CODEN: JASMAN

The Journal of the Acoustical Society of America

ISSN: 0001-4966

Vol. 113, No. 5 May 2003

(Continued)

THE JOURNAL OF THE ACOUSTICAL SOCIETY OF AMERICA VOL. 113, NO. 5, MAY 2003

CONTENTS—*Continued from preceding page*

AEROACOUSTICS, ATMOSPHERIC SOUND [28]

UNDERWATER SOUND [30]

ULTRASONICS, QUANTUM ACOUSTICS, AND PHYSICAL EFFECTS OF SOUND [35]

TRANSDUCTION [38]

STRUCTURAL ACOUSTICS AND VIBRATION [40]

(Continued)

THE JOURNAL OF THE ACOUSTICAL SOCIETY OF AMERICA VOL. 113, NO. 5, MAY 2003

CONTENTS—*Continued from preceding page*

(Continued)

THE JOURNAL OF THE ACOUSTICAL SOCIETY OF AMERICA VOL. 113, NO. 5, MAY 2003

CONTENTS—*Continued from preceding page*

BIOACOUSTICS [80]

ERRATA

ACOUSTICAL NEWS—USA

Elaine Moran
Acoustical Society of America, Suite 1NO1, 2 Huntington Quadrangle, Melville, NY 11747-4502

Editor's Note: *Readers of this Journal are encouraged to submit news items on awards, appointments, and other activities about themselves or their colleagues. Deadline dates for news items and notices are 2 months prior to publication.*

New Fellows of the Acoustical Society of America

Brigitte Schulte Fortkamp—For contributions to environmental noise awareness.

Scott D. Sommerfeldt—For research and education in active control of vibration and noise.

Floyd E. Toole—For contributions to objective measurement and subjective assessment of loudspeakers in rooms.

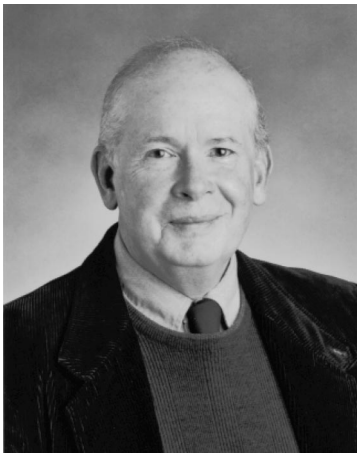

David P. Walsh—For contributions to acoustical design of education facilities.

 0001-4966/2003/113(5)/2367/6/$19.00

The First Pan American/Iberian Meeting on Acoustics held in Cancun, Mexico

The First Pan American/Iberian Meeting on Acoustics was held 2–6 December 2002 at the Fiesta Americana Grand Coral Beach Hotel in Cancun, Mexico. The meeting was jointly organized by the Acoustical Society of America (ASA), the Iberoamerican Federation of Acoustics (FIA), and the Mexican Institute of Acoustics (IMA) and comprised the 144th meeting of the Acoustical Society of America, the 3rd Iberoamerican Congress on Acoustics, and the 9th Congress of the Mexican Institute of Acoustics.

The meeting drew a total of 1330 registrants from 41 countries including 229 students (see Table I). A total of 1098 papers organized into 1112 sessions covered the areas of interest of all three cosponsoring organizations. The meeting also included 11 meetings dealing with standards.

Opening ceremonies were held on Monday morning, 2 December, and included welcoming remarks by the Meeting Cochairs and the ASA President followed by entertainment by a children's group who sang Mexican folk songs and Mayan songs and a Mariachi band (see Figs. 1 and 2). The technical sessions began on Monday afternoon followed by a welcoming reception in the exhibit area.

Two special short courses were offered on Sunday afternoon on ''Sound Quality Fundamentals'' and ''Noise Source Identification Techniques,'' and each drew about 20 participants. Two special tutorial lectures were presented on Monday and Friday evenings on Architectural Acoustics and on Industrial Noise Control. A special session titled ''Hands-On Explorations in Acoustics'' was specially organized for accompanying persons who enthusiastically participated in the demonstrations (see Fig. 3). The Womens Luncheon drew about 85 participants and over 125 students attended the Students' Reception on Wednesday evening.

The Exhibit drew 16 exhibitors and included computer-based instrumentation, sound level meters, sound intensity systems, signal processing systems, devices for noise and vibration control, and acoustical materials.

The plenary session included presentation of awards by all three cosponsoring organizations and announcements of newly elected fellows of the ASA.

ASA President Richard Stern presented five Society awards, announced the election of 15 new ASA Fellows, and presented certificates to the meeting organizers (see Figs. 4–8).

The Pioneers of Underwater Acoustics Medal was presented posthumously to Frederick D. Tappert ''for application of the parabolic equation to underwater acoustic propagation.'' Sally Tappert accepted the award on behalf of her late husband. The Silver Medal in Noise was presented to Louis C. Sutherland ''for contributions to the solution of aerospace and community noise problems, and for studies of molecular absorption and classroom acoustics.'' The Wallace Clement Sabine Award was presented to Alfred C. C. Warnock ''for broad contributions to architectural acoustics, especially on noise control in buildings and development of technical standards.'' Honorary Fellowship was conferred upon Michael Longuet-Higgins ''for fundamental contributions to surface-wave and bubble dynamics and their influence on sound in the ocean.''

TABLE I. Registration by country.

Argentina	11	Finland	1	Norway	1
Australia	8	France	30	Peru	3
Austria	4	Germany	23	Poland	4
Belgium	5	Greece	1	Portugal	8
Bolivia	1	Hong Kong	2	Russia	6
Brazil	15	India	1	Singapore	3
Canada	43	Ireland	2	South Korea	12
Chile	10	Israel	1	Spain	13
China	8	Italy	11	Sweden	5
Colombia	1	Japan	46	Taiwan	6
Cuba	1	Mexico	95	U.K.	28
Czech. Rep.	1	Netherlands	8	USA	892
Denmark	11	New Zealand	5	Venezuela	1
Ecuador	1	Nigeria	2		

FIG. 1. Children's group sings Mayan songs at the Opening Ceremonies.

FIG. 2. Mariachi Band plays a selection of Mexican and American songs at Opening Ceremonies.

FIG. 3. Participants at the special acoustics demonstration session for accompanying persons blow on a circular flute.

FIG. 4. Sally Tappert (r) accepts the Pioneers of Underwater Acoustics Medal from ASA Present Richard Stern (l).

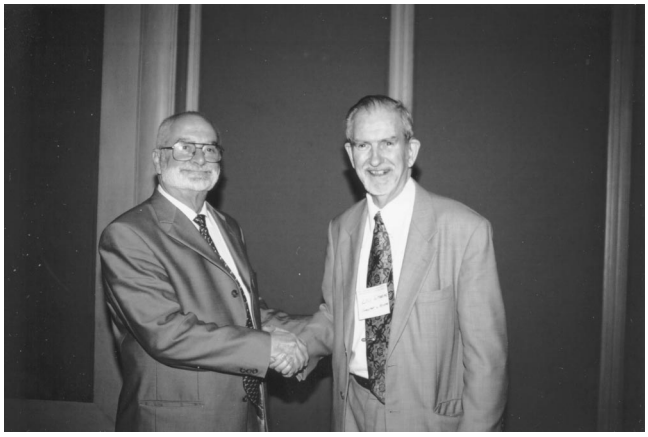

FIG. 5. ASA President Richard Stern (l) congratulates Louis C. Sutherland (r), recipient of the Silver Medal in Noise.

FIG. 6. ASA President Richard Stern (l) congratulates Alfred C. C. Warnock (r), recipient of the Wallace Clement Sabine Medal.

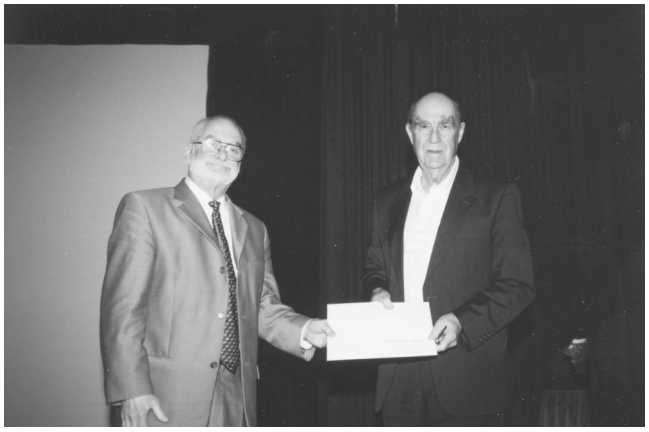

FIG. 7. ASA President Richard Stern (l) presents Honorary Fellowship certificate to Michael Longuet-Higgins (r).

FIG. 8. ASA President Richard Stern (l) presents Science Writing Award for Professionals in Acoustics to Sharem Vaezy (r).

FIG. 9. Richard Stern presents certificate acknowledging the meeting committee to James E. West. Other committee members are Rebeca de la Fuente, Kevin Shepherd, and Sergio Beristain (not in photo: Samir N.Y. Gerges and C. E. Schmid.

FIG. 10. Kevin P. Shepherd, Technical Program Chair.

FIG. 11. Recipients of award plaques from the Iberoamerican Federation on Acoustics (l to r): Sergio Beristain, Rebeca de la Fuente, Elaine Moran, Fernando Elizondo, James West, Kevin Shepherd, Rolando Menchacha, Charles Schmid, Richard Stern, Silvio Bistafa with Samir N. Y. Gerges, FIA President and Meeting Cochair.

FIG. 12. IMA President Sergio Beristain (r) presents the John William Strutt, 3rd Baron of Rayleigh Medal to Leo L. Beranek (l).

FIG. 13. IMA President Sergio Beristain (l) presents the John William Strutt, 3rd Baron of Rayleigh Medal to Per V. Bruel (r).

FIG. 14. IMA President Sergio Beristain (r) presents Herman Ludwig von Helmholtz Award to José Luis Rodríguez García.

FIG. 15. Recipients of awards in recognition of their support of the Cancun meeting.

The 2002 Science Writing Award for Professionals in Acoustics was presented to Sharem Vaezy for his article (coauthored with Roy Martin and Lawrence A. Crum) ''Acoustic Surgery'' in *Physics World*, August 2002.

Election of the following persons to Fellow grade was announced: Richard H. Campbell, Laurel H. Carney, Bruce D. Cornuelle, Peter H. Dahl, George E. Ioup, Leon M. Kerr, Hugh J. McDermott, Colette M. McKay, William C. Moss, Philip A. Nelson, Marshall H. Orr, Jack E. Randorff, Sean F. Wu, Ning Xiang, and George Zweig.

Certificates acknowledging the members of the meeting committee were presented by ASA President Richard Stern to James E. West (ASA); Samir N.Y. Gerges (FIA); and Sergio Beristain (IMA); Meeting Cochairs; Kevin P. Shepherd, Technical Program Chair; Charles E. Schmid, Vice Chair; Rebeca de la Fuente, Cultural Program Chair; and Elaine Moran, ASA Office Manager (see Fig. 9).

The ASA President introduced Kevin Shepherd, Technical Program Chair of the meeting (see Fig. 10), who extended thanks to the members of the Technical Program Organizing Committee; Kevin P. Shepherd, Technical Program Chair; Timothy F. Duda and Matthew A. Dzieciuch, Acoustical Oceanography; David A. Mann, Animal Bioacoustics; Angelo J. Campanella and David E. Marsh, Architectural Acoustics; Jeffery A. Ketterling, Biomedical Ultrasound/Bioresponse to Vibration; James P. Cottingham and Judy Cottingham, Education in Acoustics and Musical Acoustics; Elizabeth A. McLaughlin, Engineering Acoustics; Brandon D. Tinianov, Noise; James M. Chambers and Jeffery A. Ketterling, Physical Acoustics; Diane Kewley-Port, Psychological and Physiological Acoustics; Sean K. Lehman and Charles F. Gaumond, Signal Processing in Acoustics; Diane Kewley-Port and Robert F. Port, Speech Communication; Sean F. Wu, Structural Acoustics and Vibration; Michael D. Collins, Underwater Acoustics; Sergio Beristain, Rolando Menchaca, and Fernando J. Elizondo, representing the Mexican Institute of Acoustics; and Samir Y. N. Gerges, representing the Iberoamerican Federation of Acoustics.

Samir N. Y. Gerges, President of the Iberoamerican Federation of Acoustics presented plaques to the members of the meeting committee in recognition and appreciation of their efforts in organizing and operating the meeting (see Fig. 11).

Sergio Beristain, President of the Mexican Institute of Acoustics, presented three IMA awards. John William Strutt, 3rd Baron of Rayleigh Medals were presented to Leo L. Beranek and to Per V. Bruel, and the Herman Ludwig von Helmholtz Award was presented to José Luis Rodríguez García. Presentations were also made to members of the Mexican Institute of Acoustics for their support of the meeting (see Figs. 12–15).

A post-meeting tour to Chichen Itza, organized by the Mexican Institute of Acoustics, drew over 200 participants. Special acoustical effects were presented by ASA members at the pyramid of Kulkan (see Figs. 16 and 17). The tour also included visits to the Valladolid and Balancanche Caves.

RICHARD STERN
ASA President 2002–2003

FIG. 16. Meeting participants visit the pyramid of Kulkan at Chichen Itza. Pictured are Richard Stern, Richard Lyon, and Ilene Busch Vishniac.

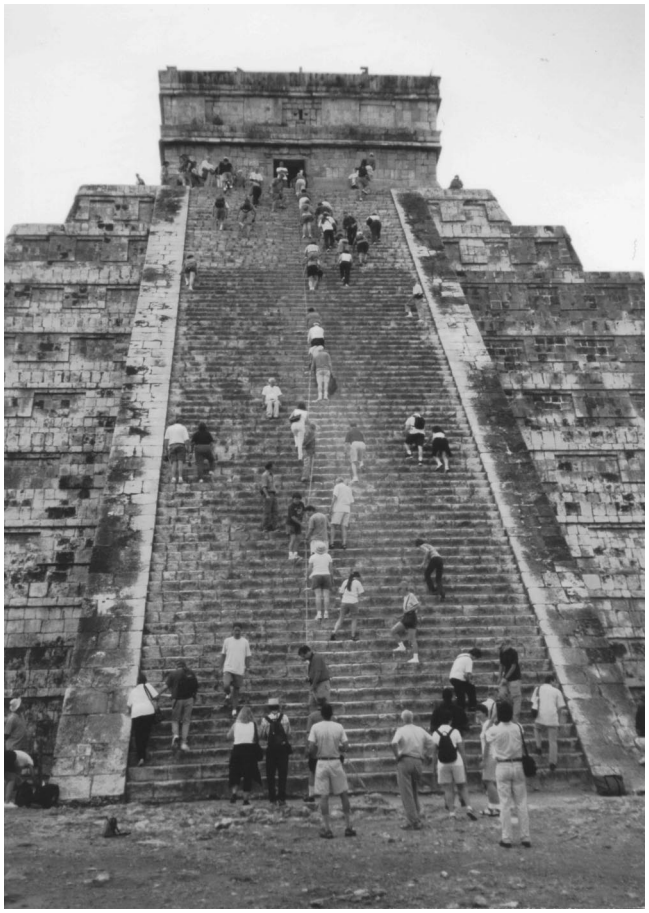

FIG. 17. Meeting participants climb the stairs of the pyramid of Kulkan during postmeeting tour.

Microscope slide collection of the auditory system of the brain stem acquired by The National Museum of Health and Medicine

The National Museum of Health and Medicine, Washington, DC, has accepted a collection of microscope slides (the ''Harrison collection''), consisting of sections through the auditory system of the brain stem in 27 different mammalian species. The collection, started in the 1960's, was produced by Martin Feldman, Ronald Irving, Bruce Warr, and Chris West, at Boston University, under grants from the National Science Foundation (J. M. Harrison, PI). The collection was gifted to the museum by Jean Moore in July 2002.

Anyone interested in working with the slides may contact the curator of neuroanatomical collections, Archie Fobbs, at 202-782-3713, or fobbs@afip.osds.mil. The assistant curator, N. Humboldt, can be found at humboltn@afip.osd.mil. The slides will be located at The Armed Forces Institute of Pathology, 6825 16th St. NW, Bldg. 54, G051, Washington, DC 20306-6000.

USA Meetings Calendar

Listed below is a summary of meetings related to acoustics to be held in the U.S. in the near future. The month/year notation refers to the issue in which a complete meeting announcement appeared.

2003

12–16 May	Symposium on Environmental Consequences of Underwater Sound (ECOUS), San Antonio, TX [www.lsro.org/ECOUS].
23–25 June	NOISE-CON 2003, Cleveland, OH [INCE Business Of-

	fice, Iowa State Univ., 212 Marston Hall, Ames, IA 50011-2153; Fax: 515-294-3528; E-mail: ibo@ince.org].
27–30 July	1st Conference on Acoustic Communication by Animals, University of Maryland, College Park, MD [Acoustical Society of America, Suite 1 NO1, 2 Huntington Quadrangle, Melville, NY 11747-4502; Tel: 516-576-2360; Fax: 516-576-2377; E-mail: asa@aip.org; WWW: http://asa.aip.org/communication.html].
5–8 Oct.	IEEE International Ultrasonics Symposium, Honolulu, HI [W. D. O'Brien, Jr., Bioacoustics Research Lab., Univ. of Illinois, Urbana, IL 61801-2991; Fax: 217-244-0105; WWW: www.ieee-uffc.org].
10–14 Nov.	146th Meeting of the Acoustical Society of America, Austin, TX [Acoustical Society of America, Suite 1 NO1, 2 Huntington Quadrangle, Melville, NY 11747-4502; Tel.: 516-576-2360; Fax: 516-576-2377; E-mail: asa@aip.org; WWW: asa.aip.org].

2004

24–28 May	75th Anniversary Meeting (147th Meeting) of the Acoustical Society of America, New York, NY [Acoustical Society of America, Suite 1 NO1, 2 Huntington Quadrangle, Melville, NY 11747-4502; Tel.: 516-576-2360; Fax: 516-576-2377; E-mail: asa@aip.org; WWW: asa.aip.org].
3–7 Aug.	8th International Conference on Music Perception and Cognition, Evanston, IL [School of Music, Northwestern Univ., Evanston, IL 60201; WWW: www.icmpc.org/conferences.html].
15–19 Nov.	148th Meeting of the Acoustical Society of America, San Diego, CA [Acoustical Society of America, Suite 1 NO1, 2 Huntington Quadrangle, Melville, NY 11747-4502; Tel.: 516-576-2360; Fax: 516-576-2377; E-mail: asa@aip.org; WWW: asa.aip.org].

Cumulative Indexes to the *Journal of the Acoustical Society of America*

Ordering information: Orders must be paid by check or money order in U.S. funds drawn on a U.S. bank or by Mastercard, Visa, or American Express credit cards. Send orders to Circulation and Fulfillment Division, American Institute of Physics, Suite 1 NO1, 2 Huntington Quadrangle, Melville, NY 11747-4502; Tel.: 516-576-2270. Non-U.S. orders add $11 per index.

Some indexes are out of print as noted below.

Volumes 1–10, 1929–1938: JASA and Contemporary Literature, 1937–1939. Classified by subject and indexed by author. Pp. 131. Price: ASA members $5; Nonmembers $10.

Volumes 11–20, 1939–1948: JASA, Contemporary Literature, and Patents. Classified by subject and indexed by author and inventor. Pp. 395. Out of print.

Volumes 21–30, 1949–1958: JASA, Contemporary Literature, and Patents. Classified by subject and indexed by author and inventor. Pp. 952. Price: ASA members $20; Nonmembers $75.

Volumes 31–35, 1959–1963: JASA, Contemporary Literature, and Patents. Classified by subject and indexed by author and inventor. Pp. 1140. Price: ASA members $20; Nonmembers $90.

Volumes 36–44, 1964–1968: JASA and Patents. Classified by subject and indexed by author and inventor. Pp. 485. Out of print.

Volumes 36–44, 1964–1968: Contemporary Literature. Classified by subject and indexed by author. Pp. 1060. Out of print.

Volumes 45–54, 1969–1973: JASA and Patents. Classified by subject and indexed by author and inventor. Pp. 540. Price: $20 (paperbound); ASA members $25 (clothbound); Nonmembers $60 (clothbound).

Volumes 54–64, 1974–1978: JASA and Patents. Classified by subject and indexed by author and inventor. Pp. 816. Price: $20 (paperbound); ASA members $25 (clothbound); Nonmembers $60 (clothbound).

Volumes 65–74, 1979–1983: JASA and Patents. Classified by subject and indexed by author and inventor. Pp. 624. Price: ASA members $25 (paperbound); Nonmembers $75 (clothbound).

Volumes 75–84, 1984–1988: JASA and Patents. Classified by subject and indexed by author and inventor. Pp. 625. Price: ASA members $30 (paperbound); Nonmembers $80 (clothbound).

Volumes 85–94, 1989–1993: JASA and Patents. Classified by subject and indexed by author and inventor. Pp. 736. Price: ASA members $30 (paperbound); Nonmembers $80 (clothbound).

Volumes 95–104, 1994–1998: JASA and Patents. Classified by subject and indexed by author and inventor. Pp. 632. Price: ASA members $40 (paperbound); Nonmembers $90 (clothbound).

BOOK REVIEWS

P. L. Marston
Physics Department, Washington State University, Pullman, Washington 99164

These reviews of books and other forms of information express the opinions of the individual reviewers and are not necessarily endorsed by the Editorial Board of this Journal.

Editorial Policy: *If there is a negative review, the author of the book will be given a chance to respond to the review in this section of the Journal and the reviewer will be allowed to respond to the author's comments. [See "Book Reviews Editor's Note," J. Acoust. Soc. Am.* ***81****, 1651 (May 1987).]*

Thermoacoustics: A Unifying Perspective for Some Engines and Refrigerators

G. W. Swift

Acoustical Society of America, American Institute of Physics Press, New York, 2002.
xi+300 pp.+CD-ROM: $70 (softcover), $50 for ASA members
ISBN: 0-7354-0065-2.

''I am thrilled by the power density and efficiency recently achieved by thermoacoustic engines and refrigerators, and I am fascinated by some of the latest developments in thermoacoustics.''

With that sentence, Dr. G. W. Swift begins a textbook that employs 21st century pedagogical tools to introduce students and researchers to a 21st century technology. In addition to a logical and complete development of this multidisciplinary subject, the 300-page textbook includes a CD-ROM with computerized animations and DELTAE software, with its own 200-page manual in searchable PDF format.

In many ways this textbook represents a milestone in the literature of acoustics. Unlike Swift's excellent 1988 review paper, ''Thermoacoustic engines,'' published in this Journal [**84**(4), 1145–1180], this textbook is destined to become the gateway by which many trained both inside *and outside* the acoustics community can enter this fascinating and challenging field. Swift's use of computer animations as an integral part of the text is sure to become more common in this century. These are not just pretty ''moving pictures.'' I consider myself to be quite well-versed in the physics of the oscillatory thermoviscous boundary layer, but I was pleased with the new insights I gained just by watching his ''Lagrangian marker'' whip through the viscous medium like a limp linguine in a sea of thick minestrone. The more complex animations can be an even richer source of intuitive insights. Certainly, forsaking the wave equation in favor of an approach more closely tied to the fundamental conservation equations, and consistent with the DELTAE software solution of complex quasi-one-dimensional acoustical networks, brings a fresh perspective that should be of interest to all of us who teach classes in acoustics. At the very least, a textbook that is independent of the software, yet consistent with it, provides a new (and welcome!) bridge between concept and computation.

Swift makes his ambitious goals clear from the start: He attempts to interweave the physical, the mathematical, and the intuitive into a coherent picture that supports his claim that thermoacoustics describes ''a mental framework, not a class of devices.'' The thermoacoustic paradigm abandons the 19th century crankshaft-based technology used to enforce control of gas motion in today's engines and refrigerators. Instead, it relies on oscillating pressure gradients to produce oscillatory gas motion, and on the oscillating gas motion to produce oscillatory pressure gradients. This ''circularity'' is inherently challenging, but it is also both fascinating in concept and elegant in its execution.

Swift's first chapter provides a short historical overview, presents some very basic concepts whose understanding is significantly enhanced by computer animations, and introduces the four examples that are used throughout the text to apply the thermoacoustic principles. He chooses two engines and two refrigerators, produced over the past ten years in his laboratory, to provide physical dimensions and to compare the results of the calculations to *actual measured performance* as the theory is developed.

Most of the audience for this book might have expertise in either the material contained in Chap. 2 or 3, but rarely would a reader new to thermoacoustics begin reading with a mastery of both. Chapter 2 provides background, nomenclature, and useful results from thermodynamics, hydrodynamics, and the transport properties of ideal gases. Chapter 3 introduces the concept of the simple harmonic oscillator and the use of complex numbers to describe oscillatory phenomena. That concept is then applied to a gas spring and one-dimensional wave propagation.

These first 68 pages set the tone for subsequent chapters and provide the first 50 relevant (and clever!) homework problems. These problems serve the goals of the text by providing the dedicated reader with guidance to the derivation of some of the results; they tie concepts to experience (What is the displacement and adiabatic temperature variation caused by ordinary speech?); and they broaden the application of the concepts (How deeply should water pipes be buried where you live?) beyond thermoacoustics.

Chapters 4–7 elucidate the theoretical framework that Swift has developed to establish his unifying perspective. He credits the pioneering work of Nikolaus Rott for development of the correct expressions for the acoustics and time-averaged energy transport within a channel that might also sustain a temperature gradient, but in Chap. 4, Swift eschews the wave equation for a coupled set of first-order differential equations that are represented by his ''five-parameter thermoacoustic impedance model.''

The coupled first-order approach has two advantages: The first is that it maintains an immediate connection between the five lumped parameters and the fundamental principles of the mass conservation (the continuity equation), momentum conservation (the Navier–Stokes equation), and energy conservation. The second advantage is that this approach is consistent with the operation of the differential equation solver that is the kernel of the DELTAE software and the structure of the complex pressure, complex volume velocity, and temperature boundary conditions between the ''segments'' that define each DELTAE model.

The lumped elements of that model are displayed on the book's front cover and a phasor representation is used to illustrate the acoustical effects of those elements. The thermoviscous functions, f_ν and f_κ, are introduced to keep track of the important viscous and thermal-relaxation effects and to quantify the behavior of Swift's ''fifth element:'' the current-controlled current source that is responsible for the production of useful work or refrigeration in thermoacoustic devices.

Chapter 5 addresses the central concept of power in thermoacoustic systems. Swift starts with a careful analysis of the mechanical power transported by the sound field. He then points out that the total power, represented by the enthalpy flux, is the conserved quantity that is of utmost importance in the application of the First Law of thermodynamics to acoustic systems that can exchange heat with external sources and sinks. Overall evaluation of the performance of such complex systems is addressed in Chap. 6 with the introduction of the concepts of lost work and entropy generation. The exergy function is then used to provide the self-consistent accounting scheme for energy production, dissipation, and transport that can take place at a variety of different temperatures within a single device. To this reviewer's best knowledge, this is the first time that such a comprehensive analysis of the energetics has appeared in either the thermoacoustic or the Stirling engine literature.

In earlier drafts of this text, Chap. 7 was entitled ''Thermoconfustics.'' Unlike the previous chapters, Chap. 7, now entitled ''Beyond Rott's Thermoacoustics,'' transcends the formal techniques of hydrodynamics, thermo-

 0001-4966/2003/113(5)/2379/3/$19.00

dynamics, and acoustics and attempts to address important issues that arise at high Reynolds number, in tortuous porous media, and when second-order effects like streaming and shock formation are significant. In many ways, this chapter is the most interesting because it provides insight into how a scientist of Swift's caliber can make progress by using dimensionless groups (similitude) and by piecing together knowledge from other disciplines to calculate useful results, even when a fundamental understanding or adequate computational techniques are unavailable.

Under these circumstances, Swift exposes another important component of the philosophy that has made him the world's acknowledged leader in the field: ''Given today's imperfect foundation, additional approximations are useful whenever they improve computational ease dramatically while only slightly reducing accuracy.'' Although he demonstrates that this philosophy can produce substantial progress, he warns his readers that such an approach ''will not find a dramatically improved point-of-view, no matter how interesting or important that might potentially be.'' I would argue that the progress that his ''approximate'' approach enables has led him to develop many of the ''dramatically improved points-of-view'' that he provides in this textbook.

The final two chapters deal with the details of thermoacoustic hardware and the strategies for measurement of acoustic and thermal performance of complete devices. The ''Hardware'' chapter covers ideal gases, stacks and regenerators, heat exchangers, resonators, buffer tubes, and electroacoustic transducers. The high-quality photographs of actual thermoacoustic components are an essential complement to the fairly brief discussion provided in the text. The 170 references allow the reader to fill in many of the missing details and provide an excellent bibliography for most of the important work in this field.

The last chapter on ''Measurements'' goes well beyond the ''mechanics'' of building adjustable acoustic loads and making accurate determinations of acoustic pressure, power, and heat flows. He suggests ''confidence building experiments'' in the early stages of testing your new apparatus. Make the easy measurements and compare them with your expectations to insure that the basic design is correct and that your sensors and signal-conditioning electronics are calibrated and functioning properly.

In this important chapter, Swift addresses how the experimentalist's point-of-view can influence how those measurements are interpreted as well as the experimental design that a particular point-of-view will dictate. His discussion is again philosophical, and is brought to a very practical level by his generous use of concrete examples that illustrate each experimental philosophy based again on the four examples. The final illustration of the ''thermoacoustic'' point-of-view is a wonderful excursion into the interplay of direct physical measurements and the interpretation and interpolation of those measurements made possible through the intelligent use of the DELTAE software.

Again, the end-of-chapter ''homework'' problems included in these last two chapters are worthy of special note. They distill two decades of experience with the design and testing of thermoacoustic hardware. They include topics from order-of-magnitude estimates of forces on stacks and the flutter of NiCr heater ribbon, to the energy released by exploding pressure vessels (resonators). The measurement exercises go from mundane, but important, calculations regarding the cutoff frequency of signal conditioning electronics to exercises that include sample experimental data from a device that did not function as designed and requires the reader to provide ''analysis and action plan toward diagnosis of this unfortunate situation.''

The text closes with two appendices. The first, entitled ''Common Pitfalls,'' is only a page and a half in length, but warns the neophyte of such ubiquitous failings as ''computer intoxication,'' ''unrealistic optimism,'' ''multi-vendor gridlock,'' and the tendency to avoid the real challenges. Among Swift's words of advice: ''Attack the hard problems early, whether they are technical or personnel, and address them immediately.''

The second appendix includes the DELTAE files for the four examples that are used throughout the text. In conjunction with the software manual contained as a searchable PDF file on the CD-ROM, the DELTAE software has become the ''language of thermoacoustics.'' The software and the software manual are co-authored with William Ward, one of Swift's long-time collaborators at Los Alamos. Anyone who masters this software can look at DELTAE ''output'' file and appreciate the most intricate details of any device and also gain nearly telepathic access to the mindset of its designer.

Although the DELTAE software and its manual are worthy of a separate review, a few more comments here are justifiable. The software interprets a sequence of ''segments.'' Each segment represents one component, from a simple straight or conical duct, to a variety of heat exchangers, stacks, and regenerators. All physical properties of the segments are expressed in MKS units. The software is a one-dimensional differential equation ''solver'' and it is **extremely fast**. My research group's most complicated file contains 37 segments and runs in under one second! The challenge in its application is making the determination of which results should be ''targets'' that the solver will try to match and which variables are to used as ''guesses'' that the solver will be allowed to vary. The solver seeks to minimize the ''length'' of the error vector that measures the difference between the targets and their targeted values. That important selection of an equal number of ''guesses'' and ''targets'' is aided by the ''thermoacoustic point-of-view'' that is described explicitly in Chap. 9, but which permeates the entire text.

Two particularly interesting ''segments'' are THERMOPHYSICAL and RPNTARGET. The THERMOPHYSICAL segment provides thermophysical properties for a range of gases, gas mixtures, and solids used in the models. Each segment uses the output of THERMOPHYSICAL internally, but it is also available as an independent ''segment'' in the model or as a convenient freestanding electronic ''handbook'' of thermodynamic and transport properties.

The RPNTARGET is a mathematical segment that lets the user easily calculate any quantity of interest using the ''reverse polish notation'' made popular by Hewlett-Packard calculators. It can take results from previous segments, manipulate them using trigonometric functions and complex arithmetic, and then make the results of the calculation available for use in other segments and by the solver as a ''target.'' I find the flexibility of the RPNTARGET provides an important tool for letting the software calculate useful performance parameters, but its real value is its ability to let the user introduce new physics into a model that is not a ''canned'' function already within DELTAE.

The Reference chapter of the manual is essentially a review of the current state-of-the-art in thermoacoustic modeling. It provides algebraic representations of the algorithms used by the program for calculation of heat exchanger performance, thermoviscous functions for various geometries, energy flow through regenerators, as well as the more mundane calculations of the compliance of a volume or the solution of the wave equation in a conical horn.

One caution: the DELTAE software is not particularly ''user friendly.'' I use the version that runs under DOS and has none of the convenience features of contemporary softwares such as pull-down menus, multiple windows, etc. The MAC version has those features. The ability to ''scroll'' through the window is much nicer than unidirectional output available under DOS. If you think you will ignore the text and manual and just run DELTAE like a video game, you will be instantly disappointed.

On the other hand, DELTAE does provide features that were clearly meant to satisfy the needs of eternally impatient experimentalists that go well beyond just the use of MKS units. For example, the BLOCKDATA segment makes it easy to import experimental results allowing direct comparison between the measurements and the model results. There is a provision to generate tabulations of results as two variables are allowed to step through user selectable limits. No provisions are made for graphical display of the results but the resulting files (header and data) can be exported to the user's favorite plotting software.

The design of DELTAE was motivated by the need to analyze electroacoustic systems with geometrically complicated gas-filled components, all of which might be at different temperatures and made of different materials. In the proper hands, the utility of DELTAE to the acoustics community should go well beyond thermoacoustics. I have used it to analyze the radiated power spectrum of Brüel & Kjaer Type 4295 OmniSource that was designed by Jean-Dominique Polack. Professor Polack wrote a finite-element code containing dozens of segments to tune the modal frequencies of the source to the values necessary to satisfy the standards for omnidirectional sound sources [ISO 140 and ISO 3382]. Using the physical dimensions provided, I made a seven-segment DELTAE file with a VESPEAKER segment representing the electrodynamic speaker at one end, a PISTBRANCH segment to apply the radiation condition at the other end, and an ISOCONE segment between the two. DELTAE quickly produced modal frequencies that agreed with Polack's results in air at room temperature to within $\pm 0.2\%$. I suspect that the use of DELTAE for design of acoustical networks like engine mufflers that sustain significant temperature gradients and contain porous media like catalytic converter ceramic substrates would be equally rewarding.

Much has been learned about thermoacoustics in the 14 years between publication of the 1988 review article and the publication of this textbook. Swift and his co-workers have again generated almost all of that improved understanding through a novel series of clever experiments and the publications generated by those experiments. Although there is still much to be learned, and many clever devices to be built and tested, thermoacoustics has evolved to a level where it now has significant commercial potential in addition to providing intellectual challenges for the rigorous education of acoustics graduate students and faculty, as it has done so well over the past two decades. The complete and systematic exposition of thermoacoustic theory and experimental technique in this new textbook should make Swift's understanding accessible to a far wider group of scientists and engineers who can go on to exploit that understanding and produce practical devices while contributing to the extension of that understanding by bringing their expertise from outside ''acoustics'' into thermoacoustics.

Only time will tell whether Swift's vision of a future populated by rooftop thermoacoustic heat pumps, thermoacoustic gas liquefiers and separators on offshore oil rigs and behind every hospital, and thermoacoustic refrigerators and air conditioners on sale in the appliance sections of major retail outlets will become a reality. There is no question about whether this highly original textbook and the unlimited available of the DELTAE software will go a long way toward making that vision a reality. For many of us who had the pleasure of reading the earlier drafts posted on the Los Alamos web site and using earlier versions of DELTAE, it already has.

STEVEN L. GARRETT
Graduate Program in Acoustics and Applied Research Laboratory
The Pennsylvania State University
P.O. Box 30
State College, Pennsylvania 16804-0030

Music and Technology in the Twentieth Century

Hans-Joachim Braun (Editor)

Johns Hopkins University Press, Baltimore, 2002.
256 pp. Price: $24.95 (hardcover) ISBN: 0801868858.

This is a collection of papers originally presented in a two-day session on *Technology and Music*, part of the 23rd Symposium of the International Committee for the History of Technology (ICOHTEC), which took place in Budapest in August 1996. To anyone even distantly interested in the subject, these papers make interesting, sometimes even fascinating, reading.

The very fact that we distinguish various ''periods'' in the history of Western music indicates that there never was a time when this musical culture was not changing. There is no question, however, that the twentieth century saw a great acceleration of this process, to the point where the duration of what we denote as a ''period'' is often measured in years, perhaps even months, rather than centuries. This acceleration is closely tied to the rapid technological advances that took place at that time, together with (in the words of editor Hans-Joachim Braun) ''the problematic identification of technical change with musical progress.''

It seems to me that, in all musical cultures and at all times, the process of composition has had to deal with two opposing needs: the need to be understood, in other words to compose in a language that is known to the listener, and the need to be original, in other words continually to violate the rules of that language. Without the first, a composition is unintelligible; without the second, it is boring. What characterized the twentieth century in particular was an exponential growth of the second need at the expense of the first; that is, of originality at the expense of intelligibility. Although this tendency can sometimes be discerned in contemporary music produced by traditional means, it surely comes into its own in the frantic technological search for new sounds, new tonalities, and new timbres as well as electronic modifications of old ones.

To set an appropriate backdrop, the book contains a number of excellent papers of historical narrative: on the growth of a particular Cleveland recording studio, by Susan Schmidt Horning; on the background of the 45 rpm record, by Alexander B. Magoun; on the history of tape recording, by Andre Millard; on the development of the synthesizer, by Trevor Pinch and Frank Trocco; on the role of the Yamaha Company, by Tatsuya Kobayashi; and on labor relations in the music industry, by James P. Kraft. But having read those, I found the real excitement in the chapters that dealt with the philosophies expressed by the people who themselves populated twentieth-century music, that is, with the thinking that led them to do the things that they did.

In this category is ''A Servile Imitation: Disputes about Machines in Music, 1910–1930,'' by Karin Bijsterveld. Here we are, of course, dealing with the early part of the century, when the quest to ''enrich the musical alphabet'' by, for example, forming orchestras consisting of assorted noise machines instead of limiting oneself to the ''dull'' palette of strings and winds, was gathering momentum. At the same time, the technique of recording music was making giant strides, and some people were worrying that mechanically (or, later, electronically) played-back music would lose the live quality (what Walter Benjamin called the ''aura'') of a real concert. Yet the same techniques, somewhat modified, also made it possible to play music that was otherwise, due (for example) to tempo or unusual pitches, unplayable by a human being.

The paper ''Soundsampling: an Aesthetic Challenge,'' by Helga de la Motte-Haber, addresses the aesthetic development of the whole century, including (toward its end) the accessibility of modern computers. It was, of course, inherent in the exponential growth of the quest for originality at the expense of intelligibility that, sooner or later, a brick wall would be encountered; in this case it was the very dramatic fact that, with a modern computer, *any sound, or combination of sounds, can be produced as easily as any other*. What started out in the beginning of the century as a drive to enrich the palette of available sounds now found itself trapped in the paradox that writing music, in the sense of realizing one's musical ideas, is now infinitely easy—but to have those ideas in the first place is infinitely hard. The challenge, it suddenly seemed, was to find a way, not to increase one's palette but (on the contrary) to diminish it.

One possible, but in my opinion limited, way out of the paradox is treated in the paper ''New Technology—New Artistic Genres,'' by Martha Brech. She describes various ways of making sound in combination with other stimuli, for example sound-producing devices with which the listeners interact, or ''sound installations'' that have a number of loudspeakers deployed in a specific space of some complexity so that the sensation of the audience extends to the acoustic and visual events interacting with each other. Insofar as these events are unpredictable (for example, because they depend on the actions of other members of the audience), the fact that a modern computer can so easily produce any programmable sound becomes less important since these sounds are not, strictly speaking, programmable. On the other hand, I find it implausible to expect that such an arrangement, which in effect removes the composition of the sound from the hands of its nominal composer, can long satisfy those urges which lead a person to want to compose in the first place.

The book is not, of course, without its shortcomings, but that is mostly unavoidable in a work with such a multiplicity of authors. Naturally, too, some papers are weaker than others, but I hesitate to go into disparaging detail when the book as a whole is so thoroughly worthwhile. One fact that I did find puzzling, however, is that neither Pierre Boulez, nor IRCAM (the very successful institute that he founded in Paris in 1970 for exploring precisely the coordination of technology and music), receives any mention at all.

GABRIEL WEINREICH
University of Michigan
Harrison M. Randall Laboratory of Physics
Ann Arbor, Michigan 48109-1120

OBITUARIES

Robert Hugh Tanner • 1915–2002

Robert Hugh Tanner, a Fellow of the Society, died on 2 November 2002 in Naples, Florida. A leading authority on electrical engineering and acoustical engineering, he continued to be active up until the time of his death.

He was born on 22 July 1915 in London, England and received his early education there, receiving a Higher Certificate from Bradford College, Berkshire (1928–1933) and a B.Sc. (Engineering) from Imperial College of Science and Technology (1933–1936). At Imperial College he received his initial exposure to acoustics while participating in an acoustical research program (1935–1936). After graduation, he worked as an audio engineer on the acoustics of coupled rooms and on broadcast audio applications for the BBC London Television Station (1938–1939).

During World War II, he served with the Royal Signals of the British Army, doing research and development in artillery sound ranging, ultra-low-frequency microphonics, sound ranging, recording, and other acoustical military applications. Following military service, he returned to the BBC Research Department, Acoustics Section (1946–1947), where he was involved in developing the world's first high definition television station and in developing audio techniques and researching the acoustics of broadcast studios and concert halls. He participated in an investigation of the acoustics of London's renowned Royal Albert Hall and received a joint patent on an automatic reverberation time meter.

In 1947, he immigrated with his family to Canada, where he began a long career with the Northern Electric Co., Ltd. (1947–1969). He was responsible for significant developments in audio, including speech-input equipment for radio and television applications, public address systems, and sound systems for theaters. He designed two innovative large master control switching systems for the Canadian Broadcasting Corporation facilities in Montreal and Winnipeg, and he developed practical studio use applications for the newly available electret microphone. In 1955, he began a parallel career in acoustical consulting, which was to last for the rest of his life. In 1960, he moved with his family to Ottawa to form Northern Electric's research and development division, Bell Northern Research. In 1962, he earned a M.Sc. from his alma mater, Imperial College, London. His Masters' thesis topic was ''The Acoustical Design of a Festival Theatre.''

In 1972, Robert Tanner was elected President of the Institute of Electrical and Electronic Engineers (IEEE), which, with then more than 170 000 members, was the largest professional organization of its type in the world. Bob was the first Canadian to hold this position. In 1974, he was awarded the McNaughton Gold Medal, the highest honor of the Canadian Region of the IEEE. Bob was also honored by the IEEE with the Pratt Award for Service and with the Activities Award for Engineering Professionals.

In 1975, he was elected a Fellow of the Acoustical Society of America; as a member, he listed his three principal technical interest areas in the Society as architectural acoustics, noise control, and musical acoustics.

He was also a Fellow of the IEEE, the Institution of Electrical Engineers of the United Kingdom, and the Engineering Institute of Canada. He was a member of the Canadian Acoustical Association and the National Council of Acoustical Consultants, and a Board Certified Member of the Institute of Noise Control Engineering. He was a Registered Professional Engineer in Florida and a Chartered Electrical Engineer in Great Britain.

In 1975, he and his wife Joan moved to Naples, Florida, where he established a consulting practice, Robert H. Tanner, PE. In 1989, he was awarded an Honorary Doctorate of Laws from Concordia University, Montreal for ''service to engineering.''

In a long and productive acoustical consulting career, he was consultant of record on over 1000 projects. He was especially proud of his work on the Philharmonic Hall in Naples, Florida. His highly diverse projects in architectural acoustics include the Stratford Festival Theatre in Ontario, the heritage restorations of the Elgin and Winter Garden Theatres in Toronto, the Palm Beach International Airport, Canada's Capital Congress Centre in Ottawa, the Canadian Embassy in Washington, DC, several buildings at the Palm Beach Community College, the Journey into Imagination at Disney World, Florida, the Saudi Arabian Air Force Academy with three mosques, auditoria, conference and lecture rooms, jet and rocket engine test cells, supersonic wind tunnels, a human centrifuge, and numerous teaching laboratories, the Communications Center in Mobile, Alabama, the Omni International in Atlanta, Georgia, the Winnipeg Convention Centre in Manitoba, an engineering building and swimming pool for Florida Atlantic University, and over 150 movie theaters (including four located just 18 inches above a Toronto Subway tunnel).

WILLIAM J. CAVANAUGH
WILLIAM W. LANG

 0001-4966/2003/113(5)/2382/1/$19.00

REVIEWS OF ACOUSTICAL PATENTS

Lloyd Rice
11222 Flatiron Drive, Lafayette, Colorado 80026

The purpose of these acoustical patent reviews is to provide enough information for a Journal reader to decide whether to seek more information from the patent itself. Any opinions expressed here are those of reviewers as individuals and are not legal opinions. Printed copies of United States Patents may be ordered at $3.00 each from the Commissioner of Patents and Trademarks, Washington, DC 20231. Patents are available via the Internet at http://www.uspto.gov.

Reviewers for this issue:

GEORGE L. AUGSPURGER, *Perception, Incorporated, Box 39536, Los Angeles, California 90039*
MARK KAHRS, *Department of Electrical Engineering, University of Pittsburgh, Pittsburgh, Pennsylvania 15261*
HASSAN NAMARVAR, *Department of BioMed Engineering, University of Southern California, Los Angeles, California 90089*
DAVID PREVES, *Starkey Laboratories, 6600 Washington Ave. S., Eden Prairie, Minnesota 55344*
DANIEL R. RAICHEL, *2727 Moore Lane, Fort Collins, Colorado 80526*
WILLIAM THOMPSON, JR., *Pennsylvania State University, University Park, Pennsylvania 16802*
ERIC E. UNGAR, *Acentech, Incorporated, 33 Moulton Street, Cambridge, Massachusetts 02138*
ROBERT C. WAAG, *Department of Electrical and Computer Engineering, Univ. of Rochester, Rochester, New York 14627*

6,474,157

43.20.Ye SONIC LEVEL MEASURING METHOD

Tyan Khak Su, assignor to International Hydrosonic Company, Limited; Hydrosonic International Company, Limited
5 November 2002 (Class 73/290); filed in the Republic of Korea 15 September 2000

An apparatus for measuring liquid level comprises a sound source mounted at one end of an air-filled waveguide and a number of sensors mounted at equal intervals along the waveguide. The device is positioned above, and aimed normally to, the liquid surface. From measurements of the transit times between the various sensors of incident and surface reflected pulses, the position of the liquid surface relative to the highest sensor is computed.—WT

6,455,982

43.25.Uv OBJECT LEVITATING APPARATUS, AN OBJECT TRANSPORTING APPARATUS EQUIPPED WITH SAID APPARATUS, AND AN OBJECT LEVITATING PROCESS

Yoshiki Hashimoto, assignor to Kaijo Corporation
24 September 2002 (Class 310/328); filed in Japan 24 December 1993

A narrow rectangular metal plate, oriented essentially horizontally, is set into flexural vibration at one of its resonances by means of an ultrasonic vibrator, which communicates with the plate via a horn that is attached rigidly to both the plate and the vibrator. A shield is wrapped around the underside of the plate and extends upward along the plate's long edges so that sound waves radiated from the plate's underside are directed along the plate's top surface in the directions from the edges toward the middle. The sound field radiated from the top of the plate is used to levitate objects, such as small metal plates, while the sound field that enters from the edges keeps the objects away from the edges. Transportation of the objects along the plate is obtained by tilting the plate away from the horizontal, by the use of a series of air jets, or by use of appropriately oriented sound sources or reflectors.—EEU

6,473,363

43.30.Wi SONAR DIRECTION FINDING

Emerson Hardy Oetzmann, assignor to Thales Underwater Systems
29 October 2002 (Class 367/120); filed 20 August 1990

By rotating the preferably cardioid directional pattern of a sonobuoy, either mechanically or electronically, additional information is obtained that aids in the determination of the bearing of the source of a received sonar signal.—WT

6,473,365

43.30.Yj SUPPORTING STRUCTURE OF HYDROPHONES FOR TOWED ARRAY SONAR SYSTEM

Chi Young Joh *et al.*, assignors to Agency for Defense Development
29 October 2002 (Class 367/154); filed in the Republic of Korea 4 August 2000

To provide isolation from extraneous sources of vibration, each cylindrical hydrophone module **1** within a long towed array is elastically supported near both ends of each cylinder by an elastic member in the form of

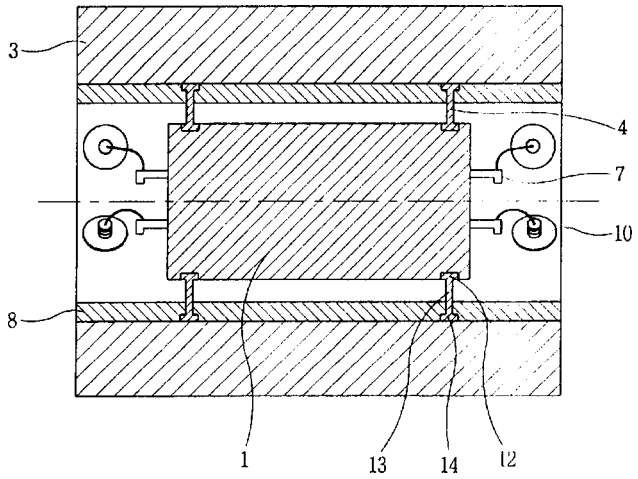

 0001-4966/2003/113(5)/2383/17/$19.00

an annular ring **4**. An axial view of this ring shows most of the cross section to be machined away so that there are only a few radial spokes actually supporting the hydrophone. The natural frequency of vibration of the hydrophone module and entrained oil mass against the compliance of these elastic supports is designed to be below the operating frequency band of the hydrophones. Tag **3** simply refers to the outer wall of the hydrophone module. The ensemble of such units is collinearly housed in an elastic hose. The entire interior of the towed array is, as usual, oil-filled.—WT

6,468,212

43.35.Yb USER CONTROL INTERFACE FOR AN ULTRASOUND PROCESSOR

Walter Guy Scott and Albert Vera, assignors to Adalberto Vara
22 October 2002 (Class 600/437); filed 3 September 1998

This is essentially a control interface that includes a software-driven display that reveals images presenting hardware control configurations for different ultrasound processors. Displayed pull-down menus provide a choice of settings for gain, image-enhancement, and other controlling parameters. A plurality of processors can be handled by this control interface, which may include the ability to recall previously scanned ultrasound images and to annotate more recently acquired images, and also to provide a checklist for medical procedures.—DRR

6,475,151

43.38.Fx AEROGEL BACKED ULTRASOUND TRANSDUCER

James D. Koger and Isaac Ostrovsky, assignors to Scimed Life Systems, Incorporated
5 November 2002 (Class 600/459); filed 13 April 2001

An ultrasound transducer is disclosed which has an acoustic backing layer made of an aerogel material. One embodiment features an aerogel backing coated with a metallized layer so that it is electrically conductive. This enables electrodes to be connected directly to the aerogel acoustic backing. Aerogels have the lowest known density of all solid materials and have sufficient strength to serve as support structure for an acoustic element.—DRR

6,453,049

43.38.Ja ACOUSTIC DIAPHRAGM

Pang-Chuan Chu and Hsiu-Yen Lee, assignors to GTI Audio Systems International, Incorporated
17 September 2002 (Class 381/152); filed in China 12 March 1999

This patent describes a paneltype loudspeaker assembly in which (a) the diaphragm is made of laminated carbon fiber layers and (b) the location of the driving point is derived from the diaphragm's center of gravity.—GLA

6,456,723

43.38.Ja ACOUSTIC DEVICE

Graham Bank and Neil Harris, assignors to New Transducers Limited
24 September 2002 (Class 381/425); filed in the United Kingdom 10 June 1999

Like its numerous predecessors, this patent from New Transducers Limited is concerned with paneltype loudspeakers, but the basic design approach is different. The fundamental frequency of bending wave modes in panel **1** is deliberately made much higher along the **y-axis** than along the

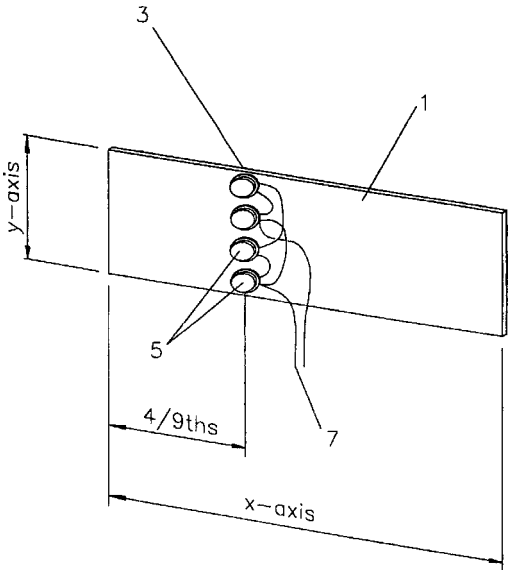

x-axis. Over a certain frequency range therefore, bending modes can be excited along the modal **x-axis** but not the nonmodal **y-axis**. As a result, sound output is essentially nondirectional horizontally whereas vertical output may drop by several dB at angles of 45 degrees or more.—GLA

6,460,651

43.38.Ja PASSIVE SPEAKER SYSTEM

Joseph Yaacoub Sahyoun, Redwood City, California
8 October 2002 (Class 181/157); filed 4 April 2000

This wobble-resistant passive radiator was first described in United States Patent 6,044,925 [reviewed in J. Acoust. Soc. Am. **108**(6), 2701

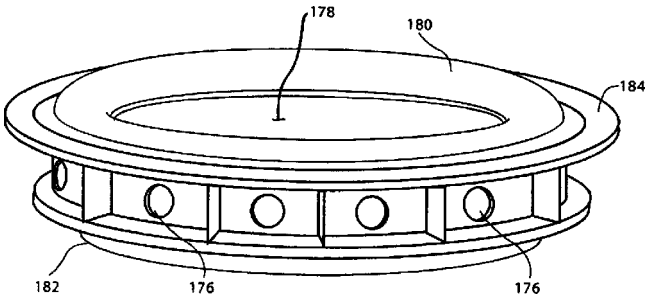

(2000)]. It now includes vents 176 to relieve air pressure buildup between opposing surrounds **180** and **182**.—GLA

6,466,676

43.38.Ja COMPOUND DRIVER FOR ACOUSTICAL APPLICATIONS

C. Ronald Coffin, Topsfield, Massachusetts
15 October 2002 (Class 381/186); filed 8 February 2001

This is the third patented version of the inventor's compound loudspeaker design. Voice coil **15** drives rear cone **25** and front cone **33**. The rear

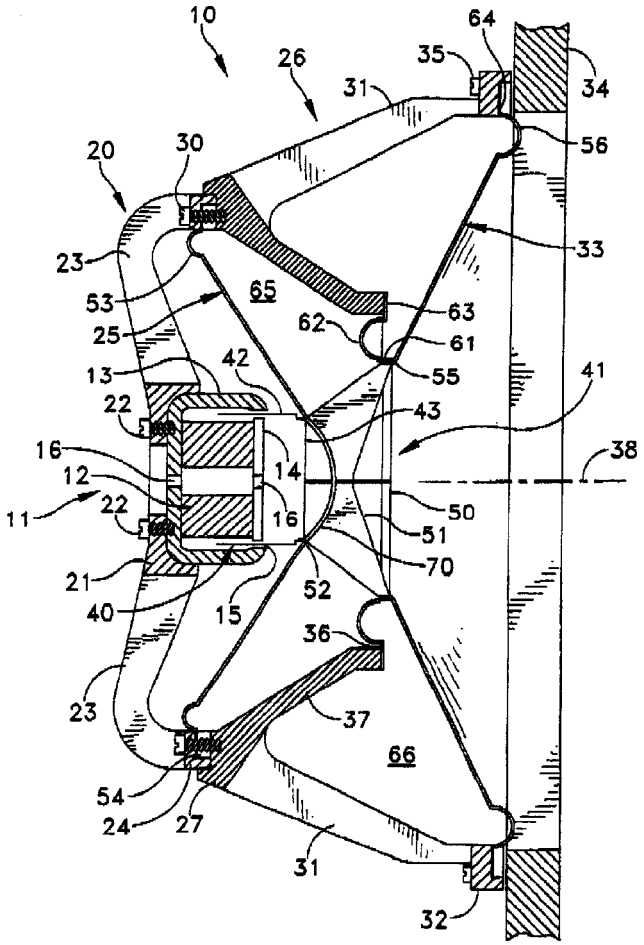

cone compresses air in chamber **65** and squirts it through center opening **41** of the front cone, thereby increasing the effective radiating area.—GLA

6,466,680

43.38.Ja HIGH-FREQUENCY LOUDSPEAKER MODULE FOR CINEMA SCREEN

William J. Gelow and Bernard M. Werner, assignors to Harman International Industries, Incorporated
15 October 2002 (Class 381/340); filed 28 June 2000

In a commercial movie theater, loudspeakers are placed behind a perforated screen. Each loudspeaker typically incorporates a high-frequency horn having controlled directional characteristics. The patent teaches that the screen not only attenuates high frequencies but spreads the high-frequency pattern as well. A waveguide design is described that compensates for screen spreading, thereby providing more nearly uniform high-frequency coverage. The patent claims are quite general, presumably allowing for specific directional characteristics to be developed for various perforation patterns and horn orientations.—GLA

6,466,682

43.38.Ja VIBRATION SPEAKER

Sang Gil An, assignor to Samsung Electro-Mechanics Company, Limited
15 October 2002 (Class 381/413); filed in the Republic of Korea 2 March 2001

The loudspeaker in your cellular phone or pager may be called upon to produce an audible signal or to generate tactile vibrations. The arrangement

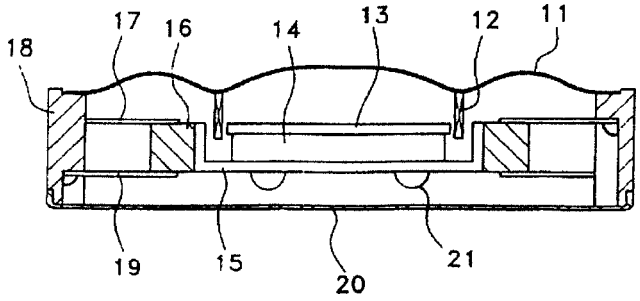

shown is intended to optimize both functions while minimizing the possibility of buzzes and rattles. Unfortunately, the patent appears to have been directly translated from Japanese and is almost impossible to follow in detail.—GLA

6,466,092

43.38.Lc DISTORTION COMPENSATION METHOD AND APPARATUS

Shigeo Kusunoki, assignor to Sony Corporation
15 October 2002 (Class 330/149); filed in Japan 16 June 2000

Although the invention is intended for use with rf amplifiers in cellular telephones, the patent claims include no such restriction. The method might be applied to class D audio amplifiers, for example. The envelope of the output signal is compared with the envelope of the input signal and any persistant difference is then funneled through distortion compensation circuitry which includes digital adders, filters, and random access memory. Today's technology allows this complex procedure to be implemented in a small, lightweight, inexpensive integrated circuit.—GLA

6,463,158

43.38.Md APPARATUS FOR PICKING UP SOUND WAVES

Franz Graf and Martin Pflüger, assignors to Joanneum Research Forschungsgesellschaft mbH; AVL List GmbH
8 October 2002 (Class 381/355); filed in Austria 21 March 2000

Binaural sound pickup normally implies the use of an artificial head, but other methods of microphone separation may provide certain advantages. The invention is a nonabsorptive wedge with microphones on or in the two angled surfaces. According to the patent, ''A reproduction of frontally impinging sound waves which is particularly true to nature can be achieved when the microphones are provided with omnidirectional characteristics.''—GLA

6,481,623

43.38.Qg CARD READER FOR TRANSMISSION OF DATA BY SOUND

Alan H. Grant and Richard J. Gambino, assignors to Privicom, Incorporated
19 November 2002 (Class 235/449); filed 12 June 2000

This portable setup is designed to read specially recorded credit card data and reproduce sound from the information contained in the magnetic stripe of the card. In one embodiment, the card reader has an electromagnetic head that reads information from the card's electromagnetic strip through an array of Hall sensors. Another embodiment makes use of a magnetic sensor based on magnetoresistive scanning. In either arrangement, the information from the card can be converted into a sequence of audio or ultrasonic signals that can be amplified and fed to a speaker. The signal can also be relayed through the speaker into a telephone receiver for transmission over telecommunication lines. Now the question arises: what will the

device be good for? The developers of the device claim usability for authorization purposes in ATM machines, room or elevator security access, personnel ID cards, etc.—DRR

6,459,798

43.38.Si SOUND-COLLECTING DEVICE

Alexander Paritsky *et al.*, assignors to Phone-Or Limited
1 October 2002 (Class 381/172); filed 15 June 2001

An adjustable beamwidth microphone is an intriguing idea. This patent describes an array of optical microphones incorporating feedback circuitry

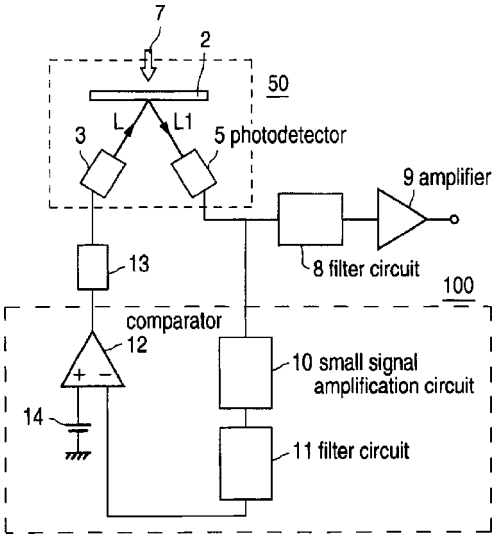

that varies beamwidth in relation to relative levels. The patent states that general off-axis sound rejection of more than 20 dB can be achieved.—GLA

6,466,136

43.38.Si MIRROR-BASED AUDIO SYSTEM FOR A VEHICLE

Jonathan E. DeLine *et al.*, assignors to Donnelly Corporation
15 October 2002 (Class 340/815.4); filed 11 July 2001

Hands-free communication is obviously easier and safer than using an ordinary cellular telephone while driving. This patent describes an arrangement incorporating or adjacent to the windshield rearview mirror. At least two microphones are included: one for the driver's voice and another to pick up general background noise. The audio system also includes a ''control''—not described further—which can process these signals to distinguish voice from noise and filter out the latter. A preferred embodiment adds a row of LEDs below the mirror to indicate whether the voice signal is satisfactory. Thus, if the driver keeps his eyes on the mirror while talking, rather than on the road ahead, he can be fairly sure that the other party is receiving an intelligible signal.—GLA

6,466,913

43.38.Vk METHOD OF DETERMINING A SOUND LOCALIZATION FILTER AND A SOUND LOCALIZATION CONTROL SYSTEM INCORPORATING THE FILTER

Seigou Yasuda and Masao Kasuga, assignors to Ricoh Company, Limited
15 October 2002 (Class 704/500); filed in Japan 1 July 1998

Using only two audio channels, a convincing phantom sound source can be located almost anywhere relative to the listener's head through the magic of head related transfer functions (HRTFs). Unfortunately, HRTFs are

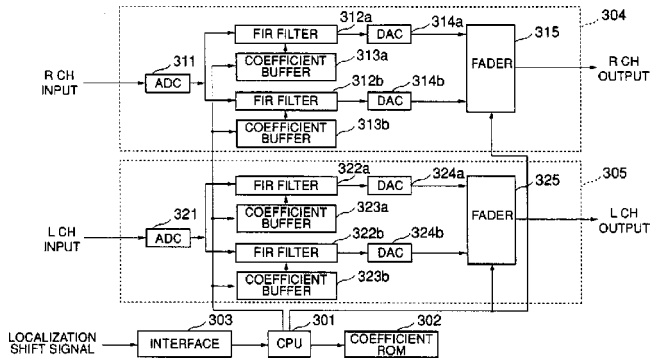

like fingerprints; they are unique to each person. Even if one records and stores HRTFs for a specific listener, each sound source location requires its own pair of transfer functions. The patent describes one method of simplifying the procedure. It also includes a useful survey of the state of the art.—GLA

6,454,252

43.40.Tm AUTOMOTIVE VIBRATION ISOLATING DEVICE

Yasuo Miyamoto, assignor to Honda Giken Kogyo Kabushiki Kaisha
24 September 2002 (Class 267/219); filed in Japan 1 August 2000

Different rubber bushings are used in the left and right suspension arms of an automobile, so that the two arms will not respond in phase to disturbances induced by road irregularities, thereby reducing the net vibration transmitted to the vehicle.—EEU

6,461,144

43.50.Ki METHOD OF CONTROLLING THERMOACOUSTIC VIBRATIONS IN A COMBUSTION SYSTEM, AND COMBUSTION SYSTEM

Ephraim Gutmark *et al.*, assignors to Alstom (Switzerland) Limited
8 October 2002 (Class 431/2); filed in Germany 7 May 1999

Noise from thermal sources in a combustion chamber, such as in a gas-turbine combustor, is reduced by the introduction of suitably phased ''antisound'' that acts on the shear layer between the fresh-gas mixture and the recirculating exhaust gas. The acoustic pressure fluctuations are measured by means of microphones or the related fluctuations in heat release are measured optically (making use of the chemiluminescence of OH molecules). Signals from these sensors are fed to a processor, which controls loudspeakers.—EEU

6,464,489

43.50.Ki METHOD AND APPARATUS FOR CONTROLLING THERMOACOUSTIC VIBRATIONS IN A COMBUSTION SYSTEM

Ephraim Gutmark *et al.*, assignors to Alstom
15 October 2002 (Class 431/1); filed in the European Patent Office 24 November 1997

Pressure oscillations in a combustion chamber are sensed via a microphone. The resulting signals are processed and used to actuate either a sound source or a device that induces vibrations in parts of the chamber's enclosure. The sound or vibrations are directed at the shear layer in the working

gas, with the idea of counteracting the formation of coherent structures and the periodic release of heat.—EEU

6,479,742

43.55.Jz AUDIO SYSTEM IN ELECTRONIC MUSICAL INSTRUMENT

Katsuhiko Torii and Tadashi Yasuda, assignors to Kabushiki Kaisha Kawai Gakki Seisakusho
12 November 2002 (Class 84/724); filed in Japan 27 March 2000

The issue here is the acoustic environment of an electric piano. The inventors propose infrared sensing to detect a back wall. If detected, then a high-pass filter is used to compensate for the attenuation of the wall.—MK

6,479,738

43.58.Hp PIANO TUNER

Donald A. Gilmore, Kansas City, Missouri
12 November 2002 (Class 84/454); filed 27 June 2001

This piano tuner is attached to the adjacent strings and the pitch is determined by finding the reciprocal of the zero crossing rate. While an

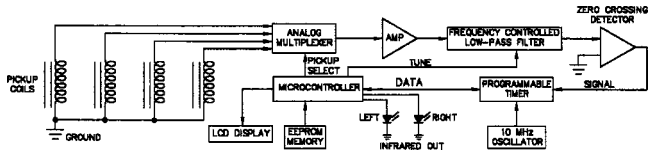

analog filter is used to extract the fundamental, a DSP approach would be easier to implement.—MK

6,471,108

43.58.Wc AUDIO AND VIDEO EFFECT STAPLER

Chien-Fa Shi, assignor to Green Lake Enterprise Company, Limited
29 October 2002 (Class 227/134); filed 27 November 2001

A common everyday object, the stapler, could become even more exciting if it was designed with the now ubiquitous sound chip.—MK

6,476,711

43.58.Wc SOUNDING-BODY DRIVING CIRCUIT AND OPERATING SOUND GENERATING APPARATUS USING THE SAME

Hajime Kitamura *et al.*, assignors to Star Micronics Company, Limited
5 November 2002 (Class 340/384.7); filed in Japan 9 April 1999

The basic premise is simple enough: the sound of a relay is a comforting signal to a machine operator. So, the patent illustrates a very simple all-digital method of generating this sound.—MK

6,478,152

43.58.Wc BEVERAGE PACKAGE WITH SOUND EFFECTS

Harold D. Mansfield, Sarasota, Florida
12 November 2002 (Class 206/446); filed 13 June 2001

Continuing in the vein of noisy beverages {such as United States Patent 6,335,691 [reviewed in J. Acoust. Soc. Am. **112**(1), 23 (2002)]}, this patent concerns a beverage container that sounds off when a bottle (or can) is placed inside it.—MK

6,468,224

43.64.Yp CALIBRATED AUDIOMETER SYSTEM

Jack C. Foreman and Leroy D. Braun, assignors to Bernafon, Incorporated
22 October 2002 (Class 600/559); filed 13 July 2001

Earphones tend to differ in their operating characteristics. In order to ensure proper mating of an audiometer and earphones after they have been calibrated together, the earphones are tagged with electronic labels that can be identified by the audiometer and recorded. When the audiometer-earphone combination is used later, the electronic label is read and compared with the recorded label, and an indication is given that the proper matching has been made, thus maintaining the calibration and ensuring that another set of earphones had not been substituted. Tagging and identification are achieved through the use of microprocessors incorporated into the audiometer.—DRR

6,473,511

43.66.Ts DISPOSABLE HEARING AID WITH INTEGRAL POWER SOURCE

John Gregory Aceti *et al.*, assignors to Sarnoff Corporation
29 October 2002 (Class 381/322); filed 5 March 1999

Most present-day hearing aids use metal-air batteries such as the zinc air type. Such batteries utilize oxygen as the activator of the battery chemistry. Described is a hearing aid design that contains a means for turning power off and on, respectively, by depriving and allowing an internally packaged battery to receive oxygen. During prolonged storage periods, the battery of a disposable hearing aid may be placed in a dormant state by preventing oxygen from reaching it. Air passageways to the battery cathode

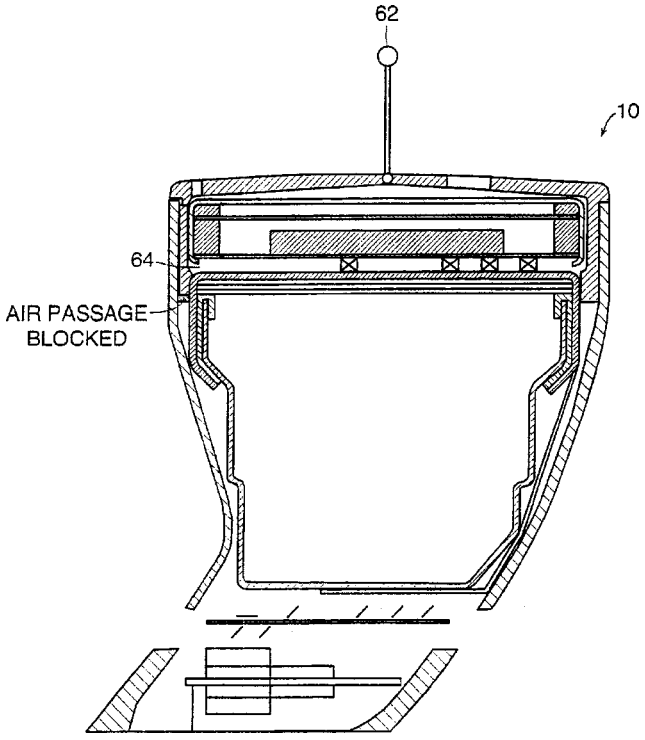

may be sealed by means of nonpermeable tape covering air ingress holes on the faceplate of a hearing aid. When the hearing aid is dispensed, the tape covering the air holes is removed with a pull tab. A sensor may be included that actuates a switch to automatically disconnect and connect the battery to the hearing aid electronics when the battery is deprived of and supplied oxygen, respectively.—DAP

6,473,513

43.66.Ts EXTENDED WEAR CANAL HEARING DEVICE

Adnan Shennib and Richard C. Urso, assignors to Insonus Medical, Incorporated
29 October 2002 (Class 381/328); filed 8 June 1999

An extended-wear, standard-size, multi-section canal hearing device containing a removable, custom cylindrical battery assembly is positioned by a physician to sit deeply within an ear canal. The disposable battery section is closest to the ear canal opening and detaches from a microphone section, both together forming a cylindrically elongated module that is suspended in a nonoccluding manner within the cartilaginous portion of the ear canal. A receiver section and a soft, surrounding, compressible sealing retainer are positioned deeply in the bony portion of the ear canal and connect

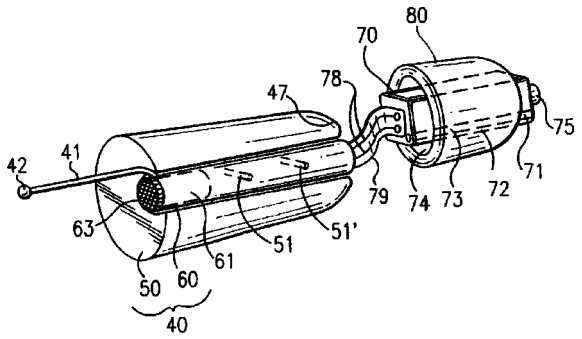

via flexible means to the microphone section. Unlike most traditional hearing aid fittings, the acoustic seal is made deep in the bony portion of the ear canal, rather than in the cartilaginous portion. The deep sound delivery system is said to reduce power consumed from the battery and improve sound quality. The flexible connection system and a small pressure equalization vent facilitate easier insertion and removal of the device. However, daily insertion and removal of the device is not needed, since power may be turned on and off remotely.—DAP

6,473,651

43.66.Ts FLUID FILLED MICROPHONE BALLOON TO BE IMPLANTED IN THE MIDDLE EAR

Janusz A. Kuzma *et al.*, assignors to Advanced Bionics Corporation
29 October 2002 (Class 607/57); filed 28 February 2000

An implantable microphone is designed to be used with cochlear implants and middle ear implantable hearing aids. The microphone is placed in the middle ear and has one fluid-filled compartment **12**...**30** consisting of a tubing connected to a thin-walled, fluid-filled balloon that contacts the tympanic membrane or stapes of the patient. A second compartment **11** within the microphone contains a transducer that converts the mechanical motion

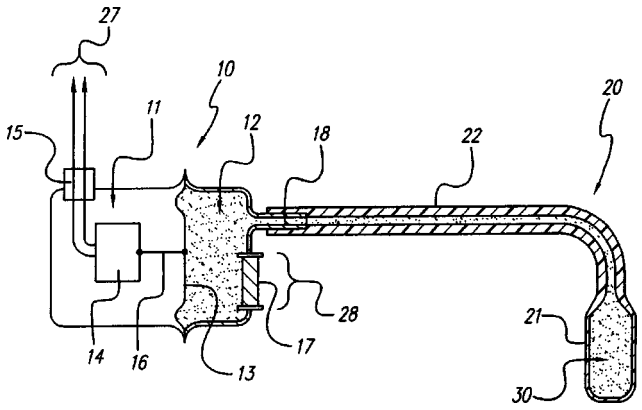

of the fluid to an electrical signal. A flexible diaphragm **13** separates the first and second compartments in the microphone and responds to mechanical movements of the fluid transmitted through the tubing from the balloon. As sound vibrations causing tympanic membrane movements are coupled through fluid communication to the flexible diaphragm, the microphone transducer detects acoustic waves resulting from fluid movement. The electrical output of the microphone is fed to the input circuitry of a cochlear implant or middle ear implantable hearing aid.—DAP

6,480,610

43.66.Ts SUBBAND ACOUSTIC FEEDBACK CANCELLATION IN HEARING AIDS

Xiaoling Fang *et al.*, assignors to Sonic Innovations, Incorporated
12 November 2002 (Class 381/321); filed 21 September 1999

A feedback cancellation method is proposed in which two cascaded narrow-band filters and a delay are used to represent the acoustic feedback path in subbands. An analysis filter bank divides both the digital audio forward signal path and the feedback path into subbands. The first filter, a training filter, models the feedback path prior to the normal use of the hearing aid. Linear prediction is used to determine the coefficients for the first filter, which can be an IIR or FIR type. Training is accomplished by driving the hearing aid receiver with a short burst of noise. Once training is completed, the coefficients for the first filter are frozen and the hearing aid feedback canceller switches into tracking mode. The estimated feedback path is subtracted on a subband basis from the forward path. A second filter, a tracking filter, is an FIR type and adapts to changes in the acoustic feedback path while the hearing aid is being worn, such as those caused by jaw movements or objects close to the ears of the wearer. Only one tap is normally required for the second filter if variations in the acoustic feedback path are mainly due to changes in the amount of sound leakage. The invention is said to provide at least 10 dB of additional stable gain before onset of acoustic feedback oscillation.—DAP

6,475,163

43.66.Yw HEARING EVALUATION DEVICE WITH PATIENT CONNECTION EVALUATION CAPABILITIES

Matthijs P. Smits *et al.*, assignors to Natus Medical, Incorporated
5 November 2002 (Class 600/559); filed 7 January 2000

This is a device for testing hearing on the basis of an evoked response to auditory clicks. The response is measured through the use of an EEG signal evoked in the patient. In one embodiment, evoked EEG responses to auditory stimuli are collected and organized into ''sweeps.'' Each sweep contains the response signal for one auditory stimulus. A predetermined number of sweeps are organized into a specific number of blocks. The device also provides for a monitoring check that the electrodes remain properly attached to the patient being tested.—DRR

6,413,092

43.70.Dn METHOD AND DEVICE FOR ENHANCING THE RECOGNITION OF SPEECH AMONG SPEECH-IMPAIRED INDIVIDUALS

Paula Anne Tallal *et al.*, assignors to The Regents of the University of California; Rutgers, The State University of New Jersey
2 July 2002 (Class 434/116); filed 5 June 2000

This review covers seven United States Patents numbered 6,413,092 through 6,413,098, which are essentially identical. The entire set results from a continuation of a single filing, now abandoned. The patents cover a device for teaching persons with a language perception deficit, similar to devices reviewed previously.—DLR

6,423,013

43.70.Dn SYSTEM AND METHOD FOR ASSESSING BREATHING AND VOCAL TRACT SOUND PRODUCTION OF A USER

Klaas Bakker *et al.*, assignors to The Board of Governors of Southwest Missouri State University
23 July 2002 (Class 600/586); filed 15 September 2000

This diagnostic system allows a user or therapist to evaluate the relative timing and interactions between breath cycles and speech production.

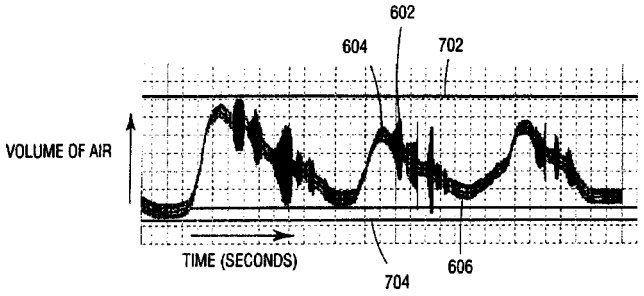

Either a thoracic or an abdominal breath sensor provides lung volume data. This data is processed together with a microphone signal and displayed to the user as feedback.—DLR

6,421,425

43.71.Ky AUTOMATED COMMUNICATIONS ASSISTANT FOR THE SOUND-IMPAIRED

Burt Joseph Bossi *et al.*, assignors to AT&T Corporation
16 July 2002 (Class 379/52); filed 17 August 1998

Two interconnect services presently available for telephone customers using a teletypewriter (TTY), typically used by hearing impaired persons, are Operator Services for the Deaf, which directly connects two TTY devices, and Telecommunications Relay Services, in which a human intermediary reads TTY text to a hearing listener and listens to normal speech, typing it in for the TTY customer. This patent covers a system for directly connecting a TTY customer onto the Internet if it is determined that the called party is also using the Internet and accepts the connection.—DLR

6,470,311

43.72.Ar METHOD AND APPARATUS FOR DETERMINING PITCH SYNCHRONOUS FRAMES

Robert Brian Moncur, assignor to Fonix Corporation
22 October 2002 (Class 704/208); filed 15 October 1999

To determine pitch synchronous frames, an optimal filter is designed based on the average energy output and delta energy. The first peak in delta energy above the average delta energy determines the optimal filtering. The

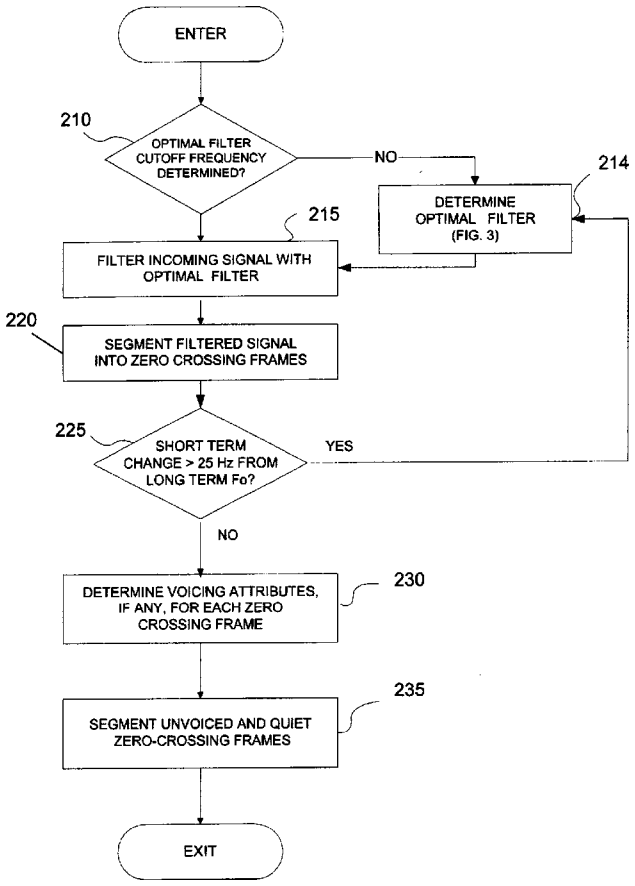

filtered signal determines the voiced periods and the unfiltered signal tracks pitch synchronous frames.—HHN

6,480,823

43.72.Dv SPEECH DETECTION FOR NOISY CONDITIONS

Yi Zhao and Jean-Claude Junqua, assignors to Matsushita Electric Industrial Company, Limited
12 November 2002 (Class 704/226); filed 24 March 1998

Speech signals are divided into frequency bands and short-term band-limited energies are compared to adaptive thresholds. The thresholds are

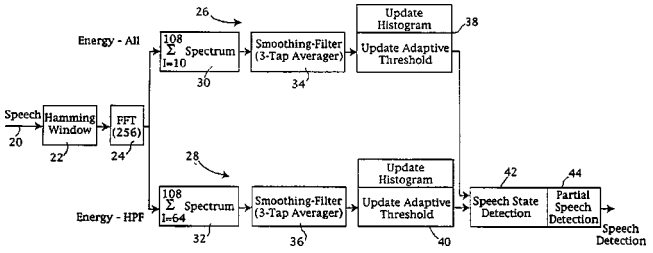

independently updated using histogram information. Endpoints are determined by a state machine.—HHN

6,411,932

43.72.Ja RULE-BASED LEARNING OF WORD PRONUNCIATIONS FROM TRAINING CORPORA

Lajos Molnar and Charles T. Hemphill, assignors to Texas Instruments Incorporated
25 June 2002 (Class 704/260); filed 8 June 1999

The ''background'' section of this patent contains an extensive and detailed summary of the various prior systems for automatically learning pronunciation rules based on a corpus of spoken words. For the purposes disclosed here, one of the prior systems, a transformation-based, error-driven learner, is chosen because of its low needs for memory and language-specific information. A phoneme-to-grapheme aligner is then added and the system is run in a feedback loop, checking pronunciations against training data, to iteratively improve the discovered pronunciation rules.—DLR

6,417,773

43.72.Ja SOUND-ACTUATED SYSTEM FOR ENCOURAGING GOOD PERSONAL HYGIENE IN TOILET FACILITIES

Gust N. Vlahos, Westchester and Robert B. Jones, River Forest, both of Illinois
9 July 2002 (Class 340/573.1); filed 21 June 2001

This audio analysis and speech synthesis device has a single, straightforward purpose. It resides in a public restroom, waiting to detect the sounds of a toilet flushing. Its sole purpose is then to play a short recorded message, advising the patron to be sure to wash his or her hands.—DLR

6,424,937

43.72.Ja FUNDAMENTAL FREQUENCY PATTERN GENERATOR, METHOD AND PROGRAM

Yumiko Kato *et al.*, assignors to Matsushita Electric Industrial Company, Limited
23 July 2002 (Class 704/207); filed in Japan 28 November 1997

This speech synthesis system uses both stored patterns and a rule system to generate natural-sounding prosodic patterns in the Japanese language. Various naturally produced patterns are stored according to a parametrization system, which is described in some detail. If a pattern is required for synthesis which is not currently available from this stored database, then a system of rules allows some characteristics of available patterns to be mixed and interpolated to produce a natural-sounding synthetic pattern.—DLR

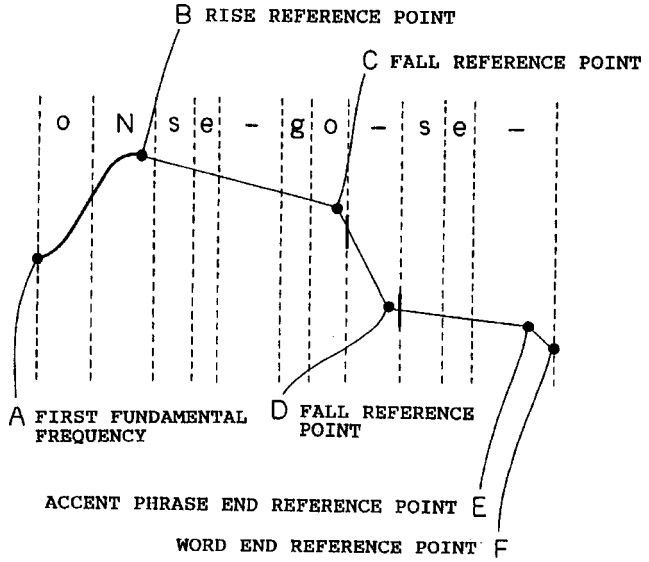

6,405,939

43.72.Ne VOICE-ACTIVATED SHOWER SYSTEM

Gino A. Mazzenga, Cranston, Rhode Island and Thomas B. Brundage, Ottawa, Kansas
18 June 2002 (Class 239/69); filed 31 May 2000

This patent appears to overlap substantially with United States Patent 6,317,717 [reviewed in J. Acoust. Soc. Am. **112**(1), 22 (2002)]. Voice control may be used to adjust water temperature and control the filling of multiple showers, tubs, or other ''containers.'' A new feature here is the ability to mix various kinds of soaps or shampoos with the controlled water stream.—DLR

6,415,257

43.72.Ne SYSTEM FOR IDENTIFYING AND ADAPTING A TV-USER PROFILE BY MEANS OF SPEECH TECHNOLOGY

Jean-Claude Junqua *et al.*, assignors to Matsushita Electric Industrial Company, Limited
2 July 2002 (Class 704/275); filed 26 August 1999

This voice-operated television viewing control system first recognizes the speaker as one of a small population using a trained model set. The speech input is then reprocessed using the selected speaker model to determine actions, such as tuner control, volume setting, etc. The system has access to an on-line program guide, as well as speaker-specific usage profiles, to assist in the utterance recognition.—DLR

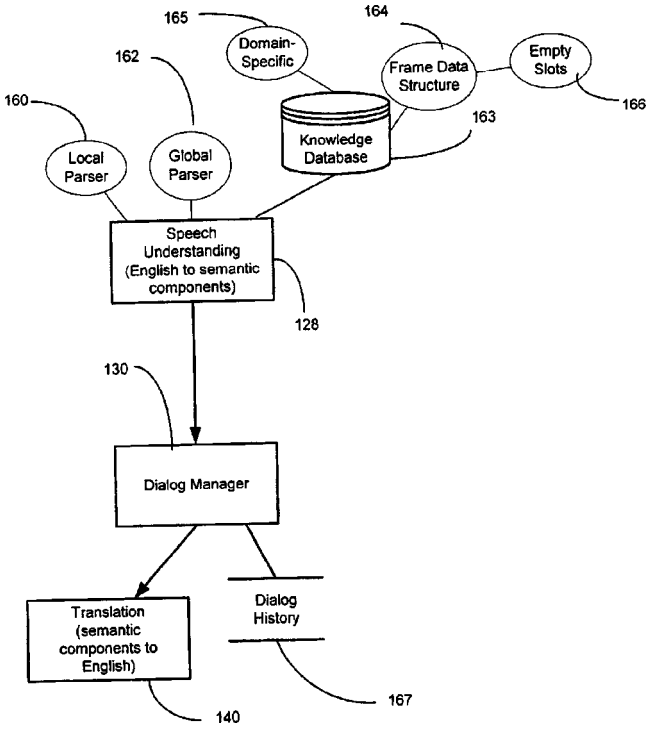

6,408,271

43.72.Ne METHOD AND APPARATUS FOR GENERATING PHRASAL TRANSCRIPTIONS

Kenneth W. Smith and Michael G. Sabourin, assignors to Nortel Networks Limited
18 June 2002 (Class 704/257); filed 24 September 1999

This speech recognizer is arranged so as to provide phonetic transcriptions of words or phrases, either for use by a speech recognition word model or for speech synthesis. The output may be reformatted for various purposes and may be arranged either as word lists or as sets of phrases.—DLR

6,408,272

43.72.Ne DISTRIBUTED VOICE USER INTERFACE

George M. White *et al.*, assignors to General Magic, Incorporated
18 June 2002 (Class 704/270.1); filed 12 April 1999

This patent describes the basic version of a common theme in voice interaction via networks. The end-user unit first processes the speech signal for a limited repertoire of commands. If not successful, the signal is passed on to more powerful processors elsewhere on the network to complete the recognition process.—DLR

6,411,934

43.72.Ne OPERATING SYSTEM, PARTICULARLY FOR COMPONENTS IN A MOTOR VEHICLE USING SPEECH RECOGNITION

Carsten-Uwe Möller and Frank Reh, assignors to DaimlerChrysler AG
25 June 2002 (Class 704/275); filed in Germany 7 March 1996

This patent describes a voice control system which operates together with a manual knob, specifically intended for use in a vehicle. The special knob may have many degrees of freedom, including sliding in any of three directions and rotating around any of three axes, and also would include a computer-controlled tactile feedback mechanism to emulate stops, detents, friction, or self-return-to-center. A voice control may be used to switch the knob to any of various functions, such as rearview mirror settings, wiper settings, radio operation, etc. Ideally, the knob's currently assigned function would be immediately apparent from the feel of the knob, precluding additional eye movements or voice commands.—DLR

6,415,258

43.72.Ne BACKGROUND AUDIO RECOVERY SYSTEM

Jeffrey C. Reynar *et al.*, assignors to Microsoft Corporation
2 July 2002 (Class 704/275); filed 6 October 1999

This device is an on-line backup system for the audio input stream to a speech recognition system. Does that sound far-fetched? Here's how it works. If you ''inadvertently'' leave the recognition system turned off and speak a command, the backup system stores the voice signal. Then when you come to your senses and turn the system on, the stored speech signal will be transmitted to the recognizer, processed, and the command executed. All is well. The recovery process may be manually monitored or controlled, if desired.—DLR

6,413,079

43.72.Ne VOICE ACTIVATED FIREPLACE CONTROL SYSTEM

David Charles Lyons and Gary Lee Butler, assignors to Heat-N-Glo Fireplace Products, Incorporated
2 July 2002 (Class 431/125); filed 10 April 2000

This voice control system is arranged to operate the gas valve in a fireplace or other gas heating system. As a safety measure, a double command is required. When an initial command is processed, the interpreted

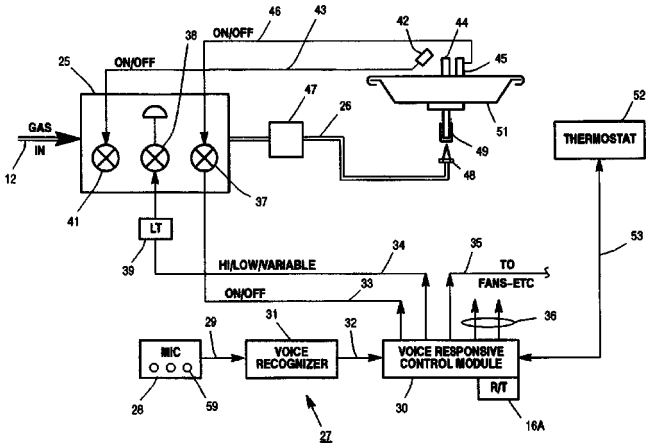

result is displayed visually. A second confirmation command is then required to actuate the desired gas setting.—DLR

6,417,769

43.72.Ne VOICE-CONTROLLED BURGLARPROOF DEVICE

Te-Chin Jan, Neihu, Taipei, Taiwan, Province of China
9 July 2002 (Class 340/541); filed 27 March 2001

This burglar alarm uses voice recognition to detect the intruder. In other words, if the thief speaks into the mic or sits down on your couch and tries to operate your voice-controlled television, the game is over. A sound

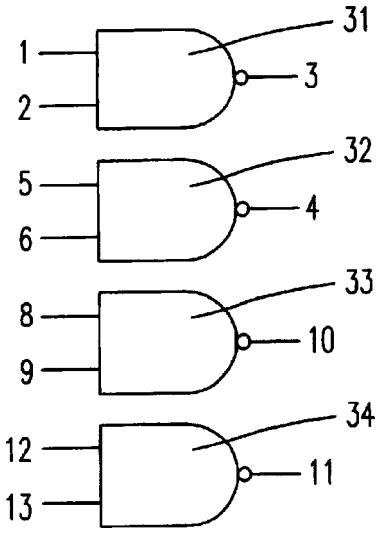

playback chip can generate a vocal warning, barking dog sounds, or other fearsome responses. Amazingly, the detector circuit seems to consist of 2 op-amps and a quad NAND gate. In accordance with standard patent procedures, the pinout of the NAND gate chip is duly disclosed.—DLR

6,418,199

43.72.Ne VOICE CONTROL OF A SERVER

Jeffrey Perrone, San Francisco, California
9 July 2002 (Class 379/88.01); filed 23 May 2000

The system described here integrates client and server operations to implement remote voice control of the network operation. Simultaneous with the network linkup over communication lines, a telephone connection is also established between the user at the client machine and a recognition system at the server. Voice control of a browser is thus mediated by a direct voice connection to the recognizer. The intended application is on-line Internet stock trading.—DLR

6,421,643

43.72.Ne METHOD AND APPARATUS FOR DIRECTING AN AUDIO FILE TO A SPEECH RECOGNITION PROGRAM THAT DOES NOT ACCEPT SUCH FILES

Jonathan Kahn *et al.*, assignors to Custom Speech USA, Incorporated
16 July 2002 (Class 704/270); filed 29 October 1999

Some personal computer speech recognition software packages are designed to accept speech input only from a microphone. When in use on a computer with an appropriate sound card, this system would provide a means to reconfigure the sound card so as to redirect audio from a prerecorded speech file into the recognition system. The interface software would reconfigure a mixer utility in order to establish the alternate input to the recognizer system. When the file playback is complete, the mixer settings would be restored from saved settings.—DLR

6,421,645

43.72.Ne METHODS AND APPARATUS FOR CONCURRENT SPEECH RECOGNITION, SPEAKER SEGMENTATION AND SPEAKER CLASSIFICATION

Homayoon Sadr Mohammad Beigi *et al.*, assignors to International Business Machines Corporation
16 July 2002 (Class 704/272); filed 30 June 1999

The speech and speaker recognition system described here is organized for processing prerecorded speech materials, such as from a teleconference or workshop session. Multiple processors or processing threads simultaneously extract a word sequence, segment the audio stream according to speaker identity, and perform a speaker recognition step on each segmented audio portion. The final result is a transcription with each speaker identified and time codes provided on a word-by-word basis. The patent provides some details of the speaker segmentation techniques.—DLR

6,424,935

43.72.Ne TWO-WAY SPEECH RECOGNITION AND DIALECT SYSTEM

George W. Taylor, assignor to Micron Technology, Incorporated
23 July 2002 (Class 704/10); filed 31 July 2000

This speech recognition system is enhanced by the ability to detect various speech dialects and to use that information to improve the recognition performance. Using an interactive question and answer method, the system queries the user for specific information, such as age, gender, education level, region of residence, etc., continually adapting the dialect characteristics using both the speech stream and the information gathered. Dialect-specific lexical terms and phonetic patterns are also consulted to aid the recognition and adaptation processes.—DLR

6,430,523

43.72.Ne CONTROL SYSTEM FOR CONTROLLING OBJECT USING PSEUDO-EMOTIONS AND PSEUDO-PERSONALITY GENERATED IN THE OBJECT

Takashi Mizokawa, assignor to Yamaha Hatsudoki Kabushiki Kaisha
6 August 2002 (Class 702/182); filed 6 April 2001

This control system for a robotic toy or for an interactive control system includes an elaborate structure of sensed external conditions and simulated internal conditions in order to synthesize an effective behavior appropriate to interaction with a human user. The internal states include such items as pseudo-personality traits and pseudo-emotional states. External sensing may include a wide variety of inputs such as temperature, brightness, time, or physical motion, in addition to an analysis of sounds picked up by a microphone. Many detailed flowcharts are provided showing the various interactions among the various states and conditions. Users of such a system are said to quickly adapt by forming various levels of emotional attachment. Whether this is appropriate in a control environment where accuracy is more important than effect may be another matter.—DLR

6,430,531

43.72.Ne BILATERAL SPEECH SYSTEM

Nathaniel Polish, assignor to Soliloquy, Incorporated
6 August 2002 (Class 704/257); filed 1 February 2000

This two-way dialogue system includes a speech recognizer, a synthesizer, and a dialogue management database which includes a history of the conversation, speaker and domain characteristics, and grammatical details as will allow natural use of pronouns, demonstratives, and other elliptic references. Various device controllers may also be attached to the system to allow actions to be taken as a result of the processed dialogue.—DLR

6,470,314

43.72.Ne METHOD AND APPARATUS FOR RAPID ADAPT VIA CUMULATIVE DISTRIBUTION FUNCTION MATCHING FOR CONTINUOUS SPEECH

Satyanarayana Dharanipragada and Mukund Padmanabhan, assignors to International Business Machines Corporation
22 October 2002 (Class 704/231); filed 6 April 2000

This patent describes nonlinear transformation methods for adaptating a speech recognition system to varying acoustic environments. Cumulative distribution function matching provides equalization between training acoustic data and test acoustic data. Cepstral or spectral vectors may be used to represent acoustic data. Cumulative distribution functions are first computed based on dimensions of speech vectors associated with both test speech and training speech data. Then a nonlinear transform mapping is computed that is based on the cumulative distribution functions associated with both test speech and training speech data. Finally, nonlinear transform mapping is applied only to those speech vectors associated with the test speech data that are similar to those of the training speech data. The advantage of such a system is said to be reduced computational requirements, resulting in substantial speed improvement over linear transform techniques.—DAP

6,470,315

43.72.Ne ENROLLMENT AND MODELING METHOD AND APPARATUS FOR ROBUST SPEAKER DEPENDENT SPEECH MODELS

Lorin Paul Netsch and Barbara Janet Wheatley, assignors to Texas Instruments Incorporated
22 October 2002 (Class 704/256); filed 11 September 1996

A garbage model covers any words or sounds for which no other model exists within the recognition system. A unique garbage model described here conforms to phonotactic language constraints to locate speech in the presence of other sounds. Methods are provided for constructing models of the located speech segments as well as locating speech in an utterance. For example, transitions are weighted by probabilities based on temporal phonotactic constraints. Hierarchical structured hidden Markov (HMM) garbage models are used to enforce syllabic constraints on the speech. HMM topologies are modified to model the onset, nucleus and final

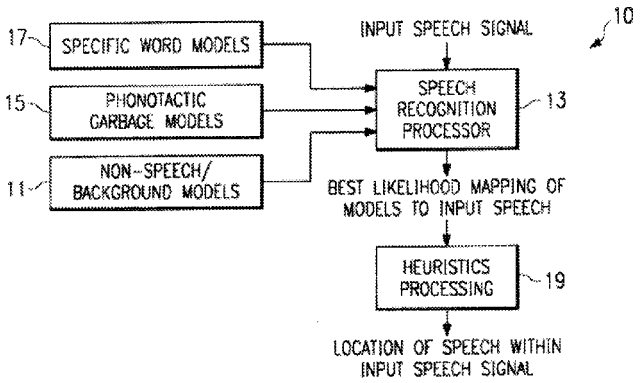

(coda) portions of a syllable. i.e., onset of a syllable may occur with a sibilant, fricative, stop or nasal; an initial sibilant may be followed by a fricative, stop or nasal; a fricative may be followed by a stop or nasal; and a stop or nasal must occur at the end of the onset. The nucleus contains the sounds of a front, low, or back vowel. The coda model allows ending a syllable with a sibilant, fricative, stop, or nasal sound. After recognition, heuristics are applied to smooth the estimated locations of speech. Frames of speech data, which are best matched by states of the garbage model, are designated as locations where speech exists. Interword silences may optionally be added to match the actual speech utterance.—DAP

6,484,141

43.72.Ne CONTINUOUS SPEECH RECOGNITION APPARATUS AND METHOD

Takashi Tomoeda, assignor to NEC Corporation
19 November 2002 (Class 704/254); filed in Japan 4 December 1998

Some speech recognition systems have the problem that a large amount of memory and calculations are required when look-ahead is performed of unigram and bigram language models. Wasteful calculation is done because some of the arcs of a tree structure dictionary and hypothesis may expand only to a word whose connection to the context is not permitted linguistically. Also, hypotheses on an arc which is developed to a word whose connection to the context is permitted linguistically may be unintentionally eliminated. This invention describes a speech recognition system containing a hypothesis storage section, a hypothesis expansion discrimination means for determining if a hypothesis may be expanded to a succeeding

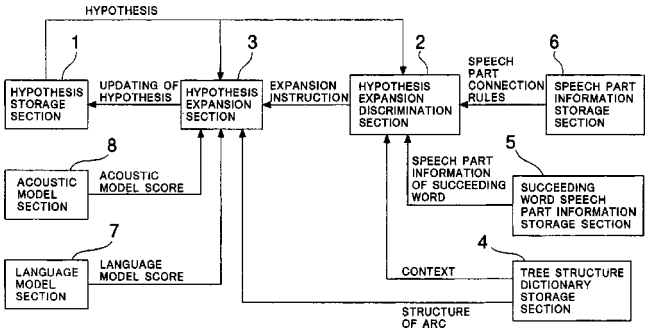

arc, and a tree structure dictionary storage section. The number of unnecessary hypotheses is said to be minimized and, as a result, speed of recognition is increased. Occurrence of scores of a hypothesis to a word not connecting linguistically to a context is said to be reduced, resulting in greater recognition accuracy.—DAP

6,424,946

43.72.Pf METHODS AND APPARATUS FOR UNKNOWN SPEAKER LABELING USING CONCURRENT SPEECH RECOGNITION, SEGMENTATION, CLASSIFICATION AND CLUSTERING

Alain Charles Louis Tritschler and Mahesh Viswanathan, assignors to International Business Machines Corporation
23 July 2002 (Class 704/272); filed 5 November 1999

This speaker identification system is designed to produce speaker labels for various portions of a body of recorded speech, such as news coverage video material. An unsupervised clustering system marks segments of the material as being spoken by different individuals. If the identity of the speaker of a portion is not currently known, that segment is assigned a generic label, such as ''unknown male.'' Operator input may be requested for additional information in such cases and if a specific label becomes available for a previously unknown portion, the new label will be attached to all segments with the same cluster characteristics.—DLR

6,411,930

43.72.Pf DISCRIMINATIVE GAUSSIAN MIXTURE MODELS FOR SPEAKER VERIFICATION

Christopher John Burges, assignor to Lucent Technologies, Incorporated
25 June 2002 (Class 704/240); filed 12 February 1999

This speaker recognition system uses a combination of techniques. A Gaussian mixture model is built in the usual way for multiple speakers. The likelihood sum of this model is then factored into two components, one related only to the Gaussian mixture model and the other specialized for discriminating among the various speakers. When arranged so as to distinguish one speaker from all others, this term may be used with a more powerful classifier such as a support vector machine.—DLR

6,472,591

43.75.Bc PORTABLE COMMUNICATION TERMINAL APPARATUS WITH MUSIC COMPOSITION CAPABILITY

Eiichiro Aoki *et al.*, assignors to Yamaha Corporation
29 October 2002 (Class 84/611); filed in Japan 25 May 2000

Imagine a cellular telephone that can compose new tunes for use as a ''ringing'' sound. The user can supply either the rhythm or pitch track (or

both) and the algorithm described in a separate Japanese patent will fill in the chords or pitches. The algorithm allows for ''feelings'' of songs to dictate the chord choice. Finally, the user can edit the score using the familiar cell phone keypad.—MK

6,469,237

43.75.Mn APPARATUS FOR OPENING AND CLOSING TOP BOARD OF GRAND PIANO

Manabu Arimori, assignor to Kabushiki Kaisha Kawai Gakki Seisakusho
22 October 2002 (Class 84/174); filed in Japan 28 October 1999

The top board of a grand piano can weigh as much as 40 to 50 kg, which means pianists risk crushed fingers and worse when trying to raise the

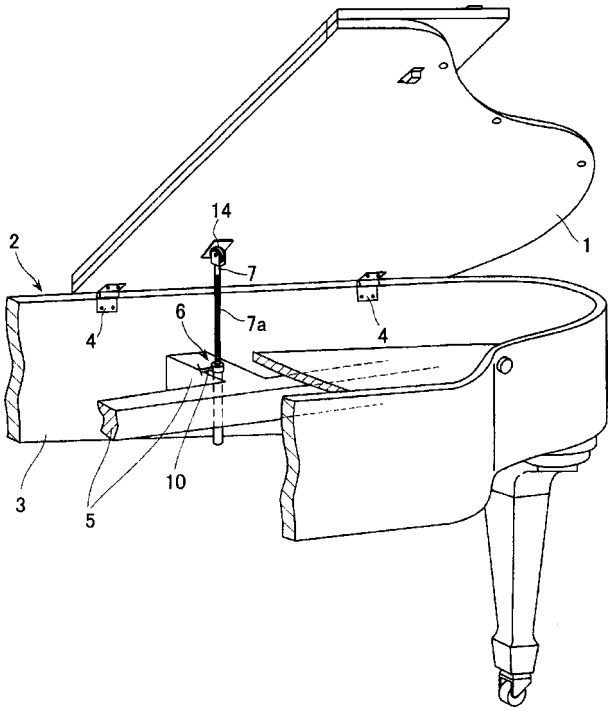

lid. The inventors simply propose adding a jack instead of the familiar wooden prop.—MK

6,476,301

43.75.Pq BAGPIPE DRONES

Ralph Robertson Hepburn, Edinburgh, the United Kingdom
5 November 2002 (Class 84/380 B); filed in the United Kingdom 24 July 1997

The inventor, comfortably situated in Edinburgh, proposes changing the drone pipes of a bagpipe so that the instrument can be practiced indoors. His improvements include reduction of pipe diameter and use of brass instead of wood.—MK

6,476,306

43.75.St METHOD AND A SYSTEM FOR RECOGNIZING A MELODY

Jyri Huopaniemi *et al.*, assignors to Nokia Mobile Phones Limited
5 November 2002 (Class 84/609); filed in Finland 29 September 2000

Automatic recognition of songs has become a hot research area. Here, the inventors propose adding word recognition to aid melody recognition. The patent is very high level and leaves too much to the imagination. Critical references to the song search literature (such as McNab) are conspicuously absent.—MK

6,472,592

43.75.Wx APPARATUS FOR AND METHOD OF ADDING SOUND SIGNAL IN SYSTEM HAVING LIMITED NUMBER OF SOUND GENERATORS

Masako Arizumi, assignor to Mitsubishi Denki Kabushiki Kaisha
29 October 2002 (Class 84/656); filed in Japan 11 May 1999

A DSP microprocessor can implement a fixed number of voices in a sample period and therefore complex program material can exhaust these finite resources. This patent proposes cutting the resource with the least time remaining, which is naive at best but easy to implement. However, even in 1999, this was obvious to those ''skilled in the art.''—MK

6,473,475

43.75.Wx SAMPLE RATE CONVERTER USING POLYNOMIAL INTERPOLATION

Bruno J. G. Putzeys, assignor to Koninklijke Philips Electronics N.V.
29 October 2002 (Class 375/350); filed in the European Patent Office 27 April 1998

It is well known that sampling rate conversion may involve the use of large upsampling rates. The proposed method uses a phase lock loop to find the time difference between the two sampling periods and then uses a sixth-order polynomial interpolator to generate the output sample.—MK

6,479,740

43.75.Wx DIGITAL REVERSE TAPE EFFECT APPARATUS

Louis Schwartz, Ansonia and G. Burnell Hohl, New Canaan, both of Connecticut
12 November 2002 (Class 84/609); filed 3 February 2001

The use of reversing tape to use the attack as the decay (and vice versa) dates back to the earliest use of magnetic tape. This patent proposes a digital version of the same by detecting note on and off events in a recording memory and playing the memory backwards. The reversed waveform is spliced in by predicting where the envelope is at midpoint. The algorithm depends critically on an exponentially damped sound—electric guitars are mentioned specifically. The technology described in the patent is curiously old fashioned for having been filed in 2001.—MK

6,468,213

43.80.Qf MEDICAL DIAGNOSTIC ULTRASOUND SYSTEM AND METHOD

Christopher B. Knell *et al.*, assignors to Ecton, Incorporated
22 October 2002 (Class 600/437); filed 14 September 1999

The diagnostic system described here employs a scan converter that uses a reprogrammable logic device for converting data from an acoustic grid (representing a subsystem of a body being scanned) into a display format. A set of instruction codes in the logic device may be changed to

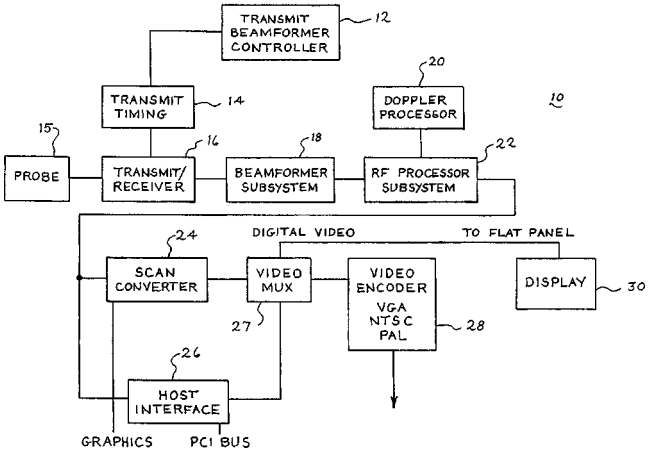

redefine the scan conversion process, providing flexibility in the scanning procedure. A single memory stores the incoming data where read and write operations are performed sequentially. The same memory may also be used to store the converted scan data.—DRR

6,471,651

43.80.Qf LOW POWER PORTABLE ULTRASONIC DIAGNOSTIC INSTRUMENT

Juin-Jet Hwang *et al.*, assignors to SonoSite, Incorporated
29 October 2002 (Class 600/459); filed 3 May 2000

The principal attractions of this device are its portability and low power requirement (no more than 25 W). The apparatus consists of an array transducer, a beamformer for delaying and combining echo signals received by the elements of the array transducer, signal processing and imaging circuitry for processing the echo signals, and a display for the processed echo signals. Power consumption economy is achieved through the use of a battery, use of an analog beamformer to avoid power-consuming A/D or D/A conversions, use of an LCD display, etc.—DRR

6,471,653

43.80.Qf TRANSESOPHAGEAL ULTRASOUND PROBE WITH MOTOR IN THE TIP FOR SCAN-PLANE ROTATION

Dag Jordfald *et al.*, assignors to GE Medical Systems Global Technology Company, LLC
29 October 2002 (Class 600/462); filed 2 November 2000

The device provides an alternative means of scanning human organs, particularly the heart. In the preferred embodiment, a transesophageal ultrasound probe that allows for scan-plane rotation includes an endoscope with a probe head connected to the distal end. A transducer with a transfer mechanism is attached to the probe head and a motor at the distal end of the endoscope connects to the transfer mechanism. The motor allows a clinician to alter the scan-plane of the transducer by rotating the transducer around an axis perpendicular to the transfer surface through the use of the transfer surface connected to the transducer. The motor is powered through an electrical wire, thus eliminating the need for mechanical linkages used in current devices.—DRR

6,468,215

43.80.Qf METHOD AND DEVICE FOR MULTI-PARAMETRIC ULTRASONIC ASSESSMENT OF BONE CONDITIONS

Armen P. Sarvazyan and Alexej Tatarinov, assignors to Artann Laboratories
22 October 2002 (Class 600/438); filed 16 July 2001

The device and method entails an ultrasonic bone scan along a trajectory over the surface of a bone being examined, e.g., a probe or a set of probes moving along the skin adjacent to the bone. The parameters measured include velocity of a longitudinal wave, velocity of a flexural wave, attenuation of both types of waves, frequency slopes of attenuation, and changes in spectral characteristics. Pulse-echo ultrasonic channels incorporated in the probes determine the thickness of soft tissue layer, so as to eliminate the influence of soft tissues on the parameters. Tools for controlling the pressure of the probes against the skin and a digital counter to measure the distance traveled by a probe along the predetermined trajectory are also described in the patent. While it is essentially the same type of device as the current ultrasonic device used in physicians' offices to detect osteoporosis, it appears to differ principally in providing for sequential bone assessment along a selected trajectory.—DRR

6,471,655

43.80.Qf METHOD AND APPARATUS FOR THE NONINVASIVE DETERMINATION OF ARTERIAL BLOOD PRESSURE

Gail D. Baura, assignor to VitalWave Corporation
29 October 2002 (Class 600/485); filed 29 June 1999

In an embodiment of this device, intended to measure mean arterial blood pressure, one or more pressure and ultrasound transducers are placed over the radial artery of a patient's wrist. The transducers transmit and receive acoustic energy, thus enabling measurement of blood velocity during periods of variable compression of the artery. During compression, the ultrasound velocity waveforms are recorded and processed through time-frequency analysis. When mean time-frequency distribution is maximal, transmural pressure equals zero and the mean pressure read by the pressure transducer equals the mean pressure within the artery.—DRR

6,475,146

43.80.Qf METHOD AND SYSTEM FOR USING PERSONAL DIGITAL ASSISTANTS WITH DIAGNOSTIC MEDICAL ULTRASOUND SYSTEMS

Paul D. Frelburger *et al.*, assignors to Siemens Medical Solutions USA, Incorporated
5 November 2002 (Class 600/437); filed 24 September 2001

This is a system that would enable using Palm Pilots and other personal digital assistants (PDAs) as part of a diagnostic medical ultrasonic system. A PDA can be used to control the ultrasound system via a wired or wireless communications link. Moreover, the PDA can use personal infor-

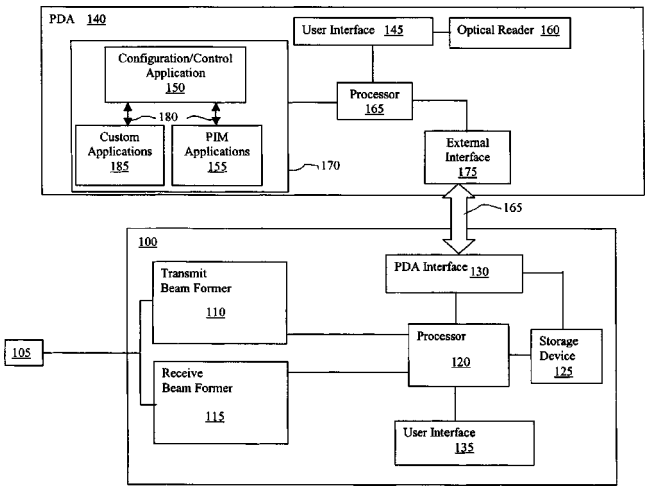

mation management (PIM) functions to permit automated control and configuration of the ultrasound system based on data stored by the PIM applications. A special interface would be incorporated into the ultrasound system to interact with the PDA.—DRR

6,475,147

43.80.Qf ULTRASONIC APPARATUS AND TECHNIQUE TO MEASURE CHANGES IN INTRACRANIAL PRESSURE

William T. Yost and John H. Cantrell, assignors to the United States of America as represented by the United States National Aeronautics and Space Administration
5 November 2002 (Class 600/438); filed 27 January 2000

The aim of this device is to measure intracranial pressure in patients by noninvasively monitoring the pulsatile components of the cerebrospinal fluid (CSF). The device works by generating an ultrasonic signal on one side of the head, which is reflected back from the other side of the head. When the reflected signal travels through the brain, pulsatile variations in the CSF cause associated phase variations in the signal. A preferred embodiment of the device uses the phase shifting capabilities of a constant-frequency, pulsed phase-locked-loop ultrasonic device (covered by United States Patent 5,214,955, also by Yost and Cantrell) to monitor this variation in CSF pulsatile components. Calibration of the device is achieved by inducing a known change in intercranial pressure, thus allowing conversion of the process signal to the changes in intercranial pressure.—DRR

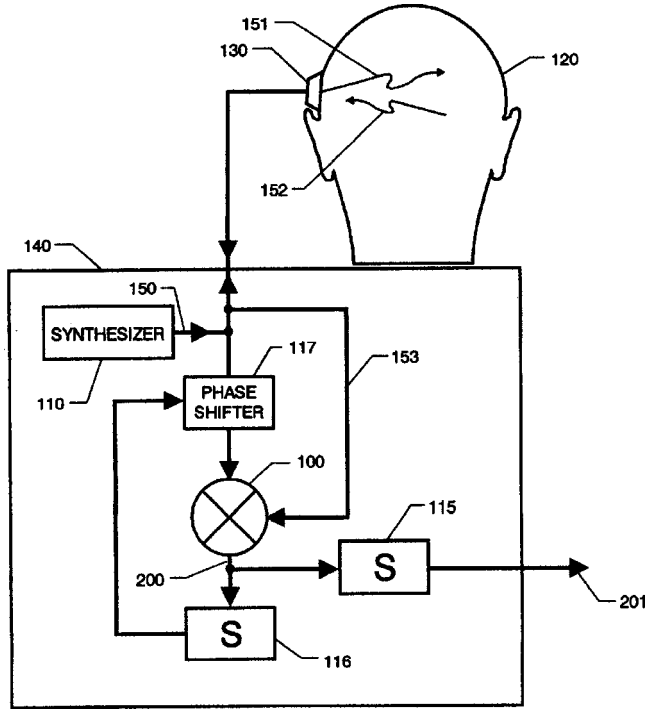

6,475,149

43.80.Qf BORDER DETECTION METHOD AND SYSTEM

Thilaka Sumanaweera, assignor to Acuson Corporation
5 November 2002 (Class 600/441); filed 21 September 2001

Both fluid and tissue data are used to locate vessel or organ borders. Fluid data, obtainable from ultrasound Doppler data, identifies tissue-to-fluid borders, such as vessel borders that are closer to the transducer. Tissue data, such as the ultrasound B-mode data, is better for identifying fluid-to-tissue borders further away from the transducer. Also, since there is no moving blood flow or fluid flow above an upper or top portion of a vessels border, fewer reverberation effects are provided for Doppler data. The detected borders are used for additional calculation or display, such as automatically estimating vessel diameter for endothelial function assessment. Other techniques, such as MRI, CAT scan, or x-ray, for imaging interior segments of a patient can also be applied.—DRR

6,482,161

43.80.Qf MEDICAL DIAGNOSTIC ULTRASOUND SYSTEM AND METHOD FOR VESSEL STRUCTURE ANALYSIS

Thilaka Sumanaweera and Linyong Pang, assignors to Acuson Corporation
19 November 2002 (Class 600/454); filed 29 June 2000

This is a system for automating the analysis of vessel structure inside the human body, particularly bifurcations such as the carotid artery. In the process of diagnosis, the bifurcation bulb (the common portion of the bifurcation) is divided as a function of a ratio of the integrals of ultrasound flow data at cross sections of the two branches. The ultrasound data representing the common portion is associated with each branch as a function of the

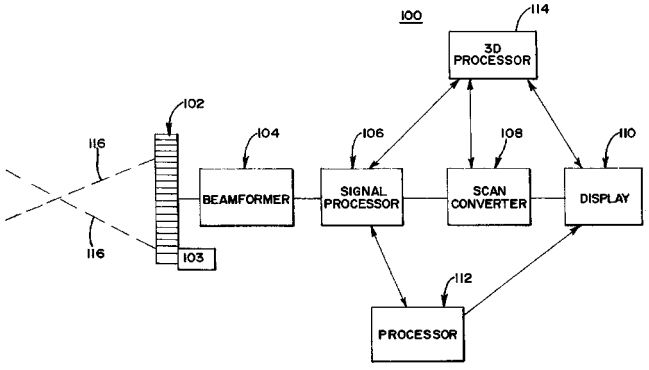

division. This association is said to be useful in flow and structural analysis. A method is also described for automatically assigning a center (i.e., medial) axis of the vessel. The center of flow is determined from flow gradient values obtained from ultrasound data associated with each vessel and from other parameters. The established central axis is used to identify constrictions or to analyze flow for medical evaluation.—DRR

6,475,170

43.80.Qf ACOUSTIC BIOSENSOR FOR MONITORING PHYSIOLOGICAL CONDITIONS IN A BODY IMPLANTATION SITE

Eyal Doron and Avi Penner, assignors to Remon Medical Technologies Limited
5 November 2002 (Class 600/587); filed 10 March 2000

In the preferred embodiment, the device contains a sensor element for measuring a physiological condition at the implantation site and for generating a signal indicating the physiological condition. The biosensor also includes a piezoelectric transducer element for an externally generated acoustic interrogation signal to trigger the sensor. The transducer element modulates the interrogation signal by using a switching element to alternate the mechanical impedance of the transducer element to transmit a signal out of the body.—DRR

6,477,405

43.80.Qf HEART-SOUND DETECTING APPARATUS, SYSTEM FOR MEASURING PRE-EJECTION PERIOD BY USING HEART-SOUND DETECTING APPARATUS, AND SYSTEM FOR OBTAINING PULSE-WAVE-PROPAGATION-VELOCITY-RELATING INFORMATION BY USING HEART-SOUND DETECTING APPARATUS

Keizoh Kawaguchi, assignor to Colin Corporation
5 November 2002 (Class 600/513); filed 12 July 2001

The extremely long title of the patent document nearly says it all. The apparatus includes a heart-sound microphone, a time-frequency analyzing device to evaluate at least a portion of the heart sound signal and an electronic device for measuring the duration of aortic valve opening phase.—DRR

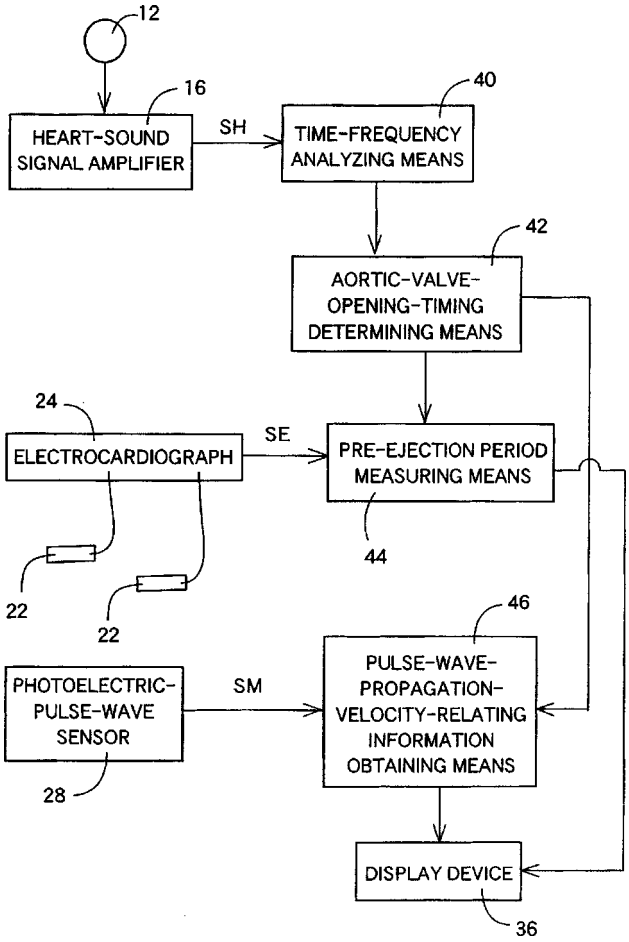

6,477,406

43.80.Qf EXTRAVASCULAR HEMODYNAMIC ACOUSTIC SENSOR

Robert Turcott, assignor to Pacesetter, Incorporated
5 November 2002 (Class 600/518); filed 5 April 2000

The device is apparently intended to act alone or to supplement the function of an implanted medical device such as a pacemaker or cardiovascular defibrillator. It functions by monitoring the hemodynamic status of a patient. A hermetic housing (e.g., a titanium ''can'') encloses the electronics and includes at least one substantially planar face to act as a diaphragm responding to acoustic waves. In response to the vibration of the diaphragm, a transducer positioned inside the housing generates a signal to the electronics portion of the device. In one embodiment the transducer is a piezoelectric element placed on the diaphragm. In a second embodiment the transducer consists of a laser interferometric source and a detector for laser light reflected from the diaphragm. The heart sound signals can be used to evaluate various cardiac arrhythmias, particularly hemodynamically stable and unstable arrhythmias.—DRR

6,478,739

43.80.Qf ULTRASONIC BREAST EXAMINATION SYSTEM

Hyundae Hong, assignor to The Procter & Gamble Company
12 November 2002 (Class 600/437); filed 11 May 2001

The device is an instrumented brassiere that contains at least two mutually opposed ultrasound transducer arrays disposed over an inner surface of the cups and at least one bladder element deployed in the shell that is configured to orient the wearer's breast properly for examination. The human breast can be noninvasively examined to detect the presence of irregularities in tissue density. The device may also include means for connecting the two mutually opposed transducer arrays to a transducer driver and means for holding the support element during use. This device may be a viable alternative to the current use of rather uncomfortable mammograms.—DRR

6,475,148

43.80.Sh MEDICAL DIAGNOSTIC ULTRASOUND-AIDED DRUG DELIVERY SYSTEM AND METHOD

John I. Jackson and Edward A. Gardner, assignors to Acuson Corporation
5 November 2002 (Class 600/439); filed 25 October 2000

This is a medical ultrasound diagnostic system that monitors and destroys drug-bearing microspheres in a specific location at a specific time in order to initiate the drug infusion. The transmit beamformer is configured to focus the beam in a sufficiently narrow area while minimizing the destruction of the microspheres outside the area of interest. A trigger that is responsive to heart or breathing cycles can be incorporated to control the instant of microsphere destruction, thus providing delivery of drugs at the most opportune time in the cycle.—DRR

6,468,286

43.80.Sh ULTRASONIC CURVED BLADE

Dominick L. Mastri and Corbett W. Stone, assignors to The United States Surgical Corporation
22 October 2002 (Class 606/169); filed 6 September 2001

This device, intended for dissection and coagulation of tissues through the use of ultrasound, appears to differ from other similar ultrasonic surgical devices principally in the geometry of the cutting blade.—DRR

6,468,219

43.80.Sh IMPLANTABLE TELEMETRIC TRANSCRANIAL DOPPLER DEVICE

Philip Chidi Njemanze, assignor to Philip Chidi Njemanze
22 October 2002 (Class 600/454); filed 24 April 2000

The system consists of a transcranial Doppler ultrasonic device, oximeter, external handheld computer, and an implantable mini-drug delivery system or external drug infusion system. The implantable ultrasonic device contains a transducer placed on the acoustic window of the temporal bone above the zygomatic arc, a voltage generator and gate, a receiver and

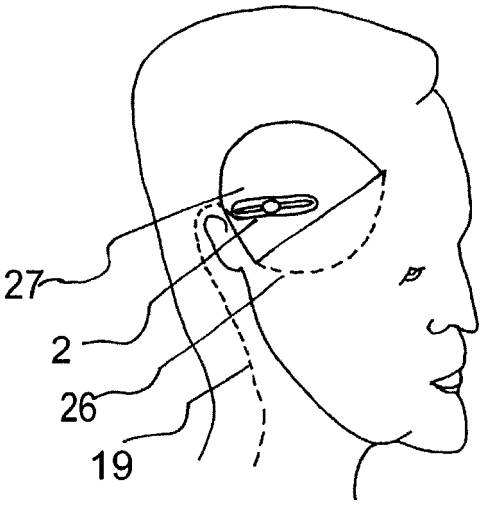

gate, and a microprocessor that can execute a spectral analysis and relay the information to the external hand-held computer via a rf transmitter/receiver. The oximeter detects the respiratory status through measurement of oxygen saturation of hemoglobin. The system can activate drug infusion for neuroprotection or treatment of thrombosis.—DRR

6,478,765

43.80.Sh APPARATUS FOR REMOVING THROMBOSIS

Robert J. Siegel and Robert E. Carter, assignors to Transon, LLC
12 November 2002 (Class 604/22); filed 9 November 1998

This device is said to take advantage of the effectiveness of applying a combination of ultrasonic energy and certain agents, including imaging agents and agents to dissolve arterial thrombosis. One embodiment alternatively uses a predetermined dose of thrombolytic agent in combination with an echo contrast agent in order to enhance the action of the thrombolytic agent in removing a thrombosis from a fistula.—DRR

6,478,754

43.80.Sh ULTRASONIC METHOD AND DEVICE FOR WOUND TREATMENT

Eilaz Babaev, assignor to Advanced Medical Applications, Incorporated
12 November 2002 (Class 601/2); filed 23 April 2001

The patent covers a method and device for spraying a wound surface to deliver drugs, kill bacteria, or cleanse a surface by noncontact application of ultrasonic waves. It is intended, for understandable reasons, that ultrasonic waves are applied without requiring direct or indirect (via a traditional coupling medium) contact between the transducer and the wound to be treated. Other noncontact sprayers have been developed and used but not

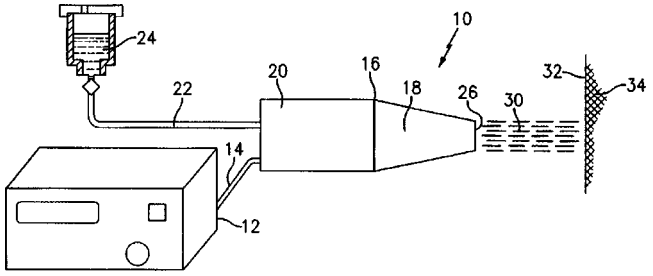

for medical purposes. The spray in this device is produced by generating liquid particles upon the liquid's exposure to the free end of an ultrasonic transducer. The ultrasonic waves cause the spray to dissipate outwardly from the distal end surface. The liquid particles can deliver drugs, kill bacteria in the wound, increase blood flow, and/or remove contaminants from the wound surface.—DRR

6,482,218

43.80.Sh WIRE-SHAPED ULTRASONIC CATHETER WITH DIAMOND COATED HEAD FOR ULTRASONIC ANGIOPLASTY

Khanh Vien Tran, Gagny, France
19 November 2002 (Class 606/169); filed 23 October 1998

This catheter is a wire-shaped ultrasonic device to be used for ultrasonic angioplasty. The catheter head is coated with a diamond powder and incorporates a cylindrical sonotrode and a thin ultrasound catheter, which together form a resonant system. The catheter itself forms a stainless steel ultrasonic waveguide.—DRR

6,468,218

43.80.Vj 3-D ULTRASOUND IMAGING SYSTEM AND METHOD

Jian-Feng Chen and Dong-Chyuan Liu, assignors to Siemens Medical Systems, Incorporated
22 October 2002 (Class 600/443); filed 31 August 2001

Echo intensity from a region of pixels is stored. The pixels are grouped into blocks and intensity histograms are computed for each block. From a comparison of each histogram with a reference, a structure likelihood value is computed to quantify the possibility that a structure of interest as opposed to noise is present in the block. Intensities likely to be noise are reduced and the resulting collection of intensities is projected onto a plane for display.—RCW

6,471,389

43.80.Vj DYNAMIC DELAY CURVE GENERATOR FOR ULTRASONIC IMAGING SYSTEM

Chen-Hua Hu *et al.*, assignors to Chung-Shan Institute of Science and Technology
29 October 2002 (Class 364/11); filed 1 December 2000

This delay curve is produced by a sequence of steps in which parameters are extracted from an ultrasonic echo signal and processed in a special algorithm to determine time delays used for focusing in a beamformer.—RCW

6,471,652

43.80.Vj ULTRASONIC DIAGNOSTIC IMAGING SYSTEM TRANSDUCER ARRAY WITH MULTILINE PATCHES

John D. Fraser *et al.*, assignors to Koninklijke Philips Electronics N.V.
29 October 2002 (Class 600/459); filed 19 July 2001

In this system, a volume of the heart wall that includes a coronary artery is scanned in three dimensions. The data are projected onto a plane to produce a coronary artery image that has the appearance of an angiogram. In the projection, signals from the coronary artery are segmented from signals from the myocardium and the heart blood pool so that the coronary arteries are distinct.—RCW

6,475,150

43.80.Vj SYSTEM AND METHOD FOR ULTRASONIC TOMOGRAPHY

Waleed Sami Haddad, assignor to The Regents of the University of California
5 November 2002 (Class 600/448); filed 1 December 2000

Images are produced from transmission mode data and also from reflection mode data. Using an iterative approach, an image of sound speed and an image of attenuation are obtained from the transmission data. Reflection mode images from a number of angles are used to calculate impedance values as well as to form a weighted impedance image. Impedance and sound speed data are combined to calculate density in the region being imaged.—RCW

6,478,742

43.80.Vj PRF ADJUSTMENT METHOD AND APPARATUS, AND ULTRASONIC WAVE IMAGING APPARATUS

Hiroaki Kataoka, assignor to GE Medical Systems Global Technology Company, LLC
12 November 2002 (Class 600/449); filed in Japan 5 November 1999

The pulse repetition frequency (PRF) is adjusted by using the maximum value of Doppler shift calculated from a sequence of transmitted pulses.—RCW

6,478,743

43.80.Vj TRANSESOPHAGEAL ULTRASOUND PROBE WITH IMAGING ELEMENT POSITION SENSOR IN SCANHEAD

Dag Jordfald *et al.*, assignors to GE Medical Systems Global Technology Company, LLC
12 November 2002 (Class 600/462); filed 16 March 2001

This probe has an articulatable scan head that contains a transducer

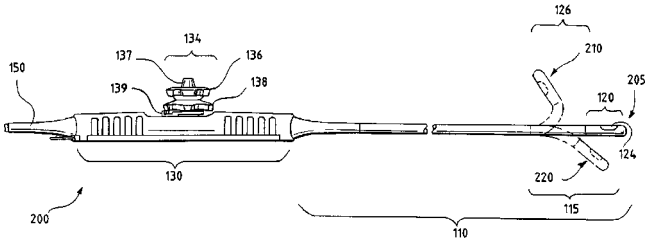

and position sensor.—RCW

6,482,162

43.80.Vj LOOP IMAGING CATHETER

Thomas C. Moore, assignor to Scimed Life Systems, Incorporated
19 November 2002 (Class 600/466); filed 20 October 2000

This catheter is designed to provide data for three-dimensional imaging of the heart or other organs with a relatively large cavity. The transducer in the catheter tip can be rotated and translated longitudinally. In addition,

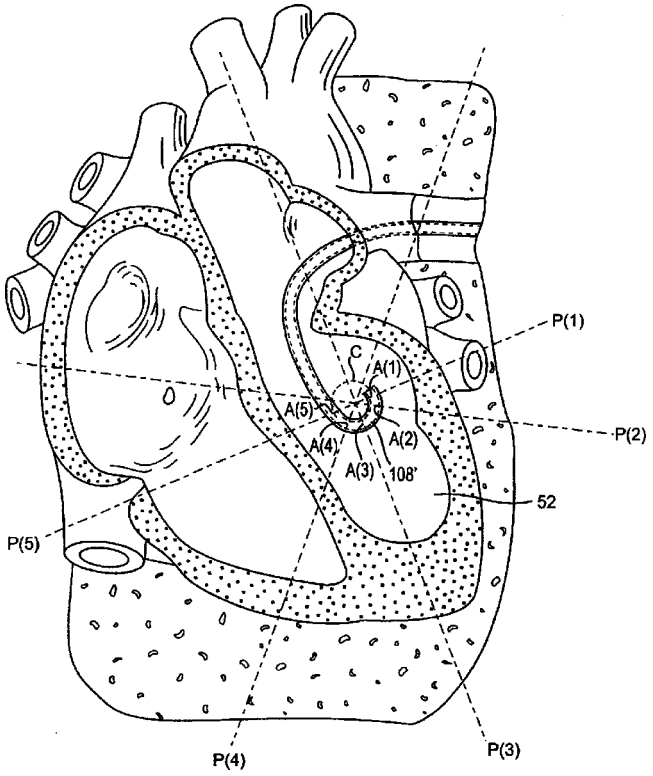

the tip of the catheter can be bent into a known and repeatable arc. The catheter can be operated to produce longitudinal scans in a sequence of planes, e.g., **P(1)**,...,**P(5)**, that are defined by the center of the arc and points, e.g., **A(1)**,...,**A(5)**, around its circumference **C**.—RCW

6,482,160

43.80.Vj HIGH RESOLUTION 3D ULTRASOUND IMAGING SYSTEM DEPLOYING A MULTIDIMENSIONAL ARRAY OF SENSORS AND METHOD FOR MULTIDIMENSIONAL BEAMFORMING SENSOR SIGNALS

Stergios Stergiopoulos and Amar C. Dhanantwari, assignors to Her Majesty the Queen in right of Canada, as represented by the Minister of National Defence
19 November 2002 (Class 600/443); filed in Canada 24 November 1999

This system employs a beamformer that accepts signals from a multidimensional array of sensors. The beamformer is divided into subapertures and each subaperture is decomposed into two sets of coherent beamformers. The first set forms beams in one direction. The second subset forms beams in another direction. The system produces high resolution three-dimensional images in real time.—RCW

Fluctuation theory and (very) early statistical energy analysis (SEA) (L)

Richard H. Lyon
RH Lyon Corp, Cambridge, Massachusetts 02138

(Received 20 July 2002; accepted for publication 24 February 2003)

The equivalence between a noise source in combination with a resistance, and a thermal bath, is a part of fluctuation theory. This observation was the motivation for the author's 1960 calculation of the power flow between modes of vibration excited by random noise sources. The resulting relation between power flow and uncoupled energy of vibration is therefore more than a thermal analogy; it is an actual representation of two thermal baths in contact. In a sense, the answer was known before the calculation was performed; the power flow had to be proportional to the differences in modal energy. The calculation merely determined the thermal conductivity of the connection. The relations for groups of modes in contact and the proportionality between power flow and actual modal energy came later. © *2003 Acoustical Society of America.* [DOI: 10.1121/1.1567274]

PACS numbers: 43.40.Hb, 43.40.Qi, 43.55.Cs [ADP]

A particle in Brownian motion is bombarded equally by impacts from all sides by the thermal bath in which it resides. But if it has a drift velocity, then the impacts from the direction it is moving toward will be a bit stronger on average, leading to a resistance to its motion in that direction. There is therefore a relation between the random impacts (spectral density S_f) and the resistance to motion R. That relation is quantified if we require the energy of each degree of freedom of the particle to reach thermal equilibrium ($\frac{1}{2}kT$) with the bath (k is Boltzmann's constant, T is the absolute temperature). The result is that the spectral density (in cyclic frequency or Hz) be[1] $S_f=4RkT$. For a resonant mode with two degrees of freedom (displacement and velocity, current and voltage, pressure and velocity potential, etc.), the equilibrium energy is $E_m=kT=S_f/4R$. (Note that engineers call a resonator a ''single degree of freedom'' device, but a physicist refers to its two degrees of freedom, each entering quadratically into the Hamiltonian.)

In 1959, the author went to the University of Manchester to work on turbulence theory, with an intention to use fluctuation theory to determine the equilibrium distribution of energy among the ''modes'' of turbulence. Such a mode is illustrated in Fig. 1, a single dof system with a broad range of frequency dependence. The excitation of such a mode is its highly nonlinear interaction with the other modes. There had been some success in estimating the turbulence spectrum for homogeneous isotropic turbulence and the hope was that fluctuation theory could be used to both broaden and focus the equilibrium spectral estimates.

Although there may still be value in the idea, I was unable to make headway with it. At the University of Minnesota, I had become interested in the modal density of structures, and that became the second or fallback focus of the Manchester work. Modal resonances had some obvious advantages; the response was narrow band and the dynamics were linear so that different frequency bands were isolated as can be seen in Fig. 1. Ordinary fluctuation theory says that all resonant modes in the system, up to the Planck limit, have the same energy of kT. But if the system is linear, one can have different frequency bands at ''different temperatures,'' and still use the concept of modal energy as the driving potential for energy flow.

The diagram in Fig. 2 illustrates how the idea was applied. Two thermal baths at different temperatures interact with attached resonators (the example uses an electrical resonant circuit). If the resonators are coupled (by magnetic flux or mutual inductance for example), we would be astonished if the power flow between them were *not* proportional to the difference in the temperatures of the bath or their uncoupled energies. Parenthetically, some commentators on SEA have thought this is a simplifying assumption. It actually makes the problem a bit harder because reciprocity cannot be invoked to aid the calculation when the resonators are uncoupled.

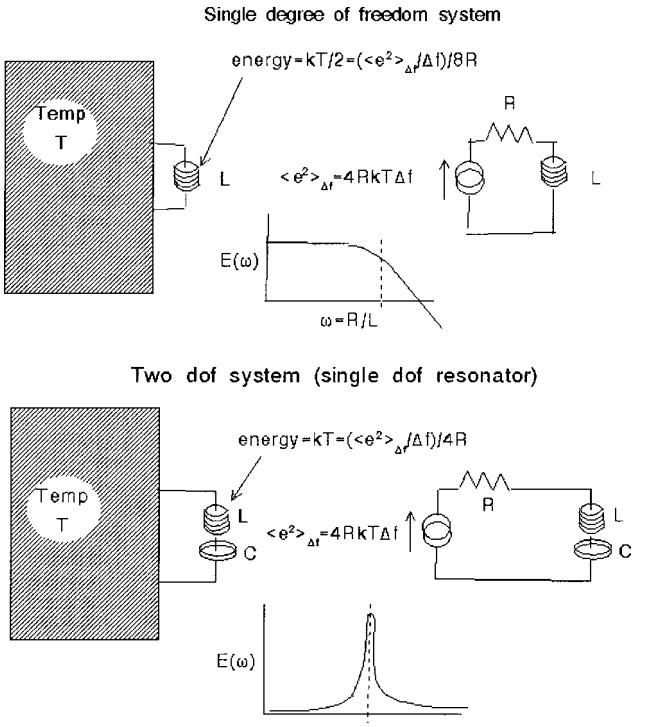

FIG. 1. One- and two-degree-of-freedom systems interacting with a thermal bath.

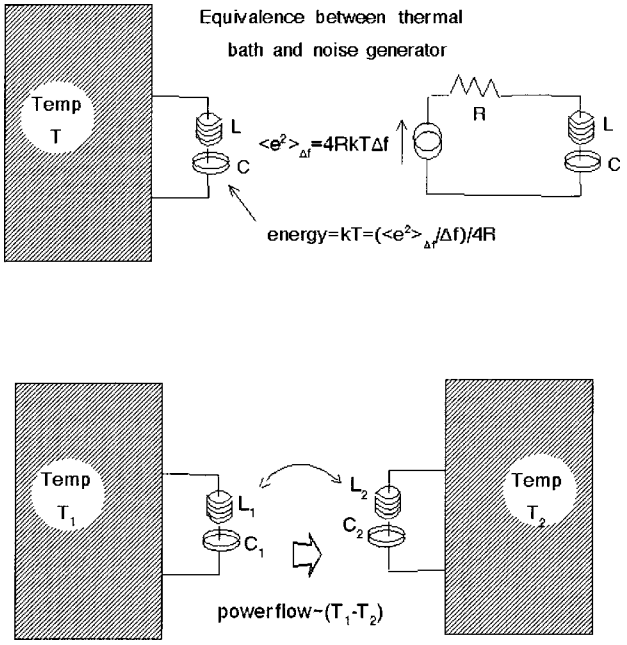

FIG. 2. Two coupled resonators at different temperatures.

The actual calculation of the power flow between modes was recorded in my notes from Manchester in February 1960, reproduced in part in Fig. 3. It is essentially a calculation for random vibration, and it gets a result for the case where one (the ''second'') resonator has a finite resistance but no random excitation. From above, $S_f/4kT \rightarrow R$ as $S_f \rightarrow 0$ and $T \rightarrow 0$, so that the second unexcited resonator is at ''absolute zero'' when it does not have noise excitation. This is a common situation in acoustical applications. The result showed that as the resistance of the second resonator vanishes, that resonator comes to energy equilibrium with the resonator that is excited by a random force. Lyon and Maidanik[2] later published this work with additions in the *Journal of the Acoustical Society of America*.

When I joined BBN in August of 1960 I became aware that Preston Smith had carried out a calculation of the interaction of a mode with a reverberant and diffuse sound field as shown in Fig. 4. It was generally assumed at the time that a sound field of noise was equivalent to a random force excitation, but the response to such a force diverges as the damping of the resonator vanishes. Smith[3] had found that in fact that the response reached a limit when the coupling represented by the radiation damping became larger than the internal damping of the mode. It was the calculation of a moment to show that this limit was the fluctuation theory value of $E_m = S_p(f)/4R_{\text{rad}}$, where S_p is the spectral density of the pressure field and $R_{\text{rad}} = \pi f^2 \rho / c$ is the point source acoustic radiation resistance.

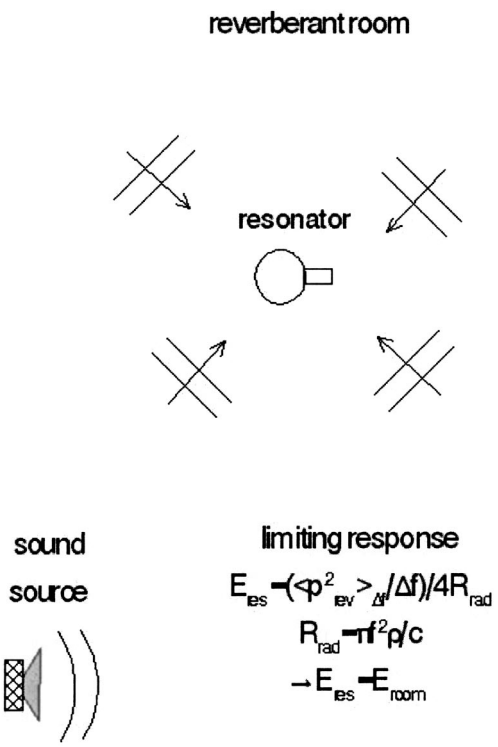

FIG. 4. Resonator in a reverberant room, with the response determined by the ''temperature'' of the room modes.

It is not at all strange that a diffuse reverberant sound field should behave like a thermal bath, since in the audible frequency range, the thermal degrees of freedom of a room are in fact its acoustical resonances. So when we excite a room with a band of noise, we are making a limited number of room modes very hot. Thankfully, the system is nearly

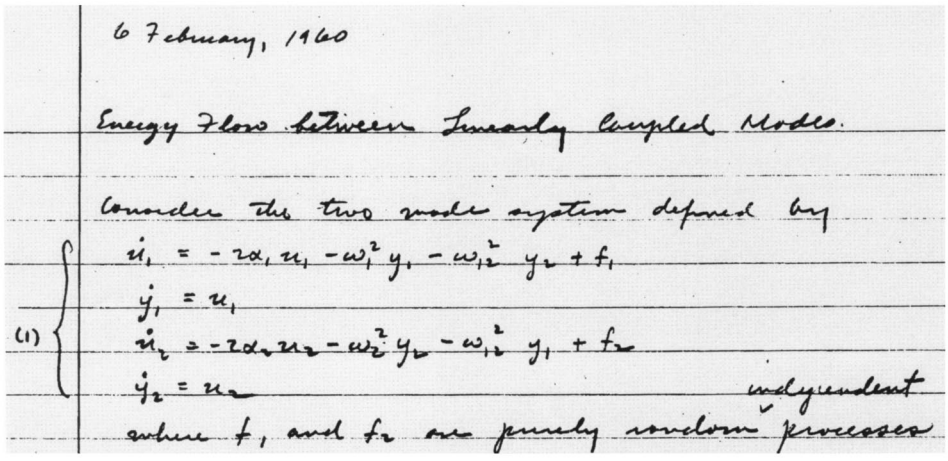

FIG. 3. Excerpt from R. H. Lyon's notebook, written in Manchester in 1960.

linear, so all of the other modes are very weakly connected and they stay cool!

In the early and mid-1960s SEA acquired a name and the applications and extensions of the theory came fast and furious. Those of us lucky to have been participants in the process feel fortunate to have been a part of that group, in that place, and at that time.

[1] J. I. Lawson and G. E. Uhlenbeck, eds., *Threshold Signals (MIT Radiation Laboratory Series*, Vol. 24 (published by McGraw-Hill, New York, 1950; reprinted by Boston Technical, Boston, 1964; reprinted by Dover, New York, 1963), Secs. 4-1–4-5.

[2] R. H. Lyon and G. Maidanik, ''Power flow between linearly coupled oscillators,'' J. Acoust. Soc. Am. **34**, 632–639 (1962).

[3] P. W. Smith, Jr., ''Response and radiation of structural modes excited by sound,'' J. Acoust. Soc. Am. **34**, 640–647 (1962).

Expression for the estimation of time-averaged acoustic energy density using the two-microphone method (L)

Justin Ghan,[a] Ben S. Cazzolato, and Scott D. Snyder
Department of Mechanical Engineering, University of Adelaide, SA 5005, Australia

(Received 12 April 2002; revised 27 January 2003; accepted 24 February 2003)

Acoustic energy density has been shown to exhibit lower spatial variance in reactive sound fields compared to the acoustic potential energy estimate offered by microphones, making it a very useful measure of the acoustic energy within an enclosure. Previously, frequency domain time-averaged energy density estimates have come about by estimating the pressure average and particle velocity between two closely spaced microphones using either analog or digital electronics. A frequency domain expression can be obtained by adding the weighted sum of the auto-spectral densities of both the pressure and particle velocity magnitude. The purpose of this letter is to derive an expression for the time-averaged acoustic energy density in the frequency domain using the auto- and cross-spectral densities between the two closely spaced microphones. The resulting expression is validated numerically. © *2003 Acoustical Society of America.* [DOI: 10.1121/1.1567273]

PACS numbers: 43.60.Qv [AJZ]

I. INTRODUCTION

Acoustic energy density is defined as the sum of the acoustic potential energy density and the acoustic kinetic energy density at a point. It has been shown[1] that energy density provides a significantly better estimate of the total acoustic energy within an enclosure than does the acoustic potential energy (estimated by microphones). Subsequently, several authors have found energy density to be an effective sensor for active noise control applications, as it measures the total energy at a point, and generally outperforms microphones.[2–6]

In the past, estimation of acoustic energy density has been made using one of two methods: time domain experiments or noise-free frequency domain simulations. The time domain method involves the use of additional electronics (either analog or digital) to calculate the pressure average and the particle velocity between the two sensing elements. The time-averaged energy density estimate can then be found by adding the weighted mean squared levels of the pressure and particle velocity. Alternatively, a frequency domain equivalent can be obtained by adding the weighted auto-spectral densities of both the pressure and particle velocity.

Estimation directly in the frequency domain has been limited to simulations where it has been assumed that the amplitudes of the pressure and particle velocity are known, which is clearly not the case in experimental measurements.

The purpose of this letter is to derive an expression for the time-averaged acoustic energy density estimate for the two-microphone method using a purely frequency domain expression suitable for experiments. The need for the additional hardware to estimate the particle velocity is then avoided.

Frequency domain expressions for estimates of potential energy density and kinetic energy density have previously been investigated.[7] However, errors have been found in these derivations.

The approach used here is similar to that used to derive the sound intensity estimate written in terms of the cross-correlation (and consequently the cross-spectral density) between the signals from two closely spaced microphones.[8,9]

The resulting analytical expression is verified using a numerical simulation in the time domain.

II. ANALYTICAL DERIVATION

The instantaneous acoustic energy density, $E_D(t)$, at a point is defined as the sum of the acoustic potential energy density and the acoustic kinetic energy density at that point, given by the expression[10]

$$E_D(t)=\frac{p^2(t)}{2\rho c^2}+\frac{\rho v^2(t)}{2}, \tag{1}$$

where $p(t)$ and $v(t)$ are the instantaneous pressure and particle velocity magnitude, respectively, at that point, c is the speed of sound, and ρ is the mean density of the fluid. The first term in the expression (1) is the acoustic potential energy density, $U(t)$, and the second term is the acoustic kinetic energy density, $T(t)$. Particle velocity is given by

$$v(t)=-\frac{1}{\rho}\int_{-\infty}^{t}\frac{\partial p(\tau)}{\partial x}\mathrm{d}\tau. \tag{2}$$

Using the two-microphone measurement method with a microphone separation distance of $2h$, pressure and particle velocity are approximated by

$$p(t)\approx\frac{p_1(t)+p_2(t)}{2} \tag{3}$$

and

$$v(t)\approx\frac{1}{2\rho h}\int_{-\infty}^{t}[p_1(\tau)-p_2(\tau)]\mathrm{d}\tau. \tag{4}$$

[a]Author to whom correspondence should be addressed. Electronic mail: justin.ghan@adelaide.edu.au

 0001-4966/2003/113(5)/2404/4/$19.00

Therefore, the instantaneous acoustic energy density is approximated by

$$E_{\mathrm{D}}(t) \approx \frac{[p_1(t)+p_2(t)]^2}{8\rho c^2} + \frac{[\int_{-\infty}^{t}[p_1(\tau)-p_2(\tau)]\mathrm{d}\tau]^2}{8\rho h^2}. \tag{5}$$

Elko[7] derives estimates for the double-sided potential energy density spectral density and the double-sided kinetic energy density spectral density in terms of the double-sided auto-spectral densities, $S_{p_1p_1}(\omega), S_{p_2p_2}(\omega)$, and the double-sided cross-spectral density, $S_{p_1p_2}(\omega)$, of the two microphone pressure signals, defined by[11]

$$S_{xy}(\omega) = \lim_{T\to\infty} \frac{1}{T} E[X^{\star}(\omega,T)Y(\omega,T)], \tag{6}$$

in which E denotes the expected value over a number of samples, and $X(\omega,T)$ is the finite Fourier transform of the time series $x(t)$,

$$X(\omega,T) = \int_0^T x(t)e^{-j\omega t}\mathrm{d}t. \tag{7}$$

Elko obtains

$$U(\omega) = \frac{1}{16\rho c^2}(S_{p_1p_1}(\omega) + S_{p_2p_2}(\omega) + 2\,\mathrm{Re}[S_{p_1p_2}(\omega)]), \tag{8}$$

$$T(\omega) = \frac{1}{16\rho\omega^2 h^2}(S_{p_1p_1}(\omega) + S_{p_2p_2}(\omega) - 2\,\mathrm{Re}[S_{p_1p_2}(\omega)]). \tag{9}$$

These expressions are incorrect, as they have been based upon the definitions

$$\overline{U} = \frac{1}{4\rho c^2} E[p(t)p^{\star}(t)], \tag{10}$$

$$\overline{T} = \frac{\rho}{4} E[v(t)v^{\star}(t)]. \tag{11}$$

For these definitions to be valid, $p(t)$ and $v(t)$ must be the complex pressure amplitude and complex velocity amplitude. However, Elko's derivation considers them to be real-valued.

The total time-averaged acoustic energy density is given by

$$\overline{E_{\mathrm{D}}} = \lim_{T\to\infty} \frac{1}{T} E\left[\int_0^T \left[\frac{1}{2\rho c^2}\cdot p^2(t) + \frac{\rho}{2}\cdot v^2(t)\right]\mathrm{d}t\right]. \tag{12}$$

Using Parseval's theorem,[11]

$$\overline{E_{\mathrm{D}}} = \lim_{T\to\infty} \frac{1}{T} E\left[\frac{1}{2\pi}\int_{-\infty}^{\infty}\left[\frac{1}{2\rho c^2}\cdot|P(\omega,T)|^2 + \frac{\rho}{2}\cdot|V(\omega,T)|^2\right]\mathrm{d}\omega\right]. \tag{13}$$

Therefore, the double-sided time-averaged acoustic energy density spectral density is

$$\overline{E_{\mathrm{D}}}(\omega) = \lim_{T\to\infty} \frac{1}{T} E\left[\frac{1}{2\rho c^2}\cdot|P(\omega,T)|^2 + \frac{\rho}{2}\cdot|V(\omega,T)|^2\right]. \tag{14}$$

From Eqs. (3) and (4),

$$P(\omega,T) \approx \frac{P_1(\omega,T)+P_2(\omega,T)}{2}, \tag{15}$$

$$V(\omega,T) \approx \frac{1}{2\rho h}\cdot\frac{P_1(\omega,T)-P_2(\omega,T)}{j\omega}. \tag{16}$$

Therefore,

$$\overline{E_{\mathrm{D}}}(\omega) \approx \lim_{T\to\infty} \frac{1}{T} E\left[\frac{1}{2\rho c^2}\left[\frac{P_1(\omega,T)+P_2(\omega,T)}{2}\right]\times\left[\frac{P_1(\omega,T)+P_2(\omega,T)}{2}\right]^{\star} + \frac{\rho}{2}\left[\frac{1}{2\rho h}\cdot\frac{P_1(\omega,T)-P_2(\omega,T)}{j\omega}\right]\times\left[\frac{1}{2\rho h}\cdot\frac{P_1(\omega,T)-P_2(\omega,T)}{j\omega}\right]^{\star}\right]. \tag{17}$$

Expanding out the brackets and using (6) yields

$$\overline{E_{\mathrm{D}}}(\omega) \approx \left(\frac{1}{8\rho c^2} + \frac{1}{8\rho\omega^2 h^2}\right)(S_{p_1p_1}(\omega) + S_{p_2p_2}(\omega)) + \left(\frac{1}{8\rho c^2} - \frac{1}{8\rho\omega^2 h^2}\right)(S_{p_1p_2}(\omega) + S_{p_2p_1}(\omega)). \tag{18}$$

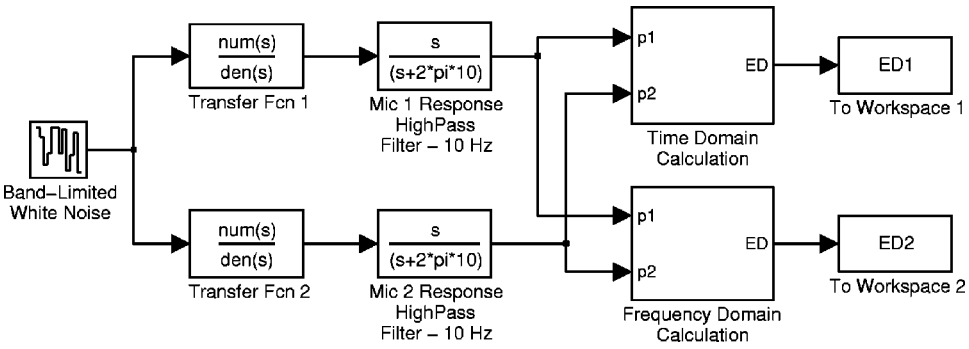

FIG. 1. The simulated sound field. The microphones (separation distance, $2h = 50$ mm) are placed at distances $r_1 = 5.00$ m and $r_2 = 5.05$ m from the monopole noise source. The source produces continuous white noise of 1.0 Pa at 1 m (94 dB re 20 μPa). Speed of sound, $c = 343\ \mathrm{m\cdot s^{-1}}$, and density of air, $\rho = 1.21\ \mathrm{kg\cdot m^{-3}}$. The "time domain calculation" submodel is shown in Fig. 2, and the "frequency domain calculation" submodel is shown in Fig. 3.

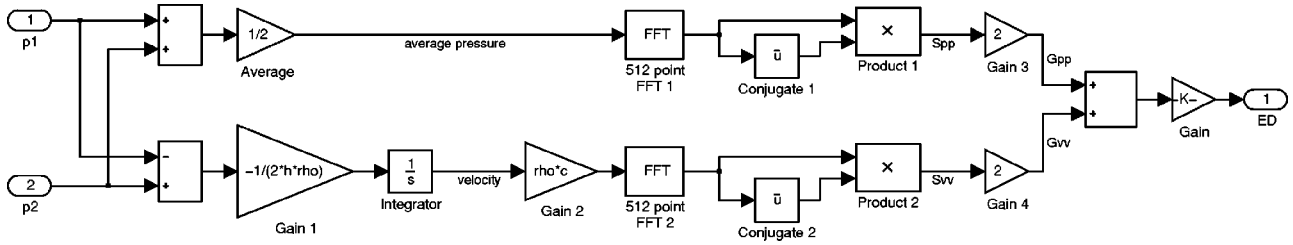

FIG. 2. Model for the calculation of the time-averaged acoustic energy density estimate as the weighted sum of the auto-spectral densities of pressure and particle velocity.

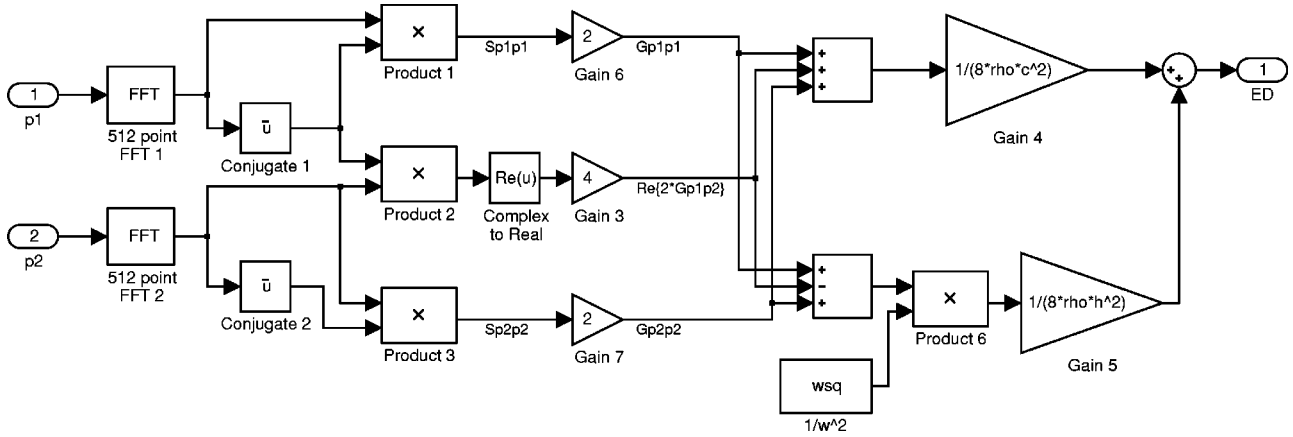

FIG. 3. Model for the calculation of the time-averaged acoustic energy density estimate using the derived expression in terms of the auto- and cross-spectral densities of the two pressure readings.

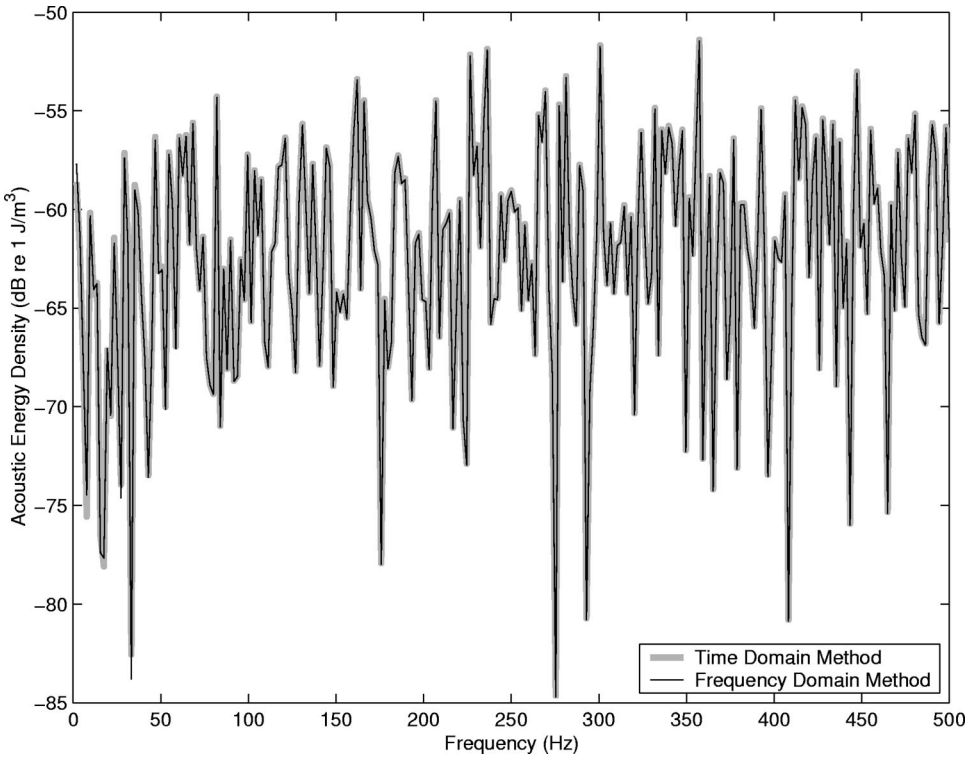

FIG. 4. Time-averaged acoustic energy density estimates using the time domain method and the frequency domain expression.

Since $S_{p_2p_1}(\omega)=S_{p_1p_2}(\omega)^\star$, the double-sided time-averaged acoustic energy density spectral density estimate is given by

$$\overline{E_{\mathrm{D}}}(\omega)\approx\left(\frac{1}{8\rho c^2}+\frac{1}{8\rho\omega^2h^2}\right)(S_{p_1p_1}(\omega)+S_{p_2p_2}(\omega))+\left(\frac{1}{8\rho c^2}-\frac{1}{8\rho\omega^2h^2}\right)(2\,\mathrm{Re}[S_{p_1p_2}(\omega)]). \quad (19)$$

This expression can easily be transformed to produce a corresponding expression for the single-sided time-averaged acoustic energy density spectral density estimate in terms of single-sided spectral densities. This is more useful in practical terms as spectrum analyzers generally calculate single-sided spectra. The single-sided time-averaged acoustic energy density spectral density estimate is given by

$$\overline{E_{\mathrm{D,1\text{-}sided}}}(\omega)\approx\left(\frac{1}{8\rho c^2}+\frac{1}{8\rho\omega^2h^2}\right)(G_{p_1p_1}(\omega)+G_{p_2p_2}(\omega))+\left(\frac{1}{8\rho c^2}-\frac{1}{8\rho\omega^2h^2}\right)(2\,\mathrm{Re}[G_{p_1p_2}(\omega)]), \quad (20)$$

where[11]

$$G_{xy}(\omega)=2S_{xy}(\omega)=\lim_{T\to\infty}\frac{2}{T}E[X^\star(\omega,T)Y(\omega,T)] \quad (21)$$

for $\omega\geqslant 0$, and $G_{xy}(\omega)$ is zero otherwise.

The correct expressions for the single-sided time-averaged potential energy density spectral density and the single-sided time-averaged kinetic energy density spectral density estimates are

$$\overline{U}_{\text{1-sided}}(\omega)\approx\frac{1}{8\rho c^2}(G_{p_1p_1}(\omega)+G_{p_2p_2}(\omega)+2\,\mathrm{Re}[G_{p_1p_2}(\omega)]), \quad (22)$$

$$\overline{T}_{\text{1-sided}}(\omega)\approx\frac{1}{8\rho\omega^2h^2}(G_{p_1p_1}(\omega)+G_{p_2p_2}(\omega)-2\,\mathrm{Re}[G_{p_1p_2}(\omega)]). \quad (23)$$

It can be seen that the estimates (8) and (9) derived by Elko give half the correct values.

III. SIMULINK SIMULATION

Referring to Fig. 1, a Simulink model was created to validate the two-microphone method for measuring acoustic energy density. The model was used to obtain the time-averaged acoustic energy density estimate both by directly calculating the pressure average and particle velocity, and also by using the derived expression (20).

The two microphone pressure signals were calculated by simulating two points in a free space pressure field generated by a white noise point source. The transfer function from a monopole point source to a sensor at distance r is

$$G(s)=\frac{1}{r}e^{-(r/c)s}, \quad (24)$$

where c is the speed of sound. These transfer functions were implemented using a second order Padé approximation in series with a gain.

The instantaneous pressure and particle velocity were estimated using Eqs. (3) and (4) (see Fig. 2). The velocity values were multiplied by ρc so that the two outputs were dimensionally consistent. They were sampled at 1000 Hz, and a frequency spectrum of each was obtained by performing a 512-point FFT (see Fig. 2). The potential and kinetic energy auto-spectral densities were calculated, then summed and scaled by the factor $1/2\rho c^2$ to produce the time-domain-based acoustic energy density spectral density estimate (see Fig. 2).

To compute an estimate directly in the frequency domain, a frequency spectrum of each of the microphone pressure readings was obtained by performing a 512-point FFT (see Fig. 3). The auto- and cross-spectral densities were then calculated, and Eq. (20) was applied to produce the frequency-domain-based acoustic energy density spectral density estimate (see Fig. 3).

A comparison of the results is shown in Fig. 4. The acoustic energy density spectral densities obtained via each method of calculation correspond closely, verifying the derived expression (20).

IV. CONCLUSIONS

An expression for the time-averaged acoustic energy density estimate has been derived using the auto- and cross-spectral densities between two closely spaced microphones. It was validated numerically using a time domain simulation in Simulink. The expression gave identical results to the traditional method using the weighted sum of the squared pressure and particle velocity.

[1] R. K. Cook and P. A. Schade, "New method for the measurement of the total energy density of sound waves," in *Proceedings of Inter-Noise 74*, 1974, pp. 101–106.

[2] S. D. Sommerfeldt and P. J. Nashif, "A comparision of control strategies for minimising the sound field in enclosures," in *Proceedings of Noise-Con 91*, 1991, pp. 299–306.

[3] P. J. Nashif and S. D. Sommerfeldt, "An active control strategy for minimising the energy density in enclosures," in *Proceedings of Inter Noise 92*, 1992, pp. 357–361.

[4] S. D. Sommerfeldt and J. Parkins, "Active control of energy density in three dimensional enclosures," J. Acoust. Soc. Am. **95**, 2989 (1994).

[5] W. Shen and J. Q. Sun, "A study of shell interior noise control," SPIE **3041**, 812–818 (1997).

[6] Y. C. Park and S. D. Sommerfeldt, "Global attenuation of broadband noise fields using energy density control," J. Acoust. Soc. Am. **101**, 350–359 (1997).

[7] G. W. Elko, "Frequency domain estimation of the complex acoustic intensity and acoustic energy density," Ph.D. thesis, The Pennsylvania State University, 1984.

[8] F. J. Fahy, "Measurement of acoustic intensity using the cross-spectral density of two-microphone signals," J. Acoust. Soc. Am. **62**, 1057–1059 (1977).

[9] J. C. Pascal and C. Carles, "Systematic measurement errors with two microphone sound intensity meters," J. Sound Vib. **83**(1), 53–65 (1982).

[10] F. Fahy, *Sound Intensity*, 2nd ed. (E&FN Spon, London, 1995).

[11] J. S. Bendat and A. G. Piersol, *Random Data-Analysis and Measurement Procedures*, 2nd ed. (Wiley, New York, 1986).

Evoked potential recording during echolocation in a false killer whale *Pseudorca crassidens* (L)

Alexander Ya. Supin[a)]
Institute of Ecology and Evolution, Russian Academy of Sciences, 33 Leninsky Prosp., 119071 Moscow, Russia

Paul E. Nachtigall, Jeffrey Pawloski, and Whitlow W. L. Au
Hawaii Institute of Marine Biology, University of Hawaii, Kailua, Hawaii

(Received 21 February 2002; revised 24 January 2003; accepted 27 January 2003)

Auditory brainstem responses (ABRs) were recorded in a false killer whale while the animal echolocated a target. The ABR collection was triggered by echolocation clicks of the animal. In these conditions, the recorded ABR pattern contained a duplicate set of waves. A comparison of ABR wave delays recorded during echolocation with those recorded during regular external stimulation with experimenter generated clicks showed that the first set of waves may be a response to the emitted click whereas the second one may be a response to the echo. Both responses, to the emitted click and to the echo, were of comparable amplitude in spite of the intensity difference of these two sounds that may differ by more than 40 dB near the animal's head. This finding indicates the presence of some mechanism of releasing responses to echoes from masking by loud emitted clicks. The evoked-potential method may be productive to investigate these mechanisms. © *2003 Acoustical Society of America.* [DOI: 10.1121/1.1561497]

PACS numbers: 43.80.Lb, 43.64.Ri [FD]

I. INTRODUCTION

Echolocating dolphins and toothed whales have to hear weak echo signals shortly after emitting intense echolocation sounds. Due to high sound velocity in water, the delay between the emitted and echo sounds may be very short, down to a few ms. To be able to distinguish the emitted clicks and echo sounds, the odontocete auditory system has to have a very high temporal resolution previously demonstrated by a variety of psychophysical and physiological data (Au, 1993; Nachtigall *et al.*, 2000; Supin *et al.*, 2001). Nevertheless, nothing is known about how loudly a dolphin hears its ongoing echolocation click and its corresponding echo, and how much ongoing clicks mask the echoes at various click intensities, target strengths, and distances.

We examined a way to answer this question by recording the brain auditory evoked potentials during natural echolocation in echolocating odontocetes. Evoked potentials directly show whether the brain responds to a sound, thus recording ABRs during echolocation may show whether or not the brain responds to both the emitted click and the echo sound. This preliminary communication describes a first attempt to find out whether this approach is feasible and demonstrates that it really is.

Among a variety of evoked-potential types previously described in whales and dolphins (Supin *et al.*, 2001), the auditory brainstem response (ABR) was used. These evoked-potentials can be recorded noninvasively from the head skin surface and are very consistent and have a rather high amplitude. Short sound clicks similar to the echolocation sounds of dolphins are appropriate stimuli to evoke ABRs (Supin *et al.*, 2001) and can be readily obtained from an animal trained to sit quietly and voluntarily wear suction-cup electrodes.

II. METHODS

A. Experimental conditions

The experiments were carried out in facilities of the Hawaii Institute of Marine Biology, Marine Mammal Research Program. The subject was a false killer whale *Pseudorca crassidens*, an approximately 20-year-old female kept in a wire-net enclosure in Kaneohe Bay, Hawaii. The animal was trained to accept suction-cup electrodes for evoked-potential recording and to ensonify and recognize targets by echolocation and to report the target's presence or absence using a go/no-go reporting paradigm.

B. Echolocation-trial procedure

The animal was trained to detect the presence or absence of a target. Both target present and target absent trials assured that the animal was indeed echolocating the target. The experimental procedure (Fig. 1) was as follows.

(*i*) Each session began with the trainer attaching the suction-cup electrodes with the following configuration; the active electrode was placed at the vertex 7–10 cm behind the blowhole, the reference electrode was placed on the animal's back near the dorsal fin. (*ii*) The animal was sent to a station that was a hoop fixed underwater at a depth of 1 m; the animal swam into the hoop in such a position that the hoop was at a level of the pectoral fins. (*iii*) In target-present trials, the trainer lowered down a target at a position just in front of the animal's head, 1.5 m from the head tip, 1 m below the water surface. The target was an aluminum cylinder 3.8 cm in diameter, 12.7 cm long, axis vertical, with a

[a)]Electronic mal: a.supin@g23.relcom.ru

 0001-4966/2003/113(5)/2408/4/$19.00

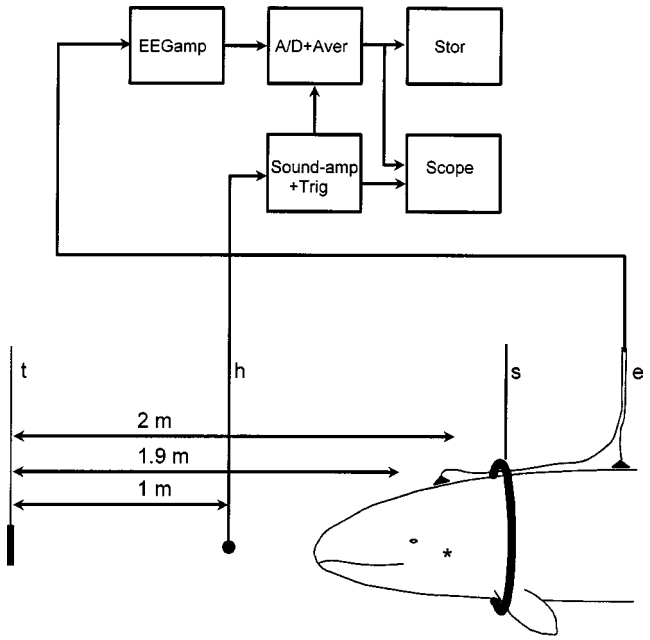

FIG. 1. Relative positions of the animal and equipment during experiments and block-diagram of data acquisition during echolocation trials. t—target (in echolocation trials) or transducer (in external-pulse trials), h—hydrophone, s—hoop station, e—electrodes, EEGamp—EEG amplifier, A/D+Aver—analog-to-digital converter and averager, Store—data storage, Sound-amp+Trig—sound amplifier and trigger, and Scope—monitoring oscilloscope. Distance from the target (transducer) to the animal's ears—2.0 m, distance to the expected sound-production region—1.9 m, distance to the triggering hydrophone—1 m.

target strength of -25 dB. Target-absent trials were exactly the same as target present trials except no target was presented. (iv) When the target was presented, the animal was required to signal its detection by leaving the hoop and touching a signal ball, then coming for the fish reward. In no-target trails, the animal was required to wait until it was signaled to leave the hoop and come for the fish reward.

Lowering down the target provoked the animal to ensonify it by a train of clicks. These clicks were recorded through a B&K-8103 hydrophone positioned in front of the animal's head at a distance of 1 m before the target, and electrical brain activity was recorded through the suction-cup electrodes, amplified by 5×10^4 within a frequency range of 200 to 5000 Hz.

Echolocation target detection performance by the animal remained high during testing. The animal was correct on 140 of the 147 target present trials and 70 of the 70 target absent trials for an overall correct performance level of 97%.

C. ABR data acquisition

To extract low-amplitude ABR from the background noise, a coherent-averaging procedure was used. The averaging was performed in two steps: within-trial on-line averaging (see block-diagram in Fig. 1) and intertrial off-line averaging. For on-line averaging, a series of echolocation clicks were recorded by the hydrophone (190–200 dB re 1 μPa p/p). These echolocation clicks were used as triggering signals. After each click, a 10-ms long window (sweep) of evoked-potential recording was picked up, all the sweeps within the trial were averaged, and the result was stored in computer memory. The number of averaged sweeps was not constant; it varied from trial to trial depending on the number of triggering clicks picked up. In target-present trials, the number of picked-up clicks was regularly from 10 to 30. Therefore, to obtain an ABR record of good signal-to-noise ratio, 20 to 40 similar trials were made during each experiment, and all records obtained in one experiment were then averaged off-line. In target-absent trials, the animal only required a few clicks to make its decision; therefore, it was not possible to collect satisfactory ABR records during target-absent trials.

D. Passive external pulse trials

For comparison, the ABR to regular passive external stimuli were recorded. For that, the animal was sent to the same position in the hoop station as in echolocation trials. A train of wideband sound clicks was emitted through a transducer placed at a position of 1.5 m in front of the animal's head tip (500 clicks, 150 dB re 1 μPa p/p, at a rate of 20/s, click peak frequency 35 kHz, bandwidth 75 kHz at a -10-dB level, 150 kHz at a -20-dB level). Responses to all clicks in the train were averaged to obtain a single ABR record; the averaging was triggered at the instant of sound emission.

III. RESULTS AND DISCUSSION

Obtained records are presented in Figs. 2(a)–(e). The ABRs to external stimuli [Fig. 2(a)] looked very similar to those described previously in a number of dolphin species (Supin *et al.*, 2001). They consisted of a number of rapid waves (each shorter than 1 ms), the latest ones designated as P and N (positive and negative, respectively) of the largest amplitude. The ABR amplitude was rather small (about 0.45 μV), which is characteristic of underwater ABR recording when potentials at the body surface are shunted by low-impedance sea water.

During echolocation, ABRs with an amplitude of 0.2 to 0.25 μV were recorded [Figs. 2(b)–(e)]. It is a little less but comparable with amplitude obtained with external stimulation. It should be noted, however, that when evoked-response averaging was triggered by signals from a hydrophone, there were possibly some number of ''false'' sweeps that were triggered by external noises, not locating clicks. These false sweeps do not contain ABRs. Being averaged together with click-triggered ABR-containing sweeps, the false sweeps may result in decreased amplitude of the records.

A distinctive feature of ABRs recorded during echolocation was a duplicate set of waves designated in Figs. 2(b)–(e) as P1–N1 and P2–N2, respectively. The delay between corresponding waves (P1 to P2, as well as N1 to N2) was 2.2 ms.

For comparative analysis of ABRs obtained during external stimulation and echolocation, all the records in Figs. 2(a)–(e) are presented in such a way that the zero point of time scale corresponds to the expected instant of sound arrival to the animal's ears. At external stimulation [Fig. 2(a)],

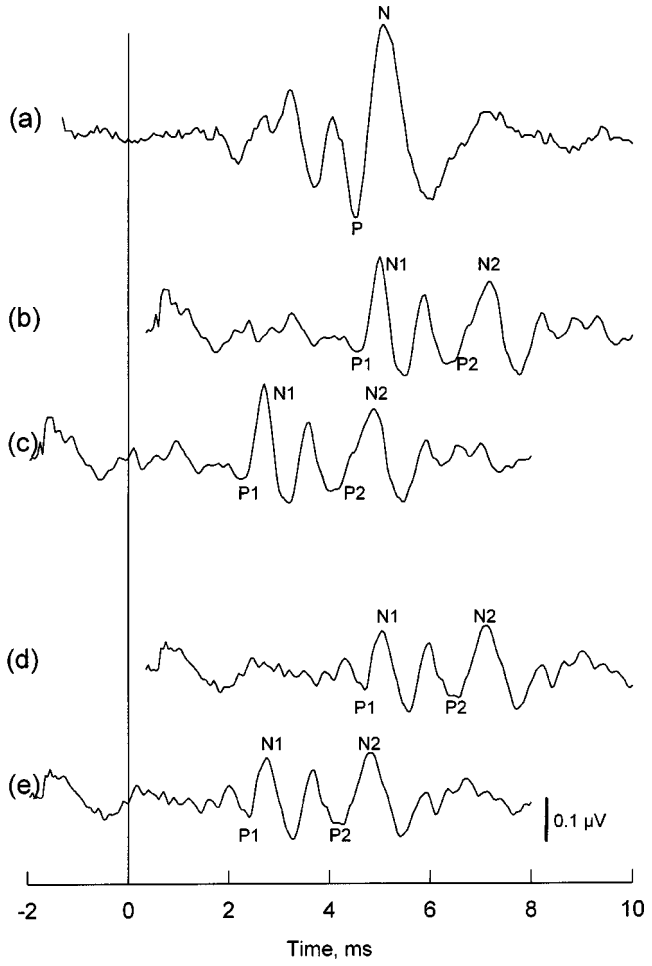

FIG. 2. ABR records. (a) ABR to external stimulus (click); P—the largest positive wave, N—the largest negative wave (negativity upward). (b) and (c) ABR to echolocation clicks at different shifts along the time scale (see text); P1 and N1—positive and negative waves assessed as a response to the emitted locating signal, P2 and N2—waves assessed as a response to the echo-signal. (d) and (e)—the same as (b) and (c), another experiment.

the record beginning corresponds to the sound emission by the transducer at a distance of 2.0 m from the ears that corresponds (taking the sound velocity of 1530 m/s) to an acoustic delay of 1.31 ms; therefore the record in Fig. 2(a) begins at a time-scale point of -1.31 ms.

In Fig. 2(b), the record obtained in echolocation conditions is presented in such a way that the zero time-scale point corresponds to the expected instant of arrival of the *sound emitted by the animal* to the animal's ears. We assumed that the distance between the region of the nasal sacs (which is an expected region of sound generation) and the triggering hydrophone was about 0.9 m which corresponds (assuming that sound velocity in body tissues is close to that in water) to an acoustic delay of 0.59 ms. The distance between the same region and the animal's ears is taken to be about 0.35 m, which corresponds to an acoustic delay of 0.23 ms. Thus, the sound reached the ears approximately $0.59-0.23=0.36$ ms *before* the triggering, so the record at Fig. 2(b) begins at a point of $+0.36$ ms. With this time positioning of the record, it becomes clear that the complex of P1–N1 waves in Fig. 2(b) corresponds well to the P–N complex of Fig. 2(a). Thus, there is a good reason to consider the P1–N1 complex as an ABR to the emitted echolocation click.

Figure 2(c) presents the same record as Fig. 2(b), but positioned in such a way that the zero time-scale point corresponds to the expected instant of arrival of the *echo sound* to the animal's ear. We took that the distance between the triggering hydrophone to the target was 1 m, which corresponded to an acoustic delay of 0.65 ms. Then, the distance from the target to the animal's ears was 2.0 m, which corresponded to an acoustic delay of 1.31 ms. Thus, we expected that the echo sound reached the animal's ears $0.65+1.31=1.96$ ms *after* triggering. So the record in Fig. 2(c) begins at a point of -1.96 ms. With such positioning, it is clear that the complex of P2–N2 waves in Fig. 2(c) corresponds well to the P–N complex in Fig. 2(a). Therefore, there is a good reason to consider the P2–N2 complex as an ABR to the echo sound.

Figures 2(d) and (e) present a record obtained in another experiment with just the same conditions as that in Figs. 2(b) and (c) and again presented twice in the same manner with the same time shifts. It demonstrates just the same relations between ABR waves obtained in external-stimulation and echolocation conditions.

Thus we can conclude that both the emitted click and echo sound evoked a definite ABR in our experiments. It is particularly noteworthy that the both of the ABRs (P1–N1 and P2–N2) are of almost equal amplitude. Meanwhile, the intensities of the emitted click and echo greatly differ. As indicated above, the target strength was -25 dB, that is, the echo level at a distance of 1 m from the target was 25 dB less than the locating click level near the target. Near the animal's ears (at a distance of 2 m from the target) or the lower jaw that may be an ''acoustic window'' (a little less than 2 m from the target), the echo intensity should be 5 to 6 dB less than at the 1-m distance. On the other hand, the emitted click intensity just in front of the animal's head (say, at a distance of 0.5 m from the sound source) is expected to be at least 10 to 12 dB higher than that near the target located at a three to four times longer distance from the sound source (near 1.5 m from the melon tip, or near 2 m from the nasal sacs). Thus, the emitted click intensity near the animal's head might be 40–43 dB higher that the intensity of perceived echo. The fact that both these signals evoked ABR of almost equal amplitude indicates that there is some acoustical (e.g., attenuation of sound transmission from the sound generator to the ears) or (and) a neurophysiological mechanism of releasing responses to echoes from masking by loud emitted clicks. The preliminary results presented herein show that the evoked-potential method may be a very productive method to investigate these mechanisms in an actively echolocating animal.

ACKNOWLEDGMENTS

The study was supported in part by the U.S. National Science Foundation's Collaboration in Basic Science and Engineering Program administered by the National Academy of Sciences, by the U.S. Office of Naval Research, and by the Russian Foundation for Basic Research, Grant No. 00-15-97769.

Au, W. W. L. (**1993**). *The Sonar of Dolphins* (Springer-Verlag, New York).
Nachtigall, P. E., Lemonds, D. W., and Roitblat, H. L. (**2000**). ''Psychoacoustic studies of dolphin and whale hearing,'' in *Hearing by Whales and Dolphins*, edited by W. W. L. Au, A. N. Popper, and R. R. Fay (Springer-Verlag, New York), pp. 330–364.
Supin, A. Y., Popov, V. V., and Mass, A. M. (**2001**). *The Sensory Physiology of Aquatic Mammals* (Kluwer, Boston).

Theory and experiment of Fourier–Bessel field calculation and tuning of a pulsed wave annular array

Paul D Fox[a)]
Ørsted.DTU, Technical University of Denmark, Building 348, DK-2800 Lyngby, Denmark

Jiqi Cheng[b)] and Jian-yu Lu[c)]
Ultrasound Laboratory, Department of Bioengineering, University of Toledo, 2801 West Bancroft Street, Toledo, Ohio 43606-3390

(Received 1 June 2001; revised 1 October 2002; accepted 16 January 2003)

A one-dimensional (1D) Fourier–Bessel series method for computing and tuning (beamforming) the linear lossless field of flat pulsed wave annular arrays is developed and supported with both numerical simulation and experimental verification. The technique represents a new method for modeling and tuning the propagated field by linking the quantized surface pressure profile to a known set of limited diffraction Bessel beams propagating into the medium. This enables derivation of an analytic expression for the field at any point in space and time in terms of the transducer surface pressure profile. Tuning of the field then also follows by formulating a least-squares design for the transducer surface pressure with respect to a given desired field in space and time. Simulated and experimental results for both field computation and tuning are presented in the context of a 10-ring annular array operating at a central frequency of 2.5 MHz in water. © *2003 Acoustical Society of America.* [DOI: 10.1121/1.1560211]

PACS numbers: 43.20.Bi, 43.20.−f, 43.38.Hz [ANN]

I. INTRODUCTION

In this article we describe a method for computing and tuning linear lossless fields from flat pulsed wave (PW) annular arrays by using a one-dimensional (1D) Fourier–Bessel series.[1,2] The use of this series allows the propagated field to be described as a polychromatic set of nondiffracting J_0 Bessel beams[3,4] giving a linear mapping between the spatial quantization levels on the transducer surface and the propagated field at any point in space. The technique leads to a new method for both the tuning and fast computation of PW annular fields.

Bessel beams are the components of polychromatic X waves[5] and have been studied extensively in recent years.[5–13] Theoretically, nondiffracting beams such as Bessel beams and X waves can propagate superluminally (at a speed $c/\cos\zeta$ where c is the speed of sound and ζ is the Axicon angle[14,15]), to an infinite distance without spreading if they are produced with an infinite aperture and energy. In practice, nearly exact X waves can still be realized with either broadband or band-limited radiators over deep depth of field[5] and for this reason, these and other related beams[7,9,10,16–21] have been studied extensively for medical imaging,[22–24] tissue property identification,[25] blood flow velocity vector measurement,[26] nondestructive evaluation of materials,[27] communications,[28] electromagnetics,[29] and optics.[4,30]

The present study draws on previous knowledge of Bessel beams and X waves to formulate a method for both computing and tuning (beamforming) the propagated field by using a set of Bessel beam basis functions. In Refs. 31 and 32 these were applied across the transducer surface to decompose the emitted field into a known set of limited diffraction Bessel beams. In this article the analysis is extended to solve for the emitted field itself as a weighted set of exact Bessel solutions to the wave equation and study the method for polychromatic (pulsed) waves. We show that the method correlates well with both previous experimental results[6] and simulations based on the Rayleigh–Sommerfeld diffraction formula. The method also allows us to tune the PW field in a least-squares sense with respect to a given desired PW field distribution by choosing the transducer surface quantization levels accordingly.

In Sec. II model definitions for the governing wave equation and structure of PW annular arrays are introduced. Section III then explains the application and interpretation of 1D Fourier–Bessel series and Sec. IV develops a method for computing the propagated field using these series. Section V gives numerical examples of the field computation for X waves and focused Gaussian pulses, comparing them also to experimental data and a classical (Rayleigh–Sommerfeld) field calculation method. In Sec. VI a least-squares field tuning design is given, followed in Sec. VII by numerical examples for X waves and focused Gaussian pulses. Finally, Sec. VIII summarizes, draws conclusions, and suggests further work.

II. MODEL DEFINITIONS

A. Propagation model

Annular arrays have circular symmetry and correspondingly the resulting propagation in linear free space is dictated by the circular-symmetric wave equation

[a)]Electronic mail: pdf@oersted.dtu.dk
[b)]Electronic mail: jcheng@eng.utoledo.edu
[c)]Electronic mail: jilu@eng.utoledo.edu

 0001-4966/2003/113(5)/2412/12/$19.00

$$\left[\frac{1}{r}\frac{\partial}{\partial r}\left(r\frac{\partial}{\partial r}\right)+\frac{\partial^2}{\partial z^2}-\frac{1}{c^2}\frac{\partial^2}{\partial t^2}\right]f(r,z,t)=0, \tag{1}$$

where $f(r,z,t)$ is the scalar field value, r is the radial distance from the cylindrical centerline, z is the outward propagation distance perpendicular to the transducer surface (sitting in the $z=0$ plane and centered around $r=0$), and c is the speed of sound (assumed real). This equation has an infinite number of Bessel beam solutions[4,5] of the form

$$\begin{aligned} &f(r,z,t,\omega)=J_0(\alpha r)e^{j\beta z}e^{-j\omega t},\\ &\beta=\sqrt{k^2-\alpha^2}:\quad k=\omega/c, \end{aligned} \tag{2}$$

where k is the wave number (real) and α any real nonnegative value ($\alpha\geqslant 0$).

Notice that for $\alpha>k$, the axial parameter $\beta=\sqrt{k^2-\alpha^2}$ becomes imaginary and in this case $f(r,z,t,\omega)$ decays exponentially rapidly in the z direction. In particular, it becomes an evanescent wave for large enough β and this will become a key property in the development of the field calculation. The other important property is that at $z=0$ the field is $f(r,0,t,\omega)=J_0(\alpha r)\cdot e^{-j\omega t}$, and therefore a pressure profile $J_0(\alpha r)e^{-j\omega t}$ at $z=0$ necessarily gives rise to a propagating Bessel beam (2). Therefore, if it is possible to describe the field over an annular transducer's surface as a sum of terms of the type $f(r,0,t,\omega)=J_0(\alpha r)e^{-j\omega t}$ with different α and β values, the propagating field in linear media becomes the summation of each individual field given by Eq. (2). And since Eq. (2) is an equation not involving costly numerical computations such as integration, this approach demonstrates potential for fast field computation.

B. PW annular arrays

We consider flat annular N-ring PW arrays of radius R with surface pressure $q(r,t)$, which are quantized spatially in the radial r direction due to their ring structure. This results in N sequentially discretized pressure profiles $q_p(t)$, where $p=1,\ldots,N$ is the ring number and $p=1$ for the inner ring with $p=N$ for the outer ring. Time and frequency domain representations $q_p(t)$ and $Q_p(\omega)$ for each ring p are linked formally by the continuous Fourier transform pair

$$\begin{aligned} Q_p(\omega)&=\int_{-\infty}^{\infty}q_p(t)e^{j\omega t}dt\\ &\Leftrightarrow q_p(t)=\frac{1}{2\pi}\int_{-\infty}^{\infty}Q_p(\omega)e^{-j\omega t}d\omega, \end{aligned} \tag{3}$$

although we assume here a sampled system with fixed pulse repeat frequency such that the system is represented by the discrete Fourier sum

$$\begin{aligned} &q_p(t_d)=\sum_{s=0}^{n_\omega}Q_p(\omega_s)e^{-j\omega_s t_d}:\quad \omega_s=s2\pi f_0\\ &Q_p(\omega_s)=\mathrm{FFT}\{q_p(t_d)\}\Leftrightarrow q_p(t_d)=\mathrm{IFFT}\{Q_p(\omega_s)\}, \end{aligned} \tag{4}$$

where n_ω is the number of nonzero Fourier frequencies, f_0 denotes fundamental frequency in hertz, and t_d denotes a discrete sampling point in time. The notation $\mathrm{FFT}\{q_p(t_d)\}$ denotes taking the fast fourier transform (FFT) of $q_p(t)$ and $\mathrm{IFFT}\{Q_p(\omega_s)\}$ denotes the inverse fast fourier transform (IFFT) of $Q_p(\omega_s)$. Hence the entire array of all N rings may then be represented as

$$\begin{bmatrix} q_1(t_d)\\ \vdots\\ q_N(t_d)\end{bmatrix}=\sum_{s=0}^{n_\omega}\begin{bmatrix} Q_1(\omega_s)\\ \vdots\\ Q_N(\omega_s)\end{bmatrix}e^{-j\omega_s t_d} \tag{5}$$

in which each entry $Q_p(\omega_s)$ for $p=1,\ldots,N$ is generally complex

$$Q_p(\omega_s)=\gamma_p(\omega_s)+j\,\delta_p(\omega_s) \tag{6}$$

with $\gamma_p(\omega_s)$ and $\delta_p(\omega_s)$ being the real and imaginary parts of $Q_p(\omega_s)$, respectively. This corresponds to each ring emitting pressure $Q_p(\omega_s)e^{-j\omega_s t_d}=|Q_p(\omega_s)|e^{j\theta_p(\omega_s)}e^{-j\omega_s t_d}=|Q_p(\omega_s)|e^{-j\omega_s(t_d-\tau_p(\omega_s))}$, where $|Q_p(\omega_s)|$, $\theta_p(\omega_s)$, and $\tau_p(\omega_s)$ are the respective ring magnitudes, phases, and time delays obtained from Eq. (6) as

$$\begin{aligned} &|Q_p(\omega_s)|=\sqrt{\gamma_p(\omega_s)^2+\delta_p(\omega_s)^2},\\ &\theta_p(\omega_s)=-j\ln(Q_p(\omega_s)/|Q_p(\omega_s)|),\\ &\tau_p(\omega_s)=\theta_p(\omega_s)/\omega_s. \end{aligned} \tag{7}$$

III. USE OF 1D FOURIER–BESSEL SERIES

A. Application of infinite series

A 1D Fourier-Bessel series[1,2] may be used to model the quantized surface pressure $q(r,\omega_s)$ at each frequency ω_s in Eq. (4) by an infinite set of known basis Bessel functions as

$$\begin{aligned} &Q(r,\omega_s)=\sum_{i=1}^{\infty}A_i(\omega_s)J_0(\alpha_i r),\\ &\alpha_i=x_i/a:\quad J_0(x_i)=0,\\ &A_i(\omega_s)=\frac{2}{a^2J_1^2(x_i)}\int_0^a q(r,\omega_s)rJ_0(\alpha_i r)dr, \end{aligned} \tag{8}$$

where $J_0(\cdot)$ is the Bessel function of the first kind of order zero and x_i in Eq. (8) are the known infinite set of (real) monotonically increasing positive solutions to $J_0(x_i)=0$. This series applies over the range $0\leqslant r\leqslant a$ for any choice of modeling aperture a, subject to $Q(a,\omega_s)=0$ due to $J_0(\alpha_i a)=J_0(x_i)=0$ for all i. (Note also that for ease of discussion, we use the term *aperture* here to refer to the modeling radius a rather the full diameter $2a$.) For annular arrays, we may therefore select any value $a>R$ since the surface pressure $Q(r,\omega_s)$ is considered to be zero for $r\geqslant R$ in the transducer plane $z=0$.

The spatial profile $Q(r,\omega_s)$ for a given ω_s is stepwise constant $Q(r,\omega_s)=Q_p(\omega_s)$ for the N rings $p=1,\ldots,N$ present over the radial range $0\leqslant r\leqslant R$. Beyond this range it becomes $Q(r,\omega_s)=0$ for $R<r\leqslant a$ and together these two consecutive ranges allow $A_i(\omega_s)$ in Eq. (8) to be evaluated analytically as

$$\begin{aligned} &A_i(\omega_s)=\sum_{p=1}^{N}C_{i,p}Q_p(\omega_s),\\ &C_{i,p}=2[r_p^+J_1(\alpha_i r_p^+)-r_p^-J_1(\alpha_i r_p^-)]/ax_iJ_1^2(x_i), \end{aligned} \tag{9}$$

where $J_1(\cdot)$ is the first-order Bessel function of the first kind and r_p^-, r_p^+ are inner and outer radii of ring p, respectively. [Hence $r_1^-=0$ (transducer center) and $r_N^+=R$ (transducer outer edge) by definition, with the kerf between successive rings being $r_p^- - r_{p-1}^+$ for $p=2,\ldots,N$.] Note also that the quantities $A_i(\omega_s)$ are complex since $Q_p(\omega_s)$ in Eqs. (4)–(6) are complex and only $C_{i,p}$ in Eq. (9) are real. See Ref. 13 for a more detailed numerical insight from the equivalent terms in the cw case.

Returning then to Eq. (8), the result is that the annular transducer pressure has now become equivalent to the infinite sum of weighted Bessel functions $Q(r,\omega_s)$. Hence, when multiplied through by their common temporal component $e^{-j\omega_s t}$, the transducer pressure becomes $Q(r,\omega_s)e^{-j\omega_s t}=\Sigma_{i=1}^{\infty}A_i(\omega_s)J_0(\alpha_i r)e^{-j\omega_s t}$ in which each weighted component $J_0(\alpha_i r)e^{-j\omega_s t}$ is a Bessel beam solution (2) to the wave equation (1) at $z=0$. Correspondingly, an infinite set of known Bessel beams propagate into the medium as

$$f(r,z,t,\omega_s)=\sum_{i=1}^{\infty}A_i(\omega_s)J_0(\alpha_i r)\cdot e^{j\beta_i(\omega_s)z}e^{-j\omega_s t},$$
$$\beta_i(\omega_s)=\sqrt{k_s^2-\alpha_i^2}:\quad k_s=\omega_s/c, \tag{10}$$

where $A_i(\omega_s)\cdot J_0(\alpha_i r)e^{j\beta_i(\omega_s)z}e^{-j\omega_s t}$ is the full Bessel solution for $z\neq 0$ to Eq. (1), $k_s=\omega_s/c$ is the wave number, and α_i, $\beta_i(\omega_s)$ are the propagation parameters in the radial and axial directions r, z, respectively.

B. Truncation to finite series

Now consider the behavior of $\beta_i(\omega_s)$ in Eq. (10) as the coefficient index i changes. The scaling parameters $\alpha_i=x_i/a$ in Eq. (8) increase monotonically with index i for a given value of a since the roots $x_i\approx\pi i-\pi/4$ increase monotonically with i by definition. Hence a change in propagation characteristics occurs for the distinct cases $\alpha_i\leqslant k_s$ and $\alpha_i>k_s$ since the wave number k_s is real and hence $\beta_i(\omega_s)$ is purely real when $\alpha_i\leqslant k_s$ but purely imaginary when $\alpha_i>k_s$. For the case of real $\beta_i(\omega_s)$, all the corresponding components in Eq. (10) propagate to infinity due to $|e^{j\beta_i(\omega_s)z}|=1$ even as $z\to\infty$. However, for the case of imaginary $\beta_i(\omega_s)$, the corresponding components usually all become evanescent since $e^{-|\beta_i(\omega_s)|z}\ll 1$ even for very small values of z in typical ultrasonic applications. Notice also from the definition of $\beta_i(\omega_s)$ in Eq. (10) that the evanescent terms $e^{-|\beta_i(\omega_s)|z}$ decay more and more rapidly with respect to z as i increases since $|\beta_i(\omega_s)|$ increases monotonically with i for all values $\alpha_i>k_s$. This means that even if a certain number of $\alpha_i>k_s$ terms are retained for a given application, all higher terms in the series may always be neglected by definition. (See Ref. 13 for a more detailed numerical discussion in the cw case.) Therefore only the nonevanescent beam components are considered for most practical purposes, and denoting $l(k_s,a)$ as the appropriate number of nonnegligible components for a given application, the infinite sum in Eq. (10) becomes replaced by the finite limited diffraction sum

$$f(r,z,t,\omega_s)=\sum_{i=1}^{l(k_s,a)}A_i(\omega_s)J_0(\alpha_i r)e^{j\beta_i(\omega_s)z}e^{-j\omega_s t}. \tag{11}$$

This truncation limit $l(k_s,a)$ may also be estimated analytically by replacing k with k_s in the expression for $l(k,a)$ derived previously in Refs. 13 and 32 to obtain

$$l(k_s,a)\approx k_s a/\pi+1/4, \tag{12}$$

which is proportional to wave number k_s and modeling aperture a, but independent of any particular transducer pressure $Q(r,\omega_s)$.

IV. THEORY FOR FIELD COMPUTATION

A. Field computation theory based on Fourier–Bessel series

When implemented over an infinite aperture ($a\to\infty$), the entire transducer plane at $z=0$ from $r=0$ to $r=\infty$ at $z=0$ becomes modeled by the Fourier–Bessel series. Then the propagating field at time t_d is given by the infinite aperture implementation of Eq. (11), namely

$$f(r,z,t_d,\omega_s)=F(r,z,\omega_s)e^{-j\omega_s t_d},$$
$$F(r,z,\omega_s)=\lim_{a\to\infty}\sum_{i=1}^{l(k_s,a)}J_0\left(\frac{x_i r}{a}\right)e^{j\beta_i(\omega_s)z}\times\left[\sum_{p=1}^{N}C_{i,p}(\gamma_p(\omega_s)+j\,\delta_p(\omega_s))\right], \tag{13}$$

and the complex terms $F(r,z,\omega_s)$ are obtained from Eqs. (11), (9), and (6). Notice from Eq. (13) that the terms $F(r,z,\omega_s)$ are Fourier coefficients mapping the transducer surface pressures $Q_p(\omega_s)=\gamma_p(\omega_s)+j\,\delta_p(\omega_s)$ to the field $f(r,z,t_d,\omega_s)$ at arbitrary positions r, z. Hence defining the total field $f(r,z,t_d)$ as the sum $\Sigma_{s=0}^{n_\omega}f(r,z,t_d,\omega_s)$ of all subfields $f(r,z,t_d,\omega_s)$ in Eq. (13) gives

$$f(r,z,t_d)=\sum_{s=0}^{n_\omega}F(r,z,\omega_s)e^{-j\omega_s t_d}$$
$$\Rightarrow f(r,z,t_d)=\mathrm{IFFT}\{F(r,z,\omega_s)\}, \tag{14}$$

which is to say that the field $f(r,z,t_d)$ may now, in principle, be evaluated rapidly as an IFFT operation for any point in space and from any set of transducer surface pressures $Q_p(\omega_s)$.

However, a numerical problem appears at this point with regard to implementation. Equation (12) indicates $l(k_s,a)\to\infty$ as $a\to\infty$, and hence an infinite number of terms need to be summed in Eq. (13) to evaluate $F(r,z,\omega_s)$. This occurs as the difference $\alpha_i-\alpha_{i-1}\approx\pi/a$ between successive α_i values in Eq. (8) decreases as a increases, and hence more and more α_i terms appear in the nonevanescent range $0\leqslant\alpha_i\leqslant k_s$ as a increases. Clearly it is impossible to compute an infinite number of terms in practice, but the following scheme may be implemented to circumvent the problem. First replace the infinite limit $a\to\infty$ in Eq. (13) with a smaller fixed value of a, such as $a=10R$. Obtain an estimate of $F(r,z,\omega_s)$ from Eq. (13) based on $a=10R$ and then increase a to $a=15R$. Obtain a revised estimate of $F(r,z,\omega_s)$ based on $a=15R$ and

compare it to the estimate obtained for $a=10R$. If significantly different, increase a to $a=20R$ and compare estimates for $a=20R$ with $a=15R$. Continue to increase a until estimates for $F(r,z,\omega_s)$ based on successive values of a effectively converge to constant values. Take the converged estimate of $F(r,z,\omega_s)$ as the final practical approximation to the limiting case $a\to\infty$ and use this value for insertion into the IFFT operation of Eq. (14). See Ref. 13 for a detailed illustration of this convergence method at a given propagation frequency.

In practice we have found that convergence typically occurs at relatively modest values of a, such as $a=20R$. Therefore $a=10R$, $a=15R$, $a=20R$ has been adopted as the default convergence test sequence for the numerical examples given later in this paper. The convergence test itself was defined as the value of a for which the change in magnitude $|F(r,z,\omega_s)|$ between latest and previous value of a dropped to within 0.1% of the magnitude $|F(r,z,\omega_s)|$ for the previous value of a. The field calculation results obtained then proved both fast and accurate when compared against the Rayleigh–Sommerfeld field calculation technique. (See Sec. V for examples and discussion.)

B. Algorithm for field calculation

The field calculation algorithm resulting from Secs. II–IV may now be summarized as follows:

(1) If not known a priori, obtain the Fourier coefficients $Q_p(\omega_s)=\mathrm{FFT}\{q_p(t_d)\}$ for $p=1,...,N$ from Eq. (4).
(2) Set frequency index to $s=0$.
(3) Select initial modeling aperture a (e.g., $a=10R$, $a=15R$, $a=20R$, etc.).
(4) Estimate the corresponding number of nonevanescent terms $l(k_s,a)$ from Eq. (12).
(5) Evaluate coefficients $C_{i,p}$ for $i=1,\ldots,l(k_s,a)$ from Eq. (9).
(6) Evaluate $F(r,z,\omega_s)$ based on Eq. (13) but with the infinite limit $a\to\infty$ removed.
(7) Increase i beyond $i=l(k_s,a)$ to ensure that evanescence occurs for z regions of interest when $\alpha_i>k$ [i.e., check for any significant changes in $F(r,z,\omega_s)$]. Stop increasing i when no significant changes are detected.
(8) Compare current evaluation of $F(r,z,\omega_s)$ with that for previous value of a. If not converged to within satisfactory limit, increase the value of a and go back to step (4).
(9) If $s<n_\omega$, increase s by 1 and go back to step (3).
(10) Evaluate the field as $f(r,z,t_d)=\mathrm{IFFT}\{F(r,z,\omega_s)\}$ from Eq. (14) based on all coefficients $F(r,z,\omega_s)$.

V. EXAMPLES OF FIELD COMPUTATION

A. Transducer geometry and simulated transducer data

For numerical examples of both field computation in this section and tuning in Sec. VII, we consider the PZT ceramic/polymer composite J_0 Bessel transducer of Lu and Greenleaf described in Ref. 6. The experimental setup for the experiment results quoted later in this paper are also described therein. The transducer is an $N=10$-ring Bessel design transducer whose ring edges are located nominally at the first 10 zeros of $J_0(\alpha r)$, where $\alpha=1202.45\ \mathrm{m}^{-1}$. In practice this transducer also has a kerf of approximately 0.2 mm, such that in terms of the notation of Sec. II B, $r_1^-=0$, $r_1^+=x_1/\alpha-\mathrm{kerf}/2$, $r_2^-=x_1/\alpha+\mathrm{kerf}/2$, and so on. The outer radius is also truncated from the nominal $R=25.48$ mm to $R=25$ mm in practice, and operating conditions are a central frequency of $f_c=2.5$ MHz ($\omega_c=15.71\ \mathrm{Mrad\,s}^{-1}$) in water at speed of sound $c=1500\ \mathrm{m\,s}^{-1}$ giving central wave number $k_c=10{,}471.98\ \mathrm{m}^{-1}$. In addition, the transfer function of the transducer is modeled as a Blackman window $B(\omega_s)$:

$$\begin{aligned} B(\omega_s)&=0.42-0.5\cos(\pi\omega_s/\omega_c)\\ &\quad+0.08\cos(2\pi\omega_s/\omega_c):\quad 0\leqslant\omega_s\leqslant 2\omega_c,\\ B(\omega_s)&=0:\quad \omega_s>2\omega_c, \end{aligned} \tag{15}$$

which exhibits zero phase shift for all ω_s, with $B(0)=0$ and $B(\omega_s)$ peaking at the central frequency $f_c=2.5$ MHz and possessing a -6 dB bandwidth of approximately $0.81f_c$. See Ref. 6 for further discussion of experimental setup and transducer characteristics. For PW studies, we assume a temporal excitation burst weighting function $g(t)$ given by

$$g(t_d)=e^{-t_d^2/t_0^2}\sin(2\pi f_c t_d), \tag{16}$$

where $t_0=0.4\ \mu$s, the burst lasts approximately one and a half cycles, and the total observation time is 20.48 μs. This gives fundamental frequency $f_0=1/20.48\ \mu\mathrm{s}=48.828$ kHz and with a maximum propagated frequency of 5 MHz due to Eq. (15), the Shannon sampling frequency is 10 MHz. In practice we implement a 100 MHz sampling rate, corresponding to sampling interval of 0.01 μs and a total number of $2048=2^{11}$ samples ($n_\omega=1024-1$ frequencies) for the FFT and IFFT operations. The excitation burst weighting $g(t_d)$ is then represented by the equivalent Fourier sum

$$g(t_d)=\sum_{s=0}^{n_\omega} G(\omega_s)e^{-j\omega_s t_d}\Rightarrow G(\omega_s)=\mathrm{FFT}\{g(t_d)\}. \tag{17}$$

Finally we define also the underlying driving function $x_p(t_d)$ similarly as

$$x_p(t_d)=\sum_{s=0}^{n_\omega} X_p(\omega_s)e^{-j\omega_s t_d}\Rightarrow X_p(\omega_s)=\mathrm{FFT}\{x_p(t_d)\}, \tag{18}$$

where $x_p(t_d)$ represents the user-defined driving function for each ring p: in our case we shall be considering X waves and focused Gaussian beams as these driving functions. Linking together $X_p(\omega_s)$, $G(\omega_s)$, and $B(\omega_s)$ in series from Eqs. (18), (17), and (15) then gives the final transmission quantization values $Q_p(\omega_s)$ and $q_p(t)$ as

$$\begin{aligned} Q_p(\omega_s)&=X_p(\omega_s)G(\omega_s)B(\omega_s)\\ &\Rightarrow q_p(t)=\mathrm{IFFT}\{X_p(\omega_s)G(\omega_s)B(\omega_s)\}, \end{aligned} \tag{19}$$

which allows the generation of either $Q_p(\omega_s)$ or $q_p(t_d)$ in Eq. (4) corresponding to any desired driving function $x_p(t_d)$. In the remainder of this section we compare the results of the Fourier–Bessel field calculation with both the Rayleigh–

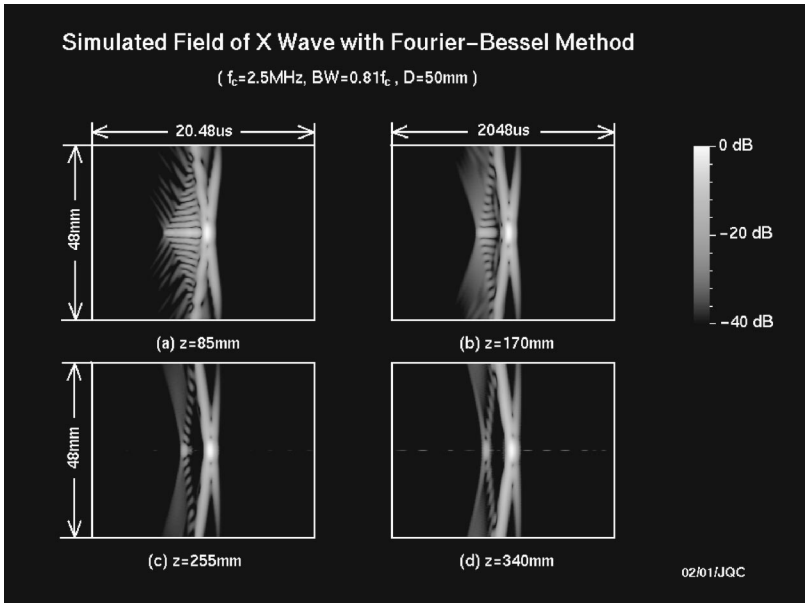

FIG. 1. Simulated fields of a zero-order band-limited X wave with Fourier–Bessel method at distances: (a) $z=85$ mm, (b) $z=170$ mm, (c) $z=255$ mm, and (d) $z=340$ mm, respectively, away from the surface of a 50-mm-diam annular array. A stepwise X wave aperture weighting and a broadband pulse drive of the array were assumed. The transmitting transfer function of the array was assumed to be the Blackman window function peaked at 2.5 MHz and with -6 dB bandwidth around $0.81f_c$. Parameters a_0 and ζ are 0.05 mm and 4°, respectively.

Sommerfeld field calculation and the experimentally measured field given in Ref. 33 for both X waves and focused Gaussian pulses. In Sec. VII we demonstrate tuning of these two types of fields with the same transducer.

B. Simulated and experimental field results

For the purposes of generating simulation data, we take $q_p(t_d)=\mathrm{IFFT}\{X_p(\omega_s)G(\omega_s)B(\omega_s)\}$ in Eq. (19) as the starting points from which to apply both the Fourier–Bessel (FB) field calculation algorithm of Sec. IV B and, for comparison/verification purposes, the more classical Rayleigh–Sommerfeld (RS) field calculation method. The driving function $x_p(t_d)$ for a (zero order) X wave[5,6] at $z=0$ on the transducer surface has frequency domain representation

$$X_p(\omega_s)=(2\pi a_0/c)e^{-a_0\omega_s/c}J_0(r_p\omega_s/c\,\sin\zeta), \tag{20}$$

where $a_0=0.05$ mm, $\zeta=4°$, $r_1=0$, $r_p=(r_p^-+r_p^+)/2$, $(p=2\cdots10)$ and $c=1500\ \mathrm{ms}^{-1}$. The focused Gaussian beam driving function $x_p(t_d)$ has frequency domain representation

$$X_p(\omega_s)=e^{-r_p^2/\sigma^2}e^{j\cdot\omega_s/c\cdot(F-\sqrt{F^2+r_p^2})}, \tag{21}$$

where $\sigma=15$ mm and the focus F is located at $F=120$ mm, with the full-width-at-half-maximum being 25 mm.

1. X wave field

Figure 1 shows the FB calculated field of a simulated X wave, where $X_p(\omega_s)$ is defined as per Eq. (20). The FB algorithm converged for all values at $a=20R$ and the field is shown at the four distances, (a) $z=85$ mm, (b) $z=170$ mm, (c) $z=255$ mm, (d) $z=340$ mm. In all four panels, the horizontal axis represents time whilst the vertical axis represents the radial position away from the center of the transducer. Figure 2 then shows the RS field calculation of the same simulated X wave as per Fig. 1. The FB and RS plots are virtually identical, and this parallel is offered as an

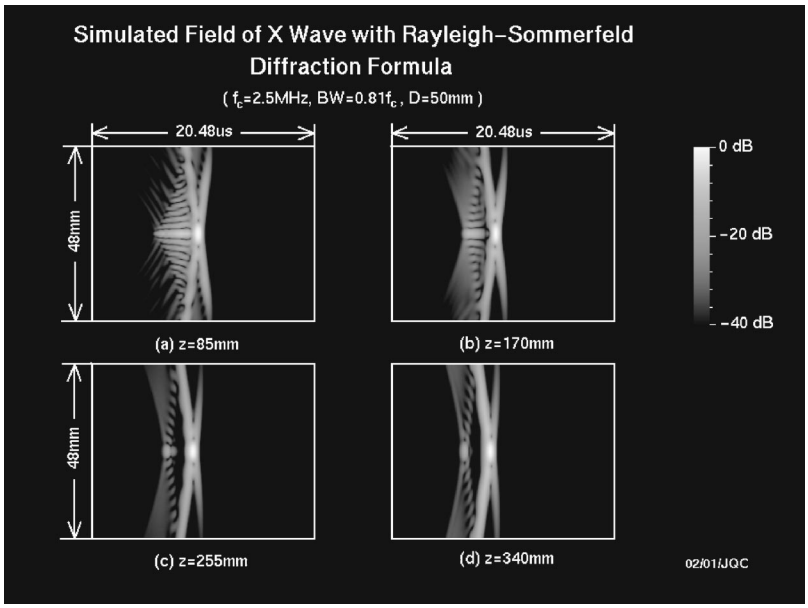

FIG. 2. The images are the same as those in Fig. 1, except that they are produced with the Rayleigh–Sommerfeld diffraction formula. The layout and the parameters used in simulation are the same as those in Fig. 1.

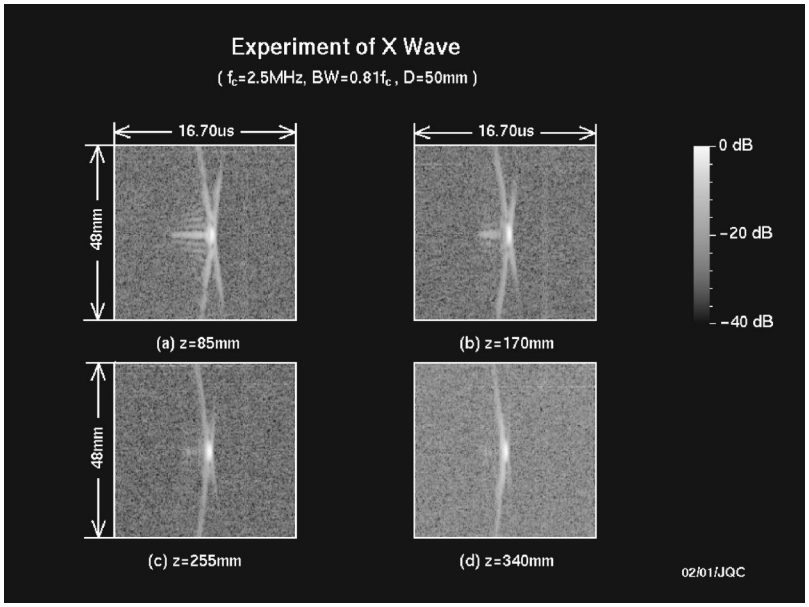

FIG. 3. Experimental results that correspond to the simulations in Figs. 1 and 2. A 10-element, 50-mm diameter, 2.5MHz central frequency, PZT ceramic/polymer composite J_0 Bessel transducer was used.

indicator of the F-B algorithm's accuracy since the R-S algorithm is widely accepted as a reliable method for field calculation. Figure 3 shows actual experimental results for the Bessel transducer of Ref. 6, which match the predicted simulated X wave fields given previously in Figs. 1 and 2. See Ref. 33 for details of experimental setup. A high level of agreement between theory and practice is observed. Notice also that the FB algorithm is applicable right up to and including the transducer surface itself since Eq. (13) applies for all $z \geqslant 0$, whereas the RS algorithm is not applicable close to the transducer surface.

When programmed in C under Linux on a Pentium III 600 MHz PC with 128 M Bytes of RAM, the FB algorithm took approximately 1 min and the RS algorithm approximately 10 h. However, a study of runtimes compared with faster computational techniques such as the impulse response method[34–39] has not yet been conducted at this point in time.

2. Gaussian field

Figure 4 shows FB field calculation for the simulated focused Gaussian pulse, where $X_p(\omega_s)$ is given by Eq. (21) and plots are shown for (a) $z=50$ mm, (b) $z=120$ mm, (c) $z=150$ mm, (d) $z=216$ mm. Figure 5 then gives the RS field calculation for the same pulse, again showing a close correlation between the FB and RS simulation methods. Finally, Fig. 6 shows experimental results except that in the experimental test of Ref. 6 the transducer had an acoustic lens added. This supplied a continuous phase shift across the transducer surface rather than the discretized phase shifts assumed in the simulation. Therefore some differences between Fig. 6 and Figs. 4 and 5 are expected. This is evidenced in the differences observed for the near field and far field panels (a) and (d) between the respective figures, al-

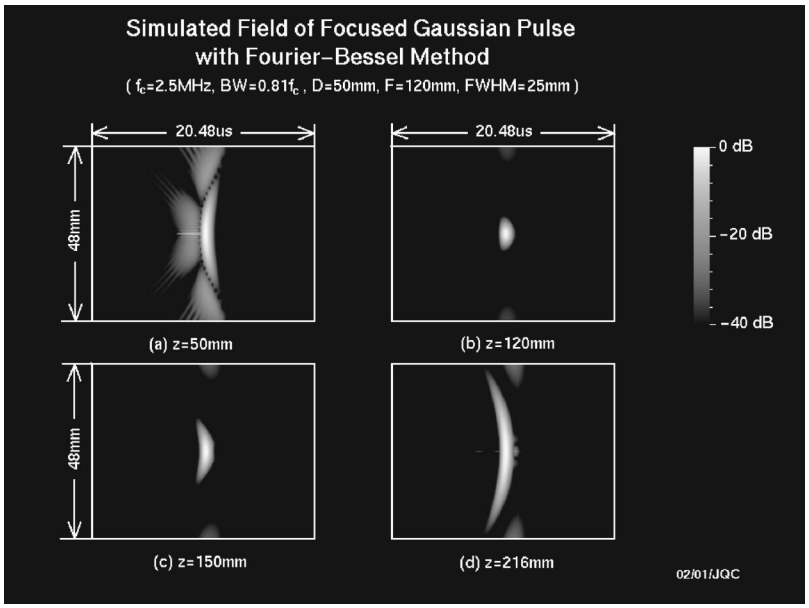

FIG. 4. Simulated fields of a focused Gaussian pulse with Fourier–Bessel method at distances: (a) $z=50$ mm, (b) $z=120$ mm, (c) $z=150$ mm, and (d) $z=216$ mm. A stepwise Gaussian aperture shading and a stepwise phase was assumed. The broadband pulse and transmitting transfer function of the array are the same as those for the X wave in Fig. 1. The FWHM of the Gaussian shading was 25 mm.

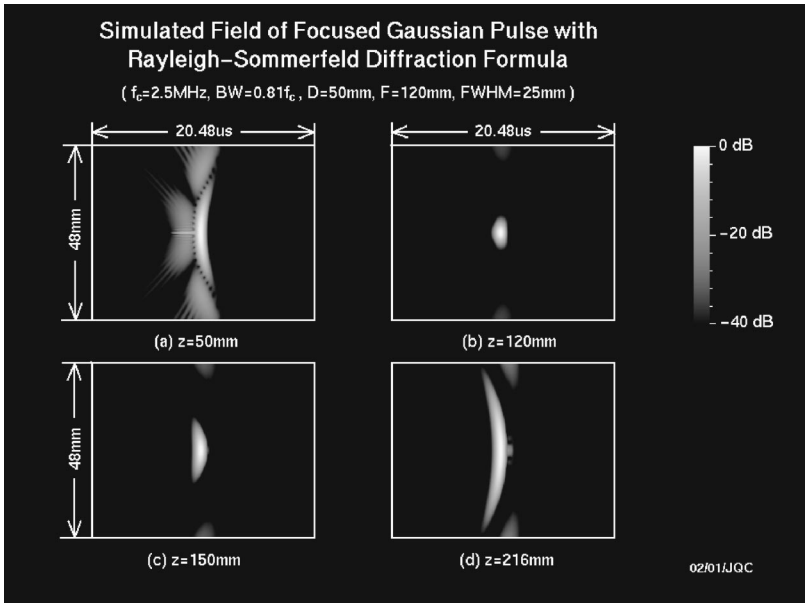

FIG. 5. The images are the same as those in Fig. 4, except that they are produced with the Rayleigh–Sommerfeld diffraction formula. The layout and the parameters used in simulation are the same as those in Fig. 4.

though the simulated and experimental pulses are very similar in the closer regions around the focus in panels (b) and (c), respectively.

VI. THEORY FOR TUNING

A. Tuning theory-based on Fourier–Bessel series

We consider now how to tune the transducer surface pressure in order to produce (as closely as physically possible) a particular desired propagating field. Assuming a given desired field $d(r,z,t_d)$ in the form

$$d(r,z,t_d)=\sum_{s=0}^{n_\omega} D(r,z,\omega_s)e^{-j\omega_s t_d}$$

$$\Rightarrow D(r,z,\omega_s)=\mathrm{FFT}\{d(r,z,t_d)\} \tag{22}$$

the tuning technique adopted will be to consider each frequency component $d(r,z,t_d,\omega_s)=D(r,z,\omega_s)\cdot e^{-j\omega_s t_d}$ of the *desired* field separately, and to minimize the sum of squared differences between it and the corresponding *physically obtainable* field term $f(r,z,t_d,\omega_s)=F(r,z,\omega_s)\cdot e^{-j\omega_s t_d}$ in Eq. (13) over a given set of field points r, z of interest. Due to the common time element $e^{-j\omega_s t_d}$ in both terms, this problem reduces to minimizing the squared sums of the Fourier coefficient differences $S(\omega_s)=\Sigma_{r,z}\|F(r,z,\omega_s)-D(r,z,\omega_s)\|^2$. Separating out $F(r,z,\omega_s)$ and $D(r,z,\omega_s)$ into real and imaginary parts then gives

$$F(r,z,\omega_s)=F^{\Re}(r,z,\omega_s)+jF^{\Im}(r,z,\omega_s),$$

$$D(r,z,\omega_s)=D^{\Re}(r,z,\omega_s)+jD^{\Im}(r,z,\omega_s), \tag{23}$$

$$S(\omega_s)=\sum_{r,z}\ ([F^{\Re}(r,z,\omega_s)-D^{\Re}(r,z,\omega_s)]^2$$

$$+[F^{\Im}(r,z,\omega_s)-D^{\Im}(r,z,\omega_s)]^2),$$

where $D(r,z,\omega_s)=\mathrm{FFT}\{d(r,z,t)\}$ from Eq. (22). Now, the

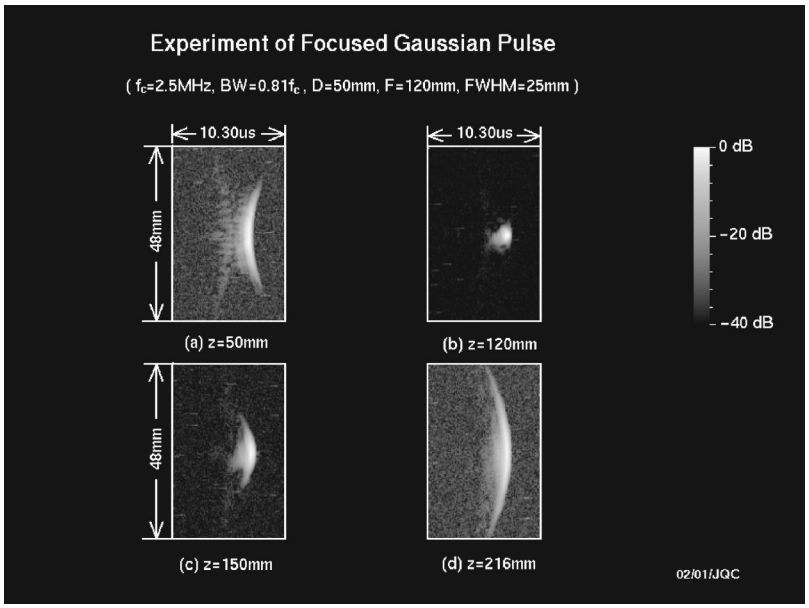

FIG. 6. Experimental results that correspond to the simulations in Figs. 4 and 5, except that in the experiment the phases applied by a lens was continuous. The same transducer for Fig. 3 was used.

obtainable field terms $F(r,z,\omega_s)$ in Eq. (13) are functions of the quantization levels $Q_1(\omega_s)\cdots Q_N(\omega_s)$ by definition, and so minimization of $S(\omega_s)$ necessarily requires adjustment of all their components $\gamma_p(\omega_s)$ and $\delta_p(\omega_s)$ as defined in Eq. (6). Then from Eqs. (13) and (6) the real and imaginary parts of $F(r,z,\omega_s)$ at all points of interest $r=r_u$, $z=z_v$ over a set of n_u radial indices $u=1\cdots n_u$ and n_v propagation indices $v=1\cdots n_v$ may then be written out as

$$\begin{bmatrix} F^{\Re}(r_1,z_1,\omega_s) \\ F^{\Im}(r_1,z_1,\omega_s) \\ \vdots \\ F^{\Re}(r_u,z_v,\omega_s) \\ F^{\Im}(r_u,z_v,\omega_s) \\ \vdots \\ F^{\Re}(r_{n_u},z_{n_v},\omega_s) \\ F^{\Im}(r_{n_u},z_{n_v},\omega_s) \end{bmatrix} = \begin{bmatrix} \lim\limits_{a\to\infty}\sum\limits_{i=1}^{l(k_s,a)} J_0\left(\frac{x_i r_1}{a}\right)\begin{bmatrix} +M^{\Re}_{i,1,1,s}, -M^{\Im}_{i,1,1,s},\ldots,+M^{\Re}_{i,N,1,s}, -M^{\Im}_{i,N,1,s} \\ +M^{\Im}_{i,1,1,s}, +M^{\Re}_{i,1,1,s},\ldots,+M^{\Im}_{i,N,1,s}, +M^{\Re}_{i,N,1,s}\end{bmatrix} \\ \vdots \\ \lim\limits_{a\to\infty}\sum\limits_{i=1}^{l(k_s,a)} J_0\left(\frac{x_i r_u}{a}\right)\begin{bmatrix} +M^{\Re}_{i,1,v,s}, -M^{\Im}_{i,1,v,s},\ldots,+M^{\Re}_{i,N,v,s}, -M^{\Im}_{i,N,v,s} \\ +M^{\Im}_{i,1,v,s}, +M^{\Re}_{i,1,v,s},\ldots,+M^{\Im}_{i,N,v,s}, +M^{\Re}_{i,N,v,s}\end{bmatrix} \\ \vdots \\ \lim\limits_{a\to\infty}\sum\limits_{i=1}^{l(k_s,a)} J_0\left(\frac{x_i r_{n_u}}{a}\right)\begin{bmatrix} +M^{\Re}_{i,1,n_v,s}, -M^{\Im}_{i,1,n_v,s},\ldots,+M^{\Re}_{i,N,n_v,s}, -M^{\Im}_{i,N,n_v,s} \\ +M^{\Im}_{i,1,n_v,s}, +M^{\Re}_{i,1,n_v,s},\ldots,+M^{\Im}_{i,N,n_v,s}, +M^{\Re}_{i,N,n_v,s}\end{bmatrix} \end{bmatrix} \begin{bmatrix} \gamma_1(\omega_s) \\ \delta_1(\omega_s) \\ \vdots \\ \gamma_N(\omega_s) \\ \delta_N(\omega_s) \end{bmatrix}, \tag{24}$$

where $M^{\Re}_{i,p,v,s}$ and $M^{\Im}_{i,p,v,s}$ are the real and imaginary parts of $C_{i,p}e^{j\beta_i(\omega_s)z_v}$, respectively ($p=1\cdots N$). This expression takes the block form

$$F(\omega_s)=M(\omega_s)T(\omega_s), \tag{25}$$

where

$$F(\omega_s)=[F^{\Re}(r_1,z_1,\omega_s),F^{\Im}(r_1,z_1,\omega_s),\ldots,F^{\Re}(r_{n_u},z_{n_v},\omega_s), F^{\Im}(r_{n_u},z_{n_v},\omega_s)]' \tag{26}$$

is the vector on the left-hand side of Eq. (24), with dimension $F(\omega_s)=\{2n_un_v,1\}$ in which the notation {*rows, columns*} indicates the numbers of *rows* and *columns*, respectively. The vector $T(\omega_s)$ is

$$T(\omega_s)=[\gamma_1(\omega_s),\delta_1(\omega_s),\ldots,\gamma_N(\omega_s),\delta_N(\omega_s)]' \tag{27}$$

appearing on the far right-hand side of Eq. (24) with dimension $T(\omega_s)=\{2N,1\}$. Finally $M(\omega_s)=\{2n_un_v,2N\}$ represents the limit as $a\to\infty$ of the large remaining matrix in Eq. (24) premultiplying $T(\omega_s)$. Similarly to $F(\omega_s)=\{2n_un_v,1\}$ in Eq. (26) we may then also define a vector $D(\omega_s)=\{2n_un_v,1\}$ as

$$D(\omega_s)=[D^{\Re}(r_1,z_1,\omega_s),D^{\Im}(r_1,z_1,\omega_s),\ldots,D^{\Re}(r_{n_u},z_{n_v},\omega_s), D^{\Im}(r_{n_u},z_{n_v},\omega_s)]', \tag{28}$$

which allows the error sum $S(\omega_s)$ in Eq. (23) to be written $S(\omega_s)=[F(\omega_s)-D(\omega_s)]'\cdot[F(\omega_s)-D(\omega_s)]$. Substituting for $F(\omega_s)=M(\omega_s)T(\omega_s)$ from Eq. (25) then gives $S(\omega_s)=[M(\omega_s)T(\omega_s)-D(\omega_s)]'[M(\omega_s)T(\omega_s)-D(\omega_s)]$ which may be minimized by adjusting all $p=1,\ldots,N$ components $\gamma_p(\omega_s)$, $\delta_p(\omega_s)$, in $T(\omega_s)$ appropriately. This is a standard linear least-squares problem with solution $T(\omega_s)=T_{ls}(\omega_s)$ given by

$$T_{ls}(\omega_s)=[M'(\omega_s)M(\omega_s)]^{-1}M'(\omega_s)D(\omega_s), \tag{29}$$

where $[M'(\omega_s)M(\omega_s)]^{-1}M'(\omega_s)$ is the Moore–Penrose pseudoinverse of $M(\omega_s)$. The existence of this pseudoinverse requires $[M'(\omega_s)M(\omega_s)]$ to be invertible, which is to say $[M'(\omega_s)M(\omega_s)]=\{2N,2N\}$ must have full rank $2N$; and since the rank of any matrix cannot exceed its lowest dimension, this cannot be achieved if the row dimension $2n_un_v$ of $M(\omega_s)=\{2n_un_v,2N\}$ is less than its column dimension $2N$. Hence we obtain the fundamental requirement $n_un_v\geqslant N$ in order to prevent $M(\omega_s)$ and thereby $M'(\omega_s)M(\omega_s)$ from being rank deficient for dimensional reasons. Assuming then that $M(\omega_s)$ is full rank for a given value of a, we also still need in practice to iterate increasing values of a to simulate $a\to\infty$ for the same reasons, as already discussed in Sec. IV A. In this case however, we calculate $T_{ls}(\omega_s)$ for each value of a and wait for the corresponding magnitudes $|T_{ls}(\omega_s)|$ to converge to within acceptable levels rather than to wait for $|F(r,z,\omega_s)|$ to converge as was the case in Sec. IV A. (See Ref. 13 for an illustration of quantization level convergence in the cw case).

In addition, consideration also needs to be given to the spatial sampling rates in the given region of interest. From Eq. (11) we observe that the nonevanescent components i of the sum propagate in the z direction as $e^{j\beta_i(\omega_s)z}$ with wavelength $2\pi/\beta_i(\omega_s)$. The shortest possible wavelength is therefore that corresponding to the maximum possible nonevanescent value of $\beta_i(\omega_s)$, namely $\beta_{\max}=k_s$ which occurs when $\alpha_i=0$ in Eq. (10). This gives a wavelength of $2\pi/k_s$, and to comply with the Shannon sampling theorem this dictates a corresponding sampling interval in the z direction of π/k_s or lower. With respect to the radial direction r, the approximation $J_0(\alpha_i r)\approx\sqrt{2/\pi\alpha_i r}\cos(\alpha_i r-\pi/4)$ from Refs. 1 and 2 allows us to approximate the radial oscillations as a cosine function of wavelength $2\pi/\alpha_i$. The minimum wavelength possible is therefore also $2\pi/k_s$, corresponding to the maximum nonevanescent value $\alpha_i=k_s$ possible in Eq. (10). This gives maximum sampling interval in the r direction also of π/k_s. Finally, considering that the highest wave number present in the system is k_{n_ω} corresponding to $s=n_\omega$, we adopt a final maximum sampling interval of $\pi/k_{n_\omega}=\pi/2k_c$

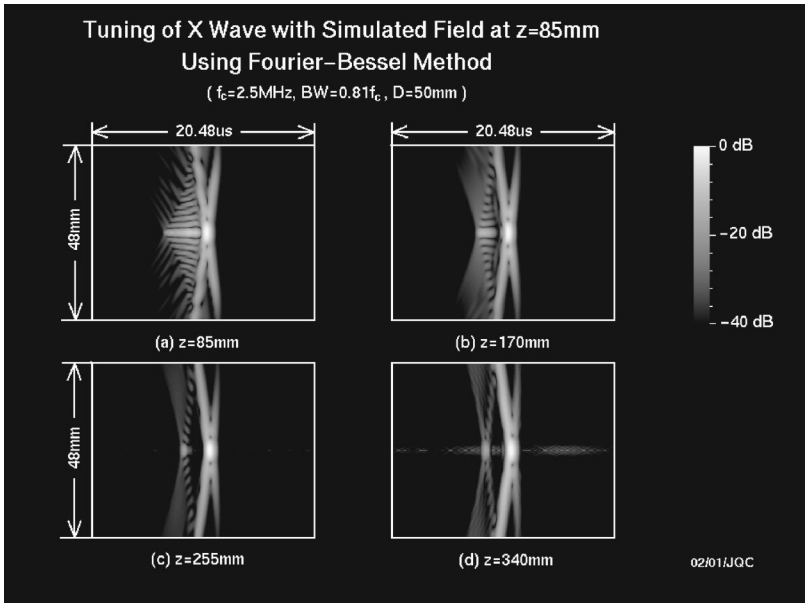

FIG. 7. Tuning results of X wave with simulated field at $z=85$ mm [Fig. 1(a)] as a desired field using Fourier–Bessel method. With the tuned weighting of the transducer, fields were reconstructed at distances: (a) $z=85$ mm, (b) $z=170$ mm, (c) $z=255$ mm, and (d) $z=340$ mm, respectively, away from the transducer surface.

$=c/2f_0n_\omega$ m in both r and z directions in order to cover the highest spatial oscillations present in the system.

B. Algorithm for tuning

From the discussion in Sec. VI A and including knowledge already gained in Secs. II–IV, the tuning algorithm becomes the following.

(1) If not known a priori, obtain Fourier coefficients $D(r,z,\omega_s)=\mathrm{FFT}\{d(r,z,t_d)\}$ from Eq. (22) for desired field. Make sure that $D(r,z,\omega_s)$ is specified at all points of interest $r=r_u$, $z=z_v$ $(u=1\cdots n_u$ and $v=1\cdots n_v)$, with sampling interval in both r and z directions being at most $\pi/k_{n_\omega}=\pi/2k_c=c/2f_0n_\omega$ m.
(2) Set frequency index to $s=0$.
(3) Select initial modeling aperture a (e.g., $a=10R$, $a=15R$, $a=20R$, etc.).
(4) Estimate the corresponding number of nonevanescent terms $l(k_s,a)$ from Eq. (12).
(5) Evaluate coefficients $C_{i,p}$ for $i=1,\ldots,l(k_s,a)$ from Eq. (9).
(6) Evaluate $M(\omega_s)$ based on Eq. (24) but with the infinite limit $a\to\infty$ removed.
(7) If necessary, continue to increase i until $\alpha_i>k$ to ensure numerically that the evanescence limit has been reached. If any of the first few evanescent terms still contribute significantly in the ranges of z of interest, include them in the sum for $M(\omega_s)$. Stop increasing i when no further terms are significant.
(8) Evaluate least-squares quantization vector $T_{ls}(\omega_s)$ from Eq. (29).
(9) Compare current evaluation of $T_{ls}(\omega_s)$ with that for previous value of a. If not converged to within satisfactory limit, increase the value of a and go back to step (4).

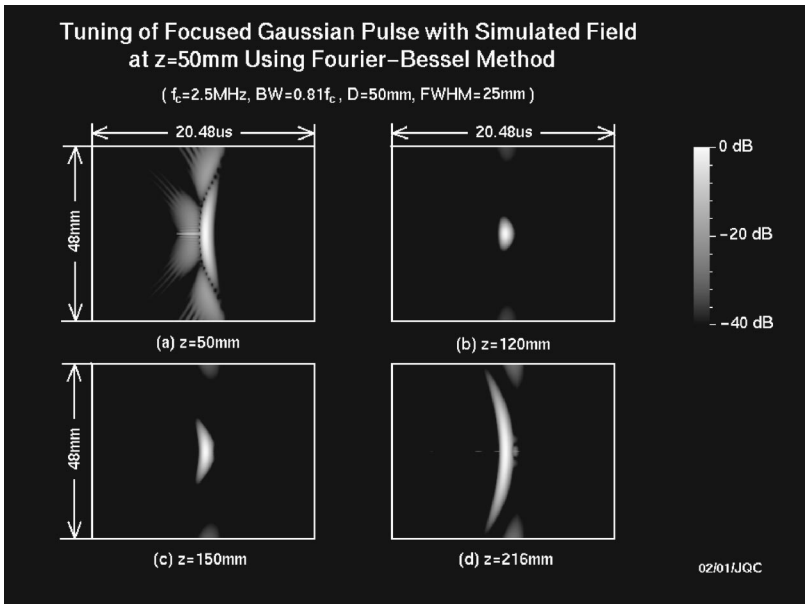

FIG. 8. Tuning results of focused Gaussian pulse with simulated field at $z=50$ mm (Fig. 4(a)) as a desired field using Fourier–Bessel method. With the tuned weighting of the transducer, fields were reconstructed at distances: (a) $z=50$ mm, (b) $z=120$ mm, (c) $z=150$ mm, and (d) $z=216$ mm, respectively, away from the transducer surface.

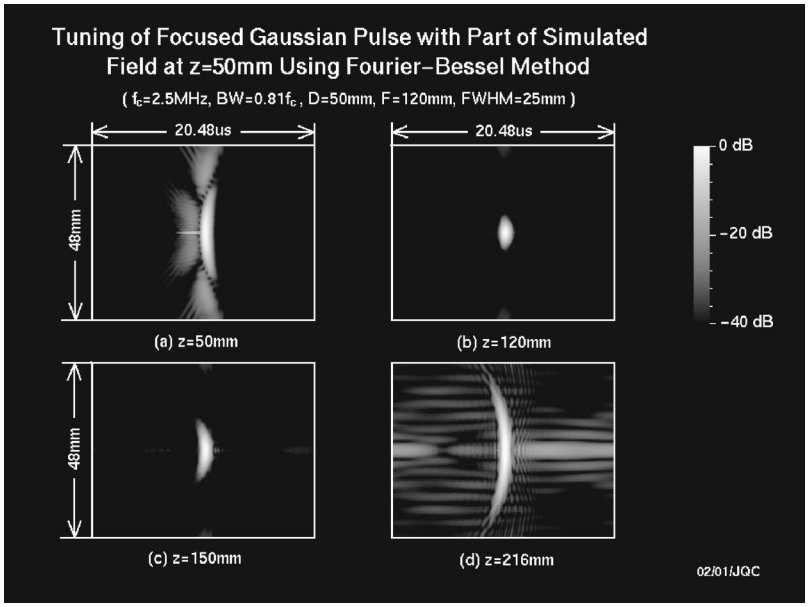

FIG. 9. Tuning results of focused Gaussian pulse with part of the simulated field at $z=50$ mm [Fig. 4(a)] as a desired field using Fourier–Bessel method. Within $r \leqslant 12$ mm, the desired field was the same as the simulated field in Fig. 4(a), otherwise it was set to zero. With the tuned weighting of the transducer, fields were reconstructed at distances: (a) $z=50$ mm, (b) $z=120$ mm, (c) $z=150$ mm, (d) $z=216$ mm.

(10) Reconstruct all quantization levels $Q_p(\omega_s)=\gamma_p(\omega_s)+j\,\delta_p(\omega_s)$ using $\gamma_p(\omega_s)$ and $\delta_p(\omega_s)$ from $T_{ls}(\omega_s)$.
(11) If $s<n_\omega$, increase s by 1 and go back to step (3).
(12) Evaluate time domain quantization values $q_p(t_d)=\mathrm{IFFT}\{Q_p(\omega_s)\}$ from Eq. (5) based on all coefficients $Q_p(\omega_s)$.

VII. EXAMPLES OF TUNING

A. X wave

Now consider tuning the transducer to produce an X wave using the algorithm of Sec. VI B. The intention here is to show that by defining a desired field as an X wave at a given location in space ($z=85$ mm), we are able to tune the transducer quantization levels so as to generate this X wave profile as closely as possible. If this is achievable, it will be evidenced by the pulse created from these quantization levels being essentially identical to the original X wave simulation already shown at the distances (a) $z=85$ mm, (b) $z=170$ mm, (c) $z=255$ mm, (d) $z=340$ mm in Fig. 1. To implement the algorithm we begin with taking the field in Fig. 1(a) as the desired field $d(r,z,t_d)$ and obtain $D(r,z,\omega_s)=\mathrm{FFT}\{d(r,z,t_d)\}$ from Eq. (22) at all sampling points $r=r_u$ of interest; namely those corresponding to a vertical line across the entire diameter of the transducer at an axial distance of $z=85$ mm into the medium. The sampling resolution in the lateral (r) direction is taken as 0.12 mm which complies with the maximum upper bound of $\pi/2k_c=0.15$ mm discussed in Sec. VI. Running the algorithm produces convergence of terms at $a=20R$ and the field resulting from the corresponding tuned transducer quantization levels is shown in Fig. 7 at distances (a) $z=85$ mm, (b) $z=170$ mm, (c) $z=255$ mm, (d) $z=340$ mm. Notice that these are essentially identical to those of Fig. 1, with only some very small differences along the central axis in the far field around $z=340$ mm in panel (d). From the extremely close similarity in propagated pulses for both original and tuned X waves simulations, we may conclude that the tuning algorithm is indeed producing the correct surface pressure profiles required to generate the desired (realizable) pulse in the medium.

B. Focused Gaussian pulses

In Fig. 8 we show the same tuning approach, but this time for the focused Gaussian pulse with desired field as per the simulated field in Fig. 4(a) at $z=50$ mm. Again, the original and regenerated fields at the tuning positions are virtually identical (Figs. 4 and 8, respectively), as are the field shots at the remaining distances (b) $z=120$ mm, (c) $z=150$ mm, (d) $z=216$ mm. This again demonstrates correct tuning of the quantization levels, but this time to produce the focused Gaussian pulse. Figure 9 shows the results once again for a focused Gaussian beam, but this time based on an adaption of the field given in Fig. 4(a). The adaption is to set the desired field at $z=50$ mm to zero beyond $r=12$ mm, which is to say a truncation of the original Gaussian profile in the radial direction. Feeding this new desired field into the tuning algorithm then gives propagating field as per panels (a)–(d) in Fig. 9. Figure 9(a) in this case remains very similar to Fig. 4(a), showing that requiring the field beyond $r=12$ mm being zero whilst at the same time keeping the

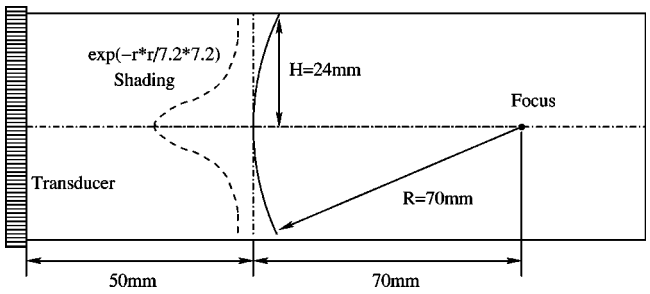

FIG. 10. Schematic diagram of an arbitrarily designed focused pulse. The pulse is 50 mm away from the transducer surface. The shape of pulse in axial direction is an arc with a height and radius of 24 and 70 mm, respectively. The weighting of the pulse in lateral (r) direction is a Gaussian function with $\sigma=7.2$ mm (FWHM=12 mm).

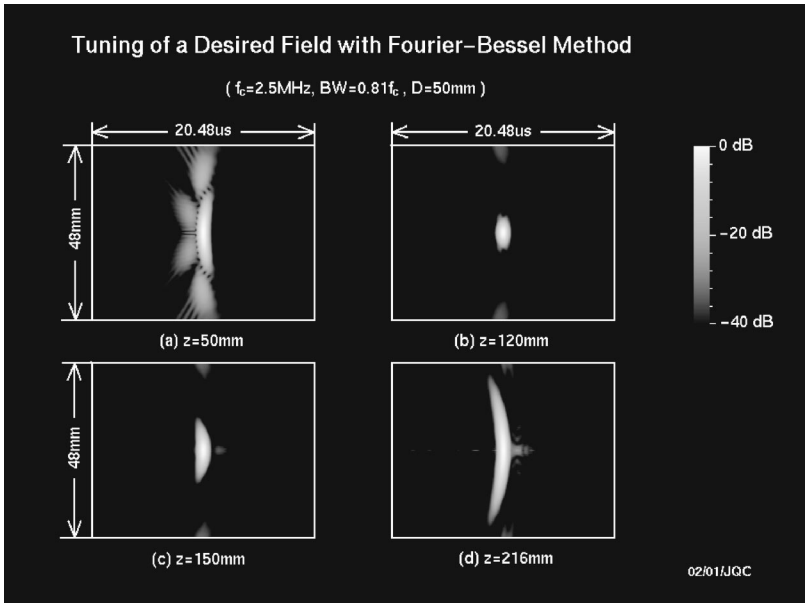

FIG. 11. Tuning results with a designed focused field at $z=50$ mm in Fig. 10 using Fourier–Bessel method. With the tuned weighting of the transducer, fields were reconstructed at distances: (a) $z=50$ mm, (b) $z=120$ mm, (c) $z=150$ mm, and (d) $z=216$ mm, respectively.

original field segment for $0 \leqslant r \leqslant 12$ mm cannot in fact be achieved. Furthermore, the attempt to attain the truncated field distribution at $z=50$ mm not only proves impossible but also leads to a considerable distortion at $z=216$ mm with respect to the original field. Therefore this example illustrates the important point that not all desired fields are achievable, merely that the algorithm tunes the field in a least-squares sense with respect to a given desired field. Hence the topic of which desired fields are realizable and which are not is one which needs further attention in future work.

To illustrate a more successful attempt, Fig. 10 then gives a schematic diagram of an alternative desired focused Gaussian pulse. The pulse is depicted as it passes through the vertical (radial) line at $z=50$ mm away from the transducer surface. The shape of the pulse in the axial direction is an arc with a height and radius of 24 and 70 mm, respectively, with the intended focus being at $z=50+70=120$ mm. The shading in the lateral direction is chosen as a Gaussian function with σ in Eq. (21) now taken as $\sigma=7.2$ mm rather than $\sigma=15$ mm previously. This selection causes the amplitude to reduce to half at $r=6$ mm, thus FWHM$=12$ mm as compared to 25 mm previously. The pulse wave front travels at a velocity $c=1500\ \mathrm{m\,s^{-1}}$ and the corresponding projection of the wave front along the radial r axis as it travels through $z=50$ mm gives the desired field $d(r,z,t)$ for the tuning algorithm. Figure 11 then gives the tuned field results at (a) $z=50$ mm, (b) $z=120$ mm, (c) $z=150$ mm, (d) $z=216$ mm. Figure 11(b) shows that the pulse focuses at $z=120$ mm as intended, and the fields in Figs. 11(a), (c), and (d) then demonstrate broadly the same propagation characteristics before and after focus as for the original Gaussian pulse considered in Fig. 4. Hence this example demonstrates a case where the desired field is actually realisable to within a satisfactory degree, in contrast to that discussed earlier in Fig. 9.

VIII. CONCLUSIONS AND FURTHER WORK

A method has been given for computing and tuning the linear lossless field of flat PW annular arrays using 1D Fourier–Bessel series. The series corresponds to a set of known Bessel beams propagating into the medium, which provides a linear mapping between the transducer surface and the field at any point in space. The method was found to be computationally fast whilst maintaining accuracy and offering computation arbitrarily close to the transducer surface. The related tuning method derived then enabled beamforming of the propagated field in a least-squares sense with respect to a given desired field. However, further work is still needed to determine which desired fields are realisable for a given transducer geometry.

Other possible developments of the current work are also evident. First, an extension to lossy media is of interest in order to model propagation in a wider set of media such as human tissue. Second, an extension to a Bessel-based technique for nonlinear propagation would useful if such progress could be made. Third, its extension to an analysis of two-dimensional (2D) arrays is of prime interest. This would require the use of 2D Fourier–Bessel series, which are capable of modeling non-circular-symmetric quantization profiles and thereby more generalized field distributions. However, whilst conceptually a straightforward progression, the use of 2D series will necessarily lead to higher computational demands due to the increased number of Bessel terms and transducer elements involved.

ACKNOWLEDGMENTS

This work was supported partially by Grant No. HL 60301 from the National Institutes of Health, USA, and No. 26-01-0178 from the Danish Science Foundation, Denmark.

[1] G. Tolstov, *Fourier Series* (Dover, New York, 1962).
[2] F. Bowman, *Introduction to Bessel Functions* (Dover, New York, 1958).
[3] J. A. Stratton, *Electromagnetic Theory* (McGraw–Hill, New York, 1941), p. 356.
[4] J. Durnin, "Exact solutions for nondiffracting beams. I. The scalar theory," J. Opt. Soc. Am. A **4**, 651–654 (1987).
[5] J.-Y. Lu and J. F. Greenleaf, "Nondiffracting X waves—Exact solutions to free-space scalar wave equation and their finite aperture realizations," IEEE Trans. Ultrason. Ferroelectr. Freq. Control **39**, 19–31 (1992).
[6] J.-Y. Lu and J. F. Greenleaf, "Ultrasonic nondiffracting transducer for

medical imaging,'' IEEE Trans. Ultrason. Ferroelectr. Freq. Control **37**, 438–447 (1990).
[7] P. R. Stepanishen and J. Sun, ''Acoustic bullets: Transient Bessel beams generated by planar apertures,'' J. Acoust. Soc. Am. **102**, 3308–3318 (1997).
[8] S. Holm, ''Bessel and conical beams and approximation with annular arrays,'' IEEE Trans. Ultrason. Ferroelectr. Freq. Control **45**, 712–718 (1998).
[9] P. R. Stepanishen, ''Acoustic bullets/transient Bessel beams: Near to far field transition via an impulse response approach,'' J. Acoust. Soc. Am. **103**, 1742–1751 (1998).
[10] P. R. Stepanishen, ''A generalized modal impulse response and Fourier transform approach to investigate acoustic transient Bessel beams and Bessel bullets,'' J. Acoust. Soc. Am. **105**, 1493–1502 (1999).
[11] J.-Y. Lu and A. Liu, ''An X wave transform,'' IEEE Trans. Ultrason. Ferroelectr. Freq. Control **47**, 1472–1481 (2000).
[12] P. D. Fox and S. Holm, ''Modelling of CW annular arrays using limited diffraction Bessel beams,'' IEEE Trans. Ultrason. Ferroelectr. Freq. Control **49**, 85–93 (2002).
[13] P. D. Fox, J. Cheng, and J.-Y. Lu, ''Fourier-bessel field calculation and tuning of a CW annular array,'' IEEE Trans. Ultrason. Ferroelectr. Freq. Control **49**, 1179–1190 (2002).
[14] J. H. Mcleod, ''The Axicon: A new type of optical element,'' J. Opt. Soc. Am. **44**, 592 (1954).
[15] C. B. Burckhardt, H. Hoffmann, and P. A. Grandchamp, ''Ultrasound axicon: A device for focusing over a large depth,'' J. Acoust. Soc. Am. **54**, 1628–1630 (1973).
[16] J. Fagerholm, A. T. Friberg, J. Huttunen, D. P. Morgan, and M. M. Salomaa, ''Angular-spectrum representation of nondiffracting X waves,'' Phys. Rev. E **54**, 4347–4352 (1996).
[17] K. Uehara and H. Kikuchi, ''Generation of near diffraction-free laser beams,'' Appl. Phys. B: Photophys. Laser Chem. **48**, 125–129 (1989).
[18] A. Vasara, J. Turunen, and A. T. Friberg, ''Realization of general nondiffracting beams with computer-generated holograms,'' J. Opt. Soc. Am. A **6**, 1748–1754 (1989).
[19] J. N. Brittingham, ''Focus wave modes in homogeneous Maxwell's equations: Transverse electric mode,'' J. Appl. Phys. **54**, 1179–1189 (1983).
[20] R. W. Ziolkowski, ''Exact solutions of the wave equation with complex source locations,'' J. Math. Phys. **26**, 861–863 (1985).
[21] R. W. Ziolkowski, D. K. Lewis, and B. D. Cook, ''Evidence of localized wave transmission,'' Phys. Rev. Lett. **62**, 147–150 (1985).
[22] J.-Y. Lu and J. F. Greenleaf, ''Pulse-echo imaging using a nondiffracting beam transducer,'' Ultrasound Med. Biol. **17**, 265–281 (1991).
[23] J.-Y. Lu, H. Zou, and J. F. Greenleaf, ''Biomedical ultrasound beam forming,'' Ultrasound Med. Biol. **20**, 403–428 (1994).
[24] J.-Y. Lu, ''2D and 3D high frame rate imaging with limited diffraction beams,'' IEEE Trans. Ultrason. Ferroelectr. Freq. Control **44**, 839–856 (1997).
[25] J.-Y. Lu and J. F. Greenleaf, ''Evaluation of a nondiffracting transducer for tissue characterization,'' IEEE 1990 Ultrasonics Symposium Proceedings 90CH2938-9, 1990, Vol. 2, pp. 795–798.
[26] J.-Y. Lu, X.-L. Xu, H. Zou, and J. F. Greenleaf, ''Application of Bessel beam for Doppler velocity estimation,'' IEEE Trans. Ultrason. Ferroelectr. Freq. Control **42**, 649–662 (1995).
[27] J.-Y. Lu and J. F. Greenleaf, ''Producing deep depth of field and depth-independent resolution in NDE with limited diffraction beams,'' Ultrason. Imaging **15**, 134–149 (1993).
[28] J.-Y. Lu and S. He, ''Optical X waves communications,'' Opt. Commun. **161**, 187–192 (1999).
[29] J. Ojeda-Castaneda and A. Noyola-lglesias, ''Nondiffracting wavefields in grin and free-space,'' Microwave Opt. Technol. Lett. **3**, 430–433 (1990).
[30] J. Durnin, J. J. Miceli, Jr., and J. H. Eberly, ''Diffraction-free beams,'' Phys. Rev. Lett. **58**, 1499–1501 (1987).
[31] S. Holm and P. D. Fox, ''Analysis of Bessel beam quantisation in annular arrays,'' Proceedings of the 22nd Scandinavian Symposium on Physical Acoustics, 1999, pp. 43, 44, Ustaoset, Norway, ISSN 1501–6773.
[32] P. D. Fox and S. Holm, ''Decomposition of acoustic fields in quantised Bessel beams,'' Ultrasonics **38**, 190–194 (2000).
[33] J.-Y. Lu and J. F. Greenleaf, ''Experimental verification of nondiffracting X waves,'' IEEE Trans. Ultrason. Ferroelectr. Freq. Control **39**, 441–446 (1992).
[34] G. E. Tupholme, ''Generation of acoustic pulses by baffled plane pistons,'' Mathematika **16**, 209–224 (1969).
[35] P. R. Stepanishen, ''The time-dependent force and radiation impedance on a piston in a rigid infinite planar baffle,'' J. Acoust. Soc. Am. **49**, 841–849 (1971).
[36] P. R. Stepanishen, ''Acoustic transients from planar axisymmetric vibrators using the impulse response approach,'' J. Acoust. Soc. Am. **70**, 1176–1181 (1981).
[37] M. Arditi, F. S. Forster, and J. Hunt, ''Transient fields of concave annular arrays,'' **3**, 37–61 (1981).
[38] J. A. Jensen, ''Field: A program for simulating ultrasound systems,'' MBEC 10th Nordic-Baltic Conference on Biomedical Imaging, 1996, Vol. 4, Supplement 1, Part 1, pp. 351–353.
[39] J. A. Jensen, ''A new calculation procedure for spatial impulse responses in ultrasound,'' J. Acoust. Soc. Am. **105**, 3266–3274 (1999).

Measuring the porosity and the tortuosity of porous materials via reflected waves at oblique incidence

Z. E. A. Fellah
National Institute of Health and Medical Research (INSERM U556), 151 cours Albert Thomas, 69424 Lyon Cedex 03, France

S. Berger and W. Lauriks
Laboratorium voor Akoestiek en Thermische Fysica, Katholieke Universiteit Leuven, Celestijnenlaan 200 D, B-3001 Heverlee, Belgium

C. Depollier
Laboratoire d'Acoustique de l'Université du Maine, UMR-CNRS 6613, Université du Maine, Avenue Olivier Messiaen, 72085 Le Mans Cedex 09, France

C. Aristégui and J.-Y. Chapelon
National Institute of Health and Medical Research (INSERM U556), 151 cours Albert Thomas, 69424 Lyon Cedex 03, France

(Received 31 October 2002; revised 21 February 2003; accepted 24 February 2003)

An ultrasonic reflectivity method is proposed for measuring porosity and tortuosity of porous materials having a rigid frame. Porosity is the relative fraction by volume of the air contained within a material. Tortuosity is a geometrical parameter which intervenes in the description of the inertial effects between the fluid filled the porous material and its structure at high frequency range. It is generally easy to evaluate the tortuosity from transmitted waves, this is not the case for porosity because of its weak sensitivity in transmitted mode. The proposed method is based on measurement of reflected wave by the first interface of a slab of rigid porous material. This method is obtained from a temporal model of the direct and inverse scattering problems for the propagation of transient ultrasonic waves in a homogeneous isotropic slab of porous material having a rigid frame [Z. E. A. Fellah, M. Fellah, W. Lauriks, and C. Depollier, J. Acoust. Soc. Am. **113**, 61 (2003)]. Reflection and transmission scattering operators for a slab of porous material are derived from the responses of the medium to an incident acoustic pulse at oblique incidence. The porosity and tortuosity are determined simultaneously from the measurements of reflected waves at two oblique incidence angles. Experimental and numerical validation results of this method are presented. © *2003 Acoustical Society of America.* [DOI: 10.1121/1.1567275]

PACS numbers: 43.20.Bi, 43.20.Hq [ANN]

I. INTRODUCTION

The ultrasonic characterization of porous materials saturated by airlike plastic foams, fibrous, or granular materials is of a great interest for a wide range of industrial applications. These materials are frequently used in the automotive and aeronautics industries or in the building trade. The determination of the properties of a medium from waves that have been reflected by or transmitted through the medium is a classical inverse scattering problem. Such problems are often approached by taking a physical model of the scattering process, generating a synthetic response for some assumed values of the parameters, adjusting these parameters until reasonable agreement is obtained between the synthetic response and the observed data. Two important parameters which appear in theories of sound propagation in porous materials[1–13] are the porosity and the tortuosity. Porosity is the relative fraction, by volume, of air contained in the connected pores in the material. Unlike other parameters included in the description of different various phenomena occurring in the acoustical propagation of porous material at high frequency range such as tortuosity,[11] viscous characteristic length,[5] and thermal characteristic length,[12] or in the low frequency range such as flow resistivity[11] and thermal permeability,[13] the porosity is a key parameter playing an important role in the propagation at all frequencies. As such, in studies of acoustical properties of porous materials, it is highly desirable to be able to measure this parameter.

Beranek[10] described an apparatus (porosimeter) used to measure the porosity of porous materials. This device was based on the equation of state for ideal gases at constant temperature (i.e., Boyle's law). Porosity can be determined by measuring the change in air pressure occurring with a known change in volume of the chamber containing the sample. In the Beranek apparatus, both pressure change and volume change are monitored using a U-shaped fluid-filled manometer. An alternate technique for measuring porosity is a dynamic method proposed by Leonard.[14] Techniques that use water as the pore-filling fluid, rather than air, are common in geophysical studies.[15,16] Mercury has been used as the pore-filling fluid in other applications.[17] However, for many materials, the introduction of liquids into the material is not appropriate. Recently a similar device to that of Beranek, involving the use of an electronic pressure transducer, was introduced by Champoux *et al.*[18] This device can be

 0001-4966/2003/113(5)/2424/10/$19.00

used to measure very slight changes in pressure accurately, and the output can be recorded by a computer.

The tortuosity α_∞, namely the structure factor k_s by Zwikker and Kosten,[11] or the parameter q^2 by Attenborough,[9] is an important parameter which intervenes in the description of the inertial interaction between the fluid and the structure in the porous material at high frequency range. In the case of cylindrical pores making an angle ϑ with the direction of propagation, $\alpha_\infty = 1/\cos^2 \vartheta$. The tortuosity can be evaluated by electrical measurements,[16] or by using a superfluid ^{4}He as the pore fluid.[5] It can also be evaluated by acoustical techniques as an ultrasonics measurement of transmitted waves.[1,3,4,19]

In this work, we present a method of measuring the porosity and the tortuosity from the measurement of acoustic wave reflected by a slab of porous material at oblique incidence. This method is based on a temporal model of the direct and inverse scattering problems for the propagation of transient ultrasonic waves in a homogeneous isotropic slab of porous material having a rigid frame initially introduced by two of the authors (Z.E.A.F and C.D) in Refs. 1–4. The viscous and thermal losses of the medium are described by the Johnson *et al.*[5] and Allard[6] model modified by a fractional calculus based method in order to be used in time domain. Reflection and transmission scattering operators of a slab of porous material are derived for an oblique incidence and thus the responses of the medium to an incident acoustic pulse are obtained.

The outline of this paper is as follows. In Sec. II, a time domain model is given, and the basic equations of wave propagation in porous material are written for an oblique incidence. Section III is devoted to the direct problem and to the expressions of the reflection and transmission kernels in the time domain at oblique incidence. Finally in Sec. IV, an experimental validation with ultrasonic measurement is treated for two plastic foams having different values of flow resistivity. The porosity and tortuosity are measured via reflected waves for different incidence angles.

II. MODEL

In the acoustics of porous materials, a distinction can be made between two situations depending on whether the frame is moving or not. In the first case, the dynamics of the waves due to the coupling between the solid frame and the fluid are clearly described by the Biot theory.[7,8] In air-saturated porous media the structure is generally motionless and the waves propagate only in the fluid. This case is described by the model of equivalent fluid which is a particular case in the Biot model, in which the interactions between the fluid and the structure are taken into account in two frequency response factors: the dynamic tortuosity of the medium $\alpha(\omega)$ given by Johnson *et al.*[5] and the dynamic compressibility of the air included in the porous material $\beta(\omega)$ given by Allard.[6] In the frequency domain, these factors multiply the density of the fluid and its compressibility respectively and represent the deviation from the behavior of the fluid in free space as the frequency increases. In the time domain, they act as operators and in the asymptotic domain (high frequency approximation) their expressions are given[1–4] by

$$\tilde{\alpha}(t) = \alpha_\infty \left(\delta(t) + \frac{2}{\Lambda} \left(\frac{\eta}{\pi \rho_f} \right)^{1/2} t^{-1/2} \right), \tag{1}$$

$$\tilde{\beta}(t) = \left(\delta(t) + \frac{2(\gamma - 1)}{\Lambda'} \left(\frac{\eta}{\pi P_r \, \rho_f} \right)^{1/2} t^{-1/2} \right). \tag{2}$$

In these equations, $\delta(t)$ is the Dirac function, Pr is the Prandtl number, η and ρ_f are, respectively, the fluid viscosity and the fluid density, and γ is the adiabatic constant. The relevant physical parameters of the model are the tortuosity of the medium α_∞ initially introduced by Zwikker and Kosten,[11] the viscous and the thermal characteristic lengths Λ and Λ' introduced by Johnson *et al.*[5] and Allard.[6] In this model the time convolution of $t^{-1/2}$ with a function is interpreted as a semi derivative operator following the definition of the fractional derivative of order ν given in Samko and colleagues[20]

$$D^\nu [x(t)] = \frac{1}{\Gamma(-\nu)} \int_0^t (t-u)^{-\nu-1} x(u) \, du, \tag{3}$$

where $\Gamma(x)$ is the Gamma function.

In this framework, the basic equations of our model can be written as

$$\rho_f \tilde{\alpha}(t) * \frac{\partial v_i}{\partial t} = -\nabla_i p \quad \text{and} \quad \frac{\tilde{\beta}(t)}{K_a} * \frac{\partial p}{\partial t} = -\nabla \cdot \mathbf{v}, \tag{4}$$

where $*$ denotes the time convolution operation, p is the acoustic pressure, $\mathbf{v}$ is the particle velocity, and K_a is the bulk modulus of air. The first equation is the Euler equation, the second one is the constitutive equation.

For a wave propagating at oblique incidence in the plane (xoz) and making an angle θ along the x-axis, these equations become

$$\begin{aligned}
&\rho_f \alpha_\infty \frac{\partial v_x(x,z,t)}{\partial t} + \frac{2 \rho_f \alpha_\infty}{\Lambda} \left(\frac{\eta}{\pi \rho_f} \right)^{1/2} \int_0^t \frac{\partial v(x,z,t')/\partial t'}{\sqrt{t-t'}} dt' \\
&\quad = -\frac{\partial p(x,z,t)}{\partial x}, \\
&\rho_f \alpha_\infty \frac{\partial v_z(x,z,t)}{\partial t} + \frac{\partial \rho_f \alpha_\infty}{\Lambda} \left(\frac{\eta}{\pi \rho_f} \right)^{1/2} \int_0^t \frac{\partial_v(x,z,t')/\partial t'}{\sqrt{t-t'}} dt' \\
&\quad = -\frac{\partial p(x,z,t)}{\partial z}, \\
&\frac{1}{K_a} \frac{\partial p(x,z,t)}{\partial t} + \frac{2(\gamma-1)}{K_a \Lambda'} \left(\frac{\eta}{\pi \rho_f P_r} \right)^{1/2} \int_0^t \frac{\partial p(x,z,t')/\partial t'}{\sqrt{t-t'}} dt' \\
&\quad = -\frac{\partial v(x,z,t)}{\partial x} - \frac{\partial v(x,z,t)}{\partial z},
\end{aligned} \tag{5}$$

where v_x, v_z are the components of the particle velocity along the axes x' and z.

In these equations, the convolutions express the dispersive nature of the porous material. They take into account the

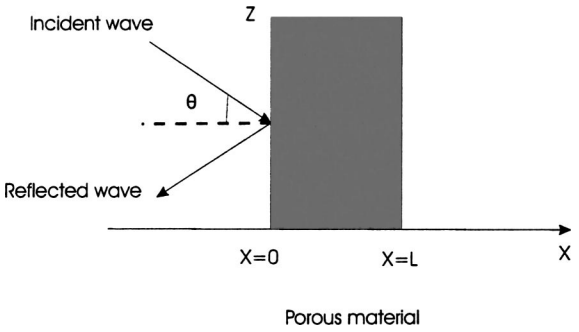

FIG. 1. Geometry of the problem.

memory effects due to the fact that the response of the medium to the wave excitation is not instantaneous but needs more time to take effect.

III. DIRECT PROBLEM

The direct scattering problem is that of determining the scattered field as well as the internal field, that arises when a known incident field impinges on the porous material with known physical properties. To compute the solution of the direct problem one needs to know the Green's function[3] of the modified wave equation in the porous medium. In that case, the internal field is given by the time convolution of the Green's function with the incident wave, and the reflected and transmitted fields are deduced from the internal field and the boundary conditions. In this section some notation is introduced. The geometry of the problem is shown in Fig. 1. A homogeneous porous material occupies the region $0 \leqslant x \leqslant L$. This medium is assumed to be isotropic and to have a rigid frame. A short sound pulse impinges at oblique incidence on the medium from the left, it gives rise to an acoustic pressure field $p(x,z,t)$ and an acoustic velocity field $\mathbf{v}(x,z,t)$ within the material, which satisfying the system of Eqs. (5), which can be written as

$$a\frac{\partial v_x(x,z,t)}{\partial t}+b\frac{\partial^{1/2} v_x(x,z,t)}{\partial t^{1/2}}=-\frac{\partial p(x,z,t)}{\partial x}, \tag{6}$$

$$a\frac{\partial v_z(x,z,t)}{\partial t}+b\frac{\partial^{1/2} v_z(x,z,t)}{\partial t^{1/2}}=-\frac{\partial p(x,z,t)}{\partial z}, \tag{7}$$

$$d\frac{\partial p(x,z,t)}{\partial t}+f\frac{\partial^{1/2} p(x,z,t)}{\partial t^{1/2}}=-\frac{\partial v_x(x,z,t)}{\partial x}-\frac{\partial v_z(x,z,t)}{\partial z}. \tag{8}$$

with

$$a=\rho_f\alpha_\infty,\quad b=\frac{2\rho_f\alpha_\infty}{\Lambda}\left(\frac{\eta}{\rho_f}\right)^{1/2},$$

$$d=\frac{1}{K_a}\quad\text{and}\quad f=\frac{2(\gamma-1)}{K_a\Lambda'}\left(\frac{\eta}{\rho_f P_r}\right)^{1/2}.$$

In the region $x\leqslant 0$, the incident pressure wave is given by

$$p^i(x,z,t)=p^i\left(t-\frac{x\cos\theta}{c_0}-\frac{z\sin\theta}{c_0}\right), \tag{9}$$

where c_0 is the velocity of the free fluid ($x\leqslant 0$); $c_0=\sqrt{K_a/\rho_f}$.

In the region $0\leqslant x\leqslant L$, the pressure wave is given by

$$p^i(x,z,t)=p^i\left(t-\frac{x\cos\theta'}{c'}-\frac{z\sin\theta'}{c'}\right), \tag{10}$$

where c' is the velocity in the porous material ($0\leqslant x\leqslant L$), and the refraction angle θ' is given by the Descartes-Snell law:[6]

$$\frac{\sin\theta}{c_0}=\frac{\sin\theta'}{c'}. \tag{11}$$

To simplify the system of equations (5), we can then use the following property:

$$\frac{\partial}{\partial z}=-\frac{\sin\theta}{c_0}\frac{\partial}{\partial t}, \tag{12}$$

which implies

$$\frac{\partial v_z}{\partial z}=-\frac{\sin\theta}{c_0}\frac{\partial v_z}{\partial t}\quad\text{and}\quad\frac{\partial p}{\partial z}=-\frac{\sin\theta}{c_0}\frac{\partial p}{\partial t}. \tag{13}$$

From Eqs. (7) and (13), we obtain then the relation

$$\frac{\partial v_z}{\partial z}=-\frac{\sin^2\theta}{c_0^2}\left(a+b\frac{\partial^{-1/2}}{\partial t^{-1/2}}\right)^{-1}*\frac{\partial p}{\partial t}. \tag{14}$$

By using Eqs. (6), (8), and (14), the equation system (6), (7) and (8) can thus be simplified to

$$a\frac{\partial v_x(x,z,t)}{\partial t}+b\frac{\partial^{1/2} v_x(x,z,t)}{\partial t^{1/2}}=-\frac{\partial p(x,z,t)}{\partial x}, \tag{15}$$

$$d\frac{\partial p(x,z,t)}{\partial t}+f\frac{\partial^{1/2} p(x,z,t)}{\partial t^{1/2}}=-\frac{\partial v_x(x,z,t)}{\partial x}+\frac{\sin^2\theta}{c_0^2}\left(a+b\frac{\partial^{-1/2}}{\partial t^{-1/2}}\right)^{-1}*\frac{\partial p(x,z,t)}{\partial t}. \tag{16}$$

From Eqs. (15) and (16), we derive the generalized lossy wave equation in the time domain along the x-axis

$$\frac{\partial^2 p(x,z,t)}{\partial x^2}-A\frac{\partial^2 p(x,z,t)}{\partial t^2}-B\frac{\partial^{3/2} p(x,z,t)}{\partial t^{3/2}}-C\frac{\partial p(x,z,t)}{\partial t}=0, \tag{17}$$

where the coefficients A, B and C are constants, respectively, given by

$$A=\frac{1}{c_0^2}(\alpha_\infty-\sin^2\theta),\quad B=\frac{2\alpha_\infty}{K_a}\sqrt{\frac{\rho_f\eta}{\pi}}\left(\frac{1}{\Lambda}+\frac{\gamma-1}{\sqrt{\mathrm{Pr}}\Lambda'}\right),$$

and

$$C=\frac{4\alpha_\infty(\gamma-1)\eta}{K_a\Lambda\Lambda'\sqrt{\mathrm{Pr}}}. \tag{18}$$

The first one is related to the velocity of the projected wave along the x-axis $c=c_0/\sqrt{\alpha_\infty-\sin^2\theta}$. The other coefficients are essentially dependent on the characteristic lengths Λ and Λ', and express the viscous and thermal interactions between the fluid and the structure. The constant B governs the spreading of the signal while C is responsible of the attenuation of the wave. Obviously, a knowledge of these three coefficients allows the determination of the parameters α_∞, Λ, and Λ'. One way to solve Eq. (17) with suitable initial and boundary conditions is by using the Laplace transform. The approach is quite simple although the inverse Laplace transform requires tedious calculi.[3] A suitable setting for the introduction of the time domain solution of the modified wave propagation equation (17) is provided by the following model.

If the incident sound wave is launched in the region $x\leqslant 0$, then the expression of the pressure field in the region at the left of the material is the sum of the incident and reflected fields

$$p_1(x,t)=p^i\left(t-\frac{x\cos\theta}{c_0}\right)+p^r\left(t+\frac{x\cos\theta}{c_0}\right),\quad x<0. \tag{19}$$

Here, $p_1(x,t)$ is the field in the region $x<0$, p^i and p^r denote the incident and the reflected fields, respectively. In addition, a transmitted field is produced in the region at the right of the material. This has the form

$$p_3(x,t)=p^t\left(t-\frac{L}{c}-\frac{(x-L)\cos\theta}{c_0}\right),\quad x>L \tag{20}$$

[$p_3(x,t)$ is the field in the region $x>L$ and p^t is the transmitted field].

The incident and scattered fields are related by the scattering operators (i.e., the reflection and transmission operators) for the material. Theses are integral operators represented by

$$\begin{aligned}p^r(x,t)&=\int_0^t\tilde{R}(\tau)p^i\left(t-\tau+\frac{x}{c_0}\right)d\tau\\&=\tilde{R}(t)*p^i(t)*\delta\left(t+\frac{x\cos\theta}{c_0}\right),\end{aligned} \tag{21}$$

$$\begin{aligned}p^t(x,t)&=\int_0^t\tilde{T}(\tau)p^i\left(t-\tau-\frac{L}{c}-\frac{(x-L)}{c_0}\right)d\tau\\&=\tilde{T}(t)*p^i(t)*\delta\left(t-\frac{L}{c}-\frac{(x-L)\cos\theta}{c_0}\right).\end{aligned} \tag{22}$$

In Eqs. (21) and (22) the functions $\tilde{R}$ and $\tilde{T}$ are the reflection and transmission kernels, respectively, for incidence from the left. Note that the lower limit of integration in Eqs. (21) and (22) is chosen to be 0, which is equivalent to assume that the incident wave front first impinges on the material at $t=0$.

The scattering operators given in Eqs. (21) and (22) are independent of the incident field used in the scattering experiment and depend only on the properties of the materials.

To derive the reflection and transmission coefficients, the boundary conditions of the flow velocity at the interfaces $x=0$ and $x=L$ are needed.[1] Using the same calculus steps given in Ref. 1, we obtain the reflection and transmission scattering operators for a slab of porous material at oblique incidence

$$\begin{aligned}\tilde{R}(t)=&\left(\frac{1-E}{1+E}\right)\sum_{n\geqslant 0}\left(\frac{1-E}{1+E}\right)^{2n}\\&\times\left[F\left(t,2n\frac{L}{c}\right)-F\left(t,(2n+2)\frac{L}{c}\right)\right],\end{aligned} \tag{23}$$

$$\tilde{T}(t)=\frac{4E}{(1+E)^2}\sum_{n\geqslant 0}\left(\frac{1-E}{1+E}\right)^{2n}F\left(t+\frac{L}{c_0},(2n+1)\frac{L}{c}\right), \tag{24}$$

with

$$E=\frac{\phi\sqrt{1-\dfrac{\sin^2\theta}{\alpha_\infty}}}{\sqrt{\alpha_\infty}\cos\theta}. \tag{25}$$

Theses expressions take into account the n-multiple reflection in the material.

In most cases of porous materials saturated by air, the multiple reflection effects can be negligible because of the high attenuation of sound waves in these media. This depends on the thickness L and the flow resistivity σ of the porous material.

In the case where the multiple reflections can be neglected, the kernel of transmission is given by

$$\tilde{T}(t)=\frac{4E}{(1+E)^2}F\left(t+\frac{L}{c},\frac{L}{c}\right),$$

and the kernel of reflection by

$$\tilde{R}(t)=r(t)+\Re(t), \tag{26}$$

with

$$r(t)=\left(\frac{1-E}{1+E}\right)\delta(t)$$

and

$$\Re(t)=-\frac{4E(1-E)}{(1+E)^3}F\left(t,\frac{2L}{c}\right). \tag{27}$$

$r(t)$ is the instantaneously response of the porous material corresponding to the reflection contribution at the first interface ($x=0$).

In the case of a semi-infinite medium when $L\to\infty$, it can be shown[1] that $F(t,2L/c)\to 0$ and $\tilde{R}(t)\to r(t)$. This means that $\Re(t)$ is equivalent to the reflection at the rear interface ($x=L$), which is the bulk contribution to the reflection. The part of the wave corresponding to $r(t)$ is not subjected to the dispersion but is simply multiplied by the factor $(1-E)/(1+E)$. This shows that although tortuosity is a bulk parameter, it may be evaluated from the wave reflected at the first interface when the porosity is known and vice versa. Although generally speaking it is easy to evaluate the tortuosity from transmitted waves[1,3,4,19,21] this is not the case for porosity because of its weak sensitivity in transmitted mode.[1] Figure 2 shows two simulated transmitted signals for a plastic foam M1. The first one (solid line) corresponds to the value

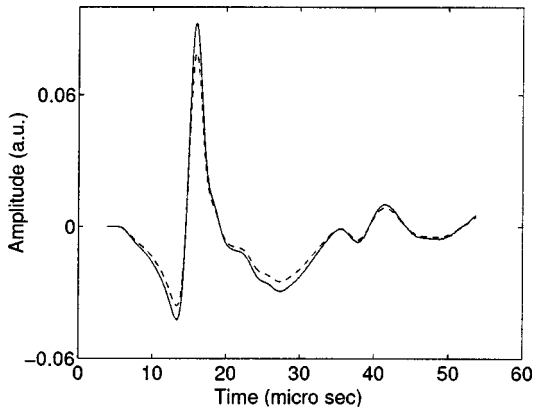

FIG. 2. Transmitted simulated signals for $\phi=0.98$ (solid line) and for $\phi=0.49$ (dashed line).

of porosity $\phi_1=0.98$ and the second one (dashed line) corresponds to $\phi_2=0.49$. The parameters of the plastic foam M1 (thickness 1.1 cm, $\phi=0.92$, $\alpha_\infty=1.25$, $\Lambda=50$ μm and $\Lambda'=150$ μm, flow resistivity $\sigma=38\,000$ Nm^{-4} s) have been determined using conventional methods.[1,3,4,19,21] Readers can see the slight difference between the two curves for a 50% difference in porosity values, which is due to the dispersion phenomenon that is governed by viscous, thermal and inertial effects contributed by α_∞, Λ and Λ' and plays a more important role in the Green function $F(t,k)$ than ϕ.

In Fig. 3 we show by numerical simulation, the difference between the reflected wave at the first interface and the total reflected wave. The difference between the two curves is marginal. This means that the wave reflected by the slab may be approximated by the reflected wave by the first interface $r(t)$ with a good level of accuracy. It is easy to verify that this approximation is valid for any incidence angle θ. In the next section, we will show, by a simple measurements, how it is the possible to determine the porosity and the tortuosity by measuring reflected wave by a slab of porous material.

IV. ULTRASONIC MEASUREMENT

In this section, we measure the tortuosity and the porosity knowing the reflection coefficient at the first interface for

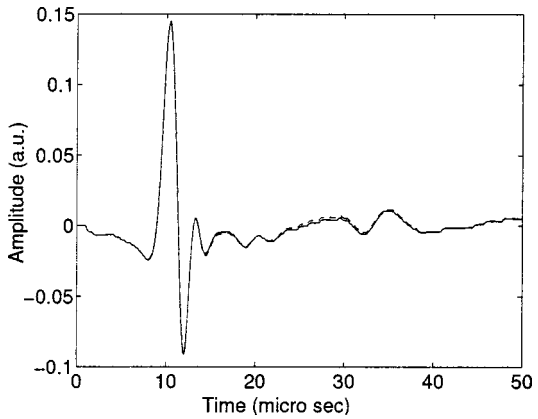

FIG. 3. Reflected wave at the first interface $x=0$ (solid line) and the total reflected wave (dashed line).

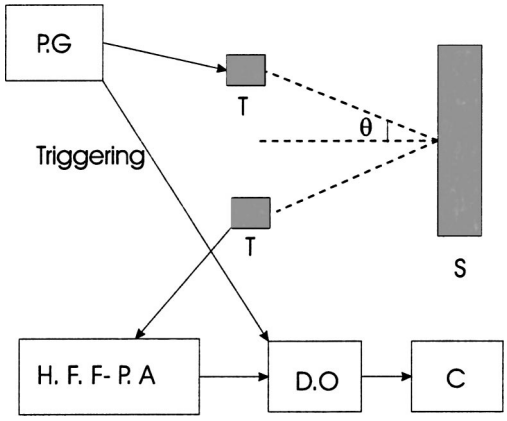

FIG. 4. Experimental set-up of the ultrasonic measurements in reflected mode P.G.: pulse generator, H. F. F-P. A: high frequency filtering-preamplifier, D.O: digital oscilloscope, C: computer, T: transducer, S: sample.

different values of the incidence angle θ. The expression of the reflection coefficient at the first interface is given by

$$r(t,\theta)=\frac{\alpha_\infty\cos\theta-\phi\sqrt{\alpha_\infty-\sin^2\theta}}{\alpha_\infty\cos\theta+\phi\sqrt{\alpha_\infty-\sin^2\theta}}\,\delta(t). \tag{28}$$

For two values of the incidence angle θ_1 and θ_2, it is easy to calculate the expression of the tortuosity function of the reflection coefficients $r_1=r(t)|_{\theta_1}$ and $r_2=r(t)|_{\theta_2}$ corresponding to the angles θ_1 and θ_2, respectively,

$$\alpha_\infty=\frac{\left(\dfrac{(1-r_2)(1+r_1)\cos\theta_2}{(1+r_2)(1-r_1)\cos\theta_1}\right)^2\sin^2\theta_1-\sin^2\theta_2}{\left(\dfrac{(1-r_2)(1+r_1)\cos\theta_2}{(1+r_2)(1-r_1)\cos\theta_1}\right)^2-1}. \tag{29}$$

Knowing the value of the tortuosity, we deduce the expression of the porosity function of θ_i and r_i by the expression

$$\phi=\frac{\alpha_\infty(1-r_i)\cos\theta_i}{(1+r_i)\sqrt{\alpha_\infty-\sin^2\theta_i}},\quad i=1,2. \tag{30}$$

As an application of this model, some numerical simulations are compared to experimental results. Experiments are carried out in air with two broadband Ultran NCT202

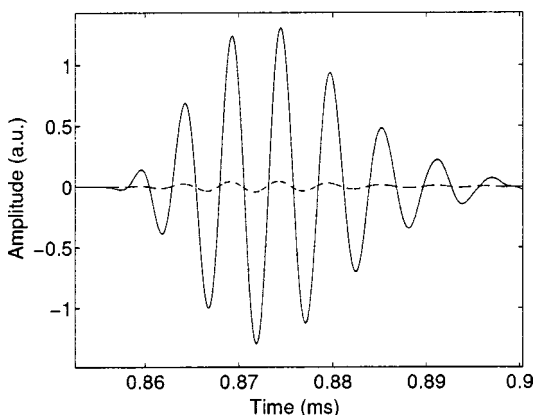

FIG. 5. Experimental incident signal (solid line) and experimental reflected signal (dashed line) by the material M2 ($\theta=0$ deg).

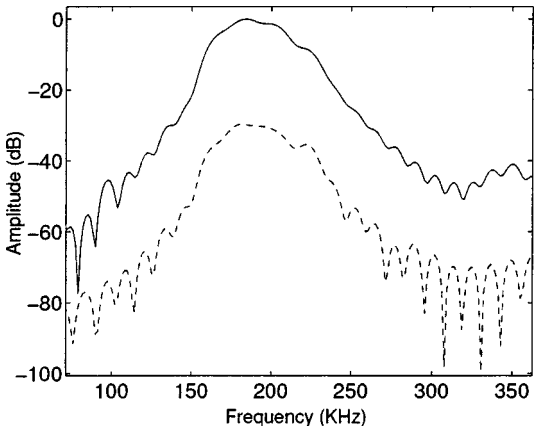

FIG. 6. Spectrum of experimental incident signal (solid line) and spectrum of experimental reflected signal (dashed line) for $\theta=0$ deg.

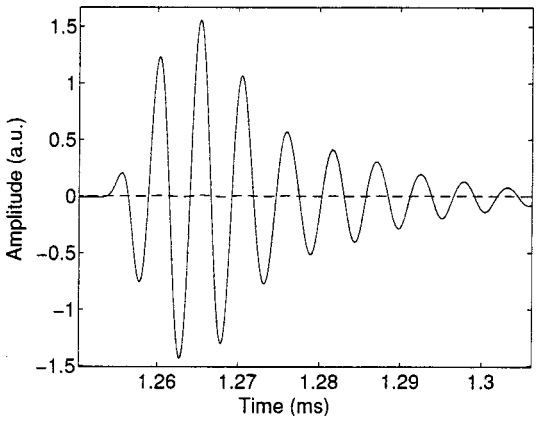

FIG. 7. Experimental incident signal (solid line) and experimental reflected signal (dashed line) by the material M2 ($\theta=53$ deg).

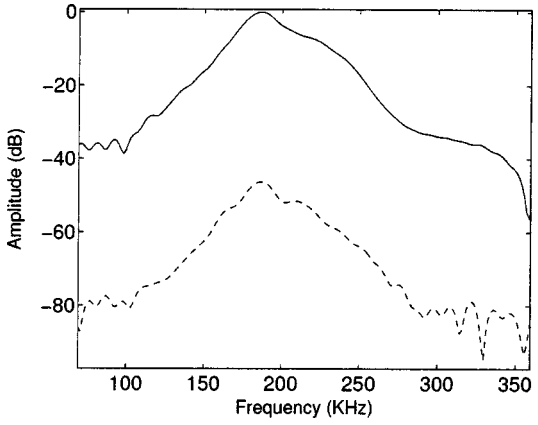

FIG. 8. Spectrum of experimental incident signal (solid line) and spectrum of experimental reflected signal (dashed line) for $\theta=53$ deg.

transducers having a 190 kHz central frequency in air and a bandwidth at 6 dB extending from 150 kHz to 230 kHz. A goniometer used in optic has been employed for the positioning of the transducers. Pulses of 400 V are provided by a 5052PR Panametrics pulser/receiver. The received signals are amplified up to 90 dB and filtered above 1 MHz to avoid high frequency noise. Electronic perturbations are removed by 1000 acquisition averages. The experimental setup is shown in Fig. 4. The distance between the transducers and the samples is 20 cm. The duration of the signal plays an important role, its spectrum must verify the condition of high frequency approximation referred to in the previous section.

The parameters of the first investigated plastic foam M2 are: resistivity $\sigma=2500\,\mathrm{Nm}^{-4}\,\mathrm{s}$, thickness 4.1 cm, $\Lambda=230\ \mu$m, and $\Lambda'=690\ \mu$m. Figure 5 shows the incident signal generated by the transducer (solid line) and the reflected signal by the plastic foam M2 (dashed line) for normal incidence. Figure 6 shows their spectra. From the spectra of the two signals, the reader can see that they have practically the same bandwidth which means that there is no dispersion. The reflected signal from the foam M2 is very small compared with the incident signal because of the low value of its flow resistivity σ.

Figure 7 represents the incident signal generated by the transducer (solid line) and the reflected signal by the plastic foam M2 (dashed line) for an incidence angle $\theta=53$ deg. Figure 8 depicts their spectra, showing that there is also no dispersion in the diffusion process. This concurs with the theory below which predicts that the reflected wave from the first interface ($x=0$) is measured and simply attenuated by the factor $(\alpha_\infty\cos\theta-\phi\sqrt{\alpha_\infty-\sin^2\theta})/(\alpha_\infty\cos\theta+\phi\sqrt{\alpha_\infty-\sin^2\theta})$. Table I gives the experimental data of the reflection coefficient for different values of the incidence angle θ and Table II give the values of the tortuosity and porosity calculated using of Eqs. (29) and (30) for each pair of incidence angles. The average value of the tortuosity obtained from these measurements is $\alpha_\infty=1.07\pm0.09$ and the average value of the porosity is $\phi=0.97\pm0.01$.

Figure 9 shows the experimental data of the reflection coefficient for different values of the incident angle θ, and the simulation of the variation of the reflection coefficient with the incident angle θ for the values of the tortuosity $\alpha_\infty=1.07$ and porosity $\phi=0.97$. The value of the porosity of the plastic foam M2 given by the porosimeter[18] is $\phi=0.98\pm0.02$, and the value of the tortuosity given by classical method[1,3,4,19,21] is $\alpha_\infty=1.06\pm0.08$. The reader can see the slight difference between the values of the porosity and tortuosity measured using this method and the other classical methods.[1,3,4,18,19,21] Figure 10 shows the comparison between the simulated reflected signal at the first interface calculated for $\alpha_\infty=1.07$ and $\phi=0.97$, and the experimental reflected signal for $\theta=17$ deg. Figure 11 shows the same comparison for $\theta=53$ deg.

TABLE I. Experimental data of the reflection coefficient for different values of the incidence angle θ (foam M2).

Incidence angle θ (deg)	0	8	14	17	23	30	35	41	53.5
Reflection coefficient r	0.033	0.0326	0.0322	0.0315	0.0300	0.0265	0.025	0.0164	0.005

TABLE II. Values of the tortuosity and porosity calculated for each pair of incidence angles θ_1 and θ_2 (foam M2).

Incidence angle θ_1/θ_2 (deg)	Tortuosity	Porosity
(a)		
0/8	1.080	0.976
0/14	1.054	0.961
0/17	1.068	0.967
0/23	1.07	0.969
0/30	1.086	0.975
0/35	1.071	0.968
0/41	1.100	0.981
0/53.3	1.039	0.954
8/14	1.039	0.954
8/17	1.063	0.965
8/23	1.069	0.968
8/30	1.085	0.975
8/35	1.070	0.968
8/41	1.100	0.981
8/53.5	1.069	0.968
14/17	1.099	0.980
14/23	1.081	0.972
14/30	1.081	0.972
14/35	1.073	0.969
14/41	1.104	0.982
14/53.5	1.070	0.977
(b)		
17/23	1.075	0.970
17/30	1.092	0.977
17/35	1.071	0.968
17/41	1.105	0.982
17/53.5	1.069	0.968
23/30	1.103	0.983
23/35	1.070	0.968
23/41	1.109	0.983
23/53.5	1.069	0.968
30/35	1.04	0.961
30/41	1.112	0.983
30/53.5	1.065	0.969
35/41	1.164	0.998
35/53.5	1.069	0.968
41/53.5	1.068	0.968

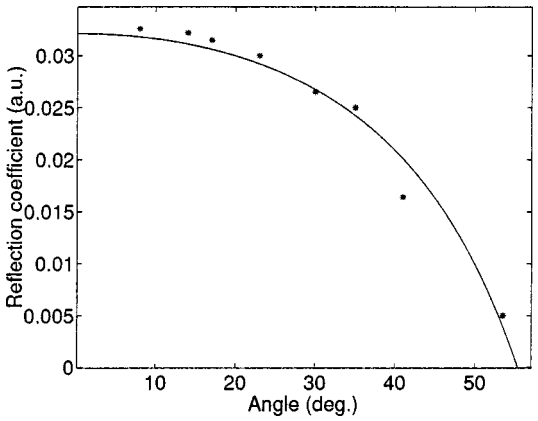

FIG. 9. Simulation of the variation of the reflection coefficient (solid line) with the incident angle θ and experimental data of the reflection coefficient (star) for the material M2.

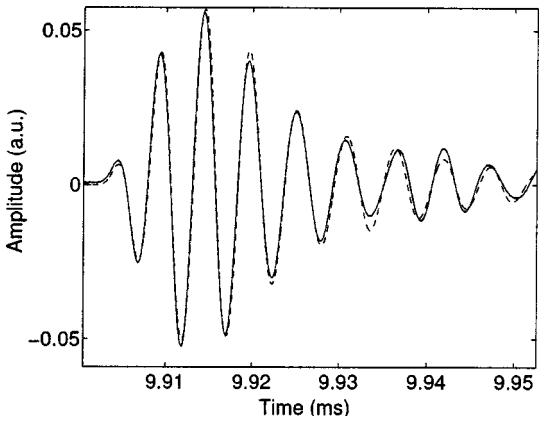

FIG. 10. Comparison between experimental reflected signal (solid line) and simulated reflected signal (dashed line) for M2 ($\theta=17$ deg).

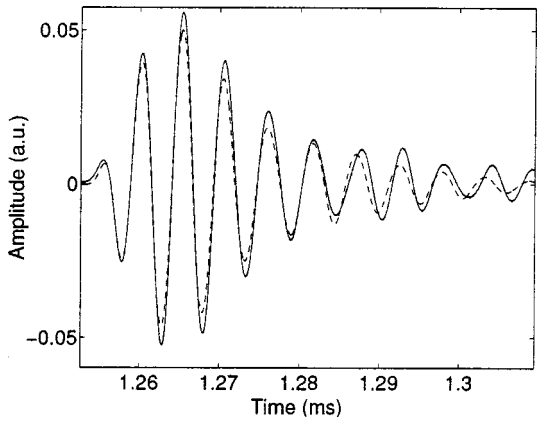

FIG. 11. Comparison between experimental reflected signal (solid line) and simulated reflected signal (dashed line) for M2 ($\theta=53$ deg).

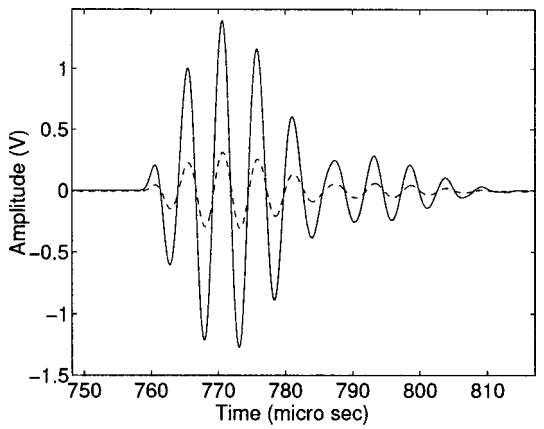

FIG. 12. Experimental incident signal (solid line) and experimental reflected signal (dashed line) by the material M3 for $\theta=13$ deg.

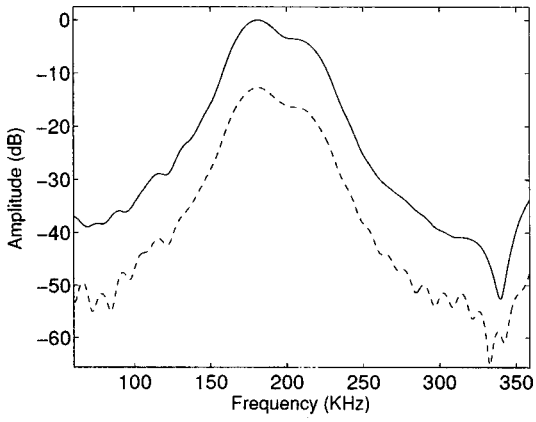

FIG. 13. Spectrum of experimental incident signal (solid line) and spectrum of experimental reflected signal (dashed line) for $\theta = 13$ deg.

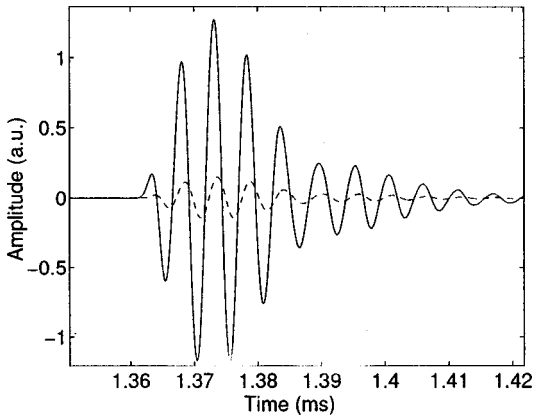

FIG. 14. Experimental incident signal (solid line) and experimental reflected signal (dashed line) by the material M3 for $\theta = 49$ deg.

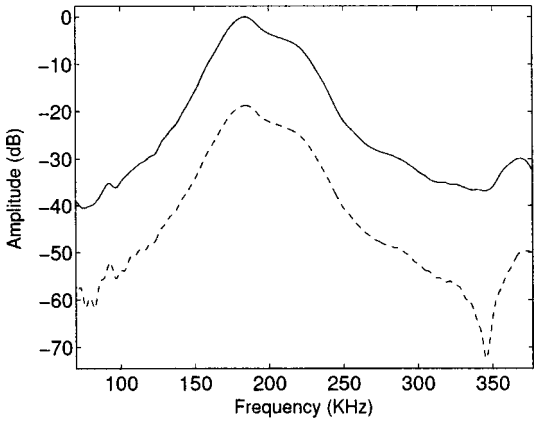

FIG. 15. Spectrum of experimental incident signal (solid line) and spectrum of experimental reflected signal (dashed line) for $\theta = 49$ deg.

TABLE IV. Values of the tortuosity and porosity calculated for each pair of incidence angles θ_1 and θ_2 (foam M3).

Incidence angle θ_1/θ_2 (deg)	Tortuosity	Porosity
(a)		
0/13.5	1.9	0.86
0/23	1.680	0.816
0/32.5	1.700	0.820
0/39.7	1.715	0.824
0/49.8	1.712	0.823
0/54	1.709	0.822
0/60.6	1.729	0.827
13.5/23	1.592	0.796
13.5/32.5	1.665	0.814
13.5/39.7	1.695	0.821
13.5/49.8	1.701	0.822
13.5/54	1.704	0.823
13.5/60.3	1.722	0.827
23/32.5	1.714	0.823
(b)		
23/39.7	1.729	0.826
23/49.8	1.719	0.824
23/54	1.719	0.824
23/60.3	1.735	0.828
32.5/39.7	1.743	0.829
32.5/49.8	1.72	0.824
32.5/54	1.721	0.824
32.5/60	1.739	0.828
39.7/49.8	1.709	0.823
39.7/54	1.713	0.824
39.7/60.3	1.738	0.821
49.8/54	1.695	0.829
49.8/60.3	1.761	0.829
54/60.3	1.801	0.832

The difference between the simulated reflected signal and experimental reflected signal is relatively weak which leads to the conclusion that the values of the tortuosity and porosity obtained are satisfactory.

Another plastic foam M3 (thickness 2.1 cm, $\Lambda = 23\ \mu$m, and $\Lambda' = 69\ \mu$m) with a higher value of the flow resistivity $\sigma = 125\,000\ \mathrm{Nm}^{-4}\,\mathrm{s}$ has been investigated. Figure 12 shows the incident and reflected signals for $\theta = 13$ deg and Fig. 13 shows their spectra. Here also, we can conclude from the two spectra that there is no dispersion. Figure 14 shows the incident and reflected signals for $\theta = 49$ deg. Figure 15 shows their spectra. For this plastic foam M3, the reflected signal is more important than the one of the foam M2 because of its high value of the flow resistivity. The approximation that the reflected signal is essentially due to the reflection at the first interface is well verified in this case.

Table III gives the experimental data of the reflection coefficient for different values of the incidence angle θ and Table IV gives the values of the tortuosity and porosity calculated with Eqs. (29) and (30) for each pair of the incidence angles. The average value of the tortuosity obtained is $\alpha_\infty = 1.72 \pm 0.02$ and the average value of the porosity obtained

TABLE III. Experimental data of the reflection coefficient for different values of the incidence angle θ (foam M3).

Incidence angle θ (deg)	0	13.5	23	32.5	39.7	49.8	54	60.3
Reflection coefficient r	0.2274	0.221	0.2106	0.1905	0.1668	0.1163	0.0864	0.024

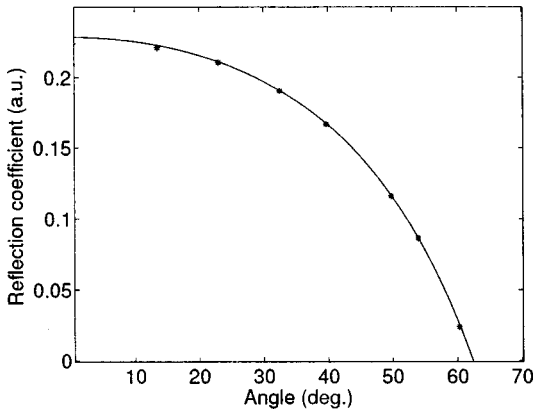

FIG. 16. Simulation of the variation of the reflection coefficient (solid line) with the incident angle θ and experimental data of the reflection coefficient (star) for the material M3.

is $\phi = 0.82 \pm 0.04$. Figure 16 shows the simulated variation of the reflection coefficient at the first interface for the value of the tortuosity $\alpha_\infty = 1.72$ and porosity $\phi = 0.82$ and experimental data of the reflection coefficient. The value of the porosity of the plastic foam M3 given by the porosimeter[18] is $\phi = 0.8 \pm 0.1$, and the value of the tortuosity obtained by classical methods[1,3,4,19,21] is $\alpha_\infty = 1.7 \pm 0.1$. Figure 17 shows the comparison between the simulated reflected signal at the first interface calculated for $\alpha_\infty = 1.72$ and $\phi = 0.8$, and the experimental reflected signal for $\theta = 13$ deg. The difference between the two results is small which leads to the conclusion that the values of the tortuosity and porosity obtained are satisfactory.

V. CONCLUSION

A method for the measurement of the porosity and the tortuosity simultaneously from the measurements of reflected waves at two oblique angles of incidence has been proposed. Generally, it is easy to evaluate the tortuosity from transmitted waves, this is not the case for porosity because of its weak sensitivity in transmitted mode. This method is an alternative to the usual method involving the use of a porosimeter introduced by Beranek and improved by Champoux *et al.* or the other ultrasonic methods developed by Leclaire *et al.*

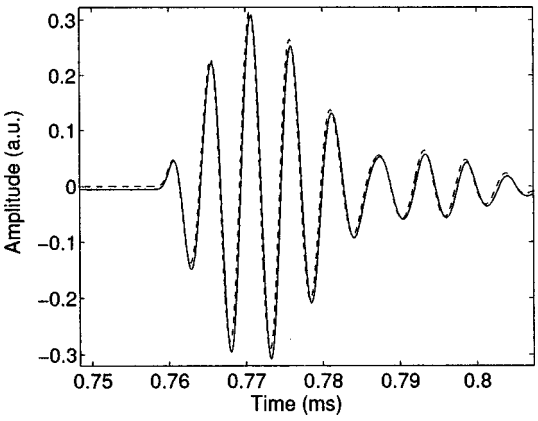

FIG. 17. Comparison between experimental reflected signal (solid line) and simulated reflected signal (dashed line) for M3 ($\theta = 13$ deg).

The method is based upon the propagation equation in time domain in a slab of porous material having a rigid frame at asymptotic domain (high frequency range). A time domain model of wave propagation in such material is worked out from the concept of fractional calculus. The kernels of the reflection and transmission scattering operators are derived giving simple relations between these operators and the parameters of the medium. Because of the high attenuation in such media, the reflected wave by the porous material can be approximated by the reflected wave at the first interface. As a consequence, it gives a simple relation between the porosity, tortuosity, incident angle and reflected wave, proving in such a way that all physical parameters of acoustic material can be evaluated from acoustic measurements.

An experimental validation of the theoretical expression of the reflection scattering operators illustrates the high level of correspondence between numerical and experimental results and show that this time domain model is well suited for the characterization of porous media via acoustic wave propagation.

ACKNOWLEDGMENT

The authors would like to express all thanks to the reviewers of the paper for their critical remarks.

[1] Z. E. A. Fellah, M. Fellah, W. Lauriks, and C. Depollier, "Direct and inverse scattering of transient acoustic waves by a slab of rigid porous material," J. Acoust. Soc. Am. **113**, 61–73 (2003).
[2] Z. E. A. Fellah and C. Depollier, "Transient acoustic wave propagation in rigid porous media: A time-domain approach," J. Acoust. Soc. Am. **107**, 683–688 (2000).
[3] Z. E. A. Fellah, C. Depollier, and M. Fellah, "An approach to direct and inverse time-domain scattering of acoustic waves from rigid porous materials by a fractional calculus based method," J. Sound Vib. **244**, 359–366 (2001).
[4] Z. E. A. Fellah, C. Depollier, and M. Fellah, "Application of fractional calculus to the sound waves propagation in rigid porous materials: Validation via ultrasonic measurements," Acust. Acta Acust. **88**, 34–39 (2002).
[5] D. L. Johnson, J. Koplik, and R. Dashen, "Theory of dynamic permeability and tortuosity in fluid-saturated porous media," J. Fluid Mech. **176**, 379–402 (1987).
[6] J. F. Allard, *Propagation of Sound in Porous Media: Modeling Sound Absorbing Materials* (Chapman and Hall, London, 1993).
[7] M. A. Biot, "The theory of propagation of elastic waves in fluid-saturated porous solid. I. Low frequency range," J. Acoust. Soc. Am. **28**, 168–178 (1956).
[8] M. A. Biot, "The theory of propagation of elastic waves in fluid-saturated porous solid. II. Higher frequency range," J. Acoust. Soc. Am. **28**, 179–191 (1956).
[9] K. Attenborough, "Acoustical characteristics of porous materials," Phys. Lett. **82**, 179–227 (1982).
[10] L. L. Beranek, "Acoustic impedance of porous materials," J. Acoust. Soc. Am. **13**, 248–260 (1942).
[11] C. Zwikker and C. W. Kosten, *Sound Absorbing Materials* (Elsevier, New York, 1949).
[12] Y. Champoux and J. F. Allard, "New empirical equations for sound propagation in rigid frame fibrous materials," J. Acoust. Soc. Am. **91**, 3346–3353 (1992).
[13] D. Lafarge, P. Lemarnier, J. F. Allard, and V. Tarnow, "Dynamic compressibility of air in porous structures at audible frequencies," J. Acoust. Soc. Am. **102**, 1995–2006 (1996).

[14] R. W. Leonard, ''Simplified porosity measurements,'' J. Acoust. Soc. Am. **20**, 39–41 (1948).
[15] E. Guyon, L. Oger, and T. J. Plona, ''Transport properties in sintered porous media composed of two particles sizes,'' J. Phys. D **20**, 1637–1644 (1987).
[16] D. L. Johnson, T. J. Plona, C. Scala, F. Psierb, and H. Kojima, ''Tortuosity and acoustic slow waves,'' Phys. Rev. Lett. **49**, 1840–1844 (1982).
[17] J. Van Brakel, S. Modry, and M. Svata, ''Mercury porosimetry: State of the art,'' Powder Technol. **29**, 1–12 (1981).
[18] Y. Champoux, M. R. Stinson, and G. A. Daigle, ''Air-based system for the measurement of porosity,'' J. Acoust. Soc. Am. **89**, 910–916 (1991).
[19] P. Leclaire, L. Kelders, W. Lauriks, N. R. Brown, M. Melon, and B. Castagnède, ''Determination of viscous and thermal characteristics lengths of plastic foams by ultrasonic measurements in helium and air,'' J. Appl. Phys. **80**, 2009–2012 (1996).
[20] S. G. Samko, A. A. Kilbas, and O. I. Marichev, *Fractional Integrals and Derivatives: Theory and Applications* (Gordon and Breach Science, Amsterdam, 1993).
[21] N. Brown, M. Melon, V. Montembault, B. Castagnède, W. Lauriks, and P. Leclaire, ''Evaluation of viscous characteristic length of air-saturated porous materials from the ultrasonic dispersion curve,'' C. R. Acad. Sci. Paris, **322**, 121–127 (1996).

Finite difference computation of head-related transfer function for human hearing

Tian Xiao and Qing Huo Liu[a)]
Electrical and Computer Engineering, Duke University, Durham, North Carolina 27708

(Received 29 April 2001; revised 12 November 2002; accepted 24 January 2003)

Modeling the head-related transfer function (HRTF) is a key to many applications in spatial audio. To understand and predict the effects of head geometry and the surrounding environment on the HRTF, a three-dimensional finite-difference time domain model (3D FDTD) has been developed to simulate acoustic wave interaction with a human head. A perfectly matched layer (PML) is used to absorb outgoing waves at the truncated boundary of an unbounded medium. An external source is utilized to reduce the computational domain size through the scattered-field/total-field formulation. This numerical model has been validated by analytical solutions for a spherical head model. The 3D FDTD code is then used as a computational tool to predict the HRTF for various scenarios. In particular, a simplified spherical head model is compared to a realistic head model up to about 7 kHz. The HRTF is also computed for a realistic head model in the presence of a wall. It is demonstrated that this 3D FDTD model can be a useful tool for spatial audio applications. © *2003 Acoustical Society of America.* [DOI: 10.1121/1.1561495]

PACS numbers: 43.20.Fn, 43.20.Px [VWS]

I. INTRODUCTION

Humans have a remarkable ability to localize a sound source using the sound heard at the two ears. Sound waves that reach the ears are affected by interactions with the listener's torso, head and pinnae, etc. The collective effects of the interactions are captured as the head-related transfer function (HRTF). For a particular source location, the HRTF is a frequency response function which is defined as the ratio of complex sound pressure level (SPL) at the eardrum to the SPL at the location of the center of the head when the listener is absent.[1] The HRTF holds the key to many applications in spatial audio.

The computation of the HRTF is essentially a typical acoustical scattering problem. The listener can be viewed as a scattering object surrounded by a homogeneous background air. Of course, walls, floors, and other environmental surfaces also have effects on the sound field which must be taken into account to produce proper rendering of spatial sound. However, because of the huge computational demand, simulation of the HRTF with all these environmental effects is still beyond the reach of current full-wave methods. Similar to earlier works,[2–8] here we will focus on scattering by a human head with only limited environmental effects, for example, from a wall.

A boundary element method (BEM) was applied by Katz[4,7–9] to solve this problem where the complex head geometry is modeled and the head is assumed homogeneous. This method has the following advantages: (a) it requires surface-only discretization resulting in a reduction in the dimensionality of the problem, and (b) it handles the far-field radiation condition automatically.[1] In the BEM, the scatterer surface is discretized using several elements (e.g., plane-triangular). To represent the solution accurately, the element size used in the discretization is determined by the frequency, with the sampling criterion requiring four elements per wavelength[7] (this number is inadequate in our opinion). In the numerical literature, 10 or 20 elements per wavelength are suggested for an adequate accuracy.[1] Thus, at a high frequency a large numerical problem has to be solved.

In this work, the HRTF was computed using the Fourier transform of the time domain results at the eardrums. A three-dimensional finite-difference (3D FDTD) method was developed to obtain the time domain results. A perfectly matched layer (PML)[10] is used to eliminate the artificial reflection from the truncated boundary of unbounded medium. An external source outside the computation domain is utilized to reduce the computational domain size. There are two important advantages with such an approach: (a) the whole frequency band of interest is obtained in one single time-domain simulation, and (b) the simulation for sound sources with a complex spectral structure can be created without convolution. Numerical validation for this 3D FDTD method has been performed against exact analytical solutions for a spherical head model. The finite-difference code is then used as a computational tool to predict the HRTF for various scenarios. In particular, a simplified spherical head model is compared to a realistic head model up to about 7 kHz. The HRTF is also computed for a realistic head model in the presence of a wall. It is demonstrated that this 3D FDTD model can be a useful tool for spatial audio applications.

II. FORMULATION

The computation of the head-related transfer function (HRTF) is a key to many applications in spatial audio, because all of the acoustic cues resulting from scattering of the incident sound by the torso, head, pinnae, walls and other environmental surfaces can be in principle captured by the HRTF. For a particular source location, the HRTF is a fre-

[a)]Author to whom correspondence should be addressed. Electronic mail: qhliu@ee.duke.edu

 0001-4966/2003/113(5)/2434/8/$19.00

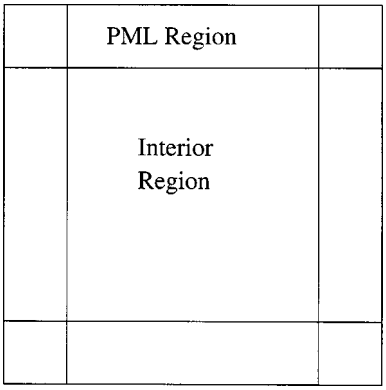

FIG. 1. Computational domain with an interior region and a PML boundary region.

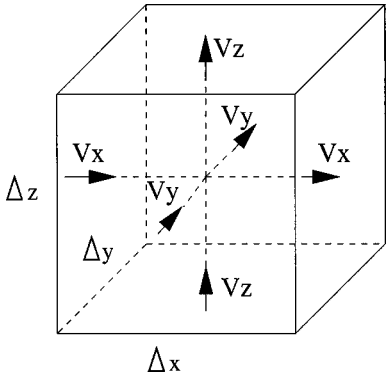

FIG. 2. The relative locations of field components in a unit cell of the staggered finite difference grid.

quency response function which is equal to the ratio of sound pressure level (SPL) at the eardrum to the SPL at the location of the center of the head when the listener is absent.[1] Thus, the HRTF can be represented by

$$H=20\log_{10}\left|\frac{\mathcal{F}\{p(\mathbf{r}_e,t)\}}{\mathcal{F}\{p_{\mathrm{inc}}(\mathbf{r}_c,t)\}}\right|, \tag{1}$$

where $p(\mathbf{r}_e,t)$ is the sound pressure at the eardrum $\mathbf{r}=\mathbf{r}_e$, $p_{\mathrm{inc}}(\mathbf{r}_c,t)$ is the pressure of the incident sound at the center of head $\mathbf{r}=\mathbf{r}_c$ when the listener is absent, and $\mathcal{F}$ denotes the temporal Fourier transform. The HRTF depends on many factors including the shape of the head and pinnae, spatial orientation of the head relative to the source of sound, the room environment, proportions of the body, and others.

To model the HRTF, a linear inhomogeneous, absorptive medium with space-dependent density $\rho(\mathbf{r})$, sound speed $c(\mathbf{r})$, and absorption coefficient $\gamma(\mathbf{r})$ is considered. The pressure field $p(\mathbf{r},t)$ and particle velocity $\mathbf{v}(\mathbf{r},t)$ field satisfy the basic Newton's law of motion and equation of continuity,

$$\rho\frac{\partial\mathbf{v}(\mathbf{r},t)}{\partial t}=-\nabla p, \tag{2}$$

$$\frac{\partial p}{\partial t}+\gamma(\mathbf{r})c^2(\mathbf{r})p(\mathbf{r},t)=-\rho(\mathbf{r})c^2(\mathbf{r})\nabla\cdot\mathbf{v}(\mathbf{r},t)+f_s(\mathbf{r},t), \tag{3}$$

where $f_s(\mathbf{r},t)$ is the volume source density of pressure injection rate (Pa/s). Our aim is to calculate the pressure and velocity fields when a listener and an arbitrary acoustic source are present.

A. The FD scheme and perfectly matched layer

Here we briefly summarize the FD scheme and the PML absorbing boundary condition; for more details, the reader is referred to Ref. 10. The PML is introduced as an ABC outside the scattering objects as shown in Fig. 1. The stretched coordinates are used in PML in order to absorb outgoing waves as proposed for electromagnetic waves and elastic waves in Refs. 11–18. In the frequency domain, if the complex coordinate-stretching variable is chosen as

$$e_\eta=a_\eta+i\frac{\omega_\eta}{\omega}\quad(\eta=x,y,z), \tag{4}$$

the operator ∇_e expressed in terms of the complex coordinate-stretching variables is

$$\nabla_e=\sum_{\eta=x,y,z}\hat{\eta}\,\frac{1}{e_\eta}\frac{\partial}{\partial\eta}. \tag{5}$$

Then, by replacing ∇ with ∇_e, Eqs. (2) and (3) are modified in stretched coordinates as

$$-i\omega\rho\mathbf{v}(\mathbf{r},\omega)=-\sum_{\eta=x,y,z}\hat{\eta}\,\frac{1}{e_\eta}\frac{\partial p(\mathbf{r},\omega)}{\partial\eta}, \tag{6}$$

$$-i\omega p(\mathbf{r},\omega)+\gamma(\mathbf{r})c^2(\mathbf{r})p(\mathbf{r},\omega)=-\rho(\mathbf{r})c^2(\mathbf{r})\sum_{\eta=x,y,z}\frac{1}{e_\eta}\frac{\partial v_\eta(\mathbf{r},\omega)}{\partial\eta}+f_s(\mathbf{r},\omega), \tag{7}$$

where a time dependence of $e^{-i\omega t}$ is implied. In a PML region, the real part $a_\eta\geqslant 1$ is a scaling factor, and the imaginary part $\omega_\eta\geqslant 0$ represents a loss in the PML. In a regular non-PML region, one has $a_\eta=1$ and $\omega_\eta=0$. The proof of zero reflections for a PML interface follows that in Ref. 13.

With the split fields defined as

$$p=\sum_{\eta=x,y,z}p^{(\eta)},\quad f_s=\sum_{\eta=x,y,z}f_s^{(\eta)}, \tag{8}$$

Eqs. (6) and (7) can be reformulated as

$$a_\eta\rho\frac{\partial v_\eta}{\partial t}+\omega_\eta\rho v_\eta=-\frac{\partial p}{\partial\eta}, \tag{9}$$

$$a_\eta\frac{\partial p^{(\eta)}}{\partial t}+(a_\eta\gamma c^2+\omega_\eta)p^{(\eta)}+\omega_\eta\gamma c^2\int_{-\infty}^{t}p^{(\eta)}(\mathbf{r},t')dt'=-\rho c^2\frac{\partial v_\eta}{\partial\eta}+a_\eta f_s^{(\eta)}(\mathbf{r},t)+\omega_\eta\int_{-\infty}^{t}f_s^{(\eta)}(\mathbf{r},t')dt', \tag{10}$$

after replacing $-i\omega$ by $\partial/\partial t$ to obtain the time domain equations.

A finite-difference scheme is used to solve Eqs. (9) and (10). The staggered grid in Fig. 2 is applied. In this staggered grid, the pressure field p is located at the cell center, while the velocity field components are located at the cell's face centers. The unbounded medium is truncated into a finite computational domain with a total of $N_x\times N_y\times N_z$ cells. If

the finite-difference cell sizes are Δx, Δy, and Δz in the x, y, and z directions, respectively, the pressure field and velocity field components are discretized as[10]

$$p^{(\eta)}(j_x,j_y,j_z,n)\equiv p^{(\eta)}[(j_x+\tfrac{1}{2})\Delta x,(j_y+\tfrac{1}{2})\Delta y,(j_z+\tfrac{1}{2})\Delta z,n\Delta t], \tag{11}$$

$$v_\eta(j_x,j_y,j_z,n)\equiv v_\eta[(j_x+\tfrac{1}{2}\epsilon_{x\eta})\Delta x,(j_y+\tfrac{1}{2}\epsilon_{y\eta})\Delta y,(j_z+\tfrac{1}{2}\epsilon_{z\eta})\Delta z,(n+\tfrac{1}{2})\Delta t], \tag{12}$$

where

$$\epsilon_{\eta_1\eta_2}=1-\delta_{\eta_1\eta_2},\quad \delta_{\eta_1\eta_2}=\begin{cases}1, & \text{if } \eta_1=\eta_2,\\ 0, & \text{if } \eta_1\neq\eta_2.\end{cases} \tag{13}$$

With this discretization, the time and spatial derivatives with respect to x are approximated by central differencing as

$$\frac{\partial p^{(\eta)}(j_x,j_y,j_z,n+\frac{1}{2})}{\partial t}\approx\frac{p^{(\eta)}(j_x,j_y,j_z,n+1)-p^{(\eta)}(j_x,j_y,j_z,n)}{\Delta t}, \tag{14}$$

$$\frac{\partial v_\eta(j_x,j_y,j_z,n-\frac{1}{2})}{\partial t}\approx\frac{v_\eta(j_x,j_y,j_z,n)-v_\eta(j_x,j_y,j_z,n-1)}{\Delta t}, \tag{15}$$

$$\frac{\partial p^{(\eta)}(j_x+\frac{1}{2},j_y,j_z,n)}{\partial x}\approx\frac{p^{(\eta)}(j_x+1,j_y,j_z,n)-p^{(\eta)}(j_x,j_y,j_z,n)}{\Delta x}, \tag{16}$$

$$\frac{\partial v_\eta(j_x+\frac{1}{2},j_y,j_z,n)}{\partial x}\approx\frac{v_\eta(j_x+1,j_y,j_z,n)-v_\eta(j_x,j_y,j_z,n)}{\Delta x}. \tag{17}$$

The spatial derivatives with respect to y and z directions are similarly approximated. The integrations in Eqs. (9) and (10) are computed by using the simple trapezoidal rule. After all these approximations, Eqs. (9) and (10) become time-stepping equations

$$v_\eta(j_x,j_y,j_z,n)=f_{1\eta}v_\eta(j_x,j_y,j_z,n-1)+f_{2\eta}[p(j_x,j_y,j_z,n)-p(j_x-\delta_{x\eta},j_y-\delta_{y\eta},j_z-\delta_{z\eta},n)], \tag{18}$$

$$p^{(\eta)}(j_x,j_y,j_z,n+1)=f_{3x}p^{(\eta)}(j_x,j_y,j_z,n)+f_{4\eta}p_I^{(\eta)}(j_x,j_y,j_z,n)+f_{5\eta}[v_\eta(j_x+\delta_{x\eta},j_y+\delta_{y\eta},j_z+\delta_{z\eta},n)-v_\eta(j_x,j_y,j_z,n)]+f_{6\eta}f_s(j_x,j_y,j_z,n+\tfrac{1}{2}), \tag{19}$$

where

$$f_{1\eta}=\frac{a_\eta/\Delta t-\omega_\eta/2}{a_\eta/\Delta t+\omega_\eta/2},\quad f_{2\eta}=-\frac{1}{(a_\eta/\Delta t+\omega_\eta/2)\rho\Delta\eta}, \tag{20}$$

$$f_{3\eta}=\frac{a_\eta/\Delta t-(a_\eta\gamma c^2+\omega_\eta)/2}{D_{\eta v}},\quad f_{4\eta}=-\frac{\omega_\eta\gamma c^2\Delta t}{D_{\eta v}}, \tag{21}$$

$$f_{5\eta}=-\frac{\rho c^2}{D_{\eta v}\Delta x},\quad f_{6\eta}=\frac{1}{D_{\eta v}}, \tag{22}$$

$$p_I^{(\eta)}(j_x,j_y,j_z,n)=\tfrac{1}{2}p^{(\eta)}(j_x,j_y,j_z,0)+\sum_{l=1}^{n}p^{(\eta)}(j_x,j_y,j_z,l), \tag{23}$$

and

$$D_{\eta v}=a_\eta/\Delta t+(a_\eta\gamma c^2+\omega_\eta)/2+\omega_\eta\gamma c^2\Delta t/2. \tag{24}$$

Equations (18) and (19) constitute a leapfrog system for v_η and $p^{(\eta)}(\eta=x,y,z)$. Given a particular source excitation and the starting fields, that is the pressure field and the particle velocity field at $n=0$, the time-stepping system provides the wave field solution for the entire grid.

B. External source

The above FD scheme includes sources in the computation domain. However, when the source is far from the scattering objects, a large space including the source and the scattering objects needs to be considered. To reduce the computational domain size, an external source method is utilized by using the scattered-field/total-field formulation well known in computational electromagnetics.[19] In this method, the total field is split into the incident and scattered fields, and the computational domain is divided into two regions by a virtual closed interface enclosing the scattering objects. The total field is solved in the inner region, while the scattered field is solved in the outer region. The pressure and particle velocity fields $(p_1,\mathbf{v}_1)$ in the inner region and $(p_2,\mathbf{v}_2)$ in the outer region satisfy the basic Newton's law and equation of continuity,

$$\rho(\mathbf{r})\frac{\partial\mathbf{v}_1(\mathbf{r},t)}{\partial t}=-\nabla p_1, \tag{25}$$

$$\frac{\partial p_1}{\partial t}+\gamma(\mathbf{r})c^2(\mathbf{r})p_1(\mathbf{r},t)=-\rho(\mathbf{r})c^2(\mathbf{r})\nabla\cdot\mathbf{v}_1(\mathbf{r},t), \tag{26}$$

$$\rho_0\frac{\partial\mathbf{v}_2(\mathbf{r},t)}{\partial t}=-\nabla p_2, \tag{27}$$

$$\frac{\partial p_2}{\partial t}+\gamma_0c_0^2p_2(\mathbf{r},t)=-\rho_0c_0^2\nabla\cdot\mathbf{v}_2(\mathbf{r},t)+f_s(\mathbf{r},t), \tag{28}$$

as well as the boundary conditions on the common virtual interface

$$p_1=p_2,\quad \mathbf{v}_1\cdot\mathbf{n}=\mathbf{v}_2\cdot\mathbf{n}, \tag{29}$$

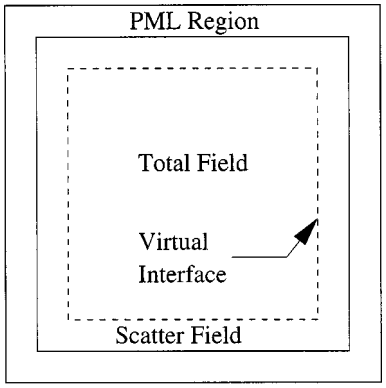

FIG. 3. Cross-section of the computation domain with rectangular PML boundary and virtual interface.

where it is assumed that no source exists on and inside the interface; for the outer region ρ, c and γ are, respectively, constants ρ_0, c_0 and γ_0, and $\mathbf{n}$ is the unit normal vector of the interface.

In the absence of the scatterer, the incident sound fields $(p_{\text{inc}}, \mathbf{v}_{\text{inc}})$ in the outer region (as well as in the interior region) satisfy the equations

$$\rho_0 \frac{\partial \mathbf{v}_{\text{inc}}(\mathbf{r},t)}{\partial t} = -\nabla p_{\text{inc}}, \tag{30}$$

$$\frac{\partial p_{\text{inc}}}{\partial t} + \gamma_0 c_0^2 p_{\text{inc}}(\mathbf{r},t) = -\rho_0 c_0^2 \nabla \cdot \mathbf{v}_{\text{inc}}(\mathbf{r},t) + f_s(\mathbf{r},t). \tag{31}$$

But since the field outside the interface can be written as the sum of the incident and scattered fields, i.e., $p_2 = p_{\text{inc}} + p_{\text{sct}}$ and $\mathbf{v}_2 = \mathbf{v}_{\text{inc}} + \mathbf{v}_{\text{sct}}$ where p_{inc} and $\mathbf{v}_{\text{inc}}$ are incident fields and p_{sct} and $\mathbf{v}_{\text{sct}}$ are scattered fields in the outer region, by subtracting (30) from (27), and (31) from (28), we arrive at the equations for the scattered fields p_{sct} and $\mathbf{v}_{\text{sct}}$,

$$\rho_0 \frac{\partial \mathbf{v}_{\text{sct}}(\mathbf{r},t)}{\partial t} = -\nabla p_{\text{sct}}, \tag{32}$$

$$\frac{\partial p_{\text{sct}}}{\partial t} + \gamma_0 c_0^2 p_{\text{sct}}(\mathbf{r},t) = -\rho_0 c_0^2 \nabla \cdot \mathbf{v}_{\text{sct}}(\mathbf{r},t), \tag{33}$$

in the outer region. Note that, naturally, there are no source terms in these scattered-field equations, thus eliminating the need to include the source in the computational domain.

The incident fields p_{inc} and $\mathbf{v}_{\text{inc}}$ can be solved by analytical method for point sources and plane wave source. With the known incident fields, (25)–(26), (32)–(33) and (29) constitute the complete governing equations.

The PML is applied outside the virtual interface to absorb the scattering wave. In the finite-difference scheme, a computational domain with the PML and virtual interface is schematically shown in Fig. 3. Note that the total fields p_1 and $\mathbf{v}_1$ in the inner region as well as the scattering fields p_{sct} and $\mathbf{v}_{\text{sct}}$ satisfy the same equations except for the the difference in medium properties ρ, c and γ. So the both sets of fields can be treated according to (18) and (19), except that the source term in (19) is now absent. On the virtual interface, care must be taken in bookkeeping to make the fields inside and outside to satisfy the boundary conditions (29). Specifically, the incident fields must be appropriately added or subtracted for the nodes on and immediately near the virtual interface. Assume that the fields on the virtual interface are defined as the total fields in the inner region; the virtual interface coincides with the normal velocity components, and is the surface of the cuboid defined by $[j_{x1}, j_{x2}] \otimes [j_{y1}, j_{y2}] \otimes [j_{z1}, j_{z2}]$. Then on the face of $j_x = j_{x1}$, for example, the velocity component v_x must be updated as

$$\begin{aligned} v_x(j_x, j_y, j_z, n) = {} & f_{1x} v_x(j_x, j_y, j_z, n-1) \\ & + f_{2x}[p(j_x, j_y, j_z, n) - p_{\text{sct}}(j_x - 1, \\ & j_y, j_z, n) - p_{\text{inc}}(j_x - 1, j_y, j_z, n)], \end{aligned} \tag{34}$$

for $j_x = j_{x1}$, $j_{y1} \leqslant j_y \leqslant j_{y2} - 1$, $j_{z1} \leqslant j_z \leqslant j_{z2} - 1$. Similarly, the pressure field $p^{(x)}$ immediately left of this face, i.e., $j_x = j_{x1} - 1$, must be updated as

$$\begin{aligned} p_{\text{sct}}^{(x)}(j_x, j_y, j_z, n+1) = {} & f_{3x} p_{\text{sct}}^{(x)}(j_x, j_y, j_z, n) \\ & + f_{4x} p_{\text{sct},I}^{(x)}(j_x, j_y, j_z, n) \\ & + f_{5x}[v_x(j_x + 1, j_y, j_z, n) \\ & - v_{\text{inc},x}(j_x + 1, j_y, j_z, n) \\ & - v_x(j_x, j_y, j_z, n)], \end{aligned} \tag{35}$$

for $j_x = j_{x1} - 1$, $j_{y1} \leqslant j_y \leqslant j_{y2} - 1$, $j_{z1} \leqslant j_z \leqslant j_{z2} - 1$. Similar procedures are taken for the other five faces of this virtual interface.

III. NUMERICAL RESULTS

We have implemented the FD algorithm with the PML and external source. To validate the algorithm, the numerical results are compared with the analytical solutions for a spherical head model. Two kinds of sources are used to excite the acoustic wave fields. One is a monopole source, the other is plane wave source. The incident waveform is the first derivative of the Blackman–Harris window function.[12,20] The central frequency of the time function is chosen as 3 kHz, giving a usable frequency band up to about 7 kHz. The FD code is first validated and then used as a computational tool to predict the HRTF for various scenarios. Since the sources are external to the computational domain, the starting time $t = 0$ in the following temporal responses is chosen to be the arriving time at a reference point in the computation domain. In all following examples, the normalized frequency f_n is defined by

$$f_n = \frac{2\pi a}{c_2} f,$$

where $c_2 = 340$ m/s is the sound velocity in air, and $a = 0.08$ m is the nominal mean radius of a sphere used in this study.

A. Validation of the FDTD algorithm

A rigid sphere has been used as an approximate head model to serve as a guide to the study of the HRTF. Here we use such a spherical model to validate the finite-difference algorithm because its analytical solutions for the monopole and plane wave sources are available.

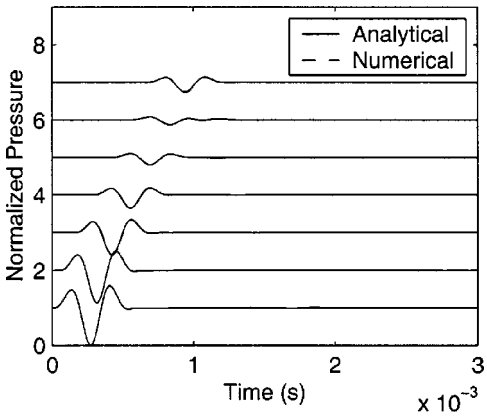

FIG. 4. 3D FDTD results and analytical solutions for a rigid spherical head model with a monopole source.

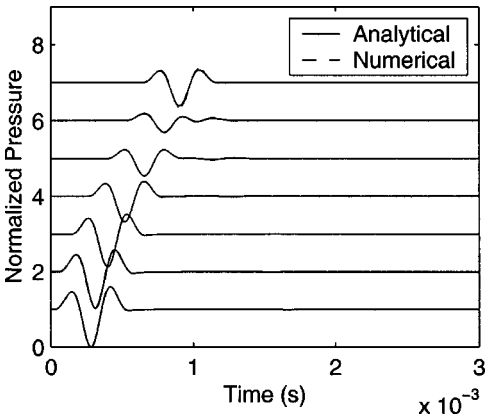

FIG. 6. 3D FDTD results and analytical solutions for a rigid spherical head model with a plane wave source.

The test case for the finite-difference algorithm is a rigid sphere (radius $a=0.08$ m) with $\rho_1=1\times10^{10}$ kg/m^3, $c_1=340$ m/s and $\gamma_1=0$ s/m^2 surrounded by a lossless background medium with $\rho_2=1$ kg/m^3, $c_2=340$ m/s and $\gamma_2=0$ s/m^2. Such a rigid medium is a very good approximation to the actual sound wave interaction with the human head. Two kinds of sources, a point source and a plane wave, are applied to validate the algorithm.

1. A monopole source interacting with a sphere

A monopole source is located at $z_s=0.24$ m from the center of the sphere. The temporal responses and transfer functions for seven points on the sphere surface are computed at every 30° from 0° to 180°. A discretization of $\Delta x=\Delta y=\Delta z=1\times10^{-3}$ m and $\Delta t=1.5\times10^{-6}$ s is chosen for the 3D FDTD program. The total number of cells is $N_x\times N_y\times N_z=200\times200\times200$. The temporal response for analytical and numerical results are given in Fig. 4 and the HRTFs are shown in Fig. 5. For the temporal response, Fig. 4 shows the excellent agreement between the numerical and analytical results. The HRTF in Fig. 5 also shows an excellent agreement at low frequencies, although the error is slightly larger at high frequencies as expected. This error at high frequencies results from a lower sampling per wavelength for high frequencies. According to our experience, this finite difference scheme should be much faster than boundary element method, though there is no BEM software available for us right now (the CPU time reported in Ref. 8 is 28 h for one single frequency of 5.4 kHz). There are some reasons to support our belief. First, HRTFs are obtained by the Fourier transformation of the time domain results in this FDTD method. Unlike BEM, we do not need to compute the transfer functions frequency by frequency. The frequency responses with broad band can be obtained by one single computation. Second, an efficient, simple, staggered finite difference scheme is used to obtain the time domain results. For example, for this relatively large case, a problem with size of $N_x\times N_y\times N_z=200\times200\times200$, 2000-time-step computation requires about 320 min on a SUN Ultra 60 computer.

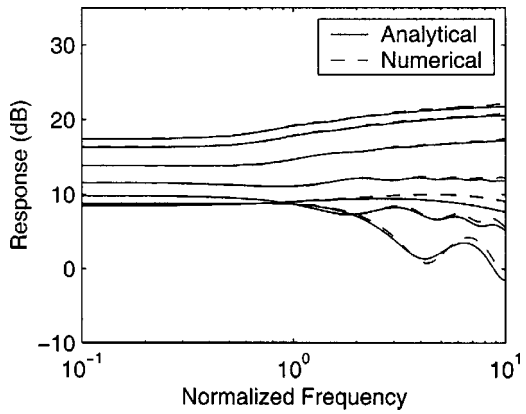

FIG. 5. Spherical head-related transfer function for a monopole source. The frequency is normalized with $c_1/2\pi a$, where a is the radius of the sphere, and c_1 is the sound speed in the air.

2. A plane wave incident on a sphere

A plane wave source is also applied to validate the finite-difference algorithm. The plane wave propagates along the $-x$ direction. A discretization of $\Delta x=\Delta y=\Delta z=1\times10^{-3}$ m and $\Delta t=1.5\times10^{-6}$ s is chosen for the 3D FDTD program. The total number of cells is $N_x\times N_y\times N_z=200\times200\times200$. The temporal responses and transfer functions for seven points on the sphere surface on xy plane through the sphere center are computed at every 30° from 0° to 180°. The analytical and numerical results are given by Figs. 6 and 7. Similar to the comparison for the monopole source, the temporal response in Fig. 6 shows an excellent agree-

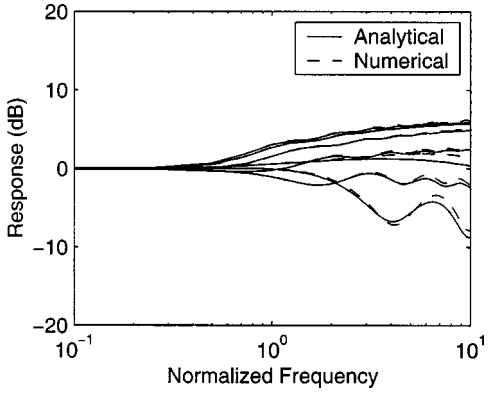

FIG. 7. Spherical head-related transfer function for a plane wave source.

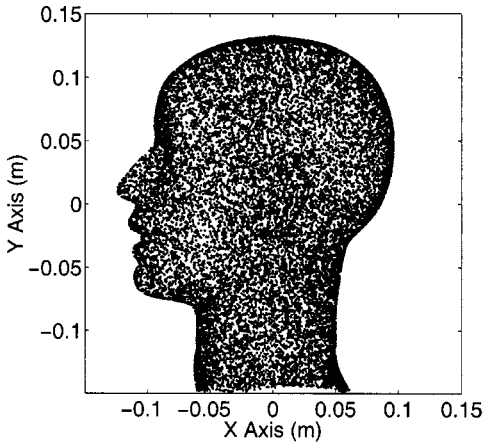

FIG. 8. The left side view of a real head model with a finely mesh surface.

ment between the numerical and analytical results. The HRTF in Fig. 7 also shows an excellent agreement at low frequencies but slightly larger error at high frequencies, as expected.

B. The HRTF computation for an actual head (Kemar model)

With the confirmation of the accuracy, the FD algorithm is then used to predict the HRTF for various scenarios. A rigid homogeneous head mode is assumed with $\rho_1=1\times10^{10}$ kg/m^3, $c_1=340$ m/s and $\gamma_1=0$ s/m^2. The geometry data of the real head (Kemar) model is from Ref. 6 which was meshed for the boundary element method. The left side view of the surface-meshed head is shown in Fig. 8. From this finely meshed surface, we created a regular FD grid by simple interpolation. The HRTFs are calculated for various cases with plane wave incidence, with the receiver slightly (17 mm) in front of the eardrum.

1. The head in a homogeneous air

A series of scenarios is considered for plane waves incident from different directions. A discretization of $\Delta x=\Delta y=\Delta z=3\times10^{-3}$ m and $\Delta t=5\times10^{-6}$ s is chosen for the 3D FDTD program. The total number of cells is $N_x\times N_y\times N_z=130\times130\times130$. Figure 9 shows the HRTF for the plane wave propagates along $\hat{x}$ (i.e., from directly in front of the head); Fig. 10 shows the HRTF for the plane wave along $-\hat{x}$ (i.e., from behind the head); Fig. 11 shows the HRTF for the plane wave along $\hat{y}$ (i.e., from below the head); Fig. 12 shows the HRTF for the plane wave along $-\hat{y}$ (i.e., from above the head); Fig. 13 shows the HRTF for the plane wave along $\hat{z}$ (i.e., from the right to left ear); and Fig. 14 shows the HRTF for the plane wave along $-\hat{z}$ (i.e., from the left to right ears). As shown by these figures, (a) the HRTFs approach 0 dB at low frequencies, and (b) the HRTFs are generally larger than those with a sphere model. This can be explained by the ears having the focusing effects on the incoming sound. (c) The focusing effects of the ears are more obvious at higher frequencies. (d) There are significant asymmetries between the responses of the left and right ears due to the geometrical differences. For these cases with the size of $N_x\times N_y\times N_z=130\times130\times130$, 1000-time-step computation requires about 40 min on a SUN Ultra 60 computer.

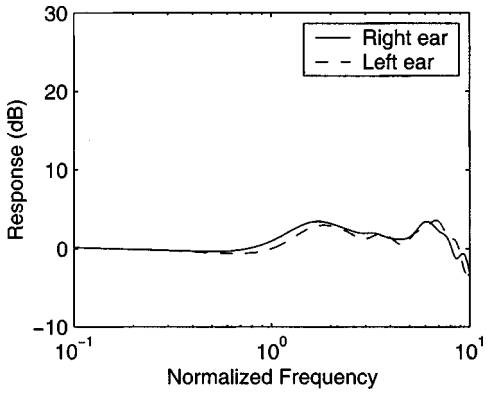

FIG. 10. HRTF for the plane wave propagating along $-x$ direction.

2. The head at a close distance from a rigid wall

Here a rigid wall parallel to the yz plane is located 6 cm behind the head. The plane wave source is directed at the direction of $\hat{x}$. A discretization of $\Delta x=\Delta y=\Delta z=3\times10^{-3}$ m and $\Delta t=5\times10^{-6}$ s is chosen. The total number of cells is $N_x\times N_y\times N_z=130\times130\times130$. The HRTF is shown in Fig. 15. From the results, we can see (a) the HRTF approaches 6 dB at low frequencies, i.e., the sound pressure is about two times that when the wall is absent and (b) the HRTF at high frequencies oscillates because of the interference from the wall.

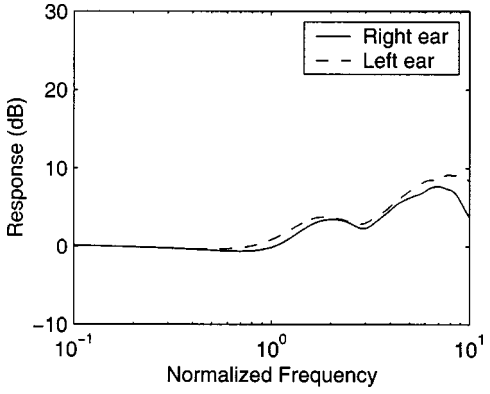

FIG. 9. HRTF for the plane wave propagating along $+x$ direction.

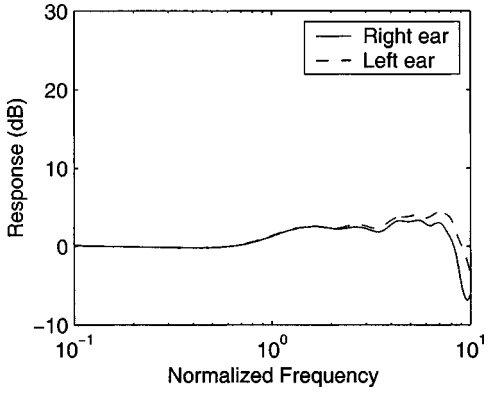

FIG. 11. HRTF for the plane wave propagating along $+y$ direction.

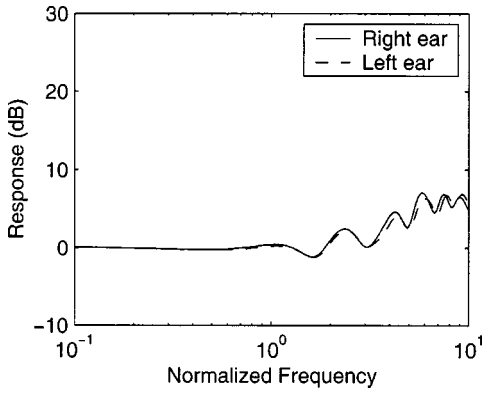

FIG. 12. HRTF for the plane wave propagating along $-y$ direction.

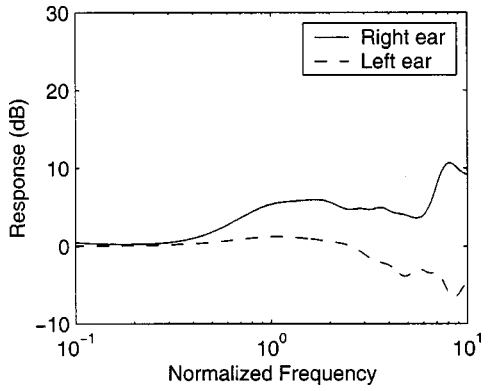

FIG. 13. HRTF for the plane wave propagating along $+z$ direction.

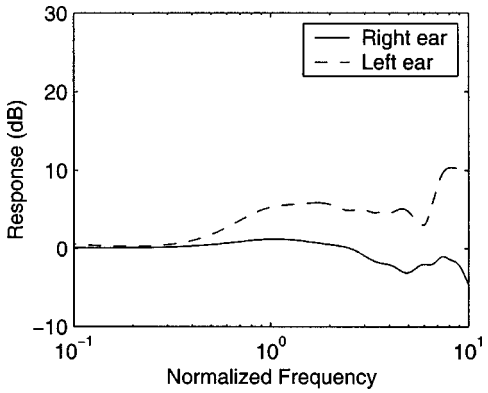

FIG. 14. HRTF for the plane wave propagating along $-z$ direction.

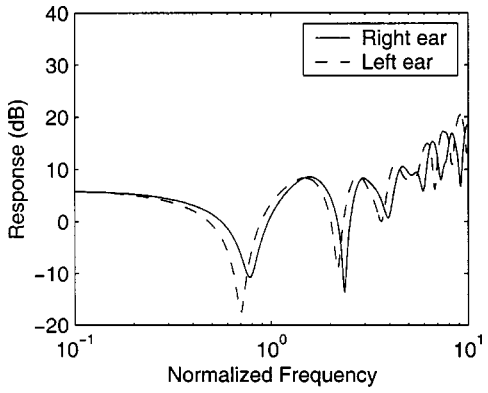

FIG. 15. HRTF with a wall for the plane wave propagating along $+x$ direction.

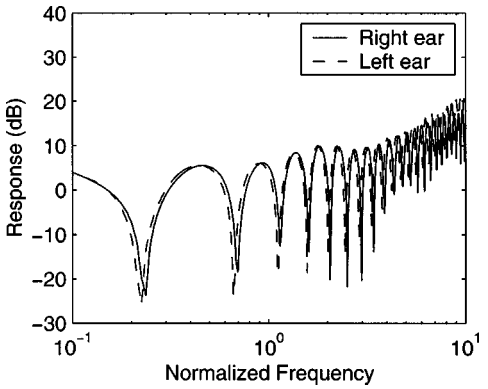

FIG. 16. HRTF with a wall for the plane wave propagating along $+x$ direction.

3. The head at a moderate distance from a rigid wall

We then model the effects of the rigid wall at a distance of 45 cm behind head. The plane wave source is incident at the same direction as the last case. A discretization of $\Delta x = \Delta y = \Delta z = 3 \times 10^{-3}$ m and $\Delta t = 5 \times 10^{-6}$ s is chosen. The total number of cells is $N_x \times N_y \times N_z = 260 \times 130 \times 130$. The HRTF is shown in Fig. 16. From the results, we can also see (a) the HRTF approaches a value slightly smaller than 6 dB at low frequencies, i.e., the sound pressure is less than about two times that when the wall is absent, and (b) the HRTF's frequency interference is more severe than the last case where the wall is closer. This is the result of the larger time separation between the incident wave and the reflected wave from the wall. In this case, since these two waves are well separated, if we only consider the time window within the first part (e.g., a window with $t \leqslant 0.003$ s), the HRTF will be identical to the case without a wall.

IV. CONCLUSION

A three-dimensional finite-difference time domain (3D FDTD) algorithm was developed to compute the head-related transfer function (HRTF). In the algorithm, a perfectly matched layer (PML) is used to absorb outgoing waves at the truncated boundary of an unbounded medium. An external source is utilized to reduce the computational domain size. The algorithm has been validated by analytical results for simple spherical head models. Several interesting results of the HRTF for a real head geometry have been modeled by the algorithm. The effects of a wall have also been considered. It is demonstrated that the 3D FDTD model can be a useful tool for spatial audio applications. On a moderate size workstation, this FDTD code can already simulate with reasonably good accuracy the HRTF for a real head in the presence of a wall up to 7 kHz. Our future work will focus on developing an even more accurate scheme to model HRTFs with more environmental effects up to a higher frequency band.

ACKNOWLEDGMENTS

With the help of Dr. Ramani Duraiswami of the University of Maryland, the finite-difference mesh used was derived from scans performed by Yuvi Kahana of the Institute of

Sound Vibration and Research, University of Southampton. The provision of this surface mesh is gratefully acknowledged. We also thank Dr. Richard Duda, Dr. Ralph Algazi, and Dr. Ramani Duraiswami for useful interactions. The work was supported by the National Science Foundation through Grant Nos. CCR-00-98140 and IIS-0086075.

[1] D. Begault, *3-D Sound for Virtual Reality and Multimedia* (Academic Press, Boston, MA, 1994).
[2] R. O. Duda and W. L. Martens, ''Range dependence of the response of a spherical head model,'' J. Acoust. Soc. Am. **104**, 3048–3058 (1998).
[3] N. A. Gumerov and R. Duraiswami, ''Modeling the effect of a nearby boundary on the HRTF,'' Proc. ICASSP-2001, Salt Lake City, UT, May 2001.
[4] Y. Kahana, P. A. Nelson, M. Petyt, and S. Choi, ''Boundary Element simulation of HRTFs and sound fields produced by virtual acoustic imaging systems,'' Audio Engineering Society, 105th Convention, Preprint 4817, San Francisco, 1998.
[5] Y. Kahana, P. A. Nelson, M. Petyt, and S. Choi, ''Numerical modeling of the transfer functions of a dummy-head and of the external ear,'' Audio Engineering Society, 16th international conference, Rovaneimi, 1999, pp. 330–345.
[6] Y. Kahana and P. A. Nelson, ''Spatial acoustic mode shapes of the human pinna,'' Audio Engineering Society, 109th Convention, Preprint 5218, Los Angeles, 2000.
[7] B. F. G. Katz, ''Measurement and Calculation of Individual Head-Related Transfer Functions using a Boundary Element Model Including the Measurement and Effect of Skin and Hair Impedance,'' Ph.D. dissertation, Graduate Program in Acoustics, Pennsylvania State University, 1998.
[8] B. F. G. Katz, ''Boundary element method calculation of individual head-related transfer function. I. Rigid model calculation,'' J. Acoust. Soc. Am. **110**, 2440–2448 (2001).
[9] B. F. G. Katz, ''Boundary element method calculation of individual head-related transfer function. II. Impedance effects and comparisons to real measurements,'' J. Acoust. Soc. Am. **110**, 2449–2455 (2001).
[10] Q. H. Liu and J. Tao, ''The perfectly matched layer for acoustic waves in absorptive media,'' J. Acoust. Soc. Am. **102**, 2072–2082 (1997).
[11] W. C. Chew and W. H. Weedon, ''A 3D perfectly matched medium from modified Maxwell's equations with stretched coordinates,'' Microwave Opt. Technol. Lett. **7**, 599–604 (1994).
[12] Q. H. Liu, ''A FDTD algorithm with perfectly matched layers for conductive media,'' Microwave Opt. Technol. Lett. **14**(2), 134–137 (1997).
[13] W. C. Chew and Q. H. Liu, ''Perfectly matched layers for elastodynamics: A new absorbing boundary condition,'' J. Comput. Acoust. **4**(4), 72–79 (1996).
[14] Q. H. Liu, ''PML and PSTD algorithm for arbitrary lossy anisotropic media,'' IEEE Microwave Guid. Wave Lett. **9**(2), 48–50 (1999).
[15] Q. H. Liu, ''Perfectly matched layers for elastic waves in cylindrical and spherical coordinates,'' J. Acoust. Soc. Am. **105**, 2075–2084 (1999).
[16] G.-X. Fan and Q. H. Liu, ''An FDTD algorithm with PML for dispersive, conductive media,'' IEEE Trans. Antennas Propag. **48**(5), 637–646 (2000).
[17] Y. Q. Zeng, J. He, and Q. H. Liu, ''The application of the perfectly matched layer in numerical modeling of wave propagation in poroelastic media,'' Geophysics **66**(4), 1258–1266 (2001).
[18] Y. Q. Zeng and Q. H. Liu, ''A staggered-grid finite-difference method with perfectly matched layers for poroelastic wave equations,'' J. Acoust. Soc. Am. **109**, 2571–2580 (2001).
[19] A. Taflove, *Computational Electrodynamics: The Finite Difference Time Domain Method* (Artech House, Norwood, MA, 1995).
[20] Q. H. Liu, F. Daube, C. Randall, E. Scheon, H. Liu, and P. Lee, ''A three-dimensional finite difference simulation of sonic logging,'' J. Acoust. Soc. Am. **100**, 72–79 (1996).

Antiplane shear wave propagation in fiber-reinforced composites[a)]

Jin-Yeon Kim[b)]
Department of Industrial, Welding and Systems Engineering, The Ohio State University and Edison Joining Technology Center, 1248 Arthur E. Adams Drive, Columbus, Ohio 43221

(Received 4 April 2002; revised 18 January 2003; accepted 27 January 2003)

A self-consistent method for analyzing antiplane shear wave propagation in two-dimensional inhomogeneous media is presented. For applications in the high-frequency range, the self-consistent condition for the effective medium is solved being supplemented with the theory of quasidynamic effective density. Comparisons with other theoretical calculations and experimental data for fiber-reinforced composites demonstrate the merits of using the present method. © *2003 Acoustical Society of America.* [DOI: 10.1121/1.1564015]

PACS numbers: 43.20.Jr, 43.35.Cg, 43.20.Fn [DEC]

I. INTRODUCTION

Due to the inherent complexity of the multiple scattering process, modeling of wave propagation in inhomogeneous media is still a challenging problem. Among other theories, the self-consistent method has been used successfully in many fields including the alloy physics[1,2] and the mechanics of composite materials[3–10] for evaluating the effective properties. The method has the advantage that the multiple scattering effects can be taken into consideration in a simple way, which greatly reduces the computational effort. It has been known that the method provides extreme values of the effective properties when the constituent properties differ very much. This may be disadvantageous when evaluating the effective properties of composites with isolated inclusions (e.g., porous solids), but it is desirable when predicting certain critical phenomena in aggregate structures.[10] Therefore, a theoretical treatment of composite media should always involve microstructural considerations.

In this paper, the condition that the effective medium should satisfy is derived based on the self-consistent formalism. Then, the practical limitations of the result in calculating the dynamic effective elastic properties are discussed. A method to circumvent the limitation is proposed combining two existing theories.[7,9] The calculated effective wave speed and coherent attenuation of fiber-reinforced composites are compared with those from other theories and also with experimental data.

II. SELF-CONSISTENT FORMULATION

The total field in an inhomogeneous medium can be considered as the sum of a mean (average) field and a fluctuating field. If the fluctuating field is due to random variation of material properties, then the mean field is naturally related to effective properties of the medium. Therefore, the effective properties can be determined by calculating the mean and the fluctuating fields. To evaluate the fluctuating field, constituents are embedded in yet-unknown effective medium in which the mean field is assumed to propagate as a plane wave in the direction $\hat{\mathbf{k}}_e$. The subscript ''e'' denotes the effective medium. Then, the effective properties are determined as those that make the fluctuating field (the scattering of the mean field due to the embedded objects) to vanish on the average. The single scattering approximation[1,2] is employed to calculate the average total multiple scattering field due to the embedded objects as

$$\langle \hat{\mathbf{k}}_e \cdot \mathbf{t} \cdot \hat{\mathbf{k}}_e \rangle = 0, \tag{1}$$

where $\mathbf{t}$ denotes the single scattering operator and the bracket ($\langle\ \rangle$) is an averaging operator. The microstructural characteristics of the inhomogeneous medium can be taken into account both in the scattering operator and in the averaging operator. This condition can be expressed in terms of the forward scattering amplitude $[f(\hat{\mathbf{k}}_e;\hat{\mathbf{k}}_e)]$ from the energy consideration[8,11]

$$\langle f(\hat{\mathbf{k}}_e;\hat{\mathbf{k}}_e) \rangle = 0. \tag{2}$$

Invoking the scattering theorem[12] that the forward-scattering amplitude is proportional to the total power abstracted during the scattering process, the self-consistent condition [Eq. (2)] states that there is no scattering when the mean field propagates in the effective medium. It should be noted that other self-consistent formulations[6,13] based on different approaches produce similar conditions for the effective medium. In the long wavelength regime, Eq. (2) can be approximated to obtain quasistatic effective properties.[7] Similar self-consistent methods have been proposed for evaluating effective electromagnetic properties of inhomogeneous dielectric media.[14,15] A simple realization of the averaging operation is the volume-weight average[5,6,8,9]

$$\sum_i v_i f(\hat{\mathbf{k}}_e;\hat{\mathbf{k}}_e) = 0, \tag{3}$$

where v_i denotes the volume fraction of the ith constituent.

Although the above self-consistent condition (vanishing of the average forward-scattering amplitude) is physically sufficient to describe the effective medium, two effective properties (density and shear modulus) cannot be determined simultaneously from the single condition. A supplementary condition is needed. This fact limits the application of Eq. (2)

[a)]This paper is dedicated to Emeritus Professor Byung-Ho Lee of KAIST, in memory.

[b)]Electronic mail: kim.896@osu.edu

 0001-4966/2003/113(5)/2442/4/$19.00

TABLE I. Elastic properties of constituents.

Materials	Density (kg/m^3)	Shear modulus (GPa)	Phase velocity (m/s)
Aluminum matrix	2720	38.7	3772
Steel fiber	7800	80.9	3220
Epoxy matrix	1260	1.98	1254
Carbon fiber	1310	21.0	4004

[or Eq. (3)] to finding dynamic effective properties of an *elastic* inhomogeneous media. Note that the above condition is sufficient for electromagnetic wave propagation in a composite medium in which a single material constant, that is, the dielectric constant, is involved. Kim *et al.*[9] attempted to calculate the effective properties by solving two nonlinear equations obtained from Eq. (3). Yang and Mal[13] used the volume-weight average density for composites having small density mismatch between constituents.

In this study, the effective density [Eq. (A2) in the Appendix] that has been derived[9] using the Sabina and Willis theory[7] for the antiplane shear wave motion in the two-dimensional composite is adopted as the supplementary condition. It should be noted that whereas the static effective density is determined as the volume-weight average density, the dynamic effective density should be determined with the consideration of the inertial interaction between constituents. Due to the approximation employed in the Sabina and Willis theory,[7] the effective density is valid in the low-frequency range. However, since the density mismatch plays an important role at frequencies near several lowest resonances, the effective density should provide a good approximation in a wide frequency range.

III. RESULTS AND DISCUSSION

Numerical calculations are performed for unidirectional fiber-reinforced composites. The material properties of constituents are listed in Table I. The matrix and fiber are denoted by subscripts "1" and "2." The results are compared with those calculated with other theories: the multiple scattering theory of Varadan *et al.*,[16] the causal differential scheme of Beltzer and Brauner,[17] the generalized self-consistent model (GSCM) of Yang and Mal,[13] and the self-consistent theory of Sabina and Willis.[7] It should be noted that a full analytical evaluation on the validity of any of the above theories is very difficult. However, all of the above theories are known to satisfy the Hashin's rigorous bound[18] in the static limit.

In Fig. 1, the normalized wave speed (c_e/c_1) and the specific attenuation capacity ($4\pi\,\mathrm{Im}[k_e]/\mathrm{Re}[k_e]$) of steel/aluminum composite with fiber volume fraction of 27% are shown. The solid lines present those from the present self-consistent method; the dashed line from Eq. (3) along with the static effective density ($\rho_e=v_1\rho_1+v_2\rho_2$); the chain-dashed line from the previous self-consistent method of Kim;[9] the dotted line from the Sabina and Willis.[7] It is noted that the present self-consistent method and the previous self-consistent method of Kim[9] agree well with each other up to $k_1a=2$. The calculation based on the static effective density shows good agreements with the above two only at low and high frequencies where the inertial motion of fibers is less important. The results from the Sabina and Willis theory deviate from other and converge to certain limits ($c_e\rightarrow c_1$ and attenuation$\rightarrow 0$) with the increase of frequency as discussed in Ref. 9.

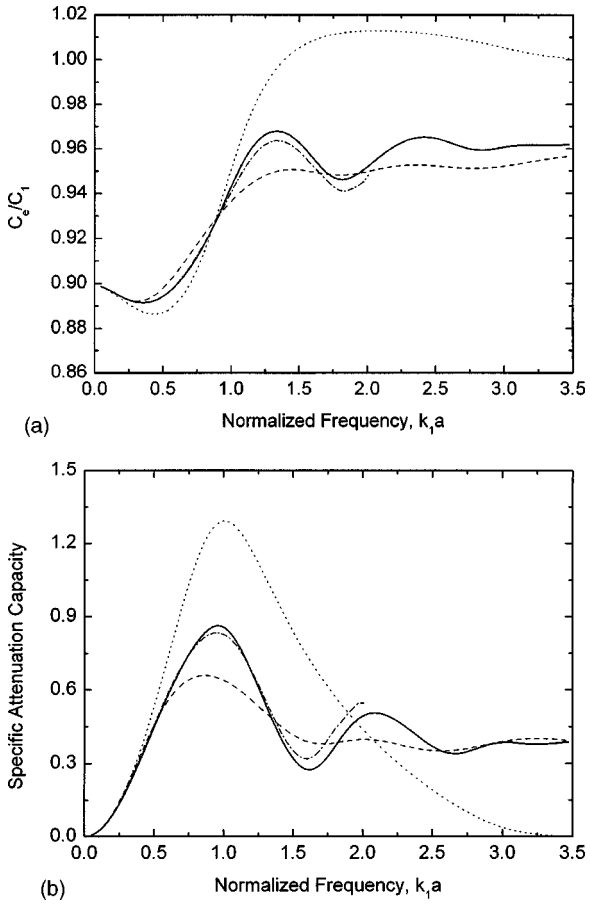

FIG. 1. Effective normalized wave speed and specific attenuation capacity versus frequency for steel/aluminum composite with fiber volume fraction of 27%. (solid line), the present method; (chain-dotted line), Kim (Ref. 9); (dashed line), Eq. (3) with static effective density; (dotted line), Sabina and Willis (Ref. 7). (a) Normalized wave speed; (b) specific attenuation capacity.

In Fig. 2, the normalized wave speed and specific attenuation in the same composite with volume fraction of 7% are shown. It is surprising that the present method, the multiple scattering theory, and the causal differential scheme predict very close values for both wave speed and attenuation in the whole frequency range. The reason for additional fluctuations in the wave-speed curve and excessively low attenuation from the GSCM are probably due to the wave interaction in the annulus of the three-phase model.

In Fig. 3, the normalized wave speed and the specific attenuation for the same composite with 27% fiber volume fraction are compared with those from other theories. It should be noted that the present method predicts the shift of the frequency of the maximum attenuation (or, correspondingly, rapid increase in wave speed). This fact illustrates the capability of the present method in considering the multiple scattering effects.

In Fig. 4 the wave speed in a carbon/epoxy composite with 46% fiber volume fraction is shown. The symbols are wave speeds measured at three different sites on the composite plate in the direction perpendicular to the fiber axis.[19] It is

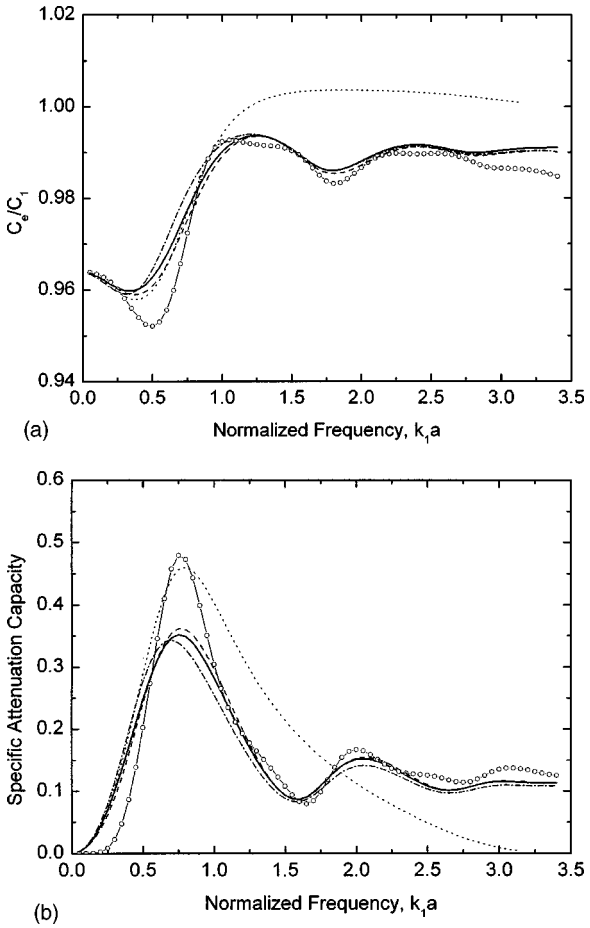

FIG. 2. Effective normalized wave speed and specific attenuation capacity versus frequency for steel/aluminum composite with fiber volume fraction of 7%. (solid line), the present method; (chain-dotted line), Beltzer and Brauner (Ref. 17); (dashed line), Varadan *et al.* (Ref. 16); (dotted line), Sabina and Willis (Ref. 7); (circle-solid line), Yang and Mal (Ref. 13). (a) Normalized wave speed; (b) specific attenuation capacity.

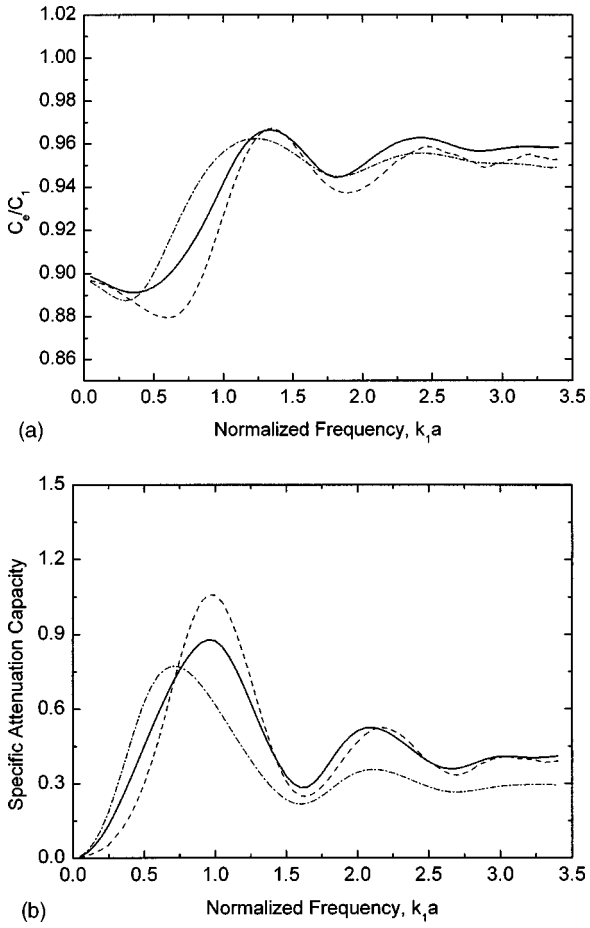

FIG. 3. Effective normalized wave speed and specific attenuation capacity versus frequency for steel/aluminum composite with fiber volume fraction of 27%. (solid line), the present method; (chain-dotted line), Beltzer and Brauner (Ref. 17); (dashed line), Varadan *et al.* (Ref. 16). (a) Normalized wave speed; (b) specific attenuation capacity.

observed that the experimental results are close to the prediction by the GSCM, which predicts the lower bound of the axial shear modulus. On the contrary, the self-consistent method predicts the axial shear modulus close to the upper bound at high volume fractions and when the constituent elastic properties contrast very high, due to the assumed microstructure models. Thus, it can be surmised that most fibers in the composite would be isolated by the matrix. However, it is also observed that the wave speeds measured at the same frequency exhibit different values. This can be attributed to the variation of the microstructural arrangement of the fibers, provided a less significant experimental error could be assumed. In the composite sample that shows higher wave speed, fibers are probably more in contact with each other so that they form several channels of fiber clusters along the wave propagation direction. A closer investigation on the dependence of wave speed on the microstructural characteristics may be explored in the future.

IV. CONCLUSION

The self-consistent method employing the quasidynamic form of the effective density has been proposed for evaluating the frequency-dependent effective wave speed and the coherent attenuation in two-dimensional inhomogeneous materials. The numerical results have been compared with those from other theories and experimental data. As well as the simplicity of the present method, reasonable agreements with other theories and experimental results should also be noted.

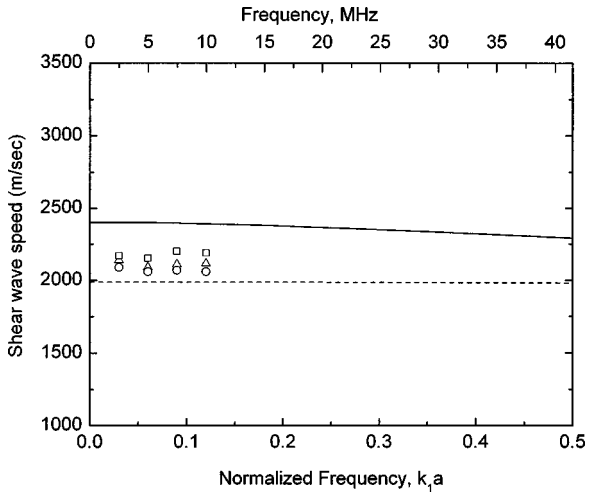

FIG. 4. Shear wave speed in carbon/epoxy composite with fiber volume fraction of 46%. (solid line), the present method; (dashed line), Yang and Mal (Ref. 13); (symbols), experiments (Ref. 19).

Analogous conditions for fiber-reinforced composites subject to in-plane wave motion and particulate composites can be derived: $\langle f_L(\hat{\mathbf{k}}_L;\hat{\mathbf{k}}_L)\rangle=0$ and $\langle f_S(\hat{\mathbf{k}}_S;\hat{\mathbf{k}}_S)\rangle=0$ to be solved together with the corresponding quasidynamic effective densities,[7,20] where f_L and f_S are scattered longitudinal and shear wave amplitudes and $\hat{\mathbf{k}}_L$ and $\hat{\mathbf{k}}_S$ are longitudinal and shear wave vectors.

APPENDIX: QUASIDYNAMIC EFFECTIVE SHEAR MODULUS AND DENSITY

Consider the antiplane shear wave propagating in a two-dimensional composite. The formulas for the effective axial shear modulus (μ_e) and the effective density (ρ_e) derived[9] using the self-consistent theory of Sabina and Willis[7] are

$$\mu_e=\mu_1+v_2h^2(k_e)(\mu_2-\mu_1)[1+\overline{S_x}(\mu_2-\mu_e)]^{-1}, \tag{A1}$$

$$\rho_e=\rho_1+v_2h^2(k_e)(\rho_2-\rho_1)[1+\overline{M_t}(\rho_2-\rho_e)]^{-1}, \tag{A2}$$

where the average of the effective wave over an inclusion, $h(k_e)$, is

$$h(k_e)=\frac{2}{k_ea}J_1(k_ea), \tag{A3}$$

and the average convolution operators, $\overline{S_x}$ and $\overline{M_t}$, are

$$\overline{S_x}=\frac{i\pi H_1(k_ea)J_1(k_ea)}{2\mu_e}, \tag{A4}$$

$$\overline{M_t}=\frac{1-i\pi H_1(k_ea)J_1(k_ea)}{\rho_e}, \tag{A5}$$

where $J_1(x)$ and $H_1(x)$ are the first and third kinds of Bessel functions of order 1 and a denotes the radius of inclusion. It should be noted that this theory provides a complex effective density.

[1] P. Soven, "Coherent-potential model of substitutional disordered alloys," Phys. Rev. **156**, 809–813 (1967).

[2] B. Velicky, S. Kirkpatrick, and H. Ehrenreich, "Single-site approximations in the electronic theory of simple binary alloys," Phys. Rev. **175**, 747–766 (1968).

[3] R. Hill, "A self-consistent mechanics of composite materials," J. Mech. Phys. Solids **13**, 213–222 (1965).

[4] B. Budiansky, "On the elastic moduli of some heterogeneous materials," J. Mech. Phys. Solids **13**, 223–227 (1965).

[5] J. G. Berryman, "Theory of elastic properties of composite materials," Appl. Phys. Lett. **35**, 856–858 (1979).

[6] C. M. Sayer and R. L. Smith, "The propagation of ultrasound in porous media," Ultrasonics **20**, 201–205 (1982).

[7] F. J. Sabina and J. R. Willis, "A simple self-consistent analysis of wave propagation in particulate composites," Wave Motion **10**, 127–142 (1988).

[8] J.-Y. Kim, J.-G. Ih, and B.-H. Lee, "Dispersion of elastic waves in random particulate composites," J. Acoust. Soc. Am. **97**, 1380–1388 (1995).

[9] J.-Y. Kim, "Dynamic self-consistent analysis for elastic wave propagation in fiber reinforced composites," J. Acoust. Soc. Am. **100**, 2002–2010 (1996).

[10] M. F. Thorpe and P. N. Sen, "Elastic moduli of two-dimensional composite continua with elliptic inclusions," J. Acoust. Soc. Am. **77**, 1674–1680 (1985).

[11] J. E. Gubernatis and E. Domany, "Effects of microstructure on the speed and attenuation of elastic waves: Formal theory and simple approximations," *Review of Progress in Quantitative Nondestructive Evaluation*, edited by D. O. Thompson and D. E. Chimenti (Plenum, New York, 1983), pp. 833–850.

[12] P. M. Morse and H. Feshbach, *Methods of Theoretical Physics* (McGraw-Hill, New York, 1953).

[13] R.-B. Yang and A. K. Mal, "Multiple scattering of elastic waves in a fiber-reinforced composite," J. Mech. Phys. Solids **42**, 1945–1968 (1994).

[14] D. Stroud and F. P. Fan, "Self-consistent approach to electromagnetic wave propagation in composite media: Application to model granular metals," Phys. Rev. B **17**, 1602–1610 (1978).

[15] G. A. Niklasson, C. G. Granqvist, and O. Hunderi, "Effective medium models for the optical properties of inhomogeneous materials," Appl. Opt. **20**, 26–30 (1981).

[16] V. K. Varadan, V. V. Varadan, and Y. Ma, "Multiple scattering of elastic waves by cylinders of arbitrary cross section. II. Pair-correlated cylinders," J. Acoust. Soc. Am. **78**, 1874–1878 (1985).

[17] A. I. Beltzer and N. Brauner, "The effective dynamic response of random composites by a causal differential method," Mech. Mater. **6**, 337–345 (1987).

[18] Z. Hashin, "On elastic behavior of fiber-reinforced materials of arbitrary transverse phase geometry," J. Mech. Phys. Solids **13**, 119–134 (1965).

[19] J. N. Park, "Ultrasonic velocity and attenuation measurements in carbon fiber reinforced plastics," Master thesis, Department of Physics in KAIST, Korea (1984).

[20] P. G. J. Bussink, P. L. Iske, J. Oortwijn, and G. L. M. M. Verbist, "Self-consistent analysis of elastic wave propagation in two-dimensional matrix-inclusion composites," J. Mech. Phys. Solids **43**, 1673–1690 (1995).

Helmholtz and parabolic equation solutions to a benchmark problem in ocean acoustics

Elisabeth Larsson
Scientific Computing, Department of Information Technology, Uppsala University, Box 337, SE-751 05 Uppsala, Sweden

Leif Abrahamsson
Division of Systems Technology, Swedish Defence Research Agency, SE-172 90 Stockholm, Sweden

(Received 1 February 2002; accepted for publication 10 February 2003)

The Helmholtz equation (HE) describes wave propagation in applications such as acoustics and electromagnetics. For realistic problems, solving the HE is often too expensive. Instead, approximations like the parabolic wave equation (PE) are used. For low-frequency shallow-water environments, one persistent problem is to assess the accuracy of the PE model. In this work, a recently developed HE solver that can handle a smoothly varying bathymetry, variable material properties, and layered materials, is used for an investigation of the errors in PE solutions. In the HE solver, a preconditioned Krylov subspace method is applied to the discretized equations. The preconditioner combines domain decomposition and fast transform techniques. A benchmark problem with upslope–downslope propagation over a penetrable lossy seamount is solved. The numerical experiments show that, for the same bathymetry, a soft and slow bottom gives very similar HE and PE solutions, whereas the PE model is far from accurate for a hard and fast bottom. A first attempt to estimate the error is made by computing the relative deviation from the energy balance for the PE solution. This measure gives an indication of the magnitude of the error, but cannot be used as a strict error bound. © *2003 Acoustical Society of America.*
[DOI: 10.1121/1.1565071]

PACS numbers: 43.20.Mv, 43.30.Ma, 43.30.Gv [ADP]

I. INTRODUCTION

The parabolic wave equation (PE) is an important propagation model in underwater acoustics.[1,2] It is an approximation of the Helmholtz equation (HE) assuming one-way propagation within an angular sector. Its usefulness in solving propagation problems in ocean acoustics is well evidenced by the PE Workshops I and II.[3,4]

In this paper, we reexamine test case II from PE Workshop II, which is a low-frequency upslope–downslope propagation problem over a penetrable, lossy seamount. This test case, or a variant with an upslope wedge only, is frequently used to demonstrate the ability of PE modeling in range-dependent environments.[5,6] The success depends on two crucial factors: a slowly varying bathymetry, and moderate density and velocity contrasts at the water/bottom interface. Usually, the sound speed of the bottom is set to 1700 m/s for which the critical grazing angle is around 28°. In uphill propagation, wave angles steepen up, and when they become larger than the critical angle, energy starts to radiate into the bottom. For ''soft and slow'' bottoms with a small depth variation, most of the energy is transmitted into the bottom within the allowed angular domain of the PE model. This is the rationale of the common phrase ''the use of PE is justified if the range dependence is weak enough.'' However, in a real-world application it might be difficult to judge whether this condition is actually satisfied. Besides the bottom characteristics, the nature of the source is of considerable importance. It is easier to maintain the requirement of a small angular spread at high frequencies, by beamforming or filtering. Nevertheless, in ocean acoustics, PE is often applied to low-frequency shallow-water environments in which the applicability of PE modeling is less obvious. In this study, we extend the upslope–downslope problem to ''hard and fast'' bottoms. When the impedance of the bottom increases, transition zones of high angles of propagation and backscattering become more pronounced. At the same time, it leads to a gradual weakening of the validity of the assumptions behind PEs. It is worthwhile to find out what actually happens when a PE is pushed to, or beyond, the limit of its ability. The approach of the present study is mainly empirical in the sense that we compare numerical solutions of HE and PE. DeSanto[7] performed a theoretical study of the relation between HE and PE solutions. A theoretical analysis of the radiation conditions at modal cutoff in an upslope wedge is given by Pierce[8,9] and by Kath *et al.*[10] In the soft and slow bottom case, it was shown analytically that practically all the energy is transmitted into the bottom in a narrow beam at the cutoff point of the incoming mode. However, for hard and fast bottoms, part of the energy is backreflected in the water layer, and there is no beamforming of the energy shed into the bottom. This is confirmed by our numerical results, which also provide quantitative information on these phenomena for a benchmark problem.

We consider HE including appropriate boundary conditions as an exact model, although it is still an ideal description of a complicated reality. Thus, the solutions to HE provide a reference for the assessment of the quality of PE

 0001-4966/2003/113(5)/2446/9/$19.00

modeling. Since there are no closed-form analytic solutions to HE in range-dependent geometries, we have to rely on numerical solutions. If we could solve HE numerically for any given problem, we would do so. The reason for using approximations such as PE models is that solving HE is often too demanding from a computational point of view. For a realistic problem, the size of the spatial domain is typically a large number of wavelengths in both the range and depth directions. Even to obtain a crude geometrical resolution of the problem would require a fixed number of degrees of freedom per wavelength. Additional degrees of freedom are needed if near-field features are present. On the other hand, lossy media and leakage of energy out of the domain might lower the resolution requirements.

In general, discretization of the two-dimensional HE with, e.g., a finite-difference or finite-element method yields systems of equations whose size increases by at least the square of the frequency f. In fact, it has been shown that in order to keep the phase error below a given relative error tolerance, the number of grid points in the range direction must grow as $f^{1+(1/p)}$ for a pth-order accurate method.[11–15] This explains why systems of equations arising from the discretized HE cannot be solved by direct solution methods except for very small problems. The main difficulty is the large memory requirements, but the computational time is also an issue. Iterative methods often converge slowly for HE problems, since the coefficient matrix is ill-conditioned, especially for large problems. Standard preconditioning techniques do not perform well. However, the range of problems for which HE can be solved is steadily expanding due to the evolution of affordable computer power as well as algorithmic progress.

A prerequisite of the present work has been the development of a new preconditioned iterative HE solver. The resolution requirements discussed above show that a higher-order method is desirable in order to reduce problem sizes. The HE solver utilizes a fourth-order accurate finite-difference method. It means that the error is reduced by a factor of 16 when the step size is halved. This high rate of convergence is also of crucial importance for the following reason. To ascertain the accuracy of the numerical HE solution, we apply the method of self-validation. It implies that the solution is computed several times on successively finer grids until convergence is attained. Then, it is imperative that a satisfactory convergence criterion is met before the computer resources have been exhausted. For the current benchmark problem, this requirement cannot be achieved by a lower-order finite-difference or finite-element method.

As an alternative to HE solvers in ocean acoustics, the COUPLE code[16,17] has been used to generate reference solutions in terms of stepwise-coupled modes. The difficulty here is the slow rate of convergence for the staircase approximation of the computational domain. In layered media, this drawback can be overcome by orthogonal mappings of layers onto rectangles.[18] Occasionally, validation of COUPLE results has been done by intermodel comparisons.[19,20] In practice, the results have proven to be good enough for benchmark solutions as presented at PE Workshop II. However, as can be seen in more detail in Sec. IV, considerably higher resolution is needed for accurate solutions of upslope propagation problems over hard and fast bottoms.

It should be noted that we are addressing two very different validation problems in this paper. The first one is to ensure that the numerical solution of HE is accurate enough to serve as a reference. The second problem, which is the main topic, is the question of model validation of PEs. Besides comparisons of HE and PE solutions to a benchmark problem, we briefly indicate how to quantify the notion of ''weak range dependence'' and how to formulate computable criteria that ascertain the accuracy of the PE model.

An account of the codes and the numerics for the PE and HE solvers is given in Secs. II and III. It is a brief survey of previous papers. A more detailed description of the new parts of the preconditioning in the HE solver is given in the Appendix. The main results appear in Sec. IV. The focus is on the numerical experiments, and their implications for model validation of PEs, rather than physical or theoretical considerations.

II. THE PE SOLVER—JEPE

The development of JEPE (Jeltsch energy-conserving PE)[21,22] is the result of a team work at the Defense Research Establishment, Stockholm, Sweden. The code is continually updated to provide extended modeling capabilities and operational improvements. A number of new ideas have been tried and found useful.

A most significant feature of JEPE is the treatment of a range-dependent bathymetry. It is assumed that the physical parameters can be grouped into layers with the water layer at the top followed by one or several sediment or bedrock layers. The layer interfaces are assumed to vary smoothly by range, and the layer thickness must not shrink to zero. In JEPE, each layer is mapped onto a rectangle by an orthogonal, boundary-fitted transformation.[23] In this way, the special precautions needed in order to avoid an appreciable systematic error in the limit of an infinitesimal staircasing are avoided.[24] The PE model and the variation of media parameters are expressed in the new coordinates. The continuity conditions of pressure and velocity can then be treated as for the horizontally stratified case. The required normal derivative at the interface is merely approximated by a centered difference formula in the transversal coordinate direction.

The computational cost of any PE implementation is dominated by the step-by-step integration in range. The integrator in JEPE is a multistep, second derivative, fourth-order accurate method by Jeltsch.[25] The scheme is implemented by an automatic selection of an optimal step size so that a preset error criterion is fulfilled. Besides being cost effective, it relieves the user from specifying the range step.

Another cost-saving device in JEPE is to apply an adaptive choice of reference wave number in the formulation of the PE. When the propagation conditions change by range, or mode stripping occurs due to lossy media, the angular spread of energy varies. This in turn may prompt a new choice of reference wave number, which is computed according to Pierce.[26]

III. THE HELMHOLTZ SOLVER—FD4HE

The implementation of the HE solver denoted by FD4HE, where FD4 stands for fourth-order accurate finite differences, was developed at the Department of Scientific Computing, Uppsala University, Uppsala, Sweden. The code was originally designed for electromagnetic wave propagation in waveguides. Due to the similarities of two-dimensional transverse magnetic (TM) wave propagation in layered materials and acoustic wave propagation in fluid layers, it was rather straightforward to adapt the code to the current needs.

In the same way as in the JEPE code, an orthogonal transformation[23] of the layers of the physical domain onto rectangles is used. Rectangular domains are well suited for finite-difference discretizations, but there are still several possible choices. For interior grid points, we use a fourth-order Numerov scheme[15] that yields a compact nine-point stencil. The compactness facilitates the implementation of boundary conditions. Continuity conditions between layers are approximated by using one-sided fourth-order differences. At the vertical boundaries, we use nonreflecting boundary conditions of Dirichlet–to–Neumann type.[27] In these boundary conditions, modal expansions of the solution at the boundaries are used. The modes are computed by solving an eigenproblem,[28] and the discretization of that is done with a fourth-order accurate finite-element method.

The first difficulty lies in the fact that the system of equations that arises is very large. Direct solution methods, e.g., band Gaussian elimination, cannot be used because of their excessive memory requirements caused by fill-in. Instead, we use an iterative solution method, where the sparsity of the coefficient matrix is exploited. Since the matrix is complex and nonsymmetric, restarted GMRES[29] is a suitable choice. Then, a second difficulty emerges. The system of equations is also very ill-conditioned, and the iterative method does not converge without preconditioning. In an earlier paper,[28] Larsson suggested a preconditioning method that works well. The equations in the system were ordered in a domain decomposition fashion. A preconditioner based on sine transform matrices was constructed for the interior unknowns. Application of the preconditioner was then performed through the Schur complement method and fast Fourier transforms. It was found that the bottleneck of the computations was to form the Schur complement. In this work, that has been greatly improved by introducing a simpler approximation for the subproblems in the interior of the subdomains, which is used only when computing the Schur complement of the preconditioner. The simpler approximation involves a staircase approximation of the domain and a two-way adiabatic approximation in the range direction. The gain compared with the original preconditioning grows with problem size, and is about a factor of 3 with respect to the number of arithmetic operations for the test problems considered here, even though the iteration count increases. A more detailed description of the preconditioning is given in the Appendix.

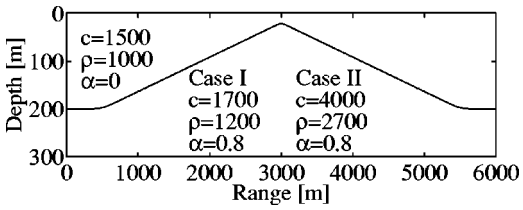

FIG. 1. Geometry of waveguide with plane symmetry and definition of media parameters, c is the speed of sound in m/s, ρ is the density in kg/m^3, and α is the absorption in dB/λ.

IV. BENCHMARK RESULTS

A. The benchmark problem

The test case is a two-layer waveguide with a symmetric bottom profile. A flat basin with a water depth of 200 m is followed by an upward-sloping bottom with an apex 22 m below the water surface. The slope of the bottom is 4°. In the experiments, we use different sound speeds and densities for the sediment layer. The extreme cases are the ''soft and slow'' and ''hard and fast'' bottoms denoted by case I and case II, respectively; see Fig. 1.

The bathymetry is slightly different from that of the second test case of PE Workshop II in two respects. First, the geometry is considered to be two-dimensional rather than three-dimensional with cylindrical symmetry. The reason is that we assume that the geometry continues with horizontal stratification outside the propagation range. This condition appears to be more realistic in cases with a significant amount of backreflection. It also facilitates the implementation of appropriate nonreflecting boundary conditions at the vertical boundaries of the computational domain. Another modification is the smoothing of corners of a polygonal bottom profile as suggested by Sundström.[30] It reduces scattering due to sharp changes in curvature, and facilitates the computation of a reference solution. For low frequencies, these alterations do not affect the main features of the original benchmark problem in any significant way. The source frequency is set to 25 Hz, and the source depth is 100 m. The source field is a modal sum of all three propagating modes at the initial range $x=0$. For computational purposes, the domain is truncated at depth $z=800$ m. Artificial absorption is introduced from $z=300$ m to $z=800$ m with a linear increase from 0.8 dB/λ to 10 dB/λ.

B. Self-validation of FD4HE

In an HE solution, the dominant error, and the error that must be suppressed by choosing a fine enough grid, is the phase error. Otto[15] has derived analytical expressions for the leading terms of the phase error for one propagating mode in a rectangular domain. Numerical experiments show that the phase error formulas give sharp predictions of the relative error. In a case with varying bathymetry, more than one propagating mode, and possibly mode coupling, it would be very difficult to analyze and derive an expression for the error. However, we can use the results for the rectangular domain as an approximate guide to a suitable mesh size. We specify a relative error tolerance τ, and then resolve according to the analytical criteria for a rectangular domain. We do

TABLE I. Self-validation of the HE solver. Given tolerances τ, and the maximum relative normwise difference between the finest solution and the coarser solutions.

	No. of points in z dir.	No. of points in x dir.	τ	max $\Delta_{\ell 0}$
Case I	479	2530	0.005	0
	403	2128	0.010	0.009
	339	1790	0.020	0.017
	305	1616	0.030	0.026
Case II	301	3008	0.0025	0
	255	2530	0.0050	0.017
	213	2128	0.0100	0.051
	179	1790	0.0200	0.088
	163	1616	0.0300	0.142

not expect to get an error bounded exactly by τ, but something of the same magnitude. For example, when more than one mode is propagating, even if the domain is rectangular, in the worst case each mode would contribute with a relative error τ.

For the convergence studies, a number of solutions on different grids have been computed for cases I and II, respectively. We will denote the computed solutions by $u_0,\ldots,u_n$, where u_0 is computed on the finest grid. For case I, $n=3$ and the problem sizes vary from about 400 000 to 1.2 million unknowns. For case II, we have used $n=4$ with problem sizes of approximately 200–900 thousand unknowns.

To get an idea of the sizes of the actual errors, we have computed relative normwise differences between the finest solution u_0 and the coarser solutions. The difference $\Delta_{\ell 0}$ for a vertical grid line was computed as

$$\Delta_{\ell 0}=\frac{\left(\int_0^{z_{\max}}\frac{1}{\rho(z)}|u_\ell-u_0|^2dz\right)^{1/2}}{\left(\int_0^{z_{\max}}\frac{1}{\rho(z)}|u_0|^2dz\right)^{1/2}}. \tag{1}$$

In Table I, a comparison between the given values of τ and the maximum values of the computed differences is shown. In Fig. 2, the differences are shown as a function of range. For a rectangular domain, a linear error growth in the direction of propagation is expected. For case I, we have linear growth, and by inspection of the differences, we conjecture that the errors are very close to τ at the outflow boundary. For case II, we get a large error growth halfway up the slope. This is probably connected with the excitation of higher modes that are not present in the source. Roughly estimated, the errors appears to be approximately of size 5τ at the outflow boundary. This reflects the more complicated behavior of the solution in case II.

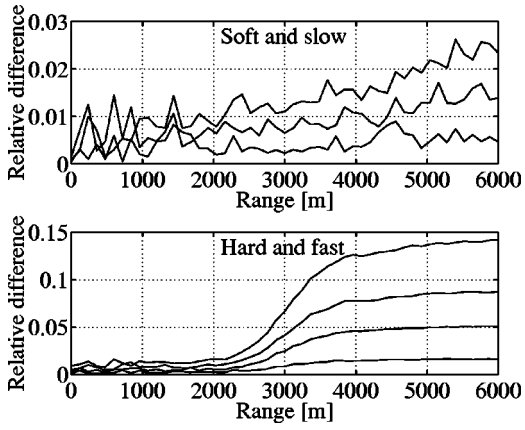

FIG. 2. Relative normwise differences between the finest and the coarser HE solutions. For case I (top) with given values of τ, from the uppermost curve and down, 0.03, 0.02, 0.01, and for case II (bottom) with $\tau=0.03$, 0.02, 0.01, 0.005.

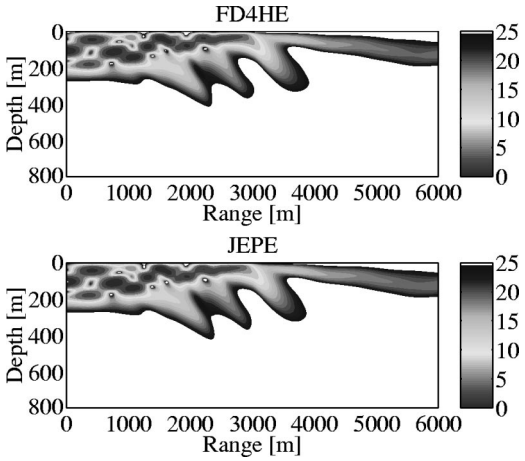

FIG. 3. Contours of the sound intensity in dB for the HE (top) and PE (bottom) solutions in case I.

A conclusion from these experiments is that the solution has converged enough to meet our requirements. Moreover, the errors on the finest grids are small compared with the differences between the HE and the PE solutions.

C. Comparison of HE and PE solutions

For the comparison of the HE and the PE solutions, we have used a wide-angle PE model due to Claerbout.[2] This model supports propagation angles below about 36°. We have compared the HE and PE solutions, both qualitatively and quantitatively. In Figs. 3 and 4, the sound intensity in dB is shown for the two solution methods applied to cases I and II. The picture for the soft and slow bottom case is well known. The source consists of three propagating modes.

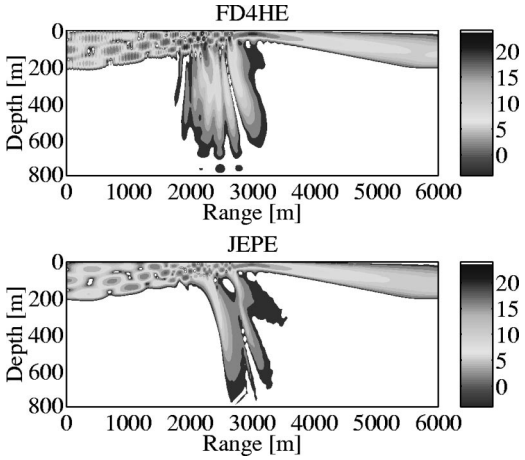

FIG. 4. Contours of the sound intensity in dB for the HE (top) and PE (bottom) solutions in case II.

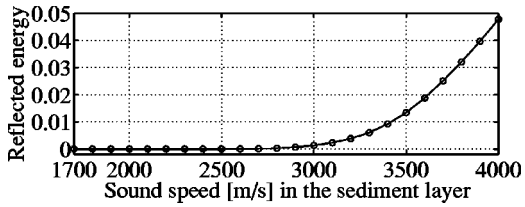

FIG. 5. Backreflected energy fraction measured at the left vertical boundary (the inflow boundary) as a function of bottom parameters. Both sound speed and density are increased linearly.

When they encounter their cutoff depths during uphill propagation, practically all the energy is transmitted into the bottom as narrow beams. The intensity contours in Fig. 3 are almost identical, whereas in the hard and fast case the solutions differ markedly. Transmission into the bottom at modal cutoff is still beam-like for the PE solution, whereas there is a wide angular spread of radiation for the HE solution. In addition, part of the energy is backreflected and still trapped in the water layer.

The relative amount of energy flux directed to the left is nearly 5%. This may seem like a rather small amount, but it is important to remember that the energy is proportional to the square of the amplitude, i.e., the total amplitude of the reflections is approximately 22%. Figure 5 shows how the backreflected energy increases by the characteristic impedance of the bottom. This picture was obtained by solving HE for a large number of cases in which ρ and c both were increased linearly from $\rho=1200$ and $c=1700$ to $\rho=2700$ and $c=4000$. The amount of backreflected energy was measured at $x=0$. It was calculated by using a modal expansion of the pressure field at $x=0$

$$u(x,z)=\sum_{m=1}^{3} A_m \exp(ik_m x)\psi_m(z) + \sum_{\mathrm{Re}\, k_m>0} B_m \exp(-ik_m x)\psi_m(z), \tag{2}$$

where the A_m coefficients are the known amplitudes in the source. Employing an approximate expression for the horizontal energy flux, yields the reflected energy fraction

$$E_r=\frac{\Sigma_{\mathrm{Re}\, k_m>0}\, \mathrm{Re}\, k_m |B_m|^2}{\Sigma_{m=1}^{3}\, \mathrm{Re}\, k_m |A_m|^2}. \tag{3}$$

In the limit case II, essentially only modes two and three are backreflected, and it was found that $|B_2|/|A_2|\approx 0.5$ and $|B_3|/|A_3|\approx 0.2$.

In Fig. 6, the normwise relative error for the PE solution, along a vertical grid line, is shown as a function of range. Here, we use the HE solution as our reference for the exact solution. The following expression was used for the error:

$$\Delta_{PE,HE}=\frac{\left(\int_0^{z_{\max}} \frac{1}{\rho(z)} |u_{PE}-u_{HE}|^2 dz\right)^{1/2}}{\left(\int_0^{z_{\max}} \frac{1}{\rho(z)} |u_{HE}|^2 dz\right)^{1/2}}. \tag{4}$$

In case I, the error has it largest value at the apex, after which it recovers. In case II, the error is 22% already at the inflow boundary. This is in accordance with the experiments above, where we predicted a total amplitude of 22% for the reflections. The HE and PE solutions use identical source functions. Therefore, the differences between the solutions at $x=0$ are solely due to reflections. Also in case II, the error recovers somewhat after the apex, but still cannot be deemed adequate.

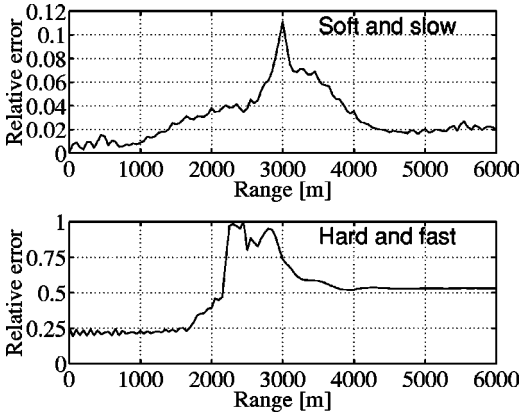

FIG. 6. Normwise relative difference between the PE and HE solutions, along a vertical grid line, as a function of range for case I (top) and case II (bottom).

Figure 7 shows how the error (4) evaluated at the apex $x=3000$ varies by the impedance of the bottom. In this picture, we have also included results for a very wide-angle PE model. As can be seen, there is a significant gain with the very wide-angle PE. However, also for this model the performance deteriorates as the bottom becomes more stiff. One reason is the excitation of modes with propagation angles larger than 60°, which is the limit often used for this model. Another reason is that there is a large amount of backreflection, which can never be approximated by a one-way model. Figures 8 and 9 show the amount of mode excitation for cases I and II over the entire range of propagation. In case I, only a small fraction of the energy propagates at large angles, and then only locally, close to the apex. The picture is different for case II. There, higher modes are excited along the upslope, and the energy in the higher modes is not at all negligible. The energy fractions were computed by doing local-mode expansions of the HE solution. An expression similar to Eq. (3) was used. However, here we relate modes with propagation angles θ_m larger than a given fixed angle to all of the modes, where

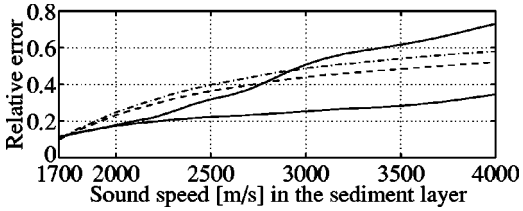

FIG. 7. Normwise relative difference between PE and HE solutions at the vertical grid line passing through the apex of the seamount. Density and sound speed in the sediment layers are varied linearly from case I to case II. The solid lines are the errors for a wide-angle PE (larger), and a very wide-angle PE (smaller). The relative deviation from the energy balance for the wide-angle (dashed line) and very wide-angle (dashed-dotted line) models are also shown.

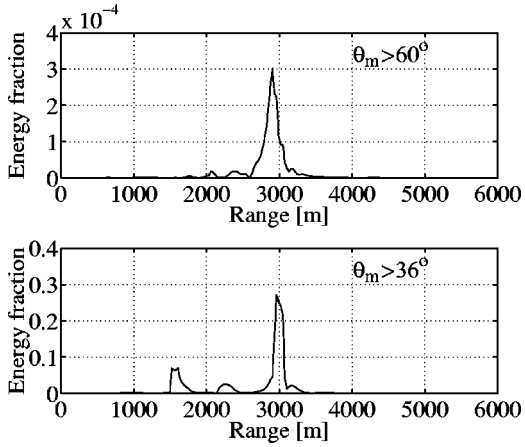

FIG. 8. Mode expansion of the HE solution for case I. The energy fractions for propagation angle θ_m larger than 36° and 60°, respectively. Note that the two scales are very different.

$$\cos\theta_m = \frac{\mathrm{Re}\, k_m}{k}, \tag{5}$$

and k is the wave number in the water layer.

In summary, the agreement between the HE and PE solutions is excellent in case I, whereas PE is incapable of handling case II. In case I, the incoming modes adapt adiabatically to the changing depth, and when the cutoff depth is encountered at an angle larger than the critical one, practically all the energy is emptied into the bottom. There is little mode interaction in this case. As the bottom becomes more stiff, there is a gradual increase of the critical grazing angle and the amount of mode excitation. At the same time, there is a weakening of the assumptions behind PE modeling. Theoretically, the situation can be improved somewhat by employing high-angle PEs, although it would be difficult to find out the ultimate borderline for any one-way model. One possibility is to invoke high-angle PEs in an adaptive way. A prerequisite for an automatic selection of an appropriate PE is a computational control device for the distribution of propagation angles within the field. We have done an experiment on self-control of the validity of PE solutions. The idea is to check the energy balance, which for the HE solution may be written

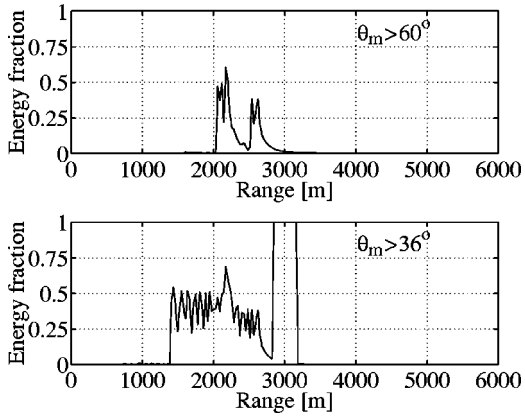

FIG. 9. Mode expansion of the HE solution for case II. The energy fractions for propagation angle θ_m larger than 36° and 60°, respectively.

$$F(0) = F(x) - \int_0^x \int_0^{z_{\max}} \mathrm{Im}\, k^2(z) |u(x',z)|^2 \; dz \; dx', \tag{6}$$

where

$$F(x) = \int_0^{z_{\max}} \mathrm{Im}\left(\frac{\partial u}{u \partial x} \right) \; dz \tag{7}$$

is proportional to the horizontal energy flux. The integral in Eq. (6) corresponds to the amount of absorbed energy due to attenuation over the range $(0,x)$. We try to construct an error indicator based on Eq. (6), which holds only approximately for PE solutions. Figure 7 shows the relative deviation from the energy balance (6) for the wide- and very wide-angle PE as a function of range. We see that the energy balance is far from being satisfied in case II. Apparently, this simple and inexpensive indicator works fairly well in this particular case. However, a comparison of the relative deviation from the energy balance and the error curves in Fig. 7 shows that the actual error is grossly overestimated for the very wide-angle PE in case II. Moreover, the estimator indicates a larger error in the very wide-angle model than in the wide-angle model, which is clearly in disagreement with the computed error results. Further work is needed to find more refined sensors.

V. SUMMARY

In conclusion, the results of the present work confirm the widely accepted belief that PE models are accurate for low-frequency propagation of acoustic waves over shallow oceans, provided that the depth variation and the density and velocity contrasts are moderate. High-angle PEs may extend the applicability to some degree. However, it is very difficult to predict when the conditions for their use are satisfied. Our calculations show that no PE model would do for hard and fast ocean bottoms with slight variations in bathymetry. The purpose of this paper has been to illuminate this issue quantitatively by accurate and comprehensive numerical solutions of the Helmholtz equation.

One difficulty of great practical concern is to develop computable criteria that measure the accuracy of the PE solution as it evolves in range. By an example, we have hinted at the possibility of introducing self-control. Evidently, indispensable tools for evaluation and further improvement of PE models are provided by the development of new, powerful HE solvers.

ACKNOWLEDGMENT

The first author would like to thank her advisor, Dr. Kurt Otto, for his constructive criticism.

APPENDIX: PRECONDITIONING OF THE ITERATIVE HELMHOLTZ SOLVER

A short description of the preconditioner constructed by Larsson[28] will be given here in order to point out the improvements implemented in this work.

First, the unknowns are separated into interface unknowns and interior unknowns. This domain decomposition type ordering yields a block system $Bu=g$ of the following form:

$$\begin{pmatrix} B_{00} & B_{01} \\ B_{10} & B_{11} \end{pmatrix} \begin{pmatrix} u_0 \\ u_1 \end{pmatrix} = \begin{pmatrix} g_0 \\ g_1 \end{pmatrix}. \tag{A1}$$

The largest block in the matrix is B_{11}, which corresponds to couplings between interior unknowns. It contains a number of subdomain problems, one for each layer in the physical domain. The subdomain problems are decoupled, except for the global nonreflecting boundary conditions at the vertical boundaries. Each subdomain problem is an HE problem with Dirichlet boundary conditions at the top and bottom boundaries. For these types of problems, effective preconditioning[14,15] techniques exist.

In a previous paper,[28] a preconditioner with the following structure was considered:

$$M = \begin{pmatrix} B_{00} & B_{01} \\ B_{10} & M_{11} \end{pmatrix}. \tag{A2}$$

The iterative method was then applied to $M^{-1}Bu=M^{-1}g$ in place of (A1). One of the steps in the preconditioning algorithm consists of solving a Schur complement system. That Schur complement of M is

$$\tilde{C} = B_{00} - B_{01}M_{11}^{-1}B_{10}. \tag{A3}$$

This is all very well, but building the Schur complement $\tilde{C}$ takes a lot of time. In this work, we have exchanged M_{11} in (A3) for an even simpler approximation in order to reduce the computational cost. The original M_{11} is a normal block approximation of the matrix B_{11}, utilizing sine transform matrices. The sine transform was chosen, because it corresponds to the analytical vertical eigenmodes of an HE problem with Dirichlet boundary conditions in a rectangular domain. This choice of M_{11} can be described as finding a least-squares approximation in a matrix sense to the original problem, but with constant coefficients for each vertical grid line within a subdomain. An important effect is also that the subdomain problems are completely decoupled.

A simpler approximation should achieve something similar, but with less arithmetic operations. In the previous work, we looked at the problem from a linear algebra point of view, and approximated the matrix. Here, we consider the continuous problem, and try to find an approximate formulation. Forming $\tilde{C}$ mainly consists of a large number of solves with M_{11} as the coefficient matrix, and the columns of B_{10} as right-hand sides. In a continuous setting, these right-hand sides correspond to source functions, and the solution vectors correspond to the solutions of a modified HE problem for those sources.

We begin by defining a modified continuous problem with properties similar to those of the discrete problem defined by M_{11}. We emphasize two properties. First, the subdomain problems must be independent of each other. Second, we want constant coefficients in the vertical direction. Then, we proceed with the source functions. The right-hand sides, i.e., the columns of B_{10}, have only a few nonzero elements. Each of those is treated as a point source in the continuous case. The strength of a source is obtained by a simple scaling of the corresponding element in B_{10}. Finally, we solve the continuous problems, and evaluate the solutions for pertinent grid points. The solution vectors obtained in this way are our approximation of $M_{11}^{-1}B_{10}$ in Eq. (A3).

The coefficients are made constant in the vertical direction by using, for each subdomain and each vertical grid line, the average value of all material properties, and requiring the bottom and interface curves to be of piecewise constant depth. All the subdomain problems are treated in the same way, and can be solved independently. We illustrate the solution process by studying one arbitrary subdomain and one right-hand side. For simplicity, we use a uniform partition of the range direction

$$h = \frac{x_{\max}}{N-1}, \quad x_j = (j-1)h, \quad j = 1,\ldots,N. \tag{A4}$$

The subdomain is divided into N slices of equal width h, but with individual constant depths d^j. Let the rectangular slice j have the vertical line $x=x_j$ as its centerline. Any parameter that is constant in the range direction within slice j is endowed with a superscript j. In slice j, there is a point source $s^j\delta(x-x_j)\delta(z-z_s)$, where s^j is the strength of the source, and (x_j, z_s) is the position. Note that s^j is zero in cells without sources, and if there are several sources in each cell, the different solutions can be superpositioned. In a rectangular domain, HE with constant coefficients is separable, i.e., we can write

$$u(x,z) = \sum_{m=1}^{\infty} \varphi_m(x)\psi_m^j(z), \qquad x_j - \frac{h}{2} \leqslant x < x_j + \frac{h}{2}, \quad j = 1,\ldots,N. \tag{A5}$$

The vertical eigenmodes are

$$\psi_m^j(z) = \sqrt{\frac{2}{d^j}} \sin\left(\frac{m\pi z}{d^j}\right). \tag{A6}$$

Insertion of the ansatz (A5) into the Helmholtz equation including the source terms yields

$$\sum_{m=1}^{\infty} (-\varphi_m''(x) - (k_m^j)^2\varphi_m(x))\psi_m^j(z) = s^j\delta(x-x_j)\delta(z-z_s), \qquad x_j - \frac{h}{2} \leqslant x < x_j + \frac{h}{2}, \quad j = 1,\ldots,N, \tag{A7}$$

where

$$k_m^j = \sqrt{k^2 - \left(\frac{m\pi}{d^j}\right)^2}, \tag{A8}$$

and k is the wave number in the current subdomain. We study a weak form of this equation, locally in slice j, by taking the scalar product with the modes ψ_n^j, which form an orthonormal basis. Then, we get

$$-\varphi_m''(x) - (k_m^j)^2\varphi_m(x) = s^j\delta(x-x_j)\psi_m^j(z_s). \tag{A9}$$

Equation (A9) tells us that the horizontal eigenfunctions should be continuous, and their derivatives should have jumps of size $-s^j\psi_m^j(z_s)$ at $x=x_j$. The solution for one mode is

$$\begin{aligned}
\varphi_m(x) &= A_m^j \exp(ik_m^j x) + B_m^j \exp(-ik_m^j x) \\
&\quad + s^j \psi_m^j(z_s) \frac{\sin(k_m^j(x-x_j))}{k_m^j}, \\
&\quad x_j - h/2 \leqslant x \leqslant x_j, \\
\varphi_m(x) &= A_m^j \exp(ik_m^j x) + B_m^j \exp(-ik_m^j x), \\
&\quad x_j < x < x_j + h/2.
\end{aligned} \tag{A10}$$

The solutions u for adjacent slices must be connected through suitable conditions of continuity. Here, we ignore couplings between different modes and the z dependence, and only enforce the continuity of the horizontal eigenfunction and its derivative between slices. Let $y_j = x_j + h/2 = x_{j+1} - h/2$ be the point where slices j and $j+1$ meet. For each mode, we get a system of equations for the unknown amplitudes A_m^j and B_m^j

$$\begin{aligned}
&A_m^j \exp(ik_m^j y_j) + B_m^j \exp(-ik_m^j y_j) \\
&\quad = A_m^{j+1} \exp(ik_m^{j+1} y_j) + B_m^{j+1} \exp(-ik_m^{j+1} y_j) \\
&\qquad + s^{j+1} \psi_m^{j+1}(z_s) \frac{\sin(k_m^{j+1}(y_j - x_{j+1}))}{k_m^{j+1}}, \\
&\qquad j = 1, \ldots, N-1, \\
&ik_m^j (A_m^j \exp(ik_m^j y_j) - B_m^j \exp(-ik_m^j y_j)) \\
&\quad = ik_m^{j+1} (A_m^{j+1} \exp(ik_m^{j+1} y_j) - B_m^{j+1} \exp(-ik_m^{j+1} y_j)) \\
&\qquad + s^{j+1} \psi_m^{j+1}(z_s) \cos(k_m^{j+1}(y_j - x_{j+1})), \\
&\qquad j = 1, \ldots, N-1.
\end{aligned} \tag{A11}$$

We also need two boundary conditions. We assume that no waves are entering the domain from the outside, and get

$$A_m^1 = 0, \quad B_m^N = 0. \tag{A12}$$

In practice, we cannot solve for all modes. Instead, we consider the number of modes that would be propagating if the attenuation was ignored. Mode m is propagating if k_m^j is real. The largest m for which the corresponding mode is propagating, at least in the deepest part of the subdomain, is given by

$$\max_j \left\lfloor \frac{\operatorname{Re} kd^j}{\pi} \right\rfloor. \tag{A13}$$

This gives us an idea of how many modes will contribute to the solution away from the vicinity of the source. We add a few extra modes for good measure, and never take less than ten. Let μ denote the number of modes that are selected for the solution. Solving the system (A11) for $m=1,\ldots,\mu$ gives us the amplitude coefficients. Consequently, the horizontal eigenfunctions are uniquely determined by Eq. (A10). For any point, the solution u can be approximated by truncating the sum in Eq. (A5) at $m=\mu$.

Overall, this method of solving the subdomain problems gives solutions very similar to the ones we want to approximate, i.e., those obtained by using the original subdomain preconditioner M_{11}. However, it seems to be difficult to capture the correct magnitude of the solution at the positions of the sources. The situation is not really improved by increasing the number of modes. It does not have to mean that the solutions are inaccurate. It could be that the matrix formulation has a slightly different effect, which is not modeled by our approximation. To cure that deficiency, an additional local solution technique is used. The equations for the unknowns in a few vertical grid lines around the source are extracted from M_{11} and B_{10}. The equations are then modified to implement homogeneous Dirichlet boundary conditions on all four boundaries. In most cases, the solutions of the local problems hardly bear any resemblance to the solutions of the subdomain problems. However, this method performs well regarding the magnitude of the solution close to the source. Although, for problems with real coefficients, some artificial damping is needed to avoid resonant solutions. The part of the local solution that is closest to the source is incorporated into our previously computed solution vector. Another difficulty is that solutions, where the sources are close to the vertical boundaries, are not good enough. This affects a few of the right-hand sides, and for those the original M_{11} matrix is used instead of the new approximation.

The great saving we make in using the new approximation is primarily that the systems of equations that are solved are of the order of the number of grid points in one spatial direction. These systems are narrow banded and relatively few, which also plays an important role. Finally, the subdomain solutions need only be evaluated in some grid points because of the sparsity of B_{01}; see Eq. (A3).

[1] F. D. Tappert, "The parabolic approximation method," in *Wave Propagation and Underwater Acoustics*, edited by J. B. Keller and J. S. Papadakis, Lecture Notes in Phys., Vol. 70 (Springer, Berlin, 1977), pp. 224–287.

[2] F. B. Jensen, W. A. Kuperman, M. B. Porter, and H. Schmidt, *Computational Ocean Acoustics* (AIP, New York, 1994).

[3] J. A. Davis, D. White, and R. C. Cavanagh, "NORDA Parabolic Equation Workshop," NORDA TN-143, Naval Ocean Research and Development Activity, Stennis Space Center, MS (1982).

[4] S. A. Chin-Bing, D. B. King, J. A. Davis, and R. B. Evans, *PE Workshop II: Proceedings of the Second Parabolic Equation Workshop* (Naval Research Laboratory, Washington, DC, 1993).

[5] F. B. Jensen and W. A. Kuperman, "Sound propagation in a wedge-shaped ocean with a penetrable bottom," J. Acoust. Soc. Am. **67**, 1564–1566 (1980).

[6] M. D. Collins, "Benchmark calculations for higher-order parabolic equations," J. Acoust. Soc. Am. **87**, 1535–1538 (1990).

[7] J. A. DeSanto, "Relation between the solutions of the Helmholtz and parabolic equations for sound propagation," J. Acoust. Soc. Am. **62**, 295–297 (1977).

[8] A. D. Pierce, "Guided mode disappearance during upslope propagation in variable-depth shallow water overlying a fluid bottom," J. Acoust. Soc. Am. **72**, 523–531 (1982).

[9] A. D. Pierce, "Augmented adiabatic mode theory for upslope propagation from a point source in variable-depth shallow water overlying a fluid bottom," J. Acoust. Soc. Am. **74**, 1837–1847 (1983).

[10] W. L. Kath, A. A. Minzoni, G. A. Kriegsmann, and E. L. Reiss, "Energy leakage and reflection in slowly varying waveguides," J. Acoust. Soc. Am. **93**, 182–187 (1993).

[11] A. Bayliss, C. I. Goldstein, and E. Turkel, "The numerical solution of the

Helmholtz equation for wave propagation problems in underwater acoustics,'' Comput. Math. Appl. **11**, 655–665 (1985).
[12] L. L. Thompson and P. M. Pinsky, ''Complex wave number Fourier analysis of the *p*-version finite element method,'' Comput. Mech. **13**, 255–275 (1994).
[13] F. Ihlenburg and I. Babuška, ''Finite element solution of the Helmholtz equation with high wave number. II. The *h*-*p* version of the FEM,'' SIAM (Soc. Ind. Appl. Math.) J. Numer. Anal. **34**, 315–358 (1997).
[14] K. Otto and E. Larsson, ''Iterative solution of the Helmholtz equation by a second-order method,'' SIAM J. Matrix Anal. Appl. **21**, 209–229 (1999).
[15] K. Otto, ''Iterative solution of the Helmholtz equation by a fourth-order method,'' Boll. Geof. Teor. Appl. **40**, 104–105 (1999).
[16] R. B. Evans, ''COUPLE: A User's Guide,'' NORDA TN-332, Naval Ocean Research and Development Activity, Stennis Space Center, MS (1986).
[17] F. B. Jensen and C. M. Ferla, ''Numerical solutions of range-dependent benchmark problems in ocean acoustics,'' J. Acoust. Soc. Am. **87**, 1499–1510 (1990).
[18] L. Abrahamsson and H.-O. Kreiss, ''Numerical solution of the coupled mode equations in duct acoustics,'' J. Comput. Phys. **111**, 1–14 (1994).
[19] R. A. Stephen, ''Solutions to range-dependent benchmark problems by the finite-difference method,'' J. Acoust. Soc. Am. **87**, 1527–1534 (1990).
[20] E. K. Westwood, ''Ray model solutions to the benchmark wedge problems,'' J. Acoust. Soc. Am. **87**, 1539–1545 (1990).
[21] L. Abrahamsson, L. Andersson, I. Karasalo, and A. Sundström, ''JEPE—a PE code for range-dependent fluid media,'' in *18th Scandinavian Symp. in Physical Acoustics* (Dept. of Physics, University of Bergen, Bergen, Norway, 1995), pp. 1–3.
[22] I. Karasalo and A. Sundström, ''JEPE—a high-order PE-model for range-dependent fluid media,'' in *Proc. 3rd European Conference on Underwater Acoustics* (Heraklion, Crete, Greece, 1996), pp. 189–194.
[23] L. Abrahamsson, ''Orthogonal grid generation for two-dimensional ducts,'' J. Comput. Appl. Math. **34**, 305–314 (1991).
[24] L. Abrahamsson and H.-O. Kreiss, ''Boundary conditions for the parabolic equation in a range-dependent duct,'' J. Acoust. Soc. Am. **87**, 2438–2441 (1990).
[25] R. Jeltsch, ''Multistep methods using higher derivatives and damping at infinity,'' Math. Comput. **31**, 124–138 (1977).
[26] A. D. Pierce, ''The natural reference wave number for parabolic approximations in ocean acoustics,'' Comput. Math. Appl. **11**, 831–841 (1985).
[27] J. B. Keller and D. Givoli, ''Exact non-reflecting boundary conditions,'' J. Comput. Phys. **82**, 172–192 (1989).
[28] E. Larsson, ''A domain decomposition method for the Helmholtz equation in a multilayer domain,'' SIAM J. Sci. Comput. (USA) **20**, 1713–1731 (1999).
[29] Y. Saad and M. H. Schultz, ''GMRES: A generalized minimal residual algorithm for solving nonsymmetric linear systems,'' SIAM (Soc. Ind. Appl. Math.) J. Sci. Stat. Comput. **7**, 856–869 (1986).
[30] A. Sundström, ''Ocean-acoustic test problems with a slowly varying bottom-slope: A missing class of benchmarks,'' in *Environmental Acoustics, Theoretical and Computational Acoustics*, edited by D. Lee and M. Schultz (World Scientific, Singapore, 1994), Vol. 2, pp. 835–848.

Power dissipation and time-averaged pressure in oscillating flow through a sudden area change

Barton L. Smith
Mechanical and Aerospace Engineering Department, Utah State University, Logan, Utah 84322

G. W. Swift
Condensed Matter and Thermal Physics Group, Los Alamos National Laboratory, Los Alamos, New Mexico 87545

(Received 11 October 2002; revised 5 February 2003; accepted 10 February 2003)

Experiments on oscillating flow at the abrupt transition between a two-dimensional channel and essentially infinite space are presented. It is shown that phenomena associated with the transition are functions of three independent dimensionless parameters including the dimensionless radius rounding the edge of the end of the channel. The effect of each of these three parameters on the time-averaged pressure difference across the transition and the acoustic power dissipation is explored by holding two parameters fixed while varying the third. Evidence is presented that the losses due to oscillatory flow in this geometry are smaller than would be expected from commonly accepted values for steady flow in similar geometry. © *2003 Acoustical Society of America.*
[DOI: 10.1121/1.1564022]

PACS numbers: 43.25.Qp, 43.25.Nm, 47.32.Ff [RR]

I. INTRODUCTION

When a fluid flows through a system, energy is lost to viscous dissipation effects including boundary layer turbulence and random motions in separated flows. These losses are often called head losses, since they result in a drop in pressure head along the flow path. When energy is dissipated in pipe bends, valves, expansions, entrances, or anything other than a length of straight pipe, the term ''minor loss'' is used.

The effects of minor losses in oscillating flow can be either detrimental or advantageous. While minor losses in steady flow are manifested by a loss of flow work (or flow energy), minor losses in oscillating flow dissipate acoustic power and create time-averaged pressure gradients. The time-averaged pressure gradient has been used to counteract streaming flows in a thermoacoustic Stirling refrigerator[1] and engine.[2] On the other hand, minor losses can result in significant power dissipation in such refrigerators and engines, and therefore may need to be minimized.

Although extensive tables[3] of losses for steady flow are available, few such data exist for oscillatory flow in any geometry, despite the fact that abrupt changes in geometry are ubiquitous in Stirling engines, thermoacoustics, and respiratory flows. Current understanding relies mostly on the assumption that the losses due to oscillatory flow can be computed by cycle averaging the losses based on steady flow data. For example, it has been assumed that the minor losses for the entrance/exit geometry in Fig. 1 are the same as for steady flow through a sudden expansion (for the outward flow) and through an entrance (for the inward flow).

Currently, at least three other research efforts are addressing oscillatory losses in sudden area changes. Wakeland and Keolian[4] have recently reported minor loss coefficients for oscillatory flow through a sharp-edged area change based on the steady-flow theory referenced below but using theoretical laminar oscillatory flow profiles. Morris *et al.*[5] are numerically studying oscillating flow in a sharp-edged two-dimensional transition with finite area ratio, while Petculescu and Wilen[6] have built an apparatus that provides very accurate pressure/flow relationships for small flow components and have recently used this apparatus to measure the losses associated with axisymmetric acoustic diodes.[7]

In steady flow through abrupt changes in geometry, minor losses are commonly accounted for by use of a minor loss coefficient:

$$K=\frac{\rho g H}{\frac{1}{2}\rho u^2} \tag{1}$$

where H is the head loss through the component, ρ is the fluid density, g is the acceleration due to gravity, and u is the velocity at the smallest cross-sectional area. The minor loss coefficient can be thought of as the ratio of dissipated flow energy per unit mass ($\Delta p/\rho$) to the kinetic energy per unit mass in the component.

One of the few minor loss coefficients that can be theoretically determined is the ''Borda–Carnot'' coefficient for steady flow through a sharp-edged expansion.[8] The common assumption of spatially uniform channel flow results in $K=1$ for flow out of the channel into infinite space. Any departure from uniform flow results in a larger loss coefficient,[4] as large as 1.5 for fully developed laminar channel flow. No data for flow from a rounded sudden expansion are known to the authors, although it seems to be commonly assumed that this geometry has similar losses to a sharp-edged expansion.[9]

Steady entrance flow through a rounded 2D opening has a minor loss coefficient that decreases with increasing r/h, where r is the edge radius and h is the channel width (see Fig. 1). For $r/D_h>0.2$, where D_h is the hydraulic diameter, K becomes constant at 0.03.[3] In the current study, $r/D_h>0.2$ for all cases.

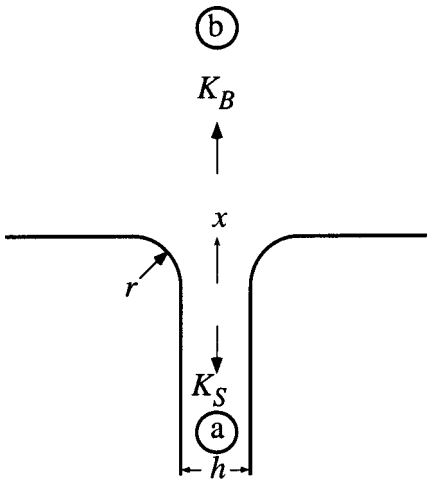

FIG. 1. Schematic of transition between a flow channel and an open space which exhibits entrance/exit flow losses. The loss coefficient during blowing is K_B and that during the suction is K_S.

This paper will discuss the results of an experimental study of effects at the rounded transition between a 2D channel and an infinite space. The results indicate that the flow is governed by three dimensionless parameters. It will be revealed that the exiting flow can, in some circumstances, expand considerably in the slot edges, resulting in smaller losses than those reported in steady flows. As will be discussed in Sec. II, calculation of minor loss coefficients from acoustic power and time-averaged pressure data requires assumptions about time-dependent inertial effects and the time-independence of minor loss coefficients that are not realistic. Therefore, we will present results in terms of acoustic power dissipation and time-averaged pressure, using minor loss coefficients only for qualitative discussion and idealized bench marks against which to compare the data. The experimental apparatus and measurement techniques are described in Sec. III and a description of the results is given in Sec. IV. Limitations to the applicability of this work and ideas for future work will be discussed in Sec. V.

II. TIME-AVERAGED PRESSURE AND LOSS COEFFICIENTS

Following Swift *et al.*,[1] minor loss coefficients for the blowing and suction cycle can be related to time-averaged pressure by writing the unsteady Bernoulli equation with loss coefficients that are assumed to be constant over each half of the cycle for flow between the points *a* and *b* in Fig. 1. It is assumed that point *b* is sufficiently far downstream that the velocity there has become negligible, and that variations in density are negligible. These equations are then averaged over a full cycle. During the blowing part of the cycle,

$$p_a+\frac{1}{2}\rho u_a^2-\frac{1}{2}K_B\rho u_a^2=p_b+\rho\int_{x_a}^{x_b}\frac{du}{dt}dx \tag{2}$$

or

$$p_a-p_b=\frac{1}{2}\rho u_a^2(K_B-1)+\rho\int_{x_a}^{x_b}\frac{du}{dt}dx, \tag{3}$$

where p is the time-varying pressure, K_B is the minor loss coefficient for the blowing stroke, u is the velocity, and the subscripts *a* and *b* refer to those locations in Fig. 1. Similarly, during the suction stroke,

$$p_a+\frac{1}{2}\rho u_a^2=p_b-\frac{1}{2}K_S\rho u_a^2+\rho\int_{x_a}^{x_b}\frac{du}{dt}dx, \tag{4}$$

$$p_a-p_b=-\frac{1}{2}\rho u_a^2(K_S+1)+\rho\int_{x_a}^{x_b}\frac{du}{dt}dx. \tag{5}$$

Averaging over a full period T,

$$\Delta P=\frac{1}{T}\int_0^{T/2}\frac{1}{2}\rho u_a^2(K_B-1)dt-\frac{1}{T}\int_{T/2}^{T}\frac{1}{2}\rho u_a^2(K_S+1)dt+\frac{\rho}{T}\int_0^T\left[\int_{x_a}^{x_b}\frac{du}{dt}dx\right]dt. \tag{6}$$

The form of the last term, which represents inertial effects, is not generally known and will be discussed further below. However, the integral over a cycle of the derivative of the periodic function u will go to zero and therefore this term can be ignored here. Rearranging, we have

$$\Delta P=\frac{\rho u_{a,\max}^2}{2}[(K_B-1)\alpha_B-(K_S+1)\alpha_S], \tag{7}$$

where

$$\alpha_B=\frac{1}{Tu_{a,\max}^2}\int_0^{T/2}u_a^2\,dt,\qquad \alpha_S=\frac{1}{Tu_{a,\max}^2}\int_{T/2}^{T}u_a^2\,dt, \tag{8}$$

ΔP is the time-averaged pressure difference, and $u_{a,\max}=\max[u_a(t)]$. If the flow is sinusoidal, then $\alpha_B=\alpha_S=1/4$ and

$$\Delta P=\frac{\rho u_{a,\max}^2}{8}(K_B-K_S-2). \tag{9}$$

In this derivation, we have assumed that u is independent of the coordinates perpendicular to x. Taking such dependence into account is much more complicated.[4,10] We have also assumed that ρ, K_B, and K_S are independent of time. Furthermore, without a second equation, we can only gain information on the difference between the loss coefficients and cannot infer anything about them individually without additional assumptions. Swift *et al.*[1] obtained a second equation for K_B and K_S by computing dissipated acoustic power, $\dot{E}=\overline{\Delta pU}$, as a function of the loss coefficients, where the overbar indicates cycle averaging and U is the volume flow rate. They argued that time-dependent inertial effects on pressure could be ignored since these are 90° out of phase with the volume flow rate. However, this assumption relies on the du/dt term being the same during blowing as it is during suction, which is to say that no nonlinear effects contribute to inertial pressure. This seems unlikely at high Reynolds number, and results from the present study indicate that this is not the case. The du/dt term can be computed using velocity data acquired as described in Sec. III between $x=0$ and point *b*. This measurement was per-

formed for $L_0/h=17$, $r/h=1.3$, and Re=354 (see definitions below). For this particular case, the difference between the magnitude of the time-average of the du/dt term during the outward stroke and inward stroke was on the same order as the time-averaged pressure. Hence, we cannot accurately compute K_B and K_S for such a case by using Eq. (9) and a similar equation for acoustic power dissipation ignoring the du/dt term. Doing so would yield an artificially high K_B and a similarly low (and perhaps negative) K_S. The present study also shows that the assumption of time-independent K_B and K_S is questionable. Because of all these complications and questionable assumptions, we will make only slight use of Eq. (9) here, presenting results in terms of ΔP and $\dot{E}$ instead of K_B and K_S.

Assuming that the aspect ratio of the slot is sufficiently large to ensure 2D flow and that the axial length of the slot is not important, the time-averaged pressure and acoustic power dissipation are functions of *r, h,* ρ, $u_{a,\max}$, the period *T*, and the viscosity μ. Dimensional analysis shows that this flow is governed by three independent dimensionless parameters. As will be shown below, the parameter r/h affects the severity of the adverse pressure gradient experienced by the exiting flow (which in turn affects the tendency for the boundary layer to separate), the Reynolds number Re $=u_{a,\max}\delta_\nu\rho/\mu$ based on the maximum velocity and the viscous penetration depth $\delta_\nu=\sqrt{\mu T/\pi\rho}$ affects turbulent transition and boundary layer thickness, and the dimensionless stroke length L_0/h, where $L_0=\int_0^{T/2}u_a\,dt$, governs the vortex pair dynamics and steady-jet tendencies.

Since it is experimentally difficult to ''dial in'' an exact value of L_0/h or Re, some variation is inevitable. Hence, for ''fixed'' cases, each of these parameters is held to within 2% of the nominal value reported.

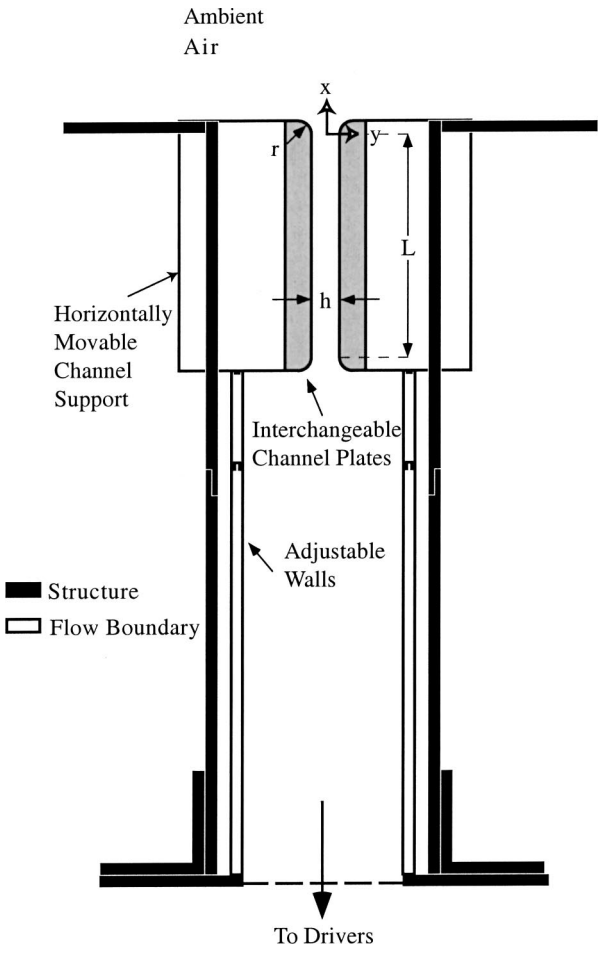

FIG. 2. Schematic of test section. The top of the test section exits to ambient conditions. The streamwise length of the channel is *L*, the cross-stream width is *h* and the spanwise depth (into the page) is *W* (not shown).

III. EXPERIMENTAL SETUP

The apparatus used in this study is shown schematically in Fig. 2. Oscillations are generated by a driver system described in an earlier paper.[11] The test section is connected to the drivers by a rectangular plenum. The flow channel is at the top of the test section and is a rectangular slot with an easily variable width *h* in the cross-stream direction *y*, a length *L* of 24.1 cm in the streamwise direction *x*, and a depth *W* of 15.2 cm in the spanwise direction into the plane of the page. Three interchangeable pairs of channel plates with edge radii $r=0.64$, 1.27, and 2.54 cm are used. The walls on the spanwise sides of the test section are made of glass to allow flow visualization or optical measurements. In air at 80 kPa (Los Alamos atmospheric pressure), the apparatus can produce oscillating velocities up to 50 m/s, and has a frequency range of $7<1/T<120$ Hz.

The flow is visualized using the double-pass shadowgraph technique.[12] The images are acquired phase locked to the driving signal with a 1000×1000-pixel 10-bit CCD camera. The necessary density gradients are generated by the addition of a small amount (less than 1% of the peak oscillating flow rate) of hydrofluorocarbon R134a introduced into the flow below the channel. The R134a is injected in a thin sheet, normally at the spanwise center of the plenum. Therefore, the resultant images should be interpreted similarly to dye or smoke sheet images.

Determination of acoustic power dissipation requires measurements of the time-varying pressure and a cross-stream average of velocity. Phase-locked velocities are measured on one cross-stream half of the slot using a single straight hot-wire probe mounted on a traverse that moves automatically from one measurement location to the next. (Cross-stream symmetry has been confirmed.) Spacing between locations is decreased near the wall to capture the large velocity gradients in the boundary layer. In all cases, 360 samples are acquired per cycle at each location, and the results are phase averaged over 250 cycles.

Oscillating flow is not a typical application of hot-wire anemometry and several unique issues must be addressed. Since the temperature inside the test section is not exactly matched to the room temperature (the drivers generate and leak some heat into the test section), it is necessary to simultaneously measure the time-varying temperature using a constant-current cold wire to correct the hot-wire data based on the measured temperature. Furthermore, since the flow is oscillatory, great care must be taken to ensure that the hot-wire sensor is not in the wake of its supporting probe body during the inward part of the cycle. This is accomplished by

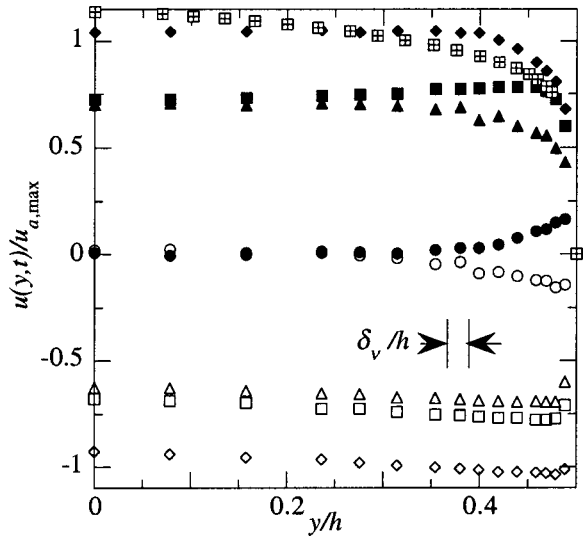

FIG. 3. Profiles of the streamwise component of velocity from the centerline $y=0$ to the wall $y=h$ at $x=0$, at eight equal increments in time through a full cycle, for $L_0/h=20$, $r/h=1.0$, and Re=905, ($\mathrm{Re}_h=u_{a,\max}h\rho/2\mu=21\,400$). The start of the cycle ($t/T=0.0$) is defined as the first time step with the volume flow rate >0. (●) $t/T=0.0$, (■) $t/T=0.125$, (◆) $t/T=0.250$, (▲) $t/T=0.375$, (○) $t/T=0.500$, (□) $t/T=0.625$, (◇) $t/T=0.750$, (△) $t/T=0.875$, (⊞) data from Hussain and Reynolds (Ref. 14) for 2D steady channel flow with $\mathrm{Re}_h=u_{\mathrm{cl}}h\rho/2\mu=23\,200$, where u_{cl} is the centerline velocity.

using a standard boundary-layer probe (where the sensor is offset laterally from the probe body) and pitching the probe body to further remove it from the flow path. The single-sensor hot-wire probe is not capable of sensing flow direction, and therefore its use is limited to regions where the flow direction is known to be along x throughout the cycle. Since the flow might separate during the inward stroke for sharp-edged slots, creating a y component of the velocity near the edges during part of the cycle, only rounded slot edges are considered. All measurements are made at the top of the straight portion of the slot, i.e., the bottom of the slot edge radius (see Fig. 1), a location that we call the exit plane and define as $x=0$. Because flow inward looks the same as flow outward to the probe, the hot-wire signal is a rectified sine wave for sinusoidal flow. Processing software detects the flow reversals and changes the velocity sign appropriately before phase averaging is performed. The result of this procedure is $u_a(y,t)$ shown in some figures below.

Since an assumption of two dimensional flow is necessary in this study, the spanwise uniformity of the flow was checked in a series of measurements with the traverse oriented in the spanwise direction. The flow at the exit plane was found to be spanwise uniform, save for the boundary layers on the spanwise edges. Fortunately, for oscillatory flow, it was found that the spanwise boundary layers have exactly the same thickness and shape as the cross-stream boundary layers which are measured as part of each data set. Therefore, the effect of the spanwise boundary layers on the average velocity can be easily accounted for.

An example of phase-averaged velocity results is shown in Fig. 3. Cross-stream profiles of the streamwise component of velocity are shown at eight points in time equally spaced through the full cycle. The profiles during the blowing stroke have a substantially thicker boundary layer than those for the suction stroke—the oscillatory boundary layer requires some streamwise distance to become established, and the entering inflow has not traversed such a distance. The accelerating flow ($t/T=0.125$) tends to be laminar (as evidenced by the maximum near the wall) while the decelerating flow ($0.25<t/T<0.375$) is turbulent, as observed previously.[13] However, the profile of the turbulent oscillating flow deviates significantly from that of steady channel flow at a similar Reynolds number. Data from Hussain and Reynolds[14] for a Reynolds number of 23 300 based on the centerline velocity and the half channel height are also shown in Fig. 3. Using a similar definition (and using the peak centerline velocity) the Reynolds number of the present data is 21 400. For steady flow, the centerline velocity is the peak of the profile and the velocity falls gradually toward the wall until the boundary layer is reached and the rate of decrease becomes much larger. However, for the oscillatory flow at $t/T=0.25$, the velocity profile is flat at the centerline value for 80% of the channel.

Nonlinear effects in the driving system result in some distortion of the average-velocity waveform. These result in second and third harmonics that on average are 1% and 2% of the fundamental, respectively. We believe that this small departure from sinusoidal flow does not alter the flow physics. However, it would cause significant errors in the normalized pressure and acoustic power if not accounted for. Pressure and acoustic power dissipation are normalized by the temporal maximum of the cross-stream averaged exit velocity squared $u^2_{a,\max}$ and cubed $u^3_{a,\max}$, respectively. As a result of the distortion, the maximum during the blowing does not generally equal the maximum during the suction. The results presented are generated by averaging pressure separately over the blowing stroke and normalizing by the blowing maximum, and doing similarly during the suction stroke. Acoustic power dissipation is normalized similarly. Since we believe that this corrects the distortion, the data will be presented as if the flow were sinusoidal.

Pressure measurements are made simultaneously with the velocity measurements using a series of piezoresistive pressure transducers mounted directly into the channel walls at seven streamwise positions. In order to avoid errors caused by the small nonlinearity of these transducers,[11] the full voltage waveforms from the transducers are digitized and a nonlinear calibration curve is used to convert voltages to pressures. These pressure measurements are extrapolated to $x=0$ to obtain exit-plane values for time-averaged pressure and acoustic power dissipation.

Referring to Eqs. (3) and (5), we see that changes in pressure between two points can come from three sources: (1) conversion of kinetic energy to flow energy due to streamwise velocity differences, (2) minor losses, and (3) time-dependent inertial effects. The time-varying pressure difference between the various measurement stations and the ambient and volume flow rate measured at $x=0$ are shown in Fig. 4 for a representative case. It should be noted that compressible effects upstream of $x=0$ are small in all cases reported here, so the volume flow rate can be assumed independent of x inside the slot. The thin solid trace is the pres-

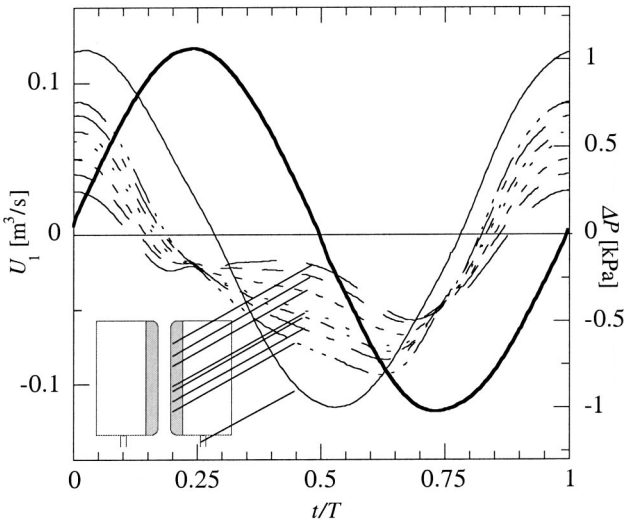

FIG. 4. Volume flow rate and pressure at various locations upstream of the exit plane for $L_0/h=20$, Re=905, $r/h=1.0$. Volume flow rate (—), pressure at $x/h=-1.1$ (— — —), $x/h=-2.1$ (– – –), $x/h=-3.1$ (---), $x/h=-4.4$ (···), $x/h=-4.9$ (–·–), $x/h=-5.9$ (–··–), $x/h=-6.9$ (–···–), below the channel (—). These curves are also labeled by the pointers to the inset which shows where the transducers are located in and below the channel.

sure measured in the large space below the channel. The velocities above and below the channel plates are similar, so there is little contribution from kinetic energy conversion to the pressure in the plenum. Pressure oscillations are dominated by linear inertial effects in the channel, as is evident from the fact that the sinusoidal pressure leads the volume flow rate by almost 90°. The deviation from 90° is due to minor losses at both ends. In addition, the pressure amplitude is somewhat greater than the ordinary inertial pressure difference because of the minor losses (which generate pressure differences that are about half of the inertial pressure difference). Near the top of the channel ($x/h=-1.1$), the length of the slug of fluid between the pressure sensor and the ambient is small while the velocity is much larger than in the ambient, and thus the pressure trace reflects only the minor losses and kinetic-energy conversion. At the lower end of the channel (e.g., $x/h=-6.9$), the pressure fluctuations must accelerate all the fluid above this location and the resultant pressure trace is a mixture of all three of these effects.

IV. RESULTS

A. Flow visualization

We begin with flow visualization. In Fig. 5, a series of instantaneous Schlieren images acquired at 12 times equally spaced through the blowing half of the cycle are shown for a case with $L_0/h=20$, $r/h=1.0$, and Re=634. The image domain is $4.2h$ wide and $3.9h$ high. The marked fluid does not arrive in the visualized domain until $t/T=0.2$. Shortly thereafter, a vortex pair is observed forming along the rounded walls of the slot edge. The locations of the vortex cores indicate that the flow has expanded considerably during the vortex pair formation process. Somewhat later in the cycle, the vortex pair leaves the exit plane and is convected down-

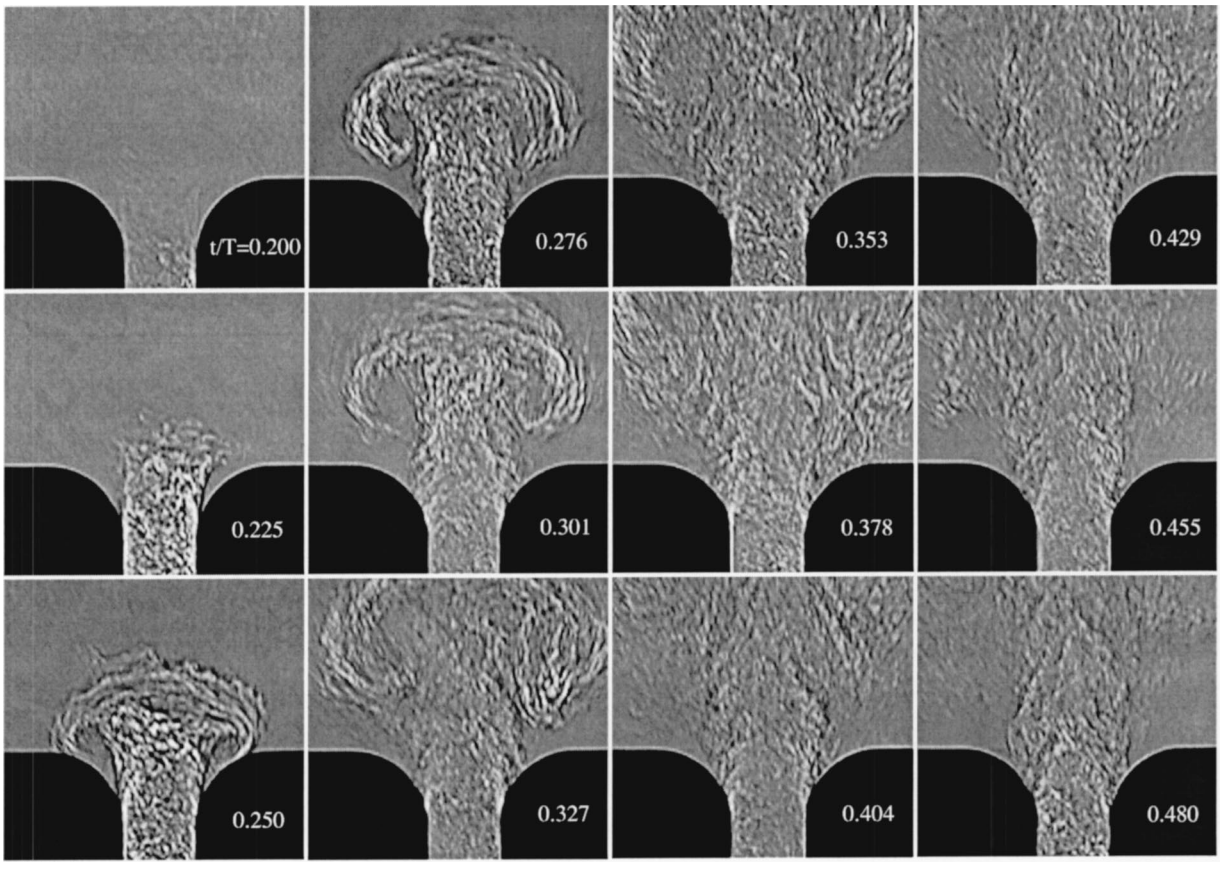

FIG. 5. Schlieren images taken at 12 equally spaced phase points during blowing cycle ($0.2<t/T<0.48$, $L_0/h=20$, Re=634, $r/h=1.0$).

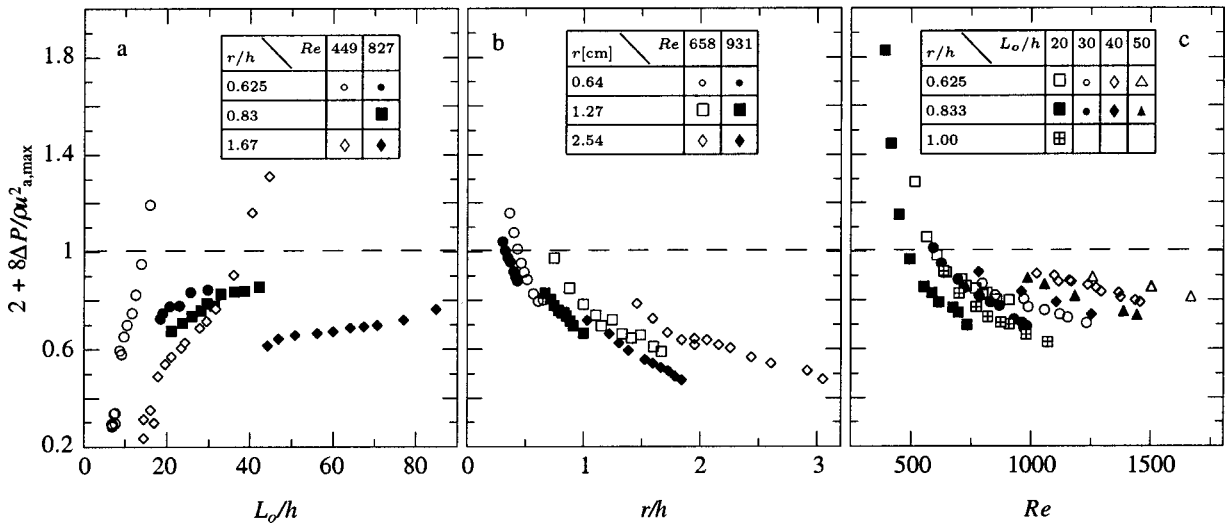

FIG. 6. Time-averaged pressure difference between $x=0$ and the ambient as a function of (a) stroke length, (b) dimensionless radius with $L_0/h=30$, and (c) Reynolds number. The dashed line at 1 is the result (Ref. 18) if $K_B=1$ and $K_S=0$.

stream ($t/T=0.276$). The turbulent vortex pair grows quickly, and a turbulent ''starting jet'' forms behind it.[15] A more subtle but surprising effect is the separation behavior near the exit radius during the latter part of the blowing stroke. The detachment point that is initially near $x=0$ moves abruptly to 45° around the exit radius on both sides of the slot after the start of the decelerating part of the blowing stroke ($t/T=0.301$). The flow remains attached downstream of $x=0$ for the remainder of the blowing stroke, although the images indicate significant fluctuations in the detachment point. As will be shown below, the attachment past $x=0$ results in deceleration of the flow, pressure recovery, and a reduced minor loss coefficient.

B. Pressure

The effects of each of the three parameters on the time-averaged pressure difference between the channel and the infinite space will be examined by fixing two parameters and varying the third. Pressure is scaled such that the normalized value is equal to K_B if $K_S \approx 0$ [see Eq. (9)] and K_B is independent of time during the blowing stroke. For the sake of describing the pressure data, it will be assumed that the suction loss is indeed negligible, as justified by the large r/h values used here.

The effect of L_0/h on the time-averaged pressure will be examined first. For very small stroke length ($L_0/h<0.01$) the oscillations do not cause separation on the outward stroke, and therefore K_B is expected to be very small. This is the region where the impedance of the nozzle is said to be linear.[16] As the stroke length becomes very large, which for a fixed velocity amplitude is equivalent to a very small frequency, the oscillatory jet should approach steady-jet behavior, for which $K_B \approx 1$. These expectations are confirmed in Fig. 6(a), where the dimensionless stroke length is varied with dimensionless radius and Reynolds number fixed (three different radii and two Reynolds-number cases are shown). These data verify that in every case the loss coefficient is small at low L_0/h and grows with L_0/h. In addition, the various cases demonstrate that the loss at a given stroke length is smaller for a larger dimensionless radius and larger Reynolds number. It is also evident that the Reynolds number has a very strong effect on the sensitivity of K_B to L_0/h.

Similarly, the effect of the dimensionless radius is determined by fixing the Reynolds number at two values (nominally Re=658 and 931) and the stroke length at $L_0/h=30$. In order to achieve the range of r/h shown, all three sets of channel plates are used. These pressure-difference data are plotted in Fig. 6(b), and several trends are apparent. The blowing loss decreases monotonically with r/h. In addition, the cases with larger Reynolds numbers have smaller losses.

The small discontinuities between the various sets of data with matched Reynolds number indicate that an additional dimensionless parameter is affecting the results. There are two possibilities: the slot aspect ratio W/h, or the stroke length relative to the slot length, L_0/L. Future researchers may want to control these parameters more carefully. Since, as stated in Sec. III, spanwise uniformity at the exit was

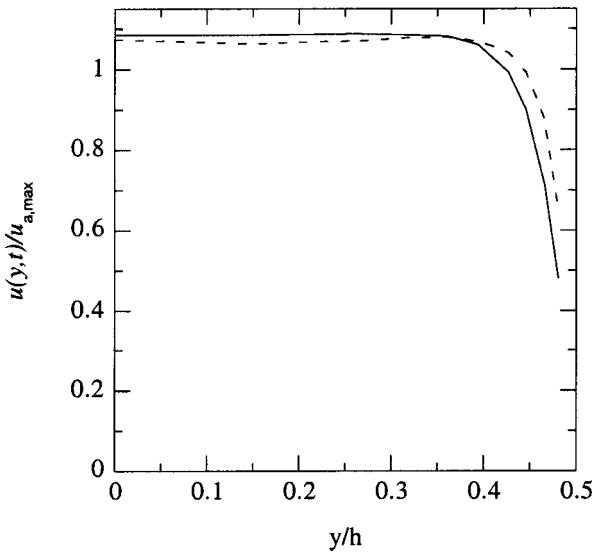

FIG. 7. Profiles of streamwise velocity at $t/T=0.25$ for $L_0/h=20$, $r/h=0.833$, and (—) Re=416, (---) Re=587.

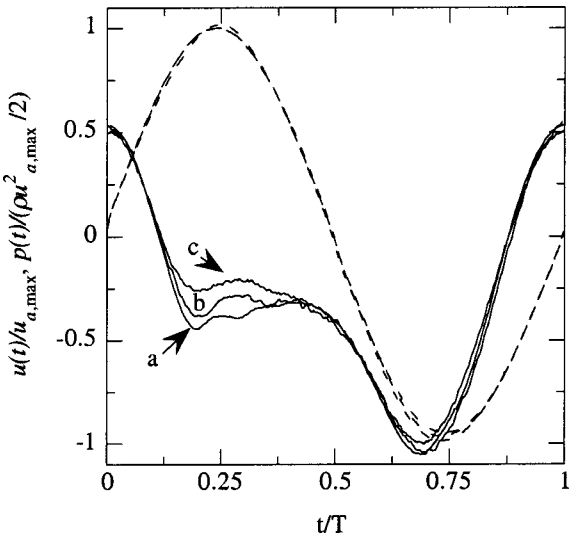

FIG. 8. Normalized cross-stream-average velocity and normalized pressure for $L_0/h=20$ and (a) Re=905, $r/h=1.0$, (b) Re=634, $r/h=1.0$, and (c) Re=645, $r/h=0.625$.

confirmed for a small-aspect-ratio case ($W/h=6.7$), we conjecture that the increase in the loss for smaller aspect ratios can only be due to spanwise nonuniformity of the flow at $x>0$. Flow visualization (not shown) confirms that the downstream flow expands more in the y direction in the spanwise center than at the spanwise edge during the blowing stroke. The slot length can impact the results only if $L_0/L>1$ since the maximum entrance length over which an oscillatory flow can develop is L_0 (the flow reverses after traversing this distance). For slots that are much shorter than L_0, the channel flow boundary layer may not develop fully. For most of the present data, including the cases in Fig. 6(b), $L<L_0$. The cross-stream velocity profiles at the peak of the blowing ($t/T=0.25$) for cases with identical r/h, L_0/h, and Re but different L_0/L are found to have only minor differences in their velocity profiles. Hence, it seems that oscillatory-flow entrance lengths are significantly less that L_0, although this is currently an open question and worthy of further study.

The Reynolds-number dependence is shown in Fig. 6(c). As stated in the discussion of Fig. 6(a) above, smaller dimensionless stroke lengths result in smaller loss coefficients at fixed Reynolds number. While at very small Re the decrease of K_B is more than linear, it becomes linear at larger Re for each of the stroke lengths and dimensionless radii considered here. The behavior of the blowing loss for fixed L_0/h and Re in Fig. 6(c) is not monotonic, which may be further evidence of aspect ratio effects. The large variation in the blowing loss at small Re is likely due to changes in the velocity profile shape associated with the transition from laminar to turbulent flow. This transition has been reported to occur near Re $=550$ for flow in smooth circular pipes.[13] Evidence for this hypothesis is provided by velocity profiles from two of the cases in Fig. 6(c), shown in Fig. 7. The higher-Re profile has a substantially thinner boundary layer than the smaller-Re case. This can potentially affect the loss coefficient because the thicker boundary layer in the smaller-Re case will likely separate from the edge radius sooner and result in a smaller pressure recovery and a larger minor loss.

The latter effect can be seen in the pressure traces shown in Fig. 8. Pressure and velocity are shown for three cases, including two from Fig. 6(c) and an additional case with the smaller of these two Reynolds numbers, the same L_0/h, and a smaller r/h. The average velocities are nearly identical and sinusoidal. For the entire suction stroke and part of the blowing stroke, the pressures are also very similar. However, before the peak of the blowing stroke ($t/T=0.25$), the effects of Re and r/h become apparent. For $r/h=1$ and Re=905 [Fig. 8(a)], there is a large pressure recovery $[p(t/T=0.185)/(\rho u_{a,\max}^2/2)=-0.44]$. Reducing the Reynolds number to 634 results in a decrease in the pressure recovery $[p(0.190)/(\rho u_{a,\max}^2/2)=-0.38$, Fig. 8(b)]. The reduction of r/h from 1.0 to 0.625 results in even less pressure recovery.

An additional flow visualization study confirmed that a larger radius or a larger Reynolds number results in increased expansion of the exiting flow, and therefore a smaller nor-

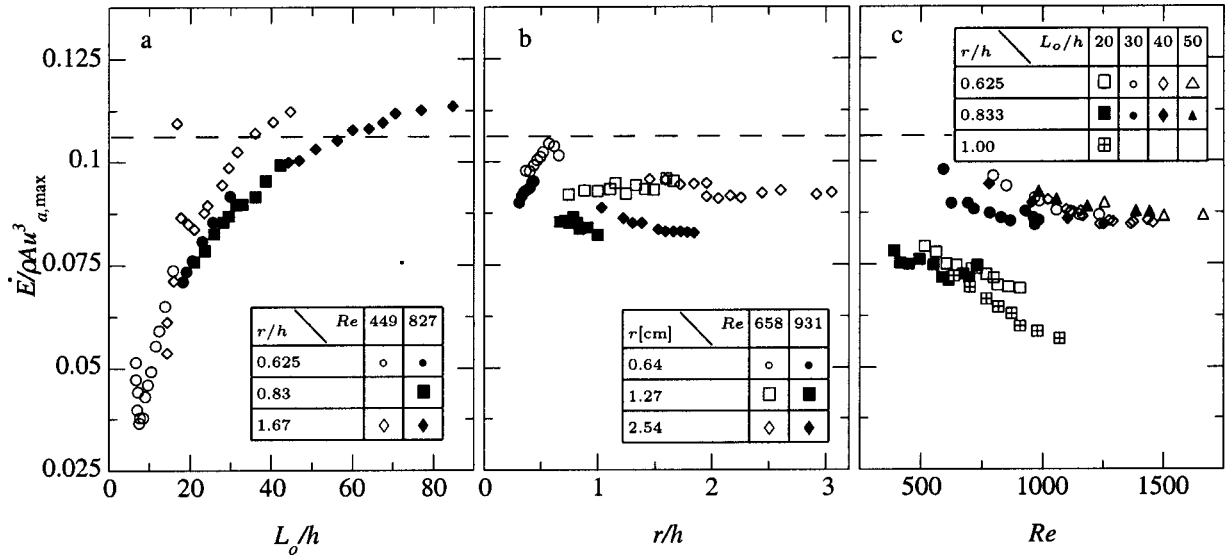

FIG. 9. Acoustic power as a function of (a) stroke length, (b) dimensionless radius with $L_0/h=30$, and (c) Reynolds number. The dashed line at $1/3\pi$ is the result (Ref. 18) if $K_B=1$ and $K_S=0$, and time-dependent inertial effects are ignored.

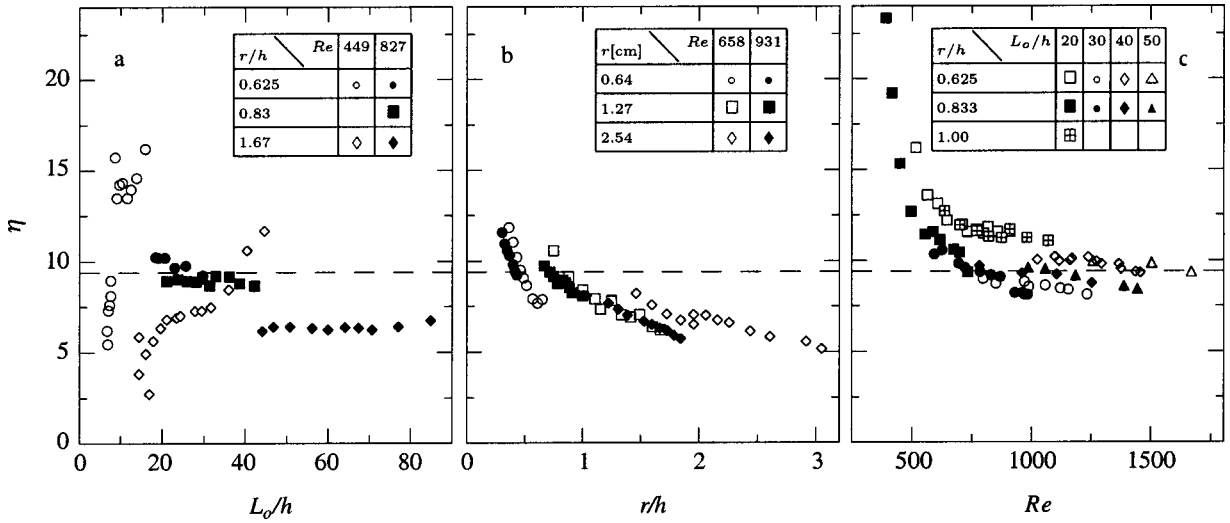

FIG. 10. The effectiveness η as a function of (a) stroke length, (b) dimensionless radius, and (c) Reynolds number. The dashed line indicates a value of 3π.

malized time-averaged pressure (and presumably a smaller blowing loss coefficient) as r/h becomes small, the effect of Re is diminished. Therefore, for a sharp-edged exit, it is likely that the losses based on the profile-based velocity scale will be a function of L_0/h only.

C. Acoustic power dissipation and effectiveness

By assuming that all of the power flowing past the exit is lost to viscous dissipation, the variations of the normalized acoustic power dissipation with each of the three parameters and over the same parameter space reported in Fig. 6 are shown in Fig. 9. Since acoustic power dissipation is the time integral of the product of pressure at $x=0$ (which goes like u^2) and u, we normalize the acoustic power dissipation with velocity cubed as suggested by Backhaus and Swift.[2] The pressure at $x=0$ is extrapolated from the nearby measurement locations.

The effect of L_0/h is shown in Fig. 9(a). Most of the data collapse on a single curve with the exception of the case with the very large radius and small Re, which has more power dissipation than the rest, including other small-Re cases. Also of note is the behavior near $L_0/h=7$. This value of stroke length was identified by Smith and Swift[17] as the boundary between time-averaged ''jetting'' behavior and reingestion of the vortex pairs generated during the blowing stroke. Clearly acoustic power dissipation increases as the reingestion process becomes more dominant (i.e., as L_0/h becomes smaller). It is also interesting to note that no such effect is detectable in the pressure data for the same cases shown in Fig. 6(a).

In contrast to the time-averaged pressure, acoustic power dissipation is a weak function of r/h, as can be seen in Fig. 9(b). In some parts of the parameter space, the behavior is not monotonic. It should be noted that a representative error for these data is ± 0.0025.

Acoustic power dissipation is shown in Fig. 9(c) to decrease with increasing Reynolds number. Data for identical L_0/h and similar r/h are more or less collapsed, as is to be expected given the weak r/h effects discussed above. It also appears that the sensitivity of the power dissipation to Re is less for $L_0/h \geqslant 30$.

As stated in Sec. I, minor losses can be used to create time-averaged pressure differences to block streaming motions or to convert oscillating flow to steady flow.[18] Ideally, we would create this time-averaged pressure difference with minimal acoustic power dissipation. It is natural to form an ''effectiveness'' parameter that is the ratio of the dimensionless time-averaged pressure difference to the dimensionless acoustic power dissipation:

$$\eta = \frac{2 + 8\Delta P/\rho u_{a,\max}^2}{\dot{E}/\rho A u_{a,\max}^3}. \tag{10}$$

Assuming[18] loss coefficients that are constant during the blowing and suction parts of the cycle, $\eta = 3\pi$ when $K_B \gg K_S$.

Using the data from Figs. 6 and 9, η is plotted versus the same three dimensionless parameters in Fig. 10. These data demonstrate that the effectiveness decreases with increasing r/h or Re. It is shown above that increasing either of these parameters improves the pressure recovery during the outward motion. A lack of this recovery is responsible for the time-averaged pressure difference desirable in some applications, so it is no surprise that improved pressure recovery can have a detrimental effect on the effectiveness. Although the effectiveness increases with stroke length for small (laminar) Re, it is a very weak function of L_0/h at larger Reynolds numbers.

V. CONCLUSIONS

The effect of minor losses on the time-averaged pressure and acoustic power dissipation generated by oscillating flow in a rounded entrance/exit between a rectangular channel and an infinite space has been investigated experimentally. Both of these quantities are functions of three dimensionless parameters: L_0/h, r/h, and Re. Cases with very small dimensionless stroke lengths tend toward linear oscillatory behav-

ior and cases with large stroke lengths tend toward steady jet flow. Increasing the exit radius reduces the adverse pressure gradient experienced by the exiting flow and allows the flow to expand more in the cross-stream direction near the exit, resulting in smaller losses. This effect can be enhanced by increasing the Reynolds number. The Reynolds number also governs the transition from laminar to turbulent flow. Laminar flow has a thicker boundary layer and thus has less tendency to expand and recover pressure which results in larger losses. It is also found that nonlinear inertial effects prevent one from making the necessary assumptions to use the equation for acoustic power dissipation to determine the blowing and suction loss coefficients separately. A parameter is defined that estimates the effectiveness of the sudden expansion for generating time-averaged pressure differences with minimal acoustic power dissipation. It is found that the effectiveness increases with decreasing r/h and Re, and increases with increasing L_0/h for laminar flow.

This work is but a small, imperfect step toward the understanding needed for the deliberate and confident use of minor loss phenomena to control streaming in thermoacoustic–Stirling engines and refrigerators. Here, we worked with $|p_a|/p_m \approx 0.01$ and $|u_a|/a \approx 0.1$, where p_m is the mean pressure and a is the sound speed, hoping that the flow could be regarded as incompressible. We were also restricted to a fixed phase between p_a and u_a, set by the impedance of the transition. In engines[2] and refrigerators[1] thus far, $|p_a|/p_m \approx 0.1$ and $|u_a|/a \approx 0.1$, so compressibility effects could be important; if so, then not only $|p_a|/\rho_m a|u_a|$ but also the phase between p_a and u_a must be important. Furthermore, here our exit geometry was unconstrained, while other design considerations typically lead to exit jets that impinge on a tube-sheet, are constrained laterally, or perhaps even interact with nearby elbows. Both axisymmetric[6,7,1] and 2D geometries[2] are to be explored. The best hope for understanding may lie with extensive numerical studies benchmarked against a few limited experimental studies.

ACKNOWLEDGMENTS

G.S. would like to acknowledge the financial support of the Division of Materials Science in DOE's Office of Science. B.S. was supported initially by Los Alamos National Laboratory LDRD funds and later by the V.P. for Research at USU. We would also like to thank Scott Backhaus for his patience and generosity through many hours of fruitful discussion.

[1] G. W. Swift, D. L. Gardner, and S. Backhaus, "Acoustic recovery of lost power in pulse tube refrigerators," J. Acoust. Soc. Am. **105**, 711–724 (1999).
[2] S. Backhaus and G. W. Swift, "A thermoacoustic-Stirling heat engine: Detailed study," J. Acoust. Soc. Am. **107**, 3148–3166 (2000).
[3] E. Fried and I. E. Idelchik, *Flow Resistance* (Hemisphere, New York, 1989).
[4] R. S. Wakeland and R. M. Keolian, "Influence of velocity profile nonuniformity on minor losses for flow exiting thermoacoustic heat exchangers," J. Acoust. Soc. Am. **112**, 1249–1252 (2002).
[5] P. J. Morris, S. Boluriaan, and C. M. Shieh, "Computational thermoacoustic simulation of minor losses through a sudden contraction and expansion," 7th AIAA/CEAS Aeroacoustics Conference, 2001, paper 2001-2272.
[6] A. Petculescu and L. Wilen, "Lumped-element technique for the measurement of complex density," J. Acoust. Soc. Am. **110**, 1950–1957 (2001).
[7] L. Wilen, A. Petculescu, and G. Petculescu, "Impedance measurements of stacks, regenerators and jet pumps," Proceedings of the 17th International Congress on Acoustics, Rome, Italy, 2001.
[8] J. K. Vennard, "One-dimensional flow," in *Handbook of Fluid Dynamics*, edited by V. L. Streeter (McGraw-Hill, New York, 1961).
[9] B. R. Munson, D. F. Young, and T. H. Okiishi, *Fundamentals of Fluid Mechanics*, 2nd ed. (Wiley, New York, 1994), Fig. 8.28.
[10] A. G. Fredrickson and R. B. Bird, "Transport phenomena in multicomponent systems," in *Handbook of Fluid Dynamics*, edited by V. L. Streeter (McGraw-Hill, New York, 1961), Eq. 6.208.
[11] B. L. Smith and G. W. Swift, "Measuring second-order time-averaged pressure," J. Acoust. Soc. Am. **110**, 717–723 (2001).
[12] G. S. Settles, *Schlieren and Shadowgraph Techniques* (Springer, New York, 2001), Fig. 3.8.
[13] M. Ohmi, M. Iguchi, K. Kakehashi, and M. Tetsuya, "Transition to turbulence and velocity distribution in an oscillating pipe flow," Bull. JSME **25**, 365–371 (1982).
[14] A. K. M. F. Hussain and W. C. Reynolds, "Measurements in fully developed turbulent channel flow," J. Fluids Eng. **97**, 568–580 (1975).
[15] M. Gharib, E. Rambod, and K. Shariff, "A universal time scale for vortex ring formation," J. Fluid Mech. **360**, 121–140 (1998).
[16] U. Ingard and S. Labate, "Acoustic circulation effects and the nonlinear impedance of orifices," J. Acoust. Soc. Am. **22**, 211–218 (1950).
[17] B. L. Smith and G. W. Swift, "Synthetic jets at large Reynolds number and comparison to continuous jets," 31st AIAA Fluid Dynamics Conference, 2001, paper 2001-3030.
[18] G. W. Swift, *Thermoacoustics: A Unifying Perspective for Some Engines and Refrigerators* (Acoustical Society of America, Publications, Sewickley, PA, 2002).

Noncontacting lateral transportation using gas squeeze film generated by flexural traveling waves—Numerical analysis

Adi Minikes[a)]
Faculty of Mechanical Engineering, Haifa 32000, Technion, Israel

Izhak Bucher[b)]
Dynamics & Mechatronics Laboratory, Faculty of Mechanical Engineering, Haifa 32000, Technion, Israel

(Received 29 July 2002; revised 24 January 2003; accepted 10 February 2003)

This paper presents the theory describing the dynamical behavior of a noncontacting lateral transportation of planer objects by means of a gas squeeze film created by traveling flexural waves of a driving surface. An oscillating motion in the normal direction between two surfaces can generate a gas film with an average pressure higher than the surrounding. This load-carrying phenomenon arises from the fact that a viscous flow cannot be instantaneously squeezed; therefore, fast vibrations give rise to a cushioning effect. Equilibrium is established through a balance between viscous flow forces and compressibility forces. When the oscillatory motion between two surfaces creates traveling waves, lateral viscous forces are generated in addition to the normal levitation forces. These forces are produced as a result of nonuniform pressure gradients in the lateral direction between the surfaces. The combination of normal and lateral forces could be used for transporting objects without any direct contact with the driving surface. The numerical algorithm in this work couples the squeeze film phenomenon, which is represented by means of finite difference equations, to model a variant of the Reynolds equation, together with the equations describing the dynamics of the floating object. Numerical simulations are presented and investigated to highlight noteworthy topics. [DOI: 10.1121/1.1564014]

PACS numbers: 43.25.Uv, 43.25.Op [MFH]

I. INTRODUCTION

In previous papers dealing with squeeze film and air bearings that are created by normal vibration between two vibrating surfaces, the analysis was carried out for the case where the mean clearance between the surfaces was predetermined.[1,2] In other words, the vibrating surface was brought (numerically) close to a fixed surface to achieve a prescribed clearance. When trying to model an applicative problem such as squeeze bearing or mass levitation, where the clearance cannot be fixed but is determined by equilibrium of forces, the analysis appearing in the literature is not suitable.

Several studies have been carried out in the field of acoustics describing the near-field levitation phenomenon.[3–5] While in a linear medium the acoustical impedance is constant since the pressure and the velocity are linearly related, in a nonlinear medium the acoustic impedance varies in time, producing a mean acoustic pressure. When an unconfined surface oscillates in a sufficiently high frequency such that the wavelength is small in comparison to the typical length of the surface, an unbounded acoustic wave is produced. If a plane target is placed in the path of such unbounded acoustic beam, the time-average pressure (defined as the Langevin radiation pressure) exerted on the target creates a levitation force. In conventional acoustic levitation, standing waves are formed between a radiating source and a reflector, and the levitation takes place near the pressure nodes in the field. In the case dealt with here, the levitated planar object acts as a reflector. In this situation the closer the object approaches the radiating source the larger the levitation force becomes.

In systems such as the one presented here, the clearance between the surfaces may be uneven; hence, the film thickness may be spatially nonuniform. As the pressure gradients and the velocity gradients in the film depend on the shape of the acoustic field, the gradients will be nonuniform as well. Therefore, in addition to normal acoustic radiation force performing the levitation, there are also acoustic viscous forces in the tangential directions. The streaming of the medium created by the radiation pressure gradients is balanced by viscous losses associated with the boundaries of the medium which create relative motion between adjacent portions of the medium producing shear deformation.

Recently, Hashimoto *et al.* have studied experimentally a method of transporting an object by exciting traveling flexural vibration waves along a plate.[3] Their experiment has confirmed the phenomenon that objects could be transported without contact. Unfortunately, in their work, a model or a numerical theory to describe the physical mechanism of the system is not provided. In addition, the parameters of the experiment were not fully investigated, leaving several inconsistencies in the results.

The present work suggests a different approach for solving the pressure field between the vibrating surface and the levitated object, which is not based on the commonly used acoustic approximation equations. Instead of solving a second-order approximations for Navier–Stokes equation in order to describe the acoustic streaming, we derive a modified nonlinear compressible Reynolds equation (which, in a

[a)]Electronic mail: minikes@technion.ac.il
[b)]Electronic mail: bucher@technion.ac.il

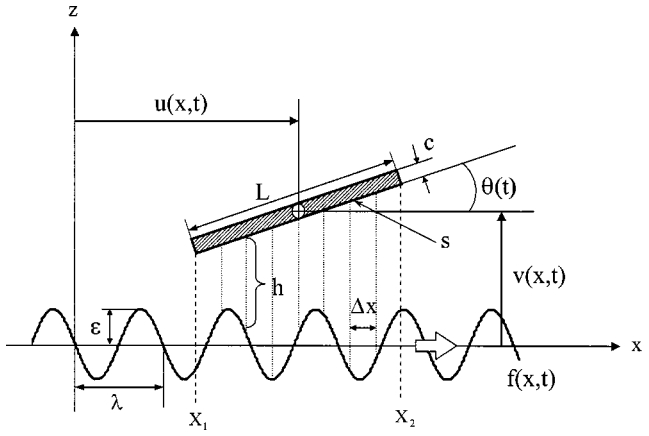

FIG. 1. Schematic layout of the system.

similar manner to acoustic equations, is derived from Navier–Stokes equations) based on a fluid mechanics approach.

This work begins by presenting the physical system and describing the governing equations of the system. Later, the numerical procedure employed for solving the coupled equations is described with suitable variable scaling and transformations. Then, we present a numerical parametric study examining the effect of the terminal speed and the nature of the traveling excitation wave on the dynamics. In the last section we discuss the influence of the acoustic radiation pressure, generated by the vibrating surface, on the boundary conditions of the squeeze film.

II. DERIVATION OF THE EQUATIONS OF MOTION

In this section the equations of motion of the overall system are developed. First, we deal with the dynamics of the squeeze film and discuss the prevailing variables. Later, the modified nonlinear compressible Reynolds equation is derived and the importance of each term is evaluated. The kinematical boundary conditions are outlined and with the dynamics of the floating object, the coupled equations of motions are developed.

Consider the case illustrated in Fig. 1, where a planar object is modeled as a rigid plate having length (L), width (b), thickness (c), and weight (m). The object is levitated and transported by a squeeze film created between the plate (s) and a traveling vibration wave that is shown on the lower surface (f). The traveling wave propagates in the positive x direction, oscillating at a frequency (ω) with an amplitude (ε) and a wavelength (λ), while the plate being rigid can be modeled using three coordinates (u,v,θ).

The fluid dynamics in the squeeze film is numerically modeled by means of finite difference equations. Since the plate is moving, the geometrical boundaries of the squeeze film are defined by the coordinates (x_1,x_2,y_1,y_2). These are determined by the geometry of the plate (L,b), the position of the plate's center of gravity (u,v), and the plate's angle of inclination (θ). The local film thickness (h) is defined by the local gap between the surfaces using spatial finite steps (Δx). For simplicity, in this paper the traveling wave progresses only in one dimension (the x direction); consequently, the pressure gradients in the y direction are symmetrical. Due to symmetry the total lateral force in the y direction vanishes, but in cases where the plate's width and length (b,L) are of the same order of magnitude, the edge effects on the gas flow in the y direction are not negligible and should be considered. In such cases the gas squeeze film needs to be treated as a two-dimensional flow (x,y plane), even though there is no motion of the plate in the y direction.

A. Reynolds equation for squeeze film

In this section we briefly derive the differential equation governing the squeeze film phenomena with some modifications for the presented case. From the modified Reynolds equation we can obtain the pressure distribution and the velocity profile in the film for determining the reactions forces excreted on the levitated plate.

In order to allow the load-carrying phenomenon to take place, the bearing dimension (L), which represents a typical length of the involved surfaces, must be much greater than the thickness of the squeezed film (h). If this restriction does not apply, the effects in the boundaries will prevent the increase of the mean pressure in the film compared to the surrounding. Furthermore, the velocity of the fluid in the normal direction is of an order of h/t and the velocities of the fluid in the lateral directions are of an order L/t, where t is the time period of the normal oscillations. Therefore, as $L \gg h$, the normal velocity of the fluid is relatively neglected compared with the lateral velocities.

Performing an order of magnitude analysis on the differential equations representing the momentum of the fluid (Navier–Stokes) and neglecting the normal velocity in the fluid reveals that the pressure gradient in the normal direction is of the order h (film thickness), while the pressure gradients in the lateral directions are of the order of unity (normalized).[6] Such typical magnitudes may suggest that the pressure gradient in the normal direction could be ignored.

For the sake of discussion, the analysis of the fluid mechanics part of the squeeze film phenomenon takes into account only the momentum in the one lateral dimension. A more complete analysis is introduced later on.

Under the above assumptions, the momentum equation in an x direction for a two-dimensional Newtonian flow reduces to

$$\rho\left(\frac{\partial v_x}{\partial t}+v_x\frac{\partial v_x}{\partial x}+v_y\frac{\partial v_x}{\partial y}\right)=-\frac{\partial p}{\partial x}+\mu\frac{\partial^2 v_x}{\partial z^2}, \tag{1}$$

where ρ, v_x, v_y, p, μ are density, velocities, pressure, and viscosity, respectively. The dilatation in the film has been neglected as its order of magnitude is of h^2 $(h \ll 1)$.[5]
The typical order of magnitude of the physical parameters that describe the gas squeeze film phenomenon, in units of cm, kg, and s, is

$$L \cong 1,\ h \cong 10^{-3},\ t \cong 10^{-4},\ v_x \cong 10^3,\ v_y \cong 10^3,\ \nu \cong 10^{-1}, \tag{2}$$

where ν is the kinematical viscosity of the gas (air in our case). It follows that the order of magnitude of the terms in Eq. (1) can be indicated by the order of the exponential power, shown under each term

$$\underset{(3+4)}{\frac{\partial v_x}{\partial t}} + \underset{(3+3)}{v_x \frac{\partial v_x}{\partial x}} + \underset{(3+3)}{v_y \frac{\partial v_x}{\partial y}} = -\frac{1}{\rho}\frac{\partial p}{\partial x} + \underset{-1+3+(2\times 3)}{\nu \frac{\partial}{\partial z}\left(\frac{\partial v_x}{\partial z}\right)}. \tag{3}$$

It is clearly seen in Eq. (3) that convective acceleration terms are smaller by 2 orders in comparison with the viscous term. Therefore, it is reasonable to neglect the contribution of the inertia forces associated with the convective acceleration to the pressure gradients.

Commonly in lubrication problems, the considered oscillation frequency of the fluid in the bearing does not exceed a magnitude of 10^3 Hz; therefore, the local acceleration term is ignored as well as the convective acceleration terms. However, when the oscillations are in the range of 10^4 Hz or more (as it is the case for this device), the local acceleration term in Eq. (3) is no longer negligible as it is of a comparable magnitude with the viscous term.

On the other hand, when levitation is considered, the film thickness is determined by equilibrium of forces in the system and cannot be initially prescribed. For relatively large levitated weight, the film thickness could decrease to such an extent that the local acceleration term will be negligible in comparison with the viscous term, even though high oscillation frequency exists.

If only the local acceleration term is considered, Eq. (1) may be reduced to

$$\frac{\partial p}{\partial x} + \rho \frac{\partial v_x}{\partial t} = \mu \frac{\partial^2 v_x}{\partial z^2}. \tag{4}$$

The boundary conditions for a squeeze film between two surfaces with the presence of relative lateral velocity and acceleration are

$$v_x(z=0)=0 \quad v_x(z=h)=\dot{u} \tag{5a}$$

$$\frac{\partial v_x}{\partial t}(z=0)=0 \quad \frac{\partial v_x}{\partial t}(z=h)=\ddot{u}, \tag{5b}$$

where $h=h(x,t)$ is the film thickness and $\dot{u}$, $\ddot{u}$ are the relative lateral velocity and acceleration, respectively.

Gross has suggested that the distribution of acceleration across the film thickness may be assumed as linear.[6] Results obtained using this simplified formulation were in good agreement with those obtained when this restricting assumption was not made. For an assumed linear acceleration profile, together with the boundary conditions in Eq. (5b), Eq. (4) could be written as

$$\frac{\partial p}{\partial x} + \rho \ddot{u}\frac{z}{h} = \mu \frac{\partial^2 v_x}{\partial z^2}. \tag{6}$$

The solution of the differential Eq. (6) under the boundary conditions in Eq. (5a) takes the form

$$v_x(z) = \frac{z}{2\mu}\frac{\partial p}{\partial x}(z-h) + \dot{u}\frac{z}{h} + \ddot{u}\frac{\rho z}{6\mu h}(z^2-h^2). \tag{7}$$

Equation (7) shows that the fluid velocity profile depends on the film thickness and the pressure gradient, and is coupled to the motion of the levitated object.

Integrating the continuity equation across the film thickness and rearranging the terms produces

$$\frac{\partial}{\partial x}\int_0^h \rho v_x dz + \frac{\partial}{\partial t}(\rho h) = 0. \tag{8}$$

Substituting the expression for the velocity profile in the gas film, as was derived in Eq. (7), into Eq. (8) produces the compressible Reynolds equation for a gas squeeze film incorporating relative lateral motion and acceleration of the surfaces

$$\frac{\partial}{\partial x}\left(\frac{\rho h^3}{\mu}\frac{\partial p}{\partial x}\right) = 12\frac{\partial}{\partial t}(\rho h) + 6\dot{u}\frac{\partial}{\partial x}(\rho h) - \ddot{u}\frac{\partial}{\partial x}\left(\frac{\rho^2 h^3}{2\mu}\right). \tag{9}$$

The density and the pressure are related by equation of state; hence, nonlinearity is introduced in Eq. (9).

The following analysis can be extended to describe the case of two-dimensional flow with lateral motion between the surfaces in both directions, meaning a relative motion in the *x,y* plane as well as in the *z* direction. For such a case, Eq. (9) becomes

$$\begin{aligned}\frac{\partial}{\partial x}\left(\frac{\rho h^3}{\mu}\frac{\partial p}{\partial x}\right) + \frac{\partial}{\partial y}\left(\frac{\rho h^3}{\mu}\frac{\partial p}{\partial y}\right) &= 12\frac{\partial}{\partial t}(\rho h) + 6\dot{u}\frac{\partial}{\partial x}(\rho h) + 6\dot{v}\frac{\partial}{\partial y}(\rho h) \\ &\quad - \ddot{u}\frac{\partial}{\partial x}\left(\frac{\rho^2 h^3}{2\mu}\right) - \ddot{v}\frac{\partial}{\partial y}\left(\frac{\rho^2 h^3}{2\mu}\right),\end{aligned} \tag{10}$$

where $\dot{v}$, $\ddot{v}$ are equivalent to $\dot{u}$, $\ddot{u}$ for the relative motion in the *y* direction. Equation (10) describes the dynamical behavior of the squeezed fluid, taking into account both time- and space-varying gap and relative acceleration. The complete dynamics requires coupling of the floating object to the supporting fluid.

B. The kinematics of the boundary and the air gap

As was mentioned earlier, the film thickness h is determined by equilibrium of forces in the system and is defined by the clearance between the vibrating surface and the levitated surface. Let the vibrating surface be a traveling wave, which vibrates at frequency (ω) with amplitudes (a_1,a_2) and wavelength (λ)

$$f(x,t) = a_1 \sin(\omega t - kx) + a_2 \sin(\omega t + kx), \quad k = 2\pi/\lambda. \tag{11}$$

In order to assure that pressure radiation will take place, the wavelength of the vibrating surface must be larger than the acoustic wavelength in the air film. This means that only above a critical vibrating frequency will levitation take place.

In practice, the mechanical imperfections make it impossible to attain a perfect traveling wave; therefore, the numerical model uses a realistic combination of two traveling waves in opposite directions. As the degree of purity of the excited wave in the positive-*x* direction increases, the standing wave ratio (SWR), which is defined by $\mathrm{SWR}=|a_1+a_2|/|a_1-a_2|$, approaches 1.

The bottom surface (*s*) of the floating object is defined geometrically by the position of the plate. Therefore, the expression describing the bottom surface's line (see Fig. 1) is

$$s(x,u,v,\theta)=v+\tan(\theta)(x-u), \quad x_1<x<x_2. \tag{12}$$

The clearance is described by

$$\begin{aligned} h(x,u,v,\theta,t)&=s(x,u,v,\theta)-f(x,t)\\ &=v+\tan(\theta)(x-u)-a_1\sin(\omega t-kx)\\ &\quad -a_2\sin(\omega t+kx). \end{aligned} \tag{13}$$

The clearance is derived from the position of the plate's center of gravity (u,v) and the plate's angle of inclination (θ), and is varying in space and time. In the present study, it is assumed that the vibrating surface is uniform along the y axis and the wave propagates only in the x direction.

C. Floating plate dynamics

Three types of external loads are exerted upon the floating plate: levitation forces, lateral forces, and rotational moments. In this section, these forces will be presented in some detail. The matrix form of the plate's equations of motion has the form

$$\begin{bmatrix} m & 0 & 0\\ 0 & m & 0\\ 0 & 0 & J \end{bmatrix} \begin{Bmatrix} \ddot{u}\\ \ddot{v}\\ \ddot{\theta} \end{Bmatrix} = \begin{Bmatrix} N_1\\ N_2\\ M_1 \end{Bmatrix}, \tag{14}$$

where m is the plate's mass, J is the inertial moment of the plate around its center of gravity, and N_1, N_2, M_1 are the lateral force, the levitation force, and the rotational moment, respectively.

The lateral forces acting on the plate are due to shear stresses in the squeeze film that develop as a result of nonuniformity of the pressure gradients in the lateral direction, and due to the relative motion between the surfaces in the lateral direction. In addition, there is drag force acting on the upper face of the plate.

For a Newtonian flow, the shear stresses in the flow acting on a plane normal to the z axis are defined by

$$\tau_{zx}=\mu\left(\frac{\partial v_z}{\partial x}+\frac{\partial v_x}{\partial z}\right)\cong\mu\frac{\partial v_x}{\partial z}. \tag{15}$$

The fluid velocity in the normal direction v_z could be neglected, as was explained in Sec. II A. Substituting Eq. (7) into Eq. (15) gives the expression for the shear stress on the bottom surface of the floating plate

$$\tau_{zx}|_{z=h}=\mu\left.\frac{\partial v_x}{\partial z}\right|_{z=h}=\frac{h}{2}\frac{\partial p}{\partial x}+\mu\frac{\dot{u}}{h}+\frac{\ddot{u}\rho h}{3}. \tag{16}$$

Equation (16) shows that the shear stresses on the plate consist of three terms. The first term is due to pressure gradients in the film. The second term depends on the relative velocity between the plates. As the relative velocity increases, this component of the stress increases until equilibrium with the pressure gradient is reached. At this stage the plate stops accelerating, the third term in the shear stress vanishes, and the plate continues at terminal steady velocity. In addition, as the film thickness h decreases, the pressure gradients increase and the shear stress in the film increases. This suggests that the terminal velocity may have a maximum value with respect to the film thickness and pressure gradients. The investigation of the dependency is beyond the scope of this paper, since the numerical model is not developed for cases involving relatively small surface densities (weight/area), as will be discussed later on.

The motion of the plate in the surrounding air generates a boundary layer on the exposed surface of the plate. The shear stresses in this boundary layer produce a drag force that resists the plate's motion. This drag force acting on the plate in the case of laminar flow is[7]

$$f_D=\tfrac{1}{2}c_D\rho_a\dot{u}^2Lb, \quad c_D=\frac{1.328}{\sqrt{\mathrm{Re}_L}}, \tag{17}$$

where Reynolds number $\mathrm{Re}_L=\dot{u}L/\nu<5\times10^5$ and ρ_a is the gas density at ambient conditions.

Integrating the shear stress along the plate's length, together with the force created by pressure acting on the plate's projected area normal to the lateral direction, and taking into account the drag force, we obtain the total lateral force (in space) as function of time acting on the plate in the x direction

$$\begin{aligned} N_1=&-\int_{x_1}^{x_2}\int_0^b \tau_{zx}|_{z=h}dy\,dx\\ &-\int_{x_1}^{x_2}\int_0^b (p-p_a)\sin(\theta)dy\,dx-f_D. \end{aligned} \tag{18}$$

Here, ρ_a is the gas pressure at ambient conditions, b is the plate's width, and the negative sign on the shear stress integration is added since the normal of the plate's bottom surface is pointing in the negative-z direction.

The total levitation force on the plate is the difference between the gravitational force of the plate and the force exerted by the stresses in the squeeze film on the plate. For small inclination angle, the viscous terms in the principal stress tensor are three orders of magnitude smaller than the pressure term.[5] Therefore, the total levitation force (in space) as function of time is taken as:

$$N_2=-mg+\int_{x_1}^{x_2}\int_0^b (p-p_a)\cos(\theta)dy\,dx. \tag{19}$$

The total rotational moment (in space) as function of time acting on the center of gravity of the plate around the y axis is defined by

$$M_1=\int_{x_1}^{x_2}\int_0^b (x-u)(p-p_a)dy\,dx. \tag{20}$$

As the plate's inclination is in the order of h/L, which is very small, the moments produced by the lateral components of the pressure are smaller by several orders of magnitudes than those in Eq. (20); therefore, they have no significant contribution to the total moment. This will be shown in Sec. III A, when the normalized equations are presented.

III. THE NUMERICAL ALGORITHM—FORMULATION

The numerical algorithm in this work couples the squeeze film phenomenon, which is represented by means of finite difference equations, together with the equations de-

scribing the dynamics of the floating plate. First, we represent the normalized equations governing the system's dynamics, then we discuss the scheme of the coupled numerical solver.

A. Normalized equations of motion of the system

In order to improve the numerical stability, it is essential to normalize the equations, especially as the dimensions governing the problem may differ by several orders of magnitudes. The dimensionless parameters

$$P=\frac{p}{p_a},\quad \Gamma=\frac{\rho}{\rho_a},\quad H=\frac{h}{h_0},\quad X=\frac{x}{L},\quad Y=\frac{y}{L},\quad T=\omega t, \tag{21}$$

are introduced, where p_a is atmospheric pressure, ρ_a is the gas density at atmospheric pressure, h_0 is the mean clearance between the surfaces, and ω is the oscillation frequency. For gas film in which polytropic flow ($p\rho^{-n}=\text{const}$) is postulated with $n=1$ for isothermal behavior, it is possible to replace Γ by P. The assumption of isothermal behavior is reasonable, as the thickness of the gas film is very thin compared to the bearing surfaces, and the heat capacity of the bearings is much larger than the heat capacity of the film. In the next section a mathematical explanation of the differences between an isothermal model and adiabatic model is provided.

Using the dimensionless parameters, the normalized Reynolds equation for two-dimensional flow with no relative motion in the y direction may be written as

$$\frac{\partial}{\partial X}\left(PH^3\frac{\partial P}{\partial X}\right)+\frac{\partial}{\partial Y}\left(PH^3\frac{\partial P}{\partial Y}\right)=\sigma\frac{\partial}{\partial T}(PH)+\Lambda_X\frac{\partial}{\partial X}(PH)-\alpha_X\frac{\partial}{\partial X}(P^2H^3), \tag{22}$$

where

$$\sigma=\frac{12\omega\mu_0L^2}{p_ah_0^2},\quad \Lambda_X=\frac{6\mu_0L\dot{u}}{p_ah_0^2},\quad \alpha_X=\frac{\rho_aL\ddot{u}}{2p_a},$$

and μ_0 is the gas viscosity at initial state. In order to derive the normalized equations describing the plate's motion, we introduce, in addition to Eq. (21), several dimensionless parameters

$$U=\frac{u}{L},\quad V=\frac{v}{h_0},\quad Z=\frac{z}{h_0},\quad \Theta=\frac{\theta}{\theta_0},\quad B=\frac{b}{L},\quad A_i=\frac{a_i}{h_0},$$

where $\theta_0=h_0/L$. As the inclination angle θ is assumed to be very small, approximating $\sin(\theta)$, $\tan(\theta)\to\theta$, and $\cos(\theta)\to1$ is permissible. The normalized Eq. (13) expressing the local film thickness takes the form

$$H=V+\frac{\Theta\,\theta_0L}{h_0}(X-U)-A_1\sin(T-kXL)-A_2\sin(T+kXL). \tag{23}$$

The normalized version of Eq. (14), describing the plate's motion, is

$$\begin{Bmatrix}\frac{\partial^2U}{\partial T^2}\\ \frac{\partial^2V}{\partial T^2}\\ \frac{\partial^2\Theta}{\partial T^2}\end{Bmatrix}=\begin{Bmatrix}-\int_{X_1}^{X_2}\int_0^B\left(\Phi_1H\left(\frac{\partial P}{\partial X}\right)+\Phi_2\frac{1}{H}\left(\frac{\partial U}{\partial T}\right)+\Phi_3PH\left(\frac{\partial^2U}{\partial T^2}\right)+\Phi_4(P-1)\Theta\right)dY\,dX-\Phi_5\left|\frac{\partial U}{\partial T}\right|^{1/2}\left(\frac{\partial U}{\partial T}\right)\\ -G+\Phi_6\int_{X_1}^{X_2}\int_0^B(P-1)dY\,dX\\ \Phi_7\int_{X_1}^{X_2}\int_0^B(X-U)(P-1)dY\,dX,\end{Bmatrix}, \tag{24}$$

where the dimensionless constants are

$$\Phi_1=\frac{h_0p_a}{2m\omega^2},\quad \Phi_2=\frac{\mu_0L^2}{h_0m\omega},\quad \Phi_3=\frac{\rho_ah_0L^2}{3m},$$

$$\Phi_4=\frac{p_a\theta_0L}{m\omega^2},\quad \Phi_5=0.664\frac{Lb}{m}\sqrt{\frac{\rho_a\mu_0}{\omega}},\quad G=\frac{g}{\omega^2h_0},$$

$$\Phi_6=\frac{p_aL^2}{m\omega^2h_0},\quad \Phi_7=\frac{12p_aL^3}{m(L^2+c^2)\omega^2\theta_0}.$$

Note that the second time derivative of U appears also in the expression of the lateral force. This will be treated in Sec. III B, where the formulation of the numerical solver is discussed.

If the moments produced by lateral components of the pressure forces were taken into consideration, it would have resulted in an additional dimensionless constant that would be similar to Φ_7 with the distinction that L^3 in the numerator would be replaced by $L^2h_0\theta_0$. As h_0 and θ_0 are several orders smaller than L, these moments will have no significant contribution to the total moment.

B. Solving the coupled equations of motion numerically

The dynamical behavior of the current system consists of the plate's dynamics coupled with compressible flow effects of the squeeze film. The equations of motion, being nonlinear, need to be integrated numerically in time to obtain the overall solution that incorporated the mutual coupling between the subsystems.

The numerical algorithm consists of two main parts: The first part consists of a finite-difference scheme in space to

descretizing the Reynolds equation. The Reynolds equation requires the instantaneous clearance between the surfaces computed from the instantaneous gap (see Fig. 1) between the floating object and the vibrating part. The initial conditions consist of the position and velocities of the free plate relative to the vibrating surface and the initial pressure distribution in the gas film. The second part of the algorithm incorporates an adaptive time integration of the coupled equations.

In the presented case, there is symmetry in the y axis along the x axis, hence allowing integrating across y from 0 to $B/2$ instead of B. This reduces by half the number of integrated variables and consequently reduces the computational cost.

By application of a finite-difference scheme in space, the Reynolds equation takes the form of a set of ordinary normalized differential equations in time

$$\begin{aligned}\sigma\left(\frac{\partial P}{\partial T}\right) &= -\sigma\frac{P_{i,j}}{H_{i,j}}\left(\frac{\partial H}{\partial T}\right)_{i,j} + H_{i,j}^2\left[\left(\frac{\partial P}{\partial X}\right)_{i,j}^2 + \left(\frac{\partial P}{\partial Y}\right)_{i,j}^2\right] \\ &+ P_{i,j}H_{i,j}^2\left[\left(\frac{\partial^2 P}{\partial X^2}\right)_{i,j} + \left(\frac{\partial^2 P}{\partial Y^2}\right)_{i,j}\right] \\ &+ 3P_{i,j}H_{i,j}\left[\left(\frac{\partial P}{\partial X}\right)_{i,j}\left(\frac{\partial H}{\partial X}\right)_{i,j} + \left(\frac{\partial P}{\partial Y}\right)_{i,j}\left(\frac{\partial H}{\partial Y}\right)_{i,j}\right] \\ &- \Lambda_X\left[\left(\frac{\partial P}{\partial X}\right)_{i,j} + \frac{P_{i,j}}{H_{i,j}}\left(\frac{\partial H}{\partial X}\right)_{i,j}\right] \\ &+ \alpha_X\left[2P_{i,j}H_{i,j}^2\left(\frac{\partial P}{\partial X}\right)_{i,j} + 3P_{i,j}^2H_{i,j}\left(\frac{\partial H}{\partial X}\right)_{i,j}\right]. \quad (25)\end{aligned}$$

The double-subscript notation i,j indicates the grid coordinate on the plane x,y, respectively. The spatial derivatives of the pressure are expressed by central-difference approximation, and the film thickness with its spatial and time derivatives are derived analytically from Eq. (23). The nondimensional parameters depend on the normalized velocity and acceleration of the plate

$$\sigma = \frac{12\omega\mu_0 L^2}{p_a h_0^2}, \quad \Lambda_X = \frac{6\mu_0\omega L^2}{p_a h_0^2}\dot{U}, \quad \alpha_X = \frac{\rho_a\omega^2 L^2}{2p_a}\ddot{U}.$$

We notice that the squeeze film is coupled with the floating plate not only by the film thickness but also by the plate's motion.

The initial state of the pressure between the plate and the vibrating surface is assumed atmospheric. The boundary conditions on the plate's edges are assumed as pressure release, meaning that the pressure near the edges of the plate is atmospheric. In practice, in cases where the excitation surface is larger than the levitating surface, the pressure on the boundaries is higher than the atmospheric pressure due to acoustic pressure radiation created by the vibrating surface. The influence of the acoustic pressure radiation on the boundaries is significant only for relatively light levitated objects when the pressure gradients in the squeeze film are small. This influence is discussed in the next section. The suitable boundary conditions (b.c.) and initial conditions (i.c.) are

$$\text{b.c.:} \quad P(X,Y,T) = 1, \quad \text{for } X,Y, \text{ on the edges}$$

$$\text{i.c.:} \quad P(X,Y,T=0) = 1.$$

Once more, application of a finite-difference scheme in space brings Eq. (25) to the form of a set of ordinary second-order normalized differential equations in time

$$\begin{Bmatrix}\ddot{U}\\ \ddot{V}\\ \ddot{\Theta}\end{Bmatrix} = \begin{Bmatrix} \dfrac{-\sum_{i,j}\left[\Phi_1 H_{i,j}\left(\dfrac{\partial P}{\partial X}\right)_{i,j} + \Phi_2\dfrac{\dot{U}}{H_{i,j}} + \Phi_4(P_{i,j}-1)\Theta\right]\Delta Y\Delta X - \Phi_5|\dot{U}|^{1/2}\dot{U}}{1+\Phi_3\Sigma_{i,j}(P_{i,j}H_{i,j})\Delta Y\Delta X} \\ -G + \Phi_6\sum_{i,j}(P_{i,j}-1)\Delta Y\Delta X \\ \Phi_7\sum_{i,j}[(X_i-U)(P_{i,j}-1)]\Delta Y\Delta X \end{Bmatrix}. \quad (26)$$

The equations of motion of the system, with consideration of the coupling effects, can be described by a state-space formulation. By defining the state-space variables vector $q = \{U,\dot{U},V,\dot{V},\Theta,\dot{\Theta},P\}^T$, the coupled state-space formulation of the entire system can be produced with Eq. (25) and Eq. (26).

IV. VERIFICATION OF THE ALGORITHM

In order to verify the validity of the numerical algorithm, we degenerate the presented case to the case of standing wave with an infinite wavelength by assigning $A_2 = 0$ and setting $k = 0$. Under these conditions, the formulation reduces to the case of a flat vibrating surface where only levitation force is exerted on the floating object. Such a case was recently investigated numerically and experimentally by Nomura *et al.* and by Minikes and Bucher.[5,8]

The study conducted by Nomura *et al.* was for the case of a vibrating flat (rigid) circular piston acting as a sound source levitating a circular disk.[5] The levitated disk is assumed to be stationary, where in reality the disk would vibrate in response to the source motion. This assumption does

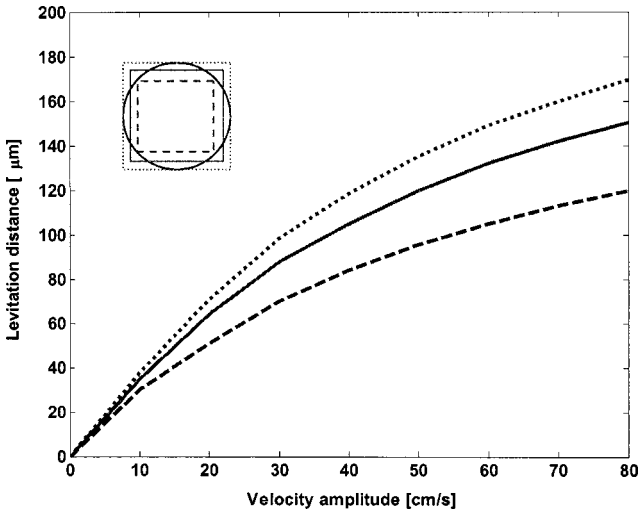

FIG. 2. Levitation distances as function of velocity amplitude the source. Solid curve: equivalent surface area; dashed curve: blocking square, dotted curve: blocked square.

not hold for a heavy levitated object, where the inertial forces of the object must be considered. In the present work there is no such restricting assumption. Additionally, Nomura *et al.* have used an adiabatic relation for a compressible fluid, while in the present work an isothermal behavior was considered. Nomura *et al.* have emphasized the influence of energy leakage on the boundaries by adopting a nonreflection condition of waves.[5] The numerical and experimental results obtained by Nomura *et al.* suggest that the energy leakage does influence the levitation distance for objects with relatively small surface densities (in the range of 1–10 [kg/m^2]). But, the results also suggest that as the surface density is increased, the influence of energy leakage decreases and the use of pressure release boundary conditions becomes suitable.[5]

The presented formulation is carried out for rectangular objects using Cartesian coordinates, while Nomura *et al.* formulated an axisymmetric model for circular objects. Therefore, the comparison is done for the same surface density but with an equivalent square surface. In addition, two bounding squares are simulated and thus the upper and lower limits are obtained by means of a square surface blocking the circular surface and a square surface blocked by the circular surface. Figure 2 shows the numerical results of the levitation distances of a square plate versus the velocity amplitudes of a vibrating source. The vibrating source has the same surface dimensions as the floating square plate, and the values of the physical and numerical parameters, under which the comparison was carried out, are summarized in Table I.

The numerical results presented in Fig. 2 are in a good agreement with the numerical and experimental results provided by Nomura *et al.*[5] We have also simulated the discussed case with an axisymmetric formulation introduced in Minikes and Bucher, where a better agreement has been achieved as the bearings geometries were identical.[8]

It is reasonable to expect differences in the results between a model assuming isothermal behavior and a model under an adiabatic behavior assumption. As was discussed in Sec. III A, for a gas film in which an isothermal polytropic flow ($p\rho^{-1}=\text{const}$) is postulated, it is possible to replace Γ by P to obtain Eq. (22). But, when adiabatic behavior is postulated, the relation between the normalized pressure and the normalized density is $\Gamma=P^{1/n}$, with $n=C_P/C_V=1.4$ for air. In such case, Eq. (22) will take the form

$$\frac{\partial}{\partial X}\left(\frac{P^{1/n}H^3}{\tilde{\mu}}\frac{\partial P}{\partial X}\right)+\frac{\partial}{\partial Y}\left(P^{1/n}H^3\frac{\partial P}{\partial Y}\right)$$
$$=\sigma\frac{\partial}{\partial T}(P^{1/n}H)+\Lambda_X\frac{\partial}{\partial X}(P^{1/n}H)-\alpha_X\frac{\partial}{\partial X}(P^{2/n}H^3). \tag{27}$$

The dimensionless parameter $\tilde{\mu}=\mu/\mu_0$ is the normalized viscosity, as it is not constant. Inspecting the analysis results of an isothermal model with the physical dimensions used in the comparison to Nomura *et al.*, it appears that the fluctuations of the normalized pressure are no more than 10%–20%. In such case, the normalized density $\Gamma=P^{1/1.4}\approx P$, as the values of P are close to 1. In addition, it is reasonable to assume that the transient period for reaching steady state is too short for allowing any thermal changes to occur, meaning that the viscosity remains constant at $\tilde{\mu}=1$. Under the above conditions, Eq. (27) may be reduced to Eq. (22). This may provide an explanation why differences in the analysis results are minor. Nevertheless, a detailed thermodynamical study is required for fully understanding the squeeze film behavior.

TABLE I. Values of the physical and numerical parameters used in the comparison with Nomura *et al.* (Ref. 5).

Parameter	Value
R_0—Disk radius	20 [mm]
L—Square's face	
Equivalent surface	$L=\sqrt{\pi}R_0$
Blocked square	$L=\sqrt{2}R_0$
Blocking square	$L=2R_0$
c—Disk thickness	2 [mm]
m—levitated mass	7.4 [gm]
ω—Frequency	19.5 [kHz]
A_1—Vibration amplitude	6.54 [μm]
ΔX—Grid interval	0.05
ΔY—Grid interval	0.05
μ_0—Air viscosity	17.9 [N·s/mm^2]
ρ_0—Air density	1 [Kg/m^3]
p_a—Ambient pressure	101 [kPa]

V. STUDYING THE SENSITIVITY OF THE SYSTEM

In this section we study the influence of several physical parameters on the behavior of the system, especially the influence on the lateral terminal velocity of the levitated object. The parameters are the standing wave ratio (SWR), the ratio between the plate's length and the wavelength (L/λ), the average vibration amplitude of the excitation surface, and the influence of the acoustic pressure radiation on the boundaries. The physical parameters and the numerical parameters under which the simulations were carried out are summarized in Table II.

TABLE II. Values of the physical and numerical parameters used in the numerical investigation.

Parameter	Value
L—Plate length	90 [mm]
b—Plate width	65 [mm]
c—Disk thickness	2.25 [mm]
ω—Frequency	19.5 [kHz]
A_1—Vibration amplitude	7.5 [μm]
p_a—Ambient pressure	101 [kPa]
μ_0—Air viscosity	17.9 [N·s/mm^2]
ρ_0—Air density	1 [Kg/m^3]
ΔX—Grid interval	0.025
ΔY—Grid interval	0.111

A. Terminal speed versus standing wave ratio (SWR)

As mentioned earlier, mechanical imperfections in a system make it almost impossible to attain a pure traveling wave. Therefore, there is a significant importance to investigate the response of the system to various standing wave ratios (SWR). Figure 3 presents the terminal velocity of the levitated plate in the presence of different SWR. The numerical results were obtained for three levitated plates with different surface densities (σ_D[kg/m^2]), and the ratio of the plate's length to wavelength (L/λ) was set to 2.37.

The numerical simulation suggests that the terminal speed of the levitated plate decreases as the ratio between the maximum amplitude and the minimum amplitude (SWR) increases. The relation between the terminal velocity and the SWR is linear when plotted on logarithmic scale. In addition, Fig. 3 indicates that the higher the surface density the lower the terminal speed of the levitated plate.

B. Terminal speed versus wavelength

When designing a system for generating traveling waves, the imposed boundary conditions make it difficult to obtain a perfect sinusoidal wave with a prescribed wavelength. Moreover, it is desired to transport plates of different lengths. Therefore, we have chosen to introduce the response

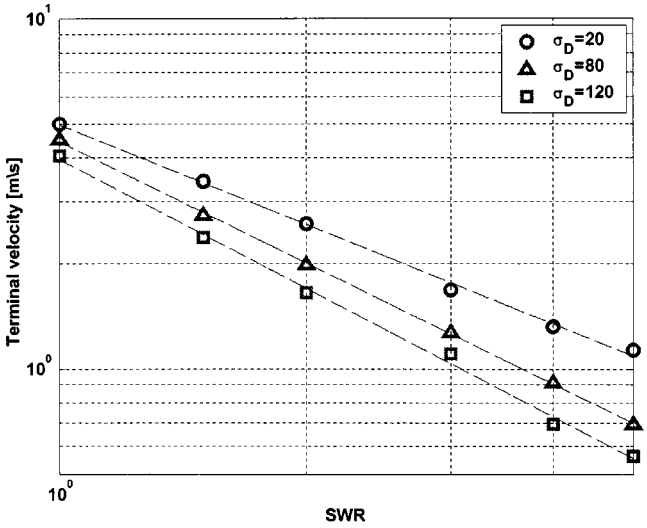

FIG. 3. Terminal velocity versus the standing wave ratio for different surface densities: σ_D=20,80,120 [Kg/m^2].

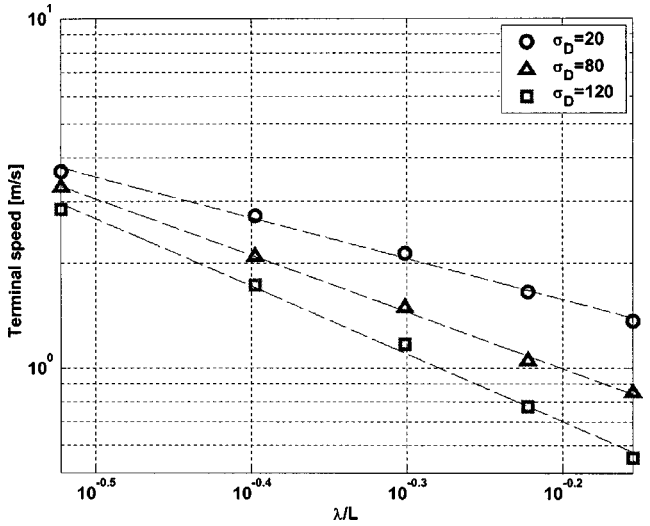

FIG. 4. Terminal velocity versus wavelength of the traveling wave for different surface densities: σ_D=20,80,120 [Kg/m^2].

of the system to the ratio between the length of the levitated plate and the wavelength of the excited traveling wave. Figure 4 presents the terminal velocity of the levitated plate for different ratios (L/λ). The numerical results were obtained for three levitated plates with different surface densities and the SWR was set to 2.

The numerical simulation suggests that the terminal speed of the levitated plate decreases as the ratio (λ/L) between the wavelength of the excited traveling wave and the plate's length increases. This relation appears to be linear when plotted on a log–log scale. In addition, as in Fig. 3, Fig. 4 indicates that the higher the surface density the lower the terminal speed of the levitated plate.

C. The pressure field and the influence of boundary conditions

Figure 5 shows how the pressure distribution in a cross section of the squeeze film varies with time for the case of excitation by a traveling wave. Two cases are presented: (a) surface density of 1.5 [Kg/m^2]; (b) surface density of 80 [Kg/m^2]. The average inclination of the plate in case (a) is Θ=12, while the average inclination of the plate in case (b) is nearly zero. As can be seen in Fig. 5(a), the pressure values on the leading edge of the plate is smaller than on the lagging edge, while in Fig. 5(b) the pressure are almost equally distributed. It appears from the numerical simulations that the average angle of attack of the plate increases as the surface density decreases.

The vibration amplitude was chosen to be 10 [μm] and the SWR was set to 2 (all the other physical and numerical parameters appear in Table II). Figure 5 shows that as the pressure distribution progresses in time, its amplitudes oscillate between maximum and minimum. This is a direct result of having a standing wave ratio greater than 1, which is obviously not a pure traveling wave.

The squeeze film equilibrium is established through a balance between viscous flow forces and compressibility forces. The pressure in the boundaries of the levitated plate influences the pressure gradients introduced in the film. The

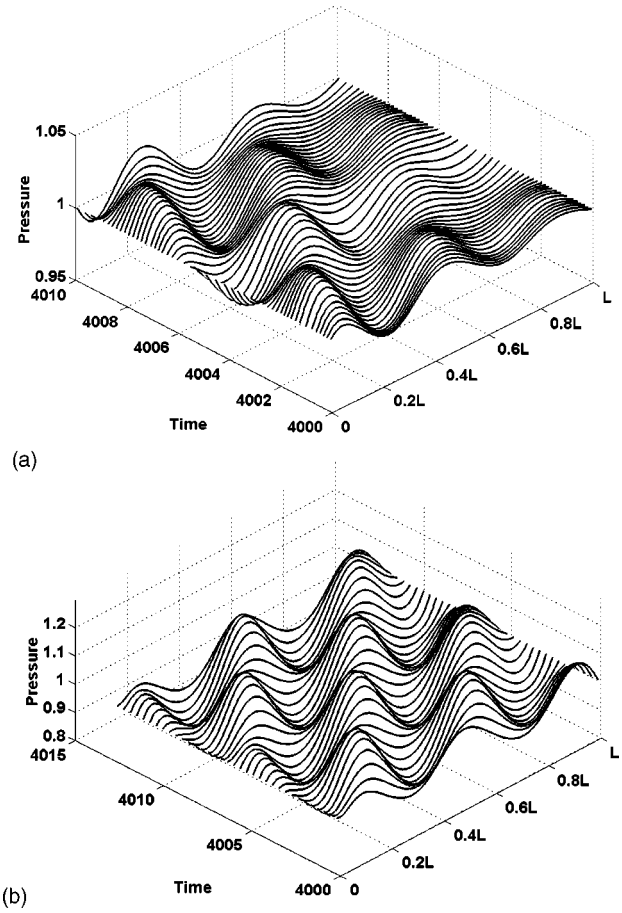

FIG. 5. Normalized pressure distribution in a cross section of the squeeze film varies with time (normalized). (a) surface density 1.5 [Kg/m^2]; (b) surface density 80 [Kg/m^2].

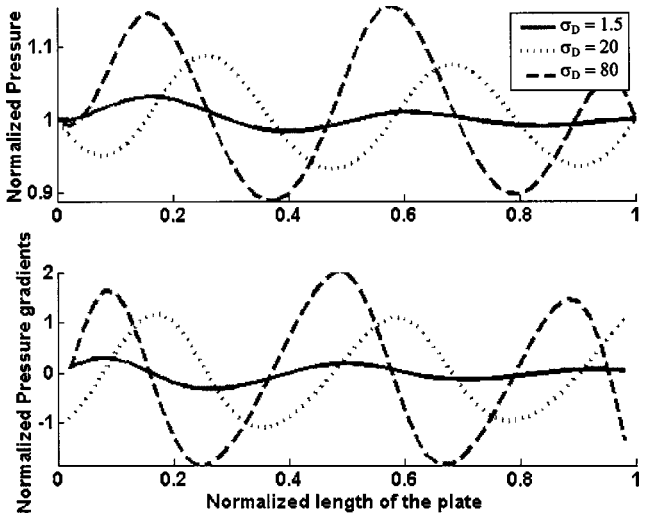

FIG. 6. Normalized pressure and gradients in a cross section of the squeeze film at an arbitrary point in time. Solid curve: surface density 1.5 [Kg/m^2], dotted curve: surface density 20 [Kg/m^2]; dashed curve: surface density 80 [Kg/m^2].

thickness of squeeze film is on the order of magnitude of a few hundreds of microns, which is much smaller than the radiated acoustic wavelength (several millimeters at 19 [kHz]). Therefore, the edges of the levitated plate are close to the vibrating surface and are exposed to mean radiation pressure higher than the ambient pressure.[8,9] The pressure values near the peripheries of the levitated object (which determine the boundary conditions) may indeed influence the film thickness and consequently the dynamical behavior.

For the load-carrying phenomenon to take place, the pressure gradients in the squeeze film must increase as the surface density of the levitated object increases. This is simply because the force excreted by the film pressure must sustain the weight of the levitated object. The influence of small changes in the radiation pressure near the boundaries decreases with the growth of the pressure gradients in the film. This implies that as the surface density of the levitated plate increases, the system dynamical behavior is less sensitive to changes in the radiation pressure near the boundaries. Figure 6 shows the normalized pressure and the normalized pressure gradients, respectively, in a cross section of the squeeze film at an arbitrary point in time (at steady state). The curves represent different levitated surface densities.

Comparing the different curves in Fig. 6, we notice that the pressure gradients in the case where the surface density is 1.5 [Kg/m^2] are significantly smaller than the pressure gradients in the case where the surface density is 80 [Kg/m^2]. Therefore, in the case of large surface densities, the pressure gradients in the film are hardly affected by a small change in the acoustic radiation pressure near edges of the levitated plate. Since the shear stresses on the levitated plate are associated with the pressure gradients in the film, the levitated distance and the terminal velocity of plates with large surface densities will hardly be affected.

VI. DISCUSSION AND CONCLUSIONS

The presented system has a complex behavior, which is governed by numerous physical parameters. We have shown that the theoretical formulation of system's dynamical behavior introduces some useful relations between the governing parameters. The simulation results suggest that the terminal velocity of the levitated plate is strongly influenced by the standing wave ratio (SWR) and the wavelength of the excitation traveling wave. The terminal velocity decreases with the increase of SWR or with the increase of the ratio (λ/L). In addition, we presented the pressure distribution in a cross section of the squeeze film and the effect of surface density on the plate's angle of attack. We concluded that the acoustic radiation pressure on the boundaries of the levitated plate is significant only for levitated plates with relatively small surface density. For such objects the pressure gradients in the squeeze film are small and therefore sensitive to pressure changes near its peripheries. The acoustic radiation pressure near the vibrating surface must be obtained in order to determine more accurately the extent of its influence on the system behavior.

The assumption made in the numerical model that the levitated plate behaves as a rigid body could deteriorate the validity of the numerical simulations. The flexibility of the levitated plate could have effects on the system dynamical behavior; therefore, a future investigation may focus on the combined dynamical behavior, which incorporates a flexible floating plate.

[1] E. O. J. Salbu, ''Compressible squeeze films and squeeze bearings,'' J. Basic Eng. **86**, 355–366 (1964).
[2] W. Wiesendanger, U. Probst, and R. Siegwart, ''Squeeze film air bearings using piezoelectric bending elements,'' in Proceedings of Fifth International Conference on Motion and Vibration Control (MOVIC2000), Sydney, Australia, pp. 181–186 (2000).
[3] Y. Hashimoto, Y. Koike, and S. Ueha, ''Transporting objects without contact using flexural traveling waves,'' J. Acoust. Soc. Am. **103**(6), 3230–3233 (1998).
[4] B. T. Chu and R. E. Apfel, ''Acoustic radiation pressure produced beam of sound,'' J. Acoust. Soc. Am. **72**(6), 1673–1687 (1982).
[5] H. Nomura, T. Kamakura, and K. Matsuda, ''Theoretical and experimental examination of near-field acoustic levitation,'' J. Acoust. Soc. Am. **111**(4), 1578–1583 (2002).
[6] W. A. Gross, *Gas Film Lubrication* (Wiley, New York, 1962).
[7] R. W. Fox and A. T. McDonald, *Introduction to Fluid Mechanics* (Wiley, New York, 1985).
[8] A. Minikes and I. Bucher, ''Coupled dynamics of a squeeze-film levitated mass and a vibrating piezoelectric disk—numerical analysis and experimental study,'' J. Sound Vib. (in press).
[9] M. P. Norton, *Fundamentals of Noise and Vibration Analysis for Engineers* (Cambridge University Press, Cambridge, 1989).

An optical fiber infrasound sensor: A new lower limit on atmospheric pressure noise between 1 and 10 Hz

Mark A. Zumberge, Jonathan Berger, Michael A. H. Hedlin, Eric Husmann, and Scott Nooner
The Cecil and Ida Green Institute of Geophysics and Planetary Physics, Scripps Institution of Oceanography, University of California—San Diego, La Jolla, California 92093-0225

Richard Hilt
Colorado College, 14 East Cache La Poudre, Colorado Springs, Colorado 80903

Rudolf Widmer-Schnidrig
Black Forest Observatory, Institute of Geophysics, Stuttgart University, Heubach 206, D-77709 Wolfach, Germany

(Received 21 June 2002; revised 17 January 2003; accepted 10 February 2003)

A new distributed sensor for detecting pressure variations caused by distant sources has been developed. The instrument reduces noise due to air turbulence in the infrasound band by averaging pressure along a line by means of monitoring strain in a long tubular diaphragm with an optical fiber interferometer. Above 1 Hz, the optical fiber infrasound sensor (OFIS) is less noisy than sensors relying on mechanical filters. Records collected from an 89-m-long OFIS indicate a new low noise limit in the band from 1 to 10 Hz. Because the OFIS integrates pressure variations at light-speed rather than the speed of sound, phase delays of the acoustical signals caused by the sensor are negligible. Very long fiber-optic sensors are feasible and hold the promise of better wind-noise reduction than can be achieved with acoustical-mechanical systems. © *2003 Acoustical Society of America.* [DOI: 10.1121/1.1566978]

PACS numbers: 43.28.Dm, 43.38.Hz [LCS]

I. INTRODUCTION

Atmospheric pressure changes that occur faster than those due to weather and slower than can be sensed by human hearing, termed infrasound, are caused by many natural and anthropogenic sources. Bolides, lightning, earthquakes, volcanoes, and ocean waves are examples of the former; supersonic aircraft and explosions are included in the latter. The Comprehensive Test Ban Treaty (CTBT) for nuclear weapons has fostered a renewed interest in infrasound in the band from 0.01 to 10 Hz. A worldwide network of 60 infrasound stations is being established to help monitor compliance with the treaty (Christie *et al.*, 2001).

Wind turbulence is a major source of noise in the infrasonic band. Hedlin *et al.* (2002), for example, reported that the noise power between 0.1 and 1 Hz in a moderately filtered microbarometer rose about 20 dB as the wind speed increased from 1 to 5 m/s. To combat this problem, researchers have developed a number of acoustical-mechanical spatial filters consisting of multiple inlet ports connected via pipes to a microbarometer in hopes of averaging out wind noise (e.g., Daniels, 1959; Burridge, 1971; Alcoverro and LePichon, 2002; Hedlin *et al.*, in press). These have proven somewhat successful, but higher frequency sampling of the pressure field is limited by time delays in these mechanical filters. An alternative would be to deploy several hundred individual sensors and data recorders over a large area, but that is not very practical.

We report here on another alternative. We have constructed a distributed pressure sensor, which averages pressure along a line by means of fiber optic sensing of strain in a long tubular diaphragm. The sensitivity to pressure changes has proven to be superior to other techniques in the band from 1 to 10 Hz. The sensor provides a continuous signal representing the instantaneous spatial average of pressure along the line described by the sensor. This average pressure $\overline{P}(t)$ at time t along path S is given by

$$\overline{P}(t)=\left(\frac{1}{L}\right)\oint_S P(s,t)ds. \tag{1}$$

In principle, the length L of path S can be made up to several km if desired.

Our original design consisted of an unconstrained optical fiber, exposed to ambient pressure, monitored with a laser interferometer. Such a design takes advantage of the fact that an optical fiber responds inherently to pressure changes via its strain-optic effect (Hocker, 1979). We formed an interferometer consisting of two optical fibers placed side-by-side (to make temperature effects common-mode) with one of them (the reference fiber) encased inside a stiff, sealed tube to shield it from pressure fluctuations. Early experiments revealed, however, that strains in the loose fibers caused noise larger than the small pressure signals we hoped to detect. This led us to the compliant tube as a means of increasing the pressure-induced strain in the fiber. This is described below.

II. DESCRIPTION OF THE INSTRUMENT

We call our new sensor, shown in Fig. 1, an optical fiber infrasound sensor (OFIS). We use a compliant, sealed tube

 0001-4966/2003/113(5)/2474/6/$19.00

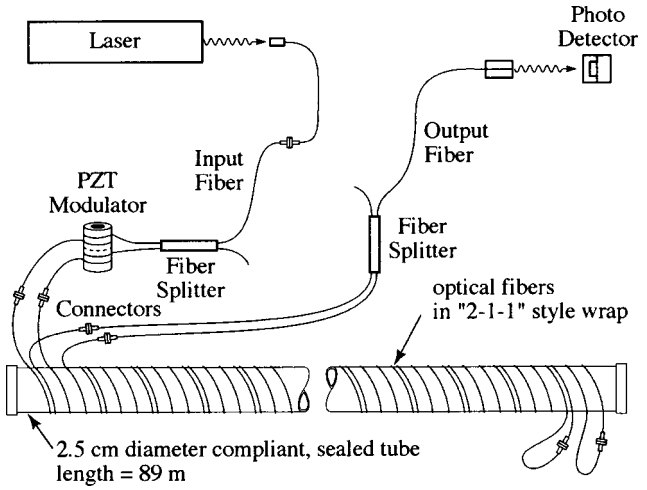

FIG. 1. The OFIS (optical fiber infrasound sensor) consists of a sealed compliant tube wrapped with a pair of optical fibers. The fibers respond to mechanical strain in the tube caused by ambient pressure changes. The "2-1-1" wrap results in one of the two fibers being strained more than the other under pressure changes. The path length difference is monitored interferometrically.

(25-mm-diam silicon rubber with 3-mm wall thickness) helically wrapped with optical fiber (SMF28 single mode with 900-μm buffer). As the ambient pressure around the tube changes, its diameter changes in response and strains the optical fiber; this strain is monitored interferometrically. This technique is sensitive to the integrated pressure along the tube, and we can build the tube almost arbitrarily long. Because the apparent pressure change inferred from the observed optical path change along a fiber wrapped around a tube of length L is governed by Eq. (1), the pressure variations having a spatial scale shorter than the total length of the sensor will be averaged away. The sensor is a true, linear, integrator whose incremental step-size is the order of the tube diameter (25 mm). Because the phase delay variation along the fiber is governed by the speed of light rather than the speed of sound as in the acoustical-mechanical filters, the response is flat up to relatively high frequencies (initial tests indicate attenuation begins around 2 kHz). The issue of how the deployment geometry [path S in Eq. (1)] affects the response is addressed in Sec. IV.

We built a wrapping machine to construct the fiber-wrapped tube depicted in Fig. 1. The compliant tubing is fed into one end of the machine at a constant rate while spools of optical fiber orbit around the tube, leaving behind helical wraps. Small electric motors control the tension on each fiber spool to maintain uniformity; similarly the feed rate of the tube and the rotation rate of the fiber spools is controlled to yield a constant spacing between the wraps. The machine also wraps a layer of silicon ribbon over the fibers to keep them in place. The interval between repeat fiber wraps is 55 mm.

To obtain immunity from slight wavelength fluctuations in the laser which illuminates the interferometer (a distributed feedback laser diode with wavelength $\lambda_1 = 1310\,\mathrm{nm}$), we use an equal-arm Mach-Zender interferometer (Hocker, 1979). In such a device, the difference in the optical path lengths of two identical optical fibers is sensed. We optimize the sensor by configuring the mechanical coupling between the optical fibers and the compliant tube such that the signal of interest affects one fiber more than the other while sources of noise have the same effect on both fibers (i.e., common mode rejection). For example, the fibers themselves have temperature coefficients, but to a good approximation, both experience the same temperature environment, and—being differential—the interferometer is unaffected. By spacing the wraps of the two fibers as shown in Fig. 1, one fiber experiences approximately twice the strain as the other as the tube deforms from pressure changes. The fibers wound closely together strengthen one another and hence strain less (for a given pressure difference) than the two isolated fibers.

The interferometer must track both increases and decreases in the optical path length difference. In order to do this, we form two fringe signals: the first is the direct signal (V_x), which is output of the photodetector in Fig. 1, the second (V_y) is generated in quadrature with the first. This is achieved with a lock-in amplifier while modulating the length difference by a small fraction of a wavelength at several hundred kHz by means of a piezoelectric crystal. The lock-in amplifier's phase is adjusted to produce the derivative of the direct fringe signal. When plotted against each other, V_x and V_y trace out an ellipse as the optical path changes. The instantaneous position on the ellipse perimeter is a measure of the optical path length difference. We recorded the two voltages V_x and V_y at 200 samples per second in the work reported here. Then we processed the records in 15-min segments by fitting the samples to an ellipse given by the parametric equations $V_x = A\sin(\phi+\delta)$ and $V_y = B\cos(\phi)$, where A and B are the amplitudes of the two fringe signals, δ is related to the eccentricity of the ellipse, and ϕ is the desired optical phase difference related to the optical path length change $dL_{\mathrm{opt}} = (\lambda_1/2\pi)\phi$. (We analyzed 15-min-long data segments because slowly varying perturbations to the polarization and the laser output power produce drift in the ellipse coefficients.) The spatially integrated, instantaneous, relative pressure $P(t)$ is given by $P(t) = (\alpha/L)\phi(t)$, where α is the empirically determined sensitivity, governed by the rheological coefficients of the rubber tube, the fibers, and the tension and spacing of the fibers. Laboratory and field experiments have determined that α is 2.52 Pa m rad^{-1}. The time series of $\phi(t)$, extracted from the records of $V_x(t)$ and $V_y(t)$, gives the record of pressure fluctuations averaged along the sensor length.

We deployed a sensor having $L = 89\,\mathrm{m}$ at our geophysical test facility, Piñon Flat Observatory, in the high desert south of Palm Springs, CA (see Fig. 2 for the location). In this deployment, we buried the sensor beneath a shallow layer of gravel to protect it from wildlife and rapidly varying thermal effects. As shown in Fig. 3, the sensor itself was below the surface by a distance of about 20 cm, covered by sorted gravel with typical rock diameter of 9 mm. Experiments in our lab showed that the acoustic attenuation produced by the gravel is insignificant at frequencies below 20 Hz. The fringe signal was continuously sampled at 200 samples per second with a 24-bit digitizer (18 bits are required to resolve 1 μPa). The data were telemetered to our

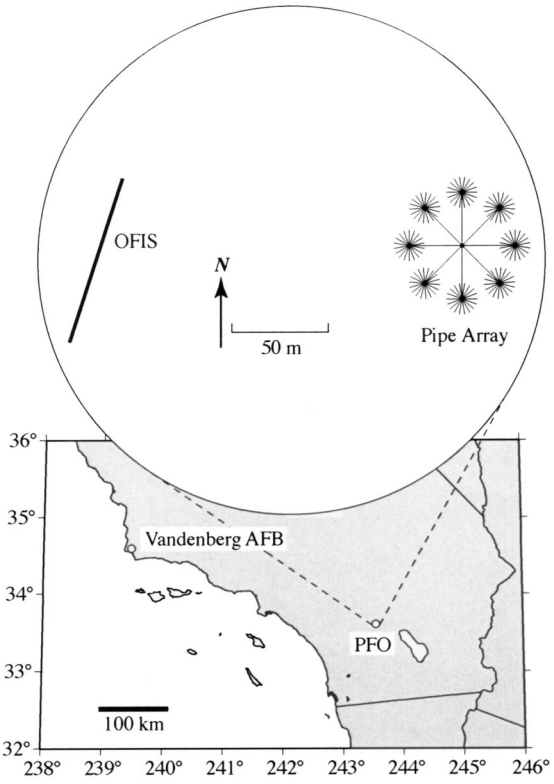

FIG. 2. Our first field test of the OFIS occurred at Piñon Flat Observatory (PFO) in the high desert just south of Palm Springs, CA. We oriented the sensor such that wave fronts from sources at Vandenberg Air Force Base would arrive parallel to the sensor. Several pipe array infrasonic sensors are also sited at PFO.

lab where the fringe signal postprocessing was performed to extract the pressure records.

After installation, we calibrated the sensor by imposing a small pressure difference (measured with a Paroscientific quartz gauge) by pumping air into the sensor tube and recording the fringe signal. A 30-cm-long capillary tube (having 0.25-mm inside diameter) connected the inside of the tube to the ambient atmosphere so that slowly changing pressure (with a time constant longer than 10 mins) would not be detected.

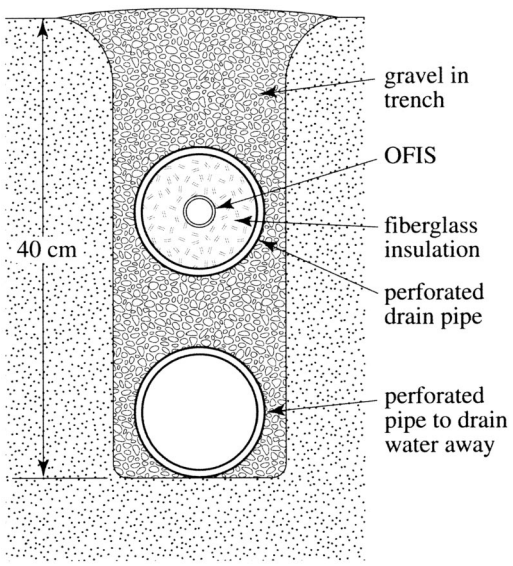

FIG. 3. This is a vertical cross section of the OFIS as it is deployed in a trench at the field site.

We have compared recordings from the new fiber-optic sensor with time series collected simultaneously from two other sensors approximately 150 m away (see the map in Fig. 2). The other sensors, described in detail elsewhere (Hedlin *et al.*, 2002), consist of two types of acoustical-mechanical filters covering a circular region 70 m in diameter connected to two microbarometers. One of the arrays, which we refer to as the Pipe Array, follows the design established for the CTBT (Christie *et al.*, 2001). A microbarometer in the center of the Pipe Array is connected to eight 27-m-long pipes extending radially in a symmetric pattern. Each of these pipes is connected to a manifold joining 18 8-m-long pipes (each open at its end) splayed into secondary symmetric patterns (see Fig. 2). This plumbing results in 144 ports each connected to the microbarometer via 35 m of solid pipe.

The Hose Array consists of eight 16-m-diam rings of compliant, microporous hose colocated with the Pipe Array ports; a point on the inner edge of each hose ring is connected to the array's microbarometer via a 19-m-long solid pipe. Spatially, the Hose Array samples essentially the same pattern as the Pipe Array, but the acoustic path lengths between points on the hose ring and the microbarometer vary from 19 to 69 m.

III. RESULTS

An example of a pressure event recorded with these sensors is displayed in Fig. 4. This is the signal produced by the launch of an Atlas II rocket from Vandenberg Air Force Base (AFB) 396 km away on 8 September 2001. Note that we purposely oriented the OFIS along an azimuth normal to the direction to Vandenberg AFB so that wave fronts from signals generated there would arrive parallel to our linear sensor (Fig. 2). The signal to noise in the OFIS record compares favorably with the other sensors operating at the same time (the records displayed in Fig. 4 have been band-pass filtered from 0.5 to 10 Hz). The Pipe Array displays the noise that results from internal resonances that have been reported elsewhere (Alcoverro and LePichon, 2002; Hedlin *et al.*, 2002). These resonances have subsequently been attenuated using strategically placed orifices in the pipe arrays deployed in support of the CTBT rendering their responses to be essentially like that of the Hose Array shown here.

Figure 5 shows the transfer function (or relative response) of the OFIS and the Hose Array computed from the time series in Fig. 4; we have plotted the ratio of the Hose Array response divided by the OFIS response. Because the Hose Array was sampled at 20 samples per second and low-pass filtered with a 9-Hz cutoff, we limit our analysis to frequencies below 10 Hz, even though the OFIS is responsive to at least 100 Hz. Note that the independent calibrations of the two sensors appear to corroborate one another: the relative response is near unity between 0.2 Hz and about 3 Hz. Because the relative response drops above 3 Hz, either the response of the Hose Array decreases there or the response of the OFIS increases. We have good evidence that it

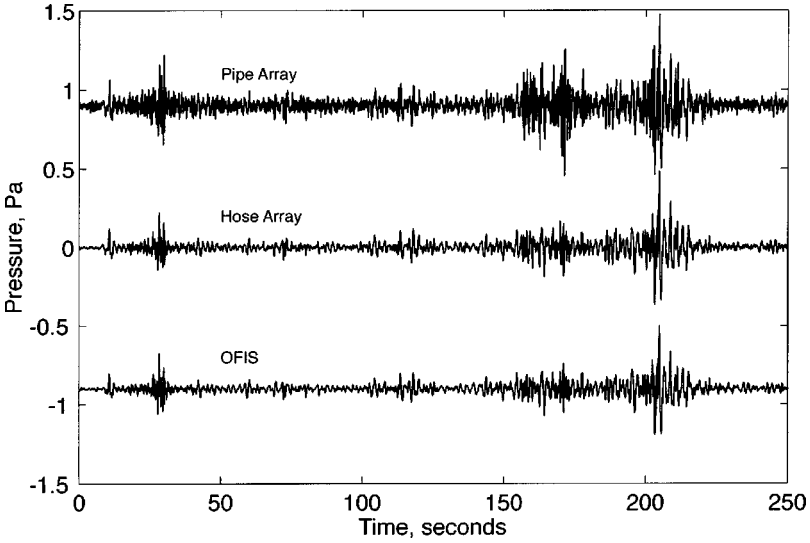

FIG. 4. These are time series of pressure variations recorded by three sensors at PFO. The source is an Atlas II rocket launch at Vandenberg AFB.

is the decrease in response of the Hose Array caused by its finite size and deployment shape that is responsible for the decrease above 3 Hz (see below).

Pressure noise increases with wind speed. To investigate the importance of wind on this sensor's performance, we computed power spectra for 440 contiguous 15-min intervals over a 4-day period for all three of the sensors described here. Two examples are shown in Fig. 6. One [Fig. 6(a)] was recorded during an interval where the average wind speed was 1.4 m/s, the other [Fig. 6(b)] at 3.3 m/s. In the low wind case, the microbarom peak at 0.2 Hz is clearly evident. It becomes obscured by ambient noise at higher wind speeds. (The wind speed during the time of the data shown in Fig. 4 was 1.8 m/s.)

Wind noise may affect the sensors slightly differently (and they are not exactly co-located). We therefore computed the minimum noise per band for all three sensors to determine the noise floor for each. After computing the 440 spectra for each sensor, we found the minimum power level in each frequency bin for each sensor. These minimum spectra are shown in Fig. 7. Each point represents the lowest 15-min-averaged power observed over the 4-day period for a specific frequency—the collection of points in these curves were not necessarily gathered in the same 15-min intervals or under the same wind speeds, they are simply the 4-day power minima irrespective of all else. Several aspects of these spectra are worth noting. First, the microbarom peak is evident in each. Second, the OFIS is slightly noisier at frequencies below 0.2 Hz. We suspect residual thermal noise is responsible. The most significant difference is that the OFIS's minimum noise per band is significantly lower than that of the others above 1 Hz; the improvement is about 23 dB at 8 Hz. We know that this represents a real improvement in the sensing methodology rather than a result of a roll-off in the frequency response of the OFIS because we examined the relative responses of the OFIS and the Hose Array (Fig.

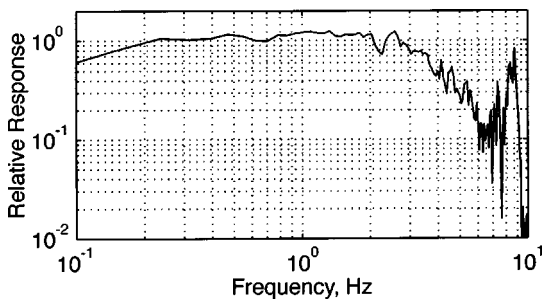

FIG. 5. The transfer function (Hose Array response divided by the OFIS response) was computed from the time series shown in Fig. 4.

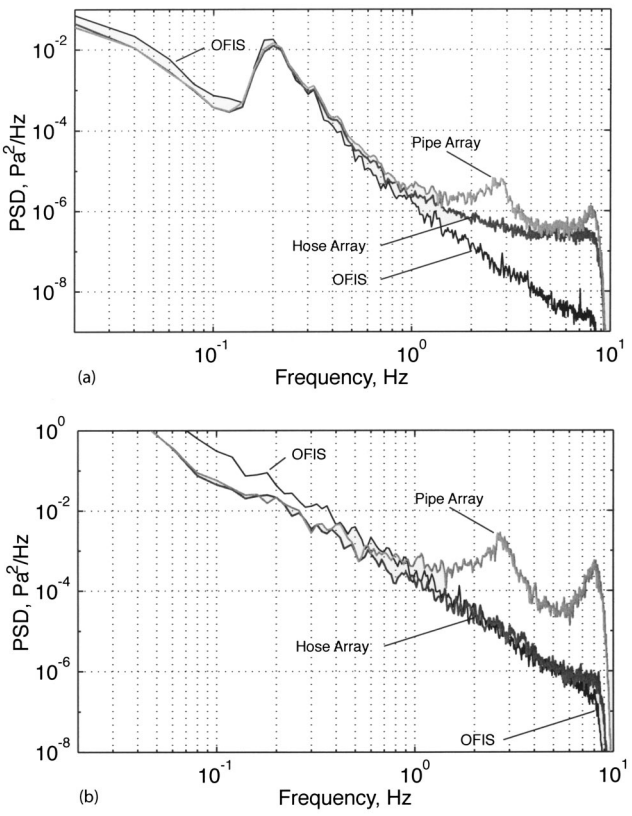

FIG. 6. (a) Power spectral densities from three sensors recorded simultaneously during a 15-min-long period when the wind speed averaged 1.4 m/s. The peak at 0.2 Hz is from the microbarom background. The peaks in the Pipe Array at 3 and 8 Hz are from internal resonances. (b) Same as (a) except the average wind speed was 3.4 m/s.

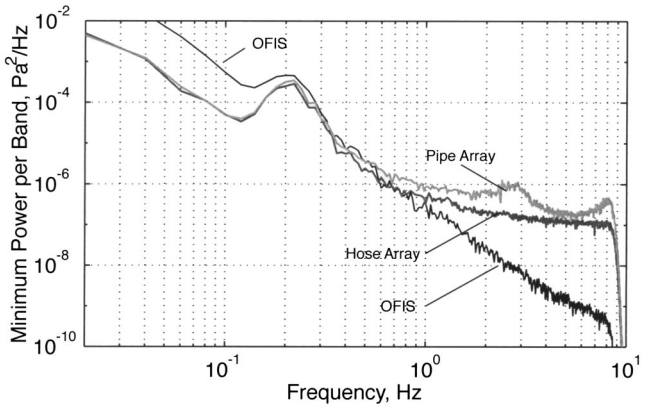

FIG. 7. Spectra were computed for each sensor for 440 15-min-long contiguous time segments. The minimum power level for each band is plotted.

5). We have seen that the response of the OFIS is flat to at least 3 Hz and is likely flat to about 1 kHz. For this case of an averaging dimension of the order of 100 m, we believe that the noise floor in Fig. 7 for the OFIS represents a new lower limit on spatially averaged ambient atmospheric pressure noise in the band from 1 to 10 Hz.

It may be that the results from the hose and pipe arrays are limited by the noise of their microbarometers (MB2000 DASE Tekelec). It has been reported that the Chaparral 4.11 sensors have lower noise (Kromer *et al.*, 1998). Standard infrasound microphones (B&K Model 4193 with preamplifier 2193, for example) have instrument noise as reported by the manufacturer's literature (Bruel & Kjaer Microphone Handbook, Vol. 1, part no. BE1447-11) some 3 to 12 dB higher than the noise levels measured by the OFIS in the frequency band 1 to 10 Hz.

IV. GEOMETRIC EFFECTS ON THE RESPONSE

As noted above, the OFIS was oriented to maximize its response to signals arriving from the direction of Vandenberg AFB. Being a line receiver, its response is directional. Pressure wave fronts add in phase along the entire length of the OFIS for wave vectors perpendicular to it. A line sensor will average over several cycles of the wave-train for arrivals from other directions if the wavelength λ_P is smaller than the sensor length L.

A pressure wave traveling in the x direction (Fig. 8) with amplitude P_0, wave number $k=2\pi/\lambda_P$, and angular frequency ω is described by

$$P(x,t)=P_0\sin(kx-\omega t). \tag{2}$$

Substituting this into Eq. (1) gives the spatial average of this wave field at time t along a straight path of length L aligned at an angle θ relative to the x direction:

$$\overline{P}(t)=\frac{1}{L}\int_0^L P_0\sin(kl\cos\theta-\omega t)\,dl \tag{3}$$

(l is the position along the averaging path). Evaluation of this integral yields the ratio R of the amplitude of the line-averaged pressure signal to the amplitude of the traveling pressure signal:

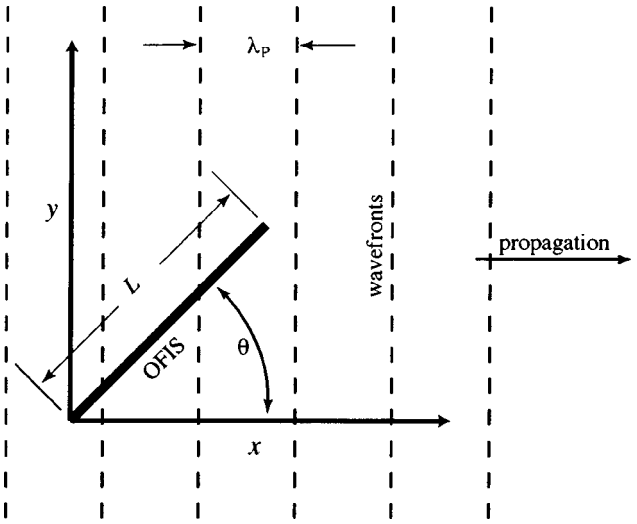

FIG. 8. The geometry for Eqs. (2)–(4).

$$R(\theta)=\frac{\sin(N\pi\cos\theta)}{N\pi\cos\theta}, \tag{4}$$

where $N=L/\lambda_P$. Figure 9 displays R vs. θ for $N=2.6$ (the solid curve) and $N=0.26$ (the dashed curve), corresponding to plane waves traveling at 340 m s^{-1} horizontally across the sensor having frequencies of 10 and 1 Hz, respectively.

Clearly, there is a frequency roll-off for a line sensor receiving distant signals from other than $\theta=90°$. An array of several line sensors oriented along differing azimuths would be required to detect high-frequency signals from all directions. While the response of a circular sensor is omnidirectional, it begins to fall off when the wavelength approaches the sensor diameter. This can be computed numerically for any shaped sensor by summing the phasor vectors for all segments of the sensor. The phase shift at each segment having position x (again for a wave traveling in the x direction) is kx. The sensor's total response R for M segments is given by the magnitude of the vector sum of the phasors from each segment:

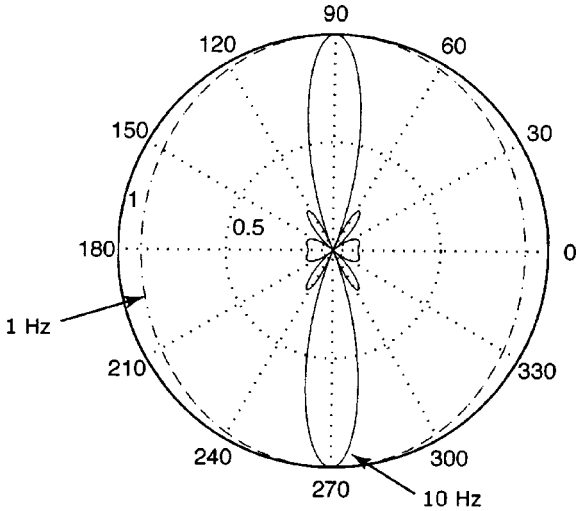

FIG. 9. The directional response of an 89-m-long OFIS is plotted for $L/\lambda_P=2.6$ (solid curve) and $L/\lambda_P=0.26$ (dashed curve).

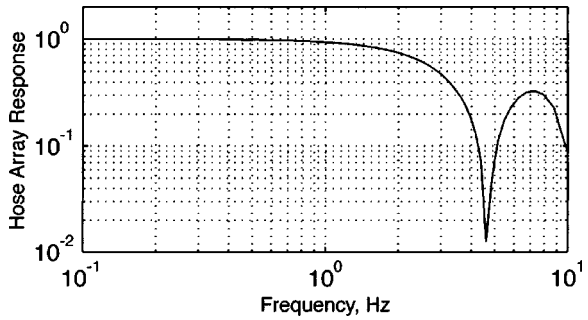

FIG. 10. The results of a numerically integrated spatial average as a function of frequency for a hose or pipe array of the geometry depicted in Fig. 2. Compare this with the observed response shown in Fig. 5.

$$R=\frac{1}{M}\left\{\left(\sum_{i=1}^{M}\cos(kx_i)\right)^2+\left(\sum_{i=1}^{M}\sin(kx_i)\right)^2\right\}^{1/2}, \qquad (5)$$

where the shape of the sensor is described by M segments each at coordinate x_i, y_i (the individual phase shifts do not depend on the y_i's because the wavefronts are assumed to be parallel to the y axis in this calculation).

This sum was computed for the geometry of the Hose Array described earlier (which is nearly the same as the geometry of the Pipe Array). Figure 10 shows the result of this numerical computation. Note that the shape of the curve in Fig. 10 agrees qualitatively with the observed transfer function between the OFIS and the Hose Array in Fig. 5. They differ somewhat in the location of the first response null (when the wavelength of the incident ray is about the same as the diameter of the Pipe Array). It is likely that other propagation effects (such as those described by Burridge, 1971) further modify the responses of the pipe arrays (it is also possible that the incident wave shown in Fig. 4 and analyzed for the comparison in Fig. 5 was not propagating horizontally). Note that this response null is purely a geometric effect resulting from our comparing a linearly deployed sensor (the OFIS) to circularly deployed sensors (the Pipe and Hose arrays) and that it will occur only for coherent waves—consequently the response null is absent from the spectra in Figs. 6 and 7 because they are dominated by ambient incoherent noise.

V. CONCLUSIONS

We have developed a new sensor for the detection of pressure variations in the infrasound band. It is less noisy than other sensors above 1 Hz, and somewhat noisier below the microbarom peak. We believe residual thermal effects in the compliant silicon tube cause this. The records we have collected reveal (as far as we are aware) a new low noise limit in the band from 1 to 10 Hz.

The prototype sensor we have built and studied is 89 m long. At this length, it reduces wind noise as well as similarly sized mechanical arrays. It would be difficult to make larger mechanical filters because the phase delays within them become more problematic as the size of the filter grows. With the OFIS, however, significantly longer lengths are possible without such problems, promising better wind noise reduction.

The directional characteristic of the linear sensor suggests that an array of them, oriented at different angles, will allow computation of direction to the source. The array arms could be made very long to reduce wind noise.

ACKNOWLEDGMENTS

Gene Herrin, Paul Golden, and Mike Sorrells provided useful insight on the effects of burying the instrument and contributed the Hose Array concept, which proved important for comparisons. This research was funded by the Defense Threat Reduction Agency under Contracts Nos. DSWA01-99-C-0056 and DTRA01-00-C-0085.

Alcoverro, B., and Le Pichon, A. (**2002**). ''Design and optimization of a noise reduction system for infrasound measurements using elements with low acoustic impedance,'' J. Acoust. Soc. Am.

Burridge, R. (**1971**). ''The acoustics of pipe arrays,'' Geophys. J. R. Astron. Soc. **26**, 53–70.

Christie, D. R., Vivas Veloso, J. A., Campus, P., Bell, M., Hoffmann, T., Langlois, A., Martysevich, P., Demirovich, E., and Carvalho, J. (**2001**). ''Detection of atmospheric nuclear explosions: the infrasound component of the International Monitoring System,'' Kerntechnik **66**, 96–101.

Daniels, F. B. (**1959**). ''Noise reducing line microphones for frequencies below 1 c/s,'' J. Acoust. Soc. Am. **31**, 529.

Hedlin, M. A. H., Alcoverro, B., and D'Spain, G. (in press). ''Evaluation of rosette infrasonic noise-reducing spatial filters,'' J. Acoust. Soc. Am.

Hedlin, M. A. H., Berger, J., and Vernon, F. L. (**2002**). ''Surveying infrasonic noise on oceanic islands,'' Pure Appl. Geophys. **159**, 1127–1152.

Hocker, G. B. (**1979**). ''Fiber-optic sensing of pressure and temperature,'' Appl. Opt. **18**, 1445–1448.

Kromer, R. P., and McDonald, T. S. (**1998**). ''Test and Evaluation of the Chaparral Physics Model 4.11 Infrasound Sensor for CTBT Infrasound Array application,'' in Proc. Infrasound Workshop for CTBT Monitoring, Santa Fe, New Mexico, 25–28 August 1997, Los Alamos National Laboratory, LA-UR-98-56.

Diffraction of sound from a dipole source near to a barrier or an impedance discontinuity

Marc Buret[a] and Kai Ming Li[b]
Department of Mechanical Engineering, The Hong Kong Polytechnic University, Hong Kong

Keith Attenborough
Department of Engineering, The University of Hull, Hull HU6 7RX, United Kingdom

(Received 5 November 2001; revised 7 January 2003; accepted 11 February 2003)

Pierce's formulation for the diffraction of spherical waves by a hard wedge has been extended to the case of the sound field due to a dipole source. The same approach is also used to extend a semiempirical model for sound propagation above an impedance discontinuity due to a dipole source. The resulting formulas have been validated by comparing their numerical solutions with that computed by summing the sound fields due to two closely spaced monopole sources of equal magnitude but opposite in phase. These new formulations are then used to develop a simple model for calculating the dipole sound field diffracted by a barrier above an impedance ground. Applications of these models relate to transportation noise prediction, particularly railway noise abatement, for which dipole sources are commonly used. The numerical predictions have been found to compare reasonably well with indoor measurements using piezoceramic transducers as dipole sources. © *2003 Acoustical Society of America.* [DOI: 10.1121/1.1566977]

PACS numbers: 43.28.En, 43.20.El [LCS]

I. INTRODUCTION

There is considerable interest in the study of noise reduction by means of screens and barriers in the context of environmental noise control. Although approximations for the calculation of the barrier insertion loss are widely used, the theoretical foundation for these studies is diffraction theory that is intimately related to corresponding solutions for electromagnetic fields.[1] An analytic solution for the sound field due to an omnidirectional point source diffracted by a hard wedge of arbitrary angle has been derived by Pierce.[2] It is often used as the basis for calculations of the screening effects due to barriers.[3] In addition, De Jong *et al.*[4] have developed a semiempirical solution for the calculation of the sound field above an admittance discontinuity, which is based on the diffraction of sound by a horizontal screen.

In view of the difficulties of computing Pierce's original solution[2] that includes Fresnel integrals, Hadden and Pierce[5] have reformulated the problem and propose an expression using simpler functions. However, more recently, Menounou *et al.*[6] have suggested a formulation of the diffraction integral by means of Hankel functions. Their approach considers the diffracted wave as being emitted by a directive line source located at the edge of the wedge. It leads to a unified formulation for the diffraction of the field due to point and line sources as well as arrays of point sources. In the case of an omnidirectional point source, it recovers Pierce's solution when asymptotic expressions are used.

The dipole field is a classical problem for the diffraction of electromagnetic waves,[1] but little can be found about the acoustic dipole and although, for example, train noise is modeled by means of a line of incoherent dipoles,[16–18] most of the methods for evaluating the shielding by barriers in the vicinity of tracks are approximations based on the solution for spherical or cylindrical waves.[18] The problem of diffraction of sound waves emitted by a dipole source has not been treated yet. Such a calculation is useful in the context of railway noise as well as for moving sources in general. It has been shown recently[7] that the sound field due to a monopole source in motion can be separated into two components: one that has the characteristics of a monopole and a second that has a dipolar behavior.

Our aim in this paper is to give a solution for the pressure field due to an arbitrarily oriented dipole diffracted by a wedge. This solution can then be used to extend De Jong's semiempirical model for propagation above an admittance step to dipole sources, as well as for the calculation of the sound field due to dipoles in the presence of barriers. Our starting point is the diffracted pressure for a monopole, as derived by Pierce.[2,8] This formulation is preferred to that given later by Hadden and Pierce[5] because of its consistency with De Jong's model[4] as well as the recent formulation of the Directive Line Source Model.[6]

The structure of the paper is as follows: in Sec. II we introduce the fundamental approach used to derive the sound field due to a dipole for the direct waves, reflected waves, and diffracted waves. In Sec. III, we discuss the use of these formulations for predicting sound in outdoor environments. Two typical cases are considered. They are namely, (1) sound propagation above an impedance discontinuity and (2) sound propagation in the presence of a barrier above the ground. In Sec. IV we present the experimental results for the validation of our theoretical formulations. Finally, Sec. V summarizes the main results obtained in the paper.

[a]On leave from the Department of Mechanical and Environmental Engineering, The Open University, Walton Hall, Milton Keynes MK7 6AA, United Kingdom.
[b]Author to whom correspondence should be addressed. Electronic mail: mmkmli@polyu.edu.hk

 0001-4966/2003/113(5)/2480/15/$19.00

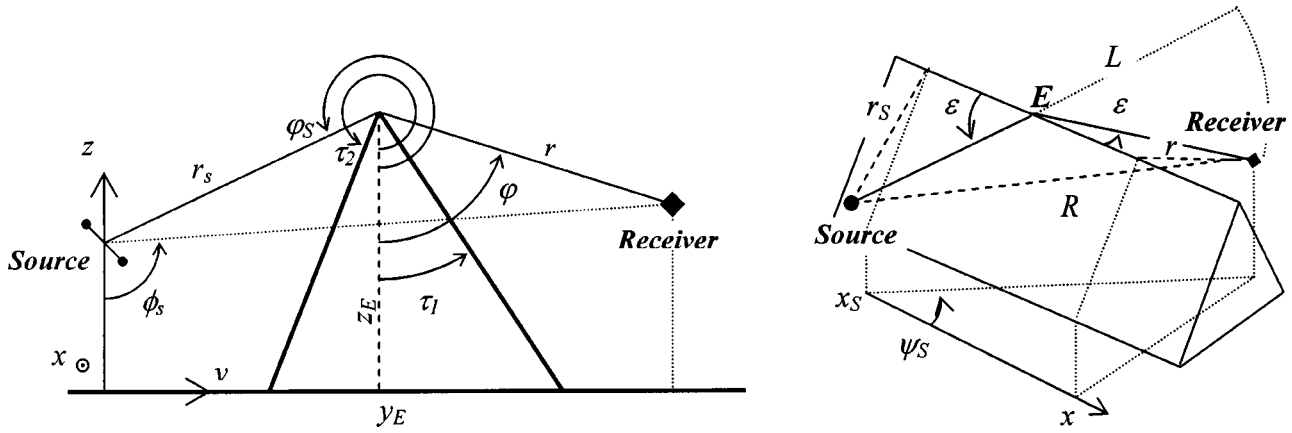

FIG. 1. Geometry for a wedge of arbitrary shape.

II. THEORETICAL FORMULATION

A. Geometrical configuration

Consider a two-dimensional wedge that has a constant cross-sectional area in the *y*-*z* plane and an arbitrary top angle $T=\tau_2-\tau_1$. The angles τ_1 and τ_2 are measured from the positive *z* axis; see Fig. 1. The wedge is acoustically hard with two reflecting planes. We choose a rectangular coordinate system such that the vertical *z* axis passes through the center of the source. The edge of the wedge is located in the direction parallel to the *x* axis and it is situated a horizontal distance of y_e and a height of z_e from the origin. In some situations, it may be more convenient to use a cylindrical polar coordinates system (r, φ, x) to specify field points from the edge of the wedge. These two coordinate systems are related according to

$$r=\sqrt{(y-y_e)^2+(z-z_e)^2}, \tag{1a}$$

$$\varphi=-\arctan\left(\frac{y-y_e}{z-z_e}\right), \tag{1b}$$

$$y=y_e+r\sin\varphi, \tag{1c}$$

$$z=z_e-r\cos\varphi, \tag{1d}$$

where the angle φ is measured from the vertical *z* axis. In the cylindrical polar coordinate system, the two sides of the wedge are located at $\varphi=\tau_1$ and $\varphi=\tau_2$. Defining a wedge index,[2]

$$\nu=\frac{\pi}{\tau_2-\tau_1}, \tag{2}$$

we can fix the shape of the wedge by specifying the parameters, ν, τ_1, and z_e.

To derive an analytical expression for the sound field due to a dipole source, it is useful to identify the source orientation by its direction cosines (ℓ_x,ℓ_y,ℓ_z) in the rectangular coordinate system as follows:

$$\begin{aligned}\ell_x&=\sin\gamma\cos\psi,\\ \ell_y&=\sin\gamma\sin\psi,\\ \ell_z&=\cos\gamma,\end{aligned} \tag{3}$$

where γ and ψ are the polar and azimuthal angles as shown in Fig. 2.

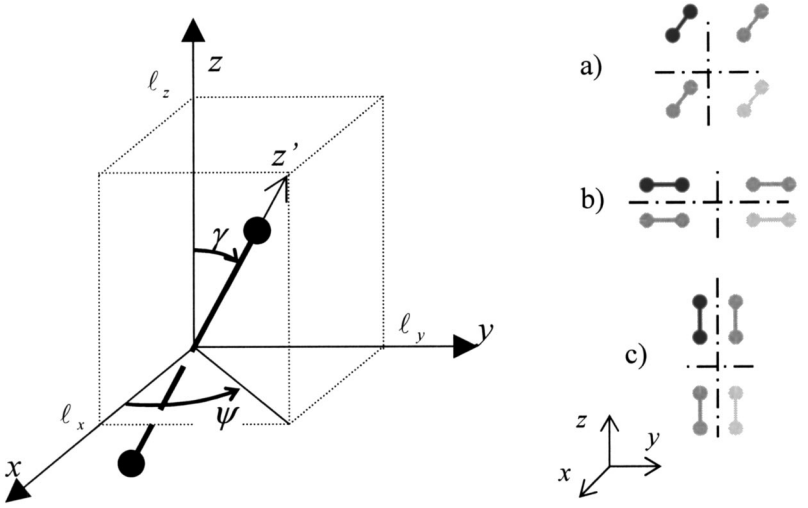

FIG. 2. Dipole orientation and direction cosines and relative orientations of a horizontal (a) along the *x* axis, (b) along the *y* axis, and vertical dipoles (c), and their images with respect to the horizontal and vertical planes.

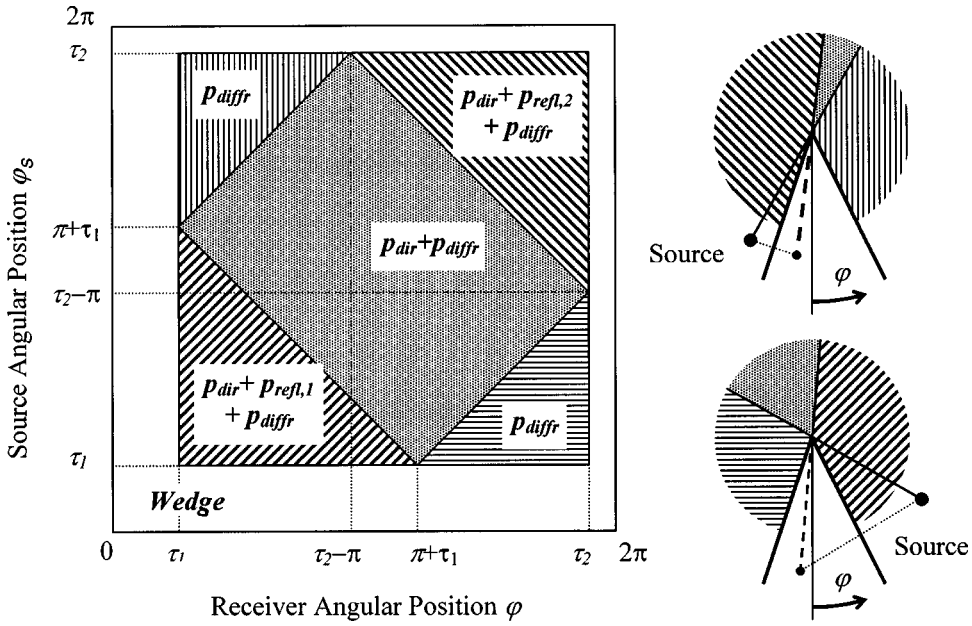

FIG. 3. Components of the pressure field in a function of the relative source and receiver positions with the faces of a wedge (τ_1 and τ_2).

B. The sound field in the vicinity of an acoustically hard wedge

The sound field can be expressed as a sum of four components: the direct wave term, two terms corresponding to the waves reflected by the planes at either sides of the wedge, and the diffracted wave as follows:

$$p_{\text{tot}} = p_{\text{dir}} + p_{\text{refl},1} + p_{\text{refl},2} + p_{\text{diffr}}. \tag{4}$$

The first three components of the total pressure may vanish depending on the source and receiver positions relative to the obstacle. The presence or absence of these components has been extensively discussed in the literature[2,5] and is summarized in Fig. 3.

The pressure field due to a dipole can be derived by considering its definition: it is the total field due to two monopoles of equal strength but 180° out of phase, infinitely close to one another.[8] The resultant sound field is given by

$$p = \lim_{|\Delta|\to 0} \frac{p_0(\mathbf{R},\mathbf{R_S}+\Delta) - p_0(\mathbf{R},\mathbf{R_S}-\Delta)}{2|\Delta|}, \tag{5a}$$

where p_0 is the pressure field due to a monopole, $\mathbf{R}$ and $\mathbf{R_S}$ are, respectively, the receiver and source coordinate vectors and the vector Δ represent the separation between the two out-of-phase monopoles, including the dipole orientation:

$$\Delta = |\Delta| \begin{pmatrix} \ell_x \\ \ell_y \\ \ell_z \end{pmatrix}. \tag{5b}$$

Consider a coordinate system (x',y',z') with the z' axis laying along the dipole axis, as illustrated in Fig. 2, Eq. (5a) can be rewritten as

$$p = \lim_{|\Delta|\to 0} \frac{p_0(x',y',z',x's,y's,z's+|\Delta|) - p_0(x',y',z',x's,y's,z's-|\Delta|)}{2|\Delta|}$$

$$= \frac{\partial p_0(x',y',z',x's,y's,z's)}{\partial z's} = \left(\frac{\partial xs}{\partial z's}\frac{\partial}{\partial xs} + \frac{\partial ys}{\partial z's}\frac{\partial}{\partial ys} + \frac{\partial zs}{\partial z's}\frac{\partial}{\partial zs} \right) p_0(\mathbf{R},\mathbf{R_S}). \tag{5c}$$

(ℓ_x,ℓ_y,ℓ_z) are the direction cosines for the z' axis and hence express (x,y,z) as functions of z'; Eq. (5c) can then be rewritten as

$$p = (\mathbf{I}\cdot\nabla_{\mathbf{S}}) p_0(\mathbf{R},\mathbf{R_S}),$$

$$\text{with } (\mathbf{I}\cdot\nabla_{\mathbf{S}}) = \left[\ell_x \frac{\partial}{\partial x_S} + \ell_y \frac{\partial}{\partial y_S} + \ell_z \frac{\partial}{\partial z_S} \right]. \tag{6}$$

C. Direct and reflected waves

The direct wave from a dipole source is well known as it is the free field solution,[8–10]

$$p_{\text{dir}} = P_0 \Theta_R \frac{1-ikR}{R^2} e^{ikR}, \tag{7a}$$

where P_0 is a pressure magnitude constant. Θ_R and R are,

respectively, directivity factor and the direct path given by

$$\Theta_R = -(\mathbf{l}\cdot\nabla_S)R$$
$$= \cos\gamma\cos\phi_S + \sin\gamma\sin\phi_S\cos(\psi_S-\psi), \quad (7b)$$

$$R = \sqrt{(x-x_S)^2+(y-y_S)^2+(z-z_S)^2}. \quad (7c)$$

The directivity factor is a function of the dipole orientation and the relative source and receiver position represented here by the incidence angle ϕ_S and the azimuthal angle ψ_S (see Fig. 1). It is interesting to note that the pressure falls as $1/R^2$ for $kR \ll 1$ and $1/R$ for $kR \gg 1$. The expressions of the directivity factor Θ_R and the direct path R can be written in the cylindrical coordinate system (r, φ, x) as follows:

$$\Theta_R = \ell_x\frac{x-x_S}{R} + \ell_y\frac{r\sin\varphi - r_S\sin\varphi_S}{R}$$
$$-\ell_z\frac{r\cos\varphi - r_S\cos\varphi_S}{R}, \quad (8a)$$

$$R = \sqrt{r^2+r_S^2-2rr_S\cos(\varphi-\varphi_S)+(x-x_S)^2}. \quad (8b)$$

The reflected waves can be calculated using a local coordinates system relative to each face of the wedge. It is then straightforward to calculate these waves in the case of a hard wedge. The sound fields due to these two components can be written in a compact form as

$$p_{\text{refl},n} = P_0\Theta_n\frac{1-ikS_n}{S_n^2}\exp(ikS_n), \quad (9a)$$

where $n=1, 2$ with the corresponding directivity factors and reflected wave paths given by

$$\Theta_n = \ell_x\frac{x-x_S}{S_n} + \ell_y\frac{r\sin\varphi + r_s\sin(\varphi_S-2\tau_n)}{S_n}$$
$$-\ell_z\frac{r\cos\varphi - r_s\cos(\varphi_S-2\tau_n)}{S_n} \quad (9b)$$

$$S_n = \sqrt{r^2+r_S^2-2rr_S\cos(\varphi+\varphi_S-2\tau_n)+(x-x_s)^2}. \quad (9c)$$

D. Diffracted wave

The wave diffracted at the edge of the wedge from a dipole source can be derived from the corresponding expression for a monopole source. Making use of Eq. (6) for the calculation of dipole fields, the diffracted pressure from a dipole source can be written as

$$p_{\text{diffr}} = (\mathbf{l}\cdot\nabla_S)D_0(\mathbf{R},\mathbf{R_S}), \quad (10)$$

where D_0 is the diffracted pressure for a monopole. Using Pierce's solution,[2] we can write the analytical solution for the diffracted pressure from a monopole source as

$$D_0 = P_0\frac{1+i}{2}\frac{\exp(ikL)}{L}[A_D(X_+)+A_D(X_-)], \quad (11a)$$

where L is the shortest path from the source to the diffraction edge to receiver,

$$L = \sqrt{(x-x_S)^2+(r+r_S)^2}. \quad (11b)$$

$A_D(X)$ is the diffraction integral:

$$A_D(X) = \frac{1}{\pi\sqrt{2}}\int_{-\infty}^{\infty}\frac{e^{-u^2}}{(\pi/2)^{1/2}X - e^{-i\pi/4}u}\,du$$
$$= \text{sgn}(X)[f(|X|) - ig(|X|)], \quad (11c)$$

where $f(X)$ and $g(X)$ are the auxiliary Fresnel functions.[2,11] The parameters, X_+ and X_-, are given by

$$X_- = \Gamma M_\nu(\alpha_-); \quad \alpha_- = \varphi - \varphi_S, \quad (11d)$$

$$X_+ = \Gamma M_\nu(\alpha_+); \quad \alpha_+ = \varphi + \varphi_S - 2\tau_1, \quad (11e)$$

with

$$\Gamma = \sqrt{krr_S/\pi L} = \sqrt{2rr_S/\lambda L} \quad (11f)$$

and

$$M_\nu(\alpha) = \frac{\cos\nu\pi - \cos\nu\alpha}{\nu\sin\nu\pi}, \quad (11g)$$

where λ is the wavelength. It is remarkable from Eqs. (11d) and (11e) that the term in X_- in the expression of the diffracted pressure in Eq. (11a) is related to the direct wave, whereas the term in X_+ is linked to the image source with respect to the wedge.

The presence of the sign function sgn(X) in Eq. (11c) means that the diffracted pressure for a monopole is not continuous. Mathematically speaking, its derivative is undefined at the points where X_+ and X_- are equal to 0. These points are the lines of sight for the direct and reflected waves. However, the total pressure field is continuous. The step in the diffracted pressure is then compensated for by the presence (or absence) of the direct or reflected wave considered and the value of the diffracted pressure on the sight lines can be calculated using the continuity of the total pressure. Before we proceed, we remark that De Jong[4] gives a slightly different formulation for the diffracted pressure due to a monopole source, making use of another form of Fresnel function than the diffraction integral A_D. Although it requires tedious manipulations on the Fresnel integrals, it is straightforward to show that this expression for the diffracted pressure wave is actually identical to Pierce's formulation.[2]

Next, we wish to derive an analytical expression for the diffracted wave due to a dipole source. As shown in Fig. 1, let ε be the angle made by the diffracted ray with the diffraction edge. According to Keller's law of diffraction, this angle is the same for both parts of the diffracted ray path[8] (source to edge and edge to receiver); thus

$$\cos\varepsilon = (x-x_S)/L \quad (12a)$$

and

$$\sin\varepsilon = (r+r_S)/L. \quad (12b)$$

The derivative of the auxiliary Fresnel functions $f(X)$ and $g(X)$ are[11]

$$f'(X) = -\pi X g(X), \quad (13a)$$

$$g'(X) = \pi X f(X) - 1. \quad (13b)$$

Hence, the diffracted wave for an arbitrarily oriented dipole can be derived by substituting Eqs. (11), (12a), (12b), (13a), and (13b) into Eq. (10):

$$p_{\text{diffr}} = P_0 \frac{1+i}{2} \Theta_L \frac{1-ikL}{L} \frac{e^{ikL}}{L} [A_D(X_+) + A_D(X_-)]$$
$$- P_0 \frac{1-i}{2} \frac{\exp(ikL)}{L} [1 - \pi X_- A_D(X_-)]$$
$$\times \left\{ \frac{X_-}{2} \left[\frac{\Theta_L}{L} + \frac{\sin\varphi_S - \cos\varphi_S}{r_S} \right] - X'_- \frac{\cos\varphi_S + \sin\varphi_S}{r_S} \right\}$$
$$- P_0 \frac{1-i}{2} \frac{\exp(ikL)}{L} [1 - \pi X_+ A_D(X_+)]$$
$$\times \left\{ \frac{X_+}{2} \left[\frac{\Theta_L}{L} + \frac{\sin\varphi_S - \cos\varphi_S}{r_S} \right] + X'_+ \frac{\cos\varphi_S + \sin\varphi_S}{r_S} \right\}, \tag{14a}$$

where Θ_L, which is the directivity factor at the point where the diffracted ray intersects the edge of the wedge, is given by

$$\Theta_L = -(\mathbf{l}\cdot\boldsymbol{\nabla}_\mathbf{S})L = \ell_x \cos\varepsilon - (\ell_y \sin\varphi_S - \ell_z \cos\varphi_S)\sin\varepsilon. \tag{14b}$$

The parameters, X'_- and X'_+, can be determined according to

$$X'_\pm = \Gamma M'_\nu(\alpha_\pm), \tag{14c}$$

where M'_ν is the derivative of M_ν with respect to its argument $\alpha_\pm$.

At high frequencies and long ranges with respect to the wavelength considered, Γ and hence $X'_\pm$ are large and the auxiliary Fresnel functions can be approximated by

$$f(X) \approx 1/\pi X, \tag{15a}$$

$$g(X) \approx 0. \tag{15b}$$

Therefore, the diffraction integral of Eq. (11c) reduces to

$$A_D(X) = \text{sgn}(X)[f(|X|) - ig(|X|)] \approx 1/\pi X. \tag{15c}$$

Figure 4 shows that for arguments greater than 1, the approximation in Eq. (15c)—shown by the dotted line—is already acceptable. The fact that $A_D(X)$ is an odd function ensures the same results for negative values of X. At high frequencies and long ranges with respect to the wavelength, the diffracted pressure as expressed in Eq. (14a) can be approximated by

$$p_{\text{diffr}} \approx P_0 \frac{1+i}{2} \Theta_L \frac{1-ikL}{L} \frac{e^{ikL}}{L} [A_D(X_+) + A_D(X_-)]. \tag{16}$$

The expression in Eq. (16) is analogous to the expression for a monopole source, but modified by the source strength factor $(1-ikL)/L$ and the directivity factor Θ_L, both typical of a dipole. Menounou's Directive Line Source Model[6] leads to a rather similar result for an array of two sources. Nevertheless, the source strength factor $(1-ikL)/L$ must then be introduced to account for the 180° difference in phase of the two point sources composing the dipole.

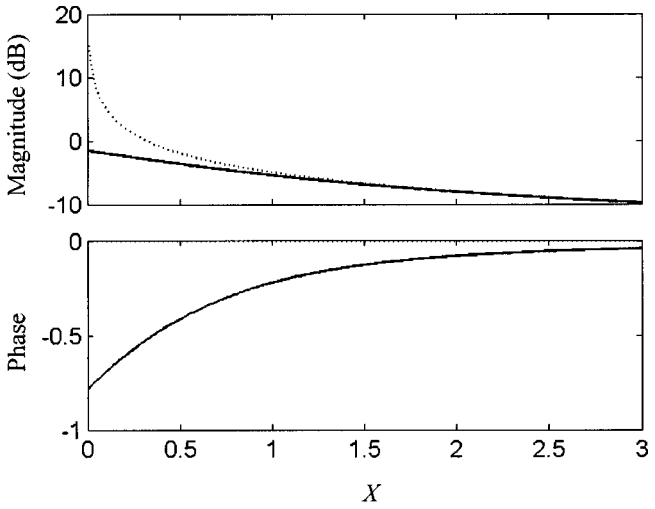

FIG. 4. Approximation of the diffraction integral $A_D(X)$ by $1/\pi X$. The exact function is shown by solid lines, its approximation represented by dotted lines.

E. Diffraction by a half-plane

A common idealization of diffraction of sound due to outdoor noise source by a barrier is that of diffraction by a thin screen, modeled by a half-plane. Diffraction by a half-plane is a classical case and can be derived by considering an infinitely thin wedge of top angle $T=0$. Hence,

$$\tau_1 = 0; \quad \tau_2 = 2\pi \quad \text{and} \quad \nu = 1/2. \tag{17}$$

The function M_ν used for the calculation of the diffracted wave can then be rewritten from Eq. (11g) as

$$M_\nu(\alpha) = -2\cos(\alpha/2). \tag{18}$$

The total sound field can be computed for a given source/receiver geometry. In Fig. 5, we show the total sound field at 1000 Hz when the receiver revolves around the edge of a half-plane. The source is located 1 m away from the edge, at $\varphi_S = 5\pi/3$ and its image is thus located at $\varphi'_S = \pi/3$ (both are marked by stars in Fig. 5). The receiver revolves at 2 m from the edge of the half-plane ($r = 2$ m). These plots show the sound field for a monopole (dotted line), a horizontal dipole (solid line), and a vertical dipole (dashed line). We remark that the axis of the horizontal dipole, which is aligned along the y axis, is perpendicular to the edge of the half-plane. Relative sound pressure levels (SPL) are used to facilitate the presentation of the theoretical results. The corresponding reference levels for different source types are chosen with the receiver located on the non-illuminated side of the half-plane at the given range, i.e., 2 m from the edge. The continuity of the total sound field on the sight lines for direct and reflected waves, marked by radial lines, is evident in the plots for all source types.

To confirm the validity of Eq. (14a) for the diffracted sound field, comparisons are made with numerical calculations using two monopoles of 180° difference in phase and very close to one another. In Fig. 5, we display these predicted results with squares for the sound field due to the horizontal dipole and triangles for that due to the vertical

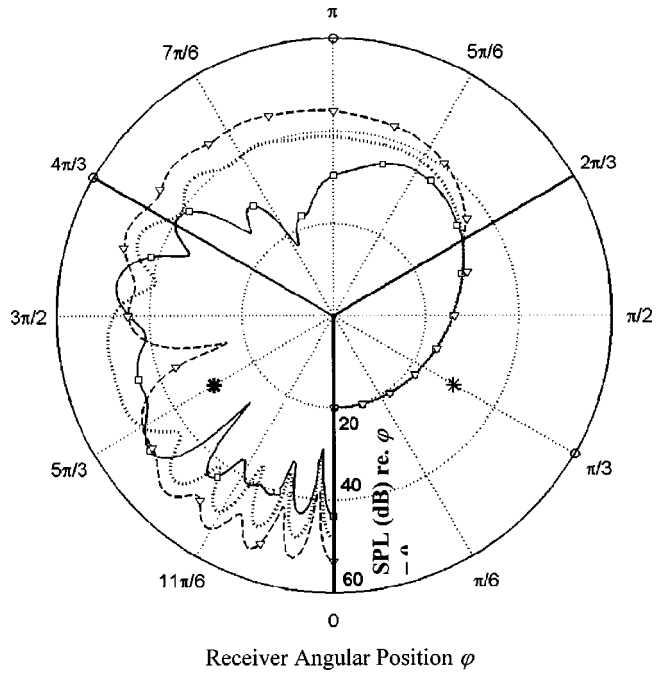

FIG. 5. The total sound field at 1000 Hz around a half-plane ($\nu=1/2$; $\tau_1=0$; $\tau_2=2\pi$) for a receiver revolving around the edge at $r=2$ m. The source is located at $\varphi_S=5\pi/3$; $r_S=1$ m; $x=x_S=0$. Three different sources are shown: a horizontal dipole (solid line), a vertical dipole (dashed line), and a monopole (dotted line). The squares and the triangles show the calculations for two monopoles with 180° out of phase and close to one another in the configuration of a horizontal and a vertical dipole, respectively. The stars show the positions of the source and its image with respect to the left-hand side of the screen. The results are referenced to the SPL when the receiver is located on the nonilluminated side of the wedge ($\varphi=\tau_1$). Solid radii represent the sight lines for direct and reflected waves.

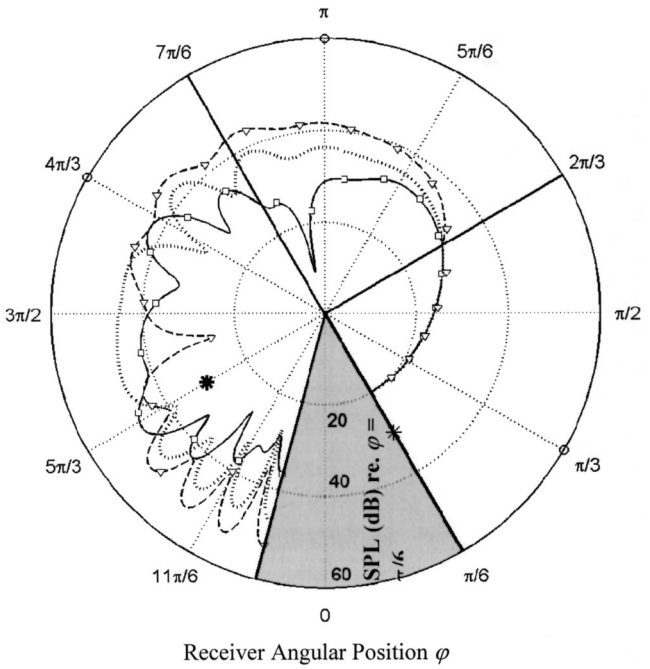

FIG. 6. The same as Fig. 5, but for a wedge of top angle $\pi/4$ ($\nu=4/7$; $\tau_1=\pi/6$; $\tau_2=23\pi/12$).

dipole. The predictions with such ''composite dipoles'' show no discernable difference with waves calculated by Eq. (14a).

In the shadow zone, all sources present the same variations in diffracted pressure, as the directivity function Θ_L is calculated at the top edge of the obstacle and is therefore independent of the receiver angular position. Outside the shadow zone, where the diffracted wave interferes with the direct wave, it is remarkable that the sound field pattern for a vertical dipole is comparable in shape to that of a monopole. This is not the case for the horizontal dipole. Different but related observations were made in the case of propagation of sound due to a dipole above ground.[10] In this case, the sound field due to a horizontal dipole (whose image has the same orientation) is very close to that due to a monopole. On the other hand, the sound field due to a vertical dipole above the ground (whose image is inverted) is somewhat different because of further interference between direct and reflected waves as well as a loss of reciprocity. Conversely, in the presence of a vertical half-plane described here, the image of the vertical dipole conserves the source orientation, whereas that of a horizontal dipole is inverted. Relative orientations of dipole sources and their images are summarized in Fig. 2. We have seen in Sec. II D that the source and its image both contribute to the diffracted pressure and hence their orientations have an important influence on its interaction with direct and reflected pressure waves.

Figure 6 displays the total sound field around the edge of a hard wedge of top angle $\pi/4$ ($\nu=4/7;\tau_1=\pi/6;\tau_2=23\pi/12$) at 1000 Hz for the same source and receiver positions. For such a narrow wedge, the pattern for a vertical dipole is again closer in shape to that of the monopole, due to the respective orientations of the source and its image. The continuity of pressure at the lines of sight is evinced and the agreement with the sound fields due to ''composite dipoles'' (squares for a horizontal dipole and a triangle for a vertical dipole) is again excellent.

Figure 7 shows the sound field for the same wedge and the same source as a function of the source–receiver offset distance $x-x_S$ for three receivers in different regions for the composition of the total pressure field. These receiver positions are shown by circles in Fig. 6. Predictions are shown for two horizontal dipolesed—along the x axis, parallel to the edge of the wedge (dashed–dotted line), and along the y axis, perpendicular to the edge of the wedge (solid line), respectively. Also shown are predictions for a vertical dipole along the z axis (dashed line) as well as a monopole (dotted line). The dipole fields are compared with the corresponding ''composite dipoles'' (crosses, squares and triangles, respectively). The agreement is again very good. The plots have been normalized to the point of null offset, except for the dipole along the x axis as the receiver is then in the midplane of the dipole and there is no sound field.

The results for horizontal and vertical dipole are undistinguishable. These calculations confirm observations made in earlier studies,[6] stating that the diffracted wave show greater directivity in the transverse direction than waves from the original source in the absence of a barrier. This is due to the behavior of the diffraction integral $A_D(X)$. Its

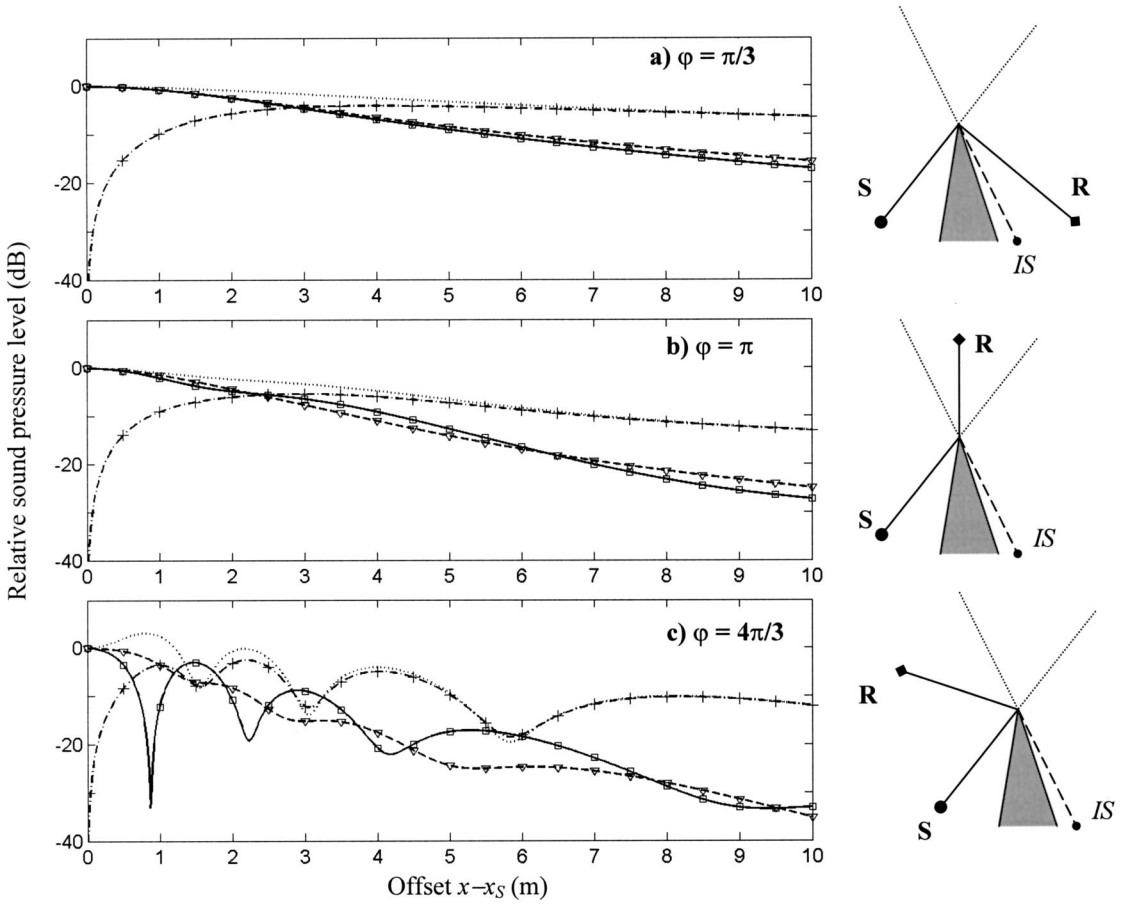

FIG. 7. The sound field at 1000 Hz in the presence of a hard wedge of top angle $\pi/4$ ($\nu=4/7$; $\tau_1=\pi/6$; $\tau_2=23\pi/12$) as a function of the source–receiver offset. The source is located at $r_S=1$ m; $\varphi_S=5\pi/3$. The receiver is located at $r=2$ m and at three positions corresponding to different compositions for the total pressure: (a) $\varphi=\pi/3$ (diffracted wave only); (b) $\varphi=\pi$ (direct wave and diffracted wave); and (c) $\varphi=4\pi/3$ (direct wave, wave reflected on the τ_2 side and a diffracted wave). These positions are shown in Fig. 6 by circles. Four different sources are shown: a horizontal dipole oriented along the y axis, perpendicular to the edge of the wedge (solid line), a horizontal dipole oriented along the x axis, parallel to the edge of the wedge (dashed–dotted line), a vertical dipole (dashed line), and a monopole (dotted line). The squares, the crosses, and the triangles show the calculations for two monopoles out of phase and close to one another in the configuration of the respective dipoles. The relative sound pressure level is referenced to its value at the point of null offset, except for the dipole along the x axis.

magnitude increases with offset, as X_- and X_+ decrease [cf. Eqs. (11d)–(11f) and Fig. 4]. This partly compensates for the decay in the sound field due to the increase in the source–receiver range. Outside the short offset range, the dipole along the x axis behaves in a way very similar to that of a monopole.

Comparing Figs. 7(a), (b), and (c) provides good insight into the influence of the direct waves and the reflections from the sides of the wedge on the total sound field. An interference pattern is observed in the region where the three components of the sound field are present. The horizontal dipole aligned along the x axis (dashed–dotted line) and the vertical dipole (dashed line) behave similarly to a monopole (dotted line) in that respect, whereas the pattern for the dipole aligned along the y axis (solid line) seems to be somewhat out of phase. This is also due to the relative orientations of the actual and image sources (see Fig. 2), which are identical for the dipole along x, almost the same for a vertical dipole and quasi-opposite for the dipole along the y axis. This figure shows that reflected waves are critical components of the total sound field.

III. TWO APPLICATIONS RELEVANT TO OUTDOOR ENVIRONMENT

A. Sound propagation above an admittance discontinuity

Several models can be found in the literature concerning the propagation of sound above a discontinuous ground. Boulanger *et al.* have given a review of these models.[12] Two of them are of interest for the present study as they make use of the solution for the diffracted pressure by a wedge. Koers' model[13] considers a wedge of top angle 180° with different admittance of each ''side.'' However, not only is such a model subject to the restrictions concerning the absorbent wedge but the sound field is not well defined when the reflection occurs at the point of discontinuity. The second model, a semiempirical one, has been proposed by De Jong.[4] It is based on the superposition of two half-planes of different admittance. The actual diffracted wave is then estimated by considering the two limiting cases: that of a hard screen in the air and that of homogeneous ground. De Jong's model has proved to give relatively good agreements with experi-

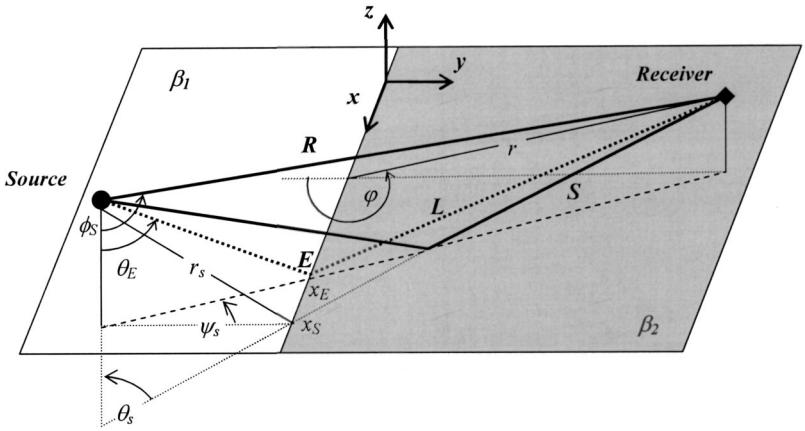

FIG. 8. Geometry for the propagation of sound above an admittance step.

mental results and with more accurate numerical calculations[12] for an omnidirectional point source. Having derived an expression for the pressure field due to a dipole diffracted by a half-plane, we shall now adapt De Jong's model to dipole sources.

After Li *et al.*,[10] the sound field due to an arbitratrily oriented dipole above a plane of specific normalized admittance β can be expressed in a close-form analytical solution as

$$p=\Theta_R\left[\frac{1-ikR}{R}\right]\frac{e^{ikR}}{R}+\Theta_S R_P\left[\frac{1-ikS}{S}\right]\frac{e^{ikS}}{S}+\Theta_Z(1-R_P)F(w)\left[\frac{1-ikS}{S}\right]\frac{e^{ikS}}{S}, \tag{19a}$$

where R and S are the direct and reflected ray paths, R_P is the plane wave reflection coefficient,

$$R_P=\frac{\cos\theta_S-\beta}{\cos\theta_S+\beta}, \tag{19b}$$

with θ_S the incidence angle of the reflected ray. The boundary loss factor, $F(w)$, is

$$F(w)=1+i\sqrt{\pi}we^{-w^2}\,\mathrm{erfc}(-iw), \tag{19c}$$

with the numerical distance w given by

$$w=(\tfrac{1}{2}ikS)^{1/2}(\cos\theta_S+\beta). \tag{19d}$$

The corresponding directivity factors are determined by

$$\Theta_R=\cos\phi_S\cos\gamma+\sin\phi_S\sin\gamma\cos(\psi_S-\psi), \tag{20}$$

$$\Theta_S=\cos\theta_S\cos\gamma+\sin\theta_S\sin\gamma\cos(\psi_S-\psi), \tag{21}$$

$$\Theta_Z=-\beta\cos\gamma+\sqrt{1-\beta^2}\sin\gamma\cos(\psi_S-\psi), \tag{22}$$

where ϕ_S is the elevation angle of the direct ray and ψ_S the azimuthal angle of the direct path connecting source and receiver shown in Fig. 8. The dipole orientation is defined by the polar and azimuthal angles γ and ψ (see Sec. II and Fig. 2).

In the presence of an admittance discontinuity on a flat reflecting ground (see Fig. 8), the pressure field for a monopole source of unit strength can be expressed as[4]

$$p_0=\frac{e^{ikR}}{R}+Q_r\frac{e^{ikS}}{S}+(Q_1-Q_2)D_0, \tag{23a}$$

where Q_1 and Q_2 are the spherical wave reflection coefficients calculated for the two types of ground,

$$Q_i=R_{p_i}+(1-R_{p_i})F(w_i),\quad \text{for } i=1,2, \tag{23b}$$

with R_{p_i} and w_i being the respective plane wave reflection coefficients and numerical distances. The parameter Q_r is the corresponding spherical wave reflection coefficient at the point of specular reflection and D_0 is the relative sound pressure of a monopole source diffracted by a horizontal half-plane with the edge coincided with the admittance discontinuity. The form of the solution for D_0 is given in a form similar to Eq. (11a) with a different configuration of source and receiver.

The sound field for a dipole of unit strength can be obtained by differentiating the expression for a monopole, the right hand side of Eq. (23a), to yield

$$p=(\mathbf{I}\cdot\nabla_\mathbf{S})\left[\frac{\exp(ikR)}{R}+Q_r\frac{\exp(ikS)}{S}\right]+(Q_1-Q_2)[(\mathbf{I}\cdot\nabla_\mathbf{S})D_0]+[(\mathbf{I}\cdot\nabla_\mathbf{S})(Q_1-Q_2)]p_{\mathrm{diffr}}, \tag{24}$$

where the operator $(\mathbf{I}\cdot\nabla_\mathbf{S})$ is given in Eq. (6) and p_{diffr} is the pressure due to the dipole source, diffracted by a horizontal half-plane whose edge coincides with the discontinuity,

$$p_{\mathrm{diffr}}\approx\frac{1+i}{2}\Theta_L\frac{1-ikL}{L}\frac{e^{ikL}}{L}[A_D(X_+)+A_D(X_-)], \tag{25a}$$

$$\Theta_L=\cos\theta_E\cos\gamma+\sin\theta_E\sin\gamma\cos(\psi_S-\psi), \tag{25b}$$

with L the diffracted ray pathlength. X_+ and X_- are defined in Eqs. (11d) and (11e) with angle φ_S measured from the negative y axis, as shown in Fig. 8. The parameter Θ_L is the directivity factor at the point E where the diffracted ray intersects the admittance discontinuity, i.e., the edge of the half-plane, as shown in Fig. 1. The parameters θ_E and ψ_S are, respectively, the elevation angle and azimuthal angle of the diffracted ray path joining source to edge to receiver.

The first bracketed term on the right hand side of Eq. (24) represents sound fields due to a dipole above the ground. Use can be made of the solution derived by Li *et al.*[10] shown in Eq. (19). The derivative of the diffracted pressure in the second term on the right-hand side of Eq. (24)

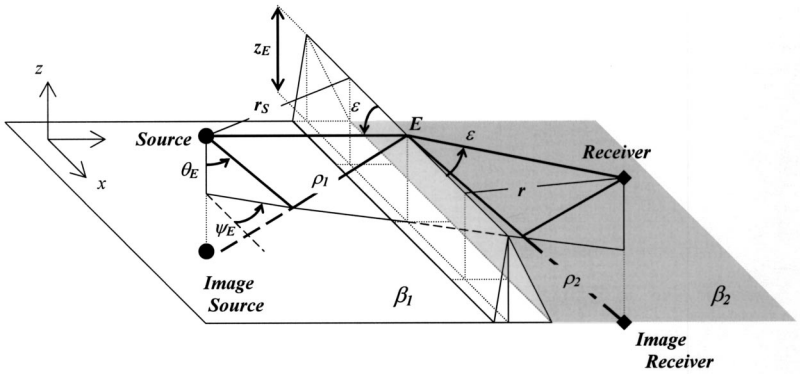

FIG. 9. Geometry for the propagation of sound in the presence of a barrier above the ground.

is the pressure due to a dipole source diffracted by a horizontal half-plane, cf. Eq. (16), with the use of appropriate parameters. The last term involves the derivative of the spherical wave reflection coefficients. In the case of a horizontal dipole, its contribution will not be significant compared with the first two terms because the variations of this reflection coefficient with horizontal distance are small. On the other hand, its influence becomes crucial in the case of a vertical dipole as the spherical wave coefficient is more sensitive to variations in height.

Li's formulation[10] is used to rewrite $(\mathbf{I}\cdot\nabla_{\mathbf{S}})Q_i$ as

$$(\mathbf{I}\cdot\nabla_{\mathbf{S}})Q_i=(\Theta_{Zi}-\Theta_S)\frac{1-ikS}{S}(1-R_{Pi})F(w_i),$$

$$\text{for}\quad i=1,2, \tag{26}$$

where Θ_S, Θ_{Z1}, and Θ_{Z2} can be determined according to Eqs. (21) and (22). Hence, Eq. (24) becomes

$$p=\Theta_R\frac{1-ikR}{R}\frac{e^{ikR}}{R}+\Theta_S\frac{1-ikS}{S}Q_r\frac{e^{ikS}}{S}$$
$$+\frac{1+i}{2}\frac{e^{ikL}}{L}\left[\Theta_L\frac{1-ikL}{L}(Q_1-Q_2)+\frac{1-ikS}{S}(\xi_1-\xi_2)\right]$$
$$\times[A_D(X_-)+A_D(X_+)], \tag{27a}$$

where

$$\xi_i=(\Theta_{Zi}-\Theta_S)(1-R_{Pi})F(w_i),\quad i=1,2. \tag{27b}$$

For near-grazing propagation and soft grounds, further approximations can be used,[10] in Eq. (27b) to simplify ξ_1 and ξ_2 as follows:

$$\xi_i\approx-2\beta_i\cos\gamma F(w_i),\quad i=1,2. \tag{27c}$$

The solution is nonsingular and continuous where the point of specular reflection crosses over the admittance discontinuity because, at the transition point, $L=S$; $\Theta_L=\Theta_S$ and $X_+=0$, which leads to $A_D(0)=-(1-i)/2$. Hence, the continuity of the solution is ensured.

B. Sound propagation in the presence of a barrier above the ground

Consider sound propagation in the presence of a barrier when source and receiver are located on either sides of a barrier with the receiver located at the shadow zone above ground. The sound field for a monopole source can then be represented by the sum of four components (see Fig. 9) corresponding to each path from source to receiver, taking into account the effect of the ground reflections. The total sound field can be expressed as

$$p_0=p_{0,S-R}+Q_1p_{0,IS-R}+Q_2p_{0,S-IR}+Q_1Q_2p_{0,IS-IR}, \tag{28}$$

where the subscripts *S, R, IS, IR* stand for the source, the receiver, the image source and the image receiver, respectively. The parameters, Q_1 and Q_2 are the reflection coefficients for the waves reflected on the source side (ground admittance β_1) and on the receiver side (ground admittance β_2). It has been found[13] that these reflection coefficients should be calculated for the respective paths joining the image source to the edge of the wedge (ρ_1) and the edge to the image receiver (ρ_2). These are calculated from geometrical considerations (see Fig. 9) as

$$\rho_1=\frac{r_S}{\sin\varepsilon}\sqrt{1-\frac{4z_e}{r_S}\left(\cos\varphi_S-\frac{z_e}{r_S}\right)\sin^2\varepsilon}, \tag{29a}$$

$$\rho_2=\frac{r}{\sin\varepsilon}\sqrt{1-\frac{4z_e}{r}\left(\cos\varphi-\frac{z_e}{r_S}\right)\sin^2\varepsilon}. \tag{29b}$$

In the case of a dipole source, the expression for the sound field can be obtained by substituting Eq. (28) into Eq. (6). This leads to

$$p=(\mathbf{I}\cdot\nabla_{\mathbf{S}})p_{0,S-R}+Q_1[(\mathbf{I}\cdot\nabla_{\mathbf{S}})p_{0,IS-R}]$$
$$+Q_2[(\mathbf{I}\cdot\nabla_{\mathbf{S}})p_{0,S-IR}]+Q_1Q_2[(\mathbf{I}\cdot\nabla_{\mathbf{S}})p_{0,IS-IR}]$$
$$+[(\mathbf{I}\cdot\nabla_{\mathbf{S}})Q_1]p_{0,IS-R}+[(\mathbf{I}\cdot\nabla_{\mathbf{S}})Q_2]p_{0,S-IR}$$
$$+\{Q_1[(\mathbf{I}\cdot\nabla_{\mathbf{S}})Q_2][(\mathbf{I}\cdot\nabla_{\mathbf{S}})Q_1]Q_2\}p_{0,IS-IR}. \tag{30}$$

However, as the reflection coefficient Q_2 is calculated for the path joining the edge of the barrier to the receiver, it is independent of the source coordinates in the vertical plane, hence,

$$(\mathbf{I}\cdot\nabla_{\mathbf{S}})Q_2=0. \tag{31a}$$

The derivative of the reflection coefficient Q_1 may here again be estimated after Li's formulation for the sound field due to a dipole above the ground,[10]

$$(\mathbf{I}\cdot\nabla_{\mathbf{S}})Q_1=(\Theta_{Z1}-\Theta_{S1})\frac{1-ik\rho_1}{\rho_1}(1-R_{P1})F(w_1), \tag{31b}$$

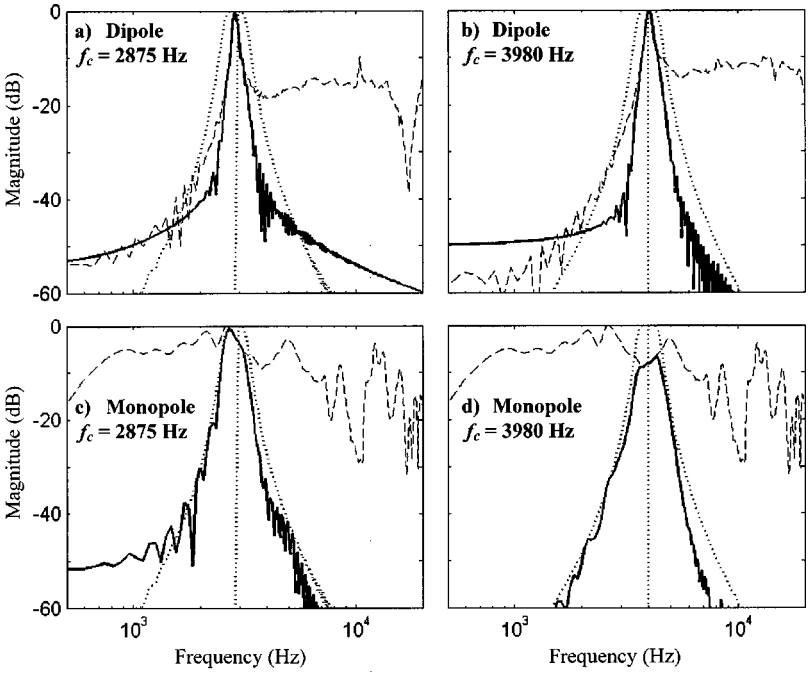

FIG. 10. Free field spectra of the sources used. The dashed lines show the broadband spectra, the solid lines the filtered spectra, and the dotted lines the third-octave band filters used. (a) Piezoceramic disk with resonant frequency $f_c = 2875$ Hz; (b) piezoceramic disk with $f_c = 3980$; (c) omnidirectional source, filtered on the third octave centered at $f_c = 2875$ Hz; (d) the same as (c) but for $f_c = 3980$ Hz.

where

$$R_{P1} = \frac{\cos\theta_E - \beta_1}{\cos\theta_E - \beta_1}, \tag{31c}$$

$$w_1 = (\tfrac{1}{2} ik\rho_1)^{1/2}(\cos\theta_E + \beta_1), \tag{31d}$$

$$\Theta_{S1} = \cos\theta_E \cos\gamma + \sin\theta_E \sin\gamma \cos(\psi_E - \psi), \tag{31e}$$

$$\Theta_{Z1} = -\beta_1 \cos\gamma + \sqrt{1-\beta_1^2} \sin\gamma \cos(\psi_E - \psi), \tag{31f}$$

with θ_E and ψ_E being the elevation and azimuthal angles of the path joining the image source to the edge of the barrier (see Fig. 9). Equation (30) can then be simplified to

$$p = p_{S-R} + Q_1 p_{IS-R} + Q_2 p_{S-IR} + Q_1 Q_2 p_{IS-IR} + (\Theta_{Z1} - \Theta_{S1})[p_{0,IS-R} + Q_2 p_{0,IS-IR}] \frac{1 - ik\rho_1}{\rho_1} \times (1 - R_{P1}) F(w_1), \tag{32}$$

where, when the receiver is in the shadow zone, p_{S-R}; p_{IS-R}; p_{S-IR}; p_{IS-IR} are the diffracted pressures for each of the four propagation paths calculated using the expression given in Eq. (16).

IV. LABORATORY MEASUREMENTS

A. Experimental setup

Measurements have been carried out in an anechoic chamber of dimension 6 m×6 m×4 m (high).

Piezoceramic disks with peak frequencies of 2875 Hz (diameter 35 mm) and 3980 Hz (diameter 27 mm) with dipole directivity have been used. Although they may be delicate to manipulate, similar disks were used successfully as dipole sources in our previous studies.[10] The impulse responses were obtained by means of a Maximum Length Sequence Analyzer[15] and then filtered on the third octave band centered on the peak frequency of the source. The sound pressure levels were then calculated by means of an integration of these filtered responses rather than on single frequencies, to ensure that small spectral instabilities linked to the change geometry do not affect the results presented here. Since the piezoceramic disks emitted quite low levels of sound, a relatively short source–receiver range up to 1.5 m was chosen in our indoor measurements. They also have been carried out with an omnidirectional source, a driver prolonged by a tube of diameter 30 mm and length 1.5 m. Here again the responses have been filtered on the third octave bands centered on the resonant frequencies of the dipole transducers. The sound pressure level is then calculated by integration of the filtered responses. The free field spectra of the various sources used are presented in Fig. 10.

The measurements were compared to theoretical predictions that have been adjusted with the filtered spectra of the corresponding sources. Hard ground was modeled by means of varnished plywood panels. Two different impedance grounds were modeled using a two-parameter model,[14] a carpet with equivalent parameters $\sigma_e = 10$ kPa s m^{-2} and $\alpha_e = 100$ m^{-1} and rough rubber mat sheets, with $\sigma_e = 8$ kPa s m^{-2} and $\alpha_e = 2000$ m^{-1}. Characterizations of these two materials by means of Excess Attenuation measurements are presented in Fig. 11. Barrier measurements have been made using a steel plate as a rigid thin screen.

B. Impedance discontinuity

In our experiments, the carpet and the rough rubber mat are used to create a mixed impedance ground surface. Figure 12 shows the variations of the sound pressure level with the percentage of the harder ground (rubber mat) on the source receiver path. The source height is 0.035 m above the rubber mat and the receiver height is 0.025 m. The source–receiver range is 0.75 m and there is no offset ($x_S = x = 0$). The data shown correspond to the measurements for a monopole (dots), a horizontal dipole along the y axis (squares), and a

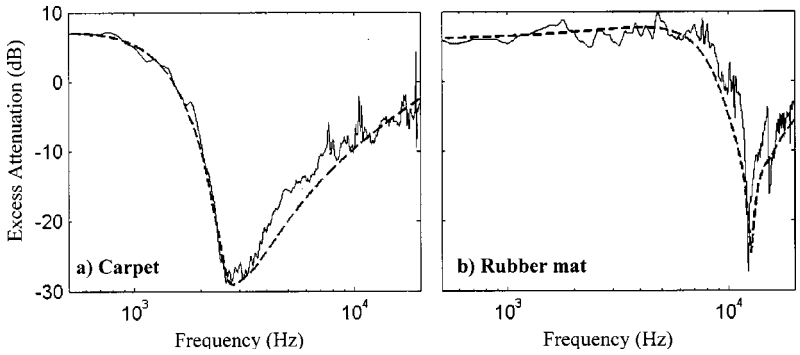

FIG. 11. Characterization of the two types of ground used. The solid lines show measurements for a separation of 0.75 m and source and receiver heights of 0.035 and 0.025 m, respectively, referenced to free field measurements. The dashed lines show predictions using a two-parameter ground model (Ref. 14) with the following values: (a) $\sigma_e = 10$ kPa s m^{-2}; $\alpha_e = 75$ m^{-1} for the carpet; (b) $\sigma_e = 8$ kPa s m^{-2}; $\alpha_e = 2000$ m^{-1} for the rubber mat.

vertical dipole (triangles). They are compared with the theory: the dotted line shows the predictions for the monopole, the solid line for the horizontal dipole, and the dashed line for the vertical dipole. The sound pressure levels have been normalized at the point of discontinuity in Figs. 12 and 13 in order to give a better comparison of the trends at this point, particularly in the change of slope observed when the surface on which the reflection occurs changes.

The continuity of the pressure field is well respected when the specular reflection occurs on the discontinuity line (about 58% of rubber mat on the source-receiver path). Nevertheless, we can observe a discrepancy in Fig. 12 between the theory and the measurements when the percentage of the harder ground tends to zero. This is also observed for a monopole source and may therefore be a fault inherent to De Jong's model. It is, however, slightly more important in the case of a dipole, probably due to the use of an approximate formula for the derivatives of the reflection coefficients. Outside this region, where the percentage of harder ground is larger, the agreement between measurements and theory is generally very good. There is a discrepancy between predictions of measurements for a vertical dipole in Fig. 12(b) for the range 50%–60% of hardest ground. In view of the good results obtained for other configurations this can be explained by a slight deviation in the orientation of the piezoceramic source used for the corresponding set of measurements.

As in the case of propagation above a homogeneous boundary,[10] we can observe from Fig. 12 that the behavior of the horizontal dipole is very similar to that of a monopole. The behavior of the vertical dipole is somewhat different. This can be explained, as mentioned earlier in Sec. II E, when commenting upon Fig. 5, by the relative orientations of the sources and their images.

Figure 13 shows the variations of the sound pressure level with source–receiver range. The source is at height 0.035 m above the rubber mat and 0.6 m away from the discontinuity ($y_e = 0; y_S = -0.6$ m). The receiver is located 0.025 m above the ground and its position varies from $y = -0.1$ m to $y = 0.9$ m. Here again, the sound field of a horizontal dipole (solid line) is almost indistinguishable from that due to a monopole (dotted line). The vertical dipole (dashed line) is more sensitive to the change in the value of the admittance, as one can observe a more important change of slope in the decrease of the sound pressure level with range when the specular reflection occurs on the second type of ground. The agreement with the experimental data for the three types of source (dots for monopole, squares and triangles for horizontal and vertical dipole, respectively) is again very good.

Figure 14 shows the variations of the sound pressure level for a horizontal dipole along the discontinuity (x axis) with the source–receiver offset $x - x_S$ (solid line for the theory and crosses for the experimental data). The results for a monopole are shown for comparison (dotted line: theory, dots: measurements). The source is 0.035 m above the rub-

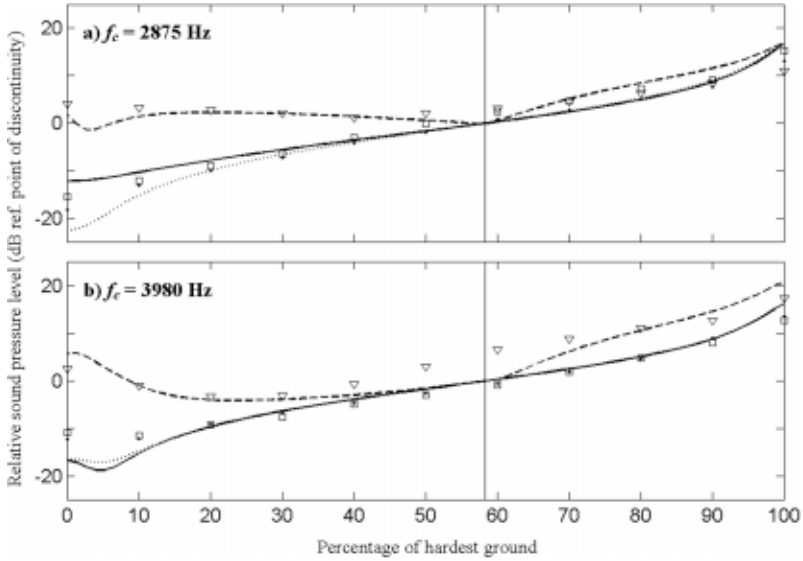

FIG. 12. Sound field above an admittance step for a monopole (dotted line for the theory; dots for the experimental data), a horizontal dipole (solid line: theory; squares: measurements) and a vertical dipole (dashed line: theory; triangles: measurements) as a function of the percentage of the hardest ground (rubber mat). The two ground models are those presented in Fig. 11. The source is located at height $z_s = 0.035$ m above the rubber mat, the receiver height is $z = 0.025$ m. The source–receiver range is $y - y_S = 0.75$ m and there is no offset ($x - x_S = 0$). The results are referenced to the predicted SPL at the point where the specular reflection occurs at the discontinuity (58% of harder ground), materialized by the vertical solid line.

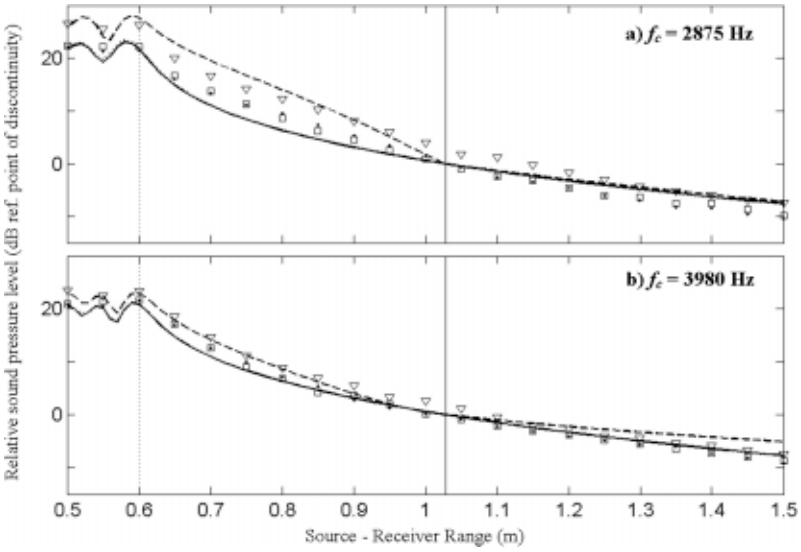

FIG. 13. Sound field above a rubber mat–carpet discontinuity for a monopole (dotted line for the theory; dots for the experimental data), a horizontal dipole (solid line: theory; squares: measurements) and a vertical dipole (dashed line: theory; triangles: measurements) as a function of the source–receiver range. The discontinuity is located at $y=0$. The source is located at height $z_S=0.035$ m above the rubber mat and at $y_S=-0.6$ m, the receiver at $z=0.025$ m. The source–receiver distance $y-y_S$ varies from 0.5 to 1.5 m and there is no offset ($x-x_S=0$). The results are referenced to the predicted SPL at the point where the specular reflection occurs at the discontinuity ($y-y_S=1.027$ m), materialized by the vertical solid line.

ber, 0.2 m away from the discontinuity and the receiver is 0.025 m above the carpet, 0.3 m away from the discontinuity. When there is no offset, there is no sound field, as the receiver is located in the midplane of the dipole source. The sound pressure level then increases with the offset following the directivity function of the source and reaches a stable value when the offset is roughly of the same order as the source–receiver distance as increases in the directivity index are compensated by longer ranges. Here again, the agreement in between the predictions and the experimental data is very good.

C. Barrier measurements

The study of the sound field in the presence of a barrier over the ground involves images with respect to the ground as well as the obstacle. This is particularly interesting in the light of the remarks we have made in Sec. II E.

Figures 15, 16, and 17 show the variations of the sound field with the receiver position when the ground is hard on both sides, hard on the source side and covered with carpet on the receiver side, and covered with carpet on both sides, respectively. The height of the screen is $z_e=0.22$ m and it is located at $y_e=0$. The source is located at $x_S=0$; $y_S=-0.3$ m; $z_S=0.1$ m and the receiver is located at $x=0$ and $z=0.05$ m. The dots show the experimental results for a monopole, the squares for a horizontal dipole along the y axis (perpendicular to the edge of the screen), and the triangles for a vertical dipole. They are compared with theoretical predictions with a dotted line for the monopole, a solid line for the horizontal dipole, and a dashed line for the vertical dipole. As in the case of the admittance discontinuity, the results shown here for the sound pressure level are based on an integration of the sound power over the third octave and centered at the resonant frequencies of the dipole sources (respectively, 2875 and 3980 Hz).

Agreement between the measurements and the predictions is very good. One may notice that, in the configuration chosen, the behavior of the dipoles is somewhat similar to that of the monopole, independently of the orientation. As we have mentioned in the beginning of this section, the image of the horizontal dipole with respect to the ground conserves the source orientation. This type of source behaves like a

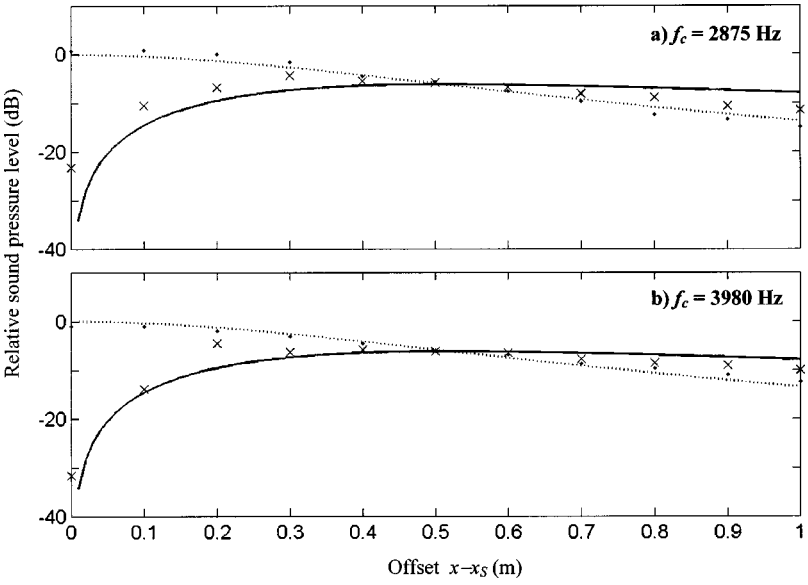

FIG. 14. Sound field above a rubber mat–carpet discontinuity for a monopole (dotted line for the theory; dots for the experimental data) and a horizontal dipole along the line of discontinuity (solid line: theory; squares: measurements) as a function of the offset $x-x_S$. The discontinuity is located at $y=0$. The source is located at $y_S=-0.2$ m, at height $z_s=0.035$ m above the rubber mat and the receiver at $y=0.3$ m, at height $z=0.025$ m above the carpet. The results for a monopole are referenced to the predicted SPL when there is no offset; those for the dipole are arbitrarily referenced.

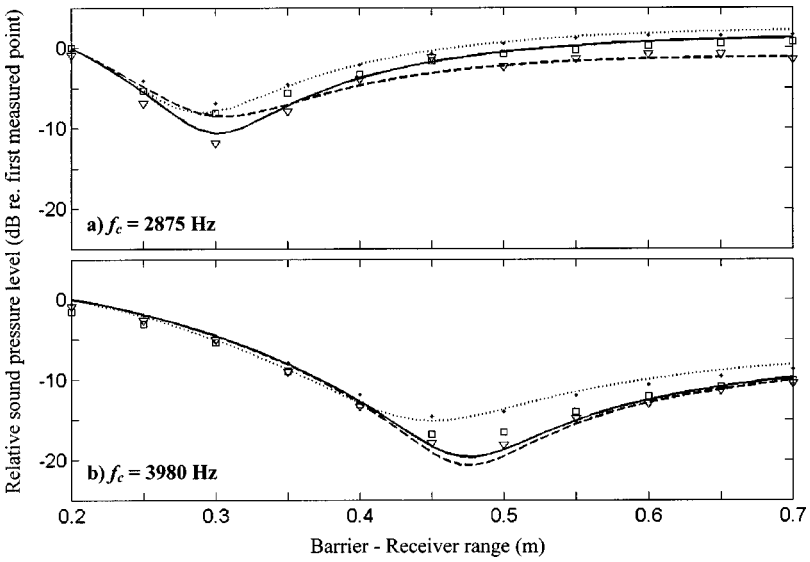

FIG. 15. Sound field diffracted by a rigid thin screen in the presence of ground for a monopole (dotted line for the theory; dots for the experimental data), a horizontal dipole (solid line: theory; squares: measurements) and a vertical dipole (dashed line: theory; triangles: measurements). The screen is located at $y_e=0$ and its height is $z_e=0.22$ m. The source coordinates are $x_S=0$; $y_S=-0.3$ m; $z_S=0.1$ m. The receiver is located at $x=0$ and $z=0.05$ m its distance from the barrier $y-y_e$ is the varying parameter. The ground on both sides is hard. The results are referenced to the total predicted SPL in the presence of the barrier at the first point considered ($y-y_e=0.2$ m).

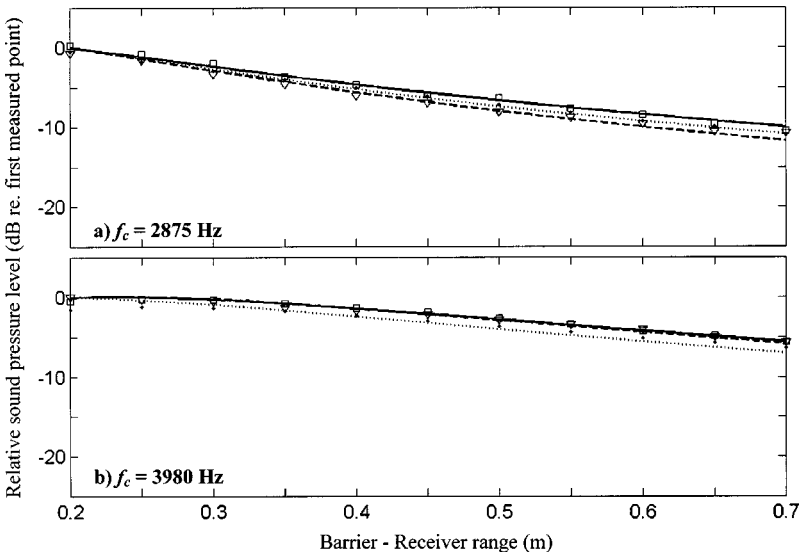

FIG. 16. The same as Fig. 15, except the ground is hard on the source side and covered with carpet on the receiver side.

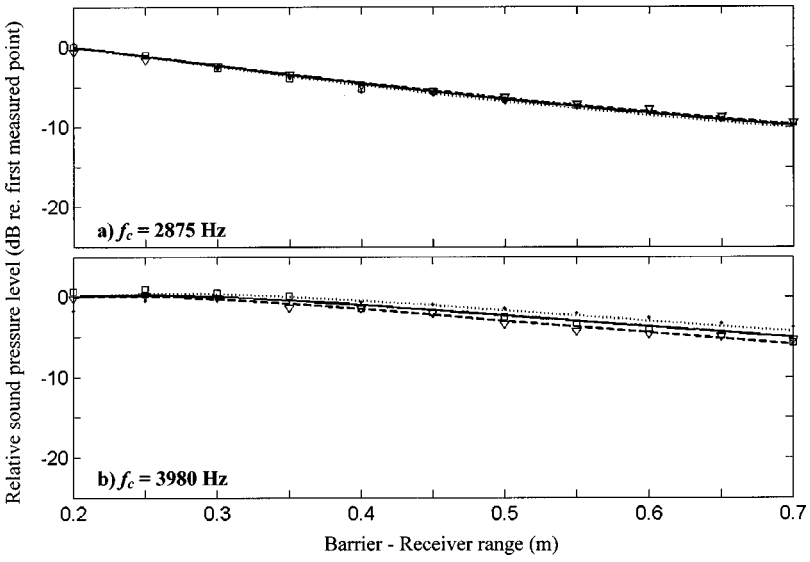

FIG. 17. The same as Fig. 15, except the ground is covered with carpet on both sides.

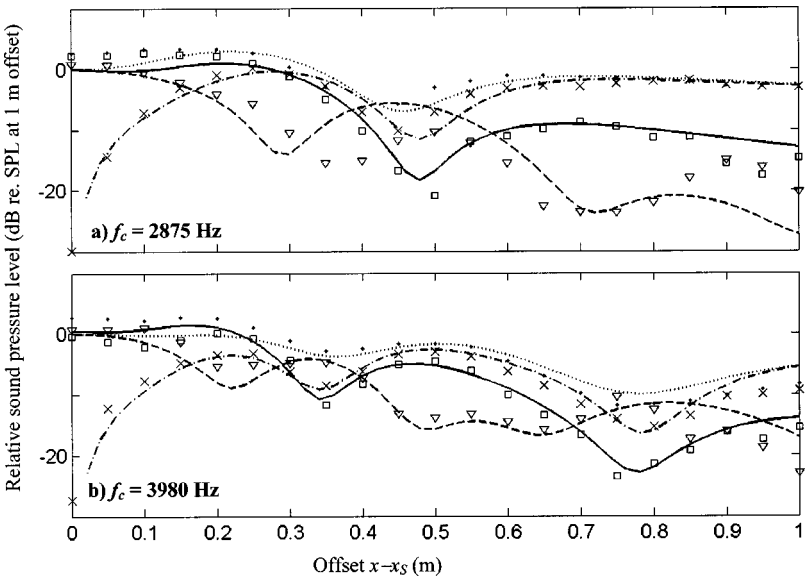

FIG. 18. Sound field as diffracted by a thin screen above hard ground as a function of the source–receiver offset $x-x_S$. Results are shown for a monopole source (dotted line: prediction; dots: measurements), a horizontal oriented along the y axis, perpendicularly to the edge of the screen (solid line: prediction; squares: measurements), a horizontal dipole oriented along the x axis, parallel to the edge (dashed–dotted line: prediction; crosses: measurements) and a vertical dipole (dashed line: prediction; triangles: measurements). The screen is 0.22 m high; both source and receiver are located at height 0.17 m; 0.1 away from the screen on each side. The results are referenced to the predicted SPL at null offset, except for the dipole along the x axis.

monopole for the ground reflection. On the other hand, its image with respect to the screen is inverted. It is the other way round for the vertical dipole whose sound field is similar to that due to a monopole as regards screen diffraction, but not for ground reflection. It appears from Figs. 15–17 that in the combination of both phenomena, the monopolar behavior is predominant. A remarkable consequence of this observation is in the acceptability of using monopole expressions as a rough estimate of the sound field due to directive sources in outdoor noise predictions involving barriers and screens for 2-D situations.

Finally, Fig. 18 shows the variations of the sound pressure level as a function of the source–receiver offset for our rigid thin screen above hard ground. Source and receiver are located relatively high above the ground: $z=z_S=0.17$ m—i.e., 0.05 m below the edge of the screen—and at a reasonably short distance away from the screen: $y=-y_S=0.1$ m. Four different sources were used: a monopole (dotted line: predictions; dots: measurements); a horizontal dipole along the y axis, perpendicular to the edge of the screen (solid line: predictions; squares: measurements); a horizontal dipole along the x axis, parallel to the edge (dashed–dotted line: predictions; crosses: measurements) and a vertical dipole (dashed line: predictions; triangles: measurements). Agreement between the experimental data and the predictions is generally very good. In view of the results shown in Fig. 18, the influence of the ground reflections is still critical, though the source and receiver are relatively high above the ground. This is confirmed by the fact that, unlike the vertical dipole and except when $kR \ll 1$, the horizontal dipoles behave in a way similar to a monopole source: with respect to the ground, the image source of a vertical dipole is inverted, whereas it keeps the original orientation in the case of a horizontal dipole. Unlike the 2-D situation, the dipole orientation seems to be crucial for the sound fields in the transverse direction when considering diffraction by a barrier in the presence of ground.

V. CONCLUDING REMARKS

A closed-form solution for the sound field due to a dipole source as diffracted by a hard wedge has been derived for arbitrary source and receiver positions. Based on Pierce's formulation for the diffraction of sound due to a point source,[2] this solution leads to an expression similar to the formulation according to Menounou's Directive Line Source Model.[6] By means of this solution for the diffracted dipole field, De Jong's semiempirical model for propagation above a ground discontinuity[4] has been extended. Similarly, an analytical formula has been derived for the calculation of the sound field due to dipole sources above the ground in the presence of a barrier. These practical cases have shown the influence of the source directivity on the prediction of the sound field. Particularly, in 2-D cases of barrier above ground, the dipole field is somewhat similar to that due to an omnidirectional point source. Nevertheless, in 3-D cases, the sound field in the transverse direction is very sensitive to the orientation of the source. This result is important in the context of screening of transportation noise where lines of incoherent dipoles may be used to model the noise source. For this reason, an extension of this work to more directional sources, such as quadrupoles, would be useful.

ACKNOWLEDGMENTS

The work reported in this paper has been conducted while one of the authors (M.B.) was on study leave at the Department of Mechanical Engineering, the Hong Kong Polytechnic University. The authors gratefully acknowledge the Research Committees of the Open University and the Hong Kong Polytechnic University for their partial financial support in this project. One of the authors (M.B.) was supported by an Open University Competitive Studentship. This work described in this paper was supported in part by EPRSC Grant No. GR L15326 and in part by the Research Grant Council of the Hong Kong SAR Government.

[1] J. J. Bowman and T. B. A. Senior, *Electromagnetic Waves and Acoustic Scattering by Simple Shapes* (North-Holland, Amsterdam, 1969).
[2] A. D. Pierce, "Diffraction of sound around corners and over barriers," J. Acoust. Soc. Am. **55**, 941–955 (1974).
[3] H. G. Jonasson, "Sound reduction by barriers on the ground," J. Sound Vib. **22**, 113–126 (1972).
[4] B. A. De Jong, A. Moekerken, and J. D. Van der Toorn, "Propagation of

sound over grassland and over an earth barrier,'' J. Sound Vib. **86**, 23–46 (1983).
[5] W. J. Hadden and A. D. Pierce, ''Sound diffraction around screens and wedges for arbitrary point source location,'' J. Acoust. Soc. Am. **69**, 1266–1290 (1981).
[6] P. Menounou, I. J. Busch-Vishniac, and D. T. Blackstock, ''Directive line source model: A new model for sound diffraction by half planes and wedges,'' J. Acoust. Soc. Am. **107**, 2973–2986 (2000).
[7] K. M. Li, M. Buret, and K. Attenborough, ''The propagation of sound due to a source moving at high speed in a refracting medium,'' *Proceedings of Euro-noise 98*, 1998, Vol. 2, pp. 955–960.
[8] A. D. Pierce, *Acoustics: An Introduction to its Physical Principles and Applications* (Acoustical Society of America, New York, 1989).
[9] P. M. Morse and U. Ingard, *Theoretical Acoustics* (McGraw-Hill, New York, 1968).
[10] K. M. Li, S. Taherzadeh, and K. Attenborough, ''Sound propagation from a dipole source near an impedance plane,'' J. Acoust. Soc. Am. **101**, 3343–3352 (1997).
[11] M. Abrahamowitz and I. Stegun, *Handbook of Mathematical Functions with Formulas, Graphs and Mathematical Tables*, 2nd ed. (Dover, New York, 1972).
[12] P. Boulanger, T. Watters-Fuller, K. Attenborough, and K. M. Li, ''Models and measurements of sound propagation from a point source over mixed impedance ground,'' J. Acoust. Soc. Am. **102**, 1432–1442 (1997).
[13] P. Koers, ''Diffraction by an absorbing barrier or by an impedance transition,'' *Proceedings of Internoise 83*, 1983, Vol. 1, pp. 311–314.
[14] K. Attenborough, ''Ground parameter information for propagation modeling,'' J. Acoust. Soc. Am. **92**, 418–427 (1997).
[15] D. D. Rife and J. Vanderkooy, ''Transfer-function measurements with Maximum Length Sequences,'' J. Audio Eng. Soc. **37**, 419–444 (1989).
[16] S. Peters, ''The prediction of Railway Noise Profiles,'' J. Sound Vib. **32**, 87–99 (1974).
[17] D. H. Cato, ''Prediction of environmental noise from fast electric trains,'' J. Sound Vib. **46**, 483–500 (1976).
[18] *Transportation Noise Reference Book*, edited by P. Nelson (Butterworths, London, 1987).

Observations of acoustic surface waves in outdoor sound propagation

Donald G. Albert[a)]
U.S. Army Cold Regions Research and Engineering Laboratory, 72 Lyme Road, Hanover, New Hampshire 03755-1290

(Received 8 October 2001; revised 6 January 2003; accepted 17 January 2003)

Acoustic surface waves have been detected propagating outdoors under natural conditions. Two critical experimental conditions were employed to ensure the conclusive detection of these waves. First, acoustic pulses rather than a continuous wave source allowed an examination of the waveform shape and avoided the masking of wave arrivals. Second, a snow cover provided favorable ground impedance conditions for surface waves to exist. The acoustic pulses were generated by blank pistol shots fired 1 m above the snow. The resultant waveforms were measured using a vertical array of six microphones located 60 m away from the source at heights between 0.1 and 4.75 m. A strong, low frequency ''tail'' following the initial arrival was recorded near the snow surface. This tail, and its exponential decay with height (z) above the surface ($\sim e^{-\alpha z}$), are diagnostic features of surface waves. The measured attenuation coefficient α was 0.28 m^{-1}. The identification of the surface wave is confirmed by comparing the measured waveforms with waveforms predicted by the theoretical evaluation of the explicit surface wave pole term using residue theory. © *2003 Acoustical Society of America.* [DOI: 10.1121/1.1559191]

PACS numbers: 43.28.En, 43.28.Fp, 43.35.Pt [LCS]

I. INTRODUCTION

In this paper experimental evidence confirming the existence of acoustic surface waves in a natural, outdoor setting is presented. Such waves require the proper ground surface impedance conditions to exist. While acoustic surface waves have been discussed for a long time in the literature, they have not been unequivocally observed in outdoor propagation experiments. Theory[1–4] predicts that these waves propagate horizontally near the ground at a phase velocity less than the velocity of sound in the air and decay exponentially with height above the surface. Laboratory measurements over hard-backed layers of felt or specially constructed model surfaces have detected these waves using both continuous and pulse sources.[3,5–16] A few outdoor experiments have revealed an increase in the received energy at low frequencies (greater than the 6 dB level expected from a rigid boundary),[3,17] but others have not detected such waves,[18] nor have they been observed in outdoor measurements over grass using pulses.[19–21] Raspet and Baird[22] give a convincing theoretical argument for their existence and Daigle *et al.*[14] present very clear evidence from indoor pulse experiments.

Theoretically, acoustic surface waves will exist when the imaginary part of the ground impedance exceeds the real part; this condition is expected for porous ground layers with a rigid backing. For outdoor experiments, one of the most favorable situations for acoustic surface waves is a thin layer of snow over frozen ground.[23,24] In this paper experiments that were conducted to search for surface waves under these favorable ground impedance conditions are discussed. The measured waves show the predicted exponential decay with height above the ground surface and the observed waveforms agree with those predicted by the theoretical evaluation of the surface wave pole using residue theory.

II. THEORY

The interaction of a spherical wave from a point source with a plane boundary is a classical problem in electromagnetics, acoustics, and seismology.[25–28] For a velocity potential ϕ, the analysis starts with the Sommerfeld representation of a monofrequency spherical wave as a sum of cylindrical waves,[25]

$$\phi = \frac{Ae^{ikr}}{r} = A\int_0^\infty \frac{e^{-\gamma|z|}}{\gamma} J_0(kr)\,k\,dk, \tag{1}$$

with J_0 the Bessel function of the first kind and zeroth order, k the radial wavenumber, z the depth coordinate, r the slant distance to the observation point, and

$$i\gamma = (k_0^2 - k^2)^{1/2}, \quad \mathrm{Re}(\gamma) > 0.$$

A coordinate transformation $k = k_0 \sin\theta$, where θ is complex[2,25] and $k_0 = \omega/c_0$ is the wavenumber in air, converts the integral in Eq. (1) into a contour integral. By substituting Hankel functions for the Bessel function and by using approximations for large kr, the reflected wave potential can be written as[2,21,25,29]

$$\phi^{\mathrm{rfl}} = A\left(\frac{k_0}{2\pi r}\right)^{1/2} e^{i\pi/4}\int_{-\pi/2+i\infty}^{-\pi/2-i\infty} e^{ik_0 r_2 \cos(\theta-\theta_0)} \times R_p(\theta)\sqrt{\sin\theta}\,d\theta, \tag{2}$$

where $R_p(\theta)$ is the plane wave reflection coefficient for angle of incidence θ and r_2 is the reflected ray path length (see Fig. 1). The integral can be evaluated by deforming the

a)Electronic mail: dalbert@crrel.usace.army.mil

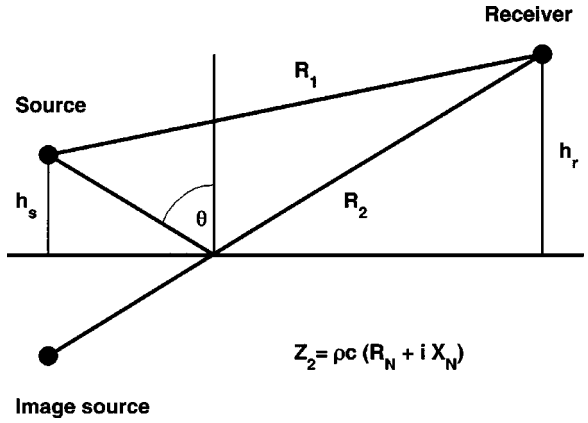

FIG. 1. Sketch of the geometry. The source and receiver are located in a homogeneous atmosphere above a plane ground surface with impedance Z_2.

contour to the steepest descent path, leading to an expression,[30–32]

$$\phi^{\mathrm{rfl}} = A\frac{e^{ik_0 r_2}}{r_2}[R_p + (1-R_p)F(w)], \tag{3}$$

where $F(w)$ is called the boundary loss factor and w is a numerical distance. The acoustic surface wave is not derived as a separate term in this approach, but if it exists [see Eq. (7) below] it is included in $F(w)$. With the addition of the direct wave term $Ae^{ik_0 r_1}/k_0 r_1$ where r_1 is the slant distance for the direct wave, the ''full waveform'' expression for the potential is obtained:

$$\frac{\phi}{A} = \frac{e^{ik_0 r1}}{r_1} + \frac{e^{ik_0 r_2}}{r_2}[R_p + (1-R_p)F(w)]. \tag{4}$$

The integrand of Eq. (2) has a pole where the denominator of the plane wave reflection coefficient,

$$R_p(\theta) = \frac{Z_2 \cos\theta - \rho c}{Z_2 \cos\theta + \rho c}, \tag{5}$$

is zero. Here $Z_2 = R + iX = \rho c(R_N + iX_N)$ is the characteristic specific impedance of the ground with normalized components R_N and X_N and a locally reacting ground surface has been assumed. The pole will give a contribution to the integral equation (2) when the deformation of the original contour to the steepest descent path crosses this pole; at grazing incidence this leads to the condition[2]

$$\left|\frac{X_N}{R_N}\right| \geq \left(1 + \frac{R_N^2}{(R_N^2 + X_N^2)^2}\right)^{-1/2}, \tag{6}$$

i.e., the surface wave exists when

$$\mathrm{Im}(Z_2) \geq \mathrm{Re}(Z_2). \tag{7}$$

Thus highly absorbing grounds will provide favorable conditions for acoustic surface waves to be observed. The contribution from the surface wave pole to the reflected pressure can be evaluated using residue theory to obtain[29,33]

$$\phi^{\mathrm{surf}} = -A\frac{k_0\beta}{2}e^{-ik_0 h\beta}H_0^{(1)}[k_0 r_2(1-\beta^2)^{1/2}], \tag{8}$$

where $H_0^{(1)}$ is the Hankel function of the first kind, $\beta = \rho c/Z_2$ and $h = h_s + h_r$ is the sum of the source and receiver heights. Donato[2] has shown that the theoretical surface wave phase velocity is

$$v = c\frac{X_N}{(1+X_N^2)^{1/2}}, \tag{9}$$

and the vertical attenuation is

$$\alpha = k_0\frac{X_N}{X_N^2 + R_N^2}. \tag{10}$$

The horizontal attenuation is the same as the decay in $H_0^{(1)} \sim r^{-1/2}$.

The acoustic pressure is related to the velocity potential by

$$P = -\rho_0\frac{\partial\phi}{\partial t} = -i\rho_0\omega\phi = \frac{P_0}{k_0 r}e^{i(k_0 r - \omega t)},$$

with

$$P_0 = -i\rho_0\omega k_0 A$$

representing the source strength in Pascals, and $-i$ representing a phase shift. Then the full waveform expression, Eq. (4), becomes

$$\frac{P}{P_0} = \frac{e^{ik_0 r1}}{k_0 r_1} + \frac{e^{ik_0 r_2}}{k_0 r_2}[R_p + (1-R_p)F(w)], \tag{11}$$

and the explicit expression for the surface wave pressure is

$$\frac{P^{\mathrm{surf}}}{P_0} = -\frac{\beta}{2}e^{-ik_0 h\beta}H_0^{(1)}[k_0 r_2(1-\beta^2)^{1/2}]. \tag{12}$$

III. EXPERIMENTAL MEASUREMENTS

A. Method

Experiments were designed to detect and identify surface waves by their chief property: their amplitude decay as a function of height above the ground surface. A microphone array was installed at an undisturbed site in Hanover, NH to obtain waveform measurements as a function of distance and height under various ground conditions, including grass, frozen ground, and various snow layers during the course of a winter. An impulsive source was selected so that the waveform characteristics could be used to identify all of the wave arrivals, rather than just recording the overall sound levels as for measurements using continuous wave sources.

The acoustic source was a .45 caliber blank pistol held at a height of 1 m and pointed toward the sensor array. A vertical array of Globe Model 100C low frequency microphones installed on a wooden tower 60 m away from the source were used as receivers. These microphones were positioned at heights of 0.5, 1, 1.5, 2, 3, and 4.75 m above the soil surface. A surface microphone (0.1 m high) also was placed at the ground or on the snow surface next to the tower just before the measurements were made (Fig. 2). The received waveforms were recorded using a Bison Model 9048 digital seismograph at a 5-kHz rate. The bandwidth of the instruments is 3 Hz to 2 kHz, but the overall bandwidth of the measurements is limited by the source output and is estimated as 5–500 Hz.

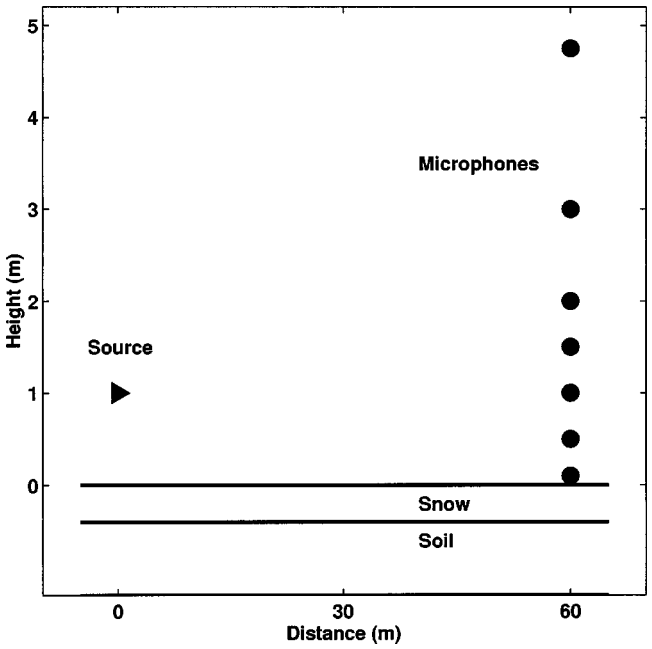

FIG. 2. Sketch of the experimental measurement geometry. The source (triangle) was a pistol firing blanks towards the microphones (circles), which were located 60 m away at heights of 0.1 m above the soil or snow surface, and 0.5, 1, 1.5, 2, 3, and 4.75 m above the soil surface. With this geometry, the grazing angle for the specularly reflected wave varied from less than 1° to 4.8°. (This sketch is not to scale, and the snow cover thickness is greatly exaggerated.)

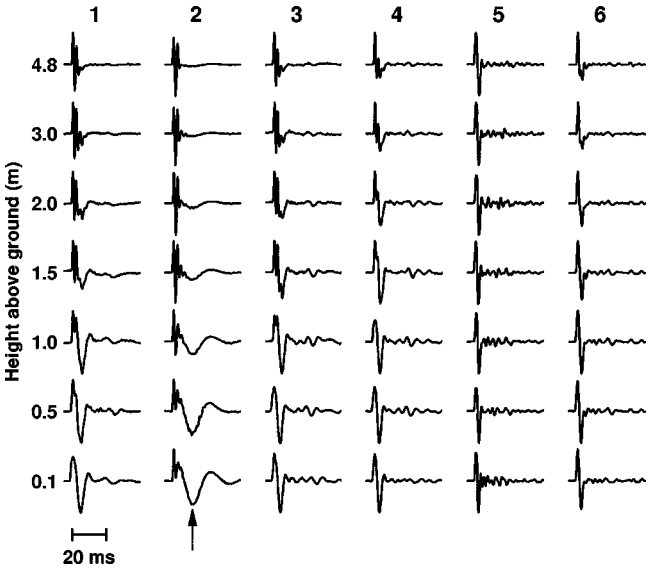

FIG. 3. Normalized low frequency microphone waveforms recorded at a 60 m range and various heights from a .45 caliber pistol shot 1 m high above the snow or ground surface. These waveforms were recorded with the same microphone array on six separate days. An arrow points to the "tail" identified as the surface wave; it is present only when snow was on the ground. Experiment numbers at the top of the columns refer to the parameters listed in Table I. Experiments 1 and 2 were conducted over dry snow covers, 3 over a wet, ripe snow cover, 4 over discontinuous wet snow, 5 over bare frozen ground, and 6 over grass. The surface wave is present in Experiments 1–4, but is strongest over the dry snow cover in Experiment 2. This case will be analyzed in the rest of the paper.

The snow and frost depths and the snow stratigraphy, temperature, density, grain size, and crystal type were determined for each snow layer present. Meterological data were collected using a Campbell Scientific Model 21X data logger. Temperatures were measured within the ground and snow and at various heights up to 5 m in the air. Wind speeds and directions were also recorded, along with relative humidity and barometric pressure.

B. Observations

Figure 3 shows the waveforms recorded by the tower microphones for one of the eight shots recorded on each of six separate occasions, in chronological order from left to right. In columns 1 and 2, the waveforms were recorded over cold, dry, continuous snow covers. The waveforms in columns 3 and 4 were recorded over wet, ripe snowpacks, with the snow cover for Experiment 4 nonuniform in depth because the snowmelt had begun. The waveforms in columns 5 and 6 were recorded over bare frozen ground and unfrozen grassland, respectively. The snow cover and ground characteristics for these measurements are given in Table I. The waveforms recorded without snow present (columns 5 and 6) show virtually no change in shape as a function of receiver height above the surface. Those recorded over snow show an initial pulse followed by a low frequency "tail" that decreases in amplitude with microphone height above the surface. This tail is identified as the acoustic surface wave. The acoustic surface wave is especially clear in the waveforms recorded during Experiment 2, over a 0.21-m-thick snow cover, so this particular experiment will be examined in the rest of this paper.

Figure 4 shows a semilogarithmic plot of the surface wave amplitude as a function of height for the eight shots recorded during Experiment 2. The absolute value of the amplitude of the negative portion of the surface wave (marked with an arrow in Fig. 3) is plotted, as these amplitudes were easy to determine without interference from the initial impulse. These values fall on a nearly straight line,

$$P(z)=P_0(r)e^{-\alpha z}, \tag{13}$$

as expected for an exponential decay where α is the decay coefficient and z the height. The slope obtained by a least squares fit (shown as a dashed line in the figure) to the lower microphones gives $\alpha=0.28\pm0.1\ \mathrm{m}^{-1}$.

Some of the deviation of the amplitudes shown in Fig. 4 from a straight line is likely to be caused by differences in microphone sensitivity. Attempts were made to calibrate the Globe microphones using a pistonphone, but difficulty in coupling the pistonphone consistently to the microphones using a special adapter made this procedure questionable, so the manufacturer's sensitivity values have been used. The figure also shows that the amplitude values for a given microphone were very consistent, indicating that the blank pistol output was also consistent from shot to shot. The microphone sensitivity differences will not affect the analysis based on waveform shape.

IV. COMPARISON WITH THEORY

To compare the measurements with theoretical predictions, a waveform inversion procedure[34] was used to derive the acoustic parameters of the snow or soil. In this method,

TABLE I. Snow cover and ground parameters for the experimental measurements shown in Fig. 3.

Experiment number	Description	Effective flow resistivity σ (kN s m^{-4})	Snow depth (cm)	Porosity Ω	Density (kg m^{-3})
1	Dry snow, flat grains	55	5	0.89	100
2	Dry snow, spherical grains	11	21	0.81	170
3	Wet ripe snow	59	5	0.68	290
4	Patchy wet snow	140	3	0.74	240
5	Frozen ground	1400	-	0.34	1600
6	Grass	300	-	0.34	1600
	Lower half space (frozen soil)	3000	-	0.27	1750

Attenborough's rigid porous, layered model of ground impedance[35,36] is used to calculate theoretical waveforms for the surface microphone using the full waveform expression, Eq. (11), above. The model parameters were varied using a simplex search algorithm until good agreement was obtained between the theoretical and the observed waveforms. Albert[34] has shown that for the low frequencies and short propagation ranges used in these experiments, a unique solution is obtained and both the meteorological conditions and the details of the snow layering are relatively unimportant. Since the acoustic wavelengths range from about 0.75 m at 400 Hz to 7.5 m at 40 Hz, sufficient accuracy is obtained by considering the snow to be a single layer on top of a frozen soil halfspace. The acoustic parameters determined by the waveform inversion method are listed in Table I.

Using this method of waveform inversion to determine the ground impedance was critical to the success in accurately modeling the acoustic surface waves. Although a forward modeling approach (guessing the snow parameters used to calculate the waveforms) was able to predict the general behavior of the waves,[37] the theoetical waveforms did not match the measured waveforms very well until this inversion method was used to accurately determine the snow parameters. This sensitivity of the waveforms to the ground impedance parameters also has been noted by Daigle and co-workers.[14]

Once the acoustic snow cover parameters were obtained by matching the observed waveforms at the surface, theoretical waveforms were calculated at the remaining measurement heights. Figure 5 compares the measured and theoetical waveforms for all of the microphone heights for Experiment 2. The waveforms agree well not only for the surface microphone, where the inversion procedure was used to derive the snow parameters, but also for all of the microphones at different heights, showing that the full waveform solution correctly predicts the surface wave decay with height. The the-

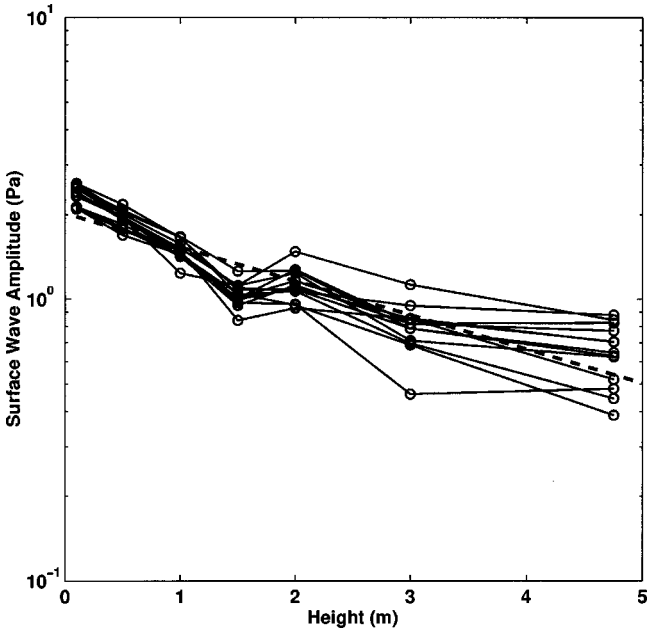

FIG. 4. Amplitude of the negative portion of the surface waveform as a function of height for eight shots recorded during Experiment 2 with a 0.21-m-thick snow cover present. A least squares fit of the measurements is shown by a dashed line and gives a decay constant of $\alpha = 0.28 \pm 0.1$ m^{-1}.

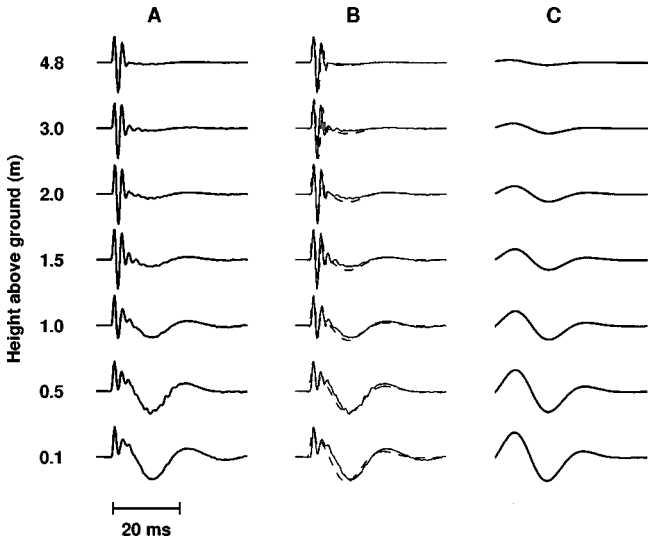

FIG. 5. A comparison between normalized measured and theoetical waveforms at a 60 m range for Experiment 2 with a 0.21-m-thick snow cover present on the ground. The parameters used in these calculations are given in Table I. Column (A) The measured waveforms as a function of height. Column (B) Overlay of the measured (solid lines) and theoretical (dashed lines) waveforms calculated using Eq. (11). Column (C) Theoretical surface wave term calculated using Eq. (12), and plotted at the same amplitude as the theoretical waveforms in Column (B).

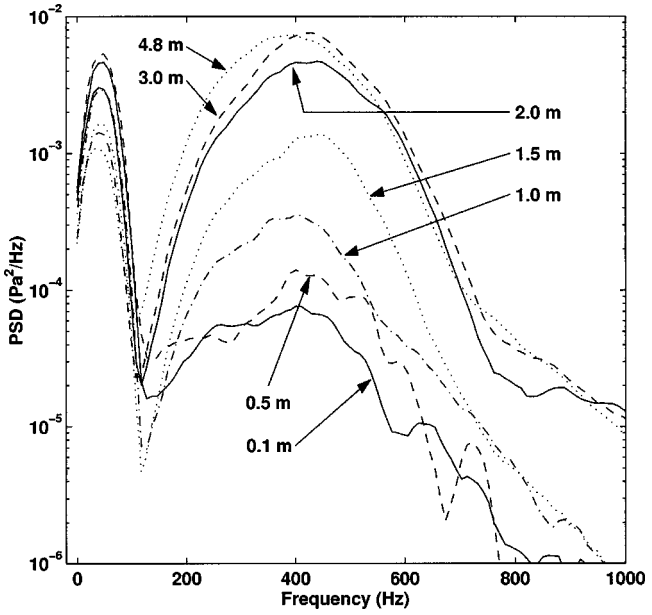

FIG. 6. Power spectral densities calculated from the measured waveforms for Experiment 2. The solid, dashed, dot–dashed, and dotted lines are the spectra for microphones at heights of 0.1, 0.5, 1, and 1.5 m, respectively. These spectra are the largest at 40 Hz and the smallest at 400 Hz. The remaining solid, dashed, and dotted lines are the spectra for microphones at 2, 3, and 4.75 m.

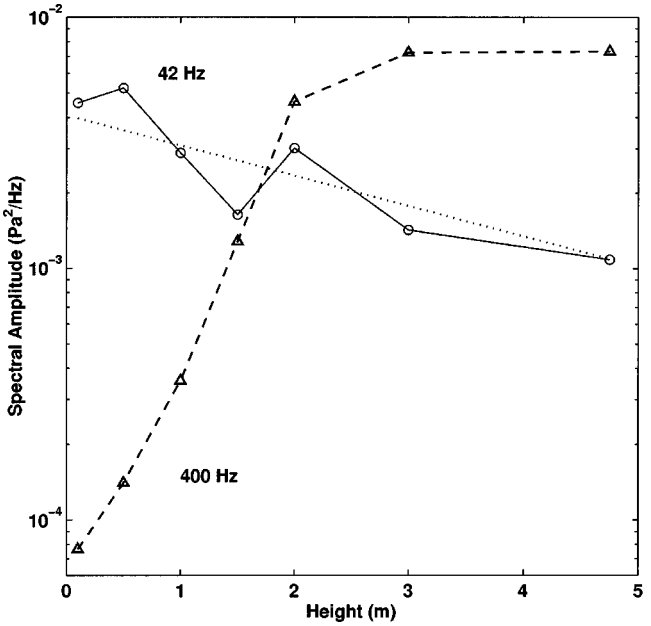

FIG. 7. The spectral amplitude as a function of height for the measured waveforms for Experiment 2, at 42 Hz (circles and solid line) and at 400 Hz (triangles and dashed line). The dotted line shows the attenuation trend for $\alpha = -0.28$ in Eq. (13) and in Fig. 4.

oretical surface wave pulses detemined using Eq. (12) are also shown in the figure. These waveforms match the shape and decay with height of the observed surface wave ''tail,'' conclusively confirming the identification of this waveform as an acoustic surface wave. The theoretical waveforms also exhibit noncausal behavior; the pressure waveform begins slightly before the direct wave arrival. This noncausal behavior is commonly observed in surface wave calculations in seismology, and arises because terms which would cancel out the early arrivals in the full waveform calculation have been neglected in the approximate surface wave expression given by Eq. (12). Nevetheless, the agreement between the measured data and the theoretical surface wave pulse from Eq. (12) is strong evidence that the acoustic surface wave has been correctly identified in the measurements.

Figure 6 shows the frequency content of the measured waveforms for Experiment 2. The calculations used the multiple window method of Thomson.[38] The peak at 42 Hz is attributed to the surface wave, and agrees approximately with the period of the waveform for the microphone at the surface (about 25 ms). As shown in Fig. 7, the spectral amplitude at this frequency decreases as the microphone height increases, and this decrease agrees with the trend determined for the surface wave in the time domain shown in Fig. 4. At 400 Hz, the largest spectral amplitudes occur for the higher microphones. These spectra show that high frequencies are attenuated and low frequencies enhanced for microphones close to the snow cover surface (Fig. 4 of Ref. 39).

The acoustic surface impedance predicted using Attenborough's model for Experiment 2 is shown in Fig. 8. This plot shows that $\mathrm{Im}(Z_2) > \mathrm{Re}(Z_2)$ for frequencies less than 115 Hz where a surface wave is expected according to Eq. (7). This result is consistent with the measured power spectra shown in Fig. 6 if we identify the low frequency portion of the spectra (with a peak at about 42 Hz) with the acoustic surface wave. The surface wave phase velocity and attenuation calculated from the impedance using Eqs. (9) and (10) are also shown in Fig. 8. The surface wave velocity is less

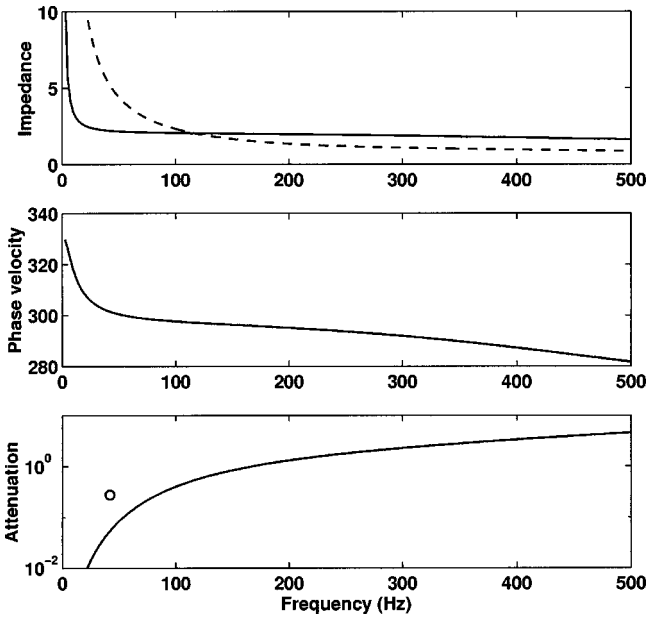

FIG. 8. Acoustic surface wave properties for Experiment 2. The top panel shows the surface impedance as predicted using Attenborough's ground impedance model and the parameters determined from the waveform inversion analysis. The real part of the impedance is given by the solid line, while the dashed line shows the absolutue value of the imaginary part. The phase velocity ($\mathrm{m\,s^{-1}}$) and attenuation ($\mathrm{m^{-1}}$) are shown in the center and bottom panels, respectively. These values were calculated using Eqs. (9) and (10) and the impedance shown in the top panel. Note that the surface wave is only expected to exist for frequencies below 115 Hz, based on Eq. (7). The circle plotted in the bottom panel is the attenuation measured in Fig. 4.

than the speed of sound in air, as expected and in agreement with the identification of the low frequency tail that arrives after the direct and reflected waves as the acoustic surface wave. The measured attenuation of 0.28 m^{-1} (from Fig. 4) is plotted at the peak frequency, 42 Hz, of the surface wave spectrum, and agrees with the theoetical attenuation, given the accuracy of the attenuation measurement as discussed above.

V. CONCLUSIONS

Acoustic surface waves have been experimentally observed propagating above a snow cover. The similarity between the observed and theoetical waveform shapes that were calculated using an explicit surface wave expression [Eq. (12)] is especially strong evidence that the identification of the observed waveforms as acoustic surface waves is correct. The acoustic surface wave for a 0.21-m-thick snow cover was observed to decay exponentially with height above the surface, with a decay constant of 0.28 m^{-1}. The results also indicate that the details of the layering within the snow are relatively unimportant, at least for these particular snow covers. Surface waves were not observed over grass or bare frozen ground, also in agreement with theoretical expectations.

ACKNOWLEDGMENTS

I thank Gilles Daigle for useful discussions at the Fourth International Symposium on Long Range Sound Propagation that led to these experiments, and for comments on early versions of the manuscript. Many of my coworkers assisted with these experiments; I would especially like to thank Steve Decato for serving as the shooter and Nancy Greeley for providing the meterological data. They also performed the snow characterization and provided additional assistance with the experiments. Thanks also goes to Steve Arcone and two anonymous reviewers for useful comments, and to the Associate Editor Lou Sutherland for many suggested improvements. This work is supported by the Directorate of Research and Development, U.S. Army Corps of Engineers.

[1] L. M. Brekhovskikh, ''Surface waves in acoustics,'' Sov. Phys. Acoust. **5**, 3–12 (1959).
[2] R. J. Donato, ''Propagation of a spherical wave near a plane boundary with complex impedance,'' J. Acoust. Soc. Am. **60**, 34–39 (1976).
[3] S. I. Thomasson, ''Sound propagation above a layer with large refractive index,'' J. Acoust. Soc. Am. **61**, 659–674 (1977).
[4] A. R. Wenzel, ''Propagation of waves along an impedance boundary,'' J. Acoust. Soc. Am. **55**, 956–963 (1974).
[5] J. Tizianel, J.-F. Allard, W. Lauriks, and L. Kelders, ''Experimental localization of a pole of the reflection coefficient of a porous layer,'' J. Sound Vib. **202**, 600–604 (1997).
[6] J. Tizianel, J. F. Allard, and B. Brouard, ''Surface waves above honeycombs,'' J. Acoust. Soc. Am. **104**, 2525–2528 (1998).
[7] W. Lauriks, L. Kelders, and J.-F. Allard, ''Surface waves and leaky waves above a porous layer,'' Wave Motion **28**, 59–67 (1998).
[8] W. Lauriks, L. Kelders, and J. F. Allard, ''Surface waves above gratings having a triangular profile,'' Ultrasonics **36**, 865–871 (1998).
[9] L. Kelders, W. Lauriks, and J. F. Allard, ''Surface waves above thin porous layers saturated by air at ultrasonic frequencies,'' J. Acoust. Soc. Am. **104**, 882–889 (1998).
[10] L. Kelders, J. F. Allard, and W. Lauriks, ''Ultrasonic surface waves above rectangular-groove gratings,'' J. Acoust. Soc. Am. **103**, 2730–2733 (1998).
[11] J. F. Allard, L. Kelders, and W. Lauriks, ''Ultrasonic surface waves above a doubly periodic grating,'' J. Acoust. Soc. Am. **105**, 2528–2531 (1999).
[12] G. Daigle and T. Embleton, ''Air–ground interface: surface waves, surface impedance and acoustic-to-seismic coupling coefficient,'' *Proceedings of the 4th International Symposium on Long-Range Sound Propagation*, NASA CP 3101, NASA, Hampton, VA, 17 May 1990, pp. 27–40.
[13] G. A. Daigle, ''Role of surface waves in outdoor noise propagation,'' *1991 International Conference on Noise Control Engineering (Inter-Noise 91)*, Noise Control Foundation, Poughkeepsie, NY, Sydney, Australia, 2–4 December 1991.
[14] G. A. Daigle, M. R. Stinson, and D. I. Havelock, ''Experiments on surface waves over a model impedance plane using acoustical pulses,'' J. Acoust. Soc. Am. **99**, 1993–2005 (1996).
[15] R. J. Donato, ''Model experiments on surface waves,'' J. Acoust. Soc. Am. **63**, 700–703 (1978).
[16] M. R. Stinson, G. A. Daigle, and D. I. Havelock, ''The formation of surface waves over a model surface,'' *Proceedings of the 5th International Symposium on Long Range Sound Propagation*, Milton Keynes, England, 24–26 May 1992, pp. 17–28.
[17] K. B. Rasmussen, ''Sound-propagation over grass covered ground,'' J. Sound Vib. **78**, 247–255 (1981).
[18] J. Nicolas, J.-L. Berry, and G. A. Daigle, ''Propagation of sound above a finite layer of snow,'' J. Acoust. Soc. Am. **77**, 67–73 (1985).
[19] C. G. Don and A. J. Cramond, ''Impulse propagation in a neutral atmosphere,'' J. Acoust. Soc. Am. **81**, 1341–1349 (1987).
[20] R. Raspet, H. E. Bass, and J. Ezell, ''Effect of finite ground impedance on the propagation of acoustic pulses,'' J. Acoust. Soc. Am. **74**, 267–274 (1983).
[21] R. Raspet, J. Ezell, and H. E. Bass, ''Additional comments on and erratum for 'Effect of finite ground impedance on the propagation of acoustic pulses' [J. Acoust. Soc. Am. **74**, 267–274 (1983)],'' J. Acoust. Soc. Am. **77**, 1955–1958 (1985).
[22] R. Raspet and G. E. Baird, ''The acoustic surface wave above a complex impedance ground surface,'' J. Acoust. Soc. Am. **85**, 638–640 (1989).
[23] G. A. Daigle (personal communication, 1990).
[24] K. Attenborough, ''Review of ground effects on outdoor sound propagation from continuous broadband sources,'' Appl. Acoust. **24**, 289–319 (1988).
[25] K. Aki and P. G. Richards, *Quantitative Seismology: Theory and Methods* (Freeman, San Francisco, 1980), Vol. 1, p. 155.
[26] W. M. Ewing, W. S. Jardetzky, and F. Press, *Elastic Waves in Layered Media* (McGraw-Hill, New York, 1957).
[27] P. M. Morse and K. U. Ingard, *Theoretical Acoustics* (Princeton University Press, Princeton, NJ, 1968), p. 927.
[28] J. A. Stratton, *Electromagnetic Theory* (McGraw-Hill, New York, 1941).
[29] C. F. Chien and W. W. Soroka, ''Sound propagation along an impedance plane,'' J. Sound Vib. **43**, 9–20 (1975).
[30] I. Rudnick, ''Propagation of an acoustic wave along a boundary,'' J. Acoust. Soc. Am. **19**, 348–356 (1947).
[31] K. U. Ingard, ''On the reflection of a spherical wave from an infinite plane,'' J. Acoust. Soc. Am. **23**, 329–335 (1951).
[32] K. Attenborough, S. I. Hayek, and J. M. Lawther, ''Propagation of sound above a porous half-space,'' J. Acoust. Soc. Am. **68**, 1493–1501 (1980).
[33] C. F. Chien and W. W. Soroka, ''A note on the calculation of sound propagation along an impedance surface,'' J. Sound Vib. **69**, 340–343 (1980).
[34] D. G. Albert, ''Acoustic waveform inversion with application to seasonal snow covers,'' J. Acoust. Soc. Am. **109**, 91–101 (2001).
[35] J. M. Sabatier, R. Raspet, and C. K. Frederickson, ''An improved procedure for the determination of ground parameters using level difference measurements,'' J. Acoust. Soc. Am. **94**, 396–399 (1993).
[36] K. Attenborough, ''Acoustical impedance models for outdoor ground surfaces,'' J. Sound Vib. **99**, 521–544 (1985).
[37] D. G. Albert, ''Observations of acoustic surface waves propagating above a snow cover,'' in Ref. 16, 1992, pp. 10–16.
[38] D. J. Thomson, ''Spectrum estimation and harmonic analysis,'' Proc. IEEE **70**, 1055–1096 (1982).
[39] D. G. Albert and J. A. Orcutt, ''Acoustic pulse propagation above grassland and snow: Comparison of theoretical and experimental waveforms,'' J. Acoust. Soc. Am. **87**, 93–100 (1990).

Backscatter from a limestone seafloor at 2–3.5 kHz: Measurements and modeling

Raymond J. Soukup[a] and Robert F. Gragg[b]
Naval Research Laboratory, Washington, DC 20375-5350

(Received 11 April 2002; revised 23 December 2002; accepted 6 January 2003)

Physics-based interface scattering models for the seafloor [H.-H. Essen, J. Acoust. Soc. Am. **95**, 1299–1310 (1994); Gragg *et al.*, *ibid.* **110**, 2878–2901 (2001)] exhibit features in their predicted grazing angle dependence. These features have a strong dependence on the assumed composition and roughness of the bottom. Verifying such predictions requires data that cover a wide range of grazing angles and involve minimal sub-bottom penetration. Such measurements were performed in the frequency band 2–3.5 kHz over an exposed limestone bottom off the Carolina coast during the second Littoral Warfare Advanced Development Focused Technology Experiment of 1996 (LWAD FTE 96-2). Direct-path bottom scattering strengths were obtained in shallow water (198–310 m deep) for grazing angles from 8° to 75° using data fusion from multiple experimental geometries coupled with careful signal processing. The processing included corrections for the surface-reflected path, other multipaths, and characteristics of the reverberation decay observed over the pulse duration at higher grazing angles. The resulting frequency and grazing-angle dependences exhibit trends consistent with theoretical predictions, and geoacoustic parameters obtained by inversion are consistent with values expected for limestone. [DOI: 10.1121/1.1558039]

PACS numbers: 43.30.Hw, 43.30.Gv, 43.30.Pc [RAS]

I. INTRODUCTION

The aim of our current research is to test theoretical predictions of the grazing angle and frequency dependence of acoustic scattering from a rough interface, using data collected from the ocean bottom or from a tank experiment. In this paper, we describe a bottom scattering dataset, collected over a limestone ocean bottom, that exhibits consistent features in its grazing angle dependence. When we perform fits to the grazing angle and frequency dependence of the data, we obtain plausible estimates of the geophysical and roughness parameters and are able to determine the relative influence of those parameters on the scattering behavior. The analysis establishes that the measured grazing angle and frequency dependencies are supportable by a physics-based model.

The general problem of characterizing seafloor scattering can be quite involved because the scattered field includes contributions from the water/bottom interface and the sub-bottom (inhomogeneous sediment volume and layering). Cable *et al.*[1] show the diversity of overall scattering levels to be expected from marine environments and compare the results to empirical models. Measurements from the series of Critical Sea Tests (CST)[2] support a variety of frequency and grazing angle dependencies in the range 100 Hz–1 kHz, showing the need for a more refined, physics-based model. In many of the CST environments, the sub-bottom, rather than the interface, was found to drive the observed scattering. Generally, bottom scattering depends on both interface and sub-bottom components, with the relative acoustic significance dependent on transmit frequency, source level, grazing angle, and bottom parameters such as sediment thickness, and attenuation.[3] Holland *et al.*[4] also examine the roles of interface and sub-bottom scattering in the 400–4000 Hz band, using a direct-path measurement technique and inferring interface and sub-bottom contributions from the characteristics of the scattering strength versus grazing angle curve. In the present paper, we provide approaches to data processing that complement the techniques used by Holland *et al.*, with a special emphasis on obtaining the widest possible range of grazing angles with a relatively simple system (single source, vertical array receiver) so that we can obtain plausible results for multiparameter inversion. The relatively high values for bottom backscatter obtained from rocky bottoms have been documented in several references.[5–7] In the present article, we focus exclusively on these types of bottoms.

Scattering from the water–sediment interface is not always dominant for a particular ocean bottom/sub-bottom, transmit frequency, grazing angle, and source level: however, a solid understanding of this scattering mechanism remains essential. This is especially true in environments with sand or rock bottoms that have a significant range of subcritical grazing angles that are important for sonar operation. Gragg *et al.*[8] have recently used the small-slope scattering theory to develop a physics-based formulation of interface scattering from elastic bottoms with stochastic roughness. This theory predicts a monostatic backscattering strength that is typically far more complex than empirical descriptions such as $\sigma = \mu + 10\log_{10}(\sin\theta)$ or $\sigma = \mu + 10\log_{10}(\sin^2\theta)$ (Lambert's Rule), where σ is the scattering strength in dB, μ is a constant, and θ is the grazing angle. Details of the monostatic formulation of the small-slope theory are given in the Ap-

[a]Electronic mail: Raymond.Soukup@nrl.navy.mil
[b]Electronic mail: Robert.Gragg@nrl.navy.mil

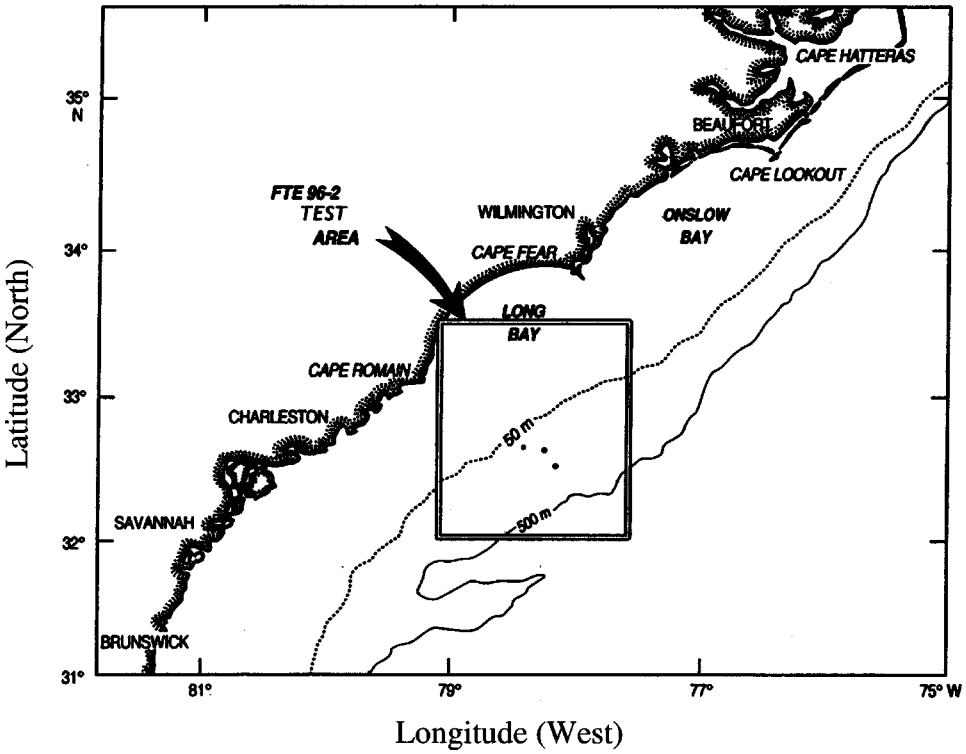

FIG. 1. LWAD FTE 96-2 test area. Bottom scattering was measured at the sites indicated by the dots.

pendix. The predicted scattering strength curve can exhibit local minima, change in behavior around the shear critical angle, or deviations from monotonic behavior. This can include regions where the predicted scattering strength decreases with increasing angle, or remains flat over a range of angles. The latter is a prominent feature of the data set we will discuss in this paper. Essen[9] has modeled grazing angle dependence for scattering from rough seafloors using perturbation theory and produced these types of features.

An investigation of the frequency and grazing angle behavior of rough interfaces calls for a dataset that lends itself to analysis at multiple frequencies over a wide range of grazing angles and that, as much as possible, involves only interface scattering. The diversity of frequencies and grazing angles makes it possible to invert for parameters of prime importance that are often difficult to measure *in situ*, such as the characteristics of the bottom roughness spectrum. In this paper, we use 2–3.5 kHz data from measurements made off the Carolina Coast in Long Bay (Fig. 1) during the 2nd Littoral Warfare Advanced Development Focused Technology Experiment of 1996 (LWAD FTE 96-2).

In Sec. II we describe the experimental design used to obtain bottom backscattering strengths in the LWAD program, and in Sec. III we discuss data processing issues related to scattering measurements in littoral water. In Sec. IV we describe the method of inverting for geoacoustic parameters from the scattering data to support the grazing angle and frequency dependence predicted by the FTE 96-2 data and the scattering model. A discussion of the issues involved in performing this analysis is given in Sec. V, and the main points of the paper are summarized in Sec. VI.

II. EXPERIMENTAL DESIGN

A. Test location

The primary focus of this paper is on the scattering data collected using 2.0, 2.5, 3.0, and 3.5 kHz transmissions during the FTE 96-2 sea test at two Long Bay sites with exposed limestone bottoms. These are designated as Sites ''Q'' and ''C'' in Fig. 2. To examine the plausibility of extrapolating scattering strength results to lower grazing angles, we will also consider measurements from a different sea test at the nearby SR2 site, which is also shown in Fig. 3. Data from Long Bay sites that were less suitable for verifying interface model predictions, because of significant sand cover, are described in Soukup and Ogden[10,11] and Kunz.[12]

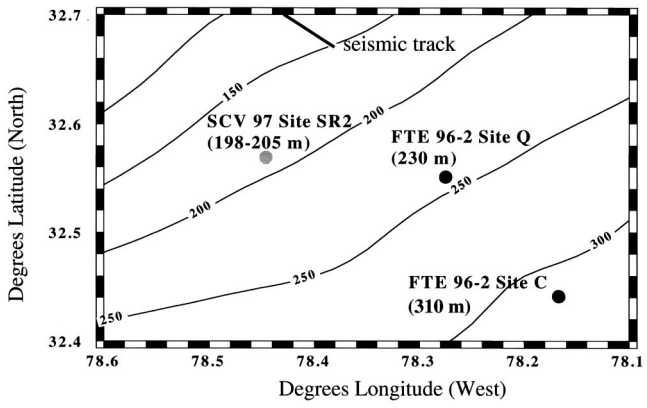

FIG. 2. Scattering sites for LWAD FTE 96-2 and SCV-97 experiments in Long Bay. Cited depths in parentheses are from the ship's fathometer, while contours come from a bathymetric database. The database captures the general downward slope of the ocean bottom, while the fathometer values are more precise. All three sites have rock bottoms. Sand cover is limited to depths shallower than about 170 m.

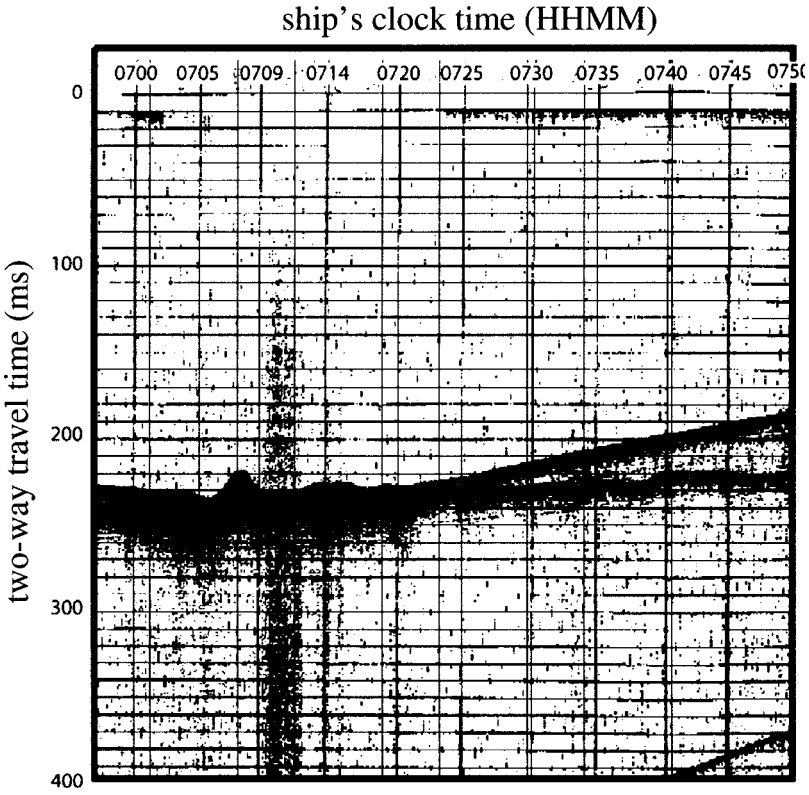

FIG. 3. Seismic trace along a track (the line in Fig. 2), roughly four miles in length, running from south-east to north-west (left to right). To the southeast, the bottom is bare limestone; to the northwest, a wedge of sand lies over the limestone (figure courtesy of Dr. Stephen W. Snyder, North Carolina State University).

In the test area shown in Fig. 2, periodic scouring by the Gulf Stream has shaped the calcareous sand sediment east of the shelf break into a wedge that tapers to seaward and ultimately effectively vanishes, as shown in the seismic trace of Fig. 3. The sand wedge ends at a water depth of 170 m. The resulting exposed bottom at greater depths is described as Miocene sequences of mostly phosphatic limestones—a bottom type that Pratt[13] considers typical of the north end of the Blake Plateau.

B. Source aperture and waveforms

In the LWAD FTE 96-2 test, an omnidirectional source and a rigid vertical line array receiving aperture were deployed on a single cable from a drifting ship, with the source located 3 m below the center of the array, producing a nearly monostatic measurement geometry. The source transmitted gated cw waveforms of 10 ms duration at each frequency, in sets of 12–15 identical repetitions separated by 3 s. These ping separation times were large enough so that the reverberation level decayed to the ambient noise level before the next transmission.

At each site, this source/receiver assembly was deployed at depths in the water column designated as ''shallow'' (35 m source depth), ''middle'' (60 or 65 m source depth), and ''deep'' (105 m source depth). In each case, the sound speed profile provided downward refracting propagation. Figure 4 shows the sound speed profiles and deployment depths. At any given frequency, the time interval between data collection for different deployment depths is typically 15–20 min, and the ship might drift as much as 0.5–0.7 nmi during this time. In our discussion below, we provide justification for the assumption that the scattering characteristics of the bottom do not change significantly due to this small displacement.

C. Receiver aperture and signal processing

The receiving aperture consisted of nine hydrophones with a spacing of 21 cm (half-wavelength at 3570 Hz), and ten beams with cosine-spaced main response axes were formed. Returns of interest came from beams 0, 1, 2, 3, and 4 that were inclined at 0°, 39°, 56°, 71°, and 84° respectively, relative to the downward direction (endfire to the vertical array). The directivity pattern for this beam subset is shown in Fig. 5. The horizontal ranges for scatterer-to-receiver paths, considering the combinations of deployment depths and water depths used during scattering runs relevant to this article, ranged from 20 to 1500 m from the source/receiver location, corresponding to ensonified ring-shaped areas ranging from 4500 to 70 000 m^2 (i.e., 0.0045–0.07 km^2). Since the source-to-interface and interface-to-receiver grazing angles coincided to within 0.5°, their average was computed and plotted as simply a single ''grazing angle.''

After beamforming, power spectra were obtained using Fourier transforms of length equal to the ping duration, the successive transforms proceeding to the end of the time series with a 90% overlap. A frequency band containing essentially all the signal energy was selected and a time series was created for each ping by including only the energy in the band. The direct arrivals for the pings were then temporally aligned and the squared reverberation envelope was averaged (prior to the conversion to decibel units) to produce a single reverberation curve for each beam and frequency bin. We obtained the transmission loss terms to and from the ensonified area by calculating geometric spreading loss along each ray path. The computed beam pattern and ray trace were used to calculate the ensonified area. From these inputs, bottom scattering strength was calculated from the sonar equation as a function of beam, frequency, and grazing angle.

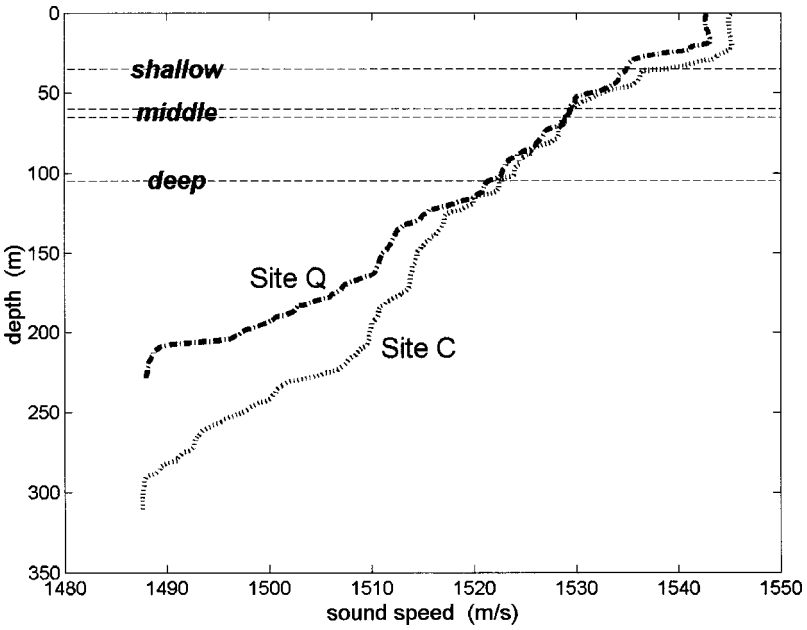

FIG. 4. Sound speed profiles and deployment depths for the FTE 96-2 experiment.

Finally, the scattering strengths were corrected for reverberation decay over the pulse length, for the surface-reflected path, and for other multipaths, as described below in Sec. III. We also confirmed that array tilt was negligible, and that the scattering from biologics was negligible compared to the scattering from the ocean bottom.

III. PROCESSING METHODOLOGY

In this section, we describe the implementation of two corrections, one relating to the problem of significant returns from paths other than the direct path, and the other relating to the problem of significant reverberation decay over the length of the transmitted signal. The application of the latter correction is further complicated by the possibility that the decay may be influenced by a change in the scattering mechanisms (e.g., near the critical angle). These corrections depend on the experimental geometry, source and receiver directionality, sound speed profile, and the grazing angle dependence arising from the specific ocean bottom. The way these corrections are applied in this paper is, to some degree, specific to the particular datasets described here, but it does illustrate aspects of the general problem of applying such corrections in other situations.

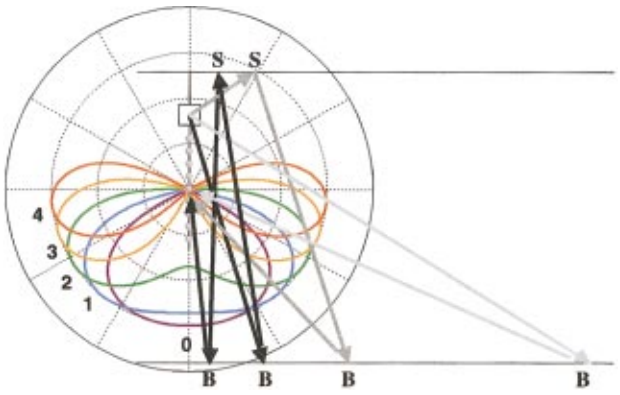

FIG. 5. Experimental geometry (not to scale) and receiver beam pattern (Hanning shaded) at 2.5 kHz for the LWAD FTE 96-2 experiment. For the actual horizontal ranges and the size of ensonified areas used for scattering strength extraction, see the text. The arrows show representative paths that produce ambiguous returns. Grid spacing: angular, 30°; radial, 10 dB.

A. Multipath corrections

In our discussion of multipaths, we use the convention of labeling paths according to the order of their boundary interactions, with B representing the direct path, BS designating a path that strikes the bottom (B) and then the surface (S) before returning to the receiver, and BSB denoting a path with three boundary interactions (Fig. 5).

When the source and receiver are relatively close to the surface, as they are for our shallow deployment geometry, the B paths and SB paths will arrive simultaneously on the same beam, but with slightly different grazing angles. Generally, for water depths sufficiently large relative to the source/receiver depth, making this grazing angle difference sufficiently small, a simple 3 dB surface-reflected path correction is applicable for $\theta < \theta_{\mathrm{SBinit}}$, where θ_{SBinit} is the grazing angle corresponding to the earliest return of an SB path.

For the experimental geometries of all FTE 96-2 deployments, we justified the use of this simple surface-reflected path correction based on the following observations.

(1) For the deep deployment, the first SB path arrives later, giving a smaller value for θ_{SBinit}. A comparison of the middle- and shallow-deployment data for $\theta < \theta_{\mathrm{SBinit}}$ to the deep-deployment data for $\theta > \theta_{\mathrm{SBinit}}$ showed that the subtraction of 3 dB would bring the shallow and mid-deployment data into agreement with the deep-deployment data. Such comparisons are feasible to support the simple 3 dB correction down to $\theta \approx 25°$.

(2) A reverberation model (BiRASP)[14] predicted equal received levels for all simultaneous B and SB paths in the grazing angle region of interest for multipath arrivals ($\theta < \theta_{\mathrm{SBinit}}$). Therefore, the SB path added an extra 3 dB to the return (i.e., a 3 dB surface-reflected path correction was supported). For these predictions, we used the empirical $\sin^2\theta$ grazing angle dependence mentioned

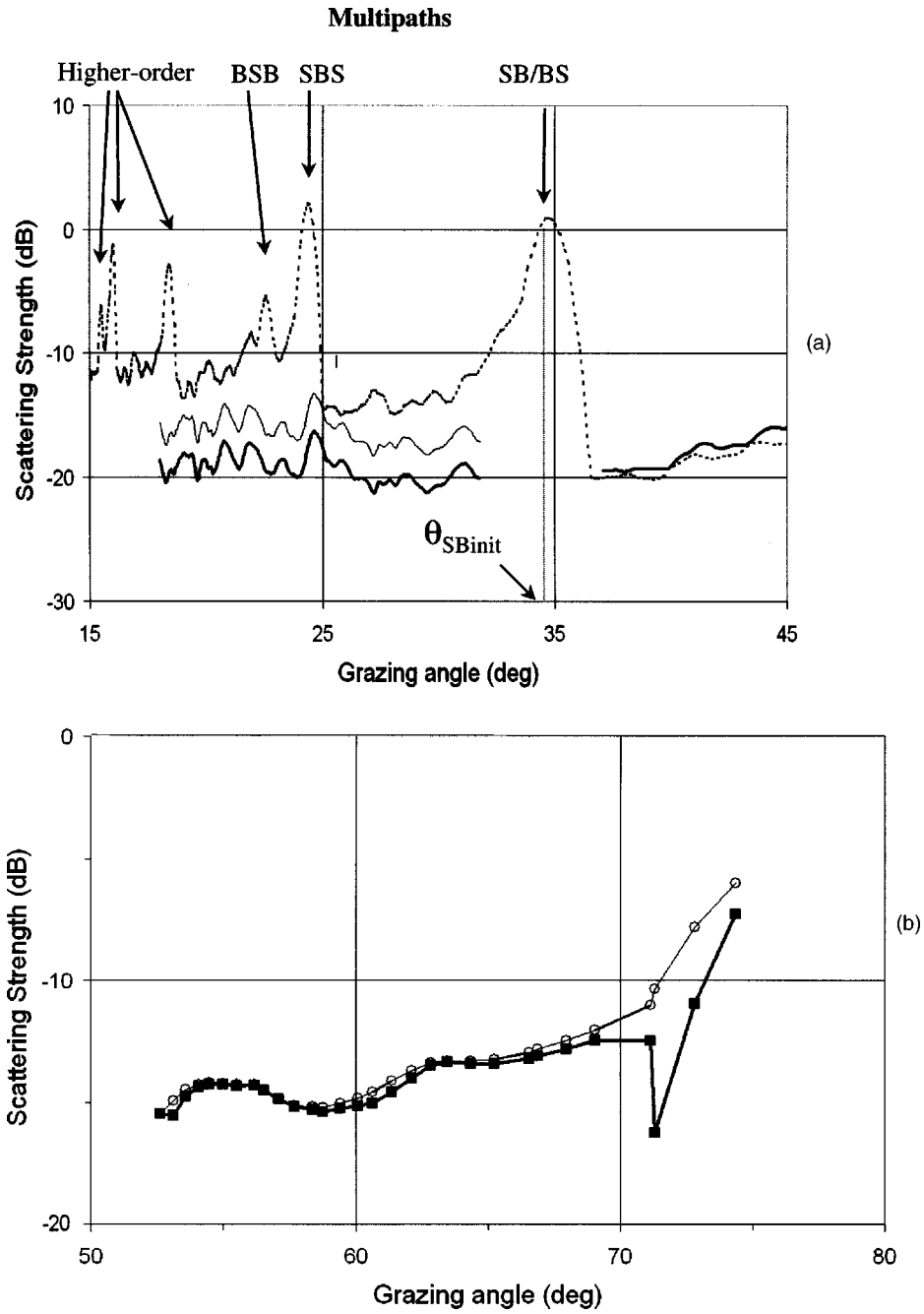

FIG. 6. Bottom scattering strengths versus grazing angle at 3 kHz from a deep deployment at site Q. (a) Application of multipath correction. The curves are phone data (dashed), uncorrected beam data (thin), and corrected beam data (thick). (b) Application of the reverberation decay correction. The curves are uncorrected beam data (thin with circles) and corrected beam data (thick with squares).

above, which is stronger than what we have observed in actual data from limestone. The maximum value of the grazing angle difference for simultaneous B and SB paths was roughly 5°, a small enough difference to produce equal contributions for the two paths. For bottoms where the scattering changes rapidly with angle, or the difference in angle between the two paths is larger, the relative contributions of the two paths would have to be estimated using this type of procedure.

Additionally, for any reasonable geophysical parameter selection, small-slope predictions within the grazing angle range of interest for surface reflections show negligible θ dependence over intervals as small as 5°. Therefore, the small-slope model itself supports a simple correction. Since we are trying to verify grazing angle predictions of this model in this paper, we have given arguments (1) and (2) that are independent of the small-slope model to support the 3 dB correction.

We now illustrate the application of this correction to a scattering curve. Figure 6(a) is an example of 3 kHz bottom scattering strength data for a single deployment at site *Q*. Multipaths, including the initial SB arrival, are most evident in the data from a single hydrophone. Performing the multipath correction produces a consistent level in the regions $\theta < \theta_{\mathrm{SBinit}}$ and $\theta > \theta_{\mathrm{SBinit}}$.

We have been discussing the correction for a particular multipath (the surface-reflected path, SB). For the other multipaths (BSB, SBS, etc.), the procedure was simply to reject peaks in the scattering strength data that coincided with obvious peaks in the single-phone return at the expected mul-

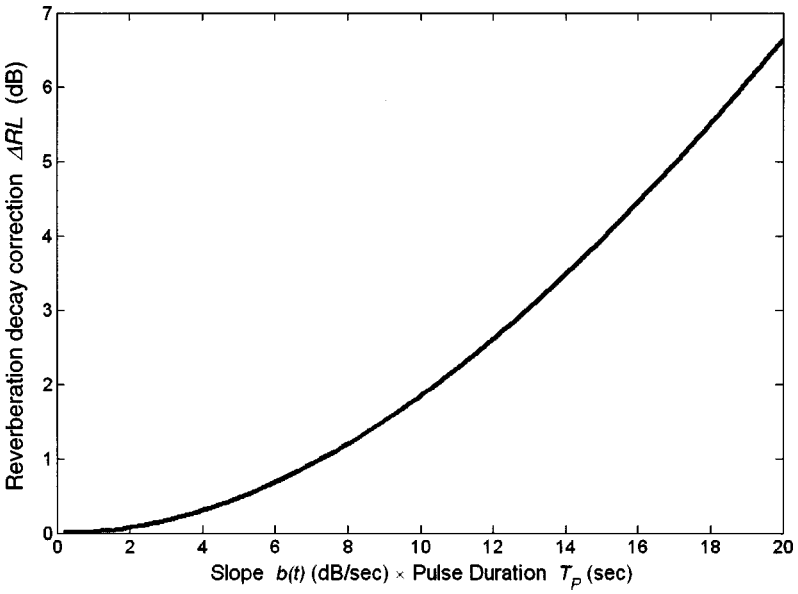

FIG. 7. Reverberation decay correction ΔRL, from Eq. (1) with $T_S = T_P$, versus the product $b(t) \times T_P$. The vertical axis gives the value to be subtracted from the reverberation level. The largest reverberation decay correction for the 3 kHz data [Fig. 6(b)], for example, was 5.9 dB.

tipath arrival angles. Instead of correcting the data at these particular angles, we omitted the data from our final scattering strength results (shown below), which were used for inverting geoacoustic parameters.

B. Reverberation decay correction

The reverberation level *RL* (in dB) generally decays with increasing time during the portion of the time series used for extracting direct-path scattering strength. When this decay is negligible over an analysis time interval (in our case, the pulse duration), the standard algorithm for extracting the scattering strength produces an unbiased result, which is then associated with the midpoint of that time interval. This even works when the decay over the time interval is substantial, *provided* that the quantity $10^{RL/10}$ is a linear function of time. Otherwise, the result is biased upward. Henyey *et al.* have devised an appropriate correction: based on the observation that the decay generally follows a power law (locally), the following reverberation decay correction, also known as the "slope correction," [15] needs to be subtracted from the backscattering strength computed for a bottom patch:[16–18]

$$\Delta RL = 10 \log_{10}\left[\frac{10^{1+b(t)T_S/20} - 10^{1-b(t)T_S/20}}{b(t)T_S \ln 10}\right] + 10 \log_{10}\left[\frac{10^{1+b(t)T_P/20} - 10^{1-b(t)T_P/20}}{b(t)T_P \ln 10}\right], \quad (1)$$

in which $b(t)$ is the local slope of the reverberation decay curve (dB versus time), and the times T_P and T_S are the pulse duration and processing resolution, respectively.

Figure 7 shows this correction as a function of the product $b(t) \times T_P$ for gated cw transmissions for which the size of our sliding Fourier transform window is equal to the signal duration, i.e., $T_S = T_P$. For other waveforms, an appropriate T_P would be necessary to reflect the range resolution of the signal.[18] Note that the computation involves the slope (i.e., first derivative) of the reverberation curve, and that large corrections can appear when there is any kind of discontinuity. For the data shown here, the large corrections occur where we would expect to see the effect of the compressional critical angle for a limestone bottom, and this information is used in the inversion procedure described in Sec. IV. At the time corresponding to this angle, we regularly observe an abrupt change in the slope of the reverberation decay. Figure 6(b) shows higher grazing angle results for the same set of pings as Fig. 6(a), and the large corrections can be seen near $\theta = 72°$. In this dataset, reverberation decay corrections are only significant near the compressional critical angle. For other direct-path scattering datasets, this correction may influence a larger set of grazing angles.[19]

Note that Figs. 6(a) and (b) represent different grazing angle regimes. For this dataset, the regions of θ for which the multipath and reverberation decay corrections were significant were disjoint, and we were able to avoid the problem of having to apply a reverberation decay correction to a part of the time series that contains an ambiguity due to the surface-reflected path.

C. Fusion of multiple-depth data

To obtain reliable data over a full range of θ, we exploited the trade-off among different deployment depths. Deeper deployments have a wider range of higher θ for which the multipath correction is zero (since the BS and SB paths occur later); however, the validity of the 3 dB surface-reflected path correction becomes highly suspect at lower θ because of the larger $\Delta\theta$ between the surface-reflected path and the direct path. Shallower deployments provide a more justifiable use of the 3 dB correction (as discussed above), but the correction must be assumed over a wider range of lower θ. Since the multipaths occur at different grazing angles for the different deployments, for almost any grazing angle we can find one deployment for which there is no interference from a multipath (other than the surface reflected path). Therefore, we can assemble the final scattering curves by fusing scattering curves from different deployments. Although the ship drifted as described above, we see excellent agreement between any two deployments at the θ

values for which both yield valid data. Therefore, we can use the multiple deployments as a means of constructing data curves over a wide grazing angle range. The combined data from different deployments appear in Sec. IV, together with the model results.

D. Scattering-strength variability

Since we average reverberation curves over a set of 10–15 pings before doing the scattering strength computation, the scattering strength data have been presented without error bars for ping-to-ping variability. This averaging makes multipaths stand out much more clearly in the time series, so that we can identify the times of multipath returns more precisely and address them through processing. To obtain a measure of variability, we could alternatively obtain scattering strength curves for individual pings and obtain a standard deviation for a fixed grazing angle over the set of pings. Although the results obtained in this manner have generally the same mean level as ours, they are not as useful in the removal of higher-order multipaths. A consistent measure of variability can be obtained by computing the scattering strengths for individual pings in this manner—the standard deviation over the ping set at a fixed grazing angle regularly falls in the range 2–4 dB, for all frequencies and deployments. This range does not apply to the observed multipaths, but rather pertains to the grazing angle subsets that are valid for extracting direct path scattering strengths.

IV. GEOACOUSTIC INVERSION

We turn now to the task of verifying the predictions of the scattering model's. In essence, this amounts to simply varying the models inputs to get the best data/model agreement. We proceed with a more exacting quantitative analysis to support the predicted grazing angle dependence given by the data and the small-slope model; namely, using the model to invert for the prevailing environmental parameters with an efficient annealing algorithm, and obtaining the best parameter values from multiple annealing results. Since simulated annealing is a ubiquitous nonlinear optimization technique[20,21] that has been used successfully in numerous parameter estimations,[22,23] we will limit our discussion to the particular problems encountered when performing an inversion with this data set.

A. Scattering model

We use the improved model recently introduced by Gragg *et al.*[8] for the interface component of bottom scattering. This formulation allows (i) fully bistatic or in-plane scattering, (ii) a homogeneous fluid or elastic bottom, and (iii) scattering computations based on small-slope or perturbation theory. It is employed here in the backscatter mode, with an elastic bottom and the small-slope option. The first two of these choices are dictated by the geometry and geophysics of the experiments. Small-slope theory was selected because it is the more accurate option, especially at high grazing angles.[8,24] Any such use of a pure *interface* scattering model, however accurate, necessarily implies that we are neglecting all scattering by sub-bottom inhomogeneities. We consider this an innocuous omission at subcritical grazing angles (roughly $\theta<70°$ for this work, as seen below).

The geoacoustic parameters of the problem are simply the densities and sound speeds of the two media. For the water, these are ρ_w and c_w; for the bottom, they are the density ρ_b and the compressional and shear speeds, c_p and c_s. The two bottom sound speeds are complex, with small negative imaginary parts that provide attenuations. We take the water/bottom interface to have isotropic roughness and a power-law spectrum:

$$S(k)=\frac{w_2}{(h_0k)^{\gamma_2}}, \tag{2}$$

with $2<\gamma_2<4$. The reference length, h_0, is essentially arbitrary.[8] We use $h_0=1$ m. This leaves the following parameters as model inputs: ρ_w, c_w, ρ_b, c_p, c_s, w_2, and γ_2.

B. Inversion technique

Before attempting any inversion, we first impose two conditions. We fix the parameters whose values are in no real doubt—$\rho_w=1000$ kg/m^3, the value for nominal standard seawater, and $c_w=1487$ m/s, an experimental *in situ* measurement. We also identify a grazing angle $\hat{\theta}$ that appears to mark the onset of sub-bottom scattering in the data (based on our association of the critical angle with the large reverberation decay corrections described above), and then limit all of our data/model comparisons to $\theta<\hat{\theta}$. With that done, inversion is simply a matter of quantifying the data-model deviation across all the experimental frequencies and allowed grazing angles by devising a cost function Φ, and then searching the appropriate region of the parameter space for the minimum of $\Phi(w_2,\gamma_2,\rho_b,c_p,c_s)$. All that remains is to specify the cost function, the search algorithm, and the search region.

1. Cost function

We examined several cost functions, all of them based on a calculation of the deviation of theory from measurement at all of the angles between the minimum measured angle, $\theta_{\min}\approx 15°$, and $\hat{\theta}$ across all four frequencies (2.0, 2.5, 3.0, and 3.5 kHz). The most direct choice, a simple rms average deviation (in decibels), performed relatively poorly. We concluded that this was due to (i) the high concentration of data points at low angles, and (ii) a ripple[25] that persists in some of the data at higher angles. These are visible, for example, in the lower left panel of Fig. 8, where the median data angle $\theta_{\text{med}}\approx 20°$ is indicated and the ripple is marked by arrows. To counter these effects, we divided the interval $\theta_{\min}\leqslant\theta\leqslant\hat{\theta}$ into N bins of size $\Delta\theta\approx 4°$ (with no overlap), and adopted the rms bin average

$$\Phi=\sqrt{\frac{1}{N}\sum_{b=1}^{N}\frac{1}{4}\sum_{f=2.0\ \text{kHz}}^{3.5\ \text{kHz}}(\sigma_b^{\text{data}}(f)-\sigma_b^{\text{model}}(f))^2}, \tag{3}$$

as the cost function. In this expression, $\sigma_b^{\text{data}}(f)$ is the measured scattering strength (in decibels) averaged over bin b at frequency f, and $\sigma_b^{\text{model}}(f)$ is the modeled scattering strength (in decibels) at the midpoint of bin b at frequency f.

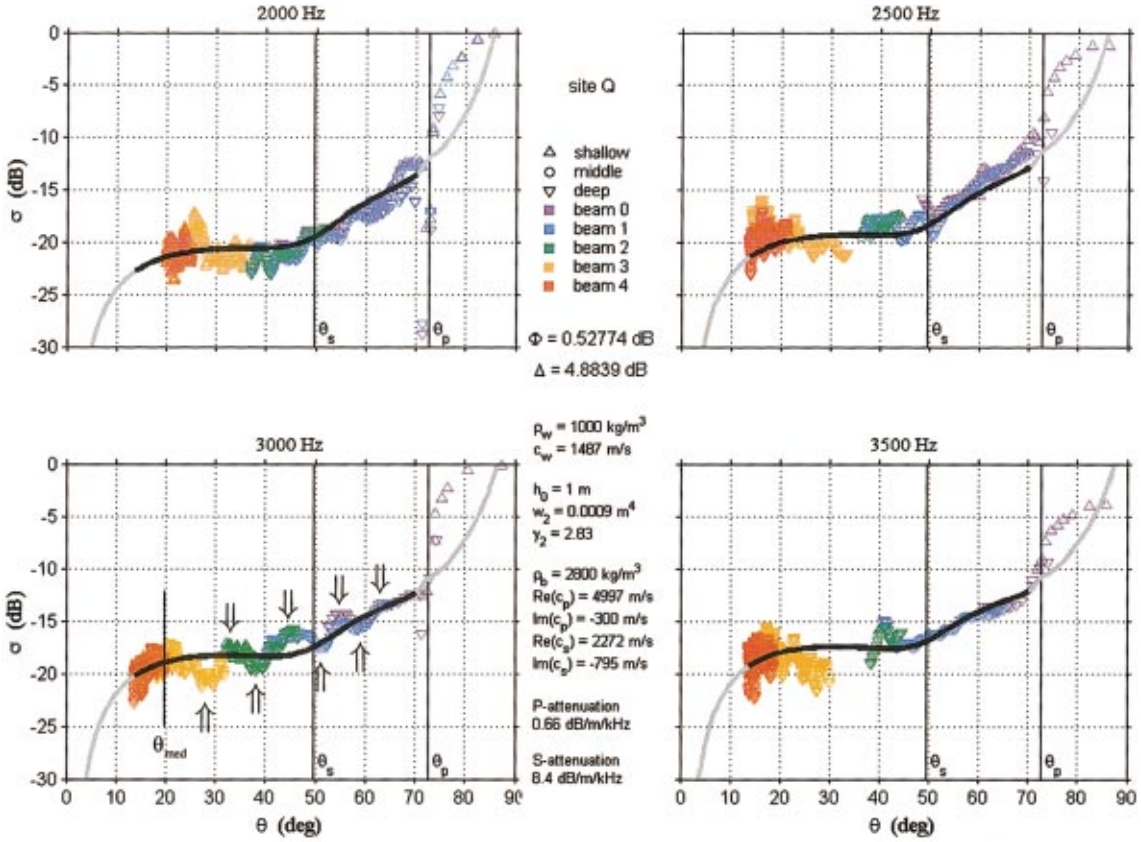

FIG. 8. Final bottom scattering strength and inversion results for site Q. The bottom scattering strength σ versus grazing angle θ is plotted for the four experimental frequencies. Symbols are experimental data. Curves are small-slope predictions using the environmental parameters obtained by inversion. These parameters are listed between the two lower graphs. In addition, the median data angle θ_{med} is shown, and the symbols ⇓ and ⇑ indicate the peaks and troughs of the ripple mentioned in the text. Data in the range $\theta \gtrsim \theta_p$ presumably involve sub-bottom scattering.

2. Search algorithm

Since the parameter space is seven-dimensional, something more efficient than a brute-force exhaustive search is called for. We chose ''amebsa,'' [26,27] an algorithm with a successful record in similar applications.[28,29] This is essentially a fast downhill simplex technique that efficiently negotiates narrow valleys in parameter space; however, it is augmented with simulated annealing to prevent trapping by local minima. Given a suitable empirically chosen cooling rate, the annealing process usually ''freezes'' into a final state of near minimum Φ well within 50 temperature steps. Straightforward annealing algorithms often have difficulty navigating long narrow valleys in state space, and coordinate rotation techniques have been developed to address the problem.[23] Since amebsa relies on simplex manipulations that are independent of coordinate orientation, we did not need to employ such techniques. We used a different approach for establishing the relative importance of parameters by examining the results of multiple runs of the annealing procedure.

3. Search region

We chose the search region within the parameter space based, as far as possible, on archival records for the geoacoustics of limestone and on roughness data from rocky seafloors. To facilitate the search, we first introduced a transformation of one of the parameters. Rather than using shear speed Re(c_s) itself as a search parameter, we actually used the compressional/shear speed ratio $\xi \equiv \text{Re}(c_p)/\text{Re}(c_s)$. This change does not materially affect the operation of the algorithm[30] and is more convenient in two respects. Hamilton has concluded from his analysis of a large collection of datasets dealing with saturated marine limestone that, although Re(c_p) and Re(c_s) exhibit considerable variation, their ratio is to be found in the interval $|\xi - 1.90| < 0.06$ ''within 95% confidence limits.'' [31] One can relax this empirical statistical rule somewhat, allowing a larger variance about the mean value, $\langle \xi \rangle = 1.90$, by taking $|\xi - 1.90| < n \times 0.06$ with $n > 1$. Linear elastic theory[32] requires that $\xi > 2/\sqrt{3}$, which can be incorporated into our formulation by taking $n \leqslant 12$. We use $n = 5$, and are thus dealing with the range $1.6 < \xi < 2.2$ (Table I).

The limits on Re(c_p) come from the observation that the compressional critical angle in the LWAD data, as indicated by large reverberation decay corrections, falls within the range $70° < \theta_p < 73°$. The low and high values for ρ_b embody the range reported in Hamilton's references.[33,34] The bounds on γ_2 and w_2 reflect our experience with seafloor spectra. The range in Table I includes the value $\gamma_2 \approx 2.64$ that we have obtained from another dataset from a scarp of the Mid-Atlantic Ridge. The range of w_2 is chosen to undershoot the corresponding scarp value, $w_2 \approx 0.0021$ m^4, because of the lower relief expected for the LWAD bottom. The high values of Im(c_p) and Im(c_s) correspond to attenuations re-

TABLE I. Inversion parameters and their high and low values.

Parameter	w_2 (m^4)	γ_2	ξ	Re(c_p) (m/s)	ρ_b (kg/m^3)	Im(c_p) (m/s)	Im(c_s) (m/s)
Low	0.0003	2.4	1.6	4348	2400	−300	−900
High	0.0009	3.0	2.2	5086	2800	−5	−5

ported for pure, homogeneous, water-saturated limestone samples (Ref. 33, Table I). The low values, corresponding to compressional and shear attenuations of approximately 0.5 and 7 dB/m/kHz, respectively, are essentially guesswork inspired by the saprolitic (weathered) nature of the bottom.

At site Q, we needed to perform an additional step to stabilize the results for some of the parameters. About half of the runs of the inversion algorithm produced small ($\lesssim$1 dB) but visible deviations from the data in limited grazing angle ranges. These runs were removed to achieve the final inversion results. This step was not necessary for site C.

C. Results

Figures in this section display the data for sites Q and C, together with typical simulation curves produced using the optimal environmental parameters that result from the inversion. In each of these figures, the theoretical curve is black in the interval $\theta_{\min} \leqslant \theta \leqslant \hat{\theta}$ and gray elsewhere. The critical angles θ_s and θ_p in each figure are calculated from the optimal values of the parameters Re(c_s) and Re(c_p). In all cases, $\hat{\theta} = 70°$.

A typical single inversion result for site Q is illustrated in Fig. 8. As the frequency increases from 2 to 3.5 kHz, the scattering strength in that figure increases by $\Delta\sigma \approx 3$ dB at the smaller grazing angles. This is consistent with the dependence $\sigma \propto f^{4-\gamma_2}$ to be expected at small θ[8]. As discussed above, there are reverberation decay corrections near θ_p in Fig. 8 at all four frequencies because the first derivative of the reverberation time series changes abruptly at θ_p. In evaluating the reverberation decay correction at such a discontinuity, we do not obtain a consistent value among different frequencies and sites; rather, we obtain an artifact that illustrates the change in a scattering mechanism that has affected the derivative of the time series. The marked data–model divergence[35] as θ exceeds θ_p suggests the onset of significant sub-bottom volume scattering at $\theta \approx \theta_p$. The optimal values of the parameters w_2, γ_2, ρ_b, Re(c_p), Im(c_p), Re(c_s), Im(c_s) are listed in the figure along with the associated cost function Φ and the maximum absolute data/model deviation, Δ. Figure 9 is the equivalent result for site C.

We have obtained very similar theoretical curves even using subsets of the allowed angles, e.g., with $\hat{\theta} = 50°$. How-

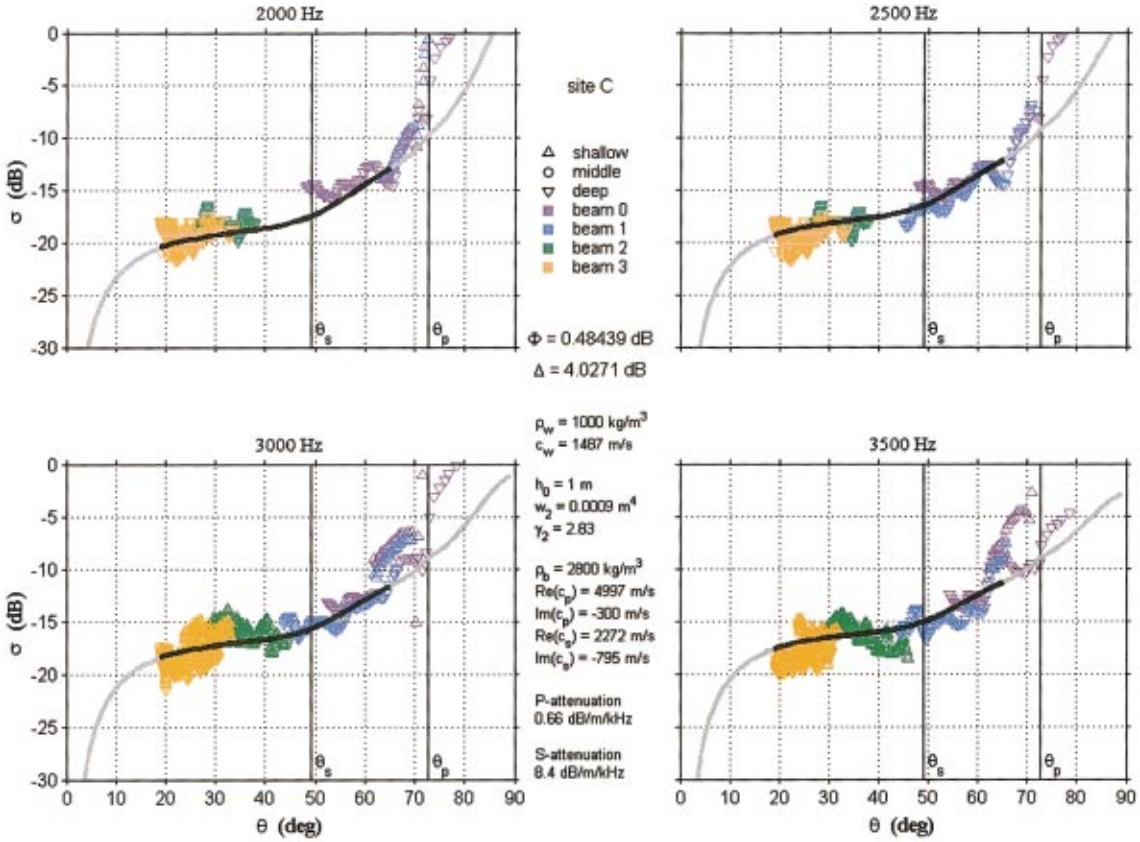

FIG. 9. Final bottom scattering strength and inversion results for site C. Bottom scattering strength σ versus grazing angle θ is plotted for the four experimental frequencies. Symbols are experimental data. Curves are small-slope predictions using the environmental parameters obtained by inversion. These parameters are listed between the two lower graphs. Data in the range $\theta \gtrsim \theta_p$ presumably involve sub-bottom scattering.

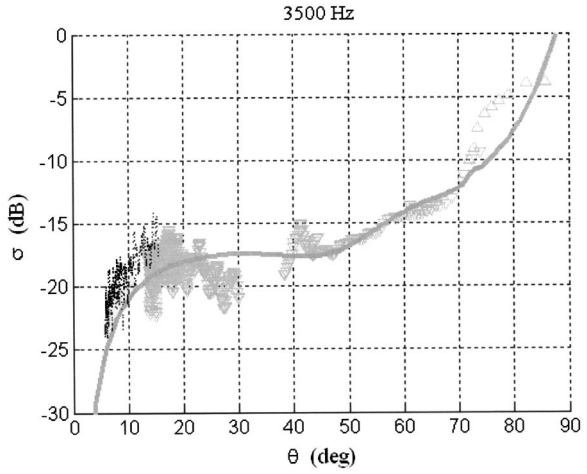

FIG. 10. The 3.5 kHz data from the SCV 97 experiment (black dots) plotted with data and model prediction (gray) for site Q of the FTE 96-2 experiment (repeated from the lower-right quadrant of Fig. 8). The SCV 97 data confirm a rapid decline in scattering strength at low grazing angles.

ever, attempts to invert based on even smaller subsets, e.g., with $\hat{\theta}<45°$ or using only data in the range $45°<\theta<70°$, met with little success. Evidently, inversion in this environment requires data over a modest bandwidth and a fairly broad range of angles. Otherwise, the system point in the annealing algorithm is too easily lured into physically dubious regions of the parameter space.

While we lack any FTE 96-2 data to confirm the rapid decline in scattering strength that the model predicts for $\theta<15°$, we can support its plausibility with data from a similar sea test, LWAD System Concept Validation 97 (SCV 97).[36] These data are from 10 ms transmissions at site SR2 (Fig. 2, 6 nmi west of site Q). This site is also in the region of exposed limestone, and the scattering levels are, in general, similar to those from FTE 96-2 at higher grazing angles. Data were obtained for a lower grazing angle interval in SCV 97 because the direct-path propagation paths extended out to longer ranges. In Fig. 10, the 3.5 kHz data and the simulation from Fig. 8 are repeated, and the lowest grazing angle 3.5 kHz SCV 97 data included. The scattering strength data decline rapidly with grazing angle, a trend that is matched by the model. Other frequencies gave a similar result.

In inversion problems, there is always the concern that the solution will not be unique. We expect to obtain fairly precise evaluations for those parameters that strongly affect the scattering for a particular type of bottom, but only ballpark estimates for the rest. Therefore, we considered ensembles of inversions for the two sites. Figures 11 and 12 present the results from these multiple runs of the annealing algorithm. Each figure is composed of seven panels, one for

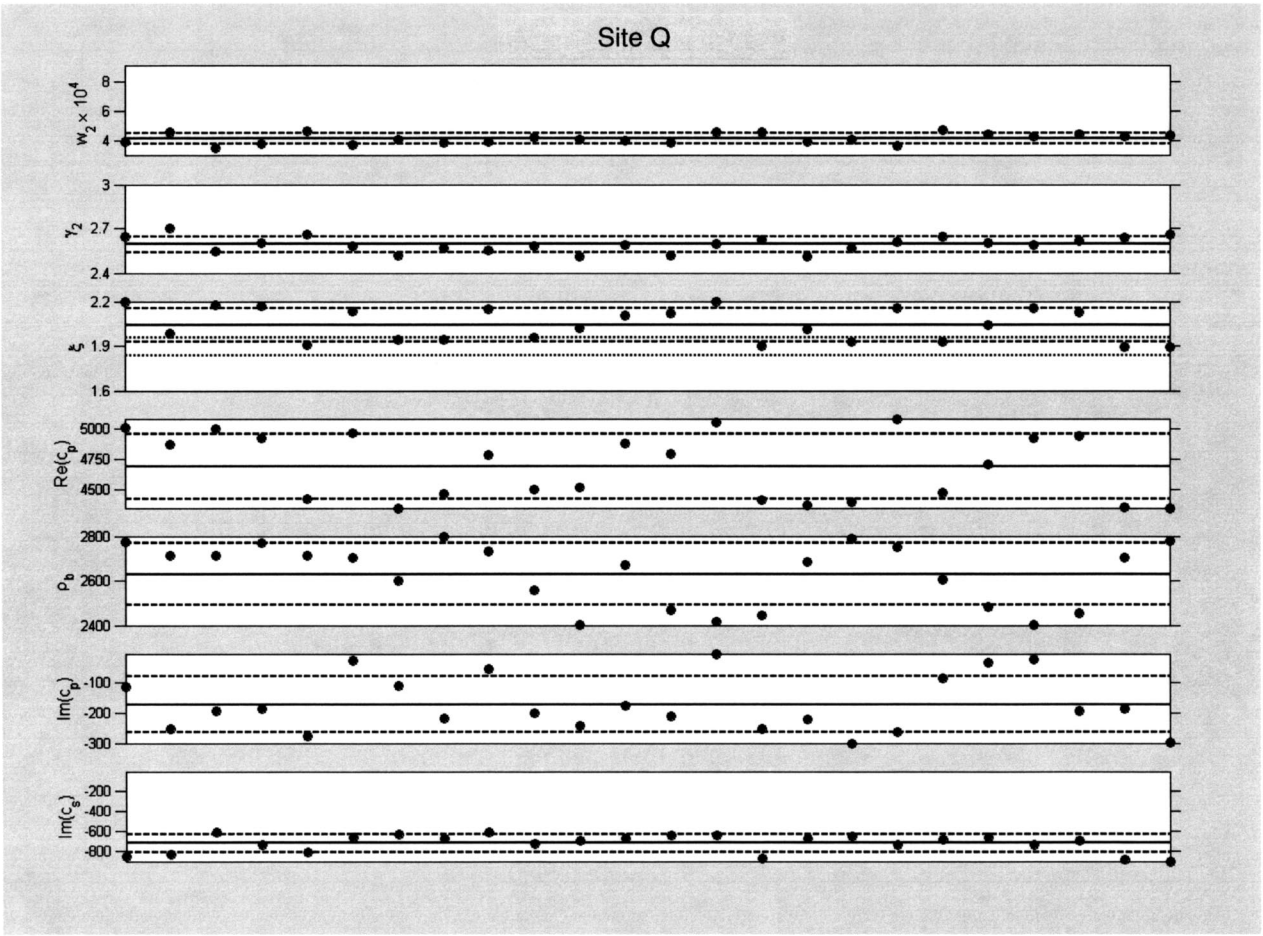

FIG. 11. The inversion results for site Q, as described in the text.

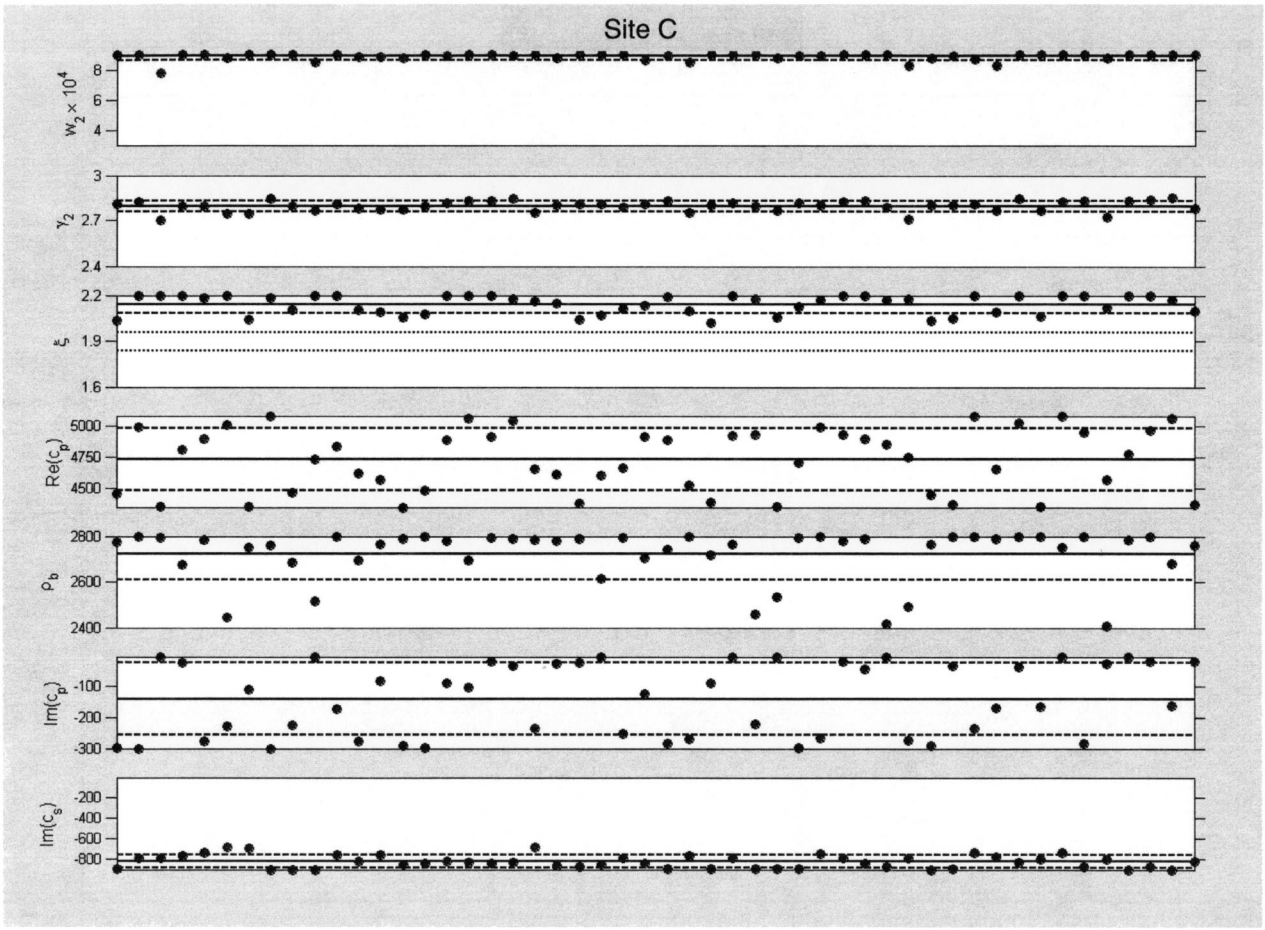

FIG. 12. The inversion results for site C, as described in the text.

each parameter. Dots represent the individual inversions, a solid line indicates the mean value for each parameter, and dashed lines mark the mean $\pm$ standard deviation. We take the means to be the inverted values of the parameters and the standard deviations to be the corresponding measures of their precision. The ξ panel also includes dotted lines at the edges of Hamilton's empirical range, $\xi = 1.90 \pm 0.06$. The outcomes for both sites are summarized in Table II. Three questions naturally arise and are addressed in the following paragraphs.

(1) Which parameters are definitively extracted by the inversion? It is clear that the bottom roughness parameters w_2, γ_2 are determined quite well at both sites. This seems natural, since the roughness spectrum is ordinarily a factor of primary importance in scattering from rough interfaces. We also benefit from the fact that the frequency dependence of the predicted scattering strength[8] is related only to the value of γ_2, and we have scattering data at multiple frequencies. The shear attenuation term $|\mathrm{Im}(c_s)|$ is also well determined, and is quite large at both sites. The sound speed ratio ξ is also fixed moderately well, but at values above Hamilton's 95% confidence interval. At site C, the bottom density ρ_b is localized within the top half of its search interval, though not at site Q. The remaining parameters, Re(c_p) and Im(c_p), apparently have the smallest influence on the scattering for this dataset, and successive runs of the annealing procedure produce a range of values that essentially cover their search intervals.

(2) Do the extracted parameter values agree between the two sites? For the three well-determined parameters, w_2 and γ_2 definitely do not, and ξ does not seem to either. There seems to be fair agreement for Im(c_s); the standard deviation intervals for the two sites overlap by about 40%. Just what all of this might mean is more problematic, since virtually

TABLE II. Summary of inversion results for sites Q and C.

Site	Parameter	$w_2 \times 10^4$ (m^4)	γ_2	ξ	Re(c_p) (m/s)	ρ_b (kg/m^3)	Im(c_p) (m/s)	Im(c_s) (m/s)
Q	Mean	4.11	2.59	2.04	4691	2630	−172	−721
	Std. dev	0.34	0.05	0.11	271	139	92	90
C	Mean	8.86	2.80	2.14	4733	2723	−141	−825
	Std. dev.	0.24	0.04	0.06	252	113	116	63

nothing is known about the typical site-to-site variation of any of these bottom parameters.

(3) Are these values believable? The values of w_2 and γ_2 are certainly within reason for naturally occurring rough surfaces. The value of ξ also seems reasonable, though somewhat high. However, from an acoustic standpoint, very little is actually known about the surficial characteristics of rock ocean bottoms in general, and nothing at all about this test area, except that the limestone is saprolitic. That characteristic may, in fact, underlie the high shear attenuation. We believe it could also reduce the shear speed and thus be responsible for the high ξ.

V. DISCUSSION

Our first objective was to produce a dataset that could be used to verify the predictions of physics-based models for scattering from a rough interface, particularly the elastic-bottom model of Gragg *et al.*[8] For this, we utilized multiple source/receiver deployments and employed corrections to eliminate both (1) multipath effects at lower grazing angles and (2) artifacts associated with rapid reverberation decay over the length of the transmission. For the surface-reflected path, a simple 3 dB correction was plausible, based on the results from the multiple deployments and the grazing angle dependence suggested by the model. The short signal duration made reverberation decay corrections small for most grazing angles, the exception being the vicinity of the critical angle. The resulting corrected dataset is suitable for testing interface scattering models over a wide range of grazing angles, and avoids the problems that arise from extrapolating model fits from a small angular interval.

For general direct-path scattering computations, the proper corrections for the data depend on several factors. Accurate reverberation for ambiguous propagation paths is a prerequisite for making the multipath corrections (including the surface-reflected path) because the experimental geometry, the sound speed profile, and the grazing angle dependence of the bottom all play a role. Furthermore, reverberation decay correction may be important over a wide range of grazing angles if the ping duration is long enough and/or the reverberation decay is rapid enough. The reverberation decay is also a function of geometry, sound speed, and bottom. In the present case, we also saw a large reverberation decay correction that corresponded to a change in physics at the critical angle. There may be other similar occurrences of large reverberation decay corrections at specific angles for more complicated (i.e., layered) bottoms. For other datasets, especially with longer waveforms, it is also possible that reverberation decay corrections may have to be applied to a range of angles. The correct treatment of multipaths and reverberation decay is important in producing a dataset that properly reflects unambiguous direct path bottom scattering.

With a suitable acoustic dataset in hand, our second objective was to support the predictions of the scattering model by using it to invert for the environmental parameters. For this, we devised a cost function to serve as a metric for the data/model disparity, defined a physically reasonable region in the parameter space, and then used a simplex/annealing scheme to search the region for the point of lowest cost. This effort also succeeded quite well. Values for the roughness parameters, the shear attenuation, and the compressional-to-shear sound speed ratio were all obtained for both sites. Although no measurements exist to serve as ground truth for any of these, the values obtained seem physically reasonably and reasonably consistent from site to site.

We have based our modeling for this paper on small-slope scattering theory—the best available formulation for scattering from a random rough interface. For the present dataset, we could actually have used perturbation theory (an asymptotic approximation) instead; the results differ slightly with a maximum difference of about 2 dB at the largest subcritical angles. In fact, perturbation-based inversions yield parameter estimates that are only slightly different and seem equally reasonable according to the criteria we have employed in this paper. Whatever scattering treatment is used, however, it is vital to include the elasticity in the bottom. Neither theory produces credible results with an artificially ''fluidized'' bottom.[8,9]

For general use, we favor small-slope theory because model studies[8] indicate that, though it is often comparable to perturbation theory, it should provide a definite improvement in situations with extended frequency ranges or bottoms that are faster (e.g., basalt) or rougher (i.e., with larger w_2) than the one encountered here. While these advantages are not yet supported by data, we are confident that the small-slope model will provide better predictive capability, allowing more accuracy and confidence when extrapolating in frequency or angle.

Our current research has turned to tank experiments that exploit scale models of ocean bottoms, employing prescription-milled materials (e.g., PVC) for a systematic treatment of the roughness and geoacoustic parameters. For bottoms such as limestone, we have seen that appropriate scattering-strength data can be used to infer plausible estimates of the relevant parameters. Tank experiments will allow us (1) to verify these inferences against the ground-truth parameter values and (2) to more closely examine the parameter regions where small-slope theory and perturbation theory diverge.

VI. CONCLUSION

The grazing angle dependence predicted by interface scattering models has been shown in papers by Essen[9] and Gragg *et al.*[8] to exhibit features that depend on the model inputs. In this paper, we were able to analyze scattering data with grazing angle dependence that includes a fast roll-off at low grazing angles (below 15°), a region of flatness that extends to the shear critical angle (15°–50°), increases rapidly between the shear critical angle and the compressional critical angle (50°–72°), and then increases even more rapidly with the onset of significant sub-bottom penetration (above 72°). The data also exhibit a slight frequency dependence that is well accounted for by the model. We were not only able to ''fit'' the grazing angle and frequency dependence, but were also able to obtain inverted geoacoustic parameters that make sense for limestone, and distinguish between parameters that play a strong role (the roughness parameters and the compressional/shear speed ratio) and pa-

rameters that are less influential (the compressional speed itself). The result is the publication of scattering data for rocky bottoms over a wide range of grazing angles that does not exhibit simple behavior but is consistent with predictions of a physics-based model.

ACKNOWLEDGMENTS

This work was supported by the Office of Naval Research. The authors are grateful for ongoing technical discussions with Dr. Roger Gauss and Dr. Daniel Wurmser of the Naval Research Laboratory. We are also grateful to Dr. David Fromm of the Naval Research Laboratory for the BiRASP model runs and review of the manuscript, and to Dr. James Fulford of the Naval Research Laboratory/Stennis Space Center for an informative discussion of saprolitic limestone bottoms.

APPENDIX A: SMALL-SLOPE BACKSCATTERING STRENGTH

For the general class of rough interface scattering theories, the scattering strength has the form

$$\sigma = P \times I. \tag{A1}$$

The dependence on interface roughness is confined to the frequency-dependent integral

$$I = \int_0^\infty e^{-\alpha u^{2\nu}} J_0(u)\, u\, du, \tag{A2}$$

in which $0 < \nu = \frac{1}{2}\gamma_2 - 1 < 1$, where γ_2 is the spectral parameter in the body of the paper. (The fractal dimension of the interface is $1+\nu$.) However, various theories yield different expressions for P, the frequency-independent prefactor that contains all of the dependence on bottom geoacoustic parameters—the density, the compressional speed and attenuation, and (if applicable) the shear speed and attenuation. There are known forms of differing complexity corresponding to perturbation theory,[9] composite roughness,[37] Kirchhoff theory,[37] and small-slope theory.[8] In this appendix we provide a summary of the form used in the body of the paper—the small-slope result specialized to a monostatic geometry. This is[8]

$$P = \frac{1}{8\pi}\left| \frac{-4(1-\rho)(k^2\xi^2+k_z^2) + 8\rho(k^2/K_s)^2\xi^2 + 4k^2(a-\xi)^2 + 4K_w^2 a^2 + 2K_s^2(a-b)^2/\rho - 4K_P^2 b^2/\rho}{4k_z k(1+a)^2} \right|^2, \tag{A3}$$

in which

$$a = \rho\frac{k_z}{k_{pz}}\left[1 - 4\left(\frac{k}{K_s}\right)^2 \frac{k_{sz}}{K_s}\frac{k_{sz}-k_{pz}}{K_s}\right],$$

$$b = \rho\frac{k_z}{k_{pz}}\left[1 - 2\left(\frac{k}{K_s}\right)^2\right], \tag{A4}$$

$$\xi = \frac{k_z}{k_{pz}}\left[1 - 2\frac{k^2 + k_{sz}k_{pz}}{K_s^2}\right].$$

In these expressions, K_w, K_p, and K_s are magnitudes of the wave vectors for acoustic waves in the water and for compressional (p) and shear (s) waves in the bottom. These three wave vectors have vertical components $k_z = -K_w \sin(\theta)$, $k_{pz} = -\sqrt{K_p^2 - k^2}$, and $k_{sz} = -\sqrt{K_s^2 - k^2}$, respectively, and share a common horizontal component, $k = K_w \cos(\theta)$.

[1] P. G. Cable, K. D. Frech, J. C. O'Connor, and J. M. Steele, "Reverberation-derived shallow-water bottom scattering strength," IEEE J. Ocean. Eng. **22**, 534–540 (1997).

[2] P. M. Ogden and F. T. Erskine, "Bottom scattering strengths measured using explosive sources in the Critical Sea Test program," Naval Research Laboratory Report 7140-97-9822, Washington, DC, 5 February, 1997.

[3] C. W. Holland and P. Neumann, "Sub-bottom scattering: A modeling approach," J. Acoust. Soc. Am. **104**, 1363–1373 (1998).

[4] C. W. Holland, R. Hollett, and L. Troiano, "Measurement technique for bottom scattering in shallow water," J. Acoust. Soc. Am. **108**, 997–1011 (2000).

[5] H. K. Wong and W. D. Chesterman, "Bottom backscattering near grazing incidence in shallow water," J. Acoust. Soc. Am. **44**, 1713–1718 (1968).

[6] R. B. Patterson, "Backscatter of sound from a rough boundary," J. Acoust. Soc. Am. **35**, 2010–2013 (1963).

[7] A. V. Bunchuk and Y. Y. Zhitkovskii, "Sound scattering by the ocean bottom in shallow-water regions (review)," Sov. Phys. Acoust. **26**, 363–370 (1980).

[8] R. F. Gragg, D. Wurmser, and R. C. Gauss, "Small-slope scattering from rough elastic ocean floors: General theory and computational algorithm," J. Acoust. Soc. Am. **110**, 2878–2901 (2001).

[9] H.-H. Essen, "Scattering from a rough sedimental seafloor containing shear and layering," J. Acoust. Soc. Am. **95**, 1299–1310 (1994).

[10] R. J. Soukup and P. M. Ogden, "Bottom backscattering measured off the south Carolina coast during Littoral Warfare Advanced Development Focused Technology Experiment 96-2," Naval Research Laboratory Memorandum Report 7140-97-7905, Washington, DC, 28 April, 1997.

[11] R. J. Soukup, "Bottom backscattering measured off the Carolina coast during the Littoral Warfare Advanced Development System Concept Validation Experiment 97 (LWAD SCV 97)," Naval Research Laboratory Report 7140-98-9885, Washington, DC, 15 June, 1998.

[12] E. L. Kunz, "Bottom backscattering measured off the Carolina coast during the Littoral Warfare Advanced Development 98-4 experiment," Naval Research Laboratory Memorandum Report 7140-99-8339, Washington DC, 26 February, 1999.

[13] R. N. Pratt, "Lithology of rocks dredged from the Blake Plateau," *Southeastern Geology*, Duke University, Vol. 13, pp. 19–38 (1971).

[14] D. M. Fromm, J. P. Crockett, and L. B. Palmer, "BiRASP—The bistatic range-dependent active system performance prediction model," Naval Research Laboratory Report 7140-95-9723, Washington, DC, 30 September, 1996.

[15] The term "slope correction" is used in Refs. 16–18. We prefer the term "reverberation decay correction" because "slope correction" has also been used to describe corrections for the physical slope of the bottom (e.g., Ref. 28).

[16] F. S. Henyey, E. I. Thorsos, and K. M. Nathwani, "Scattering strengths cannot depend on the length of a pulse," J. Acoust. Soc. Am. **98**, 2986–2987 (1995).

[17] R. C. Gauss, P. M. Ogden, J. B. Chester, and J. M. Fialkowski, "Deriving scattering strengths from nonstationary time-series data: A comparison of low-frequency surface-backscattering strengths using both impulsive and coherent sources," J. Acoust. Soc. Am. **97**, 3403 (1995).

[18] R. C. Gauss, E. I. Thorsos, and F. S. Henyey, ''Acoustic surface interaction: Advances under the Critical Sea Test program,'' J. Acoust. Soc. Am. (in preparation).
[19] For these data, the significant reverberation decay corrections correspond to the change in physical mechanism at the critical angle. Reverberation decay corrections at angles below the critical angle are less than 2 dB. However, for longer pulse durations there would have been significant reverberation decay corrections over a wide range of grazing angles. For example, using a 50 ms signal instead of a 10 ms signal would increase the product of the slope and the pulse duration (the x-axis values in Fig. 7) by a factor of 5, leading to much larger reverberation decay corrections that would have been driven by the magnitude of the reverberation decay over the pulse interval.
[20] N. Metropolis, A. W. Rosenbluth, M. N. Rosenbluth, A. H. Teller, and E. Teller, ''Equation of state calculations by fast computing machines,'' J. Chem. Phys. **21**, 1087–1092 (1953).
[21] S. Kirkpatrick, C. D. Gelatt, and M. P. Vecchi, ''Optimization by simulated annealing,'' Science **220**, 671–680 (1983).
[22] M. D. Collins, W. A. Kuperman, and H. Schmidt, ''Nonlinear inversion for ocean-bottom properties,'' J. Acoust. Soc. Am. **92**, 2770–2783 (1992).
[23] M. D. Collins and L. Fishman, ''Efficient navigation of parameter landscapes,'' J. Acoust. Soc. Am. **98**, 1637–1644 (1995).
[24] Perturbation theory is perfectly adequate for many applications involving elastic bottoms [including limestone, when the frequency range is not too great (Ref. 8)]. For this case, we thought it prudent to use the more accurate small-slope theory because, though the theoretical advantage may be only marginal, the success or failure of an inversion algorithm can hinge on such minutiae.
[25] We have been unable to explain this ripple. Its origins may lie in the deviation of the bottom characteristics from simple rough limestone. We do know that it occurs in grazing angle regimes that correspond to times before the arrivals of any multipaths, which excludes multipaths as the cause.
[26] W. H. Press and S. A. Teukolsky, ''Simulated annealing operations over continuous space,'' Comput. Phys. **5**, 426–429 (1991).
[27] W. H. Press, B. P. Flannery, S. A. Teukolsky, and W. T. Vetterling, *Numerical Recipes*, 2nd ed. (Cambridge University Press, Cambridge, 1986).
[28] H. Matsumoto, R. P. Dziak, and C. G. Fox, ''Estimation of seafloor microtopographic roughness through modeling of acoustic backscatter data recorded by multibeam sonar systems'' J. Acoust. Soc. Am. **94**, 2776–2787 (1993).
[29] R. F. Gragg and D. Wurmser, ''Theory and numerical modeling of low-frequency acoustic scattering from bubble plumes near the sea surface,'' Naval Research Laboratory Report 7140-92-9391, Washington, DC, 18 December 1992, Appendix D.
[30] We have confirmed this assertion directly. It is traceable to the fact that simplex-based algorithms are virtually coordinate independent.
[31] E. L. Hamilton, ''V_p/V_s and Poisson's ratios in marine sediments and rocks,'' J. Acoust. Soc. Am. **66**, 272–280 (1979), Table III.
[32] L. D. Landau and E. M. Lifschitz, *Theory of Elasticity*, 3rd ed. (Pergamon, New York, 1986), p. 10.
[33] L. Peselnick and I. Zietez, ''Internal friction of fine-grained limestones at ultrasonic frequencies,'' Geophysics **24**, 285–296 (1959).
[34] L. Peselnick, ''Elastic coefficients of Solenhofen limestone and their dependence upon density and saturation,'' J. Geophys. Res. **67**, 4441–4448 (1962), Table I.
[35] As $\theta \rightarrow 90°$, the situation grows more complicated: specular effects will appear in the data, but the model simulates only *non*specular scattering.
[36] For grazing angles small enough that the bottom acts like a Dirichlet boundary, the predicted behavior would be $\sigma \propto \sin^4\theta/\cos^{\gamma_2}\theta \approx \sin^4\theta$. However, indications are that this behavior would only be seen at *very* small angles, below about 5°. We do not emphasize this because (1) we have no data at such angles and (2) the theory that we are using has limited applicability at these grazing angles because it does not include shadowing.
[37] D. R. Jackson, D. P. Winebrenner, and A. Ishimaru, ''Application of the composite roughness model to high-frequency bottom scattering,'' J. Acoust. Soc. Am. **79**, 1410–1422 (1986).

Coupled perturbed modes and internal solitary waves

C. J. Higham and C. T. Tindle
Department of Physics, University of Auckland, Private Bag 92019, Auckland, New Zealand

(Received 24 May 2002; revised 24 January 2003; accepted 27 January 2003)

Coupled perturbed mode theory combines conventional coupled modes and perturbation theory. The theory is used to directly calculate mode coupling in a range-dependent shallow water problem involving propagation through continental shelf internal solitary waves. The solitary waves considered are thermocline depressions, separating well-mixed upper and lower layers. The method is fast and accurate. Results highlight mode coupling associated with internal solitary waves, and mode capture or loss to and from the discrete mode spectrum. © *2003 Acoustical Society of America.* [DOI: 10.1121/1.1561494]

PACS numbers: 43.30.Bp [WLS]

I. INTRODUCTION

Shallow water acoustic research has historically centered on the details of bottom interaction and range-dependent bathymetry. Attention has recently turned to range dependence of the water-column itself. In particular, the effects high-amplitude nonlinear internal waves have on acoustic propagation in the coastal zone.

Internal solitary waves (solitons) are prevalent when stratification is strong, and occur as propagating pulselike depressions of the thermocline. They are considered prime mechanisms leading to observed fluctuations of low-frequency signals.[1,2] Numerical propagation studies[1–7] have indicated that these signal fluctuations are a result of strong coupling of acoustic energy between normal modes as sound propagates through a soliton.

Previous related studies have largely used modal decomposition of parabolic equation (PE) models[1–5] to determine mode coupling and propagation in an internal wave field. Mode decomposition extracts the modal content of the PE generated acoustic field at each range of interest. The method employs mode orthogonality[8] and therefore requires the mode shapes be known for each range of interest. A recent simplified coupled mode approach, the sharp-interface approximation (SIA),[3,4,6] treats a soliton as a one-dimensional square well with well understood mode coupling characteristics. The applicability of this method is detailed in Ref. 3.

Both the PE with modal decomposition and the SIA give information about soliton mode coupling, but they are not a direct modal solution for internal wave problems. A full coupled mode treatment gives an exact modal solution for sufficiently small range steps. The obvious drawback—repeated solution of the wave equation for each step in range—makes this method computationally intensive and therefore somewhat impractical.

The present work employs the method of coupled perturbed modes (introduced in Ref. 9) to solve internal wave problems. The method combines perturbation theory and conventional coupled mode theory to yield a fast, direct, and accurate modal solution. Mode coupling effects are readily obtained with good accuracy.

The first use of perturbation theory in underwater acoustics was described by Williams.[10] Williams took the normal modes of a Pekeris model and used perturbation theory to find the normal modes for both linear and step sound speed profiles. A recent use of perturbation theory in a coupled mode procedure has been developed by Voronovich.[11] Voronovich uses perturbation theory to determine mode coupling matrices within a large range step where the sound speed profile is assumed to vary linearly across the range step and the normal modes at the step endpoints are known.

A brief outline of coupled modes and perturbation theory is given in Sec. II followed by a description of the soliton model in Sec. III. Numerical simulations and environment parameters are outlined in Sec. IV, with test case results using coupled perturbed modes presented in Sec. V. Using perturbation expressions, soliton coupling physics is described in Sec. VI. Discussion and conclusions are given in Sec. VII.

II. COUPLED MODES AND PERTURBATION THEORY

Coupled mode theory[12] breaks the range-dependent environment into a stepwise range independent problem. The acoustic field is found by matching the range independent solutions at the step endpoints. The range step size is reduced until the solution converges and the solution is then considered exact. Conventionally, this process requires solution of the wave equation for the mode functions at each range step.

A. Perturbation theory

Coupled perturbed mode theory assumes the normal modes of a given range step can be expanded as a linear combination of those of the previous step for small changes in the environment. These perturbed modes remove the need to repeatedly solve the depth-separated wave equation and are readily incorporated into the standard coupled mode formalism.

The application of perturbation theory to underwater acoustics is described in Refs. 9 and 10. The method may be summarized as follows. Given a set of normal modes $U_n(z)$ and eigenvalues k_n (horizontal wave numbers) for sound speed profile $c(z)$ as a function of depth z, then for a slightly different profile $\tilde{c}(z)=c(z)+\Delta c(z)$, first order perturbation theory gives the wave numbers and normal modes for this new profile as

$$\tilde{k}_n = k_n + \Delta k_n, \tag{1}$$

$$\tilde{U}_n(z) = U_n(z) + \sum_m a_{nm} U_m(z), \tag{2}$$

where

$$\Delta k_n = \frac{1}{2k_n} \int_0^\infty \frac{\Delta q(z) U_n^2(z)}{\rho(z)} \mathrm{d}z, \tag{3}$$

$$a_{nm} = \frac{1}{k_n^2 - k_m^2} \int_0^\infty \frac{\Delta q(z) U_n(z) U_m(z)}{\rho(z)} \mathrm{d}z \quad (n \neq m). \tag{4}$$

The function $q(z) = \omega^2/c^2(z)$ is defined for convenience and for small change $\Delta c(z)$ has a corresponding change $\Delta q(z)$. The a_{nn} are found by requiring the perturbed modes to satisfy mode normalization[8] giving

$$a_{nn} \approx -\frac{1}{2} \sum_{m \neq n} a_{nm}^2, \tag{5}$$

where second order perturbation terms have been included, and $\Sigma_{m \neq n} a_{nm}^2 \ll 1$ is assumed.

B. Coupled mode theory

In coupled mode theory the jth range independent step of range r is defined as the interval $r \in [r_{j-1}, r_j]$. The acoustic pressure $p(r,z)$ of the jth step for a point source in cylindrical geometry is expressed as[8]

$$p^{(j)}(r,z) \approx r^{-1/2} \sum_n A_n^{(j)} U_n^{(j)}(z) e^{ik_n^{(j)}(r - r_{j-1})}. \tag{6}$$

The mode coefficients A_n for subsequent range steps are found by matching pressure and particle velocity across the step interface. The approximate single-scatter one-way coupled mode approach of Porter *et al.*[13] gives

$$A_n^{(j+1)} = \sum_m C_{nm}^{(j)} A_m^{(j)} e^{ik_m^{(j)}(r_j - r_{j-1})}, \tag{7}$$

where

$$C_{nm}^{(j)} = \frac{1}{2} \left[\int_0^\infty \frac{U_n^{(j+1)}(z) U_m^{(j)}(z)}{\rho^{(j+1)}(z)} \mathrm{d}z + \frac{k_m^{(j)}}{k_n^{(j+1)}} \int_0^\infty \frac{U_n^{(j+1)}(z) U_m^{(j)}(z)}{\rho^{(j)}(z)} \mathrm{d}z \right]. \tag{8}$$

For the problems considered later, density is independent of range and the factor $k_m^{(j)}/k_n^{(j+1)}$ is close to unity for nearby modes as the mode shapes and wave numbers vary little between successive *small* steps. Furthermore, for modes well separated in mode number, the product $U_n^{(j+1)}(z) U_m^{(j)}(z)$ oscillates rapidly and the integrals of Eq. (8) for such mode numbers are negligible. To a good approximation Eq. (8) may therefore be replaced with

$$C_{nm}^{(j)} \approx \int_0^\infty \frac{U_n^{(j+1)}(z) U_m^{(j)}(z)}{\rho(z)} \mathrm{d}z. \tag{9}$$

This result is equivalent to matching only pressure at the step boundaries. Matching particle velocity is only important when density is a function of both range and depth.[13]

Substitution of Eq. (2) into Eq. (9), and use of mode orthogonality[8] allows analytical evaluation of the integral of Eq. (9). Combined with Eq. (7) this yields a single simple expression for the perturbed mode coefficients,[9]

$$A_n^{(j+1)} = A_n^{(j)} e^{ik_n^{(j)}(r_j - r_{j-1})} + \sum_m a_{nm}^{(j)} A_m^{(j)} e^{ik_m^{(j)}(r_j - r_{j-1})}. \tag{10}$$

An individual mode coefficient is thus a phase advanced, weighted, and summed projection of the complete set of mode coefficients of the previous step.

For $j = 1$, the $A_n^{(1)}$ are the source mode coefficients for a range independent wave guide,[8]

$$A_n^{(1)} = \sqrt{\frac{2\pi}{k_n}} \frac{e^{i\pi/4}}{\rho(z_s)} U_n(z_s), \tag{11}$$

where z_s is the depth of the source.

III. INTERNAL SOLITARY WAVES

Shallow water internal waves arise through the nonlinear interaction of oceanic tides and bottom features such as the edge of the continental shelf. They appear as pulselike depressions of the thermocline which travel shorewards in identifiable groups, or wave packets. Each packet member propagates with its shape unchanged at a constant phase velocity. Internal waves of this description are termed solitary waves or solitons.

Several internal wave studies[2–5] have modelled shallow water solitons using a stratified two-layer model of the water-column, and an analytic solution to the nonlinear Korteweg–de Vries (KdV) equation.[14] The two-layer model assumes density undergoes a stepwise transition between well-mixed (constant density) upper and lower layers. Under suitable conditions the displacement of this boundary, $\eta(r,t)$, satisfies the KdV equation:[14]

$$\eta_t + \nu \eta_r + \alpha \eta \eta_r + \beta \eta_{rrr} = 0, \tag{12}$$

where the subscripts denote partial derivatives, ν is the linear phase speed, α is the nonlinear coefficient, and β is a measure of dispersion. Solitary wave solutions to Eq. (12) take the form

$$\eta = \eta_0 \operatorname{sech}^2[(r - Vt)/L]. \tag{13}$$

The soliton velocity V and its horizontal scale-length L are related to the amplitude η_0 by

$$V = \nu + \alpha \eta_0/3, \tag{14}$$

$$L^2 = 12\beta/(\alpha \eta_0). \tag{15}$$

Packet formation can be achieved by expressing the packet as the sum of several single progressive solitons,

$$\eta(r) = \sum_\ell \eta_{0_\ell} \operatorname{sech}^2[(r - r_\ell)/L_\ell], \tag{16}$$

where r_ℓ is the center in range of the ℓth soliton.

IV. NUMERICAL MODELING

Based on the solitary wave model of Eq. (13), Preisig and Duda used PE and SIA methods to investigate the relationship between mode coupling and the physical features of a soliton,[3] and the effect modal phase and internal wave packet position have on acoustic propagation.[4] By analyzing the same problems as Preisig and Duda the present paper shows the usefulness of coupled perturbed modes in shallow water internal wave problems.

A. Model environment

The water-column is modelled on a three-layer stratified system[15] consisting of isovelocity upper and lower layers and a constant gradient intermediate layer. This intermediate layer is the thermocline, and pulselike depressions of its boundaries are described by Eqs. (13)–(15). The environment parameters are based on data from the SWARM 95 experiment.[16] The sound speed in the water-column is 1522 m/s and 1494 m/s in the upper and lower layers, respectively. The bottom has density 2000 kg/m^3 and a sound speed of 1673.3 m/s. Bottom attenuation is set to either 0.0 or 0.7 dB/λ, consistent with losses for 400 Hz in sand.

B. Numerical simulations

All acoustic field, perturbed mode functions, and coupling calculations computed in this paper were performed using MATLAB® code. Computation of exact mode functions for a given set of environmental parameters is done using ORCA, a range independent normal mode code.[17] A MATLAB subroutine calls ORCA for different sound speed profiles, and in this sense makes ORCA range-dependent. This arrangement gives an exact coupled mode solution as a reference solution to test the perturbation approximation.

V. COUPLED MODES MODELING OF INTERNAL SOLITARY WAVES

A. Single internal solitary wave

The background sound speed profile and basic environment described in Sec. IV A are shown in Fig. 1. The water depth is 50 m, and the bottom is truncated at depth 200 m with a pressure release floor that discretizes the continuum;[12] the discretized continuous modes are referred to as untrapped modes. Following Ref. 3, attenuation in the bottom is set to 0.0 dB/λ.

Included in Fig. 1 are the thermocline boundaries. The upper boundary has a background depth of 10 m, the lower boundary 20 m. Displacement of both boundaries is described by Eq. (13). The amplitude η_0 of the soliton depression investigated is 15 m, and the horizontal scale $L = 75$ m. The soliton is centered at $r = 0$ m.

The solitary wave of Fig. 1 is one of several cases used by Preisig and Duda to investigate modal content within a single soliton.[3]

1. Mode capture/loss

Modal cutoff—the transition of a mode between the discrete ('trapped') and continuous mode spectrum—is an important feature of shallow acoustics.[8] Range-dependent sound speed profiles, such as that created by the soliton depression of Fig. 1, present the possibility of a trapped (or untrapped) mode passing through cutoff. For a 400 Hz harmonic source, the acoustic environment of Fig. 1 supports 12 trapped modes outside the soliton, and 11 at the soliton center. This implies that mode 12 transits cutoff twice as sound propagates through the soliton; mode 12 is first lost from the trapped modes as the soliton center is approached, and then recaptured as the soliton recedes.

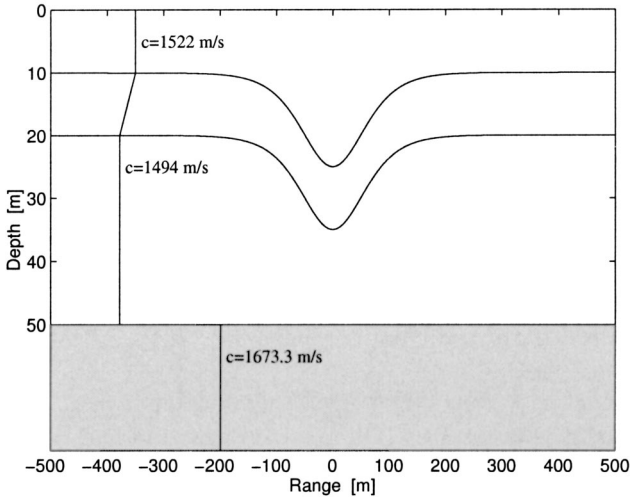

FIG. 1. Single soliton environment; see text for details.

The energy transfer that characterizes the transition from trapped to untrapped mode (or vice versa) is large and significant. This creates a difficulty for perturbation theory which is built on the premise of small and incremental changes. As explained below, the difficulty is overcome by using the exact modes in the region where a mode passes through cutoff.

Trapped modes are confined within the water-column with no energy propagation into the bottom; untrapped modes represent energy that is leaked into the bottom. These properties are characterized by the exponential tail of a trapped mode in the bottom, and the oscillatory nature of an untrapped mode in the bottom. The relative size of trapped and untrapped mode shapes in the water-column indicate the acoustical energy of the mode; trapped modes carry the bulk of the energy in the water-column. The left-hand side of Fig. 2 shows mode 12 as a trapped mode outside the soliton (solid line) and an untrapped mode at the center of the soliton (dashed line). The bottom is shaded.

Transition through cutoff, therefore, sees a mode change its shape in the bottom between exponential and oscillatory. The amplitude also changes rapidly as the mode shapes adjust to the redistribution of energy. The adjustment is not limited to the mode undergoing cutoff, but extends to adjacent modes through mode coupling. Those most affected are modes close in mode number as Eq. (4) shows coupling strength is proportional to $[k_n^2 - k_m^2]^{-1}$. Perturbation theory cannot handle this transition as the changes are rapid and large. This difficulty is easily overcome by using exact mode functions to update the field when a mode is near cutoff.

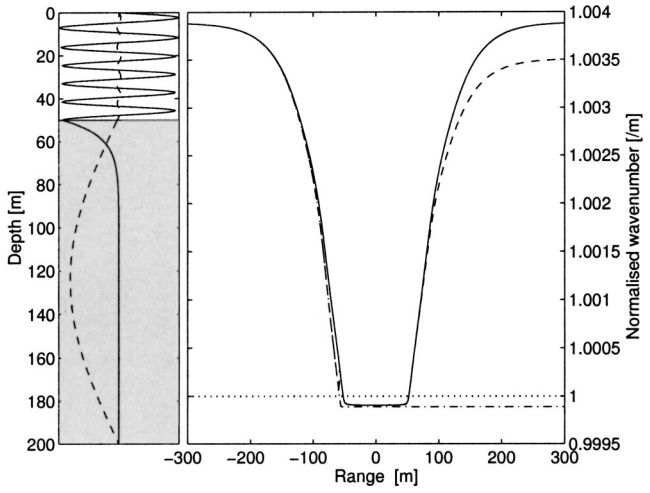

FIG. 2. Left: mode 12 outside the soliton (solid line), and at the soliton center (dashed line). Right: normalized wave number for mode 12; see text for details.

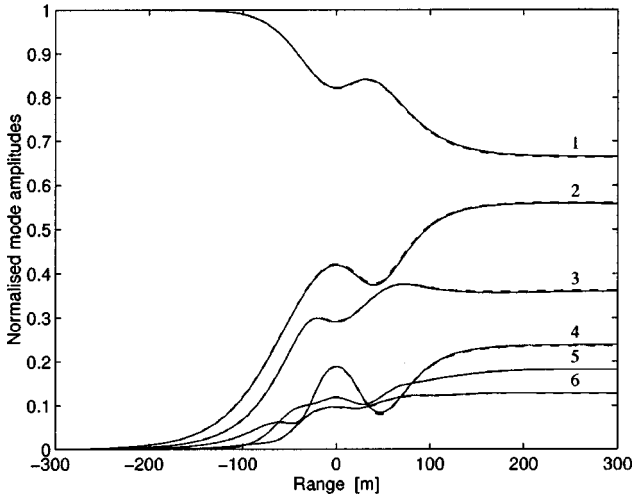

FIG. 3. Exact (solid lines) and approximate (dashed lines) normalized mode amplitudes for modes 1–6. Energy initially in mode 1 couples to other modes as the soliton is traversed. The perturbation result includes exact modes about cutoff.

Cutoff can be defined in terms of modal phase velocity v_n, or horizontal wave number k_n,

$$v_n = \omega/k_n \quad (= c_b \quad \text{at cutoff}),$$
$$\Rightarrow k_c = \omega/c_b, \tag{17}$$

where k_c is the cutoff wave number, ω is the radial frequency of the source, and c_b is the sound speed in the bottom. A mode is trapped for $k_n > k_c$, and untrapped for $k_n < k_c$. In numerical calculations, the approach of mode cutoff can be monitored through the wave numbers as the coupled perturbed mode calculation advances in range. If a value of k_n falls within some user-specified interval about k_c, the field is updated with exact mode functions. Perturbed mode functions are used outside this interval. The update interval is limited by the spacing between the cutoff wave number and the wave number of the first untrapped mode.

The right-hand side of Fig. 2 shows the wave number for mode 12 as a function of range normalized by dividing by k_c. The solid line of the exact wave number k_{12} cuts the horizontal dotted k_c line in two places. These are the cutoff points where mode 12 is first lost from the discrete spectrum, then recaptured as sound propagates through the soliton. For a left-to-right propagation direction the dotted–dashed line is the perturbation result for k_{12} with no field updates. The result clearly fails to model the wave number of mode 12 after cutoff. This is directly related to the rapid change in mode shape and amplitude of mode 12 at cutoff. By using exact mode functions for a small interval about cutoff (and perturbed mode functions elsewhere), the dashed line gives a much better approximation.

The lower order modes are trapped below the thermocline and can experience an effect similar to cutoff for changes in the thermocline depth. This process is smooth and continuous, and is modelled well by perturbation theory; an example is given in Sec. V B.

2. Mode amplitudes

The solitary wave illustrated in Fig. 1 has a rapid change of sound speed profile with range (typical of steep narrow solitons) providing a good test for coupled perturbed modes. Using 1 m range steps, the acoustic field is calculated for the range interval $[-500,500]$ m beginning at $r=-500$ m with exact mode functions. The problem is assumed to be quasi-static: the soliton properties are fixed whilst the acoustic signal propagates through the soliton. Following Ref. 3, the mode amplitudes at each step j are normalized such that $\Sigma_n |A_n^{(j)}|^2 = 1$.

The mode amplitudes of the first six trapped modes are shown in Fig. 3. The figure corresponds to Fig. 6(b) of Ref. 3 where the field initially consists only of mode 1, and the mode amplitudes were obtained by modal decomposition of a PE solution. Here, exact and perturbed mode solutions are compared in Fig. 3. To ensure the continuum is well sampled, 20 modes are used in the perturbation Eqs. (3) and (4), but only the trapped modes (12 outside the soliton) are used in the coupling expression Eq. (10) as these carry almost all the acoustical information. As the soliton trough is approached ($r=0$ m), the field which is initially entirely composed of mode 1 couples into the lower order modes. Strong net coupling is observed at the completion of the soliton traversal. This mode coupling is heavily determined by the relative phases of the modes, and is explored later in some detail.

With exact mode function updates about cutoff included, the perturbed mode amplitudes (dashed lines, Fig. 3) give an excellent approximation to the exact mode amplitudes (solid lines, Fig. 3). This accuracy is achieved with a remarkable level of efficiency. For each computational step the CPU runtime for the perturbation approximation is ~2–3% of the runtime for the equivalent exact coupled mode calculation. This is because the exact solution must numerically solve for the normal modes and wave numbers at each range step. The perturbation approximation is therefore significantly faster than the exact coupled mode approach with negligible loss in accuracy.

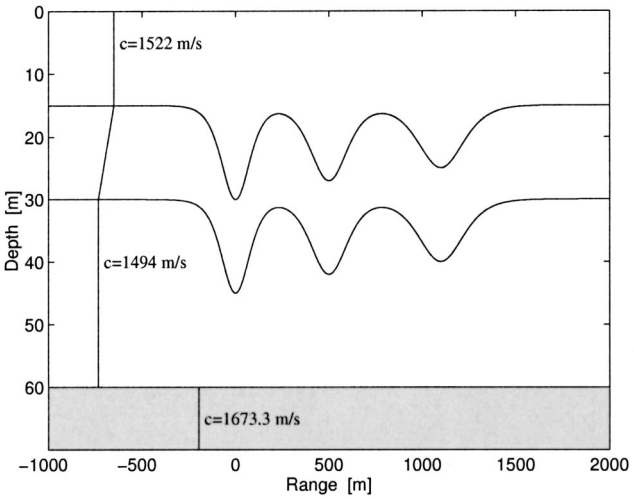

FIG. 4. Soliton packet and environment; see text for details.

It is interesting to note that Preisig and Duda considered mode coupling in an internal wave field via a perturbational approach, and concluded that perturbation theory failed to accurately describe the change in mode shapes for soliton displacements of more than a few meters.[3] The results shown here suggest otherwise.

B. Internal solitary wave packets

In a second paper, Preisig and Duda considered the effects that modal phase and solitary wave packets have on determining shallow water acoustic propagation.[4] To isolate positional packet effects, packet evolution was ignored: the packet retains the same shape with range.

The background sound speed profile and environment is illustrated in Fig. 4. The water depth is 60 m and a pressure release floor is placed at 200 m. Environment parameters are as given in Sec. IV A, with bottom attenuation set to 0.7 dB/λ. The wave packet is described by Eq. (16), and consists of three solitons. The leading soliton, the tallest and most narrow packet member for KdV solutions (and also most observations), is centered at $r_1=0$ m with amplitude $\eta_{0_1}=15$ m, and scale-length $L_1=100$ m. The trailing solitons can be described recursively. For $\ell=2$, 3,

$$\begin{aligned} r_\ell &= r_{\ell-1}+500[1+0.2(\ell-2)], \\ \eta_{0_\ell} &= \eta_{0_1}-[2(\ell-1)+1], \\ L_\ell &= L_1+30(\ell-1). \end{aligned} \tag{18}$$

The background thermocline boundary depths are 15 m and 30 m for the upper and lower boundaries, respectively. For the wave packet and environment described there is no mode capture and/or loss to, or from the discrete modes at 400 Hz.

1. Mode shapes and wavenumbers

The first five trapped modes for the soliton packet environment of Fig. 4 are illustrated in Fig. 5. The modes are plotted with arbitrary amplitude superimposed on the sound speed profile at their phase velocities. Two extremes are shown. The upper panel of Fig. 5 shows the profile and mode shapes at the center of the leading soliton where the thermocline boundaries are at maximum depression. The lower panel shows the background profile and associated mode shapes.

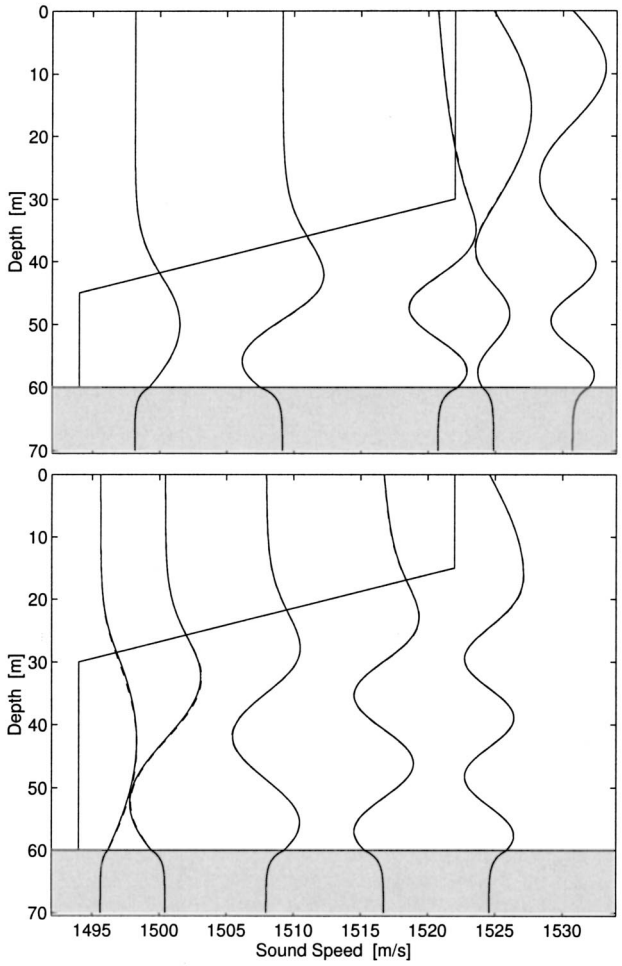

FIG. 5. Exact (solid lines) and approximate (dashed lines) mode shapes for modes 1–5 plotted at their respective phase velocities. Upper: sound speed profile at the center of the leading soliton. Lower: background sound speed profile.

For the background sound speed profile, modes 1–4 have exponential tails that extend to the surface and are examples of trapped modes that have two turning points, i.e., transition points between oscillatory and exponential dependence with depth. Modes 1–4 are trapped by the thermocline. For the same profile, mode 5 (with only a lower turning point) is completely oscillatory above the bottom with a null at the surface corresponding to surface reflected equivalent rays. The boundary between these two different types of mode shapes is defined by the sound speed in the upper water layer, $c_u=1522$ m/s. For phase velocities $v_n > c_u$ the mode shapes are oscillatory towards the surface, and for $v_n < c_u$ they are exponential.

As the modes propagate through the soliton packet, the mode shapes adjust to the changing sound speed profile. The spatial extent over which the loops of the lower order modes exist is alternatively compressed and expanded through the packet traversal. At maximum depression of the thermocline (upper panel, Fig. 5), the mode shapes are significantly different from those of the background profile (lower panel,

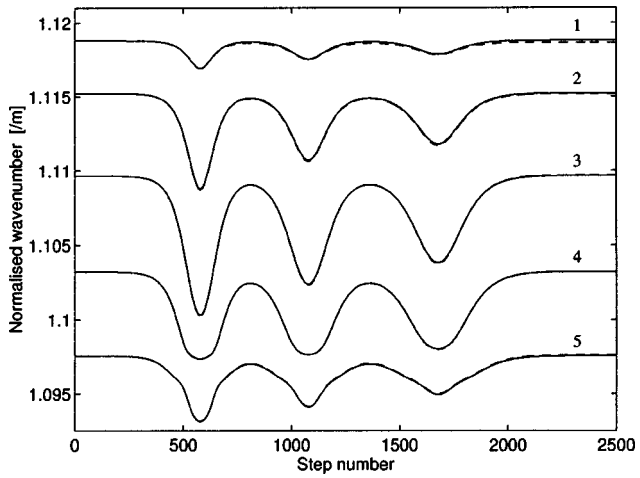

FIG. 6. Exact (solid lines) and approximate (dashed lines) normalized wave numbers for modes 1–5.

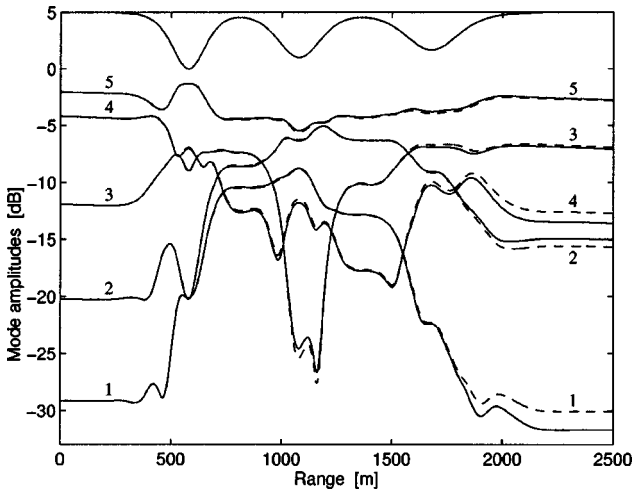

FIG. 7. Exact (solid lines) and approximate (dashed lines) mode amplitudes for modes 1–5; the curves are labeled before and after the packet traversal. The soliton packet ($r_1 = 578$ m) is included with arbitrary vertical scale at the top of the figure.

Fig. 5). In particular, mode 4 changes between exponential and oscillatory near the surface. The contrast in mode shapes between soliton trough and exterior is a good test of perturbation theory.

Included in Fig. 5 are the approximate perturbation solution for modes 1–5. These are indicated by the dashed lines. The perturbation calculation begins with the exact mode functions of the background sound speed profile, and as the packet is traversed the new mode shapes are found via Eqs. (2) and (4). The step size is 1 m and the direction of propagation is left-to-right in Fig. 4. The level of agreement is high with the approximate modes almost indistinguishable from the exact modes at the center of the lead soliton (upper panel, Fig. 5), and only just visible for the background profile after the packet is completely traversed (lower panel, Fig. 5).

A feature of Fig. 5 are the shifts in phase velocities as the modes propagate through the soliton packet. Mode 3 in particular shows a large change in phase velocity between the two profiles: 1508 m/s for the background profile and 1521 m/s at the center of the lead soliton. This is further highlighted by Fig. 6 which shows the normalized wave numbers for propagation through the above packet as a function of step number. All the curves echo the soliton packet shape of Fig. 4. Mode 3 has the largest wave number (and hence phase velocity) variations for the problem investigated. Like the mode shapes of Fig. 5, good agreement is observed in Fig. 6 between the exact wave numbers (solid lines) and the perturbation approximation (dashed lines).

2. Mode amplitudes

Moving the fixed shape soliton packet of Fig. 4 with respect to the source position, Preisig and Duda investigated the effect that mode phasing has on determining the modal content in an internal wave field. A packet position from their investigation is used here as a test case for coupled perturbed modes. The packet illustrated in Fig. 4 is positioned with the lead soliton centered at $r_1 = 578$ m, and the acoustic field is calculated from the source position ($r_s = 0$ m, $z_s = 18$ m) in 1 m steps.

The mode amplitudes of the first five trapped modes are shown in Fig. 7 along with the soliton packet shape at the top of the figure. The figure corresponds to Fig. 19 of Ref. 4 where the mode amplitudes were obtained by modal decomposition of a PE solution. Here, exact and perturbed mode solutions are compared in Fig. 7. As for the single soliton case, only the trapped modes (14 at the source range) are used in the coupling calculation; 22 modes are used in the perturbation calculations to ensure adequate sampling of the continuum. Mode coupling is different for each of the three solitons, and is strongest in the vicinities of rapid sound speed variation with range—regions where the depth of the thermocline changes most rapidly.

Beginning with exact mode functions at the source, the perturbation approximation (dashed lines, Fig. 7) determines the mode amplitudes using Eq. (10). No updates using exact mode functions for mode capture/loss are required here, and the perturbation approximation is in good agreement with the exact coupled mode result (solid lines, Fig. 7). Again, the approximate solution is significantly faster with computational savings similar to the single soliton result.

The results of Fig. 7 have been adjusted by a factor of 2 ($\sim$6 dB) to allow comparison with Fig. 19 of Ref. 4 where a factor of 2 was included.

VI. COUPLING PHYSICS

With their single soliton study[3] Preisig and Duda successfully described the physics that govern soliton mode coupling with an adiabatic invariance criterion and a simple sharp-interface model (SIA) of the soliton depression. Their later work on soliton packets[4] showed that packet coupling is linear (coupling can be resolved into single soliton coupling expressions for each packet member), and sensitive to modal phase. In the examples below the same coupling physics described by Preisig and Duda is obtained through the application of perturbation theory and standard coupled mode theory to internal solitary waves.

A. Mode coupling

Based on the condition for adiabatic invariance developed by Milder[18]—a criterion for the absence of mode coupling between mode pairs—Preisig and Duda derived an expression to determine the likelihood of any two modes coupling due to the shape of a soliton. Their expression found the increased likelihood of coupling between mode pairs was proportional to a weighted projection of the mode shapes over the thermocline layer, and proportional to the square of the mode interference length, $2\pi/(k_n-k_m)$. This sensitivity to the difference in wave numbers and the weighted projection of the mode shapes is shown explicitly by the expressions of perturbation theory.

For the soliton environments studied, the change in sound speed between adjacent range steps is nonzero only for the depth interval defined by the thermocline boundaries before and after the step interface. The limits of integration in Eq. (4) are set by this interval, $z\in[a,b]$ say, i.e.,

$$a_{nm}=\frac{1}{k_n^2-k_m^2}\int_a^b \frac{\Delta q(z)U_n(z)U_m(z)}{\rho(z)}\,\mathrm{d}z. \tag{19}$$

Physically, Eq. (19) states that for any mode pair n and m, coupling is more likely if the term $k_n^2-k_m^2$ is small or if the weighted projection of mode n onto mode m over $z\in[a,b]$ is large. The latter is more likely (assuming a fixed step size) for ranges where the depth interval is largest, i.e., where the depth of the thermocline changes most rapidly. Coupling between adjacent modes is more probable because the product $U_n(z)U_m(z)$ varies slowly for nearby modes, whereas for modes well separated in mode number it varies rapidly and the integral in Eq. (19) is small. The perturbation expression Eq. (19) confirms the effects found by Preisig and Duda with their adiabatic criterion.

B. Mode phasing

By approximating the soliton shape with a top-hat function and applying conventional one-way coupled mode theory, Preisig and Duda obtained simple mode coupling expressions for acoustic energy transfer across a step interface. This sharp-interface approximation was successfully used to explain the importance of mode phasing on net mode coupling (induced by individual solitons or soliton packets), and coupling within soliton packets.[3,4] Here the same mode phasing characteristics are quantified by Eq. (10), the perturbation approximation for the mode coefficients A_n, where the coupling coefficients C_{nm} are derived from first principles.

Essentially, Eq. (10) states that the mode coefficient $A_n^{(j+1)}$ is the sum of a set of phasors each with a different amplitude and phase, and that the phase of each phasor determines the amplitude of $A_n^{(j+1)}$ from the set of mode amplitudes for range step j. These phases are strongly dependent on both range and the wave number k_n for a given mode. As the wave number for each mode is unique, the phase of each mode coefficient advances at a different rate with range. Hence, the relative phase between any two modes for a given range determines the amount of acoustic coupling between the two.

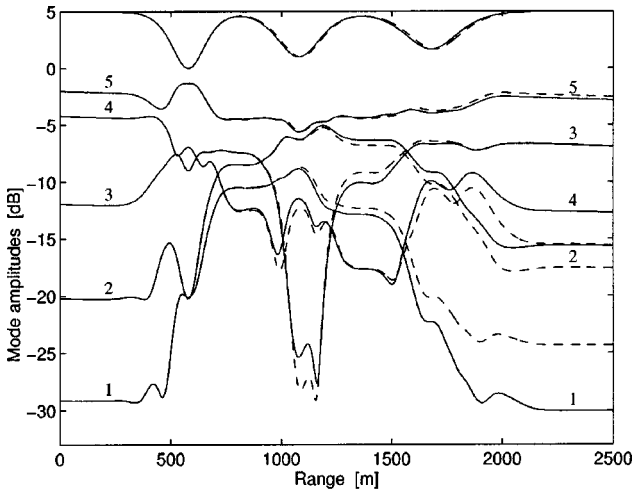

FIG. 8. Perturbed mode amplitudes for the fixed shape soliton packet of Fig. 7 (solid lines) and a slightly lengthened packet (dashed lines); see text for details. The packets are included with arbitrary vertical scale at the top of the figure.

As a solitary wave packet is a range-dependent phenomenon, the modal phase of individual modes can be quite different depending on the range r_p where the packet is first encountered. Consider the field outside the packet where the sound speed is range independent. Here the wave numbers are constant and there is no mode coupling as $\Delta q(z)=0$ in Eqs. (3) and (4). The mode coefficient expression of Eq. (10) reduces to give $A_n^{(j+1)}=A_n^{(j)}e^{ik_n(r_j-r_{j-1})}$. The mode amplitudes are clearly independent of range (no mode coupling) and the accumulated phase at some range r_p is dependent on both range and wave number. This modal phase incident on the source side of a moving packet directly determines the coupling within soliton packets, and—importantly for received signals—the output modal structure.

Packet evolution, where the spacing between the packet members gradually lengthens as the packet propagates, constantly changes the mode phasing characteristics of the packet and hence the packet induced mode coupling. At the top of Fig. 8 are two solitary wave packets. One is the fixed shape packet of Fig. 7 (solid line), the other a slightly lengthened version of that same packet (dashed line). The lead solitons of both packets coincide and the lateral shifts between the second and third members are 9 m and 15 m, respectively. These distances are equivalent to allowing the fixed shape packet to evolve slowly for 6 mins with soliton velocities 0.8, 0.775, and 0.758 m/s. This is not a change in packet position, it is simply a change of packet shape to illustrate a packet dispersion effect. The soliton velocities are comparable to the SWARM 95 data (0.6–0.8 m/s), and the 6 min window is equal to the time between successive SWARM acoustic transmissions.[16]

The lower half of Fig. 8 shows the perturbed mode amplitudes (modes 1–5) for these two slightly different length packets. The difference between the two sets of results increases as the packets are traversed. In particular the mode amplitudes of modes 1, 2, and 4 show a strong difference in output level between the two packets—approximately 3–5 dB. This is a direct result of the rapid change in mode phase

for small variations of the trailing solitons' position (the mode shapes vary slowly and have little effect), and shows for even a small variation in packet length the modal structure after the packet can be quite different.

VII. CONCLUSIONS

Internal solitary wave studies by Preisig and Duda were used as shallow water test cases for the method of coupled perturbed modes. The results presented show the method to be accurate, describing well the acoustic field in the presence of rapid range dependence due to internal solitary waves. Coupled perturbed modes correctly models changes in mode shapes and wave numbers as sound propagates through solitary waves, and also the change in mode amplitudes as a result of soliton induced mode coupling. Results were achieved with improved efficiency over a standard one-way coupled mode approach. This efficiency is achieved by removing the need to solve the depth-separated wave equation numerically for the mode functions at each range step, as is the case for standard coupled mode theory, and instead determining the mode functions for a given range step from those of the previous step.

For range-dependent sound speed profiles, modal cutoff can be important. The large transfer of energy between trapped and untrapped modes at cutoff is too great for perturbation theory and requires field updates using exact mode functions. With allowance for this phenomenon, coupled perturbed modes is a useful tool for solving range-dependent shallow water problems.

The combination of coupled modes and perturbation theory yields simple expressions for soliton mode coupling. Derived here from first principles, they directly quantify the conclusions drawn by Preisig and Duda.

The perturbation expressions describe the likelihood of mode coupling between pairs of modes, and the role of mode phasing in determining modal content. Mode phasing is strongly dependent on the source to soliton range and the spacing between packet members. Results show different net coupling for solitary wave packets of similar, but slightly different lengths, emphasizing the sensitivity of modal content on the details of solitary wave packet evolution and modal phase.

[1] Ji-xun Zhou, Xue-zhen Zhang, and Peter H. Rogers, ''Resonant interaction of sound wave with internal solitons in the coastal zone,'' J. Acoust. Soc. Am. **90**, 2042–2054 (1991).

[2] Ji-xun Zhou, Xue-zhen Zhang, Peter H. Rogers, Dezhao Wang, and Ensheng Luo, ''Anomalous sound propagation in shallow water due to internal wave solitons,'' Proc. IEEE Oceans (Engineering in harmony with the ocean), Vol. 1, pp. I-87–I-92 (1993).

[3] J. C. Preisig and T. F. Duda, ''Coupled acoustic mode propagation through continental-shelf internal solitary waves,'' IEEE J. Ocean. Eng. **22**, 256–269 (1997).

[4] T. F. Duda and J. C. Preisig, ''A modelling study of acoustic propagation through moving shallow-water solitary wave packets,'' IEEE J. Ocean. Eng. **24**, 16–32 (1999).

[5] D. Tielbürger, S. Finette, and S. Wolf, ''Acoustic propagation through an internal wave field in a shallow water waveguide,'' J. Acoust. Soc. Am. **101**, 789–808 (1997).

[6] R. H. Headrick, J. F. Lynch, J. N. Kemp, A. E. Newhall, K. von der Hedyt, J. Apel, M. Badiey, C.-S. Chiu, S. Finette, M. Orr, B. Pasewark, A. Turgot, S. Wolf, and D. Tielbuerger, ''Modelling mode arrivals in the 1995 SWARM experiment acoustic transmissions,'' J. Acoust. Soc. Am. **107**, 221–236 (2000).

[7] S. Finette, M. H. Orr, A. Turgut, J. R. Apel, M. Badiey, C.-S. Chiu, R. H. Headrick, J. N. Kemp, J. F. Lynch, A. E. Newhall, K. von der Hedyt, B. Pasewark, S. N. Wolf, and D. Tielbuerger, ''Acoustic field variability induced by time evolving internal wave fields,'' J. Acoust. Soc. Am. **108**, 957–972 (2000).

[8] F. B. Jensen, W. A. Kuperman, M. B. Porter, and H. Schmidt, *Computational Ocean Acoustics*, AIP Series in Modern Acoustics and Signal Processing (AIP Press, New York, 1994).

[9] C. T. Tindle, L. M. O'Driscoll, and C. J. Higham, ''Coupled mode perturbation theory of range dependence,'' J. Acoust. Soc. Am. **108**, 76–83 (2000).

[10] A. O. Williams, Jr. ''Some effects of velocity stucture on low-frequency propagation in shallow water,'' J. Acoust. Soc. Am. **32**, 363–371 (1960).

[11] A. Voronovich, ''Non-paprabolic marching algorithm for sound field calculation in the ocean waveguide,'' J. Comp. Acoustics, **4**, 399–423 (1996).

[12] R. B. Evans, ''A coupled mode solution for acoustic propagation in a waveguide with stepwise depth variations of a penetrable bottom,'' J. Acoust. Soc. Am. **74**, 188–195 (1983).

[13] M. B. Porter, F. B. Jensen, and C. M. Ferla, ''The problem of energy conservation in one-way models,'' J. Acoust. Soc. Am. **89**, 1058–1067 (1991).

[14] L. A. Ostrovsky and Yu. A. Stepanyants, ''Do internal solitons exist in the ocean?'' Rev. Geophys. **27**, 293–310 (1989).

[15] O. S. Lee, ''Effect of an internal wave on sound speed in the ocean,'' J. Acoust. Soc. Am. **33**, 677–681 (1961).

[16] J. R. Apel, M. Badiey, C.-S. Chiu, S. Finette, R. H. Headrick, J. N. Kemp, J. F. Lynch, A. E. Newhall, M. H. Orr, B. Pasewark, D. Tielbuerger, A. Turgut, K. von der Hedyt, and S. N. Wolf, ''An overview of the 1995 SWARM shallow water internal wave acoustic scattering experiment,'' IEEE J. Ocean. Eng. **22**, 465–500 (1997).

[17] E. K. Westwood, C. T. Tindle, and N. R. Chapman, ''A normal mode model for acousto-elastic ocean environments,'' J. Acoust. Soc. Am. **100**, 3631–3645 (1996).

[18] D. M. Milder, ''Ray and wave invariants for sofar channel propagation,'' J. Acoust. Soc. Am. **46**, 1259–1263 (1969).

Ray travel times at long ranges in acoustic waveguides

A. L. Virovlyansky
Institute of Applied Physics, Russian Academy of Science, 46 Ul'yanov Street, 603600 Nizhny Novgorod, Russia

(Received 30 November 2000; revised 3 March 2002; accepted 21 January 2003)

The Hamiltonian formalism in terms of the action-angle variables is applied to study ray travel times in a waveguide with a smooth sound speed profile perturbed by a weak range-dependent inhomogeneity. A simple approximate formula relating the differences in ray travel times to range variations of action variables is derived. This relation is applied to study range variations of the timefront (representing ray arrivals in the time-depth plane). Widening and bias of timefront segments in the presence of perturbations are considered. Qualitative and quantitative explanations are given to surprising stability of early portions of timefronts observed in both numerical simulations and field experiments. This phenomenon is interpreted from the viewpoint of Fermat's principle. By ray tracing in a realistic deep water environment with an internal-wave-induced perturbation it has been demonstrated that our approach can be used at ranges up to, at least, 3000 km. © *2003 Acoustical Society of America.* [DOI: 10.1121/1.1561491]

PACS numbers: 43.30.Cq, 43.30.Pc [SACB]

I. INTRODUCTION

The ray travel time is one of the most important and extensively studied characteristics of the wavefield in underwater acoustics. It represents an arrival time of a pulse signal propagating along a ray path connecting the source and the observation point. In field experiments such pulses, especially those propagating through steep ray paths, can often be resolved and identified even at ranges of hundreds of kilometers and longer. In many schemes of acoustic monitoring of ocean structure, ray travel times are main observables used to reconstruct variations in the environment.[1,2]

In the past decade it has been realized that ocean inhomogeneities (such as internal waves) give rise to ray chaos.[3–9] Numerical calculations have demonstrated that if a smooth sound speed profile is perturbed with a range-dependent inhomogeneity, then ray paths (or some of them) reveal extreme sensitivity to initial conditions. Trajectories which are initially neighbors move apart at an exponential rate. It might be expected that under these conditions the structure of ray arrivals becomes unpredictable and quite different from that in the unperturbed waveguide.

However, numerical simulations demonstrate that travel times of rays in the perturbed and unperturbed waveguides have common features. As it was discovered by Tappert and Tang[8] (see also Refs. 10 and 11), in the presence of perturbation the eigenray, i.e., ray connecting two fixed endpoints, splits into a cluster of new eigenrays with travel times closely spaced in the vicinity of the unperturbed arrival. In this sense, ray travel times turn out to be stable characteristics of the wave field. This property also manifests itself in comparative stability of early portions of timefronts (ray arrivals in depth-time plane) formed by steep rays.[9,12,13] It should be pointed out that besides arrival times of sound pulses a ray-based wavefield description can properly predict other characteristics of the acoustic field at long ranges in a fluctuating environment.[14–16]

In this paper we argue that rather simple analytic relations for description of ray travel time variations can be obtained by applying the Hamiltonian formalism[3,6,8,9] and expressing ray parameters via the so-called action-angle canonical variables.[3,17] The action variable, I, defines the shape of a cycle of the ray path while the angle variable, θ, indicates the position of a current ray point inside the cycle.

We derive an approximate analytic relation for the difference between travel times of perturbed and unperturbed rays. This relation provides a convenient tool to study the structure of the timefront in a range-dependent waveguide. It is demonstrated that weak inhomogeneities induced by random internal waves cause not only a widening of the timefront segments (branches) but also lead to a regular bias of segments: in the presence of perturbation the segments are biased toward early times.

Our results contribute to understanding why an early portion of the arrival pattern formed by steep rays remains stable at ranges up to a few thousand kilometers. It has been shown that this phenomenon is associated with Fermat's (Hamilton's) principle. Predictions made with our approximate analytical approach are verified by comparison with results of numerical simulations.

The paper is organized as follows. In Sec. II, a brief description of the Hamiltonian formalism in terms of the position-momentum and action-angle canonical variables is given. Approximate relations for differences in ray travel times are derived in Sec. III. They allow one to compare travel times of (i) two rays in a waveguide with a smooth (unperturbed) range-independent sound speed profile and (ii) a ray in an unperturbed waveguide and another one in a perturbed waveguide. Section IV contains results of numerical simulation carried out for a model of a stratified waveguide perturbed with range-dependent inhomogeneities induced by internal waves. It is demonstrated that our approximate formulas give rather accurate predictions at 3000-km range. In Sec. V we briefly outline the generalization of our approach to the model in which the unperturbed

waveguide adiabatically varies with range. In Sec. VI the results of this work are summarized.

II. HAMILTONIAN FORMALISM

In this section we describe the Hamiltonian formalism corresponding to the ray theory derived from the full wave equation.[3,6,9,18,19] We present expressions defining the Hamiltonian, action function (eikonal), ray equations, and canonical transformation from the position-momentum to action-angle variables.

A. Ray equations in terms of position-momentum variables

Consider wave propagation in a two-dimensional medium with the coordinates r (range) and z (depth). It is assumed that the z axis is directed downward and the plane $z=0$ is the sea surface. The ray trajectory $z(r)$ is determined by the sound speed field $c(r,z)$ and can be found from Fermat's principle[18,19] according to which the first variation of the functional

$$S=c_r\int\frac{ds}{c(r,z)}=\int dr\,n(r,z(r))\sqrt{1+\left(\frac{dz}{dr}\right)^2} \tag{1}$$

vanishes at the ray trajectory. Here $n(r,z)=c_r/c(r,z)$ is the refractive index, c_r is a reference sound speed, and $ds=dr(1+(dz/dr)^2)^{1/2}$ is the arc length. The functional S represents the so-called eikonal and it relates to the ray travel time by

$$t=S/c_r. \tag{2}$$

Formally considering Eq. (1) as an action function of some mechanical system with the r-variable playing the role of time, one can apply the standard relations of classical mechanics.[18–20] This yields explicit expressions for the momentum,

$$p=n\frac{dz/dr}{\sqrt{1+(dz/dr)^2}}, \tag{3}$$

and the Hamiltonian,

$$H=-\sqrt{n^2-p^2}. \tag{4}$$

Equations $p=n\sin\chi$ and $H=-n\cos\chi$ relate the momentum and the Hamiltonian to the ray grazing angle, χ.[9]

Expression (1) for the eikonal can now be rewritten as

$$S=\int(p\,dz-H\,dr). \tag{5}$$

Ray trajectories are governed by the Hamilton equations[8,9,17]

$$\frac{dz}{dr}=\frac{\partial H}{\partial p}=-\frac{p}{H}=\frac{p}{\sqrt{n^2-p^2}}, \tag{6}$$

$$\frac{dp}{dr}=-\frac{\partial H}{\partial z}=\frac{n\partial n/\partial z}{\sqrt{n^2-p^2}}. \tag{7}$$

Equations (1)–(7) present the Hamiltonian formalism in terms of the momentum-position canonical variables. In the remainder of this section we introduce another pair of canonically conjugated variables, namely, the action-angle variables.[3,17,19,20]

B. Action-angle variables

1. Range-independent waveguide

First, define the action-angle variables in a range-independent waveguide with $c=c_0(z)$ and, correspondingly, $n=c_r/c_0(z)=n_0(z)$. In such a waveguide the Hamiltonian remains constant along the ray trajectory:

$$H_0=-\sqrt{n_0^2(z)-p^2}=-n_0(z)\cos\chi=\text{const}. \tag{8}$$

This is Snell's law[21,22] analogous to the energy conservation law in classical mechanics. Equation (8) establishes a simple relation between the momentum p and coordinate z,

$$p=\pm\sqrt{n_0^2(z)-H_0^2}. \tag{9}$$

The action variable I is defined as the integral[3,17,20]

$$I=\frac{1}{2\pi}\oint p\,dz=\frac{1}{\pi}\int_{z_{\min}}^{z_{\max}}dz\,\sqrt{n_0^2(z)-H_0^2} \tag{10}$$

running over the cycle of ray trajectory. Here $z_{\min}$ and $z_{\max}$ are the depths of upper and lower ray turning points, respectively. Equation (10) determines "energy," H_0, as a function of the action variable, I. Note the relation

$$\frac{dH_0}{dI}=\frac{2\pi}{D}=\omega, \tag{11}$$

where D is the cycle length of the ray path, and ω is the angular frequency of spatial path oscillations.

The canonical transformation from the position-momentum, (p,z), to the action-angle, (I,θ), variables,

$$I=I(p,z),\quad \theta=\theta(p,z), \tag{12}$$

and the inverse transformation,

$$z=z(I,\theta),\quad p=p(I,\theta), \tag{13}$$

are determined by the equation[17]

$$dS=p\,dz-H_0\,dr=dG-\theta\,dI-H_0\,dr, \tag{14}$$

where $G=G(I,z)$ is the generating function. An explicit expression for $G(I,z)$ is well known.[3,17] We represent it in the form

$$G(I,z)=\begin{cases}\displaystyle\int_{z_{\min}}^{z}dz\sqrt{n_0^2(z)-H_0^2(I)}, & p>0,\\ \displaystyle 2\pi I-\int_{z_{\min}}^{z}dz\sqrt{n_0^2(z)-H_0^2(I)}, & p<0,\end{cases} \tag{15}$$

where $z_{\min}$ and $z_{\max}$ are considered as functions of I. Then the pair of coupled equations

$$p=\frac{\partial G}{\partial z}=\pm\sqrt{n_0^2(z)-H_0^2(I)}, \tag{16}$$

$$\theta=\frac{\partial G}{\partial I}$$

$$=\begin{cases} -\dfrac{2\pi H_0(I)}{D}\displaystyle\int_{z_{\min}}^{z}\frac{dz}{\sqrt{n_0^2(z)-H_0^2(I)}}, & p>0, \\ 2\pi+\dfrac{2\pi H_0(I)}{D}\displaystyle\int_{z_{\min}}^{z}\frac{dz}{\sqrt{n_0^2(z)-H_0^2(I)}}, & p<0, \end{cases} \tag{17}$$

defines the four functions present in Eqs. (12) and (13).

Note that the so-defined angle variable θ varies from 0 to 2π at a part of the trajectory beginning at one minimum and ending at the next one. To make the angle variable continuous, its value should be increased by 2π at the beginning of each new cycle. Here we assume that the cycle begins at the minimum of the trajectory. Both functions in Eq. (13) are periodic in θ with period 2π.

The ray equations in the new variables take the trivial form

$$\frac{dI}{dr}=-\frac{\partial H_0}{\partial\theta}=0, \quad \frac{d\theta}{dr}=\frac{\partial H_0}{\partial I}=\omega(I), \tag{18}$$

with the solution

$$I=I_s, \quad \theta=\theta_s+\omega(I_s)r, \tag{19}$$

where I_s and θ_s are starting values of the action and angle variables, respectively, at $r=0$.

An explicit expression for the action function (eikonal) is obtained by integrating Eq. (14). For a ray connecting points $(0,z_s)$ and (r,z_e), after some algebra we get

$$S=(I_s\omega(I_s)-H_0(I_s))r-G(z_s,I_s) + G(z_e,I_s)+I_s(\theta_s-\theta_e), \tag{20}$$

where θ_s and θ_e are angle variables at ranges 0 and r, respectively, and the value of θ_e is taken modulo 2π (θ_s never exceeds 2π). The subscript "s" marks ray parameters at $r=0$ while "e" marks parameters at the end of the trajectory. This convention will be used throughout the paper. The symbol θ_e will always designate the final value of the angle variable modulo 2π. The angle variable at the end of trajectory, θ, is related to θ_s and θ_e by

$$\theta=2\pi N-\theta_s+\theta_e, \tag{21}$$

where N is a number of minima of the ray path.

Let us emphasize an almost trivial, but crucial for our subsequent analysis, point. Canonical transformations (12) and (13) determined by the function $n_0(z)$, formally, can be applied in a waveguide with a different refractive index profile.

2. Range-dependent waveguide

In what follows we shall consider a model of sound speed field taken in the form

$$c(r,z)=c_0(z)+\delta c(r,z), \tag{22}$$

where $c_0(z)$ is a smooth (background) sound speed profile, and $\delta c(r,z)$ is a range-dependent perturbation. In this range-dependent environment where the refractive index, $n=c_r/c$, is a function of both range and depth, we define the action-angle variables using the **same** relations as in the unperturbed waveguide with the refractive index $n_0(z)=c_r/c_0(z)$.

Rewrite the Hamiltonian $H=-\sqrt{n^2-p^2}$ in the form

$$H=H_0+V, \tag{23}$$

where

$$H_0(p,z)=-\sqrt{n_0^2(z)-p^2}, \quad V(p,z,r)=-\sqrt{n^2(z,r)-p^2}+\sqrt{n_0^2(z)-p^2}\simeq\delta c/c_0. \tag{24}$$

Since our generating function G does not depend explicitly on r, the Hamiltonian in the new variables (I,θ) is obtained by simple substitution of functions (13) into the above equations. This yields

$$H(I,\theta,r)=H_0(I)+V(I,\theta,r). \tag{25}$$

The action function (eikonal), S, again can be found by integrating Eq. (14) with H_0 changed to H. Then we arrive at

$$S=\int(Id\theta-H\,dr)-G(z_s,I_s)+G(z_e,I_e) + \theta_sI_s-\theta_eI_e. \tag{26}$$

Note that Eq. (21) remains valid in a range-dependent waveguide.

The Hamilton equations now take the form

$$\frac{dI}{dr}=-\frac{\partial V}{\partial\theta}, \tag{27}$$

and

$$\frac{d\theta}{dr}=\omega+\frac{\partial V}{\partial I}. \tag{28}$$

The following two comments should be made on this definition of the action-angle variables.

(i) The action variables introduced in this way (we have followed Refs. 3 and 19) do not conserve, along the ray path even in a waveguide smoothly varying with range, i.e., our actions are not adiabatic invariants. Another definition of these variables[17] where the action does have a property of adiabatic invariance is briefly described in Sec. V.

(ii) Splitting of the Hamiltonian into a sum of the unperturbed constituent, H_0, and the perturbation, V, have been made in anticipation of our later use of some perturbation expansion based on the smallness of δc and, hence, V. However, for now we have not assumed the perturbation to be small and all the equations derived so far are exact.

III. TRAVEL TIME DIFFERENCES

In this section we derive an approximate relation for the difference in eikonals (travel times) of two rays that may have different numbers of cycles of oscillations. To distinguish between similar parameters of these two rays, param-

eters of one of them will be marked with overbars. For example, starting and final points of one trajectory will be denoted by (p_s, z_s) and (p_e, z_e), respectively, while for another trajectory we shall write $(\overline{p_s}, \overline{z_s})$ and $(\overline{p_e}, \overline{z_e})$. The symbol Δ will be used to denote the difference between any characteristic of one ray and its counterpart for another ray, e.g., $\Delta I = I - \overline{I}$, $\Delta S = S - \overline{S}$, $\Delta z_s = z_s - \overline{z_s}$, and so on. The mean value of some ray parameter and its counterpart for another ray will be designated with a tilde over the corresponding symbol. In particular, $\tilde{I} = (I + \overline{I})/2$.

We assume that both rays under consideration have large numbers of cycles N, $N \gg 1$, but the difference $\Delta N = N - \overline{N} = O(1)$. This ensures the closeness of mean cycle lengths for our rays and suggests that their actions, I and $\overline{I}$, on the average, should also be close. The difference ΔI is considered as a small parameter.

For simplicity, we also assume that the differences Δz_e and Δz_s are small compared to depth intervals spanned by rays, i.e., our rays start from close depth points, and arrive at, generally, other two close points.

A. Two rays in a range-independent waveguide

Let us begin with a pair of rays in the unperturbed waveguide with $n = n_0(z)$. Rewrite Eq. (20) as

$$S = F(I)r - G(z_s, I) + G(z_e, I) + I(\theta_s - \theta_e), \tag{29}$$

where

$$F(I) = I\omega(I) - H_0(I). \tag{30}$$

In this case $I_s = I_e$ and we have dropped the subscript at I. It follows from Eq. (11) that

$$F' = I\omega', \quad F'' = \omega' + I\omega'', \tag{31}$$

where the prime denotes differentiation with respect to I. Later on, the prime will also be used to denote a partial derivative with respect to I.

The closeness of the starting parameters of our rays ensures that the difference ΔI is small, and in the expansion

$$F(I) - F(\overline{I}) = \omega'(\overline{I})\Delta I + O(\Delta I^3) \tag{32}$$

we retain only the first term.

If we expand ΔS in a Taylor series about $\tilde{I}$, $\tilde{z}_s$, $\tilde{z}_e$, $\tilde{\theta}_s$, and $\tilde{\theta}_e$ and retain only first-order terms in small differences ΔI, Δz_s, Δz_e, $\Delta\theta_s$, and $\Delta\theta_e$, then we obtain

$$\Delta S = \tilde{I}\omega'(\tilde{I})r\Delta I - \tilde{p}_s\Delta z_s + \tilde{p}_e\Delta z_e + \tilde{I}(\Delta\theta_s - \Delta\theta_e). \tag{33}$$

In the same approximation Eqs. (19) and (21) yield

$$\Delta\theta = \omega'(\tilde{I})r\Delta I = 2\pi\Delta N - (\Delta\theta_s - \Delta\theta_e). \tag{34}$$

Substituting Eq. (34) into Eq. (12) we get

$$\Delta S = 2\pi\Delta N\tilde{I} - \tilde{p}_s\Delta z_s + \tilde{p}_e\Delta z_e. \tag{35}$$

When deriving this approximate relation, we have dropped terms proportional to r, and it may seem that Eq. (35) is valid only at short enough ranges. However, it is not so. The terms proportional to r dropped in Eqs. (33) and (34) are, on the other hand, proportional to ΔI^3 [see Eq. (32)]. According to Eq. (34), the difference ΔI can be estimated as

$$\Delta I \sim \frac{2\pi\Delta N}{\omega' r},$$

and this estimation shows that if ΔN is kept constant, then the neglected terms do not increase, but decrease with range.

In the case of $\Delta z_s = \Delta z_e = 0$, i.e., for two eigenrays connecting the endpoints $(0, z_s)$ and (r, z_e), Eq. (35) reduces to

$$\Delta S = 2\pi\Delta N\tilde{I}. \tag{36}$$

This result is known (see Refs. 23–25). In Refs. 23 and 25 it has been shown that Eq. (36) remains valid in a waveguide adiabatically varying with range.

B. Ray in a range-independent waveguide and ray in a range-dependent waveguide

To find out how the presence of a small range-dependent component of the sound speed, $\delta c(r, z)$, affects travel times, we compare a pair of rays one of which propagates in a range-independent waveguide (its parameters will be marked with overbar) and another one which propagates in a range-dependent waveguide.

Representing Eq. (28) in the form

$$d\theta = (\omega + V')dr \tag{37}$$

and substituting it into Eq. (26) we obtain

$$S = \int F(I)dr + \int (IV' - V)dr - G(z_s, I) + G(z_e, I) + I_s\theta_s - I_e\theta_e. \tag{38}$$

A similar characteristic for the unperturbed ray is given by Eq. (29) with I replaced with $\overline{I}$, z_s replaced with $\overline{z_s}$, etc. Subtract it from Eq. (38) and expand the difference in powers about parameters of the unperturbed ray. We get

$$\Delta S = \int \left[\overline{I}\omega'(\overline{I})\Delta I + \frac{1}{2}(\omega'(\overline{I}) + \overline{I}\omega''(\overline{I})\Delta I^2)\right]dr - \int (V - IV')dr + \overline{p_e}\Delta z_e - \overline{p_s}\Delta z_s + \overline{I}(\Delta\theta_s - \Delta\theta_e). \tag{39}$$

We have retained the first- and second-order terms in ΔI in the integrand and only first-order terms in small differences Δz_s, Δz_e, $\Delta\theta_s$, and $\Delta\theta_e$ determined by starting and final ray parameters.

Using Eqs. (21) and (37) we find that in the perturbed waveguide

$$2\pi N = \int \omega(I)dr + \theta_s - \theta_e + \int V'\,dr, \tag{40}$$

while in the unperturbed one

$$2\pi\overline{N} = \int \omega(\overline{I})dr + \overline{\theta_s} - \overline{\theta_e}. \tag{41}$$

Subtracting Eq. (41) from Eq. (40) and expanding the difference in a Taylor series up to terms $O(\Delta I^2)$ yields

$$2\pi\Delta N-\int\left[\omega'(\bar{I})\Delta I+\frac{1}{2}\omega''(\bar{I})\Delta I^2\right]dr-\Delta\theta_s+\Delta\theta_e$$

$$-\int V'\,dr=0. \tag{42}$$

Multiply Eq. (42) by a range-independent $\bar{I}$ and add the product to Eq. (39). Then neglecting the term

$$\Delta S_{\mathrm{negl}}=\int V'\Delta I\,dr, \tag{43}$$

we finally obtain the main quantitative result of the present paper

$$\Delta S=2\pi\Delta N\bar{I}+\bar{p}_e\Delta z_e-\bar{p}_s\Delta z_s+\frac{\omega'(\bar{I})}{2}\int\Delta I^2\,dr$$

$$-\int V\,dr. \tag{44}$$

We expect that due to the smallness of ΔI the neglected term ΔS_{negl} is small compared to the last term on the right of Eq. (44). Note that in contrast to V, whose mean value $\langle V\rangle=0$, the term ΔI^2 does not change its sign with range. For this reason the integral $\int\Delta I^2\,dr$ grows monotonically with range and we retain it.

Establishing the applicability conditions of our approximate relation (44) requires careful estimations of neglected terms. The detailed analysis of this issue is beyond the scope of the present paper (it is discussed in Ref. 26) but in the next section with an example of a realistic propagation model we demonstrate that Eq. (44) can give good predictions at ranges up to, at least, 3000 km.

IV. NUMERICAL EXAMPLE AND DISCUSSION

A. Environmental model

The unperturbed profile $c_0(z)$ [see Eq. (22)] used in our numerical simulation is typical for deep water acoustic waveguides. It is shown in the left panel of Fig. 1. The sound-channel axis, i.e., minimum of the sound speed profile, is located at a depth of 0.738 km.

We consider an internal-wave-induced sound speed perturbation, $\delta c(r,z)$, with a zero mean ($\langle\delta c(r,z)\rangle=0$) and assume that the statistics of the internal wave field is described by the empirical Garrett–Munk spectrum.[27] A numerical technique for generation of such perturbations developed by J. Colosi and M. Brown[28] has been applied. Equations (1) and (19) from Ref. 28 have been used to generate a particular realization of $\delta c(r,z)$ which is used throughout this paper. It has been assumed that the buoyancy frequency profile $\nu(z)$ is exponential, $\nu(z)=\nu_0\exp(-z/B)$, and determined by two constants: a surface-extrapolated buoyancy frequency $\nu_0=2\pi/10\,\mathrm{min}^{-1}$ and a thermocline depth scale $B=1$ km. We consider the internal wave field formed by 30 normal modes and assume its horizontal isotropy. Components of wave number vectors in the horizontal plane belong to the interval from $2\pi/100$ km^{-1} to $2\pi/4$ km^{-1}. A rms amplitude of the perturbation, $(\delta c)_{\mathrm{rms}}$, scales in depth like $\exp(-3z/2B)$ and its surface-extrapolated value

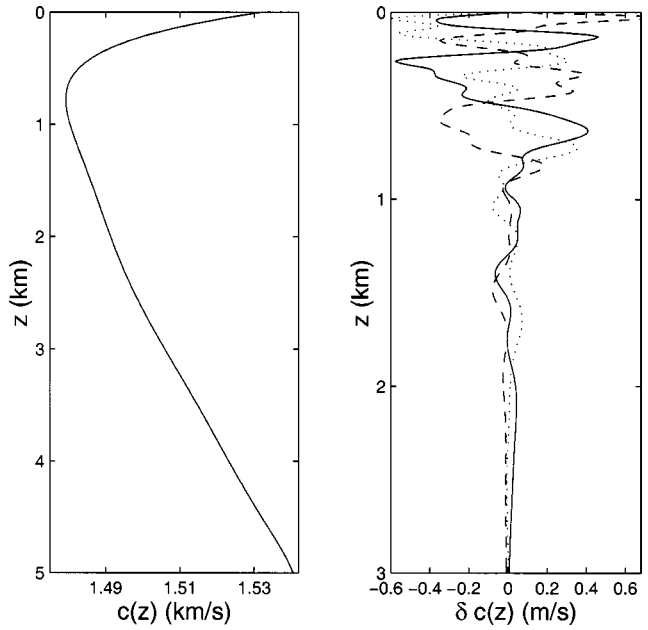

FIG. 1. Left panel: Unperturbed sound speed profile. Right panel: Sound speed perturbation versus depth at three different ranges.

in our model is about 0.5 m/s. Depth dependencies of δc at three different ranges are shown in the right panel of Fig. 1.

The angular frequency of ray trajectory oscillations in the unperturbed waveguide, ω, and its derivative with respect to the action variable are shown in Fig. 2 as functions of I.

B. Timefront in a range-independent waveguide

Figures 3 and 4 show early and late portions of the timefront at 3000-km ranges, respectively, for rays escaping a point source set at a depth of 0.78 km. The timefront in the unperturbed waveguide graphed in the upper panels of Figs. 2 and 3 has been computed using a fan of 16 000 rays with starting momenta equally spaced within an interval corresponding to launch angles $\pm12°$.

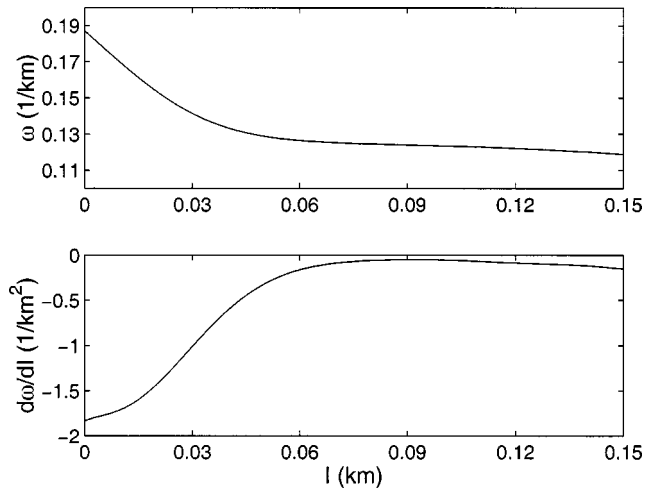

FIG. 2. Angular frequency of ray oscillations, ω (upper panel), and its derivative with respect to the action variable, $d\omega/dI\equiv\omega'$ (lower panel), versus the action variable I for rays propagating without striking the surface and the bottom.

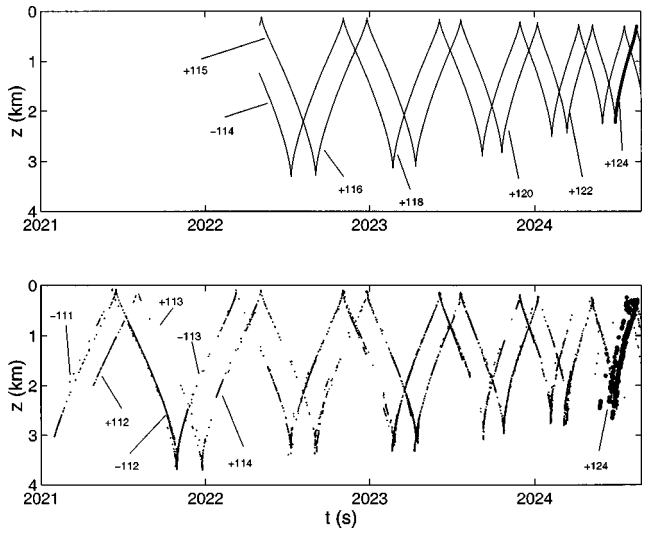

FIG. 3. Early portion of the timefront at the range 3000 km without (upper panel) and with (lower panel) internal waves present. Identifiers of rays forming some particular segments are indicated next to the corresponding segments. In the upper panel, arrivals with identifier +124 are depicted by a thick solid line. In the lower panel, arrivals with this identifier are marked by thick points.

The timefront in the range-independent waveguide has the well-known accordionlike shape consisting of smooth segments (branches).[9,21] Each segment is formed by points corresponding to arrivals of rays with the same identifier $\pm J$, where J is the number of ray turning points and symbols $+$ and $-$ correspond to rays starting upward and downward, respectively. So, we can associate each segment with the identifier of rays forming this segment. Identifiers for some particular segments in the unperturbed waveguide are indicated in the upper panels of Figs. 3 and 4. It is seen that the travel time grows with J. This is a typical situation for a deep water waveguide:[21] steep rays usually have greater cycle lengths (smaller J) and arrive earlier than flat ones.

Notice that segments formed by rays with identifiers $\pm J$ and $\pm(J-2)$ are almost parallel. Select some reference depth z_r and define the temporal shift—we denote it by $T_{\pm J,\pm(J-2)}$—between such segments as a difference in travel times of two eigenrays with identifiers $\pm J$ and $\pm(J-2)$ arriving at the depth z_r. Equation (36) with $\Delta N=1$ provides the estimation

$$T_{\pm J,\pm(J-2)}=\pi(I_{\pm J}+I_{\pm(J-2)})/c_r, \tag{45}$$

where $I_{\pm J}$ and $I_{\pm(J-2)}$ are actions of the corresponding eigenrays. At long ranges action variables of all rays forming the segment are almost equal and the right-hand side of the above equation practically does not depend on z_r.

An interesting and somewhat surprising fact following from Eq. (45) is that there exists a conservation law for temporal shifts between timefront segments. Consider a bunch of rays with launch angles within a narrow interval. Action variables of all these rays are close to some value which we denote by I_0. Beginning from a certain range r_* these rays will form at least two segments with identifiers that differ by 2. When estimating temporal shift between two such segments we shall compare rays arriving at the same depths. With this in mind, we can estimate the temporal shift as $\tau_0=2\pi I_0/c_r$. It should be emphasized that τ_0 does **not** depend on range. It means that although the number of segments formed by rays with launch angles from a given narrow angular interval grows linearly with range, temporal shifts between neighboring segments [to be more precise, between segments corresponding to identifiers $\pm J$ and $\pm(J-2)$ with J depending on range] remain approximately the same at any distance. A more detailed discussion of this issue is given in Refs. 23 and 25.

The above statement means that a simple evaluation of the action variable, I, as a function of the launch angle, χ_s, gives a considerable quantitative information on temporal structure of the pulse signal valid at arbitrary (long enough) range. If $N\gg 1$, the values of actions on the right of Eq. (45) are close and this equation can be approximated by

$$T_{\pm J,\pm(J-2)}=\tau(\chi_{\pm J,\pm(J-2)}), \tag{46}$$

where $\chi_{\pm J,\pm(J-2)}=(\chi_{\pm J}+\chi_{\pm(J-2)})/2$ with $\chi_{\pm J}$ and $\chi_{\pm(J-2)}$ being launch angles of the corresponding eigenrays and

$$\tau(\chi_s)=2\pi I(\chi_s)/c_r. \tag{47}$$

A solid line in Fig. 5 graphs $\tau(\chi_s)$ for our model of range-independent waveguide. Looking at this curve we can predict that, for example, a difference in travel times of two eigenrays with launch angles close to 7° and numbers of cycle which differ by 1, will be close to $\tau=0.19$ s at **any** (long enough) range and at **any** depth, provided such eigenrays arrive at the observation point.

Equation (46) suggests that points depicting values of $T_{\pm J,\pm(J-2)}$ against $\chi_{\pm J,\pm(J-2)}$ should lie on the curve $\tau(\chi_s)$ at any range and for any reference depth, z_r. In Fig. 5 this prediction is verified for the timefront shown in the upper panels of Figs. 3 and 4 and for a similar timefront at the range of 1500 km. Circles and triangles depict $T_{+J,+(J-2)}$ as functions of $\chi_{+J,+(J-2)}$ at 1500- and 3000-km ranges, respectively, for $z_r=0.78$ km. Travel time shifts for only even

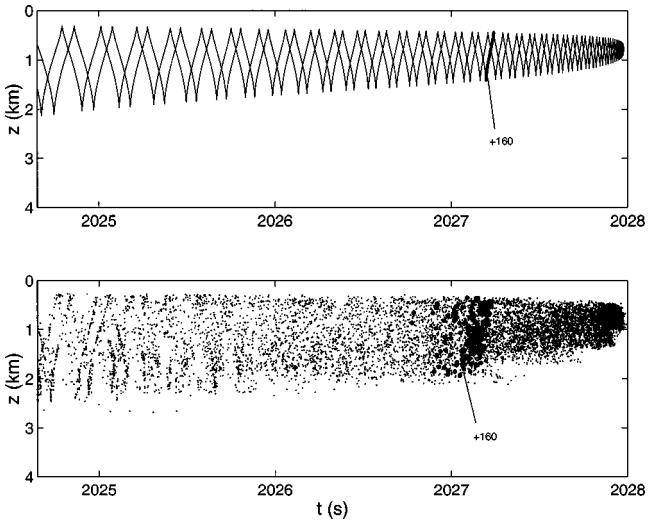

FIG. 4. Late portion of the timefront at the range 3000 km without (upper panel) and with (lower panel) internal waves present. In the upper panel, arrivals with identifier +160 are depicted by a thick solid line. In the lower panel, arrivals with this identifier are marked by thick points.

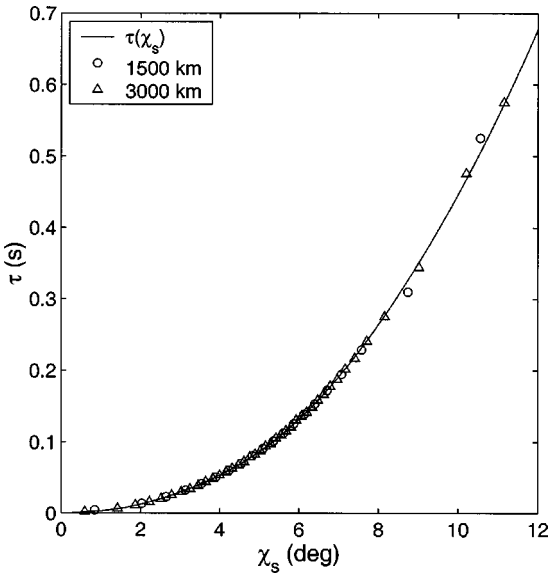

FIG. 5. The solid curve is $\tau=2\pi I(\chi)/c_r$ [see Eq. (47)]. The circles and triangles are time delays between segments with the identifiers $+J$ and $+(J-2)$ at a reference depth of 0.78 km computed for even J at 1500 km and 3000 km ranges, respectively.

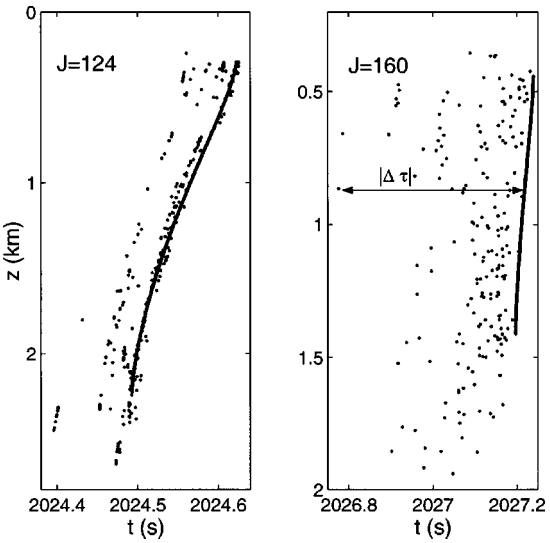

FIG. 6. Arrivals with identifiers +124 (left panel) and +160 (right panel) at the range 3000 km presented in the time-depth plane. The points and solid lines depict arrivals with and without internal waves present, respectively. The magnitude of time delay, $|\Delta\tau|$, between arrivals of the perturbed ray and an unperturbed ray with the same identifier is shown for the earliest arrival with identifier +160.

J (from 60 to 96 at 1500 km, and from 118 to 196 at 3000 km) are shown. It is clearly seen that all circles and triangles are, indeed, located close to the solid curve representing $\tau(\chi_s)$.

C. Timefront in the presence of perturbation

Early and late portions of the timefront in the perturbed waveguide at a 3000-km range are shown in the lower panels of Figs. 3 and 4. The timefront has been computed by tracing 49 000 rays with launch angles within the interval $\pm 12°$. So, the interval of launch angles is the same for both perturbed and unperturbed rays.

1. Widening and bias of timefront segments

In the lower panels of Figs. 3 and 4 we see that in the presence of weak range-dependent inhomogeneities the structure of timefront becomes more complicated: instead of infinitely thin segments of smooth curves, we have some areas filled with randomly scattered points. Although we observe the scattered points only because our fan is far too sparse to resolve what should be unbroken curves, the appearance of such regions indicates the presence of chaotic rays.

Even in the presence of perturbation giving rise to ray chaos, segments of the timefront formed by early arriving steep rays reveal a remarkable stability. The early portion of the timefront still ''remembers'' its structure in the unperturbed waveguide. This property is well known and it has been observed in both numerical simulations and field experiments.[9,12,13,29]

Points depicting arrivals of rays with the given identifier are scattered in the vicinity of the corresponding unperturbed segment. A group of arrivals formed by rays with the same identifier produces a fuzzy version of an unperturbed segment. We shall call such groups of points in the time-depth plane the fuzzy segments. Thus, every fuzzy segment, like every segment of the unperturbed timefront, is associated with some identifier. Two fuzzy segments in Figs. 3 and 4 are marked with thick points. They correspond to identifiers +124 and +160. Closer views of these groups of points are shown in Fig. 6. The left (right) panel presents arrivals with the identifier +124 (+160). Thick solid lines in both panels show the unperturbed segments with the identifiers +124 (left panel) and +160 (right panel).

In order to derive quantitative characteristics of the fuzzy segment describing its spread and bias, we introduce the quantity

$$\Delta\tau=t_p-t_u, \tag{48}$$

where t_p is the travel time of a particular perturbed ray and t_u is the travel time of an unperturbed ray with the same identifier arriving at the same depth. In words, $\Delta\tau$ represents the distance along the t-axis between the given point of the fuzzy segment and the unperturbed segment with the same identifier. In the right panel of Fig. 6 the magnitude of $\Delta\tau$ is shown for the earliest arrival. Note that $\Delta\tau$ is defined only for those rays forming the fuzzy segment whose arrival depths lie within a depth interval covered by the corresponding unperturbed segment. An approximate analytical expression for $\Delta\tau$ is readily obtained from Eq. (44) with $\Delta N=0$. Since $\Delta\tau$ is a difference in travel times of rays connecting the same endpoints, $\Delta z_s=\Delta z_e=0$ and we arrive at

$$\Delta\tau=\Delta\tau_I+\Delta\tau_V, \tag{49}$$

where

$$\Delta\tau_I=\frac{\omega'(\overline{I})}{2c_r}\int \Delta I^2\,dr, \tag{50}$$

and

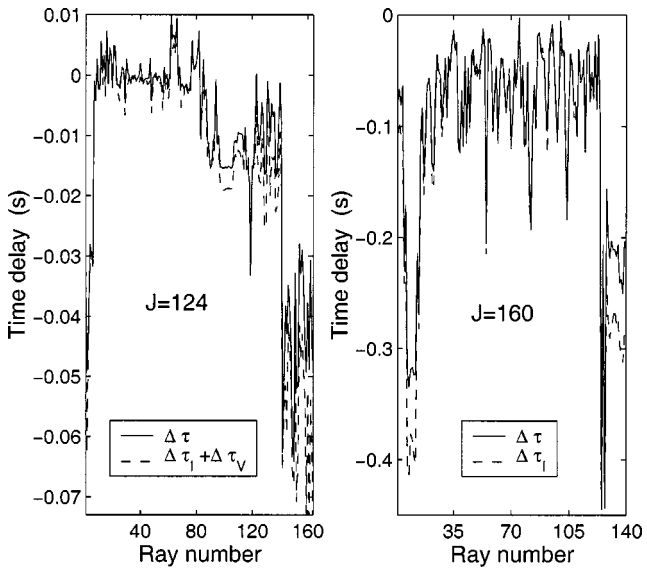

FIG. 7. Time delays, $\Delta\tau$, defined by Eq. (48), for rays with identifiers $+124$ (left panel) and $+160$ (right panel) at the range 3000 km. The solid lines represent results of the direct ray tracing, while the dashed lines are predictions made using Eq. (49). For rays with identifier $+160$ only the term $\Delta\tau_I$ in Eq. (49) has been taken into account.

$$\Delta\tau_V=\frac{1}{c_r}\int \delta c(r,z(r))dr. \tag{51}$$

The integral on the right of Eq. (51) goes along the perturbed ray. Numerical ray tracing demonstrates that for our propagation model the term $\Delta\tau_I$ usually dominates. Only for steep rays the two terms on the right of Eq. (49) may be of the same order (see Ref. 26).

In Fig. 7 we check the accuracy of Eq. (49). Values of $\Delta\tau$ predicted by Eq. (49) are compared to that obtained in numerical calculations. This is done for arrivals shown in Fig. 6. In the perturbed waveguide there are 160 fan rays with the identifier $+124$ whose depths at the 3000-km range belong to the depth interval covered by the unperturbed fan rays, i.e., between upper and lower points of a solid curve in the left panel of Fig. 6. A solid line in the left panel of Fig. 7 connects exact values of $\Delta\tau$ obtained by ray tracing, while a dashed line represents predictions provided by Eq. (49). Launch angles of perturbed rays with the identifier $+124$ belong to the interval (7°,9.5°). These rays are steep and both terms in Eq. (49) should be retained. In the right panel of Fig. 7 a similar plot is shown for 139 rays with the identifier $+160$. These rays have smaller grazing angles (their launch angles are less than 7°) and the term $\Delta\tau_V$ in this case may be neglected. Figure 7 demonstrates that Eq. (49) provides a reasonable estimation for $\Delta\tau$.

Figure 6 exhibits an important phenomenon. The perturbation causes not only diffusion of the timefront segment but it also leads to some regular bias: rays with the given identifier in the perturbed waveguide arrive, on average, earlier than unperturbed rays with the same identifier. A similar bias is observed for every fuzzy segment. An explanation to this effect follows immediately from the fact that the term $\Delta\tau_I$ in Eq. (49) usually dominates. This is true even for steep rays although in this case the term $\Delta\tau_V$ should be retained for obtaining an accurate prediction of $\Delta\tau$. The sign of $\Delta\tau_I$ is determined by the sign of the derivative $\omega'(\overline{I})$ (see Fig. 2). The latter is negative for rays propagating without reflection off the surface and bottom, because in typical deep ocean waveguides the cycle length of the refracted ray grows with the launch angle.

2. On stability of timefront segments

The spread of $\Delta\tau_I$ determines the width of fuzzy segment. An estimation of the time delay between neighboring unperturbed segments formed by rays with actions close to I is given by $\tau=2\pi I/c_r$ [see Eq. (47)]. If

$$\tau>2|\Delta\tau_I|_{\rm rms}, \tag{52}$$

then for a nonzero ΔN the first term in Eq. (44) dominates (we consider $\Delta z_s=\Delta z_e=0$) and "parallel" fuzzy segments with identifiers $\pm J$ and $\pm(J-2)$ do not overlap. Moreover, such segments remain close to their prototypes in the unperturbed waveguide and in this sense they are stable with respect to the perturbation. There are three reasons explaining why the condition (52) for steep rays is usually met at much longer ranges than for flat rays. (*i*) Actions I of steep rays, and, hence, τ are greater than that of flat rays. (*ii*) According to Eq. (50) $\Delta\tau_I$ is proportional to $\omega'(\overline{I})$. As it is seen in Fig. 2 the values of $|\omega'(\overline{I})|$ for steep rays are small compared to that for flat rays. (*iii*) Ray tracing shows that in our model the magnitude of the integral $\int\Delta I^2\,dr$ is of the same order for steep and flat rays (see Ref. 26).

It should be emphasized that the stability of fuzzy segments formed by steep rays does not mean that steep rays in the perturbed and unperturbed waveguides with the same launch angle follow practically the same paths. Come back to Fig. 3 and note that the six earliest segments in the lower panel with identifiers -111, ±112, ±113, and $+114$ have no counterparts in the upper panel. The point is that rays with these identifiers in the unperturbed waveguide have launch angles exceeding the maximum launch angle in our fan. In the presence of perturbation such rays appear because the perturbation leads to widening of the interval of ray grazing angles. It is remarkable that segments which have appeared due to scattering at random inhomogeneities are quite regular and coincide with the unperturbed segments missed in the upper panel of Fig. 3.

The smallness of $\Delta\tau_I$ that ensures stability of timefront segments can be qualitatively interpreted from the viewpoint of Hamilton's (Fermat's) principle. Indeed, present the eikonal in the form

$$S=S_0-\int V\,dr, \tag{53}$$

where $S_0=\int(p\,dz-H_0\,dr)$ and neglect the last term on the right of Eq. (53). This means neglecting the term $\Delta\tau_V$ in Eq. (49). Then

$$\Delta\tau_I=\frac{1}{c}[S_0(P)-S_0(U)], \tag{54}$$

where $S_0(P)$ and $S_0(U)$ are the values of S_0 evaluated over trajectories of perturbed (P) and unperturbed (U) eigenrays with the same identifier, i.e., with the same topology, respec-

tively. According to Fermat's principle, the ray U in the unperturbed waveguide is a stationary path of the functional S_0. The absence of linear in ΔI terms in Eqs. (44) and (50) is a consequence of this principle. Since ΔI is our small parameter, the absence of the first-order term in ΔI gives some qualitative explanation to smallness of $\Delta\tau_I$ and, hence, to stability of timefront segments.

V. RANGE-DEPENDENT UNPERTURBED WAVEGUIDE

An ocean-acoustic propagation model in the form of a superposition of a range-independent sound speed profile and a weak range-dependent perturbation responsible for emergence of ray chaos may be too idealized. In this section we briefly outline how the above results can be generalized to a more realistic model in which a weak perturbation, δc, is imposed on a smooth range-dependent sound speed field, c_0, i.e.,

$$c(r,z)=c_0(r,z)+\delta c(r,z). \tag{55}$$

First, consider another way of introducing the action-angle variables in the range-dependent waveguide[17] without dividing the Hamiltonian into the sum of an unperturbed term and a perturbation. Let us define canonical transformations (12) and (13) at every range r using Eqs. (16) and (17) evaluated for an auxiliary range-independent waveguide with the same cross section that the real waveguide has at the current range. In this case the canonical transformation is different at different ranges and the right-hand sides of Eqs. (12) and (13) as well as the generating function G now acquire an additional argument r. Note that $H=-\sqrt{n^2-p^2}$ in the new variables is a function of I and r, but not θ.[17] The Hamilton equations retain their canonical form

$$\frac{dI}{dr}=-\frac{\partial H_s}{\partial\theta},\quad \frac{d\theta}{dr}=\frac{\partial H_s}{\partial I} \tag{56}$$

with the new Hamiltonian[17]

$$H_s(I,\theta,r)=H(I,r)+\Lambda(I,\theta,r), \tag{57}$$

where

$$\Lambda(I,\theta,r)=\left.\frac{\partial G(I,z,r)}{\partial r}\right|_{z=z(I,\theta,r)}. \tag{58}$$

The term Λ is small and can be neglected if range variations in the environment are adiabatic, i.e., if the variations are small at the cycle length. Then, according to the first of Hamilton equations (56) I remains constant along the ray trajectory, i.e., the action variable defined in this way does have a property of adiabatic invariance.

However, we suppose that the above approach is not convenient for description of chaotic rays. The point is that in this case Λ is not negligible, the connection between H, Λ, and δc is nontrivial, and it is difficult to divide Hamiltonian (57) into a sum of a smooth unperturbed term and a small perturbation. But such a decomposition is needed for application of our perturbation theory.

A more appropriate approach can be developed if the unperturbed waveguide with $c(r,z)=c_0(r,z)$ is adiabatic. Then, it is convenient to introduce the action-angle variables at every range r using an auxiliary range-independent waveguide with the cross-section coinciding with that of the unperturbed waveguide. This yields the new Hamiltonian in the form

$$H_s=H_0(I,r)+V(I,\theta,r), \tag{59}$$

where $V(I,\theta,r)$ is the perturbation defined in Eq. (24) with the unperturbed refractive index n_0 now depending not only on z but on r, as well. Then the Hamilton equations

$$\frac{dI}{dr}=-\frac{\partial V}{\partial\theta}, \tag{60}$$

$$\frac{d\theta}{dr}=\omega(I,r)+\frac{\partial V}{\partial I} \tag{61}$$

look almost the same as Eqs. (27) and (28) except the angular frequency $\omega(I,r)=\partial H_0(I,r)/\partial I$ now depends on r.

The derivation of expressions for differences in ray travel times presented in Sec. III can be easily generalized to the waveguide model considered here. It turns out that in the case of adiabatic unperturbed waveguide Eqs. (35) and (44) retain their forms except the factor $\omega'(I)$ in Eq. (44) should be replaced with $\omega'(I,r)$ and put into the integrand.

VI. SUMMARY

Ray travel times in acoustic waveguides have been studied by applying the Hamiltonian formalism in terms of the action-angle variables. A comparatively simple analytic relation (44) for differences between travel times of perturbed and unperturbed rays has been derived. The use of this equation has been demonstrated in numerical simulations carried out for a model of a deep sea waveguide with inhomogeneities induced by random internal waves. By comparing to results of ray tracing, our approximate formulas have been shown to work well, at ranges up to, at least, 3000 km in spite of chaotic behavior of ray trajectories.

In the range-independent waveguide the difference in eigenray travel times is given by surprisingly simple approximate relation (36).[23–25] It establishes a kind of conservation law: the temporal shifts between the neighboring timefront segments formed by the rays with launch angles (action variables) close to some given value $\chi_0[I(\chi_0)]$ does not depend on range and up to a multiplicative constant are close to $I(\chi_0)$. It allows one to estimate differences between neighboring segments of the timefront by simple evaluation of the action variable as a function of the launch angle. Note that the term on the right of (36) is also present in Eq. (44). Moreover, this term gives the main contribution to the difference in travel times of rays with different numbers of cycles. So, Eq. (36) gives a crude estimation of temporal intervals between time front segments in the perturbed waveguide as well, unless the segments are completely destroyed by the perturbation.

The relations obtained in this paper allow one to get a quantitative description of timefront variations due to a weak range-dependent perturbation. It has been demonstrated that the perturbation leads to diffusion of time front segments and their bias toward early times. Our results also clarify why

segments formed by steep rays are significantly more stable compared to that formed by flat rays. It also has been shown that stability of ray travel times observed even for chaotic rays is associated with Fermat's (Hamilton's) principle. (See Refs. 27 and 30 for a more traditional approach for description of travel time shifts due to weak inhomogeneities.)

Equation (44) can be applied for studying of travel time shifts due to other types of inhomogeneities such as mesoscale inhomogeneities (see, e.g., Ref. 30) or that induced by large-scale seasonal or climatic variations in the environment. However, in the present paper this issue has not been addressed.

The expressions we have derived in this paper yield a comparatively simple connection between ray travel times and action variables, i.e., between different characteristics of rays. However, what is needed for solving inverse problems are simple formulas relating ray characteristics to the environmental parameters to be reconstructed. We hope that Eq. (44) can be used for obtaining such relations. The first step should be developing a perturbation approach [proceeding from ray equations (27) and (28)] to establish connection between range variations of the action and fluctuations in the environment. This important topic deserves a special investigation and has not been broached here. Some results in this direction have been obtained in Ref. 26.

In conclusion note that our approximate relations have been derived proceeding from standard equations of Hamiltonian dynamics and, in principle, they may be applied for studying different Hamiltonian systems modeled by a nonlinear oscillator subject to a weak nonstationary external perturbation. Our main relations remain valid for the ray theory taken in the parabolic equation (small angles) approximation.

ACKNOWLEDGMENTS

I thank Professor G. Zaslavsky for the benefit of our discussions on problems of quantum and wave chaos. I am grateful to Dr. I. P. Smirnov whose ray code has been used for numerical simulations. The work was supported by the U.S. Navy Grant No. N00014-97-1-0426 and by Grant No. 00-02-17409 from the Russian Foundation for Basic Research.

[1] W. Munk and C. Wunsch, ''Ocean acoustic tomography: A scheme for large scale monitoring,'' Deep-Sea Res., Part A **26**, 123–161 (1979).
[2] J. Spiesberger and K. Metzger, ''Basin-scale tomography: A new tool for studying weather and climate,'' J. Geophys. Res. **96**, 4869–4889 (1991).
[3] S. S. Abdullaev and G. M. Zaslavsky, ''Classical nonlinear dynamics and chaos of rays in wave propagation problems in inhomogeneous media,'' Usp. Fiz. Nauk **161**(8), 1–43 (1991).
[4] D. R. Palmer, M. G. Brown, F. D. Tappert, and H. F. Bezdek, ''Classical chaos in nonseparable wave propagation problems,'' Geophys. Res. Lett. **15**, 569–572 (1988).
[5] M. G. Brown, F. D. Tappert, and G. Goni, ''An investigation of sound ray dynamics in the ocean volume using an area preserving mapping,'' Wave Motion **14**, 93–99 (1991).
[6] K. B. Smith, M. G. Brown, and F. D. Tapper, ''Ray chaos in underwater acoustics,'' J. Acoust. Soc. Am. **91**, 1939–1949 (1992).
[7] K. B. Smith, M. G. Brown, and F. D. Tappert, ''Acoustic ray chaos induced by mesoscale ocean structure,'' J. Acoust. Soc. Am. **91**, 1950–1959 (1992).
[8] F. D. Tappert and X. Tang, ''Ray chaos and eigenrays,'' J. Acoust. Soc. Am. **99**, 185–195 (1996).
[9] J. Simmen, S. M. Flatte, and G.-Y. Wan, ''Wavefront folding, chaos, and diffraction for sound propagation through ocean internal waves,'' J. Acoust. Soc. Am. **102**, 239–255 (1997).
[10] D. R. Palmer, T. M. Georges, and R. M. Jones, ''Classical chaos and the sensitivity of the acoustic field to small-scale ocean structure,'' Comput. Phys. Commun. **65**, 219–223 (1991).
[11] J. L. Spiesberger and F. D. Tappert, ''Kaneohe acoustic thermometer further validated with rays over 3700 km and the demise of the idea of axially trapped energywavefront folding, chaos, and diffraction for sound propagation through ocean internal waves,'' J. Acoust. Soc. Am. **99**, 173–184 (1996).
[12] P. F. Worcester, B. D. Cornuelle, M. A. Dzieciuch, W. H. Munk, M. Howe, A. Mercer, R. C. Spindel, J. A. Colosi, K. Metzger, T. Birdsall, and A. B. Baggeroer, ''A test of basin-scale acoustic thermometry using a large-aperture vertical array at 3250-km range in the eastern north pacific ocean,'' J. Acoust. Soc. Am. **105**, 3185–3201 (1999).
[13] J. A. Colosi, E. K. Scheer, S. M. Flatte, B. D. Cornuelle, M. A. Dzieciuch, W. H. Munk, P. F. Worcester, B. M. Howe, J. A. Mercer, R. C. Spindel, K. Metzger, T. Birdsall, and A. B. Baggeroer, ''Comparisons of measured and predicted acoustic fluctuations for a 3250-km propagation experiment in the eastern north pacific ocean,'' J. Acoust. Soc. Am. **105**, 3202–3218 (1999).
[14] M. D. Collins and J. F. Lingevitch, ''Secular behavior and breakdown of chaotic ray solutions,'' IEEE J. Ocean. Eng. **24(2)**, 232–236 (1999).
[15] A. L. Virovlyansky, ''Comment on 'Mode coupling by internal waves for multimegameter acoustic propagation in the ocean' [J. Acoust. Soc. Am. **100**, 3607–3620 (1996)],'' J. Acoust. Soc. Am. **106**, 1174–1176 (1999).
[16] M. A. Wolfson and S. Tomsovic, ''On the stability of long-range sound propagation through a structured ocean,'' J. Acoust. Soc. Am. **109**, 2693–2703 (2001).
[17] L. D. Landau and E. M. Lifshits, *Mechanics* (Nauka, Moscow, 1973).
[18] M. Born and E. Wolf, *Principles of Optics* (Pergamon, Oxford, 1968).
[19] S. S. Abdullaev, *Chaos and Dynamics of Rays in Waveguide Media*, edited by G. Zaslavsky (Gordon and Breach Science, New York, 1993).
[20] G. M. Zaslavsky, *Physics of Chaos in Hamiltonian Systems* (Imperial College, Singapore, 1998).
[21] L. M. Brekhovskikh and Y. Lysanov, *Fundamentals of Ocean Acoustics* (Springer-Verlag, Berlin, 1991).
[22] F. B. Jensen, W. A. Kuperman, M. B. Porter, and H. Schmidt, *Computational Ocean Acoustics* (AIP, Woodbury, NY, 1994).
[23] A. L. Virovlyanskii, ''Travel times of acoustic pulses in the ocean,'' Sov. Phys. Acoust. **31**, 399–401 (1985).
[24] W. Munk and C. Wunsch, ''Ocean acoustic tomography: rays and modes,'' Rev. Geophys. Space Phys. **21**, 1–37 (1983).
[25] A. L. Virovlyansky, ''On general properties of ray arrival sequences in oceanic acoustic waveguides,'' J. Acoust. Soc. Am. **97**, 3180–3183 (1995).
[26] A. L. Virovlyansky, ''Ray travel times in range-dependent acoustic waveguides,'' nlin.CD/0012015.
[27] S. M. Flatte, R. Dashen, W. M. Munk, K. M. Watson, and F. Zakhariasen, *Sound Transmission Through a Fluctuating Ocean* (Cambringe U.P., London, 1979).
[28] J. A. Colosi and M. G. Brown, ''Efficient numerical simulation of stochastic internal-wave-induced sound-speed perturbation field,'' J. Acoust. Soc. Am. **103**, 2232–2235 (1998).
[29] M. G. Brown and J. Viechnicki, ''Stochastic ray theory for long-range sound propagation in deep ocean environment,'' J. Acoust. Soc. Am. **104**, 2090–2104 (1998).
[30] J. L. Spiesberger, ''Ocean acoustic tomography: Travel time biases,'' J. Acoust. Soc. Am. **77**, 83–100 (1985).

Ray dynamics in long-range deep ocean sound propagation

Michael G. Brown
Rosenstiel School of Marine and Atmospheric Science, University of Miami, Miami, Florida 33149

John A. Colosi
Woods Hole Oceanographic Institution, Woods Hole, Massachusetts 02543

Steven Tomsovic
Department of Physics, Washington State University, Pullman, Washington 99164

Anatoly L. Virovlyansky
Institute of Applied Physics, Russian Academy of Science, 6003600 Nizhny Novgorod, Russia

Michael A. Wolfson
Applied Physics Laboratory, University of Washington, Seattle, Washington 98105

George M. Zaslavsky
Courant Institute of Mathematical Sciences, New York University, New York, New York 10012

(Received 17 September 2001; revised 2 December 2002; accepted 30 January 2003)

Recent results relating to ray dynamics in ocean acoustics are reviewed. Attention is focused on long-range propagation in deep ocean environments. For this class of problems, the ray equations may be simplified by making use of a one-way formulation in which the range variable appears as the independent (timelike) variable. Topics discussed include integrable and nonintegrable ray systems, action-angle variables, nonlinear resonances and the KAM theorem, ray chaos, Lyapunov exponents, predictability, nondegeneracy violation, ray intensity statistics, semiclassical breakdown, wave chaos, and the connection between ray chaos and mode coupling. The Hamiltonian structure of the ray equations plays an important role in all of these topics. © *2003 Acoustical Society of America.* [DOI: 10.1121/1.1563670]

PACS numbers: 43.30.Cq, 43.30.Re, 43.30.Qd [DLB]

I. INTRODUCTION

The chaotic dynamics of ray trajectories in ocean acoustics have been explored in a number of recent publications.[1–17] The purpose of the present paper is to provide a review of results relating to this topic. Our exposition is brief but is intended to be self-contained. We introduce a sequence of ray-based simplifications to the mathematical description of underwater sound propagation in order to get a more complete and clear understanding of the underlying propagation physics, especially in range-dependent environments. We consider these simplifications as the starting point of developing a quantitative theory. It is our opinion that even full wave simulations cannot be used effectively without some understanding of the material described in this paper.

To make our discussion more concrete, we focus our attention on long-range propagation in deep ocean conditions. Theoretical results are emphasized, but with an eye toward analyzing measurements. For this reason considerable attention is paid to results that can be applied in the presence of complicated (nonperiodic) range-dependent ocean structure. In a separate paper many of the results presented and discussed here will be applied to the analysis of a particular data set.

In the next section we review important preliminary material. First, we introduce ray-based solutions to the Helmholtz equation. We then introduce the one-way form of the ray equations and the standard parabolic approximation. Finally, the motion of rays in a range-independent environment is discussed. For this class of problems the ray equations are integrable and the ray trajectories are most naturally described using action-angle variables. In anticipation of the material that follows, the action-angle formalism is introduced.

Section III focuses on the behavior of rays in range-dependent environments, i.e., on nonintegrable ray systems. The action-angle formalism is used here to introduce nonlinear resonances and the KAM theorem. The notion of ray chaos is discussed, as are Lyapunov exponents. Our discussion of the (well known) limitations on the predictability of isolated chaotic trajectories is complemented by a discussion of the (generally unappreciated) stability of families of chaotic trajectories. Also in this section we discuss an important connection between the background sound speed structure and ray stability.

In Sec. IV we discuss ray intensity statistics and related topics, including the distribution of finite range estimates of Lyapunov exponents. The results presented here were first described in the analysis of an idealized underwater acoustic problem, but have since been encountered in other applications. Problems associated with the important task of connecting ray intensity statistics to finite frequency wave field intensity statistics are discussed.

In Sec. V, we provide a more general, but brief, discussion of ''wave chaos''—the study of wave systems that, in the ray limit, exhibit chaotic motion. This topic falls slightly

outside the bounds of providing a review of ray dynamics, but is too important to omit. Strong results relating to this topic are dificult to obtain. Much of our discussion focuses on the question of whether semiclassical (ray-based) wave field representations break down at the so-called Ehrenfest range, which scales as $\ln(\overline{f})$ where $\overline{f}$ is the appropriately nondimensionalized wave frequency.

In Sec. VI, we describe the connection between ray chaos and mode coupling. This work builds on well-known results on ray-mode duality. The results described here provide a promising means of attacking the wave chaos problem inasmuch as finite frequency effects are built into the modal description of the wave field.

In the final section, we briefly discuss two issues. First, we discuss the principal shortcoming of our current knowledge—our relatively poor understanding of the wave chaos problem. Second, we discuss the manner in which ideas relating to deterministic chaos complement and/or conflict with more traditional ideas relating to the study of wave propagation in random media.

II. PRELIMINARY RESULTS

This section provides background material that is necessary to understand the material that is presented in the sections that follow. Starting with the Helmholtz equation we introduce the ray equations and their one-way form, the standard parabolic approximation, and the action-angle description of ray motion in range-independent environments.

A. Waves and rays

Fixed-frequency (cw) acoustic wave fields satisfy the Helmholtz equation,

$$\nabla^2 u + \sigma^2 c^{-2}(\mathbf{r}) u = 0, \tag{1}$$

where u is the acoustic pressure, $\sigma = 2\pi f$ is the angular frequency of the wave field, and $c(\mathbf{r})$ is the sound speed. We consider propagation in a vertical plane $\mathbf{r} = (z,r)$ where z is depth and r is range; the Laplacian operator in (1) is $\nabla^2 = \partial^2/\partial z^2 + \partial^2/\partial r^2$. For large kr, where $k = \sigma/c$, azimuthal spreading of sound generated by a point source can be accounted for by multiplying u by $r^{-1/2}$ if a flat Earth model is assumed, or $(r_e \sin(r/r_e))^{-1/2}$, where r_e is the radius of the Earth, if a spherical Earth model is assumed. The so-called short wave approximation can be used when

$$\sigma \gg |\nabla c|, \tag{2}$$

i.e., when the acoustic wavelength $2\pi/k$ is smaller than all length scales that characterize variations in c. Under such conditions the solution to (1) can be written as a sum of terms, each representing a locally plane wave,

$$u(\mathbf{r};\sigma) = \sum_j A_j(\mathbf{r}) e^{i\sigma T_j(\mathbf{r})}. \tag{3}$$

Substitution of the geometric ansatz (3) into the Helmholtz equation (1) gives, after collecting terms in descending powers of σ, the eikonal equation,

$$(\nabla T)^2 = c^{-2}, \tag{4}$$

and the transport equation,

$$\nabla(A^2 \nabla T) = 0. \tag{5}$$

For notational simplicity we have dropped the subscript j on T and A in (4) and (5). The solution to (4) can be reduced to the solution to the ray equations,

$$\frac{d\mathbf{r}}{d\tau} = \frac{\partial \mathcal{H}}{\partial \mathbf{p}}, \quad \frac{d\mathbf{p}}{d\tau} = -\frac{\partial \mathcal{H}}{\partial \mathbf{r}}, \tag{6}$$

and

$$\frac{dT}{d\tau} = \mathcal{L} = \mathbf{p} \cdot \frac{d\mathbf{r}}{d\tau} - \mathcal{H}, \tag{7}$$

where $\mathbf{p} = \nabla T$ is the ray slowness (also referred to as the momentum) vector and

$$\mathcal{H}(\mathbf{p},\mathbf{r}) = \tfrac{1}{2}(\mathbf{p}^2 - c^{-2}(\mathbf{r})) = 0. \tag{8}$$

The independent (timelike) variable τ satisfies $d\tau/dl = c$ where $dl = |d\mathbf{r}|$, and $d\mathcal{H}/d\tau = 0$. The sum in (3) is over all ray paths $z(r)$ that connect the source at $(z_0,0)$ and the receiver at (z,r). The ray equations (6)–(8) are seen to have Hamiltonian form, which allows many well-known results to be applied to the acoustic problem in the short wave limit. Equations (6)–(8) describe the so-called optical-mechanical analogy of wave propagation in the short wave limit.

For guided wave propagation in the direction of increasing r, the variable r can be used as the independent (timelike) variable and Eqs. (6)–(8) may be rewritten

$$\frac{dz}{dr} = \frac{\partial H}{\partial p}, \quad \frac{dp}{dr} = -\frac{\partial H}{\partial z}, \tag{9}$$

and

$$\frac{dT}{dr} = L = p\frac{dz}{dr} - H, \tag{10}$$

where $p = \partial T/\partial z$ is the z-component of the slowness vector,

$$H(p,z,r) = -\sqrt{c^{-2}(z,r) - p^2} \tag{11}$$

is minus the r-component of the slowness vector, and $dH/dr = \partial H/\partial r$. These are the so-called one-way ray equations. The formal condition for the validity of reducing the two-way ray equations (6)–(8) to the one-way ray equations (9)–(11) is that $dr/d\tau > 0$ following all rays of interest; see, e.g., Ref. 9. All subsequent analysis is based on the one-way ray equations (or a parabolic approximation to these equations, as described below), rather than the slightly more general Eqs. (6)–(8). Ray angles are defined by the condition $dz/dr = \tan\varphi$ where φ is measured relative to the horizontal. Using (9) and (11) this reduces to $cp = \sin\varphi$. An immediate consequence of Eqs. (9), independent of the form of $H(p,z,r)$, is $\partial(dz/dr)/\partial z + \partial(dp/dr)/\partial p = 0$. This is a statement of Liouville's theorem, expressing the incompressibility of flow in phase space (p,z).

The transport equation (5) can be reduced to a statement of constancy of energy flux in ray tubes. In a notation appropriate for use with the one-way ray equations, the solution to the transport equation, assuming a point source, for the jth eigenray can be written

$$A_j(z,r)=A_{0j}|q_{21}|_j^{-1/2}e^{-i\mu_j\pi/2}. \tag{12}$$

The matrix element q_{21}, defined below, describes the spreading of an infinitesimal ray bundle. At any fixed r, one has

$$\begin{pmatrix}\delta p\\ \delta z\end{pmatrix}=Q\begin{pmatrix}\delta p_0\\ \delta z_0\end{pmatrix}, \tag{13}$$

where the stability matrix

$$Q=\begin{pmatrix}q_{11} & q_{12}\\ q_{21} & q_{22}\end{pmatrix}=\begin{pmatrix}\left.\frac{\partial p}{\partial p_0}\right|_{z_0} & \left.\frac{\partial p}{\partial z_0}\right|_{p_0}\\ \left.\frac{\partial z}{\partial p_0}\right|_{z_0} & \left.\frac{\partial z}{\partial z_0}\right|_{p_0}\end{pmatrix}. \tag{14}$$

Elements of this matrix evolve according to

$$\frac{d}{dr}Q=KQ, \tag{15}$$

where Q at $r=0$ is the identity matrix, and

$$K=\begin{pmatrix}-\frac{\partial^2 H}{\partial z\partial p} & -\frac{\partial^2 H}{\partial z^2}\\ \frac{\partial^2 H}{\partial p^2} & \frac{\partial^2 H}{\partial z\partial p}\end{pmatrix}. \tag{16}$$

At caustics q_{21} vanishes and the Maslov index μ advances by one unit. (For waves propagating in three space dimensions, advances by two units are possible.) At these points diffractive corrections to (12) must be applied. The normalization factor A_{0j} is chosen in such a way that close to the source (12) matches the Green's function for the corresponding wave equation, (1) or a parabolic approximation to the one-way form of this equation. (A_{0j} is different for Helmholtz equation and parabolic equation rays; this small difference is of no consequence in any of the results presented below.) Ray intensity statistics are discussed in detail in Sec. IV.

B. The parabolic approximation

The standard parabolic wave equation is

$$-\frac{i}{\sigma}\frac{\partial\Psi}{\partial r}=\left(\frac{c_0}{2\sigma^2}\frac{\partial^2}{\partial z^2}-U(z,r)\right)\Psi, \tag{17}$$

where $u(z,r)\approx\exp(ik_0r)\Psi(z,r)$, $k_0=\sigma/c_0$,

$$U(z,r)=\frac{1}{2c_0}\left(1-\frac{c_0^2}{c^2(z,r)}\right), \tag{18}$$

and c_0 is a reference sound speed. The corresponding ray equations are (9) and (10) with $H(p,z,r)$ replaced by

$$H_{PE}(p,z,r)=\frac{c_0}{2}p^2+U(z,r). \tag{19}$$

Ray angles satisfy $c_0p=\tan\varphi$. The parabolic approximation is valid when ray angles are small and deviations of $c(z,r)$ from c_0 are small. The parabolic wave equation (17) coincides with the Schrödinger equation with r playing the role of time and σ^{-1} playing the role of Planck's constant $\hbar$. [Note that $\hbar/t$ and $(\sigma r)^{-1}$ have the same dimension as the corresponding Hamiltonians.] It is useful to note the analogy between quantum mechanics and acoustics because many tools that have been developed to study quantum chaos, discussed below, can be applied to the study of solutions of (17) or (1) under conditions in which the ray equations, (9) or (6), admit chaotic solutions. In this regard it is noteworthy that there is no direct quantum mechanical counterpart to transient sound fields as these are characterized by the simultaneous presence of a continuum of σ values. (An indirect analog, known as inverse $\hbar$ spectroscopy,[18] has been developed, however.)

C. Integrable ray systems

It is well known that when the sound speed is a function of depth only and the ocean boundaries are surfaces of constant z, the Helmholtz equation (and the parabolic wave equation) admit separable solutions. Under the same conditions the ray equations also admit simple solutions that make use of action-angle variables, and are said to be integrable. The action-angle formalism is important in the material in much of the remainder of the paper, so the essential results are presented here.

When the sound speed is a function of depth only, ray trajectories are periodic; the ray equations (9) can be transformed, via a canonical transformation, to a new set of ray equations in which the Hamiltonian $H(I)$ is a function of the new momentum variable I but is independent of the new generalized coordinate θ. In terms of the action-angle variables (I,θ), ray trajectories are described by the equations

$$\frac{d\theta}{dr}=\frac{\partial H}{\partial I}\equiv\omega(I),\quad \frac{dI}{dr}=-\frac{\partial H}{\partial\theta}=0. \tag{20}$$

The solution to these equations is simply $I=\text{const}$, $\theta(r)=\omega(I)r+\theta(0)$. These equations (and their higher dimensional counterparts) describe motion on a torus. The action variable can be written (see, e.g., Ref. 19) as a function of H (which is constant following each ray trajectory in a range-independent environment),

$$I=\frac{1}{2\pi}\oint dz\,p(H,z)=\frac{1}{\pi}\int_{\check z(H)}^{\hat z(H)}dz\,p(H,z). \tag{21}$$

The integration is over one cycle of the periodic ray trajectory, and at the turning depths $c^{-1}(\check z(H))=c^{-1}(\hat z(H))=-H$. The generating function for the canonical transformation from (p,z) to (I,θ) is

$$G(z,I)=\int^z dz'\,p(H(I),z'), \tag{22}$$

where the $H(I)$ can be obtained by inverting Eq. (21), $p=\partial G(z,I)/\partial z$, and $\theta=\partial G(z,I)/\partial I$.

III. NONINTEGRABLE RAY SYSTEMS

This section is concerned with the behavior of rays in range-dependent environments; under such conditions the ray equations define nonintegrable dynamical systems. The action-angle formalism is used to introduce nonlinear resonances and the KAM theorem. The notion of ray chaos is introduced. Lyapunov exponents and the predictability of

both isolated rays and families of rays are discussed. Also, an important connection between ray stability and the background sound speed profile is discussed.

A. Nonlinear resonances and the KAM theorem

Consider ray motion in an environment consisting of a range-independent sound speed profile to which a small range-dependent perturbation is added. Because of the smallness of the sound speed perturbation, the perturbation to H may be assumed to be additive,

$$H(p,z,r)=H_0(p,z)+\varepsilon H_1(p,z,r). \tag{23}$$

For simplicity, first consider the case where H_1 is a periodic function of r with wavelength $\lambda=2\pi/\Omega$. It is well known (see, e.g., Ref. 4) that for this class of problems canonical perturbation theory fails as nonlinear ray-medium resonances are excited for those rays whose action values I_0 in the unperturbed environment satisfy the condition

$$l\omega(I_0)=m\Omega \tag{24}$$

for any pair of integers, l and m.

A simple analysis (see, for example, Ref. 4) shows that action variables of rays captured into the resonance belong to the interval $I-\Delta I_{\max}<I<I+\Delta I_{\max}$ with

$$\Delta I_{\max}=2\sqrt{\varepsilon\overline{H}_1/|\omega'|}, \tag{25}$$

where $\omega'=d\omega(I)/dI$ at $I=I_0$, and $\overline{H}_1$ is the magnitude of H_1. The quantity $\Delta I_{\max}$ represents the width of the resonance in terms of the action variable. The width of the resonance in terms of spatial frequency can be approximately estimated as

$$\Delta\omega=|\omega'|\Delta I_{\max}/2=\sqrt{\varepsilon\overline{H}_1|\omega'|}. \tag{26}$$

The phenomenon of nonlinear ray medium resonance plays an important role in the emergence of ray chaos. If there are at least two nonlinear resonances centered at spatial frequencies ω and $\omega+\delta\omega$, chaotic motion, according to Chirikov's criterion,[20–22] takes place when the condition

$$\frac{\Delta\omega}{\delta\omega}>1 \tag{27}$$

is satisfied, i.e., when the resonances overlap leading to the stochastic instability of the system.

One might expect that, even for very small ε, all rays are captured into a nearby resonance. This turns out not to be the case. According to the KAM theorem (see, e.g., Ref. 23), for sufficiently small ε some of the tori of the unperturbed system are preserved in the perturbed system, albeit in a slightly distorted form. A condition for the applicability of the KAM theorem is that the nondegeneracy condition $\omega'\neq 0$ must be satisfied. This condition guarantees that resonances are isolated provided ε is sufficiently small. Nondegeneracy violation will be discussed in more detail below.

Realistic sound speed structure in the ocean does not have periodic range dependence, so it is important to consider a larger class of perturbation terms $H_1(p,z,r)$. In Ref. 24 it is shown that the KAM theorem applies to problems for which the perturbation term H_1 consists of a superposition of N components, each of which is periodic in range. N is assumed to be finite but is otherwise unrestricted. The spatial periods need not be commensurable and there may be depth structure associated with each periodic component. Realistic ocean sound speed structure—internal-wave-induced perturbations,[25] for example—can be described by a model of this type. A consequence is that the mixture of chaotic and regular trajectories (discussed below) that characterizes ray motion in environments with periodic range dependence applies to a much larger—and more oceanographically realistic—class of problems.

Because the mixture of chaotic and regular trajectories that characterizes ray motion in environments with periodic range dependence carries over to a much larger class of problems, there is reason to study the former (simpler) problem with the expectation that many of the observed qualitative features carry over to the larger class of problems. The principal advantage of studying ray dynamics in environments with periodic range dependence is that in systems of this type the structure of phase space can be seen by constructing a Poincaré map. To construct such a map, the ray equations (6) and (8) are integrated numerically to give $(p(r),z(r))$. The sequence of points $(p(r_0+n\lambda),z(r_0+n\lambda))$, $n=0,1,2,...$, where λ is the wavelength of the range-dependent sound speed perturbation, is then plotted. A Poincaré map constructed in this fashion is a 2-D slice of the ray motion in the 3-D space (p, z, r mod λ).

For some special problems ray dynamics and associated phase space structures can be studied using an even simpler technique which eliminates the need to numerically trace rays. An example is described in Ref. 5. Here, ray motion in a bilinear model (constant sound speed gradient above and below the sound channel axis) of the deep ocean sound channel was considered. It was shown that when the upper ocean sound speed gradient oscillates periodically in range, successive (separated by one ray cycle) iterates of axial ray angle and range satisfy

$$\begin{aligned}\phi_{n+1}&=\phi_n+\varepsilon[\sin\rho_n+\sin(\rho_n+\phi_n+\varepsilon\sin\rho_n)],\\ \rho_{n+1}&=\rho_n+\phi_n+\varepsilon\sin\rho_n+\gamma\phi_{n+1}.\end{aligned} \tag{28}$$

Here ε is the dimensionless perturbation strength, γ is the ratio of the average upper ocean sound speed gradient g to the fixed lower ocean sound speed gradient, $\phi_n=(4\pi/g\lambda)\varphi_n$ and $\rho_n=(2\pi/\lambda)r_n$. These equations define an area-preserving mapping, $\partial(\phi_{n+1},\rho_{n+1})/\partial(\phi_n,\rho_n)=1$; this condition is a discrete analog of Liouville's theorem. Because of their relative simplicity, area-preserving mappings are widely used to study properties of nonintegrable Hamiltonian systems. Some of these properties will now be described.

B. Ray chaos

Figure 1(a) shows iterates of Eq. (28) for many sets of ray initial conditions in an environment with moderately strong ($\varepsilon=0.15$) range dependence. Phase space is seen to consist of a mixture of regular and chaotic regions, often described as regular islands in a chaotic sea. For much smaller values of ε, chaotic regions occupy only thin isolated

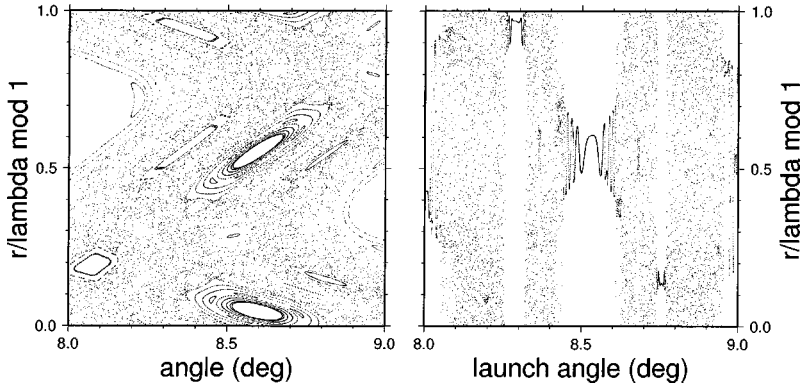

FIG. 1. Numerical simulations based on the area-preserving mapping (28) with $g=1/(30\,\mathrm{km})$, $\lambda=10\,\mathrm{km}$, $\gamma=4$, and $\varepsilon=0.15$. In both plots the ray initial conditions correspond to those of an axial point source at $r=\lambda/2$. Left panel: 500 iterates of the mapping for 50 rays whose launch angles are uniformly distributed between 8° and 9°. Right panel: range after 250 ray cycles (each corresponding to one iteration of the mapping) for 10 000 rays whose launch angles are uniformly distributed between 8° and 9°. In most regions this sampling interval is too large to resolve what should be a smooth function.

bands of phase space. Each such thin chaotic band is associated with an isolated resonance. As ε is increased, the widths of the resonances increase and nearby resonances overlap, leading to an intricate mixture of regular and chaotic regions, as seen in Fig. 1(a). Behavior of this type is typical of systems that are constrained by KAM theory. Figure 1(b) shows a plot of range versus launch angle after 250 ray cycles in the same environment, and using rays emanating from the same fixed point that was used to produce Fig. 1(a). The ray initial conditions used in both Figs. 1(a) and (b) fall on a horizontal line (at $r=\lambda/2$) through the middle of Fig. 1(a). Note that the islands that intersect this line in Fig. 1(a) are readily identifiable in Fig. 1(b). This observation is significant because plots like Fig. 1(b)—ray position versus some continuous ray label—can be constructed in environments with nonperiodic range dependence, providing a simple means of identifying islandlike structures.

At the boundaries of chaotic and regular domains—in Fig. 1(a), for example—are usually invisible cantori. These are Cantor-type invariant sets with fractal structure containing an infinity of holes. Cantori act as partial barriers that inhibit the diffusion of rays. Boundaries of chaotic regions contain small island chains around which the density of points is very high. A common phenomenon is ''stickiness'' of island boundaries; after wandering in an apparently random fashion in phase space, a chaotic trajectory may approach a stable island, and stick to its border for some (possibly long) time, during which it exhibits almost regular behavior.[26] The presence of regular islands in phase space alters the dispersion characteristics of the trajectories that lie in the surrounding chaotic sea.[26] Details depend on the structure of phase space but the phenomenon of anomalous diffusion (mean square displacements of trajectories in phase space obeying scaling laws different than those of a traditional random walk) seems to be generic.

An important property of chaotic trajectories is that they exhibit extreme sensitivity, characterized by a positive Lyapunov exponent,

$$\nu_{\mathrm{L}}=\lim_{r\to\infty}\left(\frac{1}{r}\lim_{\mathcal{D}(0)\to 0}\ln\frac{\mathcal{D}(r)}{\mathcal{D}(0)}\right). \tag{29}$$

Here $\mathcal{D}(r)$ is a measure of the separation between rays at range r. Suitable choices for $\mathcal{D}(r)$ are separations in z or p; another choice is described in Sec. IV. The Kolmogorov–Sinai entropy h_{KS} is closely related to ν_{L}. Loosely speaking, h_{KS} is a measure of information increase following a trajectory; a readable discussion of this topic can be found in Ref. 27. For bounded dynamical systems $h_{\mathrm{KS}}\sim\nu_{\mathrm{L}}$ holds; in open diffusive systems, their difference is proportional to a diffusion constant.[28] A consequence of the extreme sensitivity of chaotic rays is that the number of eigenrays connecting a fixed source and receiver grows exponentially, like $\exp(h_{\mathrm{KS}}r)$, on average in range.[1,9,12] Also, the magnitudes of the variational quantities q_{ij} [see Eq. (14)] can grow exponentially, on average, in range. Reference 17 contains a detailed discussion of this topic. A consequence of this exponential growth is that the amplitudes of chaotic rays [proportional to $|\partial z(r)/\partial p(0)|^{-1/2}$ for (9) or $|\partial\rho_n/\partial\phi_0|^{-1/2}$ for (28), assuming a point source] decay exponentially, on average, in range. Note, however, that for moderate to large r or n (measured in units of a typical value of ν_L^{-1}), plots of $\partial z(r)/\partial p(0)$ vs $p(0)$ (see Fig. 5) or $\partial\rho_n/\partial\phi_0$ vs ϕ_0 (see Fig. 1) have fractallike structure when both chaotic and regular trajectories are present.

Another consequence of extreme sensitivity of chaotic rays is that deterministic predictions using finite precision numerical arithmetic is limited to ranges less than some threshhold (which is proportional to N_b/ν_L where N_b is the number of bits used to specify the mantissa of floating point numbers). This limitation on one's ability to make deterministic predictions of chaotic ray trajectories at long range is tempered by two related factors. First, the shadowing lemma[27] guarantees that, for a large class of problems, numerically computed chaotic trajectories at long range correspond to trajectories of rays whose initial conditions are close to the specified values but are generally unknown. Second, it is easy to verify that statistical properties of discretely sampled distributions of chaotic rays (occupying, for example, a small but finite area in phase space at $r=0$) evolve in a way that does not exhibit extreme sensitivity.

A somewhat stronger form of stability of distributions of chaotic rays is illustrated in Fig. 2. In phase space an aperture-limited compact source is represented as a line segment at constant depth $z=z_0$ bounded by limiting values of p_0; this is an example of a Lagrangian manifold. Each point on such a manifold evolves in r according to the ray equations (9). As a Lagrangian manifold evolves, it gets stretched and folded, but does so without breaking or intersecting itself (owing to phase space area preservation). Figure 2 illustrates one aspect of a phenomenon that can be termed manifold

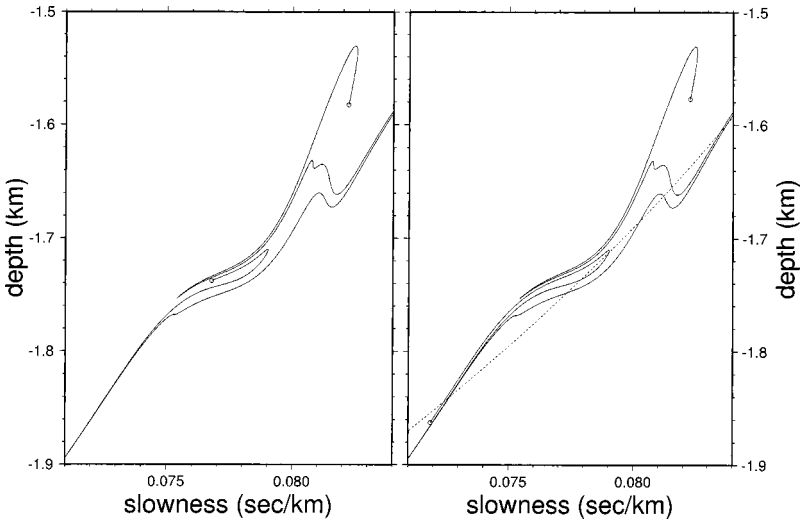

FIG. 2. Left panel: segment of a Lagrangian manifold for a fan of rays with $z(0)=-1.100$ km, $8.575° \leqslant \theta(0) \leqslant 8.625°$ at $r=500$ km in the background environment shown in Fig. 3 with an internal-wave-induced sound speed perturbation superimposed. Right panel: segment of a Lagrangian manifold for a fan of rays with $z(0)=-1.101$ km, $8.575° \leqslant \theta(0) \leqslant 8.625°$ at $r=500$ km in the same environment. The endpoints of both Lagrangian manifolds are marked with small open circles. In both panels, portions of the manifold segments, consisting of long thin tendrils, extend beyond the plot boundaries. The dashed curve in the right panel is a portion of a surface $I=$const.

stability. In this figure two Lagrangian manifolds with slightly different initial conditions are plotted in phase space at a fixed range, $r=500$ km. Each manifold has initial conditions $z=z_0$ (a constant), $8.575° \leqslant \theta_0 \leqslant 8.625°$. For one of the manifolds $z_0=1.100$ km; for the other $z_0=1.101$ km. Both manifolds evolved in the same environment, which is described below. In this environment almost all trajectories evolve chaotically, which leads to exponential growth in range of the length of each manifold. The combination of chaotic ray motion and the small difference in initial manifold depth might lead one to expect that the two manifolds should evolve very differently. Figure 2 shows clearly, however, that they have not. This can be explained by noting that phase space area is preserved. Because of this constraint, the exponential stretching of each manifold is balanced by an exponential contraction of phase space in the transverse direction. This contraction causes the two manifolds to get squeezed closer to one another. Note, however, that, in general, points on the two manifolds with the same value of θ_0 do not lie close to one another. Loosely speaking, the two manifolds have slid relative to one another while being stretched, folded, and squeezed toward one another. Trajectories with nearby initial conditions will also be squeezed toward the same locus of points. Thus, although individual trajectories exhibit extreme sensitivity under chaotic conditions, the associated exponential contraction of phase space elements imparts a surprisingly strong form of stability on continuous distributions of trajectories. The impact of manifold stability on wave field evolution and stability is considered in Ref. 29.

The environment used to produce Fig. 2 is also used in subsequent numerical work. It consists of a range-independent background profile, shown in Fig. 3, on which an internal-wave-induced sound speed perturbation field is superimposed. The background profile is a Munk[30] profile modified in the upper ocean, $c(z)=c_0(1+\varepsilon(\exp\eta-\eta-1))+c_u(z)$, with $c_0=1.49$ km/s, $\epsilon=0.0057$, $\eta=2(z-z_a)/B$, $B=1$ km, $z_a=-1.1$ km, and $c_u(z)=\delta\sin^2(\pi(z-z_a)/z_a)$ for $z>z_a$ with $\delta=0.018$ km/s. The internal-wave-induced sound speed perturbation was computed using Eq. (19) of Ref. 25 with $y=t=0$, i.e., a frozen vertical slice of the internal wave field was assumed. An exponential buoyancy frequency $N(z)=N_0\exp(z/B)$ (note that depths z are negative with $z=0$ at the sea surface) with $N_0=6$ cycles/hour was used. The dimensionless strength parameters E and μ were taken to be 6.3×10^{-5} and 17.3, respectively. Numerically, a 2^{14} point FFT was used with $\Delta k_x=2\pi/1638.4$ km, $k_{x,\max}=2\pi/1$ km and $j_{\max}=30$. It should be noted that this perturbation field is highly structured and fairly realistically describes typical deep ocean environments. Also, the assumed background profile is similar to profiles found in much of the North Atlantic Ocean.

The unpredictability associated with ray chaos is, of course, partially mitigated by finite frequency smoothing effects. This will be discussed in Sec. V. We have seen, however, that even without accounting for finite frequency smoothing, loss of predictability associated with ray chaos is less severe than might be expected due to the constraining influences of Liouville's theorem, and, for a large class of

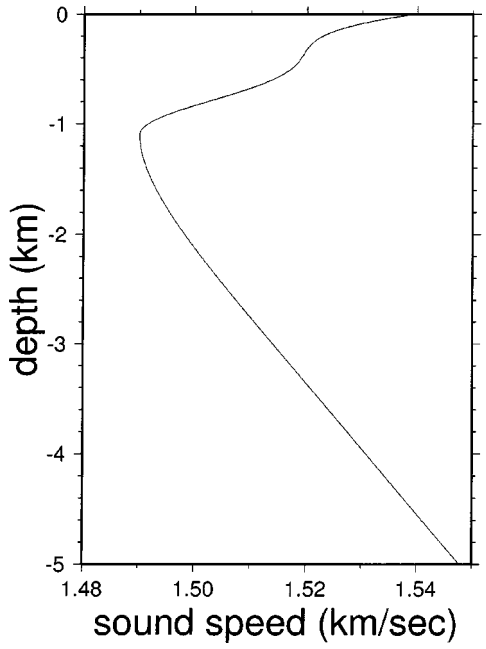

FIG. 3. Background sound speed profile used to produce Figs. 2, 4, and 5.

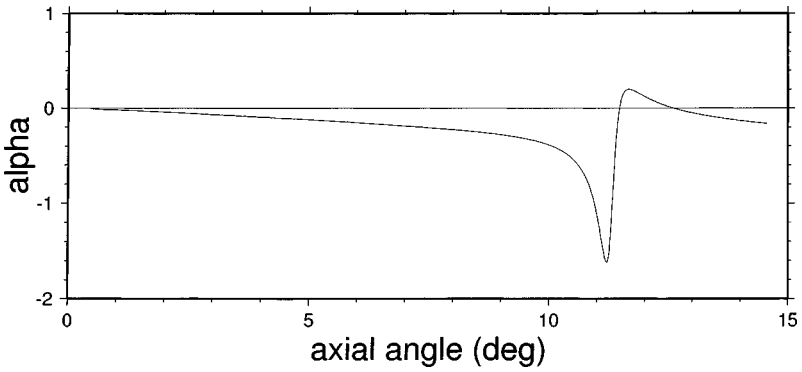

FIG. 4. Stability parameter α versus axial ray angle in the environment shown in Fig. 3.

problems, the coexistance of chaotic and nonchaotic trajectories. Because of these influences chaotic ray systems have more subtle dynamics than purely stochastic systems. Systems of the latter type arise—in studies of wave propagation in random media, for example—when sound speed perturbations to a homogeneous background are assumed to be delta correlated. The topic described in the following subsection is an example of a topic that fits naturally into a dynamical systems framework, but not into a purely stochastic framework.

C. Ray stability and ω'

Recall from Sec. III A that in order for the KAM theorem to apply the nondegeneracy condition,

$$\frac{d\omega}{dI} \neq 0, \tag{30}$$

must be satisfied in the background (range-independent) environment. Systems in which the nondegeneracy condition is violated may admit chaotic solutions, but such systems are characterized by the presence of a stochastic web[31] (or perhaps some other structure), rather than the regular island/chaotic sea mixture that characterizes chaotic systems that are constrained by KAM theory. Note, in addition, that Eqs. (26) and (27) show that $\omega' = d\omega/dI$ also plays an important role in systems that are constrained by KAM theory; if the perturbation strength $\varepsilon \overline{H}_1$ is fixed, then rays are expected to become increasingly chaotic as $|\omega'|$ increases because as $|\omega'|$ increases the number of overlapping resonances should increase. These observations suggest that ray behavior should be influenced by the background sound speed structure via the quantity ω'. Numerical evidence, including an example described below, confirms this expectation.

It is convenient to introduce, following Zaslavsky,[32] the dimensionless stability parameter

$$\alpha = \frac{I}{\omega}\frac{d\omega}{dI}. \tag{31}$$

The stability parameter $\alpha(I)$ is a property of a range-independent environment $c(z)$ and is a function of the action variable I—or some equivalent ray label such as horizontal ray slowness p_r or axial ray angle. $\alpha(I)$ can be computed from more familiar ray quantities. The angular frequency $\omega = 2\pi/R$ where R is the ray cycle distance. For Helmholtz equation rays

$$R(p_r) = 2p_r \int_{\check{z}}^{\hat{z}} \frac{dz}{(c^{-2}(z) - p_r^2)^{1/2}}, \tag{32}$$

where p_r is the r-component of the ray slowness vector, which is constant following a ray trajectory in a range-independent environment. The upper turning depth of a ray $\hat{z}(p_r)$ satisfies $c(\hat{z}(p_r)) = p_r^{-1}$, and similarly for the lower turning depth $\check{z}(p_r)$. Also, $cp_r = \cos\varphi$. The action can be written

$$I(p_r) = \frac{1}{\pi}\int_{\check{z}}^{\hat{z}} dz\,(c^{-2}(z) - p_r^2)^{1/2}. \tag{33}$$

Because $2\pi dI/dp_r = -R(p_r)$, $\alpha = (2\pi I/R^2)dR/dp_r$. This expression for α is convenient to evaluate numerically. A deep-ocean α-curve, corresponding to the sound speed profile shown in Fig. 3, is shown in Fig. 4.

In Fig. 4 zeros of α—where the nondegeneracy condition (30) is violated—are seen to be isolated. Such points are referred to in Ref. 21 as accidental degeneracies, in constast to intrinsic degeneracy where ω' vanishes for all trajectories. Parabolic equation rays in environments in which $U(z)$ is quadratic and Helmholtz equation rays in environments in which $c(z) = c_0 \cosh((z - z_0)/h)$ are intrinsically degenerate. These special problems are not realistic oceanographically. Also, it is worth noting that perturbations to intrinsically degenerate systems often break up the degeneracy, leading to phase space structure that is essentially the same as that seen in nondegenerate systems.[21] Accidental degeneracies, on the other hand, are structurally stable and, as illustrated in Fig. 4, are common in realistic deep ocean α-curves.

Reference 33 presents an extensive set of numerical simulations and some nonrigorous theoretical arguments that complement those given above in an attempt to better understand the connection between ω' and ray stability. The conclusions of that study are that ray stability is largely controlled by $|\omega'|$ and that ray instability (as measured by Lyapunov exponents, for example) increases with increasing $|\omega'|$. These statements are consistent with the argument presented above based on Eqs. (26) and (27). The connection between $|\omega'|$ and ray instability is illustrated by comparing Figs. 4 and 5. Figure 5 shows ray depth at a range of 1000 km as a function of launch angle for an axial source in the environment shown in Fig. 3 on which an internal-wave-induced sound speed perturbation was superimposed. (The internal-wave-induced perturbation used to produce Fig. 5 was identical to that used to produce Fig. 2 apart from a

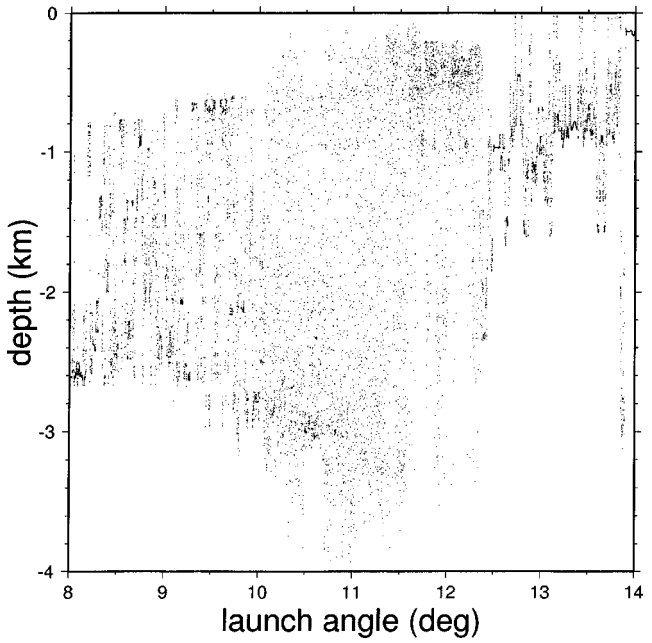

FIG. 5. Ray depth versus launch angle for an axial source at a range of 1000 km in the background environment shown in Fig. 3 with an internal-wave-induced sound speed perturbation superimposed. In most regions the sampling interval ($\Delta\theta_0 = 0.0005°$) is too large to resolve what should be a smooth function.

factor of 2 reduction in the strength parameter E.) In Fig. 5 it is seen that rays in the 10° to 12° band are evidently much less stable than those outside this band. Outside of this band there is evidence of apparently nonchaotic islandlike structures (compare to Fig. 1); inside this band, there is no indication—at the resolution shown, at least—of the presence of such structures. Note that the unstable band of rays in Fig. 5 overlies the band of rays near the peak in $|\alpha|$, corresponding to axial ray angles near 11.1°, seen in Fig. 4. The unstable band of rays seen in Fig. 5 is broader than the peak in $|\alpha|$ seen in Fig. 4. This is because rays whose initial axial angle falls slightly outside the unstable band get scattered into the unstable band. Neither Fig. 5 nor the numerical simulations shown in Ref. 33 show any evidence of structures resembling stochastic webs near isolated zeros of $|\omega'|$. Presumably this is due, in part at least, to the complexity of the internal-wave-induced sound speed perturbations that were used in the simulations, but this issue deserves to be studied more systematically.

Because significant variations in $|\omega'|$ are common in realistic models of (background) ocean structure, we expect the qualitative behavior exhibited in Figs. 4 and 5 to be fairly common in ocean acoustics. Reference 34 first investigated the connection between ray stability and the sound speed structure. Later Simmen *et al.*[14] showed that, for identical sound speed perturbation fields, characteristics of ray stability versus launch angle curves depend strongly on the background sound speed profile. Variations in $|\omega'|$ are a likely cause of the latter finding.

IV. RAY INTENSITY STATISTICS

Ray intensity distributions are discussed in this section. There are two principal reasons for investigating this topic. First, ray intensity distributions are a useful diagnostic tool to study and quantify ray dynamics,[17] especially in environments with nonperiodic range dependence where Poincaré maps cannot be constructed. Second, one expects—on the basis of the local plane wave expansion (3)—that a useful starting point for understanding wave field intensity statistics is understanding ray intensity statistics. We emphasize that gaining an understanding of ray intensity statistics is only the first step in this process, as diffraction and interference effects must be accounted for in making the transition to wave field intensity statistics. These complications will be discussed in more detail in the section that follows. The material presented here builds on the material presented in Sec. II A that relates to ray intensities.

We shall confine our attention to a discussion of ray intensity statistics in a simple idealized ocean model. A more detailed account of the results presented here can be found in Ref. 17. Some related results for the same idealized problem are presented in Ref. 16. The model consists of an unbounded homogeneous background on which an isotropic, single scale (described by a Gaussian spectrum) random perturbation is superimposed. In this idealized problem, which is the basis of much work on the study of wave propagation in random media,[35] all rays are chaotic. It should not be expected that all of the properties of ray intensity distributions in our idealized problem carry over to long-range deep ocean propagation conditions, which are characterized by the presence of a background sound channel on which strongly inhomogeneous and isotropic internal-wave-induced sound speed fluctuations with a power-law spectrum are superimposed. In spite of the idealized nature of the problem considered here, there is ample justification for studying this problem. First, this simple problem has surprisingly rich structure that must be understood before more complicated problems can be successfully attacked. Second, the results presented are expected to comprise a limiting case of those that apply to more complicated problems. And third, preliminary results suggest that many of the results presented here apply generally to systems that are far from integrable. This topic will be discussed in more detail elsewhere.

It is also worth mentioning that the results presented here are expected to apply to other fields, as well. Twinkling starlight is a familiar example, but far more exotic systems with the same dynamical foundation exist. Two such examples are the gravitational bending of light passing through galaxy clusters,[36] and quantum mechanical waves associated with the transport of low-temperature conduction electrons through semiconductor materials.[37] Recent experiments of this latter system show the electron transport breaking up into coherent channels that follow bundles of classical rays that are only weakly unstable in spite of the semiconductor acting as a random medium.[38] This is a manifestation of the remaining stable and nearly-stable rays mentioned in Sec. III in connection with the KAM theorem; such rays will show up again later in this section.

Ray stability analysis relies on the stability matrix Q defined in Eq. (13) from which a great deal of information can be deduced. The stability matrix describes the behavior of all rays that remain within an infinitesimal neighborhood

of a reference ray over the course of its propagation. As seen in Eq. (12), geometric amplitudes for a point source are controlled by the matrix element q_{21}; for a plane wave initial condition q_{22} is the relevant quantity. For pedagogical purposes, however, it is simpler to consider the trace of the matrix; for chaotic rays, its exponential rate of increase and gross statistical properties are the same as those of any of the Q matrix elements. Since Q is diagonalizable by a linear, similarity transformation

$$\Lambda = LQL^{-1} \Rightarrow \begin{pmatrix} \lambda & 0 \\ 0 & \lambda^{-1} \end{pmatrix}, \tag{34}$$

its trace is an invariant equal to the sum of the eigenvalues. The last form applies to systems with a single degree of freedom because the determinant is unity. Three distinct cases may arise. The first is $|\mathrm{Tr}(Q)|<2$ which is linked to stable motion, and it is customary to denote $\lambda = \exp(i\theta r)$. The second case is $|\mathrm{Tr}(Q)|=2$, and it is often called marginally stable because it is the boundary case between stable and unstable motion. The third case represents unstable motion, and is characterized by $|\mathrm{Tr}(Q)|>2$. There it is customary to denote $\lambda = \pm\exp(\nu r)$ where ν is positive and real.

In systems that are far from integrable, the vast majority of rays fall into this last category. Their largest Lyapunov exponent takes on an alternative form to Eq. (29), which can be expressed as

$$\nu_{\mathrm{L}} \equiv \lim_{r\to\infty} \frac{\ln|\mathrm{Tr}(Q)|}{r}. \tag{35}$$

For unstable trajectories we may approximate $\mathrm{Tr}(Q)=\lambda + 1/\lambda \approx \lambda$ with little inaccuracy. In the system described in Refs. 16 and 17 ν_{L} is the same for all rays. But finite range estimates of ν_{L}, sometimes referred to as stability exponents,

$$\nu = \frac{\ln|\mathrm{Tr}(Q)|}{r}, \tag{36}$$

generally differ from ν_{L}. If one introduces an ensemble of potentials U, each member of which generates a dynamical system with the same ν_{L}, then the ensemble average of ν converges to ν_{L}, except at very short range. The statistical properties of ν will be described in more detail below. We note here, however, that the fluctuations in ν are very important because even modest fluctuations in ν produce immense fluctuations in $\mathrm{Tr}(Q)$ which imply similar fluctuations in q_{21}. These large fluctuations in q_{21} are important because in a chaotic system at long range the number of eigenrays can be enormous, but the wave field may be dominated by a tiny fraction of these whose values of $|q_{21}|$ are small.

An analytic expression for the root mean square exponential rate of increase of $\mathrm{Tr}(Q)$ has been derived using techniques relying on Markovian assumptions:[16]

$$\mathrm{Tr}(Q)_{\mathrm{RMS}} \sim \exp(\nu' r). \tag{37}$$

where

$$\nu' \approx \left(\frac{1}{2} \int_0^\infty d\xi \left\langle \left. \frac{\partial^2 U(z;r-\xi)}{\partial z^2} \right|_{\substack{z=z_0 \\ p=p_0}} \left. \frac{\partial^2 U(z;r)}{\partial z^2} \right|_{\substack{z=z_0 \\ p=p_0}} \right\rangle \right)^{1/3}, \tag{38}$$

and the brackets, $\langle ... \rangle$, denote ensemble averaging over different realizations of the potential U. Numerical evaluation of Eq. (38) for model systems with some realism is usually necessary, but analytic results are available for simplified models such as Gaussian random single scale potentials.

Interestingly, ν' is greater than the Lyapunov exponent, independent of the range involved. In fact, with increasing range it rapidly approaches a constant. The important distinction lies in whether the ensemble averaging occurs before or after taking the natural logarithm. The fluctuations are strong enough that $\nu' > \nu_{\mathrm{L}}$ $(=\langle\nu\rangle)$ or alternatively

$$\frac{\ln\langle|\mathrm{Tr}(Q)|^2\rangle}{2r} > \left\langle \frac{\ln|\mathrm{Tr}(Q)|}{r} \right\rangle \tag{39}$$

for all appreciable r.

In the environment consisting of a homogeneous background on which a single scale Gaussian perturbation is superimposed, the probability density of ν is very nearly (except in the far tails) a Gaussian of mean ν_{L} and variance

$$\sigma_\nu^2 = \frac{\nu' - \nu_{\mathrm{L}}}{r}. \tag{40}$$

This distribution has also been observed in numerical simulations based on more realistic ocean models. This topic will be discussed in more detail elsewhere. Numerical calculations also suggest that the Gaussian statistics are obtained for each realization of the random medium just by choosing different initial conditions; i.e., an ensemble of media is not necessary. A Gaussian density for ν implies a lognormal density for $|\mathrm{Tr}(Q)|$ whose parameters are fixed by the Gaussian density's mean and variance. A property of lognormal densities is that any power of the variable also has a lognormal density. Thus, $|\mathrm{Tr}(Q)|^\gamma$ has a lognormal density as well; $\gamma = -\frac{1}{2}$ relates to the semiclassical approximation. However, note that depending on the value of γ, the lognormal density may fail as an approximation less far out in the tails.

In the limit of long range, the fluctuations in $|\mathrm{Tr}(Q)|$ grow without bound despite ν approaching ν_{L} for every ray. Just as there are highly unstable rays, there are also rays which are stable or nearly stable. The lognormal density gives a prediction for what approximate proportion is left for a given propagation range. Asymptotically, the proportion of nearly stable rays, whose stability exponent is less than some small value ν_c, decreases exponentially with range as $(a_0/4\pi r)^{1/2}\exp(-r/a_0)$ where $a_0 = 2(\nu' - \nu_{\mathrm{L}})/(\nu_{\mathrm{L}} - \nu_c)^2$.

The connection to the statistical behavior of wave field intensities arising from the lognormal density of classical ray intensities is not yet understood. There are a number of subtleties. To begin with, for long ranges of propagation, the most naive picture of semiclassical theory leads to the expectation that the wave field is made up of an extremely large number of extremely small contributions. On average, if diffusive growth in phase space is neglected, the growth of the number of eigenrays and the decay of a typical ray intensity

(squared amplitude) should occur at the same exponential rate. If this is true, energy conservation considerations dictate that at long range the constituent ray arrivals have effectively random phases. In other words, a set of N random, uncorrelated numbers of scale $N^{-1/2}$ maintains an order unity summation as $N \to \infty$. Chaotic dynamics is deterministic, and at best, the semiclassical phases generated by the dynamics are pseudo-random at long range. For shorter ranges, correlations amongst the magnitudes and phases could alter the statistical predictions. These correlations remain to be studied. Furthermore, the possibility mentioned earlier that one or few very strong terms at short range could dominate the sum increases the difficulty in finding a unique approach to an asymptotic statistical limit.

A second difficulty is that the lognormal distribution has long tails, indicative of a broad range of fluctuations. The lognormal distribution of intensities y has the form $y^{-a_0 \ln y}$ which can be verified to approach zero for large or small y faster than any power of y, but does not decay exponentially. A sum of random numbers chosen from long tailed densities may not approach a standard central theorem limit (the Lorentzian density remains Lorentzian under repeated convolution), or may approach it very slowly. For the ray chaos problem, as the number of eigenrays grows with increasing range, the breadth of the density is also increasing. If the approach to a central limit theorem is slow enough, then it might never be reached under these circumstances; the limiting density still needs to be worked out.

A third, extremely important difficulty is the appearance of caustics. Their number proliferates at the same exponential rate for chaotic systems as the number of eigenrays. At the caustics, the semiclassical expressions diverge and introduce infinities. Caustics correspond to the extremely small values of instabilities in the tail of the lognormal density where breakdown of the statistical laws are likely. The lognormal expression does not capture the physics of singularity dominated fluctuations that are characterized by twinkling exponents which depend on the types of caustics present.[39–41] Thus, some incorporation of deviations from lognormality appears to be inescapable. In addition, the presence of exponentially proliferating numbers of caustics calls into question the very relevance of semiclassical methods and their usefulness in predicting the statistical properties of the wave field. This consideration is intimately linked with discussions of the validity of the semiclassical approximation for chaotic systems of which we give an overview in the next section.

A final noteworthy complication arises in the analysis of sound fields produced by a broadband source. Interference must still be accounted for, but only among ray arrivals whose travel times fall within intervals whose duration is the reciprocal bandwidth $(\Delta f)^{-1}$ of the source. This phenomenon is further complicated when pulse shapes and phase shifts at caustics—corresponding to Hilbert transforms in the time domain—are taken into account.

V. WAVE CHAOS

''Wave chaos'' is the study of wave systems that, in the ray limit, exhibit unstable dynamics (i.e., exponential divergence of neighboring rays); the underwater sound propagation problem can be thought of as a wave chaos problem. A completely analogous definition of the phrase ''quantum chaos'' is widely used. These two subjects are similar enough that much, if not most, of the progress in either domain carries readily over into the other; we therefore do not bother to distinguish them here. It turns out that there are significant conceptual difficulties with attempting to associate wave chaos with an unbounded, exponential growth of wave field complexity in the hope that a straightforward generalization of the underlying ray chaos manifests itself. The shorthand explanation of this difficulty is often crudely stated something like ''the finite wavevector (nonzero Planck's constant $\hbar$) smooths over the intricate, fine scale details of the chaotic dynamics, not allowing them to be seen.'' The correspondence principle for chaotic systems, in fact, is quite subtle, and we avoid going into this fascinating subject except for the issue of the breakdown of semiclassical theories which we summarize next.[42] For further details though, we refer the reader to Ref. 43 for a discussion of some aspects of wave chaos in underwater acoustics, and to some recent literature relating to quantum chaos.[44,45]

The aspect of the breakdown of semiclassical theories which interests us most for the purposes of this paper is whether or not it is possible to construct, on solid theoretical ground, a ray-based theory valid beyond where ray chaos has fully developed. If not, ray-based predictions under chaotic conditions that match data in long-range propagation experiments would have to be considered accidental, and not an explanation of the essential physics of the problem. It may turn out that the eventual answer to this question is not unique, and depends upon which quantity one wishes to explain. For example, statistical predictions may be more robust than detailed, pointwise, wave field predictions. On the other hand, if the breakdown occurs on a scale much longer than that of the development of ray chaos, there remains a great deal of theoretical work to be pursued.

There is some hope for optimism in this regard. We begin by distinguishing between two classes of dynamical systems. The first class is that of simple, chaotic systems. Equations (28) define a system of this type. The equations of motion may be deceptively simple to write down, yet the solutions highly complicated, and, for all intents and purposes, analytically intractable (chaotic). The second class has complicated equations in the sense that the medium satisfies many of the criteria of randomness even though it is taken here to be deterministic (we may not know which deterministic realization is given in a particular case). One cannot take for granted the equivalence of the properties of these two classes of systems (chaotic versus random media), but we note that in certain limits there exist a number of common results (such as exponential ray instability with respect to initial conditions).

In simple chaotic systems, about which more is known concerning semiclassical breakdown, we have to be careful to distinguish three levels of dynamics: classical, quantum, and semiclassical. We emphasize that the last level should be distinguished from the classical in that it takes classical information as input, but it actually generates an approximate

construction of the quantum dynamics at the level of wave amplitudes and phases. The distinctions between time-evolving classical and quantum expectation values of operators or classical and quantum probability densities have been studied since the development of quantum mechanics. Those quantities that correspond to each other initially are known to propagate similarly before diverging over a finite time scale called the Ehrenfest time. For simplicity, we shall focus only on the fact that one cannot delay the onset of interference phenomena in the quantum dynamics beyond the Ehrenfest time, and interference is necessarily excluded from the classical dynamics. For chaotic systems, the Ehrenfest time depends logarithmically on $\hbar$,[46] and beyond this time scale one finds all manner of complications such as an exponential proliferation of rays, increasing uncertainty whether the rays can even be calculated, and proliferating caustics in semiclassical theories. There is no debate whether the classical and quantum dynamics diverge beyond the Ehrenfest time (they do by definition); the relevant debate centers upon whether a ray-based, semiclassical theory can surmount these difficulties.

There are various ''flavors'' of semiclassical approximations possible. For example, the Wigner–Weyl calculus or other constructions of pseudo-phase spaces[47] are ideally suited for exhibiting how the classical limit emerges from quantum mechanics in a semiclassical limit, but they are poorly adapted for describing interference phenomena. Indeed, mathematical proofs exist that such phase-space-based semiclassical approximations cannot be extended beyond a logarithmic time scale; see Ref. 48. In this scenario, it can be fruitful to examine smoothed features of the wave field (as opposed to pointwise comparisons), such as can be obtained through the ray-based construction of the coarse-grained Wigner function.[49] However, the development of semiclassical approaches that can be roughly described as time-dependent WKB theory handle interference naturally though multiple stationary phase (saddle point) contributions. This approach has been applied to a number of paradigms of chaos (the bakers map, the stadium, and the kicked rotor) with excellent, numerical results extending well beyond the logarithmic time scale.[50–52] Arguments leading to the expectation that the breakdown time depends algebraically on $\hbar$ have also been presented.[51–53]

Semiclassical breakdown in an idealized, but highly structured, ocean model consisting of a single realization of a ensemble with prescribed statistics has been investigated by Brown and Wolfson. They constructed the full semiclassical approximation using the classical dynamics and a Maslov–Chapman uniformization procedure. In their comparisons, they found the semiclassical approximation appeared to be working quite well beyond the onset of ray chaos.[54] This work and those quoted for simple chaotic systems are claiming that it is possible to extend a semiclassical theory for both chaotic and random media problems beyond a logarithmic time (range) scale, and, thus, that ray-based semiclassical theories are viable candidates purporting to explain the essential physics of wave chaotic dynamical problems.

VI. CHAOS AND MODE COUPLING

In this section the connection between ray chaos and mode coupling is described. The results presented provide a promising means of addressing the wave chaos problem inasmuch as finite frequency effects are built into the modal description of the wave field. The material presented here makes use of the action-angle formalism introduced in Sec. II C. The connection between ray and modal expansions of acoustic wave fields in range-independent environments is well understood (see, e.g., Refs. 55–57) and some generalizations have been derived[58–60] for range-dependent environments. Thus, it should come as no surprise that there is a quantifiable connection between ray chaos and the modal description of the wave field. Some details omitted in our presentation of this material can be found in Refs. 61 and 62. To simplify the presentation somewhat, we make use of a WKB analysis of the parabolic wave equation. Consistent with our use of the parabolic wave equation, the variables $p'=c_0 p$, $H'=c_0 H_{PE}$, $U'=c_0 U$, and $I'=c_0 I$ are used in this section after dropping the primes. Also, $S=c_0 T$ is used in place of T.

The principal result of this section is an approximate analytical expression for mode amplitudes in term of raylike quantities. We discuss how typical features of ray chaos, such as exponential growth (with range) of eigenrays contributing to the field point and coexistence of chaotic and regular ray trajectories, manifest themselves in the mode amplitude range dependence. The phenomenon of nonlinear ray-medium resonance that plays a crucial role in the emergence of ray chaos is shown to have an analog for modes which we call the mode-medium resonance.[61] According to the heuristic criterion proposed by Chirikov,[20–22] chaos is a result of an overlap of different resonances. In terms of normal modes, chaos is shown to result from overlapping mode-medium resonances leading to complicated and irregular range variations of the modal structure.

The normal mode representation of the solution to the parabolic wave equation (17) is obtained by expanding $\Psi(z,r)$ in a sum of eigenfunctions of the unperturbed Sturm–Liouville eigenvalue problem,[63,64]

$$-\frac{1}{2}\frac{d^2\psi_m}{dz^2}+k_0^2 U_0(z)\psi_m=k_0^2 E_m\psi_m, \tag{41}$$

where ψ_m and E_m are the eigenfunctions and eigenvalues, respectively:

$$\Psi(z,r)=\sum_m B_m(r)\psi_m(z). \tag{42}$$

Here it is assumed that $U(z,r)=U_0(z)+\varepsilon V(z,r)$. Each term in the sum (42) represents a contribution from an individual normal mode. In order to get simple semiclassical expressions for the amplitudes, B_m, we project the ray representation of $\Psi(z,r)$ of the form of Eq. (3) onto the normal modes. Assuming the latter to be normalized in such a way that

$$\int_{-\infty}^{\infty} dz\ \psi_m(z)\psi_n(z)=\delta_{mn}, \tag{43}$$

we need to evaluate the integrals

$$B_m(r)=\int_{-\infty}^{\infty} dz\,\Psi(z,r)\psi_m(z). \tag{44}$$

Since we consider the geometric approximation to $\Psi(z,r)$, it is natural to use the same approximation for $\psi_m(z)$. The corresponding formulas are usually referred to as the WKB approximations to the eigenfunctions.[57,63,64]

We shall assume that the potential $U_0(z)$ is smooth, has only one minimum, and its walls tend to infinity as $z \to \pm\infty$. When this assumption is combined with use of the WKB approximation, the eigenvalues of the action variable I_m are determined by the quantization rule

$$k_0 I_m = m+\tfrac{1}{2}. \tag{45}$$

Then the eigenvalues of the "energy" are given by the relation $E_m=E(I_m)$, where the function $E(I)$ is determined by Eq. (21). In the same approximation the mth eigenfunction $\psi_m(z)$ between its turning points can be represented as[57,64]

$$\psi_m(z)=\psi_m^+(z)+\psi_m^-(z), \tag{46}$$

with

$$\psi_m^{\pm}(z)=Q_m(z) \times\exp\left[\pm i\left(k_0\int_{\check{z}}^{z} dz'\,\sqrt{2[E_m-U_0(z')]}-\frac{\pi}{4}\right)\right], \tag{47}$$

$$Q_m(z)=\frac{1}{\sqrt{R_m}[2(E_m-U_0(z)]^{1/4}}, \tag{48}$$

where R_m is the cycle length of the ray in the unperturbed waveguide with $E=E_m$. In this form the eigenfunction is represented as a sum of two terms with rapidly varying phases and slowly varying amplitudes. Substituting Eqs. (46) and the ray representation of $\Psi(z,r)$ of the form (3) into Eq. (44) yields a sum of integrals which can be approximately evaluated by applying the stationary phase technique.[57] This has been done in Ref. 61. Earlier, a related result was obtained in Ref. 65. Here we present only the final expressions for B_m.

The amplitude of the mth mode at the given range r is formed by contributions from the rays whose action values are equal to that of the given mode, i.e., with

$$I=I_m. \tag{49}$$

Here I_m is defined in (45); that expression is used because the normal modes in the background environment are being used as a set of basis functions. Phase space is foliated by surfaces of constant I, defined in the background environment, so at each range, each ray falls onto one of these surfaces. Thus I on the left side of (49) may be considered as a function of range and the initial ray phase space coordinates, i.e.,

$$I=I(p_0,z_0,r). \tag{50}$$

This function is determined by the solutions to Eqs. (9) and (19), and Eq. (21). For a point source the value of z_0 is the same for all rays; substitution of Eq. (50) into Eq. (49) then yields an equation for p_0, whose solutions define the initial momenta of the rays that contribute to the mth mode. We shall refer to these as the eigenrays of the mth mode.

The process of identifying modal eigenrays is illustrated in the right panel of Fig. 2. Two curves are plotted: a surface of constant I and a segment of a Lagrangian manifold. The Lagrangian manifold corresponds, at $r=0$, to a small angular aperture point source. Each intersection of the two curves corresponds to a modal eigenray. Eleven such intersections are shown. Under chaotic conditions this number can grow exponentially in range. (In contrast, in all range-independent environments there are two modal eigenrays for each mode, independent of range, whose launch angles have opposite sign.)

The mode amplitude is given by the sum

$$B_m=\sum_n \frac{1}{\sqrt{k_0|\partial I/\partial p_0|_{p_0=p_{0n}}}} e^{ik_0\Phi_n+i\beta_n}, \tag{51}$$

where each term represents a contribution from an eigenray with an initial momentum p_{0n}. The explicit expressions for the phase terms are (since the subsequent formulas describe characteristics of a single eigenray, the subscript n is omitted)

$$\Phi=S-S_0(z,I_m)\mathrm{sgn}(p) \tag{52}$$

and

$$\beta=\left(\mathrm{sgn}\left(\frac{\partial p/\partial p_0}{\partial z/\partial p_0}\right)-\mathrm{sgn}(p)-2\mu\right)\frac{\pi}{4}. \tag{53}$$

Here z is the depth and p is the momentum of the eigenray at a range r, where S and μ are its eikonal and Maslov index, respectively.

Equations (50)–(53) provide the analytical description of mode amplitudes in a range-dependent environment through the parameters of ray trajectories, i.e., through solutions to the Hamilton equations (9). These equations reduce the mode amplitude evaluation to a procedure quite analogous to that generally used when evaluating the field amplitude at the given point. This involves solving the Hamilton (ray) equations, finding the eigenrays, and calculating ray eikonals and some derivatives with respect to initial values of ray parameters. An important point should be stressed. Although we expand the wave field using eigenfunctions of the unperturbed waveguide, smallness of the perturbation has not been assumed. Our small parameter is the acoustic wavelength, $2\pi/k$, that should be substantially smaller than any physical scale in the problem.

Having the comparatively simple expressions relating the mode amplitudes to rays, we can now discuss how the complicated ray trajectory dynamics reveals itself in the mode amplitude variations. For simplicity, we restrict our attention to a waveguide with a weak (ε is now considered as a small parameter) periodic range dependence with a spatial period $2\pi/\Omega$, and we consider the case when only one mode is excited at $r=0$, i.e.,

$$u(0,z)=\psi_m(z). \tag{54}$$

Analysis of the ray structure for this type of distributed source (see Refs. 61 and 62) shows that for all rays initial values of the action variable I are equal to I_m. A situation which we call *mode-medium resonance* occurs when the value of I_m satisfies Eq. (24). Due to the resonance, at ranges of order of $1/\Delta\omega$ there will appear a bundle of rays with the action variables I in the interval $|I-I_0|<\Delta I_{\max}$. Here I_0 is the action value of the resonant ray. This means [see Eq. (49)] that starting with such ranges, the mth mode is split into a group of $2M$ modes with

$$M=\Delta I_{\max}/k_0=2\sqrt{\varepsilon\overline{V}/|\omega'|}/k_0, \tag{55}$$

where $\overline{V}$ is the magnitude of the perturbation potential V. This expression is the modal analog of the standard expression [Eq. (25)] for the width of a ray resonance. In the case of overlapping modal resonances it is natural to expect a further broadening of a group of modes. Moreover, as we discussed earlier, the overlapping of resonances causes the emergence of ray chaos with exponential proliferation of eigenrays. Under chaotic conditions the number of eigenrays contributing to a given mode also grows exponentially with range, giving rise to a very complicated range dependence of mode amplitudes. Numerical simulations presented in Refs. 61 and 62 support these statements.

It might be assumed that that exponential proliferation of eigenrays contributing to a given mode leads to statistical independence of mode amplitude fluctuations under chaotic conditions. We expect, however, that the problem of describing mode amplitudes is considerably more rich and complicated. First, it should be recalled that generically the phase space of a chaotic Hamiltonian system contains both chaotic regions and ''stable islands'' formed by regular periodic trajectories. Some such regular rays will be eigenrays for some modes. Their contributions to modes cannot be considered as stochastic. Thus, we expect that under chaotic conditions there will be modes with amplitudes composed of two constituents: a chaotic one and a regular one. Numerical results illustrating this statement have been presented in Ref. 62. Another important phenomenon typical of chaotic dynamics, which may affect modal structure variations is stickiness, i.e., the presence of segments of a chaotic trajectory which exhibit almost regular behavior. The interval over which apparently regular behavior is observed can be long. In principle, one can presume that stickiness may cause some long-lasting correlations of mode amplitudes.[43]

Our ray-based description of normal mode amplitudes has restrictions that are very much like those of standard ray theory. In particular, at some points the contribution from an eigenray to a given mode can be infinite. This occurs when the derivative in the denominator in Eq. (51) vanishes. [The same comment applies to Eq. (59) below.] Such divergences represent analogs of standard ray theory caustics. Under conditions of ray chaos the number of such caustics grows exponentially with range, spoiling applicability of the ray-based description already at short distances. This issue is discussed in Ref. 62. On the other hand, in Ref. 62 (see also Ref. 49) it was demonstrated numerically that the approach considered in this section can properly predict squared mode amplitudes smoothed over the mode number at ranges of order of at least ten inverse Lyapunov exponents. This result is rather encouraging. It gives us hope that energy redistribution between modes can be comparatively easily analyzed using simple ray calculations at ranges of the order of a few thousand km.

So far, we have considered only a cw field. For a signal with a finite bandwidth, the mode sum must include an integration over frequency σ. The pulse signal at the point (z,r) can be represented as

$$u(z,r,t)=\sum_m u_m(z,r,t), \tag{56}$$

where

$$u_m(z,r,t)=\int d\sigma\, s(\sigma)B_m(r,\sigma)\psi_m(z,\sigma)e^{i\sigma(r/c_0-t)} \tag{57}$$

with $s(\sigma)$ being the spectrum of the initially radiated pulse. In Eq. (57) we have indicated explicitly the dependence of B_m and ψ_m on σ, which has been omitted until now. Each term, $u_m(z,r,t)$, in the sum (56) can be interpreted as a pulse carried by an individual mode and we shall call it the ''mode'' pulse. The mode pulse, in turn, can be regarded as a superposition of elementary pulses representing contributions from different terms in the sum (51):

$$u_m(z,r,t)=\sum_n \int d\sigma\, s(\sigma)G_m(z,r,\sigma)e^{i\sigma((\Phi_n+r)/c_0-t)}, \tag{58}$$

where

$$G_m(z,r,\sigma)=\frac{e^{i\beta_n}}{\sqrt{k_0 r|\partial I/\partial p_0|_{p_0=p_{0n}}}} \times\frac{2\cos(k_0\int_z^z dz'\sqrt{2[E_m-U_0(z')]}-\pi/4)}{\sqrt{R_m}[2(E_m-U_0(z)]^{1/4}}. \tag{59}$$

The above expressions depend on mode parameters with the subscript m and eigenray parameters with the subscript n. Note that both types of parameters depend on frequency. Although the trajectories of eigenrays contributing to the given mode obey frequency-independent Hamilton equations (9), their starting momenta determined by Eq. (49) depend on the eigenvalue I_m. But the latter, according to Eq. (45), does depend on frequency. Under chaotic conditions the number of terms in Eq. (58) can be huge, leading to a very complicated shape of the mode pulse.

The expectation that mode pulses are very complicated under chaotic conditions is consistent with the numerical results in Ref. 66, where broadband parabolic-equation simulations of sound transmission through a deep water acoustic waveguide with inhomogeneities induced by random internal waves are described. It was shown that, due to mode coupling, mode pulses were several times longer than was the case in the background range-independent environment, and acquired irregular shapes. In contrast, from the ray perspective, the same weak inhomogeneities caused steep eigenrays to split into clusters of eigenrays (micromultipaths) whose

travel time spreads were small and whose centroid had a travel time that was close to that of the eigenray in the background environment. (Recall also Sec. III of the present paper.) The authors of Ref. 66 concluded that ''while the high modes may be strongly affected by internal waves they are coherent enough that when they are synthesized together localized wave front results.'' A qualitative explanation of this phenomenon has been offered in Ref. 67. In that paper it was shown that mode pulses may be considerably distorted due to mode coupling already at ranges so short that chaotic ray dynamics has not yet had a chance to reveal itself and every mode is formed by contributions from only two eigenrays. It was also demonstrated how distorted pulses carried by individual modes can combine to produce much less distorted raylike pulses at the receiver.

Although the mode coupling relations presented above are not easy to test experimentally, we emphasize that these results are important because of the insight they provide into the underlying propagation physics. In this regard, it should be noted that the mode coupling relations presented above directly address the connection between ray chaos and finite frequency propagation effects, i.e., the wave chaos problem.

VII. DISCUSSION

In this paper we have reviewed results relating to ray dynamics in ocean acoustics. All of these results are intimately linked to the Hamiltonian structure of the ray equations. Most previous studies have emphasized the applicability of KAM theory to oceans with periodic range dependence and the extreme sensitivity of individual chaotic ray trajectories. To complement these ideas, considerable attention has been focused on oceans with nonperiodic range dependence, and we have discussed some forms of stability of distributions of chaotic rays. Also, we have discussed subjects such as nondegeneracy violation, ray intensity statistics, and the connection between ray chaos and mode coupling that either have not, or have only recently, been explored in an underwater acoustic context.

Although our understanding of ray dynamics is currently incomplete, it should be clear that the most pressing problem in this context is to better understand the connection between the ray dynamics and the corresponding finite frequency wave fields. For example, even the seemingly simple task of translating ray intensity statistics to wave field intensity statistics is complicated by the necessity of making an additional assumption about relative phases and correcting for diffractive effects.

It is our hope that the theoretical results presented in this paper provide a foundation for the analysis of measurements of sound fields at long range in the deep ocean. An analysis of this type will be presented in a forthcoming paper. Our long-term goal of developing tools that can be used to assist in the analysis of measurements accounts, in large part, for the considerable attention that we have devoted to ocean structures with nonperiodic range dependence.

The ideas and results that we have discussed differ in some important respects from more commonly applied ideas and results associated with the study of wave propagation in random media (WPRM). For example, in the deterministic chaos point of view, the excitation of ray-medium resonances generally leads to a mixed phase space. Most approaches to WPRM, on the other hand, invoke the assumption that the perturbation to the background sound speed structure is delta-correlated; this leads to stochasticity, but not to a mixed phase space. Also, most long-range underwater acoustic propagation WPRM theories (see, e.g., Ref. 68) assume that stochasticity is caused exclusively by internal waves. From the deterministic chaos point of view, this assumption is difficult to justify inasmuch as non-internal-wave (e.g., mesoscale) structure may excite ray-medium resonances and chaos. Although we have argued that a traditional WPRM framework is a good starting point for some purposes, such as understanding ray intensity statistics, it is unable to provide an explanation for other phenomena that we have described such as the connection between ray stability and ω'. We anticipate that, over the next decade or so, ideas relating to deterministic chaos will gradually be incorporated into theories of WPRM.

Finally, we wish to remark that the importance of ray methods is not diminished by recent advances, both theoretical and computational, in the development of full wave models, such as those based on parabolic equations. The latter are indispensible computational tools in many applications. In contrast, the principal virtue of ray methods is that they provide insight into the underlying wave physics that is difficult, if not impossible, to obtain by any other means. For this reason ray methods remain important.

ACKNOWLEDGMENTS

We thank F. Tappert and F. J. Beron-Vera for the benefit of discussions on many of the topics included in this paper. This work was supported by Code 321 OA of the U.S. Office of Naval Research.

[1] S. S. Abdullaev and G. M. Zaslavsky, ''Stochastic instability of rays and the speckle structure of the field in inhomogeneous media,'' Zh. Eksp. Teor. Fiz. **87**, 763–775 (1984) [Sov. Phys. JETP **60**, 435–441 (1985)].
[2] D. R. Palmer, M. G. Brown, F. D. Tappert, and H. F. Bezdek, ''Classical chaos in nonseparable wave propagation problems,'' Geophys. Res. Lett. **15**, 569–572 (1988).
[3] S. S. Abdullaev and G. M. Zaslavsky, ''Fractals and ray dynamics in longitudinally inhomogeneous media,'' Sov. Phys. Acoust. **34**, 334–336 (1989).
[4] S. S. Abdullaev and G. M. Zaslavskii, ''Classical nonlinear dynamics and chaos of rays in wave propagation problems in inhomogeneous media,'' Usp. Phys. Nauk **161**, 1–43 (1991).
[5] M. G. Brown, F. D. Tappert, and G. Goñi, ''An investigation of sound ray dynamics in the ocean volume using an area-preserving mapping,'' Wave Motion **14**, 93–99 (1991).
[6] F. D. Tappert, M. G. Brown, and G. Goñi, ''Weak chaos in an area-preserving mapping for sound ray propagation,'' Phys. Lett. A **153**, 181–185 (1991).
[7] M. G. Brown, F. D. Tappert, G. Goñi, and K. B. Smith, ''Chaos in underwater acoustics,'' in *Ocean Variability and Acoustic Propagation*, edited by J. Potter and A. Warn-Varnas (Kluwer Academic, Dordrecht, 1991), pp. 139–160.
[8] D. R. Palmer, T. M. Georges, and R. M. Jones, ''Classical chaos and the sensitivity of the acoustic field to small-scale ocean structure,'' Comput. Phys. Commun. **65**, 219–223 (1991).
[9] K. B. Smith, M. G. Brown, and F. D. Tappert, ''Ray chaos in underwater acoustics,'' J. Acoust. Soc. Am. **91**, 1939–1949 (1992).
[10] K. B. Smith, M. G. Brown, and F. D. Tappert, ''Acoustic ray chaos induced by mesocsale ocean structure,'' J. Acoust. Soc. Am. **91**, 1950–1959 (1992).

[11] S. S. Abdullaev, *Chaos and Dynamics of Rays in Waveguide Media*, edited by G. Zaslavsky (Gordon and Breach Science, New York, 1993).
[12] F. D. Tappert and X. Tang, ''Ray chaos and eigenrays,'' J. Acoust. Soc. Am. **99**, 185–195 (1996).
[13] G. M. Zaslavsky and S. S. Abdullaev, ''Chaotic transmission of waves and 'cooling' of signals,'' Chaos **7**, 182–186 (1997).
[14] J. Simmen, S. M. Flatté, and G.-Yu Wang, ''Wavefront folding, chaos and diffraction for sound propagation through ocean internal waves,'' J. Acoust. Soc. Am. **102**, 239–255 (1997).
[15] M. Wiercigroch, M. Badiey, J. Simmen, and A. H.-D. Cheng, ''Nonlinear dynamics of underwater acoustics,'' J. Sound Vib. **220**, 771–786 (1999).
[16] M. A. Wolfson and F. D. Tappert, ''Study of horizontal multipaths and ray chaos due to ocean mesoscale structure,'' J. Acoust. Soc. Am. **107**, 154–162 (2000).
[17] M. A. Wolfson and S. Tomsovic, ''On the stability of long-range sound propagation through a structured ocean,'' J. Acoust. Soc. Am. **109**, 2693 (2001).
[18] U. Eichman, K. Richter, D. Wintgen, and W. Sandner, ''Scaled energy spectroscopy and its relation with periodic orbits,'' Phys. Rev. Lett. **61**, 2438–2441 (1988).
[19] L. D. Landau and E. M. Lifshits, *Mechanics* (Nauka, Moscow, 1973).
[20] B. V. Chirikov, ''A universal instability of many-dimensional oscillator systems,'' Phys. Rep. **52**, 263–379 (1979).
[21] G. M. Zaslavsky and B. V. Chirikov, ''Stochastic instability of non-linear oscillations,'' Sov. Phys. Usp. **14**, 549–672 (1972).
[22] A. G. Lichtenberg and M. A. Lieberman, *Regular and Stochastic Motion* (Springer Verlag, New York, 1983).
[23] M. Tabor, *Chaos and Integrability in Nonlinear Dynamics* (Wiley-Interscience, New York, 1989).
[24] M. G. Brown, ''Phase space structure and fractal trajectories in 1 1/2 degree of freedom Hamiltonian systems whose time dependence is quasi-periodic,'' Nonlinear Process. Geophys. **5**, 69–74 (1998).
[25] J. A. Colosi and M. G. Brown, ''Efficient numerical simulation of stochastic internal-wave-induced sound speed perturbation fields,'' J. Acoust. Soc. Am. **103**, 2232–2235 (1998).
[26] G. M. Zaslavsky, M. Edelman, and B. A. Niyazov, ''Self-similarity, renormalization and phase nonuniformity of Hamiltonian chaotic dynamics,'' Chaos **7**, 159–181 (1997).
[27] E. Ott, *Chaos in Dynamical Systems* (Cambridge U. P., Cambridge, 1993).
[28] P. Gaspard and G. Nicolis, ''Transport properties, Lyapunov exponents, and entropy per unit time,'' Phys. Rev. Lett. **65**, 1693–1696 (1990).
[29] N. R. Cerruti and S. Tomsovic, ''Sensitivity of wave field evolution and manifold stability in chaotic systems,'' Phys. Rev. Lett. **88**, 054103 (2002); nlin.CD/0108016.
[30] W. H. Munk, ''Sound channel in an exponentially stratified ocean with application to SOFAR,'' J. Acoust. Soc. Am. **55**, 220–226 (1974).
[31] A. A. Chernikov, R. Z. Sagdeev, and G. M. Zaslavsky, ''Chaos: How regular can it be?'' Phys. Today **41**, 27–35 (1988).
[32] G. M. Zaslavsky, *Physics of Chaos in Hamiltonian Systems* (Imperial College, London, 1998).
[33] F. J. Beron-Vera and M. G. Brown, ''Ray stability in weakly range-dependent sound channels,'' J. Acoust. Soc. Am. (in press).
[34] T. F. Duda and J. B. Bowlin, ''Ray acoustic caustic formation and timing effects from ocean sound speed relative curvature,'' J. Acoust. Soc. Am. **96**, 1033–1046 (1994).
[35] V. I. Shishov, ''Theory of wave propagation in random media,'' Izv. Vyssh. Uchebn. Zaved., Radiofiz. **11**, 866–875 (1968).
[36] G. Hasinger, R. Giacconi, J. E. Gunn, I. Lehmann, M. Schmidt, D. P. Schneider, J. Trümper, J. Wambsganss, D. Woods, and G. Zamorani, ''The ROSAT Deep Survey IV. A distant lensing cluster of galaxies with a bright arc,'' Astron. Astrophys. **340**, L27–L30 (1998).
[37] *Mesoscopic Quantum Physics*, edited by E. Akkermans, G. Montambaux, J.-L. Pichard, and J. Zinn-Justin, Les Houches Session LXI, 1994 (Elsevier Science, Amsterdam, 1995).
[38] M. A. Topinka, B. J. LeRoy, R. M. Westervelt, S. E. J. Shaw, R. Fleischmann, E. J. Heller, K. D. Maranowski, and A. C. Gossard, ''Coherent branched flow in a two-dimensional electron gas,'' Nature (London) **410**, 183 (2001).
[39] M. V. Berry, ''Focusing and twinkling: critical exponents from catastophes in non-Gaussian random short waves,'' J. Phys. A **10**, 2061–2081 (1977).
[40] J. G. Walker, M. V. Berry, and C. Upstill, ''Measurements of twinkling exponents of light focused by randomly rippling water,'' Opt. Acta **30**, 1001–1010 (1983).
[41] J. H. Hannay, ''Intensity fluctuations beyond a one-dimensional random refracting screen in the short-wavelength limit,'' Opt. Acta **29**, 1631–1649 (1982).
[42] E. J. Heller and S. Tomsovic, ''Postmodern Quantum Mechanics,'' Phys. Today **46**(7), 38–45 (1993).
[43] B. Sundaram and G. M. Zaslavsky, ''Wave analysis of ray chaos in underwater acoustics,'' Chaos **9**, 483–492 (1999).
[44] *Quantum Chaos: between Order and Disorder: a Selection of Papers*, edited by G. Casati and B. V. Chirikov (Cambridge U. P., New York, 1995).
[45] *Chaos and Quantum Physics*, edited by M. J. Giannoni, A. Voros, and J. Zinn-Justin, Les Houches Session LII, 1989 (Elsevier Science, Amsterdam, 1991).
[46] G. M. Zaslavsky, ''Stochasticity in quantum systems,'' Phys. Rep. **80**, 157–250 (1980).
[47] N. L. Balazs and B. K. Jennings, ''Wigner function and other distribution functions in mock phase spaces,'' Phys. Rep. **104**, 347–391 (1984).
[48] D. Bambusi, S. Graffi, and T. Paul, ''Long time semiclassical approximation of quantum flows: A proof of the Ehrenfest time,'' Asymptotic Anal. **21**, 149–160 (1999).
[49] A. L. Virovlyansky and G. M. Zaslavsky, ''Evaluation of the smoothed interference pattern under conditions of ray chaos,'' Chaos **10**, 211–223 (2000).
[50] P. W. O'Connor, S. Tomsovic, and E. J. Heller, ''Semiclassical Dynamics in the Strongly Chaotic Regime: Breaking the Log Time Barrier,'' Physica D **55**, 340 (1992).
[51] M.-A. Sepulveda, S. Tomsovic, and E. J. Heller, ''Semiclassical propagation: How long can it last?'' Phys. Rev. Lett. **69**, 402–405 (1992).
[52] S. Tomsovic and E. J. Heller, ''Long-time semiclassical dynamics of chaos: The stadium billiard,'' Phys. Rev. E **47**, 282–299 (1993).
[53] M. D. Collins and J. F. Lingevitch, ''Secular behavior and breakdown of chaotic ray solutions,'' IEEE J. Ocean. Eng. **22**, 102–109 (1997).
[54] M. G. Brown and M. A. Wolfson, ''A numerical investigation of semiclassical breakdown in an idealized random medium,'' in preparation (2002).
[55] L. B. Felsen, ''Hybrid ray-mode fields in inhomogeneous waveguides and ducts,'' J. Acoust. Soc. Am. **62**, 352–361 (1981).
[56] T. Gao and E. C. Shang, ''The transformation between the mode representation and the generalized ray representation of a sound field,'' J. Sound Vib. **80**, 105–115 (1982).
[57] L. M. Brekhovskikh and Yu. Lysanov, *Fundamentals of Ocean Acoustics* (Springer-Verlag, Berlin, 1991).
[58] A. L. Virovlyansky, V. V. Kurin, N. V. Pronchatov-Rubtsov, and S. I. Simdyankin, ''Fresnel zones for modes,'' J. Acoust. Soc. Am. **101**, 163–173 (1997).
[59] A. L. Virovlyanskii and A. G. Kosterin, ''Method of smooth perturbations for the description of the fields in multimode waveguides,'' Sov. Phys. Acoust. **33**, 351–354 (1987).
[60] A. L. Virovlyansky, A. G. Kosterin, and A. N. Malakhov, ''Fresnel zones for modes and analysis of field fluctuations in random multimode waveguides,'' Waves Random Media **1**, 409–418 (1991).
[61] A. L. Virovlyansky and G. M. Zaslavsky, ''Wave chaos in terms of normal modes,'' Phys. Rev. E **59**, 1656–1668 (1999).
[62] A. L. Virovlyansky, ''Manifestation of ray stochastic behavior in a modal structure of the wave field,'' J. Acoust. Soc. Am. **108**, 84–95 (2000).
[63] L. D. Landau and E. M. Lifshits, *Quantum Mechanics* (Moscow, Nauka, 1974).
[64] F. B. Jensen, W. A. Kuperman, M. B. Porter, and H. Schmidt, *Computational Ocean Acoustics* (American Institute of Physics, New York, 1994).
[65] G. P. Berman and G. M. Zaslavsky, ''Condition of stochasicity in quantum nonlinear systems,'' Physica A **97**, 367–382 (1979).
[66] J. A. Colosi and S. M. Flatté, ''Mode coupling by internal waves for multimegameter acoustic propagation in the ocean,'' J. Acoust. Soc. Am. **100**, 3607–3620 (1996).
[67] A. L. Virovlyansky, ''Comments on 'Mode coupling by internal waves for multimegameter acoustic propagation in the ocean' [J. Acoust. Soc. Am. **100**(6), 3607–3620 (1996)],'' J. Acoust. Soc. Am. **106**, 1174–1176 (1999).
[68] S. Flatté, R. Dashen, W. Munk, K. Watson, and F. Zachariasen, *Sound Transmission through a Fluctuating Ocean* (Cambridge U.P., Cambridge, 1979).

The influence of large-scale seafloor slope and average bottom sound speed on low-grazing-angle monostatic acoustic scattering

Robert J. Greaves[a)]
Massachusetts Institute of Technology/Woods Hole Oceanographic Institution, Joint Program, Woods Hole, Massachusetts 02543

Ralph A. Stephen
Woods Hole Oceanographic Institution, Woods Hole, Massachusetts 02543

(Received 3 May 2001; revised 22 April 2002; accepted 30 January 2003)

Variations in large-scale seafloor slope and average seabed sound speed account for a significant portion of the variations in scattering intensity observed in low-grazing-angle monostatic reverberation. Numerical modeling using a finite-difference solution to the elastic wave equation is used to quantify the effect of these large-scale parameters in interpretations of reverberation data. For hard rough seafloor (e.g., basalt), the results of the modeling suggest that the monostatic backscattering strength increases with increasing large-scale seafloor slope up to a slope of about 15° dipping toward the incident direction. Once the grazing angle of the incident wavefield exceeds the critical grazing angle for the flat reference seafloor the backscattering intensity increases only slowly with increasing grazing angle. Similarly, average subseafloor sound speed has a significant effect. Seafloor with low sound speeds characteristic of soft bottoms (e.g., sediment) generate significantly weaker backscatter signals than seafloor with sound speeds characteristic of hard bottoms (e.g., basalt). The difference is that the shear waves can always be passed into soft bottoms because even for a flat seafloor there is no shear wave critical grazing angle. © *2003 Acoustical Society of America.* [DOI: 10.1121/1.1563669]

PACS numbers: 43.30.Gv, 43.30.Hw, 43.30.Ft [DLB]

I. INTRODUCTION

Elastic wavefield numerical modeling is used to predict the scattered wavefield from a variety of seabed models. The modeling simulates low-grazing-angle (<20°) monostatic scattering in reverberation experiments. These modeling results are then used to develop a quantitative description of the effect of large-scale seafloor slope and average seabed sound speed on the scattered wavefield intensity.

In a previous paper (Greaves and Stephen, 2000) we reported a similar study for variations in seafloor roughness and subbottom heterogeneity. As described there, we consider spatial characteristics that change significantly at length scales on the order of ten wavelengths or more to be ''large scale,'' whereas variations that occur in the range from a tenth to ten wavelengths to be ''wavelength scale.'' Our use of the terms ''large scale'' and ''wavelength scale'' are consistent with the discussion in Aki and Richards (1980), relating to their Fig. 13.11 (p. 749), that describes the trade-off between insonifying wavelength and the length scale of heterogeneity for a broad range of scattering problems. In the study reported here, ''wavelength'' (λ) refers to the wavelength in water at the peak frequency of the source pressure waveform. In these studies the dominant wavelength in water of the incident and scattered field is 6 m. ''Scale,'' as applied here, means the maximum spatial interval at which a feature or property can be sampled in order to measure characteristic variations in the property. Therefore, large-scale seabed characteristics, relative to the incident field wavelength of 6 m, are any features that can be accurately represented by sampling intervals greater than 60 m whereas wavelength-scale features require sampling between 0.6 and 60 m.

Field measurements of acoustic reverberation signals are usually portrayed as time average field intensities observed in specific azimuthal directions. In our numerical modeling of acoustic scattering, we quantify the effect of variations in geologic properties in terms of changes in scattered wavefield intensity. Much of the analysis of monostatic reverberation data attributes variations in the backscattered intensity to scattering from seafloor features that, by our definition, are large-scale features, such as seamounts, deep ocean ridges, and continental margins as well as canyons, gulleys, and cliffs (e.g., Preston *et al.*, 1990; Makris and Berkson, 1994; Makris *et al.*, 1995; Smith *et al.*, 1996; Makris *et al.*, 1999; Chia *et al.*, 2000), which have length scales greater than 60 m and are identified in bathymetry data sampled at 5- and 200-m intervals or larger. We believe that it is fundamental to the understanding and interpretation of scattering data to distinguish between geological features that generate scattered wavefields and those that *influence* the characteristics of a scattered field. Wavelength-scale variations in propagation properties generate the scattered wavefields while large-scale variations only influence the characteristics (e.g., modify the intensity) of the scattering. This means that if wavelength-scale variations are not imbedded in the large-scale feature, a scattered field will not be generated. As an example, we

[a)]Current address: MIT, Lincoln Laboratory, 244 Wood St., Lexington, MA 02420-9108. Electronic mail: greaves@ll.mit.edu

would say that scattering from a large seafloor ridge is generated by the wavelength-scale roughness of the seafloor on the ridge, but that the characteristics (e.g., intensity) of the scattered field are modified by the large-scale spatial characteristics (e.g., slope) of the ridge. In other words, the same wavelength-scale roughness would produce a different scattered wavefield if it is imposed on a seafloor that is flat over distances greater than about ten wavelengths than if it is imposed on a seafloor that has large-scale slope.

II. BACKGROUND

Early reports on bottom backscatter experiments remarked at the correspondence between strong backscatter intensity and large-scale seafloor features such as continental margins, seafloor ridges, or seamounts (Smith *et al.*, 1996; Makris *et al.*, 1995; Makris and Berkson, 1994; Preston *et al.*, 1990; Baggeroer and Dyer, 1986). Transmission loss was quickly recognized as an important factor. If the sound does not reach a particular patch on the seafloor, or cannot return from that patch, then strong backscatter would not be observed. Even after transmission loss was taken into account, however, the correspondence between large-scale bathymetric features (about 200-m footprints for Hydrosweep bathymetric data) and strong backscatter returns was not convincing. The presence of steep cliffs, scarps, ledges, and talus slopes was invoked based on preliminary analysis of finer-scale ''deep-tow'' imagery at 5-m resolution. It was postulated that strong backscatter correlated with the concentrations and characteristics of these features [''we have shown that prominent returns come from scarps facing the source and receiver, but we have not been able to determine whether steep cliffs (50°–90°) of exposed rock within the scarps are the dominant scatterers or more gradual talus slopes and smaller scale terraces are also important'' (Makris *et al.*, 1995)]. An important point is that the spatial scale of these features (about 100 m or so) is still much larger than the acoustic wavelength (about 6 m) of the experiment data used in these referenced analyses.

There is the continuing perception in the community that the strong scattered field from the mid-Atlantic Ridge experiment (Makris and Berkson, 1994) comes from large-scale escarpments, canyons, cliffs, or gullies as either specular reflection from steep topography or the side-lobes of isolated (truncated) antennalike radiators or facets (Ogilvy, 1991), but this is not supported in detailed analysis of reverberation data. The slopes associated with seamounts and ridges that excite the strong backscatter at the mid-Atlantic Ridge are quite small. Greaves and Stephen (1997) discuss the relationship between seafloor slope as resolved by Hydrosweep bathymetry at a resolution of 200 m to monostatic backscatter strength that was measured in the same experiment as Makris and Berkson at inside-corner and outside-corner crust near the mid-Atlantic Ridge. In the three areas near the mid-Atlantic Ridge discussed by Greaves and Stephen, seafloor slopes never exceeded 45° and rarely exceed 20°. Scattering strength was only weakly correlated with seafloor slope. One conclusion of the 1997 paper was ''the seafloor dip, on a scale of a few hundred meters, that can be resolved by Hydrosweep bathymetry data, influences, but does not determine, scattering strength. Since in detail the observed variations in scattering strength are larger than can be explained by data error or seafloor dip, it is suggested that other characteristics of steeply dipping areas, such as subsurface properties or smaller scale surface features strongly affect the level of backscattered signals.'' Analysis of finer scale (5 m) bathymetry shows higher slopes but the incident angles on 5-m patches rarely approach 90°, as shown in Fig. 7 of Makris *et al.* (1999).

Even when a patch is insonified at normal incidence, the ''specular reflection'' is negligible when the patch has dimensions comparable to an acoustic wavelength. Figures 6 and 9 of Stephen and Swift (1994) show the results of a full-wave time-domain finite-difference solution for scattering from a single patch which is one acoustic wavelength in size and is insonified at normal incidence. This is a model commonly invoked for scattering from seafloor scarps which are about a wavelength high and may be oriented at normal incidence to the insonifying field. This model of a single patch does not generate strong backscatter into the water either as a normal incidence reflection from the patch face (it is too small) or from diffraction from the corners of the patch. To support a normal incidence reflection a patch must be many wavelengths in size and there is no indication from 5-m bathymetry that such large planar patches exist. In fact, Makris *et al.* (1999) concluded that ''since the surfaces resolved by the towed-array system on the B′ scarps are not even approximately planar, there is no unique surface normal to characterize the bathymetry within the resolution footprint.'' Later in the same paper they introduce the bidirectional scattering distribution function (BSDF) ''which is a dimensionless parameter describing surface-scattering properties that are invariant in expected value to changes in transmission and projected area.'' Figures 10 and 13 of Stephen and Swift (1994) show scattering results from a surface like this, where the ''normal'' is difficult to define and the resulting scatter is essentially angle-independent (omnidirectional).

In thorough analyses of the monostatic and bistatic components of the Main Acoustics Experiment (Chia *et al.*, 2000; Makris *et al.*, 1999, 1995), Makris and co-authors discuss empirical correlations between bathymetry (at 5- and 200-m resolution) and backscatter intensity. The goal of our study has been to address the physical mechanisms responsible for anomalous backscatter. To numerically study the physics of acoustic scattering, it is necessary to describe the medium by sampling at a tenth of an acoustic wavelength or less. This is an order of magnitude finer than the finest resolution considered by Makris and co-authors. Although these papers focus exclusively on reverberations from the scarps in areas B′ and C′, there may be similar scarps that do not reverberate, and there may be features other than scarps on the seafloor that excite strong backscatter. The analysis in this paper is not restricted to the scarps at B′ and C′, nor any particular seafloor location.

Bottom backscattering is physically caused by wavelength scale (about 6 m in our case) roughness or lateral heterogeneity. There may be an indirect correlation between scattering strength and large-scale features, if the small-scale

roughness and heterogeneity themselves correlate with large-scale features or if the large-scale features change the effective geometry (for example, a large-scale slope will change the effective incidence angle). This distinction between the size of the scatterers and the size of the reverberating patch was also discussed in the backscatter analysis of Harding *et al.* (1998), for example.

Three approaches have been used to describe the bathymetric and subbottom properties that are responsible for seafloor scattering: (1) statistical descriptions (rms height, correlation lengths, etc.) applied most often to roughness (Jackson *et al.*, 1988; Thorsos, 1988), (2) facets (Dyer *et al.*, 1993; Gerstoft and Schmidt, 1991), and (3) direct observations based on various scales of bathymetric sonars, photographs, or direct sampling (Greaves, 1998; Makris *et al.*, 1995; Makris and Berkson, 1994; Preston *et al.*, 1990). Since the backscatter strength predicted from methods which use statistical descriptions is too weak to explain the observed reverberation, studies have focused on methods which could predict scattering deterministically from a small number of discrete elements or facets. These efforts were encouraged by the direct observation of seafloor scarps and fault faces which were conceptually similar to facets. Figures 6 and 9 of Stephen and Swift (1994), as explained above, show that a single facet does not generate strong backscatter into the water either as a normal incidence reflection from the facet face (it is too small) or from diffraction from the facet corners. Since this model uses a penetrable bottom (and facet) we consider the results to be more correct than models which use perfectly rigid facets (Dyer *et al.*, 1993). Other interpretations of facets are given in Figs. 1, 5, and 8 of Gerstoft and Schmidt (1991). They show that a small number of wavelength size facets (planar interfaces), which, by chance, happen to be aligned at normal incidence to the insonifying field, are also inadequate to excite strong backscatter.

In this paper, we use the time-domain finite-difference (TDFD) method to model in two dimensions the full wave scattering from seafloor features with scale lengths comparable to the wavelength of the incident acoustic field (Stephen, 2000; Stephen and Swift, 1994). Other approaches could be used with different advantages and limitations. For example, Makris and Ratilal (2001) present a thorough treatment of scattering in wave guides which includes propagation throughout the water column and scattering from objects in the water as well as from roughness at the boundaries (sea surface, ocean bottom, subbottom layers, etc.). Some differences in the approaches are as follows (a) Our paper is motivated by, and addresses primarily, bottom reverberation and scattering in a deep ocean environment (about 4000–5000-m water depth) such as the mid-Atlantic with hard basaltic bottoms; although their method is in principle applicable to deep water, the examples in Makris and Ratilal address a shallow environment (about 100-m water depth) such as a continental shelf with soft sand and silt bottoms. The different environments pose different challenges to bottom scattering methodologies. For example, in shallow water problems, the TDFD method would use point sources directly without considering incident Gaussian beams. (b) Makris and Ratilal ignore the effects of rigidity (scattered and propagating shear body waves and interface waves) in their formulation even though they consider sandy and silty bottoms which have a finite rigidity. In propagation experiments shear waves are often ignored because either (*i*) their effects can be included in an additional loss term; or (*ii*) they attenuate rapidly and do not contribute observable multi-path arrivals. In scattering experiments, however, the scattering mechanism will excite both compressional and shear body waves (as well as interface waves) in a rigid bottom regardless of the shear wave attenuation properties. In fact, in many cases in deep and shallow water, shear wave resonances are a dominant contributor to the background noise and signal-generated noise fields (Butler, 1988; Godin and Chapman, 1999). (c) Makris and Ratilal apply the notion of an isolated, finite planar interface buried in the bottom to simulate a ''riverbank.'' This is an interesting phenomenological artifice that will yield an answer to the scattering problem. It would be interesting to compare the results of this approach with other methods like the facet method of Gerstoft and Schmidt or with time-domain finite-differences. (d) A major advantage of Makris and Ratilal is that they compute results in three dimensions. It would be very challenging for a TDFD code to provide three-dimensional solutions to comparable size problems.

Some major points which we address in this paper are the following. (1) Although it is beyond the scope of this paper to compare TDFD results with perturbation, Kirchhoff, and other methods which use a statistical description of the seafloor, we do use single, discrete representations based on statistical parameters. (2) We show that through reverberation and multiple scattering from statistically rough seafloors it is possible to excite strong backscatter. Large-scale seafloor slope and average subseafloor sound speed can account for a net variation in the backscatter intensity of up to 20 dB. If we include variations in surface roughness, variations greater than 40 dB can be observed.

III. THE NUMERICAL SCATTERING CHAMBER

For the modeling, we use the numerical scattering chamber (NSC), described by Stephen and Swift (1994), to generate scattered wavefields from seafloor models with and without wavelength-scale roughness. A variety of large-scale seafloor slopes, and average subseafloor sound speed and densities are considered. The NSC solves the elastic wave equation using the second-order staggered-grid finite-difference formulation described by Virieux (1986). Although our modeling is performed in a limited 2-D model space, it is important to point out that the model is not defined as a waveguide. Radiation boundary conditions are used on all four sides of the model. Because of the finite model space the measured scattered wavefields are in the ''near-field.'' We are not including in the modeling the waveguide effects of a complete deep ocean sound speed profile (see Fig. 1 of Stephen and Swift, 1994).

In this study, the source wavefield is a Gaussian beam that is incident on a horizontal seafloor at 15° grazing angle. This is an appropriate angle for simulating monostatic backscattering data obtained in moderately deep ocean areas such as the flanks of mid-ocean ridges. The source pulse in pres-

sure is defined as the third derivative of a Gaussian curve, with the peak frequency at 250 Hz and a half-power bandwidth of one octave (170–340 Hz).

Pressure time series are calculated for grid locations along the sides and top of the scattering chamber, but only time series at grid locations in the water column (dependent on the shape of the model) are recorded. In all models a uniform grid spacing of 0.4 m ($\lambda/15$ for the 6-m dominant wavelength) was used to minimize effects of numerical grid dispersion (Kelly *et al.*, 1976). A time step (Δt) of 0.000 04 s was used to satisfy the numerical stability criteria for the second-order staggered grid calculations.

In order to complete the simulation of monostatic reverberation data, the beamforming process of Stephen and Swift (1994) is applied to the recorded scattered-field time-series data to calculate scattering coefficients as a function of scattering angle. The scattering coefficient in the monostatic backscatter direction (i.e., 15° for our modeling) is then compared as specific geologic parameters are varied. For further details on the characteristics of the NSC as utilized in our modeling the reader is referred to Greaves and Stephen (2000).

IV. VARIATION IN SOUND SPEED AND DENSITY

We consider three types of seafloor geology: basalt, sediment, and talus. Swift and Stephen (1994) suggest a basic breakdown of seafloor material into ''soft bottoms'' such as sediment, where $v_p^s > v_p^w > v_s^s$, and ''hard bottoms,'' such as basalts, where $v_p^b > v_s^b > v_p^w$, v_s and v_p being the shear and compressional wave speeds, respectively, and the superscripts denote sound speeds in water, sediment, or basalt. Also note that a flat soft bottom (sedimentary) seafloor has no shear critical grazing-angle [$\theta_c^s = \cos^{-1}(v_p^w/v_s^s) = 0$, $\forall v_s^s < v_p^w$], which means that conversion of compressional wave energy to shear wave energy that passes into the subseafloor is always possible. Talus, being a mixture of fine-grained pelagic sediment and coarse basaltic debris, has intermediate sound speed and density, but in our modeling these parameters have been set such that talus would also be described as a ''soft bottom.''

A. Seafloor models

The water column above the seafloor is represented as a homogeneous layer with compressional wave speed, $v_p^w = 1.5$ km/s, and density, $\rho^w = 1000$ kg/m^3. To represent sediment in the subseafloor models, we use $v_p^s = 1.52$ km/s, $v_s^s = 0.62$ km/s, and $\rho^s = 1500$ kg/m^3. Talus is represented by $v_p^t = 2.0$ km/s, $v_s^t = 0.88$ km/s, and $\rho^t = 1740$ kg/m^3. In representing basaltic basement, we have modeled two realistic sound speed and density descriptions: $v_p^{b1} = 3.0$ km/s, $v_s^{b1} = 1.5$ km/s, $\rho^{b1} = 2120$ kg/m^3, and $v_p^{b2} = 4.0$ km/s, $v_s^{b2} = 2.0$ km/s, $\rho^{b2} = 2500$ kg/m^3. These sound speeds correspond to Poisson's ratio of 0.33 for basalt, 0.38 for talus, and 0.4 for sediment. The basalt values were chosen based on the evidence presented by Shearer (1988) that the Poisson's ratio in the upper 500 m of oceanic basement is within the range of 0.32 to 0.38, due primarily to fracturing in these upper-crustal regions. Hamilton (1971) computed Poisson's ratios for deep sea (pelagic) sediments in the North Pacific and found them to average about 0.48, which is very close to the Poisson's ratio of fluid (0.5). We chose to use a Poisson's ratio of 0.4 in our modeling in order to maintain sufficiently high shear wave speed to allow modeling without significant grid dispersion for our 0.4-m grid spacing.

Seafloor roughness is described by two parameters, ka and $k\sigma$, where $k = 2\pi/\lambda$ is the wavenumber of the incident wavefield, and ''a'' and ''σ'' are the (auto)correlation length and standard deviation in height of the seafloor roughness, respectively. The rough seafloor is created by filtering normalized random distributions to distributions with Gaussian autocorrelations and then scaling to the desired standard deviation in height.

B. Wavefield snapshots

Figures 1 and 2 show rough seafloor model profiles and snapshots of compressional and shear wave amplitude density after 160 ms of propagation time in the NSC. Amplitude density is the square root of the energy density with the sign of the divergence and curl of the displacement field for compressional and shear density respectively (Dougherty and Stephen, 1988). For the seafloor profile shown in Fig. 1(a), the seafloor roughness is defined with $ka = 6$ and $k\sigma = 4$. The relatively smooth seafloor shown in Fig. 2(a) has $ka = 6$ but now $k\sigma = 0.5$. In both of these models the seafloor roughness is imposed on a flat seafloor, i.e., there is no large-scale seafloor slope. For each seafloor profile, snapshots are shown for subseafloor defined with the sediment, talus, and high-speed basalt model parameters. (Note that in all snapshot figures in this paper, the origin of the x axis is on the right-hand side and that the source wavefield is initiated in the upper right-hand corner such that the source wavefield, P_1, travels from right to left during the propagation modeling.) Since the modeling is based on the elastic wave equation, all possible wave types, compressional and shear waves, head waves, and interface waves are present in the snapshots. Of primary interest in this analysis are the diffractions in the water column, because they yield the backscattered acoustic wavefield.

Before discussing these modeling results we review what would be observed if the insonifying wavefield were incident on a planar seafloor (i.e., no scatterers) with the different subseafloor geological model parameters. The critical grazing angle of the compressional wave, for a model with the sediment parameters, is $\theta_{c,p}^s = 9.3°$ and with the talus parameters, $\theta_{c,p}^t = 41°$. For both the sediment model and the talus model there is no critical grazing angle for shear waves. This means that shear wave energy can be converted freely at this boundary. For the high-speed basalt model the compressional and shear wave critical grazing angles are $\theta_{c,p}^{b2} = 68°$ and $\theta_{c,s}^{b2} = 41°$.

These critical angle values tell us that for a planar seafloor with sediment properties, a compressional wavefield incident at 15° will be transmitted through the interface and also will produce converted shear waves that propagate into the subseafloor. If the subseafloor has instead the talus model properties, energy from the incident wavefield will be con-

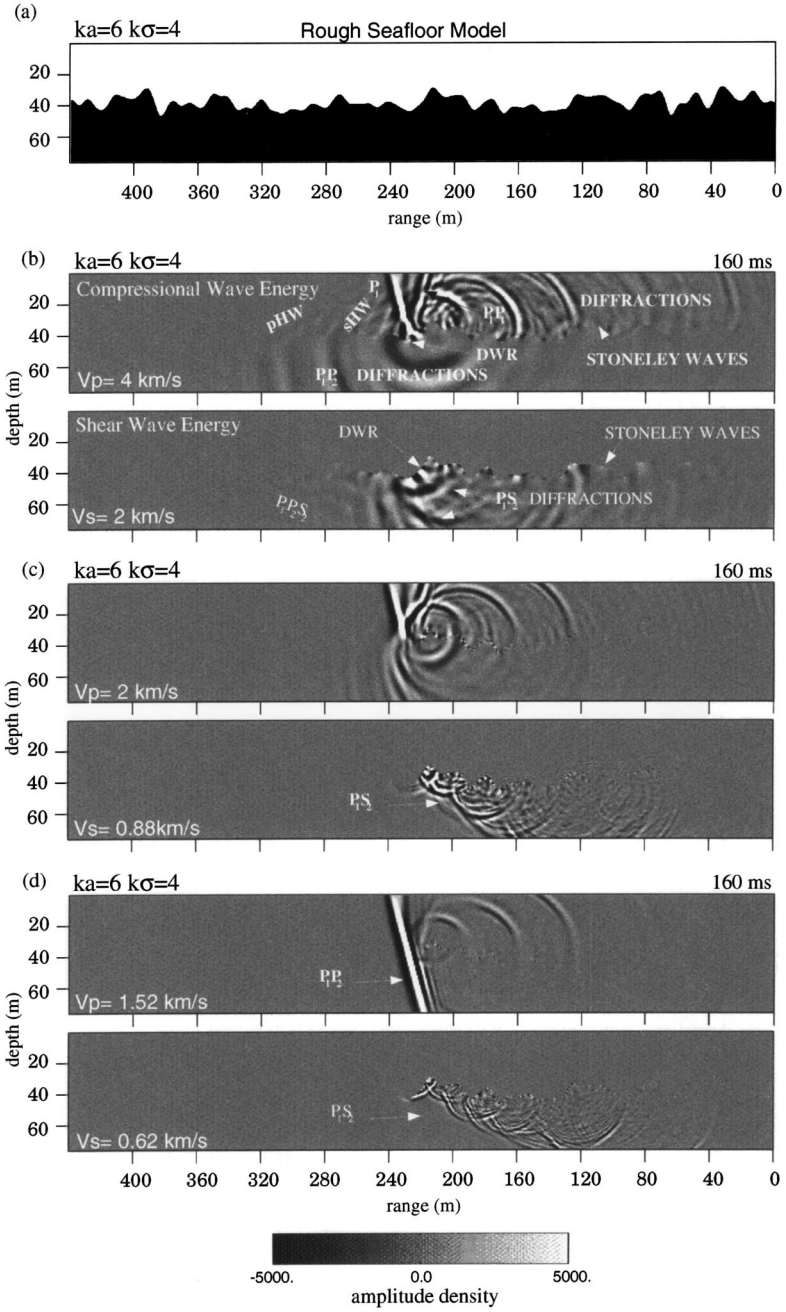

FIG. 1. Variation in the subseafloor sound speed and density of a homogeneous, rough-seafloor model alters the distribution of wavefield energy scattered into the water column and subseafloor. [Note that in all of the snapshot figures the incident wavefield (P_1) is initiated as a Gaussian-beam source-pulse in the upper right-hand corner of the model space that propagates from right to left.] These snapshots show the wavefield amplitude density at 160 ms for the $ka=6$, $k\sigma=4$, Gaussian seafloor model (a). In (b) the subseafloor parameters correspond to a basalt bottom: $v_p=4.0$ km/s, $v_s=2.0$ km/s, and $\rho=2500$ kg/m^3; in (c) they correspond to a talus bottom: $v_p=2.0$ km/s, $v_s=0.88$ km/s, and $\rho=1740$ kg/m^3; and in (d) they correspond to a sediment bottom: $v_p=1.52$ km/s, $v_s=0.62$ km/s, and $\rho=1500$ kg/m^3. For these models the critical grazing angles for compressional and shear waves at a flat seafloor are in (b) $\theta_c^P=68°$ and $\theta_c^S=41°$, in (c) $\theta_c^P=41°$ and in (d) $\theta_c^P=9°$. For (c) and (d), converted S-wave diffractions (P_1S_2) occur at all grazing angles since $\theta_c^S=0°$. For (c) and (d) shear wave energy passes into the subseafloor at all incident angles, even for a flat, homogeneous bottom. In (d) the grazing angle would be super-critical for compressional waves at a flat seafloor as well, and scattered compressional wave energy generates a wavefront that looks like a transmitted wave. The figures show that scattering of the incident wave into P-wave and S-wave energy increases as sound speed decreases. However, even at what would be subcritical grazing angles (b), both compressional and shear energy are scattered into the subseafloor. In general, as the subseafloor sound speed decreases, the amplitude of the backscattering appears to decrease.

verted to shear waves that propagate into the subseafloor but transmission of compressional waves will not occur. For the case of the basalt model, the source wavefield grazing angle is less than both the compressional and shear grazing angles, so that the incident wave is totally internally reflected.

This description of reflection and transmission at a planar interface represents the ''high-frequency approximation'' or ''geometric ray approximation'' description of wave propagation. It requires that there are no variations in the medium or interface properties small enough to cause the wavefield to scatter. Where there are such scatterers this approximation does not accurately predict or explain the resulting scattered wavefield nor the partitioning of energy. In general, scattering occurs where interface or volume heterogeneity has a radius of curvature comparable to the scale of the insonifying wavelength (Aki, 1982).

The snapshots in Fig. 1 clearly show that scattering at the rough interface send compressional waves in all directions, both into the water column and into the subseafloor, and also converts energy to shear waves that propagate in the subseafloor. The snapshot in Fig. 1(b) is from the high-speed basalt model. A flat seafloor model with this velocity contrast would have a critical grazing angle such that the geometric ray approximation would predict that no energy could be passed into the subseafloor. Since the shear wavelength is less than the compressional wavelength we expect the number of locations where shear wave scattering can occur to be greater than the number of locations where compressional wave scattering can occur, and therefore we expect a more complicated subseafloor shear wavefield than for the compressional wavefield. This is in fact what is observed.

As the subseafloor compressional and shear wave speeds

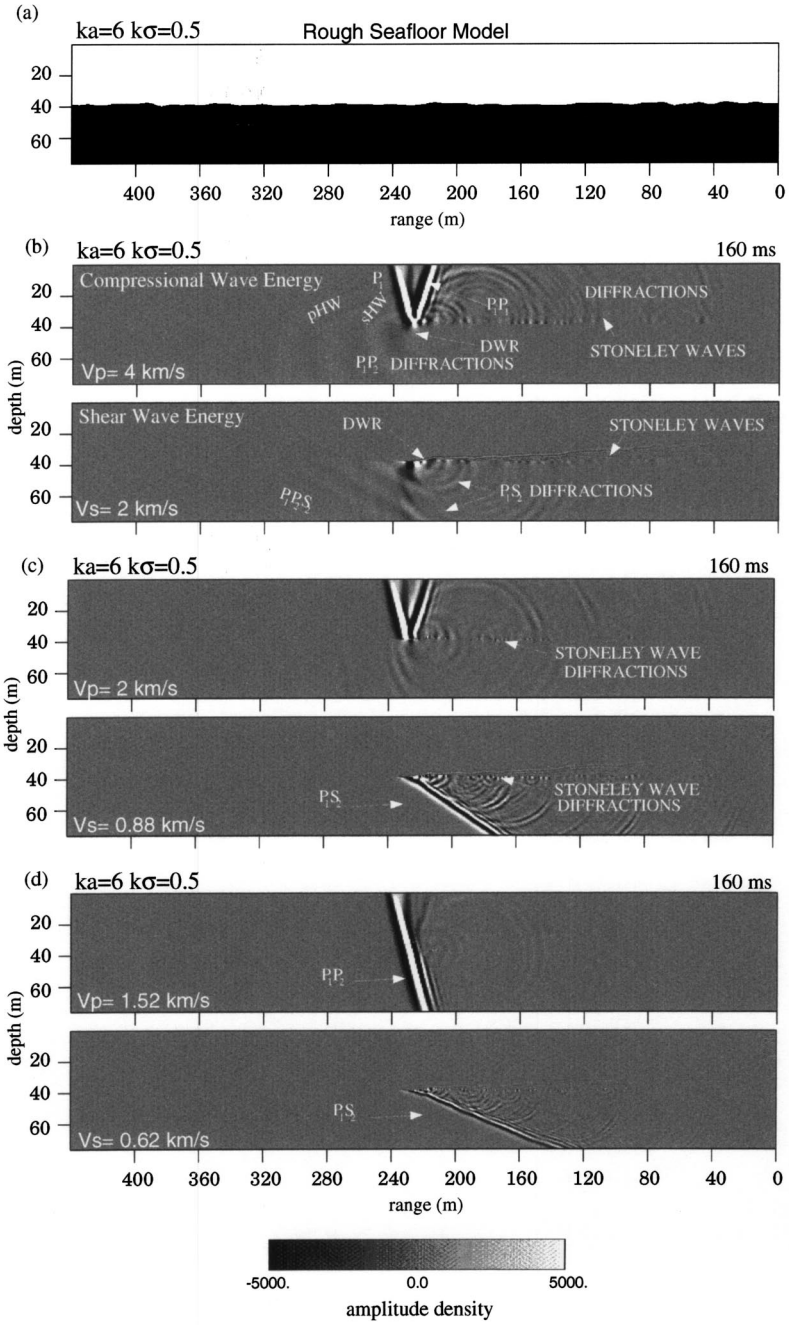

FIG. 2. This figure shows wavefield energy at 160 ms for the $ka=6$, $k\sigma=0.5$ Gaussian model (a), for the same subseafloor sound speed and density parameters as listed in Fig. 1. As expected, a decrease in interface roughness (due to the smaller value of $k\sigma$) produces less scattering in the water column (compare to Fig. 1). In all of the sound speed models, diffraction of P-wave and S-wave energy into the subseafloor is observed, but in lower sound speed models, (c) and (d), the scattered shear waves in the subseafloor look like transmitted (converted) shear waves.

decrease, the wavelengths also decrease. The same rough seafloor will have an increasing number of locations where scattering can occur. This then increases the total energy that diffracts into the subseafloor. For the talus and sediment models [Figs. 1(c) and (d) and 2(c) and (d)] the shear wave speeds are less than the water sound speed, so even for a flat seafloor there would be no shear critical angles. For subseafloor with these shear wave speeds, shear energy is excited everywhere along any seafloor structure, even a flat seafloor. Therefore it becomes difficult to distinguish between the energy transmitted (converted shear) in a ''geometric ray approximation'' context and the energy scattered from the roughness. Similarly, the sediment model in Figs. 1(d) and 2(d) have subseafloor compressional wave speed that is only slightly higher than the compressional wave speed in water and, consequently, this seafloor with no roughness would have a very small compressional wave critical angle (9°). Since the incident grazing angle is 15°, compressional energy is passed into the subseafloor regardless of the seafloor structure.

Since the seafloor profile in Fig. 2(a) is much less rough than the profile in Fig. 1(a), the resulting propagation exhibited in the snapshots in Fig. 2 appear similar to the propagation predicted by the geometric ray approximation. The basalt bottom [Fig. 2(b)] shows almost total internal reflection. The talus model snapshot, Fig. 2(c), shows a strong reflection of the compressional wave with a converted shear wavefield in the subseafloor. The sediment model snapshot, Fig. 2(d), shows both compressional and converted shear wavefields in the subseafloor that look very much like transmitted

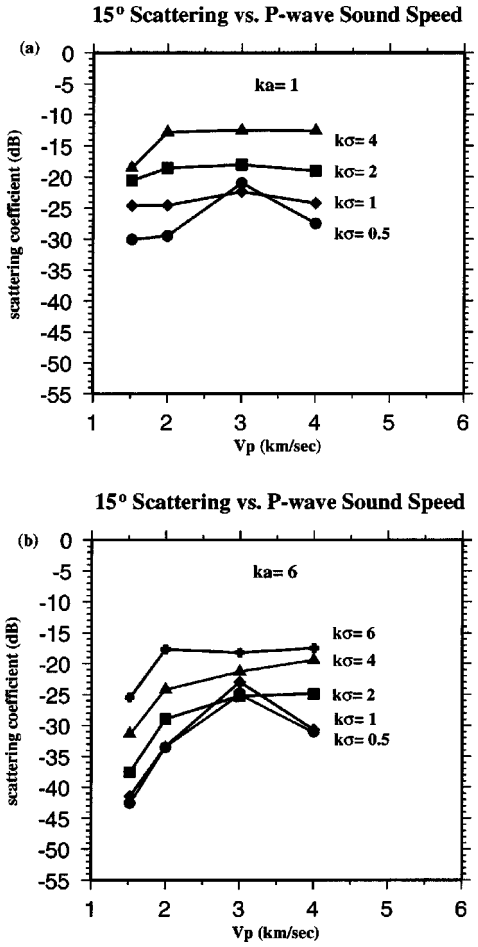

FIG. 3. In general, scattering coefficients in the 15° backscatter direction increase as subseafloor sound speed and density increase. The sensitivity is slightly weaker for models with correlation length of $ka=1$ (a) than for models with larger correlation length, $ka=6$ (b). These results also show that the backscattered signals of the lowest (sediment) velocity models are generally at least 6 dB down relative to the same models with higher subseafloor sound speed. In most cases, the points plotted represent average values from three realizations.

wavefronts. However, scattering is also observed in all of these snapshots, reminding us that these wavefields include scattering at nonplanar interfaces that is not predicted by ''ray theory'' approximations to wave propagation.

These wavefield snapshots show clearly that decreasing the amplitude of the roughness substantially decreases the magnitude of the scattered energy. The shear wavefronts for the smooth talus and sediment models [Figs. 2(c) and (d)] look very similar to the transmitted shear wavefronts for a flat seafloor with negligible scattered energy.

C. Monostatic backscattering

To compare the effects of bottom type on monostatic backscatter we use subseafloor compressional wave speed as a proxy for bottom type for a variety of rough seafloor models represented by the stochastic distribution parameters $k\sigma$ and ka (Fig. 3). Sediment is represented by $v_p^s=1.52$ km/s, talus by $v_p^t=2.0$ km/sec and basalt by $v_p^b \geqslant 3.0$ km/s. The incident grazing angle is 15° and Fig. 3 summarizes the variation in calculated scattering coefficients in the 15° backscatter direction. In all of these models, the shear wave speed and density of the subseafloor are defined by linear relationships to compressional wave speed, and, therefore, plots of scattering coefficients relative to v_s or ρ would show the same variation. Two wavelengths of roughness are considered: $ka=1$ and $ka=6$ with correlation lengths of about $\lambda/6$ and λ, respectively. For rough seafloors with $k\sigma=2$, 4 and 6 (rms heights of approximately $\lambda/3$, $\lambda/1.5$, and λ) there is a strong increase in scattering strength between sediment and talus or basalt. Most of the increase, about 7 dB on average, occurs between 1.5 and 2 km/s. We attribute this to the fact that, at low sound speeds, energy passes through the interface into the seabed. Seabeds with thick sediment cover will produce less backscatter than seabeds consisting of talus or basalt. Although basalts are represented by a large range in sound speed (3 to 4 km/s) the scattering coefficients are remarkably uniform. Scattering coefficients for rough seafloors also increase on shortening the correlation from $ka=6$ to $ka=1$ and on increasing the rms height from $k\sigma=2$ to $k\sigma=6$. For smooth seafloors, with $k\sigma=1$ or 0.5 (rms heights of $\lambda/6$ and $\lambda/12$, respectively), the effects on scattering coefficients are more variable. The strongest backscattering coefficients occur at the low basalt sound speed (3 km/s) and the weakest occur for sediments.

It is important to reiterate that our results are only for the case of a source wavefield incident at the 15° grazing angle. In this case, our results suggest that variation in backscattering is not strongly influenced by variations in the average subseafloor sound speed and density, for $v_p>2$. However, a transition from a very soft bottom, such as deep sea pelagic ooze, to hard bottoms, e.g., compacted talus or basalt, will produce at least a 5-dB increase in backscatter intensity if the seafloor roughness remains constant. This is an example of the influence of large-scale variation in seabed propagation parameters. If roughness characteristics also change at a transition zone from a soft to hard bottom, the change in backscatter intensity can be very large, e.g., a transition from a sediment bottom with $ka=6$ and $k\sigma=1$ to a hard bottom with $ka=6$ but $k\sigma=6$ would produce a variation in backscatter of about 25 dB. However, from 7 to 12 dB of this variation can be attributed to the change in wavelength-scale seafloor characteristics.

V. VARIATION IN SEAFLOOR SLOPE

Much of the analysis of acoustic reverberation data has focused on the correspondence of strong backscattering to steeply sloping seafloor areas (e.g., Makris and Berkson, 1994; Preston *et al.*, 1990). In fact, in our own analysis of some monostatic reverberation data (Greaves and Stephen, 1997) we also found this correspondence but concluded that the intensity of the backscatter could not be unambiguously correlated to the seafloor slope since the sampling rate of the bathymetry data available to calculate seafloor slope was relatively coarse. Typical bathymetry data has a nominal lateral resolution of 200 m at mid-ocean water depths (Kleinrock, 1992) and can only be used to describe large-scale seafloor features. The wavelength of the insonifying field (6 m) is more than ten times smaller than the bathymetric resolution. However, large-scale bathymetric features do have an impact on the scattered signals because they change the local

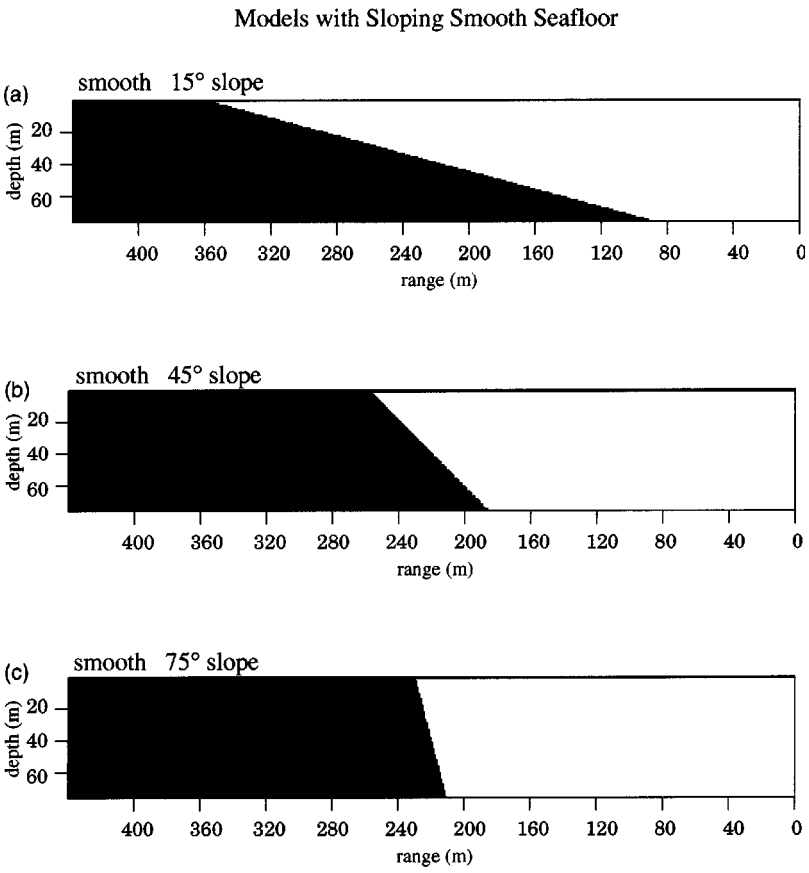

FIG. 4. Models with sloping smooth seafloor, where the slope is considered to be a large-scale feature, i.e., does not require sampling less than about ten wavelengths of the insonifying wavefield to be accurately represented. This slope influences the scattering from rough seafloor because it alters the effective grazing angle and apparent roughness of the surface. To quantify this effect, scattering from models with slopes from 0° to 75° are compared. In this figure three sloping models with smooth surfaces are shown. In each case the models are centered in the NSC in order to have the same portion of the Gaussian beam interacting with the surface. Note that the finite grid spacing adds a certain amount of "microroughness" to any model, except at 0°. Model (c), sloping 75°, represents a surface normal to the 15° incident beam.

grazing angle of the incident wavefield. In this section we analyze and quantify the influence of seafloor slope on the backscattered signal.

A. Smooth sloping seafloor

Figure 4 shows a series of smooth-seafloor models with different slope. In each model, the middle of the sloping portion is centered within the NSC grid space. In all cases, the subseafloor was defined as basalt with $v_p^b = 4.0$ km/s, $v_s^b = 2.0$ km/s and $\rho^b = 2500$ kg/m^3. As the wavefield snapshots in Fig. 5 show, the only scattering observed for these models is due to the inherent microroughness of the grid itself and the corner diffractions emanating from the terminations of the models within the model space. Both of these sources of scattering are artifacts of the finite difference modeling. The scattering from the microroughness can be considered a background "noise" level from geologically reasonable small-scale roughness (Dougherty and Stephen, 1991). Estimates of the roughness parameters attributable to this microroughness in our models are $ka = 1.5$ and $k\sigma = 0.4$ for a 15° slope and $ka = 0.57$ and $k\sigma = 0.28$ for a 45° slope. The wave types expected for a flat seafloor are the incident and reflected waves, the direct wave root, and the transmitted compressional and shear body waves. The scattering coefficients for a complete set of smooth, dipping models are shown in Fig. 6. For each model, the scattering function is dominated by a peak in the specular reflection direction. The amplitude of each peak is a function of the reflection coefficient which varies as a function of angle of incidence. Strong backscatter, well above the background level, in the source direction only occurs when the seafloor slope is 75°, i.e., is normal to the 15° incident beam.

B. Rough sloping seafloor

The sloping-seafloor models with wavelength-scale roughness shown in Fig. 7 were generated by rotating the horizontal, Gaussian-seafloor model in Fig. 7(a) to the desired slopes. Given that the horizontal model is described by $ka = 6$ and $k\sigma = 4$, these are the nominal descriptions for the dipping models also. However, a difficulty with modeling dipping interfaces in a finite model space is that it is not possible to present exactly the same surface to the incident wavefield, because the length of the actual dipping surface included in the model space varies with the dip. Also, the footprint of the incident beam varies with the dip of the seafloor (Stephen, 2000). In order to minimize this problem, we have rotated the original horizontal, rough-seafloor model about the center of the grid space, such that at least the most central portion of each sloping rough model contains the same surface and interacts with the most central portion of the incident beam. For a more accurate description of the rough surface presented in each of these dipping models, the actual values of ka and $k\sigma$ for each case are determined from the autocorrelations of the interface with large-scale dip removed. The roughness parameters calculated after the large-scale dip is removed are listed at the top of each frame in Fig. 7. The differences between $k\sigma$ of the original rough surface [Fig. 7(a)] and the dipping surfaces is less than about

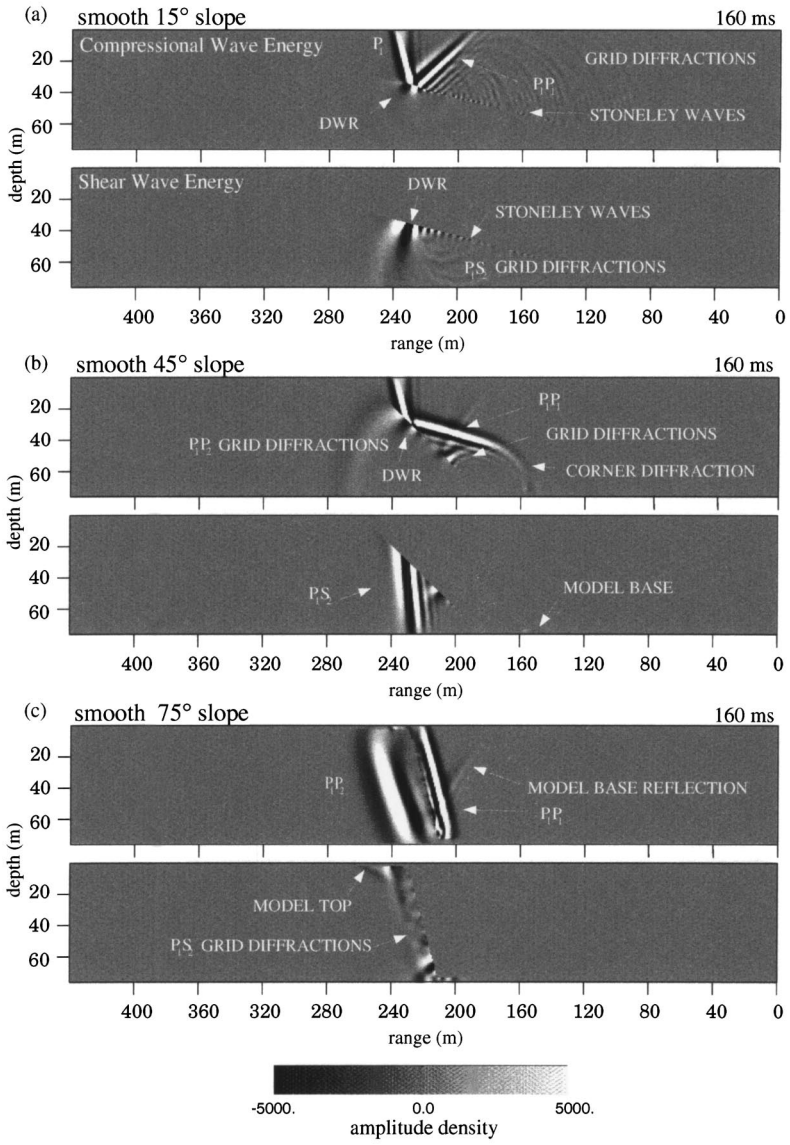

FIG. 5. The dominant waveforms in these snapshots of wavefield amplitude density are the surface reflections (P_1P_1). When the true grazing angle $\theta_g = \theta_{\text{beam}} + \theta_{\text{slope}} > \theta_c$, transmitted compressional and shear wave body waves are also observed. For these models $\theta_c^P = 68°$ and $\theta_c^S = 41°$. In (a) $\theta_g = 30°$ and no P-wave or S-wave transmission is observed. The direct wave root is present, as are low level diffractions due to the grid microroughness (referred to as grid diffractions in the figure). In (b), $\theta_g = 60°$ such that transmission of converted S-wave energy occurs. Scattering from the microroughness also generates some P-wave energy in this case and yet the direct wave root still exists because the grazing angle would be subcritical for P-waves at a flat seafloor. In (c), $\theta_g = 90°$ and the P-wave is reflected directly back in the source direction as well as being transmitted. Note that shear wave energy in (c) is due to scattering from the microroughness into the subseafloor. Note that there are some wavefield artifacts, such as the corner diffractions and the reflection from the model base at the toe of each model.

10%. The difference in *ka* is larger, up to about 20%. However, these differences are not so large that the results of the numerical modeling cannot be compared.

Comparison of the wavefield snapshots in Fig. 8 to the cases without surface roughness, Fig. 5, clearly shows that the addition of the wavelength-scale roughness causes the simple interface reflection to be destroyed by interference. Also, a much higher proportion of energy is passed (scattered) into the subseafloor. Comparison of scattering coefficients, Fig. 9(a), shows that in all models the addition of dip increases the average scattering in backward directions in comparison to the same surface with no dip. Note that the peaks associated with the reflected wave have been essentially eliminated by the interference effects of scattering from the rough surface but that relative to a smooth flat seafloor the scattering intensity from the rough sloping seafloor is as much as 40 dB higher. Figure 9(b) compares scattering coefficients in the 15° backscatter direction (including several model realizations, i.e., different realizations of the surface roughness, for each case). It is remarkable that the variation in scattering coefficient decreases substantially for slopes greater than 15°, including the case of normal incidence (75° slope).

C. Intensity versus effective grazing angle

As a means of quantifying backscatter intensity in terms of a single seafloor descriptor that includes information about both the large-scale slope and the seafloor roughness, we have derived a term that we call the effective grazing-angle.

The true grazing angle includes the grazing angle of the incident beam relative to the horizontal, θ_b, and the large-scale slope, θ_s.

$$\theta_g^{\text{true}} = \theta_b + \theta_s . \tag{5.1}$$

At this point, we take a somewhat phenomenological step in our analysis in order to incorporate some measure of the seafloor roughness parameters in the definition of the grazing angle. This is purely an attempt to include the geo-

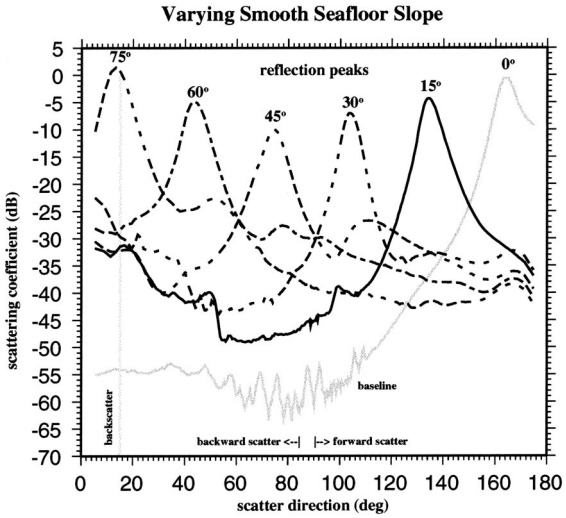

FIG. 6. The scattering coefficient functions for sloping smooth seafloor are dominated by the reflected signal. The angles labeling each function refer to the slope of each surface modeled. The variation in the amplitude of the reflection peaks is due to dependence of the reflection coefficient on the angle of incidence. The microroughness produces a signal that in the backscatter direction is about 20 dB above the signal from a baseline model having no slope.

logically significant wavelength-scale seafloor features in the interpretation of the backscatter data, and it is not based on wave propagation theory. Although there is no precedent for doing so, we add to the grazing angle an estimate of average (rms) slope (magnitude) of the interface roughness. For a seafloor defined by a stochastic Gaussian distribution, an rms slope, θ^s_{rms}, is defined by

$$\theta^s_{\mathrm{rms}} = \tan^{-1}\left(\sqrt{2}\,\frac{\sigma}{a}\right) \tag{5.2}$$

(Broschat and Thorsos, 1997). This rms slope can be attributed to either the forward or backward direction relative to the incident wavefield [i.e., $\pm\tan^{-1}(\sqrt{2}\sigma/a)$], but we have used it only in the sense of the backward (i.e., beam facing) direction. An effective grazing angle, defined here as θ_g^{eff}, is then estimated as

$$\theta_g^{\mathrm{eff}} \approx \theta_b + \theta_s + \theta^s_{\mathrm{rms}}. \tag{5.3}$$

For the horizontal, rough-seafloor model discussed above, with nominal correlation length ($ka=6$) and rms height ($k\sigma=4$), the rms slope is $\theta^s_{\mathrm{rms}}=43°$. For the same seafloor incorporated into the sloping-seafloor models, the

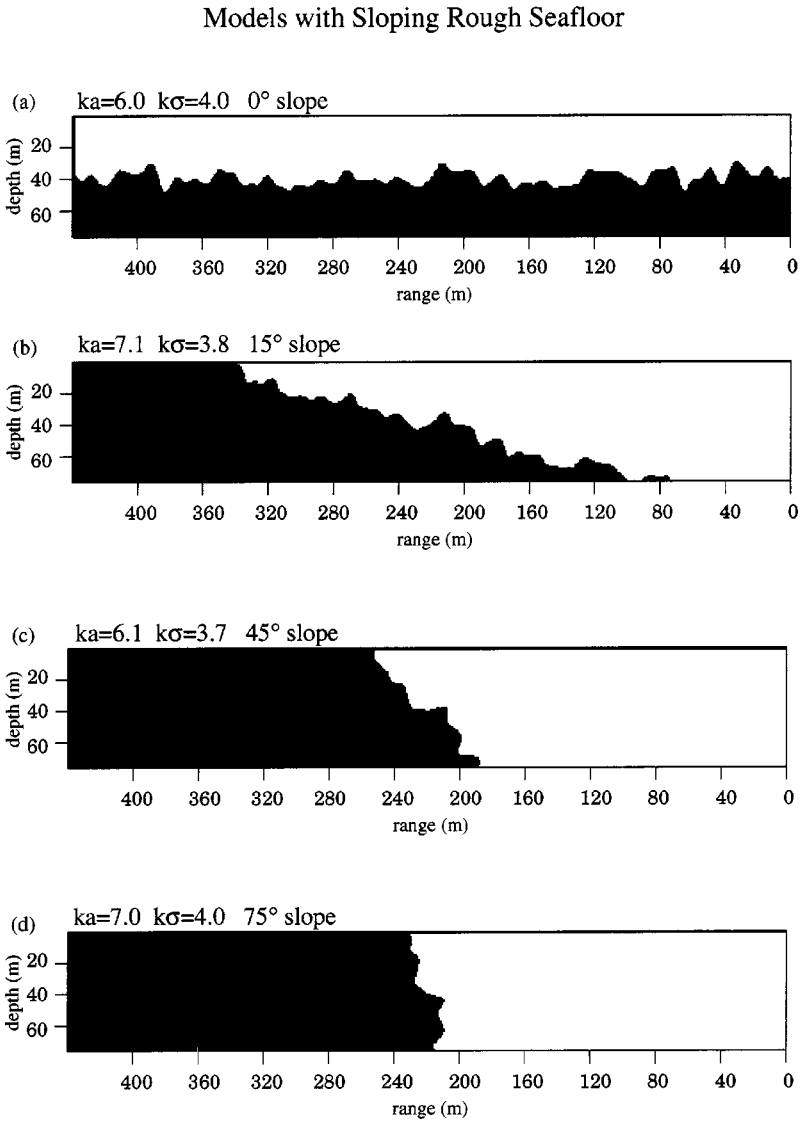

FIG. 7. A series of models with sloping rough seafloor were generated by rotating the Gaussian model in (a) to different large-scale slopes. The figure shows the sloping rough surfaces at (b) 15°, (c) 45°, and (d) 75°. Making a comparison of sloping seafloors with added roughness is difficult in a limited model chamber. Because the seafloor is truncated differently depending on angle, it is necessary to present different surfaces to the incident wavefield. To some extent this is minimized as the central portion of the rough model is always used. The roughness parameters of the original rough surface (a) are $ka=6$ and $k\sigma=4$. The roughness parameters of the portions remaining in the model after rotation have been recomputed with the slope removed and are (b) $ka=7.1$ and $k\sigma=3.8$, (c) $ka=6.1$ and $k\sigma=3.7$, and (d) $ka=7.0$ and $k\sigma=4.0$, corresponding to the rotated surfaces at 15°, 45°, and 75°, respectively.

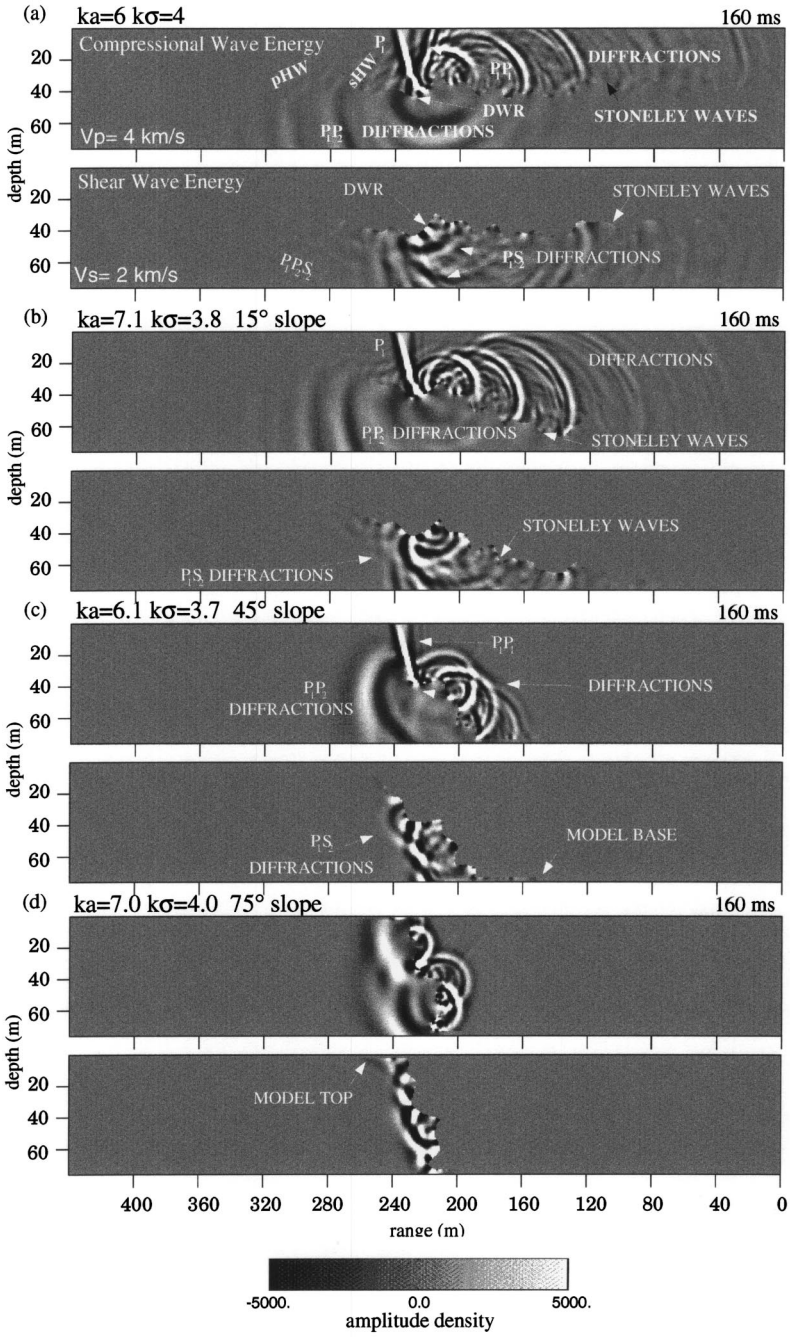

FIG. 8. As the slope of the rough surface increases, the true grazing angle of the incident wavefield increases, which according to the definition of Rayleigh roughness would increase the apparent roughness and consequently produce an increase in scattering. In the snapshots shown here, increasing the large-scale slope does not produce a consistent, nor strong, increase in scattered energy with increasing slope.

recalculated correlation lengths and rms height vary somewhat, such that the rms slope differs for each model slope and realization. The calculated rms slope for each model realization is plotted in Fig. 10(a) as a function of the large-scale slope. The average rms-slope is close to that of the horizontal model (43° in all cases), but, for any particular model realization, can deviate by as much as 5°. In Fig. 10(b), the scattering coefficients for all of the rough dipping models are plotted as a function of the effective grazing angle calculated for each model realization, as well as the true grazing angle. This new parameter does not change the fact that backscattering is much less sensitive to changes in large-scale slope above about 15° (corresponding to $\theta_g^{\text{eff}} \approx 70°$). Below this the scattering coefficients increase with θ_g^{eff} at a rate of about 0.5 dB/deg, but above $\theta_g^{\text{eff}} \approx 70°$ the rate decreases to about 0.2 dB/deg. As will be seen in the following discussion, the real value of combining the seafloor and incident wavefield characteristics to this effective grazing angle is that it leads to an important conclusion about the significance of the change in sensitivity observed in these modeling results.

VI. DISCUSSION

The numerical modeling has shown that large-scale seafloor features do influence the intensity of the scattered wavefield. However, the variation in the intensity corresponding to variation in the large-scale features is more of a bi-modal function of either velocity contrast or large-scale seafloor dip. In the following discussion we attempt to ex-

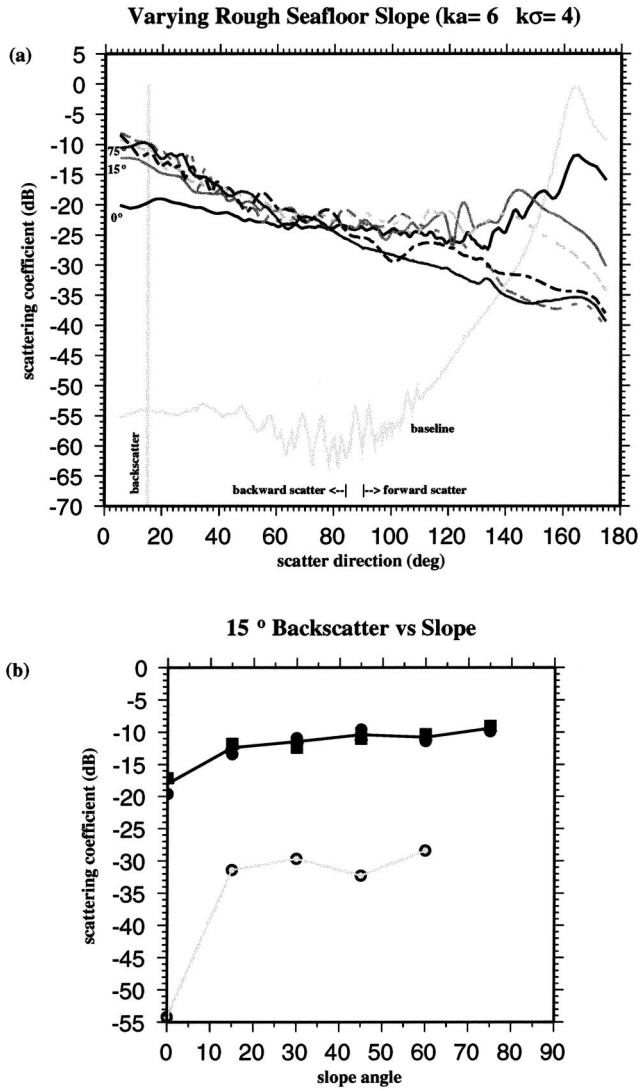

FIG. 9. (a) Scattering coefficients for sloping rough seafloor all have about the same response in the backscatter direction. This suggests that the scattering is not very sensitive to changes in average seafloor slope, at least above 15°. Only a single realization for each model has been plotted for each slope: 0° (solid black), 15° (solid gray), 30° (short gray dash), 45° (long gray dash), 60° (black dots), and 75° (solid dark gray). (b) This is clearly seen when the scattering coefficients in the 15° backscatter direction are plotted as a function of slope angle from 0° to 90°. The net increase in backscatter is about 10 dB, but almost half of this increase occurs in the change from 0° to 15° slope. The line connects the average response from three realizations of each model. In general, the backscatter from these sloping rough models ($ka=6$ and $k\sigma=4$) is about 20 dB greater than the backscattered signal of corresponding smooth (microrough) sloping seafloor models (gray circles), and are all more than 40 dB above the signal from the backscatter intensity of the baseline (flat and smooth) model.

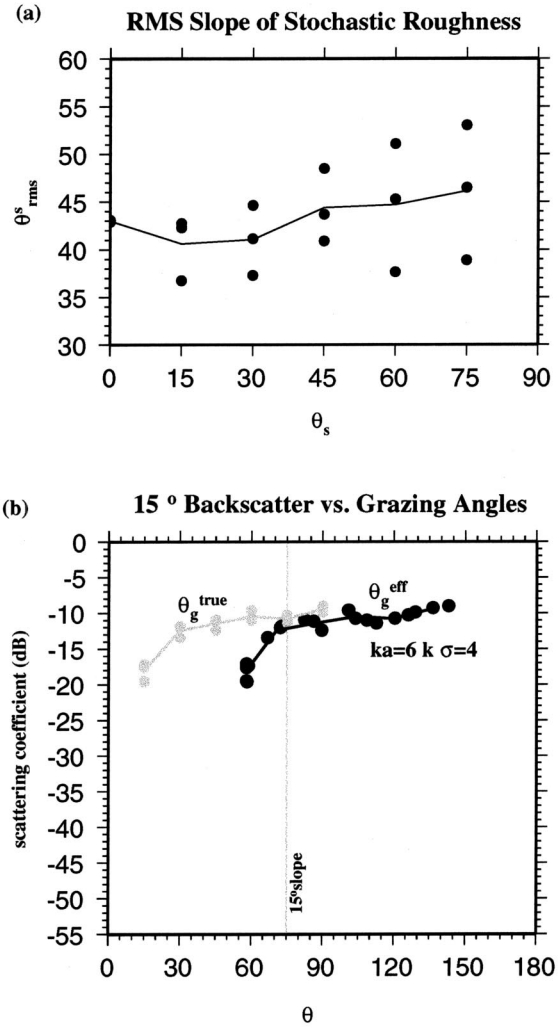

FIG. 10. An ''effective grazing angle,'' θ_g^{eff}, incorporates all seafloor structural parameters and is defined (see text) as $\theta_g^{\mathrm{eff}} \approx \theta_b + \theta_s + \theta_{\mathrm{rms}}^s = \theta_g^{\mathrm{true}} + \theta_{\mathrm{rms}}^s$. The rms slope of a Gaussian rough surface, θ_{rms}^s, is defined as $\theta_{\mathrm{rms}}^s = \tan^{-1}(\sqrt{2}\sigma/a)$. (a) For a horizontal, rough-seafloor model, where $ka=6$ and $k\sigma=4$, $\theta_{\mathrm{rms}}^s = 43°$. The actual rms grazing angle in the sloping, rough-seafloor models differs somewhat from this because of their variation in ka. The actual θ_{rms}^s calculated for each model is plotted in this figure. The solid line is the average value calculated at each large-scale slope angle, θ_s. (b) When θ_g^{eff} is computed for each of the sloping, rough-seafloor models, the scattering coefficients are more widely distributed than when plotted relative to θ_g^{true}. This plot shows that the sensitivity to increasing slope is reduced above $\theta_g^{\mathrm{eff}} \approx 73°$, which corresponds to models with seafloor slope of 15°. This suggests that changes in average seafloor slope in the range of 0° to 15° will produce a larger change in backscattered signals than the same slope variation above 15°. Further, seafloor slope modifies the backscatter signal by a maximum of about 10 dB, if roughness is constant.

plain what the influence of large-scale features can be attributed to and why the influence appears to act in this two-scale manner.

As shown in Fig. 3, a very low-speed and low-density subseafloor produces a backscatter signal that is about 3–6 dB down for $ka=1$ and 6–12 dB down for $ka=6$, relative to the signal from the same seabed with high propagation speed and density. The explanation for this is that as the propagation speed and density of the subseafloor become closer in magnitude to the values for the overlying water layer, the soft-bottom seafloor becomes more transparent to the incident wavefield. Energy passed into the subseafloor reduces the energy available for seafloor scattering. If the seafloor were not rough, the explanation would be described in terms of the critical grazing angles being less than the incident wavefield grazing angle for the soft-bottom seafloor.

Variation in the relatively high sound speed and density of hard bottoms does not produce strong corresponding variations in backscatter intensity. The explanation for this is that once the velocity and density contrast at the seafloor is strong enough to not allow much penetration through the seafloor interface by the incident wavefield, further increases

in this contrast will not change the resulting scattered field. Again, if the seafloor were not rough, this would be explained as the critical grazing angle being greater than the incident wavefield grazing angle. So, in a sense, the seabed sound speed influences the scattered field by acting as a pass/no-pass gate to incident wavefield energy. For a given incident wavefield and seafloor shape, the energy available for scattering from the surface will be constant until the wavefield insonifies a region where the propagation velocity contrast at the seafloor is sufficiently low that it becomes somewhat transparent to the incident wavefield, or in terms of a flat seafloor, that the critical grazing angle is reduced below the incident angle. Energy that does reach the subseafloor is subsequently lost to multiple scattering mechanisms at internal interfaces.

The effect of large-scale seafloor slope on backscattering is similar to that of sound speed in that it has two distinct sensitivity regions. In our modeling the transition in large-scale slope from 0° up to 15° produced an increase in backscatter intensity of about 6 dB as shown in Fig. 9(b). The transition from 15° to 75° slope only increased the intensity by another 3 dB, suggesting that the backscatter intensity is only weakly modified by changes in slope above the 15° transition point. In order to gain some understanding of how the large-scale slope influences the seafloor scattering we first consider its effect on seafloor roughness. One characterization of surface roughness is the Rayleigh roughness parameter, R_a, defined as

$$R_a = k\sigma \sin \theta_g \tag{6.1}$$

(Ogilvy, 1991). To include seafloor slope we would set $\theta_g = \theta_g^{\text{true}}$. Clearly, for a rough seafloor characterized by $k\sigma$, the Rayleigh roughness parameter increases as slope (and therefore θ_g^{true}) increases. This explains the fact that backscatter intensity increases with slope in our model results but does not explain the dramatic decrease in the rate of change above 15°.

In order to explain weakening of the sensitivity of the backscattered signal for the models with slope greater than 15° we again consider the effect of the velocity contrast at the seafloor interface, i.e., the critical grazing angle for a nonrough seafloor. For the sloping seafloor models the same hard-bottom properties of a basalt were used in each case. The shear wave and compressional wave critical grazing angles, given these parameters and a flat seafloor, would be 41° and 68°, respectively. A wavefield incident at a grazing angle above 68° would therefore be expected to pass compressional and shear energy into the subseafloor. If we consider the cross-plot of backscatter intensity and effective grazing-angle in Fig. 10(b) we see that the corner in the sensitivity curve, corresponding to models with seafloor slope of 15°, occurs at about $\theta_g^{\text{eff}} = 70°$. This strongly suggests that for seafloor slope above 15° a significant portion of the incident wavefield energy is passing into the subseafloor rather than being scattered at the seafloor and that this passage of energy increases with increasing slope. Also, the fact that the same effect is observed in the results for the smooth sloping seafloor [Fig. 9(b)], which has only microroughness, implies that this transition point is not very sensitive to the magnitude of the roughness. The microroughness parameters for the 15° smooth slope yield an effective grazing angle of about 51° and at 45° yield an effective grazing angle of about 100°. The 51° effective grazing angle is above the critical grazing angle of shear waves and the effective grazing angle of 100° is well above both the shear and compressional wave critical grazing angles for flat seafloors with these sound speed characteristics. So even for the ''smooth'' sloping seafloor wavefield energy will be passed into the subseafloor.

VII. CONCLUSION

In summary, variations in large-scale seafloor slope and average subseafloor sound speed can account for a net variation in the backscatter intensity of up to about 20 dB. If we include variations in surface roughness it is possible to observe variations greater than 40 dB. For example, a flat low-speed (1.5 km/s) seafloor with roughness parameters $ka = 6$ and $k\sigma = 0.5$ [Fig. 3(b)] has a backscatter intensity that is about 40 dB down relative to a high-speed seafloor (4 km/s) with roughness parameters $ka = 6$ and $k\sigma = 4$ and slope of 15° [Fig. 9(b)]. Such a change in seabed characteristics is not unusual since it is a good description of the transition from a sediment pond to the flank of a seafloor ridge.

When using such information for interpretation of backscatter intensity data it is important to remember that the large-scale features themselves do not cause the incident wavefield to scatter but rather change the apparent roughness characteristics of the seafloor, in some cases, and in other cases the apparent grazing angle of the wavefield. The controlling factor is the velocity contrast between the water column and the subseafloor material, which in terms of a seafloor with no roughness would be the critical grazing angle. For a seafloor with constant roughness and slope characteristics and a constant incident wavefield grazing angle, the backscattered signal will decline by at least 6 dB when a transition from hard bottom to soft bottom is encountered because energy is always able to pass into the subseafloor. Again, this is equivalent, for a flat seafloor, to the critical grazing angle of the soft bottom always being exceeded by the incident wavefield grazing angle. When the wavefield is incident on a seafloor with constant roughness and a hard-bottom sound speed but variable slope, fluctuations of up to 10 dB can be expected in the backscatter intensity as the slope varies.

ACKNOWLEDGMENTS

This work was funded by the Office of Naval Research under Grant Nos. N00014-93-1-1352, N00014-90-J-1493, N00014-95-1-0506, and N00014-96-10460. This paper is WHOI Contribution No. 10447. The authors would like to thank the Earthquake Research Institute at the University of Tokyo for a Visiting Professorship (for RAS) during which some work on this manuscript was completed.

Aki, K. (**1982**). ''Scattering and attenuation,'' Bull. Seismol. Soc. Am. **72**(6), S319–S330.

Aki, A., and Richards, P. G. (**1980**). *Quantitative Seismology, Theory and Method* (W. H. Freeman and Co., New York), Vol. 2.

Baggeroer, A. B., and Dyer, I. (**1986**). ''Long range, low frequency acoustic backscattering: a review,'' in *Ocean Seismo-Acoustics, Low-frequency Underwater Acoustics*, edited by T. Akal and J. M. Berkson (Plenum, New York), pp. 313–326.

Broschat, S. L., and Thorsos, E. I. (**1997**). ''An investigation of the small slope approximation for scattering from rough surface. Part II. Numerical studies,'' J. Acoust. Soc. Am. **101**, 2615–2625.

Butler, R. (**1988**). ''Shear wave properties of marine sediments derived from cepstral analysis of background noise,'' Geophys. Res. Lett. **8**, 836–839.

Chia, C. S., Makris, N. C., and Fialkowski, L. T. (**2000**). ''A comparison of bistatic scattering from two geologically distinct abyssal hills,'' J. Acoust. Soc. Am. **108**, 2053–2070.

Dougherty, M. E., and Stephen, R. A. (**1988**). ''Seismic energy partitioning and scattering in laterally heterogeneous ocean crust,'' Pure Appl. Geophys. **128**(1/2), 195–229.

Dougherty, M. E., and Stephen, R. A. (**1991**). ''Seismo/acoustic propagation through rough seafloors,'' J. Acoust. Soc. Am. **90**, 2637–2651.

Dyer, I., Baggeroer, A. B., Schmidt, H., and Fricke, J. R. (**1993**). ''Discrete backscatter can be dominant in rough bottom reverberation,'' in *Ocean Reverberation*, edited by D. D. Ellis, J. R. Preston, and H. G. Urban (Kluwer Academic, Dordrecht), pp. 51–57.

Gerstoft, P., and Schmidt, H. (**1991**). ''A boundary element approach to ocean seismoacoustic facet reverberation,'' J. Acoust. Soc. Am. **89**, 1629–1642.

Godin, O. A., and Chapman, D. M. F. (**1999**). ''Shear-speed gradients and ocean seismo-acoustic noise resonances,'' J. Acoust. Soc. Am. **106**, 2367–2382.

Greaves, R. J. (**1998**). ''Seismic scattering of low-grazing-angle acoustic waves incident on the seafloor,'' Ph.D. thesis, Massachusetts Institute of Technology/Woods Hole Oceanographic Institution.

Greaves, R. J., and Stephen, R. A. (**1997**). ''Seafloor acoustic backscattering from different geological provinces in the Atlantic Natural Laboratory,'' J. Acoust. Soc. Am. **101**, 193–208.

Greaves, R. J., and Stephen, R. A. (**2000**). ''Low-grazing-angle monostatic acoustic reverberation from rough and heterogeneous seafloors,'' J. Acoust. Soc. Am. **108**, 1013–1025.

Hamilton, E. L. (**1971**). ''Elastic properties of marine sediments,'' J. Geophys. Res. **76**(2), 579–604.

Harding, A. J., Hedlin, M. A. H., and Orcutt, J. A. (**1998**). ''Migration of backscatter data from the Mid-Atlantic Ridge,'' J. Acoust. Soc. Am. **103**, 1787–1803.

Jackson, D. R., Winebrenner, D. P., and Ishimaru, A. (**1988**). ''Comparison of perturbation theories for rough-surface scattering,'' J. Acoust. Soc. Am. **83**, 961–969.

Kelly, K. R., Ward, R. W., Treitel, S., and Alford, R. M. (**1976**). ''Synthetic seismograms: A finite-difference approach,'' Geophysics **41**(1), 2–27.

Kleinrock, M. C. (**1992**). ''Capabilities of some systems used to survey the deep-sea floor,'' in *CRC Handbook of Geophysical Exploration at Sea, Hard Mineral*, 2nd ed., edited by R. A. Geyer (CRC, Boca Raton, FL), pp. 35–85.

Makris, N. C., and Berkson, J. M. (**1994**). ''Long-range backscatter from the Mid-Atlantic Ridge,'' J. Acoust. Soc. Am. **95**, 1865–1881.

Makris, N. C., and Ratilal, P. (**2001**). ''A unified model for reverberation and submerged object scattering in a stratified ocean waveguide,'' J. Acoust. Soc. Am. **109**, 909–941.

Makris, N. C., Avelino, L. Z., and Menis, R. (**1995**). ''Deterministic reverberation from ocean ridges,'' J. Acoust. Soc. Am. **97**, 3547–3574.

Makris, N. C., Chia, C. S., and Fialkowski, L. T. (**1999**). ''The bi-azimuthal scattering distribution of an abyssal hill,'' J. Acoust. Soc. Am. **106**, 2491–2512.

Ogilvy, J. A. (**1991**). *Theory of Wave Scattering from Random Rough Surfaces* (Institute of Physics, Bristol, Great Britain).

Preston, J. R., Akal, T., and Berkson, J. (**1990**). ''Analysis of backscattering data in the Tyrrhenian Sea,'' J. Acoust. Soc. Am. **87**, 119–134.

Shearer, P. M. (**1988**). ''Cracked media, Poisson's ratio and the structure of the upper oceanic crust,'' Geophys. J. **92**, 357–362.

Smith, K. B., Hodgkiss, W. S., and Tappert, F. D. (**1996**). ''Propagation and analysis issues in the prediction of long-range reverberation,'' J. Acoust. Soc. Am. **99**, 1387–1404.

Stephen, R. A. (**2000**). ''Optimum and standard beam widths for numerical modeling of interface scattering problems,'' J. Acoust. Soc. Am. **107**, 1095–1102.

Stephen, R. A., and Swift, S. A. (**1994**). ''Modeling seafloor geoacoustic interaction with a numerical scattering chamber,'' J. Acoust. Soc. Am. **96**, 973–990.

Swift, S. A., and Stephen, R. A. (**1994**). ''The scattering of a low-angle pulse beam from seafloor volume heterogeneities,'' J. Acoust. Soc. Am. **96**, 991–1001.

Thorsos, E. I. (**1988**). ''The validity of the Kirchhoff approximation for rough surface scattering using a Gaussian roughness spectrum,'' J. Acoust. Soc. Am. **83**, 78–92.

Virieux, J. (**1986**). ''P-SV wave propagation in heterogeneous media: Velocity-stress finite-difference method,'' Geophysics **51**(4), 889–901.

Microseism and infrasound generation by cyclones

Samuel P. Bowen and Jacques C. Richard
Chicago State University, Chicago, Illinois 60628

Jay D. Mancini, Vassilios Fessatidis, and Benjamin Crooker
Fordham University, Bronx, New York 10458

(Received 3 July 2001; revised 12 February 2003; accepted 19 February 2003)

A two-dimensional cylindrical shear-flow wave theory for the generation of microseisms and infrasound by hurricanes and cyclones is developed as a linearized theory paralleling the seminal work by Longuet-Higgins which was limited to one-dimensional plane waves. Both theories are based on Bernoulli's principle. A little appreciated consequence of the Bernoulli principle is that surface gravity waves induce a time dependent pressure on the sea floor through a vertical column of water. A significant difference exists between microseisms detected at the bottom of each column and seismic signals radiated into the crust through coherence over a region of the sea floor. The dominant measured frequency of radiated microseisms is matched by this new theory for seismic data gathered at the Fordham Seismic Station both for a hurricane and a mid-latitude cyclone in 1998. Implications for Bernoulli's principle and this cylindrical stress flow theory on observations in the literature are also discussed. © *2003 Acoustical Society of America.*
[DOI: 10.1121/1.1567277]

PACS numbers: 43.30.Nb, 43.28.Dm, 43.28.Hr, 43.40.Ph [SAC-B]

I. INTRODUCTION

The phenomena of storm-generated microseisms, the low frequency and low intensity seismic signals recorded on land-based seismometers that are associated with storms moving across water, has been observed by many scientists over the years. A very thorough review of such ''radiated'' microseisms and the related infrasound effects has been written by Tabulevich[1] and contains qualitative data that offers insights into the causes of microseisms. Through many years of observations, Tabulevich and colleagues observed that microseisms were closely associated with moving cyclones passing over water and that the cyclonic nature of the storm was essential, there being no significant microseisms associated with linear wave fronts. She conducted triangulation studies to locate the sources of microseisms and identified specific storms as had others. For example, as early as 1940, Ramirez[2] used three seismographs to triangulate cyclones using microseismic signals. More recently, other observers[3] using arrays of seismometers have closely associated microseisms with strong cyclonic storms at sea.

The study reported in this paper was carried out to collect detailed data on large cyclones, both hurricanes and mid-latitude cyclones, in order to test various theories predicting the dominant microseism frequency and other properties of the observed ''radiated'' microseisms as detected by land-based seismometers. While developing the new theory it became clear that certain distinctions between radiated microseisms and sea floor detected microseisms needed to be clarified. While the cyclone data and theory are the main focus of this paper, some attention will be paid to these distinctions.

The foundational theoretical study of the radiation of microseisms from the sea floor to land-based seismometers was carried out by Longuet-Higgins[4] (LH), who used Bernoulli's principle, linearized hydrodynamic equations and one-dimensional plane waves moving across the surface of the water to explore possible mechanisms by which microseisms could be generated. One of the first important questions that LH addressed was the apparent contradiction between the fact that surface gravity waves are restricted to a narrow region near the surface and the evidence that pressures at the sea floor are an essential part of microseism generation. How could waves restricted to the surface have an impact on the sea floor pressures? There are essentially two different mechanisms that resolve this apparent contradiction. The first mechanism is the application of the Bernoulli principle to each vertical column of water connecting the surface to the sea floor. Bernoulli's principle states that the sum of the pressure, the kinetic energy per unit volume, and the potential energy per unit volume must have the same value at all points in the column, even if any of these variables are varying in time. The immediate consequence of this is that the pressure time dependence at the base of a column of water is determined by the time dependence of the surface gravity waves at the top of the column, and this effect is independent of the depth. The second mechanism,[5] to be discussed below, is the generation of acoustic waves through the nonlinear interaction of surface gravity waves. The resulting acoustic waves are not damped with depth and their propagation down to the sea floor provides a generation mechanism for microseisms.

LH's most often quoted result is the observation that a standing wave is the only one-dimensional plane wave structure which can generate radiated microseisms. In most of the literature, it has not been widely appreciated that this part of LH's analysis applies only to the radiation of seismic signals through the earth's crust to distant seismographs. As is discussed below, Bernoulli's principle alone is adequate to generate microseisms detected at a fixed sea bottom location. Also the generation of a seismic signal radiating into the

 0001-4966/2003/113(5)/2562/12/$19.00

crust and scaling with the size of the storm requires a wave with spatial coherence and persistence.

LH also observed that Bernoulli's principle implies that the kinetic energy of the surface wave gives rise to pressure fluctuations on the sea floor, which will be observed at twice the frequency of the surface wave. This $2f$ signal is a direct consequence of Bernoulli's principle and expresses a nonlinearity in the sense that the square of the velocity in the kinetic energy produces the effect on the pressure. The $2f$ signal is not exclusively a sign that nonlinear interactions between surface gravity waves are involved in the production of that signal.

In contrast to the studies by Tabulevich which are interpreted exclusively through Bernoulli's principle, a prominent school of thought has focused on the generation of acoustic waves by nonlinear interactions between surface gravity waves. From this perspective, microseisms are caused by the acoustic waves which are not damped with depth under the surface. The chief proponent of this effect has been Kibblewhite who has developed mechanisms for producing these acoustic waves in great detail.[6] The initial motivation for the consideration of these nonlinear effects was a hydrophone study by Nichols,[7] who concluded that nonlinear mechanisms must be involved since the $2f$ peak was so prominent. It is worth noting that Nichols included LH's work as part of this nonlinear theory and did not definitively distinguish between the two generation mechanisms listed above. Kibblewhite and colleagues[6] have worked out a number of details of the generation and consequences of acoustic waves generating microseisms. The dominant gravity waves that are assumed to be involved in microseism generation are pairs of waves moving in almost opposite directions.

The decisive researcher in this school has been Webb, who has conducted a number of exceptionally well-crafted experiments with carefully gathered data to probe the fine structure of a wide variety of theories. He collected sea-floor microseism data[8] at several depths and sites in the Pacific. Much of this data represented the microseisms generated by the ''equilibrium'' wave distribution above the detector, but some interesting data was collected for what appears to be a mid-latitude cyclone which passed near the site. He also collected fascinating data on microseisms under the frozen ice pack in the Beaufort Sea.[9] This very quiet data offers further data to distinguish between competing theories. Finally, he explored the interesting idea of the ''climatology'' [10] of bottom detected microseisms by seeking to predict the microseism spectrum from the wave height distribution associated with the surface. While these data are not central to the present work, a brief discussion of several of these measurements from the point of view of the Bernoulli principle is presented at the end of this paper.

The Longuet-Higgins conclusion about standing waves has been part of the guiding foundation for experiments on microseisms over the years since his paper. Because a standing wave can be obtained from the linear combination of two oppositely traveling waves with equal amplitudes, several observers sought to find standing waves caused by reflections from shore emplacements, harbors, and partially enclosed bodies of water. The equality of amplitudes is essential for the formation of a standing wave. In few of these cases was consideration made of the possible change in amplitude from various reflections considered. Tabulevich among others attempted to have the wind waves ahead of a moving cyclone and those which follow the storm, and move in opposite directions, combining to form standing waves, even when these two winds were not present at the same point at the same time. Other discussions have associated standing waves with wind direction changes and cross winds.[8] Detailed measurements by Kibblewhite and Ewans[11] at the Maui Development site were also interpreted as being caused by waves running into a recently changing wind and thus possibly encountering oppositely moving waves of similar amplitude. In general, searches for one dimensional, plane, standing waves as a cause of microseisms have been inferential, that is, mostly without direct observations. Careful, well-instrumented shallow ocean bottom observations[12] found no evidence of standing waves, or even significant reflected waves from nearby shores. On the other hand, several studies with under water pressure detectors and seismometers observed microseisms in the presence of swell[13] from far away storms and shore, wind,[8] and what would be expected to be predominantly traveling waves.

This paper is presented in the conviction that all of the consequences of the linear theory based on Bernoulli's principle need to be more deeply examined, and that there exists a wave form, other than one-dimensional, plane standing waves, not considered by LH, that can give rise to microseisms. In particular, cylindrical waves on the two-dimensional air–fluid interface around the center of a cyclone can also generate microseisms and rationalize much of the existing data in the literature. The role of the wind and the cyclonic nature of the storms associated with microseisms is explored below.

In the following sections, the LH study for one-dimensional plane waves on the surface and its relationship to microseism development is reviewed. Emphasis will be given to the difference between stationary bottom measurements and extensive coherent area sources for radiated microseisms. Briefly discussed are two different approaches to microseism generation which parallel the wind generation of water waves,[14] namely, the resonance theory of Phillips[15] and the shear flow theory of Miles.[16] A resonance theory of microseism generation is found to agree with the LH traveling wave null results in the absence of viscosity, but does predict a double frequency peak whose amplitude is probably too small to be observed in land-based seismometers. A two-dimensional theory, the cyclonic shear flow theory, is developed that exhibits double frequency peaks in the microseism spectra, the frequency of which depends on the cylindrical velocity structure of the atmospheric storm and the associated flow in the water. This theory will be applied to two different kinds of cyclonic storms: tropical hurricanes which are represented by a vortex line with an eye wall, centered on the storm, and mid-latitude cyclones which have almost circular isobars and a constant radial pressure gradient about their center. This shear flow theory is compared to land-based seismic measurements of two different storms in 1998: a Nor'easter in January and Hurricane Bonnie in Au-

gust. Good success is achieved in predicting the frequency of the double frequency peak from first principles and several other features of Bonnie. In the last section, consequences of these ideas are applied to observations of Tabulevich, Kibblewhite, and Ewans, and climatology of microseisms, and sea-floor spectral measurements of Webb.

II. REVIEW OF GOVERNING EQUATIONS FOR INCOMPRESSIBLE FLUIDS

In this section the notation and background for gravity waves is established. The beginning is the Navier–Stokes equation for the force on a mass of material of density ρ and velocity u. Following Mei,[17] yields the momentum equation of motion:

$$\frac{\partial u}{\partial t}+u\cdot\nabla u=-\nabla\left(\frac{P}{\rho}+gz\right)+\nu\nabla^2 u, \tag{1}$$

where ν is the constant kinematic viscosity, P is the pressure, and g is the local acceleration of gravity, and the z axis is pointing upward. When the flow is laminar and the viscosity is small, a velocity potential Φ approximately determines the velocity u through

$$u=\nabla\Phi. \tag{2}$$

Substituting into the Navier–Stokes equation yields for Φ the following equation:

$$\nabla\left(\frac{\partial\Phi}{\partial t}+\frac{1}{2}|\nabla\Phi|^2-\nu\nabla^2\Phi\right)=-\nabla\left(\frac{P}{\rho}+gz\right). \tag{3}$$

Without the viscosity this equation leads to the Bernoulli principle that

$$\frac{\partial\Phi}{\partial t}+\frac{1}{2}|\nabla\Phi|^2+\frac{P}{\rho}+gz=C(t), \tag{4}$$

where $C(t)$ is a constant in space, dependent only, possibly on time. Because $C(t)$ does not depend on depth, the pressure at the sea floor (the coordinate system has the unperturbed surface at $z=0$ and the sea floor at $z=-h$), where $\nabla\Phi, \partial\Phi/\partial t\to 0$ as $z\to -h$,

$$\frac{\partial\Phi}{\partial t}+\frac{1}{2}|\nabla\Phi|^2+\frac{P(0)}{\rho}+gz=\frac{P(-h)}{\rho}-gh. \tag{5}$$

In the following discussion the continuity equation and the boundary conditions are written for the surface and bottom of the body of water, assuming that all quantities have a $e^{-i\omega t}$ time dependence. Viscous effects are kept to lowest order where necessary, but the $|\nabla\Phi|^2$ terms are neglected.

Given that the coordinate system has the unperturbed surface at $z=0$ and the sea floor at $z=-h$, the equation of continuity for the velocity potential is

$$\nabla^2\Phi=0, \quad -h<z<0. \tag{6}$$

The velocity at the sea floor must vanish so the following condition on the normal derivative of the velocity potential must hold:

$$\frac{\partial\Phi}{\partial n}=0, \quad z=-h. \tag{7}$$

The kinematic boundary condition at the free surface is that the changes in the surface are caused by the velocity field of the fluid, so the time rate of change of the surface position must be equal to the speed of the fluid in the vertical direction:[17]

$$\frac{\partial\eta}{\partial t}=\frac{\partial\Phi}{\partial z}, \quad z=0. \tag{8}$$

Combining this surface boundary condition with the equation of motion for Φ yields the equivalent of a wave equation at the surface,

$$\frac{\partial^2\Phi}{\partial t^2}+g\frac{\partial\Phi}{\partial z}-\nu\nabla^2\frac{\partial\Phi}{\partial t}=-\frac{1}{\rho}\frac{\partial P_a}{\partial t}, \quad z=0. \tag{9}$$

Assuming that the surface of the water bears a wave with wave vector k, $\eta=Ae^{ikx}$ yields the following dispersion relation for gravity waves propagating along the surface:

$$\omega(k)^2=gk\tanh(kh), \tag{10}$$

and these waves are damped exponentially with depth.

As with any physical system it is expected that if an atmospheric pressure disturbance with a velocity v matching the gravity wave phase velocity for some wave vector k,

$$v=\sqrt{\frac{g\tanh(kh)}{k}}=\frac{\omega(k)}{k}, \tag{11}$$

there should be some sort of resonant interaction.

Precisely this resonant effect has been considered by Phillips[15] in the study of transient wave development in the ocean.[14]

III. REVIEW OF THE LONGUET-HIGGINS STUDY

The excitation of gravity waves in the linearized theory above for an incompressible fluid is localized to within a few wavelengths of the surface since the waves are damped out with increasing depth. However, the time dependence of the surface gravity waves can be transmitted to the ocean floor through the column of water between the surface and the floor via the Bernoulli principle. For laminar flow this principle relates the atmospheric pressure at the surface P_a to the pressure $P(x,y,-h)$ at a depth h on the floor

$$P_a+\rho g\,\eta(x,y,t)+\tfrac{1}{2}\rho v(x,y,\eta,t)^2=P(x,y,-h)-\rho gh, \tag{12}$$

where $v(x,y,\eta,t)$ is the velocity of the surface waves at the surface point (x,y), $\eta(x,y,t)$ is the water surface profile about $z=0$, ρ is the density of the water, g is the local acceleration of gravity, and it is assumed that the bottom velocity of the water is zero. From this principle the pressure at a point $(x,y,-h)$ on the bottom should show the time dependence of the surface gravity waves

$$P(x,y,-h)=P_a+\rho g(h+\eta(x,y,t))+\tfrac{1}{2}\rho v(x,y,\eta,t)^2. \tag{13}$$

Consider as a simple example, a vertically oriented traveling wave with wave vector k and angular frequency ω,

$$\eta(x,y,t)=A\sin(kx-\omega t), \tag{14}$$

$$v(x,y,0,t)=\omega A\cos(kx-\omega t). \tag{15}$$

The bottom pressure at a fixed position $(x,y,-h)$ will have the following time dependences:

$$P(x,y,-h)=P_a+\rho g(h+A\sin(kx-\omega t)) + \tfrac{1}{2}\rho\omega^2A^2\cos(kx-\omega t)^2. \tag{16}$$

Thus, if a single frequency traveling wave from some source, like a hurricane or typhoon, passes over a point x, this simple traveling wave would generate a pressure power spectrum with peaks at ω and 2ω. Such observations have clearly been made with the bottom placed seismic and pressure observations of Sutton and Barstow.[13]

The Longuet-Higgins well-known conditions about standing waves being necessary for surface radiated microseisms are not applicable to signals received at a single point on the bottom. The measurements and observations of this paper and the LH original study deal with the radiation of seismic signals from the ocean floor and their propagation through the surface and body of the earth to a distant seismometer. This distinction is clarified in the following paragraphs.

Longuet-Higgins began his study by looking at the generation of seismic waves by a source induced on the floor of the ocean. For simplicity, in the following discussion, an approximate Green's function for the propagation of the seismic signal through the surface of the earth will be used instead of a more detailed Green's function that reflects the surface boundary conditions and curvature of the earth. The more complete Green's function shares the property of depending on coherence in the source region for signal propagation so our arguments below will remain valid for the more accurate formulas.

For simplicity, assume a storm occupies surface over a rectangular sea-floor section of length L and width W with an area $L\times W$, which region is a distance R from the seismometer, then the vertical displacement $\mathbf{s}$ of the seismometer at a frequency ω is given approximately in the far field region[18] by

$$\mathbf{s}(R,\omega)=\frac{e^{i(\omega/c_s)R}}{c_s^2\rho_s R}W\int_0^L P(x,y,-h,\omega)dx, \tag{17}$$

where c_s is the velocity of sound in the earth's crust, ρ_s is an average density of the solid in the crust, and for the following examples it will be assumed that all plane waves are traveling along the x direction and there is no other dependence perpendicular to the x axis. This assumption reduces a surface integral over the area to the linear integral multiplied by W.

The primary assumption of Longuet-Higgins was that detectable radiated seismic signals are those in which the integral of the bottom pressure over an area is proportional to that area. To borrow language from thermodynamics, the signal has to be extensive in the area and energy of the storm. In our explicitly simplified example, the pressure integral should be proportional to L.

Examining the effect of the gravitational potential energy term on this region, shows that

$$\rho gW\int_0^L \sin(kx-\omega t)dx=\frac{\rho g}{k}W(\sin(kL-\omega t)+\sin(\omega t)), \tag{18}$$

which is not proportional to the area, vanishes (as noted by LH) whenever kL is a multiple of 2π, and will thus not scale with the size of the storm unless $k=0$, i.e., a stationary wave.

A similar observation can be found for the kinetic energy from the traveling surface gravity waves,

$$\int_0^L \rho v^2\,dx=W\frac{1}{2}\rho\omega^2A^2\frac{1}{k}(\cos(kL-\omega t)\sin(kL-\omega t) + \cos(\omega t)\sin(\omega t)+kL). \tag{19}$$

The time-dependent contribution for this one-dimensional plane traveling wave is not of order L unless $k=0$, as before.

Longuet-Higgins then asked whether there was any form of one-dimensional plane wave which would, through the kinetic energy, exert a force on the whole area and thus produce a detectable signal. In a straightforward manner he showed that a standing plane wave could produce a signal on the ocean floor that would scale with the area of the storm. The vertical velocity due to such a standing wave is given by

$$v=\omega A\cos(kx)\cos(\omega t), \tag{20}$$

and the kinetic energy integral has a positive integrand $\cos(kx)^2$ and becomes

$$\int_0^L \rho v^2\,dx=W\frac{1}{2}\rho\omega^2A^2\frac{1}{k} \times(\cos(kL)\sin(kL)+kL)\cos^2(\omega t), \tag{21}$$

which has an extensive, time-dependent contribution to the pressure at twice the wave frequency.

The current study began by asking if there is another type of wave disturbance on the surface which would give rise to an extensive force on the floor of the ocean. The search led to the examination of the two extreme types of theories for the generation of surface waves following the work of Phillips and Miles, and to examine two-dimensional cylindrical waves that are generated under wind fields of both the tropical hurricane and the mid-latitude cyclone.

IV. WAVE RESPONSE TO ATMOSPHERIC PRESSURE PROFILE: RESONANCE THEORY

If a large storm with its attendant pressure profile $P(x-vt)$ is moving through a region, Phillips'[19] resonance theory of wave excitation argues that those waves whose phase velocity is the same as the moving storm will be strongly excited. This resonance condition of matching the phase velocity selects a dominant wave vector satisfying the following equation.

$$kv=\omega(k). \tag{22}$$

Evaluating this condition for $\omega(k)=\sqrt{gk}$, valid for deep water, yields

$$\omega_v=vq=\omega(q)=\frac{g}{v} \tag{23}$$

and

$$q=\frac{g}{v^2}. \tag{24}$$

The resonance theory thus predicts a microseism frequency that is strongly dependent on the velocity of the storm.

A fairly straightforward calculation, in the limit of vanishing viscosity, yields the following for one of the surface wave velocities:

$$U=\frac{g\tilde{P}\left(\frac{g}{v^2}\right)}{2\rho v^2}\sin\left(\frac{g}{v}\left(t-\frac{x}{v}\right)\right), \tag{25}$$

where $\tilde{P}(g/v^2)$ is the spatial Fourier transform of the moving pressure profile $P(x)$. Note, however, that this is a traveling wave and hence does not contribute to distant seismometer signals (a consequence of the LH theorem for traveling waves).

Including the viscosity to lowest order in this resonance theory does give rise to a small peak at twice the resonance frequency, but its magnitude is proportional to the viscosity of the water and thus the signal would be very small.

There is another major problem with the resonance theory. It predicts that the frequency generated by a storm will become very large as the velocity of the storm approaches zero. As is discussed below, the hurricane Bonnie stopped or slowed considerably three times in its lifetime, twice at sea and once while it reversed directions at the Carolina coast and returned to sea. The dominant frequency of Bonnie's microseismic power spectrum is almost constant, velocity independent and does not obey this velocity dependence g/v_s. This flatly contradicts the resonance model.

V. GENERATION OF MICROSEISMS BY A SLOWLY MOVING HURRICANE: CYLINDRICAL SHEAR FLOW THEORY

In this section a theory is derived in which the atmospheric winds around a cyclone excite resonant excitations of the surface gravitational waves.

The treatment of the problem is in cylindrical coordinates with the quiescent surface of the sea at $z=0$. White[20] in his book on viscous flow discusses a classical cylindrical problem that had been earlier analyzed by von Karman.[21] This problem involved the flow of fluid near a infinite rotating disk with a no-slip boundary condition between the disk and fluid. The fluid velocity is expressed in terms of the cylindrical components

$$\mathbf{v}=v_r\mathbf{e}_r+v_\varphi\mathbf{e}_\varphi+v_z\mathbf{e}_z, \tag{26}$$

where the unit vectors $\mathbf{e}_r,\mathbf{e}_\varphi,\mathbf{e}_z$ form the standard orthonormal basis for cylindrical coordinates. Because of the expected cylindrical symmetry, these three velocity components and the pressure should be independent of φ, the azimuthal angle.

The governing equations include, the continuity equation

$$\frac{1}{r}\frac{\partial(rv_r)}{\partial r}+\frac{\partial v_z}{\partial r}=0, \tag{27}$$

the radial component of the momentum equation

$$\frac{\partial v_r}{\partial t}+v_r\frac{\partial v_r}{\partial r}+v_z\frac{\partial v_r}{\partial z}-\frac{v_\varphi^2}{r}=-\frac{1}{\rho}\frac{\partial p}{\partial r}+\nu\left(\frac{\partial^2 v_r}{\partial r^2}+\frac{1}{r}\frac{\partial v_r}{\partial r}+\frac{\partial^2 v_r}{\partial z^2}-\frac{v_r^2}{r}\right), \tag{28}$$

the azimuthal component of the momentum equation

$$\frac{\partial v_\varphi}{\partial t}+v_r\frac{\partial v_\varphi}{\partial r}+v_z\frac{\partial v_\varphi}{\partial z}-\frac{v_r v_\varphi}{r}=\nu\left(\frac{\partial^2 v_\varphi}{\partial r^2}+\frac{1}{r}\frac{\partial v_\varphi}{\partial r}+\frac{\partial^2 v_\varphi}{\partial z^2}-\frac{v_\varphi^2}{r}\right), \tag{29}$$

and the axial component of the momentum equation

$$\frac{\partial v_z}{\partial t}+v_r\frac{\partial v_z}{\partial r}+v_z\frac{\partial v_z}{\partial z}=-\frac{1}{\rho}\frac{\partial p}{\partial z}+\nu\left(\frac{\partial^2 v_z}{\partial r^2}+\frac{1}{r}\frac{\partial v_z}{\partial r}+\frac{\partial^2 v_z}{\partial z^2}\right). \tag{30}$$

For von Karmen's study, the boundary conditions were no slip at the disk and no viscous effects far from the disk except azimuthal flow, i.e., at $z=0$, $v_r=v_z=0$, $v_\varphi=r\Omega$, $p=0$, and as $z\to\infty$, $v_r=v_\varphi=0$. For this infinite rotating disk problem, von Karman deduced that the components v_r/r, v_φ/r, v_z, and p are all functions of z alone and was able to reduce this problem to one of the coupled ordinary differential equations, which he solved numerically.

The problem being studied here is very similar. A large storm is rotating above the water, but with a different set of boundary conditions. In the vertical direction, the kinematic condition is that the change in the surface height $z=\eta(r,\varphi)$ is determined by the vertical flow at the surface such that

$$\frac{\partial\eta}{\partial t}=v_z. \tag{31}$$

However, the other boundary condition at the liquid vapor interface has to do with the transverse stress τ,

$$\tau_{\text{int}}=\left(\mu\frac{\partial v_\varphi}{\partial z}\right)_{\text{liq}}=\left(\mu\frac{\partial v_\varphi}{\partial z}\right)_{\text{gas}}. \tag{32}$$

The boundary condition at the gas–liquid interface can be expressed using a drag coefficient C_D for the atmosphere above the water,

$$\tau_D=\left(\mu\frac{\partial v_\varphi}{\partial z}\right)_{z=\eta}=\frac{1}{2}C_D\rho_{\text{air}}V_{\text{wind}}^2, \tag{33}$$

since it is only in the φ direction that we find the major wind velocity.

As a first approximation, the convectional derivatives are neglected and an approximate solution of the resulting linear system is sought, since the frequencies and velocities of interest are quite small. Oscillatory solutions are sought

for the fluid motion due to the wind velocity. A Fourier time transform of all quantities $v_r(\omega)$, $v_\varphi(\omega)$, $v_z(\omega)$, and $p(\omega)$, are taken and it is assumed that everything has a time dependence of $e^{i\omega t}$. It is also assumed that the hurricane has the shape of a vortex flow[22] around the z axis, with a velocity given by

$$v_\varphi = \begin{cases} \Omega r, & r \leqslant a, \\ \Omega a^2/r & r \geqslant a, \end{cases} \tag{34}$$

where the rotational frequency of the hurricane is labeled Ω and a is the effective eye radius. Incorporating the body force due to gravity at the surface, into the linearized Navier–Stokes equations, yields

$$\frac{1}{r}\frac{\partial(rv_r)}{\partial r} + \frac{\partial v_z}{\partial z} = 0, \tag{35}$$

the radial component of the momentum equation

$$i\omega v_r = -\frac{1}{\rho}\frac{\partial p}{\partial r} - g\frac{\partial \eta}{\partial r} + \nu\left(\frac{\partial^2 v_r}{\partial r^2} + \frac{1}{r}\frac{\partial v_r}{\partial r} + \frac{\partial^2 v_r}{\partial z^2} - \frac{v_r^2}{r}\right), \tag{36}$$

the azimuthal component of the momentum equation

$$i\omega v_\varphi = \nu\left(\frac{\partial^2 v_\varphi}{\partial r^2} + \frac{1}{r}\frac{\partial v_\varphi}{\partial r} + \frac{\partial^2 v_\varphi}{\partial z^2} - \frac{v_\varphi^2}{r}\right), \tag{37}$$

and the axial component of the momentum equation

$$i\omega v_z = -\frac{1}{\rho}\frac{\partial p}{\partial z} - g\frac{\partial \eta}{\partial z} + \nu\left(\frac{\partial^2 v_z}{\partial r^2} + \frac{1}{r}\frac{\partial v_z}{\partial r} + \frac{\partial^2 v_z}{\partial z^2}\right). \tag{38}$$

Introducing the vertical boundary condition, yields

$$i\omega\eta = v_z, \tag{39}$$

so that

$$\frac{\partial \eta}{\partial r} = \frac{1}{i\omega}\frac{\partial v_z}{\partial r} \tag{40}$$

and

$$\frac{\partial \eta}{\partial z} = \frac{1}{i\omega}\frac{\partial v_z}{\partial z}. \tag{41}$$

Now, seeking an approximate solution, an assumption is made about the factor structure of the solutions to derive separable ordinary differential equations. That is,

$$v_r(r,\varphi,z,\omega) = J(r,\omega)F(z,\omega), \tag{42}$$

$$v_z(r,\varphi,z,\omega) = H(r,\omega)F(z,\omega), \tag{43}$$

$$v_\varphi(r,\varphi,z,\omega) = G(r,\omega)F(z,\omega), \tag{44}$$

$$p + \rho g z = L(r,\omega)F(z,\omega), \tag{45}$$

which implies that all four functions have the same z dependence.

The continuity equation is found to be separable,

$$\frac{1}{r}\frac{\partial(rv_r)}{\partial r} + \frac{\partial v_z}{\partial z} = 0 = \frac{1}{r}\frac{\partial(rJ)}{\partial r}F + H\frac{\partial F}{\partial z},$$

and adopting β as a separation constant,

$$\frac{1}{H(r)}\frac{\partial(rJ(r))}{\partial r} = -\frac{1}{F(z)}\frac{dF}{\partial z} = -\beta. \tag{46}$$

The equation for a dimensionless $F(z)$ can be solved immediately

$$F(z) = F_0 e^{\beta z}, \tag{47}$$

which vanishes as $z \to -\infty$. At this stage, our consideration is effectively limited to an infinitely deep ocean. The following is then obtained:

$$H(r) = -\frac{1}{\beta}\left[\frac{\partial J}{\partial r} + \frac{J(r)}{r}\right]. \tag{48}$$

Now because $F(z)$ is a factor in all equations, set $F_0 = 1$ and factor it out of all equations at the surface to obtain

$$i\omega J = -\frac{1}{\rho}\frac{dL}{dr} - \frac{g}{i\omega}\frac{\partial H}{\partial r} + \nu\left[\frac{\partial^2 J}{\partial r^2} + \frac{1}{r}\frac{\partial J}{\partial r} + \left(\beta^2 - \frac{1}{r^2}\right)J\right], \tag{49}$$

$$i\omega G = \nu\left[\frac{\partial^2 G}{\partial r^2} + \frac{1}{r}\frac{\partial G}{\partial r} + \left(\beta^2 - \frac{1}{r^2}\right)G\right], \tag{50}$$

$$i\omega H = -\frac{\beta}{\rho}L - \frac{g}{i\omega}\beta H + \nu\left[\frac{\partial^2 H}{\partial r^2} + \frac{1}{r}\frac{\partial H}{\partial r} + \left(\beta^2 - \frac{1}{r^2}\right)H\right]. \tag{51}$$

The boundary condition for the horizontal stress is

$$\frac{\partial v_\varphi}{\partial z} = \frac{\tau_D}{\mu} = \frac{1}{\mu}\frac{1}{2}C_D\rho_{\text{air}}V_{\text{wind}}^2, \quad z = \eta. \tag{52}$$

Since $v_\varphi = G(r)F(z)$,

$$G(z)\beta e^{\beta\eta} = \beta G(z) = \frac{\tau_D}{\mu} = \frac{1}{2\mu}C_D\rho_{\text{air}}V_{\text{wind}}^2, \tag{53}$$

assuming that the displacement of the surface is small, $\beta\eta < 1$.

The boundary condition at the surface may be rewritten as

$$\beta G(r) = \frac{1}{2\mu}C_D\rho_{\text{air}}\begin{cases} (\Omega r)^2, & r \leqslant a, \\ (\Omega a^2/r)^2, & r \geqslant a, \end{cases} \tag{54}$$

or

$$\beta G\left(\frac{r}{a}\right) = \frac{1}{2\mu}C_D\rho_{\text{air}}(\Omega a)^2\begin{cases} (r/a)^2, & r/a \leqslant 1, \\ (a/r)^2, & r/a \geqslant 1. \end{cases} \tag{55}$$

So, if $V_{\max} = \Omega a$, including one factor of $V_{\max}$ in the definition of β and the other factor in the definition of $G(r/a)$, since $G(r/a)$ must have units of velocity, yields an expression for β:

$$\beta = \frac{1}{2\mu_{\text{water}}}C_D\rho_{\text{air}}(\Omega a) = \frac{1}{2\mu_{\text{Sea}}}C_D\rho_{\text{air}}V_{\max}. \tag{56}$$

Our solution for $G(r/a)$ can be determined by the Hankel transform $K(u)$ of the first order Bessel function

$$\int K(u)J_1\left(u\frac{r}{a}\right)du = G\left(\frac{r}{a}\right) = V_{\max}\begin{cases} (r/a)^2, & r/a \leqslant 1, \\ (a/r)^2, & r/a \geqslant 1. \end{cases} \tag{57}$$

These conditions determine the value of the separation constant β. In the comparisons with observation the temperature dependence of the viscosities, densities, and velocities near the ocean surface is used for the evaluation of β. There are no adjustable parameters in β.

In the next few steps an approximate frequency dependence is sought and the viscosity, to lowest order, is included to give a broadening to the resonances. For the axial component of velocity at the surface, this yields

$$\left[i\omega + \frac{g\beta}{i\omega} - \nu\beta^2 \right] H(r) = -\frac{\beta}{\rho} L(r) \tag{58}$$

or

$$H(r) = i\frac{\omega\beta}{\rho} \frac{L(r)}{\omega^2 - g\beta + i\nu\beta^2\omega}. \tag{59}$$

Observe the resonance in $H(r,\omega)$ at the frequency

$$\omega = \sqrt{g\beta} \tag{60}$$

or

$$f_\beta = \frac{1}{2\pi}\sqrt{g\beta}. \tag{61}$$

This resonance will not depend on how fast the hurricane is moving but rather on the maximum wind speed of the storm,

$$f_\beta = \frac{1}{2\pi}\left(\frac{gC_D\rho_{\text{air}}V_{\max}}{2\mu_{\text{H}_2\text{O}}} \right)^{1/2}. \tag{62}$$

White notes that Blasius developed a drag coefficient for a flat plate as a function of a Reynolds number Re_a, which depends on the disk radius a, in this case, the eyewall radius,

$$C_D = \frac{1.328}{\sqrt{\text{Re}_a}}, \tag{63}$$

where

$$\text{Re}_a = \frac{V_{\max}a}{\upsilon} \tag{64}$$

and υ is the kinematical viscosity of air.

The parameter β thus depends on the maximum velocity of the hurricane $V_{\max}$, the effective eyewall radius a, and the temperature, density, and viscosity of the air and water. All of these parameters are accessible from the National Hurricane Center[23] (NHC) archival data, if the eyewall radius is determined by a fit from the reported external wind fields that surround the hurricane.

VI. COMPARISON OF HURRICANE BONNIE DATA WITH THE CYLINDRICAL SHEAR FLOW MODEL

Using the Fordham Seismic Station, seismic signals were recorded at each hour for most of the movement of hurricane Bonnie in August 1998. Each 1024 points of data were recorded from August 21 at 0900Z to August 30 at 2200Z on each hour at a frequency of 20 Hz using a vertical seismometer and were collected in one large data file using a 23 bit A to D converter. Data on the location, wind fields at various radii, wind speed, and velocity of movement of the storm were collected and recorded from advisories issued by the NHC. The effective eyewall radius a was determined by fitting the observed wind speeds in four quadrants at various distances from the storm as reported by the NHC advisories.

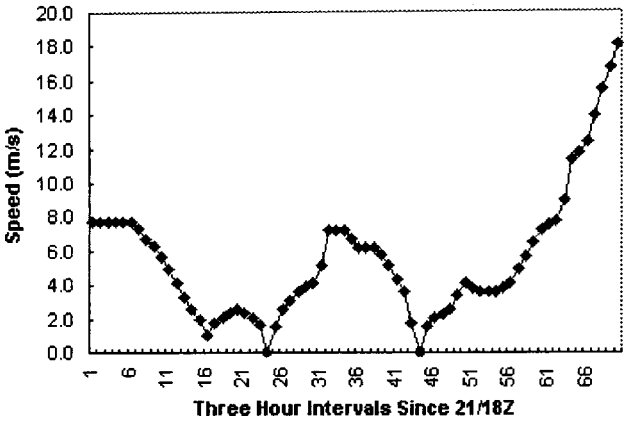

FIG. 1. Speed of Hurricane Bonnie as estimated by the National Hurricane Center at 3 hour intervals since August 21 at 1800Z.

The first step of this study is to construct the velocity of the hurricane. These results are included in Fig. 1. This shows the NHC reported velocity as Bonnie carried out a motion that had the hurricane essentially motionless near a time of reporting an advisory in three different locations. The first two times the storm slowed down and stopped it was far at sea and intensified while motionless over warm water. The third time the storm stopped it had just made landfall on the Carolina coast and turned back to go out to sea again before passing to the north and northeast.

For the following discussion it is necessary to acquaint the reader with graphing conventions followed in the rest of this paper. The frequencies at which Fourier coefficients have been measured are integer multiples of 1/51.25 Hz. This fundamental unit is imposed by our sampling rate and collection time. In all of the following plots of Hurricane Bonnie data, the integral number of such units, which we call frequency index units are plotted. The physical frequency can be obtained by multiplying the frequency index unit by 0.0195 Hz. The time intervals at which power spectrum data are compared with the NHC data are 3 hour intervals which correspond to the time interval between the two different types of advisories issued while a hurricane is monitored. In some references below, the notation 21/18Z is used to designate, August 21, 1998 at 1800 hours Zulu. Occasionally, reference is made to an hour by the designation fd50, which designates the 50th power spectrum recorded by the Fordham seismometer.

In order to get a better idea of whether seismometer data are signals being generated by the hurricane and not New York noise, it is useful to plot in Fig. 2 the total radiated intensity between the 4th and 40th frequency index unit as a function of time and compare it to a theoretically expected intensity from each hurricane location. This frequency range includes all microseisms and should capture the nonzero frequency intensity which is radiated by the hurricane. Along with the observed radiated intensity, Fig. 2 also contains a normalized plot of the inverse squared arc length distance

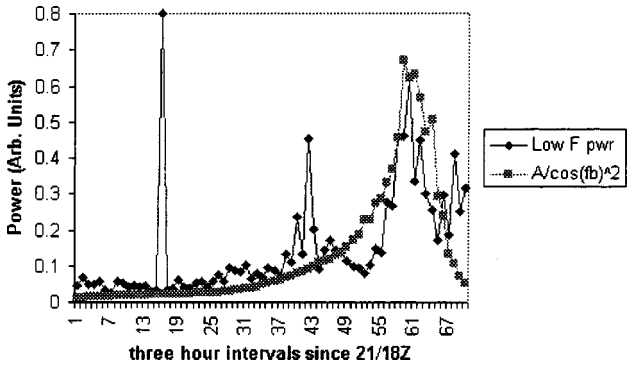

FIG. 2. Low frequency seismometer power (arbitrary units) and the normalized inverse squared distance between Bonnie and Fordham versus 3 hour intervals since August 21 at 1800Z.

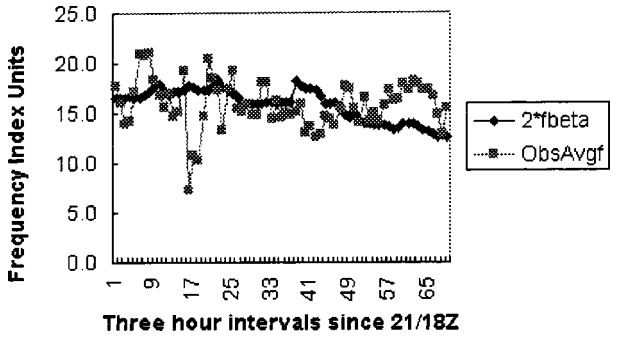

FIG. 3. The observed average frequency and the theoretical double frequency from the cylindrical shear flow theory versus 3 hour intervals since August 21 at 1800Z.

along the surface of the earth from the hurricane to the seismometer site. This inverse squared arc length is labeled $1/\cos(fb)^2$ where fb is the angular separation of the hurricane and Fordham on the surface of the earth. This $A/\cos(fb)^2$ function is scaled to match the received power at the point of closest approach and gives a rough measure of the expected intensity signals generated by the storm. This distance dependence should roughly track the radiated intensity of the microseisms by the hurricane source.

Several features of Fig. 2 require comment. First, the intensity as a function of time and distance is fairly close to the inverse squared arc length distance. This suggests that most of this signal is from the hurricane and not from noise in the vicinity of the seismometer. Second, there are two very anomalous peaks that are much more intense than the other points. In fact, the first point (Interval 16, fd50, 23/15Z) has actually been truncated to make the graphic observable. The actual value is almost 75 times more than the value plotted here. The second peak (Interval 43, fd135, 27/03Z) is the correct value as plotted.

What is happening at these two intensity peaks? Careful correlation with the hurricane location indicates that these two peaks are generated when the hurricane is stationary. The first time Bonnie is at sea and the second peak represents the reversal upon landfall and the return to the sea. The third peak in Fig. 2 is due to the intensity variation as the hurricane reaches its closest point to Fordham and then passes on to the northeast.

Figure 2 gives confidence that measured signals are from the hurricane Bonnie. The next test will be to see if the dominant peaks, essentially the average frequency, of the power spectrum is close to the prediction of $2\,f_\beta$, which is expected if the kinetic energy is integrated over the circular area of the storm. A positive integrand is expected since the velocity is squared in the cylindrical area of integration. Parameters are chosen to match the temperatures of the south Atlantic and derived other variables from the data on Hurricane Bonnie from the NHC.

Figure 3 plots the observed average frequency and twice the resonant frequency $2\,f_\beta$ as a function of the advisories issued by the NHC. In these plots the frequency is measured by the frequency index l, the actual value of the frequency is $0.0195\times l$ Hz.

The agreement between the average observed frequency and $2\,f_\beta$ indicates that the kinetic energy is the contribution to the pressure at the bottom of the ocean even though the hurricane is moving. A small translation of the cylindrical coordinates by a translation velocity v_T does not seem to make much of a difference. Consider the velocity of fluid under a moving hurricane (assumed here in the x direction) the kinetic energy expression will be

$$\tfrac{1}{2}(v_T\mathbf{e}_x+v_r\mathbf{e}_r+v_\varphi\mathbf{e}_\varphi+v_z\mathbf{e}_z)(v_T\mathbf{e}_x+v_r\mathbf{e}_r+v_\varphi\mathbf{e}_\varphi+v_z\mathbf{e}_z) \quad (65)$$

which becomes

$$\tfrac{1}{2}(v_T^2+v_\varphi^2+v_r^2+v_z^2+2v_Tv_r\mathbf{e}_r\cdot\mathbf{e}_x+2v_Tv_\phi\mathbf{e}_\phi\cdot\mathbf{e}_x). \quad (66)$$

The last two terms average out when integrated over ϕ while the first two terms have no time dependence and so make no contribution. The two terms $v_r^2+v_z^2$ both will exhibit the $2\,f_\beta$ frequency.

So, the remaining question to be answered is what is happening at the points where the hurricane has stopped. The hint can be seen in Fig. 3 at the location of the first peak. The average frequency is almost exactly at f_β. The explanation returns to the Bernoulli equation and the contribution of the gravitational potential energy, which has a resonance at f_β,

$$g\rho\,\eta(r,\omega)=g\rho\,\frac{v_z}{i\omega}=\frac{g\rho H(r)}{i\omega}=g\beta\,\frac{L(r)}{\omega^2-g\beta+i\nu\beta^2\omega}. \quad (67)$$

As noted by LH and discussed above, if such a oscillation moves along the surface as a traveling wave, it does not make a significant contribution to radiated microseisms. However, if there is no translational motion, then an oscillation in the vertical direction will be coherent and give rise to an excitation on the floor at the frequency $\sqrt{g\beta}$. If the storm is motionless, the gravitational potential energy of the surface should be seen in the microseism spectrum.

It is useful to examine the power spectrum as measured by the spectrometer to describe these phenomena. Two different plots of the power spectrum are shown below, the first of these will be 3 hours before the hurricane stops at (Interval 16, fd50, 23/15Z) and will show behavior similar to most hours of microseism production.

The spectrum (fd47,23/12Z) in Fig. 4 is fairly typical for a moving hurricane. There is a dominant peak close to the frequency $2\sqrt{g\beta}$ as well as a number of other smaller peaks

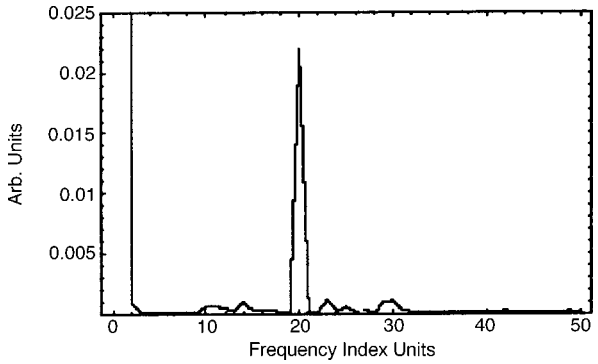

FIG. 4. The microseism power spectrum at the 47th hour of data plotted in frequency index units of 0.195 Hz.

which fluctuate in time. Notice that the maximum vertical scale of this graph is 0.025 arbitrary units, which is typical of the spectrum in this early path of the hurricane. Figure 5 shows the power spectrum for the 50th hour (df50,23/15Z) during which the hurricane was motionless. Notice immediately that the vertical scale here is 4.0, a factor of 160 larger than the previous figure. Note also the significant change in the location of this peak as well as the large increase in intensity. While the much smaller peak in Fig. 4 was very close to $2\sqrt{g\beta}$, the spectrum in Fig. 5 is dominated by the very large peak very close to $\sqrt{g\beta}$. At the hour 50 (fd50, 23/15Z) the frequency of the peak is between 8.75 and 9.0 frequency index units. The calculated value of f_β. is found to be 8.87 units.

At the second intensity peak (fd130, 26/20Z) the peak location is approximately 11 frequency index units and the theoretical value of f_β is about 9. The peak is not quite as large as the case for the 50th hour, but it must be remembered that much of the hurricane was over land when it stopped and moved back onto the sea. A smaller signal from the remaining part of the hurricane over the ocean should be expected.

In Fig. 1 there was a third time in which the NHC reports a zero velocity for Bonnie. This was at (Interval 23, fd75, 24/15Z). A review of a number of measured power spectrum near this time show spectra with f_β peaks dominant at fd70–fd73 and fd79–fd81. None of these lower frequency peaks is as large as observed at fd50. Even though the NHC reports the hurricane having zero velocity in a three hour

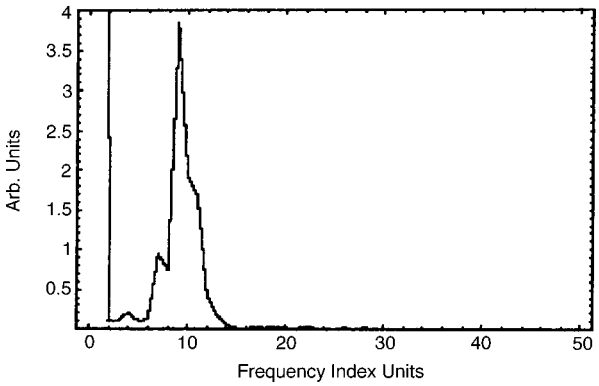

FIG. 5. Microseism power spectrum at the 50th hour plotted versus frequency index units of 0.195 Hz.

period, our data would indicate the velocity was slowly changing and was zero before and after the advisory at 24/15Z.

A similar analysis of the times around the third peak near Interval 60 in Fig. 5 shows that the spectrum is concentrated at frequencies closer to $2\sqrt{g\beta}$ and there is no shift to a lower frequency during this period. The microseisms generated here appear to arise primarily from the kinetic energy terms in Bernoulli's equation.

The power spectrum at different hours was never exactly the same. Most of the largest peaks are close to the $2\sqrt{g\beta}$ frequency as shown in Fig. 4, although there is some variation with time. The parameters that have been used to calculate β are averages computed over the whole lifetime of the hurricane and the real values must change with time more quickly than indicated by our data. This theory clearly is only a first approximation in which fluctuations are ignored. In spite of this limitation, it appears that this vortex theory captures much of the radiated microseism generation by this hurricane.

VII. EXTENSION OF THE CYLINDRICAL STRESS FLOW MODEL TO MID-LATITUDE CYCLONES

A second study was carried out with the Fordham Seismic Station during the passage of a strong Nor'easter which moved up the East Coast in January 1998. Seismic data were gathered when the storm was close to Fordham so the storm would dominate the seismic data. The data were collected for January 21 and 22 and average frequencies of the microseisms were tabulated hourly for this time period. A series of satellite images and detailed surface weather maps[24] were used to map the location of the storm and estimate its speed, size, and pressure.

The preceding theory for hurricanes was based on the assumption that the storm structure resembled a vortex with an eyewall parameter a and a maximum velocity $V_{\max}$. The structure of the mid-latitude cyclone is quite different. In the next few paragraphs the cylindrical stress–flow model is adapted to this atmospheric structure.

The striking structure of mid-latitude cyclones as represented by our nor'easter is that the isobars are approximately circular and that the pressure gradient is radial and essentially constant. A balancing of the Coriolis force and the pressure gradient forces induces the main winds to be predominantly azimuthal.

The equations of motion for the air above the sea are derived in a cylindrical coordinate system that rotates about the local zenith with a Coriolis rotation frequency Ω_c. Letting v_r and v_ϕ be the radial and azimuthal velocities of the air at the bottom of the cyclone and at the surface of the water, yields the following equations (without viscosity):

$$\frac{\partial v_r}{\partial t} - 2\Omega_c v_\phi - \frac{v_\phi^2}{r} = \Omega_c^2 r - \frac{1}{\rho_{\text{air}}}\frac{\partial P}{\partial r}, \tag{68}$$

$$\frac{\partial v_\phi}{\partial t} + 2\Omega_c v_r + \frac{v_r v_\phi}{r} = 0. \tag{69}$$

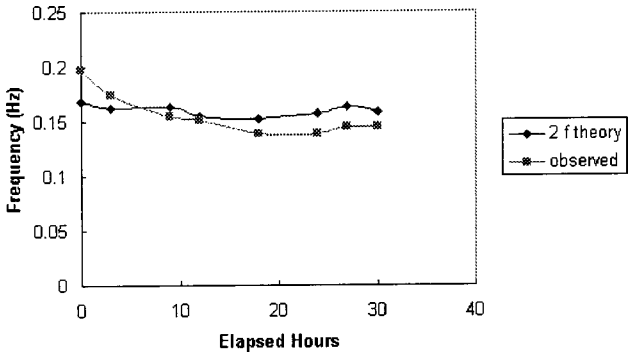

FIG. 6. Theoretical and observed 2f frequencies for the mid-latitude cyclone microseisms.

To find the steady state solution, set the derivatives on the left-hand side to zero and solve the remaining equations. This implies that $v_r=0$ and that v_ϕ depends on r in a simple fashion. In order to write this, impose the assumption that the radial pressure gradient of the pressure is constant. It may then be evaluated by measuring the pressure difference ΔP between the outermost isobar and the center, and the radius R_c of the cyclone between these same two points. Defining the maximum azimuthal air velocity

$$(v_\phi)_{\max}=\frac{1}{4\Omega_c}\frac{\Delta P}{\rho_{\text{air}}R_c}, \tag{70}$$

and a characteristic length for the velocity variation

$$a=\frac{1}{\Omega_c^2}\frac{\Delta P}{\rho_{\text{air}}R_c}, \tag{71}$$

yields the steady state solution for the azimuthal velocity

$$v_\phi=4(v_\phi)_{\max}\sqrt{\frac{r}{a}}\left(1-\sqrt{\frac{r}{a}}\right). \tag{72}$$

Inserting these into the boundary condition between the air and water and using the Blasius drag coefficient results in

$$\beta G(z)=\frac{1.328\rho_{\text{air}}\sqrt{\nu_{\text{air}}}(4(v_\phi)_{\max})}{2\mu\sqrt{R_c(v_\phi)_{\max}}}\times 4(v_\phi)_{\max}\frac{r}{a}\left(1-\sqrt{\frac{r}{a}}\right)^2. \tag{73}$$

Following factorization, and the same process as before, we find that β is given by

$$\beta=\frac{1.328\rho_{\text{air}}\sqrt{\nu_{\text{air}}}(4(v_\phi)_{\max})}{2\mu\sqrt{R_c(v_\phi)_{\max}}}. \tag{74}$$

By combining appropriate temperatures, densities, viscosities and measured pressure differences ΔP and average radii R_c from the surface weather maps,[24] the predicted stress–flow frequencies f_β are calculated for this storm.

The comparison of the average measured microseism frequency and the double frequency $2f_\beta$ were tabulated and the results are shown in Fig. 6. As can be seen, the difference between the theoretical and observed frequencies varies from 3% to 10%. Again, there have been no adjustable parameters in any of the theoretical calculations.

VIII. COMPARISONS WITH OTHER OBSERVATIONS

This study was originally stimulated by the work of Tabulevich and it would be gratifying to extend its predictions against her carefully gathered data. The data supplied for a cyclone observed crossing the Caspian Sea in 1956 minimally provides the required data, including a sketch of isobars. Inserting best guesses for values needed to calculate $2f_\beta$ for a mid-latitude cyclone, a 10% to 25% difference is found between experimental and theoretical periods. Similar sets of observations over Lake Baikal and the Okhotsky Sea were more ambiguous. Otherwise, the theory generated here satisfies most of Tabulevich's observations concerning the essential role of a cyclonic storm structure in generating microseisms.

While the main purpose of this paper has been to explain microseisms radiated from cyclonic storms, it is worthwhile to address the question of the equilibrium microseisms spectrum as measured from the sea floor. This question of the ''climatology'' of microseisms has been studied carefully by Webb[10] and compared with bottom measured spectra measured at different sites in the Pacific. The fundamental premise underlying Webb's treatment is that acoustic waves generated by gravity wave pairs are responsible for the equilibrium microseism spectrum observed in measurements. As a model of the sea for this calculation Webb used a gravity wave height versus frequency distribution suggested by Pierson and Moskowitz.[25] Webb carries out a careful and thorough study of the distribution of acoustic waves generated by gravity wave interactions and their approach to equilibrium.

From the perspective postulated by the current authors, the spectrum should be a direct consequence of the surface wave distribution as expressed through Eq. (13). A calculation of the frequency dependent pressure at the bottom of the sea through the Bernoulli principle was carried out in direct comparison with the theory and experiment of Webb.

If the consequence of the Bernoulli principle is recognized and the contribution of the non-linearly generated acoustic waves is ignored, the equilibrium spectrum should be a direct reflection of the equilibrium wave height distribution. The sea-floor pressure fluctuations $\Delta p(\omega)$ at a frequency ω should be given by

$$\Delta p(\omega)=\frac{1}{2}\rho\int v(x,y,\eta,t,t)^2e^{i\omega t}\,dt, \tag{75}$$

where $v(x,y,\eta,t,t)$ is the surface gravity wave velocity at the surface. The equilibrium distribution for this velocity was calculated using the same wave height distribution $H(\omega)$ as discussed by Webb

$$v(x,y,\eta,\Delta t)=\frac{1}{2}\int\frac{d\omega}{2\pi}\omega H(\omega)e^{-i\omega t}. \tag{76}$$

Approximate calculations of the pressure power spectrum for this wave distribution as normalized by Webb and the direct calculation of the pressure power spectrum was carried out and the comparison is Fig. 7 where the two thin lines are digitized graphs from Webb of experimental data in the Pacific, the next thicker line is Webb's calculation for winds of 10 m/s based on acoustic waves, and the broadest line is the

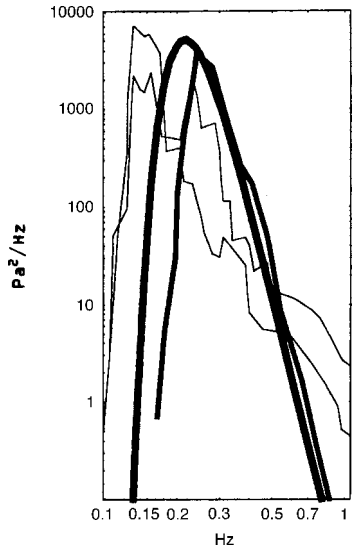

FIG. 7. Comparison of equilibrium microseism spectrum: (thin lines) observations in Pacific, (middle thickness) spectrum calculated by Webb, (heaviest line) spectrum from direct Bernoulli principle.

direct Bernoulli spectrum based on the same Pierson and Moskowitz spectrum for a steady wind of 10 m/s. It should be noted that both of the theoretical predictions are at higher frequencies than the observations, but that the Bernoulli result extends to lower frequencies than the nonlinear results of Webb.

The detailed microseism and wave spectrum data collected by Kibblewhite and Ewans[11] was originally interpreted as evidence of the nonlinear interaction of surface gravity waves to create acoustic waves. The data can be seen to support the Bernoulli principle as well. The time course of microseism events are much better explained by the approach and passing of the anticyclone with the maximum occurring at the point of closest approach of the storm center. This behavior should parallel the observations of Hurricane Bonnie in an earlier section of this paper. Kibblewhite and Ewans also present a log–log plot of a very large data set of pressure fluctuations at a given frequency versus the wave amplitude at the same frequency. Given the uncertainty that the wave amplitudes are not measured near the center of the cyclonic storm, the equations above for the pressure at a given frequency due to the Bernoulli principle immediately give rise to a slope of 2 on the log–log plot. The width of the scatter on this plot may be understood in terms of the scatter of the frequencies

$$\ln(\Delta p(\omega)) = \ln(\tfrac{1}{2}\rho\omega^2) + 2\ln(H(\omega)). \tag{77}$$

A further application of the Bernoulli principle for sea bottom pressure is suggested by the intriguing study of microseisms under the ice covered Beaufort Sea.[9] Relatively sharp resonances are observed in a very quiet environment under the ice layer. In this paper it was assumed by Webb that an acoustic wave guide theory could achieve similar resonances by assuming standing wave resonances in the wave guide for a particular depth and boundary condition. However, as expressed in this reference, the resonant conditions (depth and boundary conditions) do not closely correspond to the conditions on the depth and sea-floor covering of the Beaufort Sea. Furthermore, since the floor of the sea is very fluid and covered with a deep layer of sediment, it would be expected that the resonances would have been wider due to acoustic losses at both boundaries.

An alternative theory for these sharp resonances is suggested by the presence of the ice layer and the Bernoulli principle. If there are very low frequency shear waves excited along the length of the ice pack section over the bottom detectors, these waves should have an influence on the floor pressure due both to the potential and kinetic energy of such waves. If the length of distance between major cracks or discontinuities of the ice island is L and the velocity of sound in the ice is c, then the low lying modes (standing wave frequencies) of the ice layer would be given by $f=(c/L)n$ where $n=1,2,3,4,5,\ldots$. If these frequencies are present in the Bernoulli expression for the bottom pressure, the effects of the potential energy f and kinetic energy $2f$ of these surface modes should appear as the following multiples of the lowest mode: 1, 2, 3, 4, 5, 6, 8, 10, 12, 14. The even frequency peaks should be larger than the odd peaks should they represent both a potential and kinetic energy contribution. The odd peaks will represent only the potential energy. If the lowest mode is chosen to be the peak at 0.077 Hz, then all of these modes are clearly seen except for 3, 5, and 8,10. The location for the third and fifth frequency multiple would occur on the sides of large and wide peaks for 2 and 4. Near the required locations are slight shoulders which could be these modes potential energy modes. Since these modes represent a contribution from the potential energy and all even frequencies are also from the kinetic energy contribution, it is likely to be harder to observe these two odd frequencies. The frequencies at 8 and 10 are not clearly resolved in the data, but there is a broad peak at 9 times the base frequency which could be an unresolved combination of these two peaks. The other peaks do correspond well with the remaining multiples. Taking reasonable values for the velocity of sound in ice[26] obtained from the Army Cold Weather Laboratory, the length of the ice island would be about 10 miles.

Finally, the application of the mid-latitude cyclone cylindrical stress–flow model of this paper to the time evolution of microseisms observed on the bottom of the Pacific[8] in February 1983 as a presumably, cyclonic storm passed over or near to the detectors would offer a further test of these ideas.

IX. CONCLUSION AND NEED FOR FURTHER STUDY

The cylindrical stress–flow model for the generation of microseisms developed here has displayed much success in predicting the average frequencies of microseisms and their dependence on environmental variables. At the same time there are many details that have been left unexamined in this paper. The average or dominant frequencies were well predicted, but the other peaks which appear in microseism power spectra have not been examined. The fluctuations from the mean motion which was assumed have been ignored as has any explanation of the lifetime broadening of the microseisms themselves. Experimentally microseisms

appear as short wave trains less than 10 cycles in duration. Neither the wave train length or the arrival statistics of microseisms have been explained yet.

The ideas in this paper do not argue directly against the nonlinear generation of acoustic waves by gravity waves which has come to dominate the theoretical treatments of microseisms. The objective of this paper is to argue that the direct application of the Bernoulli principle can explain much of the observed phenomena by itself. Further study should lead to assessment of the roles of these two distinct mechanisms.

The distinction between measuring pressure variations at a point on the sea floor (at the foot of a column of water) and the conditions necessary to detect a radiated seismic signal at a distant seismometer has been delineated. This distinction should eliminate the need to search for reflected and/or standing waves over the sea floor detectors since coherence over a wide area is not required.

Most of the study in this paper has been directed toward radiated microseisms which can only be detected with seismometers. These same effects should be evident as infrasound and an effort at detecting such signals near large bodies of water as storms pass over would be an important further test of these ideas.

ACKNOWLEDGMENTS

The principal author (S.B.) would like to acknowledge the hospitality of the Fordham Physics Department during several visits. Finally, without the readily accessible archives and staff of the National Hurricane Center and the National Climatic Data Center, none of this work would have been possible. The help of Dr. Donald G. Albert of the Army Cold Weather Research Center on velocities of ice is gratefully acknowledged.

[1] V. N. Tabulevich, *Microseisms and Infrasound Waves* (Springer, Verlag, 1992).
[2] J. E. Ramirez, ''An experimental investigation of the nature and origin of microseisms at St. Louis, Missouri, Parts One and Two,'' Bull. Seismol. Soc. Am. **30**, 35–84 (1940); **30**, 139–174 (1940).
[3] R. K. Cessaro and W. W. Chan, ''Wide-angle triangulation array study of simultaneous primary microseism sources,'' J. Geophys. Res., [Oceans] **94**, 15555–15563 (1989).
[4] M. S. Longuet-Higgins, ''Theory of the origin of microseisms,'' Philos. Trans. R. Soc. London, Ser. A **243**, 1–35 (1950).
[5] A. C. Kibblewhite and C. Y. Wu, ''The generation of infrasonic ambient noise in the ocean by nonlinear interactions of ocean surface waves,'' J. Acoust. Soc. Am. **85**, 1935–1945 (1989); ''A reexamination of the role wave–wave interactions in ocean noise generation,'' *ibid.* **85**, 1946–1957 (1989); A. C. Kibblewhite and C. Y. Wu, ''The theoretical description of wave-wave interactions as a noise source in the ocean,'' *ibid.* **89**, 2241–2252 (1991).
[6] B. Hughes, ''Estimates of underwater sound (and infrasound) produced by non-linearly interacting ocean waves,'' J. Acoust. Soc. Am. **60**, 1032–1039 (1976).
[7] R. H. Nichols, ''Infrasonic ambient ocean noise measurements: Eleuthera,'' J. Acoust. Soc. Am. **69**, 974–981 (1981).
[8] S. C. Webb and C. S. Cox, ''Observations and modeling of seafloor microseisms,'' J. Geophys. Res., [Oceans] **91**, 7343–7358 (1986).
[9] S. C. Webb and A. Schultz, ''Very low frequency ambient noise at the seafloor under the Beaufort Sea icecap,'' J. Acoust. Soc. Am. **91**, 1429–1438 (1992).
[10] S. C. Webb, ''The equilibrium oceanic microseism spectrum,'' J. Acoust. Soc. Am. **92**, 2141–2157 (1992).
[11] A. C. Kibblewhite and K. C. Ewans, ''Wave-wave interactions, microseisms, and infrasonic ambient noise in the ocean,'' J. Acoust. Soc. Am. **78**, 981–994 (1985).
[12] M. V. Trevorrow, T. Yamamoto, A. Turgut, and D. Goodman, ''Measurements of ambient seabed seismic levels below 1.0 Hz on the shallow eastern US continental shelf,'' J. Acoust. Soc. Am. **86**, 2318–2327 (1989); D. Goodman, T. Yamamoto, M. Trevorrow, C. Abbott, A. Turgut, M. Badiey, and K. Ando, ''Directional spectra observations of seafloor microseisms from an ocean bottom seismometer array,'' *ibid.* **86**, 2309–2317 (1989).
[13] G. H. Sutton and N. Barstow, ''Ocean bottom microseisms from a distant supertyphoon,'' Geophys. Res. Lett. **23**, 499–502 (1996).
[14] B. Kinsman, *Wind Waves* (Prentice-Hall, Englewood Cliffs, NJ, 1965).
[15] O. M. Phillips, ''On the generation of waves by turbulent wind,'' J. Fluid Mech. **2**, 417–445 (1957).
[16] J. W. Miles, ''On the generation of surface waves by shear flows,'' J. Fluid Mech. **3**, 185–204 (1957).
[17] C. C. Mei, *The Applied Dynamics of Ocean Surface Waves* (World Scientific, Singapore, 1989).
[18] P. M. Morse and H. Feshbach, *Methods of Theoretical Physics* (McGraw-Hill, New York, 1953), p. 809.
[19] B. Kinsman, *Wind Waves* (Prentice Hall, Englewood Cliffs, NJ, 1965), p. 543.
[20] F. M. White, *Viscous Fluid Flow* (McGraw-Hill, New York, 1974).
[21] F. M. White, *Viscous Fluid Flow* (McGraw-Hill, New York, 1974), pp. 165 and 265.
[22] P. M. Morse and H. Feshbach, *Methods of Theoretical Physics* (McGraw-Hill, New York, 1953), p. 158.
[23] National Hurricane Center, http://www.nhc.noaa.gov
[24] National Climatic Data Center, http://www.ncdc.noaa.gov
[25] W. J. Pierson and L. Moskowitz, ''A proposed spectral form for fully developed wind seas based on the similarity theory of S. A. Kitaigorodskii,'' J. Geophys. Res. **69**, 5181–5190 (1964).
[26] Army Cold Weather Research Center, http:/www.crrel.usace.army.mil

An iterative implementation of rotated coordinates for inverse problems

Tracianne B. Neilsen
Applied Research Laboratories, The University of Texas at Austin, P.O. Box 8029, Austin, Texas 78713-8029

(Received 3 May 2002; revised 18 October 2002; accepted 24 January 2003)

A generalized inversion method is presented that uses a rotated coordinates technique [Collins and Fishman, J. Acoust. Soc. Am. **98**, 1637–1644 (1995)] in simulated annealing to invert for both the location of an acoustic source and parameters that describe the ocean seabed. The rotated coordinates technique not only aids in the inversion process but also indicates the coupling of the source and environmental parameters and the relative sensitivities of the cost function to changes in the various parameters. The information obtained from the rotated coordinates provides insights into how the inversion problem can be effectively decoupled. An iterative process consisting of multiple simulated annealing runs that each use a different set of rotated coordinates is demonstrated. This multistep algorithm is called systematic decoupling using rotated coordinates and is especially helpful when inverting for a large number of unknown parameters. The cost function minimized in the inversion algorithm is model-data cross-hydrophone spectra summed coherently over frequency and receiver pairs. The results of applying this inversion method to simulated data are presented in this paper. [DOI: 10.1121/1.1562912]

PACS numbers: 43.30.Pc [WLS]

I. INTRODUCTION

An iterative, efficient generalized inversion scheme to obtain the location of an acoustic source and the characteristics of the ocean environment is presented. The primary goals of the method are to minimize the number of *a priori* decisions and the number of forward calls required to obtain reliable estimates of the parameters. The approach uses multiple sets of broadband rotated coordinates to systematically decouple the parameters in such a way that the most sensitive parameters are found first. Initial tests of the method, using simulated data, are presented in this paper.

Matched-field processing (MFP) is widely used for source localization. Historically, MFP was first performed using complex spectra at a single frequency recorded on a vertical line array (VLA). To overcome ambiguities inherent to single-frequency MFP, broadband MFP was introduced. For a review of the literature about MFP, the reader is referred to Refs. 1 and 2, and the references provided therein. One problem facing MFP efforts is environmental mismatch: the use in MFP of replica vectors that are computed from inaccurate environmental information.[3]

To obtain better environmental information, a variety of matched-field inversion methods, often referred to as environmental or geoacoustic inversion methods, have been developed. Examples of environmental inversion methods are provided in Refs. 4–21 and the references therein. The general goal of environmental inversion methods is to find the properties of the ocean environment that minimize a matched-field cost function or, equivalently, that maximize the correlation between acoustic data and corresponding modeled values. In real cases, environmental inversion results are often hampered by inaccurate information about the source location.

The inversion algorithms most commonly used for environmental inversion can be divided into three categories: local, global, and hybrid methods. Local inversion methods use the gradients of the cost function and tend to find the minimum closest to the starting position. Global inversion methods, such as simulated annealing[6–8] and genetic algorithms,[9] are based on random jumps that cover more of the cost function search space and thus are more likely to find the global minimum instead of becoming trapped in a local minimum. Hybrid models combine a gradient method with a global method to increase efficiency.[10–13]

In the underwater environment, there is often a correlation between how various parameters influence acoustic propagation. While genetic algorithms are not strongly affected[14] by these parameter correlations or couplings, simulated annealing inversions, in which the physical parameters are varied directly to search for the minimum, are affected. The problems caused by parameter couplings in simulated annealing can be overcome by adding a gradient component to the global search. Hybrid inversions, such as those described in Refs. 10–13, represent ways in which this may be done. Another option is to employ a rotated coordinate system to navigate the parameter search space. The rotated coordinates, which are based on gradient information, are better aligned with the primary features of the search space than are the standard physical parameters.

The method of rotated coordinates was introduced in Ref. 15 and has been used in simulated annealing to obtain environmental parameters accurately and efficiently. The rotated coordinates correspond to the orthogonal transformation that diagonalize the covariance matrix of the cost function gradient. In Refs. 15–17, inversions are performed using rotated coordinates calculated from single-frequency data. Because the individual frequencies are sensitive to different parameters, each single-frequency inversion yields accurate estimates for the parameters that are most sensitive at that frequency. In Ref. 15, the single-frequency results are combined to yield reliable estimates for more of the environmental parameters. In Ref. 18, rotated coordinates calculated for

 0001-4966/2003/113(5)/2574/13/$19.00

broadband data are used in geoacoustic inversion. A similar reparametrization based on diagonalizing the model covariance matrix is employed in Ref. 19, in sampling at the critical temperature, and in Refs. 20 and 21, in a Bayesian inversion technique based on a fast Gibbs sampler algorithm to obtain both source and environmental parameters.

The method presented here builds on previous work and expands the possibility for efficiently obtaining reliable parameter estimates. The current work is based on a coherent broadband cost function, introduced in Ref. 2, in which correlations between modeled and measured cross spectra are summed coherently over multiple frequencies. This fully coherent cost function has been applied to broadband matched-field processing analysis.[2,22] The rotated coordinates obtained from the coherent broadband cost function describe the relative sensitivities of the broadband acoustic field to changes in the parameters and the couplings between the parameters.

In the current work, both the source location and the shallow water environment are assumed to be unknown. The three parameters that define the source location are depth, range, and bearing to the horizontal line array (HLA). By allowing both the source and environmental parameters to vary in the inversion, there is the potential to overcome the difficulties of both environmental mismatch in MFP and inaccurate source information in environmental inversion. Examples of previous inversions for both source and environmental parameters include Refs. 20 and 23. Rotated coordinates calculated for both source and environmental parameters provide insights into the parameter couplings and relative sensitivities of the cost function to changes in the parameters over the specified bounds. The rotated coordinates confirm the general parameter hierarchy accepted by the underwater acoustics community:[23] the cost function is much more sensitive to changes in the source parameters than to changes in the environmental parameters when large bounds are allowed on all the parameters.

The wide range of sensitivities of the cost function to changes in the various parameters makes it extremely difficult to obtain reliable estimates of a large number of parameters from a single inversion. The details underlying this difficulty are explained in Sec. III. A method called systematic decoupling using rotated coordinates (SDRC) has been developed to address this problem. In the SDRC approach, multiple sets of broadband rotated coordinates, corresponding to subsequently smaller parameter bounds, are used in a series of inversions to obtain the desired parameter estimates. As shown in this paper, the SDRC method can obtain reliable estimates for the sensitive parameters very efficiently and robustly. The SDRC inversion algorithm is a generalized, iterative inversion technique that can be employed with any cost function, parameter set, or forward model.

The remainder of the paper is organized as follows. In Sec. II, the method of rotated coordinates is presented. The systematic decoupling approach is explained in Sec. III. The performance of the SDRC method to invert for source and environmental parameters is then evaluated using simulated data. Conclusions and current work are discussed in Sec. IV.

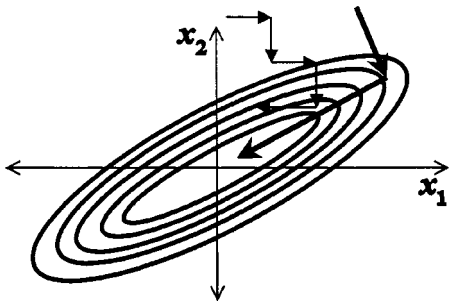

FIG. 1. Contours of a two-dimensional cost function that depict how the parameters x_1 and x_2 are coupled. The thin arrows illustrate the steps taken by an inversion method when the physical parameters are varied. The bold arrows indicate the directions of the steps when rotated coordinates are employed.

II. ROTATED COORDINATES

The basic concept of rotated coordinates is to use information about the coupling of the parameters to more efficiently navigate the search space in an inversion algorithm.[15] In general, rotated coordinates define directions approximately parallel and perpendicular to the prominent valleys of the cost function search space and thus are an efficient parametrization for the inversion. Figure 1 illustrates possible contours of a two-dimensional cost function. In this example, parameters x_1 and x_2 are coupled, and the resulting valley in the search space is oriented obliquely to the standard parameter axes. In a traditional inversion method, the standard coordinates x_1 and x_2 are varied as illustrated by the thin arrows in Fig. 1. In contrast, the bold arrows in Fig. 1 indicate a parametrization for navigating the search space when rotated coordinates are used. Rotated coordinates increase both the efficiency and the robustness of an inversion.

The rotated coordinates correspond to the orthogonal transformation that diagonalizes the covariance matrix of the cost function gradient $\mathbf{K}$. The rotated coordinates are calculated by performing an eigenvalue decomposition (EVD) of $\mathbf{K}$, where the elements of $\mathbf{K}$ are defined as

$$K_{ij} = \int_{\Omega} \frac{\partial E}{\partial x_i} \frac{\partial E}{\partial x_j} d\Omega. \tag{1}$$

A dimensionless parameter array $\mathbf{x}$ is used so it is meaningful to compare the partial derivatives of the cost function E with respect to the individual elements of $\mathbf{x}$. The dimensionless parameters $\mathbf{x}$ are obtained by dividing each physical parameter a_i by $(a_{\max,i} - a_{\min,i})$, where $\mathbf{a}_{\max}$ and $\mathbf{a}_{\min}$ contain the minimum and maximum values of the physical parameters. Ω contains the dimensionless bounds on the integration: $\{\mathbf{x}_{\max}, \mathbf{x}_{\min}\}$. An efficient Monte Carlo integration scheme is used to approximate the integral.[15,24] At each point in the Monte Carlo integration, numerical partial derivatives are evaluated:

$$\frac{\partial E}{\partial x_i} = \frac{E(x_i + \Delta x_i) - E(x_i - \Delta x_i)}{2\Delta x_i}, \tag{2}$$

where Δx_i is chosen such that Eq. (2) gives good local derivatives.

An EVD of $\mathbf{K}$ yields its eigenvectors $\{\mathbf{v_i}\}$ and the eigenvalues $\{s_i\}$. The eigenvectors $\{\mathbf{v_i}\}$ are referred to as the ro-

TABLE I. Case 1 based on the Workshop97 WA case. The values used to generate the simulated data set for case 1 and the bounds on the nine parameters that define the parameter search space and the bounds for the integration, Ω in Eq. (1). The variables are defined in the text.

Parameters	True	Min.	Max.
z_s-m	26.42	10	30
r_0-km	2.22	2.00	2.40
h_w-m	115.3	110	120
h_1-m	27.1	10	50
ρ_1-g/cm^3	1.54	1.4	1.85
c_1-m/s	1516	1500	1600
$c_{1\text{bot}}$-m/s	1573	1550	1750
ρ_2-g/cm^3	1.85	1.60	2.0
c_2-m/s	1751	1600	1800

tated coordinates and provide information about the parameter coupling. The eigenvalues $\{s_i\}$ identify the relative sensitivities of the cost function E to changes in the corresponding eigenvectors. Thus, the eigenvectors associated with the largest eigenvalues correspond to the combination of standard parameters that, when varied over the bounds Ω, affect the cost function the most. The coupling and the relative sensitivities of the parameters, reflected in the eigenvectors and eigenvalues of **K**, depend on the bounds of the multidimensional integration Ω. When large bounds are allowed for a parameter, the parameter is more likely to be represented in an eigenvector associated with a larger eigenvalue than when smaller bounds are used.

The bounds Ω are selected on the basis of the specific case being studied and can reflect the uncertainty of the initial values. In the first set of examples (case 1), the bounds specified for the nine unknowns in Table I are used to calculate the rotated coordinates. The latter examples (case 2) use larger parameter bounds on 15 parameters, defined in Table II, similar to bounds that might be used when little is known about the source or the environment. The large bounds in Table II cover a wide range of source positions and the majority of physical values for the ocean sediments.[25] In both case, no external constraints are used to match physical sediment properties (to match high sound speeds with high densities, for example).

TABLE II. Case 2: The correct environmental values for the case 2 simulated data set and the bounds on the 15 parameters that define the parameter search space and the bounds for the integration, Ω in Eq. (1). The variables are defined in the text in Sec. II C.

Parameters	True	Min.	Max.
z_s-m	40	1	70
r_0-km	2.218	0.1	10.0
θ-deg.	−18.2	−90	90
h_1-m	25	2	50
ρ_1-g/cm^3	1.37	1.0	3.0
c_1-m/s	1510	1490	1800
α_{11}-dB/m/kHz	0.005	0.0	0.5
gc_1-1/s	1.0	0.0	5.0
α_{12}-dB/m/kHz	0.008	0.0	0.5
h_2-m	50	2	80
ρ_2-g/cm^3	2.0	1.0	3.0
$rc_2 = c_2/c_{1\text{bot}}$	1.14	0.9	1.3
α_{21}-dB/m/kHz	0.06	0.0	0.5
gc_2-1/s	0.2	0.0	5.0
α_{22}-dB/m/kHz	0.12	0.0	0.5

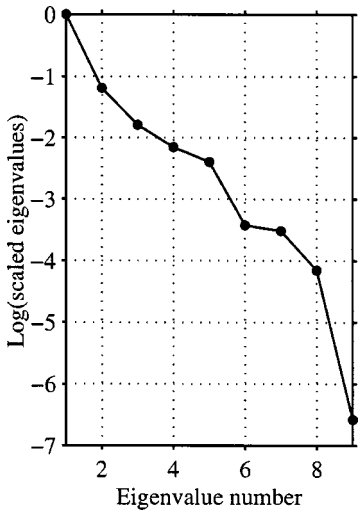

FIG. 2. Example of eigenvalues for case 1 data described in Sec. II C, calculated using the bounds defined in Table I and 720 points in the Monte Carlo integration. The eigenvalues are scaled by the largest eigenvalue; the log of the resulting scaled eigenvalues is shown.

An example of the eigenvalues and the eigenvectors of **K** is given in Figs. 2 and 3. The cost function E is defined in Eq. (3), and details of the simulated data set (case 1) are given in Sec. II C. The parameter array **x**, includes nine values that describe the source location, the water depth h_w, a sediment layer, and a half-space. The two source parameters are z_s and r_0, which correspond to the source depth and the range from the source to the horizontal line array (HLA). The four unknown parameters for the sediment layer are thickness h_1, density ρ_1, and compressional sound speed at the top and bottom of the layer c_1 and $c_{1\text{bot}}$. The two unknowns in the half-space are density ρ_2 and compressional sound speed c_2. The bounds Ω for the Monte Carlo integration of Eq. (1) are shown in Table I. The resulting scaled

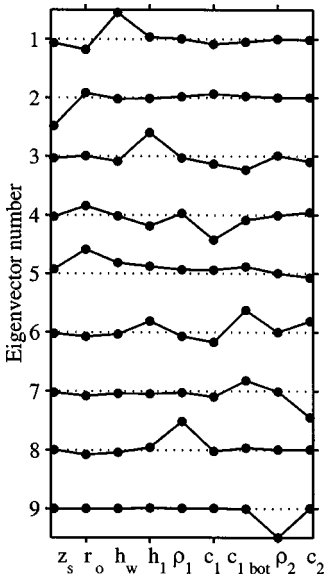

FIG. 3. Example of eigenvectors corresponding to the eigenvalues in Fig. 2. Parameters that have large amplitudes in an eigenvector are coupled.

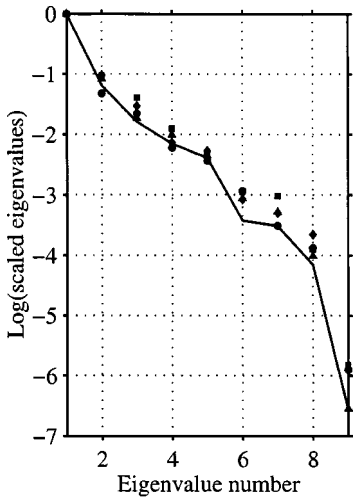

FIG. 4. Comparison of scaled eigenvalues, similar to Fig. 2, obtained when 30 (circles), 60 (diamonds), 120 (squares), 360 (triangles), 720 (line) Monte Carlo samples are used to approximate the integral in Eq. (1).

eigenvalues and eigenvectors are shown in Figs. 2 and 3, respectively.

The eigenvectors in Fig. 3 or, equivalently, the rotated coordinates indicate which standard parameters are coupled in this example. In the first eigenvector, the elements corresponding to h_w, r_0, and c_1 have the largest values, indicating they are coupled: changes in h_w will most likely decrease the cost function if the corresponding changes are also made in r_0 and c_1 as shown in the first eigenvector. Likewise, in the second eigenvector, z_s, r_0 and c_1 are coupled, indicating the second most likely way to decrease the cost function. The third eigenvector indicates a coupling between h_1, h_w, c_1, $c_{1\text{bot}}$, and c_2, and so forth.

The eigenvalues indicate the relative sensitivity of the cost function to changes in the eigenvectors over the specified parameter bounds. In Fig. 2, the eigenvalues have been scaled by the largest one, and the log of the resulting scaled eigenvalues is plotted. The eigenvalue associated with the first eigenvector is significantly larger than the remaining eigenvalues. Therefore, the parameters that have the most influence on the cost function, when allowed to vary over the bounds in Table I, are represented in the first eigenvector.

One question about the calculation of the rotated coordinates concerns the convergence of the Monte Carlo approximation to the integral in Eq. (1). To address how the number of Monte Carlo points affects the rotated coordinates, Figs. 4 and 5 show the scaled eigenvalues and rotated coordinates when 30 (circles), 60 (diamonds), 120 (squares), and 360 (triangles) Monte Carlo samples are included in the approximation of the integral. The solid lines indicates the values when 720 samples are used, as shown in Figs. 2 and 3. The different sets of scaled eigenvalues in Fig. 4 are comparable, and the parameters represented in the first several eigenvectors in the various cases in Fig. 5 are the same, with the ocassional exception of a negative sign. When the bounds on the parameters are larger, the agreement between the sets of rotated coordinates often degrades slightly with increasing parameter number. For the iterative algorithm presented in this paper, however, only the structure of the first few rotated

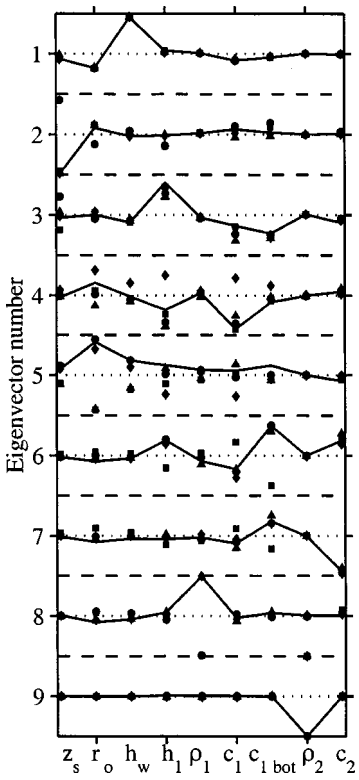

FIG. 5. Comparison of rotated coordinates, similar to Fig. 3, obtained when 30 (circles), 60 (diamonds), 120 (squares), 360 (triangles), and 720 (lines) Monte Carlo points are used, as in Fig. 4. The horizontal dashed lines separate the eigenvectors.

coordinates is important because only the rotated coordinates with relatively large eigenvalues are used in the inversion.

A. Cost function

The rotated coordinates technique can be used with any cost function. In our method, a coherent broadband cost function is employed so that the broadband features of the search space are reflected in the rotated coordinates. The cost function used in our analysis was first introduced in Ref. 2 and is defined as

$$E(\mathbf{x}) = 1 - C(\mathbf{x}), \tag{3}$$

where $C(\mathbf{x})$ is the coherent broadband correlation between data and model cross spectra for the set of source and environmental parameters $\mathbf{x}$:

$$C(\mathbf{x}) = \sum_f \sum_j \sum_{i>j} D_i(f) D_j^*(f) M_i^*(f,\mathbf{x}) M_j(f,\mathbf{x}), \tag{4}$$

where i and j indicate the receivers, and f denotes frequency. $D_i(f)$ is the measured spectra on the ith hydrophone at frequency f and is normalized such that

$$\sqrt{\sum_f \sum_j \sum_{i>j} |D_i(f) D_j^*(f)|^2} = 1. \tag{5}$$

The source and environmental parameters in $\mathbf{x}$ are used to calculate the modeled spectral values $M_i(f,\mathbf{x})$ for the ith hydrophone at frequency f, which are normalized in the same manner:

$$\sqrt{\sum_{f}\sum_{j}\sum_{i>j}|M_i(f,\mathbf{x})M_j^*(f,\mathbf{x})|^2}=1. \tag{6}$$

It is important to note that the diagonal elements in Eq. (4) are not included in the coherent sum. There are two reasons for the exclusion of the diagonal terms. First, the exclusion reduces the severity of the side lobes in the ambiguity patterns. Second, the exclusion increases the coherence gain of the signal relative to assumed incoherent noise.[2]

B. Simulated annealing

The rotated coordinates are used to construct the explicit expression for the parameter perturbations in the simulated annealing optimization. Specifically, at each step in the inversion, a single eigenvector j is perturbed, and the new values of the standard dimensionless coordinates $\mathbf{x}'$ are

$$\mathbf{x}'=\mathbf{x}+\tfrac{1}{2}\gamma^3\mathbf{v_j}, \tag{7}$$

where γ is randomly selected from the interval $(-1, 1)$. The cubed power of the random number γ in Eq. (7) allows large perturbations, but tends towards small perturbations, as described in Ref. 15, and is efficient with the linear cooling schedule used in the fast simulated annealing algorithm.[8] In the inversion, each eigenvector is used one time to vary the parameters, as shown in Eq. (7), before the temperature is reduced. From Eq. (7), it is clear that a single rotated coordinate can vary all the physical parameters.

C. Numerical results for traditional and rotated coordinates annealing

To evaluate the ability of the rotated coordinates inversion method to find source and environmental parameters, two simulated data sets are used. The first data set considered is based on the WA case from the 1997 Geoacoustic Inversion Workshop[4] (Workshop97) and consists of broadband signals received on an evenly-spaced HLA. The nine unknowns correspond to source position, water depth, single sediment layer and half-space properties. In the second case, a realistic tapered HLA is used, and the environment is described by two sediment layers over a half-space. In case 2, larger bounds are allowed on the source location and environmental parameters. The range-independent normal mode model ORCA[26] is used to generate the synthetic broadband data. The data $D_i(f)$ and the modeled values $M_i(f)$, which are computed by ORCA for the examples presented in this paper, are compared using the cost function in Eq. (3). For the following examples, 40 frequencies, evenly spaced between 50 and 250 Hz, are included in the sum over frequencies.

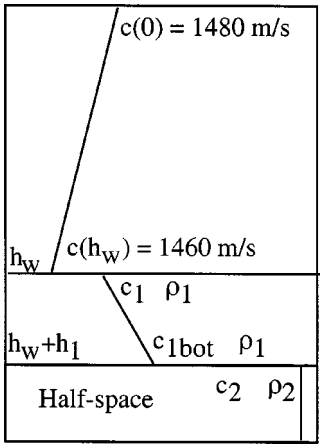

FIG. 6. Environment for the simulated data for case 1. The values of the environmental parameters are listed in Table I.

1. Case 1

Simulated data for case 1 is based on the WA case from Workshop97, which is illustrated in Fig. 6. The nine unknowns are source depth and range, z_s and r_0, water depth h_w, four sediment parameters, thickness h_1, density ρ_1, and compressional sound speed at the top and bottom of the layer c_1 and $c_{1\text{bot}}$, and two half-space parameters, density ρ_2 and compressional sound speed c_2. The parameter values used to generate the data and the bounds on the search space are given in Table I. The synthetic data set consists of broadband complex spectra values received on a 51-element, evenly spaced HLA with total horizontal aperture of 500 m at a depth of 75 m. The resulting scaled eigenvalues and rotated

TABLE III. Comparison of solutions obtained by a simulated annealing inversion algorithm when standard coordinates (third column) and the various sets of rotated coordinates in Fig. 5 are varied. The bounds in Table I are used to calculate the rotated coordinates and to define the inversion search space Ω. The total number of forward calls to the model, on the last line, includes the calculation of the rotated coordinates. The correct values are shown in Table I.

	Initial values	phys. coords.	720 pts.	360 pts.	120 pts.	60 pts.	30 pts.
z_s-m	20	26.3	26.6	26.7	26.4	26.4	26.5
r_0-km	2.00	2.213	2.221	2.231	2.203	2.217	2.207
h_w-m	100	115.2	115.6	115.5	114.9	115.3	115.0
h_1-m	50	25.5	26.4	26.1	26.6	26.7	25.1
ρ_1-g/cm^3	1.5	1.58	1.61	1.64	1.59	1.64	1.71
c_1-m/s	1550	1524	1518	1516	1517	1519	1520
$c_{1\text{bot}}$-m/s	1700	1558	1572	1572	1567	1568	1558
ρ_2-g/cm^3	2.0	1.76	1.63	1.98	1.63	1.78	1.94
c_2-m/s	1800	1708	1711	1703	1723	1723	1701
E	0.768	0.007	0.009	0.008	0.006	0.006	0.009
Calls		80 000	31 500	24 300	22 300	19 200	18 750

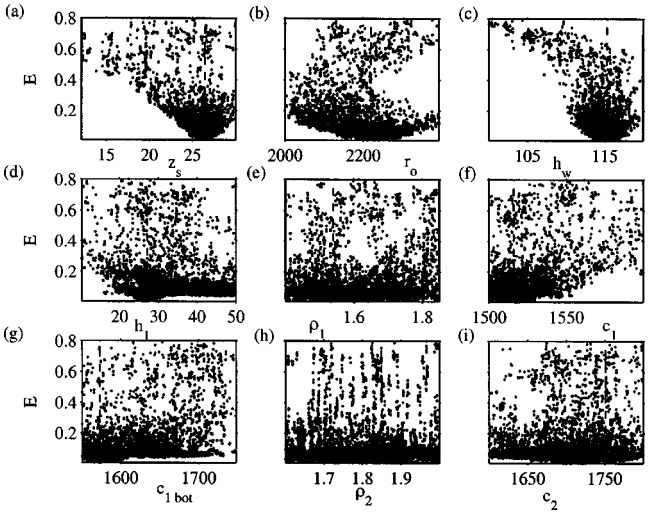

FIG. 7. Scatter plots of the cost function versus the individual parameters for all the states visited in the inversion detailed in Table III.

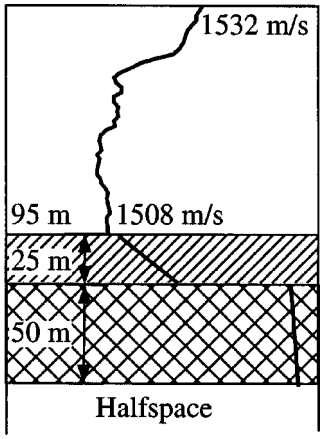

FIG. 8. Environmental model for case 2 simulated data.

coordinates obtained using various number of points to approximate the integral in Eq. (1) are shown in Figs. 2–5.

Table III shows the results of inversions when the physical and the rotated coordinates are varied. The initial parameter values are given in the second column. The third column contains the inversion results from classical simulated annealing using the physical parameters. The remaining columns show the inversion results when the various sets of rotated coordinates shown in Fig. 5 are used in fast simulated annealing as described previously. Similar cost function values and parameter estimates are found in all cases. The rotated coordinates' inversions are, however, more efficient.

The variations in the parameter estimates result from the non-uniqueness of the inverse problems using the cost function and the input data. To illustrate this uncertainty, plots of the cost function E as a function of the individual parameters at all states visited in the inversion are considered in Fig. 7. The width of the distributions for low values of E indicate both the sensitivity, or lack of sensitivity, to changes in the parameters and provide estimates of the uncertainty in the inversion results.

2. Case 2

As the number of unknowns in the inversion increases, both the traditional annealing method and the rotated coordinates method have more difficulty finding good parameter estimates. To illustrate these difficulties, a simulated data set, referred to as case 2, is used. The source location and the properties of the shallow ocean environment in this example are given in the second column of Table II. The realistic downward refracting sound speed profile is shown in Fig. 8. The water depth is 95 m. The 52 receivers are located on a tapered, bottom-mounted array that covers a horizontal aperture of 568 m.

In case 2 there are 15 unknown parameters. The three source parameters that identify the source location are z_s, r_0, and θ, which correspond to the source depth, the range,

TABLE IV. Inversion results of case 2 data for the parameters that define the source location and the two sediment layers when standard coordinates (fourth column) and rotated coordinates (fifth column) are varied. The bounds on the parameters for both the rotated coordinates calculation and the inversion are found in Table II. The parameter numbers in the first column are used for identification in Figs. 10 and 11.

No.	Parameter	Initial values	Results: standard	Results: rotated	Correct values
1	z_s-m	6	19.1	39.5	40
2	r_0-km	5.0	2.224	2.228	2.218
3	θ-deg	90	−18.2	−18.2	−18.2
4	h_1-m	40	32.3	25.2	25
5	ρ_1-g/cm^3	1.80	1.70	1.51	1.37
6	c_1-m/s	1700	1521	1504	1510
7	α_{11}-dB/m/kHz	0.05	0.033	0.015	0.005
8	gc_1-1/s	0.05	0.004	1.47	1.0
9	α_{12}-dB/m/kHz	0.05	0.41	.013	0.008
10	h_2-m	20	80	39.8	50
11	ρ_2-g/cm^3	1.6	1.05	2.3	2.0
12	$rc_2 = c_2/c_{1\text{bot}}$	0.912	1.17	1.114	1.14
13	α_{21}-dB/m/kHz	0.01	0.002	0.228	0.06
14	gc_2-1/s	0.005	0.02	2.95	0.2
15	α_{22}-dB/m/kHz	0.01	0.17	0.49	0.12
	E	0.995	0.161	0.073	0.005
	Forward calls		80,000	29,000	

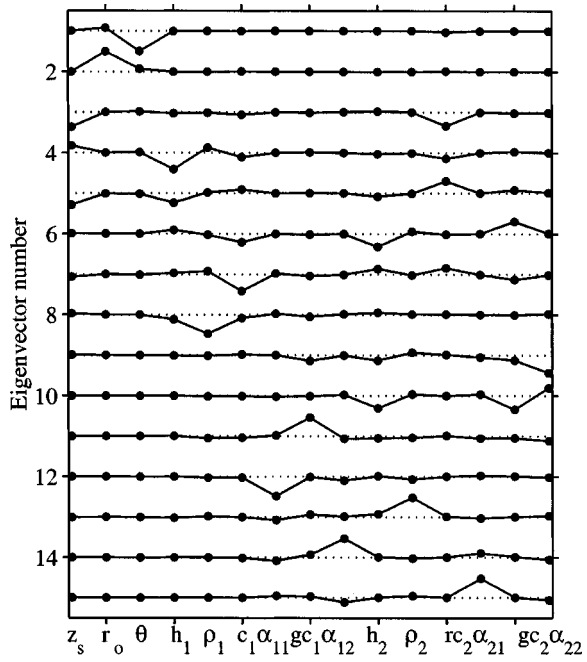

FIG. 9. Rotated coordinates for case 2 data employed in inversion shown in Table IV.

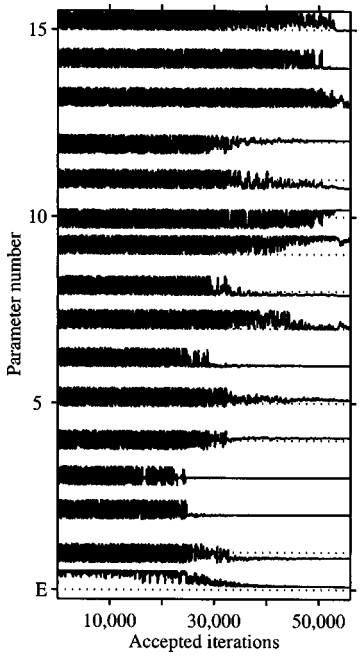

FIG. 10. The accepted values in the inversion using standard coordinates for the cost function E and the 15 parameters detailed in Table III. The horizontal lines indicate the correct parameter values.

and the bearing from the source to the horizontal line array (HLA). Each of the two sediment layers $i=1,2$ is characterized by six parameters: thickness h_i, density ρ_i, compressional sound speed at the top of the layer c_i, or ratio of the compressional sound speeds at the interface $rc_i = c_i/c_{i-1\text{bot}}$, gradient of the compressional sound speed in the layer gc_i, and compressional attenuations at the top and bottom of the layer, α_{i1} and α_{i2}. The half-space parameters are held fixed.

Table IV shows the results when both standard annealing with physical parameters and fast annealing with rotated coordinates are used to find the 15 parameters that define the source location and the two sediment layers using the case 2 data. The rotated coordinates used in this example, shown in Fig. 9, are calculated using 120 points to evaluate the integral in Eq. (1) over the bounds given in Table II. Figures 10 and 11 show the progression of the standard and the rotated coordinates inversions. Both methods obtain good estimates for the most sensitive parameters, r_0, θ, c_1, and rc_2. The rotated coordinates method also yields reasonably close values for two other parameters, z_s and h_1, and, in addition, takes less time than the standard annealing method.

In summary, the inversion method presented here uses coherent broadband rotated coordinates related to the parameter couplings to navigate the parameter search space and to find the parameters **x** that minimize the cost function in Eq. (3). The efficiency of the inversion is improved when rotated coordinates are used.

III. SYSTEMATIC DECOUPLING

The ability of the rotated coordinates method to find good estimates for a large number of parameters in a single inversion is not guaranteed. To improve the robustness of the rotated coordinates inversions, the method of systematic decoupling using rotated coordinates (SDRC) has been developed. In this section, traditional techniques used to improve annealing results are discussed. Motivation for use of the SDRC method is provided, and the SDRC method is described. Examples are given to illustrate how the SDRC method improves the likelihood and the efficiency of obtaining reliable estimates for the sensitive parameters.

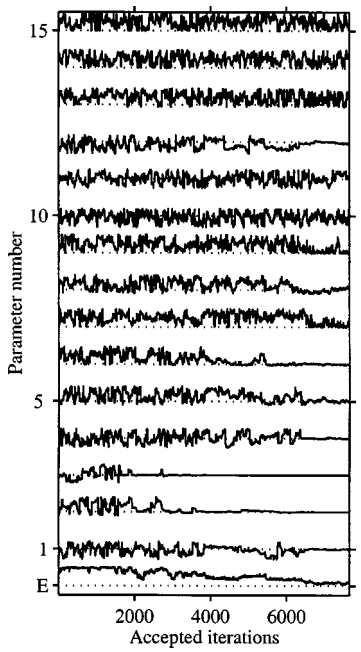

FIG. 11. The accepted values in the inversion using the rotated coordinates in Fig. 9 for the cost function E and the 15 parameters detailed in Table III. The horizontal lines indicate the correct parameter values.

TABLE V. Example of SDRC method to obtain estimates for three source parameters and three sediment parameters. The numbers in the first column correspond to the parameter numbers in Figs. 12 and 13.

No.	Parameter	Initial	Step 1	Step 2	Step 3	Step 4	Step 5	Correct
1	z_s-m	6	5.4	23	36.9	40.3	40.9	40
2	r_0-km	5.0	4.279	2.196	2.042	2.170	2.218	2.218
3	θ-deg	90	−20.0	−18.4	−18.3	−17.8	−18.2	−18.2
4	h_1-m	5.0	11.2	41.9	49.8	23.2	25.2	25
5	c_1-m/s	1600	1587	1518	1495	1506	1510	1510
6	gc_1-1/s	0.0025	4.77	3.37	4.33	0.58	1.07	1.0
	E	0.997	0.85	0.40	0.33	0.14	0.032	0.005
	n_{var}		2	4	5	6	6	

A. How to obtain good estimates with simulated annealing

Several methods have been developed to improve the results of simulated annealing. Some of these techniques are to adjust the initial temperature, the cooling schedule (in traditional annealing), and the convergence criteria. Additional methods often used to obtain better inversion results include trying multiple initial values and reducing the bounds on the parameter search space. Another scheme is to divide the parameters into two or more groups and to initially vary only the parameters in the first group while holding the rest fixed. Then, the parameters in the second group are varied while the others are held at the values obtained by the first inversion. The pattern is repeated. An example of this grouping method is found in Ref. 27. While the basic idea of decoupling the parameter set is useful, some unsatisfactory aspects of this grouping method are that (1) the user must decide how to group the parameters, and (2) there is the possibility that holding sensitive parameters at initial or intermediate incorrect values badly influences the results.

While these different refining techniques result in better annealing estimates, they are most useful when the user knows *a priori* the values he wants to obtain. In the case of experimental or other real data, one rarely has the luxury of knowing the correct answers. A primary goal in the present work is to improve the robustness of simulated annealing by developing an algorithm that works well when little is known about the correct values of the parameters and that depends less on the specific values chosen for the annealing temperature, the convergence criteria, the initial parameter values, and the parameter bounds.

B. Motivation

The underlying problem that hampers inversion efforts for a large number of unknown parameters is that less sensitive parameters cannot be reliably obtained if the value of the cost function is large because of errors in the more sensitive parameters. At relatively large values of the cost function, there are a wide range of values for the less sensitive parameters that give the same cost function value. The cost function must be reduced by finding good estimates for the most sensitive parameters before estimates of the less sensitive parameters can be found. Thus, the basic idea underlying the SDRC algorithm is to find estimates for the most sensitive parameters first, to reduce the bounds on those parameters in Ω, and then to find estimates for the less sensitive parameters. SDRC is accomplished by a series of inversions using multiple sets of rotated coordinates, each set corresponding to subsequently smaller sets of parameter bounds on the integration Ω_i. Each inversion is referred to as a step.

While the SDRC method is reminiscent of the grouping method discussed at the end of the previous section, the important difference is that the user does not make the decisions. The number of rotated coordinates used to vary the parameters during each inversion is determined by the properties of the cost function, which are based on the data. Specifically, for each set of rotated coordinates, the eigenvalues are used to decide which rotated coordinates to vary in that inversion. The rotated coordinates used in the inversion are termed the primary rotated coordinates. The primary rotated coordinates are defined as those with scaled eigenvalues within β of the largest eigenvalue, where β is typically chosen to be 40 or 60 dB to include eigenvalues within two or

TABLE VI. Bounds Ω_i on the six parameters for the rotated coordinates calculation in the last four steps of the SDRC inversion given in Table V. The bounds on the rotated coordinates calculation in step 1 Ω_1 are listed in Table II. The bounds in Table II define the limits on the annealing search space for all five steps.

	Step 2		Step 3		Step 4		Step 5	
Parameter	min	max	min	max	min	max	min	max
z_s-m	1	70	1	70	20	60	30	50
r_0-km	1.5	6.5	1.7	2.7	1.7	2.3	2.0	2.3
θ-deg	−23	−16	−23	−16	−23	−16	−19	−17
h_1-m	2	50	2	50	2	50	2	50
c_1-m/s	1495	1800	1495	1800	1495	1800	1495	1600
gc_1-1/s	0	5	0	5	0	5	0	5

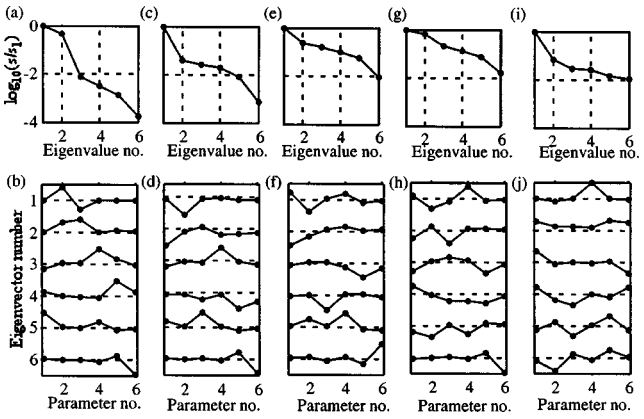

FIG. 12. Eigenvalues and eigenvectors for the SDRC inversion detailed in Table V: step 1 in (a) and (b), step 2 in (c) and (d), step 3 in (e) and (f), step 4 in (g) and (h), step 5 in (i) and (j).

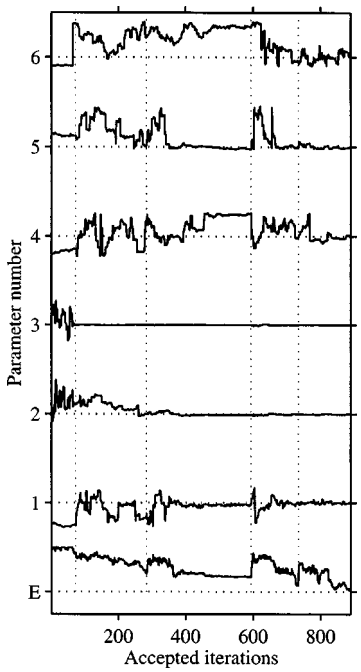

FIG. 13. Accepted parameter states from the five step SDRC inversion detailed in Table V. The horizontal lines indicate the correct parameter values. The vertical lines divide the steps listed in Table V. The cost function increases at the beginning of each step because the initial temperature is reset to a high value.

three orders of magnitude of the largest one. While only a subset of the rotated coordinates are employed in the inversion, each rotated coordinate can potentially change all the physical parameter values.

The physical parameters represented in the primary rotated coordinates change as the bounds on the integration Ω are adjusted. As the bounds on a parameter decrease, the likelihood also decreases that the parameter has a significant value in a primary rotated coordinate. In the SDRC method, each step corresponds to a new set of parameter bounds Ω_i, so that the parameters represented in each set of primary rotated coordinates are most likely to differ. Specifically, each parameter is represented in a primary rotated coordinate when the cost function has been reduced to a level at which it is sensitive to changes in that parameter. In this manner, all sensitive parameters can potentially be found regardless of the initial values and the parameter bounds. There are cases where the data is not sensitive to changes in a specific parameter, independent of the accuracy of the remaining parameter. In such cases, no reliable information about that parameter can be found.

It should be noted here that the success of the SDRC method is independent of the exact number of Monte Carlo points used to approximate the integral in Eq. (1) because the principal features of the primary rotated coordinates are independent of the number of samples, as shown in Fig. 5.

TABLE VII. Results of an SDRC inversion for the 15 parameters that define the source location and the two sediment layers. n_{var} is the number of rotated coordinates used in each step to vary the parameters. The numbers in the first column correspond to the parameter numbers in Fig. 14.

No.	Parameter	Initial	Step 1	Step 2	Step 3	Step 4	Step 5	Correct
1	z_s-m	6	7.6	20.5	38.0	39.6	39.6	40
2	r_0-km	5	2.318	2.347	2.187	2.179	2.218	2.218
3	θ-deg.	90	−19.4	−18.1	−18.2	−18.1	−18.2	−18.2
4	h_1-m	40	39.7	2.3	24.0	24.1	25.0	25
5	ρ_1-g/cm^3	1.8	1.85	2.43	1.11	1.41	1.39	1.37
6	c_1-m/s	1700	1669	1537	1519	1505	1505	1510
7	α_{11}-dB/m/kHz	0.05	0.048	0.098	0.43	0.036	0.013	0.005
8	gc_1-1/s	0.0025	4.76	4.30	1.32	1.76	1.37	1.0
9	α_{12}-dB/m/kHz	0.05	0.05	0.049	0.18	0.035	0.009	0.008
10	h_2-m	20.0	19.5	41.3	46.5	71.1	50.2	50
9	α_{12}-dB/m/kHz	0.05	0.05	0.049	0.18	0.035	0.009	0.008
10	h_2-m	20.0	19.5	41.3	46.5	71.1	50.2	50
11	ρ_2-g/cm^3	1.6	1.63	1.45	2.22	2.43	2.31	2.0
12	$rc_2=c_2/c_{1\text{bot}}$	0.91	0.92	0.97	1.11	1.14	1.14	1.14
13	α_{21}-dB/m/kHz	0.01	0.10	0.11	0.31	0.05	0.09	0.06
14	gc_2-1/s	0.005	0.067	1.36	1.51	0.72	0.094	0.2
15	α_{22}-dB/m/kHz	0.01	0.032	0.49	0.18	0.49	0.13	0.12
	E	0.995	0.64	0.36	0.20	0.083	0.019	0.005
	n_{var}		2	5	9	11	13	

TABLE VIII. Bounds Ω_i for the rotated coordinates calculation in the SDRC inversion described in Table VII. The bounds in Table II are used to calculate the rotated coordinates used in the first step and define the annealing search space for all five inversions.

	Step 2		Step 3		Step 4		Step 5	
Parameter	min	max	min	max	min	max	min	max
z_s-m	1	70	1	70	25	50	35	45
r_0-km	0.1	5.0	2.0	2.7	2.1	2.3	2.15	2.25
θ-deg.	−21	−17	−21	−17	−19	−17.5	−18.7	−17.5
h_1-m	2	50	2	50	2	50	23	26
ρ_1-g/cm^3	1.0	3.0	1.0	3.0	1.0	3.0	1.0	1.8
c_1-m/s	1490	1800	1490	1800	1490	1800	1495	1530
α_{11}-dB/m/kHz	0.0	0.5	0.0	0.5	0.0	0.5	0.0	0.5
gc_1-1/s	0.0	5.0	0.0	5.0	0.0	5.0	0.0	1.5
α_{12}-dB/m/kHz	0.0	0.5	0.0	0.5	0.0	0.5	0.0	0.5
h_2-m	2	80	2	80	30	80	30	80
ρ_2-g/cm^3	1.0	3.0	1.0	3.0	1.0	3.0	1.0	3.0
$rc_2 = c_2 / c_{1\text{bot}}$	0.9	1.3	0.9	1.3	1.0	1.3	1.1	1.2
α_{21}-dB/m/kHz	0.0	0.5	0.0	0.5	0.0	0.5	0.0	0.5
gc_2-1/s	0.0	5.0	0.0	5.0	0.0	5.0	0.0	5.0
α_{22}-dB/m/kHz	0.0	0.5	0.0	0.5	0.0	0.5	0.0	0.5

C. The SDRC algorithm

The SDRC method proceeds as follows. With large bounds on all parameters, the rotated coordinates are calculated. The primary rotated coordinates are used to vary the parameters in simulated annealing. The bounds in Ω_1 on the most sensitive parameters, those represented in the first one or two rotated coordinates, are reduced. Using the reduced bounds Ω_2, a new set of rotated coordinates is calculated. The solution from the first step provides the initial values for the second rotated coordinates annealing, performed using the second set of primary rotated coordinates. The parameter bounds are reduced again to form Ω_3, new rotated coordinates are calculated, and another simulated annealing run is performed. This pattern is repeated until all possible parameters are found. It is important to note that while the bounds on the integration for the calculation of the rotated coordinates are being reduced between the steps, the bounds on the annealing search space are never changed. In this manner, the rotated coordinates describe the features of a smaller and smaller region of the search space. The initial large bounds on the annealing search space are maintained to reduce the possibility of confining the search to the vicinity of a local minima.

1. Example of an SDRC inversion for six parameters

An example of an SDRC inversion to obtain estimates for the source location and three sediment parameters is described in Tables V and VI and Figs. 12 and 13. The data for case 2 and 30 Monte Carlo points are used to calculate the rotated coordinates. The third column of Table V gives the initial parameter values and cost function E. The next five columns give the results of the individual inversions (referred to as steps) performed when the bounds Ω_i shown in Table VI are used to calculate the rotated coordinates. The large bounds shown in Table II define the bounds on the annealing search space for all five inversions. The results from step 1 are used as the initial values for step 2, and so forth. Table V also shows the number of primary rotated coordinates n_{var} employed in each step. The initial annealing temperature of each step is $T_0 = 10$.

The rotated coordinates and eigenvalues calculated for each set of bounds are shown in Fig. 12. The eigenvalues and rotated coordinates calculated with the large bounds listed in Table II are shown in Figs. 12(a) and (b). Two of the rotated coordinates have scaled eigenvalues within 40 dB of the largest eigenvalue, so they are used to vary the parameters in step 1 of the SDRC inversion. The parameters r_0 and θ have the largest components in the first two rotated coordinates; thus, they are primarily varied in the first step. In the second step, where the bounds on r_0 and θ have been reduced, four rotated coordinates have eigenvalues within 40 dB of the largest eigenvalue, as shown in Figs. 12(c) and (d), and these

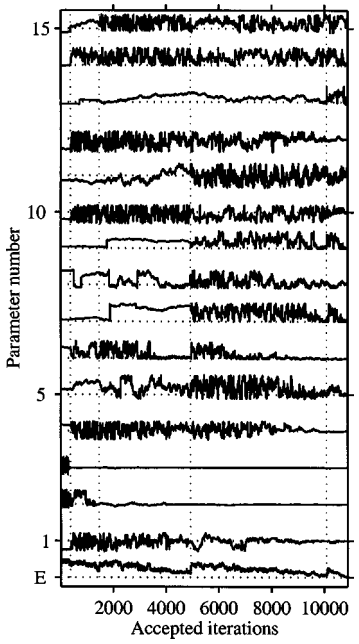

FIG. 14. Progression of the five-step SDRC inversion detailed in Table VII. The vertical lines divide the steps.

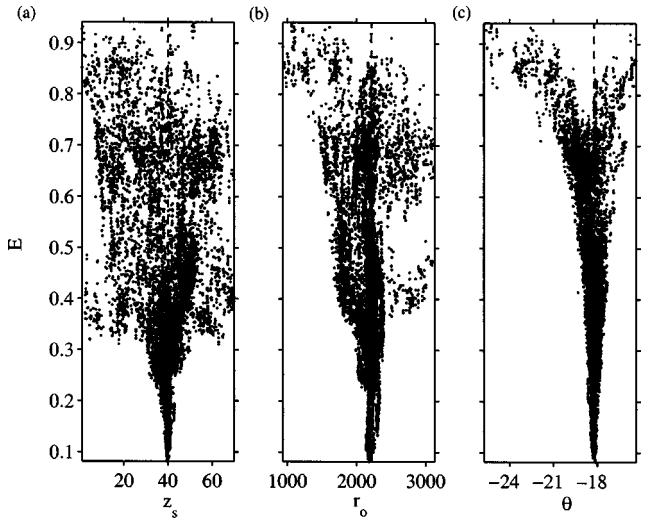

FIG. 15. Scatter plots of the cost function versus (a) z_s, (b) r_0, and (c) θ for the parameter states sampled in the inversion detailed in Table VII.

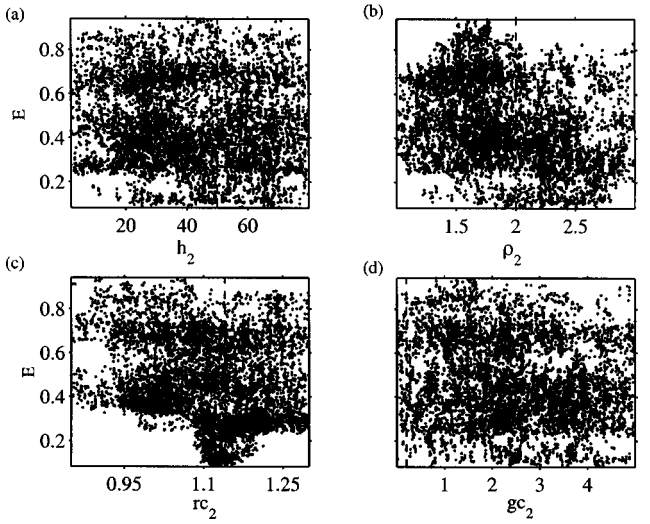

FIG. 17. Scatter plots of the cost function versus the (a) h_2, (b) ρ_2, (c) c_2, and (d) gc_2 for the parameter states sampled in the inversion detailed in Table VII.

four are employed in the annealing. The resulting estimates for r_0 and θ are close to the correct answers. Over the reduced parameter bounds Ω_2, r_0 is approximately decoupled from the other parameters because the element corresponding to r_0 is the only large value in the first rotated coordinate. The bounds on r_0 are again reduced. In the third step, Figs. 12(e) and (f), the first five rotated coordinates, which have eigenvalues within 40 dB of the largest eigenvalue are used. The results show a significant improvement in the estimate of z_s. The bounds on r_0 and z_s are decreased, and all six of the rotated coordinates calculated for step 4, Figs. 12(g) and (h), have scaled eigenvalues within 40 dB of the largest eigenvalue. The sediment thickness now has the largest value in the first rotated coordinate and is, consequently, the parameter estimate most improved during this step. Bounds are again reduced, and the resulting scaled eigenvalues for step 5 are all within 20 dB of the largest value, as shown in Figs. 12(i) and (j). Additional steps could be performed to lower the cost function further.

Approximately 7800 forward calls (including the calculations of the rotated coordinates) are made in this five-step process that obtains good estimates for all six parameters. Figure 13 shows the 874 states that are accepted during the five inversions. Accepted iterations 1 to 73 in Fig. 13 correspond to the states accepted during step 1, accepted iterations 74 to 284 represent the progress during step 2, and so forth. The vertical lines in Fig. 13 are placed at the end of each inversion step. During the iterations associated with step 1, when only two rotated coordinates are used, parameters 1, 4, 5, and 6, corresponding to z_s, h_1, c_1 and gc_1 are not varied significantly. Likewise, parameter 2, θ, is not varied significantly after step 1, and parameter 3, r_0, is not varied much in steps 4–5. The jumps in the cost function at the beginning of each step are caused by resetting the initial temperature to a large value at the beginning of each new inversion.

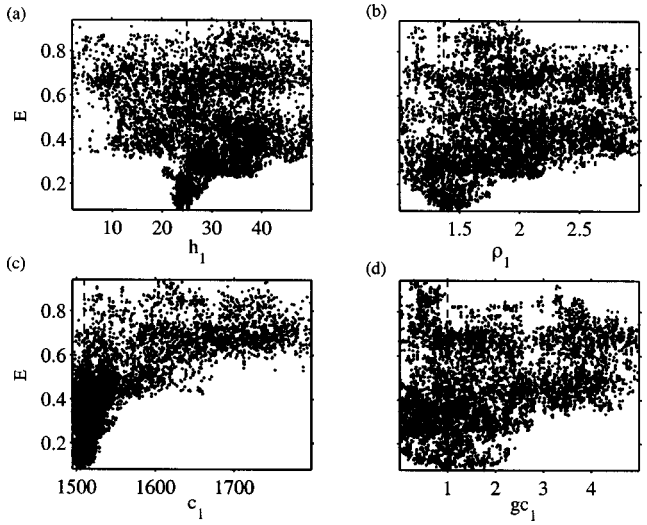

FIG. 16. Scatter plots of the cost function versus the (a) h_1, (b) ρ_1, (c) c_1, and (d) gc_1 for the parameter states sampled in the inversion detailed in Table VII.

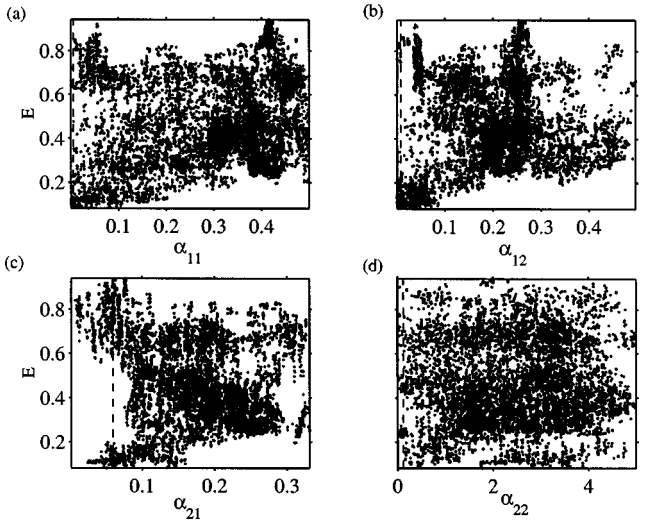

FIG. 18. Scatter plots of the cost function versus the (a) α_{11}, (b) α_{12}, (c) α_{21}, and (d) α_{22} for the parameter states sampled in the inversion detailed in Table VII.

2. Example of an SDRC inversion for 15 parameters

The example of an SDRC inversion for six parameters in the previous section is given to illustrate the SDRC algorithm. The advantages of the SDRC algorithm are more apparent when the number of unknowns in the inversion is larger. The results are now presented for an SDRC inversion for 15 unknown parameters that define the source location and the properties of the two sediment layers for the case 2 data introduced in Sec. II C. Table VII gives the initial parameter values and the results after each of the five inversions, referred to as steps. The bounds used to calculate the rotated coordinates in each step are shown in Table VIII.[28] Thirty Monte Carlo points are used in the calculation of the rotated coordinates. The starting annealing temperature in steps 1–4 is 10 but is reduced to 0.5 for the final step. The number of rotated coordinates employed in each step n_{var} is shown at the bottom of Table VII. In steps 1–3, the rotated coordinates with scaled eigenvalues within two orders of magnitude of the largest value are used to vary the parameters. In steps 4 and 5, those with scaled eigenvalues within three orders of magnitude of the largest value are used to allow the least sensitive parameters to be varied in the final steps.

The progression of the SDRC inversion is shown in Fig. 14. The vertical lines separate the inversion steps. The only parameters varied significantly in the first step are r_0 and θ. During step 2, z_s, r_0, h_1, c_1, h_2, rc_2, and gc_2 have large values in the primary rotated coordinates and are varied. Most of the parameters are varied during steps 3–5. The least sensitive parameter α_{21} is not varied substantially until the last step.

Approximately 30 000 forward calls were made to complete the SDRC inversion shown in Table VII. The SDRC method not only obtained better estimates for more of the parameters but also made approximately only 1000 more forward calls than in the single rotated coordinates case shown in Table IV.

Inversion results are more meaningful when estimates of the uncertainties in the results are included. A qualitative estimate of the uncertainty in the results can be obtained by examining scatter plots of the cost function E versus the parameter values for all the states visited in the inversion in Figs. 15–18. In Fig. 15, the source parameters z_s (a), r_0 (b), and θ (c) have very small uncertainties, which is reasonable since they are the most sensitive parameters. The next most sensitive group of parameters, h_1, ρ_1, c_1 [in Figs. 16(a)–(c)], and rc_2 [in Fig. 17(c)] have reasonable distributions and relatively small uncertainties. Approximate upper bounds can be seen on the distributions for gc_1 [in Fig. 16(d)], α_{11}, and α_{12} [in Figs. 18(a) and (b)]. The parameters for layer 2, other than rc_2, have very wide distributions in Figs. 17 and 18 indicating that, using the case 2 data, the cost function is not sensitive to changes in these parameter.

In summary, examples have been given to illustrate how the SDRC inversion method can obtain reliable estimates for the sensitive parameters in an efficient manner.

IV. CONCLUSIONS

The SDRC inversion method has been introduced in this paper as a generalized, iterative inversion technique. The basic SDRC algorithm proceeds as follows. An initial set of rotated coordinates is calculated. A complete simulated annealing run is performed using the rotated coordinates with significant eigenvalues to compute the perturbations [Eq. (7)]. The bounds on the integration for the parameters represented in the primary eigenvectors are reduced. A new set of rotated coordinates is calculated, and another simulated annealing run is performed that begins at the parameter values obtained by the previous run. These steps are repeated until reasonable estimates have been found for the desired parameters.

Although the SDRC method is based on a rotated coordinates technique that has been reported previously, the work presented here is unique in several ways. The iterative SDRC algorithm is more efficient and able to find good estimates for more parameters than either standard annealing or a single rotated coordinates inversion. The ability of the SDRC method to obtain good estimates for the most sensitive parameters without accurate knowledge of the less sensitive parameters indicates that the SDRC method has the potential to be useful in real acoustic applications in which reliable estimates of the most sensitive parameters are needed very quickly.

The SDRC method has been introduced using the cost function in Eq. (3), ORCA,[26] a range-independent forward model, and a traditional representation of the source and environmental parameters. The SDRC method is a powerful general inversion technique that can be used with any cost function, forward model, or set of parameters. The SDRC method has also been applied to range-independent, experimental, broadband VLA data[29] and to simulated, range-dependent HLA data with added white Gaussian noise.[30]

ACKNOWLEDGMENTS

This research was sponsored by the Office of Naval Research. The author wishes to thank Dr. David P. Knobles, Dr. Robert A. Koch, Dr. Brian R. LaCour, Dr. Ethan P. Honda, and Dr. Craig S. Macinnes for their helpful comments and discussions regarding this work and the reviewers for their insightful comments.

[1] A. Tolstoy, *Matched Field Processing for Underwater Acoustics* (World Scientific, New Jersey, 1993).
[2] E. K. Westwood, "Broadband matched-field source localization," J. Acoust. Soc. Am. **91**, 2777–2789 (1992).
[3] Section 3.8 of Ref. 1 contains a good summary of how environmental mismatch degrades MFP results.
[4] A. Tolstoy, N. R. Chapman, and G. Brooke, "Workshop '97: Benchmarking for geoacoustic inversion in shallow water," J. Comput. Acoust. **6**, 135–150 (1998).
[5] *Full Field Inversion Methods in Ocean and Seismo-Acoustics*, edited by O. Diachok, A. Caiti, P. Gerstoft, and H. Schmidt (Kluwer Academic, Dordrecht, The Netherlands, 1995).
[6] S. Kirkpatrick, C. D. Gelatt, Jr., and M. P. Vecchi, "Optimization by simulated annealing," Science **220**, 671–680 (1983).
[7] W. L. Goffe, G. D. Ferrier, and J. Rogers, "Global optimization of statistical functions with simulated annealing," J. Econometr. **60**, 65–99 (1994).

[8] H. Szu and R. Hartley, ''Fast simulated annealing,'' Phys. Lett. A **122**, 157–162 (1987).
[9] P. Gerstoft, ''Inversion of seismoacoustic data using genetic algorithms and *a posteriori* probability distributions,'' J. Acoust. Soc. Am. **95**, 770–782 (1994).
[10] P. Gerstoft, ''Inversion of acoustic data using a combination of genetic algorithms and the Gauss-Newton approach,'' J. Acoust. Soc. Am. **97**, 2181–2190 (1995).
[11] M. R. Fallat and S. E. Dosso, ''Geoacoustic inversion via local, global, and hybrid algorithms,'' J. Acoust. Soc. Am. **105**, 3219–3230 (1999).
[12] M. R. Fallat, P. L. Nielsen, and S. E. Dosso, ''Hybrid geoacoustic inversion of broadband Mediterranean Sea data,'' J. Acoust. Soc. Am. **107**, 1967–1977 (2000).
[13] M. Haire, ''Geoacoustic Inversion Using a Hybrid Optimization Algorithm,'' M. Sc. thesis, University of Texas at Austin, 2001.
[14] While the author has not used genetic algorithms, one of the reviewers indicated that genetic algorithms are not affected by parameter correlations because the perturbations are not limited to the parameter axes.
[15] M. D. Collins and L. Fishman, ''Efficient navigation of parameter landscapes,'' J. Acoust. Soc. Am. **98**, 1637–1644 (1995).
[16] R. J. Cederberg and M. D. Collins, ''Application of an improved self-starter to geoacoustic inversion,'' IEEE J. Ocean. Eng. **22**, 102–109 (1997).
[17] J. F. Lingevitch and M. D. Collins, ''Estimating elastic sediment properties with the self-starter,'' Wave Motion **31**, 157–163 (2000).
[18] J. S. Perkins, M. D. Collins, D. K. Dacol, L. T. Fialkowski, and J. F. Lingevitch, ''Parameter coupling in broadband geoacoustic inversion,'' J. Acoust. Soc. Am. **109**, 2394 (2001).
[19] L. Jaschke and N. R. Chapman, ''Matched field inversion of broadband data using the freeze bath method,'' J. Acoust. Soc. Am. **106**, 1838–1851 (1999).
[20] S. E. Dosso, ''Quantifying uncertainty in geoacoustic inversion. I. A fast Gibbs sampler approach,'' J. Acoust. Soc. Am. **111**, 129–142 (2002).
[21] S. E. Dosso and P. L. Nielsen, ''Quantifying uncertainty in geoacoustic inversion II: Application to broadband, shallow-water data,'' J. Acoust. Soc. Am. **111**, 143–159 (2002).
[22] D. P. Knobles and S. K. Mitchell, ''Broadband localization by matched-fields in range and bearing in shallow water,'' J. Acoust. Soc. Am. **96**, 1813–1829 (1994).
[23] M. D. Collins and W. A. Kuperman, ''Focalization: Environmental focusing and source localization,'' J. Acoust. Soc. Am. **90**, 1410–1422 (1991).
[24] W. H. Press, A. Teukolsky, W. T. Vetterling, and B. P. Flannery, *Numerical Recipes in FORTRAN: The Art of Scientific Computing* (Cambridge University Press, Cambridge, 1992), Sec. 7.8.
[25] E. L. Hamilton, ''Geoacoustic modeling of the seafloor,'' J. Acoust. Soc. Am. **68**, 1313–1340 (1980).
[26] E. K. Westwood, C. T. Tindle, and N. R. Chapman, ''A normal mode model for acousto-elastic environments,'' J. Acoust. Soc. Am. **100**, 3631–3645 (1996).
[27] D. P. Knobles, R. A. Koch, E. K. Westwood, and T. Udagawa, ''The inversion of ocean waveguide parameters using a nonlinear least squares approach,'' J. Comput. Acoust. **6**, 83–97 (1998).
[28] For the initial investigation discussed in this paper, the bound reduction was done manually. A systematic, automated bound reduction process is presented in Ref. 30.
[29] T. B. Neilsen and D. P. Knobles, ''A generalized inversion method: Simultaneous source localization and environmental inversion,'' J. Acoust. Soc. Am. **111**, 2388 (2002).
[30] T. B. Neilsen and D. P. Knobles, ''Geoacoustic inversion of range-dependent data with added Gaussian noise,'' submitted July 2002 to IEEE J. Ocean. Eng. Special Issue on Geoacoustic Inversion in Range-Dependent Shallow-Water Environments.

Broadband matched-field processing: Coherent and incoherent approaches

Cristiano Soares[a] and Sérgio M. Jesus[b]
SiPLAB–FCT, Universidade do Algarve, Campus de Gambelas, 8000-Faro, Portugal

(Received 2 January 2002; revised 7 October 2002; accepted 30 January 2003)

Matched-field based methods always involve the comparison of the output of a physical model and the actual data. The method of comparison and the nature of the data varies according to the problem at hand, but the result becomes always largely conditioned by the accurateness of the physical model and the amount of data available. The usage of broadband methods has become a widely used approach to increase the amount of data and to stabilize the estimation process. Due to the difficulties to accurately predict the phase of the acoustic field the problem whether the information should be coherently or incoherently combined across frequency has been an open debate in the last years. This paper provides a data consistent model for the observed signal, formed by a deterministic channel structure multiplied by a perturbation random factor plus noise. The cross-frequency channel structure and the decorrelation of the perturbation random factor are shown to be the main causes of processor performance degradation. Different Bartlett processors, such as the incoherent processor [Baggeroer *et al.*, J. Acoust. Soc. Am. **80**, 571–587 (1988)], the coherent normalized processor [Z.-H. Michalopoulou, IEEE J. Ocean Eng. **21**, 384–392 (1996)] and the matched-phase processor [Orris *et al.*, J. Acoust. Soc. Am. **107**, 2563–2375 (2000)], are reviewed and compared to the proposed cross-frequency incoherent processor. It is analytically shown that the proposed processor has the same performance as the matched-phase processor at the maximum of the ambiguity surface, without the need for estimating the phase terms and thus having an extremely low computational cost. [DOI: 10.1121/1.1564016]

PACS numbers: 43.30.Wi, 43.30.Pc, 43.60.Cg [DLB]

I. INTRODUCTION

The introduction of physical models in underwater acoustic signal processing has been one of the most significant advances ever in this field.[1–3] Defining a physical model for a given practical scenario allows for a consistent inclusion of *a priori* information on the signal estimation processor. That *a priori* information consists of the environmental characteristics of the propagation scenario which, by means of the solution of the wave equation on that scenario, restricts the received acoustic pressure to a well-defined class of expected signals. It is that reduction of the class of expected signals that provides the highest performance gain in terms of parameter estimation.

Since the definition of a physical model requires the knowledge (or the assumption) of a number of environmentally measurable quantities, the performance of the processor becomes dependent on those quantities. Conversely, if the emitted and received signals are known (or measurable) then it is, in principle, possible to estimate the environmental characteristics of the media of propagation—that is the base of the various *matched-field* (MF) based techniques being developed in the last two decades: Matched-field processing (MFP) for source localization, matched-field tomography (MFT) for ocean properties and matched-field inversion (MFI) for geoacoustic parameter estimation.

There are at least two aspects that emerge by their relevance to the success of MF based techniques: one is the ability of a given MF processor to accurately pinpoint the source location while rejecting sidelobes, and the other is the impact of erroneous or missing environmental information (known as model mismatch) in the final parameter estimate. This study addresses the first aspect, regarding sidelobe rejection, while considering that the processor is working on a mismatch free situation. In that case, the capacity of detecting the correct acoustic field among very close similar candidates (the so-called discrimination) largely depends on the degree of complexity of the received acoustic pressure field. As an example, a single tone will have two discriminating parameters: the amplitude and the phase. If a broadband signal is transmitted, there are as many amplitudes and phases as discrete frequencies, and the complexity of the received signal is naturally increased leading to a higher MF discrimination. This problem is similar—but not equal—to the detection problem encountered in classical spectrum estimation.

There are a number of different ways to combine MF information across frequency that can be classified in two broad groups: the conventional incoherent methods, that are based on the direct averaging of the autofrequency inner products (average of real numbers) and the, say, less conventional methods, that perform a weighted average of the cross-frequency inner products where the weights are the frequency compensated phase shifts. The latter are generally called coherent broadband methods since they combine complex inner products.

Incoherent MF methods were first proposed by Baggeroer *et al.*,[4] where geometric averaging was found to be ef-

[a]Electronic mail: csoares@ualg.pt
[b]Electronic mail: sjesus@ualg.pt

fective to reduce ambiguous Bartlett and minimum variance (MV) MFP sidelobes in a shallow-water simulation study. The same principle was used in a countless number of studies since then. More recently, the frequency domain coherent approach was first suggested by Tolstoy.[5] Michalopoulou recognized that incoherent processors discarded useful information contained in the off-diagonal terms of the cross-frequency data covariance matrix.[6] Coherent Bartlett and MV processors based on the formulation of ''supervectors'' containing field vectors of the frequencies to be processed were proposed and successfully applied on tracking a sound source in the Hudson Canyon data set.[7] Czenszak and Krolik proposed a coherent minimum variance beamformer with environmental perturbation constrains (MV–EPC) designed for a short vertical array.[8] Very recently Orris *et al.* proposed a matched-phase coherent processor that accounts for the relative phase relationships between frequencies.[9] Those phases are assumed to be unknown and are searched as free parameters.

In that classification, time domain methods play a different role but can, to some extent, be included in the coherent class. Time domain methods were first suggested by Clay[10] under the form of an optimum matched-filter for source localization. The same technique was used by Li *et al.*[11] in laboratory experimental data. Also Frazer *et al.*[12] tested Clay's technique with simulated data and a single hydrophone. In 1992, Miller *et al.*[13] showed, with computer simulations, that it is possible to localize short duration acoustic signals in a range-dependent shallow water environment. The same approach was followed by Knobles *et al.*[14] with bottom moored sensors using a broadband coherent matched-field processor proposed by Westwood.[15] Time domain source localization was actually achieved with real data by Brienzo *et al.*[16] using data received on a vertical array in a deep water area on the Monterrey fan. The technique used was a combination of time domain filtering for each sensor (matched-filter) and then a space domain beamformer.

Despite the considerable amount of work on broadband methods there is a lack of understanding on why and when a coherent method provides a better detection or localization performance than an incoherent method. This is the main topic addressed in the present study, that starts by presenting a physical-based linear data model with suitable random perturbation terms as opposed to the traditional fully stochastic model. Under this model, it is shown that the advantage of using the cross-frequency terms resides in its ability to reject noise, while its disadvantage is that the result is limited by the correlation of the random phase terms together with the deterministic correlation of the channel response across frequency. An efficient algorithm for combining cross-frequency information is derived that is shown to have an equivalent localization performance than that of the matched-phase coherent processor with a much lower computational burden. Then, the performance of the coherent and incoherent processors are compared for different number of frequencies using simulated data. Real data analysis is presented to support the physical-based model as well as for justifying the distributions of the random perturbation terms. Finally, a real data example shows the effect of a wise selection of frequency bands on the final match of the model to the data.

II. DATA MODEL

A. The physical data model

A widely used data model for M farfield point sources emitting narrowband signals received in a L-sensor array is given by

$$\mathbf{y}(t)=\mathbf{A}(\varphi)\mathbf{s}(t)+\mathbf{u}(t), \tag{1}$$

where $\mathbf{y}(t)$ is the L-sensor array received acoustic pressure, $\mathbf{A}(\varphi)$ is the $L\times M$ steering matrix, which entries are the appropriate delays for each array sensor and each source m at bearing φ_m, $\mathbf{s}(t)$ is an M-dimensional vector with the M source inputs at time t and $\mathbf{u}(t)$ is the observation additive noise. A common assumption is to consider that the additive noise is white, Gaussian, zero-mean and uncorrelated with the signals $\mathbf{s}(t)$, that themselves are zero-mean and uncorrelated stochastic processes. This model is useful for describing a field of dependent noise sources emitting through a nondispersive unbounded media and received on a horizontal array. When dealing with shallow water dispersive scenarios, deterministic sources and nonhorizontal arrays this model is unable to account for the complexity of the received field as a mixture of correlated (partially) deterministic signal reflections from sea bottom and sea surface.

An alternative approach is to start from the wave equation and directly calculate its solution with appropriate boundary conditions and environmental assumptions (e.g., azimuth and range independent isotropic media, spatial point source, etc.). In a cylindrical two-dimensional coordinate system, the acoustic pressure measured at receiver depth z_l due to a point source at range r and depth z_s can be written[17]

$$p(z_l,t;r,z_s)=\frac{-i}{2\pi}\int\sum_{j=1}^{J_M} s(\omega)\frac{\Psi_j(z_l)\Psi_j(z_s)}{\sqrt{rk_j}} \times e^{-i(k_j r-\pi/4)-\gamma_j r}e^{i\omega t}\,d\omega, \tag{2}$$

where $s(\omega)$ is the source spectrum, $\{\Psi_j(\,),j=1,...,J_M\}$ are the waveguide mode functions, and k_j and γ_j are the mode horizontal wave numbers and mode attenuation coefficients, respectively; J_M is the number of discrete modes supported by the waveguide.

Under the ray approximation the received acoustic pressure, using the same notation, can be written as

$$p(z_l,t;r,z_s)=\frac{1}{2\pi}\int\sum_{j=1}^{J_R} a_j s(\omega)e^{-i\omega\tau_j}e^{i\omega(t+|\pi/2\omega|)}d\omega, \tag{3}$$

where the number of eigenrays J_R, the ray amplitudes a_j and the delays τ_j, fully characterize the propagation channel for the specific source and receiver locations, $(0,z_s)$ and (r,z_l), respectively.

Assuming the propagation channel as a linear filter, allows for writing the received signal as the frequency product between the source signal $s(\omega)$ and the channel transfer function $h(\omega)$, defined as the sum of modal terms (or rays)

for a particular source–receiver location. Thus, a suitable model for the array-received signal from an harmonic source at frequency ω would be

$$y(z_l,\omega;r,z_s)=h(z_l,\omega;r,z_s)s(\omega)+u(z_l,\omega), \tag{4}$$

where $u(z_l,\omega)$ is a zero-mean stochastic process representing additive observation noise and where $h(z_l,\omega;r,z_s)$ can be easily deduced either from (2) or from (3) depending on which model—normal mode or ray model—is being used. It is a common assumption to consider the observation noise to be wide-sense time stationary. Taking into account the Fourier transform properties for sufficiently long observation times it can be considered that the frequency samples of u are asymptotically uncorrelated.

If the source input $s(t)$ is deterministic, signal detection using model (4) becomes a problem of detecting a deterministic signal in white noise, which optimal solutions are well known.

In the past decade, with the development of methods for acoustic inversion using deterministic signals, it has been observed that repeated emissions at very high SNR resulted in successive receptions suffering rapid changes in short time intervals possibly caused by small scale environmental perturbations, source and/or receiver motion, and sea surface and bottom roughness, which, partially or all together, contribute to unmodeled fluctuations in the signal part of (4).

Since such changes cannot be attributed to the noise due to the high SNR, a complex random factor $\alpha=|\alpha|\exp(j\phi)$ can be included such that the data model is written as

$$\mathbf{y}(\omega,\theta_0)=\alpha(\omega)\mathbf{h}(\omega,\theta_0)s(\omega)+\mathbf{u}(\omega), \tag{5}$$

where a more compact notation has been adopted by introducing a vectorial notation for the L-sensor array as $\mathbf{y}=[y(z_1),y(z_2),\ldots,y(z_L)]^t$ and similar definitions for $\mathbf{h}$ and $\mathbf{u}$, the channel transfer function and the additive observation noise, respectively; $s(\omega)$ is the source spectrum at frequency ω and θ_0 is a vector with the relevant parameters under estimation. The noise process $\mathbf{u}$ is assumed to be uncorrelated from sensor to sensor and with random factor α. Note that random factor α is space invariant but is assumed to be frequency dependent. For the design of optimal estimators it is useful to consider that α is zero-mean and Gaussian distributed. Whether that assumption is verified in practice is the subject of the next section.

B. Random signal perturbation factor

This section deals with the distribution of the random signal perturbation factor α, introduced in the linear physical model (5). It is a common assumption to consider that random factor to be complex zero-mean Gaussian distributed,[4] which implies that the module of α follows a Rayleigh distribution and that its phase is uniformly distributed in $[-\pi,\pi]$.[18] In case that the real and/or imaginary parts of the acoustic pressure are not zero mean then the envelope follows a Rice distribution while the phase term does not appear to be uniform nor Gaussian distributed (see Appendix A).

In order to obtain an empirical distribution of the signal random perturbation, only possible using real data, one has to, first, assume that the signal-to-noise ratio (SNR) is sufficiently high, to be able to neglect the influence of the noise $\mathbf{u}$, and second, assume that the deterministic part of the signal, i.e., $\mathbf{h}(\omega,\theta_0)s(\omega)$ is time-stationary or slowly varying. Under these two assumptions a possible estimator, $\hat{\alpha}$, of the random factor α at frequency ω is

$$\hat{\alpha}_n=\frac{y_n}{y_0}\approx\frac{|\alpha_n|}{|\alpha_0|}e^{j(\phi_n-\phi_0)}, \tag{6}$$

where y_n, α_n, and ϕ_n are obtained for time snapshot n and for an arbitrary frequency and receiver. This would imply that the distribution of $|\hat{\alpha}|$ would be Rayleigh or Rice depending on whether α is zero-mean or not with, however, a change on the amplitude axis due to the normalization constant $|\alpha_0|$. As an alternative and, if the stationarity assumption for $\mathbf{h}(\omega,\theta_0)s(\omega)$ is suspected not to hold, another estimator can be sought using a time sliding estimator as

$$\hat{\alpha}_n=\frac{y_n}{y_{n-1}}\approx\frac{|\alpha_n|}{|\alpha_{n-1}|}e^{j(\phi_n-\phi_{n-1})}. \tag{7}$$

In this case the interpretation is a bit more elaborated since the module of α is the ratio of two Rayleigh (or Rice) random variables and the phase term is the difference between two uniform variables if α is zero mean. It is shown in Appendix B that the ratio of two independent Rayleigh distributed random variables gives a nearly Cauchy distributed random variable and that the difference of two uniformly distributed and independent random variables gives a probability density function (pdf) for the resulting random variable that is triangular in $[-2\pi,2\pi]$. Results obtained on real data using estimators (6) and (7) are shown in Sec. VI.

III. SECOND ORDER STATISTICS AND BROADBAND MODEL FORMULATION

The correlation matrix can be directly written from (5) as

$$\begin{aligned}\mathbf{C}_{yy}(\omega,\theta_0)&=E[\mathbf{y}(\omega,\theta_0)\mathbf{y}^H(\omega,\theta_0)]\\&=E[|\alpha(\omega)|^2]|s(\omega)|^2\mathbf{h}(\omega,\theta_0)\mathbf{h}^H(\omega,\theta_0)\\&\quad+\sigma_u^2(\omega)\mathbf{I},\end{aligned} \tag{8}$$

where all terms have been previously defined and superscript H denotes conjugate transpose. Equation (5) gives the essential description of the received data model in the narrowband case. When a time-limited signal (impulse) is emitted by the source, a significant band of frequencies of the acoustic channel is excited giving rise to the need for a broadband formulation. In order to introduce, as much as possible, a common frame for the narrowband and broadband cases, we define an extended vector as

$$\underline{\mathbf{y}}=[\mathbf{y}^T(\omega_1),\mathbf{y}^T(\omega_2),\ldots,\mathbf{y}^T(\omega_K)]^T, \tag{9}$$

where superscript T denotes matrix transpose and K is the total number of discrete frequency bins. In that case, the broadband model can be written as

$$\underline{\mathbf{y}}(\theta_0)=\mathbf{H}(\theta_0)\underline{\tilde{\mathbf{s}}}+\underline{\mathbf{u}}, \tag{10}$$

where $\tilde{\underline{\mathbf{s}}}$ is a K-dimensional random vector which entries are $s(\omega_k)\alpha(\omega_k)$, i.e., the source spectrum multiplied by the random perturbation factor at each frequency $\omega_k \in [\omega_1, \omega_K]$; the matrix $\mathbf{H}(\theta_0)$ is

$$\mathbf{H}(\theta_0) = \begin{bmatrix} \mathbf{h}(\omega_1,\theta_0) & 0 & \cdots & 0 \\ 0 & \mathbf{h}(\omega_2,\theta_0) & \cdots & 0 \\ \vdots & \vdots & \ddots & \vdots \\ 0 & 0 & \cdots & \mathbf{h}(\omega_K,\theta_0) \end{bmatrix}, \tag{11}$$

where the noise extended vector $\underline{\mathbf{u}}$ has an obvious notation similar to (9). It is interesting to write the correlation matrix for model (10), which cross-frequency block matrix is given by

$$\mathbf{C}_{yy}(\omega_i,\omega_j) = \begin{cases} |s(\omega_i)|^2 \mathbf{h}(\omega_i,\theta_0)\mathbf{h}(\omega_i,\theta_0)^H E[|\alpha(\omega_i)|^2] + \sigma_u^2(\omega_i)\mathbf{I}, \\ \quad i=j, \\ s(\omega_i)s^*(\omega_j)\mathbf{h}(\omega_i,\theta_0)\mathbf{h}^H(\omega_j,\theta_0)E[\alpha(\omega_i)\alpha^*(\omega_j)], \\ \quad i\neq j, \end{cases} \tag{12}$$

where the term $E[\alpha(\omega_i)\alpha^*(\omega_j)]$ denotes the correlation of the perturbation factor across frequency. Note that unlike the autofrequency entries ($i=j$) the cross-frequency terms ($i \neq j$) are noise free. This is due to the well-known property of the Fourier transform for time-stationary processes that gives uncorrelated cross-frequency bins which might be also useful if spatially correlated noise is present. In practice, with finite observation time, that property is only asymptotically verified, which is often sufficient. In expression (12), for $i \neq j$, there are three contributions: the source cross-spectrum term $s(\omega_i)s^*(\omega_j)$, the cross-frequency acoustic channel structure term $\mathbf{h}(\omega_i,\theta_0)\mathbf{h}^H(\omega_j,\theta_0)$ and the perturbation factor correlation $E[\alpha(\omega_i)\alpha^*(\omega_j)]$. The first term is source dependent and will not be of concern here. The second term is channel dependent and may significantly vary with environmental conditions, source position (range and depth) and receiving array geometry. The third term on expression (12), for $i \neq j$, concerns the correlation of the perturbation factor and is impossible to obtain from simulations.

IV. BARTLETT MATCHED-FIELD PROCESSING

The Bartlett processor is possibly the most widely used estimator in MF parameter identification. The parameter estimate $\hat{\theta}_0$ is given as the argument of the maximum of the functional

$$P(\theta) = E[\hat{\mathbf{w}}^H(\theta)\mathbf{y}(\theta_0)\mathbf{y}^H(\theta_0)\hat{\mathbf{w}}(\theta)], \tag{13}$$

where the replica vector estimator is determined as the vector $\mathbf{w}(\theta)$ that maximizes the mean quadratic power,

$$\hat{\mathbf{w}}(\theta) = \arg\max_{\mathbf{w}} E[\mathbf{w}^H(\theta)\mathbf{y}(\theta_0)\mathbf{y}^H(\theta_0)\mathbf{w}(\theta)], \tag{14}$$

subject to $\mathbf{w}^H(\theta)\mathbf{w}(\theta)=1$. In the narrowband case, using model (5) in (14) gives the well-known nontrivial solution

$$\hat{\mathbf{w}}_{NB}(\theta) = \frac{\mathbf{h}(\theta)}{\sqrt{\mathbf{h}^H(\theta)\mathbf{h}(\theta)}}, \tag{15}$$

where the denominator is a normalization scalar and the numerator contains the signal structure as ''seen'' at the receiving array. This is simply the classical matched filter for the particular parameter location θ. Substituting (15) in (13) gives the well-known generalized conventional narrow band beamformer for parameter θ. If the search is made over θ and the maximum is selected, then an optimum mean least-squares estimate $\hat{\theta}_0$ of θ_0 is obtained.

In the broadband case, the estimator of the replica vector is given in terms of frequency extended vectors using model (10), thus

$$\hat{\underline{\mathbf{w}}}_{BB}(\theta) = \arg\max_{\underline{\mathbf{w}}} \{\underline{\mathbf{w}}^H(\theta)\mathbf{H}(\theta_0)E[\tilde{\underline{\mathbf{s}}}\tilde{\underline{\mathbf{s}}}^H]\mathbf{H}^H(\theta_0)\underline{\mathbf{w}}(\theta)\}, \tag{16}$$

where the expectation of the signal matrix $\tilde{\underline{\mathbf{s}}}\tilde{\underline{\mathbf{s}}}^H$ relates to the correlation of the perturbation factor α across frequency, weighted by the source power cross spectrum $s^*(\omega_i)s(\omega_j)$. No closed form for $\hat{\underline{\mathbf{w}}}_{BB}(\theta)$ can be given in this case without explicit knowledge of that signal matrix. There are a number of possible implementations that represent suboptimal versions of (16) with different assumptions for the structure of the perturbation correlation and signal weighting matrix. A few cases are reviewed in the next section and a new computational effective alternative to existing techniques is also proposed.

A. Broadband incoherent processor

The so-called incoherent broadband Bartlett processor, originally proposed in Ref. 4, implicitly assumes that the random factor is simply $E[\alpha(\omega_i)\alpha^*(\omega_j)] = \sigma_\alpha^2 \delta_{ij}$, i.e., that the random perturbations are uncorrelated across frequency and have a constant power. Using that expression of the correlation of α in (12), plugged in (16) and solved for $\mathbf{w}$ gives

$$\hat{\underline{\mathbf{w}}}_{\text{inc}}(\theta) = \frac{\mathbf{H}(\theta)\underline{\mathbf{s}}}{\|\mathbf{H}(\theta)\underline{\mathbf{s}}\|}, \tag{17}$$

where $\underline{\mathbf{s}}$ is a K-dimensional vector which entries are $s(\omega_k)$. Thus, by replacement into (13), allows to obtain the processor expression

$$P_{\text{inc}}(\theta) = \frac{\sigma_\alpha^2 \sum_{k=1}^K |s(\omega_k)|^2 \mathbf{h}^H(\omega_k,\theta)\mathbf{C}_{yy}(\omega_k,\omega_k)\mathbf{h}(\omega_k,\theta)}{\|\mathbf{H}(\theta)\underline{\mathbf{s}}\|^2} \tag{18}$$

which is nothing more than a source power weighted sum of the diagonal matched-filtered autofrequency block matrices of the extended correlation matrix $\mathbf{C}_{yy}$. Notice that if σ_α had been assumed to be frequency dependent, a factor $\sigma_\alpha(\omega_k)$ would appear as weighting the terms in the summation in (18). In the case of a flat source power spectrum, Eq. (18) reduces to a simple summation of the quadratic terms across the discrete band of frequencies. When the source power spectrum is unknown but not flat, an unweighted incoherent processor is generally used which leads to the suboptimal incoherent broadband conventional estimator proposed in Ref. 4.

B. Broadband coherent processor

Although there is good evidence that for many of the real underwater propagation channels most of the energy is concentrated along the main diagonal of the cross-spectrum correlation matrix (the autofrequency terms) it is also clear that the same autofrequency terms would carry the noise power as it can be seen in expression (12). One of the motivations when performing coherent processing is to take advantage of the noiseless cross-frequency terms of (12). These cross-frequency terms have no noise but the signal information they contain may also be reduced, according to both the channel cross-frequency structure and the cross-frequency correlation of the random perturbation factor, as explained in the preceding section. This explains why in most studies, concerned with coherent processing, only the cross-frequency off-diagonal terms were used, excluding the diagonal autofrequency information.[9] There are actually several broadband coherent processors depending on the assumptions made for approximating the cross-frequency perturbation terms of the signal matrix $E[\tilde{\mathbf{s}}\tilde{\mathbf{s}}^H]$ of (16).

1. Coherent normalized processor

The *coherent normalized processor* (COH–N) has been proposed by Michalopoulou[7,19] and attempts to eliminate the source spectrum–perturbation weighting across frequency. At each frequency ω_i, a normalized model vector is defined as

$$\mathbf{n}_x(\omega_i,\theta_0)=\frac{\mathbf{x}(\omega_i,\theta_0)}{x_l(\omega_i,\theta_0)}, \tag{19}$$

where $x_l(\omega_i,\theta_0)$ is the signal received at sensor l. The choice of l depends on the actual signal-to-noise ratio (SNR) at that particular sensor. In a high SNR situation, if the noise contribution at sensor l is neglected, the normalized data model becomes

$$\mathbf{n}_x(\omega_i,\theta)\approx\mathbf{n}_h(\omega_i,\theta_0)+\frac{\mathbf{u}(\omega_i)}{h_l(\omega_i,\theta_0)s(\omega_i)\alpha(\omega_i)}. \tag{20}$$

Matching this model with an extended normalized replica vector yields a perfect match for the signal and a strongly correlated structure for the noise field due to the noise term in (20). In that case the *coherent-normalized* replica vector is written as

$$\hat{\mathbf{w}}_{\text{coh-}n}(\omega_i,\theta)=\mathbf{n}_h(\omega_i,\theta)=\frac{\mathbf{h}(\omega_i,\theta)}{h_l(\omega_i,\theta)}, \tag{21}$$

and using that expression in the Bartlett processor gives

$$\begin{aligned}P_{\text{coh-}n}(\theta)&=\sum_{i=1}^{K}\sum_{j=1}^{K}\mathbf{n}_h^H(\omega_i,\theta)\mathbf{n}_h(\omega_i,\theta_0)\mathbf{n}_h^H(\omega_j,\theta_0)\mathbf{n}_h(\omega_j,\theta)\\&\quad+\mathbf{n}_h^H(\omega_i,\theta)\mathbf{C}_{n_un_u}(\omega_i,\omega_j)\mathbf{n}_h(\omega_j,\theta),\end{aligned} \tag{22}$$

where $\mathbf{C}_{n_un_u}(\omega_i,\omega_j)$ is the cross-frequency correlation matrix of the normalized additive noise vector $\mathbf{n}_u$ defined in the second term of (20). Expression (22) shows a perfectly coherent match for the signal model part when $\theta=\theta_0$, and a noise term residual which is a constant when $i=j$, due to the white noise assumption, and has a correlation structure for $i\neq j$ that is highly dependent on the cross-frequency correlation of the perturbation $\alpha(\omega)$.

2. Matched-phase coherent processor

Another approximation to the broadband coherent processor has been recently proposed by Orris[9] where the correlation terms are explicitly included in the replica vector as unknowns and have therefore to be estimated. A new replica vector is defined as

$$\underline{\mathbf{w}}_{\text{coh-mp}}(\theta)=[\mathbf{h}^T(\omega_1,\theta)e^{j\hat{\phi}_h(\omega_1)},\ldots,\mathbf{h}^T(\omega_K,\theta)e^{j\hat{\phi}_h(\omega_K)}]^T, \tag{23}$$

where the phase terms $[\hat{\phi}_h(\omega_k);k=1,...,K]$ are the estimates that maximize the output power upon summation over sensor and frequency. Taking into account that, when carrying out that summation, each term has its complex conjugate, the energy contained in the imaginary part is lost. The unknown phase terms ϕ_h are estimated in such a way as to minimize that loss which, ideally, requires the unknown phase terms to be symmetric to the phase of the signal matrix terms in (12). If that is achieved all terms turn into real numbers and the sum is carried out in phase. In that case, and for a flat spectrum source, this processor is optimum. Replacing (23) in the Bartlett processor expression gives

$$\begin{aligned}P_{\text{coh-mp}}(\theta)=\sum_{i=1}^{K}\sum_{l=1}^{K}&\mathbf{h}^H(\omega_i,\theta)\mathbf{C}_{yy}(\omega_i,\omega_l)\\&\times\mathbf{h}(\omega_l,\theta)e^{-j[\hat{\phi}_h(\omega_i)-\hat{\phi}_h(\omega_l)]}.\end{aligned} \tag{24}$$

In practice, the problem associated to the matched-phase processor, according to Orris,[9] is the computation load necessary to obtain the estimates $\hat{\phi}_h$ of the phase shifts ϕ_h, for an exhaustive search over a realistic parameter space. That computation load is of the order of $o=J^K\times M\times N$, where J is the number of samples for the phase in $[0,2\pi]$, K is the number of frequencies and $M\times N$ is the θ parameter search grid (e.g., range versus depth). In practice, and as mentioned by Orris,[9] if the source location and relative phases have to be exhaustively searched, computation complexity limits the number of frequencies to $K=3$ while for a larger number of frequencies efficient search algorithms (e.g., simulated annealing) were proposed.

C. The cross-frequency incoherent processor

The cross-frequency incoherent processor is proposed in this paper and represents an alternative to overcome the computational burden of the matched-phase processor while keeping the same performance. This processor stems from the simple idea that the phase corrections for the surface maximum ($\theta=\theta_0$) are

$$\phi_h(\omega_i)-\phi_h(\omega_j)=\angle s(\omega_i)s^*(\omega_j)E[\alpha(\omega_i)\alpha^*(\omega_j)], \tag{25}$$

for all $i,j=1,...,K$ which can be seen by direct inspection of (12) and where $\angle$ means "phase of." When these corrections are correctly set the value of the maximum is just the sum of a series of real numbers, which are the modules of the quadratic terms across frequency, i.e.,

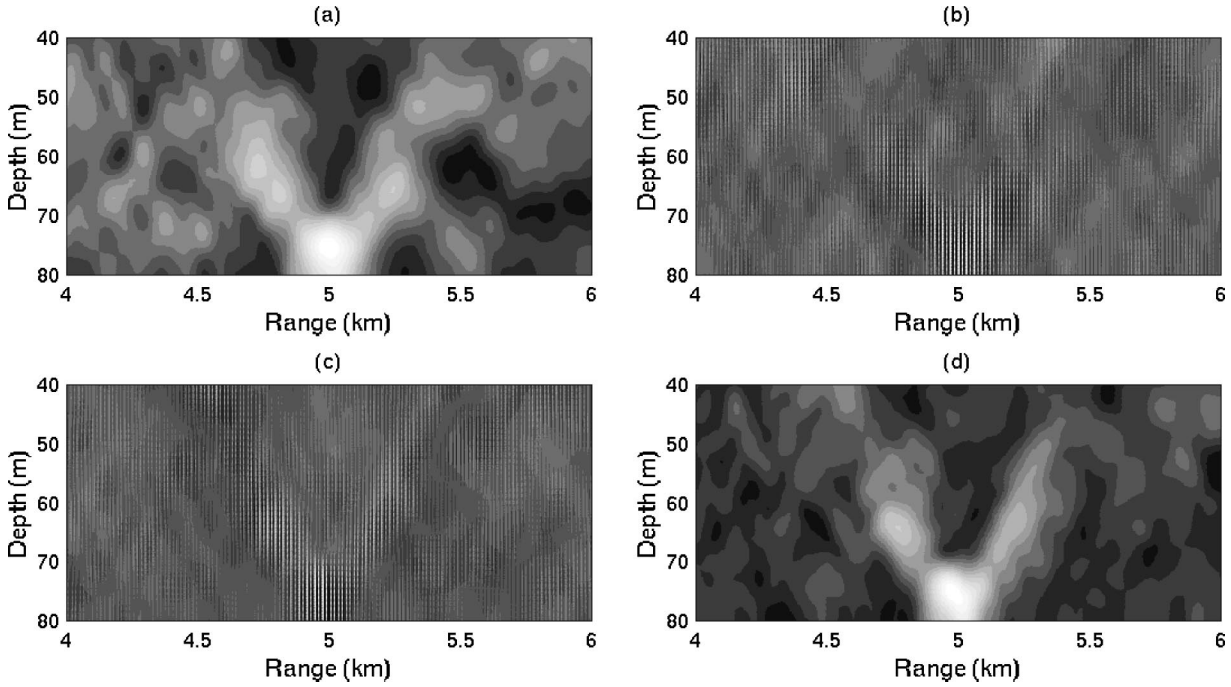

FIG. 1. Ambiguity surfaces computed with synthetic data generated without perturbation factor for the ADVENT'99 scenario at frequencies 300, 400, 500, and 600 Hz, at SNR $=-8$ dB and for the following processors: (a) incoherent conventional, (b) coherent normalized, (c) matched-phase coherent, and (d) incoherent cross frequency.

$$P_{\text{inc-xf}}(\theta)=\sum_{i=1}^{K}\sum_{j=1}^{K}\left|\mathbf{h}^{H}(\omega_i,\theta)\mathbf{C}_{yy}(\omega_i,\omega_j)\mathbf{h}(\omega_j,\theta)\right|. \tag{26}$$

The value of the maximum of the ambiguity surface obtained with (26) is exactly the same as that obtained with (24) with absolutely no phase parameter search. Therefore, the peak would have the same height and the same location, however the aspect of the resulting surface would be much different between the cross-frequency and the matched-phase processors: the former would have a smooth appearance, much like the incoherent processor, and the latter would have extremely narrow peaks distributed along the surface with, however, an overall envelop that is very similar to that of the cross-frequency incoherent processor. Examples on simulated data are given in the next section.

V. SIMULATION RESULTS

This section shows a few simulated data examples of the application of broadband MF processors to source localization. The data was simulated using the C-SNAP model[20] in a 80 m deep range-independent shallow water scenario similar to that of the ADVENT'99 experiment.[21] The acoustic source is placed at 76 m depth and at 5 km range from a 32-sensors vertical array. The source is emitting a series of multitones between 300 and 600 Hz with 100 Hz increment. The signals were generated in the frequency domain using (4) with an SNR of -8 dB and the correlation matrix was estimated using 32 snapshots. The noise level was set accordingly to the following SNR definition:

$$\text{SNR}_{\text{dB}}=10\log\frac{\sum_{k=1}^{K}\sigma_s^2(\omega_k)}{\sum_{k=1}^{K}\sigma_u^2(\omega_k)}, \tag{27}$$

where

$$\sigma_s^2(\omega_k)=\frac{E[\|\mathbf{h}(z_l,\omega_k,r,z_s)s(\omega_k)\|^2]}{L} \tag{28}$$

and

$$\sigma_u^2(\omega_k)=\frac{E[\|\mathbf{u}(\omega_k)\|^2]}{L}. \tag{29}$$

Figure 1 shows the range-depth ambiguity surfaces obtained for the above referred broadband Bartlett processors, P_{inc} (a), $P_{\text{coh-}n}$ (b), $P_{\text{coh-mp}}$ (c), and $P_{\text{inc-xf}}$ (d). In cases (b), (c), and (d) only the cross-frequency terms were used. As expected, the incoherent processors (a) and (d), gave similar smooth surfaces with a lower sidelobe structure for the cross-frequency processor. The coherent processors (b) and (c) also gave similar responses with a large number of very narrow peaks (up to only 1 m wide in range) that are due to a perfect alignment of the surfaces for all grid points. By formulating the matched-phase and the incoherent cross-frequency processors in terms of normal modes, it can be shown that the corresponding ambiguity surfaces are oscillating functions of the distance modulated by an amplitude factor that is the same in both processors. The peaky structure shown by the coherent processors results from a periodic phase alignment of the correlation terms at each pair of frequencies. At low SNR the coherent normalized processor (b), rapidly degrades due to the SNR limitation pointed out in (20). As explained above the matched-phase and the cross-frequency incoherent processors have analytically the same source detection performance with comparable peak-to-sidelobe ratios of 2.5 dB and 2.0 dB, respectively. Note that for the coherent processors a subsampling of the ambiguity surface in range can hide the sidelobe structure. The detection performance of the

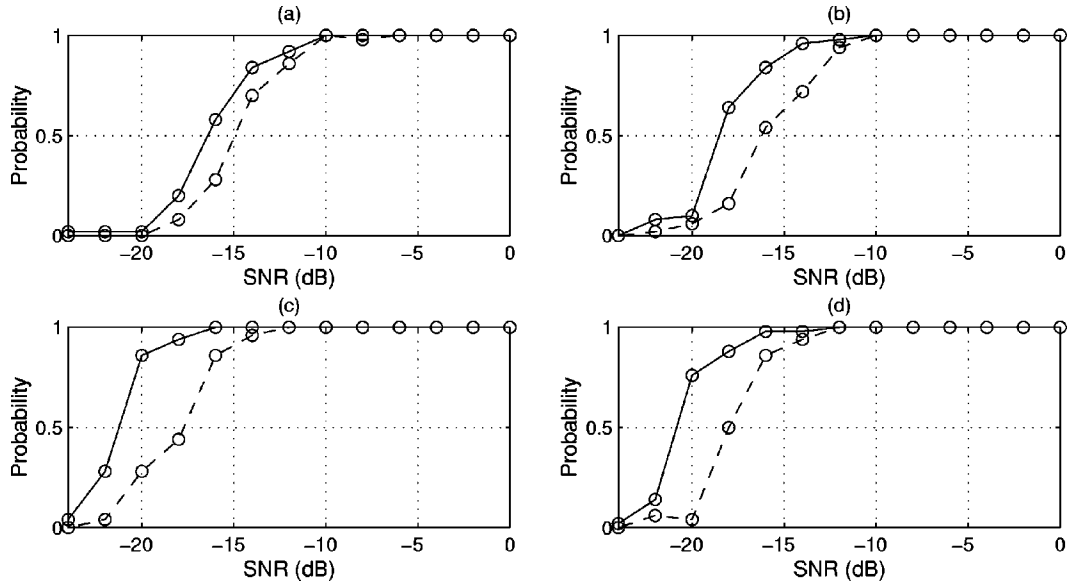

FIG. 2. Probability of correct source localization obtained on ADVENT'99 conditions simulated data for the broadband incoherent processor (dashed) and broadband cross-frequency processor (continuous) in the frequency band [500, 600] Hz for the following number of frequencies: 4(a), 7(b), 16(c) and also 16 but in the band [400, 700] Hz.

cross-frequency incoherent processor is shown in Fig. 2 for the model without perturbation. This performance was measured in terms of probability of correct source localization by determining how often the peak appeared at the correct location in 50 realizations. The environment is always that of the ADVENT'99 experiment. The effect of increasing the number of frequencies within a relatively small frequency band of 100 Hz around 550 Hz is shown in plots (a) to (c) of Fig. 2, where the number of frequencies is 4, 7, and 16, respectively. It can be noticed that the performance of the cross-frequency incoherent processor is always superior to that of the conventional (autofrequency) incoherent processor due to the higher number of frequencies involved and to the noise immunity, despite the inevitable decrease in channel structure power transmission at certain cross frequencies off the main diagonal. The number of ambiguity surfaces increases as K for the incoherent processor and as $K\times(K-1)/2$ for the cross-frequency incoherent processor. That fact results in a steady increase of the difference in performance with the number of discrete frequencies from 4 to 7 and then to 16. With 16 frequencies there is a gain in detection performance estimated to approximately 4 dB at useful detection probabilities. The result shown in plot (d) was obtained for a number of frequencies equal to 16 [the same as in plot (c)] but within a frequency band enlarged to 300 Hz, always centered at 550 Hz. The result is that there is a slight decrease of the performance of both processors, while that decrease is stronger for the incoherent cross frequency, thus there is a net loss of performance of the cross-frequency processor relative to the incoherent autofrequency processor. Other tests performed for relatively small number of closely spaced discrete frequencies clustered around center frequencies along the whole band gives better results than uniformly distributed frequencies in the same band.

In practice, with real data, these performance predictions obtained in simulation have to be balanced by the correlation of the perturbation factor across-frequency contributing to a net decrease of performance when enlarging the bandwidth around a given center frequency. That fact clearly favors the solution of using the proposed cross-frequency incoherent operating in closely spaced frequencies clustered at various frequencies in the useful band.

VI. A REAL DATA EXAMPLE

The ADVENT'99 data set was used as to provide a real world example for the assertions made in the preceding sections. The ADVENT'99 experiment took place during the month of May of 1999, in a nearly range independent area on the Strait of Sicily, Italy. The approximate depth of the area was 80 m and the acoustic signals were transmitted from a bottom mounted sound source and received on a 31-hydrophone vertical array. Various signal sequences at different frequencies and repetition rates were used. Also, the vertical array was successively located at ranges of approximately 2, 5, and 10 km. A complete description of the experimental setup can be found in Siderius *et al.*[21]

A. The perturbation factor

In order to justify the perturbation factor distribution, a signal tone at 200 Hz was extracted from the time series recorded during 18 hours on a mid-water-depth hydrophone at 10 km range from the signal source. The signal-to-noise ratio is expected to be$>$20 dB at that frequency, and the additive noise is assumed negligible compared to the signal term. Figure 3 shows the estimated pdf's based on the histograms obtained for the module—(a) and (c)—and for the phase—(b) and (d). In plots (a) and (b), module and phase pdf's are estimated using the normalization proposed in (6). It can be seen that the module is approximately Rayleigh distributed, with parameter $\lambda=1$ due to the normalization by y_0, while the phase is noncentered (also due to the normal-

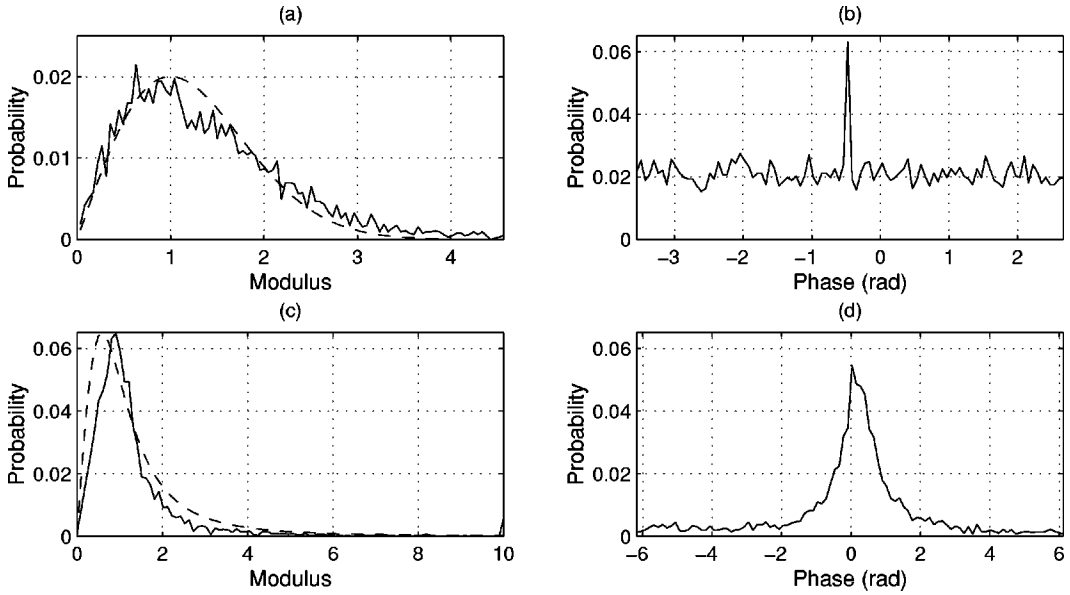

FIG. 3. Estimated probability density functions of signal perturbation factor from the ADVENT'99 data set at 200 Hz: using first element normalization for the module (a) and phase (b); using a sliding window along time for module (c) and phase (d).

ization), almost uniform in $[-\pi,\pi]$ with an outstanding peak at $\phi=-0.5$ rad of unknown nature. Instead, the sliding normalization of (7), applied in the same data set, provides the results shown in plots (c) and (d) for the module and phase, respectively. The module—plot (c)—is in this case approximately distributed according to the approximate Cauchy given by (B2), while that of the phase—plot (d)—does not resembles to a triangular function as a result from the difference of two uniformly distributed random variables. The distribution is approximately symmetric in $[-2\pi, 2\pi]$, but has a much narrower peak than expected for a triangular shaped pdf. Due to the complicated form of the expression of the phase pdf in the noncentered case [Appendix A, Eq. (A14)], it is difficult to theoretically predict what could be the expected pdf for the phase random variable $\phi_n-\phi_{n-1}$. Some numerical simulations using expression (A14) and realistic values for σ suggest that a bell-shaped centered pdf as that of Fig. 3(d) can most likely be obtained for $m_a>0$ and $m_b \approx 0$. [Note that the empirical distribution of Fig. 3(d) is, according to the theory, the autocorrelation of two identical pdf's as that obtained in (A14)]. A similar behavior was verified on the ADVENT'99 data set at various frequencies in the interval [200,1500] Hz, with however, an increasing broadening of the peak of the phase pdf with frequency. A broader pdf means a larger value for σ which is a well known effect leading to highly variable phase shifts at high frequency making it difficult to accurately predict. This discussion brings a key question for broadband applications, that is to determine which is the degree of correlation of the signal across frequency.

Using the same ADVENT'99 data set along a wide frequency band [200,1600] Hz, the correlation of the perturbation factor using the normalization (6) was estimated. The result is shown in Fig. 4 where a broad diagonal along the whole frequency band can be observed. Additional effects of frequency bandpass of the two transducers used to cover this wideband of frequencies can be seen on the artificially low levels of energy in the diagonal at about 800 Hz, which is the overlap transit in frequency band.

In order to obtain a complete view of the received signal correlation along frequency one has to add the deterministic effect of the channel correlation. As an example, a scenario similar to that of the ADVENT'99 was simulated to compute the cross-array coherence of the acoustic channel across the frequency band of interest. Figure 5 shows the result of the expression

$$\mathbf{C}_h(\omega_i,\omega_j)=\mathbf{h}^H(\omega_i)\mathbf{h}(\omega_j), \tag{30}$$

for $\omega_i,\omega_j\in[200,1600]$ Hz. It can be easily noticed from that figure that the energy is not concentrated on a single diagonal but on a band of frequencies around that diagonal. The bandwidth varies with frequency and with source–receiver geometry (not shown), e.g., it tends to be larger at longer ranges due to stronger multipath. There is also a sig-

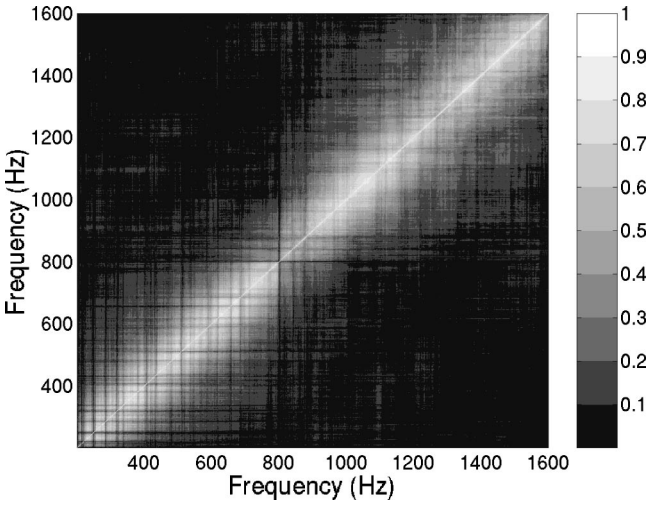

FIG. 4. Estimated correlation of normalized signal perturbation factor over the band 200–1600 Hz using the LFM data of the ADVENT'99 experiment at 5 km source–receiver range.

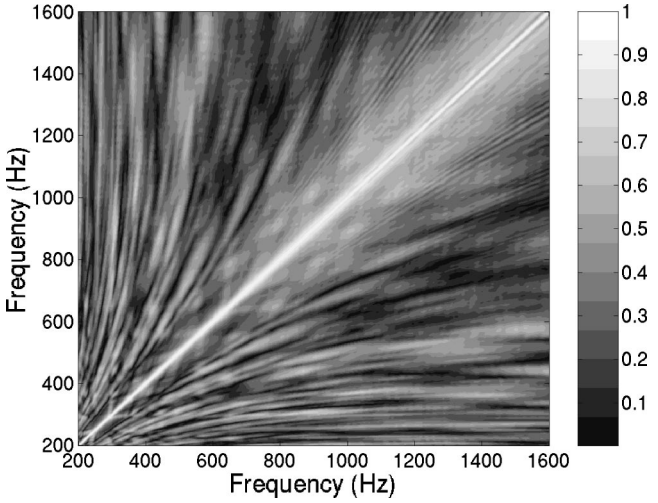

FIG. 5. Channel coherence of simulated acoustic field in the band 200–1600 Hz in the ADVENT'99 conditions with a source–receiver range of 5 km.

nificant amount of energy well apart from the diagonal due to mode interference.

These two last Figs. 4 and 5 can be compared by means of a third figure that is the frequency correlation matrix of the signals received at 5 km range during the ADVENT'99 sea trial (Fig. 6). The first comment is that the resemblance between this figure and that obtained with simulated data is striking. It appears that the cross-frequency energy spread out of the diagonal is largely attenuated when compared with the synthetic data example, that is particularly true in the low frequency range but is also evident at high frequencies where the main diagonal lobe is narrower. An estimation of the effective -3 dB bandwidth shows that at least 100 Hz are available throughout the analyzed frequency range between 200 and 1600 Hz. Comparison of Figs. 5 and 6 should be done under the assumption that the latter contains information on the source spectrum level that might alter the result. Note that the values plotted in the last three figures were normalized, so there is no information on the relative levels of each term on the final observed signal.

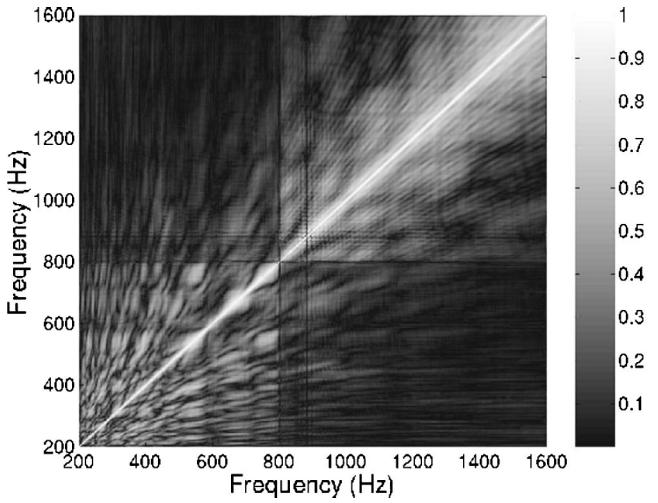

FIG. 6. Estimated correlation of received signal over the band 200–1600 Hz using the LFM data of the ADVENT'99 experiment at 5 km source–receiver range.

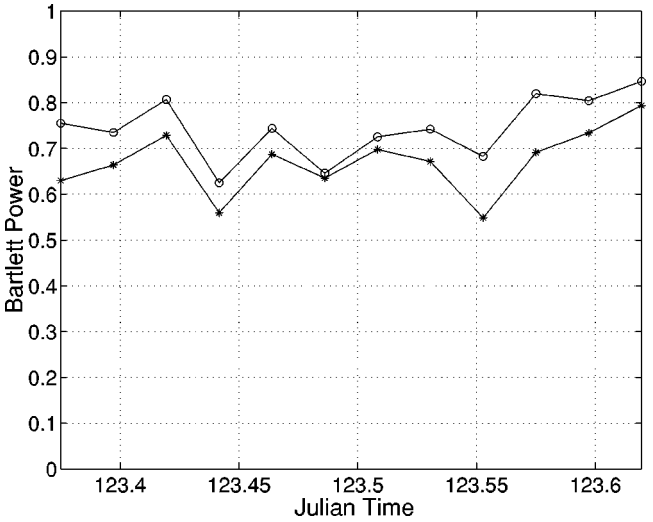

FIG. 7. Bartlett power for source localization using the cross-frequency incoherent processor in the 5 km range ADVENT'99 data set: 200 Hz frequency band clustered processing (○) and 600 Hz wide band processing (∗).

B. Broadband MFP

The results shown in the preceding section suggest that due to the limited correlation of the perturbation factor, cross-frequency broadband processors should preferably operate on relative narrow bands of 100 or 200 Hz than on wide frequency bands. In order to illustrate that point with a real data example, a series of vertical array observations at 5 km range and in the band 400–1000 Hz was drawn from the ADVENT'99 data set and processed with the proposed cross-frequency incoherent Bartlett processor for range-depth source localization purpose. Figure 7 shows the Bartlett power results obtained during approximately five consecutive hours of data for two processing schemes: the seven tones at 100 Hz spacing between 400 and 1000 Hz were processed in a single frame (∗) and the same tones were processed in three groups of three frequencies each (○)—groups (400,500,600), (600,700,800), and (800,900,1000). The number of cross-frequency terms is 21 in the first scheme and nine in the second scheme. Despite that difference the Bartlett power, i.e., the value of the normalized peak in the final ambiguity surface at the correct source location, is always higher for the processing in the clustered band than in the wide band. The range-depth source localization performance was the same for both processors. The grouping of frequencies in a limited band acts as an automatic scheme to exclude the correlation terms that yield worst SNR at the processor's output caused by low cross correlation of the signal components.

VII. CONCLUSION

For many years, underwater acoustic signal processing was devoted to the detection and/or localization of narrowband or broadband random sources using a multisensor horizontal array. Localization here meant bearing estimation, which was the main scope of a wide, yet powerful, suite of techniques. That situation has dramatically changed with the wide spread of physical model codes being able to predict the acoustic channel propagation characteristics at various

ranges and depths and in different environmental conditions with practical relevance. These are the generically called matched-field (MF) techniques, that are used not only for detecting and localizing submerged targets but also, and more importantly, to probe the ocean (ocean tomography) and the seafloor (geoacoustic inversion). From a purely signal processing point of view, the problem has lost most of its interest since the knowledge of an image of the received signal limits the range of (optimum) methods to the well-known matched filter. However, numerous tests with real data have shown that physical models, at least in their present form, can not account for acoustic channel fluctuations between the source and the receiver(s).

This paper approaches the problem of modeling the received signal as a mixture of a deterministic structure, that can be predicted by a suitable acoustic model, and a random perturbation factor that is supposed to be space invariant (within the physical sensor array limits) and time variant. Estimation of that perturbation factor on the ADVENT'99 data set has shown that its amplitude was approximately Rayleigh distributed but its phase did not follow a uniform distribution as it is assumed in many texts. Those distributions were apparently frequency invariant with, however, a consistent variance increase for the random perturbation phase term. It was also shown, based on the same real data set, that a band of frequencies extending to 100 Hz can be safely assumed to contain a significant channel and random perturbation cross-frequency signal correlation.

Making use of that data model allowed for derivations of optimum broadband MF processors, according to the various assumptions on the signal and perturbation factor correlation across frequency. The uncorrelated perturbation assumption led to the well-known incoherent broadband processor. The often used unweighted processor was shown to be optimum only on the flat source spectrum case. Other coherent broadband processors proposed in the literature are shown to provide either suboptimum performance in real noisy situations or to have serious limitations in terms of the number of frequencies processed in a reasonable computation time. An alternative incoherent algorithm is proposed that is shown to have the same detection performance as the matched-phase coherent processor. That processor—the incoherent cross-frequency processor—is able to process any number of frequencies with only a slightly larger computation time than that of the incoherent processor with however, the advantage of using the asymptotically noise-free cross-frequency terms and without making any use of the source spectrum. In that sense the proposed incoherent cross-frequency processor can be compared with that developed by Westwood,[15] since neither used the source spectrum knowledge with, however, one main difference that is that the former uses cross-frequency terms while the latter only used autofrequencies. Finally, a simple simulated test on realistic conditions, illustrated the detection performance of the proposed cross-frequency incoherent processor when compared with the autofrequency incoherent processor for a well chosen frequency band relative to the band of coherence of the underwater channel. It was concluded that the cross-frequency processor always outperformed the autofrequency processor clearly showing that it was advantageous to chose clustered sets of closely spaced discrete frequencies instead of an equivalent number of uniformly distributed frequencies along the whole band.

ACKNOWLEDGMENTS

The authors would like to thank Jürgen Sellschopp, Martin Siderius and Peter Nielsen responsible for the ADVENT'99 experiment design and data collection, and the SACLANT Undersea Research Center for providing the data of the ADVENT'99 experiment. This work was partially financed by Fundação para a Ciência e a Tecnologia–FCT, Portugal, under Contract No. ATOMS,PDCTM/P/MAR/15296/1999.

APPENDIX A: ENVELOPE AND PHASE DISTRIBUTIONS

Let $\alpha = a + jb$ be a random variable such that

$$a{:}N(0,\sigma^2) \quad \text{and} \quad b{:}N(0,\sigma^2), \tag{A1}$$

where a and b are uncorrelated, in which case it is well known that the polar notation $\alpha = |\alpha|\exp(j\phi)$ implies that

$$|\alpha|{:}R\left[\sigma\sqrt{\frac{\pi}{2}},\sigma^2\left(2-\frac{\pi}{2}\right)\right],$$

$$\Phi{:}U_{-\pi,\pi}\left(0,\frac{\pi}{\sqrt{3}}\right),$$

where R and U designate Rayleigh and Uniform distributions, respectively. The question is to determine the distribution of $V = |\alpha|$ and Φ when a and b are not zero mean. So, let us assume that

$$a{:}N(m_a,\sigma^2), \quad b{:}N(m_b,\sigma^2),$$

with joint probability density function (pdf)

$$p_{A,B}(a,b) = \frac{1}{2\pi\sigma^2}\exp\left[-\frac{(a-m_a)^2+(b-m_b)^2}{2\sigma^2}\right]. \tag{A2}$$

It is known that the square module $Y = A^2 + B^2$ follows a noncentral chi-square distribution $\chi^2(s)$ with the noncentrality parameter $s^2 = m_a^2 + m_b^2$. The pdf of Y is given by

$$p_Y(y) = \frac{1}{2\sigma^2}\exp\left(-\frac{y+s^2}{2\sigma^2}\right)I_0\left(\frac{\sqrt{y}s}{\sigma^2}\right), \quad y \geqslant 0 \tag{A3}$$

where I_0 is the zeroth-order modified Bessel function of first kind. Thus a simple change of variable $R = \sqrt{Y}$ gives us the pdf of R as

$$p_R(r) = p_Y(r^2)|J|, \tag{A4}$$

where $J = 2r$ is the Jacobian of the transformation giving

$$p_R(r) = \frac{r}{\sigma^2}\exp\left(-\frac{r^2+s^2}{2\sigma^2}\right)I_0\left(\frac{rs}{\sigma^2}\right), \quad r \geqslant 0, \tag{A5}$$

which represents a Rice distribution with parameter $s^2 = a^2 + b^2$.

For the phase ϕ the calculation is more elaborated and the result is not easy to interpret. Let us first make the transformation

$$\begin{cases} V^2 = A^2 + B^2 \\ \Phi = \arctan(B/A) \end{cases} \Leftrightarrow \begin{cases} A = V\cos\Phi, \\ B = V\sin\Phi, \end{cases} \tag{A6}$$

with the Jacobian, $|J|=v$, thus the joint pdf of the new variables (V,Φ) is

$$p_{V,\Phi}(v,\phi) = p_{A,B}(a,b)|J| = \frac{v}{2\pi\sigma^2}\exp\left[-\frac{(v\cos\phi-m_a)^2+(v\sin\phi-m_b)^2}{2\sigma^2}\right]. \tag{A7}$$

The marginal distribution can be obtained as

$$p_\Phi(\phi)=\int_0^\infty p_{V,\Phi}(v,\phi)dv. \tag{A8}$$

The first step to solve the integral obtained by replacing (A7) in (A8) is to develop the sum of squares in the exponent to get (only for the exponent)

$$-\frac{1}{2\sigma^2}[v^2-2v(m_a\cos\phi+m_b\sin\phi)+m_a^2+m_b^2], \tag{A9}$$

which can be made a square of the sum, by subtracting and adding the term $(m_a\sin\phi-m_b\cos\phi)^2$ which gives for the pdf,

$$p_\Phi(\phi)=\frac{1}{2\pi\sigma^2}e^{-(m_a\sin\phi+m_b\cos\phi)^2/2\sigma^2}\times\int_0^\infty v\exp\left\{-\frac{[v-(m_a\cos\phi+m_b\sin\phi)]^2}{2\sigma^2}\right\}dv. \tag{A10}$$

Performing a change of variable $z=v-(m_a\cos\phi+m_b\sin\phi)$ reduces to

$$p_\Phi(\phi)=\frac{1}{2\pi\sigma^2}e^{-(m_a\sin\phi-m_b\cos\phi)^2/2\sigma^2}\times\int_{-(m_a\cos\phi+m_b\sin\phi)}^\infty ze^{-z^2/2\sigma^2}dz+\cdots+\frac{m_a\cos\phi+m_b\sin\phi}{2\pi\sigma^2}e^{-(m_a\sin\phi-m_b\cos\phi)^2/2\sigma^2}\times\int_{-(m_a\cos\phi+m_b\sin\phi)}^\infty e^{-z^2/2\sigma^2}dz. \tag{A11}$$

The first integral equates to

$$\exp\left[-\frac{(m_a\cos\phi+m_b\sin\phi)^2}{2\sigma^2}\right], \tag{A12}$$

that gives by replacement in (A11) and by knowing that the second integral is even, allows for changing the sign of the integration bounds

$$p_\Phi(\phi)=\frac{\exp\left(-\frac{m_a^2+m_b^2}{2\sigma^2}\right)}{2\pi\sigma^2}+\cdots+\frac{m_a\cos\phi+m_b\sin\phi}{2\pi\sigma^2}\times e^{-(m_a\sin\phi-m_b\cos\phi)^2/2\sigma^2}\times\int_{-\infty}^{m_a\cos\phi+m_b\sin\phi}e^{-z^2/2\sigma^2}dz. \tag{A13}$$

Now, a small change of variable $\lambda=z/\sigma$ allows to view this last integral as the distribution function of a standard normally distributed random variable as

$$p_\Phi(\phi)=\frac{\exp\left(-\frac{m_a^2+m_b^2}{2\sigma^2}\right)}{2\pi\sigma^2}+\cdots+\frac{m_a\cos\phi+m_b\sin\phi}{2\pi\sigma}\times e^{-(m_a\sin\phi-m_b\cos\phi)^2/2\sigma^2}\times\int_{-\infty}^{(m_a\cos\phi+m_b\sin\phi)/\sigma}e^{-\lambda^2/2}d\lambda. \tag{A14}$$

It is not possible to continue any further knowing the difficulties to calculate the integral in the second term. Available approximate expressions exist for large $m_a\cos\phi+m_b\sin\phi/\sigma$ but that assumption does not makes much sense for the problem at hand.

APPENDIX B: ESTIMATING THE RANDOM PERTURBATION FACTOR DISTRIBUTION

Let α_n and α_{n-1} be two independent Rayleigh distributed random variables with pdf's,

$$p_\alpha=\frac{\alpha}{\lambda}e^{-\alpha^2/2\lambda^2},\quad \alpha\geqslant 0. \tag{B1}$$

The random variable Z defined as $Z=\alpha_n/\alpha_{n-1}$ can be shown to follow a pdf as

$$p_Z(z)=\frac{2\lambda_n^2}{\lambda_{n-1}^2}\frac{z}{(z^2+\lambda_n^2/\lambda_{n-1}^2)^2},\quad z\geqslant 0. \tag{B2}$$

Separately, if Φ_n and Φ_{n-1} are two independent Uniformly distributed random variables in $[-\pi,\pi]$, then it can be easily demonstrated that the pdf of the random variable $\Delta\Phi=\Phi_n-\Phi_{n-1}$ is given by the correlation between the pdf's of the two random variables Φ_n and Φ_{n-1}, i.e.,

$$p_{\Delta\Phi}(\Delta\phi)=\int_{-\infty}^\infty p_{\Phi_n}(\Delta\phi+\tau)p_{\Phi_{n-1}}(\tau)d\tau, \tag{B3}$$

which, can be easily evaluated for Uniform distributions as

$$p_{\Delta\Phi}(\Delta\phi)=\begin{cases}\frac{1}{8\pi^2}(2\pi-\Delta\phi), & -2\pi\leqslant\Delta\phi\leqslant 2\pi,\\ 0, & \text{otherwise.}\end{cases} \tag{B4}$$

[1] H. P. Bucker, "Use of calculated sound fields and matched-detection to locate sound source in shallow water," J. Acoust. Soc. Am. **59**, 368–373 (1976).

[2] M. J. Hinich, "Maximum-likelihood signal processing for a vertical array," J. Acoust. Soc. Am. **54**, 499–503 (1973).

[3] A. B. Baggeroer, W. A. Kuperman, and P. N. Mikhalevsky, "An overview

of matched field methods in ocean acoustics,'' IEEE J. Ocean. Eng. **18**, 401–424 (1993).
[4] A. B. Baggeroer, W. A. Kuperman, and H. Schmidt, ''Matched field processing: Source localization in correlated noise as an optimum parameter estimation problem,'' J. Acoust. Soc. Am. **83**, 571–587 (1988).
[5] A. Tolstoy, ''Computational aspects of matched field processing in underwater acoustics,'' in *Computational Acoustics*, edited by D. Lee, A. Cakmak, and R. Vichnevetsky (North-Holland, Amsterdam, 1990), Vol. 3, pp. 303–310.
[6] Z.-H. Michalopoulou, ''Matched-field processing for broadband source localization,'' IEEE J. Ocean. Eng. **21**, 384–392 (1996).
[7] Z.-H. Michalopoulou, ''Source tracking in the Hudson Canyon experiment,'' J. Comput. Acoust. **4**, 371–383 (1996).
[8] S. P. Czenszak and J. L. Krolik, ''Robust wideband matched-field processing with a short vertical array,'' J. Acoust. Soc. Am. **101**, 749–759 (1997).
[9] G. J. Orris, M. Nicholas, and J. S. Perkins, ''The matched-phase coherent multi-frequency matched field processor,'' J. Acoust. Soc. Am. **107**, 2563–2575 (2000).
[10] C. S. Clay, ''Optimum time domain signal transmission and source location in a waveguide,'' J. Acoust. Soc. Am. **81**, 660–664 (1987).
[11] S. Li and C. S. Clay, ''Optimum time domain signal transmission and source location in a waveguide: Experiments in an ideal wedge waveguide,'' J. Acoust. Soc. Am. **82**, 1409–1417 (1987).
[12] L. N. Frazer and P. I. Pecholcs, ''Single-hydrophone localization,'' J. Acoust. Soc. Am. **88**, 995–1002 (1992).
[13] J. H. Miller and C. S. Chiu, ''Localization of the sources of short duration acoustic signals,'' J. Acoust. Soc. Am. **92**, 2997–2999 (1992).
[14] D. P. Knobles and S. K. Mitchell, ''Broadband localization by matched fields in range and bearing in shallow water,'' J. Acoust. Soc. Am. **96**, 1813–1820 (1994).
[15] E. K. Westwood, ''Broadband matched-field source localization,'' J. Acoust. Soc. Am. **91**, 2777–2789 (1992).
[16] R. K. Brienzo and W. S. Hodgkiss, ''Broadband matched-field processing,'' J. Acoust. Soc. Am. **94**, 2821–2831 (1993).
[17] I. Tolstoy and C. S. Clay, *Ocean Acoustics: Theory and Experiments in Underwater Sound* (AIP, New York, 1966).
[18] W. B. Davenport, Jr. and W. L. Root, *An Introduction to the Theory of Random Signals and Noise* (IEEE Press, New York, 1987).
[19] Z.-H. Michalopoulou, ''Robust multi-tonal matched-field inversion: A coherent approach,'' J. Acoust. Soc. Am. **104**, 163–170 (1998).
[20] C. M. Ferla, M. B. Porter, and F. B. Jensen, ''C-SNAP: Coupled SACLANTCEN normal mode propagation loss model,'' Memorandum SM-274, SACLANTCEN Undersea Research Center, La Spezia, Italy, 1993.
[21] M. Siderius, P. L. Nielsen, J. Sellschopp, M. Snellen, and D. G. Simons, ''Experimental study of geo-acoustic inversion uncertainty due to ocean sound-speed fluctuations,'' J. Acoust. Soc. Am. **110**, 769–781 (2001).

Material property estimation in thin plates using focused, synthetic-aperture acoustic beams

Dong Fei,[a] D. E. Chimenti, and Sorin V. Teles
Center for Nondestructive Evaluation and Department of Aerospace Engineering and Engineering Mechanics, Iowa State University, Ames, Iowa 50011

(Received 27 June 2002; revised 24 January 2003; accepted 27 January 2003)

The method developed here exploits the wide angular range of focused acoustic probes and the large synthetic aperture of scanned transducers to permit a rapid and reliable estimation of material properties in thin plates. It is found in several tests with various materials that estimates of elastic behavior using this method agree with contact measurements to within less than 5%. The method utilizes transmission (or reflection) coefficient reconstruction for an infinite thin plate, across a wide range of frequency and wave number, from which elastic property estimates are made. Data collected over a large synthetic acoustic aperture are processed with temporal and spatial Fourier transforms applied to change the acquired data from the coordinate and time domains to the wave number and frequency domains. Extrinsic real-beam effects on the data are accounted for with a complex transducer point analysis. Transmission measurements yield reconstructed data extending to the mode cutoffs, permitting easy and nearly unambiguous estimation of a subset of the elastic stiffnesses. For anisotropic plates, elastic stiffnesses are estimated with an inversion procedure that uses only limited data carefully selected from different portions of the measured scattering coefficient. Estimates are made by reconstructing in a stepwise fashion, based on sensitivity studies, where only one stiffness is estimated from the data at any one time, restricting the optimization to a robust one-dimensional search.
[DOI: 10.1121/1.1561496]

PACS numbers: 43.35.Cg, 43.20.Mv [YHB]

I. INTRODUCTION

The characterization of elastic material properties has occupied many researchers in ultrasonics for nearly half a century. More recently, it has become important for the assurance of aircraft structural integrity to estimate stiffnesses in composite laminates. Work has appeared within the past ten or so years in which elastic properties of composite materials have been the focus of the investigation.[1–13] Hosten *et al.*,[1] studied lossy media using inhomogeneous waves, whereas Weaver *et al.*[2] used transient waves generated by a point source to characterize composite laminates. Karim *et al.*,[3] attempted to fit all elastic stiffnesses in one calculation to data from selected Lamb wave measurements. An energy approach was taken by Karunasena *et al.*[4] to calculate plate wave dispersion, and Deschamps and Hosten[5] evaluated the effect of viscous damping on plate waves. Properties of thick composites were studied by Hsu and Margetan using acousto-ultrasonics.[6] Through-transmission pulse propagation methods based on time-of-flight were applied by Rohklin and Wang[7] to deduce the elastic stiffnesses of plates, without the need for group-velocity methods. Point-source techniques were used by Veidt and Sachse[8] to analyze plate wave propagation in composites.

A critical realization was made by Rohklin and Chimenti,[9] who demonstrated that isolated areas of the plate wave dispersion curves have predominant influence on specific elastic stiffnesses. We draw on this finding for advances reported in this article. A synthetic-aperture method to use information in the transducer spatial-frequency spectrum was introduced by Safaeinili *et al.*[10] to characterize viscoelastic properties of materials in air-coupled acoustic measurements. The effects of transducer beams and geometry was the subject of an in-depth experimental and theoretical study by Lobkis *et al.*[11] Further characterization experiments in air were carried out by Hosten *et al.*[12] An extension of synthetic-aperture scanning in fluid-coupled experiments by Lobkis *et al.*[13] demonstrated a robust technique to estimate the large in-plane composite stiffness. While a number of works are cited here, space limitations prevent the mention of many other contributions. A recent review article[14] includes further discussion of much of this additional work.

In our own recent studies[15,16] we have employed highly focused transducers to greatly speed the acquisition of the spatial frequency spectral information from thin plates to estimate the reflection coefficient (RC) and to deduce its associated plate wave dispersion spectrum. We exploit the wide angular beam spread of highly focused cylindrical transducers to generate a broad spatial frequency spectrum, permitting us to map in a single coordinate scan the zeroes of the plate RC. Detailed modeling of the transducer beam effects on the receiver voltage with either planar or focused transducers has permitted us to isolate the contributions of extrinsic experimental elements, such as transducer size, location, and focal length from intrinsic material properties. This separation is critical for accurate property estimation, because the extrinsic experimental effects on the spectrum of RC zeroes can be as large as those caused by the material properties of the plate.[11]

[a]Author to whom correspondence should be addressed. Current address: Caterpillar, Inc., (41) Technical Center-E/854, P.O. Box 1875, Peoria, IL 61656-1875. Electronic mail: fei_dong@cat.com

In this work we extend this principle to fluid-coupled transmission measurements, and at the same time present a reliable method to infer elastic properties from plate wave data acquired in a focused, synthetic aperture scan. Reflection measurements have the advantage of single-side access, but because of geometric restrictions on the transducers, the mode cutoffs and their neighboring regions (phase-match angles of 3° or less) are nearly impossible to access experimentally. In a transmission geometry the transducers can be easily aligned to very small orientation angles, including zero, making it possible to map out all the mode cut-offs within the transducer frequency bandwidth. Because the mode cutoff frequencies have a simple relationship to either the longitudinal or shear wave velocities in the thickness direction of the plate, the associated longitudinal and shear stiffnesses can be determined directly and simultaneously from a single transducer scan. This method provides a complete elastic property estimation procedure for an isotropic plate and is of particular significance to characterize thin plates for which it is often difficult to apply contact transducers to measure shear stiffnesses. For an anisotropic plate, because the longitudinal and shear stiffnesses in the thickness direction are directly estimated using the mode cutoff frequencies, the reliability of the elastic property inversion procedure is greatly improved. A related method has been previously used by Xu *et al.*[17] in a $V(z)$ geometry with a line-focused transducer to reconstruct the reflection function of immersed plates. Recently, Lee[18] further improved the $V(z)$ method to measure the dispersion curves of leaky Lamb waves. Unlike the synthetic aperture method, however, the $V(z)$ methods scan the transducer normal to the plate and the wave number of the leaky Lamb waves (which propagate along the plate) is measured indirectly. The data processing procedure is therefore inherently more complex and less accurate than that of the synthetic aperture method.

The remaining properties of an anisotropic plate are inferred by using data from isolated portions of the dispersion spectrum. We introduce and demonstrate a method, based on a highly selective data targeting procedure, that reduces greatly the redundancy inherent in plate wave dispersion data, while avoiding possible instabilities that can occur in multidimensional parameter optimization. Most plate wave material property characterization studies performed to date have attempted to deduce elastic stiffnesses from a full set of data in a single iterative calculation using various well-known multiparameter fitting schemes. The difficulty with such an approach, and its major disadvantage, is that the highly redundant plate wave dispersion data are not equally sensitive to all elastic properties in all parts of the dispersion spectrum. The problem is compounded by the fact that more than one set of elastic stiffnesses can often be made to fit the same experimental dispersion data acceptably well if all available elastic parameters in an anisotropic medium are adjusted all at once. A careful study of the characteristics of the dispersion data has shown that it is possible to get every individual stiffness in a targeted, stepwise manner.[15] By targeting the extraction of elastic properties to specific portions of the dispersion spectrum and fitting only one stiffness at a time, a complicated and possibly error-prone multi-dimensional optimization scheme can be avoided, in favor of a highly stable and reliable one-dimensional procedure. The result is an accurate and repeatable estimate of elastic stiffnesses. Although these estimates are final results in themselves, it would be possible to use them as input to a global polishing routine that could then optimize the entire data set.

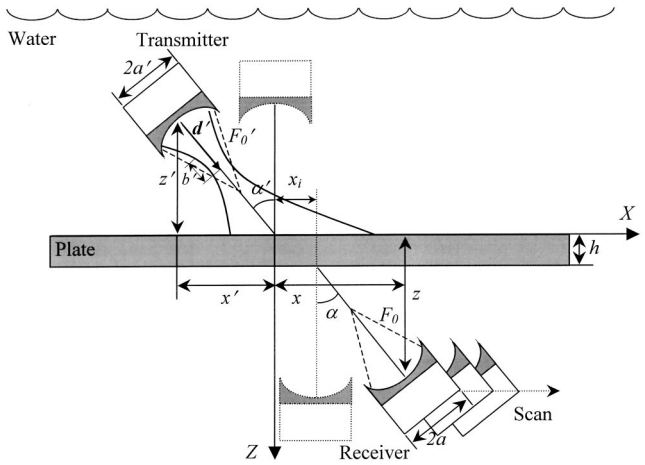

FIG. 1. Geometric configuration used in the experiment and calculation. The orientation angle of the transmitting and receiving transducers, respectively α' and α, can both be zero.

II. MEASUREMENT PRINCIPLE AND MODEL

To maximize the range of spatial frequencies sampled in a single coordinate scan, we employ highly focused transducers. In the measurement geometry shown in Fig. 1, the transmitting probe has a radius of a' and a focal length of F_0', and the receiver has a radius of a and a focal length of F_0. The central axes of the transmitter and receiver are oriented, respectively, at α' and α with respect to the z axis. The distances from the aperture centers of the transmitter and the receiver to the plate are z' and z, respectively. Conventionally, the transmitter and the receiver are aligned to nominally the same angle and in transmission can be oriented normal to the plate, i.e., α' and α equal to zero, as shown by the sketches in dashed lines in Fig. 1.

In this section we employ the complex transducer point (CTP) approach[16,19–21] to model the focused transducers as a prelude to developing an expression for the receiver voltage at a single frequency and receiver position. We then analyze the calculated voltage using a synthetic aperture scan technique and arrive at theoretical predictions of the processed experimental signals in the $k-f$ (wave-number-frequency) domain, where the comparison between model and experiment is made. The method of the rapid reconstruction of the transmission coefficient (TC) is also discussed below, followed by a description of the reconstruction strategy for elastic stiffnesses of both isotropic and anisotropic plates. Because a planar transducer can be considered to be a curved aperture with an infinite focal length, the following analysisis equally applicable to measurements using a pair of identical planar transducers.

A. Receiver voltage in the $x-f$ domain

A linear and electroacoustically reciprocal Gaussian beam transducer, used either as a transmitter or a receiver,

can be replaced by a CTP whose position is a complex spatial coordinate, according to the following operation,[20]

$$\mathbf{r}\rightarrow\tilde{\mathbf{r}}=\mathbf{r}+\mathbf{d}+i\mathbf{b}, \tag{1}$$

where vector $\mathbf{r}=(x,y,z)$ is the real location of the transducer aperture center, vector $\tilde{\mathbf{r}}=(\tilde{x},\tilde{y},\tilde{z})$ is a complex vector specifying the location of CTP in the complex plane, vector **d** is the transducer Gaussian beam waist location relative to the transducer aperture center, and vector **b** specifies the transducer beam direction and its Fresnel length. The directions of vectors **d** and **b** are the same: both are in the beam direction. The magnitude of vector **b**, or the Fresnel length b, is related to the $1/e$ beam width at the waist location W through $b=\frac{1}{2}k_fW^2$, where $k_f(=\omega/c_f)$ is the fluid wave number, ω is the circular frequency, and c_f is the sound speed in the fluid. The beam width at the waist location W and the distance between the waist location and the transducer aperture center d, which is also the magnitude of vector **d**, are given by[22]

$$W=W_0\frac{\beta}{(1+\beta^2)^{1/2}},\quad d=\frac{F_0}{1+\beta^2}, \tag{2}$$

where $\beta=2F_0/(k_fW_0^2)$, F_0 is the transducer focal length, and W_0 is the beam width at the transducer aperture. A good estimate is given by $W_0=0.752a$,[11,22] where a is the radius of the transducer aperture. For planar transducers, we simply let F_0 be infinite, and we have that $d=F_0/(1+\beta^2)=k_f^2W_0^4F_0/(k_f^2W_0^4+4F_0^2)\rightarrow 0$, which means the beam waist is at the aperture center, and thus $W=W_0$.

To model the receiver voltage in the configuration shown in Fig. 1, we apply the CTP model to both the transmitting and receiving transducers and obtain the following complex coordinates, respectively, for the transmitter and the receiver:

$$\begin{aligned}&\tilde{x}'=x'+d'\sin\alpha'+ib'\sin\alpha',\quad \tilde{y}'=y',\\&\tilde{z}'=z'+d'\cos\alpha'+ib'\cos\alpha',\end{aligned} \tag{3}$$

$$\begin{aligned}&\tilde{x}=x-d\sin\alpha-ib\sin\alpha,\quad \tilde{y}=y,\\&\tilde{z}=z-d\cos\alpha-ib\cos\alpha.\end{aligned} \tag{4}$$

By applying Auld's reciprocity theorem[23] at a single receiver position x and measurement frequency f, the receiver voltage $V(x,f)$ can be synthesized from the spectral decomposition of the complex transmitter point source, weighted by the plane wave scattering coefficient,[20,21]

$$\begin{aligned}V(x,f)=&-\frac{1}{8\pi^2}\gamma(\omega)\omega\rho_f\int_{-\infty}^{\infty}\int_{-\infty}^{\infty}T(k_x,k_y,f)\\&\times\frac{\exp[ik_x(\tilde{x}-\tilde{x}')+ik_y(\tilde{y}-\tilde{y}')-ik_z(\tilde{z}-\tilde{z}')]}{k_z}\\&\times dk_x\,dk_y,\end{aligned} \tag{5}$$

where $\gamma(\omega)$ is the combined frequency response of both transducers and their associated electronics, ρ_f is the mass density of the coupling fluid, T is the plane-wave transmission coefficient for the fluid-loaded plate, and k_x, k_y, and $k_z(=\sqrt{k_f^2-k_x^2-k_y^2})$ are, respectively, the x, y, and z components of the wave vector of the angular spectrum plane-wave components.

B. Receiver voltage in the *k–f* domain and TC reconstruction

The case we analyze here is that of a two-dimensional beam. This construct models well our experimental arrangement with its cylindrically focused transducers. We assume that both the transmitter and receiver have a two-dimensional beam distribution (sheet beam) in the $x-z$ plane with no y dependence in any field variable. In that case the receiver voltage given by Eq. (5) simplifies to

$$\begin{aligned}V(x,f)=&-\frac{1}{4\pi}\gamma(\omega)\omega\rho_f\int_{-\infty}^{\infty}T(k_x,0,f)\\&\times\frac{\exp[ik_x(\tilde{x}-\tilde{x}')-ik_z(\tilde{z}-\tilde{z}')]}{k_z}dk_x,\end{aligned} \tag{6}$$

where $k_z=\sqrt{k_f^2-k_x^2}$. Scanning to construct a synthetic aperture is equivalent to forming the spatial Fourier transform of the receiver voltage as a function of both x and f. By applying a spatial Fourier transform to $V(x,f)$ given by Eq. (6) and using a straightforward derivation,[16,21,24] we obtain an expression for the receiver voltage in the $k-f$ domain $V(k,f)$,

$$\begin{aligned}V(x,f)=&-\tfrac{1}{2}\gamma(\omega)\omega\rho_fT(k,0,f)\\&\times\frac{\exp\{ik[-(d+ib)\sin\alpha-\tilde{x}']-ik_z(\tilde{z}-\tilde{z}')\}}{k_z}.\end{aligned} \tag{7}$$

Now substitute the complex coordinates given by Eqs. (3) and (4) into Eq. (7), and we have

$$\begin{aligned}V(k,f)=&-\tfrac{1}{2}\gamma(\omega)\omega\rho_fT(k,0,f)\\&\times\exp\{-ik_f[x'\sin\theta+(z-z')\cos\theta\\&+d\cos(\theta-\alpha)+d'\cos(\theta-\alpha')]\\&+k_f[b\cos(\theta-\alpha)+b'\cos(\theta-\alpha')]\},\end{aligned} \tag{8}$$

where $\theta[=\arcsin(k/k_f)]$, is the phase-match angle or the incident angle of a particular plane-wave component in the transmitter's angular spectrum. The magnitude of $V(k,f)$ is given by

$$\begin{aligned}|V(k,f)|&=\frac{1}{2}\gamma(\omega)\omega\rho_f|T(k,0,f)|\frac{\exp\{k_f[b\cos(\theta-\alpha)+b'\cos(\theta-\alpha')]\}}{k_f\cos\theta}\\&\cong\frac{1}{2}\gamma(\omega)\omega\rho_f|T(k,0,f)|\frac{\exp[k_f(b+b')]\exp[-k_fb(\theta-\alpha)^2]\exp[-k_fb'(\theta-\alpha')^2]}{k_f\cos\theta}.\end{aligned} \tag{9}$$

The above derived equation has positive exponential terms that are not valid for large $k_f b$ and $k_f b'$. In numerical evaluation of this equation, one needs to normalize the amplitude of the two CTPs by $\exp(-k_f b)$ and $\exp(-k_f b')$, respectively, i.e., the following equation should be used instead:

$$
\begin{aligned}
&|V(k,f)| \\
&\quad = \tfrac{1}{2}\gamma(\omega)\omega\rho_f |T(k,0,f)| \\
&\qquad \times \frac{\exp\{k_f[b(\cos(\theta-\alpha)-1)+b'(\cos(\theta-\alpha')-1)]\}}{k_f \cos\theta} \\
&\quad \cong \tfrac{1}{2}\gamma(\omega)\omega\rho_f |T(k,0,f)| \\
&\qquad \times \frac{\exp[-k_f b(\theta-\alpha)^2]\exp[-k_f b'(\theta-\alpha')^2]}{k_f \cos\theta}. \qquad (10)
\end{aligned}
$$

The normalization makes the transducer field at the aperture center unity for all frequencies without changing its profile.

From Eqs. (8) and (9) the effects of the extrinsic experimental parameters and intrinsic material properties on the $k-f$ domain receiver voltage are easily identifiable. First, the heights of the transmitter and the receiver, respectively, z' and z, affect only the phase and not the magnitude of $V(k,f)$. Second, the beam spread of the transmitter and receiver, dependent on the Fresnel length b' and b, or the waist beam width W' and W, determines the angular range of $V(k,f)$. The angular beam width $\Delta\theta(=1/\sqrt{2k_f b}=1/\{k_f W\})$ is determined by the transducer Fresnel length b or the waist beam width W. In the receiver voltage expression the combined beam contribution from the transducers is the product of the individual transducer beam contributions, as is the case with the electronic frequency response. To achieve the best experimental match, we use identical transducers and align them to the same incident angles. Then, $b=b'$, $a=a'$, and $\alpha=\alpha'$, in which case Eq. (10) simplifies to

$$
|V(k,f)| \cong \frac{1}{2}\gamma(\omega)\omega\rho_f |T(k,0,f)| \frac{\exp[-2k_f b(\theta-\alpha)^2]}{k_f \cos\theta}. \qquad (11)
$$

The above equation is also applicable to planar transducer leaky wave measurements by expressing the Fresnel length as $b=\frac{1}{2}k_f(0.752a)^2$.

Equations (8) and (9) also show that the plane-wave TC, both its magnitude and phase, can be reconstructed completely in a 2D measurement. The orientation angle and the angular beam spread of both transducers determine the angular range of the reconstructed TC. To obtain a rapid mapping of the TC, the Fresnel lengths b and b' should be as small as possible to permit wide beams. A transducer of a small Fresnel length can be achieved either by decreasing the transducer aperture size or by decreasing the focal length. The former enhances the diffraction effect, and the latter the focusing effect. Using highly focused transducers is a more effective way to achieve a large angular beam spread, because aperture size is related to sensitivity. The combined electronic frequency response spectrum $\gamma(\omega)$ in all the above equations can be determined experimentally, although for focused transducers this may not be an easy task.

In this work with focused beams we find for two identical focused probes in a confocal geometry, the measured voltage at any frequency or position is essentially identical to that produced by the field of either device and sampled by a point receiver.[25] To construct a more realistic model of the experiment one could incorporate a set of Gaussian beam functions via the CTP, whose coherent sum accurately models the sidelobe behavior of a focused transducer and whose pupil function cuts off sharply at its maximum acceptance angle. We have recently demonstrated this more elaborate modeling approach[16] in a paper on reflection function modeling with focused beams. In the experiments in this work, we instead employ the expedient of acquiring a reference scan without the sample present to use in conjunction with a pseudoinverse filter to suppress the effects of sidelobes in the measured transmission function plots, which results in cleaner images that can be more accurately and easily compared to the plane-wave calculations. Although the CTP model will not be directly used in elastic property reconstruction of plate materials, the model and its associated discussions play an important role in helping one to understand the principle of our measurement procedure. The model can also be used to determine the optimal measurement parameters, including transducer aperture size, focal length, and orientation angle, to rapidly get the desired dispersion curves for material elastic property reconstruction.

C. Elastic stiffness reconstruction

The TC is the intrinsic physical parameter that carries the elastic information of the plate material. The main structural characteristics of the TC are the plate wave dispersion curves. The relationship between the dispersion curves and the individual elastic stiffnesses is complicated owing to the distribution of energy in the various partial wave components in the plate. A carefully applied optimization procedure is therefore often necessary in order to reconstruct individual stiffnesses from the plate wave transmission (or reflection) spectrum. There are, however, a few exceptions. For example, it is well known that the mode cutoff frequencies of an istropic plate are related in a simple way to either the longitudinal wave velocity, V_L, or the shear wave velocity, V_S, in the plate thickness direction

$$
f_{S,A} = \begin{cases} \dfrac{V_{S,L}}{2h}N & (N=0,2,4,\ldots), \\ \dfrac{V_{L,S}}{2h}N & (N=1,3,5,\ldots), \end{cases} \qquad (12)
$$

where h is the plate thickness, f_S and f_A are the cutoff frequencies of the symmetric and antisymmetric modes, respectively. Equation (12) is also applicable to an anisotropic plate if the plate material is orthortropic and the material axes are aligned with axes x, y, and z. For such a plate, the guided waves in the $x-z$ plane can be analyzed using the same partial-wave approach as in an isotropic plate. At zero wave numbers, the partial waves become pure longitudinal and shear waves in the plate thickness direction. The cutoff frequencies can be used to determine the longitudinal and shear stiffnesses directly in an isotropic or anisotropic medium,

with almost no need for optimization. The longitudinal mode cutoff frequencies are commonly used to determine the longitudinal stiffness, whereas the use of the shear mode cutoff frequencies in an immersion measurement is somewhat counterintuitive. When the orientation angles of the transducers are both zero, the pure shear wave motion in the plate can neither be generated nor be detected in an ideal fluid-coupled transmission measurement. Nevertheless, experimental results show that for materials with low attenuation, the dispersion spectrum near the shear mode cutoff frequencies can be easily measured in a simple low orientation-angle scan. With our focused probes, of course, there is a large range of plane waves incident on the plate, including many capable of shear-wave generation. Based on the data from the transmission peak spectrum, we are able to acquire limiting frequencies that are almost identical to the shear cutoff frequencies. A simple low orientation-angle scan thus provides a complete elastic property estimation procedure for isotropic plates.

For anisotropic plates, we have previously introduced a stepwise, targeted procedure to extract elastic stiffnesses from the measured dispersion data.[15] In this procedure we choose carefully how we make use of the dispersion spectrum data by concentrating on portions of the dispersion behavior where dependence on elastic properties is limited to a few of the full complement of elastic stiffnesses. We then proceed to obtain the elastic stiffnesses incrementally, beginning with parts of the dispersion curves where only one or two stiffnesses affect the plate wave behavior, and continue to add data from curves where other stiffnesses can be easily extracted, until all relevant stiffnesses have been inferred. The mode cutoff frequencies are very special targeted data; they are exclusively dependent on either longitudinal or shear stiffness in the plate thickness direction. By using the mode cutoff and near cutoff transmission data to directly determine or estimate the longitudinal and shear stiffnesses in the thickness direction, the robustness of the optimization process is further enhanced. The choice of the optimization algorithm is also not critical here. Because we reconstruct one parameter at a time, any one of several robust one-dimensional optimization algorithms is sufficient. Typically, a single parameter search is much easier and more reliable to use than multidimensional routines.[26] In this work, we have used a simple golden-section optimization algorithm, although any equivalent method would work as well. The used object function is $\Sigma_{i=1}^{N}(Ve_i - Vm_i)^2$, where N is the total number of selected data points for reconstruction, Ve_i and Vm_i, are the measured transmission maxima and model-predicted transmission maxima, respectively.

To illustrate the stepwise, targeted stiffness reconstruction method, we use a silicon plate as an example. The material is cubic with three independent elastic stiffnesses: C_{11}, C_{13}, and C_{55}. Using the nominal values[23] for the density, C_{11}, C_{13}, and C_{55}, we calculated the plane wave TC in the $k-f$ domain along [1 0 0] of a 1.0 mm thick silicon plate that is immersed in water. The results is shown in Fig. 2 as an image whose gray scale is proportional to the absolute value of the TC. The image format will be used extensively for presenting both model and experimental results in the $k-f$ domain. Referring to Fig. 2, in the $k-f$ domain a line through the origin has a constant slope of k/f, which can be uniquely converted into a phase-match angle θ in the coupling fluid, according to $\sin\theta = c_f k/2\pi f$. Based on this relationship we label the phase-match angles at the upper and right frames of the image so that the angular range of the $k-f$ domain data can be seen clearly.

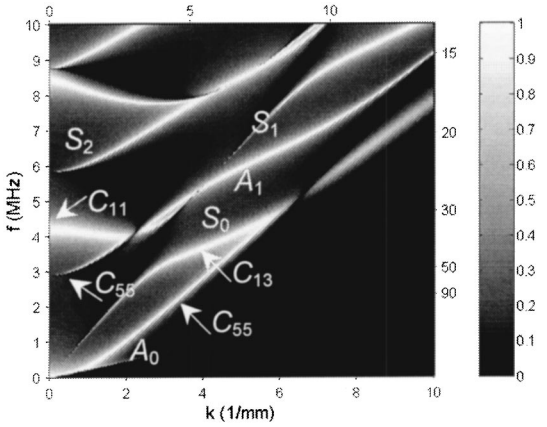

FIG. 2. The plane-wave TC along [1 0 0] of a 1.0 mm thick silicon plate immersed in water and the sensitivity of its associated dispersion spectrum to individual elastic stiffnesses.

In Fig. 2, the regions indicated by arrows show the portions of the dispersion spectrum that are sensitive to C_{11}, C_{13}, and C_{55}. The three stiffnesses can be reconstructed in the order of C_{55}, C_{11}, and C_{13}.[15] Figure 3 illustrates how the dispersion spectrum converges in the reconstruction process. In Fig. 3, the dispersion curves based on the nominal stiffness values are plotted in (a)–(d) as gray lines for comparison. To begin the reconstruction process, the three stiffnesses are assumed to have a 20% difference from their corresponding nominal values (C_{11n}, C_{55n}, and C_{13n}), i.e., $C_{11}=1.2C_{11n}$, $C_{55}=1.2C_{55n}$, and $C_{13}=1.2C_{13n}$, even

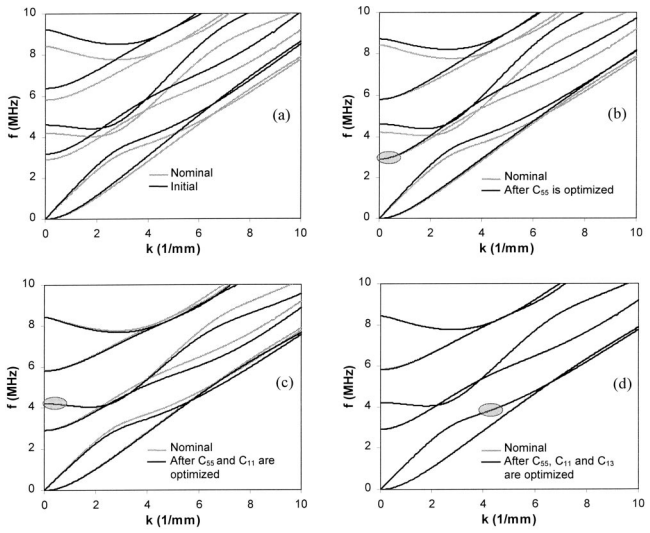

FIG. 3. A step-by-step comparison of the dispersion curves based on the nominal and optimized elastic stiffnesses of a 1 mm silicon plate in a stepwise, targeted elastic property reconstruction process. (a) Initial estimation, (b) after C_{55} is optimized, (c) after C_{55} and C_{11} are optimized, and (d) after C_{55}, C_{11}, and C_{13} are optimized. The targeted data used for optimizing the individual stiffness at every step are marked in gray areas.

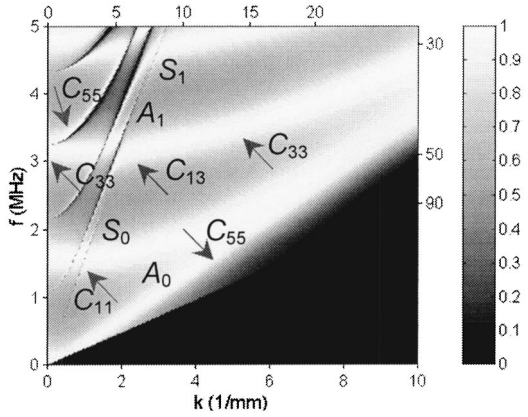

FIG. 4. The plane-wave TC along the fiber direction of a 1.0 mm thick graphite/epoxy laminate immersed in water and the sensitivity of its associated dispersion spectrum to individual elastic stiffnesses.

though if we use mode cutoff frequencies, we can get a much better estimate for C_{11} and C_{55}. The calculated dispersion curves based on the initial stiffness values are shown in Fig. 3(a) as black lines, from which their difference from the nominal dispersion spectrum is seen clearly. To get C_{55} in the first step, both the A_0 mode and the mode cutoff of the A_1 mode can be used as the targeted data for C_{55}. The A_0 mode is very strong in amplitude but the A_1 mode cutoff gives a direct estimation of C_{55}. Here we use the transmission maxima near the mode cutoff of the A_1 mode shown in Fig. 2 as the targeted data for C_{55}. The first step optimization gives $C_{55}=0.992C_{55n}$. The dispersion curves are calculated again, and the results are shown in Fig. 3(b) as the black lines. The two sets of dispersion curves overlap in both targeted regions for C_{55}. In the second step, A_1 mode is used as the targeted data for C_{11}. The optimization yields $C_{11}=1.000C_{11n}$. From the calculated dispersion curves in Fig. 3(c), dispersion curves converge in the targeted region for C_{11}, and that the optimization of C_{11} has little effect on the targeted regions for C_{55}. As the third step, C_{13} is optimized using the targeted data shown in Fig. 2, giving $C_{13}=0.997C_{13n}$. The comparison between nominal and optimized dispersion curves is shown in Fig. 3(d). After only three one-dimensional searches, the optimized dispersion curves are already almost identical to the nominal dispersion curves.

The stepwise, targeted stiffness reconstruction procedure can also be applied to a more complex material, such as a uni-axial composite laminate. The material can be considered as transversely isotropic with five independent elastic stiffnesses, C_{11}, C_{13}, C_{33}, C_{44}, and C_{55} (assuming x is the fiber direction). Among the five stiffnesses, C_{11}, C_{13}, C_{33}, and C_{55} can be deduced from measurements in the x direction, and C_{33} and C_{44} from those in the y direction. The y measurement is in the plane of isotropy and is therefore similar to the isotropic plate case. Here, we discuss the x measurement only. Figure 4 presents a plot of the magnitude of the plane wave TC in the $k-f$ domain for a 1.0 mm thick uniaxial graphite/epoxy laminate immersed in water. The gray scale is proportional to the absolute value of the TC. The regions indicated in Fig. 4 by the arrows are the portions of the dispersion spectrum sensitive to individual elastic stiffnesses based on prior sensitivity studies[9,27] of the TC. To obtain the elastic stiffnesses we use the mode cutoff frequencies to determine C_{33} and make an initial estimate of C_{55}. We also use the slope of the low-frequency part of the S_0 mode to estimate C_{11}.[4,13] We then use an optimization algorithm to operate on the targeted data for C_{11}, C_{13}, and C_{55}, and to obtain the three stiffnesses in order: first C_{11}, then C_{55}, and finally C_{13}.

There are three factors in the successful application of the stepwise, targeted stiffness reconstruction method: (1) identify the targeted data for individual stiffnesses and determine the order of their reconstruction, (2) develop a reasonably good initial guess for all the stiffnesses, and (3) acquire a wide angular range of dispersion data. The first of these can be determined from the sensitivity study of the TC. A good estimate of the stiffnesses can be obtained from mode cutoffs and other characteristics of the dispersion spectrum, as well as *a priori* information. The availability of dispersion data over a large angular range is very desirable, because the targeted regions of the different stiffnesses are often located at widely different angles. Fortunately, by using the highly focused transducers in a synthetic aperture transmission scan as discussed previously, dispersion curve mapping in a large angular range is not only possible, but it can also be done in a very efficient manner.

III. EXPERIMENTAL PROCEDURE

A detailed description of the experimental system can be found in Ref. 16. To perform a synthetic aperture scan, the receiver transducer is scanned along the plate while other geometric parameters are held constant. The receiver voltage is sampled as a time signal at each coordinate position. The spatial scan step size and the sampling time interval are, respectively, much less than the smallest wavelength and the time period of the plate wave modes of interest. The scan step varies from 0.1 mm to 1.0 mm, depending on the transducer type, orientation, position, and sample properties. The total number of scan steps is between 200 and 300. The received signals in a scan decay naturally temporally and by energy leakage spatially. The time window and the scan range are set to be wide enough to collect all the received signals of a significant amplitude (typically larger than several percent of the maximum signal amplitude in the scan). The received signals outside of the time and spatial ranges are very small and can be ignored.[15] The scan ranges are therefore taken to be effectively infinite in both time and space. A LabVIEW user interface has been developed on the PC to control the scan and data acquisition process. The acquired scan data are further processed using FORTRAN and MATLAB programs.

Experiments have been performed on both isotropic and anisotropic plate samples. The isotropic plates include a 1.60 mm thick aluminum plate with a density of 2.78×10^3 kg/m^3, and a 3.00 mm thick steel plate with a density of 7.90×10^3 kg/m^3. The anisotropic plates consist of a [001] cut 525 μm thick silicon wafer with a density of 2.33×10^3 kg/m^3 and two composite laminates: one is a uniaxial T300/CG-914 $[0]_8$ graphite-epoxy laminate with a thickness of 0.92 mm and a density of 1.60×10^3 kg/m^3, and the other

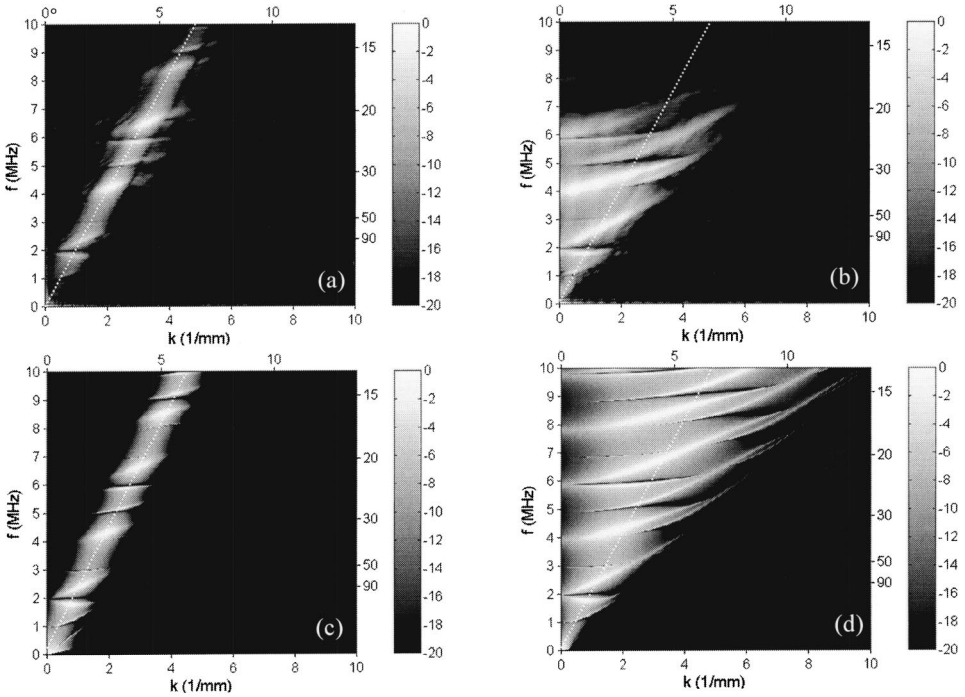

FIG. 5. A comparison between the synthetic aperture scan results using planar and focused transducers. (a) and (b) are the processed data in the $k-f$ domain in dB. (c) and (d) are the model calculations in dB. In (a) and (c) the transducers are a pair of 12.7 mm diameter planar transducers at 6°. In (b) and (d) a pair of focused transducers with a diameter of 25.4 mm and a focal length of 102 mm is used, also at 6°. The sample is a 1.60 mm thick aluminum plate in water.

is a bi-axial laminate $[0/90]_{3S}$ of AS/4-3501 with a thickness of 1.58 mm and a density of 1.62×10^3 kg/m^3. Four pairs of focused transducers have been used for the measurement. The first pair (Panametrics V305) is spherically focused and has a center frequency of 2.25 MHz, a diameter of 19.1 mm and a focal length of 25.4 mm, which can effectively map out about 40° of dispersion spectrum at a time. The second pair (Panametrics V308) has the same diameter and focal length but is cylindrically focused and has a higher frequency of 5 MHz. Another 5 MHz spherically focused transducer pair (Panametrics 309) has a diameter of 25.4 mm, a focal length of 102 mm, and an phase-match angular coverage of about 10°. The last pair (Panametrics V311) is cylindrically focused and has a center frequency of 10 MHz, a diameter of 12.7 mm, and a focal length of 50.8 mm. The angular coverage is the same as that of the previous pair.

For each sample we first perform the synthetic aperture scan to measure the TC and its dispersion spectrum in the $k-f$ domain. We then use the targeted reconstruction procedure to extract the elastic stiffnesses from the obtained dispersion spectrum. As an independent check on our reconstruction results, we also perform contact-mode longitudinal and shear wave measurements to deduce several ultrasonic velocities.

IV. RESULTS AND DISCUSSION

A. Rapid TC reconstruction

As we have seen in Sec. II, the transducer beam influences the $k-f$ domain results of a synthetic transducer aperture scan. The orientation angle and the angular beam spread of the two transducers determine the angular range of the measured dispersion data. Figure 5 shows a comparison between the scan results obtained by planar and focused transducers on a polycrystal, rolled 1.60 mm thick aluminum plate. For the planar transducer scan, two nominally identical planar transducers (Ultran L37-5, 5 MHz center frequency, 9.53 mm in diameter) have been used. Both transducers are oriented at 6° and positioned at 100 mm from the plate. The scan has been performed for x_i from -18.0 mm to 22.0 mm at a scan step size of 0.2 mm. The length of the time window is 10 μs and the sampling frequency is 50 MHz. The acquired $x-t$ domain data are transformed into the $k-f$ domain using two consecutive Fourier transforms in the t and x coordinates, respectively. The $k-f$ domain result is then normalized by the maximum value of the data set and converted into decibel scale. The result is shown in Fig. 5(a). Assuming $\gamma(\omega)=1$ and using the same data normalization procedure, Eq. (11) has been used to predict the $k-f$ domain voltage. The result is shown in Fig. 5(c). The model predicts the main features of the experimental result quite well. In both Figs. 5(a) and (c), the $k-f$ domain data of discernible amplitude are concentrated near the transducer orientation angle of 6°, and they have a nearly constant cross-sectional width in the $k-f$ domain. The bright and dark features within the band of data near 6° indicate transmission peaks and minima corresponding to various guided wave modes in the plate. Because the angular beam spread of both transducers is relatively small, we are able to view only a very narrow portion of the entire TC.

For the scan with focused transducers, a pair of spherically focused transducers (Panametrics V309) with a center frequency of 5 MHz, a diameter of 25.4 mm, and a focal length of 102 mm has been used. The transmitter and the receiver are also oriented at 6° and positioned at 100 mm from the plate. Such an arrangement forms a nearly confocal geometry. The measurement results, however, are found to be relatively insensitive to the vertical positions of the transducers, as long as the two transducers are not too far from, or too close to, the plate. The scan has been performed for x_i from -18.0 mm to 15.0 mm at a step of 0.2 mm, as before. The sampling frequency is also 50 MHz, and the time win-

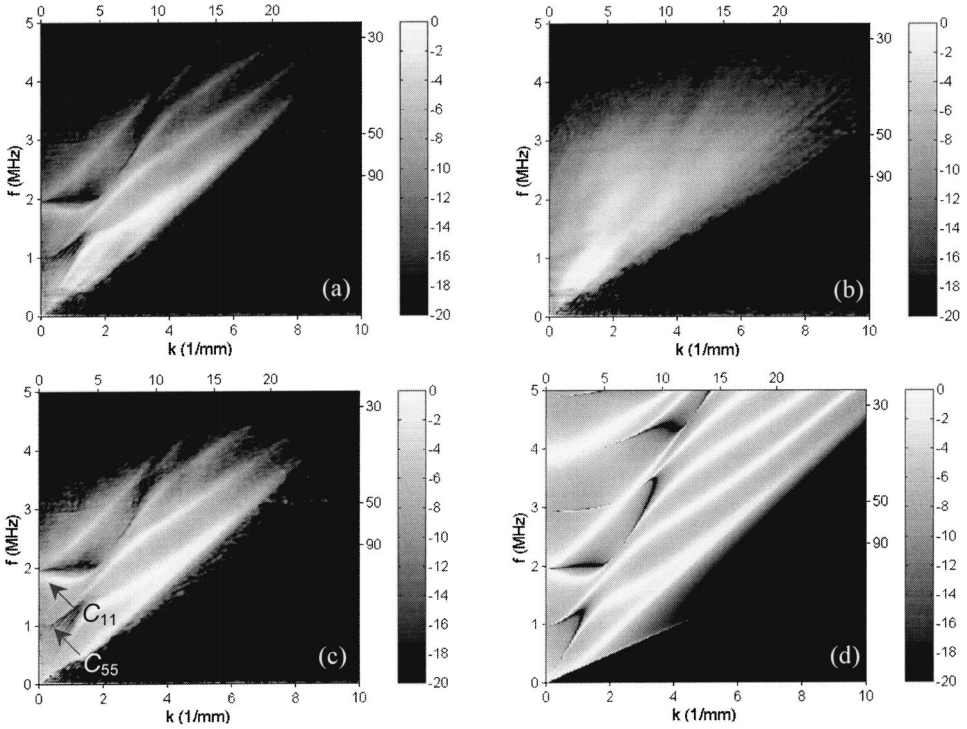

FIG. 6. Rapid reconstruction of the TC on an aluminum plate using a 20° transducer scan. (a) the sample scan result in the $k-f$ domain in dB, (b) the reference scan result in the $k-f$ domain in dB, (c) the reconstructed TC in dB, and (d) the calculated TC in dB.

dow is 10 μs in length. Figure 5(b) shows the data in the transformed $k-f$ domain in dB. These data display a much broader pattern than the $k-f$ domain result from the planar transducers [Fig. 5(a)]. The data of discernible magnitude in the focused transducer scan have a constant angular span, whereas the data in the planar transducer scan have a constant cross-sectional width. The focused transducer scan gives a much wider field of view of the dispersion spectrum. By taking advantage of the angular beam spread of the focused transducers, we are able to view the plate dispersion spectrum for the phase-match angles between 0° and 12°, although both transducers are oriented at a single angle of 6°. The plate mode cutoffs have also been mapped out clearly. Another difference here is that in the $k-f$ domain results for the focused transducers [Fig. 5(b)], we can see some nonuniform background features. These features are consequences of transducer sidelobe effects not suppressed in the measurement, or modeled in the calculation. In fact, the focused receiver has detected the structure of the transmitted acoustic field.[25] The sidelobe effects are nearly invisible in the $k-f$ domain result by planar transducers [Fig. 5(a)] owing to the averaging of the signal phase over the receiver surface in the reception process. The $k-f$ domain data calculated using the 2D model are shown in Fig. 5(d). The dispersion structures in the experimental and model results are very similar. The background features owing to sidelobe effects are not observable in the model result because the model assumes that both transducers have a Gaussian beam profile and therefore exhibit no sidelobe effects. For the results shown in Figs. 5(a) and (b), the $k-f$ domain data contain the contribution from not only the transducer beams, but also the transducer frequency responses.

To reconstruct the TC in a form more compatible with our Gaussian beam model, we perform a reference scan and normalization mentioned in Sec. II. Figure 6 shows an example demonstrating rapid TC reconstruction using a pair of highly focused transducers with the aid of a reference scan. The probes are a pair of spherically focused transducers (Panametrics V305) with a center frequency of 2.25 MHz, a diameter of 19.1 mm, and a focal length of 25.4 mm. Both transducers are oriented at 20°. The scan is first performed on the 1.60 mm thick aluminum plate. A reference scan is then performed under the same experimental settings but with the plate sample absent. The experimental data with the plate are shown in the transformed $k-f$ domain in Fig. 6(a) and without the plate in Fig. 6(b). In the $k-f$ domain result with the sample [Fig. 6(a)], we see clearly five plate wave modes, A_0, S_0, A_1, S_1, and S_2, whereas the reference scan result [Fig. 6(b)] contains only the contributions of the transducer beams and their frequency responses. Because this pair of transducers is highly focused (the ratio of a to F_0 is 0.375), the $k-f$ domain data in the sample and reference scans both have a large angular distribution. We are able to map the dispersion curves for phase-match angles as small as 0°, that is, up to the mode cutoffs, and out to larger than 40°. Such a wide angular coverage would require many measurements if planar transducers were used instead. The $k-f$ domain results from the sample and reference scans are combined using a pseudoinverse filter, and the result is shown in Fig. 6(c). The image grayscale represents the magnitude of the reconstructed TC on a dB scale, where light is high and dark is low. The predicted plane-wave TC, based on the elastic properties of the plate sample and the coupling fluid, is shown in Fig. 6(d). We can see that in the effective measurement regions, 0°–45° in phase-match angle and 0–3.5 MHz in frequency, the TC has been very well reconstructed. The loci of TC maxima represented in Fig. 6(c) serve as the basis for an accurate determination of the elastic behavior of the plate.

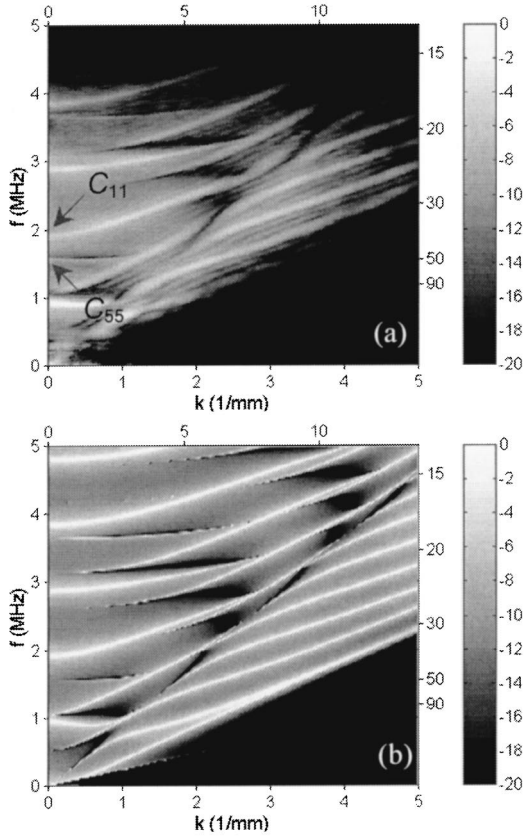

FIG. 7. Rapid TC reconstruction on the 3.0 mm thick steel plate using a 0° transducer scan. (a) The reconstructed TC in dB, and (b) the calculated TC in dB based on the reconstructed elastic stiffnesses.

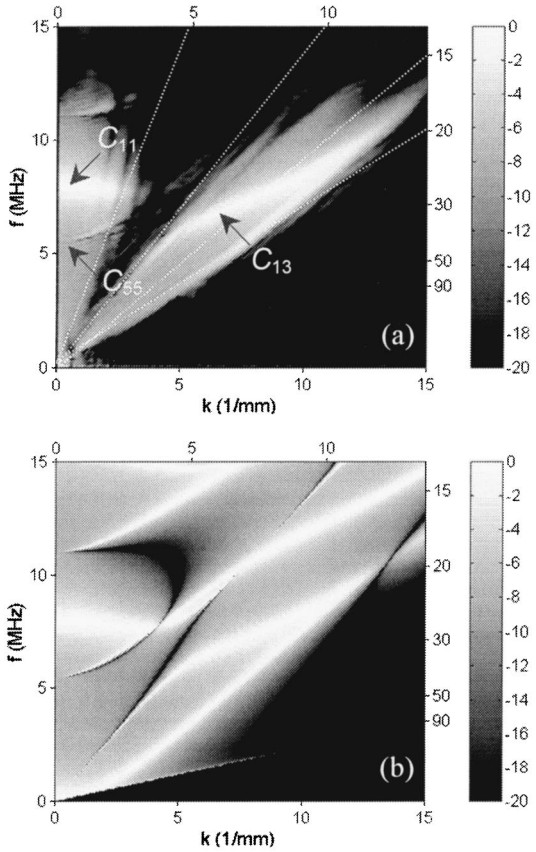

FIG. 8. Rapid TC reconstruction on the 525 μm thick silicon wafer. (a) The reconstructed TC in dB from the 0° and 15° transducer scans, and (b) the calculated TC in dB based on the reconstructed elastic stiffnesses.

B. Characterizing isotropic plates

For isotropic plates with low acoustic attenuation, a small (or zero) transducer orientation angle scan can be used to map out the mode cutoff regions to get both the longitudinal and shear stiffnesses directly. A 3.0 mm thick steel plate is used as the sample, together with a pair of 2.25 MHz spherically focused transducers (Panametrics V305, 19.1 mm in diameter, and 25.4 mm in focal length) at zero orientation angles in a nearly confocal geometry. The scan range for x_i is from -30.0 mm to 30.0 mm at a step size of 0.2 mm. The sampling frequency is 25 MHz, and the length of the time window is 20 μs. The results are shown in Fig. 7. The TC has been effectively mapped out in an angular range from 0° to 25°. Because this sample is relatively thick, we are able to discern in the experimental data of Fig. 7(a) quite a few plate modes. Although unlabeled in the figure, these modes include the A_1, S_1, A_2, S_2, A_3, and S_3; moreover, the cutoffs of several of these six modes at zero wave number are also clearly visible. Using those cutoff frequencies only, we deduce $C_{11}=267$ GPa and $C_{55}=79.0$ GPa. To check our reconstruction results, we use the two reconstructed parameters to calculate the plane-wave TC spectrum, and the result is shown in Fig. 7(b). We can see the excellent agreement between the measured and calculated TC in the effective k and f ranges, although only the cutoff frequencies have been used to determine the two elastic stiffnesses. To make an independent check on the reconstruction results, we have also used a 10 MHz contact-mode longitudinal wave transducer and a 5 MHz contact-mode shear wave transducer to measure the longitudinal velocity V_L and the shear wave velocity V_S. The results are $V_L=5.76\times10^3$ m/s and $V_S=3.13\times10^3$ m/s, which give $C_{11}=265$ GPa and $C_{55}=78.5$ GPa. The percentage difference between the results by reconstruction and the contact measurement is a respectable 0.4% and 1.1%, respectively, for C_{11} and C_{55}.

C. Characterizing anisotropic plates

To begin we examine a 525 μm thick silicon wafer. Because the sample is relatively thin, we have used a pair of cylindrically focused transducers with a higher frequency of 10 MHz (Panametrics V311, 12.7 mm in diameter, 50.8 mm in focal length) for the measurement. This pair of transducers has a relatively smaller angular beam spread of about 10°. We have made two scans with the transducers at 0° and 15°, respectively, and summed the scan results in the $k-f$ domain. The combined $k-f$ domain result is shown in Fig. 8(a). To reconstruct the three stiffnesses, we first use the cutoff frequencies of the A_1 and S_1 modes mapped in the scan at 0° to determine C_{55} and C_{11}, respectively. We then run the optimization procedure on the S_0 mode mapped during the 15° scan to reconstruct C_{13}. The reconstructed elastic stiffnesses are 165, 59.1, and 77.9 GPa, respectively, for C_{11}, C_{13}, and C_{55}. The nominal values[23] are $C_{11}=166$ GPa, $C_{13}=63.9$ GPa, and $C_{55}=79.7$ GPa. The difference is about 2% or less for C_{11} and C_{55}. The reconstructed

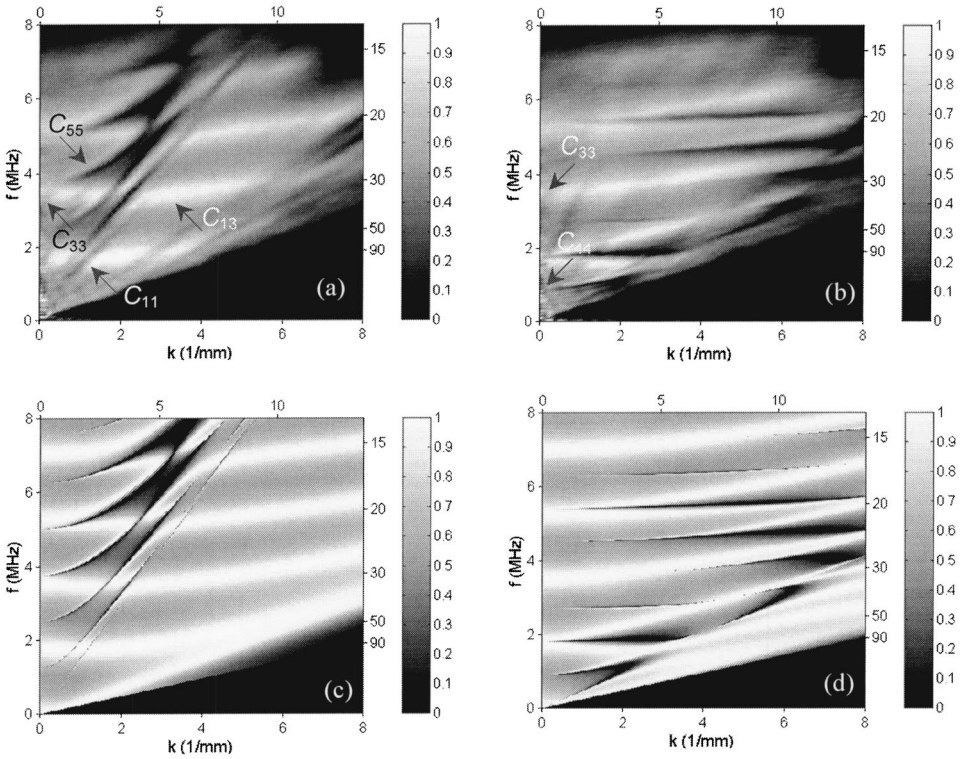

FIG. 9. Rapid TC reconstruction on the uniaxial laminate. The reconstructed TC in the $k-f$ domain is shown in (a) for the x measurement and (b) for the y measurement. The transducer orientation angle is 15° for both measurements. The calculated TC in the $k-f$ domain based on the reconstructed elastic stiffnesses is shown in (c) for the x measurement and (d) for the y measurement.

stiffness C_{13}, however, shows a difference of 7.5% from the nominal value. This relatively large difference may be caused by the sample preparation or small errors in orientation. The calculated plane-wave TC using the reconstructed elastic parameters is shown in Fig. 8(b), and the agreement with the experimental data is very good in the effective measurement regions.

Because of the importance of engineered materials, we have studied a further anisotropic plate sample: a 0.92 mm thick uniaxial T300/CG-914 $[0]_8$ graphite-epoxy laminate. For this sample we have made two synthetic aperture scans: one in the fiber direction (along the x axis), for C_{11}, C_{13}, C_{33}, and C_{55}, and the other in a direction normal to the fibers (along the y axis), for C_{33} and C_{44}. In both measurements we have used a pair of 5 MHz cylindrically focused transducers (Panametrics V308, 19.1 mm in diameter, and 25.4 mm in focal length). Figures 9(a) and (b) show the reconstructed TC in the $k-f$ domain from the x- and y-axis scans, respectively. The reconstructed elastic stiffnesses are 138, 3.3, 4.3, and 8.6 GPa, respectively, for C_{11}, C_{13}, C_{44}, and C_{55}. Elastic stiffness C_{33} has been reconstructed independently from both the x and y measurements: we find 15.6 GPa from the x measurement and 16.3 GPa from the y measurement. Figures 9(c) and (d) show the calculated plane-wave TC using the reconstructed elastic parameters, for the above two measurements. We see that the dispersion structure is fit very well in almost all parts of the dispersion spectrum, although the elastic stiffnesses have been reconstructed based only on a small portion of the dispersion data. To make a preliminary verification of the reconstruction results, we have also measured different ultrasonic velocities including $V_{33}(=\sqrt{C_{33}/\rho}$, is the longitudinal velocity in the thickness direction), $V_{13}(=\sqrt{C_{55}/\rho}$, is the shear wave velocity parallel to the fibers), $V_{23}(=\sqrt{C_{44}/\rho}$, is the shear wave velocity normal to the fibers) and $V_{S_0 11}(=\sqrt{(C_{11}-C_{13}^2/C_{33})/\rho}$, is the low-frequency phase velocity of the S_0 mode in the fiber direction). The results are $V_{33}=3.15\times10^3$ m/s, $V_{13}=2.29\times10^3$ m/s, $V_{23}=1.64\times10^3$ m/s, and $V_{S_0 11}=9.54\times10^3$ m/s, which have a difference of less than 3% from the respective velocities calculated based on reconstructed stiffnesses.

The final anisotropic plate sample we have tested is a bi-axial composite laminate with a lay-up geometry of $[0/90]_{3S}$. A bi-axial laminate with a general ply lay-up can be considered as an orthortropic material with nine independent elastic stiffnesses: C_{11}, C_{12}, C_{13}, C_{22}, C_{23}, C_{33}, C_{44}, C_{55}, and C_{66}. Among those stiffnesses, C_{11}, C_{13}, C_{33}, and C_{55} can be determined from the scan in the x direction whereas C_{22}, C_{23}, C_{33}, and C_{44} can be measured in the y direction. The remaining elastic stiffnesses are C_{12} and C_{66}. Although C_{12} can be determined in principle from a measurement away from axes of symmetry, it shares the ambiguity of the other off-diagonal stiffnesses, C_{13} and C_{23}. These three stiffnesses are generally small compared to the other elastic properties. They have little influence on either the dispersion behavior or on the static mechanical properties and are therefore difficult to measure accurately in our experiment. The remaining elastic stiffness C_{66} can be measured according to the method outlined in Ref. 24. For this particular laminate sample, the average effective elastic properties are the same in the x and y directions, i.e., $C_{11}=C_{22}$, $C_{13}=C_{23}$, and $C_{44}=C_{55}$. We have measured the sample, therefore, only in the x direction. A pair of 2.25 MHz focused transducers (Panametrics V305, 19.1 mm in diameter, and 25.4 mm in focal length) at a 15° incident angle has been used, and the $k-f$ domain results are shown in Fig. 10(a). We can clearly identify the S_0 and A_1 modes. Using our targeted scheme, the stiffnesses have been found to be

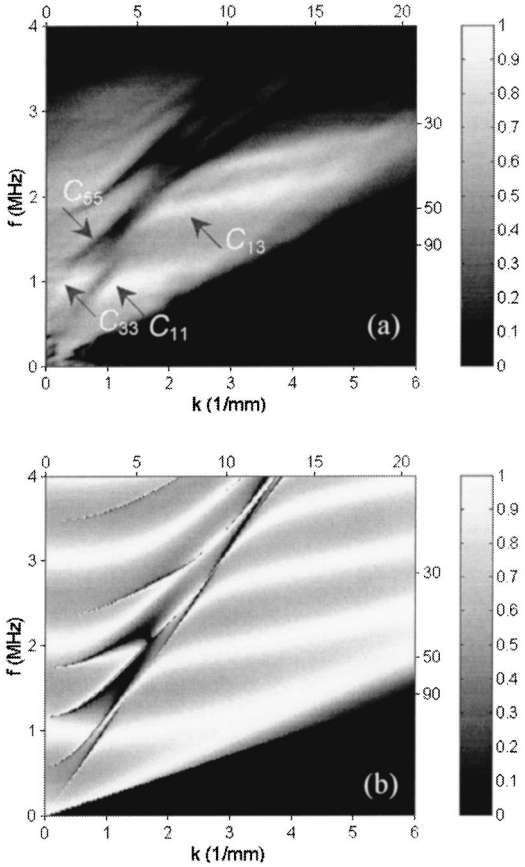

FIG. 10. Rapid TC reconstruction on the 1.58 mm thick biaxial graphite/epoxy laminate $[0/90]_{3S}$. The measurement is performed in the x-axis direction with transducers aligned at 15°. (a) The reconstructed TC in the $k-f$ domain; and (b) the calculated TC based on the reconstructed elastic stiffnesses from (a).

70.0, 7.9, 16.4, and 5.5 GPa, respectively for C_{11}, C_{13}, C_{33}, and C_{55}. Those same stiffnesses are then used as input to calculate the TC spectrum, and the results, shown in Fig. 10(b), may be compared with the experimental transmission maxima shown in frame (a). Here also, the model calculation agrees well with the experimental result. Corroborating contact longitudinal and shear wave measurements yield $V_{33}=3.19\times10^3$ m/s, $V_{13}=1.88\times10^3$ m/s, and $V_{S_0 11}=6.70\times10^3$ m/s, and those of the immersion data give $V_{33}=3.17\times10^3$ m/s, $V_{13}=1.88\times10^3$ m/s, and $V_{S_0 11}=6.39\times10^3$ m/s, where disparities are below 5%. Of course, the contact experiments are also subject to their own set of experimental uncertainties and measurement errors.

V. SUMMARY AND CONCLUSIONS

The synthetic aperture scan technique using highly focused transducers has been applied to fluid-coupled plate transmission experiments to deduce the plate's TC. We have developed and demonstrated a method to reconstruct the plate transmission coefficient over wide ranges of wave number and frequency. Both model analysis and experiments have demonstrated that by using the large angular beam spread of highly focused transducers, it is possible to measure almost the entire angular range accessible by phase-matched water coupling with the transmitting and receiving transducers at a single orientation angle. We have shown that the mode cutoffs and low phase-match angle dispersion data that are difficult to obtain in a reflection setup can be easily mapped out in the transmission geometry and used accurately to determine elastic properties of the plate. The remaining stiffnesses for an anisotropic plate are effectively reconstructed through a stepwise, targeted optimization of carefully selected dispersion data to maximize sensitivity to stiffnesses that are sought and at the same time restrict the search for optimal values to a series of one-dimensional optimizations. Experiments have been performed on both isotropic and anisotropic plates, and the measurement results show a disparity of 5% or less from contact acoustic estimates or handbook values for most of the elastic stiffnesses.

ACKNOWLEDGMENTS

This work has been supported in part by the Institute for Physical Research and Technology at Iowa State University.

[1] B. Hosten, M. Deschamps, and B. R. Tittmann, "Inhomogeneous wave generation and propagation in lossy anisotropic solids. Application to the characterization of viscoelastic composite materials," J. Acoust. Soc. Am. **82**, 1763–1770 (1987).
[2] R. L. Weaver, W. Sachse, and L. Niu, "Transient ultrasonic waves in a viscoelastic plate: Applications to materials characterization," J. Acoust. Soc. Am. **85**, 2262–2267 (1989).
[3] M. R. Karim, A. K. Mal, and Y. Bar-Cohen, "Inversion of leaky Lamb wave by simplex algorithm," J. Acoust. Soc. Am. **88**, 482–491 (1990).
[4] W. Karunasena, R. L. Bratton, S. K. Datta, and A. H. Shah, "Elastic wave propagation in laminated composite plates," J. Eng. Mater. Technol. **113**, 411–418 (1991).
[5] M. Deschamps and B. Hosten, "The effects of viscoelasticity on the reflection and transmission of ultrasonic waves by an orthotropic plate," J. Acoust. Soc. Am. **91**, 2007–2015 (1992).
[6] D. K. Hsu and F. J. Margetan, "Analysis of acousto-ultrasonic signals in unidirectional thick composites using the slowness surfaces," J. Compos. Mater. **26**, 1050–1061 (1992).
[7] S. I. Rokhlin and W. Wang, "Double through-transmission bulk wave method for ultrasonic phase velocity measurement and determination of elastic constants of composite materials," J. Acoust. Soc. Am. **91**, 3303–3312 (1992).
[8] M. Veidt and W. Sachse, "Ultrasonic evaluation of thin, fiber-reinforced laminates," J. Compos. Mater. **28**, 329–342 (1994).
[9] S. I. Rohklin and D. E. Chimenti, "Reconstruction of elastic constants from ultrasonic reflectivity data in a fluid-coupled composite plate," in *Review of Progress in QNDE*, edited by D. O. Thompson and D. E. Chimenti (Plenum, New York, 1990), Vol. 9, pp. 1411–1418.
[10] A. Safaeinili, O. I. Lobkis, and D. E. Chimenti, "Air-coupled ultrasonic estimation of viscoelastic stiffness in plates," IEEE Trans. Ultrason. Ferroelectr. Freq. Control **43**, 1171–1180 (1996).
[11] O. I. Lobkis, A. Safaeinili, and D. E. Chimenti, "Precision ultrasonic reflection studies in fluid-coupled plates," J. Acoust. Soc. Am. **99**, 2727–2736 (1996).
[12] B. Hosten, D. A. Hutchins, and D. W. Schindel, "Measurement of elastic constants in composite materials using air-coupled ultrasonic bulk waves," J. Acoust. Soc. Am. **99**, 2116–2123 (1996).
[13] O. I. Lobkis, D. E. Chimenti, and H. Zhang, "In-plane elastic property characterization in composite plates," J. Acoust. Soc. Am. **107**, 1852–1857 (2000).
[14] D. E. Chimenti, "Guided waves in plates and their use in materials characterization," Appl. Mech. Rev. **50**, 247–284 (1997).

[15] D. Fei and D. E. Chimenti, ''Single-scan elastic property estimation in plates,'' Acoustics Research Letters Online **2**, 49–54 (2001).
[16] D. E. Chimenti and D. Fei, ''Scattering coefficient reconstruction in plates using focused acoustic beams,'' Int. J. Solids Struct. **39**, 5495–5513 (2002).
[17] W.-J. Xu, M. Ourak, M. Lematre, and G. Bourse, ''Measurement of reflectance function for layered structures by pulsed wave $V(z)$ inversion,'' in *Review of Progress in QNDE*, edited by D. O. Thompson and D. E. Chimenti (American Institute of Physics, New York, 2000), Vol. 19, pp. 1183–1189.
[18] Y.-C. Lee, ''Measurements of dispersion curves of leaky Lamb waves using a lens-less line-focus transducer,'' Ultrasonics **39**, 297–306 (2001).
[19] G. A. Deschamps, ''Gaussian beam as a bundle of complex rays,'' Electron. Lett. **7**, 684–685 (1971).
[20] S. Zeroug, F. E. Stanke, and R. Burridge, ''A complex-transducer-point model for emitting and receiving ultrasonic transducers,'' Wave Motion **24**, 21–40 (1996).
[21] H. Zhang and D. E. Chimenti, ''Two- and three-dimensional complex-transducer-point analysis of beam reflection from anisotropic plates,'' J. Acoust. Soc. Am. **108**, 1–9 (2000).
[22] R. B. Thompson and E. F. Lopes, ''The effects of focusing and refraction on Gaussian ultrasonic beams,'' J. Nondestruct. Eval. **4**, 107–123 (1984).
[23] B. A. Auld, *Acoustic Fields and Waves in Solids*, 2nd ed. (Krieger, Malabar, FL, 1990), Vols. I and II.
[24] O. I. Lobkis and D. E. Chimenti, ''Three-dimensional transducer voltage in anisotropic materials characterization,'' J. Acoust. Soc. Am. **106**, 36–45 (1999).
[25] V. M. Levin, O. I. Lobkis, and R. G. Maev, ''Investigation of the spatial structure of acoustic fields by a spherical focusing transducer,'' Sov. Phys. Acoust. **36**, 391–395 (1990).
[26] W. H. Press, S. A. Teukolsky, W. T. Vetterling, and B. P. Flannery, *Numerical Recipes in FORTRAN: The Art of Scientific Computing* (Cambridge University Press, London, 1992), Chap. 10.
[27] W. P. Rogers, ''Elastic property measurement using Rayleigh-Lamb waves,'' Res. Nondestruct. Eval. **6**, 185–208 (1995).

Elastic wave thermal fluctuations, ultrasonic waveforms by correlation of thermal phonons

Richard L. Weaver[a] and Oleg I. Lobkis
Theoretical and Applied Mechanics, University of Illinois, 104 South Wright Street, Urbana, Illinois 61801

(Received 10 October 2002; accepted for publication 10 February 2003)

It is widely recognized that acoustic degrees of freedom coupled to a thermal bath have amplitudes which fluctuate with a mean square proportional to temperature; this is the basis for the Debye theory of the heat capacity of insulating solids. It is shown here that these elastic wave thermal phonons have correlation functions identical to the system's ultrasonic Green's function, and furthermore that thermal noise in ultrasonic detectors should have correlation functions equivalent to conventional waveforms obtained by active transmission and reception. This suggests the possibility of doing ultrasonics without a source. Theory for the identity is presented, and several room temperature laboratory confirmations are conducted in the frequency range 0.1–1.0 MHz. The thermal nature of the origin of these correlations is established by comparing their strength with theoretical expectations. Applications are discussed. [DOI: 10.1121/1.1564017]

PACS numbers: 43.35.Gk, 43.40.Hb, 43.60.Cg [ADP]

I. INTRODUCTION

It has recently been argued and demonstrated[1] that an ultrasonic diffuse field has correlations equal to the local ultrasonic Green's function. Exact equality was shown to deteriorate if the field is insufficiently diffuse, or if it has an imperfectly flat spectrum, or if the transducers used to detect the diffuse field have significant phase. The thesis was illustrated in the laboratory.[1]

In that illustration, the source of the diffuse field was a distant piezoelectric transducer excited by an impulse. Its spectrum was therefore not flat, but rather highly colored by the source transducer's response function, and by the local impedance near the source. Further complications arose from the decay of the diffuse field. In the absence of compensation for that decay, the low amplitude late time parts of the diffuse field contribute only weakly to the correlation function, yet they contain as much information as the earlier times. Even after compensation for the spectrum of the source and the decay of the diffuse field, it was found that a fixed deterministic source generates an imperfectly diffuse field, and leads to an imperfect recovery of the local response. Part of the discrepancy was perhaps due to the uncorrected phase of the receiving transducer, but part may have been due to imperfect compensations and/or imperfectly diffuse fields.

A recent letter[2] reported measurements that avoid these difficulties by employing the diffuse field offered by thermal fluctuations in the specimen. At frequencies below $kT/h \approx 6$ TeraHz (where h is Planck's constant, k is Boltzmann's constant, $k=1.38\times10^{-23}$ J/deg, and T is absolute temperature) thermal fluctuations are known to have a flat spectrum, with each natural mode (phonon state) of vibration being randomly excited in a Gaussian process with equal mean energy kT.[3] The fluctuation-dissipation theorem[4,5] indicates that the amplitude and phase of each mode fluctuate, with a coherence time equal to the absorption time of an ultrasonic excitation of that mode. This field is truly diffuse, it has a flat spectrum, and it does not decay in time. Except for its weakness, these features make it ideal for the purposes of constructing local responses by autocorrelation. That such constructions are feasible was nevertheless demonstrated[2] with ''pulse-echo'' waveforms using a single transducer for both source and detector. Here we report further studies of ultrasonic thermal fluctuation correlation, and demonstrate that the technique works well with other transducers, and less well with still others. It is shown that ''pitch-catch'' waveforms (those transmitted by one transducer and received by another) may be constructed in this way also. It is found that certain issues related to transducer design are relevant for the quality and character of the construction.

By the standards of conventional ultrasonics the mean thermal energy in each mode, $kT \approx 4.2\times10^{-21}$ J, is extremely small. The corresponding root mean square ultrasonic displacement amplitude at 1 MHz, in a band of width 1 MHz is about 3 fm, roughly the classical radius of the electron. The small energy kT may be compared with the work done, on a typical mode, by a calibrated ultrasonic source consisting of a broken glass capillary.[6] Such a source is modeled as a point step force of magnitude $F_o \sim 10$ N. The rise time of the step force is about 200 ns, so the spectrum of this source has little structure below 1 MHz. The work done by such a load on a mode of frequency ω is $F_o^2/6\,M\,\omega^2$ times a random quantity of order unity (with mean value unity) equal to the participation[7] of the mode at the position of the source. M is the mass of the specimen. Taking $M \sim 1$ kg, $F_o \sim 10$ N and $\omega = 6\times10^6$ rad/s, one finds that the broken capillary source applies an average energy per mode of $\sim 1.4\times10^{-13}$ J, 75 dB greater than thermal.

While thermal excitations are weak, there are transducers with signal-to-noise ratios of this order.[8] Such a transducer, it would appear, generates a level of noise of which a significant fraction is due to thermal phonons in the speci-

[a]Electronic mail: r-weaver@uiuc.edu

men. The remainder is presumably due to ambient acoustic noise in the environment, thermal phonons in the transducer, or electronic thermal fluctuations in the receiver circuit. For such transducers there is therefore a possibility that their noise could be processed in such a manner as to isolate the contributions of the phonons and reveal sample properties and sample geometry.

In the next section we present a theoretical derivation of the relationship between the correlations of a thermal phonon field and conventional ultrasonic waveforms. Then in order to estimate whether such correlations can be obtained in the laboratory, the thermal phonon sensitivities of three commercial transducers are assessed quantitatively. One transducer is found for which a significant part of the noise is thermal fluctuations in the body with which it is in contact. The laboratory system used to correlate thermal noise is then described, and comparisons are made between correlations and signals obtained by conventional means. The waveforms determined by different methods are found to be substantially identical. That the correlations are thermal in origin is confirmed by comparing their strength with theory.

Detection of thermal ultrasonic fields is not new. Recent advances in acoustic thermography[9] have allowed remote measurements of temperature and calibration of underwater transducers. The present work differs in that we focus on the correlations of thermal noise signals and establish an identity between those correlations and waveforms obtained by conventional active methods.

II. CORRELATIONS OF THERMAL FLUCTUATIONS

The cross correlation between the thermal ultrasonic signals detected by two transducers is equivalent to the direct ''pitch-catch'' signal that passes from one transducer to the other. The auto-correlation of thermal signals in one transducer is equivalent to the direct pulse-echo signal from that transducer. This section derives these identities in two distinct fashions. The first considers a passive ultrasonic receiver in contact with a thermal phonon field. The second considers the impedance presented by the transducer and amplifier and makes no reference to the specimen. An identity between correlations and ultrasonic waveforms is derived in each case, and in each case a few caveats are emphasized.

A. Correlations of a thermal phonon field

The material displacement in an elastodynamic field in a finite body may be expressed in modal form by

$$\phi(\mathbf{x},t)=\mathrm{Re}\sum_{n=1}^{\infty} a_n\mathbf{u}_n(\mathbf{x})\exp\{i\omega_n t\}, \tag{1}$$

where the a_n are the complex modal amplitudes. The $\mathbf{u}_n$ are the vector-valued displacement mode shapes; they are real and orthonormal:

$$\int \rho\mathbf{u}_n\cdot\mathbf{u}_m\, d^3\mathbf{x}=\delta_{nm}.$$

Thus the total energy in the field (1) is

$$\frac{1}{2}\sum_{n=1}^{\infty}\omega_n^2|a_n|^2.$$

A statement that the field ϕ is diffuse with real spectral power density F implies that the modal amplitudes are uncorrelated random variables

$$\langle a_n a_m^*\rangle=\delta_{nm}F(\omega_n), \tag{2}$$

where F is smooth on the scale of the modal spacings. If the field is due to thermal fluctuations at temperature T, each mode has an equal expected energy, kT. Thus $F(\omega)=2kT/\omega^2$. If the field is thermal, the a_n's vary slowly and randomly in time, with

$$\langle a_n(t)a_m^*(t')\rangle=\delta_{nm}2kT/\omega_n^2\exp\{-\gamma_n|t-t'|\},$$

where γ is the decay rate of mode n.

It is a simple matter to construct the cross correlation of the displacement fields at x and y. For times τ short compared to decay times $1/\gamma$, one finds

$$\langle\phi(\mathbf{x},t)\,\phi(\mathbf{y},t+\tau)\rangle=\frac{1}{2}\mathrm{Re}\sum_{n=1}^{\infty}F(\omega_n)\mathbf{u}_n(\mathbf{x})\mathbf{u}_n(\mathbf{y})\times\exp\{-i\omega_n\tau\}. \tag{3}$$

The brackets in the above represent an average. The correlation may be affected by integrating in t over a long interval L, in which case the integration must be followed by dividing by L. After setting $F=2kT/\omega^2$ and taking a derivative $d/d\tau$, this is readily recognized as essentially kT times the Green's dyadic $\mathbf{G}_{xy}$ governing propagation from x to y:

$$\mathbf{G}_{xy}(\tau)=\sum_{n=1}^{\infty}\mathbf{u}_n(\mathbf{x})\mathbf{u}_n(\mathbf{y})\frac{\sin\omega_n\tau}{\omega_n}\quad(\text{for }\tau>0,\quad 0\ \text{otherwise}). \tag{4}$$

The time derivative of the expression (3) differs from the actual Green's dyadic by a scaling factor involving kT, and by its support for negative τ. It is therefore useful to define an *extended* and acausal Greens dyadic $\mathbf{G}^{\text{extended}}$ using Eq. (4) without the restriction to positive τ:

$$\mathbf{G}^{\text{extended}}(\tau)=\mathbf{G}(\tau)-\mathbf{G}(-\tau).$$

If the field ϕ is detected by transducers at $\mathbf{x}$ and $\mathbf{y}$, with receiver functions $\mathbf{R_x}$ and $\mathbf{R_y}$, then the waveforms produced by the transducers are

$$\begin{aligned}V_x(t)&=\mathbf{R}_x*\phi+N_x(t)\\&=\mathrm{Re}\sum_{n=1}^{\infty}a_n\tilde{\mathbf{R}}_x(\omega_n)*\mathbf{u}_n(x)\exp\{i\omega_n t\}+N_x(t),\\V_y(t)&=\mathbf{R}_y*\phi+N_y(t)\\&=\mathrm{Re}\sum_{n=1}^{\infty}a_n\tilde{\mathbf{R}}_y(\omega_n)*\mathbf{u}_n(y)\exp\{i\omega_n t\}+N_y(t),\end{aligned} \tag{5}$$

where $*$ indicates a temporal and spatial convolution and a vector inner product, and $*$ indicates only the spatial convolution and vector inner product:

$$\mathbf{R}_x * \phi(\mathbf{x},t) \equiv \int_{-\infty}^{t} \mathbf{R}_x(t-t') * \phi(t')\, dt'$$

$$= \int_{-\infty}^{t} \int_A \mathbf{R}_x(\mathbf{x}', t-t') \cdot \phi(\mathbf{x}', t')\, d^2x'\, dt'.$$

The inner integration is over the area A of the transducer face. N_x and N_y are nonphononic noise signals, presumably uncorrelated with each other and with the thermal phonon field. If these two waveforms are cross correlated, one finds

$$C_{xy}(\tau) = \langle V_x(t) V_y(t+\tau) \rangle$$

$$= \frac{1}{2} \mathrm{Re} \sum_{n=1}^{\infty} F(\omega_n) \tilde{\mathbf{R}}_x(\omega_n) * \mathbf{u}_n \mathbf{u}_n * \tilde{\mathbf{R}}_y^*(\omega_n)$$

$$\times \exp\{-i\omega_n \tau\}. \tag{6}$$

The asterisk superscript indicates a complex conjugation. On setting $F = 2kT/\omega^2$ and taking a derivative $d/d\tau$, one finds

$$P_{xy}(\tau) \equiv dC(\tau)/d\tau = kT \mathbf{R}_x * \mathbf{G}_{xy}^{\text{extended}} * \mathbf{R}_y^{\text{t.r.}}, \tag{7}$$

where the superscript t.r. indicates a time reversal operation. The result is the convolution of transducer functions with the extended Green's dyadic. This is kT times the signal which would be received in the transducer at x due to an impulsive source applied to the transducer at y,

$$V_{xy} = \mathbf{R}_x * \mathbf{G}_{xy} * \mathbf{S}_y, \tag{8}$$

except for two reservations. The transducer at y must have a receiver function $\mathbf{R}_y$ whose time-reversed form is identical to its source function $\mathbf{S}_y$. This is generally not the case. While ultrasonic piezoelectric transducers are generally reciprocal, $\mathbf{R} \sim \mathbf{S}$, they are also causal, so $\mathbf{R}$ has support only for nonnegative times. Its time-reversed form will have support only for nonpositive times. A causal transducer function that is symmetric in time can have support only at $t=0$, e.g., $\mathbf{R} \sim \delta(t)$. Few ultrasonic transducers may be approximated as having such simple responses. A second caveat notes that replacing the Green's function with the extended Green's function must be permitted.

To gain some understanding of what Eq. (7) actually indicates, it is useful to define a ring-time, Δ, of each of the transducers at x and y, Δ being the duration of the response of the transducer after it is excited by an impulse. Thus $\mathbf{R}_x$ has support over an interval $[0, \Delta_x]$ and $\mathbf{R}_y^{\text{t.r.}}$ has support on $[-\Delta_y, 0]$. We also note that $\mathbf{G}^{\text{extended}}(\tau) = \mathbf{G}(\tau) - \mathbf{G}(-\tau)$ and $\mathbf{G}_{xy} = \mathbf{G}_{yx}$. Thus,

$$dC_{xy}(\tau)/d\tau = kT \mathbf{R}_x * [\mathbf{G}_{xy} - \mathbf{G}_{xy}^{\text{t.r.}}] * \mathbf{R}_y^{\text{t.r.}}$$

$$= kT[\mathbf{R}_x * \mathbf{G}_{xy} * \mathbf{R}_y^{\text{t.r.}}]$$

$$- kT[\mathbf{R}_y * \mathbf{G}_{yx} * \mathbf{R}_x^{\text{t.r.}}]^{\text{t.r.}}. \tag{9}$$

The first of these terms can be seen to be a hypothetical pitch-catch signal. It is the response at x to a hypothetical source at y, a source with a time function which is the reverse of the receiver function of the transducer at y. This first term has support over a range $[-\Delta_y, \infty]$. If x and y are far enough apart that all signals propagate with a delay of at least De, then this waveform has support on a narrower interval $[\mathrm{De} - \Delta_y, \infty]$. The second term is the time-reversed image of a different hypothetical signal. It has support on the interval $[-\infty, \Delta_x - \mathrm{De}]$. If we confine our attention to the interval $[\Delta_x - \mathrm{De}, \infty]$ (i.e., the first term, mostly positive τ), $dC_{xy}/d\tau$ is a conventional signal. It is not precisely the signal that is generated by pulsing y and receiving at x, but is similar to it, especially if the transducer at y is sufficiently wide band, with small Δ_y. Roughly speaking, it is the actual pitch-catch signal, advanced in time by an amount of order Δ_y.

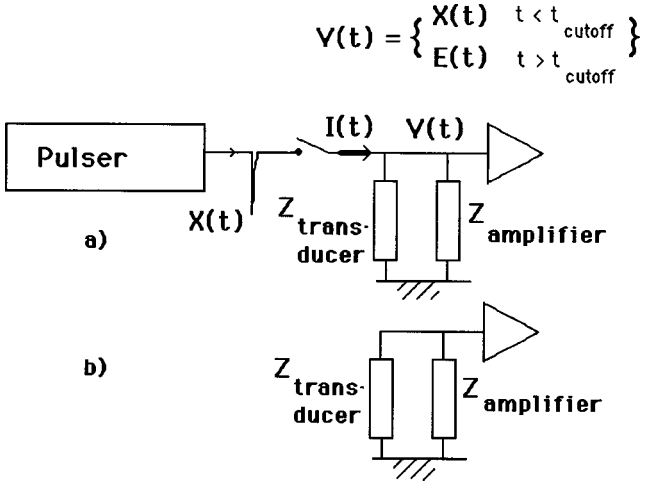

FIG. 1. (a) Simplified pulse/echo circuit diagram. The excitation pulse $X(t)$ is essentially impulsive. Its details are determined by the impedance of the pulser and to a lesser extent by the impedance $Z = [1/Z_{\text{transducer}} + 1/Z_{\text{amplifier}}]^{-1}$ of the transducer and amplifier. At times before cutoff while the switch is closed, V is $X(t)$; at times after cutoff while the receiver is isolated from the pulser and I is zero, V is $E(t)$ the pulse echo signal. (b) Circuit diagram in thermal correlation mode.

In the event that V_x is correlated with itself, with the intent of constructing a pulse-echo signal, most of the above argument is unmodified. The only difference is the effect of the noise $N_x(t)$. One finds for

$$P_{xx}(\tau) = dC_{xx}(\tau)/d\tau$$

$$= kT \mathbf{R}_x * \mathbf{G}_{xx}^{\text{extended}} * \mathbf{R}_x^{\text{t.r.}} + dC_{Nx\ Nx}(\tau)/d\tau \tag{10}$$

that the recovered waveform contains, in addition to pulse echo waveforms, contributions from the autocorrelation function of the nonphononic noise.

B. Transducer impedance and the fluctuation-dissipation theorem

The identity (10) between pulse/echo signals and autocorrelations of thermal fluctuations may also be obtained by a very different analysis[2] in which the properties of the specimen enter only by means of the impedance which the transducer presents to the electronic circuit. Electro-acoustic impedances are treated in a unified manner in the literature. See, for example, the text by Kino.[10] Here we take the impedance as given and do not closely analyze the transducer.

In pulse/echo configuration a large excitation voltage spike $X(t)$ of short duration is applied to a transducer and amplifier, as in Fig. 1(a). $X(t)$ is typically approximated as a simple exponential $V_0 \exp(-t/RC)$ with RC dominated by the properties of the pulser and equal to about 20 ns. A diode

bridge or switch or other nonlinear circuit isolates the transducer from the pulser after a short time t_{cutoff} of the order of a microsecond. During the excitation phase a current $I(t)$ passes through the transducer and amplifier. After the pulser is isolated, at $t>t_{\text{cutoff}}$, the current $I(t)$ becomes precisely zero. At such times, $t>t_{\text{cutoff}}$, the pulse echo signal $E(t)$ is given by

$$E(t)=\int_0^{t_{\text{cutoff}}} I(\tau)Z(t-\tau)\ d\tau, \quad t>t_{\text{cutoff}},$$
$$\tilde{E}(\omega)=\tilde{I}(\omega)Z(\omega). \tag{11}$$

In practice nonlinear elements in the amplifier can, at short times, still be in the process of recovering from the assault $X(t)$. For this reason the signal reported by the amplifier at the shorter times is reliably given by (11) only after the amplifier has recovered. Inasmuch as echo signals like E contain information on specimen geometry, and inasmuch as I is relatively independent of the specimen, Eq. (11) indicates that echo information must be present in Z.

The precise form of the pulse/echo signal $E(t)$ depends on both impedance Z and early values of $I(t)$. $I(t)$ is given in terms of the excitation pulse $X(t)$ and the early time values of the impedance

$$I(t)=\int_0^{t} X(\tau)Z^{\text{inv}}(t-\tau)\ d\tau, \quad t<t_{\text{cutoff}},$$
$$\tilde{I}(\omega)\approx V_o RC/\overline{Z}(\omega), \tag{12}$$

where Z^{inv} is the convolution operator inverse to Z. This inverse operation is effected easily in the frequency domain by a simple division, as in the second line of (12). The overbar indicates a smoothing operation in the frequency domain, corresponding to a confinement to early times $t<t_{\text{cutoff}}$ in the time domain.

Combining (11) and (12), one finds

$$\tilde{E}(\omega)=V_o RCZ(\omega)/\overline{Z}(\omega). \tag{13}$$

The pulse echo signal is, at times after the pulser is isolated and after the amplifier recovers, Z itself deconvolved with the smoothed (short time) $\overline{Z}$.

This result may be compared with a simple application of the fluctuation-dissipation theorem.[5] When the pulser is disconnected as in Fig. 1(b), thermal noise in the receiver circuit has a spectral power density $S(\omega)$ (the Fourier transform of V's autocorrelation function C) given by the theorem

$$S(\omega)=\int C(\tau)\exp\{-i\omega\tau\}d\tau$$
$$=2kT\,\text{Re}[Z(\omega)]=kT(Z(\omega)+Z^*(\omega)), \tag{14}$$

where Z is causal, the Fourier transform of a function without support at negative times. The inverse Fourier transform of the above is, at positive times such that Z^* vanishes, $Z(t)$. P is the time derivative of V's autocorrelation function; its Fourier transform is $i\omega$ times $S(\omega)$; therefore

$$\tilde{P}(\omega)=i\omega S(\omega)=kTZ(\omega)=i\omega\overline{Z}\frac{kT}{V_o RC}\tilde{E}(\omega). \tag{15}$$

Except for the factor $i\omega\overline{Z}$, and a constant, P is identical to E.

The desired identity between P and E follows if the transducer and amplifier offer an early time impedance $\overline{Z}$ that is purely capacitive, $\overline{Z}=1/i\omega C_{TA}$. Deviation from pure capacitance will preserve a relation, but distort the identity. That there must be some resistive part to $\overline{Z}$ is obvious; the transducer must be doing some work on the specimen. Nevertheless, we expect in practice that the resistive part is small. Our measurements of the autocorrelation function of V at small τ show $C_{xx}(\tau)=\langle V_x(t)V_x(t+\tau)\rangle_t$ to be of the form of a delta function (a resistive part) plus a step function (the capacitive part). The impulse under the delta-function part is about 20 ns times the amplitude of the step function, indicating that the capacitative part will dominate as long as $t_{\text{cutoff}}>20$ ns, i.e., as long as the cutoff time is late enough to allow the transducer and amplifier to drain their excess charge [originating in $X(t)$] back through the pulser. We conclude that $P\approx E$.

This latter argument does not easily lend itself to treatment of waveforms obtained by pulsing one transducer and receiving at another, and their relation to cross correlation functions. It may be that the theory of thermal cross correlations (e.g., Ref. 4) will be applicable to that extension.

This section concludes by drawing attention to a small mystery. Each of the two arguments indicates that there is a near-identity between time derivatives of autocorrelations of thermal noise and pulse/echo signals. But their conditions differ. The first argument states that precise identity requires the transducers to have sharp responses in the time domain, and little ringing. The second argument states that precise identity requires that the short-time ($<t_{\text{cutoff}}$) impedance of transducer and amplifier be capacitive. These conditions appear to be very different.

III. SPEED OF CONVERGENCE, DEVICE SENSITIVITY, AND NOISE

A priori estimates of the degree of averaging necessary before the Green's function actually emerges from the correlation are possible. Such a theory would define a correlation function

$$C_{xy}^L(\tau)=\frac{1}{L}\int_0^L V_x(t)V_y(t+\tau)dt \tag{16}$$

as an average over a finite, but presumably large, interval L. As L approaches infinity, C^L approaches the correlation function discussed above. At finite L,C must have random deviations from $\langle C\rangle$, deviations that could be estimated theoretically using the known Gaussian autocorrelations of the modal amplitudes a_n discussed in Eq. (1). The magnitude of the required L could be set by insisting that these deviations be small compared to typical values of $\langle C\rangle$. Critical to such a calculation would be a prior assessment of the relative strengths of the first and second terms of (5), the phononic and noise contributions to the signals V.

Such a calculation would appear to be possible, but sufficiently lengthy as to be outside the scope of this paper. In lieu of that, it is possible to estimate the required magnitude of L by noting that reasonable convergence was obtained in

Ref. 1, when the diffuse field was generated by a third transducer acting as a diffuse field source, after an integration time of several tens of ms. This provides a lower limit for the present case, in which the signals V are partly phononic, i.e., ultrasonic (and thus similar to the fields generated in Ref. 1) and partly non-ultrasonic noise $N(t)$. A rough estimate is therefore constructed in the form: L must be greater than several tens of ms divided by the fraction of the noise power due to thermal phonons.

Estimates of that fraction may be made by measuring the total power spectral density of V, and comparing with the strength of signal noise due to the phonons. The former quantity is easily measured. The latter quantity requires knowledge of transducer sensitivity; this can be obtained from a diffuse field measurement using a calibrated source.

A normal step force of magnitude F_o applied to the free surface of a finite elastic body does an average work per mode of frequency ω of

$$\text{Work} = pF_o^2/6M\omega^2, \tag{17}$$

where p is the participation factor defined in Ref. 7, equal to 2.3 for a Poisson ratio of 0.33. (It would be unity, $p=1.0$, if the load could be applied at a generic internal point. The actual value of p for a specific mode depends on the amplitude of the mode at the position of the load.) The resulting diffuse field is detected by a transducer, which reports a signal $W(t)$. The power spectral density of that signal, at times before the field has suffered any significant decay, and after normalizing by Eq. (17), is a measure of the transducer's sensitivity. Correspondingly we normalize the square of the Fourier transform of $W(t)$,

$$|\text{FFT}W(t)|^2 \quad 6M\omega^2/pF_o^2. \tag{18}$$

This is the square of the response divided by the energy per mode in the sample. Thus it is the average sensitivity of the transducer to diffuse modal energy. This may be compared to the power spectral density of the thermal noise signal V_x [see Eq. (5)] at position x, normalized by the phonon energy per mode kT

$$|\text{FFT}V_x(t)|^2/kT. \tag{19}$$

Thus the spectral power in each signal is normalized by the energy per mode in the sample. If the normalized powers are equal, then the thermal noise signal V_x is entirely phononic. If the latter is greater, then the noise signal V_x also has contributions from electronic and other noise sources. Theory tells us that the latter quantity cannot be smaller than the former. The ratio of these two quantities is a kind of absolute sensitivity-to-noise ratio, a figure of merit for the transducer

$$\text{S.t.N.} = |\text{FFT}W(t)|^2 \quad 6kTM\omega^2/pF_o^2|\text{FFT}V_x(t)|^2. \tag{20}$$

The required L is estimated to be several tens of ms, divided by the S.t.N.

Equation (20) was evaluated for three different transducers. Figure 2(a) shows the power spectral density (as represented by the square of the fast Fourier transform) of 12.8 ms of noise signal V obtained from a Valpey-Fisher pin transducer coupled to a 7.6 kg roughly cubic but irregularly shaped aluminum block, amplified by 40 dB, and digitized at 5 MSa/s. It also shows the square of the Fourier transform of the (40 dB amplified) first 12.8 ms $W(t)$ detected after the breaking of a glass capillary. The frequency-dependent S.t.N. obtained from Eq. (15) using $F_o = 10$ N is also shown. It is clear that the noise signal from this pin transducer is mostly nonphononic. This transducer and receiver circuit has a poor sensitivity-to-noise ratio. Even at its peak sensitivity, the pin-transducer's noise is 92% nonphononic. More typical values are 98%.

The same procedure was also applied to other transducers. Figure 2(b) shows that the model WD Acoustic-Emission transducer from Physical Acoustics Corporation has similar sensitivity, and much less noise. The inset evaluates Eq. (20) and shows that a significant part of this transducer's noise signal is phononic. The results from a Digital Wave model B1025 Acoustic Emission transducer are shown in Fig. 2(c). This transducer has an intermediate S.t.N.

The technique cannot be applied to assess the sensitivity-to-noise ratios of higher frequency (>1 MHz) transducers, as the calibrated broken capillary step source lacks high-frequency components.

IV. LABORATORY IMPLEMENTATION

We have attempted to reconstruct local responses from thermal fields in simple blocklike structures of dimensions of the order of several cm. Two distinct measurements were made. The noise from the highly sensitive WD Acoustic Emission transducer was autocorrelated and the result compared to its conventional pulse-echo signal, at early and late times. Comparisons for the less sensitive but better damped transducer from Digital Wave were studied also. Then the noise from the two transducers was cross correlated, and the result compared with a conventional signal obtained by transmitting from one transducer and receiving in the other. In all cases the comparisons showed that conventional waveforms are indeed recovered by this kind of correlation.

A. Pulse echo waveforms from autocorrelation in one transducer

Figure 3 shows a simple configuration in which a transducer is coupled to the center of one face of a cylindrical aluminum block (17.8 cm diameter, 10.2 cm thickness, mass 6.8 kg) using a light oil. Its noise signal was amplified by 100 dB, low-pass anti-alias filtered at 0.9 MHz, and digitized at 12.5 MSa/s into 2.56-ms windows. The transducer, battery-powered amplifier, and sample were isolated in a grounded foil-covered box (a Faraday shield) that eliminated interference from a local radio station broadcasting at 580 kHz. Each 32 000 byte waveform was passed to a PC running LabView and Fourier transformed. The spectrum was absolute-value squared, inverse Fourier transformed, and time differentiated. The whole process required about $\frac{1}{3}$ s. This was repeated many times, and the result averaged. The resulting τ-dependent waveform could be observed on the PC screen as the averaging proceeded, allowing the operator to judge when the averaging had converged. Good convergence was generally obtained within several seconds of real time, i.e., after some 100 ms of noise had been collected. The

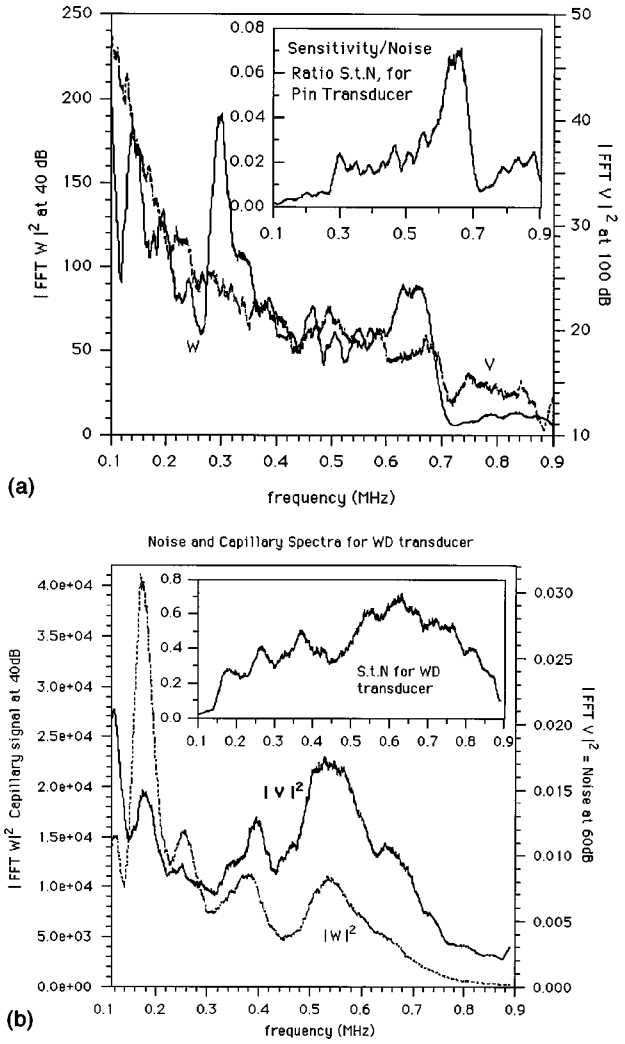

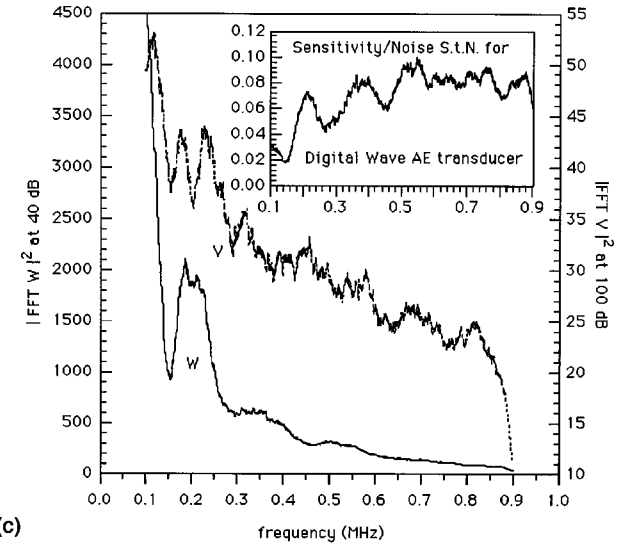

FIG. 2. (a) The spectra of 12.8 ms of noise, and 12.8 ms of broken-capillary signal, both from a Valpey-Fisher Pin transducer amplified by 40 dB, passed through a low-pass anti-aliasing filter with a cutoff at 900 kHz, and digitized at 2.5 MSa/s. A factor of $2T/N^2=2.5\times10^{-5}$ (where $T=12.8$ ms, N is the number of samples, and $N=T$ times the sampling rate) converts these numbers into units of V^2/MHz; thus typical signal levels were of the order of tens of mV. Equation (20) is evaluated in the inset, where it may be seen that the majority of the noise is nonphononic. (b) Comparison of noise and broken capillary spectra for the Physical Acoustics Corporation WD transducer. Equation (20) is evaluated in the inset (with a correction for the differing amplifications) where it may be seen that about half the noise is phononic. (c) Comparison of noise and broken capillary spectra for the Digital Wave *B*1025 transducer. Equation (20) is evaluated in the inset (with a correction for the differing amplifications) where it may be seen that about 6% of the noise is phononic.

plots below report the result after 500 such averages were made, for a total of 1.28 s of raw thermal fluctuation data collected in about 2 min of real time. All waveforms shown were digitally filtered between 100 and 900 kHz, to remove high-frequency noise and remove the contributions of low-frequency ambient vibrations.

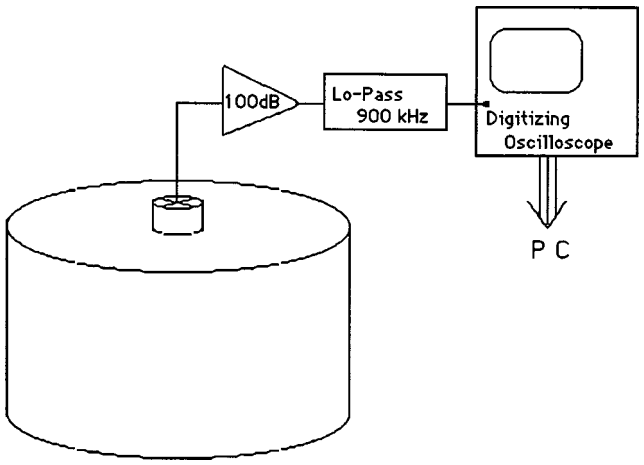

FIG. 3. The simple configuration in which the noise from a single Acoustic Emission transducer was captured and autocorrelated. On command from the *PC*, 32 000 8-bit samples of successive noise were collected by the oscilloscope, passed to the *PC*, and autocorrelated. This step was repeated and the autocorrelation was averaged.

This process was first applied for the case of the 15-mm-diam Physical Acoustics "WD" transducer, the device identified as having the best S.t.N. Figure 4(a) compares its correlation signal P with its conventional pulse-echo signal. The two waveforms are almost identical (and similar to Fig. 2 of Ref. 2 which was obtained in the same way). Each shows the main features which one expects in a pulse-echo signal. The first and second reflections from the opposite side are clear, as is the arrival of a Rayleigh wave from the edges of the sample. The chief consistent difference between the two waveforms is a constant 1.1 μs shift that was applied to the pulse/echo waveform before plotting; the direct pulse/echo signal arrived slightly later than indicated in the plot. The shift is ascribed to the effect of the low-pass filter, which adds a phase delay to the direct signal, but whose phase drops out due to the modulus-squared in the factor $|R|^2$ in the correlation construction. That the filter is responsible for the shift was confirmed by removing it from the circuit; the result is noisier, but the need for the shift is absent. The presence of two factors of the amplitude of the anti-aliasing filter in P_{xx} but only one in the direct pulse/echo signal is an additional complication.

Differences may also be due to some contamination from long-lived correlations of the nonphononic noise, as predicted in Eq. (10). The waveforms differ much more at

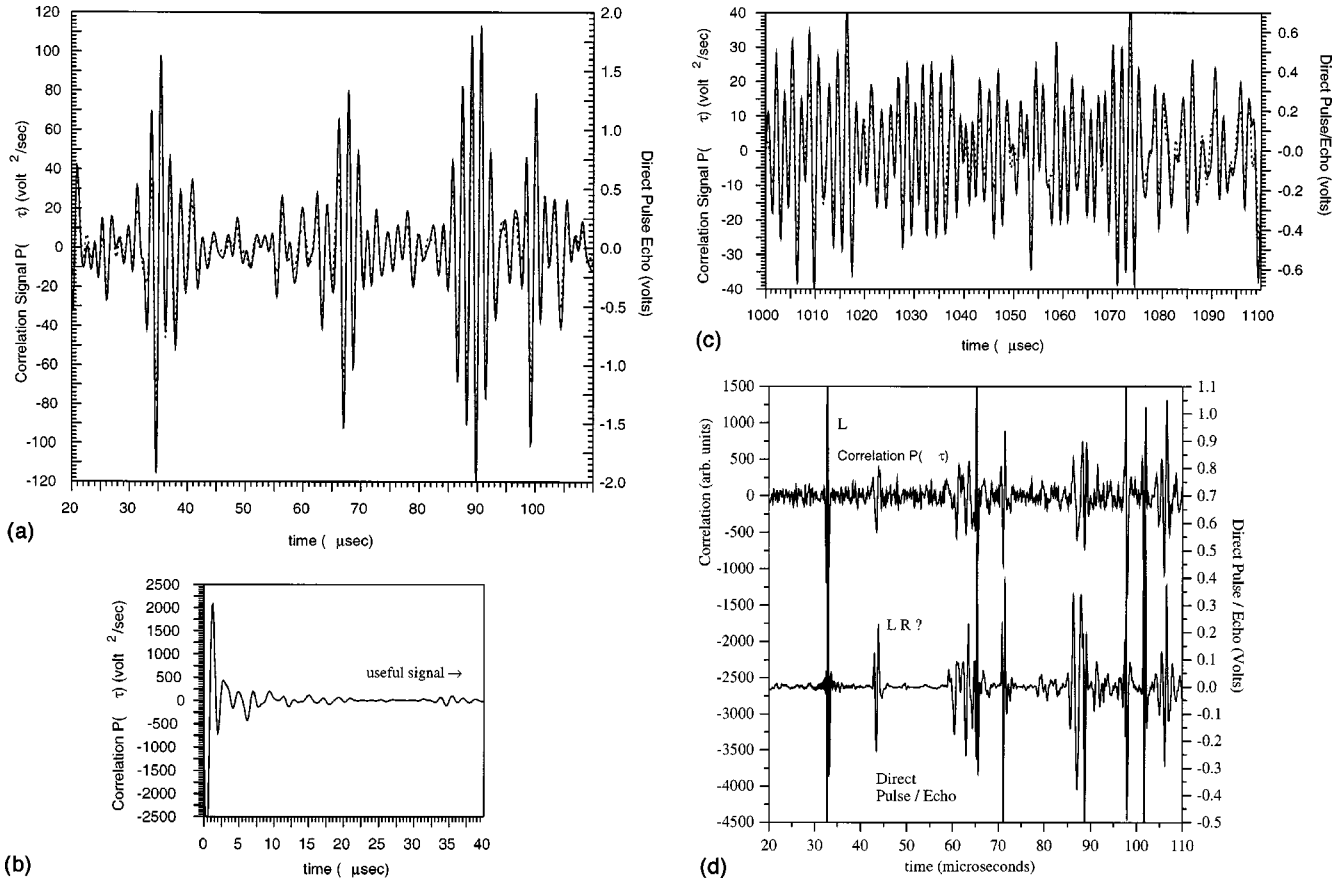

FIG. 4. (a) P_{rr}, the time derivative of the autocorrelation of the (100 dB amplified) noise from the WD transducer in the position indicated in Fig. 3 is very similar to the (1.1 μs shifted) pulse echo signal obtained from the same configuration. Ray arrivals may be identified, although the long ring-time of the transducer tends to obscure them. The round trip travel time of a longitudinal wave is 34 μs; two round trips require 68 μs. Each of these arrivals is apparent. A Rayleigh wave reflected from the circumference would arrive at about 60 μs. The strong arrival at about 90 μs is consistent with an *S*-ray shed from the transducer edge and retroreflected from a far bottom corner. (b) Early time part of the autocorrelation signal. Exact correspondence with direct pulse-echo signals (not shown) at very early times is not expected, as the latter is heavily influenced by the nonlinear properties of the amplifier as it recovers from the main bang. Nevertheless, major features were found to correspond, even for times as early as a few microseconds. (c) Comparison of pulse echo signal *E* and correlation signal *P* at late times, also with applied 1.1 μs shift. (d) Comparison for Digital Wave B1025 Transducer. The correlation signal is taken from 50 000 thermal fluctuation waveforms, each digitized at 25 MSa/s, low-pass filtered at 4.5 MHz into windows of 1.28-ms duration. This transducer has substantially sharper time-domain behavior but its sensitivity is much less. The sharper time-domain behavior has allowed the feature labeled as LR to become clear. LR has an arrival time equal to that of a surface skimming longitudinal ray which mode converts to a returning Rayleigh wave. This correlation function was assembled in 5 h of real time.

early times [shown in Fig. 4(b)] where the nonphononic noise is expected to contribute. That noise has a not-insignificant amplitude, but is weak enough and confined to early enough times that it does not overly contaminate the interesting echoes in the phononic part.

The correlation retains its correspondence with the pulse echo signal even at late times. Figure 4(c) shows the comparison at times close to 1 ms, after typical phonons have traveled over 3 m and each waveform is diffuse. This figure was obtained for a different sample, an irregular aluminum block of size similar to that of the cylinder used in Figs. 4(a) and (b).

The same comparison was also carried out for the much less sensitive 8-mm-diam Digital Wave transducer. Figure 4(d) presents the noise correlation signal and the direct pulse echo signal from that transducer when it is applied in the center of one face of the cylindrical sample. This transducer has a much sharper time-domain response, and the arrivals are more clear. The regimes of near-zero signal show the residual noise more clearly than was apparent in Fig. 4(a). The residual noise is intrinsically greater also, and only minimized by extensive extra averaging to create Fig. 4(d). While Fig. 4(a) was obtained after 1 s of raw thermal data capture, Fig. 4(d) was based on more than 1 min of raw signal, and 5 h of real time.

Attempts to construct pulse/echo waveforms from correlations of thermal fluctuations in commercial ultrasonic transducers were less successful than for the Acoustic Emission transducers. Panametrics wideband contact transducers, models V1048 (3.5 MHz central frequency, 1-in. diameter), and V109 (5 MHz, 0.5 in.) are designed to have excellent performance in pulse-echo and pitch-catch when excited by typical NDE ultrasonic pulsers. But their internal structure can be more complicated than that of Acoustic Emission transducers. Model V1048, for example, was found to have a resistive internal DC impedance of 4 Ohms, while Model V109, was found to have a DC impedance of 900 pf (purely capacitive, like that of the AE transducers and the pin transducers). After several hours of averaging with Model V1048, no discernable sign of an echo was forthcoming. With sev-

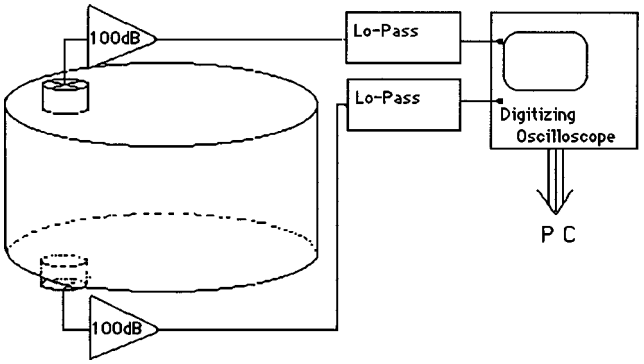

FIG. 5. Diagram of configuration for cross-correlating thermal noise signals from a pair of transducers and thereby constructing pitch-catch signals.

eral hours of averaging, Model V109 did show echoes, but the signal-to-noise ratios remained poor. It was not possible to construct S.t.N. estimates for these transducers, as they have poor response at the low frequencies for which the broken capillary provides a calibrated source. It is nevertheless to be expected that they have comparable state-of-the-art conventional sensitivities for normal use. It is our suspicion that these transducers contain hidden electronic elements that degrade their low-amplitude responses and violate the assumptions implicit in the present thesis.

B. Pitch-catch waveforms from cross correlation between two transducers

In a separate measurement, the two Acoustic Emission transducers were applied with oil couplant to opposite faces of the cylindrical body as in Fig. 5. The noise from each was amplified 100 dB and captured simultaneously in a two-channel digitizer at 5 MSa/s into 32 000 8-bit words of 6.4-ms duration each. Each such waveform was Fourier transformed; the cross-spectral density was formed $V_x(\omega)V_y^*(\omega)$, and the result averaged over some 5000 independent captures (for a total of 32 s of raw data, taking about 40 min of real time). An inverse Fourier transform and a time derivative completed the thermal signal processing.

Figure 6(a) shows the result of this process. The waveform recovered from the cross correlation is compared to that obtained by a direct pitch-catch measurement obtained by pulsing one and receiving with the other. The correspondence may be compared with that of Fig. 4. There are two points of similarity and difference needing discussion.

The absence of a large correlation signal at short times [as was seen in Fig. 4(b)] is one difference. In Fig. 4, the correlation signal at early times is an order of magnitude greater than the useful part of the signal. This is not the case in Fig. 6. The difference is due to a lack of correlation between the nonphononic noises N_x and N_y. The correlation that does exist is ascribed to imperfect isolation of the grounds.

The main arrivals (L, $3L$, and $5L$) are clearly seen in Fig. 6(a), in both the correlation P and in the direct signal. The most striking difference between them is the oscillatory precursor before the arrivals in the correlation, but not in the direct signal. This can be understood by referring to the discussion following Eq. (9) where it may be seen that the

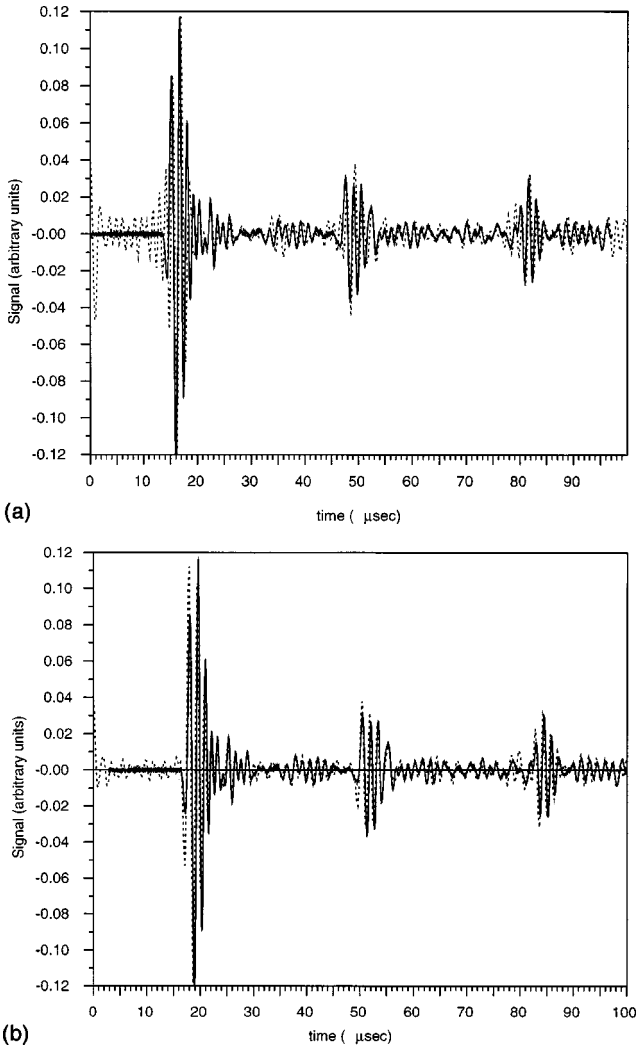

FIG. 6. (a) A direct pitch-catch signal (solid line) between two transducers is compared to the result of a cross correlation (dashed line) of thermal noise. The signals have been scaled to the same peak value, and the direct signal has been shifted back in time by a constant 2.9 μs and multiplied by -1. The waveforms are largely identical; the differences are consistent with theory. The cross-correlation signal was obtained from 32 s of raw data, acquired in a period of about 40 min of real time. (b) The direct signal of (a) (solid line) is compared to the result of the cross correlation (dashed line) of thermal noise at negative values of τ. The signals have been scaled to the same peak value, and the direct signal has been multiplied by -1.

transducer at "y" (in this case the WD transducer) contributes in a time-reversed manner. The same plot for the case in which the transducers are switched (or more simply, when we plot the time-reversed image of the cross correlation at negative τ) is shown in Fig. 6(b). Now it is the shorter ring-time transducer from Digital Wave that enters by means of its time-reversed function, and the precursor is much less pronounced.

V. CONFIRMATION OF THERMAL NATURE OF CORRELATION SIGNAL

The correspondence found above between conventional signals and those recovered by correlating the noise is in accord with the theory presented above. Thermal phonon fields should correlate in precisely that fashion. But the assertion that the observed correlations are in fact due to ther-

mal phonons, and not to some other effect, has not yet been proved. In this section the strength of the observed correlation field is compared to theoretical expectations.

The autocorrelation C_{xx} is contaminated by the autocorrelation of the nonphononic noise. Thus its strength cannot be compared directly to the known strength of the phonons. But at late times τ, the correlation field is presumably entirely phononic (the nonphononic parts having little correlation at large τ.) To establish the phononic nature of this part of the autocorrelation signal it is therefore necessary to examine the later times, after the waveform has become diffuse.

At times τ long after the ring time of the transducers, it is permitted to replace G^{extended} with G in (10), and to neglect the noise-noise autocorrelation. On writing G as a modal expansion (4), one obtains, for the autocorrelations of the signal in receiver r,

$$P_{rr}=dC(\tau)/d\tau$$
$$=kT\ \ R\ \ \copyright\left[\sum_m\ u_r^m\ \ u_r^m\frac{\sin\omega_m\tau}{\omega_m}\right]\copyright\ \ R^{\text{t.r.}}, \tag{21}$$

where $R(t)$ is the receiver transfer function, and u_r^m is the spatial overlap and vector inner product between the mth mode and the receiver $\mathbf{R}$. $R(t)\ u_r^m=\mathbf{R}_r*\mathbf{u}^m$. © indicates a conventional convolution in time. P_{rr} has dimensions of voltage^2/time. On performing the convolutions and invoking the large τ condition

$$P_{rr}=dC(\tau)/d\tau=kT\sum_m\ |\tilde{R}(\omega_m)|^2u_r^mu_r^m\frac{\sin\omega_m\tau}{\omega_m}. \tag{22}$$

A narrow-band filter $B(t)$ is convolved with this expression; the result is squared and time averaged. If that time averaging is carried out over a long time period comparable to or greater than the ''break time'' (equal to the inverse of the average eigenfrequency spacing Δf), then the cross terms fall out. If the time averaging is over a shorter interval, the matter is a bit more complex.[11] After dropping the cross terms,

$$\langle P_{rr}^2\rangle_B=(kT)^2\sum_m\ |\tilde{R}(\omega_m)|^4\overline{(u_r^m)^4}\left\langle\frac{\sin^2\omega_m\tau}{\omega_m^2}\right\rangle|\tilde{B}(\omega_m)|^2$$
$$=\frac{1}{2}(t\ \ kT)^2\sum_m\ |\tilde{R}(\omega_m)|^4\overline{(u_r^m)^4}\ \ |\tilde{B}(\omega_m)|^2/\omega_m^2. \tag{23}$$

If B is narrow compared to the variations in $|R|$, this sum may be replaced with an approximate integral,

$$\langle P_{rr}^2\rangle=\frac{1}{2\omega_b^2}(kT)^2|\tilde{R}(\omega_b)|^4\overline{(u_r^m)^4}D\int\ |\tilde{B}(\omega)|^2\,d\omega$$
$$=\frac{(kT)^2|\tilde{R}(\omega_b)|^4\overline{(u_r^m)^4}Db}{2\omega_b^2}, \tag{24}$$

where b is the bandwidth of the filter, $b=\int|B|^2\,d\omega$, ω_b is the filter's central frequency, and D is the modal density.[12] The root mean square value of the late time part of the band-passed waveform P is the square root of this,

$$\text{rms}_B\{P_{rr}\}=\frac{(kT)|\tilde{R}(\omega_b)|^2\overline{(u_r^m)^2}\sqrt{Db}}{\omega_b}, \tag{25}$$

where we have assumed that the mean fourth power of the modal overlap is twice (not thrice) the mean square. Recent work has established that a value of 3 is more correct, but is effectively reduced to 2 by eigenfrequency correlations that are important at times before the break time[11,13,14] due to the cross terms in the square of (22) that do not drop out. By taking this ratio to be 2 rather than 3, we are assuming the time averaging is carried out over an interval short compared to the break time.

It is apparent that the thermal nature of P could be confirmed by measuring it at various specimen temperatures. This was done and the rms value of P was found to decrease by about 12% as the heated specimen slowly cooled from 57 °C to 27 °C, a 10% drop in absolute temperature. This is in accord with Eq. (25), but it cannot be taken as a confirmation. There are two sources of systematic error that must be considered. Transducer, and couplant, efficiency may change with temperature. Temperature falling in real time as data is taken leads to a correlation function with degraded amplitude, due to interferences between waveforms from different conditions, with different wavespeeds. These effects must be accounted for or eliminated before using this method to confirm the thermal nature of the correlation signal.

As an alternative, Eq. (25) may also be used to measure temperature if the transducer sensitivity can be determined. This may be done by comparing (25) to the mean square of the transducer-calibration signal W discussed in Sec. II, excited by a step force $F_oH(t)$ at position z, and acquired by the same receiver and amplifier:

$$W(t)=R\copyright\left[\sum_m\ u_r^mu_z^m\frac{\sin\omega_mt}{\omega_m}\right]\copyright F_oH(t)$$
$$=F_oR\copyright\left[\sum_m\ u_r^mu_z^m\frac{1-\cos\omega_mt}{\omega_m^2}\right]. \tag{26}$$

After passing this through the filter B, evaluating it at times long after the ring time of the receiver and the ring time of the filter, and then squaring and time averaging, one obtains

$$\langle W(t)^2\rangle_B=|\tilde{R}(\omega_b)|^2\,\frac{DbF_o^2}{2\omega_b^4}\,\overline{(u_r^m)^2}\,\overline{(u_z^m)^2} \tag{27}$$

(B is taken to have no response at zero frequency). The last factor is known theoretically[7] to be $p/3M$. In aluminum $p=2.3$ if the source z is a normal force on the surface. M is the mass of the body.

A comparison of (25) and (27) shows that the root mean square of the band-passed late time correlation signal P_{rr} is proportional to the mean square calibration signal W, with a proportionality that depends on temperature and other quantities that are known. The sensitivity $|R|$ of the receiver and modal contacts u_r with the receiver drop out. These considerations allow one to design an ultrasonic bolometer to measure temperature by means of the formula

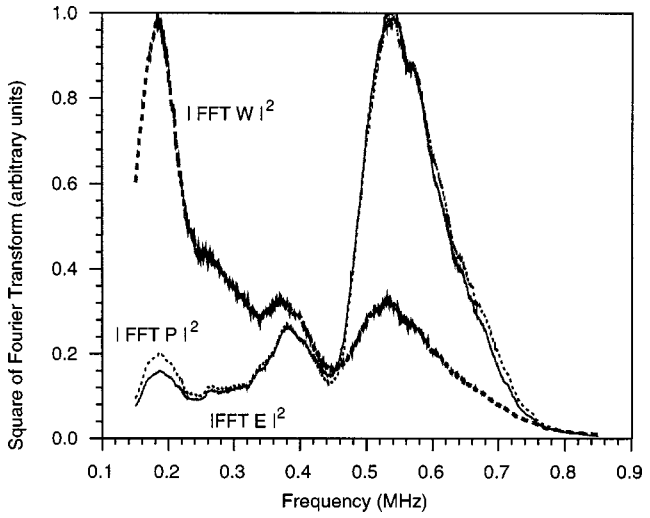

FIG. 7. Comparison of the power spectra of the correlation signal P_{rr} (dotted line), the direct pulse/echo signal $E(t)$ (thin solid line), and the signal detected after breaking a glass capillary $W(t)$ (heavy dashed line). Each was constructed from data at times between 1 and 9 ms, a period in which nonphononic noise does not contribute, and in which there is little absorption.

$$kT = \frac{\mathrm{rms}_B\{P\}}{\mathrm{rms}_B\{W\}} \frac{\sqrt{Db}F_o^2 p}{6M\omega_b^3}. \tag{28}$$

The temperature as determined from this formula may be compared with the known sample temperature, in order to confirm the thermal phonon origin of the waveform P.

Equation (28) was evaluated for the high-sensitivity Acoustic Emission transducer from Physical Acoustics Corporation. Figure 7 shows the late time (after 1 ms, before 9 ms) power spectra of P_{rr} and the directly obtained pulse-echo signals obtained in the irregular block discussed previously. As expected, and consistent with their time domain similarity seen in Fig. 4, they are virtually identical. Differences are ascribed to an imperfectly reciprocal transducer or to the presence of two factors of the anti-aliasing filter in P_{rr} and only one such factor in the pulse echo signal, or to some enhancement of the ambient noise at low frequencies, above that of the thermal fluctuations. The figure also shows the power spectrum of W, with a frequency dependence having features like those of P, because it also bears the influence of the transducer response. The curves have been multiplied by arbitrary factors to bring them to the same scale.

The result of the construction (28) is shown in Fig. 8, where the strength (in degrees K) of the ultrasonic noise source is evaluated in several distinct 40-kHz bands. The spectra of W and P_{rr} were taken as in Fig. 7. F_o was taken to be 10 N, consistent with the numbers reported in the literature and with our own measurements. (F_o was not measured in the ultrasonic test, but it was measured in several independent tests, and found to vary between 9 and 10 N.) M was measured at 7.6 kg. The agreement between the recovered temperature and the known room temperature of 293 K is good.

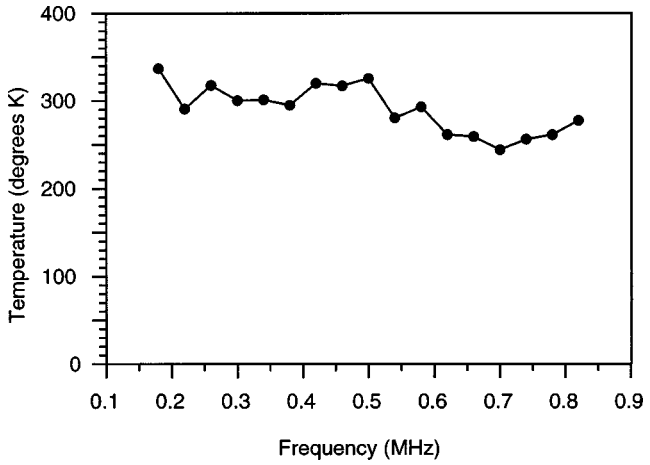

FIG. 8. Temperature recovered using Eq. (28) and the spectra of Fig. 7.

VI. CONCLUSIONS

That correlations of thermal phonon fields are identical to ultrasonic response functions is perhaps not widely recognized, but appears to be clear from the theory. The astonishing result follows that the correlation functions of the thermal noise in a detection device should be equivalent to conventional ultrasonic waveforms. It might have been imagined, however, that electronic noise in an amplifier, or thermal noise generated within a transducer, would dominant the phonon noise and that the identity would thus be impossible to realize in the laboratory. Our ability to resolve such correlations, even with poorly sensitive transducers, is a function of the short correlation range of the electronic noise. The electronic noise does not have correlations at the large values of τ where the acoustic noise is most interesting.

This result suggests the possibility of doing ultrasonics without a source. Whether a diffuse field is provided by ambient vibrations, by distant sources, or by thermal fluctuations, it now appears that such a field allows a lone receiver to generate conventional waveforms by autocorrelation of its diffuse signal. This is fascinating in its own right, and may have utility whenever sources are unavailable.

Possible applications include autocorrelations of seismic coda signals and microseismic activity, if one can be assured that the random-looking signal is diffuse. Recent indications are that the coda is indeed diffuse.[15] Seismic coda correlations might be particularly attractive with lunar, or the planned Europan, seismic records.

Sources are not expensive in MHz laboratory ultrasonics; applications there are perhaps unlikely. The advantages may be more apparent in the sea. It has been known for nearly half a century[16] that ambient thermal acoustic fluctuations in sea water dominate the noise background at frequencies above 100 kHz. The possibility of correlating passive sonar to detect quiet objects is rather intriguing, and potentially complementary to the technique termed ''acoustic daylight.'' [17]

At frequencies above a GHz, laboratory ultrasonics is increasingly difficult, and yet this is the regime in which modern materials and microstructures are providing challenges for materials characterization. Thermal fluctuations

are greater at higher frequencies, displacement amplitudes scale with $f^{1/2}$, and strain amplitudes with $f^{3/2}$. Thus it may be that ultrasonic waveform creation by correlations of thermal noise will scale well to higher frequencies.

ACKNOWLEDGMENTS

RW thanks Chris Fortunko who inspired this work by mentioning (in 1994) that he had built a transducer whose noise was at the limit provided by thermal mechanical fluctuations. Chris is greatly missed. We also thank Henrique Reis for lending us the Digital Wave transducer and Mike Weissman for discussions. This work was supported by the National Science Foundation through Grant No. 9988645.

[1] O. I. Lobkis and R. L. Weaver, ''On the emergence of the Greens function in the correlations of a diffuse field,'' J. Acoust. Soc. Am. **110**, 3011–3017 (2001).
[2] R. L. Weaver and O. I. Lobkis, ''Ultrasonics without a source, thermal fluctuation correlations at MHz frequencies,'' Phys. Rev. Lett. **87**, 134301 (2001).
[3] That each mode of vibration has expected energy of kT is routine in thermal physics and is discussed in most statistical mechanics textbooks. For example, C. Kittel, *Thermal Physics* (Wiley, New York, 1969), Chap. 16; 2nd ed. (Freeman, San Francisco, 1980).
[4] L. D. Landau and E. M. Lifschitz, *Statistical Physics*, 2nd ed. (Addison–Wesley, Reading, MA, 1970), pp. 343–391.
[5] H. B. Callen and T. A. Welton, ''Irreversibility and Generalized Noise,'' Phys. Rev. **83**, 34–40 (1951).
[6] T. M. Proctor, F. R. Breckinridge, and Y.-H. Pao, ''Transient waves in an elastic plate: Theory and experiment compared,'' J. Acoust. Soc. Am. **74**, 1905–1907 (1983); F. R. Breckinridge, C. E. Tschiegg, and M. Greenspan, ''Acoustic Emission: Some applications of Lamb's Problem,'' J. Acoust. Emiss. **1**, 173–178 (1982).
[7] R. Weaver, ''Diffuse elastic waves at a free surface,'' J. Acoust. Soc. Am. **78**, 131–136 (1985).
[8] E. S. Boltz and C. M. Fortunko, ''Determination of the absolute sensitivity of a piezoelectric displacement transducer,'' in *Review of Progress in Quantitative Nondestructive Evaluation*, edited by D. O. Thompson and D. E. Chimenti (Plenum, New York, 1996), Vol. 15, pp. 939–945.
[9] A. V. Erofeev and V. I. Pasechnik, ''Calibration of Piezoelectric transducers by thermal acoustic radiation,'' Acoust. Phys. **41**(4), 565–566 (1995); A. A. Anosov, K. M. Begrachev, and V. I. Pasechnik, ''Measurements of thermal acoustic radiation from a human hand,'' *ibid.* **44**(3), 248–254 (1998).
[10] G. S. Kino, *Acoustic Waves: Devices, Imaging, and Analog Signal Processing* (Prentice Hall, Englewood Cliffs, NJ, 1987), Chap. 1.4.
[11] R. Weaver and J. Burkhardt, ''Weak Anderson localization and enhanced backscatter in reverberation rooms and quantum dots,'' J. Acoust. Soc. Am. **96**, 3186–3190 (1994).
[12] Modal density D equal to modes per frequency interval ω is approximated in isotropic solids at short wavelengths $\lambda \ll$ system dimension, by $D = V\,\omega^2[2/c_s^3 + 1/c_L^3]/2\pi^2$, where V is system volume, and c_s and c_L are the shear and longitudinal wave speeds.
[13] J. de Rosny, A. Tourin, and M. Fink, ''Coherent backscattering of an elastic wave in a chaotic cavity,'' Phys. Rev. Lett. **84**, 1693–1696 (2000).
[14] R. L. Weaver and O. I. Lobkis, ''Enhanced Backscattering and Modal Echo of Reverberant Elastic Waves,'' Phys. Rev. Lett. **84**, 4942–4945 (2000).
[15] R. Hennino, N. Trégourès, N. M. Shapiro, L. Margerin, M. Campillo, B. A. van Tiggelen, and R. L. Weaver, ''Observation of equipartition of seismic waves,'' Phys. Rev. Lett. **86**, 3447–3450 (2001).
[16] R. H. Mellen, ''The thermal noise limit in the detection of underwater acoustics,'' J. Acoust. Soc. Am. **24**, 478–480 (1952).
[17] J. R. Potter, ''Acoustic imaging using ambient noise—some theory and simulation results,'' J. Acoust. Soc. Am. **95**, 21–33 (1994).

Guided waves propagating in sandwich structures made of anisotropic, viscoelastic, composite materials

Michel Castaings[a] and Bernard Hosten[b]
Laboratoire de Mécanique Physique, Université Bordeaux 1, UMR CNRS 5469 351, Cours de la Libération, 33405 Talence Cedex, France

(Received 20 February 2001; revised 1 October 2002; accepted 14 January 2003)

The propagation of Lamb-like waves in sandwich plates made of anisotropic and viscoelastic material layers is studied. A semi-analytical model is described and used for predicting the dispersion curves (phase velocity, energy velocity, and complex wave-number) and the through-thickness distribution fields (displacement, stress, and energy flow). Guided modes propagating along a test-sandwich plate are shown to be quite different than classical Lamb modes, because this structure does not have the mirror symmetry, contrary to most of composite material plates. Moreover, the viscoelastic material properties imply complex roots of the dispersion equation to be found that lead to connections between some of the dispersion curves, meaning that some of the modes get coupled together. Gradual variation from zero to nominal values of the imaginary parts of the viscoelastic moduli shows that the mode coupling depends on the level of material viscoelasticity, except for one particular case where this phenomenon exists whether the medium is viscoelastic or not. The model is used to quantify the sensitivity of both the dispersion curves and the through-thickness mode shapes to the level of material viscoelasticity, and to physically explain the mode-coupling phenomenon. Finite element software is also used to confirm results obtained for the purely elastic structure. Finally, experiments are made using ultrasonic, air-coupled transducers for generating and detecting guided modes in the test-sandwich structure. The mode-coupling phenomenon is then confirmed, and the potential of the air-coupled system for developing single-sided, contactless, NDT applications of such structures is discussed. [DOI: 10.1121/1.1562913]

PACS numbers: 43.35.Mr [DEC]

I. INTRODUCTION

Lamb modes are commonly used for ultrasonic, nondestructive testing (NDT) of industrial structures since they allow fast and efficient control to be done. A wide range of publications can be found on the propagation of Lamb waves in various media such as plates or pipes made of either single or stratified, isotropic or anisotropic, elastic or viscoelastic material layers. A selection of papers dealing with plate modes is given in Refs. 1–6. These works help in understanding the behavior of Lamb waves, thus making it possible to optimize the choice of particular modes for detecting specific defects in tested plates.[7,8] Numerical predictions and/or experiments have demonstrated the potential of Lamb waves for detecting flaws.[9–13] However, among all the media of investigation, sandwichlike plates, made of two skins plus a thick core in between, have rarely been considered.[14–19] These types of structures are used more and more in aircraft design for their high mechanical performances and low weights. These assembles are usually made of anisotropic, viscoelastic materials with strongly different acoustic impedances. Moreover, skins do not necessarily have the same thickness, thus making the whole structure not have the mirror symmetry. The choice of Lamb waves for testing such structures has been motivated because of their high potential for quickly testing quite a long range of the specimen. However, before a NDT process gets set up, it is necessary to fully understand the propagation of Lamb-type modes in nonsymmetric sandwich plates made of viscoelastic materials. This is the purpose of this paper, which presents both numerical predictions and experiments carried out on a test sandwich plate made of two glass-epoxy composite skins of different thicknesses, plus a rigid foam core.

A general model (2-D or 3-D model) based on the well-known transfer matrix method[20,21] has been developed for predicting the propagation of guided waves in stratified plates made of anisotropic and viscoelastic material layers, whatever their number and stacking sequence are. The current study is limited to a two-dimensional, plain strain problem since the plane of propagation is supposed to coincide with planes of symmetry of the anisotropic material layers constituting the test sandwich plate. The dispersion curves (phase velocity, energy velocity and complex wave-number versus frequency) and the through-thickness mode shapes (displacement, stress and energy flow distributions) are plotted, showing that guided waves in this sandwich structure are very different than classical Lamb modes. First of all, the mode shapes are neither symmetric nor antisymmetric with respect to the middle plane of the sample because this does not have mirror symmetry. Moreover, the viscoelastic material properties imply complex roots of the dispersion equation to be found that show coupling between some modes in specific zones of the dispersion curves. Gradual variation

[a]Electronic mail: castaings@lmp.u-bordeaux.fr
[b]Electronic mail: hosten@lmp.u-bordeaux.fr

from zero to nominal values of the imaginary parts of the viscoelastic moduli shows that the mode-coupling effect generally depends on the level of material viscoelasticity. Focus is made on a specific coupling zone, showing that dispersion curves for two modes get connected together under the effect of viscoelasticity, and that both strong attenuation and energy flow normal to the skin-foam interfaces are associated to this phenomenon. However, around a particular frequency, a mode coupling is shown to exist whether the medium is viscoelastic or not. In order to physically understand this observation, focus is made on this specific zone by investigating the complex wave-numbers, as well as the through-thickness energy flow distributions, and by comparing the analytical predictions to those obtained using finite element software[22] that models the propagation in structures made of elastic, anisotropic materials. This analysis showed the existence of a mode that is attenuated in the purely elastic plate, since it has a complex wave-number, but that does not carry energy along the plate.

Experiments have also been made using ultrasonic, air-coupled transducers for generating and detecting guided modes in the test-sandwich structure. It has been found that some modes can be launched and received if the two transducers are used at one side of the specimen, and not at the other side, and vice versa. The predicted, nonsymmetric mode shapes of these particular waves explain this phenomenon. Measurements of the phase velocity have been made in order to confirm the mode-coupling phenomenon. Finally, the phase velocity and through-thickness displacement and stress distributions of some of the guided modes are shown to be not sensitive to the viscoelastic material properties of the sandwich plate, thus making the FE software appropriate for modeling the interaction of these modes with defects, for further studies.

In this study, the test plate has been supplied by an industrial company. It is a sandwich structure made of two anisotropic viscoelastic material skins, separated by a rigid, isotropic, viscoelastic core, designed for a specific aerospace purpose. The choice of this structure for studying the mode-coupling phenomenon was motivated by the NDT ultrasonic-based application which is to set up. However, from the scientific point of view, the plate does not necessarily have to be a sandwich medium, neither of the skins have to be made of anisotropic materials, for the mode-coupling phenomenon to be observed. This trend comes from an attenuation mechanism due to viscoelastic losses that makes the wave-number complex so that the otherwise hidden complex branches become unmasked and exhibit their influence. Similar results have been observed for a single layer made of a highly viscoelastic material.[23] One originality of the present paper compared to these previous works is the low level of viscoelasticity required for the mode-coupling to be observed in the case of the sandwich plate. Even when this is modeled as an elastic medium, the mode-coupling exists, thus meaning that the geometry of the sandwich structure is an essential cause of this phenomenon. Another originality is the focus on the physical behavior of the guided waves when the mode-coupling occurs, by investigating the variations with the level of viscoelasticity of the phase velocity, of the attenuation and also of the power flow transfers through the internal interfaces of the sandwich plate.

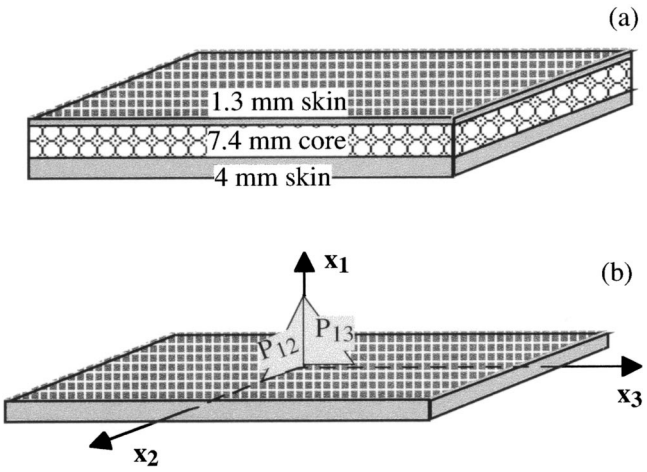

FIG. 1. (a) Schematic of test sandwich plate; (b) coordinate axis used for defining the viscoelastic moduli of individual elements.

II. DESIGN OF SANDWICH STRUCTURE

The test-sandwich plate used in this study is made of a 1.3-mm-thick skin, a 7.4-mm-thick core, and a 4-mm-thick skin, so it does not have mirror symmetry, as shown in Fig. 1(a). The two skins are made of 2D woven, glass fibers and epoxy matrix plies, and the core is made of a rigid foam. These materials are supposed to be quadratic and isotropic, respectively. The stiffness tensor that links stresses to strains according to Hooke's law[24] is represented by the following matrix, using the usual contracted notation for the indices:

$$\mathbf{C}_{ij}=\begin{bmatrix} C_{11} & C_{12} & C_{13} & 0 & 0 & 0 \\ - & C_{22} & C_{23} & 0 & 0 & 0 \\ - & - & C_{33} & 0 & 0 & 0 \\ - & - & - & C_{44} & 0 & 0 \\ - & \text{symmetric} & - & - & C_{55} & 0 \\ - & - & - & - & - & C_{66} \end{bmatrix}. \quad (1)$$

To describe the viscoelastic properties of these materials, the $\mathbf{C}_{ij}$ matrix is complex. Its elements are noted $C_{ij}=C'_{ij}+iC''_{ij}$, where C'_{ij} represents the material stiffness, and C''_{ij} the material viscosity. They are defined in the coordinate axis shown in Fig. 1(b). Seven complex moduli have been measured on a 3.1-mm-thick glass-epoxy material plate, immersed in water, using an ultrasonic, through-transmission technique described in Ref. 25. Two complex moduli have been measured on an 8.2-mm-thick foam material plate, placed in air, using an ultrasonic, through-transmission technique described in Ref. 26. Extra measurements using conventional, contact transducers have also been made to estimate values of C_{ij}, which could not be identified with the water-immersion or air-coupled techniques. The whole set of C_{ij} thus obtained confirms that the glass-epoxy material possesses the quadratic symmetry (plane P_{12} identical to plane

TABLE I. Measured thickness (in mm), density (in kg/m^3) and viscoelastic moduli (in GPa) for the glass epoxy and foam materials constituting the sandwich structure.

Material	Thickness	Density	C_{11}	C_{22}	C_{12}	C_{66}
Glass epoxy	3.1	1560	$13.7\pm i0.4$	$20.4\pm i0.6$	$6.6+i0.3$	$3.7+i0.14$
Foam	8.2	140	$0.6+i0.04$	⋯	⋯	$0.1+i0.01$

P_{13}) and that the foam is an isotropic material. Some of the measured C_{ij} will be used as input data for the numerical models described in the next section. These are given in Table I.

III. NUMERICAL MODELS

A. Semi-analytical model

The model used for predicting the dispersion curves is based on the transfer matrix method[20,21] that was initially intended for modeling wave propagation through stratified media. This method has already been adapted by Hosten and Castaings[27] for modeling heterogeneous plane waves through stratified plates made of anisotropic and viscoelastic layers, and for predicting the reflection and transmission coefficients of an incident plane wave. The purpose of the current project is to extend this model for simulating the propagation of leaky, guided modes (Lamb, SH, Rayleigh,...) along any direction of stratified plates made of anisotropic, viscoelastic materials. This work has begun with consideration of propagation of Lamb and SH modes along homogeneous anisotropic material plates.[6] In this paper, restriction is made to the case of Lamb waves propagating in planes of symmetry of the material layers. The direction of propagation chosen here is direction x_2, so the plane of propagation is plane P_{12} formed by the pair of axis (x_1,x_2). According to the measured values of C_{ij}, for the skins and for the foam, this plane is identical to plane P_{13} formed by the pair of axis (x_1,x_3). Four complex C_{ij} are therefore necessary for modeling the propagation along the skins (C_{11}, C_{22}, C_{12}, and C_{66}) and two for the core (C_{11} and C_{66}). These are given in Table I.

From a general point of view, the stratified plate is made of n solid layers. A transfer matrix that links the displacement and stress components from one surface of each layer j $(1\leqslant j\leqslant n)$ to the other is written according to the following relation:

$$\begin{bmatrix} u_2 \\ u_1 \\ \sigma_1 \\ \sigma_6 \end{bmatrix}_{\substack{j\text{-layer} \\ \text{bottom surface}}} = \underbrace{\begin{bmatrix} A_{11} & A_{12} & A_{13} & A_{14} \\ A_{21} & A_{22} & A_{23} & A_{24} \\ A_{31} & A_{32} & A_{33} & A_{34} \\ A_{41} & A_{42} & A_{43} & A_{44} \end{bmatrix}}_{j\text{-layer transfer matrix}} \begin{bmatrix} u_2 \\ u_1 \\ \sigma_1 \\ \sigma_6 \end{bmatrix}_{\substack{j\text{-layer} \\ \text{top surface}}} \tag{2}$$

using the usual contracted notation for the indices,[24] i.e., $\sigma_1=\sigma_{11}$ and $\sigma_6=\sigma_{12}=\sigma_{21}$. The routine for calculating the elements A_{pq} $(p,q=1,2,3,4)$ is given in Ref. 27. The displacement and stress components are defined in the coordinate axis shown in Fig. 2. This figure also illustrates that the whole displacement and stress fields in each layer result from the superposition of four bulk heterogeneous plane waves: one quasi-longitudinal (QL) wave and one quasi-shear (QT) wave, propagating downward (d) and upward (u) in the layer. The two components of the total displacement vector, at any position (x_1,x_2) in the plane of propagation, and at a given time t, are the sum of the displacement components of each partial wave, so written as follows:

$$\begin{aligned} u_1(t,x_1,x_2) &= \sum_{m=1}^{4} u_1^m(t,x_1,x_2) \\ &= \sum_{m=1}^{4} A^m P_1^m e^{i(\omega t-k_1^m x_1-k_2^m x_2)} \\ u_2(t,x_1,x_2) &= \underbrace{\sum_{m=1}^{4} u_2^m(t,x_1,x_2)}_{\text{sum of partial waves}} \\ &= \sum_{m=1}^{4} A^m P_2^m e^{i(\omega t-k_1^m x_1-k_2^m x_2)}, \end{aligned} \tag{3}$$

where $\mathbf{u}=A^m\mathbf{P}^m e^{i(\omega t-\mathbf{k}^m\cdot\mathbf{x})}$ is the displacement vector corresponding to each partial heterogeneous plane wave, using the following notations: A^m is the complex amplitude, $\mathbf{P}^m=(P_1^m,P_2^m)$ is the polarization vector, ω is circular frequency, $\mathbf{k}^m=(k_1^m,k_2^m)$ is the complex wave vector, $\mathbf{x}=(x_1,x_2)$ is the spatial coordinate vector, and m is the type of plane wave ($m=1$, 2, 3, or 4 for modes QL^d, QL^u, QT^d or QT^u, respectively). The stress components are then obtained from the generalized Hooke's law.[24] According to the boundary conditions at the internal solid–solid interfaces of the plate, i.e., the continuity of displacements and stresses, the transfer matrix, noted A, of the whole plate is then ob-

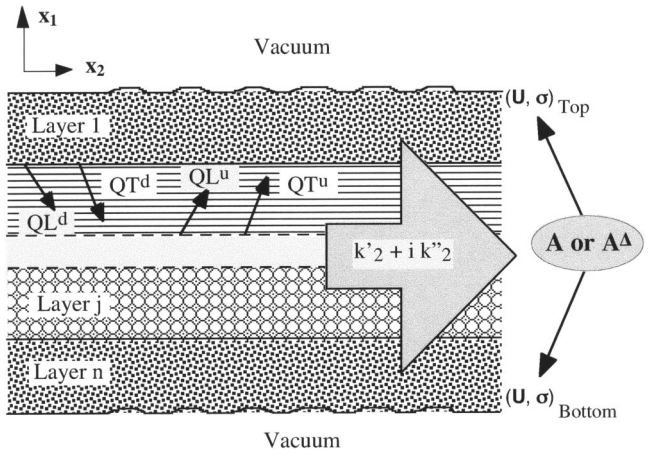

FIG. 2. Schematic of the superposition of partial plane waves in each layer forming guided modes along the stratified plate.

tained by multiplying together all individual transfer matrices A_j:

$$A=\prod_{j=n}^{1} A_j. \tag{4}$$

This matrix links the displacement and stress components at one surface of the plate (top) to those at the other surface (bottom).

In the actual study, the plates are always placed in air, which can be considered as a nonviscous fluid. Therefore, the boundary conditions at the two surfaces of the plate imply the normal displacement component u_1 and the stress components σ_1 and σ_6 to be continuous. Moreover, since the acoustic impedance of the air is negligible compared to that of the tested material plates,[28] a simplification that considers that leakage in air is equivalent to that in vacuum, i.e., null, can be made. These simplified boundary conditions lead to the following system of equations:

$$\begin{bmatrix} u_2 \\ u_1 \\ 0 \\ 0 \end{bmatrix}_{\text{bottom}} = \underbrace{\begin{bmatrix} A_{11} & A_{12} & A_{13} & A_{14} \\ A_{21} & A_{22} & A_{23} & A_{24} \\ A_{31} & A_{32} & A_{33} & A_{34} \\ A_{41} & A_{42} & A_{43} & A_{44} \end{bmatrix}}_{\text{Plate transfer matrix}} \begin{bmatrix} u_2 \\ u_1 \\ 0 \\ 0 \end{bmatrix}_{\text{top}}. \tag{5}$$

The resolution of this system leads to the dispersion equation, which depends on the material layers properties (density, thickness, orientation and complex elastic moduli) and two variables, f and k_2, where f is the frequency, and $k_2 = k_2' - ik_2''$ is the complex wave-number of a guided mode propagating along the direction x_2:

$$F(\underbrace{f,k_2}_{\text{variables}},\underbrace{\rho,h,C_{ij},\varphi}_{\text{layers}}) = A_{31}A_{42} - A_{41}A_{32} = 0. \tag{6}$$

Solutions to this equation are couples, noted (f,k_2). They are obtained using a numerical process based on the dichotomy method to find initial solutions at specific frequencies, plus the Newton–Raphson method used to follow these roots as the frequency changes. The real part, k_2', of k_2, is related to the phase velocity of the mode by the classical relation $V_{ph} = 2\pi f/k_2'$, while the opposite of the imaginary part, i.e., k_2'', represents its attenuation. It is important to note that stable solutions cannot be obtained for large frequency-thickness products, due to the well-known numerical instabilities of the transfer matrix method.[29] To avoid this problem, the transfer matrices in (2) and (4) are decomposed in 2 by 2 subdeterminants using the Delta operator method.[30] The dispersion equation in (6) is recognized as a 2 by 2 subdeterminant of the global transfer matrix A, which is then always accurately calculated. Thus, sought solutions (f,k_2) can be reliably obtained. These solutions are used in turn for plotting the dispersion curves, i.e., the phase velocity, the energy velocity, the real wave-number and/or the attenuation versus frequency. In a recent publication,[23] it is shown that for nonattenuated waves propagating in elastic media, the group velocity $V_g = \partial\omega/\partial k$ is identical to the component along the plate of the energy velocity vector defined by

$$\mathbf{V}_e = \frac{\int_{-h/2}^{h/2} \mathbf{P}\, dx_1}{\int_{-h/2}^{h/2} \int_0^T E\, dx_1 dt}, \tag{7}$$

where $\mathbf{P}$ is the time-averaged Poynting vector defined by Eq. (8c), E is the total energy density in the plate, T is the temporal period and h is the plate thickness. However, if the materials are viscoelastic and/or the plate is coupled to a fluid, the definition of the group velocity is shown to have no physical meaning. Experimental data indicated that the use of the above energy velocity definition is valid for such situations.[23] This remark is of importance here since the sandwich plate is made of viscoelastic materials. Therefore, the component along direction x_2 of the energy velocity vector will be plotted later for the test-sandwich structure, whether the viscoelasticity is considered or not.

Solutions (f,k_2) are also used for plotting the through-thickness displacement, stress and energy flow distributions, at a given frequency, i.e., components $U_1(x_1)$ and $U_2(x_1)$ of the displacement vector given by Eq. (8a), components $\sigma_1(x_1)$, $\sigma_2(x_1)$ and $\sigma_6(x_1)$ of the stress vector given by Eq. (8b), and components $P_1(x_1)$ and $P_2(x_1)$ of the Poynting vector given by Eq. (8c). This latest quantity represents the average power flow carried by the mode over a temporal period, at each position through the plate thickness, and for a guide supposed to have a unit width in the direction normal to the plane of propagation, i.e., along x_3, where $\bar{\bar{\boldsymbol{\sigma}}}$ is the stress tensor and $\mathbf{v} = \partial\mathbf{u}/\partial t$ is the particle velocity in the plane of propagation (* is the complex conjugate symbol):

$$\begin{aligned} \mathbf{u}(x_1,x_2,t) &= \begin{pmatrix} U_1(x_1) \\ U_2(x_1) \end{pmatrix} e^{i(\omega t - k_2 x_2)} \\ &= \underbrace{\begin{pmatrix} U_1(x_1) \\ U_2(x_1) \end{pmatrix}}_{\substack{\text{Power-normalized} \\ \text{through-thickness} \\ \text{displacement}}} \underbrace{e^{-k_2'' x_2}}_{\text{attenuation}} \underbrace{e^{i(\omega t - k_2' x_2)}}_{\text{phase term}} \end{aligned} \tag{8a}$$

$$\begin{aligned} \mathbf{T}(x_1,x_2,t) &= \begin{pmatrix} \sigma_1(x_1) \\ \sigma_2(x_1) \\ \sigma_6(x_1) \end{pmatrix} e^{i(\omega t - k_2 x_2)} \\ &= \underbrace{\begin{pmatrix} \sigma_1(x_1) \\ \sigma_2(x_1) \\ \sigma_6(x_1) \end{pmatrix}}_{\substack{\text{Power-normalized} \\ \text{through-thickness stress}}} \underbrace{e^{-k_2'' x_2}}_{\text{attenuation}} \underbrace{e^{i(\omega t - k_2' x_2)}}_{\text{phase term}} \end{aligned} \tag{8b}$$

$$\mathbf{P}(x_1,x_2) = -\frac{1}{2}\mathrm{Re}(\bar{\bar{\sigma}}\mathbf{v}^*) = \underbrace{\begin{pmatrix} P_1(x_1) \\ P_2(x_1) \end{pmatrix}}_{\substack{\text{Power-normalized} \\ \text{through-thickness} \\ \text{energy flow}}}. \tag{8c}$$

The displacement and stress vectors expressed in Eq. (8) are actually normalized by the power flow carried by the mode through the whole plate thickness (along direction x_2), for a unit width of the guide in direction x_3, and averaged over a temporal period. The Poynting vector is normalized by the square of this flow. This insures comparison to be possible between the various displacement, stress or energy fields of

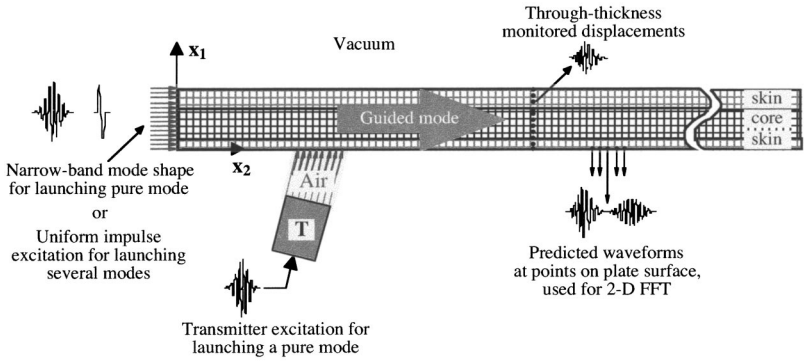

FIG. 3. Schematic of the finite element modeling of the sandwich plate.

any modes and for any frequencies. This normalization factor is expressed by Eq. (9):

$$P_n = \sqrt{\left| \int_{-h/2}^{h/2} \mathbf{P}\cdot\mathbf{x}_2 dx_1 \right|}. \tag{9}$$

This model takes into account the attenuation of guided modes due to the anisotropic viscoelastic properties of the material layers. The choice of number of layers and stacking sequence is very flexible and the plate can either have mirror symmetry or not. The model can also consider propagation out of planes of symmetry and/or leakage in a surrounding perfect fluid, but this is not the purpose of the present paper. It is considered as a semi-analytical model since as many as possible closed form solutions are expressed, like for example the elements of the transfer matrices, and the through-thickness fields. However, solutions like the roots of the dispersion equation require numerical packages to be used.

B. Finite element model

This section describes a numerical analysis package, which was developed at Imperial College in London, UK, to model the propagation of plate, waves and their interaction with defects.[22] Simulated plates are considered as free plates (i.e., placed in vacuum), and can be made of one or several different layers made of either isotropic or anisotropic elastic materials. This tool is based on the finite element (FE) method and includes an explicit central difference routine for producing a time marching solution. Therefore it is possible to vary the characteristics of the exciting temporal signal, i.e., the center frequency, the number of cycles and the envelope. The excitation can be produced at any point of the mesh, as displacements or forces. The response of the plate to various types of excitation is modeled by calculating the displacements at every point of the spatial mesh that defines the plate, as a function of time. Specific points of the mesh can be monitored, thus showing the time response at particular locations in/on the plate. Monitoring a series of points along the plate is usually done for processing a two-dimensional Fourier transform which converts the time-position, predicted data into a frequency-wave-number diagram.[31,32] Such a diagram is very useful since it allows the phase velocity and amplitude (or decay in amplitude, i.e., attenuation) of various modes propagating along the plate to be plotted versus the frequency, whether these modes are pure or superimposed. This processing will also be applied to our experimental data for measuring the phase velocities of modes produced in the test-sandwich plate. The FE code is also associated to specific interfaces used for modeling the excitation and/or the reception by finite transducers, the angle, the diameter, the spatial distribution and the position above the plate of which can vary. More details about these options can be found in Refs. 12 and 13.

In the current study, the sandwich plate is modeled by three layers, which are meshed and joined together by their sides according to Fig. 3. Their thicknesses are 1.3, 7.4, and 4 mm for the first skin, the core and the second skin, respectively. They all have the same length of 500 mm, which is usually high enough for avoiding any reflection from the hand sides, at the monitoring points (except for one particular case that will be mentioned later). The plate is considered as infinitely wide in the direction x_3 normal to the plane of propagation, i.e., plane strain condition is considered. The plane of propagation is formed by the axis x_1 and x_2. It coincides with a plane of symmetry for all layers. Therefore, the two skins properties are modeled by four real elastic moduli (C'_{11}, C'_{22}, C'_{12}, and C'_{66}) and the core properties by two real elastic moduli (C'_{11} and C'_{66}), the values of which are given in Table I. The excitation of guided modes was produced in two main different ways. The first type of excitation was a through-thickness displacement distribution, applied at one end of the structure. This excitation was either a wide-frequency-band, uniform distribution for launching several guided modes, or a narrow-frequency-band, single mode-shape distribution for launching a pure mode. In both cases, monitoring series of points along the plate allowed two-dimensional Fourier transforms to be processed, so leading to sets of phase velocity versus frequency data that were compared to the dispersion curves obtained from the analytical solutions. The second type of excitation was simulating a finite air-coupled transducer placed at one surface of the specimen, as that used in the experiments (see next section). This transmitter is modeled by the pressure distribution that it is supposed to locally apply at one plate surface, depending on its angular orientation and frequency excitation, which were changed according to the pure mode, which was suited to be launched. The incident beam was supposed to be collimated.[12] In-plane (x_2 direction) and normal-to-plane (x_1 direction) displacements were monitored at points located in the through-thickness of the plate. These were used for plotting the mode shapes at a given frequency, which were compared in turn to through-thickness displacement distributions predicted using Eq. (8a). The various options for forcing

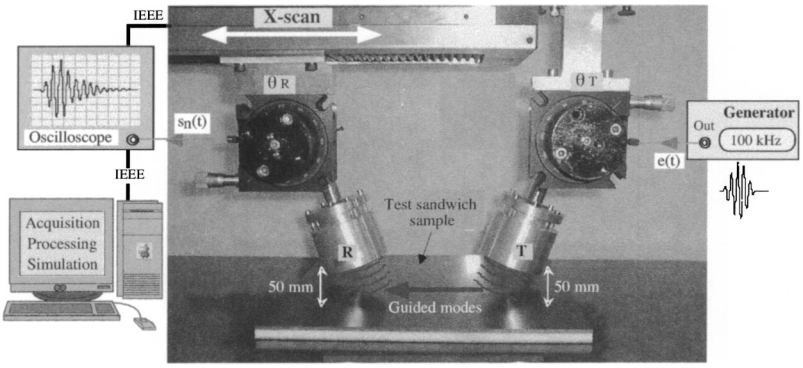

FIG. 4. Experimental setup.

and/or monitoring points of the FE mesh are presented on the schematic of Fig. 3.

IV. EXPERIMENTS

Air-coupled ultrasonic transducers are used for generating and detecting guided modes in the test-sandwich plate. These transducers are electrostatic elements with a 45-mm diameter, circular cross-section. Their frequency bandwidth is centered at 200 kHz with −15 dB points at 50 and 400 kHz. More details can be found on such prototypes in Ref. 33. As shown in Fig. 4, one transmitter and one receiver are placed at one side of the specimen, and are oriented at angles optimised for selective coupling with guided modes that can propagate in the plate. The analytical model described in previous section predicts these angles. The receiver is moved away the transmitter, by a motorized translation stage, so varying the distance of propagation of the guided modes in order to measure a series of temporal signals visualized on a scope. As mentioned in the previous section, a two-dimensional Fourier transform is applied to each set of experimental waveforms for quantifying the phase velocities of modes produced in the testsandwich plate.

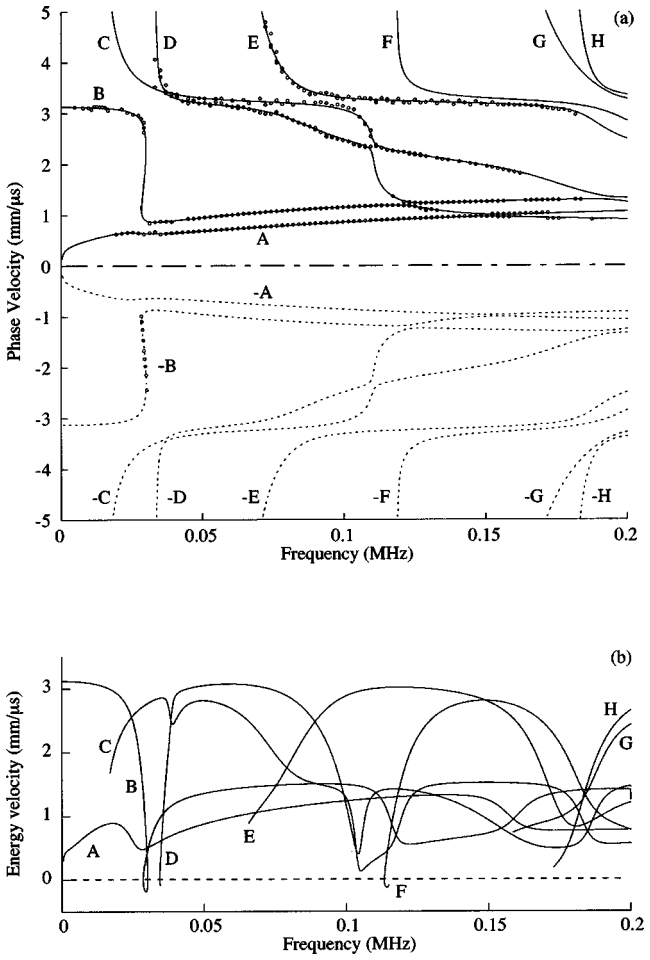

FIG. 5. Real solutions of analytical model (lines) compared to FE predictions (○○○) for guided modes along the elastic sandwich plate; (a) positive (———) and negative (---) phase velocities and (b) energy velocities corresponding to positive phase velocities only.

V. RESULTS

A. Real solutions for elastic materials

First of all, the simulation of guided modes propagating along the sandwich structure without taking into account the material viscoelastic properties is considered. This was first done by searching real solutions of Eq. (6) and by considering real elastic moduli as input data. Figure 5 presents the phase and energy velocities thus obtained. It is interesting to note that these dispersion curves are quite different than classical dispersion curves for Lamb modes. This is due to the fact that guided modes propagating in the test-sandwich plate are neither symmetric nor antisymmetric modes because the plate does not have mirror symmetry. Then, the FE software that models purely elastic materials was used. To launch several modes at the same time, a uniform, through-thickness, displacement distribution was applied in both directions, at the left-hand side of the meshed plate. The exciting signal was a two-cycle, 100-kHz center frequency, Hanning-windowed burst, having a frequency bandwidth comprised between 10 and 180 kHz, at −20 dB. Three series of 167 points were then monitored along 250-mm-long lines parallel to the plate, every 1.5 mm, at positions $x_1 = 0$, 8, and 12.7 mm, respectively, in the plate thickness. Therefore, the first series was at the thin skin surface, the second series was roughly in the middle of the core, and the last series was at the thick skin surface. The location of these monitored points (to the right of the excitation) was a way to model modes having positive energy velocities in the x_2 direction only. Processing two-dimensional Fourier transforms from these data led to a big set of phase velocity values in the frequency range of investigation. This technique allows modes with positive or negative phase velocities to be selected since the Fourier transform is defined the whole space $[-\infty, +\infty]$ of

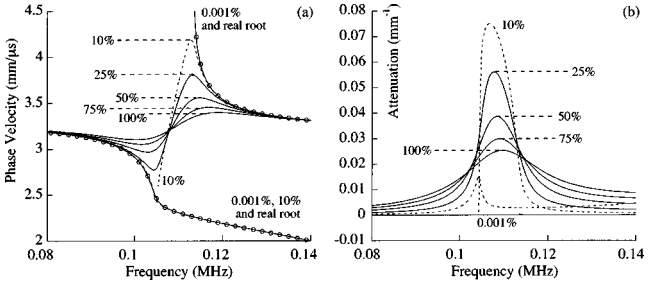

FIG. 6. Effect of material viscoelasticity rate on complex solutions (lines) of analytical model, plus real solutions (○○○), for mode C around 110 kHz; (a) phase velocity and (b) imaginary part of wave-number.

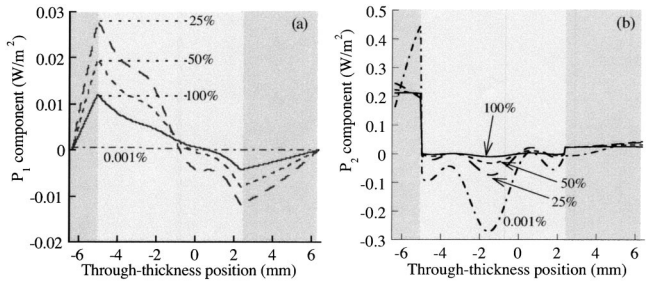

FIG. 7. Through-thickness distribution of unit-power Poynting vector for various viscoelasticity levels for mode C at 110 kHz; (a) component in direction x_1 and (b) component in direction x_2.

wave-numbers. The upper part of Fig. 5(a) (positive phase velocities) shows that the FE predictions are in good agreement with the dispersion curves plotted from the real solutions of the dispersion equation. This correlation gives a general good confidence in both the analytical and the finite element codes, used for modeling guided waves in stratified plates made of elastic, anisotropic materials. However, if careful attention is paid on specific zones of these curves, some differences can be seen between the FE and the analytical predictions. For instance, real positive solutions of Eq. (6) show that the phase velocity of the lowest-order dilatational mode (mode B) is multiple-valued around 30 kHz where it sharply drops from 3.2 mm/μs to about 1.0 mm/μs. This result is not confirmed by the set of positive phase velocities obtained from the FE plus 2D-FFT process, which supplies positive phase velocities decreasing from 3.2 to 2.6 mm/μs, up to 29.5 kHz, no positive solutions between 29.5 kHz and 31.2 kHz, and then solutions around 1.0 mm/μs above 31.2 kHz. However, if negative phase velocities are selected by the 2D-FFT technique applied to the FE results, then very good agreement with the dispersion curves plotted from negative real solutions of Eq. (6) is obtained, as shown by the lower part of Fig. 5(a). This result means that the branch between 29.5 and 31.2 kHz corresponds to a different mode than those obtained below 29.5 kHz and above 31.2 kHz. Figure 5(b) presents the energy velocity curves that correspond to positive phase velocities only. It is clear that where the positive phase velocities form a positive slope between 29.5 and 31.2 kHz, the energy velocity is negative. From a physical point of view, this is equivalent to having a negative slope formed by negative phase velocities and a positive energy velocity, i.e., dots in the lower part of Fig. 5(a). The multiple-valued curve (mode B) plotted in the upper part of Fig. 5(a) is then an artifact due to the resolution of the dispersion equation (6) in the real positive plane. This is very similar to the case of the s_1 mode that propagates along free, elastic, isotropic plates. Indeed, it is shown in Ref. 24 that the dispersion curve for this particular mode is actually composed of two branches of real positive wave-numbers, the energy velocity being positive for one branch and negative for the other one. This latest is actually identified as the s_2 mode propagating in the opposite direction as that of s_1. In fact, the connection of the lower real branch of positive energy velocity to the upper real branch of ''negative energy velocity'' is an artifact due to the resolution of the dispersion equation in the real plane. For the same reasons, similar results are obtained for mode D around 34.5 kHz and mode F around 114 kHz.

B. Complex solutions for viscoelastic materials

Complex solutions of Eq. (6) are now sought in order to quantify the effect of material viscoelasticity on wave propagation. The material viscoelastic rate is gradually increased by varying the imaginary parts of the viscoelastic moduli, from 0.001% to 100% of the nominal values given in Table I. From a numerical point of view, in the case of the lowest level of viscoelasticity, it is necessary to input C''_{ij} values not exactly equal to zero in order to ensure convergence on complex solutions. However, for such small values of the C''_{ij}, the sandwich plate can be considered as an elastic medium. From a general point of view, the viscoelasticity generates a mode coupling effect demonstrated by connections between some of the dispersion curves together. As an example, Fig. 6 shows the coupling of two modes, labeled D and F in Fig. 5, between 80 and 140 kHz. As expected when the viscoelasticity level is negligible, i.e., when the C''_{ij} are equal to 0.001% of their nominal values, the dispersion curves (phase velocity and attenuation) are unchanged whether real or complex solutions are sought. When the C''_{ij} are equal to 10% of their nominal values, the phase velocity of the mode labeled F in Fig. 5 does no longer follow a vertical asymptote, but it drops off while its attenuation gets very high, and the mode labeled D in Fig. 5 has an unchanged phase velocity but a nonzero attenuation. In this situation, still two independent modes exist. However, as seen in Fig. 6(a), as soon as the C''_{ij} are equal to or greater than 25% of their nominal values, the two phase velocity curves of modes D and F get connected together, so that a single curve is obtained forming a squabble shape that is less pronounced as the viscoelasticity rate increases. Figure 6(b) shows that this phenomenon is accompanied by a relatively strong attenuation that diminishes from 0.055 to 0.025 mm^{-1}, i.e., from 4.7 to 2.1 dB/cm, as the C''_{ij} increase from 25% to 100% of their nominal values, at 110 kHz. However, below 104 kHz and above 114 kHz, i.e., on both sides of the frequency at which the mode coupling occurs, the attenuation gets stronger as the C''_{ij} values increase.

The two components of the Poynting vector have also been plotted for this mode, using Eq. (8c), at frequency 110 kHz, and for several rates of the viscoelasticity. Figure 7(a) shows that the flow of energy in direction normal to the plate

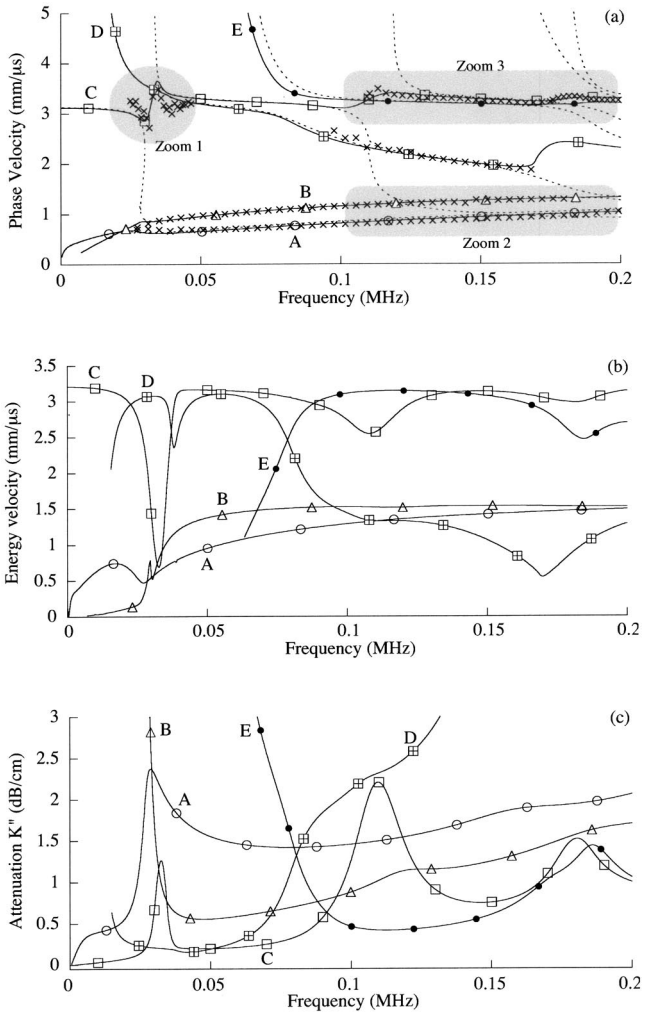

FIG. 8. Dispersion curves for guided modes propagating along the sandwich plate; (a) phase velocity, (b) energy velocity, (c) attenuation; analytical model for elastic (---) or viscoelastic (——— and symbols) plate and ($\times\times\times$) experiments.

(direction x_1) is null if the structure is made of elastic materials, i.e., the energy flow is strictly parallel to direction x_2 at any position through the plate thickness. However, as soon as the viscoelasticity level is high enough for the mode-coupling to occur, i.e., for C''_{ij} equal to or greater than 25% of their nominal values, energy is transferred through the skin-foam interfaces. The amount of this normal power flow (in direction x_1) tends to diminish as the viscoelasticity level increases. Simultaneously, it is observed that the mode gets less attenuated since the ratio of imaginary to real parts of the wave-number drops off by a factor of 2 when the C''_{ij} increase from 25% to 100% of their nominal values. Figure 7(b) shows that the power flow in direction x_2 is essentially carried both by the thin skin and by the foam if the materials have a low level of viscoelasticity, and that it gets more concentrated in the thin skin as the viscoelastic material properties increase. Similar phenomena as those described above have been observed at other frequencies where mode coupling occurs. For example, as seen in Fig. 8 that presents dispersion curves up to 200 kHz, both for the elastic plate (dashed lines) and for the full level of viscoelasticity (plain lines), modes labeled B and C in Fig. 5 get coupled around 120 kHz, modes A and B around 160 kHz, modes C and D around 104 kHz and around 183 kHz, etc. It can therefore be concluded that the material viscoelastic properties produce, at specific frequencies, a mode coupling effect that implies connections between some of the dispersion curves, and that is accompanied by a strong attenuation, and by transfer of energy through the skin-core interfaces. The viscoelasticity also makes some parts of the real dispersion curves disappear, and crossing points between the new curves possible. New labels are used for the various modes since the dispersion curves are strongly different than those obtained from real solutions. For instance, the new mode formed by the connection of curves D and F of Fig. 5, between 80 and 140 kHz, is labeled mode C.

Non-null normal components (in direction x_1) of the Poynting vector have already been observed for the mode s_3 propagating with high attenuation in a single, viscoelastic, HPPE material layer, at low frequency.[23] As shown in this reference, this mode has a phase velocity curve that exhibits connections between several dispersion curves obtained from real solutions, due to an attenuation mechanism coming from either the material viscoelasticity or leakage into a surrounding fluid. The phenomenon is therefore very similar to that studied in the present paper, except that in the case of our viscoelastic, free sandwich plate many more connections occur even for a very low rate of viscoelasticity. Indeed, when this rate is chosen equal to 25% of the nominal level, the attenuation coefficients α_L and α_T (in Np/wavelength) for the individual components of the sandwich plate are about two to ten times smaller than those given in Ref. 23. The geometry of the sandwich plate is therefore likely to be one reason for the mode-coupling occurrence, i.e., in favor of exchanges of energy through the internal interfaces. This will be confirmed later in Sec. V C. In the same way, it has been checked that no mode-coupling occurred in the case of the propagation along the individual components of the sandwich plate (skin or core), although the nominal level of viscoelasticity was considered in the model. This means that the material viscoelasticity is not the only reason for the mode-coupling to exist in the sandwich plate.

Figure 8(a) compares the phase velocity curves predicted for the elastic structure (dashed lines) and for the fully viscoelastic one (plain lines) to experimental data measured using the air-coupled transducers, as described in Sec. IV. In order to check whether these measurements confirm the mode-coupling phenomenon or not, three zoomed regions are presented in Fig. 9. Concerning the new mode C mentioned above, Fig. 9(c) shows that the tendency of the experimental data agrees much more with the complex root solutions (solid line) than with the real ones (dashed line). Figure 9(b) also shows that the experimental phase velocities confirm the coupling between modes B and C of Fig. 5 around 120 kHz, between modes A and B around 160 kHz, and between modes C and D around 183 kHz, since none of the measured data follow the dashed line representing the uncoupled modes. The mode-coupling phenomenon is therefore quite well confirmed by these measurements, thus indicating that the complex roots of the dispersion equation correspond to realistic solutions for guided waves propagating

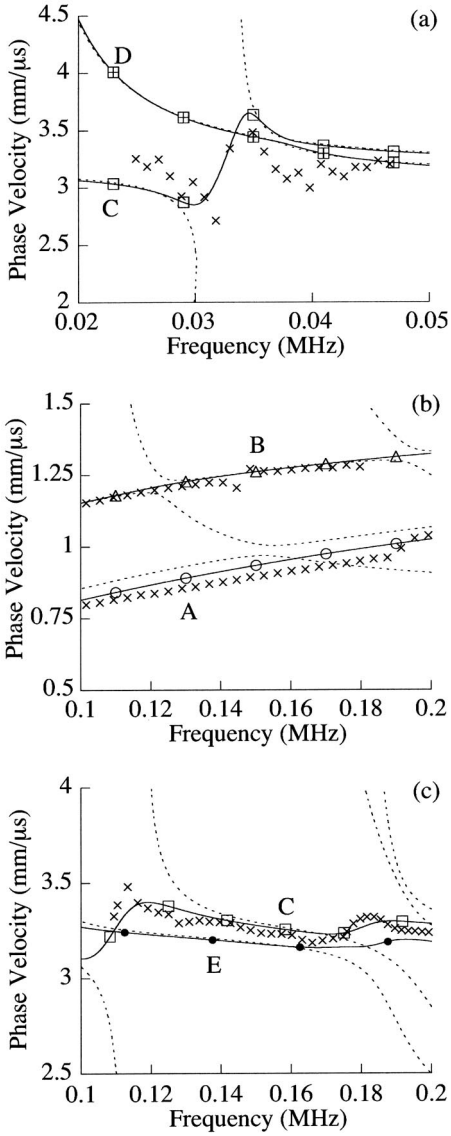

FIG. 9. Zooms on phase velocity dispersion curves presented in Fig. 8(a); (a) zoom 1: mode C, 20–50 kHz, (b) zoom 2: modes A and B, 100–200 kHz, (c) zoom 3: mode C, 100–200 kHz, (——— and symbols) complex solutions of analytical model, (---) real solutions of analytical model and (×××) experiments.

along this viscoelastic sandwich plate. The energy velocity and the attenuation of these waves are also presented by Figs. 8(b) and 8(c), respectively. Sharp variations of the energy velocity are visible for most of the coupling zones, thus

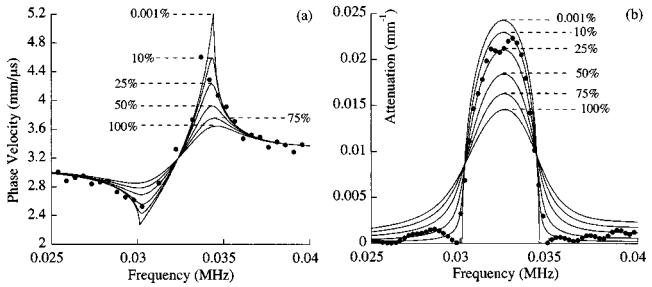

FIG. 10. Effect of material viscoelasticity rate on complex solutions of analytical model (———) compared to FE predictions (···), for mode C around 33 kHz; (a) phase velocity and (b) imaginary part of wave-number.

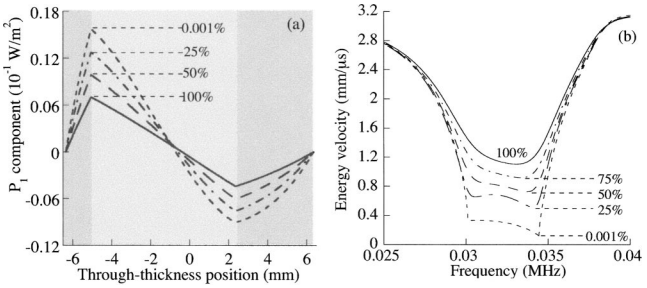

FIG. 11. Effect of material viscoelasticity on transfer of energy for mode C; (a) through-thickness distribution of component in direction x_1 of unit-power Poynting vector at 33 kHz and (b) component in direction x_2 of energy velocity around 33 kHz.

indicating that this phenomenon is likely to be associated to strong dispersion of the propagation. The attenuation is obtained from the imaginary part of the complex wave-number roots, converted from mm^{-1} to dB/cm, as a more convenient unit for NDT applications. It is confirmed that the mode coupling is systematically associated to an increase of attenuation, as said before. The attenuation of the various modes supposed to propagate along the sandwich plate is often quite high, i.e., greater than 0.5 dB/cm (50 dB/m), even in the low-frequency range of investigation. Since aeronautic structures are likely to be about one or several meters long rather than of a few centimeters, a careful choice of guided modes with low attenuation will be needed in real applications.

C. Particular attenuated mode

An interesting particular case is now investigated. It corresponds to mode B in Fig. 5 that was previously considered because its real solutions were multiple-valued around 30 kHz. Figure 10(a) shows that the phase velocity curve plotted from complex roots of the dispersion equation presents a continuous coupling occurring between this lowest-order dilatational mode and a higher-order mode labeled mode D in Fig. 5. As shown in Fig. 10(b), this coupling is accompanied by a strong imaginary part of the wave-number. The interesting point here is that this mode coupling even exists if the viscoelasticity level is negligible, i.e., when the C''_{ij} values are equal to 0.001% of their nominal values, indicating that the mode is attenuated even if the medium is elastic. In order to quantify the effect of the material viscoelasticity on the attenuation of the mode, the ratio between the imaginary and real parts of its wave-number has been calculated for several level of viscoelasticity, at frequency 33 kHz. This ratio decreases from about 39% to 23% when the C''_{ij} values increase from 0.001% to 100% of their nominal values. The Poynting vector and the energy velocity have been calculated for this mode, at frequency 33 kHz, and for several rates of viscoelasticity. Figure 11(a) that presents the component in direction x_1 of the Poynting vector shows that energy is transferred through the skin-core interfaces, and that the level of these exchanges gets stronger as the viscoelasticity diminishes. Figure 11(b) shows that the energy velocity (component in direction x_2) tends towards zero, around 33 kHz where the mode-coupling occurs, when the material is almost

elastic. This means that the mode does not carry energy along the platelike complex modes already identified in elastic free layers.[24] When the material viscoelastic properties are increased, the energy velocity increases, thus meaning that the nature of the mode is changing since it carries energy along the viscoelastic plate.

To confirm that this attenuated mode exists if the sandwich plate is purely elastic, a specific FE calculation has been run by applying its exact, through-thickness displacement distribution, at the left-hand side of the meshed sandwich plate. The two components U_1 and U_2 of this displacement distribution have been calculated by injecting in Eq. (8a) the complex wave-number obtained for the lowest level of viscoelasticity, at 33 kHz. The temporal excitation in the FE model was then a five-cycle toneburst having a center frequency of 33 kHz, thus producing energy in the 25–40-kHz bandwidth at −30 dB. In-plane displacements (in direction x_2) were monitored at points located 2 mm away from the surface of the thick skin, i.e., where other modes which are supposed to exist at the same frequency produce a negligible in-plane displacement compared to that created by mode C. These points were placed from 16 to 200 mm away from the excited edge. The scale in time was extended up to 1.4 ms and the plate length was fixed equal to 2 m, so that even the slowest components of mode C were properly modeled without being overlapped in time by the fastest components that could be twice reflected from the plate edges. The amplitude of these displacements is not presented here but it definitively reduces by 96%, at 33 kHz, as the position along the plate gets from 16 to 100 mm away from the input. This latest position precisely corresponds to one wavelength, at this frequency, thus confirming that this mode does not carry energy along the plate. Then, the two-dimensional Fourier processing mentioned in Sec. III B was applied to this set of displacements. Dots in Fig. 10 correspond to the FE results. The very good agreement obtained between the FE and analytical predictions, both for the phase velocity and the attenuation, validate the existence of the attenuated mode in the elastic sandwich plate.

Finally, experimental data of the phase velocity are also presented in Fig. 8(a), and a zoom of the mode C around 33 kHz is shown in Fig. 9(a). The strong attenuation of this mode and the small normal-to-plate displacement that it produces at the skin surfaces prevented two air-coupled transducers to be used for its generation/detection. In order to insure a high level of the energy input to this mode, a piezoelectric contact transmitter was coupled to one end of the sandwich plate. A ten-cycle, 33-kHz toneburst was then applied to this element, so that it created a fairly uniform through-thickness in-plane displacement that was suitable for launching the mode C with a relatively strong energy. The amplitude of the normal-to-plate displacement produced by this mode at the thin skin surface was then high enough for measurements to be made using an air-coupled receiver as those presented in Sec. IV. However, 100-time averaging was necessary for increasing the signal-to-noise ratio, so that processing was possible. This receiver was moved along the plate from 20 to 200 mm away from the emitter, with a 10-mm step. The set of signals captured for each position were processed using the 2D-FFT technique. As seen in Fig. 9(a), the quality of the phase velocity measurements is a bit poor compared to data measured for other modes, which are much easier to generate-detect. However, the reproducibility of these measured phase velocities and the elbow shape they form show a reasonable agreement with the predicted results.

TABLE II. Configuration data used for modeling finite transmitter excitation producing a pure mode

Mode	Incident angle (degrees)	Center frequency (kHz)	Frequency bandwidth (kHz) at −20 dB
A	25	100	85–115
B	17.3	100	85–115
D	10	140	118–165

D. Through-thickness displacement and stress fields

The overall good results obtained up to this point confirm the efficiency of the numerical and experimental tools used in this study. The potential of air-coupled transducers for launching and/or detecting guided modes in sandwich structures has been shown, so they may be used for developing single-sided, contactless, NDT applications which are aimed in this project. The choice of a particular mode for detecting specific defects will depend on the ability of the transducers to generate/detect it, on its level of attenuation according to the size of the sample to be tested, and on its sensitivity to various types of defects (holes, delaminations, disbonds, ...), based on the through-thickness shape (displacement and stress) that it produces when propagating.[7,8] The FE software is an interesting feature for this latest point since it allows the interaction of guided modes with defects to be modeled. However, since the present model is restricted to simulate purely elastic materials, it is necessary to carefully select zones in the dispersion curves where the viscoleasticity has negligible effects. Figure 8(a) clearly shows that some parts of the phase velocity curves remain unchanged when the viscoelastic properties of the materials are taken into account. This is the case for modes A and B at 100 kHz, and mode D at 140 kHz, for example. However, to fully guarantee that these modes are insignificantly affected by the viscoelastic properties, it is necessary to carefully look at the through-thickness, displacement and stress field distributions that they produce when propagating. In this purpose, these fields have been predicted using the analytical model with and without taking into account the material viscoelastic properties, for modes A and B at 100 kHz, and for mode D at 140 kHz. Then, the FE software has been used to predict the through-thickness displacements that are generated when the excitation is produced by a virtual, finite, air-coupled transmitter, oriented at an angle and excited in a local frequency region, together corresponding to one of the three previous specific zones of the dispersion curves where the viscoelasticity has little effect. For each run, the transmitter was simulated as a line strip source (2-D model) of 30 mm long, and the excitation was a ten-cycle, hanning-windowed toneburst. Table II summarizes extra data specific to these various cases.

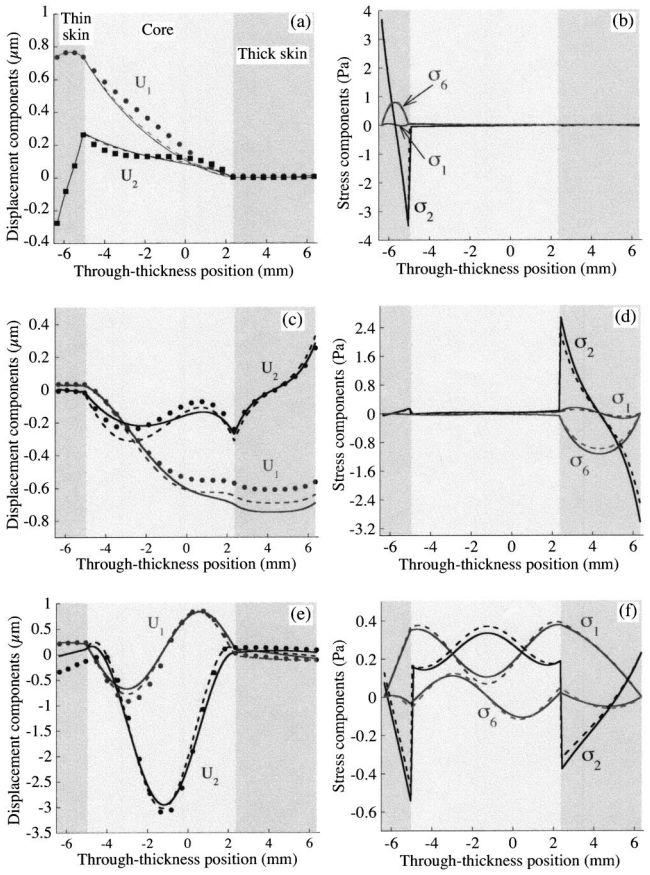

FIG. 12. Through-thickness unit-power displacement components (a, c, e) and unit-power stress components (b, d, f) without viscoelasticity (---) and with viscoelasticity (———), plus FE data (···); (a and b) mode A at frequency 100 kHz, (c and d) mode B at frequency 100 kHz and (e and f) mode D at frequency 140 kHz.

Displacements in both directions x_1 and x_2 were monitored at points distributed through the sandwich thickness, located 100 mm away the excitation area. These were normalized so that the normal component (U_1) at the thin skin surface be equal to that predicted by the analytical solution, which uses a unit-power normalization factor. In this way, the fields predicted by the two models have comparable order of magnitude. Figures 12(a)–(f) confirm that modes A and B at 100 kHz, and mode D at 140 kHz are very slightly sensitive to the viscoelastic properties, since the changes in the analytical predictions of both displacement and stress distributions are very small whether the viscoelasticity is taken into account or not. The FE through-thickness displacements are then in good agreement with both of these analytical predictions. Therefore, if one of these modes is considered as incident on a defect, then the FE model is likely to simulate properly the local interaction phenomenon, i.e., the amplitudes in the vicinity of the defect of the various modes produced by mode conversion. However, since such modes would probably have different attenuations, specific terms like $e^{-k''_m \Delta x_2}$, where k''_m is the attenuation of a given scattered mode m and Δx_2 is a distance away from the defect, would be needed for predicting the diffracted field at any position along the structure. This may be useful for positioning transducers when preparing NDT applications. Ideally, it would be more suitable to implement a viscoelasticity option in the FE software, so that no correction of the diffracted-mode amplitudes would have to be made. Moreover, such an option would allow the interaction of any incident mode with defects to be modeled, even modes having phase velocity and/or through-thickness shapes sensitive to the material viscoelasticity. This work is being done and should be efficient soon.

Figures 12(b) and (d) show that modes A and B propagating at frequency 100 kHz are skin modes producing high levels of stress in the thin or thick skins, respectively. These kinds of modes are therefore suitable for detecting defects in the skins, which can be caused by external impacts. The experimental phase velocity data measured for these two modes [see Fig. 8(a)] have been obtained by disposing the two air-coupled transducers either at the thin or thick skin side, respectively. This is due to the normal-to-plate displacement component U_1 which is continuous at the air-plate interfaces, and which is high at the thin skin side and small at the thick skin side for mode A, and vice versa for mode B. The attenuation is about 1.5 and 1 dB/cm, around 100 kHz, for modes A and B, respectively, thus making them suitable for short or average range testing, depending on the power of the transmitter.

Figures 12(e) and (f) show that mode D at frequency 140 kHz is not a skin mode, but a plate mode producing roughly the same amount of stresses through the two thins than through the core. This kind of mode is therefore suitable for detecting disbondlike defects at the skin-core interfaces, but also defects in the core, like holes or local collapses of the foam. This mode has been experimentally generated and detected by disposing the two air-coupled transducers at the thin-skin side, where it produces a normal-to-plate displacement component U_1 that is higher than that at the other plate surface. With no averaging, the signal to noise ratio at the scope was about 2, thus making the use of two air-coupled transducers not suitable for efficient industrial tests of the skin-foam interfaces or of the foam core. It would be more judicious to produce such modes using another generation system like, for example, a contact PZT transmitter that could be permanently fixed in the sandwich plate, an air-coupled receiver being moved above the specimen for wave detection. Moreover, the very high attenuation level of this mode (about 3.2 dB/cm at 140 kHz) makes a high level of input energy required for testing real structures.

VI. CONCLUSIONS

A semi-analytical model based on the Thomson–Haskell method[20,22] has been developed for predicting the dispersion curves and the through-thickness, displacement, stress and energy flow distributions of guided modes propagating along stratified plates made of anisotropic, viscoelastic material layers. Numerical predictions have been carried out for guided waves in a test-sandwich plate used in aircraft industry. Results show that guided modes very different than Lamb modes propagate in the sandwich specimen. Phase velocity measurements have been made using air-coupled transducers placed at the same side of the individual skin and core samples, thus aiming the contactless and single-sided

access conditions usually required for real industrial testing. Some modes, however, required a contact PZT transmitter to be used for improving the signal-to-noise ratio. The overall good agreement between measured and predicted phase velocities confirms that guided modes get coupled together due to the viscoelastic properties of the materials. Indeed, the dispersion curves plotted from complex roots of the dispersion equation have regions very different than those plotted from real solutions usually sought when propagation in an elastic medium is considered. Connections between modes are dependent on the viscoelasticity level, and associated both to strong attenuation and to exchange of energy through the skin-core interfaces. However, the coupling phenomenon has been shown to exist for a specific mode that is attenuated in amplitude even if the materials constituting the structure are purely elastic. In this case, this mode does not carry energy along the plate.

Finally, through-thickness, displacement and stress fields have been predicted for modes propagating along the sandwich plate. They demonstrate that these waves are neither symmetric nor antisymmetric modes like Lamb waves, due to the nonmirror symmetry of the plate. They also give information on the potential of these modes for detecting particular types of defects in the structure. The lack of sensitivity to viscoelasticity of these fields has been shown for three cases corresponding to no changes in the dispersion curves when the viscoelastic properties are taken into account. This result indicates that some modes, at specific frequencies, can be properly modeled by the FE software that is restricted to simulate the propagation and diffraction in elastic media. However, for modes having phase velocity and/or through-thickness shape sensitive to the anisotropic material viscoelasticity, this property would have to be implemented in FE codes for modeling properly scattering problems. Future works will concern the implementation of a viscoelastic option in the finite element model, and also the use of this software for modeling the diffraction of guided waves by various defects in the sandwich structure. The final aim of this project consists in setting up a single-sided, contactless, NDT technique of aircraft sandwich structures.

ACKNOWLEDGMENTS

This work was supported by the STTC and the Office National d'Etudes et de Recherches Aérospatiales. The authors are grateful to their collaborators at AIA/CP and Thales for supplying the test specimen, and also to the referees for their very helpful contribution in analyzing the results.

[1] I. A. Viktorov, *Rayleigh and Lamb Waves* (Plenum, New York, 1967).
[2] M. J. S. Lowe, ''Matrix technique for modelling ultrasonic waves in multilayered media,'' IEEE Trans. Ultrason. Ferroelectr. Freq. Control **42**(4), 525–542 (1995).
[3] J. Laperre and W. Thys, ''Experimental and theoretical study of Lamb wave dispersion in aluminium/polymer bilayers,'' J. Acoust. Soc. Am. **94**, 268–278 (1993).
[4] A. H. Nayfeh, ''The general problem of elastic wave propagation in multilayered anisotropic media,'' J. Acoust. Soc. Am. **89**, 1521–1531 (1991).
[5] C. Potel, J. F. de Belleval, E. Genay, and P. Gatignol, ''Behaviour of Lamb waves and multilayered Rayleigh waves in an anisotropic periodically multilayered medium: Application to the long-wave length domain,'' Acust. Acta Acust. **82**(5), 738–748 (1996).
[6] M. Castaings and B. Hosten, ''Lamb and SH waves generated and detected by air-coupled ultrasonic transducers in composite material plates,'' NDT & E Int. **34**(6), 249–258 (2001).
[7] J. J. Ditri, J. L. Rose, and G. Chen, ''Mode selection criteria for defect detection optimization using Lamb waves,'' in *Review of Progress in Quantitative NDE*, Vol. 11, edited by D. O. Thompson and D. E. Chimenti (Plenum, New York, 1992), pp. 2109–2115.
[8] K. Maslov and T. Kundu, ''Selection of Lamb modes for detecting internal defects in composite laminates,'' Ultrasonics **35**, 141–150 (1997).
[9] Y. Cho and J. L. Rose, ''An elastodynamic hybrid boundary element study for elastic guided wave interactions with a surface-breaking defect,'' Int. J. Solids Struct. **37**(30), 4103–4124 (2000).
[10] D. N. Alleyne and P. Cawley, ''The interaction of Lamb waves with defects,'' IEEE Trans. Ultrason. Ferroelectr. Freq. Control **39**(3), 381–397 (1992).
[11] W. Yang and T. Kundu, ''Guided waves in multilayered anisotropic plates and its use in internal defect detection,'' ASCE J. Eng. Mech. **124**, 311–318 (1998).
[12] M. Castaings and P. Cawley, ''The generation, propagation and detection of Lamb waves in plates using air-coupled ultrasonic transducers,'' J. Acoust. Soc. Am. **100**, 3070–3077 (1996).
[13] M. Castaings, P. Cawley, R. Farlow, and G. Hayward, ''Single sided inspection of composite materials using air coupled ultrasound,'' J. Nondestruct. Eval. **17**(2), 37–45 (1998).
[14] N. Bourasseau, E. Moulin, C. Delebarre, and P. Bonniau, ''Radome health monitoring with Lamb waves: experimental approach,'' NDT & E Int. **33**(6), 393–400 (2000).
[15] N. Guo and M. K. Lim, ''Lamb waves propagation in aluminium honeycomb structures,'' in *Review of Progress in Quantitative NDE*, Vol. 15, edited by D. O. Thompson and D. E. Chimenti (Plenum, New York, 1996), pp. 323–330.
[16] F. Coulouvrat and M. Rousseau, ''Lamb-type waves in a symmetric solid-fluid-solid trilayer,'' Acust. Acta Acust. **84**, 12–20 (1998).
[17] A. Safaeinili, O. I. Lobkis, and D. E. Chimenti, ''Air-coupled ultrasonic characterization of composite plates,'' Mater. Eval. **53**, 1186–1190 (1995).
[18] A. Safaeinili, O. I. Lobkis, and D. E. Chimenti, ''Air-coupled ultrasonic estimation of viscoelastic stiffnesses in plates,'' IEEE Trans. Ultrason. Ferroelectr. Freq. Control **43**, 1171–1180 (1996).
[19] M. Castaings and B. Hosten, ''The propagation of guided waves in composite, sandwich-like structures and their use for NDT,'' in *Review of Progress in Quantitative Non Destructive Evaluation*, edited by D. O. Thompson and D. E. Chimenti, AIP Conf. Proc. **20B**, 999–1006 (2001).
[20] W. T. Thomson, ''Transmission of elastic waves through a stratified medium,'' J. Appl. Phys. **21**, 89 (1950).
[21] N. A. Haskell, ''The dispersion of surface waves on multilayered media,'' Bull. Seismol. Soc. Am. **43**, 17–34 (1953).
[22] D. Hitchings, *FE77 user manual*, Department of Aeronautics, Imperial College Int. Rep., 1995.
[23] A. Bernard, M. J. S. Lowe, and M. Deschamps, ''Guided wave energy velocity in absorbing and nonabsorbing plates,'' J. Acoust. Soc. Am. **110**, 186 (2001).
[24] B. A. Auld, *Acoustic Fields and Waves in Solids* (Krieger, Malabar, FL, 1990).
[25] M. Castaings, B. Hosten, and T. Kundu, ''Inversion of ultrasonic plane-wave transmission data in composite plates to infer viscoelastic material properties,'' NDT & E International **33**(6), 377–392 (2000).
[26] M. Castaings and B. Hosten, ''Air-coupled measurement of plane-wave, ultrasonic plate transmission for characterising anisotropic, viscoelastic materials,'' Ultrasonics **38**, 781–786 (2000).
[27] B. Hosten and M. Castaings, ''Transfer matrix of multilayered absorbing and anisotropic media Measurements and simulations of ultrasonic wave propagation through composite materials,'' J. Acoust. Soc. Am. **94**, 1488–1495 (1993).
[28] J. Krautkramer and H. Krautkramer, *Ultrasonic Testing of Materials*, 3rd ed. (Springer-Verlag, Berlin, 1983).
[29] J. W. Dunkin, ''Computation of modal solution in layered, elastic media at high frequencies,'' Bull. Seismol. Soc. Am. **55**(2), 335–358 (1965).
[30] M. Castaings and B. Hosten, ''Delta operator technique to improve the Thomson Haskell method stability for propagation in multilayered anisotropic absorbing plates,'' J. Acoust. Soc. Am. **95**, 1931–1941 (1994).
[31] D. Alleyne and P. Cawley, ''A two-dimensional Fourier transform method for the measurement of propagating multimode signals,'' J. Acoust. Soc. Am. **89**, 1159–1168 (1991).
[32] B. Hosten, M. Castaings, H. Tretout, and H. Voillaume, ''Identification of

composite materials elastic moduli from Lamb wave velocities measured with single sided, contact-less ultrasonic method,'' in *Review of Progress in Quantitative Non Destructive Evaluation*, edited by D. O. Thompson and D. E. Chimenti, AIP Conf. Proc. **20B**, 1023–1030 (2001).

[33] B. Hosten, C. Biateau, M. Castaings, and D. Rozière, ''Etude et caractérisation de transducteurs à couplage par air pour l'évaluation et le contrôle non destructifs des matériaux,'' Instrume. Mesure Métrol. **1**(1–2), 169–189 (2001).

Approximation of the Struve function $\mathbf{H}_1$ occurring in impedance calculations

Ronald M. Aarts[a] and Augustus J. E. M. Janssen
Philips Research Laboratories Eindhoven, Prof. Holstlaan 4, NL-5656 AA Eindhoven, The Netherlands

(Received 23 September 2002; revised 24 January 2003; accepted 10 February 2003)

The problem of the rigid-piston radiator mounted in an infinite baffle has been studied widely for tutorial as well as for practical reasons. The resulting theory is commonly applied to model a loudspeaker in the audio-frequency range. A special function, the Struve function $\mathbf{H}_1(z)$, occurs in the expressions for the rigid-piston radiator. This Struve function is not readily available in programs such as Matlab or Mathcad, nor in computer languages such as FORTRAN and C. Therefore a simple and effective approximation of $\mathbf{H}_1(z)$ which is valid for all z is developed. Some examples of the application of the Struve function in acoustics are presented. © *2003 Acoustical Society of America.* [DOI: 10.1121/1.1564019]

PACS numbers: 43.38.Ar, 43.20.Bi, 43.40.At [AJZ]

I. INTRODUCTION

Struve functions occur in many places in physics and applied mathematics, e.g., in optics as the normalized line-spread function (de Boer *et al.*, 1994), in fluid dynamics (Newman, 1984), and quite prominently in acoustics for impedance calculations as is outlined below. The problem of the rigid-piston radiator mounted in an infinite baffle has been studied widely for tutorial as well as for practical reasons (see, e.g., Greenspan, 1979; Pierce, 1989; Kinsler *et al.*, 1982; Beranek, 1954; Morse and Ingard, 1968). The resulting theory is commonly applied to model a loudspeaker in the audio-frequency range. For a baffled piston the ratio of the force amplitude to the normal velocity amplitude, termed the piston mechanical radiation impedance, is given by

$$Z_m = \frac{-i\omega\rho}{2\pi}\int\int\int\int R^{-1}e^{ikR}\,dx_s\,dy_s\,dx\,dy. \tag{1}$$

Here $R=\sqrt{(x-x_s)^2+(y-y_s)^2}$ is the distance between any two surface points on the piston (x_s, y_s) and (x, y), respectively; ω is the frequency and ρ is the density of air. The integration limits are such that (x_s, y_s) and (x, y) are within the area of the piston. The fourfold integral in Eq. (1), known as the Helmholtz integral, was performed by Rayleigh (1896, §302) and further elaborated in Pierce (1989), with the result

$$Z_m = \rho c\pi a^2[R_1(2ka) - iX_1(2ka)], \tag{2}$$

where

$$R_1(2ka) = 1 - \frac{2J_1(2ka)}{2ka} \tag{3}$$

and

$$X_1(2ka) = \frac{2\mathbf{H}_1(2ka)}{2ka} \tag{4}$$

are the real and imaginary part of the radiation impedance, respectively. In Eqs. (2)–(4), a is the piston radius, k is the wave number ω/c, c is the speed of sound, J_1 is the first-order Bessel function of the first kind (Abramowitz and Stegun, 1972, §9.1.21), and $\mathbf{H}_1(z)$ is the Struve function of the first kind (Abramowitz and Stegun, 1972, §12.1.6). See Fig. 1 for a plot of $R_1(ka)$ and $X_1(ka)$.

The Struve function is not readily available in programs such as Matlab or Mathcad, nor in computer languages such as FORTRAN and C. High-accuracy expansions and approximations of Struve functions are available in the literature, see for instance Newman (1984) and the references therein, but these are somewhat cumbersome to use since they require separate consideration of small and large z. Also, the accuracy provided by these approximations is far beyond what is actually needed in most acoustical applications. Therefore, in the following an effective and simple approximation of $\mathbf{H}_1(z)$ which is valid for all z is developed.

II. APPROXIMATION OF THE STRUVE FUNCTION $\mathbf{H}_1(z)$

The Struve function $\mathbf{H}_1(z)$ is defined as

$$\mathbf{H}_1(z) = \frac{2z}{\pi}\int_0^1 \sqrt{1-t^2}\sin zt\,dt. \tag{5}$$

There is the power series expansion (Abramowitz and Stegun, 1972, §12.1.5)

$$\mathbf{H}_1(z) = \frac{2}{\pi}\left[\frac{z^2}{1^2 3} - \frac{z^4}{1^2 3^2 5} + \frac{z^6}{1^2 3^2 5^2 7} - \cdots\right]. \tag{6}$$

For the purpose of numerical computation this series is only useful for small values of z, ka, respectively. Equations (4) and (6) yield for small values of ka

$$X_1(ka) \approx \frac{8ka}{3\pi}, \tag{7}$$

which is in agreement with the small ka approximation as can be found in the references given earlier (see also Fig. 1). Furthermore, there is the asymptotic result (Abramowitz and Stegun, 1972, §12.1.31, §9.2.2 with $\nu=1$)

[a]Electronic mail: ronald.m.aarts@philips.com

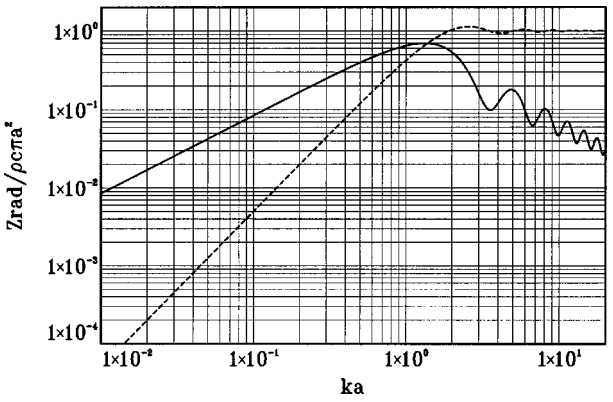

FIG. 1. Real part R_1 (dashed line) and imaginary part X_1 (solid line) of the normalized radiation impedance of a rigid disk with a radius a in an infinite baffle. (On a log log scale.)

$$\mathbf{H}_1(z)=\frac{2}{\pi}-\sqrt{\frac{2}{\pi z}}\cos(z-\pi/4)+O(1/z),\quad z\to\infty, \tag{8}$$

but this is only useful for large values of z. Equation (4) and the first term of Eq. (8) yield for large values of ka

$$X_1(ka)\approx\frac{2}{\pi ka}, \tag{9}$$

and this is in agreement with the large ka approximation as can be found in the earlier given references as well.

Below an approximation for all values of ka is developed in which only a limited number of elementary functions is involved. Integrating by parts, the integral in Eq. (5) becomes

$$\mathbf{H}_1(z)=\frac{2}{\pi}\left[1-\int_0^1\frac{t\cos zt}{\sqrt{1-t^2}}dt\right]. \tag{10}$$

The integral on the right-hand side of Eq. (10) can be written as

$$\int_0^1\frac{\cos zt}{\sqrt{1-t^2}}dt-\int_0^1\sqrt{\frac{1-t}{1+t}}\cos zt\,dt. \tag{11}$$

Using the integral representation of $J_0(z)$ (Abramowitz and Stegun, 1972, §9.1.20 with $\nu=0$) there results the exact representation

$$\mathbf{H}_1(z)=\frac{2}{\pi}-J_0(z)+\frac{2}{\pi}\int_0^1\sqrt{\frac{1-t}{1+t}}\cos zt\,dt. \tag{12}$$

The function $\sqrt{(1-t)/(1+t)}$ in the remaining integral on the right-hand side of Eq. (12) can be approximated quite well by a linear function of t. Accordingly, there holds

$$\sqrt{\frac{1-t}{1+t}}\approx\hat{c}+\hat{d}t, \tag{13}$$

where $\hat{c}$ and $\hat{d}$ are such that

$$\int_0^1\left|\sqrt{\frac{1-t}{1+t}}-(c+dt)\right|^2dt \tag{14}$$

is minimal for $c=\hat{c}$, $d=\hat{d}$. These $\hat{c}$, $\hat{d}$ are readily obtained by requiring that $\sqrt{(1-t)/(1+t)}-(\hat{c}+\hat{d}t)$ is orthogonal to the functions 1, t on $[0, 1]$, and this yields

$$\hat{c}=7\pi/2-10,\quad \hat{d}=18-6\pi, \tag{15}$$

with minimum squared error in Eq. (14) equal to 3.4×10^{-4}.

There results the approximation

$$\mathbf{H}_1(z)\approx\frac{2}{\pi}-J_0(z)+\left(\frac{16}{\pi}-5\right)\frac{\sin z}{z}+\left(12-\frac{36}{\pi}\right)\frac{1-\cos z}{z^2}, \tag{16}$$

with squared approximation error on $[0, \infty)$ equal to 2.2×10^{-4} by Parseval's formula.

It is observed that the right-hand side of Eq. (16) equals $0=\mathbf{H}_1(0)$ for $z=0$. The absolute approximation error in Eq. (16) is plotted in Fig. 2 as a function of z. For the calculation of $\mathbf{H}_1(z)$ the computer program Mathematica has been used. Using Mathematica (V.4.0.2.0) with standard precision results into an anomaly in the region of z between 26 and 30; this anomaly disappears when the standard precision is replaced by a higher one as is done for Fig. 2.

As one sees, the approximation error is small and decently spread-out over the whole z-range, it vanishes for $z=0$, and its maximum value is about 0.005. Replacing $\mathbf{H}_1(z)$ in Fig. 1 by the approximation in Eq. (16) would result in no

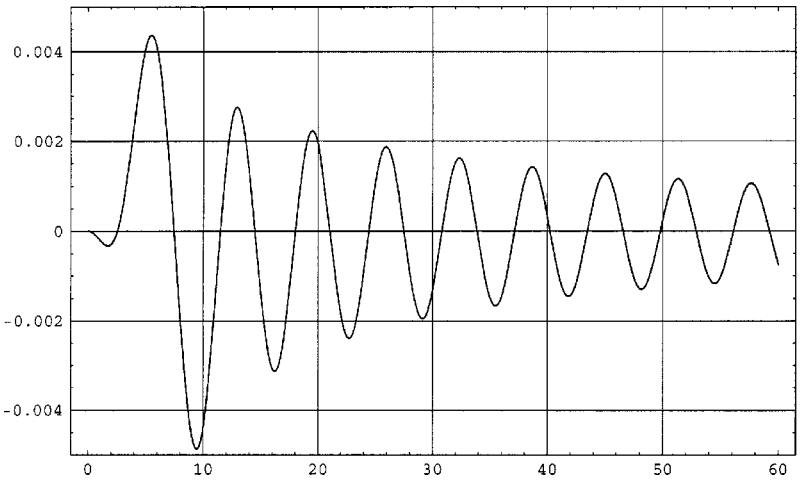

FIG. 2. The absolute error in the approximation of $\mathbf{H}_1(z)$ by Eq. (16).

visible change at all. The maximum relative error appears to be less than 1%, equals 0.1% at $z=0$, and decays to zero for $z \to \infty$.

It was found that inclusion of a quadratic and a cubic term in the approximation in Eq. (13) resulted in a decrease of the mean squared error, see Eq. (14), by only a factor of 1.5 and 6, respectively. The resulting approximation of $\mathbf{H}_1(z)$ then becomes rather awkward, both in form and numerically, while its accuracy is only marginally improved. Hence the approximation in Eq. (16) seems the best compromise between accuracy and simplicity.

III. EXAMPLE

A prime example of the use of the radiation impedance is the calculation of the radiated acoustic power of a circular piston in an infinite baffle. This is an accurate model (Beranek, 1954) for a loudspeaker with radius a mounted in a large cabinet. The radiated acoustic power is equal to

$$P_a = 0.5|V|^2 \Re\{Z_m\}, \tag{17}$$

where V is the velocity of the loudspeaker's cone, and $\Re$ denotes real part of. An example of the use of the obtained approximation of $\mathbf{H}_1$ is to calculate a loudspeaker electrical input impedance Z_{in}, which is among other parameters a function of Z_m (see Beranek, 1954; Vanderkooy and Boers, 2002). Using Z_{in}, the time-averaged electrical power delivered to the loudspeaker is calculated as

$$P_e = 0.5|I|^2 \Re\{Z_{\text{in}}\}, \tag{18}$$

where I is the current fed into the loudspeaker. Finally, the efficiency of a loudspeaker, defined as

$$\eta(ka) = P_a / P_e, \tag{19}$$

which is an important engineering parameter in the field of electro-acoustics, can be calculated. The approximation in Eq. (16) of $\mathbf{H}_1(z)$ is used in Vanderkooy and Boers (2002) to calculate Z_{in} and $\eta(ka)$.

IV. CONCLUSIONS

A simple and effective approximation of the Struve function $\mathbf{H}_1(z)$ for all values of z has been developed using only a limited number of elementary functions. The obtained approximation is in agreement with the small as well as large ka approximations known from the literature, but does not require patchwork formulas, since it is accurate for the whole ka range. The approximation can be used in various fields, with its most prominent engineering application in electro-acoustics.

ACKNOWLEDGMENTS

The authors would like to thank Professor John Vanderkooy and Paul Boers for their interest in this work.

Abramowitz, M., and Stegun, I. (**1972**). *Handbook of Mathematical Functions* (Dover, New York).

Beranek, L. (**1954**). *Acoustics* (McGraw–Hill, New York) (reprinted by ASA, 1986).

de Boer, G., Braat, J., and Janssen, A. (**1994**). ''Scan density and resolution in a laser beam pattern generator,'' Pure Appl. Opt. **3**, 623–641.

Greenspan, M. (**1979**). ''Piston radiator: Some extensions of the theory,'' J. Acoust. Soc. Am. **65**, 608–621.

Kinsler, L., Frey, A., Coppens, A., and Sanders, J. (**1982**). *Fundamentals of Acoustics* (Wiley, New York).

Morse, P., and Ingard, K. (**1968**). *Theoretical Acoustics* (McGraw-Hill, New York).

Newman, J. (**1984**). ''Approximations for the Bessel and Struve functions,'' Math. Comput. **43**, 551–556.

Pierce, A. (**1989**). *Acoustics, An Introduction to Its Physical Principles and Applications* (ASA, New York).

Rayleigh, J. (**1896**). *The Theory of Sound*, Vol. 2 (Dover, New York, 1945).

Vanderkooy, J., and Boers, P. (**2002**). ''High-efficiency direct-radiator loudspeaker systems,'' convention paper 5651 presented at the 113th AES Convention, 5–8 October 2002, Los Angeles, CA, Audio Eng. Soc.

Energy analysis of a piezoelectric body under nonuniform deformation[a)]

Boris Aronov
Acoustics Research Laboratory, Department of Electrical and Computer Engineering, University of Massachusetts at Dartmouth, 285 Old Westport Road, North Dartmouth, Massachusetts 02747-2300 and BTECH Acoustics, 1445 Wampanoag Trail, Suite 115, East Providence, Rhode Island 02915

(Received 1 May 2002; accepted for publication 30 January 2003)

One of the most powerful and clear methods for solving electromechanical transducer problems is the energy method based on the use of the Euler–Lagrange equations. The general expression is developed in a form convenient for applying the energy method to the calculation of the internal energy of a piezoelectric body under nonuniform deformation. The electrical and mechanical variables in this expression are separable under certain conditions and the underlying physics is illustrated with particular examples of bars made of piezoelectric ceramic for the case of transverse and axial polarization. In the case that the electrical and mechanical variables are not separable, the contribution of the mutual energy term to the total internal energy is expressed analytically. [DOI: 10.1121/1.1562648]

PACS numbers: 43.38.Ar, 43.38.Fx, 43.38.Pf, 43.30.Yj [SLE]

I. INTRODUCTION

One of the most powerful methods for solving vibration problems for a system with multiple energy transformations such as an electroacoustical transducer is the energy method based on the use of the variational principle which results in a set of Euler–Lagrange equations. An example of application of the Euler–Lagrange equations to calculation of flexural mode transducers can be found in Ref. 1. In order to apply the variational principles to the problems of piezoelectric electromechanical transducers in general, an expression for the appropriate thermodynamic function for an arbitrary deformed piezoelectric body has to be at hand. The objective of this paper is to develop the expression for the internal energy of a piezoelectric body with general deformation distribution in a form that is convenient for the application of the Euler–Lagrange equations.

The internal energy of a unit volume of piezoelectric ceramic material w_{int} under uniform deformation is considered in Sec. II. The concept of the electromechanical or ''convertible'' part of the internal energy is discussed. It is shown that the electrical and mechanical variables may be considered separable in this case. The analysis of the internal energy of an arbitrary piezoelectric body under nonuniform deformation of a general type, based on the integration of the internal energy of the unit volume, is presented in Sec. III. The general expression for the internal energy is obtained. It is shown that under certain conditions the electrical and mechanical variables in this expression may be considered separable as in the case of the unit volume. In the case that the condition of separation is not fulfilled, the contribution of a mutual energy term ΔW to the total internal energy is analytically derived and can be easily evaluated. The condition of separation is physically illustrated with examples of longitudinally vibrating bars with transverse and axial electric fields (the latter is considered in solid and segmented modifications). This technique is demonstrated in Sec. IV.

II. THE INTERNAL ENERGY OF A SMALL PIEZOELECTRIC VOLUME

Consider a unit volume of the piezoelectric ceramic described by an orthogonal coordinate system $\mathbf{q}_1$, $\mathbf{q}_2$, and $\mathbf{q}_3$ as illustrated in Fig. 1, in which the axis $\mathbf{q}_3$ is in the direction of the polar axis $\mathbf{P}$. Depending upon the direction of the electric field applied, the unit volume produces the extension strain [$\mathbf{E}=\mathbf{E}_3$ as shown in Fig. 1(a)] or the shear strain [$\mathbf{E}=\mathbf{E}_1$ as shown in Fig. 1(b)]. At first we will consider the most common case that $\mathbf{E}=\mathbf{E}_3$. Assuming that the piezoelectric volume is a linear system and under adiabatic condition, its internal energy is given by

$$w_{\text{int}}=w_m+w_{\text{el}}=\tfrac{1}{2}S_iT_i+\tfrac{1}{2}D_3E_3, \tag{1}$$

where $w_m=S_iT_i/2$ and $w_{\text{el}}=D_3E_3/2$ are the independent mechanical and electrical energies supplied by external sources, S_i and T_i are the strains and stresses ($i=1,2,\ldots,6$), and D_3 and E_3 are the charge density and electric field.

If the unit piezoelectric element is considered as an energy converter in the ''receive mode'' (when the energy enters only from the mechanical side), then the internal energy density is

$$w_{\text{int}}=w_m=\tfrac{1}{2}S_iT_i. \tag{2}$$

In the ''transmit mode'' (when the energy enters only from the electrical side)

$$w_{\text{int}}=w_{\text{el}}=\tfrac{1}{2}D_3E_3. \tag{3}$$

The equations of state (piezoelectric equations) for a unit volume may be represented in the following forms:

$$T_i=c_{ik}^{E}S_k-e_{3i}E_3, \tag{4a}$$

$$D_3=e_{3i}S_i+\epsilon_{33}^{S}E_3, \tag{4b}$$

[a)]The results of this work were reported in part at the 136th Meeting of the Acoustical Society of America [J. Acoust. Soc. Am. **104**, 1845(A) (1998)].

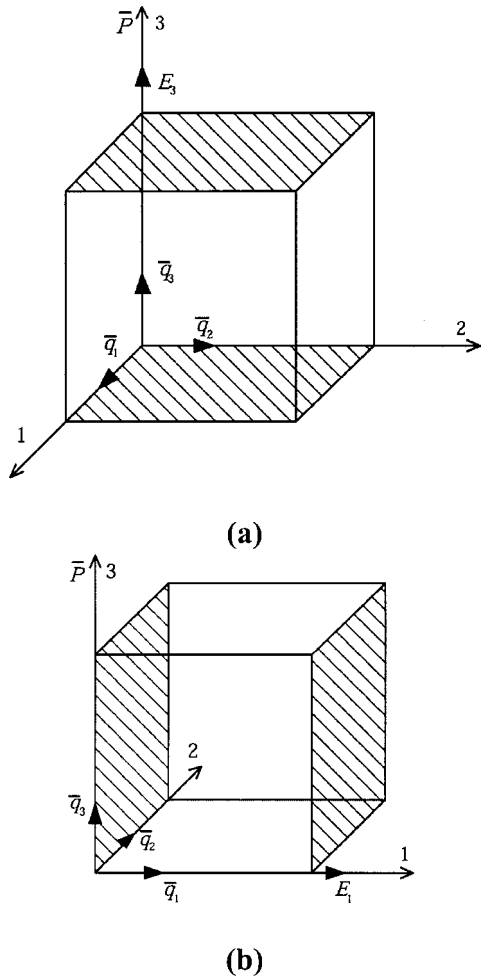

FIG. 1. The typical element of a piezoelectric ceramic body: (a) to produce the extensional deformation; (b) to produce the shear deformation.

with the electric field and strain as independent variables, or

$$S_i = s_{ik}^E T_k + d_{3i} E_3 , \tag{5a}$$

$$D_3 = d_{3i} T_i + \epsilon_{33}^T E_3 , \tag{5b}$$

with the electric field and stress as independent variables. The standard notations of the piezoelectric material constants, as they are defined in Ref. 2, are used in Eqs. (4) and (5) and the common convention of the summation with respect to repeated indices is applied. The piezoelectric equations in the form of Eq. (4) are more convenient for a general theoretical analysis because the strains as independent variables are directly linked with the transducer surface vibration and therefore with the acoustic field. On the other hand, the piezoelectric equations in the form of Eq. (5) are more convenient for a particular transducer analysis because in practical designs the conditions of one-dimensional stress are often fulfilled and therefore Eq. (5) can be simplified.

In this paper the analysis of the internal energy is restricted to the transmit mode. Results for the receive mode can be obtained in a similar way or by reciprocity. After substituting D_3 obtained from Eq. (4b) in Eq. (3), the internal energy in the transmit mode will be obtained in the form of

$$w_{\text{int}} = w_{\text{el}} = \tfrac{1}{2}\epsilon_{33}^S E_3^2 + \tfrac{1}{2} e_{3i} S_i E_3 . \tag{6}$$

Let us denote the first term

$$w_{\text{el}}^S = \tfrac{1}{2}\epsilon_{33}^S E_3^2 , \tag{7}$$

as the electrical energy of a clamped piezoelectric element (at $S_i = 0$) and the second term

$$w_{\text{em}} = \tfrac{1}{2} e_{3i} S_i E_3 , \tag{8}$$

as the electromechanical energy. If it is assumed that the unit volume is under the ideal mechanical boundary conditions (i.e., there is no external exchange of mechanical energies), we have $S_i T_i = 0$. Using the piezoelectric equation (4a) and taking into account the condition of $S_i T_i = 0$, we arrive at the expression

$$w_{\text{em}} = \tfrac{1}{2} e_{3i} S_i E_3 = \tfrac{1}{2} c_{ik}^E S_k S_i . \tag{9}$$

The right-hand term in this expression is the mechanical energy of a piezoelectric element at constant electric field, and it can be denoted as

$$w_m^E = \tfrac{1}{2} c_{ik}^E S_k S_i . \tag{10}$$

Now, Eq. (9) becomes

$$w_{\text{em}} = w_m^E . \tag{11}$$

This means that the electromechanical energy can be considered as a part of the electrical energy supplied to a piezoelectric element which is transformed into the mechanical energy of deformation. Equation (9) shows that w_{em} is positive, and therefore it can be used in the form of the equivalent absolute value $|w_{\text{em}}|$ regardless of the signs of the entering factors.

When the state of the unit volume is characterized by free deformation (i.e., $S_i \neq 0$), it should be noted that $T_i = 0$ by virtue of the boundary condition $S_i T_i = 0$. Therefore, we can define the electrical energy supplied to the piezoelectric unit volume as $w_{\text{el}} = w_{\text{el}}^T$ (electrical energy of a piezoelectric element free of stress). Considering this and summarizing Eqs. (7) through (11), the expression for the internal energy in Eq. (6) can be represented as follows:

$$w_{\text{int}} = w_{\text{el}}^T = w_{\text{el}}^S + |w_{\text{em}}| = w_{\text{el}}^S + w_m^E . \tag{12}$$

If the piezoelectric equations (5) are used when considering Eq. (3) for w_{int}, then the state of the unit volume under the action of the electric field E_3 is characterized by $T_i \neq 0$ and $S_i = 0$. Therefore, $w_{\text{el}} = w_{\text{el}}^S$ and the following representation of Eq. (3) is obtained as

$$w_{\text{int}} = w_{\text{el}}^S = \tfrac{1}{2}\epsilon_{33}^T E_3^2 + \tfrac{1}{2} d_{3i} E_3 T_i , \tag{13}$$

where

$$-\tfrac{1}{2} d_{3i} E_3 T_i = \tfrac{1}{2} s_{ik}^E T_i T_k . \tag{14}$$

The terms in these relations are the same components of the internal energy as in the previous case but expressed in different variables. Therefore, they may be denoted as

$$w_{\text{el}}^T = \tfrac{1}{2}\epsilon_{33}^T E_3^2 , \tag{15}$$

$$w_m^E = \tfrac{1}{2} s_{ik}^E T_i T_k , \tag{16}$$

$$w_{\text{em}} = -\tfrac{1}{2} d_{3i} E_3 T_i . \tag{17}$$

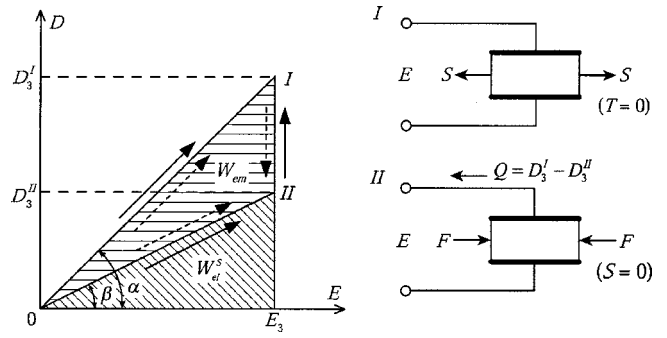

FIG. 2. The energy state diagram of a unit piezoelectric volume: tan $\alpha = \epsilon_{33}^S$, tan $\beta = \epsilon_{33}^T$; the way of transition to the "free" state is shown by the solid arrows and the way of transition to the "clamped" state is shown by the dashed arrows.

Note that the electromechanical energy density w_{em} in Eq. (17) is always positive in spite of the negative sign, as it follows from Eq. (14). However, it is also useful to prove this statement independently by applying the conventional rule of signs to the right-hand part of Eq. (17). In the case that $i=3$, $d_{33}>0$ and the positive electric field E_3 (applied in the positive direction of the polar axis **P**) in a clamped piezoelectric element generates compression, which is in convention a negative variable as $T_3<0$. In the case that $i=1$, $d_{31}<0$ and a positive electric field E_3 generates tension, which is in convention a positive variable as $T_1>0$. In both cases the quantity $w_{\text{em}}=-d_{3i}E_3T_i$ is positive and w_{em} may be replaced by $|w_{\text{em}}|$ in order to avoid any confusion introduced by the negative sign. Thus, Eq. (13) for w_{int} may be represented as follows:

$$w_{\text{int}}=w_{\text{el}}^S=w_{\text{el}}^T-|w_{\text{em}}|=w_{\text{el}}^T-w_m^E. \tag{18}$$

Equations (12) and (18) describe w_{int} for different mechanical conditions, namely, for the free and clamped unit volume. These states correspond to the points I and II in the diagram shown in Fig. 2. If the unit volume is subjected to an external force F so as to clamp it, i.e., to transit its energy state into position II, then the charge $Q=D_3^{\text{I}}-D_3^{\text{II}}$ flows into the electrical energy source, while the electric field E_3 remains constant. The part of the internal energy of the piezoelectric volume, which is converted in the electrical form, is equal to w_{em}. Therefore, the electromechanical energy w_{em} can also be considered as the convertible part of the internal energy. According to Eqs. (12) and (18), the electrical (E_3) and mechanical variables (S_i or T_i) in the expression for the internal energy of a unit volume can be considered separable under the conditions that w_{el}^S and w_{el}^T are calculated with the dielectric constants ϵ_{33}^S and ϵ_{33}^T correspondingly, and w_m^E is calculated with the elastic constants c_{ik}^E or s_{ik}^E.

III. THE INTERNAL ENERGY OF THE PIEZOELECTRIC VOLUME UNDER NONUNIFORM DEFORMATION

Let us now consider a piezoelectric ceramic body under the ideal mechanical boundary condition, i.e., under the condition that it does not exchange mechanical energy with its surroundings. Under this assumption

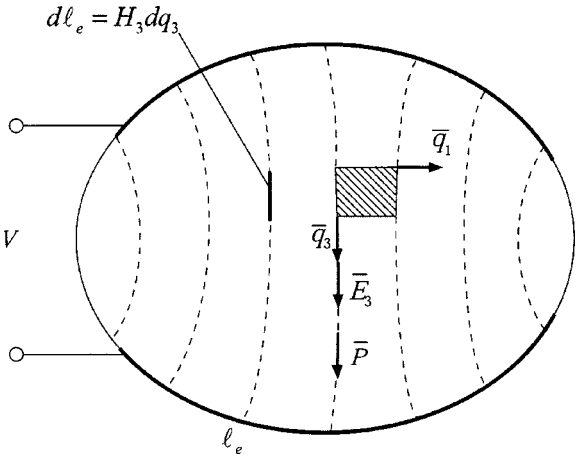

FIG. 3. Piezoelectric body represented in the crystallographic coordinate system.

$$\int_{\Sigma} \mathbf{f}\cdot\boldsymbol{\xi}\, d\Sigma = 0, \tag{19}$$

where $\mathbf{f}$ and $\boldsymbol{\xi}$ are the acting force and displacement on the surface Σ of the body.

The internal energy of the piezoelectric body W_{int} may be found by integrating the internal energy w_{int} of its typical element over the volume $\tilde{V}$ of the body

$$W_{\text{int}}=\int_{\tilde{V}} w_{\text{int}} d\tilde{V}. \tag{20}$$

To carry out the integration for an arbitrary piezoelectric body shown in Fig. 3, the orthogonal crystallographic coordinate system $\mathbf{q}_1$, $\mathbf{q}_2$, $\mathbf{q}_3$ is used, in which $\mathbf{q}_3$ is in the direction of the polar axis **P**. The configuration of the coordinate system depends both on the geometry of the body and on the electrode shape. In the general case the elemental volume is represented as $d\tilde{V}=h_1h_2h_3\, dq_1\, dq_2\, dq_3$ and $dl_i = h_i\, dq_i$ is an elemental length along the coordinate line. In Eq. (20), the density of the internal energy in Eq. (6) may be used in association with Eqs. (7)–(10), but the following considerations have to be taken into account.

A peculiarity in the energy conversion of the elemental volume inside the piezoelectric body may occur due to possible mechanical and electrical interactions between this element and the neighboring parts of the body. In the process of deformation the elemental volume may generate mechanical reactions on the part of the neighboring elements. In this case, when using Eq. (4a) in order to derive the relation for w_{em} similar to Eq. (9), one has to use the stress $T_i=T_{ri}$, where T_{ri} is the stress of the mechanical reaction, instead of $T_i=0$ as it was in the case of the ideal boundary condition. The electromechanical energy in the unit volume becomes

$$w_{\text{em}}=w_m^E-\tfrac{1}{2}T_{ri}S_i, \tag{21}$$

instead of Eq. (11) for the ideal boundary condition. Therefore

$$\int_{\tilde{V}} w_{\text{em}} d\tilde{V}=\int_{\tilde{V}} w_m^E\, d\tilde{V}-\frac{1}{2}\int_{\tilde{V}} T_{ri}S_i\, d\tilde{V}. \tag{22}$$

Applying the Green's theorem to the last term, which is of pure mechanical origin, and taking into account the boundary condition in Eq. (19), we arrive at

$$\int_{\tilde{V}} T_{ri}S_i \, d\tilde{V} = \int_{\Sigma} \mathbf{f}\cdot\boldsymbol{\xi} \, d\Sigma = 0. \tag{23}$$

Thus, Eq. (22) becomes

$$\int_{\tilde{V}} w_{\mathrm{em}} d\tilde{V} = \int_{\tilde{V}} w_m^E \, d\tilde{V}, \tag{24}$$

i.e., the same as if Eq. (11) was used regardless of the mechanical interactions inside the body.

The electrical interactions between elements inside the body can result in the fact that the electric field distribution in a deformed body (let it be denoted by E_3') may differ from the one in a clamped body E_3 under the condition that the same voltage is applied. Therefore, when integrating the internal energy density w_{int}, one has to know the distribution of E_3' over the volume of the body with respect to E_3. As the piezoelectric body is dielectric without free electric charges inside

$$\nabla\cdot\mathbf{D} = \frac{1}{h_1h_2h_3}\left[\frac{\partial(D_1h_2h_3)}{\partial q_1} + \frac{\partial(D_2h_1h_3)}{\partial q_2} + \frac{\partial(D_3h_1h_2)}{\partial q_3}\right] = 0. \tag{25}$$

When $\mathbf{E}$ is parallel to $\mathbf{q}_3$, this leads to $D_1 = D_2 = 0$, and

$$D_3h_1h_2 = \mathrm{const}. \tag{26}$$

Let us now apply Eq. (4b) to the elemental volume of the body in Fig. 3 with substitution of E_3' for E_3. Multiplying both sides of Eq. (4b) by h_1h_2, integrating along the electric field line ℓ_e ($d\ell_e = d\ell_3 = h_3dq_3$), and taking into account Eq. (31), we obtain

$$D_3 = \frac{\epsilon_{33}^S}{\ell_e h_1h_2}\int_0^{\ell_e} E_3'h_1h_2h_3 \, dq_3 + \frac{e_{3i}}{\ell_e h_1h_2}\int_0^{\ell_e} S_ih_1h_2h_3 \, dq_3. \tag{27}$$

The first term in this relation represents the charge density $\epsilon_{33}^S E_3$ due to the electric field E_3 in the clamped body under the applied voltage. The second term represents the charge density generated by the deformation of the body due to the piezoelectric effect. Substituting D_3 expressed by Eq. (27) into Eq. (4b), we obtain the electric field inside the vibrating body E_3' in the form

$$E_3' = E_3 + \frac{e_{3i}}{\epsilon_{33}^S \ell_e h_1h_2}\int_0^{\ell_e} S_ih_1h_2h_3 \, dq_3 - \frac{e_{3i}S_i}{\epsilon_{33}^S}. \tag{28}$$

Thus, the electric field E_3 has to be replaced with E_3' in Eqs. (6) for w_{int} and (20) for W_{int}. This yields

$$W_{\mathrm{int}} = \frac{1}{2}\int_{\tilde{V}} \epsilon_{33}^S (E_3')^2 d\tilde{V} + \frac{1}{2}\int_{\tilde{V}} e_{3i}E_3'S_i d\tilde{V}. \tag{29}$$

When integrating in Eq. (29) after substituting E_3' by its expression in Eq. (28), the assumption that h_1h_2 is independent of q_3 can be adopted for practically all the piezoelectric ceramic transducer designs. (Otherwise the poling electric field in the piezoelectric elements would be nonuniform, which would result in a poor quality of polarization.) Under this assumption, and taking into account that $\int_0^{\ell_e} H_3 dq_3 = \ell_e$, the integration in Eq. (29) becomes straightforward and leads to the following results:

$$\frac{1}{2}\int_{\tilde{V}} \epsilon_{33}^S (E_{33}')^2 d\tilde{V} = \frac{1}{2}\int_{\tilde{V}} \epsilon_{33}^S E_3^2 d\tilde{V} + \frac{1}{2}\frac{e_{3i}^2}{\epsilon_{33}^S}\int_{q_1,q_2}\left[\int_0^{\ell_e} S_i^2h_3 \, dq_3 - \frac{1}{\ell_e}\left(\int_0^{\ell_e} S_ih_3 dq_3\right)^2\right] h_1h_2 \, dq_1 \, dq_2, \tag{30}$$

$$\frac{1}{2}\int_{\tilde{V}} e_{3i}S_iE_3' d\tilde{V} = \frac{1}{2}\int_{\tilde{V}} e_{3i}S_iE_3 d\tilde{V} - \frac{e_{3i}^2}{2\epsilon_{33}^S}\int_{q_1,q_2}\left[\int_0^{\ell_e} S_i^2h_3 \, dq_3 - \frac{1}{\ell_e}\left(\int_0^{\ell_e} S_ih_3 \, dq_3\right)^2\right] h_1h_2 \, dq_1 \, dq_2. \tag{31}$$

Here, the symbol $\int_{q_1q_2}$ means integration over the equipotential surface. In addition to Eqs. (30) and (31), Eq. (24) may be rewritten as follows:

$$\int_{\tilde{V}} w_{\mathrm{em}} d\tilde{V} = \int_{\tilde{V}} e_{3i}S_iE_3' \, d\tilde{V} = \int_{\tilde{V}} w_m^E \, d\tilde{V}. \tag{32}$$

For simplification, the following designations for the terms in Eqs. (30) and (31) are introduced:

$$W_{\mathrm{el}}^S = \frac{1}{2}\int_{\tilde{V}} \epsilon_{33}^S E_3^2 \, d\tilde{V}, \tag{33}$$

for the electrical energy of a clamped body

$$W_{\mathrm{em}} = \frac{1}{2}\int_{\tilde{V}} e_{3i}E_3S_i \, d\tilde{V}, \tag{34}$$

for the electromechanical energy, and

$$W_m^E = \int_{\tilde{V}} w_m^E \, d\tilde{V}, \tag{35}$$

for the mechanical energy of the body due to deformation, and

$$\Delta W=\frac{e_{3i}^2}{2\epsilon_{33}^S}\int_{q_1,q_2}\left[\int_0^{\ell_e} S_i^2 h_3\, dq_3 - \frac{1}{\ell_e}\left(\int_0^{\ell_e} S_i h_3\, dq_3\right)^2\right] h_1 h_2\, dq_1\, dq_2, \tag{36}$$

as the additional term which depends both on the strain distribution and on the configuration of electric field in the clamped body.

Both $W_{\rm el}^S$ and $W_{\rm em}$ have to be calculated using the electric field E_3 in the clamped body. (In the case that $\mathbf{E}=\mathbf{E}_3$, i.e., **E** is parallel to the polar axis **P**, this is the configuration of the crystallographic coordinate system.) W_m^E has to be calculated with the elastic constants at the constant electric field.

From Eq. (36) it follows that $\Delta W=0$, when $\partial S_i/\partial q_3=0$, i.e., in the case that strains do not change along the electric field line.

Finally, taking into account Eqs. (30)–(32) and the designations in Eqs. (33)–(36), the expression for $W_{\rm int}$ in Eq. (29) can be represented as follows:

$$W_{\rm int}=W_{\rm el}^S+W_{\rm em}=W_{\rm el}^S+W_m^E+\Delta W. \tag{37}$$

In the particular case that $\partial S_i/\partial q_3=0$, the expression for $W_{\rm int}$ becomes

$$W_{\rm int}=W_{\rm el}^S+W_{\rm em}=W_{\rm el}^S+W_m^E, \tag{38}$$

i.e., formally the same result is obtained as for a small body under uniform deformation [see Eq. (38)]. In this case, *the electrical and mechanical variables in the expression for* $W_{\rm int}$ *can be considered separable* in the sense that the internal energy of the body can be determined as the sum of the electrical energy evaluated with the permeability value ϵ_{33}^S and the mechanical energy evaluated with the elastic constants c_{ik}^E or s_{ik}^E at a constant electric field.

Up to this point the case that electric field is parallel to the polar axis ($\mathbf{E}=\mathbf{E}_3$) was considered. If the electric field is perpendicular to the polar axis [$\mathbf{E}=\mathbf{E}_1$ as shown in Fig. 1(b)], then the typical element of a piezoelectric body produces shear deformation. The procedure exactly analogous to the preceding gives the following expressions for the components of the internal energy density:

$$w_{\rm el}^S=\frac{1}{2}\epsilon_{11}^{S_5}E_1^2,\quad w_m^E=\frac{1}{2}c_{55}^E S_5^2=\frac{1}{2}\frac{T_5^2}{s_{55}^E},$$
$$w_{\rm em}=\tfrac{1}{2}e_{15}S_5E_1=\tfrac{1}{2}d_{15}T_5E_1. \tag{39}$$

All the components of the internal energy and the corresponding parameters of a piezoelectric body may be obtained by integrating these expressions over the volume. Under the assumption that h_2h_3 does not depend on q_1, the general expression for ΔW is

$$\Delta W=\frac{k_{15}^2}{1-k_{15}^2}\frac{1}{s_{55}^E}\int_{q_2,q_3}\left[\int_0^{\ell_e} S_5^2 h_1\, dq_1 - \frac{1}{\ell_e}\left(\int_0^{\ell_e} S_5 h_1\, dq_1\right)^2\right] h_2 h_3\, dq_2\, dq_3. \tag{40}$$

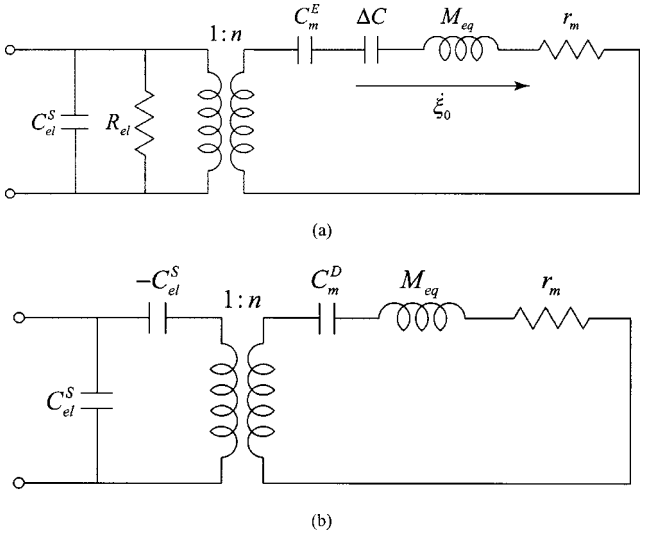

FIG. 4. The equivalent circuit of a transducer with one mechanical degree of freedom: (a) the general representation (the case in which the electrical and mechanical coordinates are separable, i.e., $\Delta W=0$, the compliance ΔC should be excluded); (b) the Mason's equivalent circuit for an end-electroded bar vibrating in the fundamental mode.

If the shear strains do not change along the electric field (i.e., $\partial S_5/\partial q_1=0$), then $\Delta W=0$ and the electrical and mechanical variables can be considered separable as in the previous case where the electric field is parallel to the polar axis.

Let us assume that the piezoelectric body has one mechanical degree of freedom. The distribution of displacements inside the body can be represented as $\xi(r,t)=\xi_0(t)\theta(r)$, where $\xi_0(t)$ is the displacement of a reference point on the surface of the body and $\theta(r)$ is a nondimensional function of the geometrical coordinates, which does not change in the frequency range under consideration. Then, all the components of the $W_{\rm int}$ may be expressed by ξ_0 as the generalized mechanical coordinate and by the voltage V as the generalized electrical coordinate, namely

$$W_{\rm el}^S=\frac{C_{\rm el}^S V^2}{2},\quad W_m^E=\frac{K_m^E\xi_0^2}{2}=\frac{\xi_0^2}{2C_m^E},$$
$$W_{\rm em}=\frac{1}{2}V\xi_0 n,\quad \Delta W=\frac{\Delta K\xi_0^2}{2}=\frac{\xi_0^2}{2\Delta C}, \tag{41}$$

where $C_{\rm el}^S$ is the electrical capacitance of a clamped body, K_m^E and C_m^E are the equivalent rigidity and compliance ($K_m^E=1/C_m^E$), n is the electromechanical transformation coefficient, and $\Delta K=1/\Delta C$ is the additional rigidity of the vibrating body, which is associated with the energy ΔW. Generally, the equivalent electromechanical circuit of such a transducer with one mechanical degree of freedom can be represented as shown in Fig. 4(a). In the particular case that electrical and mechanical variables are separable ($\Delta W=0$), the circuit element ΔC should be excluded.

IV. TRANSDUCER EXAMPLES

A. Longitudinally vibrating bar

Consider the internal energy related parameters for a thin longitudinally vibrating bar of piezoelectric ceramics

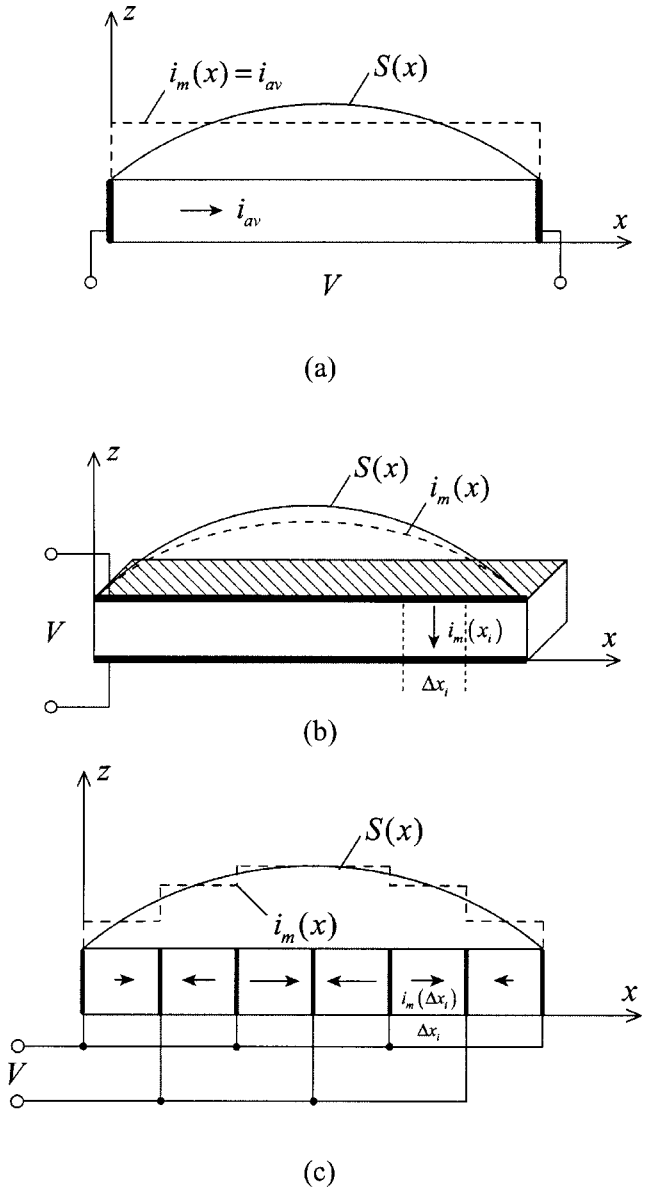

FIG. 5. Longitudinal fundamental mode vibration in the piezoelectric bars: (a) end-electroded; (b) side-electroded; (c) segmented and axially polarized.

with different electrical boundary conditions as illustrated in Fig. 5. Assuming that the bar vibrates in the fundamental mode $\xi=\xi_0\cos(\pi x/\ell)$, it represents a mechanical system with one degree of freedom. Since all the stresses in the bar are zero except for the one in the longitudinal direction, the piezoelectric equations (5) with independent stresses are appropriate. For this particular case Eqs. (5) can be represented in the following form:

$$T_i=\frac{S_i}{s_{ii}^E}-\frac{d_{3i}}{s_{ii}^E}E_3,\quad D_3=\frac{d_{3i}}{s_{ii}^E}S_i+\epsilon_{33}^{S_i}E_3. \tag{42}$$

In Eq. (42), $i=1$ for the transverse polarization as shown in Fig. 5(b), and $i=3$ for the axial polarization, as shown in Figs. 5(a) and (c). Also, $\epsilon_{33}^{S_i}=\epsilon_{33}^T\cdot(1-k_{3i}^2)$, where k_{31} and k_{33} are the coupling coefficients of the piezoelectric material.

The internal energy densities of the longitudinally vibrating bar evaluated according to Eqs. (7) and (9) are given by

$$w_{\rm el}^S=w_{\rm el}^{S_i}=\epsilon_{33}^{S_i}\frac{E_3^2}{2},\quad w_m^E=\frac{S_i^2}{2s_{ii}^E},\quad w_{\rm em}=\frac{d_{3i}}{2s_{ii}^E}S_iE_3. \tag{43}$$

For the bars under consideration, the equivalent parameters defined by Eq. (41) may be obtained by integrating the internal energy densities in Eq. (43) according to Eqs. (33)–(36). It has to be taken into account in the process of integration that the strain is $S_i=-\xi_0(\pi/\ell)\sin(\pi x/\ell)$ and in the case of the transverse polarization $\partial S_1/\partial q_3=\partial S_1/\partial z=0$ (therefore $\Delta W=0$). After calculation, the equivalent parameters for various cases are determined as shown in the following.

(a) For the end-electroded bar (axial polarization)

$$C_{\rm el}^{S_3}=\epsilon_{33}^T(1-k_{33}^2)\frac{bt}{\ell},\quad K_m^E=\frac{1}{C_m^E}=\frac{\pi^2tb}{2s_{33}^E\ell},$$
$$n=\frac{2d_{33}bt}{s_{33}^E\ell},\quad \Delta K=K_m^E\cdot k_{33}^2\frac{(1-8/\pi^2)}{(1-k_{33}^2)}, \tag{44}$$

where t, b, and l are the thickness, width, and length of the bar, respectively. The end-electroded bar is the most typical representation of a transducer with nonuniform strain distribution along the electrical field which results in the additional rigidity ΔK associated with the energy ΔW. Thus, $\Delta K=0.2K_m^E$ in the case that PZT-4 is used with $k_{33}^2\doteq0.5$. This effect is represented by the compliance ΔC in the equivalent circuit shown in Fig. 4(a). The Mason's equivalent circuit (Ref. 2) shown in Fig. 4(b) represents the same end-electroded bar vibrating in the fundamental mode. The parameters C_m^D and $-C_{\rm el}^S$ in Fig. 4(b) are responsible for the effect of the internal energy component $W_m^E+\Delta W$ instead of the use of C_m^E and ΔC in Fig. 4(a). The representation of the circuit in Fig. 4(a) has an advantage, as the term $-C_{\rm el}^S$ in Fig. 4(b) does not have a clear physical meaning.

(b) For the side-electroded bar (transverse polarization)

$$C_{\rm el}^{S_1}=\epsilon_{33}^T(1-k_{31}^2)\frac{b\ell}{t},\quad K_m^E=\frac{1}{C_m^E}=\frac{\pi^2tb}{2s_{11}^E\ell},$$
$$n=\frac{2bd_{31}}{s_{11}^E},\quad \Delta K=0. \tag{45}$$

The side-electroded bar is a typical case that electrical and mechanical variables are separable ($\Delta W=0$). The equivalent circuit for the transducer looks like Fig. 4(a) without ΔC and obviously coincides with the common equivalent circuit for a side-electroded bar vibrating in the fundamental mode.

(c) For the segmented axially polarized bar

$$K_m^E=\frac{\pi^2tb}{2s_{33}^E\ell},\quad C_{\rm el}^{S_3}=\epsilon_{33}^T(1-k_{33}^2)\frac{btN^2}{\ell},$$
$$K_m^E=\frac{\pi^2tb}{2s_{33}^E\ell},\quad n=\frac{2d_{33}btN}{s_{33}^E\ell}, \tag{46}$$

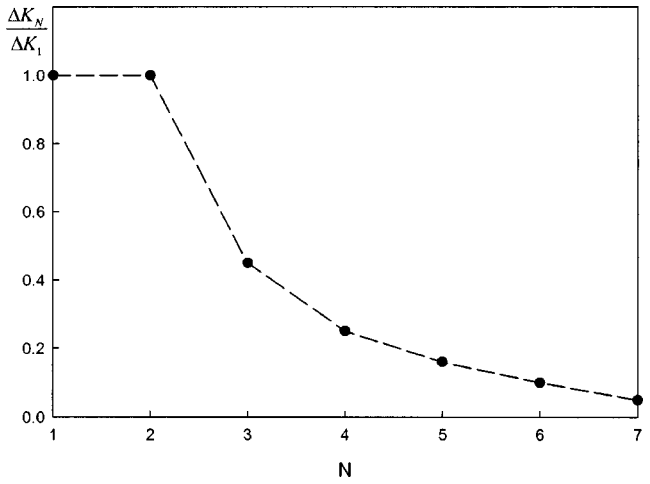

FIG. 6. The ratio $\Delta K_N/\Delta K_1$ as a function of the number of segments N.

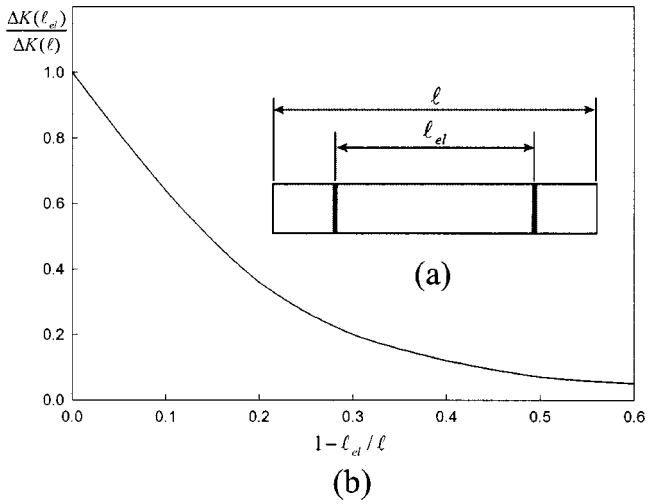

FIG. 7. Effect of the electrodes imbedded in a piezoelectric bar: (a) location of the electrodes; (b) $\Delta K(\ell_{el})/\Delta K(\ell)$ as a function of separation between electrodes.

$$\Delta K_N = K_m^E \frac{k_{33}^2}{1-k_{33}^2}\left[\int_0^{\ell}\sin^2\frac{\pi x}{\ell}dx - \frac{N}{\ell}\sum_{i=1}^{N}\left(\int_{\Delta x\cdot(i-1)}^{\Delta x\cdot i}\sin\frac{\pi x}{\ell}dx\right)^2\right] = K_m^E\frac{k_{33}^2}{1-k_{33}^2}\left[1-\beta\cdot\frac{\sin^2\frac{\pi}{2N}}{(\pi/2N)^2}\right]. \quad (47)$$

In Eq. (47) $\beta=1$ at $N\geqslant 2$ and $\beta=2$ at $N=1$, which corresponds to the preceding case of the solid axially polarized bar. The ratio $\Delta K_N/\Delta K_1$ versus the number of segments N is represented in Fig. 6. For a number of segments greater than six on a half wavelength of deformation it can be seen that $\Delta K_6<0.1\Delta K_1$, and in practice $\Delta K_{N\geqslant 6}$ is negligible. For instance, in the case of PZT-4, $\Delta K_6<0.02K_m^E$. With $\Delta K_N \ll K_m^E$ (conventionally, at $N\geqslant 6$ if the modern PZT ceramic is used), the equivalent circuit for the axially poled segmented bar is qualitatively the same as the equivalent circuit for the transverse polarized bar, as shown in Fig. 5(b), because $1/\omega\Delta C\ll 1/\omega C_m^E$ and $1/\omega\Delta C$ can be neglected. This reflects the fact that the conversion of energy in these two cases occurs qualitatively in the same manner and it differs from the case of the axially polarized solid bar.

In order to explain the physical difference in the quality of energy conversion between the transverse polarized, axially polarized solid, and axially polarized segmented bars, let us assume that the bar is divided into small elements Δx as shown in Fig. 5, and consider these elements as the individual elemental energy converters. The electrical energy which is utilized by the elements may be represented as

$$w_{\rm el}(x)=[w_{\rm el}^S(x)+w_{{\rm el}.m}(x)]\sim[i_s(x)+i_m(x)]. \quad (48)$$

The "$\sim$" sign indicates the proportionality, $w_{\rm el}^S(x)$ and $i_s(x)$ are the electrical energy and the current through the element in the case that the bar is clamped, $w_{{\rm el}.m}(x)$ and $i_m(x)$ are the motional part of electrical energy utilized by the element and the motional current through the element due to the deformation of the whole bar. The motional part of the electrical energy consumed by the element is $w_{{\rm el}.m}(x)\sim i_m(x)\cdot E_3(x)$. The part of the electrical energy, which is converted into the mechanical energy in the course of the element deformation, is $w_m^E(x)$ and according to Eq. (9) it is proportional to the strain, i.e., $w_m^E(x)\sim S(x)\cdot E_3(x)$, where $E_3(x)$ is the electric field in the element. Thus, the ratio $w_m^E(x)/w_{{\rm el}.m}(x)\sim S(x)/i_m(x)$ gives the part of the motional electrical energy that is converted into the mechanical form by the element of the vibrating bar with the coordinate x.

In the case of the transverse piezoelectric effect the electrodes of the bar distribute the motional current in such a way that $i_m(x)\sim S(x)$ (actually $i_m=d_{31}S_1/s_{11}^E$) and $w_m^E(x)/w_{{\rm el}.m}(x)=$const. There is no electrical interaction between elements of the bar. The distribution of the motional electrical energy between the elements of the mechanical system occurs in exact accordance with their contribution to the electromechanical conversion.

In the case of the axially polarized solid bar $i_m(x)=i_{\rm av}$, where $i_{\rm av}$ is the average current, which flows through all the elements while $S(x)\sim\sin(\pi x/\ell)$. Accordingly, $w_m^E(x)/w_{{\rm el}.m}(x)\sim\sin(\pi x/\ell)$. This means that, although the elements located near the ends contribute nearly nothing to electromechanical conversion, they consume the same amount of the motional electrical energy as the elements located in the middle part of the bar that is actually contributing the most. The distribution of the motional electrical energy in this case is "unfair." The electrical interaction between the elements takes place in a manner that the "strong" elements of the bar feed the "weak" ones. In order to obtain the same amount of the mechanical energy, relatively more electrical energy is needed than in the preceding case of the transverse electric field.

In the case of a segmented bar, the electrodes inserted into the bar distribute the motional current between segments in accordance with the average strain $S_{3{\rm av}}(\Delta x_i)$ within a segment, $i_m(\Delta x_i)\sim S_{\rm av}(\Delta x_i)$. Therefore, we have $w_m^E/w_{{\rm el},m}\sim S_3(x_i)/S_{3{\rm av}}(\Delta x_i)$. With increasing the number of segments, $\Delta x_i=l/N\to 0$ and $S_3(x_i)/S_{3{\rm av.}}(\Delta x_i)\to 1$. [It can be assumed that $S_{3{\rm av.}}(\Delta x)\doteq S_3(x)$ at $N>6$ for a half-wavelength of deformation.] The distribution of the motional

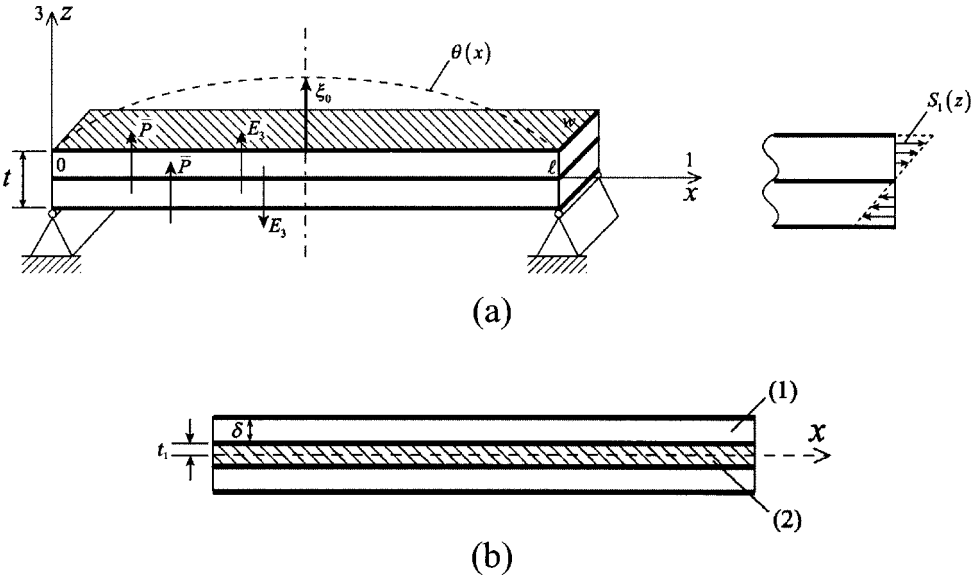

FIG. 8. Piezoelectric beam under flexure: (a) uniform beam; (b) trilaminar beam. (1—piezoelectric layers; 2—inactive material, t_1—separation between piezoelectric layer and neutral plane.)

energy becomes almost as ''fair'' as in the case of the transverse electric field. Thus, the conversion of energy in these two cases qualitatively takes place in the same manner as in the case without the electrical interaction between elements.

It is clear that the most inadequate consumption of the motional electrical energy in the axially polarized solid bar takes place near the ends of the bar, where strains are especially small. Therefore, it is interesting to consider the case that the electrodes are imbedded in the bar at some distance from the ends as shown in Fig. 7(a). Using Eq. (36), where the integration is fulfilled over the length of the bar between the electrodes, yields

$$\frac{\Delta K(\ell_{\rm el})}{\Delta K(\ell)}=\frac{1}{1-8/\pi^2}\cdot\frac{\ell_{\rm el}}{\ell}\left[1+\frac{\ell}{\pi\ell_{\rm el}}\cdot\sin\frac{\pi\ell_{\rm el}}{\ell}-2\frac{\sin^2(\pi\ell_{\rm el}/2\ell)}{(\pi\ell_{\rm el}/2\ell)^2}\right]. \tag{49}$$

This function is depicted in Fig. 7(b), from which it can be concluded that $\Delta K(\ell_{\rm el})$ may be neglected at $\ell_{\rm el}/\ell<0.5$.

B. Beams under flexure

Piezoelectric transducers with mechanical systems in the shape of thin beams, plates, and shells vibrating in flexure and employing the transverse piezoelectric effect represent one more example for the case that the strain changes in the direction of electric field. The distribution of strains in direction perpendicular to the neutral surface in these systems does not depend on their configuration in the horizontal plane and on the boundary conditions. Therefore, consider for simplicity a thin, rectangular, simply supported piezoelectric beam as shown in Fig. 8(a), vibrating in the fundamental mode $\theta(x)=\sin(\pi x/\ell)$. From the general expression for the strain $S_1(z,x)=-z\xi_0\partial^2\theta/\partial x^2$, it follows in this case that

$$S_1(z,x)=z\xi_0\frac{\pi^2}{\ell^2}\sin\frac{\pi x}{\ell}. \tag{50}$$

For the same reason as in the case of the longitudinally vibrating bars, the corresponding piezoelectric equations in Eq. (42) and expressions for the energy densities in Eq. (43) are applicable. Upon substituting S_1 in Eq. (50) into Eqs. (35) and (36), and after simple manipulation, it follows

$$W_m^E=\frac{1}{2s_{11}^E}\int_V S_1^2\cdot d\tilde{V}=\frac{\xi_0^2}{2}\cdot\frac{\pi^4 wt^3}{48\ell^3 s_{11}^E}=\frac{\xi_0^2}{2}\cdot K_m^E, \tag{51}$$

where

$$K_m^E=\frac{\pi^4}{48}\cdot\frac{wt^3}{\ell^3 s_{11}^E}, \tag{52}$$

is the equivalent rigidity of the beam, and

$$\Delta W=\frac{\xi_0^2}{2}\frac{d_{31}^2}{\epsilon_{33}^{S_1}s_{11}^E}K_m^E\left[1-\frac{2}{t}\frac{(\int_0^{t/2}zdz)^2}{\int_0^{t/2}z^2dz}\right]=\frac{\xi_0^2}{2}\Delta K. \tag{53}$$

After integrating the terms in the brackets and taking into account that $d_{31}^2/\epsilon_{33}^{S_i}s_{11}^E=k_{31}^2/(1-k_{31}^2)$, we arrive at

$$\Delta K=0.25\frac{k_{31}^2}{1-k_{31}^2}K_m^E. \tag{54}$$

If the transducers are made of PZT ceramic materials, in which case $k_{31}^2\doteq 0.1$, then $\Delta K\doteq 0.03K_m^E$ can be neglected as compared to K_m^E.

In practice, it is more common to use the flexural-type transducers of the trilaminar passive mechanical system design with the piezoelectric layer removed from the neutral plane, as shown in Fig. 8(b). In this design $\Delta K/K_m^E$ drops as the separation between the piezoelectric layer and the neutral plane increases exactly for the same reason as in the case of

a longitudinally vibrating bar with embedded electrodes. If we assume that Young's moduli of the active and passive materials are approximated the same, then

$$\frac{\Delta K(\delta)}{\Delta K(t/2)} = \frac{\left(\frac{2\delta}{t}\right)^2}{3\left(1-\frac{2\delta}{t}\right)+\left(\frac{2\delta}{t}\right)^2}, \tag{55}$$

where δ is the thickness of the piezoelectric layer. From Eq. (55) it follows that at $\delta/t \leqslant 0.4$ the term ΔK can be neglected even if the single crystal materials are used having very high coupling coefficients ($k_{31} \doteq 0.5$).

V. CONCLUSIONS

The general expression for the internal energy of a nonuniformly deformed piezoelectric body was described. It was shown that the electrical and mechanical generalized coordinates in the expression for the internal energy are separable in most cases of practical interest, when strains do not change (or change insignificantly) along the electric field. That is, the components W_{el}^{S}, W_{m}^{E}, and W_{em} of the internal energy can be evaluated independently as long as the electric field in the clamped transducer body and the strain distribution in the vibrating transducer body are known.

Thus, the problem of the transducer analysis falls into two separate categories: the evaluation of the electric field in the transducer body as a passive dielectric, and the vibration analysis of the transducer mechanical system as a passive anisotropic body (according to anisotropy of the elastic parameters of the piezoelectric material at constant electric field).

When strains change significantly along the electric field, the additional energy term ΔW of a mutual electric and mechanical nature has to be introduced into the expression for the internal energy. This term may result in small corrections to the solutions obtained by the separate analysis of the dielectric and passive mechanical system. The energy ΔW is expressed analytically and can be evaluated in any particular case. The underlying physics explaining the origin of the additional energy term as the result of the electrical interaction between elements in a nonuniformly strained piezoelectric body was illustrated with examples of thin piezoelectric ceramic bars with transverse and axial electric fields longitudinally vibrating in the fundamental mode.

It is shown that in the case of a solid end-electroded bar the nonuniform strain distribution along the electric field results in the additional rigidity of the bar ΔK related to the energy ΔW. This effect is accounted for in the equivalent circuit of the vibrating bar by including an additional term ΔC in series with the bar compliance C_{m}^{E}, as shown in Fig. 4(a).

The expression was also derived which allows the evaluation of the rigidity ΔK depending on the electrical field configuration and the strain distribution in each particular case. The analysis of this expression showed that the additional rigidity may be neglected and the electrical and mechanical variables can be considered separable in the vast majority of practical transducer types.

ACKNOWLEDGMENTS

The author wishes to thank Dr. David A. Brown and Tetsuro Oishi for their cooperation and assistance in revising and preparing the paper for publication. This work was supported in part by BTECH Acoustics, ONR 321SS Elswick and Lindberg, and SBIR N02-066.

[1] F. J. Rosato, "Lagrange equations applied to flexural mode transducers," J. Acoust. Soc. Am. **57**, 1397 (1975).

[2] D. A. Berlincourt, D. R. Curren, and H. Jaffee, "Piezoelectric and Piezomagnetic Materials and their Function in Transducers," in *Physical Acoustics*, edited by W. P. Mason (Academic, New York, 1964), Vol. IA.

Flexural waves on narrow plates

Andrew N. Norris[a)]
Department of Mechanical & Aerospace Engineering, Rutgers University, 98 Brett Road, Piscataway, New Jersey 08854-8058

(Received 16 July 2002; revised 24 January 2003; accepted 28 January 2003)

Flexural wave speeds on beams or plates depend upon the bending stiffnesses which differ by the well-known factor $(1-\nu^2)$. A quantitative analysis of a plate of finite lateral width displays the plate-to-beam transition, and permits asymptotic analysis that shows the leading order dependence on the width. Orthotropic plates are analyzed using both the Kirchhoff and Kirchhoff–Rayleigh theories, and isotropic plates are considered for Mindlin's theory with and without rotational inertia. A frequency-dependent Young's modulus for beams or strips of finite width is suggested, although the form of the correction to the modulus is not unique and depends on the theory used. The sign of the correction for the Kirchhoff theory is opposite to that for the Mindlin theory. These results indicate that the different plate and beam theories can produce quite distinct behavior. This divergence in predictions is further illustrated by comparison of the speeds for antisymmetric flexural, or torsional, modes on narrow plates. The four classical theories predict limiting wave speeds as the plate width vanishes, but the values are different in each case. The deviations can be understood in terms of torsional waves and how each theory succeeds, or fails, in approximating the effect of torsion. Dispersion equations are also derived, some for the first time, for the flexural edge wave in each of the four ''engineering'' theories. © *2003 Acoustical Society of America.* [DOI: 10.1121/1.1561493]

PACS numbers: 43.40.Cw, 43.40.Dx [JJM]

I. INTRODUCTION

The wave number of a flexural wave in a beam of rectangular cross-section or in a plate is $k=(\omega^2 m/D)^{1/4}$ according to classical (Kirchhoff, Euler–Bernoulli) theory, where D is the bending stiffness, m is the mass density (per unit length or area) and ω is the circular frequency. The bending stiffness for the beam is $D=EI$, while that of the plate of the same thickness as the beam is $D=EI/(1-\nu^2)$, where E is Young's modulus, I is the moment of inertia of the cross-section, and ν is Poisson's ratio. The appearance of the factor $1/(1-\nu^2)$ can be explained in terms of the different assumptions in each theory. Both make use of the Kirchhoff kinematic assumption; the plate theory assumes plane stress, while the beam theory is based on the assumption of uniaxial stress. The factor can therefore be attributed to the different assumed forms for the stress in the structure. The uniaxial stress approximation is clearly reasonable for a beam, bar, or rod that is thin in the cross directions, both transverse and lateral. The transverse direction is defined as the direction perpendicular to the plate, and a beam of rectangular cross-section can therefore be considered as the limit of a plate where the lateral dimension is small.

The purpose of this paper is to examine how the beam and plate theories are reconciled, that is, how the transition occurs between the uniaxial and plane stress theories. We will demonstrate explicitly how the beam limit occurs, and in particular will examine the leading order correction to beam theory that includes the dependence on the lateral width. The analysis is performed in the context of several classical theories—the four engineering theories,[1] beginning with the Kirchhoff theory for orthotropic plates and we show that the beam theory prediction for the wave number falls out in the limit of zero plate width. The analysis yields surprising differences. Thus, the four theories contribute different physical aspects which lead to serious differences in the high-frequency limit, but they all agree in the low or quasi-static limit where the Euler–Bernoulli predictions remains inviolate. In this context, the results here show the surprising result, a surprise to the author anyway, that the first correction to the beam theory prediction from the four theories are all distinct. While the main results are for flexural waves symmetric about the center line of the beam or plate, we also analyze the situation where the flexural wave is totally antisymmetric about the center line, and again demonatrate that the four theories provide distinct predictions. Comparison of the symmetric and asymmetric modes offers some explanation for the variations in the prediction for the first correction to the flexural wave (symmetric case).

The methodology adopted here uses known plate theories as the starting point to examine the narrow plate limit. One could also begin with the exact theory of elasticity and derive reduced order theories appropriate to the narrow plate. This approach is outlined briefly in Appendix B for a reduced order model consistent with the Kirchoff hypothesis, generating a uni-dimensional beam theory. It is shown that the predictions of this reduced order model are entirely consistent with those found using the Kirchhoff plate theory. It is expected that similar connections could be obtained between the present results for the Mindlin plate theory and a higher order reduced parameter model for narrow plates that includes shear and rotary inertia,[2] but the analysis is overly complicated and beyond the present study.

a)Electronic mail: norris@jove.rutgers.edu

We begin in the next section with the classical plate equations, and derive the dispersion relation for waves propagating in a plate of finite lateral width. A mode which is symmetric about the center line is shown to exist for all frequencies, and it reduces to the beam mode in the appropriate limit. We also show that this mode has the flexural edge wave speed[3] as asymptote for large width. Subsequent sections consider the same problem in the context of the refined models, the Kirchhoff–Rayleigh and Mindlin plates theories. In each case we illustrate how the appropriate beam theory naturally drops out in the limit as the lateral width becomes small, and we derive the leading order correction to the beam theory that includes the width for asymptotically small values. Modes asymmetric about the plate center line are also examined for the four theories, and the behavior of the lowest order mode as the width vanishes is examined, and compared with the symmetric results.

II. KIRCHHOFF PLATE THEORIES

The classical Kirchhoff theory ignores shearing of cross sections and rotational inertia, effects that are included in the Mindlin plate theory, discussed in the next section. We first consider the classical theory, and then the related Kirchhoff–Rayleigh theory which includes rotational inertia. Both theories are examined in the context of orthotropic plates for greater generality.

A. Classical Kirchhoff plate theory

The plate occupies $-\infty<x<\infty$, $-b\leqslant y\leqslant b$, $-h\leqslant z\leqslant h$, with flexural motion in the z- direction. The governing equations for the displacement $w(x,y,t)$, in the absence of external loading, are[4]

$$\frac{\partial Q_x}{\partial x}+\frac{\partial Q_y}{\partial y}=m\frac{\partial^2 w}{\partial t^2}, \tag{1}$$

$$\frac{\partial M_x}{\partial x}+\frac{\partial M_{xy}}{\partial y}-Q_x=0, \tag{2}$$

$$\frac{\partial M_{xy}}{\partial x}+\frac{\partial M_y}{\partial y}-Q_y=0, \tag{3}$$

where $m=2\rho h$ is the mass density per unit area. The plate is assumed to be orthotropic with axes of symmetry in the x and y directions, for which the moments M_x, M_y, and M_{xy} are

$$M_x=-D_x\frac{\partial^2 w}{\partial x^2}-D_0\frac{\partial^2 w}{\partial y^2}, \tag{4}$$

$$M_y=-D_y\frac{\partial^2 w}{\partial y^2}-D_0\frac{\partial^2 w}{\partial x^2}, \tag{5}$$

$$M_{xy}=-2D_{xy}\frac{\partial^2 w}{\partial x\partial y}. \tag{6}$$

Substituting from Eqs. (2)–(6) into (1) yields the flexural wave equation

$$D_x\frac{\partial^4 w}{\partial x^4}+2(D_0+2D_{xy})\frac{\partial^4 w}{\partial x^2\partial y^2}+D_y\frac{\partial^4 w}{\partial y^4}+m\frac{\partial^2 w}{\partial t^2}=0. \tag{7}$$

This possesses a wave solution of the form $w(x,t)=\mathrm{Re}[Ae^{i(k_x x-\omega t)}]$, where k_x is the wave number of a wave traveling in the x direction in a plate of infinite width, and for later use we also define the analog for the y direction,

$$k_x=\left(\frac{m\omega^2}{D_x}\right)^{1/4}, \tag{8a}$$

$$k_y=\left(\frac{m\omega^2}{D_y}\right)^{1/4}. \tag{8b}$$

Consider, for instance, the limiting case of an isotropic plate, for which the bending stiffnesses reduce to

$$D_x=D_y=D,\quad D_0=\nu D,\quad D_{xy}=\tfrac{1}{2}(1-\nu)D, \tag{9}$$

with

$$D=\frac{EI}{1-\nu^2},\quad I=\frac{2}{3}h^3, \tag{10}$$

where ν is Poisson's ratio and E is the Young's modulus, and, hence, $k_x=((1-\nu^2)m\omega^2/EI)^{1/4}$. By comparison, the flexural wave number in a beam, a purely 1D construct, is $k=(m\omega^2/EI)^{1/4}$. In the following we will determine how this factor of $(1-\nu^2)$ arises, simultaneously examining the analogous situation for the orthotropic plate. We note here that an orthotropic plate composed of an anisotropic material with in-plane extensional (Young's) moduli E_1 and E_2, shear modulus G_{12}, and generalized Poisson's ratios ν_{12} and ν_{21} related by $\nu_{12}E_2=\nu_{21}E_1$ has

$$D_x=\frac{IE_1}{1-\nu_{12}\nu_{21}},\quad D_y=\frac{\nu_{21}}{\nu_{12}}D_x,$$
$$D_0=\nu_{21}D_x,\quad D_{xy}=IG_{12}. \tag{11}$$

In general, the bending stiffnesses D_x, D_y, D_0, and D_{xy} satisfy the inequalities $D_x+D_y>0$, $D_xD_y-D_0^2>0$, $D_{xy}>0$, as a result of the fact that the flexural strain energy is necessarily a positive quantity.

Our approach is to consider the beam as the limit of a plate of vanishing width. In order to take the proper limit we must enforce free-free boundary conditions on the edges $y=\pm b$, viz.,

$$M_y(x,\pm b,t)=0,\quad V_y(x,\pm b,t)=0,\quad -\infty<x<\infty, \tag{12}$$

where $V_y=Q_y+\partial M_{xy}/\partial x$ is the Kirchhoff shear force.[4] We consider time harmonic solutions of the form $w(x,y,t)=\mathrm{Re}[W(y)e^{i(kx-\omega t)}]$. The most general solution that is symmetric about the center line $-\infty<x<\infty$, $y=0$, is

$$W(y)=A_1\cosh\gamma_1 y+A_2\cosh\gamma_2 y, \tag{13}$$

where the transverse wave numbers $\gamma_{1,2}$ are

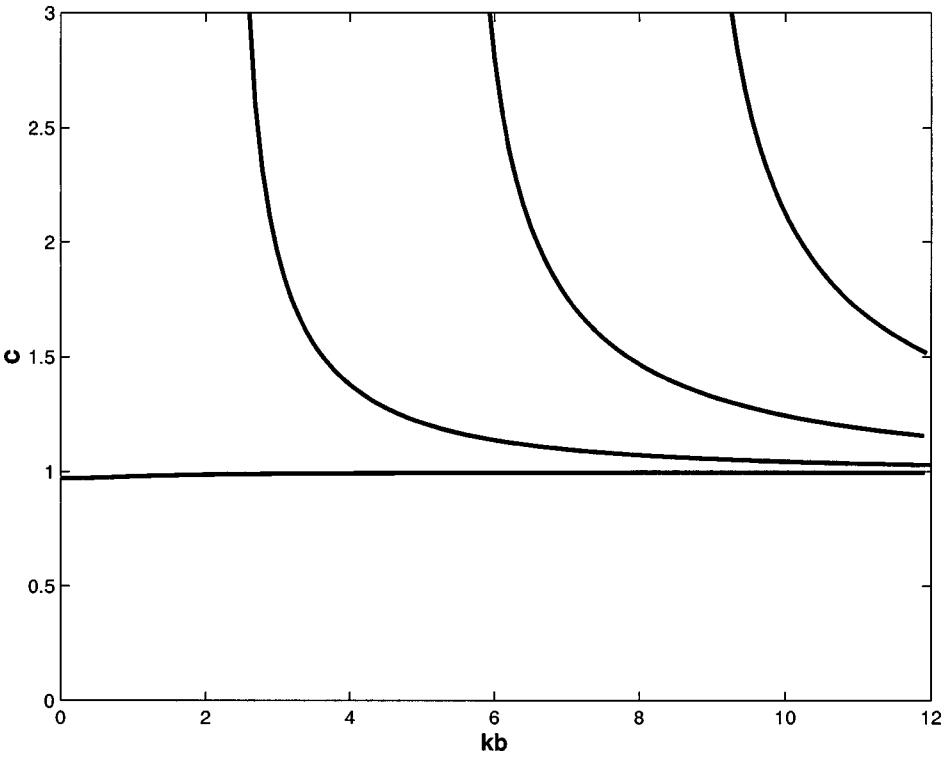

FIG. 1. Dispersion curves for symmetric flexural modes on a strip of width $2b$, from Kirchhoff theory, Eq. (16) for an isotropic plate with $\nu=\frac{1}{3}$. The quantity plotted is the phase speed $c=k_\infty/k$ relative to the speed on a plate of infinite width, $k_\infty^4=m\omega^2(1-\nu^2)/EI$.

$$\gamma_j=\left\{\left(\frac{D_0+2D_{xy}}{D_y}\right)k^2+(-1)^j\left[\left(\frac{D_0+2D_{xy}}{D_y}\right)^2k^4+\frac{D_x}{D_y}(k_x^4-k^4)\right]^{1/2}\right\}^{1/2},\quad j=1,2. \tag{14}$$

Note that $\gamma_2>0$, while γ_1 is positive for subsonic ($k>k_x$) solutions, and pure imaginary, $\gamma_1=i|\gamma_1|$, for supersonic ($k<k_x$) solutions. Applying the boundary conditions (12) gives the simultaneous equations

$$\begin{bmatrix}(D_0k^2-D_y\gamma_1^2)\cosh\gamma_1 b & (D_0k^2-D_y\gamma_2^2)\cosh\gamma_2 b\\ [(D_0+4D_{xy})k^2-D_y\gamma_1^2]\gamma_1\sinh\gamma_1 b & [(D_0+4D_{xy})k^2-D_y\gamma_2^2]\gamma_2\sinh\gamma_2 b\end{bmatrix}\begin{bmatrix}A_1\\A_2\end{bmatrix}=\begin{bmatrix}0\\0\end{bmatrix}, \tag{15}$$

from which the dispersion relation follows as

$$(D_0k^2-D_y\gamma_1^2)^2\gamma_1^{-1}\coth\gamma_1 b-(D_0k^2-D_y\gamma_2^2)^2\gamma_2^{-1}\coth\gamma_2 b=0. \tag{16}$$

The relation $\gamma_1^2+\gamma_2^2=(2D_0+4D_{xy})k^2/D_y$ has been used in simplifying Eq. (16).

The first few dispersion curves are plotted in Fig. 1 versus the nondimensional parameter k_xb for an isotropic plate. The nondimensional speed plotted is $c=k_x/k$, which characterizes the wave number of the wave in the x direction. Solutions with $c<1$ ($c>1$) correspond to waves that are subsonic (supersonic) relative to the reference phase speed

$$v_x\equiv\frac{\omega}{k_x}=\left(\frac{D_x\omega^2}{m}\right)^{1/4}. \tag{17}$$

Note the appearance in Fig. 1 of the modes at discrete frequencies, which in general occur when $k=0$, at discrete values of k_yb satisfying

$$\tan k_yb+\tanh k_yb=0,\quad \text{symmetric cut off}, \tag{18}$$

where k_y, defined in Eq. (8b), is the wavenumber of a wave traveling in the y direction in a plate of infinite width (see Table I).

In addition to these modes, the symmetric solution displays a mode that exists at arbitrarily low values of k_xb,

TABLE I. The first five cutoff frequencies for the Kirchhoff plate model, Eqs. (16) and (49), follow from these values of x, according to $k_yb=\pi x$.

Symmetric: $\tan(\pi x)+\tanh(\pi x)=0$.	0	$x=0.7528$	1.7500	2.7500	3.7500
Asymmetric: $\tan(\pi x)-\tanh(\pi x)=0$	$x=0$	1.2499	2.2500	3.2500	4.2500

which is the mode that reduces to the flexural wave on a beam. Before considering this limit, we note that the large-b asymptote of this mode in Fig. 1 is reached when $k_x b \gg 1$, for which (16) reduces to

$$(D_0 k^2 - D_y \gamma_1^2)^2 \gamma_2 - (D_0 k^2 - D_y \gamma_2^2)^2 \gamma_1 = 0. \tag{19}$$

This has a unique positive root[5] at $k = k_x / c_{\text{edge}}$ where $0 < c_{\text{edge}} \leqslant 1$ is given by

$$c_{\text{edge}}^4 = 1 - \frac{(\sqrt{D_0^2 + 4D_{xy}^2} - 2D_{xy})^2}{D_x D_y}. \tag{20}$$

The speed of a flexural wave guided by the free edge of a semi-infinite isotropic elastic thin plate was first derived by Konenkov,[3] and later by Sinha[6] and by Thurston and McKenna.[7] The flexural edge wave speed for an isotropic plate was also derived from the modes of a thin plate of finite width by taking the limit in which the width becomes infinite.[8] The edge wave decays exponentially with distance from the edge, similar to a Rayleigh wave on an elastic half-space. The existence of the edge wave on orthotropic thin plates was demonstrated by Norris,[5] who first derived the explicit expression (20). Abrahams and Norris[9] showed that it can also exist in the presence of fluid loading, a result which is perhaps surprising. However, the existence is restricted to very light fluid loading conditions: for example, thin plates of aluminum or plexiglass can support edge waves in air, although not in water.[9] The classical Kirchhoff plate theory predicts a speed for the edge wave which is in constant proportion to the flexural wave speed. The constant of proportionality is independent of the frequency and depends only on the Poisson's ratio, being slightly less than unity and equal to unity when the Poisson's ratio vanishes. As noted by Thurston and McKenna,[7] this equality reflects the fact that a flexural wave traveling parallel to the edge of a thin plate of zero Poisson's ratio gives no bending moment or shear and hence automatically satisfies the free edge conditions of the classical plate theory.

We now turn to the beam limit by considering small but nonzero width, specifically $k_x b \ll 1$, by taking the leading order terms in $\coth(\gamma_{1,2} b)$. Using $\coth \xi = 1/\xi + \xi/3 + \mathrm{O}(\xi^3)$, Eq. (16) simplifies to

$$\left(D_x - \frac{D_0^2}{D_y} \right) k^4 - m\omega^2 + \frac{4D_0^2 D_{xy}}{3D_y^2} k^6 b^2 + \mathrm{O}(k^8 b^4) = 0, \tag{21}$$

which may be rewritten

$$k^4 = \frac{m\omega^2}{D^*}, \tag{22}$$

with modified stiffness D^*,

$$D^*(b) = D_x \left[1 - \frac{D_0^2}{D_x D_y} + \frac{4D_0^2 D_{xy}}{3D_x D_y} \frac{k_y^2 b^2}{\sqrt{D_x D_y - D_0^2}} + \mathrm{O}(k^4 b^4) \right]. \tag{23}$$

Substituting from (11) gives $D^* = E^* I$, with effective Youngs modulus

$$E^* = E_1 \left[1 + \frac{4G_{12}}{3E_2} \nu_{12} \nu_{21} (k_{x0} b)^2 + \mathrm{O}(k^4 b^4) \right], \tag{24}$$

where k_{x0} is the wave number of simple beam theory, $k_{x0} = (m\omega^2 / E_1 I)^{1/4}$. Thus, the beam flexural wave number that includes the leading order correction is $k = (m\omega^2 / E^* I)^{1/4} + \mathrm{O}(b^4)$.

Equation (24) suggests that the first correction to the beam limit for nonzero width $b > 0$ can be interpreted as an *increase* in uniaxial stiffness. The increase is proportional to $b^2 \sqrt{\omega}$, and the leading order approximation assumes $k_{x0} b \ll 1$. In the case of isotropy, we have

$$E^* = E \left[1 + \frac{2\nu^2 k_0^2 b^2}{3(1+\nu)} \right] + O(k_0^4 b^4), \tag{25}$$

and k_0 is the beam flexural wave number. The veracity of this leading order correction is verified by the straight line approximation in Fig. 2, which shows the nondimensional relative phase speed $c = k_\infty / k$ versus the $(k_\infty b)^2$ where k_∞ is the flexural wave number of a plate, i.e., $k_\infty = k_0 (1 - \nu^2)^{1/4}$.

B. Kirchhoff–Rayleigh plate theory

The equation of motion of an orthotropic plate is again Eq. (1), but now the effect of rotational inertia is included as follows:

$$\frac{\partial M_x}{\partial x} + \frac{\partial M_{xy}}{\partial y} - Q_x = -\rho I \frac{\partial^3 w}{\partial t^2 \partial x}, \tag{26}$$

$$\frac{\partial M_{xy}}{\partial x} + \frac{\partial M_y}{\partial y} - Q_y = -\rho I \frac{\partial^3 w}{\partial t^2 \partial y}, \tag{27}$$

The moments are as before, Eqs. (4)–(6), and the governing equation for flexural displacement becomes

$$D_x \frac{\partial^4 w}{\partial x^4} + 2(D_0 + 2D_{xy}) \frac{\partial^4 w}{\partial x^2 \partial y^2} + D_y \frac{\partial^4 w}{\partial y^4} + m \frac{\partial^2 w}{\partial t^2} - \rho I \nabla^2 \frac{\partial^2 w}{\partial t^2} = 0. \tag{28}$$

The wave number of a wave traveling in the x direction in a plate of infinite width, formerly given by Eq. (8), is now

$$k_x = \left(\frac{\rho I \omega^2}{2D_x} + \sqrt{\left(\frac{\rho I \omega^2}{2D_x} \right)^2 + \frac{m\omega^2}{D_x}} \right)^{1/2}. \tag{29}$$

Despite the more sophisticated theory, it can be shown following the same procedures as before that the dispersion relation for the plate of finite lateral width $2b$ is again given by Eq. (16), but where $\pm \gamma_{1,2}$ are now roots of

$$D_y \gamma^4 - [2(D_0 + 2D_{xy}) k^2 - \rho I \omega^2] \gamma^2 + D_x k^4 - \rho I \omega^2 k^2 - m\omega^2 = 0. \tag{30}$$

The wave number for the edge wave is defined by (19), derived from (16) in the limit $b \to \infty$, where γ_1 and γ_2 are roots of (30). The equation for the edge wave number may be expressed as a quartic in k^2. At high frequencies it becomes nondispersive, and reduces to a cubic in k^2.

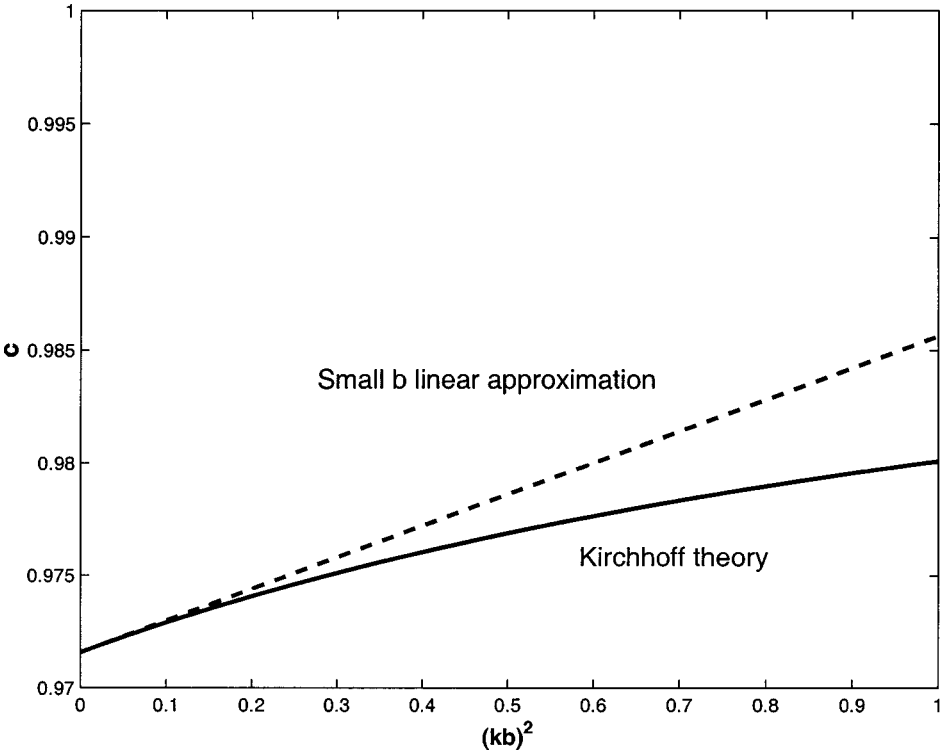

FIG. 2. The relative phase speed $c=k_x/k$ of the lowest symmetric mode versus $(k_\infty b)^2$ (frequency) for an isotropic plate ($\nu=\frac{1}{3}$) using Kirchhoff theory. The zero frequency limit is $(1-\nu^2)^{1/4}$. The dashed straight line is the small-b leading order correction based on Eq. (25).

We now examine the behavior of this plate theory as the width b vanishes. Expanding (16) to first order in b^2, subject to the constraint (30) on $\gamma_{1,2}$, yields

$$\left[1+\frac{D_0}{3}k^2b^2\right][(D_xD_y-D_0^2)k^4-D_y\rho I\omega^2k^2-D_ym\omega^2]$$
$$+\frac{D_0^2}{3D_y}k^4b^2(4D_{xy}k^2-\rho I\omega^2)+\mathrm{O}(b^4)=0. \tag{31}$$

The limiting wave number as $b\to 0$ therefore solves

$$(D_xD_y-D_0^2)k^4-D_y\rho I\omega^2k^2-D_ym\omega^2=0, \tag{32}$$

that is, it is given by (29) with D_x replaced by $D^*(0)$ of Eq. (23). This is the precisely the prediction according to Kirchhoff–Rayleigh beam theory.

Based upon the leading order equation (32), we may simplify (31) so that the first-order correction satisfies the following,

$$[(D_xD_y-D_0^2)k^4-D_y\rho I\omega^2k^2-D_ym\omega^2]$$
$$+\frac{D_0^2}{3D_y}k^4b^2(4D_{xy}k^2-\rho I\omega^2)+\mathrm{O}(b^4)=0. \tag{33}$$

Unlike the previous case of the simple Kirchhoff theory, it does not seem possible to interpret this result in terms of an effective stiffness alone. No simplification is apparent even if we consider the isotropic version of (33),

$$[EIk^4-\rho I\omega^2k^2-m\omega^2]+\frac{\nu^2}{3}k^4b^2\left(\frac{2EIk^2}{1+\nu}-\rho I\omega^2\right)$$
$$+\mathrm{O}(b^4)=0. \tag{34}$$

In particular, this equation cannot be expressed using the modified stiffness of (25) alone.

III. MINDLIN AND SHEAR PLATE THEORIES

Mindlin's theory contains the rotational inertia of the Kirchhoff–Rayleigh theory plus a shear correction. Based on the previous analysis for the Kirchhoff–Rayleigh theory it would seem likely that the Mindlin theory will not yield a simpler result, and probably more complicated than (34). Despite the extra refinements in Mindlin's theory we will see that the first correction to the beam theory, or Timoshenko's theory, only involves an effective stiffness. In fact, it will emerge that the leading order correction for the shear theory is identically zero.

A. Mindlin plate theory

The wave numbers for straight crested waves in an isotropic Mindlin plate and in a Timoshenko beam of the same thickness $2h$ are solutions of quadratic equations for k^2:

$$k^4-(k_S^2+k_P^2)k^2-k_S^2k_P^2+k_F^4=0, \tag{35}$$

$$k^4-(k_S^2+k_{P0}^2)k^2-k_S^2k_{P0}^2+k_{F0}^4=0, \tag{36}$$

respectively. Here,

$$k_P=\omega\sqrt{\frac{\rho(1-\nu^2)}{E}},\quad k_F=\left(\frac{m\omega^2(1-\nu^2)}{EI}\right)^{1/4},$$
$$k_{P0}=\omega\sqrt{\frac{\rho}{E}},\quad k_{F0}=\left(\frac{m\omega^2}{EI}\right)^{1/4}\quad\text{and}\quad k_S=\frac{\omega}{\alpha}\sqrt{\frac{\rho}{\mu}}, \tag{37}$$

where μ is the shear modulus and α is a nondimensional factor, with $0<\alpha\leqslant 1$.[4] The details of the Mindlin plate theory are in Appendix A, where the following dispersion relation for a plate of width $2b$ is derived,

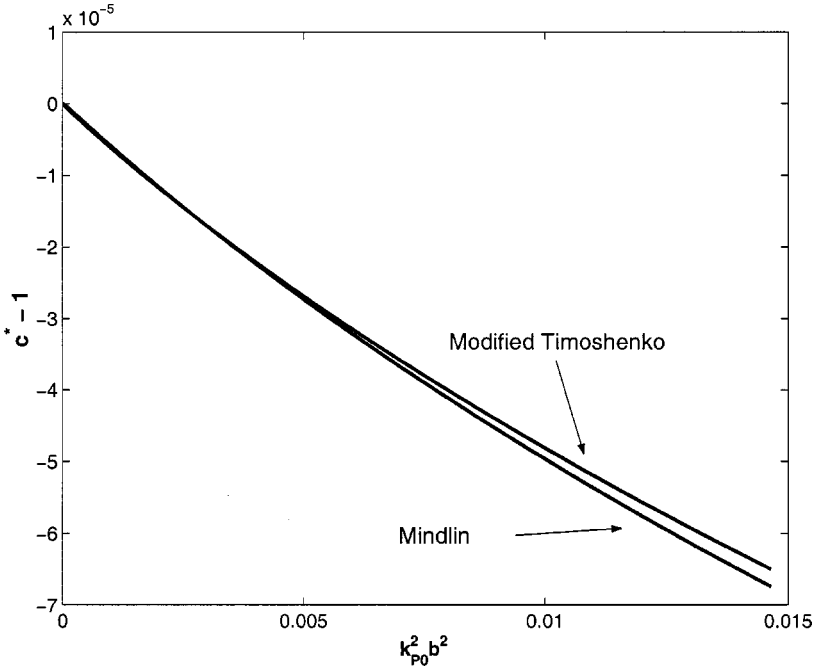

FIG. 3. Comparison of the lowest order symmetric mode for the Mindlin plate theory, and the prediction using the Timoshenko beam equation (43) and the modified Young's modulus of (45). The ratio $b/h=0.2$. The speed $c^*=k_{\mathrm{Tim}}/k$, where k_{Tim} is Timoshenko wave number and k is either the Mindlin wave number or the wave number predicted by the modified Timoshenko dispersion equation.

$$\left(k^2-\frac{k_1^2}{1-\nu}\right)^2(k_S^2-k_1^2)k_2^2\gamma_1^{-1}\coth(\gamma_1 b)$$
$$-\left(k^2-\frac{k_2^2}{1-\nu}\right)^2(k_S^2-k_2^2)k_1^2\gamma_2^{-1}\coth(\gamma_2 b)$$
$$+k^2k_S^2(k_1^2-k_2^2)\gamma_3\coth(\gamma_3 b)=0. \tag{38}$$

The three wavenumbers k_j, $j=1,2,3$, in this equation are defined in Eq. (A9), and $\gamma_j=\sqrt{k^2-k_j^2}$, $j=1,2,3$. Note that k_1 and k_2 are roots of the Mindlin equation (35).

It is interesting to note that the dispersion relation for the Kirchhoff–Rayleigh theory falls out of Eq. (38) by setting k_S to zero or, equivalently, allowing $\alpha\to\infty$. In the limit of infinite width, (38) reduces to

$$\left(k^2-\frac{k_1^2}{1-\nu}\right)^2(k_S^2-k_1^2)k_2^2\gamma_1^{-1}-\left(k^2-\frac{k_2^2}{1-\nu}\right)^2$$
$$\times(k_S^2-k_2^2)k_1^2\gamma_2^{-1}+k^2k_S^2(k_1^2-k_2^2)\gamma_3=0. \tag{39}$$

This equation has been examined by Norris *et al.*[10] who showed that it possesses a root at all frequencies. In the high-frequency limit $k_{S,P}h\gg 1$, the edge wave speed becomes nondispersive, and equal to the Rayleigh wave speed in plane stress,[10] given by

$$(2k^2-k_T^2)^2-4k^2(k^2-k_T^2)^{1/2}(k^2-k_P^2)^{1/2}=0, \tag{40}$$

where $k_T^2=\omega^2\rho/\mu$. Also, the cutoff frequencies of Eq. (38) for the plate of finite width are given by

$$(k_S^2-k_1^2)k_1\cot k_1 b-(k_S^2-k_2^2)k_2\cot k_2 b=0. \tag{41}$$

These define the modal cut-on frequencies, which are infinite in number but include $\omega=0$. We now consider the mode that exists down to zero frequency: the flexural mode.

Unlike the previous expansions for the Kirchhoff plate models, greater care is necessary with the Mindlin theory. Thus, in addition to the assumption $kb\ll 1$, we now need to further specify that $b\ll h$. The latter is required because when we allow the frequency to tend to zero we have $k_3 b=\mathrm{O}(b/h)$, and therefore the consistent small-b limit is reached by allowing $k_j b\ll 1$, $j=1$, 2, 3. We shall return to this point later.

By considering $kb\ll 1$ and $b\ll h$, we find that $\gamma_j b\ll 1$, $j=1$, 2, and by using the leading order approximation $\coth\xi=1/\xi+\mathrm{O}(\xi)$, combined with (A9), it can be shown that Eq. (38) reduces to Eq. (36), which is precisely the dispersion relation for a flexural wave on a Timoshenko beam. Using the two-term approximation of $\coth\xi$ plus the leading order approximation given by (36), we find that the first correction to the wave number satisfies

$$k^4-(k_S^2+k_{P0}^2)k^2-k_S^2k_{P0}^2+k_{F0}^4-\frac{\nu^2}{3}(1-\nu^2)$$
$$\times b^2k_{P0}^2(k_{P0}^2k^2+k_S^2k_{P0}^2-k_{F0}^4)+\mathrm{O}(k^8b^4)=0. \tag{42}$$

The derivation of Eq. (42) was performed using the symbolic algebra program Maple. It may be written as

$$k^4-(k_S^2+k_{P*}^2)k^2-k_S^2k_{P*}^2+k_{F*}^4+\mathrm{O}(k^8b^4)=0, \tag{43}$$

where

$$k_{P*}=\omega\sqrt{\frac{\rho}{E^*}},\quad k_{F*}=\left(\frac{m\omega^2}{E^*I}\right)^{1/4}, \tag{44}$$

and

$$E^*=E\left[1-\frac{\nu^2}{3}(1-\nu^2)k_{P0}^2b^2+\mathrm{O}(b^4)\right]. \tag{45}$$

The approximation to the flexural wave number based on (43)–(45) is compared with the exact prediction from Mindlin theory in Fig. 3. We note the agreement between the lowest order mode and the asymptotic approximation. We also note that the effective Young's modulus of Eq. (45) is

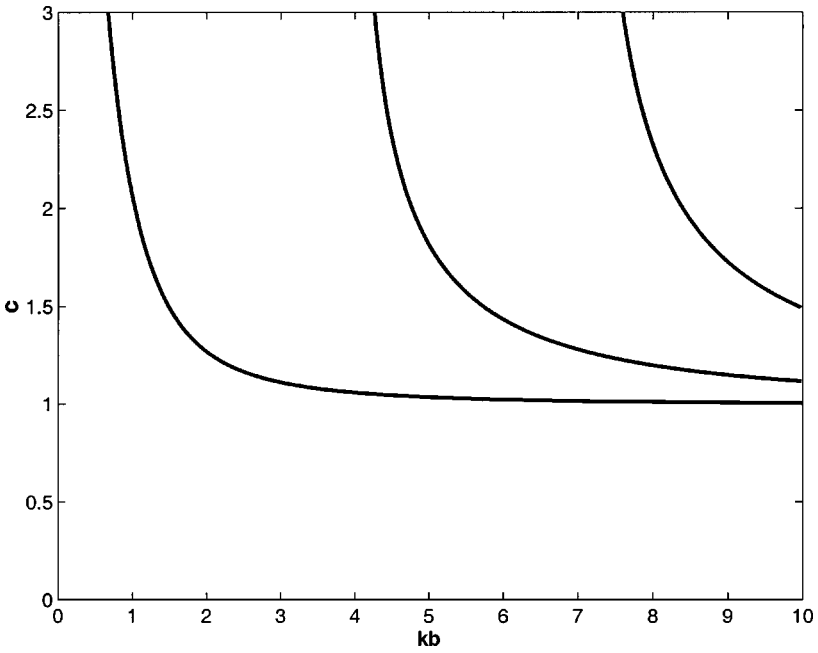

FIG. 4. Dispersion curves for the phase speed $c=k_\infty/k$ for the asymmetric modes on a plate of width $2b$ according to Kirchhoff theory, Eq. (49). Note the existence of the mode down to zero frequency, see Eq. (54).

different in form from that for the Kirchhoff theory, Eq. (25), but defer discussion until later.

B. Shear plate theory

Shear plate theory is a simplified version of Mindlin's theory, as it only considers the shear correction to the Kirchhoff model without the rotational inertia effects. Thus, the model is described by Eqs. (1)–(3) and (A3); the analysis is similar to that for the Mindlin theory, and requires a three-wave solution which is identical with the Mindlin solution if the replacement $k_P\to 0$ is made in (A9). Thus, instead of Eq. (A9), we have

$$k_j^2=\frac{1}{2}k_S^2-(-1)^j\sqrt{\frac{1}{4}k_S^4+k_F^4},\quad j=1,2,\quad k_3^2=3\frac{\alpha^2}{h^2}. \tag{46}$$

The dispersion relation so obtained is formally equivalent to (38), and therefore the asymptotic approximation that results is the same as for the Mindlin plate. That is, the limiting wave number reduces to the pure shear beam theory prediction as $b\to 0$. The edge wave solutions ($b\to\infty$) are also given by the Mindlin equation (39), and in the limit of high frequency the edge wave becomes nondispersive, with $k\to k_S$.

However, because $k_P=0$, we find that the first correction to the leading order equation is identically zero. That is, the narrow plate limit is given by (43) and (44) with

$$E^*=E[1+\mathrm{O}(b^4)]. \tag{47}$$

IV. ASYMMETRIC MODES

We have seen how the beam theory prediction follows from the limit of plate solutions that are symmetric about the centerline $y=0$. We now consider the analogous situation for asymmetric modes or, more correctly, pure antisymmetric modes satisfying $w(x,-y,t)=-w(x,y,t)$. These are plate modes which possess no limit in the beam theories. However, as we will see, these modes all reduce to dispersionless waves, which can be understood in terms of *torsion* rather than flexure. The question arises then whether the plate theories reduce to the correct torsional limits. As before, we consider the four engineering theories in sequence.

A. Kirchhoff plate theory

The general solution that is asymmetric about the center line $-\infty<x<\infty$, $y=0$, is

$$W(y)=A_1\sinh\gamma_1 y+A_2\sinh\gamma_2 y. \tag{48}$$

Applying the boundary conditions (12) on the free edges gives the dispersion relation (see Fig. 4).

$$(D_0k^2-D_y\gamma_1^2)^2\gamma_1^{-1}\tanh\gamma_1 b-(D_0k^2-D_y\gamma_2^2)^2\gamma_2^{-1}\tanh\gamma_2 b=0. \tag{49}$$

Setting $k\equiv 0$ implies that the cutoff frequencies satisfy

$$\tan k_y b-\tanh k_y b=0,\quad \text{asymmetric cut off.} \tag{50}$$

These are enumerated in Table I, and include zero, indicating a mode exists for all nonzero values of b.

Expanding the asymmetric dispersion relation (49) to leading order in $k_x b\ll 1$ gives

$$4D_{xy}k^2-\frac{b^2}{3D_y}\{[D_0+4D_{xy}]k^4+D_xD_y(k_x^4-k^4)\}+\mathrm{O}(b^4)=0. \tag{51}$$

The only consistent solution is $kb=\mathrm{O}(k_xb)^2$, with

$$k^2=\frac{m\omega^2b^2}{12D_{xy}}+\mathrm{O}(b^4). \tag{52}$$

Note that the limiting wave is nondispersive, since $v=\omega/k$ is independent of frequency. Thus, using $D_{xy}=IG_{12}$ gives

$$v^2=\frac{4G_{12}h^2}{\rho b^2}+\mathrm{O}(b^0). \tag{53}$$

In the isotropic case ($G_{12}=\mu$), we find the limiting wave speed $v\to v_0$ as $\omega\to 0$,

$$v_0=\frac{2h}{b}c_T, \tag{54}$$

where $c_T=\sqrt{\mu/\rho}$ is the bulk transverse wave speed. We will discuss this limit later in terms of torsion theory.

B. Kirchhoff–Rayleigh plate theory

The dispersion relation for asymmetric modes is again (49), but where now we have the identities, from (30),

$$\begin{aligned} &D_y(\gamma_1^2+\gamma_2^2)=(2D_0+4D_{xy})k^2,\\ &D_y\gamma_1^2\gamma_2^2=D_xk^4-\rho I\omega^2k^2-m\omega^2. \end{aligned} \tag{55}$$

The equation for cutoff frequencies ($k=0$) is also (50), implying the existence of a mode with a cutoff at zero frequency.

The mode with zero cutoff may be examined using Eq. (55), yielding

$$\begin{aligned} &4D_{xy}k^2-\rho I\omega^2-\frac{b^2}{3D_y}\{[(D_0+4D_{xy})k^2-\rho I\omega^2]^2\\ &\quad+D_xD_y(k_x^4-k^4)-D_y\rho I\omega^2k^2\}+\mathrm{O}(b^4)=0. \end{aligned} \tag{56}$$

Hence,

$$k^2=\frac{\rho I\omega^2}{4D_{xy}}\left(1+\frac{b^2}{h^2}\right)+\mathrm{O}(k^4b^2). \tag{57}$$

This is again nondispersive, with limiting phase (wave) speed for the isotropic plate

$$v_0=\frac{2c_T}{\sqrt{1+b^2/h^2}}. \tag{58}$$

Again, we defer discussion of this result until later.

C. Mindlin plate theory

It may be shown using the same procedure as for the symmetric modes that the dispersion relation for asymmetric modes according to the Mindlin theory is

$$\begin{aligned} &\left(k^2-\frac{k_1^2}{1-\nu}\right)^2(k_S^2-k_1^2)k_2^2\gamma_1^{-1}\tanh(\gamma_1 b)\\ &\quad-\left(k^2-\frac{k_2^2}{1-\nu}\right)^2(k_S^2-k_2^2)k_1^2\gamma_2^{-1}\tanh(\gamma_2 b)\\ &\quad+k^2k_S^2(k_1^2-k_2^2)\gamma_3\tanh(\gamma_3 b)=0. \end{aligned} \tag{59}$$

Setting $k=0$ implies that the cutoff frequencies satisfy

$$(k_S^2-k_1^2)k_1\tan k_1b-(k_S^2-k_2^2)k_2\tan k_2b=0, \tag{60}$$

which includes zero as a cut-on frequency.

Retaining the first two terms in the expansion of (59) in terms of b yields

$$\begin{aligned} &k_p^2\left(1-\frac{k^2b^2}{3}\right)+\frac{b^2}{3}\left\{-(1-\nu^2)k^4+2k^2\left[(1+\nu)k_p^2-2\frac{k_F^4}{k_S^2}\right]\right.\\ &\quad\left.+k_p^4+k_F^4\right\}+\mathrm{O}(b^4)=0. \end{aligned} \tag{61}$$

The dominant terms in (61) for both small b and low frequency are

$$k_p^2+\frac{b^2}{3}k_F^4\left[1-4\frac{k^2}{k_S^2}\right]\sim 0. \tag{62}$$

Hence the limiting value of the phase speed $v=\omega/k\to v_0$ at zero frequency is

$$v_0=\frac{2\alpha c_T}{\sqrt{1+h^2/b^2}}, \tag{63}$$

which is discussed in the next section.

D. Mindlin shear theory

If the rotational inertia is ignored and the pure shear theory is employed, then formally the result can be obtained from the analysis for the Mindlin theory by taking the limit of $k_P\to 0$. The outcome is that expression (62) simplifies to

$$\frac{b^2}{3}k_F^4\left[1-4\frac{k^2}{k_S^2}\right]\sim 0, \tag{64}$$

or $k=k_S/2$. Thus, the zero frequency limit for the phase speed becomes in this case

$$v_0=2\alpha c_T. \tag{65}$$

Note that the resulting wave number is independent of both the half-width b and the semithickness h.

V. DISCUSSION

We have derived the dispersion relations for symmetric and asymmetric modes on a plate of finite width according to the four engineering theories. In the limit of zero width, $b\to 0$, each plate theory predicts that the symmetric mode has the wave number of the corresponding beam theory. The four plate theories also predict the existence of an edge wave solution in the limit of infinite width, $b\to\infty$. The edge wave speed for the Kirchhoff theory is given by (20), and by (39) for the Mindlin and Mindlin-shear theories, respectively. In the high-frequency limit only the Kirchhoff edge wave remains dispersive; the other three theories predict constant but different values for the edge wave speed. We have also examined the behavior of the asymmetric mode in the narrow plate limit, and found in each case that the mode is nondispersive at zero frequency, but with different limiting values. We now discuss the symmetic and asymmetric cases in more detail.

A. Symmetric or flexural mode

The two main results are Eqs. (25) and (45), for the effective Young's moduli of narrow plates or beams of rectangular cross section. By writing the fundamental Kirchhoff beam wave number as $m\omega^2/EI=3k_{P0}^2/h^2$, where k_{P0} is defined in (37), the corrections to the beam theories can be expressed

$$\frac{E^*}{E}-1=\begin{cases}\dfrac{2\nu^2}{\sqrt{3}(1+\nu)}\dfrac{k_{P0}b^2}{h}+\mathrm{O}(b^4), & \text{Kirchhoff},\\ -\dfrac{\nu^2}{3}(1-\nu^2)k_{P0}^2b^2+\mathrm{O}(b^4), & \text{Mindlin},\\ 0+\mathrm{O}(b^4), & \text{Mindlin-Shear only}.\end{cases} \tag{66}$$

The Kirchhoff–Rayleigh theory is not included as it does not reduce to an effective Young's modulus E^*.

The effective stiffness differs for each theory, and the differences are significant in terms of the leading order dependence on the width. Thus, the signs for the correction in (66) are such that in Kirchhoff theory the beam is stiffened, it softens for the Mindlin theory, and in the Mindlin-shear theory the leading order correction is identically zero. In addition to this fundamental deviation between the conflicting theories, we note the distinct frequency dependence of the correction terms: linear in ω for the Kirchhoff correction, and quadratic for the Mindlin plate theory. It is interesting to note that the latter does not depend on the shear correction factor α. Yet, when we consider the Mindlin theory without the rotational inertia, that is the pure shear theory, the correction vanishes. These asymptotic corrections have been verified by numerical examples, see Figs. 2 and 3.

It is perhaps useful to compare the corrections in (66) with the well-known corrections to the various beam theories as a function of frequency. In this case the variation depends on the beam semi-thickness h, which enters into the beam theories as follows:

$$k^2h^2=\sqrt{3}k_{P0}h+\begin{cases}0, & \text{Kirchhoff},\\ \frac{1}{2}k_{P0}^2h^2+\mathrm{O}(k_{P0}^3h^3), & \text{Kirchhoff–Rayleigh},\\ \frac{1}{2}k_S^2h^2+\mathrm{O}(k_S^3h^3), & \text{Mindlin–shear only},\\ \frac{1}{2}(k_S^2+k_{P0}^2)h^2+\mathrm{O}(k_S^3h^3), & \text{Mindlin}.\end{cases} \tag{67}$$

Each of the refinements to the classical Kirchhoff or Euler–Bernoulli beam theory predicts an increase in the wave number, with the increase dependent on the model. Furthermore, the leading order correction in each case has the same frequency and thickness dependence, that is, each correction in (67) is quadratic in frequency and in the beam thickness, and may be characterized by another effective Young's modulus, E^{**}, where

$$\frac{E^{**}}{E}-1=-\sqrt{\tfrac{2}{3}}k_{P0}h\times\begin{cases}0, & \text{Kirchhoff},\\ 1+\mathrm{O}(k_{P0}^2h^2), & \text{Kirchhoff–Rayleigh},\\ 2(1+\nu)/\alpha+\mathrm{O}(k_{P0}^2h^2), & \text{Mindlin–shear only},\\ 1+2(1+\nu)/\alpha+\mathrm{O}(k_{P0}^2h^2), & \text{Mindlin}.\end{cases} \tag{68}$$

It is interesting to now compare Eqs. (66) and (68), which summarize the leading order corrections for plate width and beam thickness, respectively. Beam thickness has the consistent effect of reducing the effective Young's modulus for each of the refinements to the classical Kirchhoff beam theory. However, the finite width of the plate affects each model quite differently, as it leads to an initial increase in E^* for the Kirchhoff plate theory, and a decrease for the Mindlin theory. The distinction between the beam and plate models can be explained as a Poisson effect, which disappears when $\nu=0$. Thus, for very wide plates, both models reduce to the plane stress limit, for which $E^*\to E/(1-\nu^2)\geqslant E$, with equality only if $\nu=0$. Note that Eq. (66) retains this feature, as all the corrections to E^* are $\mathrm{O}(\nu^2)$, with frequency-dependent factors. The surprising feature of Eq. (66) is that Mindlin theory initially predicts a decrease in the stiffness, although it eventually does increase to the plane stress value as kb increases. In fact, numerical experiments indicate that the prediction of (66) is only valid for extremely small values of $k_{P0}b$ (for which the correction is itself even smaller).

B. Asymmetric or torsional mode

The results of Sec. III are summarized by the following equation for the phase speeds $v=\omega/k$ in the zero frequency limit, from Eqs. (54), (58), (63), and (65),

$$v_0=c_T\times\begin{cases}2\dfrac{h}{b}, & \text{Kirchhoff},\\ 2\left(1+\dfrac{b^2}{h^2}\right)^{-1/2}, & \text{Kirchhoff–Rayleigh},\\ 2\alpha, & \text{Mindlin–shear only},\\ 2\alpha\left(1+\dfrac{h^2}{b^2}\right)^{-1/2}, & \text{Mindlin}.\end{cases} \tag{69}$$

Note that these are all nondispersive, yet it is remarkable how they provide quite different results.

Each of these limiting values can be understood as an approximation to the torsional mode for a plate. A proper analysis for the torsional wave in the zero frequency or quasistatic limit requires an estimate of the torsional rigidity C, from which the wave speed is calculated as $v=\sqrt{C/\rho J}$, where J is the centroidal moment of inertia.[4] The rectangular cross-section of the plate implies $J=(b^2+h^2)A/3$, where $A=4bh$. The torsional stiffness of a rectangular rod is not available in closed form, although it does satisfy the inequal-

ity $C<\mu J$, implying that $v<c_T$. However, we may approximate C for rectangular cross sections that are far from square,[11] thus

$$C=\frac{\mu}{3}A^2\times\begin{cases}\dfrac{h}{b} & \text{for } b\gg h,\\ \dfrac{b}{h} & \text{for } b\ll h.\end{cases} \tag{70}$$

Hence, in the two extreme but interesting cases of very wide and extremely narrow plates, the torsional wave speed is

$$v=c_T\times\begin{cases}2\left(1+\dfrac{b^2}{h^2}\right)^{-1/2} & \text{for } b\gg h,\\ 2\left(1+\dfrac{h^2}{b^2}\right)^{-1/2} & \text{for } b\ll h.\end{cases} \tag{71}$$

Referring to Eq. (69) we see that the Kirchhoff and Kirchhoff–Rayleigh plate theories each predict the correct behavior for wide plates, $b\gg h$, in the quasistatic limit. However, neither is correct in the limit of interest here, when the plate is narrow, $b\ll h$. In that case the Kirchhoff theory predicts an unphysically large speed, and the Kirchhoff–Rayleigh theory gives a finite limit, $v_0\to 2c_T$, which is also incorrect (and unphysically large). Only the Mindlin theory predicts the correct behavior for $b\ll h$, if α is taken to be unity, which is not unreasonable. The shear-only model predicts a finite limiting speed, which is incorrect. Thus we are led to conclude that of the four theories only Mindlin's gives a proper limit for very narrow plates.

This result is perhaps surprising. A very narrow plate with $b\ll h$ undergoing asymmetric ''flexural'' motion is more aptly described as a plate oriented at 90° with the motion similarly rotated. Despite this extreme test of the model, Mindlin's plate theory is capable of predicting the correct limiting wave speed—the speed of a torsional wave. Finally, it should be noted that the Mindlin expansion of (61) is not sufficient to give the wide plate torsional wave limit. The reason for this is as follows. Let $\lambda=b/h\gg 1$, and $\epsilon=k_Tb\ll 1$, such that $\epsilon\lambda=o(1)$. Then, multiplying the expression (61) by b^2 to make it nondimenional, we find that it is $O(\epsilon^2\lambda^4)$ and this arises from the single term $-4b^4k^2k_F^4/(3k_S^2)$. In order to cancel this leading order term we need to expand (59) to at least the next order, but leave that as a separate exercise for the interested reader.

VI. CONCLUSION

We have examined the transition between the plate and beam regimes and how both the symmetric (flexural) and asymmetric (torsional) modes depend upon the width of the plate in the lateral direction. Analytical asymptotic predictions for narrow plates have been illustrated by numerical results, and suggest the use of a frequency-dependent Young's modulus for describing the flexural wave on beams or strips of finite width, although the form of the correction to the modulus is not unique and depends on the theory used. The sign of the correction for the Kirchhoff theory is opposite to that for the Mindlin theory. Analysis of the asymmetric or torsional mode also displays quite distinct behavior for the four classical engineering theories applied to narrow plates. It is argued that only the Mindlin theory provides a realistic result in this case, and by extension, the Mindlin theory is recommended for considering the symmetric (flexural) waves in beams of rectangular cross-section and finite width.

As part of the analysis we have also derived the dispersion equations for edge-guided waves in each of the four classical plate theories. This is given by Eq. (19) for orthotropic plates in the Kirchhoff theory, with explicit solution (20). This is the only case of the four for which the edge wave is nondispersive and for which the edge wave speed has an explicit expression, as in Eq. (20). Equation (19) also defines the edge wave for the Kirchhoff–Rayleigh theory, where γ_1 and γ_2 are now defined by Eq. (30). The edge wave in the Mindlin theory with and without rotational inertia is defined by Eq. (39). The wave numbers k_1, k_2, and k_3 are defined by Eq. (A9) for the Mindlin theory, and by Eq. (46) for the Mindlin–shear theory. This is the first time that the edge wave equations have been derived or discussed for the Kirchhoff–Rayleigh and the Mindlin–shear theories.

APPENDIX A: MINDLIN PLATE THEORY

Mindlin's theory for an isotropic plate is Eq. (1), with two additional variables corresponding to angles of rotation, $\psi_x(x,y,t)$ and $\psi_y(x,y,t)$,[4] with

$$\frac{\partial M_x}{\partial x}+\frac{\partial M_{xy}}{\partial y}-Q_x=\rho I\frac{\partial^2\psi_x}{\partial t^2}, \tag{A1}$$

$$\frac{\partial M_{xy}}{\partial x}+\frac{\partial M_y}{\partial y}-Q_y=\rho I\frac{\partial^2\psi_y}{\partial t^2}, \tag{A2}$$

$$M_x=E_pI\left(\frac{\partial\psi_x}{\partial x}+\nu\frac{\partial\psi_y}{\partial y}\right),\quad M_y=E_pI\left(\frac{\partial\psi_y}{\partial y}+\nu\frac{\partial\psi_x}{\partial x}\right),$$

$$M_{xy}=\mu I\left(\frac{\partial\psi_x}{\partial y}+\frac{\partial\psi_y}{\partial x}\right), \tag{A3}$$

$$Q_x=\alpha^2 2h\mu\left(\frac{\partial w}{\partial x}+\psi_x\right),\quad Q_y=\alpha^2 2h\mu\left(\frac{\partial w}{\partial y}+\psi_y\right).$$

Note that the thickness-integrated shear modulus appearing in the shear forces Q_x and Q_y is modified by the factor α^2 in order to better approximate shear forces in the plate, and α may be chosen according to different criteria, but normally $\alpha^2\leqslant 1$.[4] We consider solutions of the form

$$\{w(x,y,t),\psi_x(x,y,t),\psi_y(x,y,t)\}=\mathrm{Re}\{W(y),\Psi_x(y),\Psi_y(y)\}e^{i(kx-\omega t)}, \tag{A4}$$

where[10]

$$W(y)=A_1\cosh\gamma_1y+A_2\cosh\gamma_2y, \tag{A5}$$

$$\Psi_x(y)=ik\beta_1A_1\cosh\gamma_1y+ik\beta_2A_2\cosh\gamma_2y+\gamma_3A_3\cosh\gamma_3y, \tag{A6}$$

$$\Psi_y(y)=\gamma_1\beta_1A_1\sinh\gamma_1y+\gamma_2\beta_2A_2\sinh\gamma_2y-ikA_3\sinh\gamma_3y, \tag{A7}$$

and

$$\gamma_j=\sqrt{k^2-k_j^2},\quad j=1,2,3,\quad \beta_j=-1+k_S^2/k_j^2,\quad j=1,2, \tag{A8}$$

$$k_j^2=\tfrac{1}{2}(k_S^2+k_P^2)-(-1)^j\sqrt{\tfrac{1}{4}(k_S^2-k_P^2)^2+k_F^4},\quad j=1,2, \tag{A9a}$$

$$k_3^2=\frac{2k_1^2k_2^2}{(1-\nu)k_S^2}. \tag{A9b}$$

The wave numbers k_P, k_F, and k_S are defined in Eq. (37). The wave number k_1 describes a straight crested flexural wave in a plate according to Mindlin's theory. The corresponding wave numbers for a Timoshenko beam are defined by Eq. (36), and are given by k_1, k_2 of Eq. (A9) with the replacements k_P, $k_F\to k_{P0}$, k_{F0}, that is, the stiffness for uniaxial extension is substituted for the plate stiffness.

The boundary conditions on $y=\pm b$ require the simultaneous vanishing of Q_y, M_y and M_{xy}, implying the dispersion relation

$$\begin{vmatrix} (1+\beta_1)\gamma_1\sinh\gamma_1 b & (1+\beta_2)\gamma_2\sinh\gamma_2 b & -ik\sinh\gamma_3 b \\ \beta_1(\gamma_1^2-\nu k^2)\cosh\gamma_1 b & \beta_2(\gamma_2^2-\nu k^2)\cosh\gamma_2 b & (1-\nu)k^2\gamma_3\cosh\gamma_3 b \\ 2ik\gamma_1\beta_1\sinh\gamma_1 b & 2ik\gamma_2\beta_2\sinh\gamma_2 b & (k^2+\gamma_3^2)\sinh\gamma_3 b \end{vmatrix}=0. \tag{A10}$$

Using row and column manipulation, this can be rearranged as

$$\begin{vmatrix} k_1^2 & k_2^2 & k_3^2 \\ k_S^2 & k_S^2 & 2k^2 \\ \left(k^2-\dfrac{k_1^2}{1-\nu}\right)(k_S^2-k_1^2)\dfrac{\coth\gamma_1 b}{\gamma_1} & \left(k^2-\dfrac{k_2^2}{1-\nu}\right)(k_S^2-k_2^2)\dfrac{\coth\gamma_2 b}{\gamma_2} & 2k^2\gamma_3\coth\gamma_3 b \end{vmatrix}=0. \tag{A11}$$

This can be further reduced to Eq. (38) by using (A9b).

APPENDIX B: A REDUCED PLATE THEORY FOR NARROW PLATES

An alternative procedure for examining the dependence of the flexural wave speed on the width of a narrow plate is to derive a theory appropriate to this limit. In this Appendix we demonstrate that the first corrections to the beam theory prediction, Eqs. (22) and (23), are obtained for the Kirchhoff theory using this approach.

Starting with the Kirchhoff kinematic ansatz, $u(x,y,z,t)=-zW_x(x,y,t)$, $v(x,y,z,t)=-zW_y(x,y,t)$, $w(x,y,z,t)=W(x,y,t)$, along with the assumption of plane stress, implies the Lagrangian density per unit area

$$\mathcal{L}(W(x,y,t))=\frac{1}{2}mW_t^2-\frac{EI}{2(1-\nu^2)}[W_{xx}^2+W_{yy}^2+2\nu W_{xx}W_{yy}+2(1-\nu)W_{xy}^2]. \tag{B1}$$

For the narrow plate, we make the further assumption

$$W(x,y,t)=w(x,t)+yp(x,t)+\frac{y^2}{2}q(x,t). \tag{B2}$$

Substituting into (B1) and integrating over the plate width $-b<y<b$ yields a Lagrangian density per unit length

$$\mathrm{L}(w,p,q)=\mathrm{L}_0(w,q)+\mathrm{L}_1(p), \tag{B3}$$

with decoupled terms

$$\mathrm{L}_0(w,q)=\frac{m}{2}(w_t^2+Kq_t^2+Jw_tq_t)-\frac{EI}{2(1-\nu^2)}[w_{xx}^2+q^2+Kq_{xx}^2+Jw_{xx}q_{xx}+2\nu qw_{xx}+\nu Jqq_{xx}+2(1-\nu)Jq_x^2], \tag{B4}$$

$$\mathrm{L}_1(p)=\frac{m}{2}Jp_t^2-\frac{EIJ}{2(1-\nu^2)}p_{xx}^2-\frac{EI}{1+\nu}p_x^2, \tag{B5}$$

where $J=b^2/3$, $K=b^4/20$. These in turn imply the Euler–Lagrange equations

$$\frac{EI}{1-\nu^2}\left(w_{xxxx}+\frac{J}{2}q_{xxxx}+\nu q_{xx}\right)+mw_{tt}+\frac{J}{2}q_{tt}=0, \tag{B6}$$

$$\frac{EI}{1-\nu^2}\left[q+Kq_{xxxx}+\frac{J}{2}w_{xxxx}+\nu w_{xx}-(2-3\nu)Jq_{xx}\right]+mKq_{tt}+\frac{J}{2}mw_{tt}=0, \tag{B7}$$

$$\frac{EI}{1-\nu^2}p_{xxxx}-\frac{2EI}{(1-\nu^2)J}p_{xx}+mp_{tt}=0. \tag{B8}$$

Note that the torsional (asymmetric) mode, p, decouples from the symmetric mode, (w,q). Dispersions relations can be easily determined for each mode from Eqs. (B6)–(B8),

$$(k^4-k_\infty^4)[1-\tfrac{2}{3}(1-\nu)k^2b^2+\tfrac{1}{45}(k^4-k_\infty^4)b^4]-\nu k^4=0, \tag{B9}$$

$$\frac{k^4}{k_\infty^4}+4c_T^2\frac{h^2k^2}{b^2\omega^2}=1, \tag{B10}$$

where $k_\infty=(m\omega^2(1-\nu^2)/EI)^{1/4}$ is the wide plate flexural wave number and $c_T=\sqrt{\mu/\rho}$. Both dispersion relations yield $k\to k_\infty$ as $b\to\infty$. A straightforward expansion of the dispersion relations in the narrow plate limit $kb\ll 1$ shows that Eq. (B9) reproduces the leading order correction of Eq. (25), while Eq. (B10) gives the constant wave speed for the Kirchhoff theory in Eq. (69). Thus, this particular reduced order plate theory for the narrow plate is entirely consistent with the Kirchoff plate theory, which is not surprising since the ansatz (B2) is a special case of the general displacement included in the Kirchhoff theory.

A similar but necessarily more complicated reduced plate theory for narrow plates is discussed by Russell and White[2] within the context of a Timoshenko-type beam model.

[1] S. M. Han, H. Benaroya, and T. Wei, "Dynamics of flexurally vibrating beams using four engineering theories," J. Sound Vib. **225**(5), 935–988 (1999).

[2] D. L. Russell and L. W. White, "The bowed narrow plate model," Elec. J. Diff. Eqs. **2000(27)**, 1–19 (2000).

[3] Y. K. Konenkov, "A Rayleigh-type flexural wave," Sov. Phys. Acoust. **6**, 122–123 (1960).

[4] K. F. Graff, *Wave Motion in Elastic Solids* (Dover, New York, 1991).

[5] A. N. Norris, "Flexural edge waves," J. Sound Vib. **171**, 571–573 (1994).

[6] B. K. Sinha, "Some remarks on propagation characteristics of ridge guides for acoustic waves at low frequencies," J. Acoust. Soc. Am. **56**, 16–18 (1974).

[7] R. N. Thurston and J. McKenna, "Flexural acoustic waves along the edge of a plate," IEEE Trans. Sonics Ultrason. **21**, 296–297 (1974).

[8] V. A. Veshev, I. I. Klyukin, D. P. Kouzov, and V. D. Lukyanov, "On oscillating energy propagation in a thin elastic plate of a finite width," Sov. Phys. Acoust. **23**, 129–131 (1977).

[9] I. D. Abrahams and A. N. Norris, "On the existence of flexural edgewaves on submerged elastic plates," Proc. R. Soc. London, Ser. A **456**, 1559–1582 (2000).

[10] A. N. Norris, V. V. Krylov, and I. D. Abrahams, "Flexural edge waves and Comments on 'A new bending wave solution for the classical plate equation'," J. Acoust. Soc. Am. **107**, 1781–1784 (2000).

[11] S. Timoshenko, *Theory of Elasticity*, 3rd ed. (McGraw-Hill, New York, 1970).

Negative group velocity Lamb waves on plates and applications to the scattering of sound by shells

Philip L. Marston[a)]
Department of Physics, Washington State University, Pullman, Washington 99164-2814

(Received 19 July 2002; revised 10 January 2003; accepted 10 February 2003)

Symmetric Lamb waves on plates exhibit anomalies for certain regions of frequency. The phase velocity appears to be double-valued [M. F. Werby and H. Überall, J. Acoust. Soc. Am. **111**, 2686–2691 (2002)] with one of the branches having a negative group velocity relative to the corresponding phase velocity. The classification of the symmetric plate modes for frequencies appearing to have a double-valued phase velocity is reviewed here. The complication of a double-valued velocity is avoided by examining mode orthogonality and the complex wave-number spectra. Various authors have noted an enhancement in the backscattering of sound by elastic shells in water that occurs for frequencies where symmetric leaky Lamb waves (generalized to case of a shell) have contra-directed group and phase velocities. The ray diagram for negative group velocity contributions to the scattering by shells [G. Kaduchak, D. H. Hughes, and P. L. Marston, J. Acoust. Soc. Am. **96**, 3704–3714 (1994)] is unusual since for this type of mode the energy on the shell flows in the opposite direction of the wave vector. Circumnavigation of the shell is not required for the leaky ray to be backward directed.
[DOI: 10.1121/1.1564021]

PACS numbers: 43.40.Dx, 43.35.Cg, 43.20.Bi [ADP]

I. INTRODUCTION

Symmetric Lamb waves on plates can have special properties recently investigated by Werby and Überall.[1] The purpose of this letter is to reexamine some of the issues raised in Ref. 1 and to consider some closely related applications to the scattering of sound by elastic shells in water. The issues considered here include: (i) the classification of the symmetric plate modes resulting in a double-valued phase velocity; (ii) the significance of the group velocity when the derivative with respect to wavenumber vanishes; and (iii) literature and results concerning plate or shell modes having group and phase velocities in opposite directions and the relevance of such modes to the scattering of sound by elastic shells in water. Some relevant recent examples pertaining to *electromagnetic waves* having a negative group velocity are noted in Sec. V in addition to the discussion of applications to shells. It is the intent of the present author that readers interested in guided waves having contra-directed group and phase velocities may find these comments helpful in reconciling several publications concerned with Lamb waves on plates and the high frequency scattering of sound by shells.

II. CLASSIFICATION OF ANOMALOUS SYMMETRIC MODES

Consider first the situation of an isotropic elastic plate in a vacuum. Werby and Überall and various other authors (e.g., Viktorov[2]) classify the symmetric modes in such a way that mode S_1 has a double-valued phase velocity V_x over a range of the frequency f. In some publications noted in Ref. 1 (see, e.g., Kaduchak *et al.*[3]) the double-valued phase velocity is avoided since the region corresponding to group and phase velocities having opposite signs (as discussed below) is classified as a ''backwards wave'' branch of the S_2 mode. (See also Ref. 4 where this branch is designated as S_2^b.) A simple justification for that choice of mode classification is given by Auld.[5] See Eqs. (10-120)–(10-122) of Ref. 5 showing that modes at the same f having differing phase velocities obey an orthogonality relationship. Auld's conclusion that the lowest frequency ''backward-wave'' symmetric branch is classified with the upper mode (the S_2 mode in the current notation) is also supported by three-dimensional plots of the complex wave number as a function of frequency (Fig. 10.14 of Ref. 5, where the modes labeled here as S_j are denoted by L_l with $l=j+1$). The analogous designation of the backwards-wave portion in plots of the complex wave number dates from the early work of Mindlin[6] and these plots are used in numerous investigations.[3–14]

Mindlin and Medick[7] plot the complex wave-number spectra for plates having Poisson's ratio σ less than, equal to, and greater than the special case of $\sigma=1/3$ noted in Ref. 1. They assign modes analogous to the choice of S_2 for the backwards-wave portion in each case. The special case of $\sigma=1/3$ is the situation where the lowest thickness–stretch and lowest symmetric thickness–shear mode frequencies are degenerate. (This σ corresponds to the case in Ref. 1 of the longitudinal speed $V_L=2V_T$ where V_T is the shear wave speed.) Achenbach (p. 235 of Ref. 13) emphasizes that a locus of solutions for real f and wave number k_x (in the notation of Ref. 1) ''are not a necessary part of a single branch.'' When modes are assigned using the orthogonality criteria of Auld[5] or the branch designations as in Achenbach,[13] the wave numbers (and phase velocities) *are single valued*. Inspection of the complex wave-number spectra shows that for real-valued wave numbers, the branch designated here as S_2^b has an upper and a lower cutoff frequency.

a)Electronic mail: marston@wsu.edu

The *lower* cutoff frequency also corresponds to the cutoff (for real wave numbers) of the properly designated S_1 mode. The *upper* cutoff frequency of the S_2^b branch is the lower of the two frequencies f_{T-ST} and f_{T-SH} for the first thickness–stretch and symmetric-thickness–shear modes of the elastic plate of thickness h. These are given from Eqs. (7a) and (7b) of Ref. 1, respectively, as $f_{T-ST}=V_L/2h$ and $f_{T-SH}=V_T/h$. The cutoff frequency for real-valued wave numbers in the ordinary branch of the S_2 mode (the upper branch) is the greater of f_{T-ST} and f_{T-SH}. Materials having $\sigma<1/3$ (such as steel) give $f_{T-SH}>f_{T-ST}$ while materials having $\sigma>1/3$ (such as aluminum) give $f_{T-SH}<f_{T-ST}$.

Inspection of the complex wave-number spectra for plates in a vacuum[4–13] reveals that except for the special case of $\sigma=1/3$, the upper threshold of the S_2^b branch and the lower threshold of the ordinary S_2 branch are connected by a loop for which the wave number k_x is purely imaginary. Numerical calculations for thin and moderately thin spherical shells in a vacuum have confirmed that the shape of the complex spectra are similar to the case of plates.[3,14] It is not always practical to trace the entire connection of the upper and lower parts of the loop as a consequence of numerical difficulties in the evaluation of the Hankel functions of complex order in the dispersion relation for shells derived using Watson-transform methodology. Figure A1 of Ref. 3 shows an example for a stainless-steel shell having a thickness-to-radius ratio $h/a=0.019\,18$ where a portion of the loop with an imaginary wave number is missing. The vertical axis is proportional to f and is expressed in terms of ka where k is the wave number in water at frequency f. Point B at the base of the loop is $ka=628$ and corresponds to f_{T-ST}. The cut-off for the ordinary S_2 mode at the upper end of the loop is at $ka=695$ and corresponds to f_{T-SH}. References 3 and 14 also examine the consequence of *fluid loading*. The changes in the complex wave-number spectra resulting from placing an aluminum shell in water are more significant than for a steel shell of the same thickness.[14] This is consistent with the analysis in Ref. 4 of the effect of varying the density of the fluid loading on a plate.

III. MODES HAVING AN EXTREMUM IN THE GROUP VELOCITY $V_{gx}=d\omega/dk_x$

In Sec. V of Ref. 1, it is emphasized that an elementary approximation for the transient response of a dispersive waveguide breaks down when dV_{gx}/dk_x vanishes but the concern is left unresolved. [See the discussion of Eq. (11) in Ref. 1.] The relevance to anomalous Lamb modes is that dV_{gx}/dk_x vanishes within the region where $d\omega/dk_x$ appears to be negative. (The notation $\omega=2\pi f$ is used.) While it is correct that the simple approximation in Eq. (11) fails, group velocity remains a useful quantity as demonstrated by Tolstoy and Clay[15] (and various other authors[16]) by expanding the phase through terms of order d^2V_{gx}/dk_x^2 (in the notation of Ref. 1) evaluated at the extremum where $dV_{gx}/dk_x=0$. The resulting approximation for the transient response has an Airy function envelope factor. The Airy function has a vanishing argument when the propagation distance is given by $V_{gx}t$ where t is the elapsed time and V_{gx} is evaluated at the stationary condition $dV_{gx}/dk_x=0$. Some readers may find it helpful to note that Wait[17] gives an analogous expansion evaluated at the extreme $dV_{gx}/d\omega=0$ and obtains an analogous approximation for the transient response. Except for the special case of vanishing or diverging V_{gx}, the approximations are expected to be similar since $dV_{gx}/d\omega=(dV_{gx}/dk_x)(dk_x/d\omega)=(dV_{gx}/dk_x)/V_{gx}$. The wave packet resulting from transient excitation has a spectral peak at or near the frequency where $dV_{gx}/dk_x=0$. Levine[16] and Lighthill[18] discuss wave-packet propagation with extremum in the group velocity in terms of a space–time caustic and the kinematics of wave crests. Various authors have calculated or demonstrated the propagation of ordinary shell modes in regions where the derivatives vanish analogous to dV_{gx}/dk_x and $dV_{gx}/d\omega$.

IV. SIGNIFICANCE OF PLATE OR SHELL MODES HAVING OPPOSITELY DIRECTED PHASE AND GROUP VELOCITIES

As noted in Sec. V of Ref. 1, $d\omega/dk_x$ can be negative giving an apparently negative value for V_{gx}. This occurs for one root in the ''double-valued'' region discussed in Ref. 1 (the S_2^b branch in the terminology discussed here in Sec. II). Some readers of Ref. 1 may find it helpful to examine the discussions in Refs. 3, 10, and 13 concerning the interpretation of those regions. Specifically in Ref. 10, the average energy flux density is evaluated for two modes having the same frequency but oppositely directed group velocities (one of which is the S_2^b branch). For the mode having $V_{gx}<0$, the total energy flux is *opposite* the direction of the phase velocity ($V_x>0$ in the notation of Ref. 1). A similar plot is given in Fig. 4 of Ref. 19 where in the present terminology the mode should be classified as S_2^b. (The direction of the energy flux is consistent with Biot's discussion of the energy transport by waves.[20]) Achenbach[13] notes that when k_x and V_{gx} have opposite signs, he prefers to take k_x (and V_x) as negative. To analyze the scattering by shells in Refs. 3, 14, and 21, it was convenient to consider quantities analogous to k_x and V_x as *positive*. This selection facilitated the specification of the wave-vector-matching condition between the incident acoustic wave in the surrounding fluid and the (fluid-loaded) S_2^b leaky Lamb wave excited on the shell in a way that was consistent with the convention used for ordinary Lamb waves. As a consequence of the negative group velocity assigned to the S_2^b branch, the direction of the leaky ray *on the shell*, Fig. 1 (taken from Fig. 3 of Ref. 3), is reversed from the normal convention. The ray theory, based on this modified ray diagram and on fluid-loaded S_2^b parameters, is supported by experimental *measurements* of backscattering by a thin steel shell in water as well as by (background-subtracted) partial-wave series calculations.[3] (The relevant ray diagram is supported by an additional experimental test shown in Fig. 7 of Ref. 3.) The deficiencies of the ray theory are the most significant (for reasons discussed in Ref. 3) near the upper cutoff of the S_2^b mode (at f_{T-ST}) where the damping is large. Ray theory comparisons[14] with partial-wave-series calculations for steel shells having $h/a=0.05$ and 0.075 and an aluminum shell having $h/a=0.075$ also support the ray diagram in Fig. 1. The ray-theoretic interpretation of the computational and experimental data is supportive of

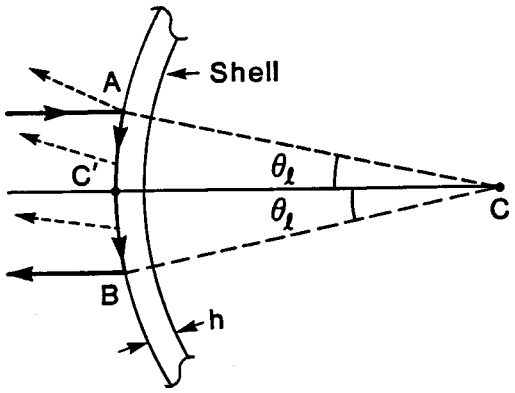

FIG. 1. Ray diagram of a leaky wave contribution to the backscattering by a fluid-loaded circular shell when the shell mode has contra-directed group and phase velocities. The acoustic wave in water couples onto the shell at *A* where the angle θ_l is determined by matching the projection (onto the shell) of the local acoustic wave vector with the wave number of the Lamb mode. The group velocity is in the counterclockwise direction and energy is transported past the specular point C'. Radiation is launched in the backscattering direction at *B* so that circumnavigation of the shell is not required for a leaky wave contribution to the backscattering. The backscattering amplitude calculated from ray theory for a spherical shell was shown by Kaduchak, Hughes, and Marston (Ref. 3) to agree with measurements. The damping of this type of guided wave is calculated to be sufficiently large that contributions from rays that circumnavigate of the shell may be neglected.

Meitzler's analysis that the energy flux is *directed opposite* to k_x when $d\omega/dk_x<0$. The time evolution of wave-packet surface displacements on a cylindrical shell also supports this interpretation.[21] The evolution of the ray diagram when a fluid-loaded plate is bent into a shell is shown in Fig. 2, which is taken from Fig. 8 of Ref. 3. The diagram in the flat-plate limit, Fig. 2(a), appears to be consistent with the observed properties of Lamb waves having contra-directed group and phase velocities. See, e.g., the plate experiments in Refs. 22–24 where the wave is classified as a branch of the S_1 mode.

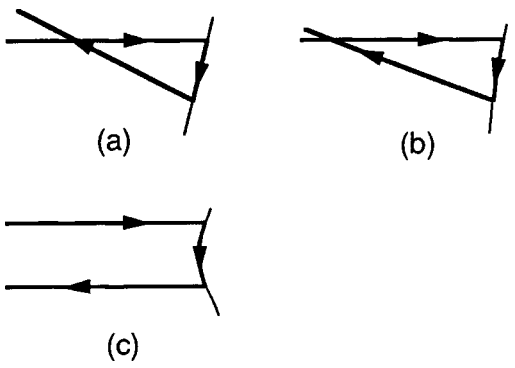

FIG. 2. The evolution of the ray diagram when a fluid-loaded plate is bent into a curved shell and the plate or shell mode has contra-directed group and phase velocities. The curvature of the elastic shell increases from (a) to (c) with (a) being the case of a plate and (c) being the circular shell shown in Fig. 1. The direction of the arrow on the plate or shell is in the direction of the energy flow (which is opposite the direction of phase progression of the leaky wave). The arrows on the left of the structure correspond to propagation of ordinary acoustic waves in water. The launching and radiation locations are determined by matching the projections (onto the shell) of the local acoustic wave vectors with the wave number of the Lamb mode.

V. DISCUSSION AND RELEVANCE TO ENERGY FLUX AND TO THE SCATTERING BY SHELLS

The difficulties of having a mode for which there are two values of the phase velocity at a given frequency are avoided by examining the evolution with frequency of the complex wave number as reviewed here in Sec. II. The resulting mode classifications satisfy the Auld's orthogonality condition.[5] A convenient notation[3,4,14,21,25,26] for lowest-frequency anomalous symmetric branch is S_2^b where *b* indicates a backwards wave having properties reviewed here in Sec. VI. (The present author originally classified the backwards wave scattering contribution of shells as associated with the S_1 mode[27] but revised the classification as noted in Appendix C of Ref. 3.) Since the energy flux is in the opposite direction of the local wave vector, the ray diagram for the S_2^b contribution to the backscattering takes the unusual form shown in Fig. 1. (This is in contrast to an *ordinary* ray diagram[27] where the energy flow on the shell from point *A* is counterclockwise). For thin spherical shells, the energy flux along a backwards ray gives a large backscattering enhancement described by ray theory.[3,14] Other authors (e.g., Refs. 28 and 29) have associated that enhancement with the S_1 leaky Lamb wave. The frequency of the enhancement lies *below* the thickness–stretch mode frequency $f_{T-ST}=V_L/2h$ for a plate of thickness *h*. When plane waves are reflected from an empty shell, the interference of the reverberating elastic longitudinal waves causes a *reduction* in the total backscattering when $f\approx f_{T-ST}$ that was analyzed using ray theory for spheres[27,30,31] and cylinders.[31] See, e.g., Fig. 8 of Ref. 27 for the case of a spherical aluminum shell. The reduction is more isolated from other scattering contributions when σ exceeds 1/3 and becomes most prominent in the limit of an empty *fluid shell* having $\sigma=1/2$. The reduction is more prominent for cylinders (Fig. 4 of Ref. 21 and Fig. 82 of Ref. 31) than for spheres and is easily seen in a measured "backscattering spectrum" for an elastic cylinder in water recently published by Ezzaidi *et al.*[32] (near the left-hand side of their Fig. 5). Ray theory can be used to separate the evaluation of the S_2^b backscattering *enhancement*[3] (with the ray diagram given here in Fig. 1) from the *reduction* in the scattering associated with the reverberating longitudinal waves.[27,30,31]

In addition to Lamb waves (and related shell modes) there are other examples where the average energy flux is directed opposite to the wavevector. This occurs for electromagnetic waves in a medium having negative permittivity and negative permeability.[33–35] The average Poynting energy flux for a tilted beam incident on a slab of such a material has been calculated[36] to have a backwards beam displacement analogous to the ray diagram for the leaky S_2^b Lamb waves on plates [Fig. 2(a)]. Another example of an elastic wave having contra-directed group and phase velocities is an out-of-plane mode of a plate with a zero-displacement boundary condition applied to one of the surfaces.[37]

[1] M. F. Werby and H. Überall, "The analysis and interpretation of some special properties of higher order symmetric Lamb waves: The case for plates," J. Acoust. Soc. Am. **111**, 2686–2691 (2002).
[2] I. A. Viktorov, *Rayleigh and Lamb Waves* (Plenum, New York, 1967).

[3] G. Kaduchak, D. H. Hughes, and P. L. Marston, ''Enhancement of the backscattering of high-frequency tone bursts by thin spherical shells associated with backward wave: Observation and ray approximation,'' J. Acoust. Soc. Am. **96**, 3704–3714 (1994). [In the secondary test of the ray theory in Fig. 7, a gain enhancement of 1000 (relative to Fig. 5) was not explicitly mentioned. For plots of the unblocked signal on the same scale as Fig. 7, see Appendix 5.D of G. Kaduchak, ''Mode threshold and transient scattering processes for high-frequency scattering of sound by elastic shells in water,'' Ph.D. thesis, Washington State University, Pullman, WA, 1994. For thesis abstract see G. Kaduchak, J. Acoust. Soc. Am. **97**, 1345 (1995).]
[4] S. I. Rokhlin, D. E. Chimenti, and A. H. Nayfeh, ''On the topology of the complex wave spectrum in a fluid-coupled elastic layer,'' J. Acoust. Soc. Am. **85**, 1074–1080 (1989).
[5] B. A. Auld, *Acoustic Fields and Waves in Solids* (Wiley, New York, 1973), Vol. 2; for other discussions of orthogonality relations see J. E. Murphy, G. Li, and S. A. Chin-Bing, ''Orthogonality relation for Rayleigh–Lamb modes of vibration of an arbitrarily layered elastic plate with and without fluid loading,'' J. Acoust. Soc. Am. **96**, 2313–2317 (1994); and W. B. Fraser, ''Orthogonality relation for the Rayleigh–Lamb modes of vibration of a plate,'' *ibid.* **59**, 215–216 (1976).
[6] R. D. Mindlin, ''Waves and vibrations in isotropic elastic plates,'' in *First Symposium on Structural Mechanics*, 1958, edited by J. N. Goodier and N. J. Hoff (Pergamon, Oxford, 1960), pp. 199–232.
[7] R. D. Mindlin and M. A. Medick, ''Extensional vibrations of elastic plates,'' J. Appl. Mech. **26**, 561–569 (1959).
[8] J. J. McCoy and R. D. Mindlin, ''Extensional waves along the edge of an elastic plate,'' J. Appl. Mech. **30**, 75–78 (1963).
[9] T. R. Meeker and A. H. Meitzler, ''Guided wave propagation in elongated cylinders and plates,'' in *Physical Acoustics*, edited by W. P. Mason (Academic, New York, 1964), Vol. 1A, pp. 111–167.
[10] A. H. Meitzler, ''Backward-wave transmission of stress pulses in elastic cylinders and plates,'' J. Acoust. Soc. Am. **38**, 835–842 (1965).
[11] P. J. Torvik, ''Reflection of wave trains in semi-infinite plates,'' J. Acoust. Soc. Am. **41**, 346–353 (1967).
[12] J. Miklowitz, *The Theory of Elastic Wave and Waveguides* (North-Holland, Amsterdam, 1978), pp. 197–209.
[13] J. D. Achenbach, *Wave Propagation in Elastic Solids* (North-Holland, Amsterdam, 1973).
[14] D. H. Hughes, ''Backscattering of sound by spherical shells in water,'' Ph.D. thesis, Washington State University, Pullman, WA, 1992; for thesis abstract see D. H. Hughes, J. Acoust. Soc. Am. **94**, 1168 (1993).
[15] I. Tolstoy and C. S. Clay, *Ocean Acoustics* (McGraw-Hill, New York, 1966), pp. 40–48.
[16] H. Levine, *Unidirectional Wave Motion* (North-Holland, Amsterdam, 1978).
[17] J. R. Wait, ''Propagation of pulses in dispersive media,'' J. Res. Natl. Bur. Stand. **69D**, 1387–1401 (1965).
[18] M. J. Lighthill, ''Group velocity,'' J. Inst. Math. Appl. **1**, 1–28 (1965).
[19] A. Bernard, M. J. S. Lowe, and M. Deschamps, ''Guided waves energy velocity in absorbing and nonabsorbing plates,'' J. Acoust. Soc. Am. **110**, 186–196 (2001).
[20] M. A. Biot, ''General theorems on the equivalence of group velocity and energy transport,'' Phys. Rev. **105**, 1129–1137 (1957).
[21] G. Kaduchak and P. L. Marston, ''Traveling wave decomposition of surface displacements associated with scattering by a cylindrical shell: Numerical evaluation displaying guided forward and backward wave properties,'' J. Acoust. Soc. Am. **98**, 3501–3507 (1995).
[22] J. Wolf, T. D. K. Nook, R. Kille, and W. G. Mayer, ''Investigation of Lamb waves having a negative group velocity,'' J. Acoust. Soc. Am. **83**, 122–132 (1988).
[23] A. Alippi, M. Germano, A. Bettucci, F. Farrelly, and G. Muzio, ''Traversal time of acoustic plate waves through a tunneling section,'' Phys. Rev. E **57**, R4907–R4910 (1998).
[24] A. Alippi, A. Bettucci, and M. Germano, ''Anomalous propagation characteristics of evanescent waves,'' Ultrasonics **38**, 817–820 (2000).
[25] L. R. Dragonette, D. M. Drumheller, C. F. Gaumond, D. H. Hughes, B. T. O'Connor, N. Yen, and T. J. Yoder, ''The application of two-dimensional signal transformations to the analysis and synthesis of structural excitations observed in acoustical scattering,'' Proc. IEEE **84**, 1249–1262 (1996).
[26] S. F. Morse and P. L. Marston, ''Meridional ray contributions to scattering by tilted cylindrical shells above the coincidence frequency: ray theory and computations,'' J. Acoust. Soc. Am. **106**, 2595–2600 (1999).
[27] S. G. Kargl and P. L. Marston, ''Ray synthesis of the form function for backscattering from an elastic spherical shell: Leaky Lamb waves and longitudinal resonances,'' J. Acoust. Soc. Am. **89**, 2545–2558 (1991).
[28] G. S. Sammelmann and R. H. Hackman, ''The acoustic scattering by a submerged, spherical shell. II: The high-frequency region and the thickness quasiresonance,'' J. Acoust. Soc. Am. **89**, 2096–2103 (1991).
[29] M. F. Werby and H. Überall, ''A systematic study of water-filled, submerged elastic spherical shells and the resolution of elastic and water-included resonances,'' J. Acoust. Soc. Am. **112**, 896–905 (2002).
[30] S. G. Kargl and P. L. Marston, ''Longitudinal resonances in the form function for backscattering from a spherical shell: Fluid shell case,'' J. Acoust. Soc. Am. **88**, 1114–1122 (1990).
[31] P. L. Marston, ''Geometrical and catastrophe optics methods in scattering,'' in *Physical Acoustics*, edited by R. N. Thurston and A. D. Pierce (Academic, Boston, 1992), Vol. 21, pp. 1–234; see Sec. 4.11, pp. 198–205.
[32] M. Ezzaidi, D. Decultot, G. Maze, and A. Moudden, ''Measure of the thickness of a cylindrical shell with a focused beam,'' NDT & E Int. **35**, 433–436 (2002).
[33] V. G. Veselago, Usp. Fiz. Nauk **92**, 517 (1964) [''The electrodynamics of substances with simultaneously negative values of ε and μ,'' Sov. Phys. Usp. **10**, 509 (1968)].
[34] D. R. Smith, W. J. Padilla, D. C. Vier, S. C. Nemat-Nasser, and S. Schultz, ''Composite medium with simultaneously negative permeability and permittivity,'' Phys. Rev. Lett. **84**, 4184–4187 (2000); R. A. Shelby, D. R. Smith, and S. Schultz, ''Experimental verification of a negative index of refraction'', Science **292**, 77–79 (2001).
[35] R. W. Ziolkowski and E. Heyman, ''Wave propagation in media having negative permittivity and permeability,'' Phys. Rev. E **64**, 056625(1–15) (2001); A. L. Pokrovsky and A. L. Efros, ''Sign of refractive index and group velocity in left-handed media'', Solid State Commun. **124**, 283–287 (2002).
[36] J. A. Kong, B-I. Wu, and Y. Zhang, ''Lateral displacement of a Gaussian beam reflected from a grounded slab with negative permittivity and permeability,'' Appl. Phys. Lett. **80**, 2084–2086 (2002).
[37] P. Kirrmann, ''On the completeness of Lamb modes,'' J. Elast. **37**, 39–69 (1995).

Radiation efficiency of convected fluid-loaded plates[a)]

Kenneth D. Frampton[b)]
Department of Mechanical Engineering, Vanderbilt University, VU Station 351592, Nashville, Tennessee 37235-1592

(Received 24 May 2002; revised 3 January 2003; accepted 23 January 2003)

The radiation of sound from geometrically simple vibrating structures into stationary fluids is well understood. However, to date, very few investigations have considered the effects of fluid convection on structural acoustic radiation. The purpose of this investigation is to quantify the effects that fluid flow has on the sound radiated from rectangular vibrating plates. The discussion includes a description of the fundamental physics associated with a simply supported, vibrating, rectangular plate imbedded in an infinite baffle and radiating into a semi-infinite convected fluid field. This is followed by a discussion of the computational approach used to calculate the plate radiation efficiency. Finally, numerical results are presented which demonstrate the effect that convection has on the radiation efficiency. The primary effect is a significant increase in radiation efficiency in the mid-wave number region, which is attributable to an effective decrease in the critical frequency. © *2003 Acoustical Society of America.* [DOI: 10.1121/1.1559173]

PACS numbers: 43.40.Rj [EGW]

I. INTRODUCTION

Sound radiation from vibrating structures has been a topic of considerable interest for quite some time. The mathematical tools available to scientists and engineers have evolved from analytic techniques, to numerical integration, and on to finite and boundary elements. As these tools have evolved so has the knowledge base concerning the sound radiation from structures of ever-increasing complexity. The radiation of sound from geometrically simple vibrating structures into stationary fluids is well understood. However, to date, only a few investigations have considered the effects that a convected fluid has on structural acoustic radiation. A thorough, fundamental understanding of these effects will inevitably improve the design and construction of a variety of engineering systems.

This work represents the merger of two previously separate disciplines: structural acoustics and aeroelasticity. These two disciplines, while having very different objectives, share many common physical and mathematical tools. Past investigations into the effects of convected fluid loading on plates (i.e., aeroelasticity) are numerous and are well summarized by Dowell.[1] These investigations focus primarily on the stability of such coupled systems. Significant effects on plate dynamics, particularly at high subsonic and supersonic Mach numbers, have been demonstrated. The importance of this body of previous work to the present effort is that the physics and mathematics associated with aeroelastic behavior can be used as a foundation for structural acoustic investigations in the presence of mean flow.

Once an understanding of the dynamics of the convected fluid-loaded structure is obtained, analysis of the resulting far-field acoustic radiation can follow from well-established methods of structural acoustics. Radiation from plates into a static fluid is well understood (particularly for simple geometries), and numerous publications are available which describe the problem in various ways. This body of knowledge will not be reviewed here; however, thorough reviews of this topic are provided by Crighton,[2] Fahy,[3] Junger and Feit,[4] and Howe.[5] One investigation that is of particular importance to this work is that by Wallace,[6] which outlines the radiation efficiency of rectangular plates without flow. The current investigation is, to a large extent, an extension of Wallace's work for the case where the fluid is convected.

A limited number of references are available concerning sound radiation from convected fluid-loaded plates. Abrahams published one of the earliest efforts in this field.[7] Abrahams' work involves a rigorous analytical treatment of the problem and is unique in that it employs asymptotic solution techniques. Work published by Atalla and Nicolas[8] presented the radiation impedance for a vibrating piston in the presence of flow. One of their conclusions was that the radiation resistance increases with increasing Mach number while the radiation reactance decreases with increasing flow. Limited results supporting this conclusion were also provided for a plate vibrating in the (1,1) and (2,2) modes. This work was followed by Sgard, Attalla, and Nicolas,[9] who employed finite elements and the extended Kirchhoff integral to calculate the radiated power. They also concluded that radiated sound power increases with increasing flow speed. It was further noted that the effects of flow could be neglected when the Mach number in air is less than 0.2. However, for heavy fluids such as water the Mach number below which flow effects can be neglected is substantially smaller. This work is particularly noteworthy in that it addresses the complex issue of flow-induced coupling, which has been neglected in most other investigations. An investigation by Wu and Maestrello[10] incorporated structural nonlinear effects into the

[a)]This work has been previously presented, in part, at the *Symposium on Flow-Induced Vibration and Noise of Thin Materials*, IMECE, Nashville, TN, November 1999 and at the *136th Meeting of the Acoustical Society of America*, Vol. 103, No. 9, Norfolk, VA, October 1998.

[b)]Assistant Professor of Mechanical Engineering, Associate Member of the Acoustical Society of America, and author to whom correspondence should be addressed. Electronic mail: ken.frampton@vanderbilt.edu

analysis. The radiated acoustic pressure was calculated in order to permit flow-induced modal coupling. However, the purpose of the work was stability analysis and not an investigation of the radiated pressure. A more recent effort by Graham[11] also concluded that the primary effect of flow was to decrease the frequency at which a mode becomes an efficient radiator. The primary metric used by Graham was the average radiation efficiency rather than the frequency-dependent radiation efficiency. One important issue addressed by Graham was that of flow-induced coupling. It was concluded that neglecting coupling is a not an unreasonable assumption, although in some situations coupling can be very important. Last, the author has published some related work that focuses on sound transmission through aeroelastic plates,[12] radiation from aeroelastic plates,[13] as well as methods for modeling the coupled fluid–structure interaction.[14] One commonality among all of these publications (with the exception of the work by Abrahams[7] and Sgard, Attalla, and Nicolas[9]) is the use of transform techniques to solve the fluid dynamic equations.

The objective of this work is to quantify the acoustic radiation efficiency of rectangular, elastic plates into a convected fluid. The theoretical development begins with the prescribed motion of a rectangular plate and the resulting generalized force due to acoustic pressures. Next, a solution to the convected wave equation is presented subject to the boundary conditions of a vibrating plate in an infinite baffle. This solution is the result of a combined transform/numerical technique.[14] This is followed by the description of a singular value decomposition technique, which casts the fluid dynamic solution in state variable form. Next, building on the approach taken by Wallace,[6] the radiation efficiency is found by normalizing the total power radiated to the far field by the kinetic energy of the plate. Numerical results are presented which validate the modeling approach and which demonstrate the effects on radiation efficiency by subsonic flows and plate aspect ratio. Finally, the implications of flow induced modal coupling are briefly discussed.

II. THEORETICAL DEVELOPMENT

The system under consideration consists of a finite, flexible, rectangular plate embedded in an infinite baffle. The plate is subjected to a semi-infinite fluid, flowing parallel to the x axis, on one side and a vacuum on the other side as depicted in Fig. 1. The plate vibration creates a pressure disturbance in the surrounding fluid, some of which propagates into the far field.

This section begins with a description of the plate motion and the relationship of this motion to the dynamic behavior of the surrounding fluid. This is followed by a description of the method employed in modeling the response of the surrounding convected fluid as well as the means for computing the radiation efficiency.

A. Plate dynamics

Consider a rectangular panel that is undergoing prescribed motion in one of its modes as described by

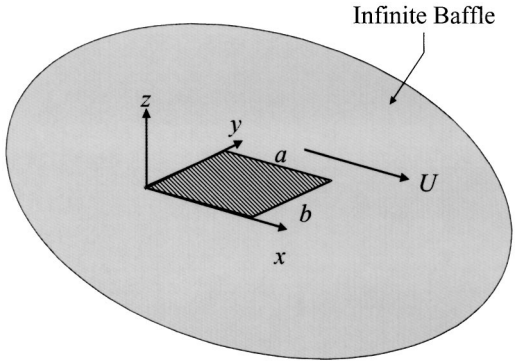

FIG. 1. Schematic of the plate and coordinate system.

$$w(x,y,t)=q_n(t)\psi_n(x,y) \quad n=1,2,3,..., \tag{1}$$

where $w(x,y,t)$ is the out-of-plane plate displacement, $\psi_n(x,y)$ is the mode shape, and $q_n(t)$ is the temporal component of the mode (i.e., the generalized coordinate) and is an arbitrary function of time. The modeling approach taken here is not inherently limited to harmonic motion nor is it limited to motion in a particular mode. Therefore, the development of the plate motion and fluid response will initially be developed assuming that the temporal component of the plate motion is arbitrary. Later, when the specific notion of radiation efficiency is considered, harmonic motion of a simply supported plate in a particular *in vacuo* mode will be assumed. Since the motion of the panel is prescribed [i.e., $q_n(t)$ is given], there is no need to proceed with a solution to the panel equations of motion. However, one important product of the modal solution approach is the expression for the aerodynamic generalized force acting on the panel as defined by[15]

$$Q_n(t)=\int_0^b\int_0^a p_a(x,y,z=0,t)\psi_n(x,y)dx\,dy, \tag{2}$$

where $p_a(x,y,z=0,t)$ is the aerodynamic pressure acting on the plate and $Q_n(t)$ is the resulting generalized force (or modal force). This generalized force is due entirely to the fluid dynamic or acoustic pressure at the surface of the plate that is created by plate motion. Developing an expression for this generalized force is the next step in finding the radiation efficiency of the plate and is considered in the next section.

B. External flow generalized forces

Historically, two distinct approaches have been used to find the acoustic pressures acting on a vibrating plate. The first approach is based on the Helmholtz–Kirchhoff integral, which is typically solved numerically.[6,8,10] A second approach is to employ spatial Fourier transform techniques requiring approximate inverse transforms obtained through asymptotic techniques.[7,11] The approach taken here falls under the latter category, although the inverse transforms are performed through numeric integration, as will be shown.

The aerodynamic generalized forces of Eq. (2), and denoted $Q_n(t)$, are found by solving the partial differential equation describing the velocity potential in an inviscid, irrotational fluid moving parallel to the x axis (also known as the convected wave equation)

$$\nabla^2\phi - \frac{1}{c_o^2}\left[\frac{\partial^2\phi}{\partial t^2} + 2U\frac{\partial^2\phi}{\partial t\partial x} + U^2\frac{\partial^2\phi}{\partial x^2}\right] = 0, \tag{3}$$

subject to the boundary conditions for a panel embedded in an infinite baffle

$$\left.\frac{\partial\phi}{\partial z}\right|_{z=0} = \begin{cases} U\dfrac{\partial w}{\partial x} + \dfrac{\partial w}{\partial t} = f(x,y,z,t) & \text{on the plate} \\ 0 & \text{off the plate,} \end{cases} \tag{4}$$

and a finiteness or radiation condition as z approaches infinity. In Eqs. (3) and (4) ϕ is the fluid velocity potential, c_o is the speed of sound, and U is the ambient flow velocity. The solution to these equations follows that of Dowell.[1] We begin by performing a double Fourier transform with respect to the x and y spatial coordinates and a Laplace transform with respect to time according to the following definitions:

$$\tilde{\Phi}(\alpha,\gamma,z,s) = \int_{-\infty}^{\infty}\int_{-\infty}^{\infty} e^{-i(\alpha x+\gamma y)}\Phi(x,y,z,s)\,dx\,dy, \tag{5}$$

$$\Phi(x,y,z,s) = \int_0^{\infty} e^{-st}\phi(x,y,z,t)\,dt. \tag{6}$$

Applying these transforms to the convected wave equation, Eq. (3), results in

$$\frac{d^2\tilde{\Phi}}{dz^2} = \tilde{\Phi}\mu^2, \tag{7}$$

where

$$\mu = \left[\frac{s^2}{c_o^2} + \frac{2Msi\alpha}{c_o} - \alpha^2(M^2-1) + \gamma^2\right]^{1/2}, \tag{8}$$

and where s is the Laplace variable, $M = U/c_o$ is the Mach number, $i = \sqrt{-1}$, and α and γ are the Fourier transform variables in x and y, respectively. Similarly, the triple transform of the boundary condition, Eq. (4), results in

$$\frac{d\tilde{\Phi}}{dz} = \tilde{F}. \tag{9}$$

The transformed version of the convected wave equation, Eq. (7), is solved subject to the transformed boundary condition of Eq. (9) to yield the transformed velocity potential on the plate surface such that

$$\tilde{\Phi}|_{z=0} = \frac{-\tilde{F}}{\mu}. \tag{10}$$

Equation (10) can be inverted with respect to the Laplace variable to yield the velocity potential in the Fourier/time domain on the surface of the plate

$$\tilde{\phi}(\alpha,\gamma,z=0,t) = -c_o\int_0^t \tilde{f}(\alpha,\gamma,\tau)\exp[-iMc_o\alpha(t-\tau)] \times \mathrm{J}_0[(\alpha^2+\gamma^2)^{1/2}c_o(t-\tau)]\,d\tau, \tag{11}$$

where $\mathrm{J}_k[\bullet]$ is a Bessel function of the first kind and of order k and τ is a dummy variable of integration. Now, in order to calculate the generalized force acting on the plate the pressure acting on the surface of the plate is required. This can be found from Bernoulli's equation, which relates the pressure to the velocity potential such that

$$p = -\rho\left(\frac{\partial\Phi}{\partial t} + U\frac{\partial\Phi}{\partial x}\right), \tag{12}$$

where ρ is the fluid density. Combining Eqs. (11) and (12) yields

$$\tilde{p}(\alpha,\gamma,z=0,t) = \rho c_o\tilde{f}(t) - \rho c_o^2(\alpha^2+\gamma^2)^{1/2}\int_0^t \tilde{f}(\tau) \times\exp[-ic_oM\alpha(t-\tau)] \times \mathrm{J}_1[c_o(\alpha^2+\gamma^2)^{1/2}(t-\tau)]\,d\tau. \tag{13}$$

At this point an inverse Fourier transform can be performed. This step is complicated by a logarithmic singularity at the leading edge or upstream edge of the plate (this singularity exists only for subsonic flows). If one is interested in determining the pressure specifically at the leading edge, this singularity does present a challenge. However, in this treatment, we are not interested in the pressure at any particular point. Rather, the generalized force on the plate is sought. Since the leading edge singularity is integrable, this challenge is avoided by integrating the pressure over the entire surface of the plate. We will therefore proceed by substituting Eq. (13) into Eq. (2). The integration with respect to x and y is performed first, followed by the inverse Fourier integrals with respect to α and γ.[16] By choosing this order of integration the leading edge singularity problem is avoided in the inversion. The result yields the fluid generalized forces on the plate such that

$$Q_n = \sum_{m=1}^{N} Q_{mn}(t), \tag{14}$$

where $Q_{mn}(t)$ is the force on the nth panel mode due to motion of the mth panel mode such that

$$Q_{mn}(t) = \sum_{m=1}^{N}[q_m(t)S_{mn} + \dot{q}_m(t)D_{mn}] + \sum_{m=1}^{N}\left[\int_0^t q_m(\tau)H_{mn}(t-\tau)\,d\tau\right] + \sum_{m=1}^{N}\left[\int_0^t \dot{q}_m(\tau)I_{mn}(t-\tau)\,d\tau\right], \tag{15}$$

and

$$S_{mn} = \frac{1}{M}\int_0^a\int_0^b \frac{\partial\psi_m}{\partial x}\psi_n\,dx\,dy, \tag{16}$$

$$D_{mn} = \frac{1}{MU}\int_0^a\int_0^b \psi_m\psi_n\,dx\,dy, \tag{17}$$

$$H_{mn} = \frac{U}{4\pi^2M^2}\int_{-\infty}^{\infty}\int_{-\infty}^{\infty} G_{mn}i\alpha\sqrt{\alpha^2+\gamma^2}e^{-i\alpha Ut} \times \mathrm{J}_1[c_ot\sqrt{\alpha^2+\gamma^2}]\,d\alpha\,d\gamma, \tag{18}$$

$$I_{mn}=\frac{1}{4\pi^2M^2}\int_{-\infty}^{\infty}\int_{-\infty}^{\infty}G_{mn}\sqrt{\alpha^2+\gamma^2}\times e^{-i\alpha Ut}\mathrm{J}_1[c_o t\sqrt{\alpha^2+\gamma^2}]d\alpha\,d\gamma, \tag{19}$$

$$G_{mn}=\int_0^a\int_0^b\psi_m(x,y)e^{-i(\alpha x+\gamma y)}dx\,dy\times\int_0^a\int_0^b\psi_n(x,y)e^{i(\alpha x+\gamma y)}dx\,dy. \tag{20}$$

The variables S_{mn} and D_{mn} are referred to as aerodynamic influence coefficients and relate the instantaneous changes in the plate generalized coordinates (modal position, q_n, and modal velocity, $\dot{q}_n$) to instantaneous changes in the aerodynamic generalized force. The influence coefficients are defined by the integrals in Eqs. (16) and (17), which can be performed analytically for most plate eigenfunctions as can Eq. (20). Since all results discussed in this work are for simply supported plates, the integrals of Eqs. (16) and (17) are evaluated in the Appendix. The aerodynamic influence functions, $H_{mn}(t)$ and $I_{mn}(t)$, are defined by integrals with no closed-form solution. Dowell used numeric integration to find the influence functions and then used numeric time-stepping algorithms to simulate the system response.[1] This approach worked well for the objective of stability analysis. However, if the objective is to perform eigenvalue analysis similar to that of Currey and Cunefare,[17] or feedback control system design,[18,19] then an approach that results in a differential equation representation of the system is desired. Such a representation is obtained here by the application of a singular value decomposition technique. The result is a state variable representation of the fluid dynamics where the plate generalized coordinates and generalized velocities are the inputs and the fluid generalized forces are the outputs. This approach is not necessarily the most efficient path toward a solution of the panel radiation efficiency. In fact, a great deal of computational economy could be had if one were to assume harmonic motion from the outset. The fact that this approach is used here is somewhat serendipitous. The approach was developed in order to permit transient analysis and to perform feedback control analysis.[12,18,19] Most importantly for the work presented here, this modeling approach enables one to readily represent the relationship between the plate motion and the fluid generalized force in transfer function form.

C. Approximation of the aerodynamic generalized forces

As stated previously, approximation of the aerodynamic generalized forces is performed using a singular value decomposition (SVD) technique originally developed as a system identification method.[20] This technique was chosen for two reasons. First, this SVD technique utilizes time-domain impulse responses to calculate the system realization. This trait lends itself well to this problem since the aerodynamic system to be modeled is characterized by aerodynamic influence functions, $H_{mn}(t)$ and $I_{mn}(t)$. These are essentially impulse responses that relate the plate motion to the generalized force. Second, the result of the SVD approach is a state-variable model that permits the use of numerous system analysis tools associated with linear systems theory.

The objective is to create a state-variable representation of the relationship between the plate motion and the aerodynamic forces, as expressed by Eq. (15). Note that Eq. (15) constructs the aerodynamic forces as outputs by convolving the influence functions with the plate generalized coordinates. This mapping can be represented in state variable form as

$$\mathbf{x}((k+1)T)=\mathbf{A}\mathbf{x}(kT)+\mathbf{B}\mathbf{u}(kT),$$
$$\mathbf{y}(kT)=\mathbf{C}\mathbf{x}(kT)+\mathbf{D}\mathbf{u}(kT), \tag{21}$$

where T is the discrete time increment and k is the time index. The system ($\mathbf{A}$,$\mathbf{B}$,$\mathbf{C}$,$\mathbf{D}$) has n states $\mathbf{x}$, p inputs $\mathbf{u}$, and m outputs $\mathbf{y}$. In this case the desired aerodynamic system input and output vectors, for a plate having N modes, are

$$\mathbf{u}=[q_1\quad q_2\quad\cdots\quad q_N\quad\dot{q}_1\quad\dot{q}_2\quad\cdots\quad\dot{q}_N], \tag{22}$$

and

$$\mathbf{y}=[Q_1\quad Q_2\quad\cdots\quad Q_N], \tag{23}$$

respectively. The creation of a state-variable aerodynamic model begins by building a block Hankel matrix of the matrix valued impulse response as follows:

$$\mathbf{H}=\begin{bmatrix}\mathbf{h}(T) & \mathbf{h}(2T) & \mathbf{h}(3T) & \cdots & \mathbf{h}((J+1)T)\\ \mathbf{h}(2T) & \mathbf{h}(3T) & \mathbf{h}(4T) & \cdots & \mathbf{0}\\ \mathbf{h}(3T) & \mathbf{h}(4T) & \mathbf{h}(5T) & \cdots & \mathbf{0}\\ \vdots & \vdots & \vdots & \ddots & \vdots\\ \mathbf{h}((J+1)T) & \mathbf{0} & \mathbf{0} & \cdots & \mathbf{0}\end{bmatrix}, \tag{24}$$

where the matrix valued impulse response for the aerodynamic system is

$$\mathbf{h}(kT)=\begin{cases}\begin{bmatrix} S_{11} & S_{21} & \cdots & S_{N1} & D_{11} & D_{21} & \cdots & D_{N1} \\ S_{12} & S_{22} & \cdots & S_{N2} & D_{12} & D_{22} & \cdots & D_{N2} \\ \vdots & \vdots & \ddots & \vdots & \vdots & \vdots & \ddots & \vdots \\ S_{1N} & S_{2N} & \cdots & S_{NN} & D_{1N} & D_{2N} & \cdots & D_{NN} \end{bmatrix} & \text{for } k=0 \\ \begin{bmatrix} H_{11}(kT) & \cdots & H_{N1}(kT) & I_{11}(kT) & \cdots & I_{N1}(kT) \\ H_{12}(kT) & \cdots & H_{N2}(kT) & I_{12}(kT) & \cdots & I_{N2}(kT) \\ \vdots & \ddots & \vdots & \vdots & \ddots & \vdots \\ H_{1N}(kT) & \cdots & H_{NN}(kT) & I_{1N}(kT) & \cdots & I_{NN}(kT) \end{bmatrix} & \text{for } k=1,2,...,J+1 \\ \mathbf{0} \quad \text{for } k>J+1. & \end{cases} \tag{25}$$

Note that the Hankel matrix, $\mathbf{H}$, is of dimension $m(J+1)$ by $p(J+1)$. The next step toward obtaining a state space realization of the system is to perform a singular value decomposition of the block Hankel matrix. The decomposition has the form

$$\mathbf{H}=U\Sigma V^T=\mathbf{U}\mathbf{V}^T, \tag{26}$$

where $\mathbf{U}$ is an $m(J+1)$ by $(J+1)$ orthogonal matrix of the eigenvectors of $\mathbf{H}\mathbf{H}^{\mathrm{T}}$, $\mathbf{V}$ is a $p(J+1)$ by $(J+1)$ orthogonal matrix of the eigenvectors of $\mathbf{H}^{\mathrm{T}}\mathbf{H}$, and the singular value matrix is

$$\Sigma=\mathrm{diag}[\sigma_1,\sigma_2,\ldots,\sigma_r,\varepsilon_{r+1},\varepsilon_{r+2},\ldots,\varepsilon_{J+1}], \tag{27}$$

with the singular values in descending order such that

$$\sigma_1\geqslant\sigma_2\geqslant\cdots\sigma_r\geqslant\varepsilon_{r+1}\geqslant\varepsilon_{r+2}\geqslant\cdots\geqslant\varepsilon_{J+1}, \tag{28}$$

and

$$\mathbf{U}=U\Sigma^{1/2},\quad \mathbf{V}=\Sigma^{1/2}V^T. \tag{29}$$

If $\mathbf{H}$ has a rank of r then the last J-r singular values, $(\varepsilon_i:i=r+1,r+2,\ldots,J+1)$, are zero. If the singular values, ε_i, are not zero but are much less than the singular values, σ_i, then the matrix is very near to rank r. In this case the singular values, ε_i, represent computational ''noise'' in the impulse responses or degrees of freedom with relatively small contribution to the system response. This property is taken advantage of in selecting the order of the final model.

A reduced order realization $(\hat{\mathbf{A}},\hat{\mathbf{B}},\hat{\mathbf{C}},\hat{\mathbf{D}})$ of order r, which omits the excess degrees of freedom, can be constructed by partitioning the SVD as follows:

$$\mathbf{H}=\begin{bmatrix} \mathbf{U}_{1,1} & \mathbf{U}_{1,2} \\ \mathbf{U}_{2,1} & \mathbf{U}_{2,2} \\ \vdots & \vdots \\ \mathbf{U}_{J,1} & \mathbf{U}_{J,2} \\ \mathbf{U}_{J+1,1} & \mathbf{U}_{J+1,2} \end{bmatrix}\begin{bmatrix} \mathbf{V}_{1,1}^T & \mathbf{V}_{2,1}^T & \cdots & \mathbf{V}_{J,1}^T & \mathbf{V}_{J+1,1}^T \\ \mathbf{V}_{1,2}^T & \mathbf{V}_{2,2}^T & \cdots & \mathbf{V}_{J,2}^T & \mathbf{V}_{J+1,2}^T \end{bmatrix}, \tag{30}$$

where the block matrices $\mathbf{U}_{i,1};i=1,2,...,J+1$ are m by r, $\mathbf{U}_{i,2};i=1,2,...,J+1$ are m by $(J+r-1)$, $\mathbf{V}_{i,1};i=1,2,...,J+1$ are p by r, and $\mathbf{V}_{i,2};i=1,2,...,J+1$ are p by $(J+r-1)$.

The reduced order realization can be defined based on these partitions as follows:

$$\hat{\mathbf{A}}=\left(\begin{bmatrix} \mathbf{U}_{1,1} \\ \mathbf{U}_{2,1} \\ \vdots \\ \mathbf{U}_{J,1} \end{bmatrix}^T\begin{bmatrix} \mathbf{U}_{1,1} \\ \mathbf{U}_{2,1} \\ \vdots \\ \mathbf{U}_{J,1} \end{bmatrix}\right)^{-1}\begin{bmatrix} \mathbf{U}_{1,1} \\ \mathbf{U}_{2,1} \\ \vdots \\ \mathbf{U}_{J,1} \end{bmatrix}^T\begin{bmatrix} \mathbf{U}_{2,1} \\ \mathbf{U}_{3,1} \\ \vdots \\ \mathbf{U}_{J+1,1} \end{bmatrix}, \tag{31}$$

$$\hat{\mathbf{B}}=\mathbf{V}_{1,1}^T, \tag{32}$$

$$\hat{\mathbf{C}}=\mathbf{U}_{1,1}, \tag{33}$$

and

$$\hat{\mathbf{D}}=\mathbf{h}(0). \tag{34}$$

So, in summary, a state-variable approximation of the aerodynamic forces on a plate can be created as follows: (1) calculate the influence coefficients from Eqs. (16) and (17); (2) numerically calculate the influence functions, $H_{mn}(t)$ and $I_{mn}(t)$ of Eqs. (18) and (19), at discrete times $t=kT$[1,14]; (3) form the block Hankel matrix of Eq. (24) based on the matrix valued impulse response of Eq. (25); (4) perform singular value decomposition of the Hankel matrix; and (5) construct the system matrices based on the SVD partitions of Eqs. (31), (32), (33), and (34). The final aerodynamic system will receive the plate generalized coordinates and generalized velocities as inputs and generate as outputs the aerodynamic generalized forces. It is important to note that the states of the resulting system have no physical significance but are of mathematical construct.

D. Radiation efficiency

The first step toward calculating the radiation efficiency is to define the radiated sound power. The power radiated by a plate vibrating in its nth mode can be calculated as follows:

$$\Pi_n=\int p_n(x,y,z=0,t)\dot{w}_n(x,y,t)dS, \tag{35}$$

where $p_n(x,y,z=0,t)$ is the surface fluid pressure created by motion of the nth panel mode and $\dot{w}_n(x,y,t)$ is the velocity of the panel vibrating in the nth mode. By substituting the modal representation of Eq. (1) into Eq. (35), the radiated power of an individual mode can be expressed as

$$\Pi_n(t)=\int_S p_n(x,y,z=0,t)\psi_n(x,y)dS\,\dot{q}_n(t). \tag{36}$$

Note that the integral of Eq. (36) is equivalent to the generalized force expression of Eq. (2), resulting in

$$\Pi_n(t)=Q_n(t)\dot{q}_n(t). \tag{37}$$

If we now assume that the system is undergoing harmonic motion, Eq. (1) becomes

$$w(x,y,t)=\psi_n(x,y)\tilde{q}_n e^{j\omega t} \quad n=1,2,3,..., \tag{38}$$

where $\tilde{q}_n$ is the modal amplitude and ω is the excitation frequency. In this case Eq. (37) becomes

$$\Pi_n(t)=Q_n\dot{q}_n e^{j\omega t}, \tag{39}$$

where $\dot{q}_n$ now represents the magnitude of the modal velocity $(j\omega q_n)$. Now, advantage can be taken of the aerodynamic state-variable model by extracting the transfer function between the nth modal velocity and the nth generalized force, $\tilde{H}_n(\omega)$.[21] However, since cross-modal coupling is not considered here, the coupling terms are omitted [i.e., $m=n$ in Eq. (15)]. The resulting relationship is

$$\tilde{Q}_n e^{j\omega t}=\tilde{H}_n(\omega)q_n e^{j\omega t}. \tag{40}$$

Incorporating the transfer function into Eq. (39) results in the instantaneous radiated sound power

$$\Pi_n(t)=\Re\{\tilde{H}_n(\omega)\}(\tilde{\dot{q}}_n e^{j\omega t})^2, \tag{41}$$

where $\Re\{\cdot\}$ indicates the real part of the argument. Thus, Eq. (41) represents the radiation to the far field. Now, the radiation efficiency is found from the time-averaged radiated power expressed as[6]

$$\langle\Pi_n\rangle=\frac{1}{T_h}\int_0^T \Re\{\tilde{H}_n(\omega)\}(\tilde{\dot{q}}_n e^{j\omega t})^2 dt=\frac{1}{2}\Re\{\tilde{H}_n(\omega)\}\tilde{\dot{q}}_n^2, \tag{42}$$

where T_b is one period of the harmonic excitation. Finally, the radiation efficiency of the nth plate mode can be expressed as[6]

$$\sigma_n=\frac{\langle\Pi_n\rangle}{\rho_o c_o ab\langle|\tilde{\dot{q}}_n|^2\rangle}=\frac{4\Re\{\tilde{H}_n(\omega)\}}{\rho_o c_o ab}, \tag{43}$$

where the spatio-temporal mean-square modal velocity of the plate is $\langle|\dot{q}_n|^2\rangle=\frac{1}{8}\tilde{\dot{q}}_n^2$ for a simply supported plate.[3] So, the radiation efficiency of the plate is proportional to the real part of the transfer function between the plate motion and fluid generalized force [as defined by Eq. (8)].

III. COMPUTATIONAL RESULTS

Results from the previously outlined theory are presented in this section. Three primary topics are covered including validation of the model, the effects of flow velocity on radiation efficiency, and the effects of plate aspect ratio on radiation efficiency. The section concludes with a brief discussion on the implications of flow-induced coupling. All results presented are for a simply supported plate. Evaluation of the influence coefficient integrals can be found in the Appendix.

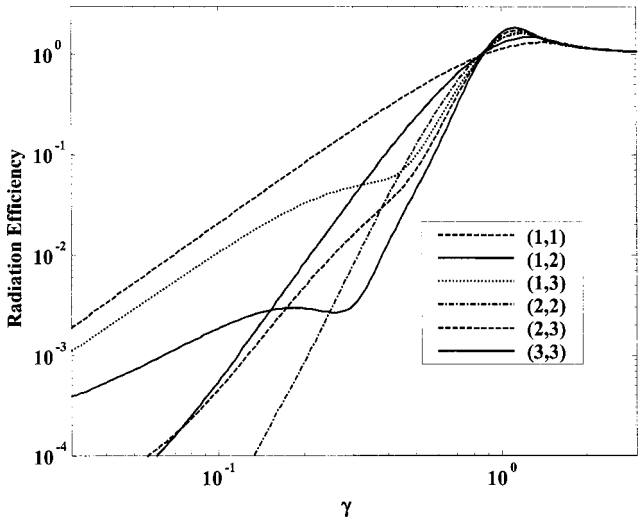

FIG. 2. Radiation efficiency of several plate modes without flow.

A. Validation of the model

The accuracy of the radiation efficiency calculations are established through comparison with results previously published by Wallace[6] for no-flow conditions and by Graham[11] for the case with flow. A plot of the radiation efficiency for several modes of a square, simply supported plate and with a Mach number of $M=0$ are shown in Fig. 2. The plot is shown with respect to the acoustic wave number normalized by the structural wave number for a simply supported mode shape

$$\gamma=\frac{k}{\sqrt{(m\pi/a)^2+(n\pi/b)^2}}. \tag{44}$$

These results compare very well with those of Wallace. Good agreement was also found for the nonzero flow conditions published by Graham. Although Graham did not provide specific radiation efficiency plots, he did include modal radiation impedance plots that are proportional to the radiation efficiency.

In general, the singular value decomposition solution method employed here demonstrated the most inaccuracy in the low wave number region. This was not a specific low-frequency weakness in the solution method. Rather, the SVD approach minimizes the error of the total area under the transfer function curve.[14] Therefore, the lowest amplitude singular values, which are related to the low-frequency components in this case, are the first to suffer from inaccuracy. An example of this inaccuracy can be seen in the (2,3) mode radiation efficiency of Fig. 2. Note the slight concavity in the curve at the lowest wave numbers. One would expect the low wave number asymptote to be a straight line (on a log–log plot). Every effort was made to establish the low wave number asymptote in this work, and all of the radiation efficiency plots shown subsequently are deemed accurate over the wave

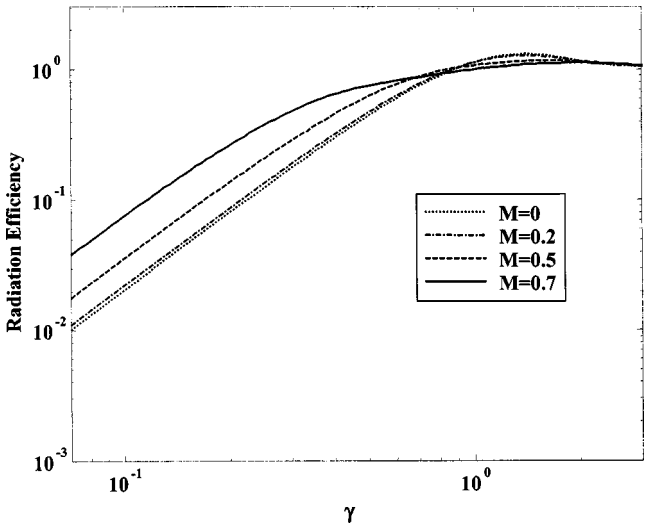

FIG. 3. Radiation efficiency of the (1,1) mode at various Mach numbers.

number region shown in the plots. Improving the accuracy of the results is simply a matter of increasing the resolution of the numerically integrated influence functions and, hence, the order of the state-variable representation.

One further item to note is that the solution method presented here is not restricted to subsonic Mach numbers. However, since it is well established that modal coupling is particularly important for supersonic flow, the results presented here are limited to subsonic Mach numbers. More comments concerning the implications of flow-induced coupling follow. The solution presented here does, however, suffer from the well-known inaccuracy of the linearized potential flow equations in the transonic region. In order to avoid such inaccuracies, the results are limited to a maximum Mach number of 0.7.

B. Effects of flow on radiation efficiency

The effect of flow on the radiation efficiency of the (1,1) plate mode is demonstrated in Fig. 3. The most notable change in radiation efficiency is that the critical frequency (the frequency at which the mode becomes an efficient radiator) decreases with increasing flow velocity. The result of convection is to increase the plate radiation efficiency in the mid-wave number domain as well as a significant increase in the total radiation efficiency of the plate. The primary cause for this shift in the critical frequency is that plate waves traveling upstream (relative to the flow) experience an effective increase in the phase speed.

This effect can be explained by considering the more simple case of radiation from a two-dimensional plate of infinite extent. In this case, the fluid still behaves according to the convected wave equation such that

$$\nabla^2 p - \frac{1}{c_o^2}\left[\frac{\partial^2 p}{\partial t^2} + 2U\frac{\partial^2 p}{\partial t\,\partial x} + U^2\frac{\partial^2 p}{\partial x^2}\right] = 0. \tag{45}$$

Assuming that the plate waves are harmonic, one can assume that the solution to Eq. (45) will be of the form

$$p(x,z,t) = P_o e^{-jk_x x} e^{-jk_z z} e^{j\omega t}. \tag{46}$$

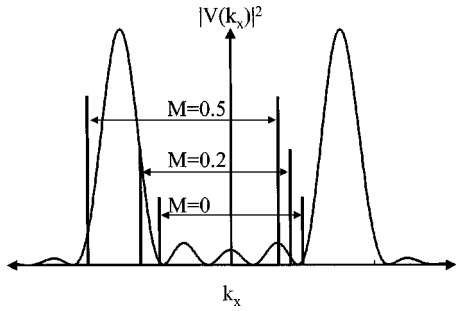

FIG. 4. The wave number spectrum of plate velocity and the changes in the supersonic region with increasing Mach number.

Substituting Eq. (46) into Eq. (45) results in

$$0 = k_x^2 + k_z^2 + \frac{1}{c_o^2}[-\omega^2 + 2U\omega k_x - U^2 k_x^2]. \tag{47}$$

Noting that the acoustic wave number is $k = \omega/c_o$ Eq. (47) then becomes

$$0 = k_z^2 + k_x^2(1-M^2) + 2Mkk_x - k^2. \tag{48}$$

In order for waves to propagate to the far field the z component of the acoustic wave number, k, must be real. It must also be positive to satisfy the finiteness condition. The boundary condition at the plate requires that the x component of the acoustic wave number equal the wave number in the plate. The result of these constraints combined with Eq. (48) is that

$$\frac{k}{M-1} < k_x < \frac{k}{M+1}, \tag{49}$$

in order for waves to propagate to the far field. (Note that if $M=0$ we are left with the familiar no-flow requirement that $-k<k_x<k$ for far-field radiation.) So, as the Mach number increases, the breadth of the radiating (or supersonic) wave number region increases (approaching infinity as $M\to 1$) and is no longer centered on $k=0$. It is well established that the radiation from finite plates is related to the wave number spectrum of the plate vibration that falls within the super-

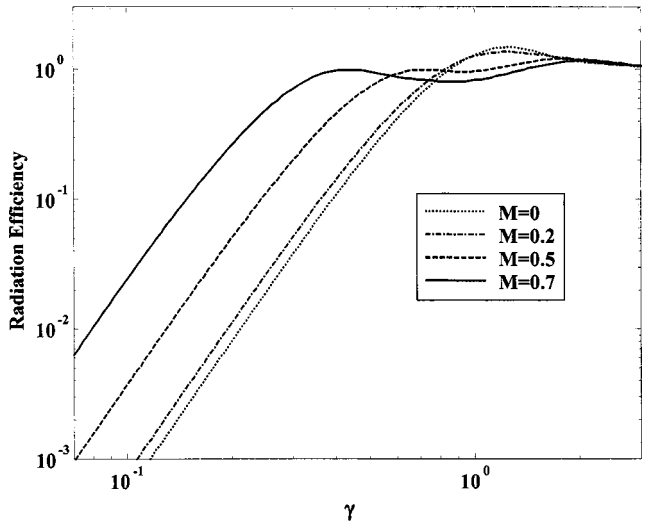

FIG. 5. Radiation efficiency of the (2,1) mode at various Mach numbers.

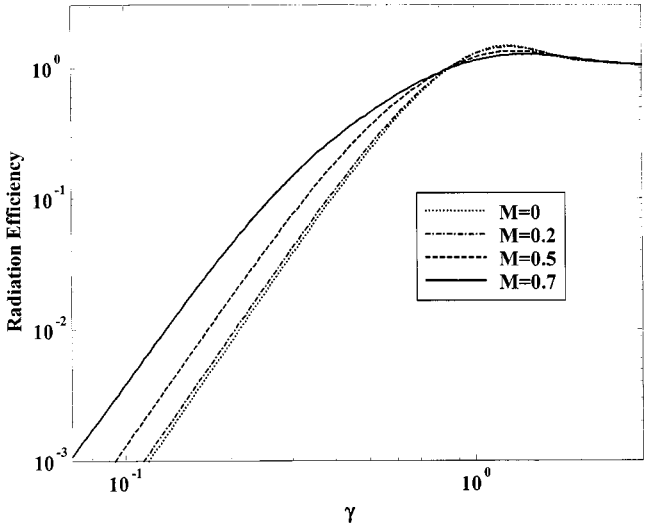

FIG. 6. Radiation efficiency of the (1,2) mode at various Mach numbers.

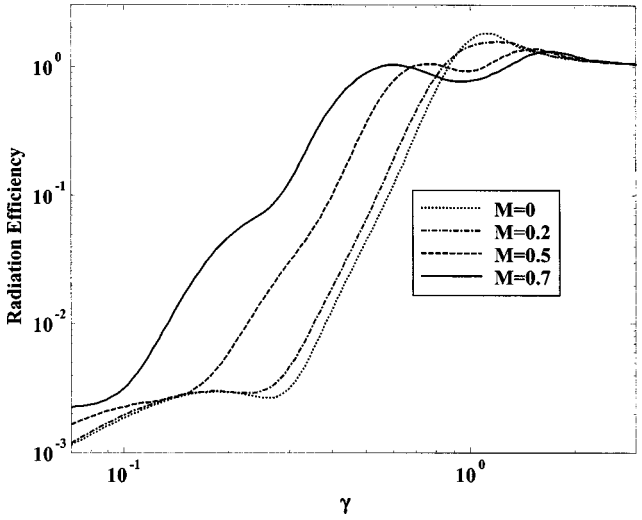

FIG. 8. Radiation efficiency of the (3,3) mode at various Mach numbers.

sonic wave number region.[3,5] So, as the Mach number increases, the width of the supersonic wave number region increases, thus enveloping more of the plate vibration wave number spectrum. This is demonstrated in Fig. 4, which shows the supersonic wave number region superimposed on the wave number spectrum for a two-dimensional plate, $|V(k_x)|^2$. The part of the plate wave number spectrum between the vertical lines is responsible for the far-field radiation. As is evident in Fig. 4, as the Mach number increases, the area under the plate vibration spectrum curve increases. In this case one would expect a particularly large increase in going from $M=0.2$ to $M=0.5$ as the supersonic wave number region envelops the spectrum peak. So, the critical frequency shift noted in Fig. 3 is caused by the broadening of the radiating wave number region.

A similar critical frequency shift is noted in the radiation efficiency of the (2,1) plate mode as shown in Fig. 5. It has been previously noted that symmetric plate modes have equal radiation efficiencies into stationary fluids.[3] Not surprisingly, this symmetry is lost in the presence of mean flow. This is demonstrated in Fig. 6, which shows the radiation efficiency for the (1,2) mode. Note that the increase in radiation efficiency is not as prominent for the (1,2) mode as for the (2,1) mode. This result holds for all modes with (odd, even) indices (odd in the flow direction, even in the lateral direction). The effect on critical frequency is most prevalent for (odd, odd) and (even, odd) modes and less so for (even, even) modes. Our subsequent attention will focus on the former.

The radiation efficiencies of the (3,1), (3,3), (5,1), and (6,1) modes are shown in Figs. 7, 8, 9, and 10, respectively. Note that, as in the previous cases, the critical frequency decreases in each case. Also note that, as the Mach number increases, a local maxima in the radiation efficiency appears above the critical frequency. This is the effect of the shift in coincidence frequency for waves propagating downstream as the supersonic region begins to envelop the plate vibration spectral peak. Also of interest in the higher mode cases (e.g., Figs. 9 and 10) are the effects on the mid-wave number region ripples. These ripples have been attributed to the onset of sidelobes in the radiation pattern.[4,6] Since lobes radiating upstream and downstream are affected differently by the

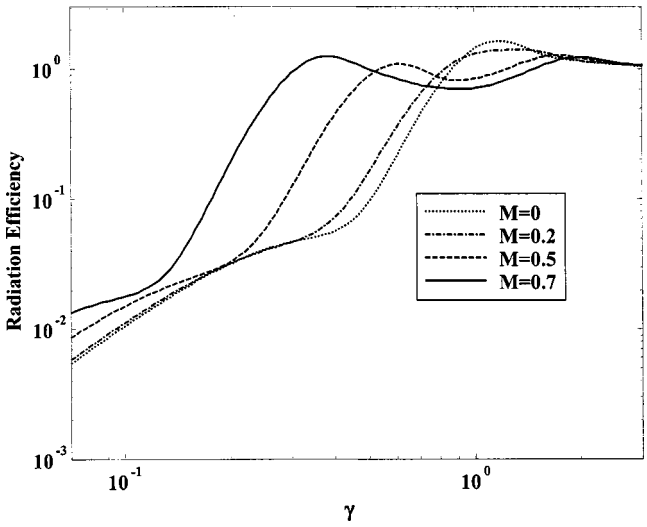

FIG. 7. Radiation efficiency of the (3,1) mode at various Mach numbers.

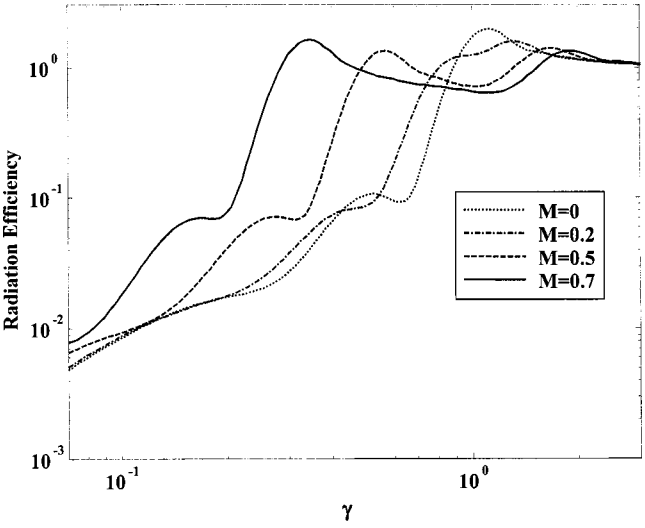

FIG. 9. Radiation efficiency of the (5,1) mode at various Mach numbers.

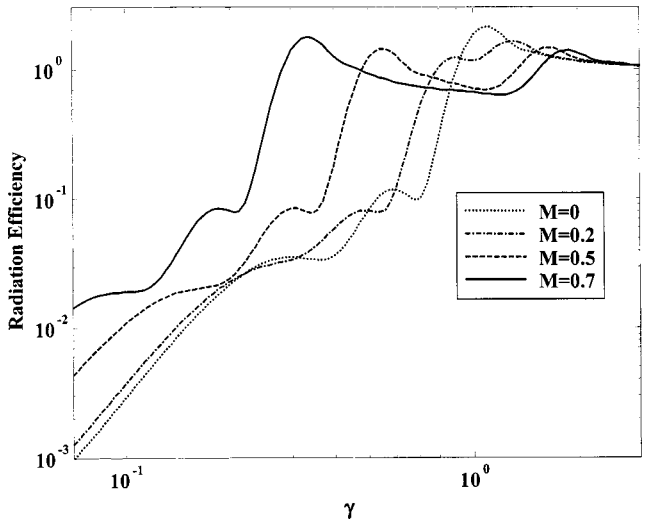

FIG. 10. Radiation efficiency of the (6,1) mode at various Mach numbers.

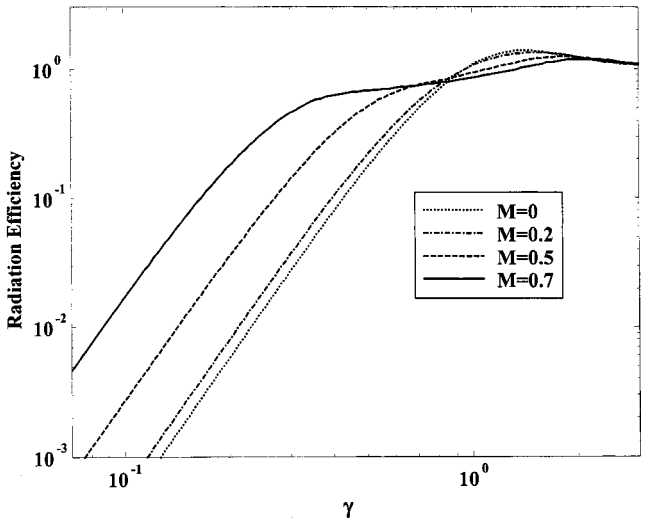

FIG. 12. Radiation efficiency of the (2,1) mode at various Mach numbers with an aspect ration of $a/b=2$.

convection, the ripples in the radiation efficiency curves are not just shifted in wave number but are also distorted relative to the no-flow case.

C. Effects of plate aspect ratio and flow on radiation efficiency

The effect of plate aspect ratio and flow on radiation efficiency is addressed in this section. The radiation efficiency of the (2,1) mode for a plate with aspect ratios of $a/b=0.5$ and $a/b=2.0$ are shown in Figs. 11 and 12, respectively. Note that, relative to the aspect ratio 1 case shown in Fig. 5, the effect of aspect ratios of less than 1 is to increase the radiation efficiency below the critical frequency. The radiation efficiency is decreased when the aspect ratio is greater than 1, as demonstrated by comparing Fig. 11 with Fig. 5. This trend was found to be true for all modes studied. This is somewhat in contrast to the findings of Wallace,[6] who noted that any departure from an aspect ratio of unity resulted in an increase in radiation efficiency. A careful comparison of Fig. 5 with Figs. 11 and 12 indicates that this trend is only weakly related to the Mach number.

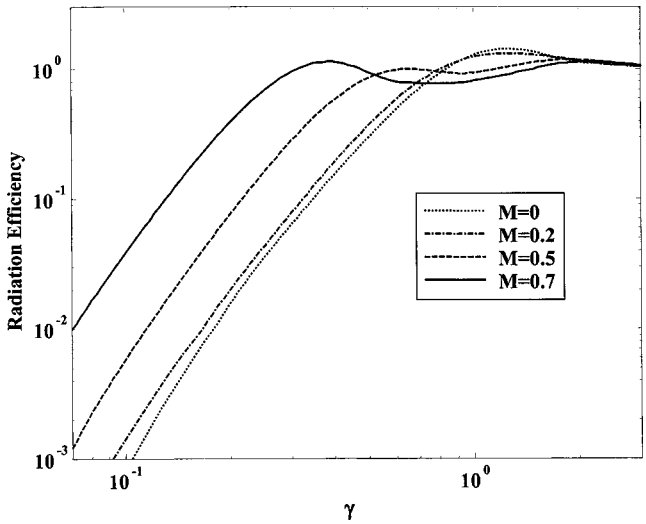

FIG. 11. Radiation efficiency of the (2,1) mode at various Mach numbers with an aspect ration of $a/b=0.5$.

D. A note on flow-induced coupling

The coupling induced by the flow has not been considered in this investigation. It is clear from the aeroelasticity literature that as the Mach number increases the effects of coupling become quite significant, particularly for supersonic flow.[1] (On a side note, according to the aeroelasticity community the nondimensional dynamic pressure, $\lambda = \rho U^2 a^3/D$, is a better indicator of coupling than the Mach Number.[1]) However, the analytical development presented here could easily accommodate intermodal coupling. This could be accomplished by including all necessary terms of the summation in Eq. (15) in the transfer function of Eq. (40). The SVD modeling technique readily supports this. The difficulty in studying the effect of coupling does not lie in the computational aspects but rather in the available analysis tools. It is traditional in structural acoustics literature to consider radiation as it relates to structural modes. However, as flow velocity increases the *in vacuo* modes of the structure are no longer orthogonal with respect to the problem. They are not, in fact, the modes of the problem at hand. Therefore, the radiation that is produced by the imposed motion of one *in vacuo* mode includes the influence of some other *in vacuo* modes.

Several methods for performing the analysis of coupled system radiation present themselves, all of which have their inherent weaknesses. One possible way to analyze this problem is to find the modes of the coupled problem and to look at the radiation from each of them. However, this presents difficulty in comparing radiation from one flow condition to another since the mode shapes, and hence the wave number content, will be different. Sgard, Attalla, and Nicolas[9] chose a novel approach based on the coherence between modes as a means to quantifying the strength of coupling. This provides some interesting insight into the effects of coupling,

but still makes comparison between different flow cases difficult. Last, the author considered the total radiation efficiency (including all modes simultaneously).[13] Assuming that enough modes are included in the analysis, an accurate result can be found that allows a fair comparison between different flow conditions. However, the complexity of the overall plate vibration makes any meaningful analysis in the wave number domain difficult. A thorough treatment of the coupled problem is left for a future effort.

IV. CONCLUSIONS

The radiation efficiency of simply supported, rectangular elastic plates into a convected fluid has been presented. The accuracy of the computational approach was established through comparison with previously published results. The most notable effect was that the critical frequency of the individual modes scales downward with increasing flow velocity. This results in a significant increase in the overall radiation efficiency of the plate, particularly in the mid-wave number region. It was noted that the primary cause of the changes in radiation efficiency is the effective increase in the plate phase velocity for waves traveling upstream. It was also noted that, contrary to findings for radiation efficiency without flow, the radiation efficiency decreases when the aspect ration of the plate is greater than 1. Finally, it was demonstrated that flow-induced modal coupling, while potentially having a significant impact on the radiation efficiency, is a rather difficult problem. The difficulty does not lie in the computation, but rather in the selection of metrics that yields a meaningful result.

APPENDIX: EVALUATION OF INFLUENCE COEFFICIENT INTEGRALS

The following section contains specific evaluations of the integrals in Eqs. (16), (17), and (20) assuming simply supported plate modes. In order to facilitate the integration the plate motion description of Eq. (1) is expanded such that

$$w(x,y,t)=q_n(t)\psi_n(x,y)=q_{pq}(t)\xi_p(x)\eta_q(y), \tag{A1}$$

where the nth mode has x and y indices of p and q, respectively. As an example the first mode corresponds to $n=1$ will likely have x and y indices of $p=1$ and $q=1$. The second mode corresponds to $n=2$ and may have x and y indices of $p=1$ and $q=2$. Substituting Eq. (A1) into Eqs. (16) and (17) results in

$$S_{mn}=\frac{1}{M}\int_0^a \frac{d\xi_p(x)}{dx}\xi_r(x)dx\int_0^b \eta_q(y)\,\eta_s(y)dy, \tag{A2}$$

$$D_{mn}=\frac{1}{MU}\int_0^a \xi_p(x)\xi_r(x)dx\int_0^b \eta_q(y)\,\eta_s(y)dy, \tag{A3}$$

$$G_{mn}=\int_0^a \xi_p(x)e^{-j\alpha x}dx\int_0^b \eta_q(y)e^{-j\gamma y}dy \times\int_0^a \xi_r(x)e^{j\alpha x}dx\int_0^b \eta_s(y)e^{j\gamma y}dy, \tag{A4}$$

where the nth mode has indices (p, q) and the mth mode has indices (r, s). Now, assuming that the plate is simply supported results in

$$\begin{aligned}&\xi_p(\mathrm{x})=\sin(p\pi x)\quad \text{for}\ \ p=1,2,3...,\\ &\eta_q(\mathrm{y})=\sin(q\pi x)\quad \text{for}\ \ q=1,2,3,....\end{aligned} \tag{A5}$$

Substituting this in Eqs. (A2), (A3), and (A4) results in

$$S_{mn}=\frac{1}{M}\int_0^a p\pi\cos(p\pi x)\sin(r\pi x)dx \times\int_0^b \sin(q\pi y)\sin(s\pi y)dy, \tag{A6}$$

$$D_{mn}=\frac{1}{MU}\int_0^a \sin(p\pi x)\sin(r\pi x)dx \times\int_0^b (q\pi y)\sin(s\pi y)dy, \tag{A7}$$

and

$$G_{mn}=\int_0^a \sin(p\pi x)e^{-j\alpha x}dx\int_0^b \sin(q\pi y)e^{-j\gamma y}dy \times\int_0^a \sin(r\pi x)e^{j\alpha x}dx\int_0^b \sin(s\pi y)e^{i\gamma y}dy. \tag{A8}$$

These integrals are available in many mathematics handbooks, resulting in[16]

$$S_{mn}=S_{pqrs}=\begin{cases}0 & \text{for}\ \ p=r\ \ \text{or}\ \ q\neq s\\ \dfrac{bpr}{2M(r^2-p^2)}[1-(-1)^{(p+r)}] & \text{for}\ \ p\neq r\ \ \text{or}\ \ q=s\end{cases}, \tag{A9}$$

$$D_{mn}=D_{pqrs}=\begin{cases}0 & \text{for}\ \ p\neq r\ \ \text{or}\ \ q\neq s\\ \dfrac{ab}{4MU} & \text{for}\ \ p=r\ \ \text{for}\ \ q=s\end{cases}, \tag{A10}$$

$$G_{mn}=G_{pqrs}=[\pi(pqrs)(ab)^2e^{-j(\alpha+\gamma)}]\cdot\left[\frac{(e^{j\alpha}-\cos(p\pi))(e^{j\gamma}-\cos(q\pi))(e^{j\alpha}\cos(r\pi)-1)(e^{j\gamma}\cos(s\pi)-1)}{(p^2\pi^2-\alpha^2)(q^2\pi^2-\gamma^2)(\alpha^2-r^2\pi^2)(\gamma^2-s^2\pi^2)}\right]. \tag{A11}$$

[1] E. H. Dowell, *Aeroelasticity of Plates and Shells* (Noordhoff, Groningen, The Netherlands, 1975).
[2] D. G. Crighton, ''The 1988 Rayleigh Medal lecture: Fluid loading—the interaction between sound and vibration,'' J. Sound Vib. **133**, 1–27 (1989).
[3] F. Fahy, *Sound and Structural Vibration* (Academic, New York, 1985).
[4] M. C. Junger and D. Feit, *Sound, Structures and Their Interaction, 2nd ed.* (The MIT Press, Cambridge, MA, 1986).
[5] M. S. Howe, *Acoustics of Fluid–Structure Interactions* (Cambridge University Press, Cambridge, UK, 1998).
[6] C. E. Wallace, ''Radiation resistance of a rectangular panel,'' J. Acoust. Soc. Am. **51**, 946–952 (1972).
[7] I. D. Abrahams, ''Scattering of sound by an elastic plate with flow,'' J. Sound Vib. **89**, 213–231 (1983).
[8] N. Atalla and J. Nicolas, ''A formulation for mean flow effects on sound radiation from rectangular baffled plates with arbitrary boundary conditions,'' J. Vibr. Acoust. **117**, 22–29 (1995).
[9] F. Sgard, N. Atalla, and J. Nicolas, ''Coupled FEM-BEM approach for mean flow effects on vibro-acoustic behavior of planar structures,'' AIAA J. **32**, 2351–2358 (1994).
[10] S. F. Wu and L. Maestrello, ''Responses of finite baffled plate to turbulent flow excitations,'' AIAA J. **33**, 13–19 (1995).
[11] W. R. Graham, ''The effect of mean flow on the radiation efficiency of rectangular plates,'' Proc. R. Soc. London **454**, 111–137 (1998).
[12] K. D. Frampton and R. L. Clark, ''Power flow in an aeroelastic plate backed by a reverberant cavity,'' J. Acoust. Soc. Am. **102**, 1620–1627 (1997).
[13] K. D. Frampton, ''Radiation efficiency of convected fluid loaded plates,'' in *Proceedings of the Symposium on Flow-Induced Vibration and Noise of Thin Materials, IMECE* (ASME, Nashville, TN, 1999).
[14] K. D. Frampton and R. L. Clark, ''State space modeling of aerodynamic forces on a plate using singular value decomposition,'' AIAA J. **34**, 2627–2630 (1996).
[15] L. Meirovitch, *Analytical Methods in Vibration* (Macmillan, New York, 1967).
[16] M. R. Spiegel, *Mathematical Handbook*, Schaum's Outline Series (McGraw-Hill, New York, 1968).
[17] M. N. Currey and K. A. Cunefare, ''The radiation modes of baffled finite plates,'' J. Acoust. Soc. Am. **98**, 1570–1580 (1995).
[18] K. D. Frampton and R. L. Clark, ''Control of sound transmission through a convected fluid loaded plate with piezoelectric sensoriactuators,'' J. Intell. Mater. Syst. Struct. **8**, 686–696 (1997).
[19] R. L. Clark and K. D. Frampton, ''Aeroelastic structural acoustic control,'' J. Acoust. Soc. Am. **105**, 743–754 (1999).
[20] S. Kung, ''A New Identification and Model Reduction Algorithm via Singular Value Decomposition,'' IEEE 12th Asilomar Conference on Circuits, Systems and Computers, 1978, pp. 705–714.
[21] T. Kailath, *Linear Systems* (Prentice-Hall, Englewood Cliffs, NJ, 1980).

Solving the hypersingular boundary integral equation in three-dimensional acoustics using a regularization relationship

Zai You Yan, Kin Chew Hung,[a] and Hui Zheng
Institute of High Performance Computing, 1 Science Park Road #01-01 The Capricorn, Singapore Science Park II, Singapore 117528

(Received 2 August 2002; revised 2 January 2003; accepted 24 January 2003)

Regularization of the hypersingular integral in the normal derivative of the conventional Helmholtz integral equation through a double surface integral method or regularization relationship has been studied. By introducing the new concept of discretized operator matrix, evaluation of the double surface integrals is reduced to calculate the product of two discretized operator matrices. Such a treatment greatly improves the computational efficiency. As the number of frequencies to be computed increases, the computational cost of solving the composite Helmholtz integral equation is comparable to that of solving the conventional Helmholtz integral equation. In this paper, the detailed formulation of the proposed regularization method is presented. The computational efficiency and accuracy of the regularization method are demonstrated for a general class of acoustic radiation and scattering problems. The radiation of a pulsating sphere, an oscillating sphere, and a rigid sphere insonified by a plane acoustic wave are solved using the new method with curvilinear quadrilateral isoparametric elements. It is found that the numerical results rapidly converge to the corresponding analytical solutions as finer meshes are applied. © *2003 Acoustical Society of America.* [DOI: 10.1121/1.1560164]

PACS numbers: 43.40.Rj, 43.20.Rz, 43.20.Fn [EGW]

I. INTRODUCTION

Boundary element method based on the Helmholtz integral equation has long been applied for the analysis of acoustic radiation and scattering problems. Its significant advantages over other popular numerical techniques such as the finite difference and finite element method include a reduction of dimensionality of the problem by one, and an automatic satisfaction of the radiation boundary condition. However, the classical boundary element method for exterior acoustic problems fails to provide a unique solution at certain frequencies, which are the characteristics of the associated interior problem. The nonuniqueness is a purely mathematical problem arising from the boundary integral formulation rather than from the nature of the physical problem. A detailed description about the nonuniquness problem is presented in Ref. 1.

Several modified integral formulations have been developed to overcome the nonuniqueness problem. By far, the combined Helmholtz integral equation formulation (CHIEF) proposed by Schenck[2] in 1968 and the composite Helmholtz integral equation (CHIE) presented by Burton and Miller[3] in 1971 are the two most popular approaches. In the CHIEF method, Schenck[2] combined the surface Helmholtz integral equation with the interior Helmholtz integral equation to form an overdetermined system of equations, which was then solved using the least-squares procedure. Seybert *et al.*[4] provided a computational method based on the CHIEF method using isoparametric element formulation. Recently, Chen *et al.*[5] extended the CHIEF method to the combined Helmholtz exterior integral equation formulation to solve the interior problems. Although the CHIEF method is very simple to implement, it fails when the interior points are located on a nodal surface of the corresponding interior problem. To date, the selection of some suitable interior points still remains as a difficult problem. On the other hand, the CHIE method uses a linear combination of the Helmholtz integral equation and its normal derivative equation. It was proved that the linear combination of these two integral equations would yield a unique solution for all frequencies with a suitable complex combination coefficient, even if both the Helmholtz integral equation and its normal derivative equation suffer from the nonuniqueness problem. This method appears to be robust for numerical implementation. However, it suffers from a major drawback that hypersingular integral is involved in the normal derivative of the Helmholtz integral equation. Numerical techniques for computing nonsingular, nearly singular, and nearly hypersingular integrals can be found in the review paper by Tanaka *et al.*[6]

Burton and Miller[3] used a double surface integral method throughout the integral equation to reduce the order of the hypersingularity. Although such a technique results in numerically tractable kernels, it is computationally expensive to evaluate a double surface integral. The regularization techniques developed by Meyer *et al.*[7] and Terai[8] are valid for planar element only. Mathews[9] compared the double surface integral method[3] and the regularization technique[7] using quadratic quadrilateral isoparametric elements. It was noted that the regularization technique resulted in $1/r$ type singular integrals over the element near the point of singularity, even if a polar coordinate transformation was employed. Chien *et al.*[10] developed an approach to regularize such hypersin-

[a]Electronic mail: hungkc@ihpc.a-star.edu.sg

 0001-4966/2003/113(5)/2674/10/$19.00

gular integrals by employing certain known identities from the associated interior Laplace problems. Adaptive subdivision around singular points was needed in the numerical computation. Yang[11] successfully implemented this method in the study of acoustic scattering across a wide frequency range. Liu and Rizzo[12] developed a general form of the hypersingular boundary integral equation, which contained at most weakly singular integrals. This weakly singular form was derived by employing certain integral identities involving the static Green's function. Recently, Liu and Chen[13] made an improvement on this method with a new formulation that involves only tangential derivatives of the density function. Especially, C^0 continuous boundary elements were employed in the discretization. Wu *et al.*[14] implemented a regularized normal derivative equation, which converges in the Cauchy principal value sense rather than in the finite-part sense. This equation required the evaluation of tangential derivatives everywhere on the boundary. By taking the advantage of the properties of axisymmetric geometry, Wang *et al.*[15] successfully computed the hypersingular integrals using tangential operators. But this approach can only be applied to the problems with axisymmetric geometry. Hwang[16] regularized the hypersingular Helmholtz integral equation by some identities from the associated Laplace equations. The collocation points were chosen to be the Gauss–Legendre nodes and no interpolation function was assumed for acoustic variables. In that study, an important assumption was that the normal derivative of the dimensionless solid angle was identical to zero as point was on the surface. On the other hand, source distribution for the equipotential surface from the potential theory was employed to regularize the weak singularities. Therefore, the value of equipotential inside the domain must be calculated. A mathematical investigation about the existence of uniqueness theorems of the boundary element methods based on the Helmholtz integral equation was performed by Luke and Martin.[17] They also discussed the treatment of the hypersingular integral by the double surface integral method.

In this paper, the regularization of the hypersingular integral in the CHIE method is investigated through the double surface integral method. As stated earlier, it is computationally expensive to evaluate a double surface integral. Now by introducing the new concept of discretized operator matrix, evaluation of the double surface integral is reduced to the evaluation of the two discretized operator matrices. As a result, the computational cost for calculating CHIE is comparable to that of solving the conventional Helmholtz integral equation as the number of frequencies to be computed increases. This paper is organized into five sections. Following the Introduction, a detailed theoretical formulation of the governing equation for acoustic propagation in unbounded exterior domain is presented. Next, a discretization scheme for the surface boundary integral equations using a set of curvilinear quadrilateral isoparametric elements is discussed. A new concept of discretized operator matrix is introduced here. The double surface integral is discretized according to this new concept and the discretized operator matrix of the hypersingular integral operator N_0 is found. The hypersingularity in the integral operator N_k is eliminated using the operation $N_k - N_0$. Then, numerical calculations are performed for pulsating and oscillating sphere radiation and plane acoustic wave scattering from a rigid sphere. Three kinds of surface Helmholtz integral equations have been solved. They are the conventional Helmholtz integral equation (HIE), the normal derivative of the conventional Helmholtz integral equation (NDHIE), and the composite Helmholtz integral equation (CHIE). Finally a conclusion is drawn.

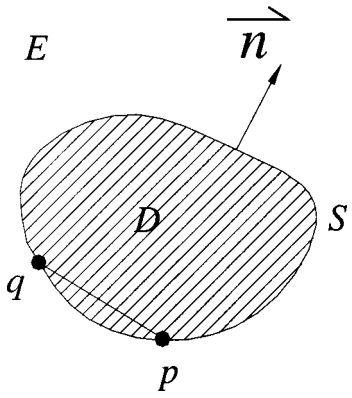

FIG. 1. Notation for a structure with smooth surface.

II. THEORETICAL DEVELOPMENT

Consider the acoustic pressure field in the exterior unbounded domain E. The acoustic field is either radiated by a finite body with smooth surface S vibrating with prescribed velocity distribution or scattered of acoustic waves from rigid surface S. The exterior infinite fluid medium is assumed to be homogeneous. Sound travels in the fluid medium with speed c and the fluid density is ρ. The normal vector at any point on the surface is taken to be the inward normal as shown in Fig. 1.

The governing differential equation[1] of the exterior acoustic domain in steady-state linear acoustics is the well-known Helmholtz equation,

$$(\nabla^2 + k^2)\varphi = 0. \tag{1}$$

The Neumann boundary condition on the boundary surface S can be expressed as

$$\frac{\partial \varphi}{\partial n} = i\omega\rho v_n. \tag{2}$$

In case of acoutic radiation, the acoustic pressure φ must satisfy the Sommerfeld radiation condition at infinity,

$$\lim_{r\to\infty} \int\int \left(\frac{\partial \varphi}{\partial r} + ikr\right)^2 dS = 0, \tag{3}$$

where φ represents the acoustic pressure, ω represents the circular frequency, k is the wave number, and v_n denotes the normal surface velocity.

By using the Green's second identity, the surface Helmholtz integral equation that satisfies the Sommerfeld radiation condition is

$$\int\int \left(\varphi(q) \frac{\partial G_k(p,q)}{\partial n_q} - G_k(p,q) \frac{\partial \varphi(p)}{\partial n_q} \right) dS_q = \frac{1}{2} \varphi(p). \tag{4}$$

The free-space Green's function G_k for the three-dimensional wave equation is

$$G_k(p,q) = e^{-ikr}/4\pi r, \quad r = |p-q|, \tag{5}$$

where p is the source point anywhere on the surface, and q is the field point on the surface, see Fig. 1. r represents the Euclidean distance between points p and q.

In operator notation,[8] Eq. (5) can be written as

$$\left[-\frac{1}{2} I + M_k \right] \varphi = L_k \frac{\partial \varphi}{\partial n}, \tag{6}$$

where

$$L_k \mu = \int\int \mu(q) G_k(p,q) dS_q, \tag{7}$$

$$M_k \mu = \int\int \mu(q) \frac{\partial G_k(p,q)}{\partial n_q} dS_q. \tag{8}$$

It is well known that the above surface Helmholtz integral equation, Eq. (4), leads to nonuniqueness solutions at certain frequencies that are the characteristics of the associated interior problem. As discussed in Sec. I, remedies to resolve the problem of nonuniqueness have been investigated by many researchers. Here, the CHIE method is studied.

The CHIE method is based on a linear combination of the surface Helmholtz integral equation, Eq. (4), and its normal derivative with respect to the source point. The resulting equation was proven to have unique solutions at all wave numbers, which can be expressed in operator notation as

$$\left\{ -\frac{1}{2} I + M_k + \alpha N_k \right\} \varphi = \left\{ L_k + \alpha \left[\frac{1}{2} I + M_k^T \right] \right\} \frac{\partial \varphi}{\partial n}, \tag{9}$$

where α, the coupling constant, is chosen to be strictly complex when wave number k is a real number. Here α takes the value $-i/k$. The integral operators N_k and M_k^T can be expressed as

$$\begin{aligned} N_k \mu &= \int\int \mu(q) \frac{\partial^2 G_k(p,q)}{\partial n_p \partial n_q} dS_q, \\ M_k^T \mu &= \int\int \mu(q) \frac{\partial G_k(p,q)}{\partial n_p} dS_q. \end{aligned} \tag{10}$$

The main drawback of the CHIE method is the numerical treatment of the hypersingular integral kernel N_k that appears in the normal derivative equation. Burton and Miller[3] used a regularization relationship, which replaces a hypersingular integral operator with two weakly singular integral operators, to deal with the hypersingularity in operator N_k. The regularization relationship used is

$$L_0 N_0 = [M_0 + \tfrac{1}{2} I][M_0 - \tfrac{1}{2} I] = M_0^2 - \tfrac{1}{4} I, \tag{11}$$

where L_0, N_0, and M_0 are integral operators identical to L_k, N_k, and M_k except that the kernels of L_0, N_0, and M_0 contain $G_0(p,q) = 1/4\pi r$ not G_k.

Therefore, the composite integral operators $L_0 N_0$ and M_0^2 are defined as

$$L_0 N_0 \mu(p) = \int\int G_0(p,q) \left\{ \int\int \frac{\partial^2 G_0(q,t)}{\partial n_q \partial n_t} \mu(t) dS_t \right\} dS_q, \tag{12}$$

$$M_0^2 \mu(p) = \int\int \frac{\partial G_0(p,q)}{\partial n_q} \left\{ \int\int \frac{\partial G_0(q,t)}{\partial n_t} \mu(t) dS_t \right\} dS_q. \tag{13}$$

According to the regularization relationship, Eq. (11), Burton and Miller[3] developed the following transformation to remove the hypersingularity in the operator N_k:

$$L_0 N_k = L_0[N_k - N_0] + L_0 N_0 = L_0[N_k - N_0] + M_0^2 - \tfrac{1}{4} I, \tag{14}$$

where

$$\begin{aligned} &L_0[N_k - N_0] \mu(p) \\ &\quad = \int\int G_0(p,q) \\ &\qquad \times \left[\int\int \frac{\partial^2 [G(q,t) - G_0(q,t)]}{\partial n_t \partial n_q} \mu(t) dS_t \right] dS_q. \end{aligned} \tag{15}$$

Then the CHIE in Eq. (9) was rewritten as

$$\begin{aligned} &L_0 \{ -\tfrac{1}{2} I - M_k + \alpha (N_k - N_0) \} \varphi + \alpha [M_0^2 - \tfrac{1}{4} I] \varphi \\ &\quad = L_0 \left\{ L_k + \alpha \left[\frac{1}{2} I + M_k^T \right] \right\} \frac{\partial \varphi}{\partial n}. \end{aligned} \tag{16}$$

In Eq. (16), the hypersingular integral operator N_k has been transformed into several weakly singular integral operators. However, the composite integral operators, such as $L_0[N_k - N_0]$ and M_0^2, are double surface integrals and these integrals must be computed for each frequency step. It is very inefficient to numerically implement such an approach. Therefore, even though it gives rise to tractable kernels, it is abandoned by most of the researchers. In this paper, the regularization relationship, Eq. (11), will be applied. A new method is proposed to discretize it. Finally a highly efficient approach is developed to solve the hypersingular integral.

III. DISCRETIZATION OF THE INTEGRAL OPERATORS

The integral operators are discretized using eight-noded, quadratic quadrilateral isoparametric surface elements which allows the integration of the interpolated variables over a three-dimensional surface to be carried out within a standard basis square in the (ξ, η) local coordinate space. The global Cartesian coordinates x are related to the nodal global coordinates x_i by

$$x(\xi, \eta) = \sum_{i=1}^{8} N_i(\xi, \eta) x_i. \tag{17}$$

$N_i(\xi, \eta)$ is the shape function[8] for the quadratic quadilateral elements with nodes numbered in counterclockwise fashion. The acoustic variables φ and $\partial\varphi/\partial n$ are approximated over each element by the shape functions, that is,

TABLE I. Comparison of computational time for different methods.

Model	Method	Per frequency step (s)	For N_0 operator (s)
24-element	Double surface integral [Eq. (16)]	148.751 67	x
	Proposed method [Eq. (35)]	1.081 555 2	0.751 080 0
	HIE [Eq. (6)]	1.041 497 7	x
96-element	Double surface integral [Eq. (16)]	8290.458	x
	Proposed method [Eq. (35)]	12.998 693	8.752 585
	HIE [Eq. (6)]	12.818 431	x

$$\varphi=\sum_{i=1}^{8} N_i\varphi_i, \quad \frac{\partial\varphi}{\partial n}=\sum_{i=1}^{8} N_i\frac{\partial\varphi_i}{\partial n}, \tag{18}$$

where φ_i represents the nodal quantity of the variable φ. With these relationships, integration of the integral operator L_k expressed in Eq. (7) can be discretized using n elements as follows:

$$\begin{aligned} L_k\varphi &= \int_S\int G_k(p,q)\varphi(q)dS_q \\ &= \sum_{j=1}^{n}\sum_{i=1}^{8}\int_{\Delta S_j}\int G_k(p,q)N_i(\xi,\eta)J(\xi,\eta)d\xi d\eta\varphi_i \\ &= B_k\{\varphi\}, \end{aligned} \tag{19}$$

where $\{\varphi\}=[\varphi_1,\varphi_2,\ldots K,\varphi_t]^T$, t is the total global node number. The square matrix B_k is defined as the discretized operator matrix of the integral operator L_k,

$$B_{ki,m}=\sum_{m=f(j,l)}\int_{\Delta S_j}\int N_l G_{kij}dS_q, \tag{20}$$

where the function $f(j,l)$ is the mapping function for the relation between element nodes and global nodes. Comparing Eq. (20) and Eq. (7), it is evident that the element of the discretized operator matrix takes the same integral form as the integral operator.

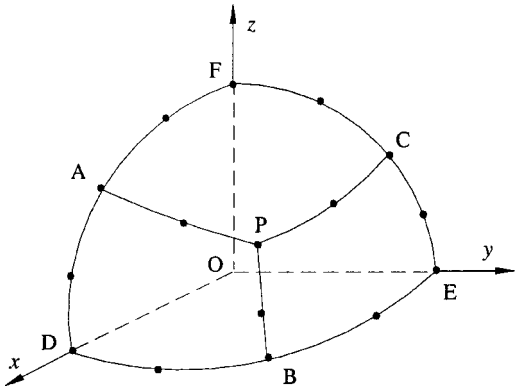

FIG. 2. Surface discretization of one octant of a sphere using 3 curvilinear quadrilateral elements.

Similarly, the discretized operator matrix A_k for the integral operator M_k is expressed as

$$A_{ki,m}=\sum_{m=f(j,l)}\int_{\Delta S_j}\int N_l\frac{\partial G_{kij}}{\partial n}dS_q, \tag{21}$$

and that for the discretized operator matrices B_0 and D_0 of the integral operators L_0 and N_0 are

$$\begin{aligned} B_{0i,m} &= \sum_{m=f(j,l)}\int_{\Delta S_j}\int N_l G_{0ij}(p,q)dS_q, \\ D_{0i,m} &= \sum_{m=f(j,l)}\int_{\Delta S_j}\int \frac{\partial^2 G_{0ij}(p,q)}{\partial n_p\partial n_q}N_l dS_q. \end{aligned} \tag{22}$$

In the past, the composite integral operator L_0N_0 in Eq. (12) was directly approximated as

$$\begin{aligned} L_0N_0\mu_i(p) &= \sum_{j=1}^{n}\int_{\Delta S_j}\int G_{0ij}(p,q) \\ &\quad\times\left\{\sum_{l=1}^{n}\int_{\Delta S_l}\int\frac{\partial^2 G_{0jl}(q,t)}{\partial n_q\partial n_t}\sum_{k=1}^{8}N_k\mu_k dS_t\right\}dS_q \\ &= \sum_{j=1}^{n}\sum_{l=1}^{n}\sum_{k=1}^{8}\int_{\Delta S_j}\int G_{0ij}(p,q) \\ &\quad\times\left\{\int_{\Delta S_l}\int\frac{\partial^2 G_{0jl}(q,t)}{\partial n_q\partial n_t}N_k dS_t\right\}dS_q\mu_k, \end{aligned} \tag{23}$$

which is obviously too computationally expensive to evaluate, and has deterred from implementing the regularization relationship, Eq. (11).

In this study, a new idea is proposed to discretized the composite integral operator L_0N_0. Assuming that

$$\psi(q)=\int_S\int\frac{\partial^2 G_0(q,t)}{\partial n_q\partial n_t}\mu(t)dS_t, \tag{24}$$

over each element, using the shape functions N_l, we have

$$\psi=\sum_{l=1}^{8}N_l\psi_l, \tag{25}$$

where ψ_l is nodal value of function ψ. Based on the definition of discretized operator matrix, Eq. (24) can be dis-

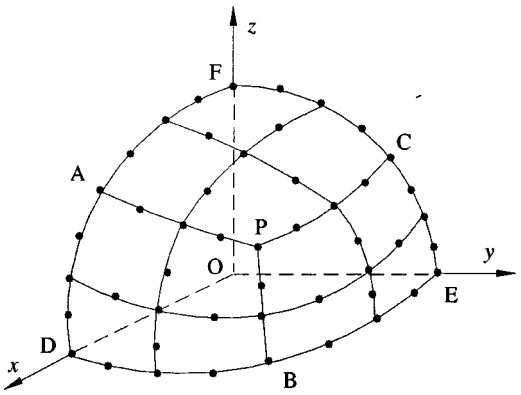

FIG. 3. Surface discretization of one octant of a sphere using 12 curvilinear quadrilateral elements.

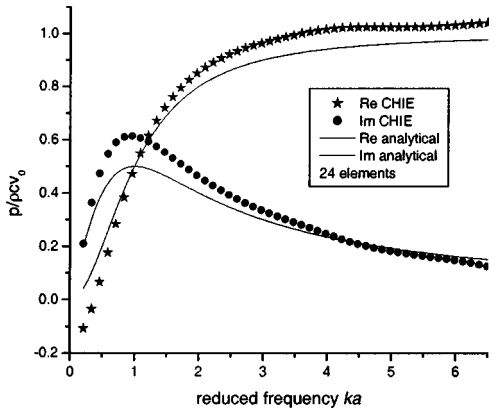

FIG. 5. Dimensionless surface acoustic pressures from a pulsating sphere using CHIE with 24 elements.

cretized and expressed in the form of discretized operator matrix,

$$\{\psi\}=D_0\{\mu\}, \tag{26}$$

where $\{\psi\}$ and $\{\mu\}$ are values at global nodes, and are constants in the integration. D_0 is the discretized operator matrix of integral operator N_0. Because N_0 is a hypersingular integral operator and the integral does not exist in either conventional or Cauchy-principal value sense. The operator matrix D_0 should be obtained in the Hadamard finite part sense.[16]

Substituting Eq. (24) into Eq. (12), we have

$$L_0N_0\mu(p)=\int\int_S G_0(p,q)\psi(q)dS_q. \tag{27}$$

The discretization of Eq. (27) can be expressed in discretized operator matrix form as

$$E_0\{\mu\}=B_0\{\psi\}, \tag{28}$$

where E_0 is the discretized operator matrix of the composite integral operator L_0N_0. Substituting Eq. (26) into Eq. (28), we have

$$E_0\{\mu\}=B_0D_0\{\mu\}. \tag{29}$$

Because the regularization relationship, Eq. (11), is an identity formulation and μ is an arbitrary function, the discretized operator matrix E_0 is equal to the product of B_0 and D_0,

$$E_0=B_0D_0. \tag{30}$$

The discretized operator matrix A_0^2 corresponding to the composite integral operator M_0^2 can be obtained in the same way. A_0 is the discretized operator matrix of integral operator M_0,

$$A_{0,im}=\sum_{m=f(j,l)}\int\int_{\Delta S_j}N_l\frac{\partial G_{0ij}}{\partial n}dS_q. \tag{31}$$

Therefore, the regularization relationship, Eq. (11), can be expressed in the form of discretized operator matrices as

$$B_0D_0=A_0^2-\tfrac{1}{4}I. \tag{32}$$

Then, we have

$$D_0=B_0^{-1}(A_0^2-\tfrac{1}{4}I). \tag{33}$$

Now the double surface integrations in the regularization relationship, Eq. (11), have been reduced to the product of surface integrations. Above all, the discretized operator matrix of the hypersingular integral operator N_0 as higher-order elements are implemented is explicitly found for the first time.

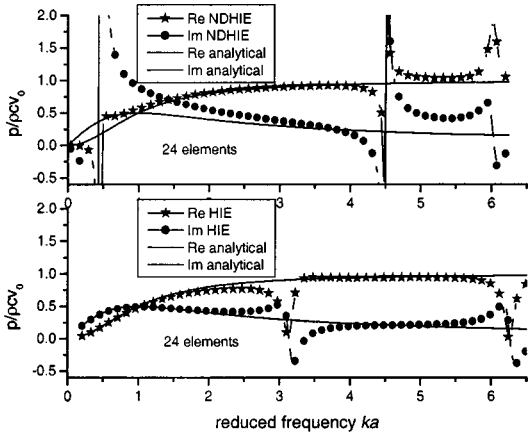

FIG. 4. Dimensionless surface acoustic pressures from a pulsating sphere using HIE and NDHIE with 24 elements.

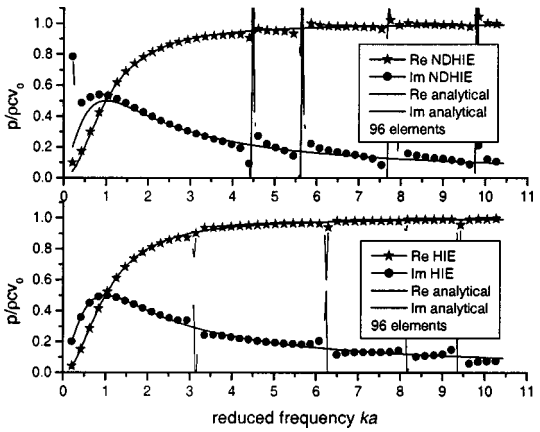

FIG. 6. Dimensionless surface acoustic pressures from a pulsating sphere using HIE and NDHIE with 96 elements.

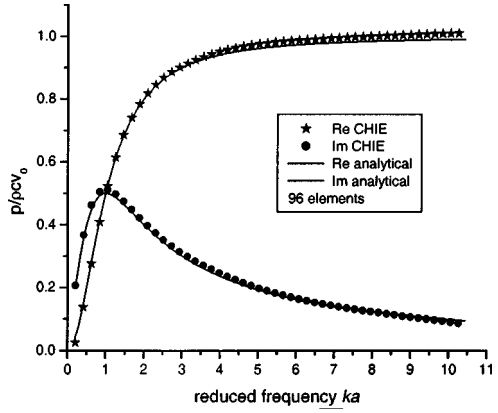

FIG. 7. Dimensionless surface acoustic pressures from a pulsating sphere using CHIE with 96 elements.

IV. TREATMENT OF THE HYPERSINGULARITY IN OPERATOR N_k

Now applying the integral operator N_0, Eq. (9) can be modified as

$$[-\tfrac{1}{2}I+M_k+\alpha[(N_k-N_0)+N_0]]\varphi = \left[L_k+\alpha\left[\frac{1}{2}I+M_k^T\right]\right]\frac{\partial\varphi}{\partial n}. \tag{34}$$

The term (N_k-N_0) has removed the hypersingularity in operator N_k. Only the term N_0 still contains hypersingularity. Using the discretized operator matrices, Eq. (34) can be discretized and expressed as

$$\left[-\frac{1}{2}I+A_k+\alpha[D+D_0]\right]\{\varphi\}=\left[B_k+\alpha\left[\frac{1}{2}I+F\right]\right]\left\{\frac{\partial\varphi}{\partial n}\right\}, \tag{35}$$

where D is the discretized operator matrix for integral operator (N_k-N_0) and F is the discretized operator matrix of integral operator M_k^T,

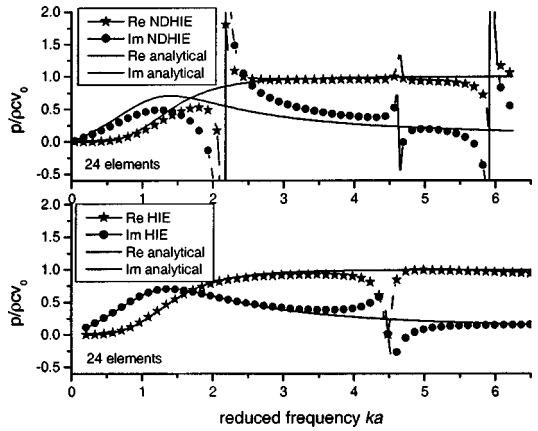

FIG. 8. Dimensionless surface acoustic pressures for an oscillating sphere using HIE and NDHIE with 24 elements as $\theta=0°$.

$$D_{im}=\sum_{m=f(j,l)}\int\int_{\Delta S_j} N_l\frac{\partial^2(G_{kij}-G_{0ij})}{\partial n_t\partial n_q}dS_q,$$
$$F_{im}=\sum_{m=f(j,l)}\int\int_{\Delta S_j} N_l\frac{\partial G_{0ij}(p,q)}{\partial n_p}dS_q. \tag{36}$$

Since the discretized operator matrix D_0 of the hypersingular integral operator N_0 has already been obtained by Eq. (33), the linear equation system in Eq. (35) can be numerically solved using a weakly singular integration scheme, such as that proposed by Lachat and Watson.[18]

As the discretized operator matrix D_0 is independent of frequency, the computational cost of solving Eq. (35) is comparable to that of solving the conventional Helmholtz integral equation, Eq. (6), as the number of frequencies to be computed increases. Table I presents the computational time for solving the problem of pulsating sphere radiation, which will be described in detail in Sec. V, using different methods. Here the computer is a Dell Latitude C610 notebook. Clearly, the new approach greatly improves the computational efficiency as compared to the technique applied in Eq. (16). For each frequency step, the computational time for the new method is very close to that for the HIE Eq. (6).

V. NUMERICAL EXAMPLES

In order to test the accuracy and efficiency of the new method, two cases of acoustic radiation and a case of plane acoustic wave scattering from rigid sphere have been computed. The two acoustic radiation problems are pulsating sphere radiation and oscillating sphere radiation. In all three examples, the surface of a sphere is, respectively, modeled using 24 and 96 curvilinear quadrilateral isoparametric elements to observe the convergence of the new method. Each octant of a sphere is discretized using 3 and 12 surface elements as shown in Figs. 2 and 3. Due to symmetry, the problems are computed in half space. For radiation problems, three linear equation systems are computed. They are the conventional Helmholtz integral equation (HIE), normal derivative equation of the conventional Helmholtz integral equation (NDHIE), and the composite Helmholtz integral equation (CHIE). Comparisons between the numerical results of these three linear equation systems clearly show the nonuniqueness problem and the effectiveness of the new method. For plane acoustic wave scattering from a rigid sphere, only the conventional Helmholtz integral equation and the composite Helmholtz integral equation are computed. These examples are computed using the in-house developed code, SSFI. This software is suitable to solve multi-domain acoustic problems, especially the problems of structural–acoustic interaction.

A. Pulsating sphere radiation

The analytical solution[10] of the acoustic pressure $\varphi(r)$ for a sphere of radius a, pulsating with an uniform radial velocity v_0, is given by

$$\frac{\varphi(r)}{\rho c v_0}=\frac{a}{r}\frac{ika}{1+ika}e^{-ik(r-a)}. \tag{37}$$

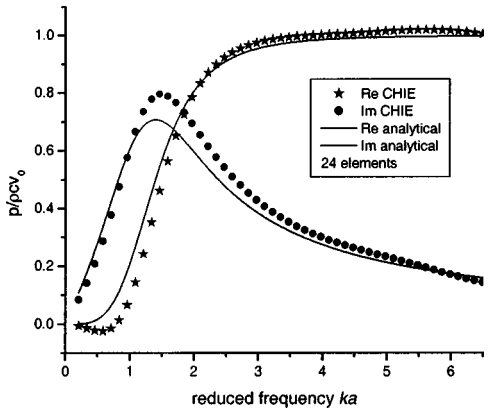

FIG. 9. Dimensionless surface acoustic pressures for an oscillating sphere using CHIE with 24 elements as $\theta=0°$.

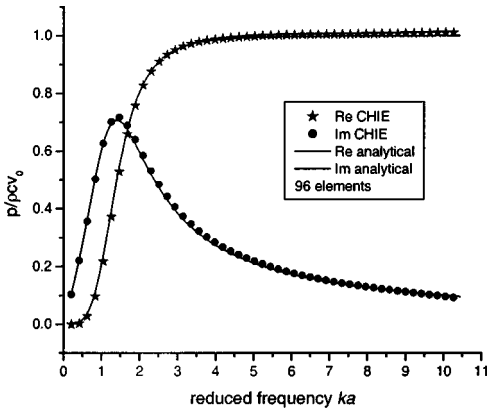

FIG. 11. Dimensionless surface acoustic pressures for an oscillating sphere using CHIE with 96 elements as $\theta=0°$.

Dimensionless surface acoustic pressures as a function of the reduced frequency *ka* are plotted in Figs. 4–7. Figures 4 and 5 present the results obtained using 24 elements. While the numerical results obtained using 96 elements are presented in Figs. 6 and 7. The comparison between the numerical results obtained using the HIE and NDHIE with the corresponding analytical solutions is shown in Figs. 4 and 6. It is evident that the HIE equation fails to provide unique solutions near $ka=\pi$, 2π, 8.13, and 3π and the NDHIE equation fails to provide unique solutions near $ka=0$, 4.493, 5.616, 7.725, and 9.784. On the other hand, the numerical results calculated using the CHIE, which are plotted in Figs. 5 and 7, are unique for all the frequencies. Figure 7 shows that with a finer mesh, the numerical results obtained using the CHIE agree very well with the analytical solutions for *ka* up to 10.5.

B. Oscillating sphere radiation

The analytical solution[10] of the acoustic pressure for an oscillating sphere of radius a with a radial velocity $v_0\cos(\theta)$ is given by

$$\frac{\varphi(r)}{\rho c v_0}=\left(\frac{a}{r}\right)^2\cos(\theta)\frac{ika(1+ikr)}{2(1+ika)-k^2a^2}e^{-ik(r-a)}, \qquad (38)$$

where θ is the angle made by the radial direction and the direction of the velocity. In the following example, $\theta=0$ is along the direction of z axis.

The dimensionless surface acoustic pressures at $\theta=0$ are displayed as function of the reduced frequency in Figs. 8–11. Figures 8 and 9 show the results obtained using the model with 24 elements. The results for 96 elements model are shown in Figs. 10 and 11. The comparison between the numerical results obtained using the HIE and NDHIE with the corresponding analytical solutions is shown in Figs. 8 and 10. As can be seen, the HIE equation fails to provide unique solutions near $ka=4.493$, 7.725, and 9.349. Similarly, the NDHIE equation also suffers from the nonuniqunness near $ka=2.062$, 5.911, 5.616, 6.787, 8.521, and 9.150, whereas the numerical results calculated using the CHIE displayed in Figs. 9 and 11 are unique for all the wave numbers. Figure 11 shows that with a finer mesh discretization the surface acoustic pressures for an oscillating sphere obtained using the CHIE agree quite well with the corresponding analytical solutions for *ka* up to 10.5.

C. Plane acoustic wave scattering from a rigid sphere

To provide a further test of the new technique, the scattering of a plane acoustic wave $\varphi_I=\varphi_0 e^{-ikz}$ from a rigid sphere of radius a is computed. The analytical solution[19] of

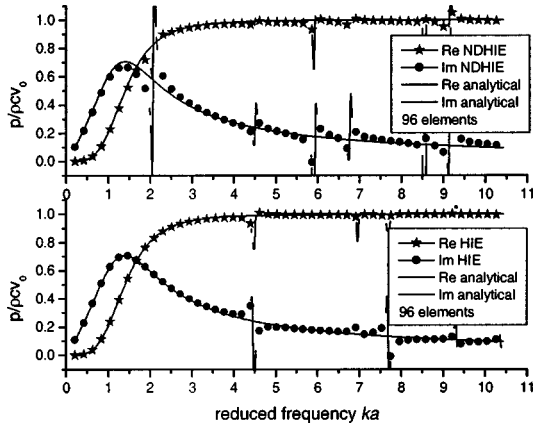

FIG. 10. Dimensionless surface acoustic pressures for an oscillating sphere using HIE and NDHIE with 96 elements as $\theta=0°$.

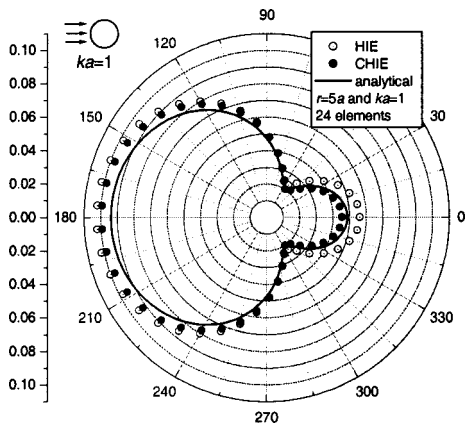

FIG. 12. The angular dependence of φ_s/φ_0 as $ka=1.0$ and $r=5a$ with 24 elements.

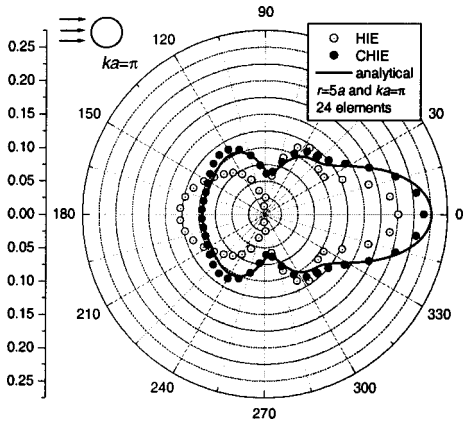

FIG. 13. The angular dependence of φ_s/φ_0 as $ka=\pi$ and $r=5a$ with 24 elements.

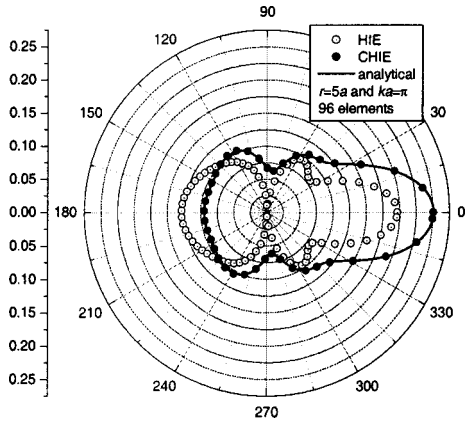

FIG. 16. The angular dependence of φ_s/φ_0 as $ka=\pi$ and $r=5a$ with 96 elements.

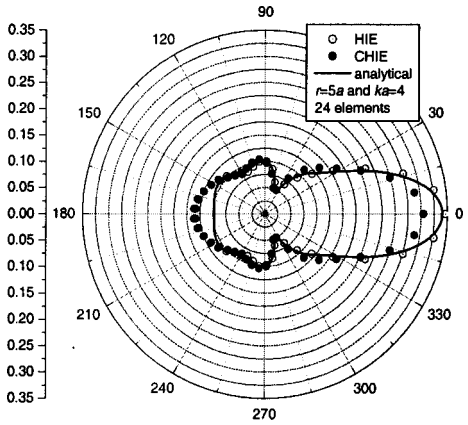

FIG. 14. The angular dependence of φ_s/φ_0 as $ka=4$ and $r=5a$ with 24 elements.

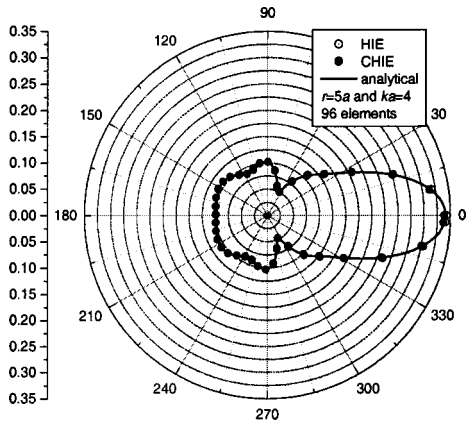

FIG. 17. The angular dependence of φ_s/φ_0 as $ka=4$ and $r=5a$ with 96 elements.

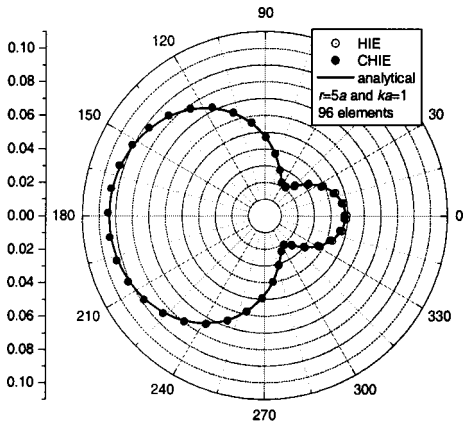

FIG. 15. The angular dependence of φ_s/φ_0 as $ka=1.0$ and $r=5a$ with 96 elements.

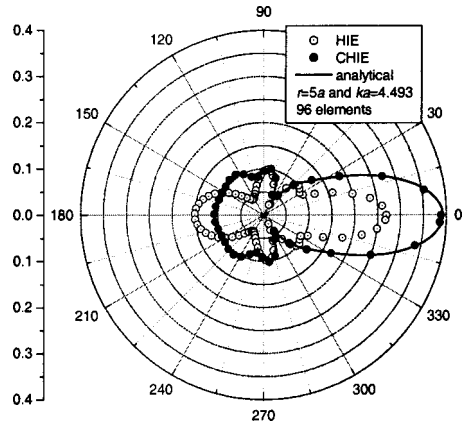

FIG. 18. The angular dependence of φ_s/φ_0 as $ka=4.493$ and $r=5a$ with 96 elements.

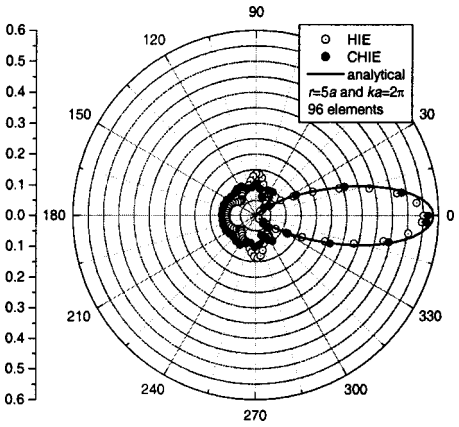

FIG. 19. The angular dependence of φ_s/φ_0 as $ka=2\pi$ and $r=5a$ with 96 elements.

the scattered acoustic pressure $\varphi_s(r,\theta)$ at a distance r from the center of the sphere and at an angle θ from the direction of the incoming wave is given by

$$\frac{\varphi_s(r,\theta)}{\varphi_0}=\sum_{m=0}^{\infty}\left[-(-i)^m(2m+1)\frac{j_m'(ka)}{h_m'(ka)}\right]h_m(kr)\times P_m(\cos\theta), \tag{39}$$

where j_m is spherical Bessel function of the first kind and h_m is spherical Hankel function of the second kind. P_m denotes Legendre polynomial of order m.

Figures 12–14 present the results obtained using the 24-element model. While Figs. 15–19 present the results obtained using the 96-element model. The results at $r=5a$ are presented. Figures 12 and 15 show the angular dependency of φ_s/φ_0 as $ka=1.0$. It is observed that the numerical results obtained using both the HIE and CHIE agree well with the analytical solutions. Figures 13 and 16 show the results at the reduced frequency $ka=\pi$. As $ka=\pi$ is one of the characteristic frequencies,[11] the scattered acoustic pressures obtained using the HIE do not agree with the corresponding analytical solutions. However, the scattered acoustic pressures obtained using the CHIE again agree very well with the analytical solutions. Figures 14 and 17 demonstrate the angular dependency of φ_s/φ_0 at $ka=4$. Comparisons between these two figures indicate that the numerical results converge rapidly as finer meshes are applied. Angular dependencies of φ_s/φ_0 at $ka=4.493$ and 2π are presented in Figs. 18 and 19, respectively. These frequencies correspond to the characteristic frequencies of either the conventional Helmholtz integral equation or its normal derivative equation. All these figures demonstrate that the new technique can overcome the nonuniqueness problem encountered in acoustic scattering analysis using the conventional Helmholtz integral equation.

VI. CONCLUSIONS

By introducing the concept of discretized operator matrix, a new method has been generated to overcome the hypersingular integral involved in the composite Helmholtz integral equation proposed by Burton and Miller.[3] The discretized operator matrix of a composite integral operator is proved to be just the product of the two discretized operator matrices corresponding to the two integral operators, which construct the composite integral operator. The double surface integrals employed by Burton and Miller[3] are discretized according to this new concept. Above all, the discretized operator matrix of the hypersingular integral operator N_0 is explicitly found for the first time as higher-order elements are implemented. Subsequently, an elimination of the hypersingularity in the integral operator N_k is implemented using the formulation N_k-N_0. The new method greatly improves the computational efficiency and has tractable integral kernels. Numerical calculations are performed for pulsating and oscillating sphere radiation and plane acoustic wave scattering from a rigid sphere with curvilinear quadrilateral isoparametric elements being employed. As finer meshes are applied, the numerical results agree quite well with the corresponding analytical solutions. Here surface of the object is constrained to be smooth enough. Further investigations will extend the new technique to problems with arbitrary shape structure.

[1] R. D. Ciskowski and C. A. Brebbia, *Boundary Element Methods in Acoustics* (Computational Mechanics, Souththampton, Boston, 1991).
[2] H. A. Schenck, "Improved integral formulation for acoustic radiation problems," J. Acoust. Soc. Am. **44**, 41–58 (1968).
[3] A. J. Burton and G. F. Miller, "The application of integral equation methods to the numerical solution of some exterior boundary value problems," Proc. R. Soc. London, Ser. A **323**, 201–210 (1971).
[4] A. F. Seybert, B. Soenarko, F. J. Rizzo, and D. J. Shippy, "An advanced computational method for radiation and scattering of acoustic waves in three dimensions," J. Acoust. Soc. Am. **77**, 362–368 (1985).
[5] I. L. Chen, J. T. Chen, S. R. Kuo, and M. T. Liang, "A new method for true and spurious eigensolutions of arbitrary cavities using the combined Helmholtz exterior integral equation formulation method," J. Acoust. Soc. Am. **109**, 982–998 (2001).
[6] M. Tanaka, V. Sladek, and J. Sladek, "Regularization techniques applied to boundary element methods," Appl. Mech. Rev. **47**, 457–499 (1994).
[7] W. L. Meyer, W. A. Bell, and B. T. Zinn, "Boundary integral solutions of three dimensional acoustic radiation problems," J. Sound Vib. **59**, 245–262 (1978).
[8] T. Terai, "On calculation of sound fields around three dimensional objects by integral equation methods," J. Sound Vib. **69**, 71–100 (1980).
[9] I. C. Mathews, "Numerical techniques for three dimensional steady-state fluid-structure interaction," J. Acoust. Soc. Am. **79**, 1317–1325 (1986).
[10] C. C. Chien, H. Rajiyah, and S. N. Atluri, "An effective method for solving the hyper-singular integral equations in 3-D acoustics," J. Acoust. Soc. Am. **88**, 918–937 (1990).
[11] S.-A. Yang, "Acoustic scattering by a hard and soft body across a wide frequency range by the Helmholtz integral equation method," J. Acoust. Soc. Am. **102**, 2511–2520 (1997).
[12] Y. J. Liu and F. J. Rizzo, "A weakly-singular form of the hypersingular boundary integral equation applied to 3-D acoustic wave problems," Comput. Methods Appl. Mech. Eng. **96**, 271–287 (1992).
[13] Y. J. Liu and S. H. Chen, "A new form of the hypersingular boundary integral equation for 3-D acoustics and its implementation with C0 boundary elements," Comput. Methods Appl. Mech. Eng. **173**, 375–386 (1999).
[14] T. W. Wu, A. F. Seybert, and G. C. Wan, "On the numerical implementation of a Cauchy principal value integral to insure a unique solution for acoustic radiation and scattering," J. Acoust. Soc. Am. **90**, 554–560 (1991).
[15] W. P. Wang, N. Atalla, and J. Nicolas, "A boundary integral approach for acoustic radiation of axisymmetric bodies with arbitrary boundary conditions valid for all wave numbers," J. Acoust. Soc. Am. **101**, 1468–1478 (1997).

[16] W. S. Hwang ''Hyper-singular boundary integral equations for exterior acoustic problems,'' J. Acoust. Soc. Am. **101**, 3336–3342 (1997).
[17] C. J. Luke and P. A. Martin, ''Fluid-solid interaction: Acoustic scattering by a smooth elastic obstacle,'' SIAM (Soc. Ind. Appl. Math.) J. Appl. Math. **55**, 904–922 (1995).
[18] J. C. Lachat and J. O. Watson, ''Effective numerical treatment of boundary integral equations,'' Int. J. Numer. Methods Eng. **10**, 991–1005 (1976).
[19] M. C. Junger, ''Sound scattering by thin elastic shells,'' J. Acoust. Soc. Am. **24**, 366–373 (1952).

Evaluation of decay times in coupled spaces: Bayesian decay model selection[a),b)]

Ning Xiang[c)]
National Center for Physical Acoustics and Department of Electrical Engineering, University of Mississippi, 1 Coliseum Drive, University, Mississippi 38677

Paul M. Goggans
Department of Electrical Engineering, University of Mississippi, Anderson Hall, University, Mississippi 38677

(Received 28 May 2002; revised 23 November 2002; accepted 24 January 2003)

This paper applies Bayesian probability theory to determination of the decay times in coupled spaces. A previous paper [N. Xiang and P. M. Goggans, J. Acoust. Soc. Am. **110**, 1415–1424 (2001)] discussed determination of the decay times in coupled spaces from Schroeder's decay functions using Bayesian parameter estimation. To this end, the previous paper described the extension of an existing decay model [N. Xiang, J. Acoust. Soc. Am. **98**, 2112–2121 (1995)] to incorporate one or more decay modes for use with Bayesian inference. Bayesian decay time estimation will obtain reasonable results only when it employs an appropriate decay model with the correct number of decay modes. However, in architectural acoustics practice, the number of decay modes may not be known when evaluating Schroeder's decay functions. The present paper continues the endeavor of the previous paper to apply Bayesian probability inference for comparison and selection of an appropriate decay model based upon measured data. Following a summary of Bayesian model comparison and selection, it discusses selection of a decay model in terms of experimentally measured Schroeder's decay functions. The present paper, along with the Bayesian decay time estimation described previously, suggests that Bayesian probability inference presents a suitable approach to the evaluation of decay times in coupled spaces. [DOI: 10.1121/1.1562151]

PACS numbers: 43.55.Br, 43.55.Ka [MK]

I. INTRODUCTION

A previous paper[1] discussed estimation of the decay times in coupled spaces using a Bayesian parameter estimation approach given that the number of decay rates is already known. However, in most decay time determinations, the number of decay rates (modes) is not always readily known. Eyring[2] pointed out that energy decay functions on a logarithmic scale are not generally linear for coupled spaces having different natural reverberation times or even for a single room with nonuniformly distributed absorption and no diffusing scheme. In effect, the sound energy decay in a single-space room can be of multi-rate character. Therefore, the practical application of the proposed decay time evaluations is not only the analysis of sound decay in coupled spaces but also in single spaces, such as in those reverberation chambers which often yield inconsistent absorption data, probably due to lack of diffusion. In contrast, single-rate energy decay can also be observed in coupled spaces, depending on the size of the coupling aperture, the position of the sound receiver, and the natural reverberation time of each space. Often acousticians have to answer the question, ''How many decay rates are present in the collected data?'' before the relevant decay times can be properly estimated. As discussed in previous works,[1,3,4] decay functions obtained from measured room impulse responses using Schroeder's backward integration[5] contain inherent characteristic curvature towards the upper limit of the integration. This characteristic curvature impedes identification of different decay modes. Visual inspection of Schroeder decay functions will not always reveal the number of decay rates. An algorithmic determination of decay order (number of decay rates) is needed in practice.

The subject of the present paper is the application of Bayesian probability theory to the problem of estimating the number of decay rates present in Schroeder decay functions. The Bayesian method essentially calculates the probability of decay models with different decay order based on the experimentally measured data. The Bayesian literature refers to this as model comparison and selection (MCS).

A model-based approach using a generalized least square (LS) principle[4] can also estimate decay times. The LS approach and all other parameter estimations, including Bayesian decay time estimation,[1] are all subject to the question of how many decay modes are present in the measured data. In resolving this question, the Bayesian approach proves to be more comprehensive than the LS approach, since a Bayesian framework can provide quantitative tools for both the model selection and the parameter estimation.

Similar to the decay time estimation problem described in Ref. 1, systematic development of a Bayesian formalism for MCS starts with application of the Bayes theorem, followed by incorporation of prior information and then marginalization (defined in Ref. 1). Any interest in parameter

[a)]Portions of this work were presented at the 141st and 143rd meetings of the Acoustical Society of America [J. Acoust. Soc. Am. **109**, 2283(A) (2001); **111**, 2332(A) (2002)].
[b)]Dedicated to Prof. Dr. Jens Blauert on the occasion of his 65th birthday.
[c)]Electronic mail: nxiang@olemiss.edu

values will be pushed into the background of the current problem through marginalization. Marginalization allows attention to be focused on the probabilities for different decay in a preselected set of decay models. In Sec. III of the present paper, we develop the MCS formalism toward evaluation of the Schroeder decay functions in a step-by-step manner for the convenience of architectural acousticians. This development of the MCS relies heavily on other works,[6–12] particularly Ref. 6. In Sec. IV we discuss results obtained using the Bayesian MCS with experimentally measured decay functions from coupled spaces. Additional detailed derivations involved in the Bayesian MCS of the present paper are given in the Appendix.

II. MULTI-RATE DECAY

A previous paper[1] established a decay model for Schroeder decay functions with multiple decay modes. In the present paper, a set of these decay models $\mathbf{F}=\{F_1,F_2,\ldots,F_M\}$ is under consideration with

$$F_s(\mathbf{A}_s,\mathbf{B}_s,t_k)=\sum_{j=1}^{s+1} A_{sj}G_j(B_{sj},t_k),$$
$$0\leqslant t_k\leqslant L \quad \text{and} \quad 1\leqslant s\leqslant M, \tag{1}$$

and

$$G_j(B_{sj},t_k)=\begin{cases}\exp(-B_{sj}\cdot t_k) & \text{for } 1\leqslant j\leqslant s,\\ L-t_k & \text{for } j=m=s+1,\end{cases} \tag{2}$$

where s is the *decay order* (number of exponential decay modes), $m=s+1$ is the number of additive terms of the model, M is the total number of different models under examination, $\mathbf{A}_s=\{A_{s1},A_{s2},\ldots,A_{sm}\}$ contains *linear* parameters, $\mathbf{B}_s=\{B_{s1},B_{s2},\ldots,B_{ss}\}$ contains *nonlinear* parameters, and L represents the upper limit of the Schroeder backward integration.[5] The decay times are related to the nonlinear parameter by the expression $T_{sj}=13.8/B_{sj}$, for $1\leqslant j\leqslant s$. In this paper, time will be treated as a discrete variable t_k. The following derivations drop the subscript s of $\mathbf{A}_s$, $\mathbf{B}_s$ and all other parameters given model F_s for simplicity. As a specific case of a double-rate Schroeder decay function, the decay model with $s=2$, $m=3$ reads

$$F_2(\mathbf{A},\mathbf{B},t_k)=A_1\exp(-B_1\cdot t_k)+A_2\exp(-B_2\cdot t_k)$$
$$+A_3(L-t_k). \tag{3}$$

The third term on the right-hand side in Eq. (3) is associated with background noise in experimentally measured room impulse responses from which Schroeder decay functions are calculated. It results in the characteristic curvature that occurs towards the upper limit of the integration in a logarithmic plot of Schroeder decay functions [e.g., Fig. 1(a)]. This curvature is well documented in Refs. 1, 3, and 4 and, as previously mentioned, it impedes the determination of the decay order s.

The decay model in Eq. (1) is in the form of a general linear model.[1] It describes sound energy decay in enclosed spaces after a steady-state sound excitation in the spaces is switched off. Therefore, only positive-valued linear parameters $\mathbf{A}=\{A_1,A_2,\ldots,A_m\}$ are of primary interest for decay time determination in architectural acoustics practice, although there may exist other acoustical situations or other kinds of systems without this restriction.

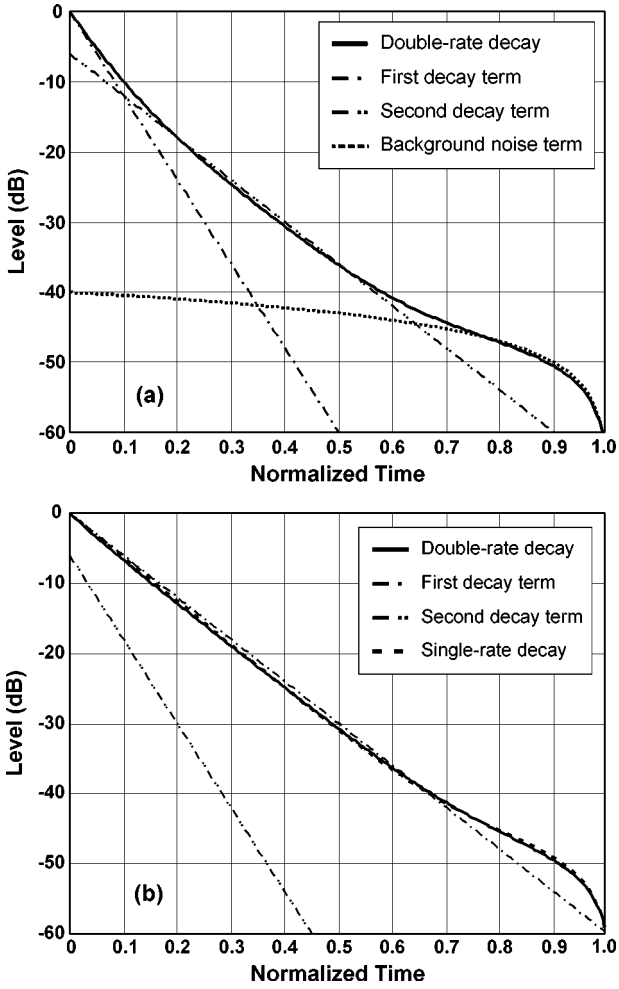

FIG. 1. Schroeder decay functions simulated using a double-rate decay model [Eq. (3)]. Normalized time scale is used for simplicity. (a) Decay parameters fulfill the conditions in Eq. (4) ($0.5=T_1<T_2=1.0$ and $10\log_{10}A_1=0$ dB; $10\log_{10}A_2=-6$ dB). (b) Decay parameters break the conditions in Eq. (4) ($1.0=T_1>T_2=0.5$ and $10\log_{10}A_1=0$ dB; $10\log_{10}A_2=-6$ dB). A single-rate decay curve with $T_1=0.96$ is also plotted for comparison. The double-rate decay curve in (b) is very close to the single-rate curve.

In addition, architectural acousticians are primarily concerned with the conditions

$$T_1<T_2<\cdots<T_s \quad \text{and} \quad A_1>A_2>\cdots>A_m>0, \tag{4}$$

as pointed out in Ref. 13. Figure 1 illustrates two opposite examples simulated using the double-rate decay model in Eq. (3). A normalized time scale is used for simplicity. In Fig. 1(a), the Schroeder decay function fulfills the conditions in Eq. (4) with $T_1=0.5$, $T_2=1.0$ and with $10\log_{10}A_1=0$ dB, $10\log_{10}A_2=-6$ dB, and $10\log_{10}A_3=-40$ dB. In Fig. 1(b), the decay parameters of the decay function break the conditions in Eq. (4) with the same linear parameters as those in Fig. 1(a) but $T_1=1.0$ and $T_2=0.5$. This double-rate decay function is very close to the single-rate one with $T_1=0.96$ as plotted in Fig. 1(b) for comparison. The smaller the parameter A_2 is relative to A_1, the closer the double-rate decay function will be to a single-rate function.

Often the decay function in Fig. 1(b) represents a sound decay process in coupled spaces sensed by a sound receiver in the primary space when the secondary space possesses a shorter natural reverberation time than that of the primary space. In this situation, the coupling aperture acts as an absorption area resulting in a shorter decay time than the natural reverberation time in the primary space. It is, therefore, reasonably to treat the energy decay in a statistical sense as a single-rate decay.

III. BAYESIAN MODEL SELECTION

This section develops Bayesian formalism for model comparison and selection (MCS). Bayesian MCS relies on the measured Schroeder decay functions to compare and select the most likely decay model(s) among a specified model set of competing decay models. The development of Bayesian MCS formalism begins with calculating the posterior probability for a competing model by applying the Bayes theorem. Bayesian MCS focuses on the posterior probabilities of the competing models rather than specific model parameters. Therefore, any interest in parameter values will be pushed into the background of the current problem through marginalization. The development needs to introduce some additional parameters when dealing with residual errors between the measured data and models and dealing with prior probabilities. Marginalization will also remove these additional parameters. Eventually the MCS is accomplished by evaluating the posterior probability for each competing model.

The decay model F_s with s decay modes among $\mathbf{F}=\{F_1,F_2,\ldots,F_M\}$ approximates the Schroeder decay function:[5]

$$d_k=F_s(\mathbf{A},\mathbf{B},t_k)+\varepsilon_k,\quad 1\leqslant k\leqslant K, \tag{5}$$

in such a way that $F_s(\mathbf{A},\mathbf{B},t_k)$ models the Schroeder decay function d_k with a residual error ε_k. As stated in Ref. 1, this error is defined as the difference between the measured data and the model and so is a function of s, $\mathbf{A}$, and $\mathbf{B}$. It includes measurement errors, fluctuations in the decay function data, and modeling errors. The current problem is specified by the background information I including the hypothesis that the data consist of a systematic part $F_s(\cdot)$ and an additive error part ε_k, and that the error has a finite-valued variance σ^2 (see Sec. III B in Ref. 1) and a set $\mathbf{F}$ of M mutually exclusive, exhaustive competing models specified by Eqs. (1) and (2).

A. Posterior probability of competing models

The probability $p(F_s|\mathbf{D},I)$ for model F_s given the Schroeder decay function $\mathbf{D}=\{d_1,d_2,\ldots,d_K\}$ and the relevant background information I can be expressed using Bayes theorem:

$$p(F_s|\mathbf{D},I)=\frac{p(F_s|I)p(\mathbf{D}|F_s,I)}{P(\mathbf{D}|I)},\quad l\leqslant s\leqslant M. \tag{6}$$

In examining mutually exclusive, exhaustive decay models in the model set $\mathbf{F}=\{F_1,F_2,\ldots,F_M\}$, $p(\mathbf{D}|I)$ is the probability of the data given only the background information I:

$$p(\mathbf{D}|I)=\sum_{s=1}^{M} p(F_s|I)p(\mathbf{D}|F_s,I). \tag{7}$$

In effect, $p(\mathbf{D}|I)$ is a normalization constant over all models. Equation (7) is the consequence of the competing models being mutually exclusive and exhaustive. For a mutually exclusive and exhaustive set of models

$$\sum_{s=1}^{M} p(F_s|\mathbf{D},I)=1. \tag{8}$$

$p(F_s|I)$ is *prior* probability for model F_s given only the information denoted by I. The proposition I represents one's state of knowledge about the models *before* obtaining the data $\mathbf{D}$ (or before analyzing the data once the data are obtained). The *global likelihood* for the data given model F_s and the information I is denoted $p(\mathbf{D}|F_s,I)$. The likelihood indicates how well the specified model fits the data. The *posterior* probability $p(F_s|\mathbf{D},I)$ is so-called because it applies *after* the data and the prior information have been taken into account.

The calculation of the posterior probability for models according to Eqs. (6) and (7) requires assignment of the prior probability for the model F_s and the calculation of the global likelihood. An appropriate uninformative prior probability given M possible models is the uniform prior probability $1/M$ that expresses no preference for any model in the model set $\mathbf{F}$. Using this prior and Eq. (7) the posterior probability for the model becomes

$$p(F_s|\mathbf{D},I)=\frac{p(\mathbf{D}|F_s,I)}{\Sigma_{s=1}^{M}p(\mathbf{D}|F_s,I)}. \tag{9}$$

Equation (9) is of central importance for the decay model selection and will be discussed in more detail in the following sections.

B. Global likelihood

The global likelihood for the data is vital to the calculation of the posterior probability for models as indicated in Eq. (9). The joint probability for the data and the model parameters $p(\mathbf{D},\mathbf{A},\mathbf{B}|F_s,I)$ can yield the global likelihood for the data $p(\mathbf{D}|F_s,I)$ in terms of

$$p(\mathbf{D}|F_s,I)=\int \mathrm{d}\mathbf{A}\,\mathrm{d}\mathbf{B}\,p(\mathbf{D},\mathbf{A},\mathbf{B}|F_s,I) \tag{10}$$

in which the domain of the integral spans the (multidimensional) parameter space of the model F_s.

Applying the product rule to the joint probability $p(\mathbf{D},\mathbf{A},\mathbf{B}|F_s,I)$ yields

$$p(\mathbf{D},\mathbf{A},\mathbf{B}|F_s,\sigma,I)$$
$$=p(\mathbf{B}|F_s,I)p(\mathbf{A}|\mathbf{B},F_s,I)p(\mathbf{D}|\mathbf{A},\mathbf{B},F_s,\sigma,I) \tag{11}$$

so that the global likelihood given the variance σ^2 for the model F_s reads

$$p(\mathbf{D}|F_s,\sigma,I)$$
$$=(\sqrt{2\pi}\sigma)^{-K}\int d\mathbf{B}\,p(\mathbf{B}|F_s,I)\int d\mathbf{A}\,p(\mathbf{A}|\mathbf{B},F_s,I)$$
$$\times\exp\left\{\frac{-1}{2\sigma^2}\sum_{k=1}^{K}[d_k-F_s(\mathbf{A},\mathbf{B},t_k)]^2\right\}. \quad (12)$$

Equation (12) incorporates the likelihood function expression for $p(\mathbf{D}|\mathbf{A},\mathbf{B},F_s,\sigma,I)$ given in the previous paper [see Eq. (9) in Ref. 1]. Since the task is to determine the posterior probability for the decay models, both the linear parameters **A** and the nonlinear **B** parameters can be treated as nuisance parameters and the explicit dependence of the likelihood on **A** and **B** can then be removed by considering all their possible values through marginalization.[1] The following section pursues the marginalization over these parameters.

C. Marginalization over amplitude A

$p(\mathbf{A}|\mathbf{B},F_s,I)$ is the prior probability of parameters **A** assuming that the nonlinear parameters **B** of a decay model F_s are given. No specific information is assumed about the values of the parameters **A** expect that their values are finite. Application of the principle of maximum entropy to assign the prior probability,[7,8] given only the finite value assumption, results in the Gaussian assignment of

$$p(\mathbf{A}|\mathbf{B},F_s,\zeta,I)=\sqrt{\lambda_1\cdots\lambda_m}(\sqrt{2\pi}\zeta)^{-m}$$
$$\times\exp\left\{\frac{-1}{2\zeta^2}\sum_{k=1}^{K}\left[\sum_{l=1}^{m}\sum_{j=1}^{m}A_lA_jG_lG_j\right]\right\}. \quad (13)$$

In Eq. (13) the dependence of $p(\mathbf{A}|\mathbf{B},F_s,\zeta,I)$ on **B** is through the function G. The variance ζ^2 is associated with the uncertainty of the model parameter **A**, and λ_j is the jth eigenvalue of the matrix g_{ij} of Eq. (10) in Ref. 1. With the addition of the new parameter ζ, the global likelihood of the data in Eq. (12) reads

$$p(\mathbf{D}|F_s,\sigma,\zeta,I)$$
$$=(\sqrt{2\pi})^{-(K+m)}\sigma^{-K}\zeta^{-m}\int d\mathbf{A}\,d\mathbf{B}\,\sqrt{\lambda_1\cdots\lambda_m}p(\mathbf{B}|F_s,I)$$
$$\times\exp\left\{\frac{-1}{2\zeta^2}\sum_{k=1}^{K}\left[\sum_{l=1}^{m}\sum_{j=1}^{m}A_lA_jG_lG_j\right]\right\}$$
$$\times\exp\left\{\frac{-1}{2\sigma^2}\sum_{k=1}^{K}[d_k-F_s(\mathbf{A},\mathbf{B},t_k)]^2\right\}. \quad (14)$$

The global likelihood of the data can further be rewritten as

$$p(\mathbf{D}|F_s,\sigma,\zeta,I)$$
$$=(\sqrt{2\pi})^{-(K+m)}\sigma^{-K}\zeta^{-m}\int d\boldsymbol{\alpha}\,d\mathbf{B}\,p(\mathbf{B}|F_s,I)$$
$$\times\exp\left\{-\sum_{j=1}^{m}\frac{\alpha_j^2}{2\zeta^2}-\frac{1}{2\sigma^2}\left[\Delta-2\sum_{j=1}^{m}\alpha_jq_j+\sum_{j=1}^{m}\alpha_j^2\right]\right\}, \quad (15)$$

using Eqs. (13) and (17) in a previous paper[1] for α_j and q_j, respectively. In Eq. (15), $\boldsymbol{\alpha}=\{\alpha_1,\alpha_2,\ldots,\alpha_m\}$ and

$$\Delta=\sum_{k=1}^{K}d_k^2. \quad (16)$$

Performing the integral over the amplitude parameters $\boldsymbol{\alpha}$ (see Appendix A), the global likelihood simplifies to

$$p(\mathbf{D}|F_s,\sigma,\zeta,I)\approx\frac{(\sqrt{2\pi}\sigma)^{-K+m}}{(\sqrt{2\pi}\zeta)^m}\int d\mathbf{B}\,p(\mathbf{B}|F_s,I)$$
$$\times\exp\left[-\Delta\left(\frac{1-\varphi}{2\sigma^2}+\frac{\varphi}{2\zeta^2}\right)\right], \quad (17)$$

where

$$\varphi=\frac{1}{\Delta}\sum_{j=1}^{m}q_j^2. \quad (18)$$

The function φ represents a normalized form of $\overline{q^2}$ defined in Eq. (20) in Ref. 1, and plays the role of *sufficient indicator* in evaluating the values of the nonlinear parameter **B**.[6]

D. Marginalization over parameter B

When an appropriate model is employed, the data determines the nonlinear parameters well, the posterior probability around the global maximum $\hat{\mathbf{B}}$ falls off rapidly, and there exists a small region in parameter space around $\hat{\mathbf{B}}$ where the normalized sufficient indicator φ in Eq. (18) can be approximated by

$$\varphi\approx\varphi|_{\mathbf{B}=\hat{\mathbf{B}}}. \quad (19)$$

The posterior density function for the nonlinear parameters **B** is multi-modal with extremes of identical value when s is greater than one. Taking the approximation in Eq. (19) and $s!$ multi-modal extremes (see Ref. 1) into account and assuming that these extremes do not overlap to any significant degree, the global likelihood in Eq. (17) becomes

$$p(\mathbf{D}|F_s,\sigma,\zeta,I)\approx\frac{(\sqrt{2\pi}\sigma)^{m-K}s!}{(\sqrt{2\pi}\zeta)^m}$$
$$\times\exp\left[-\Delta\left(\frac{1-\varphi}{2\sigma^2}+\frac{\varphi}{2\zeta^2}\right)\right]\Bigg|_{\mathbf{B}=\hat{\mathbf{B}}}$$
$$\times\int d\mathbf{B}\,p(\mathbf{B}|F_s,I). \quad (20)$$

The further development requires assignment of the prior probability $p(\mathbf{B}|F_s,I)$ for the nonlinear parameters **B** given model F_s. Here little prior information about the values of the parameters **B** is assumed, only that they have finite values. Under this assumption, application of the principle of maximum entropy results in the assignment of a Gaussian prior probability as follows:

$$p(\mathbf{B}|F_s,\gamma,I)=(\sqrt{2\pi}\gamma)^{-s}\exp\left[-\sum_{j=1}^{s}\frac{B_j^2}{2\gamma^2}\right]. \quad (21)$$

The variance γ^2 expresses the uncertainty of the nonlinear parameters **B**. Equation (21) does not express a strong opin-

ion about the parameters provided that γ is large compared to σ. This means that Eq. (21) effectively represents a constant over the range in which the likelihood function of the data is strongly peaked. Substitution of this prior probability into Eq. (20) results in the global likelihood of the data:

$$p(\mathbf{D}|F_s,\sigma,\zeta,\gamma,I)\approx\frac{(\sqrt{2\pi}\sigma)^{m-K}s!}{(\sqrt{2\pi}\zeta)^m(\sqrt{2\pi}\gamma)^s}\times\exp\left[-\Delta\left(\frac{1-\varphi}{2\sigma^2}+\frac{\varphi}{2\zeta^2}\right)-\frac{\beta}{2\gamma^2}\right]\Bigg|_{\mathbf{B}=\hat{\mathbf{B}}}, \tag{22}$$

where

$$\beta=\sum_{j=1}^{s}B_j^2. \tag{23}$$

E. Marginalization over variances

The three variances σ^2, ζ^2, γ^2 are referred to as *hyperparameters* in Bayesian literature. Although their values are unknown, marginalization can remove them from the problem. Marginalization over these hyperparameters requires multiplication of appropriate normalized prior probabilities with the global likelihood in Eq. (22), followed by integration over these parameters. Appropriate prior probabilities for these scale parameters[10] σ, ζ, and γ are Jeffreys priors.[9] However, the Jeffreys prior presents an ''improper'' probability distribution, the integral of which is not normalizable.[10] Nevertheless, the current problem can handle a bounded Jeffreys prior. Application of a normalized, bounded Jeffreys prior[6] for σ, ζ, and γ (see Appendix B) approximates the global likelihood of the data as

$$\begin{aligned}p(\mathbf{D}|F_s,\zeta_a,\zeta_b,\gamma_a,\gamma_b,\sigma_a,\sigma_b,I)&\approx(\sqrt{2\pi})^{-(K+s)}\cdot s!\\&\times\frac{\Gamma(m/2)}{2\log(\zeta_b/\zeta_a)}\frac{\Gamma(s/2)}{2\log(\gamma_b/\gamma_a)}\frac{\Gamma[(K-m)/2]}{2\log(\sigma_b/\sigma_a)}\\&\times\left\{\left(\Delta\frac{\varphi}{2}\right)^{-m/2}\left(\frac{\beta}{2}\right)^{-s/2}\left[\frac{\Delta}{2}(1-\varphi)\right]^{-(K-m)/2}\right\}\Bigg|_{\mathbf{B}=\hat{\mathbf{B}}}\end{aligned} \tag{24}$$

with ζ_a, ζ_b, γ_a, γ_b, and σ_a, σ_b being the bounds of the parameters ζ, γ, and σ, respectively. In Eq. (24), $\Gamma(x)$ is the gamma function of x. So long as models with both linear and nonlinear parameters are compared using the same data (as in the case of multi-rate decay functions), the posterior probability for the model in Eq. (9) is independent of ζ_a, ζ_b, γ_a, γ_b, and σ_a, σ_b because $\log(\zeta_b/\zeta_a)$, $\log(\gamma_b/\gamma_a)$, and $\log(\sigma_b/\sigma_a)$ will appear in both the numerator and the denominator [see Eqs. (27) and (28)]. Hence the global likelihood of the data can be simplified to

$$p(\mathbf{D}|F_s,I)\propto C[\varphi^{-m/2}\beta^{-s/2}(1-\varphi)^{-(K-m)/2}]_{\mathbf{B}=\hat{\mathbf{B}}} \tag{25}$$

with

$$C=(\sqrt{\pi})^{-s}(s!)\Gamma\left(\frac{m}{2}\right)\Gamma\left(\frac{s}{2}\right)\Gamma\left(\frac{K-m}{2}\right). \tag{26}$$

F. Model comparison and selection

To compare which one of the two models F_x and F_y is favored by the data, the ratio of the posterior probability of the two models according to Eq. (9) is evaluated:

$$O=\frac{p(F_y|\mathbf{D},I)}{p(F_x|\mathbf{D},I)}=\frac{p(\mathbf{D}|F_y,I)}{p(\mathbf{D}|F_x,I)}. \tag{27}$$

Equation (27) is referred to as the *odds*. Its logarithmic form is conventionally calculated using

$$E_{yx}=10\log_{10}\frac{p(\mathbf{D}|F_y,I)}{p(\mathbf{D}|F_x,I)} \tag{28}$$

to indicate which model is preferred. E (with dB as the unit) in Eq. (28) is often referred to in relevant Bayesian literature as *Bayesian evidence*. In addition to the model comparison, the model selection is accomplished by evaluating the posterior probability in Eq. (9) for each model throughout the specified model set **F**. Eventually, the data should favor a model with a clearly higher posterior probability.

This section has developed a Bayesian formalism of model comparison and selection (MCS). Bayesian MCS relies on the measured Schroeder decay functions to compare and select the most likely decay model(s) among a specified model set containing M competing decay models. The development of Bayesian MCS formalism begins with calculating the posterior probability for a competing model by applying the Bayes theorem. Expressing no preference for any particular decay model in advance of analyzing the data leads to the assignment of a uniform prior probability for the models. In examining a decay model within a specified, mutually exclusive, exhaustive model set, the posterior probability for a decay model relies solely on the global likelihood function. It can be proven[6] that the MCS described in this section still remains valid if something else outside the model set is not taken into account, since the MCS relies on a relative evaluation of posterior probabilities over the specified model set. Marginalization has removed all linear and nonlinear model parameters and variances arising from residual errors, from the assignment of prior probability on both linear and nonlinear parameters during the development. Eventually the model comparison and selection can be accomplished by evaluating Bayesian evidence or the posterior probability of each model by calculating the global likelihood for the data at the peak position in the nonlinear parameter space. The current paper employs Gibbs sampler (as done in Ref. 1) to determine the peak position in the nonlinear parameter space.

The analytical development arrives at the approximation of $p(\mathbf{D}|F_s,I)$ in Eqs. (25) and (26) by assuming that the nonlinear parameters associated with the peak position of the global likelihood are already well determined. Besides the mean squared value of the nonlinear parameters and some gamma function values determined by the decay order and the number of data points, the normalized sufficient indicator φ at the peak position must be calculated to yield the global likelihood of the data. The development of the MCS formal-

ism in this section has incorporated some approximations to yield a practicable end formalism. In the following section, MCS calculations using experimentally measured data will examine both their validation and the limitation of these approximations.

IV. EXPERIMENTAL RESULTS

This section employs experimentally measured Schroeder decay functions from 1:8 scale-model rooms and real halls to demonstrate how the Bayesian MCS can be applied to decay model determination associated with the decay time evaluation. All room impulse responses (RIRs) have been (octave band-pass) filtered before Schroeder decay functions[5] are calculated from them. All evaluations being discussed below use the normalized decay function data from the time limit at -5 dB to the upper limit of the integration. The upper limit of the integration is selected to be large enough to include a portion of the noise tail in each RIR.

A. Double-rate decay functions

Figure 2 illustrates a RIR measured in 1:8 scale model rooms [Fig. 2(a)], its energy decay curve [Fig. 2(b)], and the Schroeder's decay function [Fig. 2(c)]. The peak-to-noise ratio of the RIR is 53 dB. The primary room of $6.4\times5.6\times3.6$ m^3 in dimension, approximately 129 m^3 in volume of real size, in which the sound source and receiver are located, possesses a natural reverberation time of 0.5 s at 1 kHz. The secondary room of $8\times8\times7.2$ m^3 in dimension, approximately 461 m^3 in volume coupled to the primary room through a coupling aperture of 4 m^2, possesses a natural reverberation time of 1.0 s. Care had to be given to arrange most of the interior surface of both rooms as diffuse as possible within the frequency range of interest. As stated previously, recognition of the number of decay modes from the three forms of presentations in Fig. 2 is not straightforward. When using a single-rate decay model F_1, the posterior probability density function (PPDF) presents a sharp peak at 0.502 s as depicted in Fig. 3(a). Figure 2(c) contains the Schroeder single-rate model curve using this estimated parameter. The normalized sufficient indicator (NSI) φ as given in Eq. (18) around the peak position presents a relatively ''flat'' shape, but still peaked at 0.502 s as depicted in a zoomed presentation in Fig. 3(b). When using a double-rate decay model F_2, the PPDF presents two peaks with equal value over the parameter space (T_1, T_2) as depicted in Fig. 4. Either of them will serve when seeking the global maximum.[1] These 2! equal-valued peaks for dimensionality of two are well separated, meeting the assumption required in Sec. III D when simplifying Eq. (17) to Eq. (20). Figure 5 shows the distribution of the NSI over the same sub-space as given in Fig. 4(c). The NSI peaks at the same location as the PPDF with a relatively ''flat'' shape. The NSIs shown in Figs. 3 and 5 present such a flat shape as to clearly justify the approximation undertaken in Eq. (19). A double-rate model

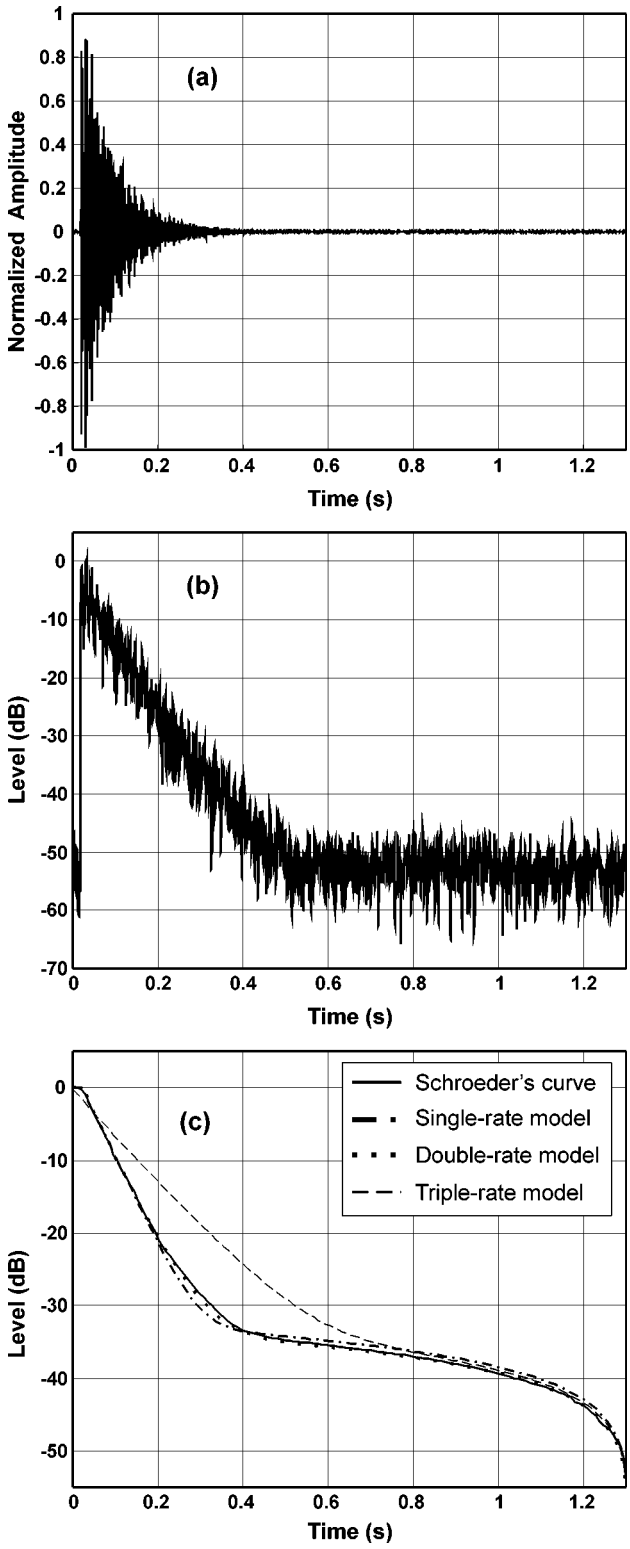

FIG. 2. Room impulse response and Schroeder decay function achieved from an experimentally measured room impulse response in two coupled scale-down model rooms. (a) Room impulse response, octave band-pass filtered at 1 kHz, the peak-to-noise ratio amounts to 53 dB. (b) Energy decay curve (ETC). (c) Schroeder decay function. The decay models with single-, double-, and three-rate modes are also depicted for comparison. Table I lists the model parameters associated with single-, double-, and three-rate model.

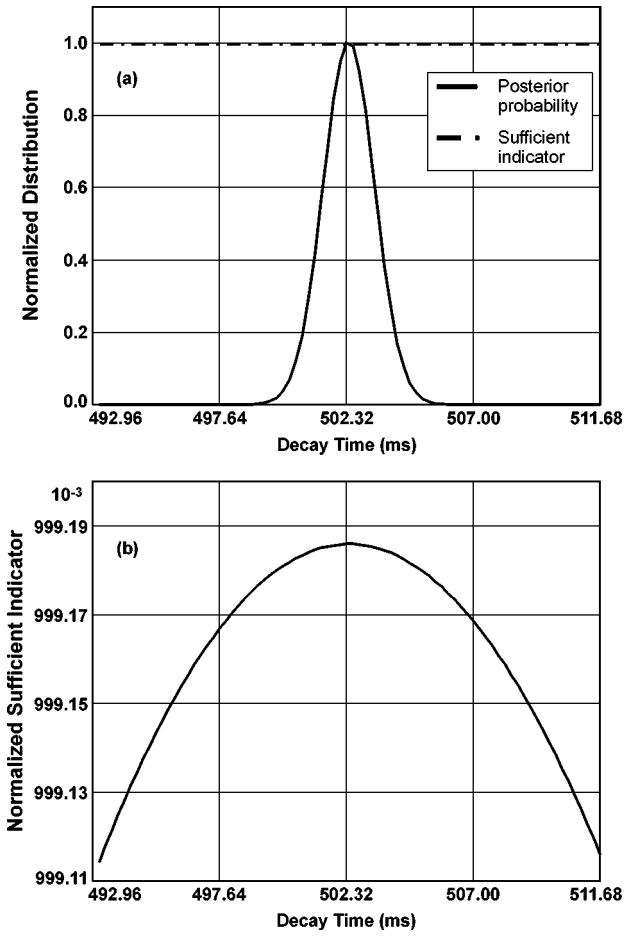

FIG. 3. Normalized posterior probability and normalized sufficient indicator when using a single-rate decay model to analyze Schroeder's decay function measured in coupled scale-down model rooms. (a) Comparison between the normalized posterior probability and the normalized sufficient indicator. (b). Normalized sufficient indicator in a zoomed scale (0.999 11–0.99 92).

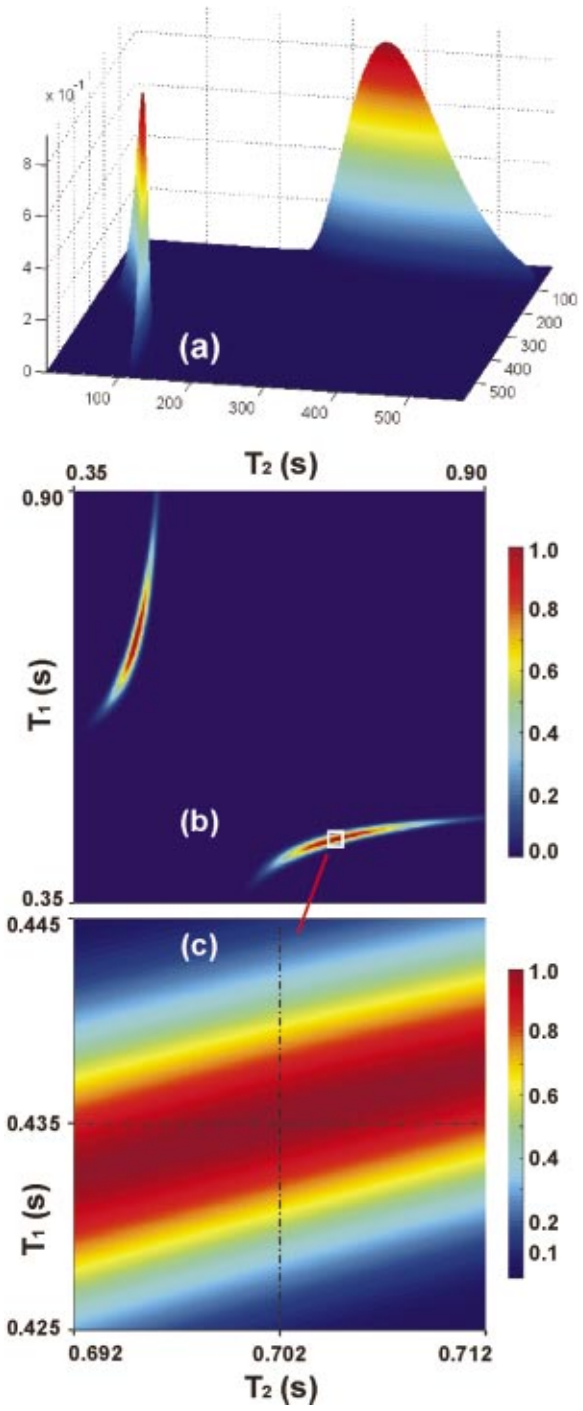

FIG. 4. Normalized posterior probability distribution evaluated over parameter space of two decay times. Two separate peaks of identical peak value are identified within this range. (a) 3-D presentation over the decay time space. A grid of 600 by 600 is defined over the decay time parameter space between 0.35 and 0.9 s. (b) 2-D presentation over the decay time parameter space between 0.35 and 0.9 s. (c) Zoomed presentation over the decay time parameter subspace of $0.425 \leqslant T_1 \leqslant 0.445$ s and $0.692 \leqslant T_2 \leqslant 0.712$ s, a grid of 84 by 84 is defined to evaluate the posterior probability.

curve using the decay parameters associated with one of peak positions is also depicted in Fig. 2(c).

Sharp peaks over the nonlinear parameter space associated with both a double-rate and a single-rate model suggest that these two decay models are competing candidates for the decay time estimation. To determine which candidate is favored by the data, Bayesian evidence E_{21} for a double-rate decay model F_2 over a single-rate decay model F_1 is determined based upon the measured data. Table I contains some relevant parameter values for evaluating $p(\mathbf{D}|F_1,I)$, $p(\mathbf{D}|F_2,I)$, and $p(\mathbf{D}|F_3,I)$. The Gibbs sampler algorithm is applied to determine these parameters. Figure 2(c) shows three decay model curves along with the measured Schroeder decay function. The Bayesian evidence $E_{21}=382.6$ dB is estimated as listed in Table I, indicating that the data [Schroeder's decay function as shown in Fig. 2(c)] strongly favors model F_2: a double-rate decay function.

Using a triple-rate decay model, the assumptions required in Sec. III D cannot be met. Investigation results illustrated in Fig. 6 may yield an explanation. Given the estimated first decay time ($T_1=0.44$ s), which can be easily verified from a small portion at the beginning of the decay function, Fig. 6 shows the PPDF over two other decay times (T_2,T_3). Two peaks are still recognizable over the two decay time parameter space ($0.5\text{ s} \leqslant T_2,\ T_3 \leqslant 1.5\text{ s}$). However, these two peaks, overlapped by each other in a significant degree, occur along the line of symmetry $T_2=T_3$. One of the peaks occurs at $T_2=T_3=0.61$ s and the other occurs at $T_2=T_3=0.87$ s with a lower peak value. In other words, the three-dimensional decay time space within a reasonable

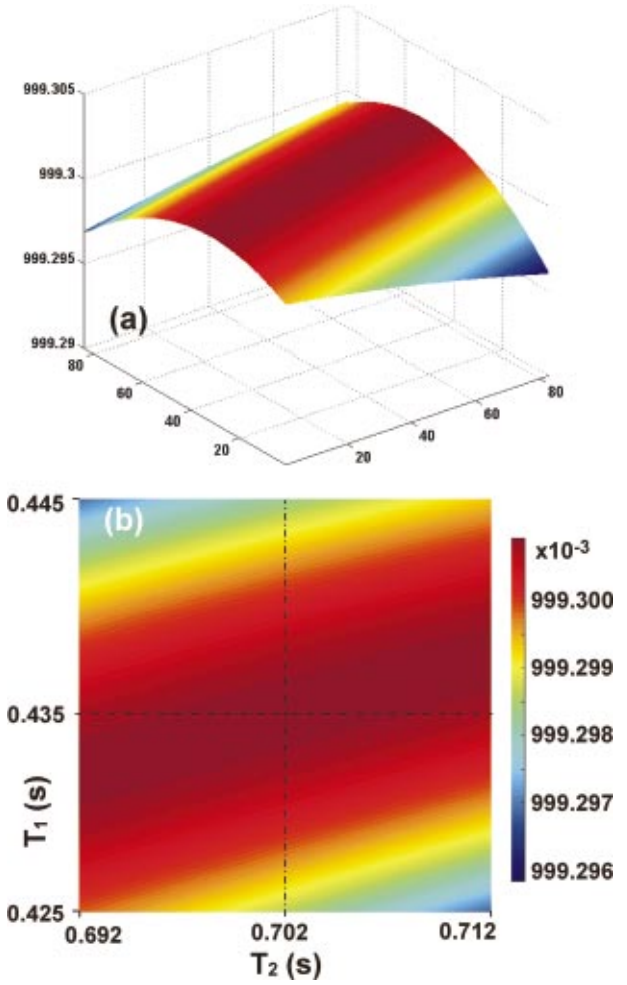

FIG. 5. Distribution of normalized sufficient indicator over parameter subspace of two decay times. In the parameter subspace of $0.425 \leqslant T_1 \leqslant 0.445$ s and $0.692 \leqslant T_2 \leqslant 0.712$ s, a grid of 84 by 84 is defined to evaluate the normalized sufficient indicator. (a) 3-D pseudo-color presentation. (b) 2-D presentation.

range does not include 3! equal-valued, spatially well-separated peaks as required when approximations are used to simplify the global likelihood from Eq. (17) to Eq. (20). It clearly shows that the data contain two distinct decay rates (T_1, T_2) rather than three decay rates. The third exponential term along with decay time T_3, as required by the triple-rate model, is redundant, and should have been removed from the current problem.

When seeking peaks in a three-dimensional parameter space, any search algorithm would converge to a point in the space associated with no reasonable parameters (T_1, T_2, T_3). Therefore, the calculation of global likelihood at the "peak" position cannot be considered as reasonable. Table I lists the relevant parameters for the triple-rate model. The evaluated linear parameters ($A_1 = -15.92$ dB, $A_2 = -6.37$ dB, and $A_3 = -6.36$ dB) associated with these nonlinear parameters break the condition in Eq. (4), especially A_2 being so close to A_3, indicating that the third decay term is redundant. It is not reasonable in this case to use the evaluated Bayesian evidence ($E_{23} = 2.2$ dB) to indicate that the data favor the model F_2. Moreover, Fig. 2(c) shows that the decay parameters evaluated using the triple-rate model do not yield a reasonable decay function when compared with the measured one.

TABLE I. The parameters associated with single-, double-, and triple-rate decay models for evaluation of a decay function measured in two scale-down coupled model rooms as depicted in Fig. 2. Peak-to-noise ratio of the room impulse response is 53 dB. The decay parameters evaluated using a triple-rate model cannot fulfill the condition in Eq. (4).

	Single-rate model F_1	Double-rate model F_2	Triple-rate model F_3
Decay order s	1	2	3
No. of terms m	2	3	4
No. of data K	1098	1098	1098
Sufficient indicator φ	0.9992	0.9993	0.9993
Linear parameter A_1 (dB)	1.898	1.27	−15.92
Decay time T_1 (s)	0.502	0.435	0.442
Linear parameter A_2 (dB)	−63.56	−4.06	−3.67
Decay time T_2 (s)	⋯	0.702	0.61
Linear parameter A_3 (dB)		−64.4	−3.66
Decay time T_3 (s)	⋯	⋯	0.87
Bayesian evidence E_{21} (dB)	⋯	382.6	⋯
Bayesian evidence E_{23} (dB)	⋯	⋯	2.2

In a similar fashion, Fig. 7 depicts the Schroeder decay function measured at 1 kHz in real coupled spaces (Student Union, University of Mississippi, University, MS). A tall (secondary) room of $36.63 \times 14.63 \times 7.77$ m^3 in dimension, approximately 4164 m^3 in volume, is coupled with a short (primary) room of $28.04 \times 18.14 \times 3.48$ m^3 in dimension, approximately 1770 m^3 in volume, through a coupling aperture of 16.56 m^2 in area. The secondary room possesses a natural reverberation time of 2.2 s at 1 kHz while the primary room has a natural reverberation time of 0.95 s. Table II lists some relevant parameters evaluated using the single-, double-, and triple-rate models, respectively. Sharp peaks of the PPDF over the parameter space can be found using both single- and double-rate models. Bayesian evidence for a double-rate model over a single-rate one is $E_{21} = 373.4$ dB. For the triple-rate model, however, given the estimated first decay time ($T_1 = 0.78$ s), the PPDF over two other decay time spaces $\{T_2, T_3\}$ within a reasonable value range does not present two equal-valued peaks off the line of symmetry $T_2 = T_3$ as required. This indicates that the third decay time T_3 is redundant and should have been removed from the problem. For the triple-rate model, calculation of the global likelihood using Eqs. (25) and (26) in a three-dimensional parameter space is not reliable and it is misleading to use the calculated evidence ($E_{23} = -2.9$ dB) for model comparison and selection. A closer look at the linear parameters (in Table II evaluated based on the nonlinear parameters reveals that $A_1 = -0.096 < 0$ and $A_2 < A_3$, breaking the conditions in Eq. (4) as well. Figure 7 illustrates that the triple-rate model evaluated with these decay parameter values cannot yield a reasonable model function.

The examples of double-rate decay functions discussed above show that the global likelihood of the data changes significantly when going from using a single-rate to a double-rate model. Among these, Bayesian model comparison and selection can provide a quantitative measure (Bayesian evidence) to indicate which model is the most probable one for proper decay time estimation. The calculated value of Bayesian evidence E is liable to vary depending on the data

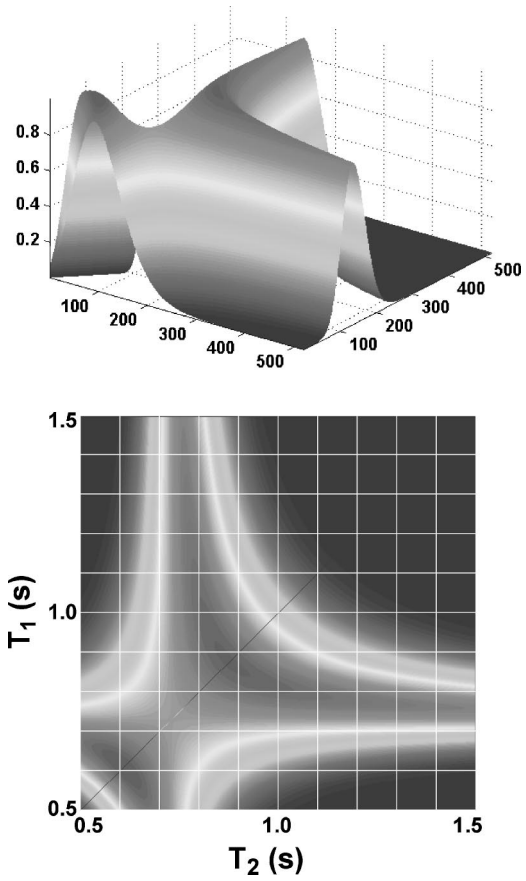

FIG. 6. Posterior probability distribution over decay time (T_2, T_3) while keeping $T_1 = 0.4421$ s. A grid of 521×521 is defined for evaluating the normalized posterior probability distribution using a triple-rate decay model. One peak with higher peak value occurs along the symmetrical line at $T_2 = T_3 = 0.61$ s. The second peak with a lower peak value occurs at $T_2 = T_3 = 0.87$ s. It indicates that third decay time T_3 is redundant and should have been removed from the problem.

and the number of data points. However, the assumptions for simplifying the global likelihood calculations cannot be met when the model order becomes higher than that favored by the data, in this case a triple-rate model. Moreover, the decay parameters evaluated using a triple-rate model break the conditions in Eq. (4), resulting in improper estimation. With even higher decay order, the nonlinear parameter space does not contain an adequate number of well-separated equal-valued peaks either. Of course, a $(K-1)$-degree equation will fit K points of experimental data. Ockham's razor tells us, however, ''an explanation of the facts should be no more complicated than necessary.''[15]

B. Single-rate decay functions

Figure 8(a) shows RIR at 2 kHz (octave) measured in the secondary room of the 1:8 scale model rooms discussed in Sec. IV A when the coupling aperture is acoustically closed. For these data, the peak-to-noise ratio is 46 dB. Its energy decay curve and the Schroeder's decay function are given in Figs. 8(b) and (c), respectively. Evaluation of the PPDF using a single-rate model yields a sharp peak at 1.047 s as shown in Fig. 9(a). In the same range, the NSI presents a flat curve. Figure 9(b) shows the NSI function at a

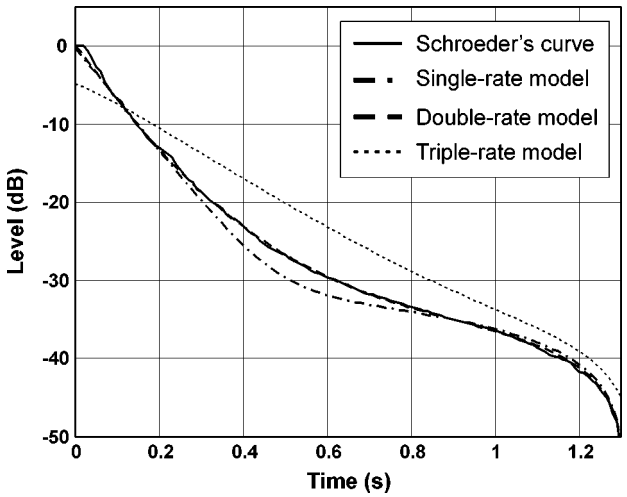

FIG. 7. Schroeder decay function achieved from an experimentally measured room impulse response in real coupled spaces (Student Union, University of Mississippi, USA). The decay models with single, double, and triple rate are also depicted for comparison. Table II lists the model parameters associated with these models.

zoomed scale. The peak of the NSI is in the same position as that of the PPDF. The NSI shown in Fig. (9) validates the simplification undertaken in Eq. (19). Table III lists the relevant model parameters evaluated at the peak position.

Evaluation of the PPDF using a double-rate model over the decay time space $\{T_1, T_2\}$ within a reasonable value range between 0.98 and 1.4 s presents only a single peak along the line of symmetry $T_1 = T_2$ (as shown in Fig. 10), indicating that the second exponential decay term of the model along with the decay time T_2 is redundant and should have been removed from the problem. In this situation the MCS cannot use the Bayesian evidence at the ''peak'' position although the search algorithm will settle to two decay parameters somewhere around the single peak in the decay time space. Note that one of two linear parameters at the ''peak'' position becomes negative as listed in Table III, breaking the conditions in Eq. (4).

TABLE II. The parameters associated with single-, double-, and triple-rate decay models for evaluation of a decay function measured in two coupled halls as depicted in Fig. 7. Peak-to-noise ratio of the room impulse response is 51 dB. The decay parameters evaluated using a triple-rate model cannot fulfill the condition in Eq. (4).

	Single-rate model F_1	Double-rate model F_2	Triple-rate model F_3
Decay order s	1	2	3
No. of terms m	2	3	4
No. of data K	1038	1038	1038
Sufficient indicator φ	0.998 01	0.998 31	0.998 31
Linear parameter A_1 (dB)	−0.553	−0.648	−0.1 (linear)
Decay time T_1 (s)	0.908	0.774	0.784
Linear parameter A_2 (dB)	−61.13	−9.572	−8.998
Decay time T_2 (s)	⋯	1.588	1.496
Linear parameter A_3 (dB)		−61.78	−5.34
Decay time T_3 (s)	⋯	⋯	1.902
Bayesian evidence E_{21} (dB)	⋯	373.4	⋯
Bayesian evidence E_{23} (dB)	⋯	⋯	−2.9

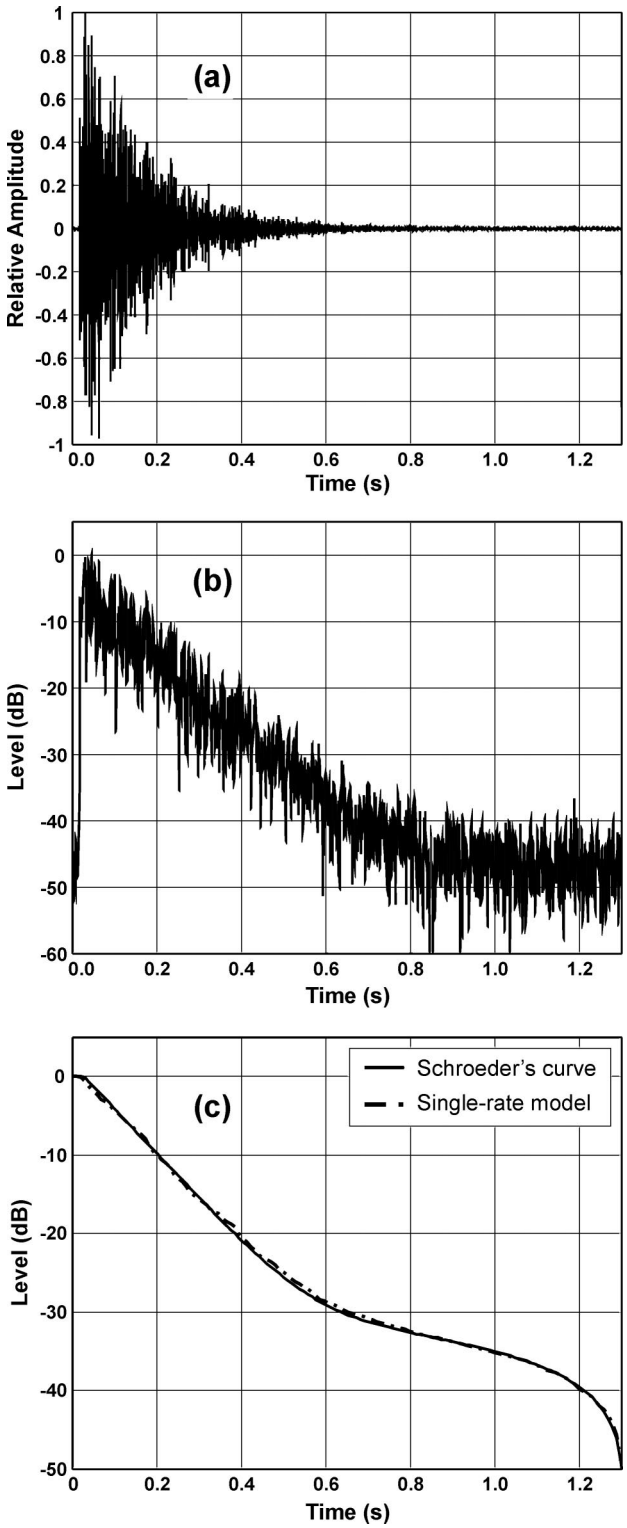

FIG. 8. Room impulse response and Schroeder decay function achieved from an experimentally measured room impulse response in one of the scale-down model rooms. (a) Room impulse response, octave band-pass filtered at 2 kHz, the peak-to-noise ratio amounts to 46 dB. (b) Energy decay curve (ETC). (c) Schroeder decay function. The decay model with single rate is also depicted for comparison. Table III lists the model parameters associated with single- and double-rate model.

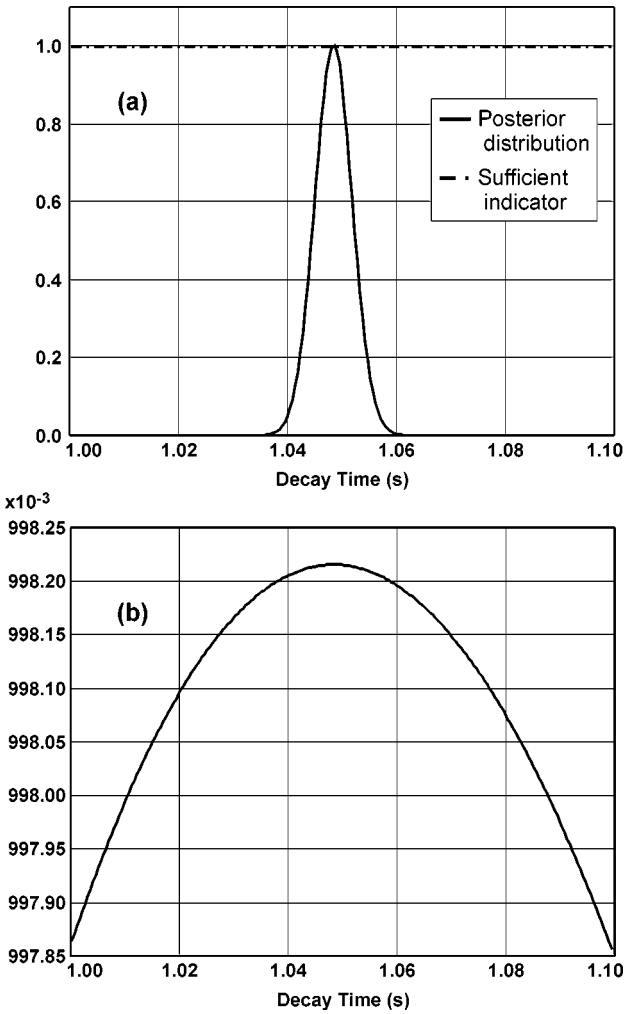

FIG. 9. Normalized posterior probability and normalized sufficient indicator when using a single-rate decay model to analyze Schroeder's decay function measured in one scale-down model room. (a) Comparison between the normalized posterior probability and the normalized sufficient indicator. (b) Normalized sufficient indicator in a zoomed scale (0.997 85−0.998 25).

C. Discussion

The present paper has described a simplified formalism for Bayesian model comparison and selection. A close comparison between Eqs. (25) and (26) of this paper and Eq. (21) of the earlier paper[1] reveals that the end formalism in Eqs. (25) and (26) can be straightforwardly extended from the Bayesian parameter estimation described in Eq. (21) of the earlier paper[1] since one of the multiplication factors $(1-\varphi)^{-(K-m)/2}$ in Eq. (25) is in the form of the Student t-distribution as given in Eq. (21) of the earlier paper.[1] Once the global optimal position in the parameter space is found, calculations of remaining factors in Eqs. (25) and (26) require insignificant effort. For this reason, both the MCS and the parameter estimation using advanced optimization approaches[1] can be accomplished hand-in-hand. Some necessary approximations, particularly that given in Secs. III C and D, make this formalism practicable in architectural acoustic applications. The examples using experimentally measured Schroeder's functions in both coupled rooms and single-space rooms confirm the validation of the simplifying steps when an adequate number of well-separated peaks exist in the corresponding nonlinear parameter space.

The exploratory examples restricted so far to the measured Schroeder functions show that the estimation of the

TABLE III. The parameters associated with single- and double-rate decay models for evaluation of a decay function measured in one 1:8 scale-down single-space room. The decay parameters evaluated using the double-rate model cannot fulfill the condition in Eq. (4).

	Single-rate model F_1	Double-rate model F_2
Decay order s	1	2
No. of terms m	2	3
No. of data K	1040	1040
Sufficient indicator φ	0.9982	0.9983
Linear parameter A_1 (dB)	1.336	7.725
Decay time T_1 (s)	1.047	1.2334
Linear parameter A_2 (dB)	−60.16	−4.617 (linear)[a]
Decay time T_2 (s)	⋯	1.279
Linear parameter A_3	⋯	−0.00 (linear)[a]
Bayesian evidence E_{12} (dB)	⋯	−75.3

[a]The linear parameters $A_2<0$ and $A_3<0$ are estimated using the double-rate model.

relevant parameters, including the global likelihood value, becomes unreliable when the model order is one more than the optimal one. Often this happens with an inadequate number of equal-valued, well-separated peaks in the given parameter space since one decay term in the model is redundant and should have been removed from the problem. In this situation, the model comparison and selection described in this paper cannot rely on the Bayesian evidence calculated in terms of the global likelihood. It has often been observed that the model parameters in this situation break the conditions in Eq. (4). In practice, the conditions expressed in Eq. (4) can provide an additional indicator to reject a decay model with a model order one higher than the optimal order. Checking the conditions in Eq. (4) requires determination of all linear parameters at the "peak" position. Equation (24) of the earlier paper[1] yields the expected value estimates of the linear parameters without substantial computational load.

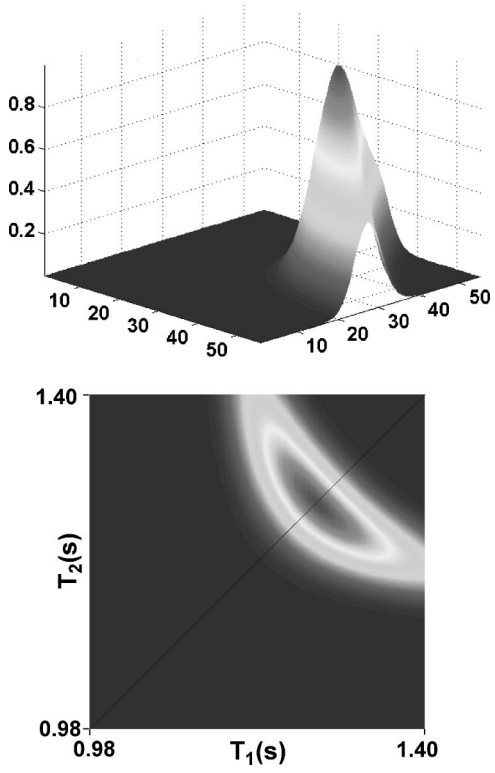

FIG. 10. Normalized posterior probability distribution over decay time (T_1, T_2). A grid of 56×56 is defined for evaluating the normalized posterior probability distribution using a double-rate decay model. A single peak occurs along the symmetrical line $T_1 = T_2$. It indicates that second decay time T_2 is redundant and should have been removed from the problem.

Optimization (search) algorithms play a crucial role in both Bayesian parameter estimation described in Ref. 1 and model comparison and selection in this paper. Advanced methods can converge to the global extreme over the parameter space of given dimensionality with a reasonable computational load. Determination of the dimensionality of the parameter space is again a MCS problem rather than an optimization problem. This is clearly the case because a search algorithm, searching for the global extreme over a three-dimensional parameter space, will converge somewhere in that space even if the actual extreme should have been in a two-dimensional parameter space. This confirms what profound thinkers say: "The trick lies not in finding the answer, but in asking the right question."[11]

V. SUMMARY AND CONCLUSIONS

Recently, acoustically coupled spaces have been drawing more and more attention in the architectural acoustics community. As a result, determination of decay times in these coupled spaces from measured Schroeder decay function data has become a more significant problem. It has long been recognized that evaluations of more than one decay time in coupled spaces requires considerable effort. A previous work[1] proposed a Bayesian parameter estimation approach to evaluating decay times. Bayesian parameter estimation can yield reasonable estimation results only when it uses an appropriate model with the correct number of decay modes (decay order) for Schroeder decay functions. The decay order should be first determined. This paper has described a model comparison and selection (MCS) procedure using Bayesian probability theory. In effect, Bayesian evidence has to be calculated for comparison between two alternative models. Given a set of competing exclusive, exhaustive decay models, the global likelihood for each model over the model set has to be evaluated based upon the measured data.

All results discussed in this paper have been restricted to exploratory examples with some necessary approximations. One needs to come back to the original step beginning with the Bayesian theorem if the assumed approximations cannot be made in specific problems. The current work also reveals some limitations associated with the described MCS applied in Schroeder's decay functions. Solutions of these problems remain for future efforts.

ACKNOWLEDGMENTS

The authors are very grateful to Professor M. R. Schroeder for his encouragement and Dr. Ch. Jaffe, Dr. W. T. Chu, and Dr. J. M. Sabatier for their valuable suggestions and constructive criticisms. Thanks are also due to Donghua Li who contributed to the data collection in the coupled scale-down models as part of his Master's degree thesis.

APPENDIX A

Equation (15) can be expressed as

$$p(\mathbf{D}|F_s,\sigma,\zeta,I)=(\sqrt{2\pi})^{-(K+m)}\sigma^{-K}\zeta^{-m}\int p(\mathbf{B}|F_s,I)V\,\mathrm{d}\mathbf{B}, \tag{A1}$$

where

$$\begin{aligned}V&=\int_{-\infty}^{\infty}\exp\left\{-\sum_{j=1}^{m}\frac{\alpha_j^2}{2\zeta^2}-\frac{1}{2\sigma^2}\left[\Delta-2\sum_{j=1}^{m}\alpha_j q_j+\sum_{j=1}^{m}\alpha_j^2\right]\right\}\mathrm{d}\boldsymbol{\alpha}\\&=\int_{-\infty}^{\infty}\exp\left\{-\frac{1}{2\sigma^2}\left[\Delta-2\sum_{j=1}^{m}\alpha_j q_j+\sum_{j=1}^{m}\frac{\zeta^2+\sigma^2}{\zeta^2}\alpha_j^2\right]\right\}\mathrm{d}\boldsymbol{\alpha}\\&=\exp\left[\frac{-\Delta}{2\sigma^2}\left(1-\frac{\varphi\zeta^2}{\zeta^2+\sigma^2}\right)\right]\\&\quad\cdot\int_{-\infty}^{\infty}\exp\left[-\frac{1}{2\sigma^2}\sum_{j=1}^{m}\left(\sqrt{\frac{\zeta^2+\sigma^2}{\zeta^2}}\alpha_j-\sqrt{\frac{\zeta^2}{\zeta^2+\sigma^2}}q_j\right)^2\right]\mathrm{d}\boldsymbol{\alpha}.\end{aligned} \tag{A2}$$

Here Δ and φ are defined in Eqs. (16) and (18), respectively. A change of variable

$$u_j=\sqrt{\frac{\zeta^2+\sigma^2}{\zeta^2}}\alpha_j-\sqrt{\frac{\zeta^2}{\zeta^2+\sigma^2}}q_j,$$

$$\mathrm{d}\alpha_j=\sqrt{\frac{\zeta^2}{\zeta^2+\sigma^2}}\mathrm{d}u_j$$

yields

$$\begin{aligned}V&=\exp\left[\frac{-\Delta}{2\sigma^2}\left(1-\frac{\varphi\zeta^2}{\zeta^2+\sigma^2}\right)\right]\\&\quad\cdot\prod_{j=1}^{m}\left\{\sqrt{\frac{\zeta^2}{\zeta^2+\sigma^2}}\left[2\int_0^{\infty}\exp\left(\frac{-u_j^2}{2\sigma^2}\right)\mathrm{d}u_j\right]\right\}.\end{aligned} \tag{A3}$$

According to Eq. (A5) in Ref. 1

$$V=(\sqrt{2\pi}\sigma)^m\left(\frac{\zeta^2}{\zeta^2+\sigma^2}\right)^{m/2}\exp\left[\frac{-\Delta}{2\sigma^2}\left(1-\frac{\varphi\zeta^2}{\zeta^2+\sigma^2}\right)\right]. \tag{A4}$$

Substitution of V in Eq. (A4) into (A1) yields

$$\begin{aligned}p(\mathbf{D}|F_s,\sigma,\zeta,I)&=(\sqrt{2\pi}\sigma)^{-K}\left(\frac{\sigma}{\zeta}\right)^m\left(\frac{\zeta^2+\sigma^2}{\zeta^2}\right)^{-m/2}\\&\quad\times\int p(\mathbf{B}|F_s,I)\\&\quad\times\exp\left[\frac{-\Delta}{2\sigma^2}\left(1-\frac{\varphi\zeta^2}{\zeta^2+\sigma^2}\right)\right]\mathrm{d}\mathbf{B}.\end{aligned} \tag{A5}$$

Assuming that prior uncertainty in the amplitudes associated with ζ^2 is much greater than σ^2, $p(\mathbf{D}|F_s,\sigma,\zeta,I)$ may be approximated[6] as

$$\begin{aligned}p(\mathbf{D}|F_s,\sigma,\zeta,I)&\approx(\sqrt{2\pi}\sigma)^{-K}\left(\frac{\sigma}{\zeta}\right)^m\int p(\mathbf{B}|F_s,I)\\&\quad\times\exp\left[-\Delta\left(\frac{1-\varphi}{2\sigma^2}+\frac{\varphi}{2\zeta^2}\right)\right]\mathrm{d}\mathbf{B},\end{aligned} \tag{A6}$$

which results in Eq. (17).

APPENDIX B

Assuming that there exist two bounds σ_a, σ_b, ζ_a, ζ_b, and γ_a, γ_b for σ, ζ, and γ, respectively, the normalized Jeffreys prior becomes

$$\begin{aligned}&p(\sigma,\zeta,\gamma,|\sigma_a,\sigma_b,\zeta_a,\zeta_b,\gamma_a,\gamma_b,I)\\&\quad=\frac{1}{\log(\sigma_b/\sigma_a)\sigma\log(\zeta_b/\zeta_a)\zeta\log(\gamma_b/\gamma_a)\gamma}.\end{aligned} \tag{B1}$$

The marginalization over these parameters reads

$$\begin{aligned}&p(\mathbf{D}|F_s,\sigma_a,\sigma_b,\zeta_a,\zeta_b,\gamma_a,\gamma_b,I)\\&\quad=\int_{\sigma_a}^{\sigma_b}\int_{\zeta_a}^{\zeta_b}\int_{\gamma_a}^{\gamma_b}p(\sigma,\zeta,\gamma,|\sigma_a,\sigma_b,\zeta_a,\zeta_b,\gamma_a,\gamma_b,I)\\&\qquad\times p(\mathbf{D}|F_s,\sigma,\zeta,\gamma,I)\mathrm{d}\sigma\,\mathrm{d}\zeta\,\mathrm{d}\gamma.\end{aligned} \tag{B2}$$

Substitution of Eqs. (B1) and (22) into Eq. (B2) yields

$$\begin{aligned}&p(\mathbf{D}|F_s,\sigma_a,\sigma_b,\zeta_a,\zeta_b,\gamma_a,\gamma_b,I)\\&\quad\approx\frac{s!}{(\sqrt{2\pi})^{K+s}}\left\{\frac{W}{\log(\zeta_b/\zeta_a)}\frac{Y}{\log(\gamma_b/\gamma_a)}\right.\\&\qquad\left.\times\frac{Z}{\log(\sigma_b/\sigma_a)}\right\}\Bigg|_{\mathbf{B}=\hat{\mathbf{B}}}\end{aligned} \tag{B3}$$

with

$$W=\int_{\zeta_a}^{\zeta_b}\zeta^{-(m+1)}\exp\left(-\Delta\frac{\varphi}{2\zeta^2}\right)\mathrm{d}\zeta, \tag{B4}$$

$$Y=\int_{\gamma_a}^{\gamma_b}\gamma^{-(s+1)}\exp\left(\frac{-\beta}{2\gamma^2}\right)\mathrm{d}\gamma, \tag{B5}$$

and

$$Z=\int_{\sigma_a}^{\sigma_b}\sigma^{-(K-m+1)}\exp\left[\frac{-\Delta(1-\varphi)}{2\sigma^2}\right]\mathrm{d}\sigma. \tag{B6}$$

Equations (B4)–(B6) are all of the same form. This form reduces to the following:

$$\int_a^b x^{2n}\exp(-yx^2)\mathrm{d}x\to\Gamma\left(n+\frac{1}{2}\right)\frac{y^{-(n+1/2)}}{2} \tag{B7}$$

when $a\to0$, $b\to\infty$. Taking Eq. (B4) as an example, by letting $x=1/\zeta$ so that $d\zeta=-\zeta^2dx$ and $\zeta_a\to0$ as $x\to\infty$ and $\zeta_b\to\infty$ as $x\to0$,

$$n=\frac{m-1}{2}\quad\text{and}\quad y=\Delta\frac{\varphi}{2}.$$

Equation (B4) can be approximately determined by

$$W \approx \Gamma\left(\frac{m}{2}\right)\left(\Delta\frac{\varphi}{2}\right)^{-m/2} \tag{B8}$$

given that the interval (ζ_a, ζ_b) is wide (so as to approximately fulfill the conditions $\zeta_a \to 0$, $\zeta_b \to \infty$). In similar fashion,

$$Y \approx \Gamma\left(\frac{s}{2}\right)\left(\frac{\beta}{2}\right)^{-s/2} \tag{B9}$$

and

$$Z \approx \Gamma\left(\frac{K-m}{2}\right)\left[\frac{\Delta(1-\varphi)}{2}\right]^{-(K-m)/2}. \tag{B10}$$

Substituting Eqs. (B8)–(B10) into Eq. (B3) results in Eq. (24).

[1] N. Xiang and P. M. Goggans, "Evaluation of decay times in coupled spaces: Bayesian parameter estimation," J. Acoust. Soc. Am. **110**, 1415–1424 (2001).

[2] F. Eyring, "Reverberation time measurements in coupled rooms," J. Acoust. Soc. Am. **3**, 181–206 (1931).

[3] W. T. Chu, "Comparison of reverberation measurements using Schroeder's impulse method and decay-curve averaging method," J. Acoust. Soc. Am. **63**, 1444–1450 (1978).

[4] N. Xiang, "Evaluation of reverberation times using a nonlinear regression approach," J. Acoust. Soc. Am. **98**, 2112–2121 (1995).

[5] M. R. Schroeder, "New method of measuring reverberation time," J. Acoust. Soc. Am. **37**, 409–412 (1965).

[6] G. L. Bretthorst, "Bayesian analysis. II. Signal detection and model selection," J. Mag. Res. **88**, 552–570 (1990).

[7] E. T. Jaynes, "Highly informative priors," in *Bayesian Statistics 2*, edited by J. M. Bernardo, M, H. Degroot, D. V. Lindley, and A. F. M. Smith (Elservier Science, Amsterdam, The Netherlands, 1985), p. 329.

[8] P. M. Woodward, *Probability and Information Theory* (Pergamon, Oxford, UK, 1964).

[9] H. Jeffreys, *Theory of Probability* (Oxford U.P., London, 1939, 3rd revised ed. 1969).

[10] D. S. Sivia, *Data Analysis: A Bayesian Tutorial* (Clarendon, Oxford, 1996).

[11] A. J. M. Garrett, "Ockham's Razor," in *Maximum Entropy and Bayesian Methods*, edited by W. T. Grandy and L. H. Schick (Kluwer Academic, The Netherlands, 1991), pp. 357–364.

[12] G. L. Bretthorst, *Bayesian Spectrum Analysis and Parameter Estimation* (Springer-Verlag, New York, 1988).

[13] L., Cremer, H. A. Müller, and T. J. Schultz, *Principles and Applications of Room Acoustics* (Applied Science, London, 1982).

[14] S. F. Gull, "Bayesian Inductive Inference and Maximum Entropy," in *Maximum-Entropy and Bayesian Methods in Science and Engineering*, Vol. 1, edited by G. J. Erickson and C. R. Smith (Kluwer Academic, The Netherlands, 1988), pp. 53–74.

[15] W. H. Jefferys and J. O. Berger, "Ockham's Razor and Bayesian Analysis," Am. Sci. **80**, 64–72 (1992).

An acoustic-logging transmission-network model (continued): Addition and multiplication ALTNs

Lin Fa and John P. Castagna
The Institute for Exploration and Development Geosciences, The University of Oklahoma, Sarkeys Energy Center, 100 East Boyd Street, Norman, Oklahoma 73019

Roberto Suarez-Rivera
TerraTek, 400 Wakara Way, Salt Lake City, Utah 84108

Peng Sun
Xi'an Petroleum Exploration Instrument Complex, Xi'an, Shaanxi 710061, People's Republic of China

(Received 20 March 2001; accepted for publication 30 January 2003)

On the basis of the acoustic-logging transmission-network (ALTN) model [Fa *et al.*, J. Acoust. Soc. Am. **111**(5), 2158–2165 (2002)] this paper puts forward concepts of addition and multiplication ALTNs, proves the reciprocity of two kinds of addition ALTNs, sets up the physical model of the multiplication acoustic array logging tool, calculates their acoustic-beam steering efficiencies, and performs experimental verification. © *2003 Acoustical Society of America.*
[DOI: 10.1121/1.1562651]

PACS numbers: 43.58.Vb, 43.58.Wc, 43.20.Bi, 43.20.Mv [SLE]

I. INTRODUCTION

The acoustic-logging process can be described as a signal transmission system. From the ALTN model,[1] it can be known that the properties of the acoustic source and receiver have great effects on the acoustic-logging signal. On the basis of the equivalent circuit of a thin spherical shell piezoelectric transducer which was given by Berlincourt, Curran, and Jaffe,[2] Fa, Castagna, and Hovem[3] considered the anti-effect of the acoustic field on the thin spherical shell transducer during its vibration in the coupling fluid medium. Then, they inducted the radiation resistance and radiation impedance[4] in the equivalent circuit and derived its electrical–acoustical and acoustical–electrical transmission functions. Using the electrical–acoustical and acoustical–electrical transmission functions of the transducer and the ALTN model, this paper aims to (1) verify the reciprocity between the source array (SA) ALTN and the receiver array (RA) ALTN; (2) put forth the concepts of addition and multiplication ALTNs; (3) calculate their acoustic-beam steering efficiency; and (4) show that the acoustic-beam steering efficiency of multiplication ALTN is the greater. This paper will also show that a corresponding source–receiver array (SRA) logging tool can improve the accuracy of the logging curve and decrease the data quantity of the acoustic-logging signal from the down-hole to the ground through a cable telemetry system (CTS).

II. MODELING

For a piezoelectric thin spherical shell transducer with average radius r_b, polarized in the radial direction with electrodes connected to the inner and outer surfaces, the expressions of its electric–acoustic and acoustic–electric transmission functions in the time domain can be written as follows:[2–4]

$$h_1(t)=K_{11}e^{-\alpha_1 t}+2K_{12}e^{-\beta_1 t}\cos(\omega_1 t+\theta_1), \tag{1}$$

$$h_3(t)=K_{31}e^{-\alpha_3 t}+2K_{32}e^{-\beta_3 t}\cos(\omega_3 t+\theta_3), \tag{2}$$

where K_{11}, K_{12}, K_{31}, and K_{32} are constants; α_1, α_3, β_1, and β_3 are the damping factors of direct and alternate terms; ω_1 and ω_3 are resonance angle frequencies of the source and receiver; and θ_1 and θ_3 are initial phase shift angles. All of them are determined by the physical and geometric parameters of the transducer and the physical parameters of the coupling fluid around the transducer.

Suppose that a fluid-filled cylindrical borehole of radius R is embedded in an infinite elastic medium and that SA and RA consist of n and m transducer elements, respectively, which are located on the borehole axis, as shown in Fig. 1. $T_i\,(i=1,2,...,n)$ is the ith transmitting transducer element in the SA; $R_l\,(l=1,2,...,m)$ is the lth receiving transducer element in the RA; ΔZ is the interval between two neighbor transmitting transducer elements in the SA, and ΔL is the interval between two neighbor receiving transducer elements in the RA. At an any point z on the borehole axis, the effect of the propagation media (the borehole fluid and the formation around the borehole) on the acoustic signals radiated by T_i can be described by[5]

$$\begin{aligned}H_{2i}(\omega,z)&=H_{di}(\omega)+H_{ri}(\omega)\\&=\frac{1}{z-(i-1)\Delta Z}\exp\{-j\omega[(i-1)\Delta t\\&\quad+[z-(i-1)\Delta Z]/V_f]\}\\&\quad+\frac{1}{(2\pi)^2}\exp[-j\omega(i-1)\Delta t]\\&\quad\times\int_{-\infty}^{+\infty}A(k_z,\omega)\exp\{j[k_z z-(i-1)\Delta Z)]\}dk,\end{aligned} \tag{3a}$$

 0001-4966/2003/113(5)/2698/6/$19.00

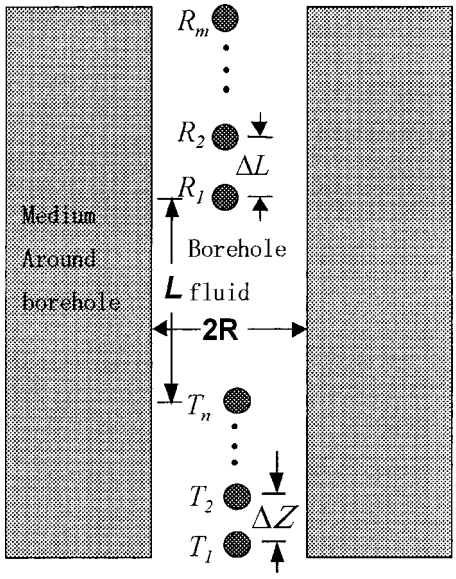

FIG. 1. Configuration of array-acoustic logging.

$$h_{2i}(t)=\int_{-\infty}^{+\infty} H_{2i}(\omega)\exp(j\omega t)d\omega, \tag{3b}$$

where k_z is the axial wave number; Δt is the excitation delay between two neighbor transmitting transducer elements in the SA; and $z-(i-1)\Delta Z$ is the separation from the ith transmitting transducer element T_i in the SA to the point z on the borehole axis.

If the driving-voltage signal excites all transmitting transducer elements in the SA in turn with excitation delay Δt, the acoustic-logging process shown in Fig. 1 can be described as a signal transmission network, as shown in Fig. 2. U_{1i} is the driving-voltage signal ($i=1,2,...,n$); $X_i[t-(i-1)\Delta t, z-(i-1)\Delta Z]$ is the acoustic signal radiated by T_i; $P_l[t,z+(l-1)\Delta L]$ is the pressure response at the space position of the lth receiving transducer element R_l ($l=1,2,...,m$) in the RA; $U_{3l}(t)$ is the electrical output signal of R_l ($l=1,2,...,m$); h_{1i} is the electrical–acoustic transmission function of T_i; h_{2l} is the acoustic transmission function of the propagation media (the borehole fluid and the formation around the borehole); and h_{3l} is the acoustic–electrical

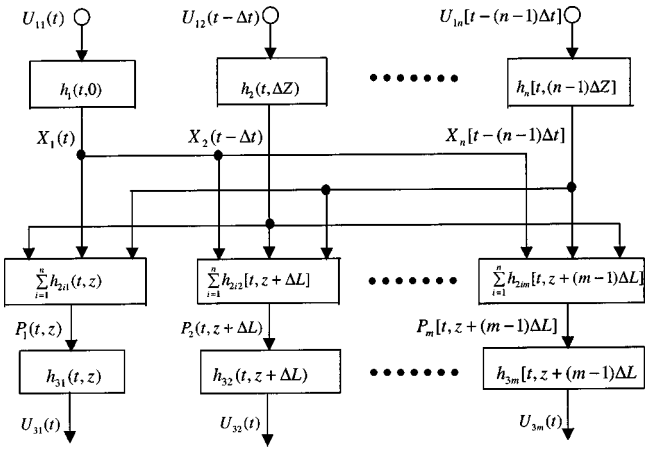

FIG. 2. Array acoustic-logging transmission network.

transmission function of R_l. The electrical output signal of the lth receiving transducer element R_l in the RA can be written as

$$U_{3l}(t,z)=\sum_{i=1}^{n} U_{1i}[t-(i-1)\Delta t]*h_{1i}(t)* \times h_{2l}[t,z-(i-1)\Delta Z+(l-1)\Delta L]*h_{3l}(t). \tag{4}$$

III. CALCULATION AND SIMULATION

The size of the borehole limits the size of the transducer element. Therefore, the lowest resonance frequency of the transducer is limited. In the following calculation, the chosen driving-voltage signal is a gated sinusoid. Suppose the transducer is made of piezoelectric material *PZT-7A* and its average radius is 44.5 mm. As an acoustic source, its resonance frequency is 20 kHz.[6] This resonance frequency is used as the frequency of a gated sinusoid to calculate the acoustic-beam steering efficiencies of SA ($m>1$ and $n=1$), RA ($m=1$ and $n>1$), and SRA ($m>1$ and $n>1$) ALTNs.

Using the phase control technology to adjust the excitation delay of the SA or the shift time of acoustic-logging signals received by the RA can improve their radiation and receiving directivities and increase the head-wave amplitude of the acoustic-logging signal. In order to make head waves of acoustic-logging signals created by all transmitting transducer elements in the SA, or received by all receiving transducer elements in the RA stack with the same phase, the excitation delay of the SA or the shift time of the acoustic-logging signals received by the RA should be[7]

$$\Delta t_0=\Delta Z/V_2 \ (\text{or} \ \ \Delta t_0=\Delta L/V_2), \tag{5}$$

where V_2 is *P*-wave velocity of formation around the borehole.

Now, we calculate the acoustic-beam steering efficiencies of the above three types of ALTNs. The driving-voltage signal of the gated sinusoid can be written as

$$U_1(t)=[H(t)-H(t-t_1)]\sin\omega_1 t, \tag{6}$$

where t_1 is the window width of the sinusoid; $H(\cdot)$ is the Heaviside unit step function; $\omega_1=2\pi f_1$ is the angular frequency (f_1 is the electrical–acoustic transmission resonance frequency of the transducer). Let $f_1=20$ kHz, $t_1=6\pi/\omega_1$, $R=0.1$ m, $L=2.44$ m, the *P*-wave velocity, *S*-wave velocity, and density of formation around borehole be 5460 m/s, 3300 m/s, and 4000 kg/m^3, and let the acoustic velocity and density of borehole fluid be 1500 m/s and 1200 kg/m^3, respectively.

For the SA ALTN, let $n=4$, $m=1$, and $\Delta Z=82$ mm. The calculated relation between the head-wave amplitude of the received acoustic-logging signal and the excitation delay is shown in Fig. 3. From Fig. 3, it can be seen that when the excitation delay abides by Eq. (5), i.e., $\Delta t=(82\ \text{mm})/(5460\ \text{m/s})=15.10\ \mu$s, the head-wave amplitude is the greatest. For the excitation delay of 15.10 μs, the calculated relation between received head-wave amplitude and

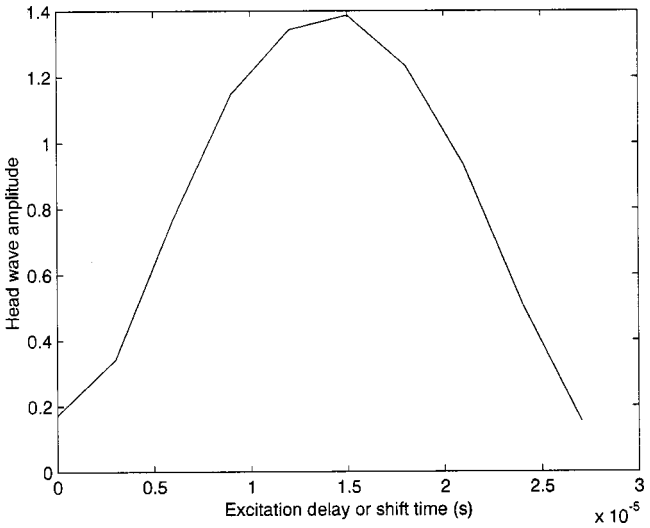

FIG. 3. Relation curve between the head-wave amplitude of received acoustic-logging signal and the excitation delay or that between the head-wave amplitude of the stacked acoustic-logging signal and the shift time.

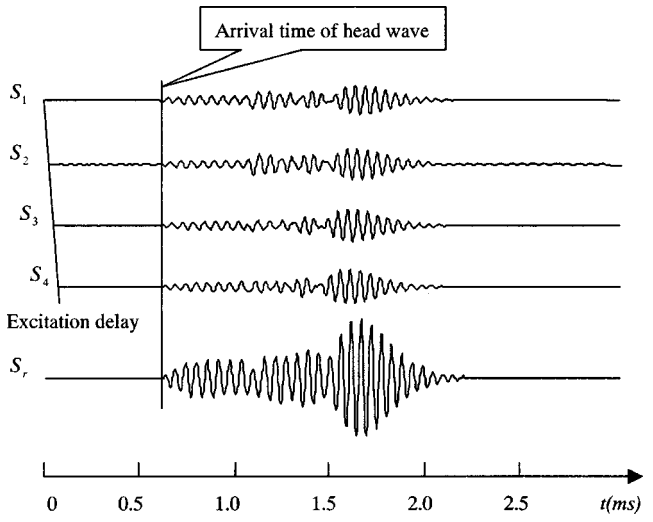

FIG. 4. Full waves of acoustic-logging signals for the SA ALTN. Where S_i ($i=1,2,3,4$) is full waves created by the ith transmitting transducer elements in the SA and S_r is full waves received by the receiver.

the transmitting transducer element number in the SA and full waves of acoustic-logging signals are shown in Table I and Fig. 4, respectively.

For the RA ALTN, let $n=1$, $m=4$, and $\Delta L=82$ mm. By adjusting shift time of acoustic-logging signals received by all receiving transducer elements in the RA, the calculated relation between the head-wave amplitudes of the stacked acoustic-logging signals and the shift time is the same as that shown in Fig. 3. For the shift time of 15.10 μs, the calculated relation between the stacked head-wave amplitude and the receiving transducer element number in the RA is the same as that shown in Table I. Figure 5 is the calculated acoustic-logging signal full waves. The stacked full wave, S_s, in Fig. 5 is the same as the received full wave, S_r, in Fig. 4.

From the above calculation, it can be seen that the effects of the SA and RA ALTNs are the same. In other words, the SA ALTN is reciprocal to the RA ALTN. Concerning the SA and RA ALTNs, when the *P*-wave velocity of the formation around the borehole is used to adjust the excitation delay of the SA or the shift time of the acoustic-logging signals received by the RA, the head-wave amplitudes of the acoustic-logging signal increase with the number of transducer elements in the SA or in the RA and abides by an approximate addition rule. Therefore, the SA and RA ALTNs are identified as the addition ALTN.

For the SRA ALTN, let $n=4$, $m=4$, $\Delta Z=82$ mm, and $\Delta L=82$ mm. First, the *P*-wave velocity of the formation around the borehole is used to adjust the excitation delay of the SA. The acoustic signals created by all transmitting transducer elements in the SA propagate in the formation around the borehole with the same phase. Then, they are received by all receiving transducer elements in the RA. Finally, the shift time of all acoustic-logging signals received by all receiving elements in the RA is adjusted. The relation between the head-wave amplitude of stacked acoustic-logging signals and the shift time is calculated as shown in Fig. 6. It can be seen from Fig. 6 that when the shift time is 15.10 μs, the *P*-wave contents of all acoustic-logging signals received by all receiving transducer elements in the RA stack with the same phase. Here, the stacked head-wave amplitude is the greatest. Let the shift time be 15.10 μs and $n=4$. The relation between the head-wave amplitude of the stacked acoustic-logging signal and the number m of receiving transducer elements in the RA is calculated as shown in Table II. The

TABLE I. For two kinds of addition (SA and RA) ALTNs, when the excitation delay or the shift time is 15.10 μs, the calculated relation between the head-wave amplitude of acoustic-logging signal and the transmitting transducer number in the SA or that between the head-wave amplitude of stacked acoustic-logging signal and receiving transducer number in the RA. Where, HWA is the abbreviation of head-wave amplitude.

n (or m)	HWA
1	0.3467
2	0.6539
3	0.9878
4	1.3234

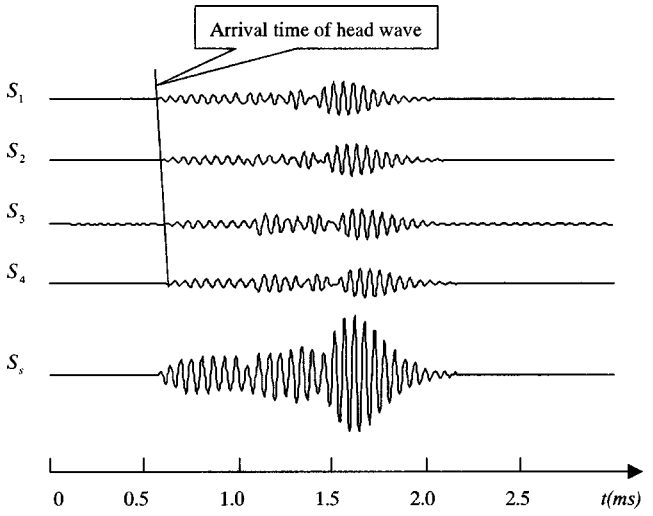

FIG. 5. Full waves of acoustic-logging signals for the RA ALTN. Where S_l ($l=1,2,3,4$) is full waves received by the lth receiving transducer elements in the RA and S_s is the full-waves stacked by S_1, S_2, S_3, and S_4.

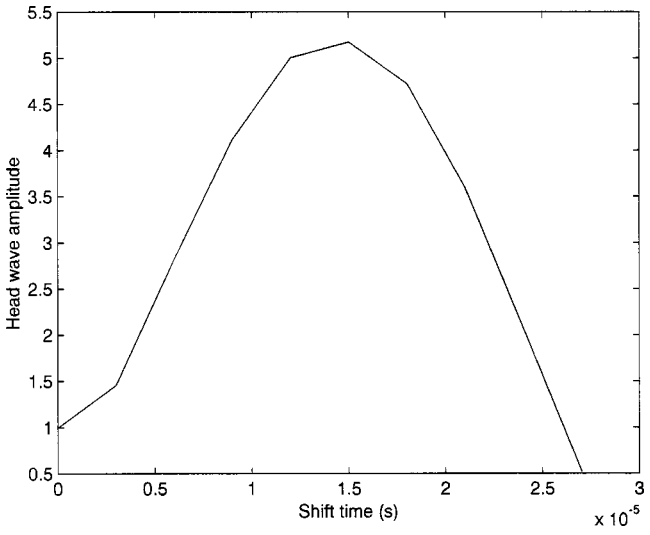

FIG. 6. Relation curve between the head-wave amplitude of stacked acoustic-logging signal and the shift time when the *P*-wave velocity is used to adjust the excitation delay of the SA for the multiplication ALTN.

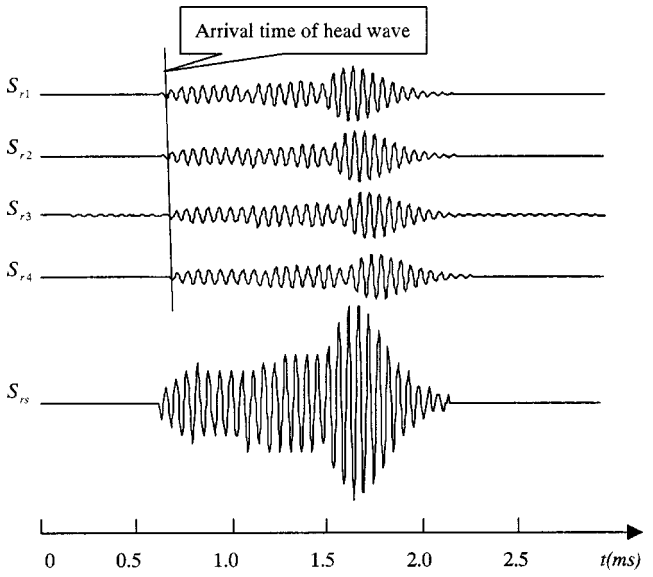

FIG. 7. Full waves of acoustic-logging signals received by all receiving transducer elements in the RA and the full waves of stacked acoustic-logging signal for the multiplication ALTN. Where S_{rl} ($l=1$, 2, 3, and 4) is the full waves received by each receiving transducer element in the RA and S_{rs} is that of the stacked acoustic-logging signal.

stacked acoustic-logging signals are calculated as in Fig. 7, respectively. The head-wave amplitude of the acoustic-logging signal for the SRA ALTN is about 16 times that of one transmitting transducer element and one receiving transducer element. The stacked head-wave amplitude increases approximately according to the pattern of the product of the transducer element number in the SA and the transducer element number in the RA. Therefore, the SRA acoustic-logging transmission network is identified as a multiplication ALTN. The relation curves shown in Fig. 3 and Fig. 6 can be converted into normalized acoustic-beam steering directivity graphs for the two addition ALTNs and the multiplication ALTN as shown in Fig. 8.[7] In this case, the radius stands for the number value of the normalized head-wave amplitude of the acoustic-logging signal; the angle unit of circumference direction is in degrees; the curve (1) is the directivities of the two kinds of addition ALTNs (SA and RA) and the curve (2) is that of the multiplication ALTN. The directivities of the addition and multiplication ALTNs have the maximal values in the direction of the critical incidence angle (15.98°) from the borehole fluid to the formation around the borehole.

There are two kinds of addition ALTNs. In the first kind, there are four transmitting elements and one receiving element in the corresponding SA acoustic-logging tool. In the second kind, there are one transmitting transducer element and four receiving transducer elements in the corresponding RA logging tool. For the multiplication ALTN, there are four transmitting transducer elements and four receiving transducer elements in the corresponding SRA acoustic-logging tool. The multiplication ALTN is approximately four times the addition ALTN for both the head-wave amplitude of the calculated logging signal and the calculated directivity. Apparently, the acoustic-beam steering efficiency of the multiplication ALTN is much greater than that of the addition ALTN. Using the SRA logging tool to perform petroleum logging, one can get a transient time curve from the SA and get another one from the RA. After performing depth alignment and averaging on the two transient curves, one can get a new transient time curve. Therefore, the accuracy of this new transient time curve is higher compared with the other

TABLE II. For the multiplication ALTN, when both excitation delay and shift time are 15.1018 μs and the SA consists of four transmitting transducer elements, the relation between the head-wave amplitude of stacked acoustic-logging signal and receiving transducer number in the RA.

m (where, choose $n=4$)	Stacked HWA
1	1.3866
2	2.7348
3	4.0186
4	5.2109

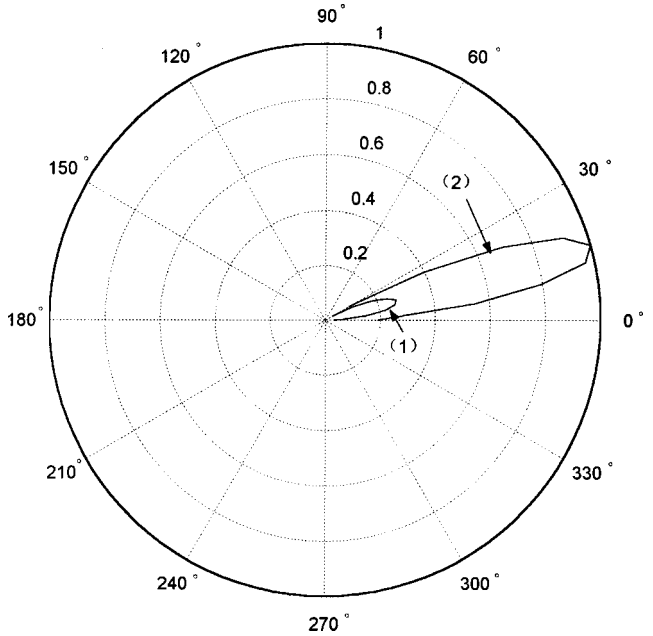

FIG. 8. Acoustic-beam steering directivities of the SA, RA, and multiplication logging transmission networks for calculation.

TABLE III. The parameters of the experimental equipment of the SA, RA, and SRA ALTNs.

n	m	ΔZ(m)	ΔL(m)	L(m)
4	4	0.082	0.082	2.44

two transient time curves. For all logging terms, the data quantity of acoustic logging is the greatest. The SRA logging tool uses a down-hole computer to calculate the dynamic excitation delay of the SA and to obtain a set of acoustic parameters of the formation. This process is equivalent to the processing four-channel acoustic-logging signals on the ground. There are only four-channel acoustic-logging data transmitting to the ground from the down-hole, which have been preprocessed in the down-hole. Therefore, compared with the RA logging tool with eight receiving transducer elements, the SRA logging tool with four transmitting transducer elements and four receiving transducer elements can reduce the data quantity transmitting from down-hole to ground through CTS during logging without loss of information quantity.

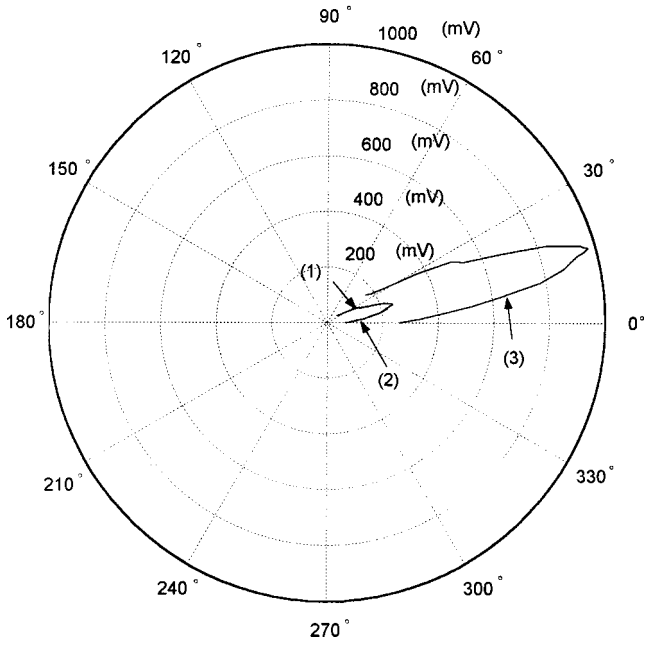

FIG. 10. Acoustic-beam steering directivities of the experimental equipment of the SA, RA, and SRA ALTNs for experimental measurement.

IV. EXPERIMENTAL VERIFICATION

Let the experimental equipment of SA, RA, and SRA ALTNs consist of combinations of four transmitting transducer elements and one receiving transducer element, one transmitting transducer element and four receiving transducer elements, and four transmitting transducer elements and four receiving transducer elements, respectively. Cylindrical shell transducers are used as the transducer elements of the SA and RA in the experiment. The electrical–acoustic transmission resonance frequency of the transducer is 20 kHz. The parameters of the three kinds of experimental equipment are shown in Table III. This experimental equipment is put in a water-filled, thin steel pipe, respectively. *P*-wave velocity, inner- and outer diameters of the steel pipe are 5640 m/s, 135 mm, and 143 mm, respectively.

In practice, the measured acoustic full waves in the water-filled steel pipe of radius R are certainly different from that in the water-filled cylindrical hole of radius R embedded in an infinite steel medium. But, the head wave of the former is a kind of quasi-*P* wave, which mainly consists of head waves of a direct refracted wave and multiple reflection waves in the steel pipe. Because the steel pipe is very thin, the travel time of the measured head wave is approximately equal to that of the direct refracted wave (i.e., the *P*-wave velocity of the steel medium). The measured results are shown in Fig. 9. Figure 9 shows that when the excitation delay Δt_0 is equal to $\Delta Z/V_2$ or the shift time Δt_0 is equal to $\Delta L/V_2$, the head-wave amplitudes measured by using the above three kinds of experimental equipment are the greatest

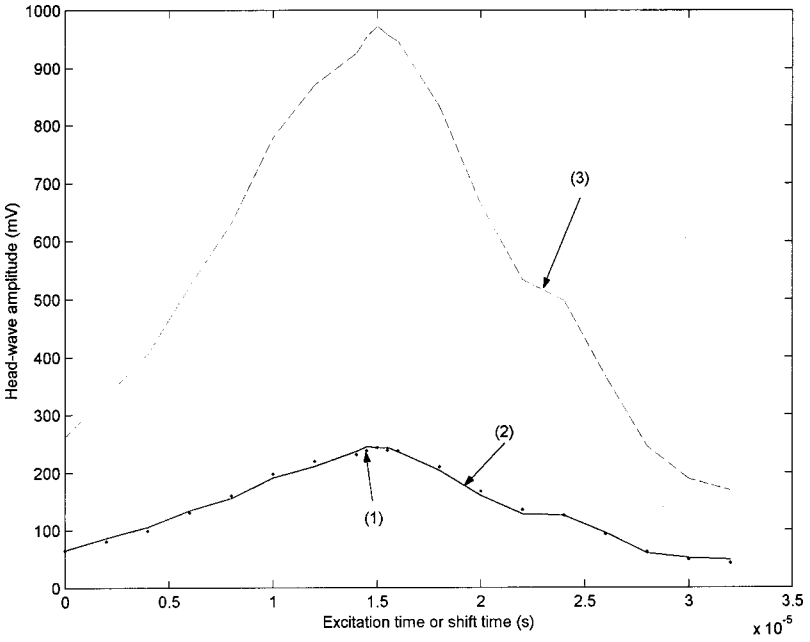

FIG. 9. Relation curves measured by experiment. The point line (1) is the relation curve between the head-wave amplitude of the received acoustic signal and the excitation delay for the experimental equipment of the SA ALTN. The solid line (2) is that between the head-wave amplitude of the stacked acoustic signals and the shift time for the experimental equipment of the RA ALTN. The dashed line (3) is that between the head-wave amplitude of the stacked acoustic signals and the shift time for the experimental equipment of the SRA ALTN when *P*-wave velocity of steel pipe is used to adjust the excitation delay.

TABLE IV. The observed relations between the transducer element number and the head-wave amplitudes of acoustic signals for the three kinds of logging tools.

SA logging tool		RA logging tool		SRA logging tool ($n=4$)	
n	HWA (mV)	m	HWA (mV)	m	HWA (mV)
1	67.50	1	65.50	1	247.05
2	140.00	2	137.00	2	493.40
3	207.00	3	198.50	3	736.48
4	247.00	4	242.00	4	972.48

as predicted for pure head waves. The measurement results shown in Fig. 9 can be converted to the acoustic-beam steering directivity graphs shown in Fig. 10 for the above three kinds of experimental equipment. The curve (1) is the directivity of the experimental equipment of the SA ALTN. The curve (2) is that of the experimental equipment of the RA ALTN and the curve (3) is that of the experimental equipment of the SRA ALTN. The curves (1) and (2) overlap so closely that they cannot be visibly distinguished. For the above three kinds of experimental equipment, when the *P*-wave velocity of steel pipe is used to adjust the excitation delay and shift time, the observed relations between the transducer element number and the head-wave amplitudes of the measured acoustic-logging signals are shown in Table IV.

It can be seen from the measured results shown in Table IV and Fig. 10 that when the *P*-wave velocity of steel pipe is used to adjust the excitation delay and shift time, the head-wave amplitude of the acoustic signal and the directivity value measured by using the experimental equipment of the SRA ALTN is approximately four times that measured by using the experimental equipment of the SA and RA ALTNs. The experimental results agree well with the theoretical prediction.

V. CONCLUSIONS

From the above formulation, calculation, experimental measurement, and analysis, some conclusions can be reached.

(1) The SA ALTN is reciprocal to the RA ALTN.
(2) The concepts of addition and multiplication ALTNs are put forward.
(3) Compared with the experimental equipment of two kinds of addition ALTNs (SA and RA), the acoustic-beam steering efficiency of the experimental equipment of the multiplication (SRA) ALTN is the greatest.
(4) The multiplication (SRA) ALTN can increase the accuracy of the measured transient time curve and greatly reduce the acoustic-logging data quantity transmitted to the ground from the down-hole by CTS without loss of logging information.

ACKNOWLEDGMENTS

We would like to thank Associate Editor Stanley L. Ehrlich and the reviewers for their insightful comments, and the Institute for Exploration and Development Geosciences, University of Oklahoma and Fusion Geophysical for their financial support. We also thank Professor Billy Wolfe and Mr. Chuck Fry for their improvement of this manuscript.

[1] L. Fa, J. P. Castagna, J. M. Hovem, and D. Dong, ''An acoustic-logging transmission-network model,'' J. Acoust. Soc. Am. **111**(5), 2158–2165 (2002).
[2] D. A. Berlincourt, D. R. Curran, and H. Jaffe, ''Piezoelectric and piezomagnetic materials and their function in transducers,'' in *Physical Acoustics*, edited by W. P. Mason (Academic, New York, 1964), Vol. 1A, pp. 223–224.
[3] L. Fa, J. P. Castagna, and J. M. Hovem, ''Derivation and simulation of source function for acoustic logging,'' 1999 IEEE International Ultrasonics Symposium Proceedings, pp. 707–710.
[4] H. Du, Z. Zhu, and X. Gong, *Basis of Acoustics* (Shanghai Science and Technology, Shanghai, 1981), Vol. 2, pp. 67–75.
[5] A. L. Kurkjian, ''Numerical computation of individual far-field arrivals excited by an acoustic source in a borehole,'' Geophysics **50**, 852–866 (1985).
[6] L. Fa, A. Lu, and P. Li, ''Relation between radiated acoustic wave signal and driving voltage for a spherical shell transducer,'' Well Logging Technol. **22**, 32–35 (1998).
[7] L. Fa and H. Ma, ''Design of a new type of array transmitting sonic sonde,'' Acta Petrolei Sinica **12**, 52–57 (1991).

Performance bounds for passive sensor arrays operating in a turbulent medium: Plane-wave analysis

S. L. Collier[a] and D. K. Wilson[b]
U.S. Army Research Laboratory, ATTN: AMSRL-CI-EE, 2800 Powder Mill Road, Adelphi, Maryland 20783-1197

(Received 27 August 2001; revised 12 December 2002; accepted 31 December 2002)

The performance bounds of a passive acoustic array operating in a turbulent medium with fluctuations described by a von Kármán spectrum are investigated. This treatment considers a single, monochromatic, plane-wave source at near-normal incidence. A line-of-sight propagation path is assumed. The primary interests are in calculating the Cramer–Rao lower bounds of the azimuthal and elevational angles of arrival and in observing how these bounds change with the introduction of additional unknowns, such as the propagation distance, turbulence parameters, and signal-to-noise ratio. In both two and three dimensions, it is found that for large values of the index-of-refraction variance, the Cramer–Rao lower bounds of the angles of arrival increase significantly at large values of the normalized propagation distance. For small values of the index-of-refraction variance and normalized propagation distance, the signal-to-noise ratio is found to be the limiting factor. In the two-dimensional treatment, it is found that the estimate of the angle of arrival will decouple from the estimates of the other parameters with the appropriate choice of array geometry. In three dimensions, again with an appropriate choice of array geometry, the estimates of the azimuth and elevation will decouple from the estimates of the other parameters, but due to the constraints of the model, will remain coupled to one another. [DOI: 10.1121/1.1554691]

PACS numbers: 43.60.Cg, 43.28.Gq [LCS]

I. INTRODUCTION

Sensor arrays are often used to estimate the orientation of wave fronts arriving from a distant source, thereby providing information on the source bearing. The fidelity of the wave-front angle-of-arrival (AOA) estimates is affected by noise (interfering sound sources) and, if present, by scattering from random inhomogeneities in the propagation environment. The random inhomogeneities distort the propagating wave fronts, causing the apparent bearing and strength of the source to fluctuate. The net effect of these distortions can be important for direction finding in both the atmosphere[1,2] and the ocean.[3,4]

The performance of a sensor array may be quantified by calculating the mean square error (MSE) between the estimated parameter (such as the AOA) and its actual value. The lower bound of the MSE is the Cramer–Rao lower bound (CRLB), which is calculated from the Fisher information (FI).[5,6] There already exists much work in the open literature that characterizes the CRLB of array processors in the presence of noise only. (See Ottersten *et al.*,[7] and references therein.) Recently, Song and Ritcey[8] directly incorporated the effects of random media on acoustic waves into the calculation of the CRLBs of the AOAs. Specifically, they considered propagation in an ocean channel with random inhomogeneities having a Gaussian spatial correlation. Using the general framework of Song and Ritcey, Wilson[9] calculated the performance bounds on AOA estimates using various correlation functions that are representative of atmospheric turbulence.

A limitation of the previous CRLB calculations for random media is that the received signals were modeled as complex, zero-mean, Gaussian random variables. The zero-mean assumption implicitly treats the case of strong scattering by the medium. However, in many practical problems the variance of the index-of-refraction fluctuations is sufficiently small, or the propagation distance is sufficiently short, that the waves have only been weakly scattered when they arrive at the receiving array. A weakly scattered wave has a mean component significantly larger than the standard deviation of the real and imaginary parts of the signal.

In this paper we provide a comprehensive analysis of the CRLBs for passive sensor arrays operating in a turbulent medium. By avoiding the zero-mean assumption, we are able to develop a model that is valid for both strong and weak scattering. To capture scattering by eddies in both the energy-containing and inertial subranges, a von Kármán spectrum is used for the turbulence.[14] Furthermore, we expand the analysis from Ref. 9 to include the propagation distance, signal-to-noise ratio (SNR), turbulence parameters, and phase of the source in the unknown parameter set. By calculating the coupling between the estimates of the AOAs and the estimates of the other parameters, we are able to determine the extent to which the estimates of the AOAs will degrade when the AOAs and other parameters are simultaneously estimated.

In the following, both two-dimensional (2D) and three-dimensional (3D) plane-wave propagation are considered. This investigation is limited to near-normal incidence at a line array (2D) and a planar array (3D). A single, monochro-

[a]Electronic mail: scollier@arl.army.mil
[b]Currently with Engineer Research and Development Center, U.S. Army Cold Regions Research and Engineering Laboratory, ATTN: CEERD-RC, 72 Lyme Road, Hanover, NH 03755-1290.

matic source and a line-of-sight propagation path are assumed. The signal model, including the first and second moments needed for the CRLB calculations, is introduced in Sec. II. The CRLB is derived in Sec. III, followed by the numerical results in Sec. IV. Concluding remarks are in Sec. V. The FI for a two-element array is given in Appendix A and lists of the symbols and acronyms are given in Appendix B.

II. THEORETICAL MODEL

Calculation of the FI requires a priori knowledge of the probability density function (PDF) of the received signal. In this section we develop a theoretical model, which incorporates the effects of turbulence on the source signal, to describe the PDF of the received signal.

Let us define the notation that shall be used throughout this paper: $[\cdot]^*$ denotes the complex conjugate, $[\cdot]^T$ the transpose, $[\cdot]^\dagger$ the Hermitian adjoint (complex conjugate transpose), and $\langle\cdot\rangle$ the ensemble average or expectation value.

Consider an array with N sensors. We assume that the signal at each sensor results from: (1) the wave that has propagated from the source of interest with ϕ and θ as the azimuthal and elevational AOAs, respectively, and (2) random noise. Let $\mathbf{p}(\phi,\theta,t)$ and $\mathbf{n}(t)$ be the respective time-varying complex envelopes of the two contributions. These vectors are column vectors with N elements, one element corresponding to each sensor. The source contribution is time dependent because of the random turbulent effects. The noise, which is also time dependent, may result from wind noise or other competing acoustic sources. The total received signal is

$$\mathbf{s}(\phi,\theta,t)=\mathbf{p}(\phi,\theta,t)+\mathbf{n}(t). \tag{1}$$

Let us assume that the source and the noise signals are uncorrelated and that the noise signals at the sensors are mutually uncorrelated with equal variance. Let us further assume that the noise component has a complex Gaussian distribution with a zero mean and variance σ_n^2. Although exact solutions for the pressure field of the source and its PDF are unknown, solutions to its first and second moments can be found in the literature. We therefore approximate that $\mathbf{p}$ has a complex Gaussian distribution with mean (or first moment) $\boldsymbol{\mu}$ and covariance matrix $\mathbf{C}_p$, whose elements are

$$\mu_i=\langle p_i\rangle, \quad [\mathbf{C}_p]_{ij}=\langle p_i p_j^*\rangle-\mu_i\mu_j^*. \tag{2}$$

We use the results in the open literature for acoustic wave propagation in a random medium to determine the first moment μ_i and the second moment $\langle p_i p_j^*\rangle$ as discussed in Sec. II A. The total signal $\mathbf{s}$ is thus Gaussian distributed with mean $\boldsymbol{\mu}$ and covariance

$$\mathbf{C}=\mathbf{C}_p+\sigma_n^2\mathbf{I}_N, \tag{3}$$

where $\mathbf{I}_N$ is the $N\times N$ identity matrix.

This signal model, in which the real and imaginary parts are Gaussian random variables with equal covariances, is reasonable for strong or weak scattering in the presence of strong diffraction (the Rytov extension region). It is not suited to situations where both scattering and diffraction are weak (geometric acoustics), in which case the phase variance dominates the signal behavior.[10,11]

Admittedly, the signal and noise statistics observed in the atmosphere and ocean often deviate significantly from the idealized assumptions used in this paper. For example, turbulent pressure fluctuations from the atmospheric wind (usually called "wind noise") often exhibit notable correlations over scales of several meters.[12] In some frequency ranges, signals that have propagated through the atmosphere exhibit a combination of low amplitude variance and high phase variance that is inconsistent with the present Gaussian model.[13] It would be desirable in future work to address the significance of these discrepancies between the idealized model and the actual signal and noise properties.

A. First and second moments

The pressure field associated with a sound wave propagating in a moving random medium is characterized by a closed set of fluid dynamic equations. The small-angle parabolic and Markov approximations may be used to obtain the statistical moments of the sound field in closed form. These approximations are valid in far field, for small scattering angles, and for $\mathcal{L}\gg\lambda>\ell$, where λ is the wavelength, and $\mathcal{L}$ and ℓ are the outer (integral) and inner (Kolmogorov) length scales of the turbulence, respectively. We use the solutions for the first and second moments of the pressure field as given by Ostashev,[14] who generalized the results in Refs. 11 and 15 to include fluctuations in the medium velocity. The solution for the second moment is, however, strictly valid for normal incidence across two sensors.

Consider a sound wave that is propagating with wave number $\mathbf{k}$, $k=2\pi/\lambda$, where λ is the wavelength of the source. Let the vector from the center of the array normal to the plane of the source be $\mathbf{r}=-r\hat{\mathbf{k}}=r\hat{\mathbf{r}}$, so that r is the propagation distance of the wave front to the center of the array. Let $[\cdot]^\perp$ and $[\cdot]^\parallel$ denote the components of a vector transverse and parallel to $\hat{\mathbf{r}}$, respectively. The azimuthal and elevational AOAs, ϕ and θ, are measured with respect to the center of the array, so that $\hat{\mathbf{r}}=[\cos\phi\cos\theta, \sin\phi\cos\theta, \sin\theta]^T$. An illustration is given in Fig. 1. Let $\mathbf{r}_i'=[x_i', y_i', z_i']^T$ be the vector from the center of the array to the ith sensor. We define $\mathbf{r}_i=\mathbf{r}-\mathbf{r}_i'$, so that $r_i^\parallel=|\mathbf{r}_i\cdot\hat{\mathbf{r}}|$ is the propagation distance of the wave front to the ith sensor. Let us also define $\boldsymbol{\rho}_{ij}=\mathbf{r}_i-\mathbf{r}_j=\mathbf{r}_j'-\mathbf{r}_i'$ to be the separation vector between the jth and ith sensors.

From Ref. 14, the first moment at the ith sensor is

$$\mu_i=p_H(\mathbf{r}_i)e^{-\gamma r_i^\parallel}, \tag{4}$$

where γ is the extinction coefficient for the first moment and p_H is the sound field in the absence of random inhomogeneities. For a plane wave

$$p_H(\mathbf{r}_i)=p_0 e^{i\Phi_i}, \tag{5}$$

where p_0 is the pressure amplitude of the source (a real-valued constant) and Φ_i (also real valued) is the total phase at the ith sensor. As we have defined $\mathbf{r}$ and $\mathbf{r}_i$ to be from the array plane to the source plane, it follows that

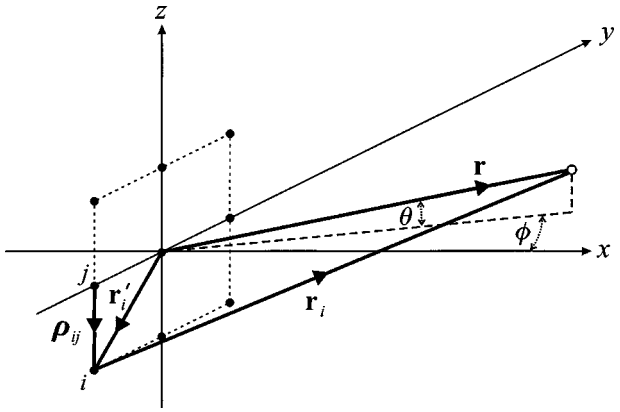

FIG. 1. Coordinate system. The closed circles represent the sensors. The open circle represents the point in the plane of the source at which $\mathbf{r}$ is normal to the wave front. The azimuthal and elevational AOAs, ϕ and θ, are defined with respect to $\hat{\mathbf{r}}$.

$$\Phi_i = \chi - \mathbf{k}\cdot\mathbf{r}_i, \tag{6}$$

where χ is the phase of the source. Now from Ref. 14, the second moment for *normal* incidence across sensors i and j, i.e., when $r_i^{\parallel} = r_j^{\parallel}$ and hence $\boldsymbol{\rho}_{ij}^{\perp} = \boldsymbol{\rho}_{ij}$, is

$$\langle p_i p_j^* \rangle = p_H(\mathbf{r}_i) p_H^*(\mathbf{r}_j) e^{-\alpha(\rho_{ij}^{\perp}) r_i^{\parallel}} = p_0^2 e^{i\Phi_{ij}} e^{-\alpha(\rho_{ij}^{\perp}) r_i^{\parallel}}, \tag{7}$$

where $\alpha(\rho)$ is the extinction coefficient for the second moment and Φ_{ij} is the total phase difference between the ith and jth sensors,

$$\Phi_{ij} = \Phi_i - \Phi_j = -\mathbf{k}\cdot\boldsymbol{\rho}_{ij}. \tag{8}$$

The extinction coefficient for the moments are related by

$$2\gamma = \alpha(\rho = \infty). \tag{9}$$

In order to apply the results of Ref. 14 to oblique incidence, we assume that the attenuation of the first moment and of the second moment may be approximated by the values for normal incidence. We take the first moment at the ith sensor to be

$$\mu_i \approx p_H(\mathbf{r}_i) e^{-\gamma r}, \tag{10}$$

where $p_H(\mathbf{r}_i)$ is still determined from Eqs. (5) and (6). [Recall that for normal incidence, $r_i^{\parallel} = r$ for every i.] We are thus assuming that the largest source of variation of the first moment between the center of the array and the ith sensor is due to the phase not the attenuation. Equation (10) is valid if, for every i and j,

$$e^{-\gamma r_i^{\parallel}} \approx e^{-\gamma r_j^{\parallel}} \approx e^{-\gamma r}, \tag{11}$$

i.e., if the attenuation of the first moment is approximately constant across the array. The second moment is approximated as

$$\langle p_i p_j^* \rangle \approx p_H(\mathbf{r}_i) p_H^*(\mathbf{r}_j) e^{-\alpha(\rho_{ij}) r}, \tag{12}$$

where again $p_H(\mathbf{r}_i)$ and $p_H^*(\mathbf{r}_j)$ are determined from Eqs. (5) and (6). This approximation holds if for every i and j,

$$\alpha(\rho_{ij}^{\perp}) \approx \alpha(\rho_{ij}), \tag{13}$$

$$e^{-\alpha(\rho_{ij}) r_i^{\parallel}} \approx e^{-\alpha(\rho_{ij}) r_j^{\parallel}} \approx e^{-\alpha(\rho_{ij}) r}. \tag{14}$$

A consistent form of the first and second moments must be used to ensure that the covariance matrix $\mathbf{C}_p$ is positive semi-definite. For example, as

$$[\mathbf{C}_p]_{ij} = \langle p_i p_j^* \rangle - \langle p_i \rangle \langle p_j^* \rangle = p_0^2 [e^{-\alpha(\rho_{ij}) r} - e^{-2\gamma r}] e^{i\Phi_{ij}}, \tag{15}$$

in the limit $\rho_{ij} \to \infty$,

$$[\mathbf{C}_p]_{ij} \to p_0^2 [e^{-2\gamma r} - e^{-2\gamma r}] e^{i\Phi_{ij}} = 0, \tag{16}$$

as it should.

Due to the constraints of the approximations in Eqs. (11), (13) and (14), as well as the small-angle parabolic approximation, we restrict our investigation to near-normal incidence to: (1) a linear array for propagation in 2D and (2) a planar array for propagation in 3D. In this way, the wave front arrives with near-normal incidence across every pair of sensors in the array. It should be noted that all of the information on the angles of arrival is contained in the phase terms. Therefore, the limitation to near-normal incidence is consistent with the limitations of direction finders that use phase differences to determine the wave front's angle of arrival.

An advantage to this formulation of the first and second moments is that the resulting covariance matrix $\mathbf{C}_p$ and mean $\boldsymbol{\mu}$ may be written in terms of the mutual coherence function (MCF) matrix $\boldsymbol{\Gamma}$, a steering vector $\boldsymbol{s}$, and a steering matrix $\boldsymbol{\mathcal{S}}$. We define the ij element of the MCF matrix to be the positive square root of

$$\Gamma_{ij}^2 = \frac{\langle p_i p_j^* \rangle \langle p_i^* p_j \rangle}{\langle p_i p_i^* \rangle \langle p_j p_j^* \rangle}. \tag{17}$$

In the literature, the distinction between the second moment and the MCF is not always made for a plane wave. For the treatment here,

$$\Gamma_{ij} = |\langle p_i p_j^* \rangle| / p_0^2 = e^{-\alpha(\rho_{ij}) r}. \tag{18}$$

The minimum value of the MCF occurring for $\rho_{ij} = \infty$ is $\Gamma_{\min} = e^{-2\gamma r}$. The steering vector is defined to be

$$\boldsymbol{s} = [e^{i\mathbf{k}\cdot\mathbf{r}_1}, e^{i\mathbf{k}\cdot\mathbf{r}_2}, \cdots, e^{i\mathbf{k}\cdot\mathbf{r}_N}]^{\dagger}. \tag{19}$$

The steering matrix represents the phase delay between the sensors due solely to the difference in propagation length. It is given by

$$\boldsymbol{\mathcal{S}} = \boldsymbol{s} \otimes \boldsymbol{s}^{\dagger}, \quad \mathcal{S}_{ij} = \exp(-i\mathbf{k}\cdot\boldsymbol{\rho}_{ij}), \tag{20}$$

where $\otimes$ is the Kronecker product (the direct or tensor product). Therefore

$$\boldsymbol{\mu} = p_0 \Gamma_{\min}^{1/2} e^{i\chi} \boldsymbol{s}, \tag{21}$$

$$\mathbf{C}_p = p_0^2 \, \boldsymbol{\Gamma} \odot \boldsymbol{\mathcal{S}} - p_0^2 \, \boldsymbol{\Gamma}_{\min} \boldsymbol{\mathcal{S}}, \tag{22}$$

where $\odot$ is the Hadamard product[16] (element-by-element multiplication).

B. Turbulence model

The extinction coefficients depend on the structure of the random medium. For an incident plane wave the extinction coefficient for the second moment[14,17,18] is

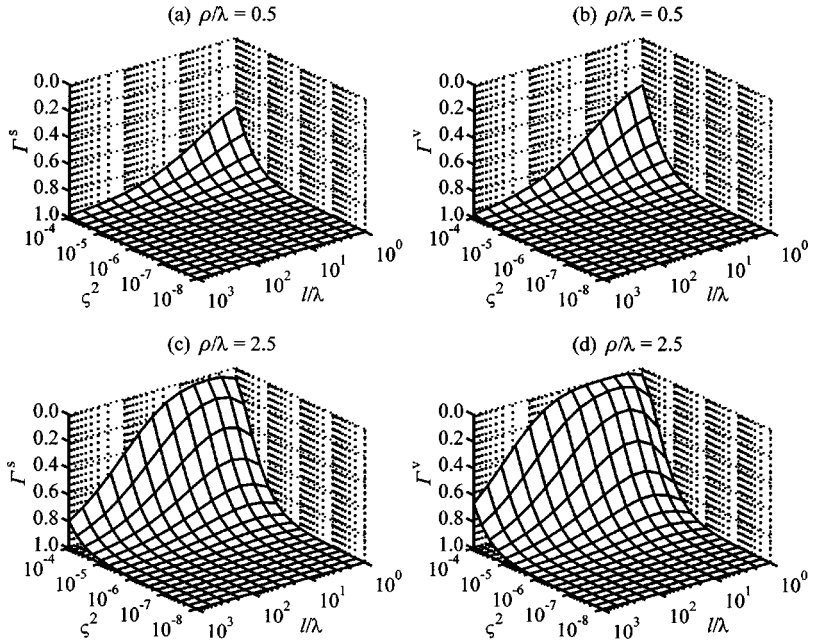

FIG. 2. Coherence for von Kármán spectra: (a) and (c) are for a scalar spectrum; (b) and (d) are for a vector spectrum. All calculations are for $r/\lambda = 500$.

$$\alpha(\rho) = 2\pi k^2 [f(0) - f(\rho)], \tag{23}$$

where $f(\rho)$ is the 2D (or projected) correlation function for the sound-speed fluctuations. For most random media, including turbulence, $\alpha(\rho)$ initially increases monotonically with increasing ρ, but when ρ exceeds $\mathcal{L}$, $\alpha(\rho)$ asymptotically approaches a constant value. Since $f(\rho) \to 0$ in the limit $\rho \to \infty$, this constant value is simply 2γ, given by

$$2\gamma = 2\pi k^2 f(0) = 2\varsigma^2 k^2 \mathcal{L}, \tag{24}$$

where ς^2 is the index of refraction variance. Hence the second moment initially decreases with increasing ρ, and eventually ''saturates'' at a fixed minimum value.

The performance of atmospheric acoustic sensor arrays depends on the turbulence structure in the part of the turbulence spectrum corresponding to the sensor spacing.[9] In typical situations, the sensor spacing may be within the energy-containing subrange, the inertial subrange, or both. Therefore, in this paper we use the isotropic, homogeneous von Kármán model for the turbulence spectrum, which describes the inertial subrange of the spectrum more realistically than the commonly used Gaussian models, yet still behaves reasonably in the energy-containing subrange.[19] The von Kármán form for the 2D correlation function is dependent upon the source of the sound speed fluctuations: a scalar field is induced by temperature or humidity fluctuations and a vector field is induced by wind velocity fluctuations. The 2D correlation functions for a scalar field f_s and a vector field f_v, may be written in the form (see Eq. (49) in Ref. 18 and Eq. (7.112) in Ref. 14)

$$f_s(\rho, \varsigma^2, l) = \frac{2\varsigma^2 l}{\sqrt{\pi}\Gamma(1/3)} \left(\frac{\rho}{2l}\right)^{5/6} K_{5/6}\left(\frac{\rho}{l}\right), \tag{25}$$

$$f_v(\rho, \varsigma^2, l) = \frac{2\varsigma^2 l}{\sqrt{\pi}\Gamma(1/3)} \left(\frac{\rho}{2l}\right)^{5/6} \left[K_{5/6}\left(\frac{\rho}{l}\right) - \frac{\rho}{2l} K_{1/6}\left(\frac{\rho}{l}\right)\right], \tag{26}$$

where $l = \Gamma(1/3)\mathcal{L}/[\sqrt{\pi}\Gamma(5/6)]$ is a characteristic length scale of the turbulence, $\Gamma(x)$ is the gamma function, and $K_\nu(x)$ is the modified Bessel function of order ν. The equation for f_s in this paper differs somewhat from that of Ref. 9 due to the manner in which the scalar energy spectrum was defined in that paper. The equation in this paper is consistent with the more standard definition found in Ref. 14.

The MCF for both a scalar, Γ^s_{ij}, and a vector, Γ^v_{ij}, von Kármán spectrum is plotted in Fig. 2 as a function of the index-of-refraction variance, ς^2, and the characteristic length scale normalized by the wavelength, l/λ. In presenting the results, it is natural to use normalized length scales, (e.g., r/λ, d/λ, etc.), as then the coherence has no explicit wavelength dependence. In Figs. 2(a) and (b) the MCFs are calculated for $\rho_{ij}/\lambda = 0.5$ and $r/\lambda = 500$. The coherence for both spectra decreases significantly in the regions where the index-of-refraction variance is large, $\varsigma^2 \sim 10^{-4}$, and the normalized characteristic length scale is small, $1 < l/\lambda < 10$. (The MCF is actually dependent upon the product $\varsigma^2 r/\lambda$; therefore, the y axis alternatively represents an increase in r/λ for fixed ς^2.) In Figs. 2(c) and (d) the same is calculated but for $\rho_{ij}/\lambda = 2.5$. The larger sensor separation leads to a more rapid decrease in the MCFs as functions of the turbulence parameters. For both sensor separations the MCF for the vector spectrum is more sensitive to the changes in the turbulence parameters, and its minimum with respect to the turbulence parameters (for a fixed finite sensor separation and normalized propagation distance) is smaller than that for the scalar spectrum. The function $\Gamma_{\min}$ (the minimum value of the MCF as a function of sensor separation ($\rho_{ij} = \infty$) for fixed propagation distance and fixed turbulence parameters) is the same for both a scalar and a vector spectrum. It is plotted in Fig. 3. Even though its value is only dependent upon the product $\varsigma^2 r l/\lambda^2$, it is plotted versus the same turbulence parameters at $r/\lambda = 500$ for ease of comparison with Fig. 2.

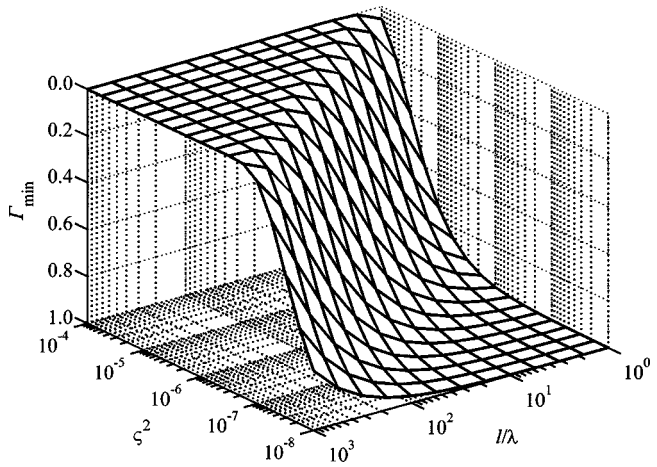

FIG. 3. Minimum coherence ($\rho_{ij}=\infty$) for von Kármán spectra, $\Gamma_{\min}=e^{-2\gamma r}$. Calculation is for $r/\lambda=500$.

III. FORMULATION

Having completed the theoretical model, we proceed to formulate the FI. We begin by reviewing the Cramer–Rao theory. We then proceed to analytically calculate the CRLBs for the cases of no turbulence and a two-element array operating in turbulence. These cases will provide valuable insight into the behavior of the full results. We specifically address factors, such as array geometry, that affect the coupling of the parameter estimates.

A. Cramer–Rao lower bound

Consider the complex random vector $\mathbf{s}$. Suppose that the PDF of $\mathbf{s}$ is parametrized by the $\mathcal{N}\times 1$ real vector $\mathbf{\Theta}=[\Theta_1, \Theta_2, \ldots, \Theta_{\mathcal{N}}]^T$. The elements of $\mathbf{\Theta}$ are the real unknown parameters to be estimated (for example, the angles of arrival). The Cramer–Rao theorem[5,6] states that for any unbiased estimator $\hat{\mathbf{\Theta}}$,

$$\langle(\Theta_\nu-\hat{\Theta}_\nu)^2\rangle\geqslant[\mathbf{J}^{-1}(\mathbf{\Theta})]_{\nu\nu}, \tag{27}$$

where $\mathbf{J}(\mathbf{\Theta})$ is the $\mathcal{N}\times\mathcal{N}$ Fisher information (FI) matrix. The right-hand side of Eq. (27) is the Cramer–Rao lower bound (CRLB). The CRLB of Θ_ν is the minimum MSE between the estimator $\hat{\Theta}_\nu$ and its actual value Θ_ν. We define

$$\sigma_\nu=\sqrt{[\mathbf{J}^{-1}]_{\nu\nu}} \tag{28}$$

and loosely refer to either σ_ν or σ_ν^2 as the CRLB of Θ_ν, as the meaning should be evident from the units involved.

The λ-νth element of the FI matrix is related to the probability likehood function $\wp(\mathbf{s};\mathbf{\Theta})$ (the PDF of $\mathbf{s}$ with $\mathbf{\Theta}$ as a parameter) by

$$[\mathbf{J}(\mathbf{\Theta})]_{\lambda\nu}=-\left\langle\frac{\partial^2\ln\wp(\mathbf{s};\mathbf{\Theta})}{\partial\Theta_\lambda\partial\Theta_\nu}\right\rangle, \tag{29}$$

where the expectation is taken with respect to $\wp(\mathbf{s};\mathbf{\Theta})$ and the derivatives are evaluated at the true value of $\mathbf{\Theta}$.

Suppose that $\mathbf{s}$ is a complex Gaussian random vector with covariance matrix $\mathbf{C}(\mathbf{\Theta})$ and mean $\boldsymbol{\mu}(\mathbf{\Theta})$. Its likelihood function may be written as[5]

$$\wp(\mathbf{s};\mathbf{\Theta})=\frac{1}{\pi^N\det[\mathbf{C}(\mathbf{\Theta})]}\times\exp\{-[\mathbf{s}-\boldsymbol{\mu}(\mathbf{\Theta})]^\dagger\mathbf{C}^{-1}(\mathbf{\Theta})[\mathbf{s}-\boldsymbol{\mu}(\mathbf{\Theta})]\}. \tag{30}$$

The corresponding FI for M independent and identically distributed data sets is[5]

$$J_{\lambda\nu}=M\,\mathrm{tr}\left(\mathbf{C}^{-1}\frac{\partial\mathbf{C}}{\partial\Theta_\lambda}\mathbf{C}^{-1}\frac{\partial\mathbf{C}}{\partial\Theta_\nu}\right)+2M\,\mathrm{Re}\left(\frac{\partial\boldsymbol{\mu}^\dagger}{\partial\Theta_\lambda}\mathbf{C}^{-1}\frac{\partial\boldsymbol{\mu}}{\partial\Theta_\nu}\right), \tag{31}$$

where the functional dependence on $\mathbf{\Theta}$ is implied. For $\mathcal{N}$ unknown parameters, $\mathbf{J}$ is an $\mathcal{N}\times\mathcal{N}$ matrix. And for N sensors in the array, $\mathbf{s}$ and $\boldsymbol{\mu}$ are column vectors of length N and $\mathbf{C}$ is an $N\times N$ matrix. Let us use the convention that λ, $\nu\in[1,2,\ldots,\mathcal{N}]$ are the indices on the unknown parameters and $i,j\in[1,2,\ldots,N]$ are the indices on the sensors.

The minimum value of the CRLB of Θ_ν occurs when Θ_ν is the only unknown parameter, and is given by $1/J_{\nu\nu}$. We define

$$\sigma_{\nu_0}^2=1/J_{\nu\nu}. \tag{32}$$

As the number of unknowns increases, σ_ν^2 will increase.

For example, suppose that there are two unknowns. For λ and ν cyclic (e.g., if $\lambda=1$ then $\nu=2$),

$$\sigma_\lambda^2=\frac{1}{J_{\lambda\lambda}-J_{12}^2/J_{\nu\nu}}=\sigma_{\lambda_0}^2\frac{1}{1-\zeta_{12}}, \tag{33}$$

where ζ_{12} is the coupling, or partial correlation, given by

$$\zeta_{12}=\frac{J_{12}^2}{J_{11}J_{22}},\quad 0\leqslant\zeta_{12}\leqslant 1. \tag{34}$$

Only if $J_{12}=0$ does $\sigma_\lambda^2=\sigma_{\lambda_0}^2$, and the estimates of Θ_1 and Θ_2 are said to be uncoupled. As ζ_{12} increases, σ_λ^2 increases from its minimum value of $\sigma_{\lambda_0}^2$, and a degradation of the estimates of Θ_1 and Θ_2 results. The quantity ζ_{12} thus provides a measure of the strength of the coupling between, and hence degradation of, the estimates of Θ_1 and Θ_2: if $\zeta_{12}=0$, the estimates are uncoupled and the CRLBs retain their minimum values; if $\zeta_{12}\ll 1$, the estimates of Θ_1 and Θ_2 are weakly coupled and the CRLBs increase only slightly; and if $\zeta_{12}=1$, the estimates are fully coupled, the CRLBs are infinite, and hence neither Θ_1 nor Θ_2 can be estimated. It is therefore advantageous to determine the conditions under which the estimates of Θ_1 and Θ_2 will decouple.

B. FI of theoretical model

We write the elements of the mean vector and total covariance matrix to be used in the calculation of the FI as

$$\mu_i=p_0e^{-\gamma r}e^{i\Phi_i}=p_0\Gamma_{\min}^{1/2}e^{i\Phi_i}, \tag{35}$$

$$C_{ij}=p_0^2\left\{[e^{-\alpha(\rho_{ij})r}-e^{-2\gamma r}]e^{i\Phi_{ij}}+\frac{\sigma_n^2}{p_0^2}\delta_{ij}\right\}$$

$$=p_0^2\left[(\Gamma_{ij}-\Gamma_{\min})e^{i\Phi_{ij}}+\frac{\sigma_n^2}{p_0^2}\delta_{ij}\right], \tag{36}$$

where δ_{ij} is the Kronecker delta function and

$$\Phi_i=\chi+kr-k(x_i'\cos\phi\cos\theta+y_i'\sin\phi\cos\theta + z_i'\sin\theta), \tag{37}$$

$$\Phi_{ij}=k(x_j'-x_i')\cos\phi\cos\theta+k(y_j'-y_i')\sin\phi\cos\theta + k(z_j'-z_i')\sin\theta. \tag{38}$$

The signal-to-noise ratio is related to the noise variance by $\mathrm{SNR}=p_0^2/\sigma_n^2$. For a plane wave, p_0 is a constant, and we treat either the SNR, or its inverse 1/SNR, as the unknown. In this way the exact value of p_0 is not needed for the calculation of the FI, as its dependence in the FI cancels.

The FI may now be readily calculated from Eq. (31) for those parameters we wish to consider as unknowns: ϕ, θ, χ, r, l, ς^2, and SNR. Note that the source phase χ must be treated as an unknown when a nonzero mean is considered. We address this point later. While the derivatives of the covariance matrix and mean with respect to these parameters are straightforward, the derivatives with respect to the turbulence parameter l are tedious. For brevity, the derivatives are not presented here.

Numerical difficulties may arise when trying to invert the FI matrix, **J**. Consider the diagonal terms of this matrix. The contributions from the propagation distance r and characteristic length scale l may differ by over ten orders of magnitude. This scale discrepancy may also occur for other parameters. We construct a diagonal matrix **D**, whose elements are the inverse of the square roots of the diagonal elements of the FI matrix, $D_{\lambda\nu}=J_{\lambda\nu}^{-1/2}\delta_{\lambda\nu}$. The matrix $\mathbf{A}=\mathbf{DJD}$ may now be easily inverted by standard numerical techniques. The inverse of the FI matrix is then numerically computed from $\mathbf{J}^{-1}=\mathbf{DA}^{-1}\mathbf{D}$.

C. No turbulence

Let us begin by examining the case of no turbulence. In the absence of turbulence

$$\boldsymbol{\mu}=p_0[e^{i\Phi_1},\ e^{i\Phi_2},\ \ldots,\ e^{i\Phi_N}]^T,\quad \mathbf{C}=\sigma_n^2\mathbf{I}_N. \tag{39}$$

The elements of the FI matrix are

$$J_{\lambda\nu}=\frac{MN}{\sigma_n^4}\frac{\partial\sigma_n^2}{\partial\Theta_\lambda}\frac{\partial\sigma_n^2}{\partial\Theta_\nu}+2M\frac{p_0^2}{\sigma_n^2}\sum_{i=1}^{N}\frac{\partial\Phi_i}{\partial\Theta_\lambda}\frac{\partial\Phi_i}{\partial\Theta_\nu}. \tag{40}$$

Let us consider the AOAs and source phase as unknowns, and the propagation distance and noise variance as knowns. It follows that

$$J_{\phi\phi}=2Mk^2\cos^2\theta\frac{p_0^2}{\sigma_n^2}\sum_{i=1}^{N}(x_i'\sin\phi-y_i'\cos\phi)^2, \tag{41}$$

$$J_{\theta\theta}=2Mk^2\frac{p_0^2}{\sigma_n^2}\sum_{i=1}^{N}(x_i'\cos\phi\sin\theta+y_i'\sin\phi\sin\theta - z_i'\cos\theta)^2, \tag{42}$$

$$J_{\chi\chi}=2MN\frac{p_0^2}{\sigma_n^2}, \tag{43}$$

$$J_{\phi\theta}=2Mk^2\cos\theta\frac{p_0^2}{\sigma_n^2}\sum_{i=1}^{N}[(x_i'^2-y_i'^2)\cos\phi\sin\phi\sin\theta + x_i'y_i'(\sin^2\phi-\cos^2\phi)\sin\theta-x_i'z_i'\sin\phi\cos\theta + y_i'z_i'\cos\phi\cos\theta], \tag{44}$$

$$J_{\phi\chi}=2Mk\cos\theta\frac{p_0^2}{\sigma_n^2}\sum_{i=1}^{N}(x_i'\sin\phi-y_i'\cos\phi), \tag{45}$$

$$J_{\theta\chi}=2Mk\frac{p_0^2}{\sigma_n^2}\sum_{i=1}^{N}(x_i'\cos\phi\sin\theta+y_i'\sin\phi\sin\theta - z_i'\cos\theta). \tag{46}$$

Therefore, the estimate of the source phase χ will decouple from the estimates of ϕ and θ for every value of ϕ and θ if

$$\sum_{i=1}^{N}x_i'=\sum_{i=1}^{N}y_i'=\sum_{i=1}^{N}z_i'=0, \tag{47}$$

i.e., if the center of the array is located at the origin. (If r is unknown, the estimate of r will also decouple from the estimates of ϕ and θ if Eq. (47) is satisfied.) The estimates of ϕ and θ will decouple from one another if

$$\sum_{i=1}^{N}y_i'^2=\sum_{i=1}^{N}x_i'^2,\quad \sum_{i=1}^{N}x_i'y_i'=\sum_{i=1}^{N}x_i'z_i'=\sum_{i=1}^{N}y_i'z_i'=0. \tag{48}$$

Symmetric planar array configurations such as a circular array with sensors placed at equal angular intervals, or a rectangular grid with sensors placed at the lattice points, meet these requirements provided that the array is located in the xy plane and that the array center is located at the origin. (If both r and χ are unknown, then the quantity $\chi'=kr+\chi$ (the phase of the signal at the array center) may be treated as the unknown, and the same results hold. Nielsen[20] has performed an analysis for a multiple-frequency, far-field, sine wave signal imbedded in Gaussian noise. The conditions he found for the estimates of the elevation, azimuth, and phase at the array center to decouple are the same as for the case presented here. Among the literature which examine array configurations that result in the decoupling of the angle estimates, Refs. 21–23 may be of interest to the reader.)

Also note that none of the elements of the FI given in Eqs. (41)–(46) is dependent upon the value of χ. This is expected as the value of the source phase should not effect the estimates of the other parameters. Close inspection of the second term of Eq. (31) reveals that its dependence in the FI should cancel regardless of whether we consider turbulence or not.

Suppose that the center of a sensor array is located at the origin so that the estimates of the angles of arrival ϕ and θ are uncoupled from the estimate of the source phase χ. Moreover, suppose that the sensors are configured so that Eq. (48) is satisfied, and hence the estimate of ϕ is uncoupled from the estimate of θ. Then the CRLBs of the AOAs are

$$\sigma_\phi^2 = J_{\phi\phi}^{-1} = \left[2Mk^2 \cos^2\theta \frac{p_0^2}{\sigma_n^2} \sum_{i=1}^{N} x_i'^2 \right]^{-1}, \tag{49}$$

$$\sigma_\theta^2 = J_{\theta\theta}^{-1} = \left[2Mk^2 \frac{p_0^2}{\sigma_n^2} \sum_{i=1}^{N} (x_i'^2 \sin^2\theta + z_i'^2 \cos^2\theta) \right]^{-1}. \tag{50}$$

At $\theta = \pi/2$, the CRLB of ϕ is singular. Therefore, an array whose sensors are located so that Eq. (48) is satisfied cannot be used to obtain an estimate of the azimuthal AOA of a plane wave that is propagating along the z axis. Specifically, a planar array must be located in the xy plane in order for Eq. (48) to be satisfied. Thus it cannot be used to obtain an estimate of the azimuth of a normally incident wave. Due to the limitations discussed in Sec. II A, we want to investigate waves that arrive at near-normal incidence to a planar array. Therefore in the full simulation, the estimates of the azimuth and elevation will always be coupled as we cannot choose the xy plane as the array plane.

It was noted earlier that, as we are considering the case with a nonzero mean, the source phase χ in Eq. (6) must be included as an unknown. For the case of no turbulence, it can be readily shown that not considering the source phase as an unknown yields misleading results. For example, consider a linear array that is located along the y axis. Suppose that r and the SNR are known. If the azimuth ϕ is treated as the only unknown, $\sigma_\phi^{-2} = 2M\ k \cos^2\phi (p_0^2/\sigma_n^2)\ \Sigma_i y_i'^2$. Thus we could choose a coordinate system that is infinitely far away from the sensors, so that $y_i' \to \infty$, and hence $\sigma_\phi \to 0$. However, if both ϕ and χ are treated as unknowns, $\sigma_\phi^{-2} = 2M\ k \cos^2\phi (p_0^2/\sigma_n^2)\ \Sigma_{i,j}(y_i' - y_j')^2$. Thus the CRLB of ϕ is only dependent on the separation of the sensors, regardless of the choice of coordinate system, as we intuitively expect. Second, let us again consider a linear array along the y axis. Let us further assume that its center is located at the origin so that the estimates of ϕ and r, (as well as ϕ and χ), decouple. Treating r but not χ as an unknown, it is found that $\sigma_r^2 = \sigma_n^2/(2M\ Nk^2 p_0^2)$, i.e., the propagation distance can be determined to within a constant times 1/SNR for a plane wave with a single sensor array. But if χ is included as an unknown, we find that the FI submatrix for r and χ is singular, therefore neither r nor χ can be estimated. Clearly, the source phase χ must be included in Φ_i for the nonzero mean case.

D. Two-element array operating in turbulence

The CRLBs for a two-element array operating in turbulence may be calculated analytically, albeit tediously. Though this case is not physically practical, many of the characteristics that are evidenced here also manifest themselves in the more complex systems. For the interested reader, the FI for a two-element array is given in Appendix A. In deriving Eqs. (A2)–(A4), no assumptions are made about the form of the derivatives of the total covariance matrix or mean vector [refer back to Eqs. (35) and (36)]. In deriving Eqs. (A5) and (A6), it is assumed that $\partial\tilde{\mu}/\partial\Theta_\lambda = \partial a/\partial\Theta_\lambda = \partial\beta/\partial\Theta_\lambda = 0$, where $\tilde{\mu} = |\mu_i| = p_0^2 e^{-\gamma r}$, $a = C_{11} = C_{22} = p_0^2 - \tilde{\mu}^2 + \sigma_n^2$, and $\beta = |C_{12}| = |C_{21}| = p_0^2 e^{-\alpha(\rho_{ij})r} - \tilde{\mu}^2$.

Let us begin by examining the coupling between the AOA estimate and the estimates of the other parameters. Suppose that $\Theta_\lambda = \phi$. Inspection of Eq. (A6) reveals that the estimate of ϕ is uncoupled from the estimate of any parameter of which Φ_i is independent. Therefore, as Φ_i is independent of l, ς^2, and SNR, the estimates of these parameters are uncoupled from the estimate of ϕ. Now if $\Theta_\nu = \chi$, $\partial\Phi_i/\partial\chi = 1$, and substituting this quantity into Eq. (A6) we find

$$J_{\phi\chi} = \frac{2M\tilde{\mu}^2}{a+\beta}\left(\frac{\partial\Phi_1}{\partial\phi} + \frac{\partial\Phi_2}{\partial\phi}\right) = \frac{2M\tilde{\mu}^2 k}{a+\beta}[(x_1' + x_2')\sin\phi - (y_1' + y_2')\cos\phi]. \tag{51}$$

Thus the estimates of ϕ and χ will be uncoupled provided $x_1' = -x_2'$ and $y_1' = -y_2'$. Similarly, $J_{\phi r} = kJ_{\phi\chi}$ as $\partial\Phi_i/\partial r = k$. Hence, the estimates of r and ϕ will also be uncoupled when $x_1' = -x_2'$ and $y_1' = -y_2'$.

Let $x_1' = x_2' = 0$ and $y_1' = -y_2' = d/2$. Then the CRLB of ϕ is $1/J_{\phi\phi}$, which from Eq. (A5) is

$$\sigma_\phi^2 = \frac{p_0^4[1 - e^{-2\alpha(d)r}] - 2p_0^2\tilde{\mu}^2[1 - e^{-\alpha(d)r}] + \sigma_n^2(2p_0^2 - 2\tilde{\mu}^2 + \sigma_n^2)}{Mk^2d^2\cos^2\phi\{2p_0^4 e^{-2\alpha(d)r} + p_0^2\tilde{\mu}^2[1 - 3e^{-\alpha(d)r}] + \tilde{\mu}^2\sigma_n^2\}} \tag{52}$$

$$= \frac{1 - \Gamma_{12}^2 - 2\Gamma_{\min}(1 - \Gamma_{12}) + \frac{\sigma_n^2}{p_0^2}\left(2 - 2\Gamma_{\min} + \frac{\sigma_n^2}{p_0^2}\right)}{Mk^2d^2\cos^2\phi\left[2\Gamma_{12}^2 + \Gamma_{\min}(1 - 3\Gamma_{12}) + \frac{\sigma_n^2}{p_0^2}\Gamma_{\min}\right]}. \tag{53}$$

For $\tilde{\mu} = 0$, the result presented in Ref. 9 for a zero mean is recovered. Whether or not the mean is incorporated, when $\phi = 0$, the source is broadside to the sensors, and the performance is maximal. When $\phi = \pi/2$, the source is in line with the sensors, and the solution is singular. Though $\phi = \pi/2$ is not consistent with the small-angle approximation, the solution should be singular at $\phi = \pi/2$ as we have not directly incorporated the angular restrictions of the propagation

model (discussed in Sec. II A) into the calculation of the CRLB.

Let us now examine the couplings between the estimates of the other parameters. Suppose that $\Theta_\lambda = \chi$. Again, the estimate of χ is uncoupled from the estimate of any parameter of which Φ_i is independent: l, ς^2, and SNR. Now for $\Theta_\nu = r$,

$$J_{\chi r} = \frac{2M\tilde{\mu}^2}{a+\beta}\left(\frac{\partial \Phi_1}{\partial r} + \frac{\partial \Phi_2}{\partial r}\right) = \frac{4M\tilde{\mu}^2 k}{a+\beta}. \tag{54}$$

Therefore the estimates of r and χ will always be coupled. For Θ_λ, $\Theta_\nu \in [r, l, \varsigma^2, \text{SNR}]$, Eqs. (A2) and (A3) must be used to calculate $J_{\lambda\nu}$. As $J_{\lambda\nu} \neq 0$ in general, the estimates of these parameters are coupled.

E. Linear array operating in turbulence

Let us now consider a linear array ($N > 2$) operating in turbulence. Unfortunately, this case does not lend itself to being evaluated analytically. Numerically, we find that the estimate of ϕ remains uncoupled from the estimates of l, ς^2, and SNR (or 1/SNR). However we find (again numerically) that placing the center of the array at the origin is no longer a sufficient condition for the estimate of ϕ to decouple from the estimates of r and χ: In addition, the line array must have mirror symmetry about the origin, though the stronger condition of uniform spacing is not needed. The results are independent of the value of χ, as we noted earlier they should be.

F. Planar array operating in turbulence

For 3D propagation in turbulence, we assume that the wave is propagating near the x axis and thus take the yz plane to be the plane of the array. As noted earlier, the estimates of θ and ϕ are coupled for this choice. Numerically, the estimates of θ and ϕ are still found to be uncoupled from the estimates l, ς^2, and SNR (or 1/SNR). As with the 2D case, we find (numerically) that placing the center of the array at the origin is no longer sufficient for the estimates of θ and ϕ to decouple from the estimates of r and χ: A symmetric array configuration such as a rectangular grid with mirror symmetry in y about the origin and mirror symmetry in z about the origin must be used, again the stronger condition of uniform spacing is not necessary. The results are independent of the value of χ.

IV. RESULTS

We now present the CRLBs of the AOAs for arrays operating in turbulence. We begin by examining the results for the simple two-element array, and then proceed to present the results for the linear and planar arrays. A brief comment is made about the CRLBs of the other parameters.

A. Two-element array

Consider a two-element array whose center is located at the origin. The CRLB of ϕ for this case was given in Eqs. (52) and (53). According to Eq. (53), the quantity $M\,k^2 d^2 \cos^2\phi \sigma_\phi^2$ depends only on $\Gamma_{\min}$, Γ_{12}, and σ_n^2/p_0^2. This quantity is plotted in Figs. 4 and 5. The figures correspond, respectively, to weak scattering ($\Gamma_{\min} = 0.9$), and strong scattering ($\Gamma_{\min} = 0.1$).

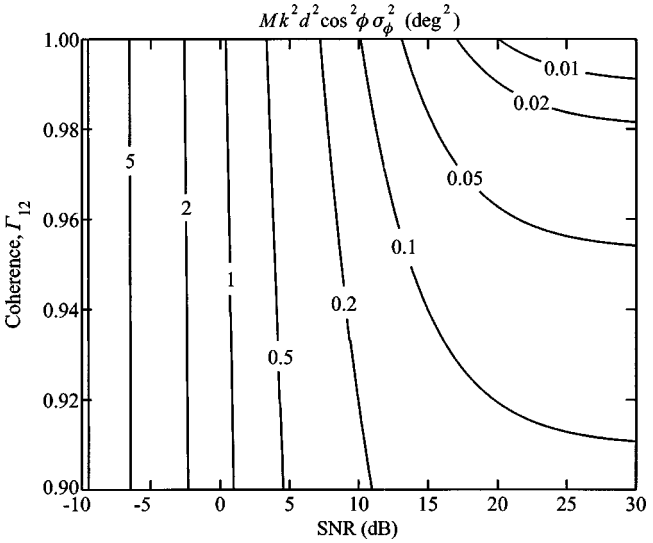

FIG. 4. Weak scattering for a two-element array, $\Gamma_{\min} = 0.9$.

Figures 4 and 5 demonstrate that for high SNR (greater than about 20 dB for weak scattering and 10 dB for strong scattering), the performance of the array becomes nearly independent of SNR, depending primarily on the coherence Γ_{12}. Conversely, at low SNR (less than about 5 dB for weak scattering), the performance becomes nearly independent of coherence, depending primarily on the SNR. For strong scattering at low and moderate SNR, and CRLB actually is strongly affected by both coherence and SNR.

B. Linear array

The CRLB of ϕ was examined in detail in Ref. 9 for 2D propagation using the zero-mean assumption. The results presented here for a nonzero mean use a modified version of the scalar field 2D correlation function f_s as noted earlier. For the 2D propagation calculations, we consider a linear array with five sensors spaced in equal intervals of d. The origin is taken to be the array center so that the estimate of ϕ is uncoupled from the estimates of all the other parameters.

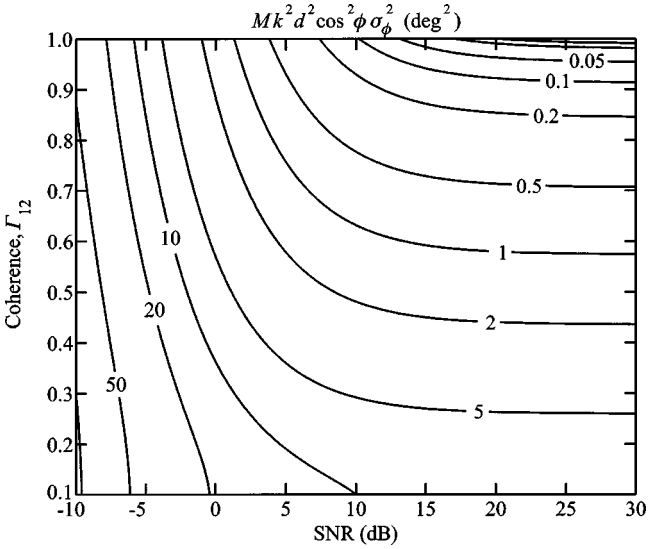

FIG. 5. Strong scattering for a two-element array, $\Gamma_{\min} = 0.1$.

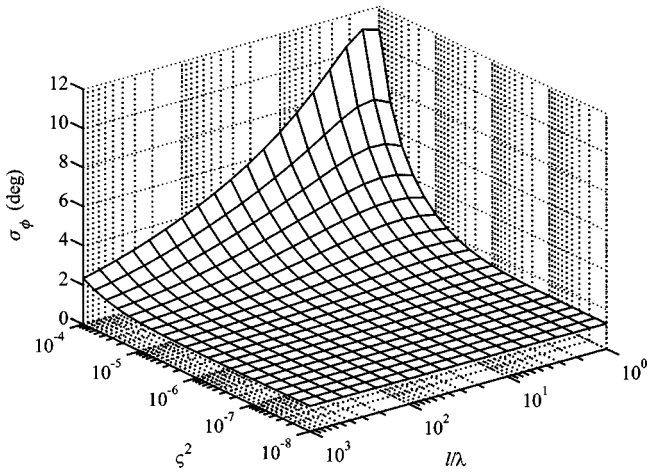

FIG. 6. CRLB of ϕ for broadside incidence on a uniformly spaced linear array as a function of turbulence parameters. Calculation is for $r/\lambda=500$, SNR$=10$ dB, $N=5$, $d/\lambda=0.5$, and a scalar von Kármán spectrum.

As the CRLB (σ) for M independent and identically distributed data sets is $1/\sqrt{M}$ times the CRLB (σ) for one data set, all results are presented for $M=1$.

The CRLB of ϕ for broadside incidence is plotted as a function of index-of-refraction variance, ς^2, and normalized characteristic length scale, l/λ, in Fig. 6 for fixed values of the other parameters listed in the Figure title. A scalar von Kármán spectrum is used. A peak is evident in σ_ϕ at the larger values of ς^2 and smaller values of l/λ. In this region both Γ_{ij} and $\Gamma_{\min}$ are approaching their minimum values as functions of the turbulence parameters. (The location of the maximum of the CRLB shown in Fig. 6 varies slightly from the locations of the minimums of the coherence functions depicted in Figs. 2 and 3 because of the contributions to the covariance matrix and mean from every pair of sensors in the array.) In fact, in the limit that Γ_{ij} and $\Gamma_{\min}$ simultaneously approach zero, $\sigma_\phi^2\rightarrow\infty$ as $\mathbf{C}\rightarrow\sigma_n^2\mathbf{I}_N$ and $\boldsymbol{\mu}\rightarrow 0$. For small values of ς^2 and of l/λ, both Γ_{ij} and $\Gamma_{\min}$ are approaching the maximum value of 1.0, and hence σ_ϕ^2 is approaching the limit of $(k^2d^2\cos^2\phi p_0^2/\sigma_n^2)^{-1}$ for no turbulence. In Fig. 7 the

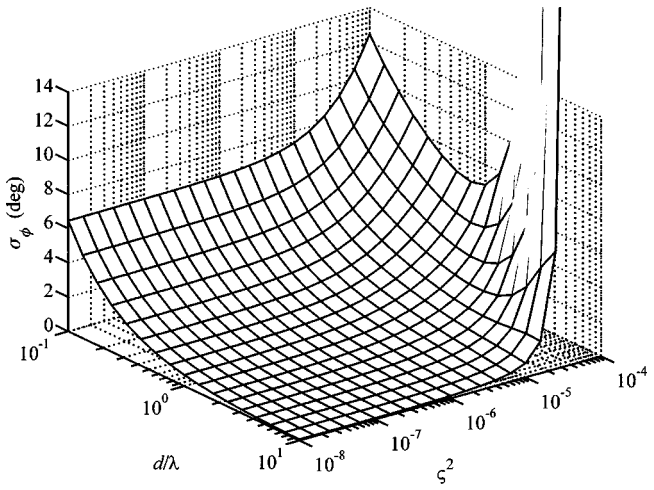

FIG. 7. CRLB of ϕ for broadside incidence on a uniformly spaced linear array as a function of normalized sensor separation and index-of-refraction variance. At large values of d/λ and ς^2, σ_ϕ is approaching infinity. Calculation is for $l/\lambda=10$, $r/\lambda=500$, SNR$=10$ dB, $N=5$, and a scalar von Kármán spectrum.

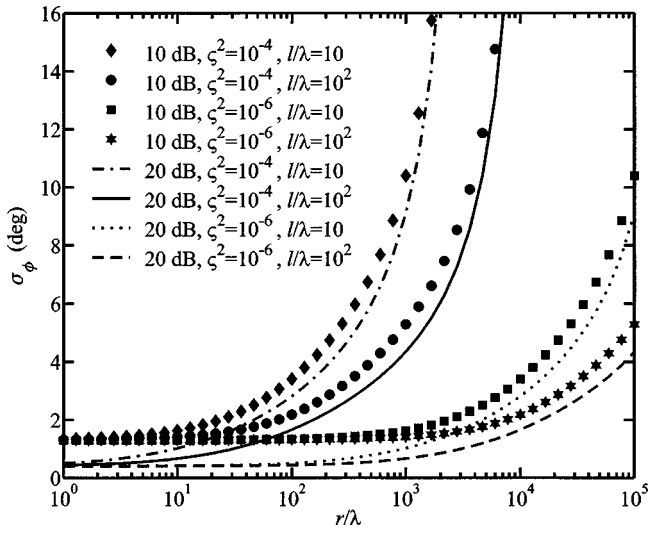

FIG. 8. CRLB of ϕ for broadside incidence on a uniformly spaced linear array as a function of normalized propagation distance. All curves are for $d/\lambda=0.5$, $N=5$, and a scalar von Kármán spectrum.

CRLB of ϕ for broadside incidence is plotted as a function of d/λ and ς^2 for fixed values of the other parameters, and a scalar von Kármán spectrum. For large values of d/λ and ς^2, σ_ϕ is rapidly approaching infinity. Again, the peak in σ_ϕ occurs when Γ_{ij} and $\Gamma_{\min}$ simultaneously approach their minimum values. The shapes of these curves are similar for different values of the SNR, with the value of σ_ϕ increasing with decreasing SNR, provided that the SNR is not too low that it dominates the performance (refer to Sec. IV A and the following paragraphs).

In Fig. 8 the CRLB of ϕ for broadside incidence is examined as a function of the normalized propagation distance r/λ for a couple of values of ς^2 and l/λ. The closed points (lines) correspond to a SNR of 10 dB (20 dB) for every value of r/λ. For small values of r/λ ($r/\lambda\lesssim 10$), σ_ϕ is limited by the SNR. As r/λ increases, σ_ϕ is driven primarly by the values of the turbulence parameters, in particular, the index-of-refraction variance. For $\varsigma^2=10^{-6}$, the performance degrades with increasing r/λ, especially for $r/\lambda\gtrsim 10^4$. And for $\varsigma^2=10^{-4}$, the performance degrades almost exponentially for $r/\lambda\gtrsim 10^3$ when $l/\lambda=100$ and for $r/\lambda\gtrsim 10^2$ when $l/\lambda=10$. These results can be understood by examining the behavior of the $\Gamma_{\min}$ and Γ_{ij}.

The CRLB of ϕ for other values of ϕ has the same behavior as for $\phi=0$, with σ_ϕ increasing slightly. In Fig. 9, σ_ϕ is plotted versus ϕ for two values of each r/λ, l/λ, ς^2, and SNR. A scalar von Kármán turbulence spectrum is used. For $\varsigma^2=10^{-6}$ depicted in the upper graph (a), σ_ϕ is most sensitive to the SNR; whereas, for $\varsigma^2=10^{-4}$ depicted in (b), σ_ϕ is most sensitive to changes in the values of the turbulence parameters.

The results for a vector von Kármán spectrum are similar to those of the scalar spectrum: the shapes are nearly identical, but the value of σ_ϕ is for the most part larger. In Fig. 10 the ratio $\sigma_\phi^v/\sigma_\phi^s$ is plotted as a function of ς^2 and l/λ for normal incidence. The superscripts v and s, respectively, refer to a vector and a scalar spectrum. Note that the largest

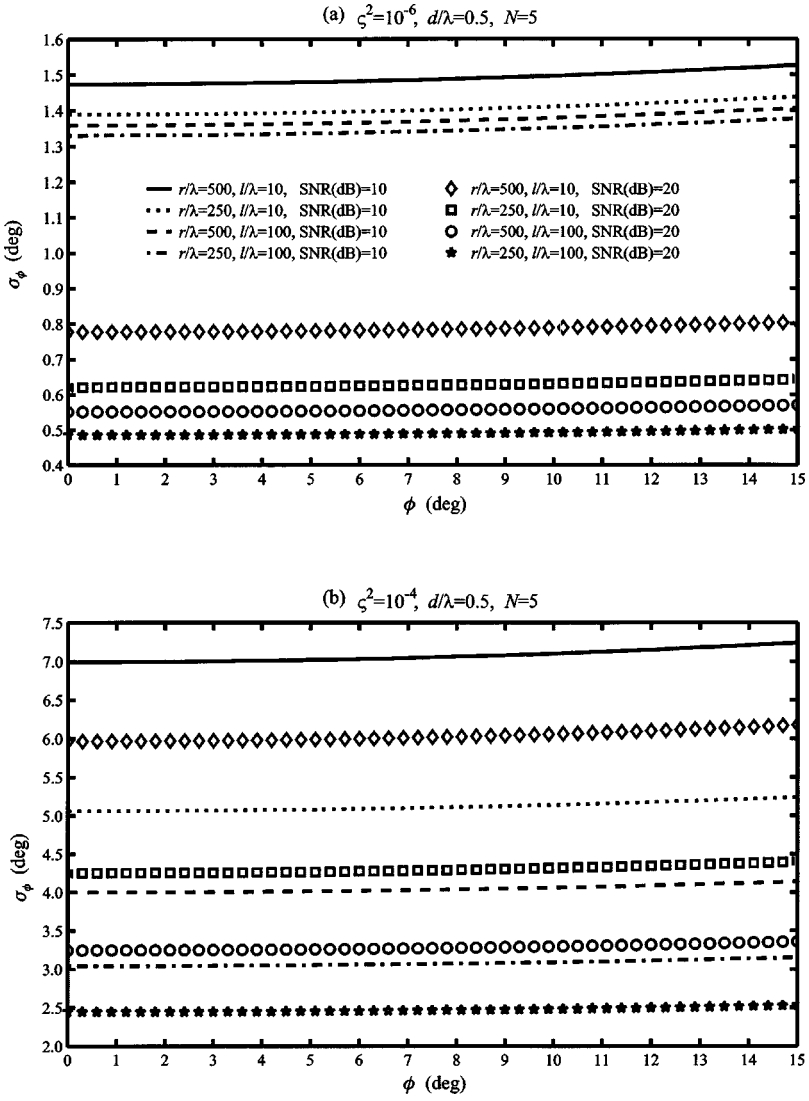

FIG. 9. Angular dependence of σ_ϕ for incidence on a uniformly spaced linear array. A scalar von Kármán spectrum is used. The legend applies to (a) and (b).

difference occurs in the regions where Γ_{ij}^v is appreciably smaller than Γ_{ij}^s.

C. Planar array

Let us now examine the results for propagation in 3D. The array geometry considered for this analysis is a 4×4 square grid with spacing of d. As noted earlier, we take the array plane to be the yz plane and place the center of the array at the origin. Thus even though the estimates of ϕ and θ are coupled to one another, they are uncoupled from the estimates of the remaining parameters. Again all results presented are for $M=1$.

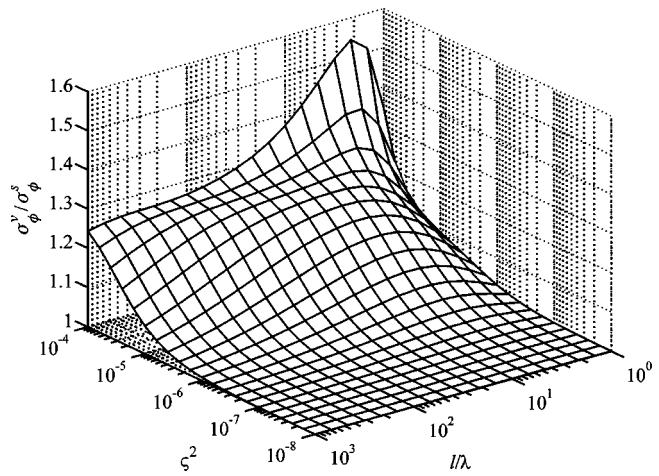

FIG. 10. The ratio $\sigma_\phi^v/\sigma_\phi^s$ for broadside incidence on a uniformly spaced linear array as a function of turbulence parameters. Calculation is for $r/\lambda=500$, SNR$=10$ dB, $N=5$, and $d/\lambda=0.5$.

The values of σ_ϕ, σ_θ, σ_{ϕ_0}, and σ_{θ_0} are the same for normal incidence due to symmetry. (Recall that σ_ϕ is the CRLB of ϕ when both ϕ and θ are unknown, σ_{ϕ_0} is the CRLB of ϕ when ϕ is the only unknown, and $\sigma_\phi \geqslant \sigma_{\phi_0}$.) In Fig. 11, σ_ϕ for normal incidence is plotted as a function of ς^2 and l/λ for fixed values of the other parameters. A scalar von Kármán turbulence spectrum is used. We see the same behavior as for the 2D case. The peak in σ_ϕ corresponds to the region where both Γ_{ij} and $\Gamma_{\min}$ are small. The shape is similar to that in 2D, but the overall values are smaller, especially for large values of ς^2 and small values of l/λ. This is expected as a 4×4 array in 3D should provide more information than a five-point linear array in 2D. The behavior for other values of ϕ and θ is similar. The CRLB of ϕ as a function of d/λ and ς^2 for broadside incidence is given in Fig. 12. Again the results are similar to the 2D case, but the overall values are smaller.

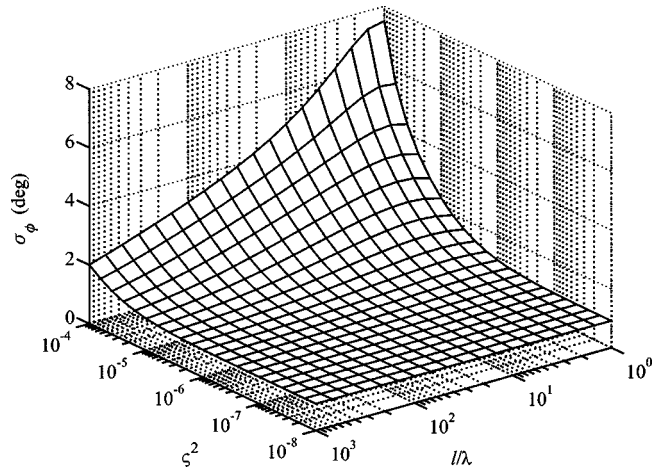

FIG. 11. CRLB of ϕ and θ for normal incidence on a symmetric planar array as a function of turbulence parameters. At $\phi=\theta=0$, $\sigma_\phi=\sigma_\theta=\sigma_{\phi_0}=\sigma_{\theta_0}$ due to symmetry. Calculation is for $r/\lambda=500$, SNR$=10$ dB, $N_y=N_z=4$, $d/\lambda=0.5$, and a scalar von Kármán spectrum.

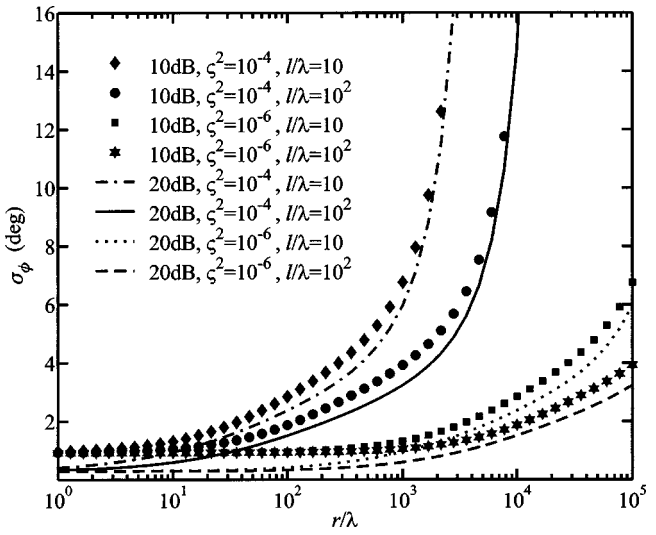

FIG. 13. CRLB of ϕ and θ for normal incidence on a symmetric planar array as a function of normalized propagation distance. All curves are for $N_y=N_z=4$, $d/\lambda=0.5$, and a scalar von Kármán spectrum.

In Fig. 13, σ_ϕ for normal incidence is examined as a function of the normalized propagation distance r/λ for a couple of values of the SNR, ς^2, and l/λ. As with the 2D case, the performance degrades most rapidly with increasing r/λ for $\varsigma^2=10^{-4}$; for the 3D case, however, the near exponential rise in σ_ϕ now occurs at slightly larger values of r/λ.

As in the 2D case, the behavior of σ_ϕ and σ_θ for a vector von Kármán spectrum is similar to that for a scalar von Kármán spectrum: the CRLBs for the vector spectrum increase most significantly over those for the scalar spectrum in the regions where Γ^v_{ij} is appreciably smaller than Γ^s_{ij}. The ratio of the CRLB of ϕ for a vector spectrum to that of a scalar spectrum, $\sigma^v_\phi/\sigma^s_\phi$, is plotted as a function of ς^2 and l/λ in Fig. 14 for normal incidence.

Figure 15 examines σ_ϕ and σ_θ as functions of ϕ and θ for a scalar von Kármán spectrum. The first column is for $\varsigma^2=10^{-4}$ and $l/\lambda=10$, and the second column for $\varsigma^2=10^{-6}$ and $l/\lambda=10$. From Figs. 15(a) and (b), we see that for small angles $\sigma_\phi(\phi,\theta)=\sigma_\phi(\theta,\phi)$. This symmetry is also seen, though not presented here, for small angles in the no-turbulence case. Figures 15(c) and (d) give σ_ϕ as a function of ϕ for fixed values of θ. Now, σ_θ, on the other hand, is dependent upon θ but is independent of ϕ, as indicated in Figs. 15(e) and (f). Again this is the same behavior as in the no-turbulence case. Though not presented here, both σ_{ϕ_0} and σ_{θ_0} are dependent on ϕ and θ. In Fig. 16, the coupling $\zeta_{\phi\theta}$ [as defined in Eq. (34)] is plotted versus ϕ for fixed values of θ. The coupling is in fact weak, only on the order of 10^{-3}. To within the numerical accuracy of this calculation, we find that $\zeta_{\phi\theta}$ for this array geometry is the same as for the no turbulence case:

$$\zeta_{\phi\theta}=\frac{\sin^2\phi\sin^2\theta}{\cos^2\theta+\sin^2\phi\sin^2\theta}\approx\phi^2\theta^2-\frac{1}{3}\phi^4\theta^2+\frac{2}{3}\phi^2\theta^4, \tag{55}$$

regardless of the value of r/λ, d/λ, SNR, l/λ, or ς^2, and regardless of the von Kármán spectrum used.

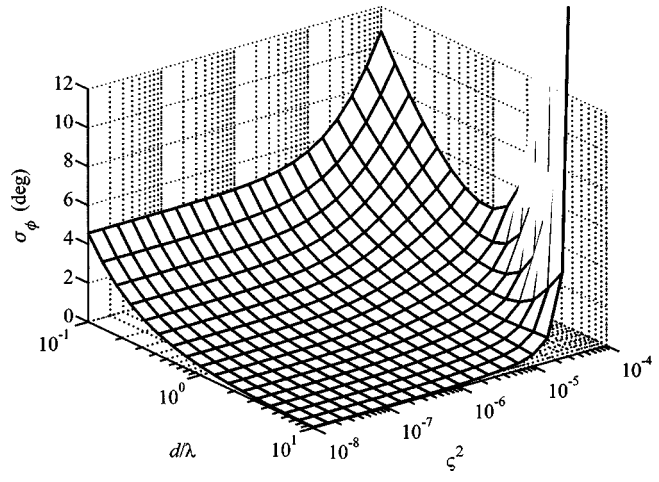

FIG. 12. CRLB of ϕ and θ for normal incidence on a symmetric planar array as a function of normalized sensor separation and index-of-refraction variance. Calculation is for $l/\lambda=10$, $r/\lambda=500$, SNR$=10$ dB, $N_y=N_z=4$, and a scalar von Kármán spectrum.

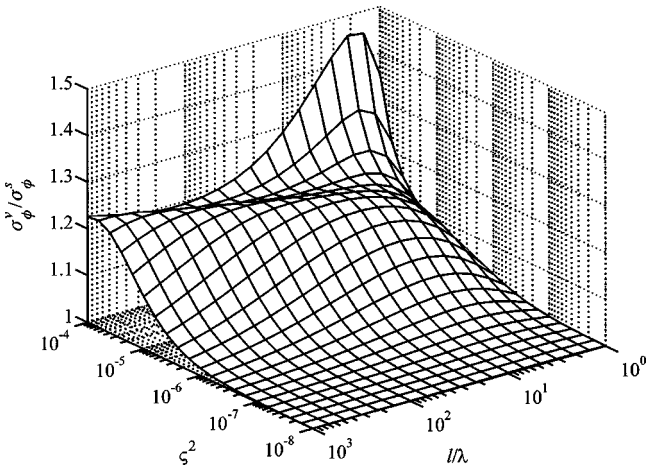

FIG. 14. The ratio $\sigma^v_\phi/\sigma^s_\phi$ for normal incidence on a symmetric planar array as a function of turbulence parameters. The calculation is for $r/\lambda=500$, SNR$=10$ dB, $N_y=N_z=4$, and $d/\lambda=0.5$.

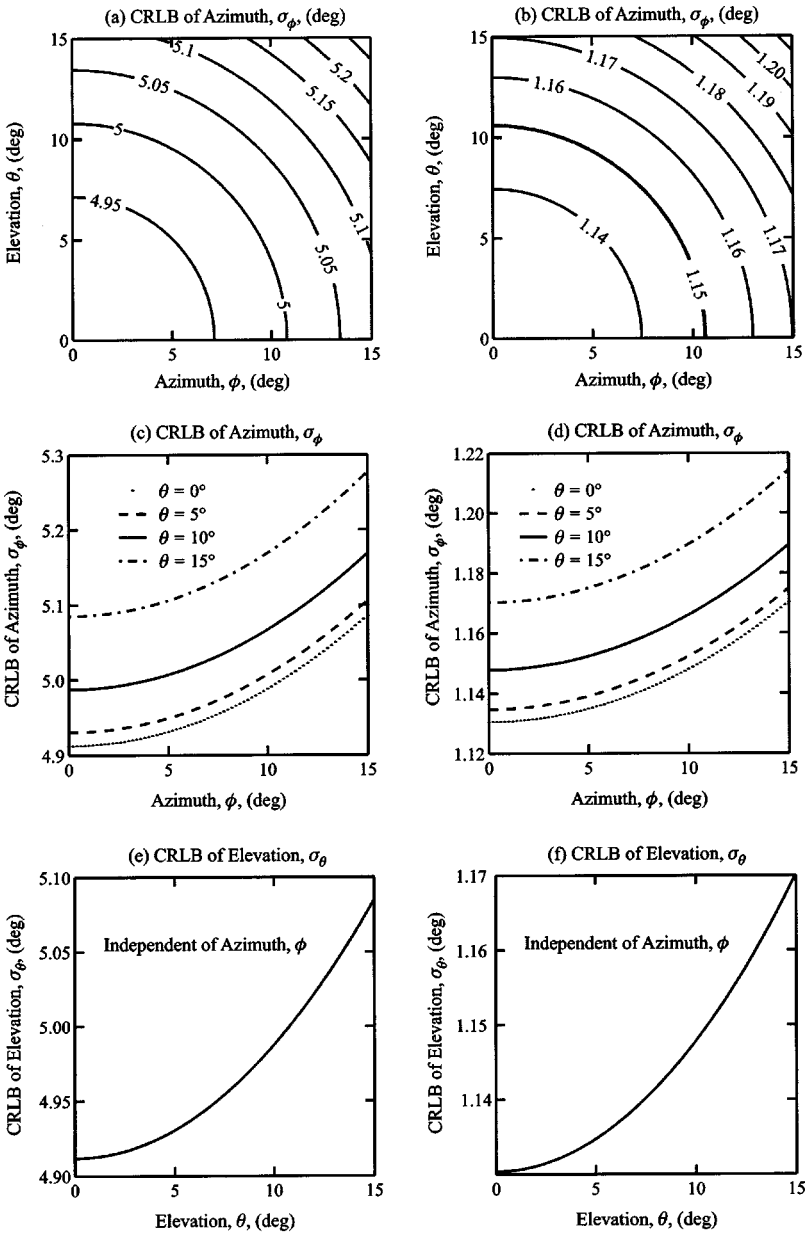

FIG. 15. Angular dependence of σ_ϕ and σ_θ for incidence on a symmetric planar array. The first column is for $\varsigma^2 = 10^{-4}$ and the second column is for $\varsigma^2 = 10^{-6}$. All curves are for $l/\lambda = 10$, $r/\lambda = 500$, SNR = 10 dB, $N_y = N_z = 4$, $d/\lambda = 0.5$, and a scalar von Kármán spectrum.

D. CRLBs of other parameters

It is interesting to consider the possibility of using the signal behavior at the array to deduce the propagation distance of the wave front and the properties of the turbulence field. For large values of ς^2 and small values of l/λ, we find (numerically) that for $\Theta_\nu \in [l/\lambda, \varsigma^2, r/\lambda]$, σ_ν/Θ_ν may be significantly less than 1, particularly for a large number of independent and identically distributed samples M. This can be explained from the fact that the array provides information on the propagation distance and turbulence parameters only when the scattering is strong. (In weak scattering, the SNR dominates the array performance, so that the effect of the turbulence is not evident.) For other values of the turbulence parameters, we find $\sigma_\nu/\Theta_\nu \gg 1$. Therefore, the regions in which σ_ϕ is strongly dependent upon Θ_ν correspond to the regions in which σ_ν/Θ_ν is smallest; similarly the regions in which σ_ϕ is nearly independent of Θ_ν, correspond to the regions in which Θ_ν cannot be estimated from the model presented here. It should be noted that there are models based von Kármán's spectrum that calculate the turbulence parameters in the energy-containing subrange of the turbulence.[17,18] These models consider contributions to the sound speed variations from wind and temperature fluctuations produced by both shear and buoyancy instabilities and will likely be more accurate.

V. CONCLUSIONS

We have examined the performance bounds of acoustic arrays operating in turbulence with fluctuations described by a von Kármán spectrum. The analysis featured three main improvements upon earlier work: (1) the performance bounds were generalized to weak as well as strong scattering, (2) multiple unknowns such as the propagation distance of the wave front and the turbulence parameters were incorporated, (3) AOA estimates for three-dimensional problems (i.e., two bearing angles) were considered. However, certain

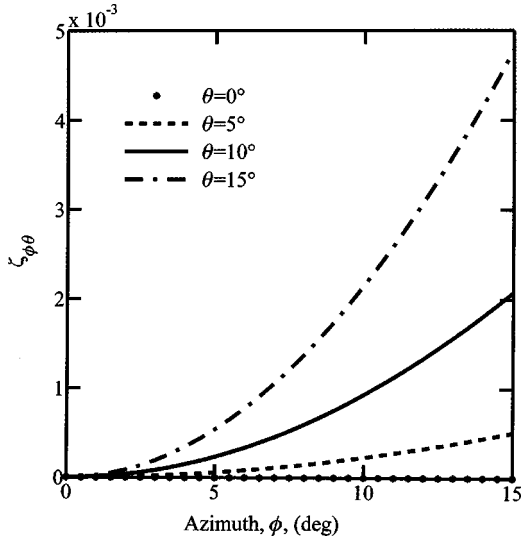

FIG. 16. Coupling between the estimates of ϕ and θ. This quantity is only dependent on ϕ and θ.

approximations had to be made in order to apply the results for the second moment from the theory of waves propagating in an inhomogeneous medium. Because of these approximations, this investigation is limited to near-normal incidence at a planar array for 3D propagation and at a linear array for 2D. However, in this model the information about the direction of arrival is derived solely from the phase terms. Therefore, this limitation to near-normal incidence is consistent with the limitations of direction finders that use phase differences to determine the wave front's angle of arrival.

Our primary interest in this paper was to analyze the Cramer–Rao lower bounds of the estimates of the angles of arrival. For an incident plane wave, we have found that an appropriate choice of coordinate system and array geometry leads to the decoupling of the estimates of the AOAs from the estimates of the propagation distance and phase of the source. The estimates of the AOAs are found to be uncoupled from the estimates of the SNR and turbulence parameters, regardless of array geometry. In order to remain consistent with the approximations for the moments, we had to choose a coordinate system that resulted in the coupling of the estimates of the azimuth and elevation; the coupling, however, was small. For large values of the index-of-refraction variance and moderate to small values of the normalized characteristic length scale, we have found that the CRLBs of the AOAs increase significantly at large propagation distances. However, for smaller values of the index-of-refraction variance and normalized propagation distance, the SNR is the limiting factor.

The results in this paper demonstrate that scattering by atmospheric turbulence significantly affects the performance of acoustic sensor arrays. While only a single array with a simple geometry (line array in 2D, square grid in 3D) was considered in this analysis, the results indicate that the effects of atmospheric turbulence should be included in performance bounds calculations for other more complicated systems as well. This analysis would benefit from an improved model of the second moment for oblique incidence. Future efforts should also attempt to incorporate the additional phenomena of ground reflections and refraction by atmospheric wind and temperature gradients. These phenomena will likely have considerable impact on the ability to estimate the elevation. However, numerical techniques will probably be required to model these complications.

ACKNOWLEDGMENTS

S.L.C. was supported by an American Society for Engineering Education postdoctoral fellowship during the execution of this work. The authors are grateful to B. M. Sadler and A. Swami of ARL, V. E. Ostashev of NOAA/Environmental Technology Laboratory, and R. J. Kozick of Bucknell University for many helpful discussions.

APPENDIX A: FISHER INFORMATION FOR TWO-ELEMENT ARRAY

Let us write the mean and covariance matrix for a simple two-element array as

$$\boldsymbol{\mu}=\tilde{\mu}\begin{bmatrix} e^{i\Phi_1} \\ e^{i\Phi_2} \end{bmatrix}, \quad \mathbf{C}=\begin{bmatrix} a & \beta e^{i\Phi_{12}} \\ \beta e^{-i\Phi_{12}} & a \end{bmatrix}, \tag{A1}$$

where $\tilde{\mu}$, a, β are real valued. From Eqs. (35) and (36), $\tilde{\mu}=p_0 e^{-\gamma r}$, $a=C_{11}=C_{22}=p_0^2-\tilde{\mu}^2+\sigma_n^2$, and $\beta=|C_{12}|=|C_{21}|=p_0^2 e^{-\alpha(\rho_{12})r}-\tilde{\mu}^2$. If Θ_λ and Θ_ν are unknown parameters, then

$$\begin{aligned} &\mathrm{tr}\left(\mathbf{C}^{-1}\frac{\partial \mathbf{C}}{\partial \Theta_\lambda}\mathbf{C}^{-1}\frac{\partial \mathbf{C}}{\partial \Theta_\nu}\right) \\ &=\frac{2}{(a^2-\beta^2)^2}\left[(a^2+\beta^2)\left(\frac{\partial a}{\partial \Theta_\lambda}\frac{\partial a}{\partial \Theta_\nu}+\frac{\partial \beta}{\partial \Theta_\lambda}\frac{\partial \beta}{\partial \Theta_\nu}\right)\right. \\ &\quad -2a\beta\left(\frac{\partial a}{\partial \Theta_\lambda}\frac{\partial \beta}{\partial \Theta_\nu}+\frac{\partial a}{\partial \Theta_\nu}\frac{\partial \beta}{\partial \Theta_\lambda}\right) \\ &\quad \left.+\beta^2(a^2-\beta^2)\frac{\partial \Phi_{12}}{\partial \Theta_\lambda}\frac{\partial \Phi_{12}}{\partial \Theta_\nu}\right] \end{aligned} \tag{A2}$$

and

$$\begin{aligned} \mathrm{Re}\left(\frac{\partial \boldsymbol{\mu}^\dagger}{\partial \Theta_\lambda}\mathbf{C}^{-1}\frac{\partial \boldsymbol{\mu}}{\partial \Theta_\nu}\right)=\frac{1}{a^2-\beta^2}\left\{2(a-\beta)\frac{\partial \tilde{\mu}}{\partial \Theta_\lambda}\frac{\partial \tilde{\mu}}{\partial \Theta_\nu}\right. \\ +\tilde{\mu}^2\left[a\left(\frac{\partial \Phi_1}{\partial \Theta_\lambda}\frac{\partial \Phi_1}{\partial \Theta_\nu}+\frac{\partial \Phi_2}{\partial \Theta_\lambda}\frac{\partial \Phi_2}{\partial \Theta_\nu}\right)\right. \\ \left.\left.-\beta\left(\frac{\partial \Phi_1}{\partial \Theta_\lambda}\frac{\partial \Phi_2}{\partial \Theta_\nu}+\frac{\partial \Phi_1}{\partial \Theta_\nu}\frac{\partial \Phi_2}{\partial \Theta_\lambda}\right)\right]\right\}. \end{aligned} \tag{A3}$$

Thus, for $\xi=\lambda$ or ν,

$$J_{\xi\xi}=\frac{2M}{(a^2-\beta^2)^2}\left\{(a^2+\beta^2)\left[\left(\frac{\partial a}{\partial\Theta_\xi}\right)^2+\left(\frac{\partial\beta}{\partial\Theta_\xi}\right)^2\right]-4a\beta\frac{\partial a}{\partial\Theta_\xi}\frac{\partial\beta}{\partial\Theta_\xi}+\beta^2(a^2-\beta^2)\left(\frac{\partial\Phi_{12}}{\partial\Theta_\xi}\right)^2\right\}+\frac{2M}{a^2-\beta^2}\left\{2(a-\beta)\left(\frac{\partial\tilde{\mu}}{\partial\Theta_\xi}\right)^2+a\tilde{\mu}^2\left[\left(\frac{\partial\Phi_1}{\partial\Theta_\xi}\right)^2+\left(\frac{\partial\Phi_2}{\partial\Theta_\xi}\right)^2\right]-2\beta\tilde{\mu}^2\frac{\partial\Phi_1}{\partial\Theta_\xi}\frac{\partial\Phi_2}{\partial\Theta_\xi}\right\}. \tag{A4}$$

For the special case when $\partial a/\partial\Theta_\lambda=\partial\beta/\partial\Theta_\lambda=\partial\tilde{\mu}/\partial\Theta_\lambda=0$, but there are no restrictions on the derivatives with respect to Θ_ν,

$$J_{\lambda\lambda}=\frac{2M\beta^2}{a^2-\beta^2}\left(\frac{\partial\Phi_{12}}{\partial\Theta_\lambda}\right)^2+\frac{2M\tilde{\mu}^2}{a^2-\beta^2}\left\{a\left[\left(\frac{\partial\Phi_1}{\partial\Theta_\lambda}\right)^2+\left(\frac{\partial\Phi_2}{\partial\Theta_\lambda}\right)^2\right]-2\beta\frac{\partial\Phi_1}{\partial\Theta_\lambda}\frac{\partial\Phi_2}{\partial\Theta_\lambda}\right\}, \tag{A5}$$

$$J_{\lambda\nu}=\frac{2M\beta^2}{a^2-\beta^2}\frac{\partial\Phi_{12}}{\partial\Theta_\lambda}\frac{\partial\Phi_{12}}{\partial\Theta_\nu}+\frac{2M\tilde{\mu}^2}{a^2-\beta^2}\left[a\left(\frac{\partial\Phi_1}{\partial\Theta_\lambda}\frac{\partial\Phi_1}{\partial\Theta_\nu}+\frac{\partial\Phi_2}{\partial\Theta_\lambda}\frac{\partial\Phi_2}{\partial\Theta_\nu}\right)-\beta\left(\frac{\partial\Phi_1}{\partial\Theta_\lambda}\frac{\partial\Phi_2}{\partial\Theta_\nu}+\frac{\partial\Phi_1}{\partial\Theta_\nu}\frac{\partial\Phi_2}{\partial\Theta_\lambda}\right)\right], \tag{A6}$$

and $J_{\nu\nu}$ is given by Eq. (A4) with $\xi=\nu$.

APPENDIX B: NOMENCLATURE

1. Symbols

$[\cdot]^*$	Complex conjugate
$[\cdot]^{\parallel}$	Component parallel to $\hat{\mathbf{r}}$
$[\cdot]^{\perp}$	Component perpendicular to $\hat{\mathbf{r}}$
$\langle\cdot\rangle$	Ensemble average or expectation value
$\odot$	Hadamard product, elementwise product of matrices, $\mathbf{A}\odot\mathbf{B}=[A_{ij}B_{ij}]$
$[\cdot]^\dagger$	Hermitian adjoint (complex conjugate transpose)
$\otimes$	Kronecker product of matrices (direct or tensor product)
$\sim$	On the order of
$[\cdot]^T$	Transpose

2. Integers and subscripts

M	Number of independent and identically distributed data sets
N	Number of elements in the array
$\mathcal{N}$	Number of unknown parameters
i, j	Indices on elements of the array
λ, ν	Indices on unknown parameters

3. Matrices and vectors

$\mathbf{C}$	Covariance matrix for total pressure field, $N\times N$
$\mathbf{C}_p$	Covariance matrix for pressure field of source, $N\times N$
$\mathbf{I}_N$	Identity matrix, $N\times N$
$\mathbf{J}$	Fisher information matrix, $\mathcal{N}\times\mathcal{N}$
$\mathbf{k}$	Wave number vector, $\mathbf{k}=-k\hat{\mathbf{r}}$
$\mathbf{n}$	Noise pressure field, column vector with N elements
$\mathbf{p}$	Pressure field of source, column vector with N elements
$\mathbf{r}$	Vector from center of array perpendicular to plane of source
$\hat{\mathbf{r}}$	Unit vector in direction of $\mathbf{r}$, $\hat{\mathbf{r}}=[\cos\phi\cos\theta,\ \sin\phi\cos\theta,\ \sin\theta]^T$
$\mathbf{r}_i'$	Vector from center of array to ith sensor, $\mathbf{r}_i'=[x_i',\ y_i',\ z_i']^T$
$\mathbf{r}_i$	Defined as $\mathbf{r}_i=\mathbf{r}-\mathbf{r}_i'$
$\mathbf{s}$	Total pressure field, column vector with N elements
$\boldsymbol{s}$	Steering vector, column vector with N elements
$\boldsymbol{\mathcal{S}}$	Steering matrix, $N\times N$
$\boldsymbol{\Gamma}$	Mutual coherence matrix, $N\times N$
$\boldsymbol{\mu}$	First moment (mean) of pressure field of source, column vector with N elements
$\boldsymbol{\rho}_{ij}$	Vector from jth to ith sensor, $\boldsymbol{\rho}_{ij}=\mathbf{r}_i-\mathbf{r}_j=\mathbf{r}_j'-\mathbf{r}_i'$
$\boldsymbol{\Theta}$	Column vector of unknown parameters, $\mathcal{N}$ elements

4. Functions and scalar quantities

d	Separation between adjacent sensors in a uniformly spaced array
$f_s(\rho_{ij})$	Two-dimensional correlation function for a scalar field, as a function of sensor separation
$f_v(\rho_{ij})$	Two-dimensional correlation function for a vector field, as a function of sensor separation
k	Wave number
$K_\nu(x)$	Modified Bessel function of order ν evaluated at x
l	Characteristic length scale of turbulence, $l=\Gamma(1/3)\mathcal{L}/[\sqrt{\pi}\Gamma(5/6)]$
$\mathcal{L}$	Outer (integral) length scale of turbulence
ℓ	Inner (Kolmogorov) length scale of turbulence
$p_H(\mathbf{r}_i)$	Pressure field in a homogeneous medium at the ith sensor
p_0	Pressure amplitude of source
$\langle p_i p_j^*\rangle$	Second moment of source pressure field between the ith and jth sensors
r	Propagation distance of wave front to the center of the array
$\alpha(\rho_{ij})$	Extinction coefficient for second moment of the pressure field, as a function of sensor separation
χ	Phase of the source
δ_{ij}	Kronecker delta function
γ	Extinction coefficient for the first moment of the pressure field
$\Gamma(x)$	Gamma function evaluated at x
Γ_{ij}	Mutual coherence between ith and jth sensors, a function of sensor separation ρ_{ij}
$\Gamma_{\min}$	Minimum value of Γ_{ij} occurring for $\rho_{ij}=\infty$, $\Gamma_{\min}=\Gamma_{ij}(\rho_{ij}=\infty)$
λ	Wavelength (when symbol not used as subscript)
μ_i	First moment (mean) of pressure field at ith sensor, $\mu_i=\langle p_i\rangle$
ϕ	Azimuthal angle of arrival
Φ_i	Total phase of signal received at the ith sensor, $\Phi_i=\chi-\mathbf{k}\cdot\mathbf{r}_i$
Φ_{ij}	Difference in total phase between ith and jth sensors, $\Phi_{ij}=\Phi_i-\Phi_j$

ρ_{ij}	Separation between ith and jth sensors
σ_n^2	Noise variance
σ_ν^2	Cramer–Rao lower bound of Θ_ν, $\sigma_\nu^2=[\mathbf{J}^{-1}]_{\nu\nu}$
$\sigma_{\nu_0}^2$	Cramer–Rao lower bound of Θ_ν when Θ_ν is the only unknown, $\sigma_{\nu_0}^2=1/J_{\nu\nu}$
ς^2	Index-of-refraction variance
θ	Elevational angle of arrival
$\zeta_{\lambda\nu}$	Coupling (partial correlation) between the estimates of Θ_λ and Θ_ν

5. Acronyms

AOA	Angle of arrival
CRLB	Cramer–Rao lower bound
FI	Fisher information
MCF	Mutual coherence function
MSE	Mean square error
SNR	Signal-to-noise ratio
2D	Two dimensions or two-dimensional
3D	Three dimensions or three-dimensional

[1] D. K. Wilson, C. R. Tate, D. C. Swanson, and D. M. Reichard, ''Acoustic scintillations and angle-of-arrival fluctuations observed outdoors with a large planar vertical michrophone array,'' Acoust. Res. Lett. Online **106**, L24–L29 (1999).

[2] B. G. Ferguson, ''Variability in the passive ranging of acoustic sources in air using a wave front curvature technique,'' J. Acoust. Soc. Am. **108**, 1535–1544 (2000).

[3] B. J. Uscinski and D. E. Reeve, ''The effect of ocean inhomogeneities on array output,'' J. Acoust. Soc. Am. **87**, 2527–2534 (1990).

[4] E. Y. Gorodetskaya, A. I. Malekhanov, A. G. Sazontov, and N. K. Vdovicheva, ''Deep-water acoustic coherence at long ranges: Theoretical prediction and effects on large-array signal processing,'' IEEE J. Ocean. Eng. **24**, 156–171 (1999).

[5] S. M. Kay, *Fundamentals of Statistical Signal Processing: Estimation Theory* (PTR Prentice Hall, Englewood Cliffs, NJ, 1993).

[6] L. L. Scharf, *Statistical Signal Process: Detection, Estimation, and Time Series Analysis* (Addison–Wesley, Reading, MA, 1991).

[7] B. Ottersten, M. Viberg, P. Stoica, and A. Nehorai, ''Exact and large sample maximum likelihood techniques for parameter estimation and detection in array processing,'' J. Acoust. Soc. Am. **99**, 1370–1379 (1996).

[8] B.-G. Song and J. A. Ritcey, ''Angle of arrival estimation of plane waves propagating in random media,'' J. Acoust. Soc. Am. **99**, 1370–1379 (1996).

[9] D. K. Wilson, ''Performance bounds for acoustic direction-of-arrival arrays operating in atmospheric turbulence,'' J. Acoust. Soc. Am. **103**, 1306–1319 (1998).

[10] *Sound Transmission Through a Fluctuating Ocean*, edited by S. M. Flatté (Cambridge University Press, Cambridge, 1979).

[11] A. Ishimaru, *Wave Propagation and Scattering in Random Media* (IEEE Press, Piscataway, NJ, 1997).

[12] H. E. Bass, R. Raspet, and J. O. Messer, ''Experimental determination of wind speed and direction using a three microphone array,'' J. Acoust. Soc. Am. **97**, 695–696 (1995).

[13] D. E. Norris, D. K. Wilson, and D. W. Thomson, ''Correlations between acoustic travel-time fluctuations and turbulence in the atmospheric surface layer,'' Acustica **87**, 677–684 (2001).

[14] V. E. Ostashev, *Acoustics in Moving Inhomogeneous Media* (E & FN Spon, London, 1997).

[15] S. M. Rytov, Yu. A. Kravtsov, and V. I. Tatarskii, *Principles of Statistical Radiophysics 4: Wave Propagation Through Random Media* (Springer, New York, 1989).

[16] R. A. Horn and C. R. Johnson, *Matrix Analysis* (Cambridge University Press, New York, 1993).

[17] V. E. Ostashev and D. K. Wilson, ''Relative contributions from temperature and wind velocity fluctuations to the statistical moments of a sound field in a turbulent atmosphere,'' Acustica **86**, 260–268 (2000).

[18] D. K. Wilson, ''A turbulence spectral model for sound propagation in the atmosphere that incorporates shear and buoyancy forcings,'' J. Acoust. Soc. Am. **108**, 2021–2038 (2000).

[19] D. K. Wilson, J. G. Brasseur, and K. E. Gilbert, ''Acoustic scattering and the spectrum of atmospheric turbulence,'' J. Acoust. Soc. Am. **105**, 30–34 (1999).

[20] R. O. Nielsen, ''Estimation of azimuth and elevation angles for a plane wave sine wave with a 3-D array,'' IEEE Trans. Signal Process. **42**, 3274–3276 (1994).

[21] R. O. Nielsen, ''Azimuth and elevation angle estimation with a three-dimensional array,'' IEEE J. Ocean. Eng. **19**, 84–86 (1994).

[22] A. N. Mirkin and L. H. Sibul, ''Cramer–Rao bounds on angle estimation with a two-dimensional array,'' IEEE Trans. Signal Process. **39**, 515–517 (1991).

[23] Y. Hua and T. K. Sarkar, ''A note on the Cramer–Rao bound for 2-D direction finding based on 2-D array,'' IEEE Trans. Signal Process. **39**, 1215–1218 (1991).

Source motion mitigation for adaptive matched field processing[a)]

Lisa M. Zurk,[b)] Nigel Lee, and James Ward
MIT Lincoln Laboratory, 244 Wood Street, Lexington, Massachusetts 02420

(Received 30 November 2001; revised 23 December 2002; accepted 23 December 2002)

Application of adaptive matched field processing to the problem of detecting quiet targets in shallow water is complicated by source motion, both the motion of the target and the motion of discrete interferers. Target motion causes spreading of the target peak, thereby reducing output signal power. Interferer motion increases the dimensionality of the interference subspace, reducing adaptive interference suppression. This paper presents three techniques that mitigate source motion problems in adaptive matched field processing. The first involves rank reduction, which enables adaptive weight computation over short observation intervals where motion effects are less pronounced. The other two techniques specifically compensate for source motion. Explicit target motion compensation reduces target motion mismatch by focusing snapshots according to a target velocity hypothesis. And time-varying interference filtering places time-varying nulls on moving interferers not otherwise suppressed by adaptive weights. The three techniques are applied to volumetric array data from the Santa Barbara Channel Experiment and are shown to improve output signal-to-background-plus-noise ratio by more than 3 dB over the standard minimum-variance, distortionless response adaptive beam-former. Application of the techniques in some cases proves to be the difference between detecting and not detecting the target. [DOI: 10.1121/1.1561817]

PACS numbers: 43.60.Gk, 43.30.Wi [JCB]

I. INTRODUCTION

This paper presents and applies three ''motion mitigation'' techniques for improving adaptive matched field processing detection of quiet, moving targets in shallow-water environments.

Detection and localization of targets in shallow-water environments is a challenging problem for which it is well-known that plane-wave beamforming is inadequate because channel-specific acoustic multipath is not accounted for.[1] By contrast, matched field processing (MFP) accounts for coherent acoustic multipath in shallow water by employing a propagation model to construct appropriate steering (or ''replica'') vectors. Conventional (nonadaptive) matched field processing tends to suffer from beampatterns with high sidelobes, which can obscure quiet target detection in the presence of strong interferers. *Adaptive* matched field processing (AMFP) reduces interferer sidelobes by computing data-dependent weight vectors based on sample covariance matrix (SCM) inversion.[2–4]

It is well known, however, that AMFP performance degrades quickly in less-than-ideal conditions.[1,3] In particular, moving sources (both targets and interferers) can degrade AMFP performance severely, especially for large arrays with small beamwidths.[5] Target motion spreads target energy across several beams, reducing output signal power and resulting in poorer target detection and localization. Interferer motion increases the dimensionality of the interference subspace, reducing adaptive interference suppression and again resulting in poorer weak target detection.

One way to mitigate source motion is to apply rank reduction, which allows adaptive weight computation over shorter observation intervals where sources move less and are quasi-stationary. In much of the literature, rank reduction for AMFP is performed in eigenvector space.[6–8] The drawback to this is that eigenvectors have no inherent physical basis, so eigenvector-based rank reduction is usually achieved with no regard for information provided by the propagation physics. By contrast, several authors[9–11] have shown the utility of transforming the data into acoustic mode space, with a physically based modal basis; mode-space rank reduction to date, however, still employs eigenvectors.[11] The first motion mitigation technique presented here performs mode-based rank reduction (MBRR) by selecting the reduced-rank mode space according to physical considerations. In addition to the general benefits of rank reduction, this technique provides both filtering of surface interferers and broadening of beamwidths in the output beamformer, both of which further mitigate motion effects. MBRR does require accurate computation of the acoustic modes, so it is somewhat sensitive to environmental mismatch and it requires a capable array; this is discussed further in Sec. IV.

For processing over *long* observation intervals (in order

[a)]Portions of this work were presented in ''3D adaptive matched field processing for a moving source in a shallow water channel,'' Proceedings of the IEEE Oceans '99 Conference, Seattle, WA, September 1999; in ''Evaluation of reduced-rank adaptive matched field processing algorithms for passive sonar detection in a shallow-water environment,'' Proceedings of the 33rd Asilomar Conference, Pacific Grove, CA, November 1999; in ''Adaptive matched field processing for a moving target in a noisy shallow water channel,'' Proceedings of the Adaptive Sensor Array Processing (ASAP) Workshop, Lexington, MA, March 2000; and in ''Interference rejection for passive sonar using prior information with adaptive matched field processing,'' Fifth European Conference on Underwater Acoustics, Lyon, France, July 2000.

[b)]Electronic mail: zurk@ll.mit.edu

to minimize adaptive bias loss[2]), various techniques seek to address either target motion (by compensation) or interferer motion (by filtering). In the former category, the concept of matched-field tracking[12,13] has been proposed to mitigate target motion effects by adjusting the matched field replica vectors according to a target velocity hypothesis; however, matched field tracking can only produce nonadaptive output. By contrast, the second motion mitigation technique presented here performs explicit target motion compensation (ETMC) by focusing the *data* (snapshots), not the replicas, according to the target velocity hypothesis. This allows computation of target-motion-compensated *adaptive* output. The concept of focusing snapshots is found in broadband source localization problems,[14,15] but there the focusing is done in frequency (for wideband but stationary sources), not in space (as done in MFT and ETMC for narrowband but moving sources).

To address the interference motion problem over long observation times, data-based, time-varying interference filtering has been proposed previously in other contexts[16,17] and has recently been proposed for matched field processing.[18–21] The idea is to filter moving interferers, which are not effectively nulled by normal adaptive processing, on a snapshot-by-snapshot basis, under the assumption that the principal eigenvectors for each snapshot represent the interferers to be filtered. This technique fails, however, whenever the target itself is loud relative to the interferers. The third motion mitigation technique presented here performs *model*-based, time-varying interference filtering (MTIF) that makes use of external track information to place location-based nulls on interferers. Note that MTIF does not require association of the interferer with eigenvectors of the data; however, it does require accurate modeling of the interference space and is thus sensitive to (environment and track) mismatch. A hybrid algorithm is also presented that combines information from both the model-based and data-based techniques.

All three of the proposed techniques are demonstrated on vertical line array (VLA) data obtained from the Santa Barbara Channel Experiment (SBCX).[22] Section II presents the basic AMFP framework used in this work. Section III describes in detail the three techniques of improving AMFP performance on moving sources (reduced-rank mode space processing, explicit target motion compensation, and time-varying interference filtering). Section IV shows the results of applying the techniques to SBCX data and the improvement they provide over standard AMFP output and over existing motion mitigation techniques. Finally, Sec. V summarizes the conclusions of this work and suggests some areas for further work.

II. ADAPTIVE MATCHED FIELD PROCESSING FRAMEWORK

This section presents the basic AMFP framework used throughout the paper.

Defining $\Theta=(r,\phi,z)$ as the three-dimensional spatial position in range, azimuth, and depth, the MFP output for an N-element array at frequency f_0, time t_0, and direction Θ can be written as

$$P(f_0,t_0,\Theta)=\vec{w}^H(f_0,t_0,\Theta)\hat{\mathbf{K}}(f_0,t_0)\vec{w}(f_0,t_0,\Theta), \quad (1)$$

where $\vec{w}(f_0,t_0,\Theta)$ is the $N\times 1$ weight vector based on the corresponding replica vector $\vec{v}(f_0,t_0,\Theta)$, and where $\hat{\mathbf{K}}(f_0,t_0)$ is the $N\times N$ sample covariance matrix discussed in the following. For conventional matched field processing (CMFP),[23] the weights in Eq. (1) are normalized replica vectors:

$$\vec{w}_c(f_0,t_0,\Theta)=\vec{v}(f_0,t_0,\Theta)/N, \quad (2)$$

where the replica vector is normalized such that $|\vec{v}(f_0,t_0,\Theta)|^2=N$, so that the CMFP weight vector $\vec{w}_c(\cdot)$ in Eq. (2) achieves unity gain on target.

Adaptive matched field processing computes a weight vector that is dependent on the sample covariance matrix as well as the replica vector. The AMFP results in this paper are based on the high-resolution minimum-variance, distortionless-response (MVDR) filter.[2,3] The diagonally loaded MVDR (or MVDR-DL) weight vector is given by

$$\vec{w}_m(\cdot)=\frac{(\hat{\mathbf{K}}(f_0,t_0)+\sigma_d^2(\cdot)\mathbf{I})^{-1}\vec{v}(\cdot)}{\vec{v}(\cdot)^H(\hat{\mathbf{K}}(f_0,t_0)+\sigma_d^2(\cdot)\mathbf{I})^{-1}\vec{v}(\cdot)}, \quad (3)$$

where the MVDR weight vector $\vec{w}_m(\cdot)=\vec{w}_m(f_0,t_0,\Theta)$ is based on the replica vector $\vec{v}(\cdot)=\vec{v}(f_0,t_0,\Theta)$ and a position-dependent diagonal load level $\sigma_d^2(\cdot)=\sigma_d^2(f_0,t_0,\Theta)$. The load level is chosen to be large enough to satisfy a white noise gain constraint[4] (WNGC)

$$\vec{w}_m^H(\cdot)\vec{w}_m(\cdot)\leqslant\frac{\beta}{N}, \quad (4)$$

where the constant β is a ''relaxation'' parameter, defined as the factor by which the weight norm in Eq. (4) is allowed to exceed the ''white noise gain'' of $1/N$ [which is the value of $\vec{w}_m^H(\cdot)\vec{w}_m(\cdot)$ with no loading when $\hat{\mathbf{K}}(f_0,t_0)=\mathbf{I}$]. The WNGC load level that just satisfies Eq. (4) can be efficiently found through iterative searching,[8] which is the method employed here. Diagonally loading the MVDR weight vector minimizes the effects of poorly estimated components of the SCM $\hat{\mathbf{K}}(f_0,t_0)$ (due to insufficient snapshots, for example) as well as the effects of target self-nulling due to mismatch.

MFP weights are computed over a finite set of spatial coordinates Θ, and MFP results are typically displayed via a spatial *ambiguity surface* measuring MFP output power [from Eq. (1) above] versus spatial variables (range, depth, and/or bearing).

In this paper, the $N\times N$ sample covariance matrix $\hat{\mathbf{K}}(f_0,t_0)$ in Eq. (3) is computed using a time average of snapshots taken from FFT data at the frequency of interest:

$$\hat{\mathbf{K}}(f_0,t_0)=\frac{1}{L}\sum_{l=-L/2}^{L/2-1}\vec{x}(f_0,t_0+l\Delta t)\vec{x}(f_0,t_0+l\Delta t)^H, \quad (5)$$

where $\vec{x}(f,t)$ denotes the $N\times 1$ snapshot computed at frequency f and time t, f_0 is the center frequency, t_0 is the ''center time,'' and L is the number of snapshots. With nonoverlapping FFT windows, the estimate in Eq. (5) requires an observation period of $T=L\Delta t$ for each covariance computation, where Δt is the FFT window length.

The baseline AMFP output for this paper is the power output in Eq. (1) computed using the MVDR-DL weight vector in Eq. (3) and the sample covariance matrix in Eq. (5). In all subsequent sections of this paper, the dependence of $\vec{v}$, $\vec{w}$, $\hat{\mathbf{K}}$, and $\mathbf{P}$ on the center frequency f_0 and center time t_0 is suppressed and assumed implicitly, except where needed for clarity.

III. AMFP MOTION MITIGATION

A. Quantifying motion effects for MFP

The effect of source motion on MFP detection is best understood by considering the intrinsic cell size of a matched field processor (equivalent to the beamwidth of a plane wave beamformer). The width of an MFP ''cell'' in a given spatial dimension (range, depth, or bearing) is defined as the distance between the half-power points of the CMFP beampattern in that dimension, where the gain of the beampatter is one half (3 dB below) its maximum value. MFP achieves relatively fine resolution due to the deterministic phasing of acoustic modes. Rough expressions of the range and depth cell sizes can be obtained by considering the span of horizontal and vertical wavenumbers of the propagating modes. Letting k_M denote the horizontal wavenumber and k_{z_M} the vertical wavenumber of the Mth mode (representing the highest propagating mode with significant energy), the following are approximate expressions for the MFP range and depth cell sizes C_R and C_Z, respectively:[9,24,25]

$$C_R = \frac{2\pi}{k_1 - k_M}, \tag{6}$$

$$C_Z = \frac{\pi}{k_{z_M}}, \tag{7}$$

where k_1 is the wavenumber of the first mode (the mode that propagates nearly horizontally). The MFP bearing cell size is well-approximated by the corresponding expressions in plane wave beamforming:

$$C_\phi \approx \lambda/L \quad \text{(near broadside)} \tag{8}$$

$$C_\phi \propto \sqrt{\lambda/L} \quad \text{(near endfire)}, \tag{9}$$

where L is the horizontal array extent and λ is the acoustic wavelength. Note that a straight VLA has no horizontal extent, but a tilted VLA has a small horizontal extent.

The effect of *target* motion over a given observation time T is to disperse the energy of the target in the MFP ambiguity surface across several MFP cells. One can define target ''motion loss'' as the loss in peak target power due to target motion, with the loss computed relative to the power of a stationary target. If the target is thought to be at position Θ but in reality transits through Θ over time, the motion loss (in dB) as a function of Θ is given by

$$ML(\Theta) = -10\log_{10}\left[\frac{1}{L}\sum_{l=1}^{L}\cos^2(\vec{x}_{t_l}, \vec{w}(\Theta))\right], \tag{10}$$

where

$$\cos^2(\vec{x}_{t_l}, \vec{w}(\Phi)) \triangleq \frac{|\vec{w}^H(\Theta)\vec{x}_{t_l}|^2}{|\vec{w}(\Theta)|^2|\vec{x}_{t_l}|^2} \tag{11}$$

represents the beam offset between the target signature $\vec{x}_{t_l}$ at time t_l and the MFP weight vector $\vec{w}^H(\Theta)$ for the assumed target position Θ. For a stationary target, assuming no other sources of mismatch, $\cos^2(\vec{x}_{t_l}, \vec{w}(\Theta)) = 1$ and $ML(\Theta) = 0$ dB. For CMFP, expression (11) reduces to $\cos^2(\vec{x}_{t_l}, \vec{v}(\Theta))$, because the weight vector $\vec{w}_c(\Theta)$ is a scalar multiple of the replica vector $\vec{v}(\Theta)$. $ML(\Theta)$ quantifies an upper bound to signal-to-background-plus-noise-ratio (SBNR) loss due to target motion, specifically the ''signal'' portion of SBNR. [SBNR loss due to target motion may be less than $ML(\Theta)$ if, to begin with, the weight vector $\vec{w}(\Theta)$ is mismatched with the assumed (stationary) target at position Θ.] This loss can be estimated by using Eqs. (6) and (7) to calculate the number of cells transited by the target during the observation time T, which may then be used to bound the allowable radial velocity. For example, in the SBCX environment, the 3 dB range cell size in Eq. (6) is approximately 10λ. If a source in this environment moves in range with a radial velocity greater than $10\lambda/T$, its motion loss in Eq. (10) is greater than 3 dB.

The effect of *interferer* motion over a given observation time T is to spread interferer energy across the eigenvalue spectrum of the sample covariance matrix. The result of this is that moving interferers consume adaptive degrees of freedom (DOF) and limit the adaptive nulling capability of the AMFP weight vector (3). The number of adaptive DOF consumed by a moving interferer is roughly equivalent to the number of resolution cells [given again by Eqs. (6) and (7) above] that the interferer transits during the observation time.

B. Motion mitigation by mode-based rank reduction (MBRR)

One philosophy for mitigating source motion is to compute AMFP weights over shorter observation intervals where sources–both target and interferers—move less and are quasi-stationary, thus limiting motion loss. Shorter observation intervals, however, mean fewer data snapshots for SCM computation, and it is well known that MVDR power output is biased low if not enough snapshots are available.[2,26,27] Rank reduction is one method of decreasing the number of snapshots needed. (There is a limit, however, as to how short the observation time T can be; this limit is determined by the number of snapshots needed to estimate all discrete sources in the data, including the target.)

Rank reduction for AMFP involves computing a reduced-rank approximation of the sample covariance matrix $\hat{\mathbf{K}}$ in Eq. (5). Most commonly, this is done using the eigenvector (EV) decomposition of $\hat{\mathbf{K}}$, given by

$$\hat{\mathbf{K}} = \mathbf{U}\mathbf{\Sigma}\mathbf{U}^H = \sum_{i=1}^{N} \sigma_i^2 \vec{u}_i \vec{u}_i^H, \tag{12}$$

where $\mathbf{U} = [\vec{u}_1 \vec{u}_2 \cdots \vec{u}_N]$ is an orthogonal matrix whose columns are comprised of the eigenvectors $\vec{u}_i$ of $\hat{\mathbf{K}}$ and $\mathbf{\Sigma} = \mathrm{diag}(\sigma_1^2, \sigma_2^2, \ldots, \sigma_N^2)$ is a diagonal matrix whose diagonal elements are comprised of the eigenvalues σ_i^2 of $\hat{\mathbf{K}}$. Transformation from phone space (snapshots $\vec{x}$) to EV space is represented as $\vec{x}_e = \mathbf{T}_e \vec{x}$, where the $N \times N$ eigenvector transformation matrix is given by $\mathbf{T}_e = \mathbf{U}^H$. Eigenvector-space rank reduction is then achieved by retaining P out of N

elements of $\vec{x}_e$, which is equivalent to applying an eigenvector filter Φ_e: $\vec{x}_{e_R}=\Phi_e\vec{x}_e=\Phi_e\mathbf{T}_e\vec{x}$, where Φ_e is a diagonal matrix with 1's (corresponding to retained eigenvectors) and 0's (corresponding to filtered eigenvectors) as its diagonal entries.

The drawback to EV-based rank reduction is that eigenvectors have no inherent physical basis, so the rank reduction is usually achieved with no regard for information provided by the propagation physics. The most common example of eigenvector-based rank reduction is to retain the eigenvectors corresponding to the largest eigenvalues, which is essentially what is done in the well-known dominant mode rejection (DMR) algorithm.[6] Other techniques exist for EV-based rank reduction in which the criterion for retaining eigenvectors is based at least in part on correlation with the replica vector look direction; examples of this include the signal coherence criterion[8] and the direct-form-cross-spectral metric, which was proposed and examined by the authors.[28,29] However, the latter techniques require computation of a different reduced-rank EV subspace with each look direction and are thus computationally expensive.

AMFP rank reduction that is both physically based and computationally simple is made possible by transformation of both data and replicas into acoustic mode space. The acoustic mode functions are the mathematical descriptions of the physical phenomena assumed by normal mode propagation models, and the number of *independent* mode functions is limited to the number of propagating modes. Further, for a fully spanning, upright VLA, the propagating acoustic mode functions form an approximately orthonormal basis (note, however, that vertical aperture is essential to the formation of an orthonormal modal basis).

Modal decomposition makes use of the normal mode expansion of the acoustic pressure field $p(r,z)$ at receiver range r and depth z due to a source at depth z_s, which is approximated (in the far field) by

$$p(r,z)=\frac{j}{\rho(z_s)\sqrt{8\pi}}e^{-j\pi/4}\sum_{i=1}^{M}\Psi_i(z_s)\Psi_i(z)\frac{e^{jk_ir}}{\sqrt{k_ir}}, \quad (13)$$

where $\Psi_i(\cdot)$ are the acoustic mode functions, $\rho(z_s)$ is the water density at the source depth, k_i is the horizontal wavenumber associated with the ith mode, and M is the number of "propagating" modes for which k_i does not have significant imaginary part. The expression in Eq. (13) may be rewritten as

$$p(r,z)=\sum_{i=1}^{M}\alpha_i(z_s)f_i(r,z), \quad (14)$$

where the constants $\alpha_i(z_s)$ may be thought of as coefficients in the modal expansion,

$$\alpha_i(z_s)=\frac{je^{-j\pi/4}}{\rho(z_s)\sqrt{8\pi}}\Psi_i(z_s), \quad (15)$$

and where the functions $f_i(r,z)$ are the attenuated acoustic mode functions:

$$f_i(r,z)=\Psi_i(z)\frac{e^{jk_ir}}{\sqrt{k_ir}}. \quad (16)$$

To account for array tilt, the range r in Eq. (16) may be replaced by an "adjusted" range $r+\Delta r$, with the element-dependent offset Δr varying for each hydrophone (i.e., for each receiver depth z).

In vector notation, Eq. (14) may be rewritten as

$$\vec{p}=(\mathbf{F}_m\odot\Gamma)\vec{a}, \quad (17)$$

where $\mathbf{F}_m$ is the $N\times M$ modal decomposition matrix whose ith column is the attenuated mode function $f_i(r,z)$ in Eq. (16), sampled at the depths of the array hydrophones; where $\odot$ stands for element-by-element multiplication; where Γ is a matrix of phase terms that takes into account the effects of array tilt; and where $\vec{a}$ is the $M\times 1$ vector of mode coefficients α_i. Equivalently, the transformation of an $N\times 1$ "phone-space" data snapshot $\vec{x}$ to an $M\times 1$ mode-space snapshot $\vec{x}_m$ can be written as

$$\vec{x}_m=\mathbf{T}_m\vec{x}, \quad (18)$$

where the $\mathbf{T}_m$ is the $M\times N$ mode transformation matrix computed as

$$\mathbf{T}_m=\{(\mathbf{F}_m\odot\Gamma)^H(\mathbf{F}_m\odot\Gamma)\}^{-1}(\mathbf{F}_m\odot\Gamma)^H. \quad (19)$$

The transformation matrix $\mathbf{T}_m$ in Eq. (19) is essentially that proposed in previous papers on mode-space MFP.[9,11] The inverse in Eq. (19) can be unstable, especially if $M>N$ and $\mathbf{F}_m^H\mathbf{F}_m$ is less than full rank; in this case, small or zero eigenvalues of $\mathbf{F}_m^H\mathbf{F}_m$ may be dropped in order to compute the (pseudo)inverse.[11]

The first of three motion mitigation techniques proposed here is mode-based rank reduction (MBRR). This is achieved by retaining P out of M elements of $\vec{x}_m$ in Eq. (18), which is equivalent to applying a mode filter Φ_m:

$$\vec{x}_{m_R}=\Phi_m\vec{x}_m=\Phi_m\mathbf{T}_m\vec{x}, \quad (20)$$

where Φ_m is a diagonal matrix with 1's (corresponding to retained modes) and 0's (corresponding to filtered modes) as its diagonal entries. For example, $\Phi_m=\mathrm{diag}(1,...,1,0,...,0)$ retains the first few (lower-order) modes and filters the rest.

MBRR can succeed where EV-based techniques do not because the mode functions have physical structure that can be exploited to separate submerged targets and surface interferers. (Successful eigenvector separation of nonorthogonal sources requires different source powers, which will not always be the case. Equal-power nonorthogonal sources will not be separated well using eigenvectors.) For example, because only higher-order modes are strongly excited at the water surface and because lower-order modes often contain a significant portion of the energy for sources at depth, one potentially effective MBRR technique is to retain only the lower-order modes (and to filter the higher-order modes). Of course, the success of mode-based surface-submerged source separation may vary with environment.

In addition to allowing adaptive processing with fewer snapshots, MBRR thus has the added benefit of filtering surface energy while not suffering significant signal gain degradation for targets at depth. Further, filtering of the higher-

order modes has the effect of increasing the intrinsic MFP range cell size by decreasing the denominator of Eq. (6). Thus, AMFP motion effects are further mitigated, as both target and interferers transit fewer mode-space MFP cells than phone-space MFP cells, resulting in less target motion loss and fewer interferer DOF. It is also true, however, that the increased cell size results in decreased source localization accuracy.

C. Motion mitigation by explicit target motion compensation (ETMC)

A second philosophy for mitigating source motion is to compute AMFP weights over long observation intervals T but to compensate explicity for source motion. Processing over long observation intervals, if done properly, increases the accuracy of the adaptive weight computation and increases incoherent integration gain. Over long observation intervals, however, both target and interferer motion have to be accounted for.

The second of three motion mitigation techniques proposed here is explicit target motion compensation (ETMC), which combats target motion loss over long observation intervals. This is accomplished by adjusting the amplitude and phase across each data snapshot $\vec{x}(f_0,t_l)$ in Eq. (5) so that the target appears stationary. It is important to note that ETMC (as well as other target motion compensation techniques) compensates for the motion of a *single* source; it cannot effectively compensate for different motions of multiple sources. The amplitude/phase adjustment is determined by applying a velocity hypothesis to the target to predict the target position at each time t_l, and then by comparing the target replica vector at each position (computed via a propagation model) with the replica vector at a chosen, ''focus'' position. Assuming uncorrelated sensor data, the adjustment for the kth sensor at time t_l is given by

$$\Psi_l(k)=e^{-j\Delta\phi_l(k)}\Delta\alpha_l(k), \tag{21}$$

where $\Delta\phi_l(k)$ is the phase difference between the response of the kth hydrophone for the predicted target position at time t_l and the response of the kth hydrophone for the target focus position; and where $\Delta\alpha_l(k)$ is the corresponding target amplitude ratio. Computation of the correct compensations $\Delta\phi_l$ and $\Delta\alpha_l$ thus requires both an accurate target velocity hypothesis and accurate propagation modeling.

Once each snapshot has been ''compensated,'' the resulting covariance matrix contains the signature of a target that has been ''focused'' to the focus point. The focus point is any position along the target track (during the observation interval) to which motion will be compensated; a single focus point is chosen for a given observation interval T. Perfect compensation produces output equivalent to that for a stationary target at the focus point; this theoretically recovers whatever target motion loss has occurred during the observation interval. In this paper, the predicted position of the target in the *middle* of the observation period is chosen as the focus point.

It is important to distinguish ETMC with matched field tracking (MFT) algorithms,[12,13] which adjust the replica vectors $\vec{v}$ according to the target velocity hypothesis, while keeping the data (snapshots and SCM) fixed. Because the adaptive weight computation in Eq. (3) requires multiple snapshots for a given replica vector, target motion compensation for *adaptive* MFP requires adjustment of the data while keeping the replica vectors fixed. The latter is what is done in ETMC. Another significant difference is computational: MFT requires compensation of every replica vector with each snapshot in time, whereas ETMC requires only the adjustment of the snapshot itself. Again, it is important to note that both techniques can only compensate for the motion of a single source.

D. Motion mitigation by model-based, time-varying interference filtering (MTIF)

The last of three motion mitigation techniques proposed here is model-based, time-varying interference filtering (MTIF), which combats interference motion loss over long observation intervals. Interference filtering involves spatial filtering of an interferer, in which the data is projected onto a subspace that is orthogonal to the (estimated) interference subspace. Because interferers move, the rank of the interference subspace estimate over the entire observation interval T can be quite large, and filtering of the data by this ''long-time'' interference subspace estimate may result in undesirable reduction of the target peak. The solution to this problem is to apply a *time-varying* spatial filter to the data that removes an *instantaneous* estimate of the interference subspace *at each snapshot*; the instantaneous subspace is likely low-rank because it is estimated over a very short observation time.

The spatial interference filter is the orthogonal projection complement $\mathbf{I}-\Phi(\Phi^H\Phi)^{-1}\Phi^H$ of the interference subspace estimate Φ. This filter is applied to each snapshot, and the filtered snapshot is then target-motion-compensated as detailed earlier. The resulting filtered and compensated snapshot is then used as in Eq. (5) to compute the sample covariance matrix $\hat{\mathbf{K}}$.

Clearly, the most important aspect of the interference filtering technique is estimating the interference subspace. Data-based estimation assumes that the interferer is the strongest source in the data and is captured by the principal eigenvector(s) of the ''instantaneous covariance matrix'' computed for each snapshot. By contrast, MTIF makes use of external track information for the interferer to build a location-based interference subspace estimate. Hybrid estimation combines information from both. The three methods are detailed in the following.

1. Data-based interference filtering

The data-based method of interference filtering (similar to what Cox terms ''multi-rate adaptation''[18]) assumes that the interference is strong and can be estimated with a small number of snapshots J, fewer than the total number of snapshots L. At each time t_l, an instantaneous covariance matrix $\hat{\mathbf{K}}_{\text{inst}}$ is computed with J snapshots (centered on the lth snapshot):

$$\hat{\mathbf{K}}_{\text{inst}}=\sum_{j=l-J/2}^{l+J/2}\vec{x}_j\vec{x}_j^H. \tag{22}$$

The M principal eigenvectors[16,17] of this instantaneous covariance matrix are then used to estimate Φ, the instantaneous interference subspace: $\Phi_{\text{data}}=[\vec{u}_1\vec{u}_2\cdots\vec{u}_M]$, where $\{\vec{u}_i\}_{i=1}^{M}$ are the principal eigenvectors of $\hat{\mathbf{K}}_{\text{inst}}$. The success of the data-based method relies on the assumption that the interference and target subspaces are distinct in eigenvector space; specifically, it is assumed that that interferer comprises the only strong source in the data. Problems arise if the target is loud relative to the interferer (in which case the target will be part of the interference estimate and will itself be filtered). The data-based method also assumes that the interferer can be estimated well with J snapshots; problems arise if the interferer still moves significantly during the computation of Eq. (22).

2. Model-based interference filtering

Model-based, time-varying interference filtering (MTIF)[19–21] constructs its spatial filter assuming that some prior knowledge of the interferer's position is available. An example might be the tracking of a merchant ship by an airborne asset in the region. In order to estimate the interference subspace, a propagation model is used to determine the acoustic signature (replica vector) for an interferer at the given position. To protect against inaccuracies in the interferer position, the interference subspace is computed using M replica vectors spanning a spatial region centered at the instantaneous position estimate of the interferer: $\Phi_{\text{model}}=[\vec{v}(\Theta_0)\vec{v}(\Theta_1)\cdots\vec{v}(\Theta_{M-1})]$, where $\Theta_1,\ldots,\Theta_{M-1}$ represent neighboring coordinates in range and depth (and possibly bearing) to the center coordinate Θ_0. The amount of range and depth ''padding'' that is necessary is determined by the accuracy of the prior knowledge (the greater the uncertainty in the position of the interferer, the larger M should be); any padding increases the size of the interference subspace estimate. Padding is also necessary when environmental information is uncertain, in which case more replica vectors are needed to describe a given interferer. Clearly, this method is dependent on accurate external information, but it does not make any assumptions about interferer versus target strength (in contrast to the data-based method).

3. Hybrid interference filtering

The hybrid method of interference filtering combines information from both the data-based and model-based approaches. To accomplish this, the model-based replica vectors $\{\vec{v}_m\}_{m=1}^{M}$ that span the presumed interferer position are projected onto the data-based interference subspace spanned by the principal eigenvectors of $\hat{\mathbf{K}}_{\text{inst}}$. The hybrid interference subspace is then formed by selecting only those replica vectors with significant projection onto the data: $\Phi_{\text{hybrid}}=\{\vec{v}_m\}$, $\vec{v}_m^H\Phi_{data}\geqslant\gamma$, where γ is an adjustable parameter between 0 and 1 representing the minimum acceptable projection. Higher values of γ produce more conservative interference subspace estimates; in the examples below, $\gamma=0.6$, requiring fairly (but not extremely) high correlation between replicas in the model subspace and the data. In general, the greater one's confidence in the model (versus the data), the lower γ should be. Note that the hybrid method essentially uses Φ_{model} except where the interference model is deemed inaccurate (as measured by correlation with Φ_{data}).

IV. RESULTS

In this section, the three AMFP motion mitigation techniques proposed earlier are applied to data from the Santa Barbara Channel Experiment (SBCX). Baseline AMFP performance is computed using the MVDR-DL weight vector in Eq. (3).

Results are presented in the form of MFP ambiguity surfaces (or derivatives), with the implicit assumption that detection is done in the spatial domain. Note that because of the redundancy in MFP steering vectors, it is inherently difficult to perform detection on MFP ambiguity surfaces. Performance is quantified by output SBNR (signal-to-background-and-noise ratio), which for an ambiguity surface is calculated as the ratio (in dB) of the output signal peak relative to the level of the background (consisting of output noise, interference, and possibly strong source sidelobes). The background level is defined as the 25th percentile of the ordered output powers on the ambiguity surface. For strong discrete sources, the 25th percentile measure may reflect source sidelobes, which are not traditionally considered background. However, it should be pointed out that for detection in the spatial domain, discrete interferer sidelobes often comprise the ''background,'' especially for data taken in heavy-shipping-density environments where interferers are constantly present. Thus, a processor that lowers sidelobes not only improves localization but also improves detection in the spatial domain, and this is reflected in both the 25th percentile measure and in the resulting SBNR.

The SBCX experiment was conducted in April 1998 in the 200-m-deep littoral waters of the Santa Barbara Channel.[22] One of the passive acoustic sensors deployed during the experiment was a 150-hydrophone volumetric array called the full-field processing (FFP) array. The FFP array consisted of five 30-phone VLAs arranged in a pentagonal configuration. The combination of vertical and horizontal aperture allowed full, three-dimensional localization in range, depth, and bearing.

One of the acoustic sources deployed during SBCX was a J15-3 transducer that was towed by a research vessel, the Acoustic Explorer (AX). The J15-3 was used to generate a comb sequence of 12 tones at approximately 159 dB re 1 μPa source level. The AX contained an onboard GPS receiver for platform position information, and a nearby radar station produced track information for surface vessels in the SBCX area.[22] The SBCX site bathymetry is shown in Fig. 1. Replica vectors were computed by using the KRAKEN normal mode program[30] to generate mode functions and wavenumbers for water depths ranging from 50 to 260 m. A two-dimensional adiabatic approximation was then applied to derive *range-dependent* replica vectors (with the range dependence due to varying site bathymetry). The replicas were computed using a geoacoustic model that consisted of two sediment layers overlaying an acoustic half-space; the parameters used for the sediment were obtained from previous investigation in this area and are given in Table I. The

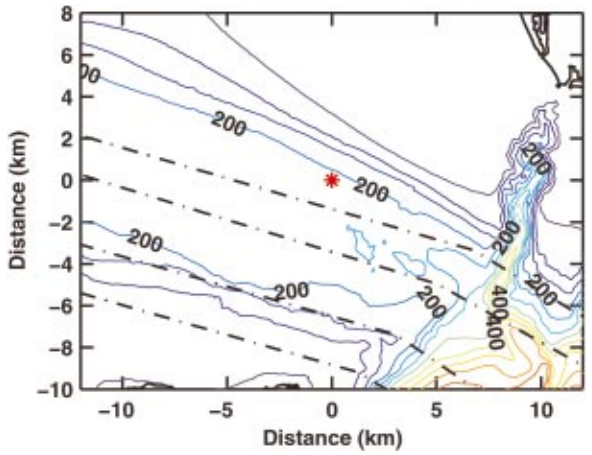

FIG. 1. SBCX site bathymetry. Dashed lines indicate shipping lanes. The map origin is the FFP array, indicated by the red asterisk. The California coastline is in the northeast corner of the map.

sound speed profile (SVP) for the water column was measured experimentally in several regions throughout the duration of the experiment; the replicas were computed using an average SVP shown in Fig. 2.

Figure 3 shows processing of data from a single VLA ($N=30$ phones) for 300 s at 235 Hz, one of the comb frequencies. Time-averaged covariance estimation was used with $\Delta t=1$ s, resulting in 300 snapshots over 300 s. CMFP and AMFP output were computed using the CMFP weight vector in Eq. (2) and the AMFP weight vector in Eq. (3), respectively, and the results are shown in Figs. 3(a) and (b). Note that the 90.4 dB peak of the CMFP surface, according to the sonar equation, equals SL-TL-MM, with source level SL=159 dB, transmission loss TL ~60 dB for a 2 km source, and mismatch MM ~8.4 dB due to both motion and steering vector mismatch. The AMFP peak of 87.4 dB is lower because of greater mismatch. The CMFP output in Fig. 3(a) displays the characteristically high sidelobes of nonadaptive MFP processing; this is manifested by the measured background level of 84 dB, resulting in an output SBNR of 6.4 dB. The AMFP output in Fig. 3(b) displays significantly lower sidelobes than CMFP; the background level is 76.3 dB and the SBNR is 11.1 dB. However, the motion of the target over 300 s (about 780 m in range) has resulted in peak dispersion; the motion loss from Eq. (10) is ~7.3 dB (vs 5.8 dB for CMFP). Motion loss is greater for AMFP than for CMFP because of the higher resolution of the adaptive weight vectors.

Figure 4 demonstrates motion mitigation via MBRR

TABLE I. Parameters for geoacoustic model used in SBCX data: z=depth from surface; c_c=compressional sound speed; ρ=density; α_c=compressional wave attenuation.

z (m)	c_c (m/s)	ρ (g/cm^3)	α_c (dB/λ)
209	1607	1.95	0.37
309	1702	1.95	0.37
309	1862	1.98	0.035
609	2374	1.98	0.035
609	2374	2.03	0.04

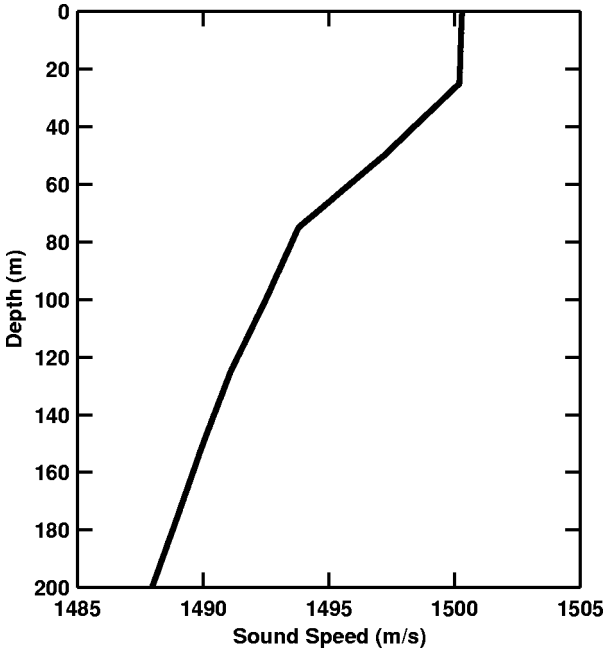

FIG. 2. Typical shallow-water, downward-refracting sound speed profile (SSP) used in all KRAKEN computations and obtained from averaging multiple measurements.

(mode-based rank reduction). First, Figs. 4(a) and (b) show eigenvector-based and mode-based AMFP rank reduction, respectively, for the full 300 s processed in Fig. 3. The eigenvector-based rank reduction in Fig. 4(a) is achieved using dominant mode rejection (DMR) with rank 10 (compared to the array size of 30). For the long observation time, snapshots are plentiful (300 snapshots for $\Delta t=1$ s FFT window), so rank reduction is not necessary for computational purposes. Indeed, as has been observed previously by the authors,[7,29] reduced-rank DMR displays poorer sidelobe rejection than the full-rank MVDR-DL. The result, in this case, is that the background level increases by 3.1 dB over the full-rank MVDR-DL to 79.4 dB, and the output SBNR decreases by 3 dB to 8.1 dB. For the long observation time, then, there is no reason to perform eigenvector-based rank reduction.

By contrast, MBRR is highly effective over the long observation time because of wider cell-widths in the reduced-rank mode space. Figure 4(b) shows MBRR achieved by retaining the ten lowest-order modes. The range resolution for the reduced-rank mode result—estimated from Eq. (6), but with k_M replaced by k_P, the highest propagating mode *in the reduced-rank subspace*—is approximately 346 m, compared to the 68 m resolution of the full-rank result. The result of this wider cell-width is a higher target peak (90.3 dB compared to 87.4 dB in the full-rank result) and a 4.4 dB increase in output SBNR (15.5 to 11.1 dB), because the target has transited fewer MFP cells over the 300 s observation time and there is correspondingly less motion loss [5.2 dB compared to 7.3 dB for the full-rank case, using Eq. (10)]. Note that basic sonar equation computations (assuming that transmission loss follows a cylindrical spreading law) dictate that a 3 dB increase in output SBNR results in a doubling of detection range; thus, the 4.4 dB

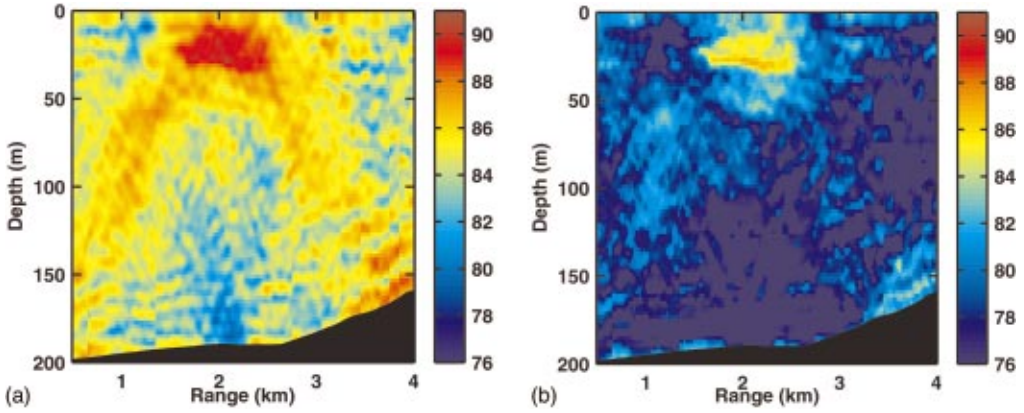

FIG. 3. Ambiguity surfaces from VLA data ($N=30$ phones) for a 235 Hz tone processed with an observation time of $T=300$ s and FFT window $\Delta t=1$ s. The range of the AX (according to GPS) was 1.67–2.45 km from the array. Nonadaptive CMFP output in (a) displays characteristically high sidelobes, with output SBNR 6.4 dB. Adaptive MVDR-DL output in (b) shows lower sidelobes but a dispersed peak due to target motion; output SBNR is ~11.1 dB. Estimated target motion loss is 7.3 dB due to the 0.78 km motion of the target in range during the 300 s observation time. Colorbar units are dB *re* 1 μPa/Hz.

increase in output SBNR is significant. Figure 4(b) vividly illustrates, then, the motion mitigation over long observation times provided by adaptive MBRR.

The more typical application of rank reduction however, involves very short time intervals over which source motion is less pronounced. Figures 4(c) and (d) show reduced-rank AMFP output over 11 s (11 snapshots) of data within the original 300 s observation period; during these 11 s, the target transited less than one full range cell-width (resulting in little motion loss). Eigenvector-based rank reduction using rank-10 DMR in Fig. 4(c) performs poorly because there are too few snapshots to effectively reject all sidelobes in eigen-

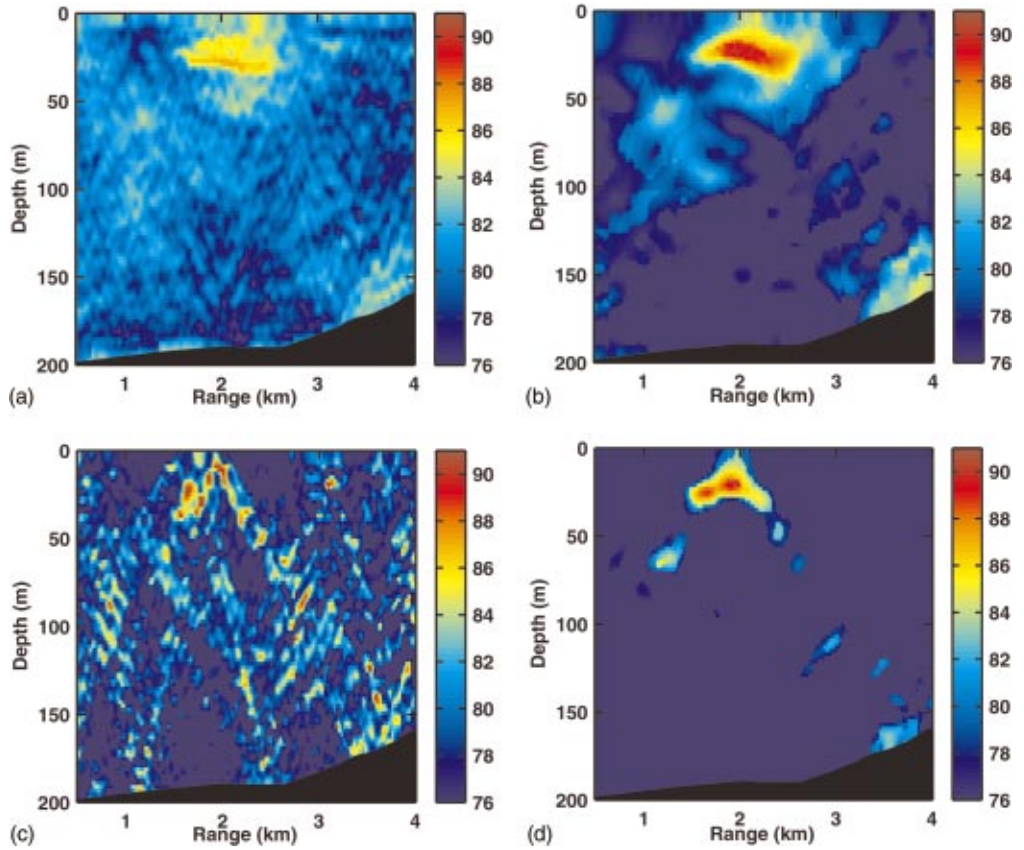

FIG. 4. Reduced-rank AMFP surfaces for the same data as in Fig. 3. (a) and (b) Rank-10 DMR and Rank-10 mode space AMFP for $T=300$ s of data. Rank-10 DMR in (a), as expected, has higher sidelobes than full-rank MVDR-DL in Fig. 3(b), resulting in lower output SBNR of 8.1 dB. Rank-10 mode space in (b) is less sensitive to motion (because of wider MFP cells in reduced mode space), resulting in less motion loss (5.2 dB vs 7.3 dB for the full-rank case), a higher signal peak (almost 3 dB better than full-rank MVDR), and output SBNR of 15.5 dB. (c) and (d) Rank-10 DMR and Rank-10 mode space AMFP for $T=11$ s (11 snapshots) of data. Rank-10 DMR in (c) is ineffective because the reduced-dimension eigenvalue spectrum no longer allows adequate sidelobe nulling; the output SBNR is 16.9 dB, but there are multiple peaks within 3 dB of the target peak. Rank-10 mode space in (d) is highly effective because significant filtering occurs during modal rank reduction; the background level drops to 67 dB, resulting in an output SBNR of 22.4 dB. Colorbar units are dB *re* 1 μPa/Hz.

vector space. Even though the measured output SBNR is high (16.9 dB), there are several ''false'' peaks of nearly the same power as the main target peak, so the target has not been unambiguously detected. By contrast, the rank-10 mode-space result (ten lowest-order modes retained) in Fig. 4(d) displays excellent sidelobe rejection and an unambiguous target peak (output SBNR ~22.4 dB). The reason for this is twofold: first, the ten lowest-order modes represent all the significant propagating modes at the 235 Hz frequency, so rank-10 AMFP output is still meaningful in mode space; second, the wider cell-widths in the reduced-rank mode space effectively ''group'' neighboring ambiguity peaks into larger peaks regions. Figure 4(d) illustrates that when computing reduced-rank AMFP output over very short observation intervals to mitigate motion, mode space provides a physically meaningful and intelligent way to perform the rank reduction.

Over both short and long observation times, the distinguishing feature for adaptive MBRR is its wider cell widths. This can be advantageous, since the coarser MFP cells reduce the number of ''beams'' that need to be formed to cover a given search region adequately. However, the coarser MFP cells also result in poorer localization, making it more likely for interferers to reside within one cell width of the target and thus appear in the same peak region as the target. The latter is not as great a concern as it may appear, given the potential with MFP for range, depth, *and* bearing discrimination.

It is important to note that the success of mode-based processing requires enough environmental information to compute the modal decomposition in Eq. (14) accurately. The SBCX environment was fairly well characterized, but not extraordinarily so, as the mode functions in the above-discussed results were computed using historical geoacoustic parameters (Table I) and an average SVP (Fig. 2), neither of which is entirely accurate for the SBCX data. Thus, it can be reasonably stated that mode-space processing is only somewhat sensitive to environmental mismatch. Computing the modal decomposition accurately also requires an array capable of resolving the modes; the SBCX VLA, which is almost fully spanning, is an example of the latter.

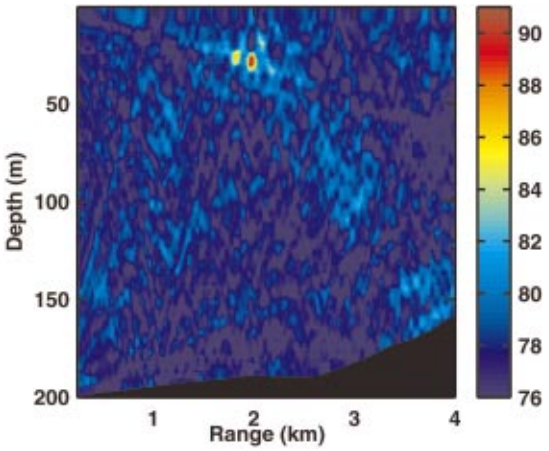

FIG. 5. Target-motion-compensated AMFP output for the same data as in Fig. 3, also processed for observation time $T=300$ s. The plot shows the signal focus that results when motion compensation is applied using the GPS track with a focus range of 2.0 km from the array. Target motion compensation adjusts the amplitude and phase of each snapshot according to a given velocity hypothesis. The signal peak is 91.1 dB [compared to 87.4 dB for uncompensated MVDR output in Fig. 3(b)], resulting in an output SBNR of 14.4 dB. Colorbar units are dB *re* 1 μPa/Hz.

In contrast to the motion mitigation provided by reduced-rank mode-based processing, ETMC (explicit target motion compensation) as detailed in Sec. III C uses target track hypotheses to correct for target motion explicitly. Figure 5 shows ETMC AMFP output over the 300 s observation interval processed in Fig. 3. The result is a focused target

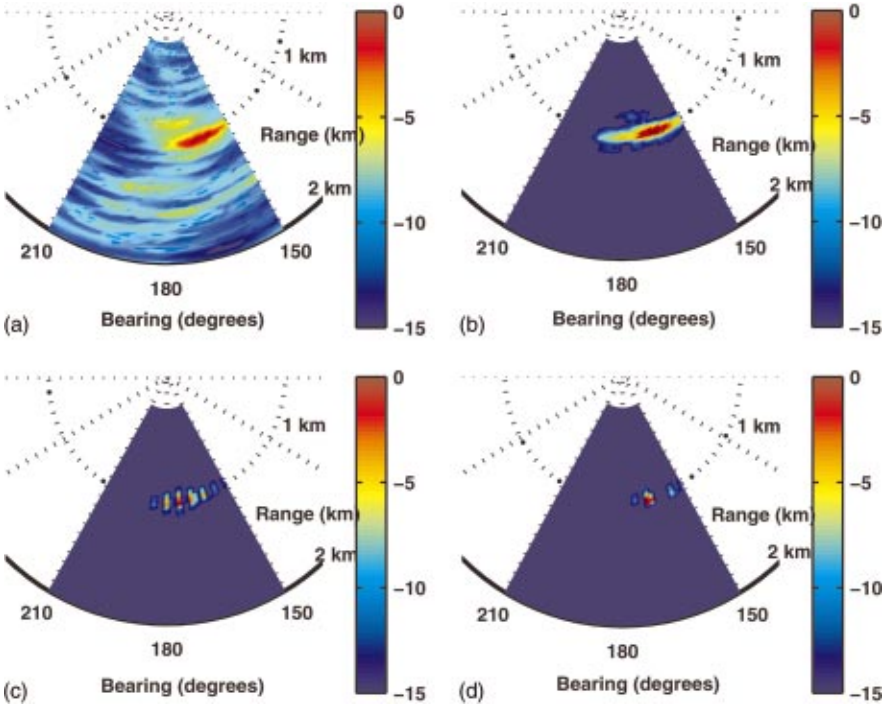

FIG. 6. Target motion compensation in bearing, applied to data from multiple VLAs. Results are range-bearing ambiguity surfaces for 1–3 VLAs processed coherently on a 235 Hz tone over observation time $T=120$ s, using FFT window $\Delta t=1$ s. The single VLA result in (a) shows coarse bearing localization due to the tilt of the VLA. Coherent processing of two VLAs should give additional azimuth resolution due to the 130 m horizontal baseline, but the uncompensated result in (b) is equivalent to incoherent array averaging because of motion decorrelation effects. Motion-compensated results for two VLAs (c) and three VLAs (d) give the expected azimuthal resolution and full, coherent array gain.

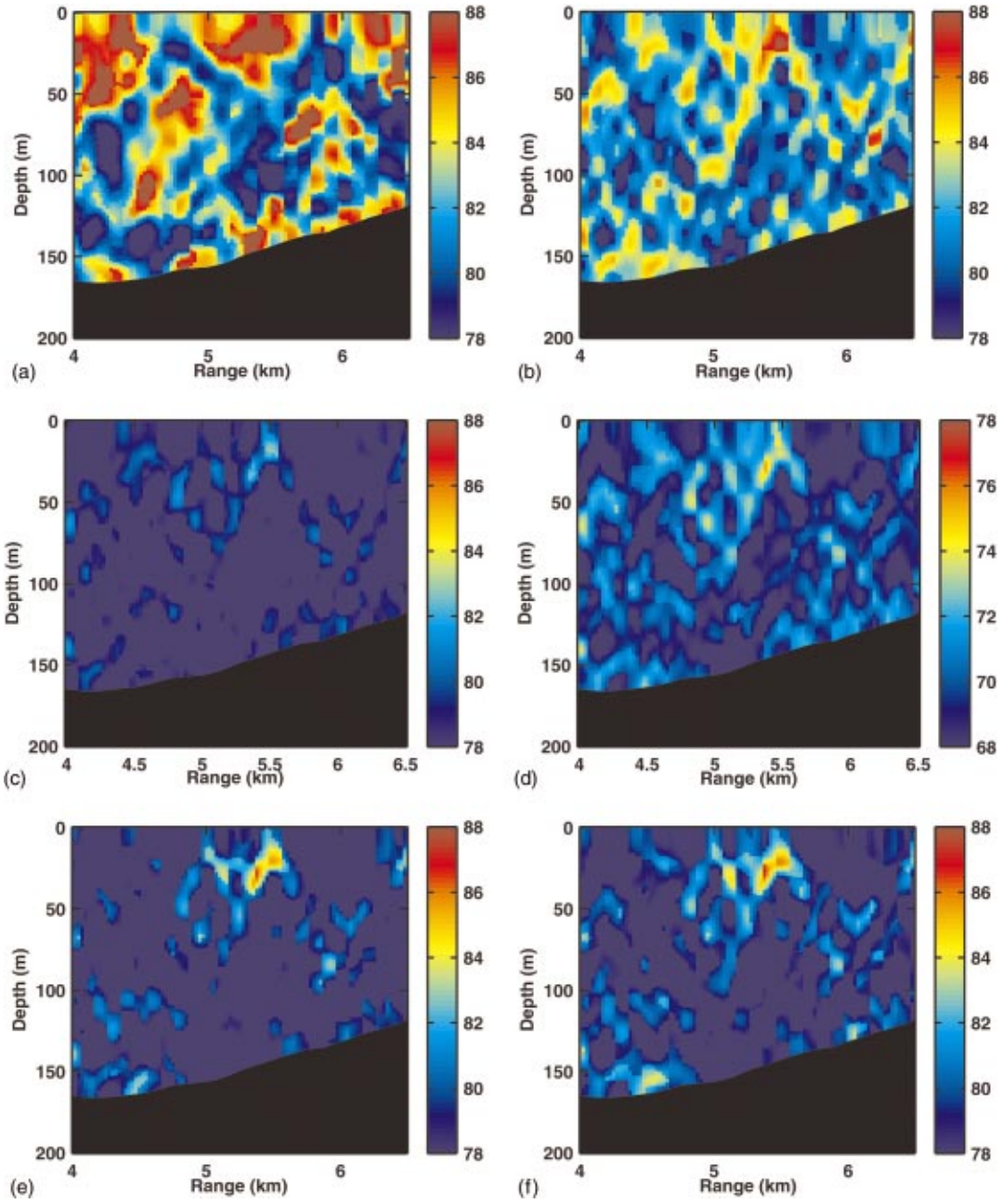

FIG. 7. Time-varying interference filtering of AMFP output at 94 Hz (time-averaged covariance matrix, $T=200$ s, $\Delta t=1$ s). The AX was 5.05–5.75 km from the array at the same time a surface ship was traveling in the eastbound shipping lane (~6.7 km from the array), with estimated interference level 163 dB. (a) The unfiltered result with output SBNR 7.8 dB; however, the target is not unambiguously detected because of interferer sidelobes. (b) The result after motion compensation only (output SBNR remains 7.8 dB but the target is localized). (c) Data-based filtering followed by motion compensation, with the principal eigenvector used to estimate the instantaneous interference subspace; the resulting output SBNR is 6.8 dB, a decrease from the unfiltered result due to undesired target filtering. (d) Data-based filtering with two principal eigenvectors; the resulting output SBNR is again 6.8 dB, but altogether too much of the target has been filtered (target peak 12.2 dB below the unfiltered result—note the lower colorbar). (e) Model-based filtering followed by motion compensation, with $M=7$ replica vectors used to estimate the instantaneous interference subspace; the resulting output SBNR is 11.2 dB. (f) Hybrid filtering, with $M=7$ and $\gamma=0.6$; the resulting output SBNR is 10.8 dB. Both model-based and hybrid filters produce good results for this scenario because the interferer position was approximately known (from a radar track) and the acoustic propagation model was accurate. Colorbar units are dB *re* 1 μPa/Hz.

peak (91.1 dB, compared to 87.4 dB for the uncompensated AMFP result) and output SBNR improvement of 3.3 dB (11.1 to 14.4 dB). Note that in this particular example, the true target track was approximately known, so the output is close to a best-case result. Further research is needed to determine the sensitivity of the motion compensation algorithm to target track accuracy.

A second example of ETMC, this time in the bearing dimension, is illustrated in Fig. 6. In this example, range-bearing AMFP output is shown for data from multiple VLAs (recall that the FFP array in SBCX contained five VLAs), processed at 235 Hz over $T=120$ s, using a $\Delta t=1$ s FFT window. For a single VLA [Fig. 6(a)], the array tilt of the VLA (approximately 15°) allows coarse azimuthal localization. The addition of a second VLA [Fig. 6(b)] should provide finer resolution and coherent array gain, but target motion—the differential Doppler across the two VLAs—introduces a time-varying phase that prevents any coherent

processing of the two VLAs; the result is then an incoherent sum of single-VLA outputs (with the same target peak region). Note that the motion compensation expression in Eq. (21) contains a phase correction that accounts for the modally dependent Doppler signatures. After correcting for this phase, the compensated surface for two VLAs [Fig. 6(c)] shows the grating pattern one would expect from a sparse horizontal aperture. Processing of three VLAs with motion compensation [Fig. 6(d)] results in a single strong peak with array gain $10\log_{10}3\approx5$ dB higher than the single-VLA result. It is important to note once again that ETMC is designed for a single source and that the SBNR improvement seen in the above two examples is not guaranteed for multiple sources.

All of the results to this point have demonstrated improved AMFP output on a single, moving target. For data that also include an interferer, the third motion mitigation technique is necessary, that of MTIF (model-based, time-varying interference filtering). Figure 7 shows AMFP output for data containing a loud, moving interferer located ~6.7 km from the FFP array (at another bearing) in addition to the AX towed source located ~5.5 km from the array. The processing was done at frequency 94 Hz (another of the comb frequencies), with observation time $T=200$ s and FFT window $\Delta t=1$ s. The basic AMFP result in Fig. 7(a) is contaminated by sidelobes from the loud interferer, to the point that the target is not detectable. The measured output SBNR is 7.8 dB, but there are several peaks higher than the target peak (at 5.5 km range and 15 m depth). Target motion compensation [Fig. 7(b)] focuses target energy to the correct location, but sidelobes from the interferer remain; the output SBNR remains 7.8 dB, but the only peak of the ambiguity surface is the target. In Figs. 7(c) and (d), data-based interference filtering using one and two principal eigenvectors, respectively, is used to remove the interferer sidelobes. Because the target and the interferer have nearly the same phone-level (source level minus transmission loss) power in this example, the target has been incorporated into the eigenvector estimate of the interferer subspace, resulting in undesired filtering of the target; the resulting output SBNR of 6.8 dB for both Figs. 7(c) and (d) is actually lower than the unfiltered result. By contrast, Fig. 7(e) demonstrates the use of MTIF to remove the interferer sidelobes. The MTIF (model-based) result uses a rough estimate of the interferer position (derived here from a radar track) to generate a time-varying, location-based null on the interferer; the interferer space has dimension $M=7$, to account for potential inaccuracies in the interferer track information. Application of MTIF increases output SBNR to 11.2 dB, an increase of 3.4 dB over the unfiltered result. In Fig. 7(f), hybrid interference filtering is used to remove the interferer sidelobes. The hybrid method uses the model-based interference subspace estimate (again with dimension $M=7$) but eliminates any replicas from the interferer space estimate that do not have high correlation with the principal eigenvectors of the data (as measured by the correlation parameter $\gamma=0.6$). The effect of this is greater protection of the target peak (87.6 vs 86.6 dB for the model-based output) at the expense of less sidelobe rejection (background level approximately 1.5 dB higher than the model-based output). The output SBNR of 10.8 dB for the hybrid output is still 3 dB higher than that for the unfiltered output in Fig. 7(a). This example is a case where the model-based (and hybrid) interference filtering techniques perform well (because of accurate interferer track information) but the data-based filtering technique performs poorly (because the target is loud relative to the interferer).

There are cases, however, when the interferer track is unknown, so data-based interference filtering is the only option; the following example is one such case. Figure 8 shows range-time AMFP output derived from range-depth ambiguity surfaces by taking the maximum over a set of depths. Output was generated using FFT window $\Delta t=16$ s; the data contain both a loud, moving surface interferer and a weaker acoustic source at depth. Figure 8(a) is the basic ''surface'' AMFP result, generated from surface depths 0–20 m. The track of the interferer is clearly visible, with ~15 dB interferer-to-noise ratio at its closest point of approach, at 38 min. Figure 8(b) applies data-based interference filtering in which $M=2$ principal eigenvectors (computed using $J=7$ snapshots at each time instant) are used to generate the interferer null; the result is effective removal of nearly all interferer energy. Figure 8(c) is the basic ''submerged'' AMFP result, generated from depths 50 to 55 m that include the target depth. The target track is now visible, but it is still obscured by sidelobes from the surface interferer. Applying data-based interference filtering as above, in Fig. 8(d), results in effective removal of the interferer sidelobes and retention of the now-distinct target track. The SBNR improvement from applying data-based interference filtering at depth is up to 10 dB where the target and interferer tracks cross in range.

V. CONCLUSIONS

This paper proposed three techniques to improve AMFP performance for detecting quiet, moving targets. Each of the techniques was demonstrated on data examples to provide 3 dB or more improvement in output SBNR over basic AMFP output. Basic AMFP suffers both from target motion, in which the target moves across several resolution cells during the observation time and the target peak is reduced, and from interferer motion, in which the moving interferer occupies several adaptive degrees of freedom and reduces adaptive nulling capability.

The first motion mitigation technique, mode-based rank reduction, reduces the effects of both target and interferer motion over long observation times by increasing the effective size of the MFP resolution cells. Both target and interferers move across fewer resolution cells for a given observation time, and motion loss is correspondingly reduced. The technique was demonstrated on a data example in which target motion loss was reduced and output SBNR was increased by 4.4 dB compared to the basic, full-rank AMFP output. The technique is only somewhat sensitive to environmental mismatch, but it does require an array capable of resolving the acoustic modes (such as the SBCX VLA used in the data examples of this paper). Future work should examine the effectiveness of mode-based rank reduction for tactical horizontal line arrays.

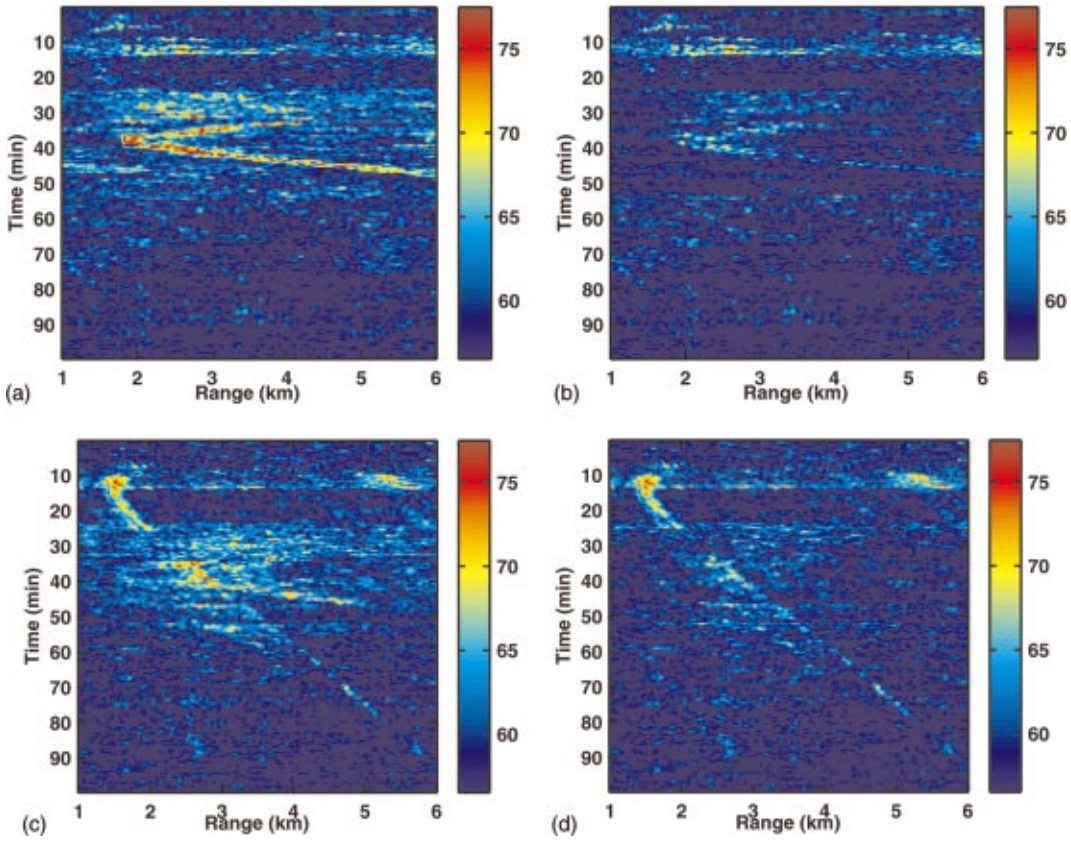

FIG. 8. AMFP range-time tracks, processed with FFT window $\Delta t = 16$ s. Data include both a loud surface interferer and a weak acoustic source at depth, with the interferer approximately 30 dB louder. Plots (a) and (b) are derived from range-depth ambiguity surfaces focused at depths near the surface (less than 20 m depth). The data in (a) have not been filtered, and the ship track is clearly seen with INR at CPA of 15 dB (CPA is at $t = 38$ min). Data-based filtering with $M = 2$ eigenvalues and $J = 7$ snapshots has been applied in (b), and the ship energy has been effectively removed. Plots (c) and (d) are derived from range-depth ambiguity surfaces focused at depths near the target depth of 50 m. The data in (c) have not been filtered, and sidelobes from the surface interferer are still visible. After applying data-based filtering as in (b), the result in (d) removes the interferer sidelobes and retains the target track. SBNR improvement from data-based interference filtering is up to 10 dB where the tracks cross in range. Colorbar units are dB *re* 1 μPa/Hz.

The second motion mitigation technique, explicit target motion compensation, reduces the effect of target motion over long observation times by using a hypothesized target track to focus data snapshots; done accurately, target motion compensation eliminates target motion loss (for a single target). This technique was demonstrated on the same data example to provide both improved output SBNR (3.3 dB better) and improved source localization over the basic, uncompensated AMFP result. Even greater SBNR gains are possible with more accurate target tracks. However, one of the open questions with this technique (and a focus for future work) is how sensitive it is to inaccuracies in the assumed target track and to environmental mismatch, both of which would reduce the effectiveness of the focusing operation. Also, it should be noted again that the technique is designed for a single source; another interesting question is how motion compensation might be combined with interference filtering to handle data with multiple sources.

The third motion mitigation technique, model-based time-varying interference filtering, reduces the effect of interference motion by placing a time-varying null on the interferer; done accurately, interference filtering removes interferer sidelobes entirely and increases output SBNR (potentially by a very large amount if the interferer is loud relative to the target). The model-based filtering technique was demonstrated on a data example in which a radar track was used to form an interference null based approximately on the location of the interferer, resulting in unambiguous detection of the target (not possible in the basic AMFP result) and a 3.4 dB increase in output SBNR over the basic, unfiltered AMFP output. Again, even greater SBNR gains are possible with more accurate interferer tracks. Greater protection of the target peak is achievable with the hybrid interference-filtering technique (combining elements of model-based and data-based filtering), at the expense of less interference nulling; hybrid filtering produced a 3 dB output SBNR increase in the same example. It is important to note that the use of external information for the model-based filtering technique removes the need to associate interferers with principal eigenvectors, which is a potential weakness of the data-based filtering method (when the target is loud relative to the interferer). However, accurate track and environmental information is needed for model-based filtering to succeed, and future work should investigate how sensitive the technique is to mismatch.

All three of the techniques presented here require intelligent application of external information. Mode-based rank reduction (the least dependent of the three techniques on external information) requires some knowledge of the number of significant propagating modes in the data. Target motion

compensation requires an accurate target track hypothesis. And model-based interference filtering requires an accurate interferer track. To varying degrees, as mentioned earlier, all three techniques require accurate environmental information. Future work should examine the robustness of these techniques to inaccuracies in the assumed external information.[31]

ACKNOWLEDGMENTS

This work was sponsored by DARPA-ATO under Air Force Contract No. F19628-00-C-0002. Opinions, interpretations, conclusions, and recommendations are those of the authors and are not necessarily endorsed by the Department of Defense. The authors wish to thank Andrew Gronosky for help in formatting many of the figures in the paper and Brian Tracey for various technical consultations during the writing of the paper. The authors are also grateful for the efforts involved in the SBCX data collection under Newell Booth of SPAWAR, and for the efforts of Peter Daly of MIT and Robert Greene of SAIC in computing SBCX array shapes.

[1] A. Baggeroer, W. Kuperman, and P. Mikhalevsky, ''An overview of matched field methods of ocean acoustics,'' IEEE J. Ocean. Eng. **18**, 401–424 (1993).
[2] J. Capon and N. Goodman, ''Probability distributions for estimators of frequency wavenumber spectra,'' Proc. IEEE **58**, 1785–1786 (1970).
[3] H. Cox, ''Resolving power and sensitivity to mismatch of optimum processors,'' J. Acoust. Soc. Am. **54**, 771–785 (1973).
[4] H. Cox, R. Zeskind, and M. Owen, ''Robust adaptive beamforming,'' IEEE Trans. Acoust., Speech, Signal Process. **35**, 1365–1376 (1987).
[5] A. Baggeroer and H. Cox, ''Passive sonar limits upon nulling multiple moving ships with large aperture arrays,'' in Proceedings of the 33rd Asilomar Conference, 1999, pp. 103–108.
[6] H. Cox and R. Pitre, ''Robust DMR and multi-rate adaptive beamforming,'' in Proceedings of the 31st Asilomar Conference, 1997, pp. 920–924.
[7] N. Lee, L. Zurk, and J. Ward, ''Evaluation of reduced-rank, adaptive matched field processing algorithms for passive sonar detection in a shallow-water environment,'' in Proceedings of the 33rd Asilomar Conference, 1999, pp. 876–880.
[8] Y. Lee, P. Mikhalevsky, H. Freese, and J. Hanna, ''Robust adaptive matched-field-processing,'' in Proceedings of the IEEE Oceans '93 Conference, 1993, pp. 387–392.
[9] E. Shang, C. Clay, and Y. Wang, ''Source depth estimation in waveguides,'' J. Acoust. Soc. Am. **77**, 1413–1418 (1985).
[10] T. Yang, ''A method of range and depth estimation by modal decomposition,'' J. Acoust. Soc. Am. **82**, 1736–1745 (1987).
[11] T. Yang, ''Effectiveness of mode filtering: A comparison of matched-field and matched-mode processing,'' J. Acoust. Soc. Am. **87**, 2072–2084 (1990).
[12] H. Bucker, ''Matched-field tracking in shallow water,'' J. Acoust. Soc. Am. **96**, 3809–3811 (1994).
[13] L. Fialkowski *et al.*, ''Matched-field source tracking by ambiguity surface averaging,'' J. Acoust. Soc. Am. **110**, 739–746 (2001).
[14] H. Hung and M. Kaveh, ''Focussing matrices for coherent signal-subspace processing,'' IEEE Trans. Signal Process. **36**, 1272–1281 (1988).
[15] J. Krolik and D. Swingler, ''Multiple broad-band source location using steered covariance matrices,'' IEEE Trans. Signal Process. **37**, 1481 (1989).
[16] B. Freburger and D. Tufts, ''Rapidly adaptive signal detection using the principal components inverse (PCI) method,'' in Proceedings of the 31st Asilomar Conference, 1997, pp. 765–769. The philosophy behind time-varying eigenvector filtering is essentially that of the so-called ''principal component inverse'' method, though the specific application of the filtering presented here, within the context of MVDR weight computation, is different.
[17] D. Tufts, R. Kumaresan, and I. Kirsteins, ''Data adaptive signal estimation by singular value decomposition of a data matrix,'' Proc. IEEE **70**, 684–685 (1982).
[18] H. Cox, ''Multi-rate adaptive beamforming (MRABF),'' in Proceedings of the 2000 Sensor Array and Multichannel Signal Processing Workshop, Boston, MA, pp. 306–309.
[19] L. Zurk, N. Lee, and J. Ward, ''Adaptive matched field processing for a moving target in a noisy shallow-water channel,'' in Proceedings of the 2000 Adaptive Sensor Array Workshop, Lexington, MA, pp. 103–107.
[20] L. Zurk and J. Ward, ''Model-based and data-based matched field processing of moving sources in a shallow water channel,'' J. Acoust. Soc. Am. **107**, 2889 (2000).
[21] L. Zurk, N. Lee, and J. Ward, ''Interference rejection for passive sonar using prior information with adaptive matched field processing,'' in Proceedings of the Fifth European Conference on Underwater Acoustics, Lyon, France, 2000.
[22] N. Booth, ''Santa Barbara Channel Experiment (SBCX) Data Report,'' Space and Naval Warfare Systems Center, 1998.
[23] H. Bucker, ''Use of calculated sound fields and matched field detection to locate sound sources in shallow water,'' J. Acoust. Soc. Am. **59**, 368–373 (1976).
[24] B. Tracey, N. Lee, L. Zurk, and J. Ward, ''Array design and motion effects for matched field processing,'' J. Acoust. Soc. Am. **108**, 2645 (2000).
[25] L. Zurk, B. Tracey, and J. Munro, ''Signal degradation mechanisms for passive localization of acoustic sources in shallow water,'' in Progress in Electromagnetic Research Symposium 2000, Cambridge, MA.
[26] I. Reed, J. Mallett, and L. Brennan, ''Rapid convergence rate of adaptive arrays,'' IEEE Trans. Aerosp. Electron. Syst. **10**, 853–863 (1974).
[27] N. Lee and N. Pulsone, ''Performance of sample-covariance-based adaptive sonar detectors,'' in Proceedings of the 34rd Asilomar Conference, 2000, pp. 668–672.
[28] J. Ward, A. Baggeroer, and L. Zurk, ''Rapidly adaptive matched field processing for nonstationary environments,'' in Proceedings of the 1998 Adaptive Sensor Array Workshop, Lexington, MA.
[29] N. Lee, L. Zurk, and J. Ward, ''Evaluation of reduced-rank, adaptive matched field processing for shallow-water target detection,'' in Proceedings of the 2000 Adaptive Sensor Array Workshop, Lexington, MA, pp. 25–30.
[30] M. Porter, ''The KRAKEN normal mode program,'' Technical Report No. SM-245, SACLANT Undersea Research Centre, 1991.
[31] L. Zurk, N. Lee, and J. Ward, ''3D adaptive matched field processing for a moving source in a shallow water channel,'' in Proceedings of the IEEE Oceans '99 Conference, Vol. 2, pp. 728–731.

Optimal detection of crack echo families in elastic solids

Daniel E. Asraf and Mats G. Gustafsson
Signals and Systems Group, Department of Material Science, Uppsala University, Box 528, 751 20 Uppsala, Sweden

(Received 11 December 2001; revised 21 January 2003; accepted 13 February 2003)

Optimal detection of a striplike crack residing in an isotropic elastic solid with coarse microstructure by means of ultrasonic nondestructive evaluation (NDE) is considered. A physics-based approach to derive an optimal detector, which achieves the theoretical limitations constrained by the underlying physics, is presented. State-of-the-art physical models of crack echoes and of stochastic backscattering from the material structure in elastic solids are introduced and unified with the theory of optimal detection to yield a practically useful nonlinear filter bank implementation of the optimal detector. Monte Carlo simulations of the detection performance for the special case of a striplike crack with uncertain angular orientation are presented in the form of receiver operating characteristics (ROCs). These new results represent the physical limitations for detecting a crack under the stated conditions and serve as performance bounds to which other detectors should be compared. A physics-based generalized likelihood ratio (GLR) detector, which relies on the same nonlinear filter bank as the optimal detector, is also presented for the special case of a striplike crack. A comparison between the optimal and the GLR detectors shows that the GLR detector only slightly reduces the performance. [DOI: 10.1121/1.1566976]

PACS numbers: 43.60.Cg, 43.35.Zc, 43.40.Le, 81.70.Cv [JCP]

I. INTRODUCTION

In this paper we consider the problem of optimal detection of crack echoes in elastic solids with coarse microstructures. This is a common problem in ultrasonic nondestructive evaluation (NDE) of materials, in which an acoustic pulse is transmitted into a test specimen and the echoes from inhomogeneities in the material are analyzed in order to determine the presence of defects. For many industrial applications, such as power plant and air craft inspection, it is important to develop fast defect detectors with high performance.

Optimal detectors for crack echoes that achieve the theoretical limitations constrained by the underlying physics have not been presented previously. However, the growing body of advanced elasto-dynamical models[1–4] and computational resources now make it feasible to accurately compute realistic defect echoes and realizations of clutter caused by backscattering from the material microstructure. Accurate numerical modeling of defect echoes and clutter is a significant advantage as it opens the possibility to design such detectors.

A key issue in the development of an optimal detector is how to unify the advanced numerical models of the crack echoes and of the clutter with the classical theory of optimal detection. In this paper such a unification is presented for the problem of detecting families of echoes from a striplike crack yielding a practically useful optimal detector implementable by means of a nonlinear filter bank. A physics-based generalized likelihood ratio (GLR) detector is also derived and used for comparison with the optimal detector. Two separate state-of-the-art numerical models are used, one for defect scattering and one for clutter noise generation. The defect scattering model is an adjusted (see Appendix A for some details) version of a recently published model by Mattsson *et al.*[3] in which the echo from a striplike crack residing in an elastic solid is derived based on Auld's electromechanical reciprocity relation.[5] The clutter noise model is a significant modification (including a new approximations to speed up the calculations) of the model presented by Yalda *et al.*[4] where the ultrasonic backscattering from a polycrystalline material is treated by assuming single scattering from ensembles of single-crystal, spherical grains with random locations and orientations.

Three main results are reported. The first is the detector design methodology, which is independent of the numerical models used herein and easily extendable to other types of defects. The second main result is a physical formulation of the detection problem as a binary hypothesis test expressed in terms of the underlying physical variables describing the material and the crack. The third main result consists of a set of receiver operating characteristic (ROC) curves for the optimal detector applied to the particular problem of detecting a striplike crack with unknown angular orientation. These ROC curves represent the physical limitations for detecting a crack under the stated conditions and serve as performance upper bounds to which other detectors should be compared.

The perhaps closest area in which there is an active interest in unifying statistical signal processing with physical modeling, in order to utilize as much *a priori* information about the underlying problem as possible, is that of matched field processing (MFP).[6–11] The MFP framework in conjunction with composite binary hypothesis testing was employed by Bucker[6] for the problem of detecting an unknown source by means of a passive sonar. Also briefly presented[7,8] is a methodology for the joint detection/estimation problem for weak signals by means of MFP but the focus of MFP has mainly been devoted to physical model based parameter estimation in the case of strong signals.

 0001-4966/2003/113(5)/2732/10/$19.00

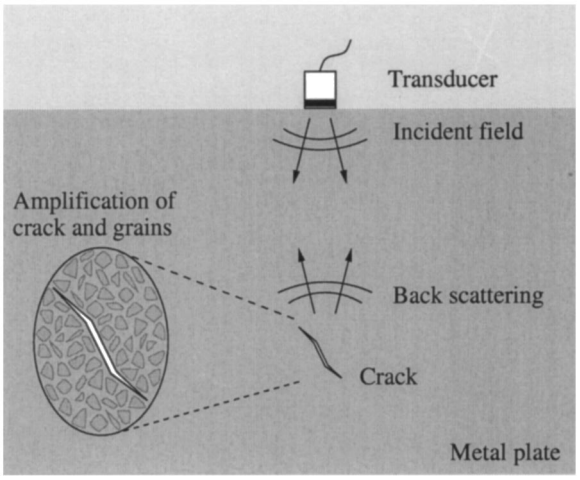

FIG. 1. Sketch of the geometry for the pulse-echo crack detection problem. The material crystallites are illustrated in the inserted amplification of the crack.

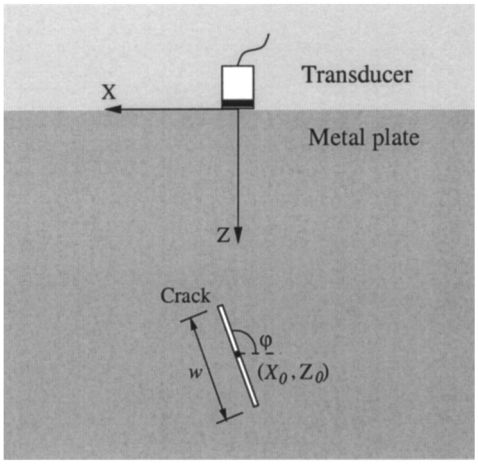

FIG. 2. The geometry of the striplike crack model showing the parameters specifying the cracks width w, center location $[X_0, Z_0]$ and angular orientation φ with respect to the X-axis.

Detectors for defects in elastic solids have also been designed without quantitative physical modeling. A well known approach, detection using split spectrum processing (SSP),[12,13] relies on qualitative physical reasoning about interference phenomena in grainy materials but no explicit mathematical models of the echo signals and clutter noise are employed. In a more recent approach, explicit mathematical models of echoes and clutter were used to derive detectors[14–16] with competitive performance on real ultrasonic data. However, as in a work by Premus *et al.*,[17] which was devoted to a hydro acoustical application, the detectors were not based on any explicit physical modeling of the signals to be detected.

This paper is organized as follows. In Sec. II, the problem of detecting a family of strip-like cracks residing in an elastic solid with a coarse microstructure is introduced and the related physical models of the crack echoes and the clutter are presented. In Sec. III, the optimal crack echo family detector is presented based on the proposed unification of the theory of optimal detection with numerical physical modeling of crack echoes and clutter. A physics-based GLR detector is also introduced. Section IV presents the performance, in terms of ROC curves, of the proposed detectors for the case of a striplike crack with unknown angular orientation. Finally, Sec. V contains a short summary and a discussion about future work.

II. PHYSICAL MODELING OF CRACK ECHO FAMILIES AND CLUTTER

Consider the problem of detecting a crack residing in an isotropic elastic material with a coarse microstructure using an ultrasonic NDE system. A sketch of the experimental scenario is shown in Fig. 1. In the pulse-echo set up considered here, a piezoelectric transducer is assumed to be unfocused, to have perfect fluid contact to the test specimen and to generate a transient compressional wave-pulse with a normal angle of incidence with respect to the elastic solid. This field is scattered by inhomogeneities in the solid and received by the same transducer, which converts the backscattered wave field into an electric signal. The signal generated by the backscattered field from the grains in the solid are considered to be the clutter and the signal generated by the backscattered field from the crack is the crack echo to be detected. The rest of this section is devoted to the physical models of the crack echo and the clutter which are used to derive an optimal crack echo family detector.

A. Modeling echoes from strip-like cracks

The crack to be detected is modeled as open and striplike with an infinite length in the Y-direction. The parameters specifying a crack is thus the width w, location $[X_0, Z_0]$ and angular orientation φ with respect to the X-direction, see Fig. 2.

In a real testing situation, all or some of the crack parameters w, $[X_0, Z_0]$ and φ are often *a priori* unknown from one inspection to another. A P-dimensional ($P \leqslant 4$) vector θ containing the unknown parameters is introduced. Using a Bayesian approach,[18] the uncertainty about the unknown parameters is modeled by means of a stochastic variable Θ with the probability density function (pdf) $p_\Theta(\theta)$ and realizations θ. Since the backscattered field may be regarded a function of θ, the uncertainty about θ is transformed into an uncertainty about the recorded backscattered crack echo signal. Let $\mathbf{s}(\theta) = [s(1;\theta), \ldots, s(N;\theta)]^T$ be a column vector of N time samples of the backscattered crack echo signal for a particular value of θ, where T denotes the transpose operator. Then the ensemble of crack echo signals for all possible values of θ, below denoted $\mathcal{S}$, may be expressed as

$$\mathcal{S} = \{\mathbf{s}(\theta) \in \mathbb{R}^N | \, \theta \in \Omega\}, \tag{1}$$

where Ω is the set of possible values of θ.

Following the approach by Mattsson *et al.*,[3,19,20] the crack echo signal in the frequency domain $S(\omega;\theta)$, for a particular value of θ, is expressed as[3]

$$S(\omega;\theta) = \delta\Gamma(\omega;\theta)\beta(\omega), \tag{2}$$

where ω is the frequency, $\delta\Gamma(\omega;\theta)$ is the electrical transmission coefficient[5] and $\beta(\omega)$ is the probe efficiency factor.[21] The electrical transmission coefficient is obtained via Auld's

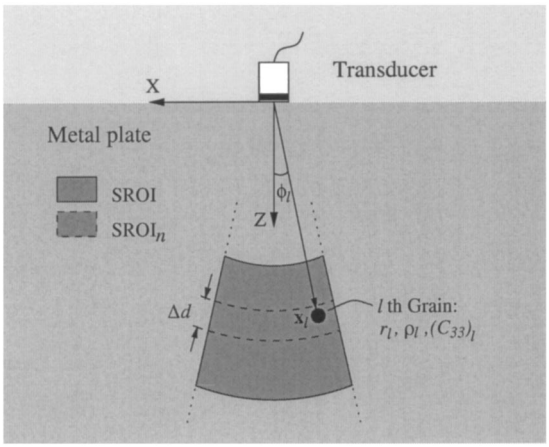

FIG. 3. Sketch over the clutter noise model geometry illustrating the SROI and the lth grain residing in the nth sub region, SROI$_n$.

reciprocity relation.[5] By assuming a striplike crack with spring boundary conditions, Auld's reciprocity relation reduces to[3]

$$\delta\Gamma(\omega;\theta)=\frac{j\omega}{4P}\int_{\mathbf{x}\in S_c}\Delta U(\mathbf{x},\omega;\theta)\cdot\mathbf{t}(\mathbf{x},\omega;\theta)\cdot\mathbf{n}_{S_c}\,dS(\mathbf{x}), \tag{3}$$

where P is the electrical feeding power, ΔU is the crack opening displacement (COD), $\mathbf{n}_{S_c}$ is an outward unit normal vector to the crack surface S_c, and $\mathbf{t}$ is the traction on the crack surface induced by the probe generated incident field. The time domain crack echo signal, $s(\theta)$, is obtained by first computing the spectral amplitude of the crack echo from Eq. (2) at N equidistant frequencies in the frequency band of $\beta(\omega)$ and then performing an inverse discrete Fourier transformation. These computations are made with a modified version of a numerical package by Mattsson *et al.* In the original numerical implementation by Mattsson *et al.*, the displacement field generated by the emitting transducer is assumed to be constant for all frequencies when computing the integrand in Eq. (3) while at the same time assuming a constant electrical feeding power P into the transducer. These assumptions are not satisfied in our case, therefore the implementation was slightly modified to yield a frequency dependent displacement field. For details see Appendix A.

B. Clutter noise

The clutter noise model is based on the work by Yalda *et al.*,[4] where the backscattering is caused by grains within a predefined *spatial region of interest* (SROI), see Fig. 3. The borders of the SROI are defined by the beam pattern of the transmitting probe and a *time window of interest* (TWOI), which is chosen to only include grains in the far field. The model differs from the one proposed by Yalda *et al.*[4] in the following aspects:

- The testing configuration is modeled as pulse-echo contact testing.
- The transducer is modeled as unfocused.
- New approximations are introduced to reduce the computational complexity.

The mathematical implications of these modifications are presented below.

The fluid model[22–24] is employed to describe the elastic wave propagation. Since only far field scattering and small-angles of incidence are considered, this model is known to be accurate. In the fluid model, the z component of the particle displacement, u_z, is assumed to be dominating and therefore the only one included in the computations. Hence, the general expression for the incident displacement field, u_z^i, at a point $\mathbf{x}_l$ caused by a transmitting probe is, due to the assumptions and simplifications mentioned above, expressed as[22]

$$u_z^i(\omega,\mathbf{x}_l)=\beta_{ea}(\omega)\int_{\mathbf{x}\in S_T}\frac{\exp\left\{j\left(\frac{\omega}{c}\|\mathbf{x}-\mathbf{x}_l\|\right)\right\}}{\|\mathbf{x}-\mathbf{x}_l\|}dS(\mathbf{x}). \tag{4}$$

Here, c is the sound speed in the solid, S_T is the transmitting probe surface and β_{ea} is a frequency dependent conversion factor between electrical power and acoustical power of the piezoelectric crystal. A well known far field approximation of the surface integral in Eq. (4), for the case of a circular transducer with radius a, yields[22]

$$u_z^i(\omega,\mathbf{x}_l)\approx\beta_{ea}(\omega)2\pi a^2\frac{\exp\left\{j\frac{\omega}{c}\|\mathbf{x}_l\|\right\}}{\|\mathbf{x}_l\|}\frac{J_1\left(a\frac{\omega}{c}\sin\phi_l\right)}{a\frac{\omega}{c}\sin\phi_l}, \tag{5}$$

where $J_1(\cdot)$ is a Bessel function of order one. The expression for the incident field in Eq. (5) contains one factor, $\exp\{j\omega/c\|\mathbf{x}_l\|\}/\|\mathbf{x}_l\|$, that describes a spherically spreading wave and one factor, $J_1(a\omega/c\sin\phi_l)/(a\omega/c\sin\phi_l)$, that describes the angular dependence of the spherical wave amplitude, i.e., the beam pattern. The beam pattern is used to define the SROI as the set

$$\left\{\mathbf{x}_l\left|\frac{J_1\left(a\frac{\omega}{c}\sin\phi_l\right)}{a\frac{\omega}{c}\sin\phi_l}>b\right.\right\}, \tag{6}$$

where b is a constant which specifies the width of the SROI.

The incident field locally near the scatterer is assumed (approximated) to behave like a plane compressional wave. The scattered displacement field, u_z^s, by a grain located in the far field is therefore expressed as[21]

$$u_z^s(\omega,\mathbf{x})=u_z^i(\omega,\mathbf{x}_l)A_l(\omega)\frac{\exp\left(j\frac{\omega}{c}\|\mathbf{x}_l-\mathbf{x}\|\right)}{\|\mathbf{x}_l-\mathbf{x}\|}, \tag{7}$$

where $A_l(\omega)$ is the compressional wave backscattering amplitude of the grain. Using the Born approximation it is expressed as[4]

$$A_l(\omega)=\frac{\omega^2}{4\pi c^2}\left[\frac{\delta\rho_l}{\rho}+\frac{1}{c^2\rho}(\delta C_{33})_l\right]G(\omega,r_l). \tag{8}$$

Here $\delta\rho_l=\rho_l-\rho$ is the difference between the density of the grain, ρ_l, and the host medium density ρ. Furthermore,

$(\delta C_{33})_l=(C'_{33})_l-(C_{33})_{\text{host}}$ expresses the difference between the elasticity tensor element $(C'_{33})_l$ of the grain and the corresponding element $(C_{33})_{\text{host}}$ of the host medium.[4] $G(\omega,r_l)$ is the *shape-factor*[4] for a spherical grain with radius r_l.

The measured electric signal, $V_l(\omega)$, is assumed to be proportional to the average wave field over the receiving transducer surface, S_T, that is[23]

$$V_l(\omega)=\beta_{ae}(\omega)\langle u^s(\omega,\mathbf{x}_l)\rangle = \frac{\beta_{ae}(\omega)}{S_T}\int_{\mathbf{x}\in S_T} u_z^i(\omega,\mathbf{x}_l)A_l(\omega) \times\frac{\exp\left(j\frac{\omega}{c}\|\mathbf{x}-\mathbf{x}_l\|\right)}{\|\mathbf{x}-\mathbf{x}_l\|}dS_T(\mathbf{x}), \tag{9}$$

where $\beta_{ae}(\omega)$ is a frequency dependent conversion factor from acoustical power to electrical power for the piezoelectric crystal. For the case of a circular transducer a similar approach as in the approximation of Eq. (4) yields

$$V_l(\omega)\approx\beta(\omega)\frac{\exp\left\{j2\frac{\omega}{c}\|\mathbf{x}_l\|\right\}}{\|\mathbf{x}_l\|^2}A_l(\omega)\frac{J_1^2\left(a\frac{\omega}{c}\sin\phi_l\right)}{\left(a\frac{\omega}{c}\sin\phi_l\right)^2}, \tag{10}$$

where $\beta(\omega)=\beta_{ea}(\omega)\beta_{ae}(\omega)$ is the probe efficiency factor. To account for the effects of material attenuation the expression in Eq. (10) is multiplied by the exponentially decreasing factor[4] $\exp\{-\alpha d\}$, where α is an attenuation coefficient and d is the distance of propagation. Omitting multiple reflections, by inserting Eq. (8) into Eq. (9), assuming that the $\delta\rho_l=0$ (as in Yalda *et al.*[4]) and that the SROI contains L number of grains, the total electric signal, $V(\omega)$, is expressed as the superposition

$$V(\omega)=\sum_{l=1}^{L}V_l(\omega)\exp\{-2\alpha\|\mathbf{x}_l\|\} =\beta(\omega)\frac{\omega^2}{4\pi\rho c^4}\sum_{l=1}^{L}\frac{\exp\left\{2\left(j\frac{\omega}{c}-\alpha\right)\|\mathbf{x}_l\|\right\}}{\|\mathbf{x}_l\|^2} \times(\delta C_{33})_l G(\omega,r_l)\frac{J_1^2\left(a\frac{\omega}{c}\sin\phi_l\right)}{\left(a\frac{\omega}{c}\sin\phi_l\right)^2}. \tag{11}$$

To determine the spectral distribution of the energy of the noise (its color) and also to alleviate much of the computational complexity in Eq. (11), the SROI is decomposed into N sub regions SROI_n, which are slices perpendicular to the propagation direction of the incident wave, see Fig. 3. The slices are confined by the borders of the SROI and their thickness are here taken to be $\Delta d=T_s c$, where T_s is the sampling interval. The distance from the transducer to the center of the n:th slice is denoted R_n. All grains in a spatial sub region are approximated to have the same distance to the transducer. Hence $\|\mathbf{x}_l\|\approx R_n$ for the set $\{l|\mathbf{x}_l\in\text{SROI}_n\}$. This is a reasonable approximation if Δd is small and results in the following approximation of the expression in Eq. (11):

$$V(\omega)\approx\beta(\omega)\frac{\omega^2}{4\pi\rho c^4}\sum_{n=1}^{N}\frac{\exp\left\{2\left(j\frac{\omega}{c}-\alpha\right)R_n\right\}}{R_n} \times\sum_{l=1}^{L_n}(\delta C_{33})_l G(\omega,r_l)\frac{J_1^2\left(a\frac{\omega}{c}\sin\phi_l\right)}{\left(a\frac{\omega}{c}\sin\phi_l\right)^2}. \tag{12}$$

Assuming the grains to be uniformly distributed in the SROI and to have random sizes and anisotropy, the variables L_n, ϕ_l, $(C'_{33})_l$ and r_l are all stochastic and naturally modeled as independent. Therefore $J_1^2(a\omega/c\sin\phi_l)/(a\omega/c\sin\phi_l)^2$, $(\delta C_{33})_l$ and $G(\omega,r_l)$ may also be modeled as independent random variables.

With reference to the central limit theorem, the second sum in Eq. (12) is approximated by a frequency and position dependent zero mean Gaussian random variable, $Q_n(\omega)$, with the variance $\sigma^2_{Q_n}(\omega)$. Details of the derivation of $\sigma_{Q_n}(\omega)$ is found in Appendix B. In this case, Eq. (12) reduces to

$$V(\omega)\approx\beta(\omega)\frac{\omega^2}{4\pi\rho c^4}\sum_{n=1}^{N}\frac{\exp\left\{2\left(j\frac{\omega}{c}-\alpha\right)R_n\right\}}{R_n}Q_n(\omega). \tag{13}$$

Finally, the time domain clutter noise signal, $\mathbf{v}=[v(1),\ldots,v(N)]$, is also obtained by an N-point frequency sampling followed by an inverse Fourier transformation as described in Sec. II A. Since the frequency domain clutter signal is a linear combination of zero mean Gaussian random variables, its inverse Fourier transform will also be zero mean Gaussian. Hence, the vector $\mathbf{v}$ is a realization of an N-dimensional stochastic variable $\mathcal{V}$ with a Gaussian pdf $p_{\mathcal{V}}(\mathbf{v})$.

III. DETECTION OF CRACK ECHO FAMILIES

The objective of a detector is to determine the presence or absence of a crack when presented a measured signal, $\mathbf{y}=[y(1),\ldots,y(N)]^T$, from the receiving probe, in Fig. 1. This problem can be cast as a hypothesis test between H_0, under which $\mathbf{y}$ only contains a realization of the clutter $\mathbf{v}$, and H_1, in which $\mathbf{y}$ contains a crack echo signal, $\mathbf{s}(\theta)$, contaminated by additive clutter noise. The crack echo signal $\mathbf{s}(\theta)$ is drawn from the crack echo signal family $\mathcal{S}$, defined in Eq. (1), according to the pdf $p_\Theta(\theta)$. Thus, the hypothesis problem of interest is

$$H_0:\ \mathbf{y}=\mathbf{v},\qquad H_1:\ \mathbf{y}=\mathbf{s}(\theta)+\mathbf{v}. \tag{14}$$

In other words, $\mathbf{y}$ is a realization of a stochastic variable $\mathcal{Y}$, which has two possible pdfs $p(\mathbf{y}|H_0)$ and $p(\mathbf{y}|H_1)$ under H_0 and H_1, respectively.

When deriving an optimal detector for the hypothesis problem in Eq. (14), different definitions of optimality can be

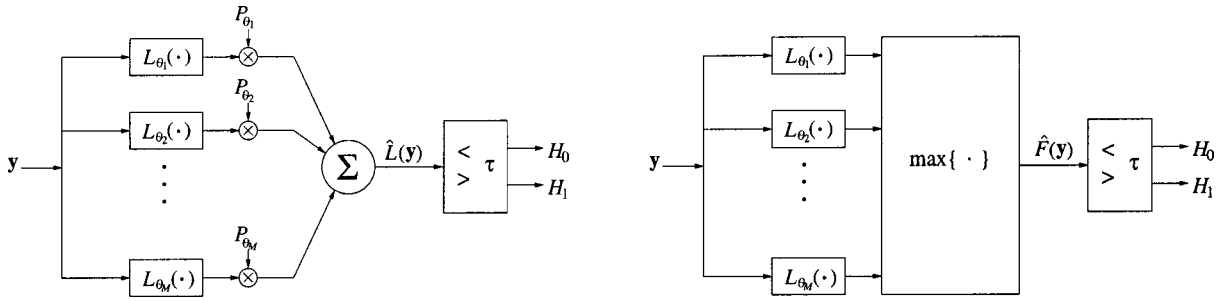

FIG. 4. Block diagrams of numerical implementations of the optimal detector (left) and the suboptimal GLR detector (right).

adopted. The most well known are Neyman–Pearson (NP), Bayes, and minimax.[25] All these criteria imply the use of the likelihood ratio $L(\mathbf{y})=p(\mathbf{y}|H_1)/p(\mathbf{y}|H_0)$ as detection test statistic and a decision rule of the form

$$L(\mathbf{y}) \underset{H_1}{\overset{H_0}{\lessgtr}} \tau, \tag{15}$$

where τ is a threshold determined by the particular optimality criterion. In the NP case, which was adopted in the detector performance simulations in Sec. IV B, τ is set to give a desired probability of false alarm.

Thus, the key issue in deriving such optimal detectors is to compute the likelihood ratio. By exploiting the physical models derived in the previous section, the pdfs of $\mathcal{Y}$ can be expressed as $p(\mathbf{y}|H_0)=p_{\mathcal{V}}(\mathbf{y})$ and $p(\mathbf{y}|H_1)=\int_\Omega p_{\mathcal{V}}(\mathbf{y}-s(\theta))p_\Theta(\theta)d\theta$, which yields the likelihood ratio

$$L(\mathbf{y})=\int_\Omega L_\theta(\mathbf{y})p_\Theta(\theta)d\theta, \tag{16}$$

where

$$L_\theta(\mathbf{y})=\frac{p_{\mathcal{V}}(\mathbf{y}-\mathbf{s}(\theta))}{p_{\mathcal{V}}(\mathbf{y})} \tag{17}$$

is the conditional likelihood ratio.

The likelihood ratio is determined numerically by a discretization of the probability distribution p_Θ at M sample points θ_m, yielding

$$\hat{L}(\mathbf{y})=\sum_{m=1}^{M} L_{\theta_m}(\mathbf{y})P_{\theta_m}, \tag{18}$$

where $P_{\theta_m}=p_\theta(\theta_m)\Delta\theta$ and $\Delta\theta$ is the volume around each sampling point. Hence, $\hat{L}(\mathbf{y})$ is *a numerical approximation* of the likelihood ratio $L(\mathbf{y})$ which, for all nonpathological cases, can be made arbitrarily good.

Based on the conditional likelihood ratio in Eq. (17), expressed in terms of the clutter and the crack echo pdfs, it is straight forward to derive a GLR detector for the hypothesis problem in Eq. (14). This physics-based GLR detector consists of the test statistic

$$\hat{F}(\mathbf{y})=\max_m[L_{\theta_m}(\mathbf{y})] \tag{19}$$

and the threshold test

$$\hat{F}(\mathbf{y}) \underset{H_1}{\overset{H_0}{\lessgtr}} \tau_{\mathrm{GLT}},$$

where τ_{GLT} can be selected according to the different decision criteria. This detector is suboptimal but still attractive since, in contrast to the optimal detector, it does not require knowledge about the *a priori* pdf $p_\Theta(\theta)$.

Implementation of the optimal detector using Eq. (18) and Eq. (15) is performed by means of the filter bank structure presented as a block diagram in the left part of Fig. 4. Similarly, the GLR detector is also implemented by means of the same filter bank, as shown in the right part of Fig. 4.

In Sec. II B, it was shown that the clutter noise from materials with a coarse microstructure like stainless steel and copper may be accurately modeled as a zero mean colored Gaussian process. Thus, as also have been shown by others,[4,15,26] it is relevant to assume $\mathcal{V}\sim\mathcal{N}(\mathbf{0},\Sigma_{\mathcal{V}})$, where $\mathcal{N}$ denotes a Gaussian distribution with the covariance matrix $\Sigma_{\mathcal{V}}$. This assumption yields an explicit expression for the conditional likelihood ratio in Eq. (17) as[25]

$$L_\theta(\mathbf{y})=\exp\{\mathbf{s}(\theta)^T\Sigma_{\mathcal{V}}^{-1}\mathbf{y}-\tfrac{1}{2}\mathbf{s}(\theta)^T\Sigma_{\mathcal{V}}^{-1}\mathbf{s}(\theta)\}. \tag{20}$$

In the argument to the exponential function we can identify $\mathbf{s}(\theta)^T\Sigma_{\mathcal{V}}^{-1}$ as the well known *matched filter* which can be efficiently implemented as a finite impulse response filter. A useful implementation of the optimal detector test statistic is obtained by using Eq. (20) in Eq. (18) yielding

$$\hat{L}(\mathbf{y})=\sum_{m=1}^{M}\exp\{\mathbf{s}(\theta_m)^T\Sigma_{\mathcal{V}}^{-1}\mathbf{y}-\tfrac{1}{2}\mathbf{s}(\theta_m)^T\Sigma_{\mathcal{V}}^{-1}\mathbf{s}(\theta_m)\}P_{\theta_m}. \tag{21}$$

The corresponding GLR detector test statistic $\hat{F}$ takes the form

$$\hat{F}(\mathbf{y})=\max_m[\exp\{\mathbf{s}(\theta_m)^T\Sigma_{\mathcal{V}}^{-1}\mathbf{y}-\tfrac{1}{2}\mathbf{s}(\theta_m)^T\Sigma_{\mathcal{V}}^{-1}\mathbf{s}(\theta_m)\}]. \tag{22}$$

In conclusion, for clutter noise that can be accurately modeled as a zero mean colored Gaussian stochastic process, the methodology presented in this work may be summarized as follows:

Summary of Methodology for Gaussian Clutter

- *Sample the crack echo signal family by computing echoes for different parameter settings θ_m. This results in crack echo signals $\mathbf{s}(\theta_m)$.*
- *Compute realizations of the clutter noise and use them to estimate the covariance structure (color) of the clutter pro-*

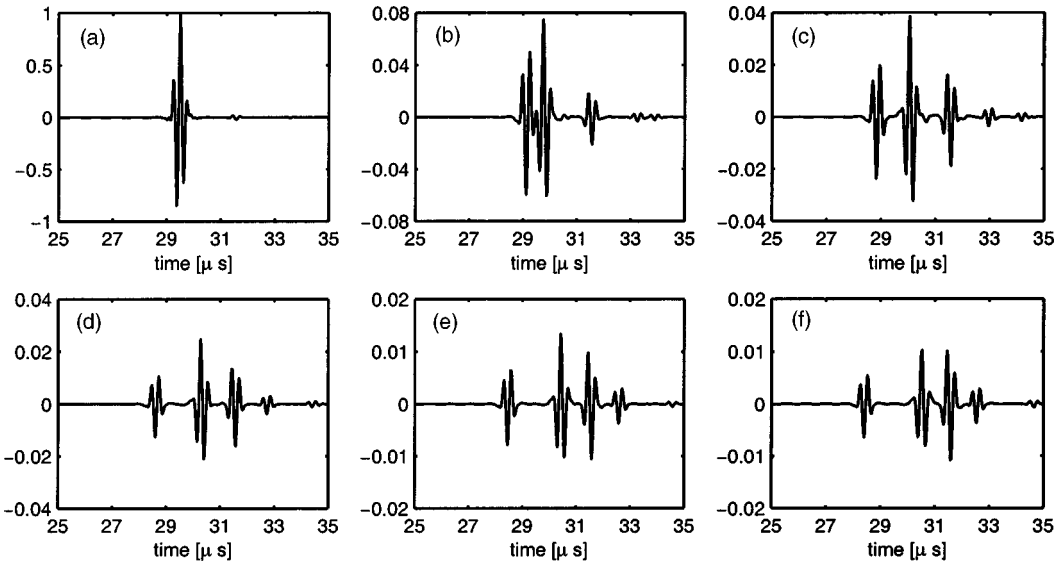

FIG. 5. Signals from the signal family $\mathcal{S}$, induced by crack scattering. The signals shown here are generated with the different angular orientations $\varphi = 0°$ (a), 18° (b), 36° (c), 54° (d), 72° (e), and 90° (f).

cess. This results in an estimate of the covariance matrix $\Sigma_{\mathcal{V}}$.

- *Use the crack echoes and the estimated covariance matrix to implement the optimal crack echo family detector test statistic as in Eq. (21) or the suboptimal GLT detector test statistic as in Eq. (22).*

One should note that the methodology is not restricted to the particular choice of crack echo signal model used here nor to the case of Gaussian clutter. Crack echo family detection in non-Gaussian clutter may also be considered but the discrete sum implementations in Fig. 4 may then no longer be simplified into a filter bank consisting of classical matched filters. One should also note that a fundamental limitation of the filter bank implementation of the crack echo family detectors above is the computational complexity. For a problem with K unknown parameters which need to be discretized into M different intervals, the number of filters in the filter bank is M^K, i.e., the number of filters grows exponentially with the number of parameters K. Thus, except for problems with few unknown parameters, one has to consider suboptimal family detectors with lower complexity. One obvious approach to decrease the computational complexity of the family detectors in Fig. 4 is to reduce the number of filters in the filter bank. This would correspond to a smaller value of M above. However, in the case of the optimal detector, this would of course also result in a less accurate approximation of the integral in Eq. (18). Ideally one should find a filter bank with as few filters as possible that still gives a reasonable approximation of the likelihood ratio.

IV. DETECTION PERFORMANCE SIMULATION

A. Problem specification

Consider detection of a striplike crack with unknown angular orientation residing in isotropic stainless steel with parameters specified in Appendix C. The unknown parameter vector θ is in this case reduced to the angular orientation, i.e., $\theta = \varphi$, and the uncertainty is described by the pdf

$$p_\Theta(\theta) = \begin{cases} \dfrac{1}{K}\exp\left\{-\dfrac{(\theta-\mu_\theta)^2}{2\sigma_\theta^2}\right\}, & \text{if } 0° \leqslant \theta \leqslant 90°, \\ 0, & \text{elsewhere,} \end{cases} \tag{23}$$

where $K = \int_0^{90} e^{-(\theta-\mu_\theta)^2/2\sigma_\theta^2} d\theta$, $\mu_\theta = 45$ and $\sigma_\theta^2 = 20$. Such a pdf may model a case when the test specimen regularly is subject to some specific (angular dependent) stress causing cracks to develop more likely in some particular direction [e.g., $\varphi = 45°$ as in Eq. (23)]. The length of the crack is $w = 6$ mm with position $X_0 = 0$ mm and $Z_0 = 85$ mm, see Fig. 2.

Assume a circular transducer with radius $a = 5$ mm and efficiency factor[3]

$$\beta(\omega) = \begin{cases} \sin^2\left(\pi \dfrac{|\omega|-\omega_1}{\omega_2-\omega_1}\right), & \omega_1 \leqslant |\omega| \leqslant \omega_2, \\ 0, & \text{otherwise,} \end{cases} \tag{24}$$

where the upper and lower frequencies are $\omega_2 = 6.68$ MHz and $\omega_1 = 1.32$ MHz, respectively. Hence, the center frequency of the probe is 4 MHz and the -3 dB bandwidth is 2.68 MHz, yielding a relative bandwidth of 67%.

Figure 5 presents a few members of the crack echo family for the scenario described above. The crack echoes are normalized with the maximum amplitude $\max_{\theta,n}\{s(n;\theta)\}$ and computed in the time window $t = [22,36]$ μs using the sampling frequency $F_s = 40$ MHz, resulting in $N = 561$ samples.

B. Quantitative simulation results

The detection performance is quantified in terms of receiver operating characteristic (ROC) curves, where the probability of detection, P_D, is displayed versus the probability of false alarm P_F. Estimates of the ROC curves were obtained by applying the proposed detectors to two Monte Carlo simulated signal sets using different detection thresholds τ. The two signal sets, each contained 60.000 time-series of the measured signal $\mathbf{y}$, under H_0 and H_1, respec-

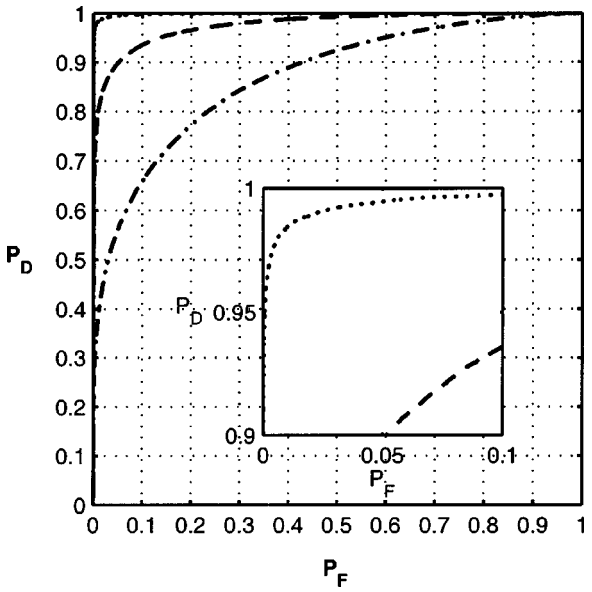

FIG. 6. ROC curves showing upper-bounds for detection given SNR=1 (dotted) SNR=0.1 (dashed) and SNR=0.01 (dash-dotted). The figure inserted is a magnification of the upper left region in order to better visualize the behavior of the ROC curve for the optimal detector for SNR=1.

tively. These time-series were generated using the time window and sampling frequency mentioned above.

In order for the two signal sets to model different signal-to-noise-ratio (SNR) scenarios (i.e., different detection difficulties), the clutter realizations were scaled in relation to the normalized crack echoes to obtain the SNRs 1, 0.1, and 0.01, where the SNR is defined as the energy deflection:[25]

$$\mathrm{SNR}=\frac{(E_1\{\|\mathbf{y}\|^2\}-E_0\{\|\mathbf{y}\|^2\})^2}{\mathrm{Var}_0\{\|\mathbf{y}\|^2\}}. \tag{25}$$

$\mathrm{Var}_0\{\cdot\}$ denotes the variance operator under H_0, $E_0\{\cdot\}$, and $E_1\{\cdot\}$ are the expectation operators under H_0 and H_1, respectively.

The optimal detector: The optimal detector was implemented according to Eq. (21) with $M=90$ number of filters as a result of the parameter discretization $\Delta\theta=1°$. The discretization was based on a work by Chapman *et al.*,[2,27] where it is shown that incident angular variations in the order of 1° yield small variations in the backscattering amplitude.

ROC curves for the three different SNRs were computed and are presented in Fig. 6. These ROCs represent the detection upper bounds and are an immediate reflection of the underlying physical constrains inherent in the NDE scenario described above.

The optimal detector is also used to compute the minimum achievable probability of error (MAPE) according to[28]

$$P_E^*=\pi_1 P_M(\tau^*)+\pi_0 P_F(\tau^*), \tag{26}$$

where π_0 and π_1 are the *a priori* probabilities for H_0 and H_1, respectively, $P_M(\tau^*)$ is the probability of miss, and $P_F(\tau^*)$ is the probability of false alarm when $\tau^*=\pi_0/\pi_1$. In this NDE context, the MAPE has the appealing feature of being an information theoretic lower bound for the crack detection error. Furthermore, the MAPE belongs to the class of Ali–Silvey divergence measures[29,30] and can thereby serve as a rigorous measure of the detection difficulty (i.e., separation of the input signal pdfs under the two hypotheses). The SNR, on the other hand, reflects the ''true'' detection difficulty only if the pdfs of the input signal, **y**, under the two hypotheses in Eq. (14) are Gaussian. In our case, the pdf of **y** under H_0 is Gaussian while the pdf of **y** under H_1 is not, due to the uncertainty of the parameter θ and its nonlinear relationship to $s(\theta)$. Table I presents the MAPEs corresponding to the three different SNRs. The MAPEs were obtained from Eq. (26) by estimating $P_F(\tau^*)$ and $P_M(\tau^*)$ by applying the optimal detector with $\tau^*=\pi_0/\pi_1$ to the Monte Carlo simulated data sets.

TABLE I. Table presenting the different levels of detection difficulty in terms of P_E^* and SNR. The P_E^* values are computed by means of Monte Carlo estimates of the probability of false alarm and the probability of miss for the optimal detector with $\tau^*=\pi_0/\pi_1$.

SNR	P_E^*
1	0.013
0.1	0.076
0.01	0.213

Low complexity detectors: As mentioned in Sec. III, it is desirable to decrease the computational complexity of the optimal detector. In Fig. 7, the ROCs for three low complexity detectors are presented together with the ROC for the optimal detector as the upper bound. The low complexity detectors were obtained by increasing the discretization step $\Delta\theta$, which reduced the number of filters in the filter bank.

As can be seen in Fig. 7, the NP performance loss when reducing the full ($\Delta\theta=1°$) filter bank (solid) to a filter bank corresponding to a discretization of θ by $\Delta\theta=10°$ (dashed) is very small. This indicates that the optimal crack echo fam-

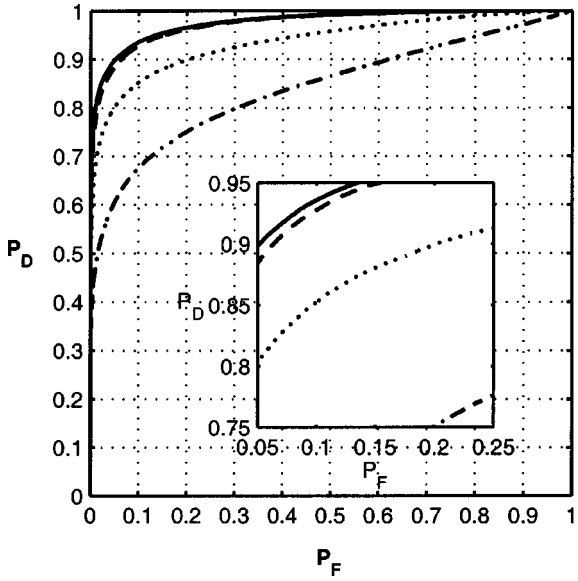

FIG. 7. ROC curves showing decreasing detection performance for the low complexity detectors relative to the optimal detector (solid). The three low complexity detectors were implemented with a θ discretization of $\Delta\theta=10°$ (dashed), $\Delta\theta=18°$ (dotted), and $\Delta\theta=30°$ (dash-dotted). The level of difficulty for the detection problem was SNR=0.1 or $P_E^*=0.076$. The figure inserted is a magnification of the upper left region in order to visualize the separation of the optimal and the low complexity ($\Delta\theta=10°$) ROC curves more clearly.

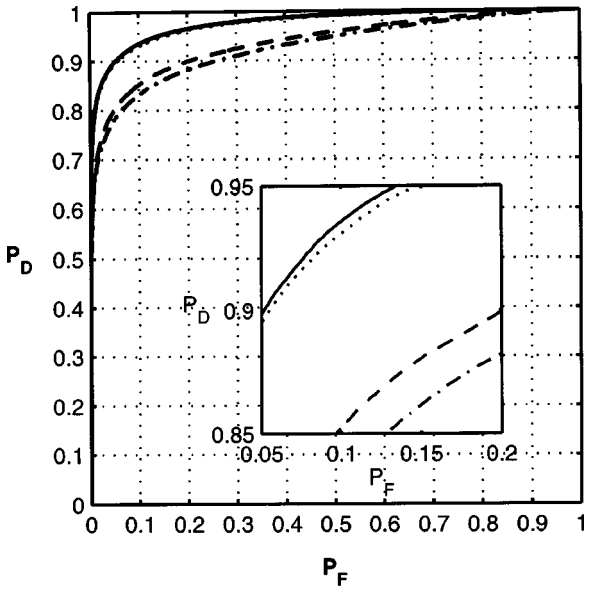

FIG. 8. ROC curves for the optimal detector (solid) and the GLR detector (dotted), both with $\Delta\theta=1°$. Also presented here are the low complexity detector (dashed) and the low complexity GLR detector (dash-dotted). Both low complexity detector versions have $\Delta\theta=18°$. All ROCs are generated for SNR$=0.1$ or $P_E^*=0.076$. The figure inserted is a magnification of the upper left region in order to better visualize the separation of the ROC curves.

ily detector can be implemented with a much more sparse sampling than $\Delta\theta=1°$ without a significant performance loss.

Optimal vs GLR detectors: Two GLR detectors were implemented according to Eq. (22), with a θ discretization of $\Delta\theta=1°$ (i.e., full filter bank) and $\Delta\theta=18°$ (low complexity), respectively. A comparative performance study between the optimal and the GLR detectors, together with their low complexity approximations, is presented in Fig. 8 in terms of ROCs. As expected, the optimal detector demonstrates a slightly better performance than the full filter bank GLR detector. Also for the low complexity approximations of the two detector structures, one finds that the GLR detector has a slightly reduced performance.

V. CONCLUSIONS

The problem of optimal detection of ultrasonic crack echoes in elastic solids with coarse microstructures has been considered. A detector design methodology which yields a practically useful nonlinear filter bank implementation of the optimal detector was proposed. This approach unifies physical numerical modeling with the theory of optimal detection in order to give a detector which reaches the theoretical limitation constrained by the underlying physics. It should be stressed that the proposed detector design methodology is easily extended to include other types of defects and also to a broad range of other detection problem where physical models of signals and noise are available.

An explicit link between the hypothesis problem and the introduced statistical physical models for the crack echoes and material clutter was also established. In particular, it was shown that the clutter can be described by a colored Gaussian process, where the color (covariance) is specified by the material parameters.

A quantitative study of the detector performance of the optimal detector for the special case of striplike cracks with unknown angular orientations yielded new results reflecting the physical limitations of detecting a crack under the stated conditions. These results, presented in the form of ROC curves, are performance upper bounds to which other detectors should be compared. A physics-based GLR detector was derived and applied to the crack detection problem and was shown to yield a performance which is close to the bounds constrained by the underlying physics.

The general approach presented in this work may be developed in many directions. One interesting direction for future work would be a more rigorous treatment of the detection problem in which the scaling of the amplitudes of the clutter noise and crack echoes agree exactly. Then different noise levels could be obtained by changing, e.g., the grain density of the material. Moreover, robustness issues for the proposed detectors need to be investigated further. The detector robustness could for example be quantified by maintained detection performance against model errors, incorrect *a priori* pdf assumptions, etc. Another important direction for future work would be to develop robust, low complexity, approximations of the optimal detector for problems with several unknown parameters and validate them on real and simulated data.

ACKNOWLEDGMENTS

The authors would like to thank Tommy Öberg and Ping Wu at Uppsala University for very valuable discussions and comments on earlier versions of the manuscript and Johan Mattsson at the Swedish defense research agency for providing the numerical package for the crack scattering computations. The authors also thank Tomas Olofsson, Catharina Carlemalm, Ingvar Nedgård, and Elias Parastates for critically reading the earlier versions of the manuscript. D. E. Asraf was supported by the Swedish defense research agency project X2201.

APPENDIX A: CRACK SCATTERING NUMERICS

In Mattsson's[3] original implementation of Auld's electromechanical transmission coefficient, $\delta\Gamma$ in Eq. (3), the integrand in the expression for $\delta\Gamma$ is computed using an incident field with unit displacement amplitude, $U_0=1$ across the spatial region defined by the probe surface S_T. In other words, the integral is computed using the mechanical power[31]

$$P_{\text{mech}}(\omega)=\tfrac{1}{2}S_T c\rho\omega^2 U_0^2, \tag{A1}$$

where c is the sound velocity and ρ is the density of the wave propagation media. Unfortunately, when computing the final expression for $\delta\Gamma$, the integral is normalized by the *electrical* feeding power set to unity, $P=1$.

Since the electromechanical power conversion factors for the probe are included in the probe efficiency factor β and not in $\delta\Gamma$, the electrical and mechanical energies must

agree. For a given value of the electrical power P, this is achieved by scaling the displacement amplitude according to

$$U_0(\omega)=\frac{1}{\omega}\sqrt{\frac{2P}{S_T c\rho}},\quad \omega\neq 0. \tag{A2}$$

APPENDIX B: CLUTTER NOISE NUMERICS

This Appendix explains how to generate samples from the probability distribution function (pdf) of the frequency dependent stochastic variable Q_n in Eq. (13) which is expressed as

$$Q_n(\omega)=\sum_{l=1}^{L_n}(\delta C_{33})_l G(\omega,r_l)\frac{J_1^2(ka\sin\phi_l)}{(ka\sin\phi_l)^2}=\sum_{l=1}^{L_n} q_l, \tag{B1}$$

where

$$q_l=(\delta C_{33})_l G(\omega,r_l)\frac{J_1^2(ka\sin\phi_l)}{(ka\sin\phi_l)^2} \tag{B2}$$

is a set of independent stochastic variables. According to the central limit theorem, for large values of the number of grains, L_n, the pdf $p_{Q_n}(Q_n)$ of $Q_n(\omega)$ may be approximated by a Gaussian stochastic variable $\mathcal{N}(\mu_{Q_n},\sigma_{Q_n})$.

To generate realizations from P_{Q_n} one may employ the identity

$$p_{Q_n}(Q_n)=\int p_{Q_n|L_n}(Q_n|L_n)p_{L_n}(L_n)dL_n \tag{B3}$$

and follow a two step procedure: (1) Generate a sample L_n from $p_{L_n}(L_n)$. (2) Generate a sample Q_n from the conditional pdf $p_{Q_n|L_n}(Q_n|L_n)$. In order to follow this two step procedure one has to determine the conditional pdf $p_{Q_n|L_n}(Q_n|L_n)$. Employing the central limit theorem, one finds that $p_{Q_n|L_n}(Q_n|L_n)$ may be approximated by the conditional Gaussian pdf $\mathcal{N}(\mu_{Q_n|L_n},\sigma_{Q_n|L_n})$ where $\mu_{Q_n|L_n}(\omega)=E\{Q_n|L_n\}$ and $\sigma^2_{Q_n|L_n}(\omega)=E\{Q_n^2|L_n\}-\mu^2_{Q_n|L_n}$.

First the mean $\mu_{Q_n|L_n}$ is determined as

$$\begin{aligned}\mu_{Q_n|L_n}(\omega)&=L_nE\{q_l\}\\&=L_nE\{(\delta C_{33})\}E\{G(\omega,r_l)\}\\&\quad\times E\left\{\frac{J_1^2\left(a\frac{\omega}{c}\sin\phi_l\right)}{\left(a\frac{\omega}{c}\sin\phi_l\right)^2}\right\}.\end{aligned} \tag{B4}$$

Since $\delta C_{33}=C'_{33}-(C_{33})_{\text{host}}$ and the elastic stiffness of the host medium is taken to be the Voigt-averaged stiffness,[4,32] i.e., $E\{C'_{33}\}=(C_{33})_{\text{Voigt}}=(C_{33})_{\text{host}}$, one gets $E\{(\delta C_{33})\}=0$ and thus, $\mu_{Q_n|L_n}=0$. Since the identity $E\{(\delta C_{33})\}=0$ also implies that $E\{q_l\}=0$, it is then straight forward to determine the variance $\sigma^2_{Q_n|L_n}$ as

$$\sigma^2_{Q_n|L_n}(\omega)=E\{Q_n^2|L_n\}=L_nE\{q_l^2\}=L_n\sigma_l^2. \tag{B5}$$

Here σ_l^2 is the variance of q_l and may be expressed as

$$\sigma_l^2(\omega)=E\left\{(\delta C_{33})^2G(\omega,r_l)^2\frac{J_1^4\left(a\frac{\omega}{c}\sin\phi_l\right)}{\left(a\frac{\omega}{c}\sin\phi_l\right)^4}\right\}. \tag{B6}$$

If the crystallites possess cubic symmetry (e.g., stainless steel, which is considered here) it has been shown that[32] $E\{(\delta C_{33})^2\}=16[C_{11}^2-2C_{11}C_{12}+C_{12}^2-4C_{11}C_{44}+4C_{12}C_{44}+4C_{44}^2]/525=K$. Thereby the variance $\sigma_l^2(\omega)$ can be reduced to

$$\sigma_l^2(\omega)=KE\{G^2(\omega,r_l)\}E\left\{\frac{J_1^4\left(a\frac{\omega}{c}\sin\phi_l\right)}{\left(a\frac{\omega}{c}\sin\phi_l\right)^4}\right\}. \tag{B7}$$

The mean value integrals for the two remaining factors $E\{G^2(\omega,r_l)\}$ and $E\{J_1^4(a\omega/c\sin\phi_l)/(a\omega/c\sin\phi_l)^4\}$ are here computed by means of Monte Carlo sampling.

In this work, the number of grains, L_n, is modeled as the outcome of a stochastic variable $\mathcal{L}_n$, which is dependent on the volume, V_n, of the SROI_n and the distribution of the grains in the elastic solid. The grains are assumed to be uniformly distributed in the test specimen, which results in the following multinomial distribution for $\mathcal{L}_n$:

$$p_{\mathcal{L}_1,\ldots,\mathcal{L}_N}(L_1,\ldots,L_N)=\frac{L!}{L_1!\times\ldots\times L_N!}P_1^{L_1}\times\ldots\times P_N^{L_N}. \tag{B8}$$

$L=\Sigma_n L_n$ is the total number of grains in the SROI and $P_n=V_n/(\Sigma_n V_n)$ is the probability that a grain is residing in SROI_n.

In summary, in the approach taken here, an outcome of the stochastic variable $Q_n(\omega)$, for a pre-defined frequency ω, is obtained by first generating outcomes of the number of grains L_n in the SROI_n according to Eq. (B8). Then a Gaussian random number generator is employed to generate a realization from the pdf $\mathcal{N}(0,\sqrt{L_n}\sigma_l(\omega))$.

APPENDIX C: HOST MATERIAL PARAMETERS

The material is modeled as an isotropic stainless steel, with the stiffness matrix elements $C_{11}=C_{22}=C_{33}=280.2$ GPa, $C_{12}=C_{21}=C_{13}=C_{31}=C_{23}=C_{32}=114.0$ GPa, $C_{44}=C_{55}=C_{66}=82.6$ GPa and all other elements equal to zero. The density of the specimen is $\rho=8420$ kg/m^3, the sound velocity is $c=5800$ m/s and the material attenuation coefficient $\alpha=1.1$ dB/cm.

The micro structural crystals are modeled as spherical grains with Gaussian distributed radii with mean[32] $\mu_g=52\,\mu$m and standard deviation $\sigma_g=10\,\mu$m (the negative part of the distribution is neglected). The density of the grains are taken to be 100 000 grains per cubic cm. The borders of the SROI due to the transducer beam width are defined by allowing for an amplitude ratio of $b=0.5$ in Eq. (6).

[1] A. Boström and H. Wirdelius, "Ultrasonic probe modeling and nondestructive crack detection," J. Acoust. Soc. Am. **97**, 236–284 (1995).
[2] R. K. Chapman, "A system model for the ultrasonic inspection of smooth

planar cracks,'' J. Nondestruct. Eval. **9**, 197–211 (1990).
[3] J. Mattsson, A. J. Niklasson, and A. Eriksson, ''3D ultrasonic crack detection in anisotropic materials,'' Res. Nondestruct. Eval. **9**, 59–79 (1997).
[4] I. Yalda, F. Margetan, and R. Thompson, ''Predicting ultrasonic grain noise in polycrystals: A Monte Carlo model,'' J. Acoust. Soc. Am. **99**, 3445–3455 (1996).
[5] B. Auld, ''General electromechanical reciprocity relations applied to the calculation of elastic wave scattering coefficients,'' Wave Motion **1**, 3–10 (1979).
[6] H. P. Bucker, ''Use of calculated sound fields and matched-field detection to locate sound sources in shallow water,'' J. Acoust. Soc. Am. **59**, 368–373 (1976).
[7] E. J. Sullivan and D. Middleton, ''Estimation and detection issues in matched-field processing,'' IEEE J. Ocean. Eng. **18**, 156–167 (1993).
[8] D. Middleton and R. Esposito, ''New results in the theory of optimum detection and estimation of signals in noise,'' Probl. Peredachi Inf. **6**, 3–20 (1970).
[9] M. Hinich, ''Maximum likelihood signal processing for a vertical array,'' J. Acoust. Soc. Am. **54**, 499–503 (1972).
[10] M. Hinich, ''Array design for measuring source depth in a horizontal waveguide,'' SIAM (Soc. Ind. Appl. Math.) J. Appl. Math. **32**, 800–805 (1977).
[11] M. Hinich and E. Sullivan, ''Maximum-likelihood passive localization using mode filtering,'' J. Acoust. Soc. Am. **85**, 214–219 (1989).
[12] V. Newhouse, N. Bilgutay, J. Saniie, and E. Furgason, ''Flaw-to-grain echo enhancement by split-spectrum processing,'' Ultrasonics **20**, 59–68 (1982).
[13] N. Bilgutay, U. Bencharit, R. Murthy, and J. Saniie, ''Analysis of a nonlinear diverse clutter suppression algorithm,'' Ultrasonics **28**, 90–96 (1990).
[14] M. Gustafsson, ''Detection of spatio-temporal ultrasonic transient families using filter banks and neural nets,'' in *Proceedings of the 8th International Conference on Artificial Neural Networks, ICANN98* (Springer Verlag, New York, 1998), pp. 227–232.
[15] M. Gustafsson and T. Stepinski, ''Studies of split spectrum processing, optimal detection and maximum likelihood amplitude estimation using a simple clutter model,'' Ultrasonics **35**, 31–52 (1997).
[16] M. Gustafsson, ''Nonlinear split spectrum processing using optimal detection,'' IEEE Trans. Ultrason. Ferroelectr. Freq. Control **43**, 109–124 (1996).
[17] V. Premus, D. Alexandrou, and L. Nolte, ''Full-field optimum detection in an uncertain, anisotropic random wave scattering environment,'' J. Acoust. Soc. Am. **98**, 1097–1110 (1995).
[18] K. Fukunaga, *Introduction to Statistical Pattern Recognition* (Academic, San Diego, 1990).
[19] J. Mattsson and A. Niklasson, ''Ultrasonic 2d-sh crack detection in anisotropic solids,'' J. Nondestruct. Eval. **16**, 31–41 (1997).
[20] A. Eriksson, J. Mattsson, and A. J. Niklasson, ''Modeling of ultrasonic crack detection in anisotropic materials,'' NDT & E Int. **33**, 441–451 (2000).
[21] R. Thompson and T. Gray, ''A model relating ultrasonic scattering measurements through liquid-solid interfaces to unbounded medium scattering amplitudes,'' J. Acoust. Soc. Am. **74**, 1279–1290 (1983).
[22] L. Schmerr and A. Sedov, ''An elastodynamic model for compressional and shear wave transducers,'' J. Acoust. Soc. Am. **86**, 1988–1999 (1989).
[23] X. Tang, M. Toksoz, and C. Cheng, ''Elastic wave radiation and diffraction of a piston source,'' J. Acoust. Soc. Am. **87**, 1894–1902 (1990).
[24] A. Lhemery, ''Impulse-response method to predict echo responses from defects in solids. Part i. Theory,'' J. Acoust. Soc. Am. **98**, 2197–2208 (1995).
[25] V. Poor, *An Introduction to Signal Detection and Estimation* (Springer, New York, 1994).
[26] K. Donohue, ''Maximum likelihood estimation of a-scan amplitudes for coherent targets in media of unresolvable scatterers,'' IEEE Trans. Ultrason. Ferroelectr. Freq. Control **39**, 422–431 (1992).
[27] R. K. Chapman, ''Application of elastic scattering theory for smooth flat cracks to the quantitative prediction of ultrasonic defect detection and sizing,'' Nucl. Energy **22**, 319–333 (1983).
[28] S. M. Kay, *Fundamentals of Statistical Signal Processing: Detection Theory* (Prentice-Hall, New Jersey, 1993).
[29] M. Basseville, ''Distance measures for signal processing and pattern recognition,'' Signal Process. **18**, 349–369 (1989).
[30] D. Boekee and J. V. D. Lubbe, ''Some aspects of error bounds in feature selection,'' Pattern Recogn. **11**, 353–360 (1979).
[31] L. W. Schmerr, *Fundamentals of Ultrasonic Nondestructive Evaluation: A Modeling Approach* (Plenum, New York, 1998).
[32] F. Margetan, R. Thompson, and I. Yalda-Mooshabad, ''Backscattered microstructural noise in ultrasonic toneburst inspection,'' J. Nondestruct. Eval. **13**, 111–136 (1994).

Transmission mode time-reversal super-resolution imaging

Sean K. Lehman[a)]
Lawrence Livermore National Laboratory, Livermore, California 94550

Anthony J. Devaney[b)]
Northeastern University, Boston, Massachusetts 02115

(Received 10 May 2002; revised 13 February 2003; accepted 13 February 2003)

The theory of time-reversal super-resolution imaging of point targets embedded in a reciprocal background medium [A. J. Devaney, ''Super-resolution imaging using time-reversal and MUSIC,'' J. Acoust. Soc. Am. (to be published)] is generalized to the case where the transmitter and receiver sensor arrays need not be coincident and for cases where the background medium can be nonreciprocal. The new theory developed herein is based on the singular value decomposition of the generalized multistatic data matrix of the sensor system rather than the standard eigenvector/eigenvalue decomposition of the time-reversal matrix as was employed in the above-mentioned work and other treatments of time-reversal imaging [Prada, Thomas, and Fink, ''The iterative time reversal process: Analysis of the convergence,'' J. Acoust. Soc. Am. **97**, 62 (1995); Prada *et al.*, ''Decomposition of the time reversal operator: Detection and selective focusing on two scatterers,'' J. Acoust. Soc. Am. **99**, 2067 (1996)]. A generalized multiple signal classification (MUSIC) algorithm is derived that allows super-resolution imaging of both well-resolved and non-well-resolved point targets from arbitrary sensor array geometries. MUSIC exploits the orthogonal nature of the scatterer and noise subspaces defined by the singular vectors of the multistatic data matrix to form scatterer images. The time-reversal/MUSIC algorithm is tested and validated in two computer simulations of offset vertical seismic profiling where the sensor sources are aligned along the earth's surface and the receiver array is aligned along a subsurface borehole. All results demonstrate the high contrast, high resolution imaging capabilities of this new algorithm combination when compared with ''classical'' backpropagation or field focusing. Above and beyond the application of seismo-acoustic imaging, the time-reversal super-resolution theory has applications in ocean acoustics for target location, and ultrasonic nondestructive evaluation of parts.
 [DOI: 10.1121/1.1566975]

PACS numbers: 43.60.Pt, 43.35.Zc [JCB]

I. INTRODUCTION

We consider the situation illustrated in Fig. 1 in which an arbitrary configuration of sources and receivers probe a medium containing a number of discrete scatterers. We assume a generalized multistatic measurement mode in which the scattered wave field resulting from the incident or probing wave generated by each transmitter is measured at all receiver locations. In the usual multistatic measurement mode the transmitters and receivers are co-incident corresponding to a *reflection measurement mode*. Here we will not impose this restriction and, indeed, will be most interested in a *transmission measurement mode* where the sources and receivers are all distinct. Our goal in this paper is to extend the usual (reflection mode) theory[1] of time-reversal imaging to this generalized configuration and also to extend the theory of super-resolution imaging presented in Ref. 1 to this more general case. Besides allowing the measurement configuration to be arbitrary we will also not require the background medium in which the scatterers are contained to be nonreciprocal (see discussion later). Although a reflection mode experiment using a coincident but decimated receiving array demonstrated the possibility of noncoincident arrays,[2] the theory was never derived nor formalized to a truly arbitrary transceiver configuration.

Section II develops the forward scattering model under the (distorted wave) Born approximation that underlies most treatments of time-reversal imaging. Section III introduces fundamental time-reversal concepts and theory. Section IV reviews the theory of subspace signal processing[3–5] first applied to time-reversal imaging in Ref. 1. In this section we develop a generalized version of the multiple signal classification (MUSIC) algorithm presented in Ref. 1 for performing super-resolution imaging of both well-resolved as well as non-well-resolved targets. The generalized MUSIC algorithm is tested and validated in two computer simulations of offset vertical seismic profiling (VSP) in Sec. V. The offset VSP examples employ a set of surface acoustic sources and a set of distinct borehole receivers as illustrated in Fig. 2. The first of the two simulations employs ideal (Born approximation) data while the second example is based on a two-dimensional finite-difference time-domain (FDTD) simulation for a set of buried cylinders.

II. THE MULTISTATIC DATA MATRIX

We consider a wave probing data acquisition system (either acoustic or electromagnetic) consisting of a set of N_t

a)Electronic mail: lehman2@llnl.gov
b)Electronic mail: tonydev2@aol.com

 0001-4966/2003/113(5)/2742/12/$19.00

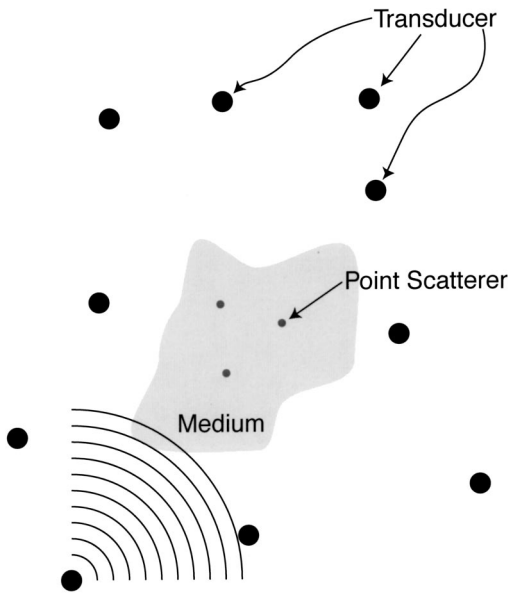

FIG. 1. An arbitrary configuration of transceivers are used to probe a medium.

transmitters and a set of N_r receivers such as illustrated in Fig. 1. The transmitters are individually excited and generate incident wave fields that propagate into a background medium containing a number of discrete scatterers. The incident wave field generated from any given source interacts with the scatterers and generates a total wave field (incident plus scattered) that satisfies the Lippman–Schwinger equation[6]

$$\psi_j(\mathbf{R}_i^r,\omega)=\psi_j^{\mathrm{inc}}(\mathbf{R}_i^r,\omega) + k_0^2(\omega)\int d\mathbf{r}\, G(\mathbf{R}_i^r,\mathbf{r},\omega)O(\mathbf{r},\omega)\psi_j(\mathbf{r},\omega), \tag{1}$$

where $G(\mathbf{r},\mathbf{r}',\omega)$ is the Green's function of the background medium, $\mathbf{R}_i^r$ is the location of the ith receiver, $\psi_j(\mathbf{r},\omega)$ is the total field resulting from the incident field $\psi_j^{\mathrm{inc}}(\mathbf{r},\omega)$ generated by the jth source. $O(\mathbf{r},\omega)$ is the unknown *object profile* (also known as the *object distribution function* or *scattering potential*) characterizing the buried targets and is given by

$$O(\mathbf{r},\omega)\equiv\frac{k^2(\mathbf{r},\omega)}{k_0^2(\omega)}-1, \tag{2}$$

where $k(\mathbf{r},\omega)$ is the wave number of the total medium (background plus targets) and $k_0(\omega)$ the wave number of the background medium alone.

The total field ψ_j consists of the sum of the incident wave from the transmitter plus the *scattered wave* generated by the interaction of the incident wave with the targets. It follows from Eq. (1) that the scattered wave measured at receiver i due to source j is given by

$$\psi_j^{\mathrm{scatt}}(\mathbf{R}_i^r,\omega)=k_0^2(\omega)\int d\mathbf{r}\, G(\mathbf{R}_i^r,\mathbf{r},\omega)O(\mathbf{r},\omega)\psi_j(\mathbf{r},\omega), \tag{3}$$

where $\psi_j^{\mathrm{scatt}}(\mathbf{R}_i^r,\omega)\equiv\psi_j(\mathbf{R}_i^r,\omega)-\psi_j^{\mathrm{inc}}(\mathbf{R}_i^r,\omega)$. The raw data at frequency ω thus forms an $N_r\times N_t$ matrix $K=\{K_{i,j}\}$ whose i,j element is given by

$$K_{i,j}(\omega)=k_0^2(\omega)\int d\mathbf{r}\, G(\mathbf{R}_i^r,\mathbf{r},\omega)O(\mathbf{r},\omega)\psi_j(\mathbf{r},\omega). \tag{4}$$

If we define the column vectors

$$g_r(\mathbf{r},\omega)\equiv[G(\mathbf{R}_1^r,\mathbf{r},\omega),G(\mathbf{R}_2^r,\mathbf{r},\omega),\ldots,G(\mathbf{R}_{N_r}^r,\mathbf{r},\omega)]^T, \tag{5a}$$

$$\psi(\mathbf{r},\omega)\equiv[\psi_1(\mathbf{r},\omega),\psi_2(\mathbf{r},\omega),\ldots,\psi_{N_t}(\mathbf{r},\omega)]^T, \tag{5b}$$

we can rewrite Eq. (4) in the symbolic form

$$K(\omega)=k_0^2(\omega)\int d\mathbf{r}\, g_r(\mathbf{r},\omega)O(\mathbf{r},\omega)\psi^T(\mathbf{r},\omega), \tag{6}$$

where the superscript T stands for the transpose operation and where we have used the r subscript on the Green's function vector to denote that it corresponds to the receiver array.

The data matrix K is called the *generalized multistatic data matrix* and is the key quantity that is employed in most data inversion schemes for subsurface imaging. In diffraction tomography[7,8] this matrix is used in conjunction with a *slant stacking*[9,10] algorithm to generate plane wave data which are then input into a *filtered backpropagation algorithm*[7] to generate an ''image'' of the target [the object profile $O(\mathbf{r},\omega)$]. In the case where the transmitters and receivers are co-located (reflection geometry) the multistatic matrix can be employed to perform time-reversal imaging[11,12] which is especially useful for locating targets that are small relative to a wavelength, even if the targets are buried in inhomogeneous media whose Green's functions are not precisely known. We describe the process of time-reversal imaging in Sec. III.

Born Approximation. In many cases of interest the effect of the targets on the incident wave field ψ_j is small so that to a first approximation the total field ψ_j within the integral defining the scattered field in Eq. (3) can be set equal to the incident field $\psi_j^{\mathrm{inc}}(\mathbf{r},\omega)$. This is called the *Born approximation* and is employed in the vast majority of imaging and inversion schemes. More precisely, this is called the *distorted Born approximation* since the background medium is not required to be constant. However, we will interpret the Born

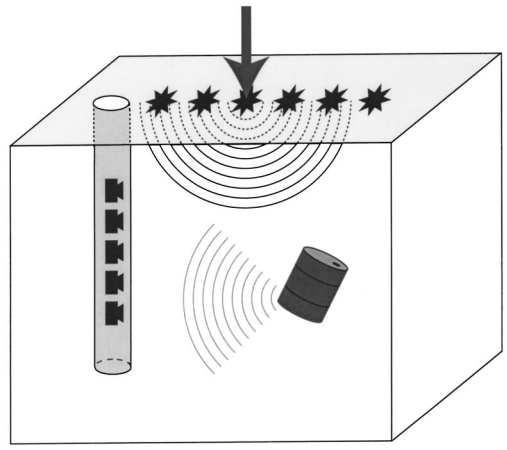

FIG. 2. Acoustic bore hole tomography scenario. A series of surface sources extend radially outward from a receiver chain inserted in a bore hole. The sources are excited individually and the scattered field measured at the receivers.

approximation within this more general context and not differentiate between uniform (constant) and nonuniform backgrounds except when noted. Another simplification results in cases where the sensor elements are small relative to the wavelength. In this case the incident waves ψ_j^{inc} are proportional to the Green's functions; i.e.,

$$\psi_j^{\text{inc}}(\mathbf{r},\omega)=P_j(\omega)G(\mathbf{r},\mathbf{R}_j^t,\omega), \tag{7}$$

where $P_j(\omega)$ is the incident pulse, or source excitation, spectrum, and $\mathbf{R}_j^t$ is the transmitter location. Within the Born approximation, the multistatic response matrix defined in Eq. (6) assumes the form

$$K(\omega)=k_0^2(\omega)\int d\mathbf{r}\, g_r(\mathbf{r},\omega)O(\mathbf{r},\omega)g_t^T(\mathbf{r},\omega), \tag{8}$$

where g_r is the Green's function vector associated with the receiver array and defined in Eq. (5a) and

$$g_t(\mathbf{r},\omega)\equiv[P_1(\omega)G(\mathbf{r},\mathbf{R}_1^t,\omega),P_2(\omega)\times G(\mathbf{r},\mathbf{R}_2^t,\omega),\ldots,P_{N_t}(\omega)G(\mathbf{r},\mathbf{R}_{N_t}^t,\omega)]^T \tag{9}$$

is the Green's function vector associated with the transmitter array. Physically, g_t is generated by a source and propagates from that source point into the target region while g_r is generated by a target scattering point and propagates from that source point into the sensor array.

From this point on we will employ Eq. (8) as our working definition of the multistatic response matrix. Thus, we will assume that the (distorted wave) Born approximation can be employed and that the incident wave fields generated from the sources are the background Green's functions. This second assumption is done only for convenience and can easily be removed. However, the use of the Born approximation is not easily removed from the theory although there has been some work along these lines.[13] For the sake of ease of notation we will also suppress the frequency variable ω in all of the following developments with the understanding that all equations are in the frequency domain at frequency ω.

III. TIME-REVERSAL IMAGING

In the general case where all of the transmitters are simultaneously activated, the data measured at the receivers are given by an expression of the form

$$v=Ke,$$

where $v(\omega)$ is the linear array of output signals (usually voltages in most receiver systems), viewed as an N_r dimensional column vector, measured at the receiver terminals, $e(\omega)$ is the N_t dimensional column vector of applied source excitations, and K is the $N_r\times N_t$ multistatic matrix. As mentioned earlier we will not explicitly display the frequency variable ω in subsequent equations. In time-reversal imaging the object profile $O(\mathbf{r})$ consists of a sum of M disjoint profiles $O_m(\mathbf{r})$ each centered at a spatial location $\mathbf{X}_m$ and each having an effective size that is small relative to the wavelength; i.e.,

$$O(\mathbf{r})\equiv\sum_{m=1}^{M} O_m(\mathbf{r}-\mathbf{X}_m)\approx\sum_{m=1}^{M}\tau_m\delta(\mathbf{r}-\mathbf{X}_m), \tag{10}$$

where the τ_m are the scattering coefficients. The goal of time-reversal imaging is to estimate the location $\mathbf{X}_m$ and strength τ_m of each scatterer. If we substitute Eq. (10) into Eq. (8) we obtain

$$K=k_0^2(\omega)\sum_{m=1}^{M}\tau_m g_r(\mathbf{X}_m)g_t^T(\mathbf{X}_m), \tag{11}$$

where

$$\tau_m=\int d\mathbf{r}\, O_m(\mathbf{r}), \tag{12}$$

and where we have made use of the assumption that the targets are small relative to the wavelength.

A. Transmitter and receiver array point spread functions

Classical coherent imaging from arrays is performed by *backpropagating* a coherent wave that is measured across an array into the space from which it propagated. If $\psi(\mathbf{R}^r)$ denotes such a wave measured at the receiver array then the back propagation of ψ is defined mathematically via

$$\chi(\mathbf{r})=\sum_{j=1}^{N_r} G^*(\mathbf{r},\mathbf{R}_j^r)\psi(\mathbf{R}_j^r), \tag{13}$$

where the superscript asterisk denotes the complex conjugate operation, χ is the backpropagated wave, and $\psi(\mathbf{R}_j^r)$ the measured coherent wave across the receiver array. The backpropagated wave $\chi(\mathbf{r})$ is the ''best'' estimate of the measured coherent wave that can be deduced from the measured data.

Now assume that the incident coherent wave to the receiver is the Green's function $G(\mathbf{R}^r,\mathbf{X})$ resulting from a source location at $\mathbf{X}$. We then find using Eq. (13) that the backpropagated field corresponding to the measured Green's function is

$$H_r(\mathbf{r},\mathbf{X})=\sum_{j=1}^{N_r} G^*(\mathbf{r},\mathbf{R}_j^r)G(\mathbf{R}_j^r,\mathbf{X})=g_r^\dagger(\mathbf{r})g_r(\mathbf{X}). \tag{14}$$

The backpropagated field $H_r(\mathbf{r},\mathbf{X})$ is a function both of the field point at which it is evaluated as well as the source point location $\mathbf{X}$ and is the *best image of the source point that can be formed from measurement of the Green's function across the receiver array.* This quantity is called the *receiver array coherent point spread function* (PSF). In a similar fashion one can define the transmitter array PSF as

$$H_t(\mathbf{r},\mathbf{X})=g_t^\dagger(\mathbf{r})g_t(\mathbf{X}). \tag{15}$$

We will not discuss the importance and use of the above PSFs at this time but will shortly encounter both of these quantities in connection with time-reversal imaging.

B. Singular value decomposition of the multistatic matrix

The theory of generalized time-reversal imaging depends on the ability to perform a singular value decomposition (SVD) of the multistatic data matrix K. In particular, we consider the singular system

$$Ke_j=\sigma_j v_j, \tag{16a}$$

$$K^\dagger v_j=\sigma_j e_j, \tag{16b}$$

where j labels the singular system e_j, v_j, σ_j, and the multistatic data matrix of Eq. (11) represents a mapping from the transmitter to receiver spaces:

$$K: \quad C^{N_t}\rightarrow C^{N_r}. \tag{17}$$

In a similar manner, its adjoint, $K^\dagger$, represents a mapping from the receiver to transmitter spaces:

$$K^\dagger: \quad C^{N_r}\rightarrow C^{N_t}, \tag{18}$$

where

$$K^\dagger=k_0^2(\omega)\sum_{m=1}^{M}\tau_m^* g_t^*(\mathbf{X}_m)g_r^\dagger(\mathbf{X}_m). \tag{19}$$

The normal equations for the system of Eqs. (16a) and (16b) are

$$K^\dagger Ke_j=\sigma_j^2 e_j, \tag{20a}$$

$$KK^\dagger v_j=\sigma_j^2 v_j, \tag{20b}$$

where the $N_t\times N_t$ matrix,

$$T\equiv K^\dagger K,$$

is the well-known *time-reversal matrix*. The singular vectors $\{e_j\}_{j=1}^{N_t}$ are orthonormal and span the space C^{N_t} while the singular vectors $\{v_j\}_{j=1}^{N_r}$ are orthonormal and span the space C^{N_r}. There are a total of $\min(N_t,N_r)$ singular values $\sigma_j\geqslant 0$.

If we substitute the expression for the K matrix given in Eq. (11) into Eqs. (16a) and (16b) we obtain

$$k_0^2(\omega)\sum_{m=1}^{M}\tau_m\, g_r(\mathbf{X}_m)\, g_t^T(\mathbf{X}_m)\, e_j=\sigma_j v_j, \tag{21a}$$

$$k_0^2(\omega)\sum_{m=1}^{M}\tau_m^* g_t^*(\mathbf{X}_m)g_r^\dagger(\mathbf{X}_m)v_j=\sigma_j e_j. \tag{21b}$$

It follows from the above-given equations that for $\sigma_j>0$ the singular vectors v_j are linear combinations of the receiver array Green's function vectors $g_r(\mathbf{X}_m)$ while the singular vectors e_j are linear combinations of the complex conjugates of the transmitter array Green's function vectors $g_t^*(\mathbf{X}_m)$. An important special case occurs when these two sets of Green's function vectors are orthogonal, i.e., when the following two equations are satisfied:

$$H_r(\mathbf{X}_m,\mathbf{X}_{m'})\equiv g_r^\dagger(\mathbf{X}_m)\, g_r(\mathbf{X}_{m'})\, =\|g_r(\mathbf{X}_m)\|^2\delta_{m,m'}, \tag{22a}$$

$$H_t(\mathbf{X}_m,\mathbf{X}_{m'})\equiv g_t^\dagger(\mathbf{X}_m)g_t(\mathbf{X}_{m'})=\|g_t(\mathbf{X}_m)\|^2\delta_{m,m'}, \tag{22b}$$

where $\delta_{m,m'}$ is the Kronecker delta function and

$$\|g_r(\mathbf{X}_m)\|^2=g_r^\dagger(\mathbf{X}_m)g_r(\mathbf{X}_m),$$

$$\|g_t(\mathbf{X}_m)\|^2=g_t^\dagger(\mathbf{X}_m)g_t(\mathbf{X}_m)$$

are the squared norms of the Green's function vectors evaluated at the target point $\mathbf{X}_m$. If Eq. (22a) holds then we say that *the targets are well resolved by the receiver array* while if Eq. (22b) holds we say that *the targets are well resolved by the transmitter array*. When both equations hold then the targets are well resolved with respect to both the transmitter and receiver arrays.

The rational for the above-mentioned terminology is apparent if we simply note that the inner products in Eqs. (22a) and (22b) are, respectively, the PSFs $H_r(\mathbf{X}_m,\mathbf{X}_{m'})$ and $H_t(\mathbf{X}_m,\mathbf{X}_{m'})$. Thus, for example, the inner product $g_r^\dagger(\mathbf{X}_m)g_r(\mathbf{X}_{m'})$ is *the image of a point target located at* $\mathbf{X}_{m'}$ *formed at point* $\mathbf{X}_m$ *by the receiver array*. An entirely analogous interpretation can be given the inner product $g_t^\dagger(\mathbf{X}_m)g_t(\mathbf{X}_{m'})$; i.e., as *the image of a point target located at* $\mathbf{X}_{m'}$ *formed at point* $\mathbf{X}_m$ *by the transmitter array.* The case of *well-resolved targets* thus corresponds to the case where the targets are sufficiently well separated that the PSF of either the transmitter or receiver array does not significantly overlap any target other than the one on which it is focused.

C. Well-resolved targets

For the case of well-resolved targets it is easy to show that *the singular system* $\{e_j,v_j,\sigma_j>0\}$ *can be related in a one-to-one manner with the* $M\leqslant\min(N_t,N_r)$ *scattering targets.* Indeed, it follows at once from the orthogonality of the Green's function vectors that the singular vectors having nonzero singular values for well-resolved targets are given by

$$e_j=\frac{g_t^*(\mathbf{X}_j)}{\|g_t(\mathbf{X}_j)\|}, \tag{23a}$$

$$v_j=\frac{g_r(\mathbf{X}_j)}{\|g_r(\mathbf{X}_j)\|}, \tag{23b}$$

where $j=1,2,\ldots,M$. Moreover, the nonzero singular values σ_j are given by

$$\sigma_j=k_0^2(\omega)|\tau_j|\|g_t(\mathbf{X}_j)\|\|g_r(\mathbf{X}_j)\|. \tag{24}$$

We conclude that *the scatterer strengths are computed directly from the singular values* which, in turn, are readily computed from the measured multistatic data matrix K. Moreover, *the singular vectors give the location of the targets*. Indeed, the coherent image formed using the singular vector e_j will generate the PSF of the transmitter array centered at $\mathbf{X}_j$ while the coherent image formed using the singular vector v_j will generate the PSF of the receiver array centered at $\mathbf{X}_j$. It is, of course, possible to have well-resolved targets only if their number $M\leqslant\min\{N_r,N_t\}$.

IV. PSEUDOSPECTRUM

For well-resolved targets, the $\{e_j\}_{j=1}^{N_t}$ and $\{v_j\}_{j=1}^{N_r}$ form two orthonormal sets which span the C^{N_t} and C^{N_r} spaces,

TABLE I. Mathematical relations of the transmitter and receiver spaces defined by the transmitter and receiver singular vectors. N_σ is the number of singular values.

Transmitter C^{N_t} space	Receiver C^{N_r} space
$Ke_j=\sigma_j v_j,\ j=1,\ldots,M$	$K^\dagger v_j=\sigma_j e_j,\ j=1,\ldots,M$
$Ke_j=0,\ j=M+1,\cdots,N_\sigma$	$K^\dagger v_j=0,\ j=M+1,\ldots,N_\sigma$
$e_j^\dagger e_{j'}=\delta_{jj'}$	$v_j^\dagger v_{j'}=\delta_{jj'}$
$\mathcal{S}^t\equiv\text{span}\{e_j,\ j=1,\ldots,M\}$	$\mathcal{S}^r\equiv\text{span}\{v_j,\ j=1,\ldots,M\}$
$\mathcal{N}^t\equiv\text{span}\{e_j,\ j=M+1,\ldots,N_\sigma\}$	$\mathcal{N}^r\equiv\text{span}\{v_j,\ j=M+1,\ldots,N_\sigma\}$
$C^{N_t}=\mathcal{S}^t\oplus\mathcal{N}^t$	$C^{N_r}=\mathcal{S}^r\oplus\mathcal{N}^r$
$N_\sigma\equiv\min(N_t,N_r)$	

respectively. The transmitter and receiver spaces may be subdivided into "signal" and "noise" subspaces spanned, respectively, by the singular vectors having nonzero singular values $\sigma_j>0$ and the singular vectors having zero singular values $\sigma_j=0$. This decomposition, which is summarized in Table I, is a generalization of the same type of decomposition used in Ref. 1 for the case where the transmitter and receiver arrays are coincident (reflection mode case) and which lead directly to a generalized MUSIC algorithm[14,3–5] for generating super-resolved images of the targets.

To develop a MUSIC algorithm for the more general case of noncoincident transmitter and receiver arrays we consider the transmitter and receiver Green's function vectors, $g_t(\mathbf{r})$ and $g_r(\mathbf{r})$, as defined in Eqs. (5a) and (9), respectively. When the point at which these Green's function vectors falls upon a scatterer location, $\mathbf{X}_j$, we have

$$\left.\begin{aligned} e_j^T g_t(\mathbf{X}_j)&=\frac{1}{\|g_t(\mathbf{X}_j)\|}g_t^\dagger(\mathbf{X}_j)g_t(\mathbf{X}_j)=\|g_t(\mathbf{X}_j)\| \\ v_j^\dagger g_r(\mathbf{X}_j)&=\frac{1}{\|g_r(\mathbf{X}_j)\|}g_r^\dagger(\mathbf{X}_j)g_r(\mathbf{X}_j)=\|g_r(\mathbf{X}_j)\| \end{aligned}\right\} \quad \text{for } j=1,\cdots,M, \tag{25}$$

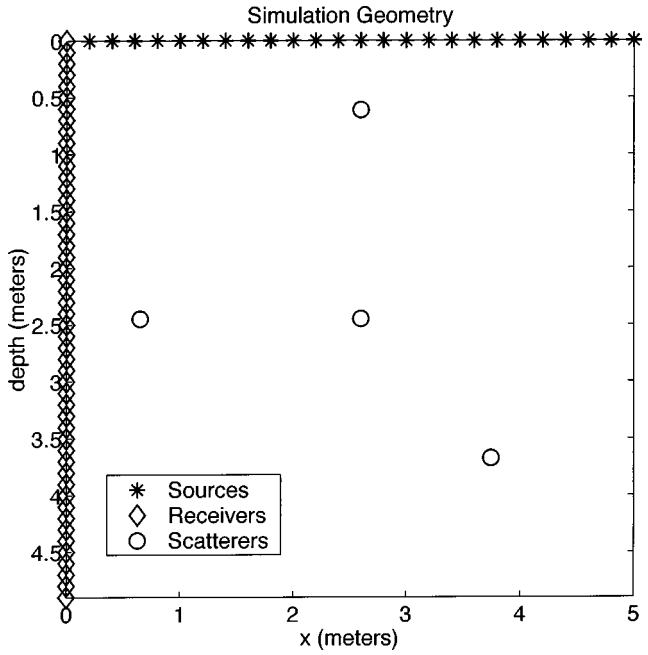

FIG. 4. The asterisks indicate the surface source locations. The diamonds indicate the bore hole receiver locations. There are 25 sources with a separation of 0.2 m, and 50 receivers with a separation of 0.1 m.

and

$$\left.\begin{aligned} e_{j'}^T g_t(\mathbf{X}_j)&=0 \\ v_{j'}^\dagger g_r(\mathbf{X}_j)&=0 \end{aligned}\right\} \quad \text{for } j'=M+1,\cdots,\min(N_t,N_r), \tag{26}$$

where we have used the definitions of the e_j and v_j singular vectors from Eqs. (23a) and (23b). For other evaluation points, that is, for spatial locations, $\mathbf{r}$, which are not scatterer locations, we have

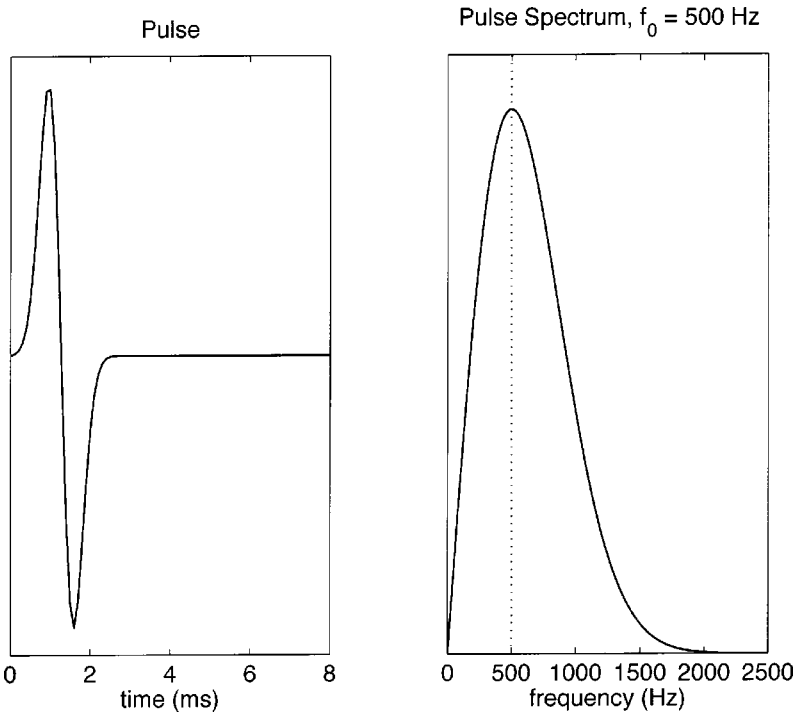

FIG. 3. Incident pulse and its spectrum with a peak frequency of 500 Hz.

TABLE II. Born simulation parameters of four point scatterers.

Number of sources, N_{src}	25
Number of receivers, N_{rcv}	50
Source spacing, Δsrc	0.2 m
Receiver spacing, Δrcv	0.1 m
Number of point scatterers	4
Scattering strength, τ_m	1
Scatterer locations	(2.60, 2.45) m
	(0.65, 2.45) m
	(2.60, 0.61) m
	(4.55, 4.29) m
Background velocity, v_{gnd}	365.76 m/s
Pulse peak frequency, f_0	500 Hz
Wavelength at 500 Hz, λ_0	0.73 m
Imaging sample interval, Δh	0.02 m

$$\left.\begin{aligned} e_{j'}^T g_t(\mathbf{r}) \neq 0 \\ v_{j'}^\dagger g_r(\mathbf{r}) \neq 0 \end{aligned}\right\} \quad \text{for } j' = M+1,\ldots,\min(N_t,N_r), \text{ and } \mathbf{r} \neq \mathbf{X}_j. \tag{27}$$

Consider the following sum of the inner products of the singular vectors and transceiver Green's function vectors:

$$Q(\mathbf{r}) \equiv \sum_{jM+1}^{\min(N_t,N_r)} [|e_j^T g_t(\mathbf{r})| + |v_j^\dagger g_r(\mathbf{r})|]. \tag{28}$$

When we evaluate Eq. (28) at any scatterer location, $\mathbf{r} = \mathbf{X}_j$, we have

$$Q(\mathbf{X}_j) \equiv 0, \quad \text{for } j = 1,\ldots,M,$$

where we have used the orthogonality property of Eq. (26). We now define the *pseudospectrum* to be

$$P(\mathbf{r}) \equiv \frac{1}{\sum_{j=M+1}^{\min(N_t,N_r)} [|e_j^T g_t(\mathbf{r})| + |v_j^\dagger g_r(\mathbf{r})|] + \sigma_r}, \tag{29}$$

where σ_r is a regularization parameter. For well-resolved scatterers, $P(\mathbf{r})$ will have distinct peaks at each of the scatterer locations. We note the expression in Eq. (29) combines the transmitters and receivers into a "super-array" with steering vectors e_j^T applied to the transmitters, and $v_j^\dagger$ applied to the receivers.

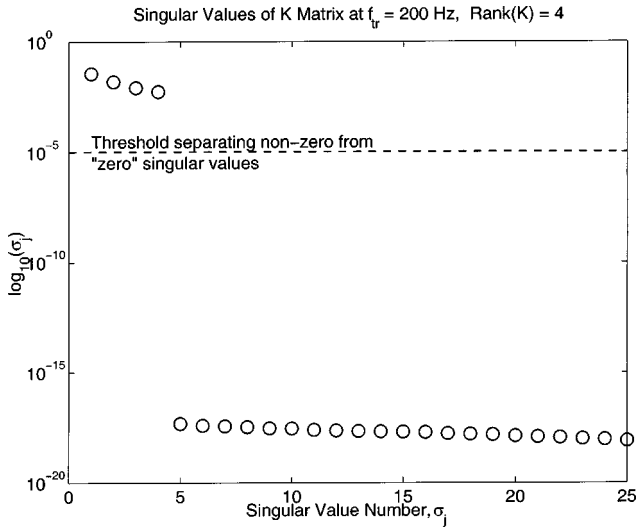

FIG. 5. Singular values of the Born simulation at a time-reversal frequency of 200 Hz.

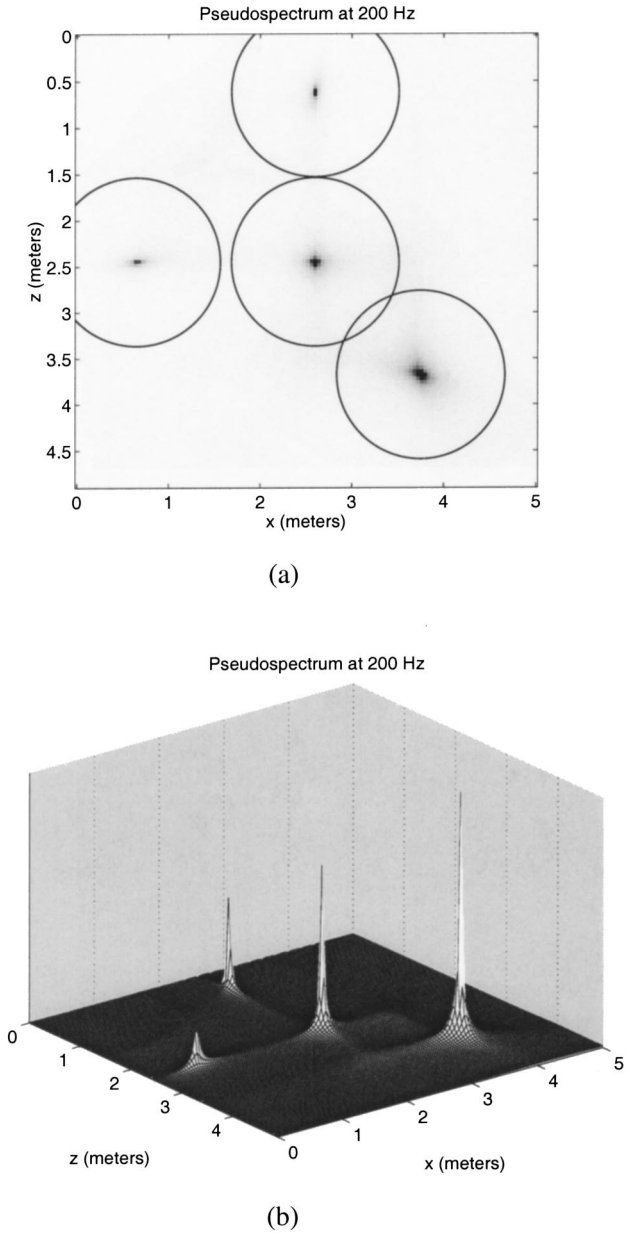

FIG. 6. Born simulation pseudospectrum results at 200 Hz. (a) Reconstructed image with an inverse gray color map. The black circles have a half-wavelength radius and indicate the "classical" resolution limit. (b) Mesh plot.

V. EXAMPLES

As examples, we consider the case of using vertical offset seismic profiling (VSP) to image a buried waste pit. Particularly, we consider the geometry of Pit-9 located at the Idaho National Engineering and Environmental Laboratory, one of the United States' national energy laboratories. Pit-9 has been instrumented with a series of steel cased bore holes approximately 5.5 m deep. A receiver chain in each bore hole measures the field from sources excited along a line extended radially outward approximately 8 m from the bore hole. The

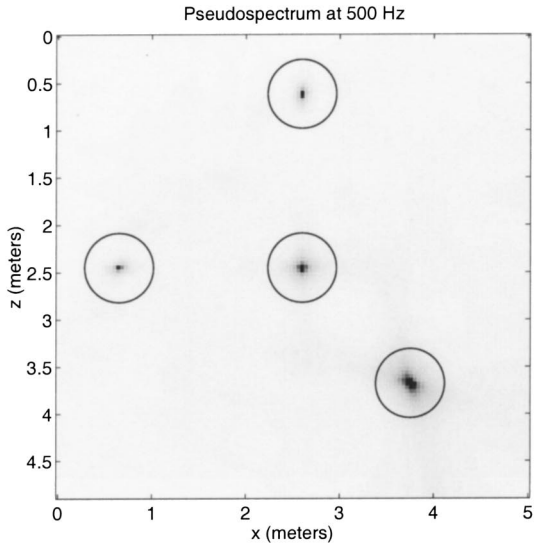

(a)

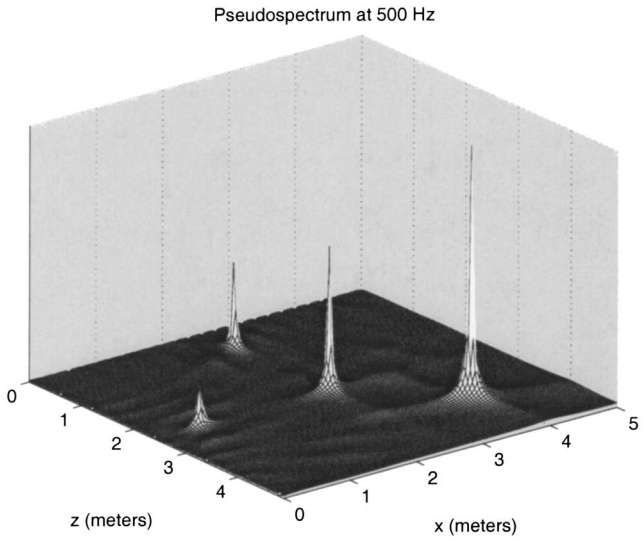

(b)

FIG. 7. Born simulation pseudospectrum results at 500 Hz. (a) Reconstructed image with an inverse gray color map. The black circles have a half-wavelength radius and indicate the ''classical'' resolution limit. (b) Mesh plot.

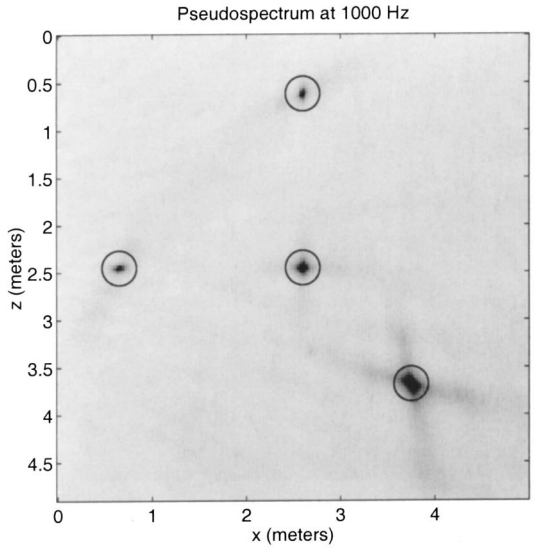

(a)

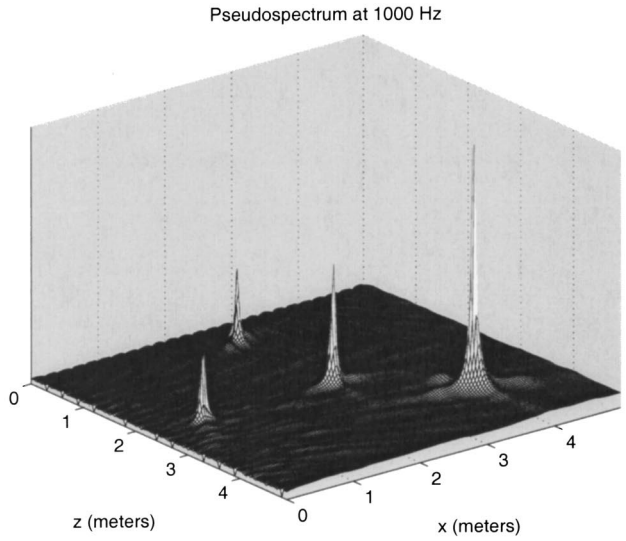

(b)

FIG. 8. Born simulation pseudospectrum results at 1000 Hz. (a) Reconstructed image with an inverse gray color map. The black circles have a half-wavelength radius and indicate the ''classical'' resolution limit. (b) Mesh plot.

source consists of a metal plate on the surface of the ground struck by a hammer. This data collection scenario is depicted in Fig. 2.

Based on our knowledge of the test pit geometry, the incident field spectrum, and the spacing and extent of the transmitter and receiver arrays, it appears that the buried targets are well resolved with respect to both the transmitter and receiver arrays. Thus, we assume that both Eqs. (22a) and (22b) hold and we may use the time-reversal technique to form images of the subsurface structures.

We present two examples: a proof-of-principle based upon the exact forward model of Eq. (8); and a two-dimensional finite-difference time-domain (FDTD) simulation using E3D, an explicit 2D/3D elastic propagation code designed for modeling seismic waves, developed at Lawrence Livermore National Laboratory.[15–20]

A. Proof-of-principle

The proof-of-principle is based upon the forward Born approximation model with a set of four distinct point scatterers, that is, Eq. (3) with the total field replaced by the incident field, and with an object described by Eq. (10) with $M=4$. The scattering coefficients, τ_m, were all set to one.

The incident pulse is described by the first derivative of a Gaussian, or ''DOG'' pulse, given by

$$p(t)=-e^{1/2}\omega_0(t-t_0)e^{-(\omega_0(t-t_0))^2/2}, \tag{30}$$

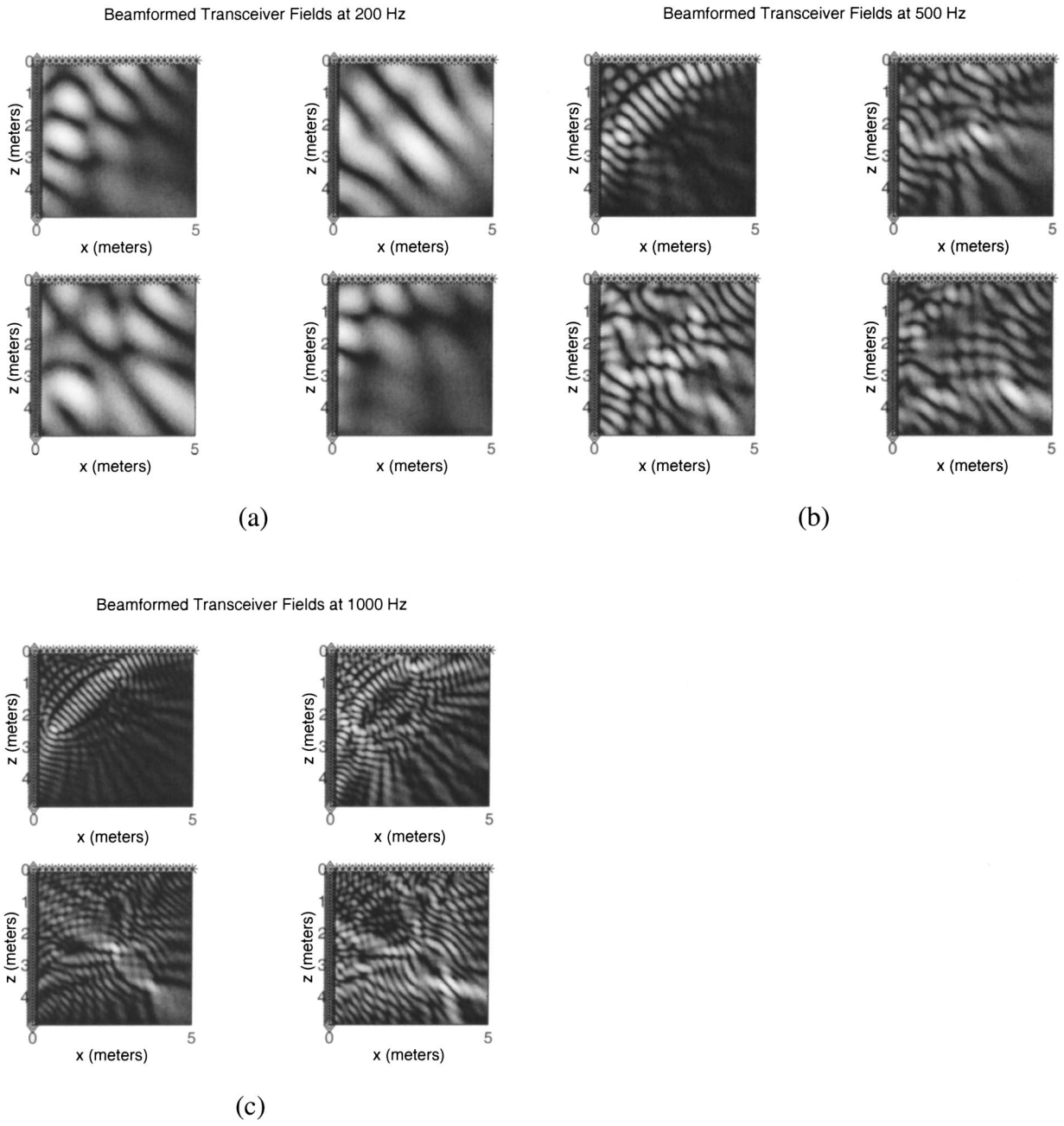

FIG. 9. Born simulation focused transducer field results at time-reversal frequencies (a) 200 Hz, (b) 500 Hz, (c) 1000 Hz.

where $\omega_0 \equiv 2\pi f_0$ and f_0 is the peak frequency of the pulse in hertz. Antenna characteristics are not modeled, thus Eq. (30) is assumed to be the governing form of the incident field. We chose the peak frequency, f_0, to be 500 Hz. The pulse and its spectrum are shown in Fig. 3. The geometry of the simulation, approximately that of Pit-9, is depicted in Fig. 4. The surface sources are represented by the asterisks, the bore hole receivers by the diamonds. There are four point scatterers as indicated in the figure. The scatterers have equal scattering amplitudes. The simulation parameters are listed in Table II.

We performed reconstructions at time-reversal frequencies of 200, 500, and 1000 Hz. The singular values of the multistatic data matrix are shown in Fig. 5 at the 200 Hz time-reversal frequency. The rank of the multistatic data matrix was 4 as expected. The results at 500 and 1000 Hz are similar and are not shown. In this ideal noise-free case, we clearly see the distinction between the nonzero and ''zero'' singular values representing the scatter and noise subspaces, respectively.

The pseudospectrum reconstruction results at each of the time-reversal frequencies are shown in Figs. 6, 7, and 8. Each figure shows an inverted gray scale image and a mesh rendering of the pseudospectrum. The circles superposed on the gray scale images have a radius of a half time-reversal frequency wavelength. They indicate the ''classical'' resolution limit of the reconstruction. In all cases, we observe a resolution of the point scatterer better than a wavelength. In ''classical'' reconstructions, we would only anticipate a resolution no better than a half-wavelength. This is confirmed in the images of Fig. 9 which show ''classical'' reconstructions

TABLE III. FDTD simulation parameters of four cylindrical scatterers.

Number of sources, N_{src}	25
Number of receivers, N_{rcv}	50
Source spacing, Δsrc	0.2 m
Receiver spacing, Δrcv	0.1 m
Background velocity, v_{gnd}	365.76 m/s
Scatterer velocity, $v_{\text{scatt}}=1.1\times v_{\text{gnd}}$	402.34 m/s
Shear velocity, v_{sh}	36.58 m/s
Background density, ρ_{gnd}	2.65 g/cm^3
Scatterer density, $\rho_{\text{scatt}}=1.1\times\rho_{\text{gnd}}$	2.92 g/cm^3
Scatterer diameter	0.58 m
Pulse peak frequency, f_0	500 Hz
Imaging sample interval, Δh	0.02 m

of the point scatterers. The images were formed by back-propagating or focusing the singular vectors associated with the scatter singular values. Mathematically the images show the field created by

$$\psi_m(\mathbf{r})=e_m^T\cdot g_t(\mathbf{r})+v_m^\dagger\cdot g_r(\mathbf{r}), \tag{31}$$

where $m=1,2,3,4$. The scatterers are unresolved in the 200 Hz images. They are partially resolved in the 500 Hz images but not sufficiently so to distinguish them from field side lobes. They are reasonably identifiable in the 1000 Hz images. The MUSIC images show both superior resolution and contrast than the focused field reconstructions.

B. Finite-difference time-domain simulation

The proof-of-principle example was used to confirm the theory. Following that, we performed a two-dimensional FDTD simulation of four buried cylinders using seismic ground parameters similar to those found at Pit-9. The simulation parameters are listed in Table III. In order to remain within the Born approximation region of validity, we chose a scatterer velocity and density that was 10% larger than the background velocity and density. The entire domain, including the scatterers, had a uniform shear velocity. We did not model the surface or the water of the bore hole. For each source, two FDTD simulations were performed: one with the scatterers, that is, an ''object run;'' and the other with just the background, that is, a ''background run.'' The scattered fields used in the time-reversal algorithm were taken as the difference between the ''object run'' and the ''background run.'' This is how we performed the incident pulse removal to obtain the scattered field time series. We emphasize that the time-reversal model and imaging algorithm developed in Secs. II–IV, do not account for the properties of shear and density. Nor do they account for the multiple scattering events (although the simulation was designed so as to make multiple scattering events small).

The incident pulse is identical to that of the proof-of-principle example as shown in Fig. 3. The simulation domain grid is identical to that of the proof-of-principle with the addition of padding to avoid numerical reflections from the boundary. The velocity and density grid domains are presented in Fig. 10.

We performed reconstructions at three time-reversal frequencies of 200, 500, and 1000 Hz. Due to the increased complexity of the physical scattering mechanism, the singular values, shown in Fig. 11, lack the high contrast between nonzero and ''zero'' singular values as those of the proof-of-principle example. This reflects the fact the multistatic data matrix was full rank. The selection of the threshold between nonzero and ''zero'' singular values was based upon the largest decrease in singular value magnitude when plotted on a logarithmic graph. This lack of distinction is due to many factors not included in the model such as the contributions of shear and density, and small multiple scattering. Additionally, Chambers has shown that a single scatterer can have multiple singular values corresponding to its physical properties.[21]

The pseudospectrum reconstructions are presented in Figs. 12, 13, and 14 for the 200, 500, and 1000 Hz, time-reversal frequencies, respectively. We show inverted gray

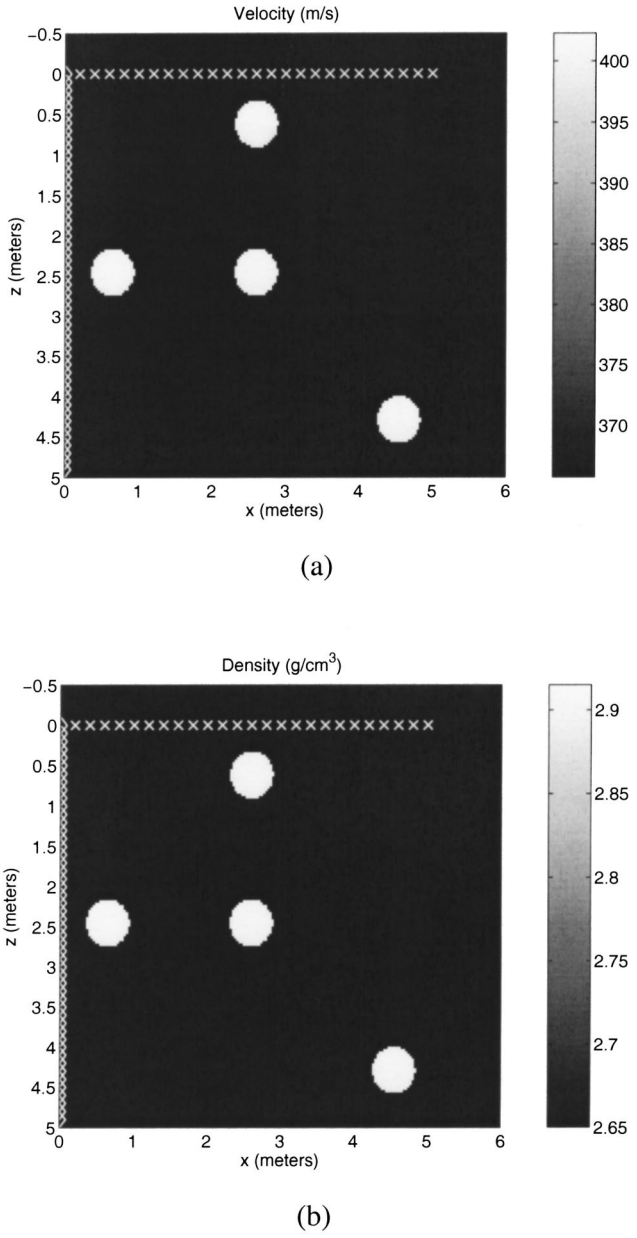

FIG. 10. FDTD grid domain. The asterisks indicate the surface source locations. The diamonds indicate the bore hole receiver locations. There are 25 sources with a separation of 0.2 m, and 50 receivers with a separation of 0.1 m. (a) Velocity domain; (b) density domain.

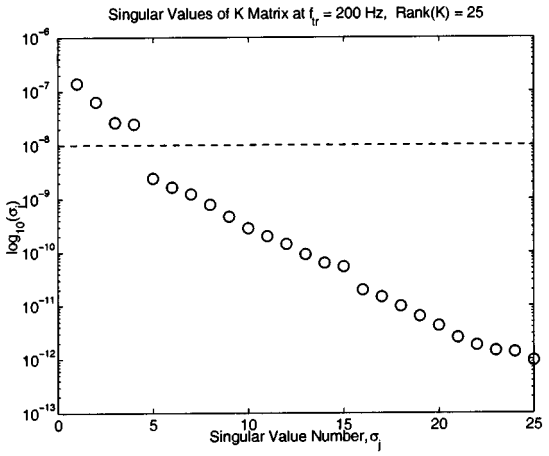

(a)

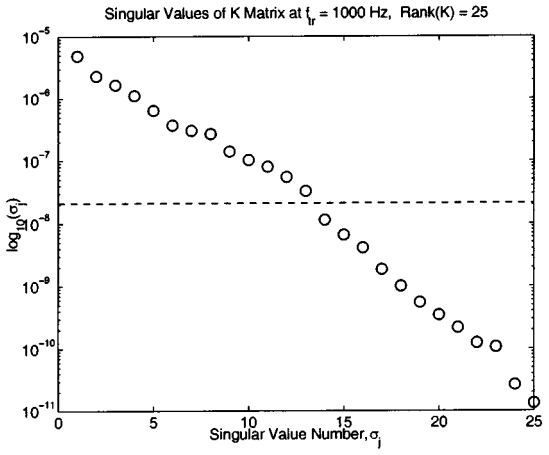

(c)

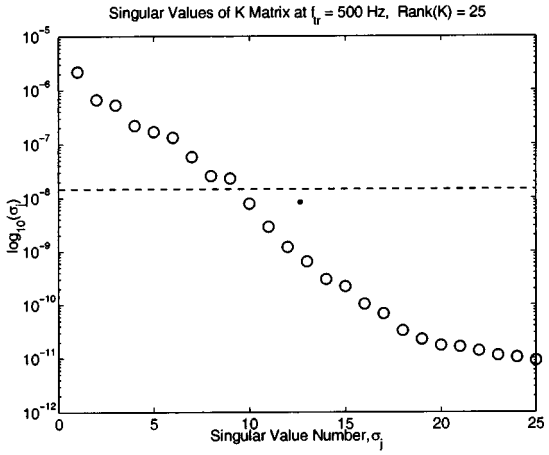

(b)

FIG. 11. Singular values of the FDTD simulation multistatic data matrix at frequencies (a) 200 Hz, (b) 500 Hz, (c) 1000 Hz.

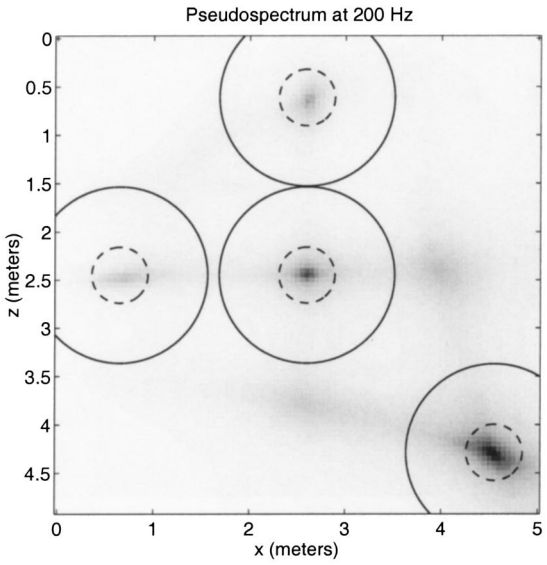

(a)

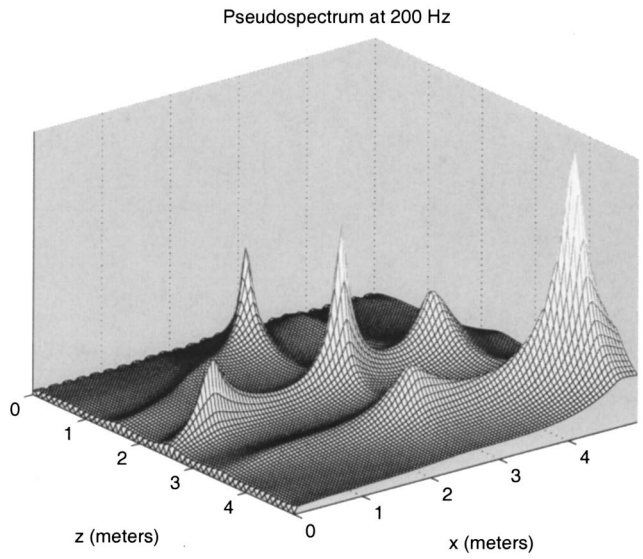

(b)

FIG. 12. FDTD simulation pseudospectrum results at 200 Hz. (a) Reconstructed image with an inverse gray color map. The solid black circles have a half-wavelength radius and indicate the ''classical'' resolution limit. The dashed circles represent the outline of the cylindrical scatterer. (b) Mesh plot.

scale images and mesh rendering of the reconstructions. The closed circles superposed on the gray scale images have a radius of a half time-reversal frequency wavelength. The dashed circles indicate the outline of the scatterers.

All the reconstructions show the cylinders with high resolution and contrast. The 200 Hz pseudospectrum also shows ''false'' reconstructions due to scattering interactions between cylinders. These multiple scattering events are not included in the forward model used in the time-reversal theory.

VI. CONCLUSIONS

We derived the generalized theory for transmission mode time-reversal imaging for arbitrary transceiver number and location. Although not implementable in practice, that is, ''in the field'' in real time, we proved that transmission mode time-reversal is achievable *a posteriori* from the scattered field time series as measured at the receivers. We used the singular value decomposition of the scattering matrix rather

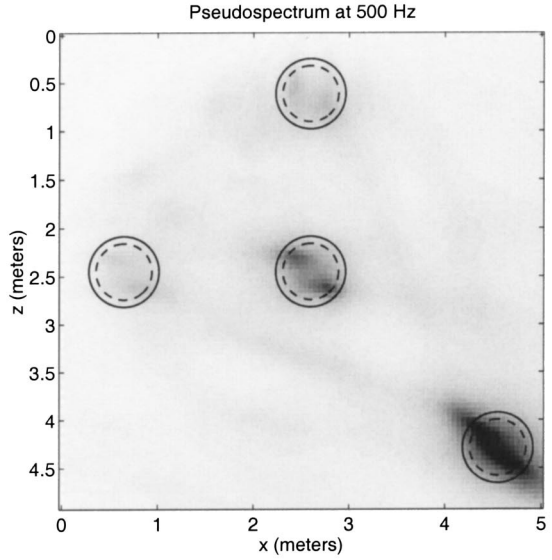

(a)

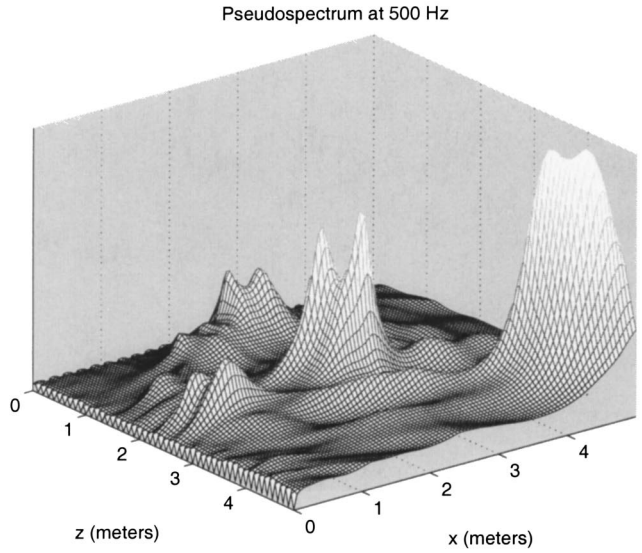

(b)

FIG. 13. FDTD simulation pseudospectrum results at 500 Hz. (a) Reconstructed image with an inverse gray color map. The solid black circles have a half-wavelength radius and indicate the ''classical'' resolution limit. The dashed circles represent the outline of the cylindrical scatterer. (b) Mesh plot.

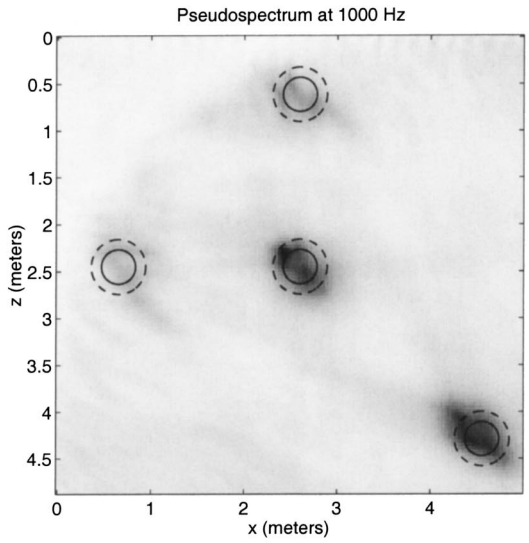

(a)

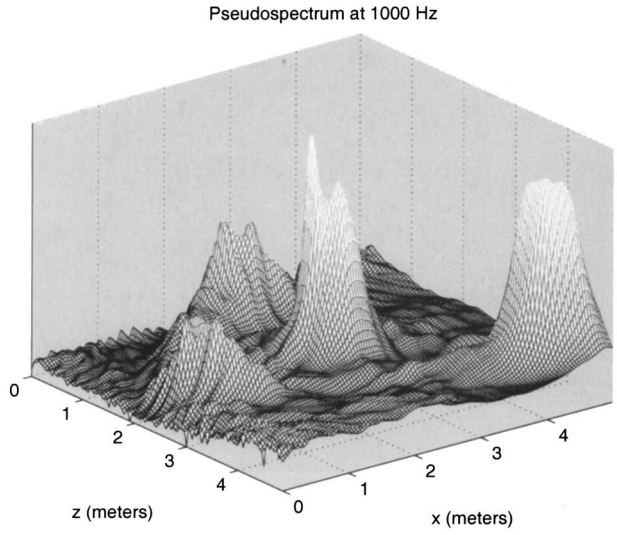

(b)

FIG. 14. FDTD simulation pseudospectrum results at 1000 Hz. (a) Reconstructed image with an inverse gray color map. The solid black circles have a half-wavelength radius and indicate the ''classical'' resolution limit. The dashed circles represent the outline of the cylindrical scatterer. (b) Mesh plot.

than the standard eigenvector decomposition. Exploiting the orthogonal nature of the singular values, we employed the orthogonal subspace concepts of MUSIC and developed an algorithm to form images of point scatterers embedded in a medium. We validated the theory using a proof-of-principle example based upon the exact forward scattering model. We then applied the theory to a realistic two-dimensional scattering simulation of buried cylinders. The results show high contrast, high resolution images, and are excellent considering the simulation included physical properties not accounted for in the forward model.

Future work must include a study on the singular value spectra and how multiple singular values are associated with the multiple physical properties of the scatterer. As this research is intended to locate objects buried in a two layer medium, that is, the ground, we will also generalize the algorithm using a two layer Green's function.

ACKNOWLEDGMENTS

This work was performed under the auspices of the U.S. Department of Energy by University of California Lawrence Livermore National Laboratory under Contract NO. W-7405-Eng-48. A.J.D. supported by contracts from AFOSR, DARPA, and DoE.

[1] A. J. Devaney, ''Super-resolution imaging using time-reversal and MUSIC,'' J. Acoust. Soc. Am. (to be published).
[2] C. Prada, M. Tanter, and M. Fink, ''Flaw detection in solid with the D.O.R.T. method,'' IEEE Ultrason. Symp. Proc. 679–683 (1997).
[3] C. Therrien, *Discrete Random Signals and Statistical Signal Processing* (Prentice–Hall, Englewood Cliffs, NJ, 1992).
[4] P. Stoica and R. Moses, *Introduction to Spectral Analysis* (Prentice-Hall, Englewood Cliffs, NJ, 1997).
[5] H. Wang and M. Kaveh, ''Coherent signal-subspace processing for the detection and estimation of angles of arrival of multiple wide-band sources,'' IEEE Trans. Acoust., Speech, Signal Process. **ASSP-33**, 823–831 (1985).
[6] R. G. Newton, *Scattering Theory of Waves and Particles*, 2nd ed. (Springer, New York, 1982).
[7] A. J. Devaney, ''A filtered backpropagation algorithm for diffraction tomography,'' Ultrason. Imaging **4**, 336–350 (1982).
[8] A. C. Kak and M. Slaney, *Principles of Computerized Tomographic Imaging* (IEEE, 1988), ISBN 0-7803-0447-0.
[9] A. J. Devaney, ''Geophysical diffraction tomography,'' IEEE Trans. Geosci. Remote Sens. **GE-22**, 3–13 (1984).
[10] A. J. Devaney and D. Zhang, ''Geophysical diffraction tomography in a layered background,'' Wave Motion **14**, 243–265 (1991).
[11] C. Prada, J. L. Thomas, and M. Fink,'' The iterative time reversal process: Analysis of the convergence,'' J. Acoust. Soc. Am. **97**, 62–71 (1995).
[12] C. Prada, S. Manneville, D. Spoliansky, and M. Fink, ''Decomposition of the time reversal operator: Detection and selective focusing on two scatterers,'' J. Acoust. Soc. Am. **99**, 2067–2076 (1996).
[13] R. K. Snieder and J. A. Scales, ''Time-revered imaging as a diagnostic of wave and particle chaos,'' Phys. Rev. E **58**, 5668–5675 (1998).
[14] R. O. Schmidt, ''Multiple emitter location and signal parameter estimation,'' IEEE Trans. Antennas Propag. **AP-34**, 276–280 (1986).
[15] A. R. Levander, ''Fourth-order finite-difference p-sv seismograms,'' Geophysics **53**, 1425–1436 (1988).
[16] S. Larsen and J. Grieger, ''Elastic modeling initiative. iii. 3-D computational modeling,'' Soc. Expl. Geophys. Conf. Proc. **68**, 1803–1806 (1998).
[17] S. Larsen, M. Antolik *et al.*, ''3D simulations of scenario earthquakes in the San Francisco Bay area,'' EOS Trans. Am. Geophys. Union **78**, 487 (1997).
[18] R. Madariaga, ''Dynamics of an expanding circular fault,'' Bull. Seismol. Soc. Am. **66**, 639–666 (1976).
[19] J. Virieux, ''P-SV wave propagation in heterogeneous media: Velocity-stress finite-difference method,'' Geophysics **51**, 889–901 (1986).
[20] S. Larsen and D. Harris, ''Seismic wave propagation through a low-velocity nuclear rubble zone,'' Technical report, Lawrence Livermore National Laboratory, 7000 East Avenue, Livermore, CA 94550, 1993.
[21] D. H. Chambers and A. K. Gautesen, ''Time reversal for a single spherical scatterer,'' J. Acoust. Soc. Am. **109**, 2616–2624 (2001).

Reciprocal maximum-length sequence pairs for acoustical dual source measurements[a)]

Ning Xiang[b)]
National Center for Physical Acoustics and Department of Electrical Engineering, University of Mississippi, University, Mississippi 38677

Manfred R. Schroeder
Drittes Physikalisches Institut, Universität Göttingen, Bürgerstraße 42-44, D-37073 Göttingen, Germany

(Received 3 August 2002; revised 14 November 2002; accepted 18 November 2002)

In this paper we propose and demonstrate a method to obtain simultaneous dual source–receiver impulse responses in acoustical systems using binary maximum-length sequences (MLS). A binary MLS and its reversed-order sequence form a reciprocal MLS pair. Their correlation property includes a two-valued ''pulse-like'' autocorrelation function and a relatively smaller-valued cross-correlation function. This unique property, along with other number-theory properties, makes the reciprocal MLS pair suitable for simultaneous dual source cross-correlation measurements. In the measurement of a dual source system, each of the reciprocal MLS pairs simultaneously excite one of two separate sources, one or several receiver signals cross-correlate in turn with each of the MLS pairs, resulting in impulse responses associated with two separate sources. The proposed method is particularly valuable for system identification tasks with multiple sound/vibration sources and receivers that have to be accomplished in a limited time period. A fast algorithm called a fast MLS transform is exploited for the cross-correlation. In this paper we propose a fast MLS transform pair for the reciprocal MLS pairs. Its efficiency lies in the requirement of one single permutation matrix for a pair of two fast MLS transforms. Its feasibility and usefulness in the acoustical measurements are demonstrated using experimental results. [DOI: 10.1121/1.1561498]

PACS numbers: 43.60.Qv, 43.58.Gn, 43.55.Mc [JCB]

I. INTRODUCTION

A wide acceptance of binary maximum-length sequences (MLS or M sequences) measurement technology in the acoustics community is due to MLS' excellent number-theory properties. One of the key characteristics of the MLS is their two-valued periodic autocorrelation function. It is this autocorrelation property that is exploited in most of the applications of MLS. The advanced MLS measurement technique is based on a fast algorithm termed a *Fast M-sequence Transform* (FMT) by Cohn and Lempel[1] in which the impulse response-related system identification tasks can be accomplished efficiently. In addition, MLS, as excitation signals, possess a high signal power and low peak factors. Along with the inherent cross-correlation mechanism for system identification, a high noise immunity in measurement results can be obtained. Recent acoustical applications of the MLS measurement technique can be found, among others, in architectural acoustics,[2–7] audiology,[8–10] ultrasonics,[11,12] psychoacoustics,[13,14] underwater acoustics,[15] and physical acoustics.[16,17]

In this paper we propose a technique using a reciprocal pair of MLS in simultaneous dual-source channel measurements. Impulse responses between two separate sources and one or several receivers of acoustical systems can be determined simultaneously. The simultaneous dual-source measurements exploit the cross-correlation properties of reciprocal MLS pairs that are considerably less widely known and understood than the autocorrelation functions. It is this property that makes simultaneous dual-source measurements feasible. This technique is of practical significance for a number of acoustical investigations in physical acoustics, ultrasonics, and architectural acoustics. Particularly, some measurement tasks of an acoustical system under test with multiple sound/vibration sources have to be accomplished in a limited time period. In Sec. II we briefly introduce some number-theory properties pertaining to the technique. In Sec. III we then describe a convenient algorithm for the FMT and in Sec. IV derive a permutation matrix for the reciprocal MLS pairs. In Sec. V we discuss some acoustical experiments designed for a demonstration of the usefulness of the properties and the convenience of the algorithm.

II. BASIC PROPERTIES OF BINARY MLS

An n-stage linear feedback shift-register device can generate a binary periodic sequence $\{a_i\}$ with $a_i \in \{0,1\}$. When its feedback taps are appropriately connected, the periodic sequences arrive at their maximum period length of $L=2^n-1$. In this case, the sequences are referred to as maximum-length sequences (MLS). A characteristic polynomial $f(x)$ expressing its feedback connection is then referred to as *primitive*. The positive integer n is said to be the degree of the MLS as well as its primitive polynomial (PP). In math-

[a)]Dedicated to Dr. Jens P. Blauert on the occasion of his 65th birthday. Parts of this work have been presented at the 141st meeting of the Acoustical Society of America [J. Acoust. Soc. Am. **109**, 2418(A) (2001)].

[b)]Author to whom correspondence should be addressed. Electronic mail: nxiang@olemiss.edu

ematical treatment MLS are convenient in their binary form $a_i \in \{0,1\}$ while a bipolar form $m_i \in \{-1,+1\}$ is often used in practice to generate waveforms with $m_i = 1 - 2a_i$.

MLS enjoy a number of attractive properties that make them widely useful in broad scientific and engineering fields. In this section we briefly review some basic properties pertaining to the following discussion with respect to the application of reciprocal MLS pairs. A detailed description and definitions can be found in Refs. 18–23.

A. Decimation of MLS

If $\{a_i\}$ is an MLS of length $L = 2^n - 1$, a decimation $\{a_{qi}\}$ of sequence $\{a_i\}$ yields another MLS $\{b_i\}$ of the same degree with $b_i = a_{qi}$, if and only if (see Ref. 18) the greatest common divider of positive integers q and L equals one, $\gcd(q,L) = 1$. q is said to be a proper decimation factor. The index operation $q \cdot i$ of $\{a_{qi}\}$ and all others throughout this paper are evaluated modulo L.

A decimation factor of 2 results in the same MLS $\{b_i\}$ with $b_i = b_{2i}$ only for a unique initial state of the linear feedback shift register for every individual PP $f(x)$. This special class of MLS is designated as characteristic,[25] also as an idempotent,[19] self-similar[26] MLS. Without restriction on a specific initial state, a decimation factor of 2 or even 2^k will generally yield a phase-shifted MLS associated with the same PP,[18] with k being a positive integer. Recently, Xiang *et al.*[26] described an algorithm for determining the initial state according to Gold.[25] The self-similar, characteristic MLS substantiated in terms of this invariant decimation have found applications in ultrasonic measurement techniques.[26] They are also of practical significance for the technique proposed in this paper.

With some other proper decimation factors, decimation may yield distinctly different MLS generated by distinctly different PP of the same degree. This variant decimation property is worth mentioning together with reciprocal MLS pairs and their cross-correlation property in the following.

B. Primitive elements over GF(2^n) and trace orthogonal basis

A primitive polynomial (PP) $f(x) = \sum_{j=0}^{n} c_j x^j$ exactly expressing the feedback connections of the linear feedback shift register with its coefficients c_j over a finite field, called a Galois field GF(2), has a close connection with the elements of GF(2^n). Given a PP $f(x)$ of degree n, one can always find an element ν of GF(2^n) such that $f(\nu^{-1}) = 0$.[20] ν is a primitive element of GF(2^n) and so is ν^{-1}, namely $f(\nu) = 0$. The characteristic MLS has a close relation to the trace operator of an element α over GF(2^n).[20] The trace of an arbitrary element $\alpha \in \mathrm{GF}(2^n)$ is defined by

$$\mathrm{Tr}(\alpha) = \sum_{k=0}^{n-1} \alpha^{2^k}. \tag{1}$$

And a basis $\Omega = \{\omega_0, \omega_1, \ldots, \omega_{n-1}\}$ of GF(2^n) over GF(2) is termed the trace orthogonal basis (TOB) if

$$\mathrm{Tr}(\omega_i) = 1, \quad \omega_i \in \Omega \tag{2}$$

and

$$\mathrm{Tr}(\omega_i \omega_j) = 0, \quad \omega_i, \omega_j \in \Omega, \quad i \neq j. \tag{3}$$

A TOB can be considered as a special coordinate system containing n vectors $\omega_0, \omega_1, \ldots, \omega_{n-1}$ that are orthogonal to each other in a sense of the trace operator. The practical significance of a TOB for GF(2^n) lies in the fact that an arbitrary element $\nu^i \in \mathrm{GF}(2^n) - \{0\}$ can be represented by an n-tuple binary number $\{e_{i0}, e_{i1}, \ldots, e_{i(n-1)}\}$ (see Ref. 7 for more details) as

$$\nu^i = \sum_{j=0}^{n-1} e_{ij} \omega_j; \quad 0 \leq i < L \tag{4}$$

and

$$\mathrm{Tr}(\nu^i \nu^j) = \sum_{k=0}^{n-1} e_{ik} e_{jk}, \tag{5}$$

with

$$e_{ij} = \mathrm{Tr}(\nu^i \omega_j) \in \mathrm{GF}(2). \tag{6}$$

Equations (4)–(6) will be useful for the derivation in Sec. IV.

C. Reciprocal MLS and polynomials

If $\{a_i\}$ is a MLS of length $L = 2^n - 1$ generated by $f(x)$, one can derive another $\{b_i\}$ of the same degree in terms of simply reverting the sequence with

$$b_i = a_{-i}. \tag{7}$$

$\{b_i\}$ is then generated by a primitive polynomial $r(x)$ derived by simply reverting the given PP $f(x)$ of degree n:

$$r(x) = x^n f(x^{-1}). \tag{8}$$

$r(x)$ is termed the reciprocal polynomial of $f(x)$. The MLS $\{b_i\}$ generated by $r(x)$ is termed reciprocal MLS of $\{a_i\}$. A pair of reciprocal PP $f(x)$, $r(x)$ always associate with a reciprocal pair of characteristic MLS $\{a_i\}$, $\{b_i\}$, respectively. In addition, if ν is a primitive element of $f(x)$ such that $f(\nu^{-1}) = 0$, then ν^{-1} is a primitive element of $r(x)$ such that $r(\nu) = 0$.[7]

A reciprocal MLS $\{b_i\}$ of $\{a_i\}$ can also be derived from the given $\{a_i\}$ in terms of decimation with a factor of $q = L - 1$. In effect, $b_i = a_{qi} = a_{(L-1)i} = a_{-i}$, which is exactly Eq. (7) since the index operation is evaluated modulo L. If $\{a_i\}$ is a characteristic MLS, $\{b_i\}$ achieved using Eq. (7) is also a characteristic MLS. The cross-correlation function of the reciprocal MLS pairs is of practical significance for the technique being discussed in the following.

D. Correlation property of MLS

MLS are periodic pseudorandom signals. The normalized periodic autocorrelation function (PACF) of a bipolar MLS within one period is a two-valued function[4] with

$$\phi(i) = \frac{L+1}{L} \delta(i) - \frac{1}{L}; \quad 0 \leq i < L. \tag{9}$$

When the period length $L = 2^n - 1$ is large enough, the PACF of MLS approximates a unit-sample sequence:

$$\phi(i) \approx \delta(i); \quad 0 \leq i < L. \tag{10}$$

From its PACF, it is readily deduced that its power spectral density function is of broadband nature and covers the entire frequency range (except for the zero frequency). It is this well-known property of MLS that has been exploited in most applications. Figure 1(a) illustrates the normalized PACF of a MLS of degree 12 for one period.

Cross-correlation properties of MLS are considerably less widely known, particularly in the acoustics community. Cross-correlation means correlation of one bipolar MLS with another of the same degree. There exists a number of MLS pairs for which their periodic cross-correlation functions (PCCF) possess considerably smaller values in comparison to the peak value of their two-valued PACF. Golomb[18] has observed that if $\{a_i\}$ and $\{b_i\}$ are generated by different PPs, then the PCCF ϕ_{ab} takes on at least three values. An appropriate decimation of MLS will yield pairs of MLS having a relatively small three-valued PCCF. The small valued PCCF depends only on the decimation factor rather than upon individual MLS. These three-valued PCCF of MLS pairs have gained considerable attention due to their (relatively) small magnitude in spread spectrum communication systems.[22] They are termed preferred pairs of MLS.[23] In addition to the preferred three-valued PCCF, there also exist four-valued PCCFs for specific classes of MLS.[22] They are even slightly better than the three-valued pairs with respect to the small magnitude. This paper will refer to both the three-valued and four-valued MLS pairs as preferred pairs. Appropriate decimation factors leading to the preferred MLS pairs are well documented and can be found in Refs. 22–23.

The most significant feature in this context is that the cross-correlation of the reciprocal MLS pairs also have small values being close to those of three-valued MLS pairs, yet not limited to three values.[22] The normalized cross-correlation bound $l(n)$ of the reciprocal MLS pairs is dependent upon the degree n:[22,24]

$$l(n)=\frac{2^{(n+2)/2}-1}{2^n-1}. \tag{11}$$

For the applications exploiting the small peak cross-correlation properties, one should not necessarily insist on having three- or four-valued PCCF. Figures 1(b) and 1(c) illustrate the normalized PCCF of a reciprocal MLS pair with a degree of 12 for one period. For convenience of comparison, the PACF of one of MLS is also illustrated in Fig. 1(a). Table I lists the peak cross-correlation values for degree 8–24 achieved by calculating the peak cross-correlation between these reciprocal MLS pairs compared with the cross-correlation bound values $l(n)$ predicted using Eq. (11).

III. FAST MLS TRANSFORM

Applying a periodic bipolar MLS $\{m_i\}$ to a linear time-invariant system under test and receiving one period of the system response **Y** to the MLS after the system arrives at its steady state, its impulse response **h** can predominantly be determined in terms of cross-correlation between the excitation MLS and the system response to the MLS[1,7] by

$$\mathbf{h}=\mathbf{MY}, \tag{12}$$

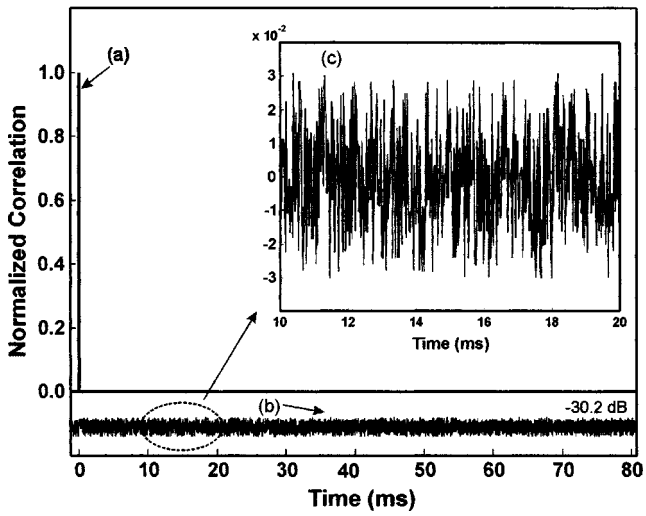

FIG. 1. Correlation functions of a MLS of degree 12 generated at sampling frequency of 50 kHz. (a) Autocorrelation function. (b) Cross-correlation function between the reciprocal MLS pair (shifted downward beneath the autocorrelation function for a convenient comparison while keeping the same amplitude scale). The peak value of the cross-correlation amounts to 0.03, 30.2 dB lower than the peak value of the autocorrelation. (c) A zoomed presentation of a segment from (b).

where **h**, **Y** are vectors of L elements. **M** represents the MLS matrix of dimension $L\times L$, its rows contain sequentially right-cyclically shifted MLS $\{m_i\}$:

$$\mathbf{M}=[M_{ij}]=[m_{j-i}]; \quad i,j=0,1,...,L-1. \tag{13}$$

Equation (12) is termed the *M sequence (MLS) transform*. Taking a bipolar $\{m_i\}$ of degree 3 as an example $\{m_i\}=\{-1,-1,-1,+1,-1,+1,+1\}$ and using its binary version $\{a_i\}$ for the MLS matrix, the binary MLS matrix **A** (binary version of **M**) becomes

TABLE I. Cross-correlation bound values $l(n)$ [Eq. (11)] and normalized peak cross-correlation values of reciprocal MLS pairs achieved experimentally by performing the fast MLS transform of reciprocal MLS.

Degree	Period length	Cross-correlation bound [Eq. (11)]	Peak cross-correlation
8	255	0.1216	0.1216
9	511	0.0881	0.090
10	1023	0.0616	0.061
11	2047	0.0437	0.043
12	4095	0.0310	0.0308
13	8191	2.198E-2	0.0222
14	14 383	1.557E-2	0.0155
15	32 767	1.012E-2	1.013E-3
16	65 535	7.797E-3	7.78E-3
17	131 071	5.517E-3	5.51E-3
18	262 143	3.903E-3	3.90E-3
19	524 287	2.760E-3	2.76E-3
20	1 048 575	1.952E-3	1.95E-3
21	2 097 151	1.381E-3	1.38E-3
22	4 194 303	9.763E-4	9.76E-4
23	8 388 607	6.904E-4	6.90E-4
24	16 777 215	4.882E-4	4.88E-4

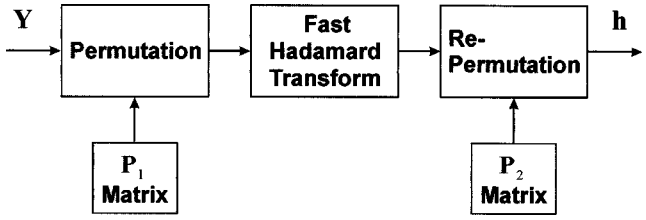

FIG. 2. Flow diagram of the Fast MLS Transform algorithm. A system response **Y** to the MLS undergoes permutation, Fast Hadamard Transform and repermutation, yielding the impulse response **h** directly in the time domain. In general, the algorithm requires two permutation matrices from the given MLS.

$$\mathbf{A}=[A_{ij}]=[a_{j-i}]=\begin{bmatrix}1&1&1&0&1&0&0\\0&1&1&1&0&1&0\\0&0&1&1&1&0&1\\1&0&0&1&1&1&0\\0&1&0&0&1&1&1\\1&0&1&0&0&1&1\\1&1&0&1&0&0&1\end{bmatrix}. \quad (14)$$

The MLS matrix in Eq. (13) is permutationally similar to Hadamard matrix:[23,27]

$$\mathbf{M}=\mathbf{P_2}\mathbf{H}\mathbf{P_1}, \quad (15)$$

where **H** is a Hadamard matrix of Sylvester-type. $\mathbf{P_1}$, $\mathbf{P_2}$ denote the permutation and the repermutation matrix, respectively. Equation (15) implies a fast algorithm, referred to as *Fast MLS Transform* (FMT) by Cohn and Lempel,[1] since the fast Hadamard transform for Hadamard matrix **H** is adopted in the calculation. Figure 2 illustrates a flow diagram for the FMT. It consists of three major steps.

(1) Permutation of the system response **Y** to the MLS being used as excitation of the system under test $(\mathbf{P_1Y})$.
(2) Fast Hadamard transform of the permuted vector $(\mathbf{H}(\mathbf{P_1Y}))$.
(3) Repermutation of the transformed vector $(\mathbf{P_2}[\mathbf{H}(\mathbf{P_1Y})])$.

An impulse response **h** results directly in the time domain right after the repermutation, except for a scale factor.[7]

Generally two permutation matrices are required by the fast MLS transform, as indicated in Eq. (15) and Fig. 2 (see, among others, Refs. 1, 4, 28). The two permutation matrices are derived from the MLS being used for the excitation signal. They are usually stored in form of indices.[7] Since the fast MLS transform performs inherently the cross-correlation between the MLS itself and the system response to the MLS, the two permutation matrices together can be considered as the original binary MLS in index form. In the following section we briefly describe an approach to construct the permutation matrices from the characteristic MLS. It yields one single permutation matrix that can be used at the same time for a pair of two reciprocal MLS.

IV. PERMUTATION MATRIX OF RECIPROCAL MLS PAIR

If $\{a_i\}$ is a characteristic MLS of degree n generated by a PP $f(x)$ and ν is a primitive element over GF(2^n), which satisfies $f(\nu^{-1})=0$, then the MLS matrix **A** can be factored using Eqs. (4)–(6) in terms of the trace operator and the TOB[7] as

$$\begin{aligned}\mathbf{A}=[A_{ij}]=[a_{j-i}]&=[\mathrm{Tr}(\nu^{-i}\nu^{j})]\\&=\left[\sum_{k=0}^{n-1}e_{(-i)k}e_{jk}\right]\\&=\mathbf{E}_2\mathbf{E}_1;\quad i,j=0,1,...,L-1.\end{aligned} \quad (16)$$

A close investigation of Eq. (16) reveals that $\mathbf{E}_1$, $\mathbf{E}_2$ are of a similar structure in such a way that the rows of $\mathbf{E}_2$ can be found in the columns of $\mathbf{E}_1$ in the reversed order except for the first row and the first column. Taking the previous MLS of degree 3 in Eq. (14) as an example, $\mathbf{E}_1$ and $\mathbf{E}_2$ become

$$\mathbf{E}_1=\begin{bmatrix}1&1&0&1&0&0&1\\1&0&1&0&0&1&1\\1&0&0&1&1&1&0\end{bmatrix} \quad (17)$$

and

$$\mathbf{E}_2^T=\begin{bmatrix}1&1&0&0&1&0&1\\1&1&1&0&0&1&0\\1&0&1&1&1&0&0\end{bmatrix}, \quad (18)$$

where T stands for transpose of a matrix. Readers can easily verify that $\mathbf{E}_2\mathbf{E}_1$ results in the binary MLS matrix **A** in Eq. (14). Matrices $\mathbf{E}_1$, $\mathbf{E}_2$ lead straightforwardly to permutation matrices $\mathbf{P}_1$, $\mathbf{P}_2$, which can be expressed in index form by converting each binary column in Eqs. (17)–(18) into a decimal number with the top row containing the insignificant bit:[7]

$$\mathbf{P}_1=(7,1,2,5,4,6,3)_{\mathrm{index}} \quad (19)$$

and

$$\mathbf{P}_2=(7,3,6,4,5,2,1)_{\mathrm{index}}. \quad (20)$$

A detailed calculation of $\mathbf{P}_1$ can be found in Refs. 3, 7. In a practical implementation, once the permutation indices $\mathbf{P}_1$ is calculated from the given MLS, the repermutation (requiring $\mathbf{P}_2$) needs to take the indices from $\mathbf{P}_1$ in the reversed order, except for the first index while the permutation takes the indices in its sequential order. The FMT using this approach is illustrated in Fig. 3, where only one permutation matrix is required.

For a given PP $f(x)$, its reciprocal MLS $\{b_i\}$ of $\{a_i\}$ is generated by its reciprocal PP $r(x)=x^n f(x^{-1})$. If ν^{-1} satisfies $f(\nu^{-1})=0$, so does $(\nu^{-1})^{-1}$ satisfy $r[(\nu^{-1})^{-1}]=0$. In a similar fashion, the reciprocal MLS matrix **B** can be factored using Eqs. (4)–(6) as[7]

$$\begin{aligned}\mathbf{B}=[b_{j-i}]&=[\mathrm{Tr}((\nu^{-1})^{j-i})]\\&=[\mathrm{Tr}(\nu^{-j}\nu^{i})]=\left[\sum_{k=0}^{n-1}e_{ik}e_{(-j)k}\right]=\mathbf{G}_2\mathbf{G}_1.\end{aligned} \quad (21)$$

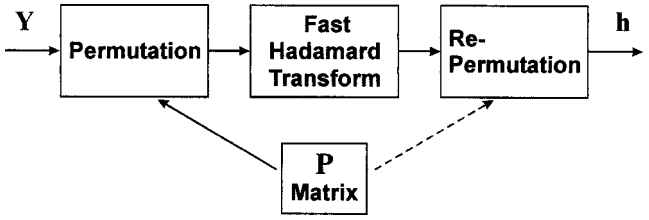

FIG. 3. Flow diagram of the Fast MLS Transform algorithm of a characteristic MLS. The algorithm requires only one permutation matrix. The dashed-line arrow from the permutation matrix to the repermutation implies that the repermutation takes the permutation indices in a reversed order while the permutation just takes its sequential order (solid arrow).

A close comparison of Eq. (21) with Eq. (16) reveals that $\mathbf{G}_1^T=\mathbf{E}_2$ and $\mathbf{G}_2=\mathbf{E}_1^T$, since the primitive element ν in Eq. (21) is the same as that in Eq. (16). This implies that the FMT for the reciprocal MLS $\{b_i\}$ uses the same single permutation matrix. Figure 4 shows the flow diagram of the FMT pair if the reciprocal MLS pair comes into practical applications that we elaborate on in the following section.

V. APPLICATIONS

In a variety of acoustical applications, a system under test can contain multiple sound/vibration sources and receivers, such as a listening situation in auditoria,[29] where, e.g., multiple loudspeakers of a sound system operate, or a number of musical instruments are played at the same time on the stage. Moreover, some impulse response-related system identification tasks with multiple sources have to be accomplished in a limited time period.[30,31] A simultaneous source measurement technique is especially needed.

A. Principle of simultaneous measurements

A system schematically illustrated in Fig. 5 is suitable for modeling the system identification tasks with multiple sources. In the figure, S_i denotes the ith source signal in the time domain while R_j denotes the jth receiver signal in the

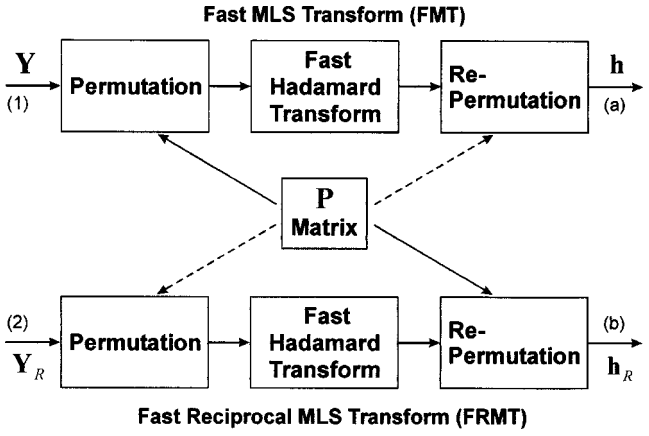

FIG. 4. Flow diagram of the Fast MLS Transform pair. The algorithms require only one permutation matrix for both the fast MLS transform (FMT) and the fast reciprocal MLS transform (FRMT). The dashed-line arrows from the permutation matrix to the permutation or repermutation imply that these permutations take the permutation indices in a reversed order while the other permutations just take their sequential order (solid arrows).

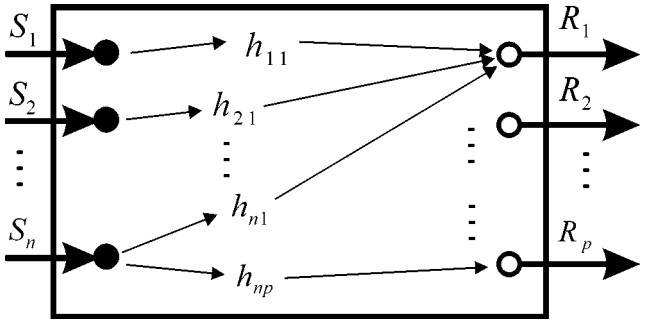

FIG. 5. System-theoretical model of a multisource and multireceiver system. All together, $n\times p$ impulse responses h_{ij} are defined between n sources and p receivers.

time domain. h_{ij} stands for an impulse response defined between the ith source and the jth receiver of a linear system.

In the presence of all source signals as required by simultaneous source channel measurements, the jth receiver yields an output signal:

$$R_j(t)=\sum_{k=1}^{n} S_k(t)*h_{kj}(t); \quad j=1,...,p, \tag{22}$$

where "*" stands for the linear convolution, assuming that the system under test can be considered as a linear time-invariant system. A cross-correlation between the ith source signal and the jth receiver signal reads as

$$S_i(t)\otimes R_j(t)=\sum_{k=1}^{n} \phi_{ik}(t)*h_{kj}(t); \quad i=1,...,n; \quad j=1,...,p, \tag{23}$$

where $\otimes$ stands for linear cross-correlation and $\phi_{ik}(t)=S_i(t)\otimes S_k(t)$ for cross-correlation between the ith and kth source signal.

For experimentally determining the impulse responses, the following PCCF of excitation signals is desirable:

$$\phi_{ik}(t)=\begin{cases}\delta(t), & \text{for } i=k,\\ 0, & \text{for } i\neq k,\end{cases} \tag{24}$$

since inserting Eq. (24) into Eq. (23) yields

$$h_{ij}(t)=S_i(t)\otimes R_j(t); \quad i=1,...,n; \quad j=1,...,p. \tag{25}$$

Equation (25) indicates that the impulse response between the ith source and the jth receiver could conveniently be determined if the simultaneous excitation signals would possess the property expressed in Eq. (24), namely, their PACF would be a unit-sample sequence while their PCCF would equal zero. Lüke[23] pointed out that signals with exactly such a cross-correlation property can neither exist nor be constructed. Fortunately, some special classes of binary MLS are most suitable candidates for the discussed tasks due to the following two reasons.

First, the cross-correlation of reciprocal and preferred pairs of binary MLS discussed in Sec. II B approximates the desired condition in Eq. (24). As expressed both in Eqs. (10) and (11), illustrated in Fig. 1 and listed in Table I, the longer the sequences are to be used, the smaller the peak cross-correlation value becomes and the closer their cross-

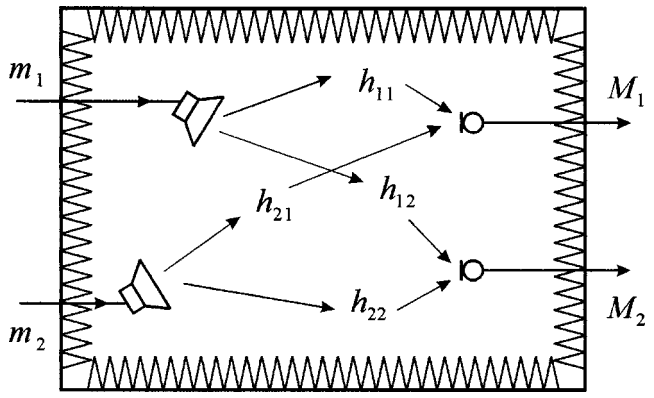

FIG. 6. Simultaneous acoustical measurement undertaken in an anechoic chamber with two sound sources and two microphones.

correlation approximate the condition in Eq. (24). Second, the FMT described in Sec. III can accomplish the operation expressed in Eq. (25) with high computational efficiency, particularly using the fast reciprocal MLS transform pair, as discussed in Sec. IV, two MLS (reciprocal pair) need only a single permutation matrix.

B. Experimental results

An exploratory experiment was carried out in an anechoic chamber, as schematically illustrated in Fig. 6, when a reciprocal MLS pair (m_1, m_2) excited two sound sources simultaneously. Each MLS of degree 13 at a sampling frequency of 30 kHz excited one sound source, respectively. Two microphones received one period of responses (M_1, M_2) to the MLS excitations after the system arrived at the steady state. Each microphone signal was then fed into input labeled by (1) of the FMT illustrated in Fig. 4 and then into the input labeled by (2) of the FRMT, respectively.

Since each microphone signal contained a linear combination of responses to the individual MLS from each sound source and the FMT pair performed the cross-correlation of each MLS to the microphone signal, the FMT [from input (1) to output (a) in Fig. 4] approximately filtered out the impulse response h_{11} and suppressed the component $m_2 * h_{21}$ with microphone signal M_1 feeding into the input labeled by (1) of the FMT. And the FRMT [from input (2) to output (b)] approximately filtered out the impulse response h_{21} and suppressed the component $m_1 * h_{11}$ with microphone signal M_1 feeding into the input labeled by (2) of the FRMT. One permutation matrix was determined using the given MLS of degree 13 for the pair of FMT and FRMT. In a similar fashion, when feeding microphone signal M_2, in turn, into the input labeled by (1) of the FMT and then into the input labeled by (2) of the FRMT, the FMT pair (in Fig. 4) approximately yielded h_{12} and h_{22}. Figure 7 shows the first 16 ms segments of four impulse responses. The peak-to-noise ratio of 30–31 dB was achieved for all four impulse responses, about 2–3 dB less than the peak cross-correlation value listed in Table I (for degree 13). A single-excitation impulse response with a peak-to-noise ratio of 53 dB, corresponding to h_{12}, but achieved from a single loudspeaker-microphone measurement using an M sequence of degree 13 is also plotted in Fig. 7 for comparison. This measurement

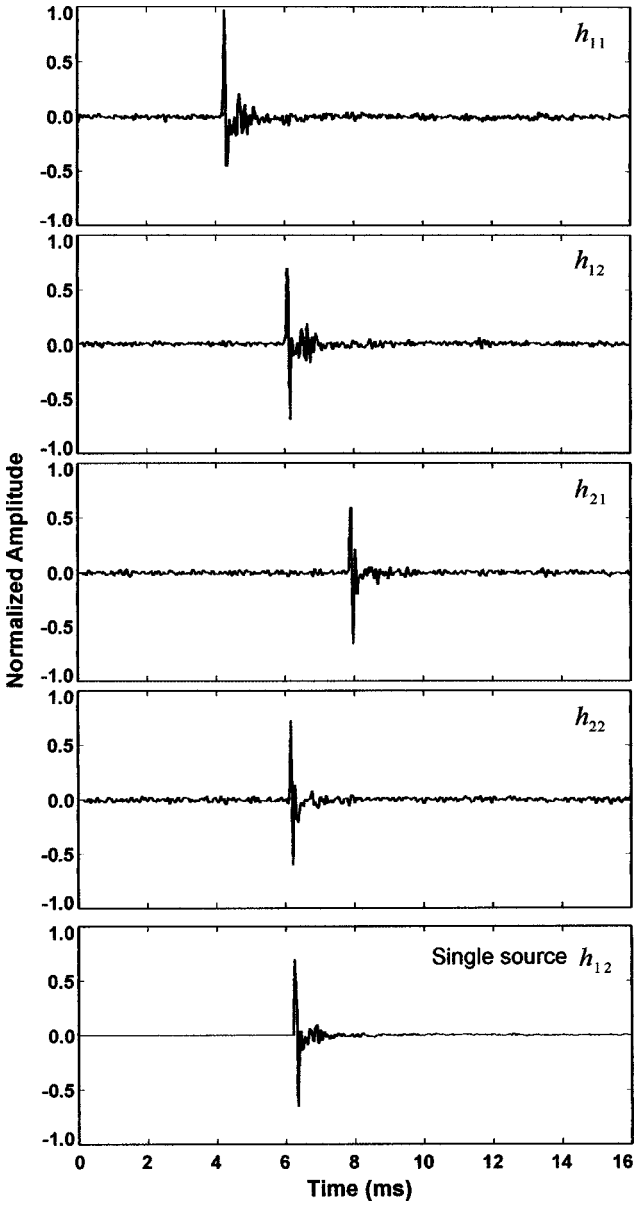

FIG. 7. Segments of impulse responses simultaneously measured in an anechoic chamber using a reciprocal MLS pair of degree 13 as excitation signals at the two (loudspeaker) source channels, respectively. Each of two microphone signals is, in turn, fed into two inputs of the FMT pair (illustrated in Fig. 4) yielding four impulse responses (h_{11}, h_{12}, h_{21}, and h_{22}). A single-source impulse response, corresponding to h_{12}, but achieved from a single loudspeaker-microphone measurement is also plotted for a comparison.

technique can be used, among others, for the study of outdoor sound propagation, as required by the experimental study in Refs. 30–31.

Another example is a simultaneous measurement of room impulse responses carried out in an auditorium (in the National Center for Physical Acoustics, The University of Mississippi) with a stereo sound system. The measurement setup is similar to the sketch in Fig. 6 but in the auditorium. A reciprocal MLS pair of degree 20, at a sampling frequency of 50 kHz, drove the pair of loudspeakers, respectively, and two microphones received one period of the responses to the simultaneous MLS excitations from both stereo loudspeakers. One permutation matrix was determined using the given

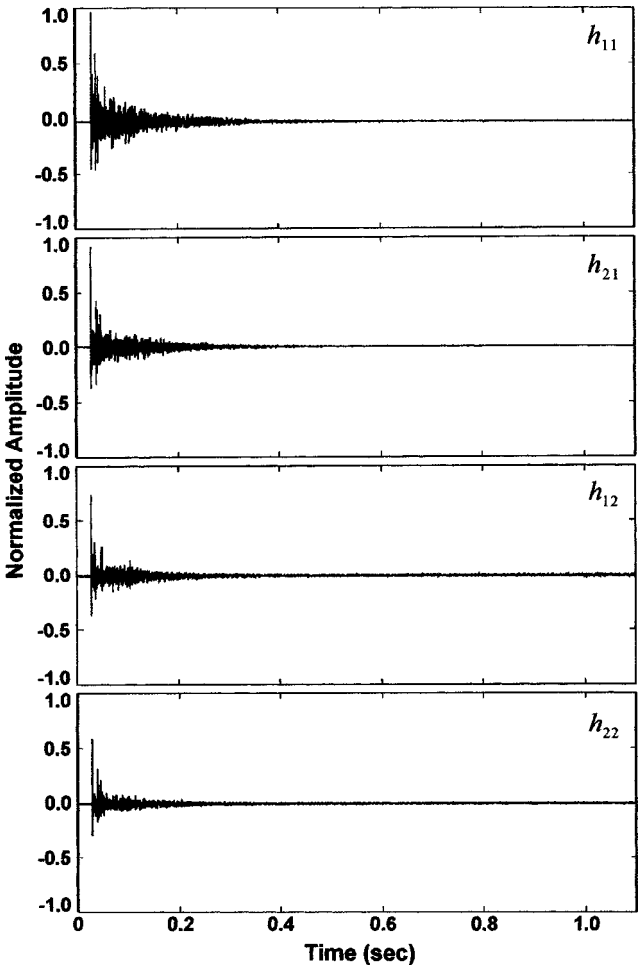

FIG. 8. Segments of room impulse responses simultaneously measured in an auditorium using a reciprocal MLS pair of degree 20 as excitation signals driving two stereo loudspeakers of a sound system, respectively. Two microphones are used for the sound receivers. Each of two microphone signals is, in turn, fed into two inputs of the FMT pair (illustrated in Fig. 4) yielding four room impulse responses (h_{11}, h_{12}, h_{21}, and h_{22}).

MLS of degree 20 for the FMT pair. Each of the two microphone signals was, in turn, fed into each input of the FMT pair, resolving two pairs of room impulse responses, as illustrated in Fig. 8. In Fig. 8, the first 1.1 s long segments of four room impulse responses are shown, the peak-to-noise ratio ranges between 42–50 dB.

C. Discussion

The peak-to-noise (P/N) ratios achieved in the two examples discussed previously can be further improved if an even longer reciprocal MLS pair can be used. The maximum achievable P/N ratio is restricted by the peak cross-correlation value of reciprocal MLS pairs listed in Table I. The PCCF between two reciprocal MLS pairs as shown in Fig. 1(b) is of a deterministic nature given the reciprocal MLS pair. Therefore, additional averages cannot significantly improve the P/N ratios if other kinds of random noise are in the measurement environment. For this reason, additional averages are not relevant for a P/N ratio improvement. Particularly, the technique employing reciprocal and preferred MLS pairs, as discussed in this paper is of practical significance especially for the simultaneous source channel measurement; a limited measurement time period is often critical in specific applications.

The separation of individual impulse responses from individual simultaneous sources is due to the excellent cross-correlation properties of reciprocal and preferred MLS pairs. The separation at the receiving ends, however, is not a big concern at all, since individual receiving channels inherently possess the separation ability. Increasing the number of receiving channels does not significantly influence the figure of achievable P/N ratio in the measured impulse responses, but increasing the number of simultaneous source channels does. Generally one more source channel leads to at least 3 dB degradation of achievable P/N ratio depending on the MLS selected.

More preferred MLS pairs need to be added to the simultaneous mode if a specific application requires more source channels given the limited measurement period. Some MLS-related sequences[22] can be employed if the number of available preferred MLS pairs cannot meet the need.

VI. CONCLUSION

The two-valued autocorrelation function of binary maximum-length sequences (MLS) has long been exploited for various applications, while considerably less attention has been given to the excellent cross-correlation property of binary MLS, particularly of reciprocal MLS. The cross-correlation function between a pair of reciprocal MLS exhibits relatively smaller values than the peak value of their autocorrelation function. It is this excellent property that makes the simultaneous dual-source measurements feasible. The measurement technique simultaneously obtains impulse responses of an acoustical system under test with two separate sound sources and one or several receivers with each of the reciprocal MLS pair exciting each of dual source channels. The impulse response measurements are based on a fast cross-correlation technique called the Fast MLS Transform. In this paper we have proposed the fast reciprocal MLS transform (FRMT) pair. The efficiency of the FRMT pair lies both in exploitation of the fast Hadamard transform algorithm and in the requirement of a single permutation matrix. In addition to the cross-correlation property, in this paper we have applied some fundamental properties of the binary MLS for a derivation of the permutation matrix from the MLS pair, including decimations, characteristic MLS, trace operations, and a trace orthogonal basis. The principle of the simultaneous dual source measurements is discussed and the efficient technique and potential acoustical applications have been demonstrated using exploratory experimental results. The technique proposed in this paper is especially of practical significance when impulse responses of acoustical systems with multiple sources and receivers have to be determined in a limited time period.

ACKNOWLEDGMENTS

The unremitting interest and support from Professor Dr. Jens Blauert have been driving the authors to continue this endeavor. The authors owe many thanks to Professor Dr.

Hans Lüke for his valuable advice and inspiration. The authors also wish to express their gratitude to Dr. H. Bass, Dr. R. Raspet, and Dr. J. M. Sabatier, who supported this work with enthusiasm. Ch. Sabatier carried out a number of experiments, some results of which have been discussed in this paper. The work was partially supported by the Deutsche Forschungsgemeinschaft.

[1] M. Cohn and A. Lempel, ''On fast M-sequences transforms,'' IEEE Trans. Inf. Theory **23**, 135–137 (1977).
[2] M. R. Schroeder, ''Integrated-impulse method measuring sound decay without using impulses,'' J. Acoust. Soc. Am. **66**, 497–500 (1979).
[3] H. Alrutz and M. R. Schroeder, ''A fast Hadamard transform algorithm for the evaluation of measurements using pseudorandom test signals,'' *Proceedings of the 11th Conference on Acoustics*, Paris, 1983, pp. 235–238.
[4] J. Borish and J. B. Angell, ''An efficient algorithm measuring the impulse response using pseudorandom noise,'' J. Audio Eng. Soc. **31**, 478–488 (1983).
[5] W. T. Chu, ''Impulse-response and reverberation-decay measurements made by using a periodic pseudorandom sequence,'' Appl. Acoust. **29**, 193–205 (1990).
[6] W. Zuomin and W. T. Chu, ''Ensemble average requirement for acoustical measurements in noisy environment using an M-sequence correlation technique,'' J. Acoust. Soc. Am. **94**, 1409–1414 (1993).
[7] N. Xiang, ''Using M-sequences for determining the impulse responses of LTI-systems,'' Signal Process. **28**, 139–152 (1992).
[8] U. Eysholdt and C. E. Schreiner, ''Maximum-length sequences—a fast method for measuring brain-stem evoked responses,'' Audiology **21**, 242–250 (1982).
[9] R. Burkard, Y. Shi, and K. E. Hecox, ''A comparison of maximum length and Legendre sequences for the derivation of brain-stem auditory-evoked responses at rapid rates of stimulation,'' J. Acoust. Soc. Am. **87**, 1656–1664 (1990).
[10] T. Schneider and D. G. Jamieson, ''A dual-channel MLS-based test system for hearing–aid characterization,'' J. Audio Eng. Soc. **41**, 583–594 (1993).
[11] M. Pollakowski, N. Xiang, and H. Ermet, ''Ultrasonic attenuation measurements using the fast maximum-length sequences transform algorithm,'' *Proceedings of the 14th ICA*, Beijing, 1992, pp. L7-2.
[12] E. Mommertz and G. Bayer, ''PC-based high frequency range M-sequence measurements using an interleaved sampling method,'' Acustica **81**, 80–83 (1995).
[13] A. Schmitz and M. Vorländer, ''Messung von Aussenohrstoßantworten mit Maximalfolgen–Hadamard-Transformation und deren anwendung bei inversions-versuchen,'' Acustica **71**, 257–268 (1990).
[14] K. Genuit and N. Xiang, ''Measurements of artificial head transfer functions for auralization and virtual auditory environment,'' *Proceedings of the 15th ICA*, Trondheim, 1995, Vol. II, pp. 469–472.
[15] H. DeFerrari and T. Birdsall, ''The application of M-sequences to sonar,'' J. Acoust. Soc. Am. **109**, 2418 (2001).
[16] M. Garai, ''Measurement of the sound-absorption coefficient *in-situ*: The reflection method using periodic pseudo-random sequences of maximum length,'' Appl. Acoust. **39**, 119–139 (1993).
[17] N. Xiang and J. M. Sabatier, ''Fast M-sequence transform for laser-Doppler based mine detection,'' *Proceedings of the SPIE Conference Signal Processing, Sensor Fusion and Target Recognition VIII*, edited by I. Kadar, 1999, Vol. 3270, pp. 390–396.
[18] S. W. Golomb, *Shift Register Sequences* (Aegean Park Press, Laguna, CA, 1982).
[19] M. R. Schroeder, *Number Theory in Science and Communication*, 2nd enl. ed. (Springer-Verlag, Berlin, 1991).
[20] A. Lempel, ''Matrix factorization over GF(2) and trace-orthogonal bases of $GF(2^n)$,'' SIAM J. Comput. **4**, 175–186 (1975).
[21] F. J. MacWilliams and N. J. Sloane, ''Pseudo-random sequences and arrays,'' Proc. IEEE **64**, 1715–1729 (1976).
[22] D. V. Sarwate and M. B. Pursley, ''Crosscorrelation properties of pseudo-random and related sequences,'' Proc. IEEE **68**, 593–619 (1980).
[23] H. D. Lüke, *Korrelationssignale* (Springer-Verlag, Berlin, 1992).
[24] T. A. Dowling and R. McEliece, ''Cross-correlation of reverse maximal-length shift register sequences,'' *SPL Space Programs Summary*, 1968, Vol. III, pp. 37–53, 192–193.
[25] R. Gold, ''Characteristic linear sequences and their coset functions,'' SIAM (Soc. Ind. Appl. Math.) J. Appl. Math. **14**, 980–985 (1966).
[26] N. Xiang and K. Genuit, ''Characteristic maximum-length sequences for the interleaved sampling method,'' Acust. Acta Acust. **82**, 905–907 (1996).
[27] A. Lempel, ''Hadamard and M-sequence transforms are permutationally similar,'' Appl. Opt. **18**, 4064–4065 (1979).
[28] E. E. Sutter, ''The fast m-transform: A fast computation of cross-correlations with binary m-sequences,'' SIAM J. Comput. **20**, 686–694 (1991).
[29] N. Xiang and J. Blauert, ''Binaural scale modeling for auralisation and prediction of acoustics in auditoria,'' Appl. Acoust. **38**, 267–290 (1993).
[30] D. K. Wilson, A. Ziemann, V. E. Ostashev, and A. G. Voronovich, ''An overview of acoustic travel-time tomography in the atmosphere and its potential applications,'' Acust. Acta Acust. **87**, 721–730 (2001).
[31] A. Ziemann, K. Arnold, and A. Raabe, ''Acoustic tomography as a method to identify small-scale land surface characteristics,'' Acust. Acta Acust. **87**, 731–737 (2001).

Stimulus-frequency-emission group delay: A test of coherent reflection filtering and a window on cochlear tuning

Christopher A. Shera[a] and John J. Guinan, Jr.
Eaton-Peabody Laboratory of Auditory Physiology, Massachusetts Eye and Ear Infirmary, 243 Charles Street, Boston, Massachusetts 02114 and Department of Otology and Laryngology, Harvard Medical School, Boston, Massachusetts 02115

(Received 4 October 2002; accepted for publication 13 January 2003)

This paper tests and applies a key prediction of the theory of coherent reflection filtering for the generation of reflection-source otoacoustic emissions. The theory predicts that reflection-source-emission group delay is determined by the group delay of the basilar-membrane (BM) transfer function at its peak. This prediction is tested over a seven-octave frequency range in cats and guinea pigs using measurements of stimulus-frequency-emission (SFOAE) group delay. A comparison with group delays calculated from published measurements of BM mechanical transfer functions supports the theory at the basal end of the cochlea. A comparison across the whole frequency range based on variations in the sharpness of neural tuning with characteristic frequency (CF) suggests that the predicted relation holds in the basal-most 60% of the cochlea. At the apical end of the cochlea, however, the measurements disagree with neural and mechanical group delays. This disagreement suggests that there are important differences in cochlear mechanics and/or mechanisms of emission generation between the base and apex of the cochlea. Measurements in humans over a four-octave range indicate that human SFOAE group delays are roughly a factor of 3 longer than their counterparts in cat and guinea pig but manifest similar trends across CF. The measurements thus reveal global deviations from scaling whose form appears quantitatively similar in all three species. Interpreted using the theory of coherent reflection filtering, the group delay measurements indicate that the wavelength at the peak of the traveling wave decreases with increasing CF at a rate of roughly 25% per octave in the base of the cochlea. The measurements and analysis reported here illustrate the rich potential inherent in OAE measurements for obtaining valuable information about basic cochlear properties such as tuning. [DOI: 10.1121/1.1557211]

PACS numbers: 43.64.Bt, 43.64.Kc, 43.64.Jb [LHC]

I. INTRODUCTION

The theory of coherent reflection filtering (Shera and Zweig, 1993b; Zweig and Shera, 1995) relates ear-canal otoacoustic measurements to the mechanical response of the organ of Corti, providing a quantitative theoretical foundation for the use of otoacoustic emissions as noninvasive probes of cochlear mechanics. The theory indicates that reflection-source otoacoustic emissions [such as stimulus-frequency emissions, or SFOAEs, evoked at low sound levels (Shera and Guinan, 1999)] arise via coherent reflection from densely and ''randomly'' distributed cochlear impedance perturbations. These perturbations may include spatial variations in outer-hair-cell (OHC) number and geometry (e.g., Engström *et al.*, 1966; Bredberg, 1968; Wright, 1984; Lonsbury-Martin *et al.*, 1988) and/or perturbations not clearly visible in conventional anatomical preparations, such as variations in OHC forces due to random, cell-to-cell variations in the number of somatic motor proteins.

Among the theory's many predictions and applications (e.g., Zweig and Shera, 1995; Talmadge *et al.*, 1998) is one of special relevance to the noninvasive measurement of cochlear tuning. Specifically, the theory predicts that reflection-source-emission group delay is determined by the group delay of the basilar-membrane (BM) mechanical transfer function at its peak. Since BM transfer functions at low levels manifest many of the characteristics of minimum-phase-shift filters (e.g., Zweig, 1976; de Boer, 1997), their bandwidths and phase slopes (i.e., group delays) are related, with sharper tuning corresponding to longer group delays. If the theory's prediction about reflection-source-emission group delay is correct, otoacoustic measurements can be used to provide a noninvasive measure of basilar-membrane group delay, and, hence, indirectly, of the frequency selectivity of cochlear tuning. In this paper we test the predicted relation between otoacoustic and BM group delays;[1] we apply these ideas to estimate the frequency selectivity of cochlear tuning in another publication (Shera *et al.*, 2002).

II. RELATING SFOAE AND BM GROUP DELAYS

The theory of coherent reflection filtering predicts that the SFOAE group delay, $\tau_{\mathrm{SFOAE}}(f)$, is approximately equal to twice the group delay of the basilar-membrane (BM) mechanical transfer function, evaluated at the cochlear location with CF equal to the stimulus frequency:

$$\tau_{\mathrm{SFOAE}}(f) \approx 2\,\hat{\tau}_{\mathrm{BM}}(f), \tag{1}$$

where $\hat{\tau}_{\mathrm{BM}}(f) = \tau_{\mathrm{BM}}[x_{\mathrm{CF}}(f), f]$. The factor of two arises be-

[a]Electronic mail: shera@epl.meei.harvard.edu

 0001-4966/2003/113(5)/2762/11/$19.00

cause reflection-source-emission group delay depends on round-trip wave travel. Derived in the next section,[2] Eq. (1) is the central relation about which the arguments of this paper revolve.

A. Computing the round-trip travel time

To derive Eq. (1) from the theory of coherent reflection filtering we approximate SFOAE group delay $\tau_{\mathrm{SFOAE}}(f)$ by the round-trip wave travel time $\tau_{\rightleftarrows}(x_{\mathrm{ref}},f)$ between the stapes and the region of reflection, assumed centered about an as yet unspecified point, $x_{\mathrm{ref}}(f)$. Since emissions at different frequencies may arise from different cochlear locations, we write $x_{\mathrm{ref}}(f)$ as an explicit function of frequency. The identification of emission group delay with cochlear round-trip travel times neglects contributions to $\tau_{\mathrm{SFOAE}}(f)$ introduced by eardrum transduction and subsequent transmission through the middle ear.[3] Measurements indicate that delays due to round-trip middle-ear transmission are small; in cat and gerbil they amount to approximately 50 μs, or only about 1 cycle at 20 kHz (Puria and Allen, 1998; Olson, 1998).

We compute the round-trip wave travel time by dividing the total distance into segments of length Δx and adding up the times required to traverse each segment. Taking the limit as $\Delta x \to 0$ yields the integral

$$\tau_{\mathrm{SFOAE}}(f) \approx \tau_{\rightleftarrows}[x_{\mathrm{ref}}(f),f] = 2\int_0^{x_{\mathrm{ref}}(f)} \frac{dx}{v(x,f)}, \tag{2}$$

where $v(x,f)$ is the group velocity at location x of waves of frequency f traveling along the cochlear spiral. The reciprocal of the group velocity is given by (e.g., Brillouin, 1946)

$$v^{-1} = \frac{1}{2\pi}\frac{\partial k}{\partial f}, \tag{3}$$

where the (real-valued) wavenumber $k(x,f)$ is 2π divided by the local wavelength [i.e., $2\pi/\lambda(x,f)$]. The wavenumber is related to the spatial derivative of the phase of the traveling wave through the equation

$$k(x,f) = -\frac{\partial \angle T}{\partial x}, \tag{4}$$

where $T(x,f)$ is the traveling wave at frequency f. Written in terms of its amplitude and phase, T has the form $T = |T|e^{i\angle T}$.

1. The region of reflection

According to the theory of coherent reflection filtering, reflection-source OAEs arise by reflection off densely and irregularly distributed cochlear impedance perturbations. At all frequencies the net backward-traveling wave is dominated by wavelets reflected within the region about the peak of the traveling wave, where the wave amplitude is much larger than it is elsewhere. The centroid of the scattering region, $x_{\mathrm{ref}}(f)$, is then the characteristic place for frequency f. In other words,

$$x_{\mathrm{ref}}(f) = x_{\mathrm{CF}}(f) \equiv \hat{x}(f), \tag{5}$$

where the diacritical hat denotes the peak of the traveling wave. Other models of reflection-source OAEs predict no such effective localization of the reflection to the region about the peak. For example, many models assume only sparse, isolated impedance discontinuities (e.g., Kemp, 1980, 1986; Zwicker, 1989); in such models reflection occurs at the site of the discontinuity, which coincides with the peak region only at certain frequencies. In other models, such as Strube's (1989), the perturbations are dense but quasi-sinusoidally distributed; reflection is then largely localized to the region where the wavelength of the traveling wave matches twice the spatial period of the assumed periodic distribution.

2. Finding the group delay

Combining Eqs. (2)–(5) yields

$$\tau_{\mathrm{SFOAE}}(f) \approx -2\int_0^{\hat{x}(f)} \frac{1}{2\pi}\frac{\partial}{\partial f}\frac{\partial \angle T}{\partial x}\,dx. \tag{6}$$

Continuity guarantees the equality of mixed partials (e.g., Apostol, 1969), so we interchange the order of differentiation in the integrand to obtain

$$\tau_{\mathrm{SFOAE}}(f) \approx -2\int_0^{\hat{x}(f)} \frac{\partial}{\partial x}\frac{1}{2\pi}\frac{\partial \angle T}{\partial f}\,dx$$

$$= 2\int_0^{\hat{x}(f)} \frac{\partial \tau_{\mathrm{BM}}}{\partial x}\,dx, \tag{7}$$

where we have used the definition of the traveling-wave group delay,

$$\tau_{\mathrm{BM}}(x,f) = -\frac{1}{2\pi}\frac{\partial \angle T}{\partial f}. \tag{8}$$

Evaluating the integral yields

$$\tau_{\mathrm{SFOAE}}(f) \approx 2\{\tau_{\mathrm{BM}}[\hat{x}(f),f)] - \tau_{\mathrm{BM}}(0,f)\}. \tag{9}$$

Since the wave speed slows considerably as it approaches the peak location (e.g., Lighthill, 1981), contributions to the travel time coming from the lower limit of integration can be neglected. We thus obtain the relation given above as Eq. (1):

$$\tau_{\mathrm{SFOAE}}(f) \approx 2\,\hat{\tau}_{\mathrm{BM}}(f), \tag{10}$$

where $\hat{\tau}_{\mathrm{BM}}(f) = \tau_{\mathrm{BM}}[\hat{x}(f),f]$.

In the above derivation we have regarded $T(x,f)$ as the traveling wave (i.e., as a function of x at fixed f). Local scaling symmetry implies that the same function $T(x,f)$ also represents the BM transfer function as a function of f at fixed x. Scaling therefore implies that empirical estimates of the traveling-wave group delay $\hat{\tau}_{\mathrm{BM}}(f)$ appearing in Eq. (1) can be obtained from measurements of the slope of the phase of BM transfer function near its peak.

III. MEASUREMENTS OF SFOAE GROUP DELAY IN THREE SPECIES

To test Eq. (1) we measured SFOAE phase over a seven-octave frequency range in two species widely used as models of mammalian hearing (cat and guinea pig). For comparison,

and for application to noninvasive estimates of cochlear tuning (cf. Shera *et al.*, 2002), we made measurements spanning four and a half octaves in humans.

A. Measurement methods

The methods and equipment used to measure SFOAEs were generally similar to those detailed previously (Shera and Guinan, 1999; Guinan, 1986). Briefly, we measured SFOAEs in guinea pigs ($n=9$) and humans ($n=9$) using a variant of the acoustic suppression method (Shera and Guinan, 1999) and in cats using either acoustic ($n=3$) or efferent ($n=5$) suppression (Guinan, 1986). In both methods, the emission is obtained as the complex (or vector) difference between the ear-canal pressure at the probe frequency measured first with the probe tone alone and then with the addition of a ''suppressor.'' The suppressor was either (1) an acoustic suppressor tone at a nearby frequency or (2) olivocochlear efferent stimulation via electrical shocks applied at the floor of the fourth ventricle. Both acoustic and efferent suppression are assumed to reduce the SFOAE at the probe frequency substantially. In all cases, probe level was approximately 40 dB SPL in the ear canal. Measurements were made versus probe frequency over at least a four-octave range with a frequency resolution sufficient to prevent ambiguities in phase unwrapping. Emission group delays, τ_{SFOAE}—defined as the negative slope of the emission-phase (in cycles) versus frequency function—were calculated from unwrapped phase responses using centered differences (e.g., Press *et al.*, 1992). Only group delays at frequencies where the emission amplitude was at least 15 dB above the measurement noise floor (typically -25 dB SPL) are included in the final data set. Since no significant differences between the delays measured using acoustic and efferent suppression were found, data from the two techniques were pooled. Details of animal care and preparation are discussed elsewhere (Guinan, 1986; Shera *et al.*, 2000). Treatment of animal and human subjects accorded with protocols established at the Massachusetts Eye and Ear Infirmary.

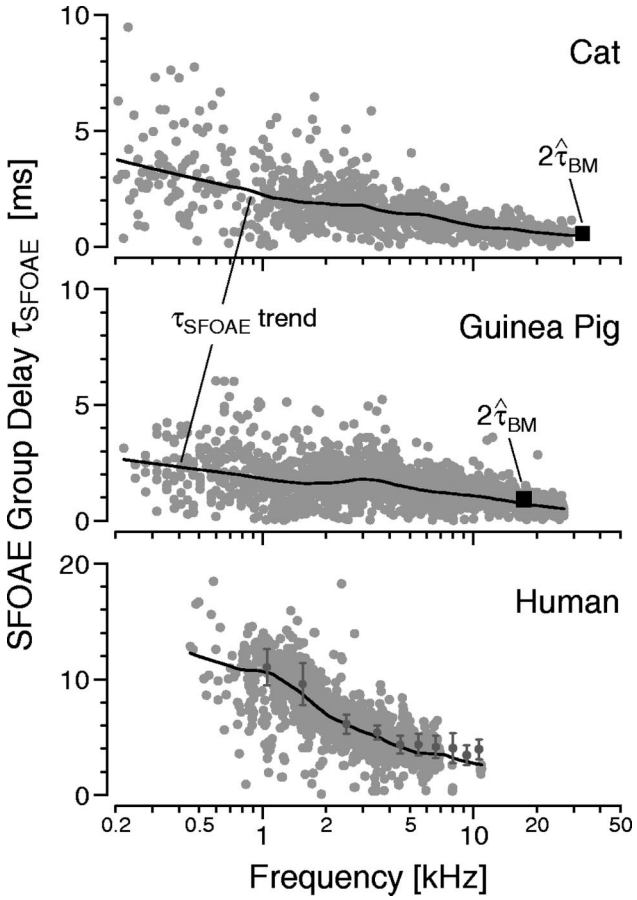

FIG. 1. Stimulus-frequency emission group delay, $\tau_{\mathrm{SFOAE}}(f)$, versus frequency in three species. The data are shown as a scatterplot (gray dots) together with loess trend lines (Cleveland, 1993) computed from the data (solid lines). Human SFOAE data from Dreisbach *et al.* (1998) are included to supplement our data at high frequencies (dots with error bars representing standard deviations). The black squares (■) provide a test of Eq. (1) in cat and guinea pig by showing values of $2\hat{\tau}_{\mathrm{BM}}$ computed from published measurements of BM mechanical transfer functions in the same species (Cooper and Rhode, 1992; Nuttall and Dolan, 1996). Like the SFOAE measurements shown here, the BM measurements were made in healthy preparations at stimulus levels of roughly 40 dB SPL. Note the difference in vertical scale between the human and animal graphs; human group delays are roughly a factor of 3 larger than those in cat and guinea pig.

B. Empirical SFOAE group delays

Figure 1 show scatterplots of our measurements of $\tau_{\mathrm{SFOAE}}(f)$ in three species together with loess trend lines (Cleveland, 1993) to guide the eye. The group delay $\tau_{\mathrm{SFOAE}}(f)$ decreases with increasing frequency, a dispersive trend consistent with time-domain measurements of the latency of click- and tone-burst-evoked emissions (e.g., Kemp, 1978; Wilson, 1980; Norton and Neely, 1987; Sisto and Moleti, 2002). For each frequency, SFOAE group delays in human are roughly a factor of 3 larger than in cat and guinea pig (see also Zwicker and Manley, 1981).

1. Origin of the variability

Although the trend line is robust both between and within individual subjects, the data points show considerable scatter. This scatter does not arise from measurement noise; indeed, the measurements are quite reproducible in each subject. Rather, the scatter comes from intrinsic variations in emission phase that are correlated with variations in emission amplitude across frequency. Intrinsic variations in emission amplitude and phase are predicted by the theory of coherent reflection filtering. To understand their origin, note that the theory indicates that SFOAEs are analogous to ''bandpass-filtered noise'' (Zweig and Shera, 1995). In this analogy, the ''noise'' is the irregular spatial arrangement and strength of the impedance perturbations that scatter the wave, and the ''bandpass filter'' results from interference among the multiple wavelets originating from the scattering region (Zweig and Shera, 1995). Unlike distortion-source emissions, whose amplitudes and phases typically vary relatively slowly with frequency, reflection-source emissions often vary considerably with frequency. For example, SFOAE amplitude spectra are often punctuated by relatively sharp notches (e.g., Fig. 9 of Shera and Guinan, 1999). According to the model, such notches result from random spatial fluctuations in the irregularities that scatter the wave. At some frequencies, wavelets scattered from different locations within the scattering region combine nearly out of phase, resulting in near cancellation of the net reflected wave.

Along with these large and small scale amplitude variations come corresponding phase variations whose effect is magnified here by taking the frequency derivative to compute the group delay.

C. Testing the predicted relation at high frequencies

We test the predicted relation [Eq. (1)] by overlaying in Fig. 1 values of $2\hat{\tau}_{\mathrm{BM}}$ computed from published measurements of basilar-membrane motion in the cat and guinea pig. Like the SFOAE measurements reported here, the BM measurements shown for comparison were made in healthy preparations at stimulus levels of roughly 40 dB SPL. Although the BM data are limited to high CFs, and to a single animal in each species, the agreement in the figure appears good in both cat and guinea pig. Computing the ratio $\tau_{\mathrm{SFOAE}}/\hat{\tau}_{\mathrm{BM}}$ allows a more quantitative comparison. The calculations yield ratios of 1.7 ± 0.2 in the cat and 1.6 ± 0.3 in the guinea pig,[4] where the error bars represent nominal 95% confidence intervals based on the uncertainties arising from the estimates of phase slope. In both species, the empirical ratios $\tau_{\mathrm{SFOAE}}/\hat{\tau}_{\mathrm{BM}}$, although significantly greater than 1, are smaller than the value 2 predicted by the theory. Note, however, that the confidence intervals given here underestimate the actual uncertainties because they do not include contributions arising from the variation in $\hat{\tau}_{\mathrm{BM}}$ between animals. Additional data are therefore needed to assess the differences among preparations and determine whether there are systematic deviations from the theoretical relation $\tau_{\mathrm{SFOAE}}\approx 2\hat{\tau}_{\mathrm{BM}}$.

IV. RELATING SFOAE GROUP DELAY TO COCHLEAR TUNING

Although SFOAE group delays are readily measured over a wide frequency range (see Fig. 1), direct comparisons between SFOAE and BM group delays are currently constrained to those few locations for which access to the basilar membrane can be obtained without significant loss of cochlear function (e.g., the squares in Fig. 1). To test whether SFOAE delays are consistent with the predictions of Eq. (1) over a broader region of the cochlea, we explore the relation between SFOAE group delay and cochlear tuning, as assessed using auditory-nerve-fiber (ANF) tuning curves.

We base our approach on the observation that at low sound levels the tuning of the basilar membrane appears nearly identical to the tuning of corresponding auditory-nerve fibers at frequencies in the tip region near CF (Narayan *et al.*, 1998). Although systematic measures of ANF group delay are not available in the basal half of the cochlea—the loss of phase locking above a few kilohertz means that cochlear phase characteristics cannot readily be obtained at high frequencies from ANF responses to tones or noise[5]—measurements of cochlear frequency selectivity are easily obtained from threshold tuning curves over the entire range of hearing. We relate BM group delay to cochlear-filter bandwidth by noting that at low levels BM transfer functions manifest many of the characteristics of minimum-phase-shift filters (e.g., Zweig, 1976; de Boer, 1997). In particular, their bandwidths and phase slopes are reciprocally related, with smaller bandwidths corresponding to steeper phase slopes (i.e., longer delays).

A. Dimensionless measures of tuning bandwidth and group delay

Our two measures of cochlear tuning—bandwidth and group delay—have different units (frequency and time, respectively). To compare them we render them dimensionless by normalizing each by the corresponding natural units of frequency and/or time. For the bandwidth, the natural frequency unit is the local characteristic frequency, f_{CF}. We therefore represent cochlear frequency selectivity using the parameter-free measure Q_{ERB}, defined as

$$Q_{\mathrm{ERB}}(f_{\mathrm{CF}}) \equiv f_{\mathrm{CF}}/\mathrm{ERB}(f_{\mathrm{CF}}), \tag{11}$$

where ERB is the equivalent rectangular bandwidth (i.e., the bandwidth of the rectangular filter with the same peak amplitude that passes the same total power).[6] Q_{ERB} is a measure of the ''sharpness'' of tuning: the smaller the bandwidth, the larger the Q_{ERB}. For the BM group delay, the natural unit of time is the reciprocal of the characteristic frequency. We define $N_{\mathrm{BM}}(f_{\mathrm{CF}})$ as

$$N_{\mathrm{BM}}(f_{\mathrm{CF}}) \equiv f_{\mathrm{CF}} \cdot \hat{\tau}_{\mathrm{BM}}(f_{\mathrm{CF}}). \tag{12}$$

$N_{\mathrm{BM}}(f_{\mathrm{CF}})$ is simply the group delay measured in periods of the characteristic frequency. In an analogous fashion we define the dimensionless SFOAE group delay by measuring time in periods of the stimulus frequency: $N_{\mathrm{SFOAE}}(f) \equiv f \cdot \tau_{\mathrm{SFOAE}}(f)$. Equation (1) implies that

$$\boxed{N_{\mathrm{SFOAE}}(f) \approx 2N_{\mathrm{BM}}(f).} \tag{13}$$

B. Frequency dependence of cochlear tuning

Figure 2 shows ANF-derived values of $Q_{\mathrm{ERB}}(f_{\mathrm{CF}})$ in cat and guinea pig. The figure illustrates that the sharpness of cochlear tuning increases gradually with CF throughout the cochlea. Although close examination of the data suggests a possible flattening of the Q_{ERB} at the highest CFs, this trend may well be a measurement artifact. Mechanical responses in the high-frequency region of the cochlea are extremely labile, and cochlear tuning at high CFs can easily be damaged (e.g., as a result of trauma caused by surgically opening the auditory bulla). As illustrated in the figure, power-law fits (straight lines on log-log axes) provide an excellent description of the overall trends in the data. Parameters for the fits are given in Table I.

C. Expected covariation of tuning bandwidth and group delay

Because bandwidth and group delay are inversely related, the product of the two (i.e., the ''tuning ratio'' $N_{\mathrm{BM}}/Q_{\mathrm{ERB}}$) is likely to vary more slowly along the cochlea than does either factor by itself. Consider, for example, representing BM tuning by a minimum-phase band-pass filter (e.g., a gammatone filter) of center frequency f_{CF}. Denote the filter bandwidth (e.g., the ERB) by Δf. If the filter phase

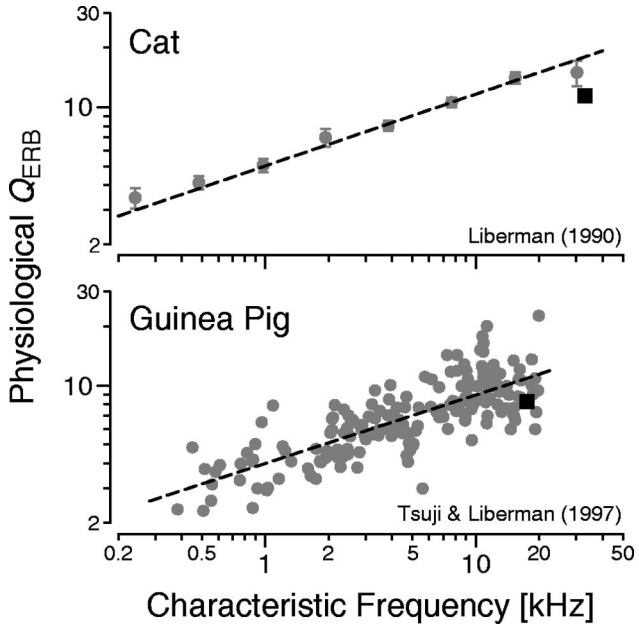

FIG. 2. Physiological values of Q_{ERB} in cat and guinea pig. In guinea pig, values of Q_{ERB} were computed from high-spontaneous-rate (high-SR) ANF threshold tuning curves (Tsuji and Liberman, 1997) using standard algorithms (Evans and Wilson, 1973). Since original tuning curves were unavailable in cat, the approximate proportionality between Q_{ERB} and Q_{10} discussed in footnote 6 was used to convert measurements of Q_{10} in high-SR fibers (Liberman, 1990) to corresponding values of Q_{ERB}. The cat data represent means and their standard errors in eight logarithmically spaced frequency bins. The dashed lines give power-law fits to the data (parameters in Table I). Shown for comparison are Q_{ERB} values (■) computed from the magnitudes of the mechanical transfer functions whose group delays appear in Fig. 1 (Cooper and Rhode, 1992; Nuttall and Dolan, 1996).

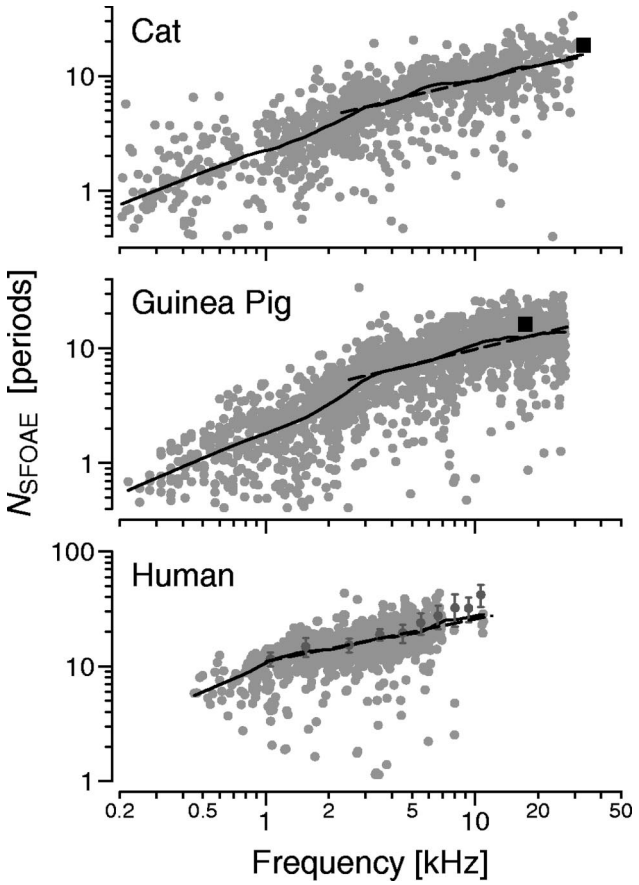

FIG. 3. N_{SFOAE} versus frequency in three species. The group-delay data (gray dots) and trends (solid lines) from Fig. 1 are replotted in dimensionless form in units of periods of the stimulus frequency. Shown for comparison are power-law fits to the data from roughly the basal-most 60% of the cochlea (dashed lines; parameters in Table I). Note that all vertical scales span two decades. Comparison with Fig. 2 demonstrates that in cats and guinea pigs the frequency dependence of $N_{SFOAE}(f)$ generally parallels the CF-dependence of the sharpness of tuning, at least in the basal half of the cochlea.

lag increases by an amount $|\Delta\phi|$ (in cycles) over the bandwidth Δf (in Hz), then the filter group delay is approximately $\hat{\tau}_{BM} \approx |\Delta\phi|/\Delta f$. The value of N_{BM}/Q_{ERB} is therefore[7]

$$N_{BM}/Q_{ERB} = \frac{\hat{\tau}_{BM} \cdot f_{CF}}{f_{CF}/\Delta f} = \hat{\tau}_{BM}\,\Delta f \approx |\Delta\phi|. \tag{14}$$

In other words, the tuning ratio N_{BM}/Q_{ERB} is simply the phase change (in cycles) across the filter bandwidth Δf. In filters of fixed type and order this phase change is largely independent of bandwidth. Since the shapes of neural tuning curves change relatively slowly with CF in the basal half of the cochlea (Liberman, 1978; Liberman and Kiang, 1978), we therefore expect Q_{ERB} and N_{BM} to vary in almost constant proportion across CF. If this is the case, Eq. (13) relating N_{BM} to N_{SFOAE} implies that Q_{ERB} and N_{SFOAE} will also vary together across CF.

TABLE I. Parameters of power-law fits to the functions $N_{SFOAE}(f)$ and $Q_{ERB}(f_{CF})$ in three species. Power-law fits (i.e., straight-line approximations on log-log axes) are an excellent approximation to N_{SFOAE} at $f > 1$ kHz and to Q_{ERB} over the entire frequency range. For each species, the parameters $\{\alpha,\beta\}$ characterizing the frequency dependence of $N_{SFOAE}(f)$ and $Q_{ERB}(f_{CF})$ in the high-frequency region of the cochlea were determined by linear regression using power-law fits of the form $y = \beta x^{\alpha}$, where y is the dependent variable and $x = f/[\text{kHz}]$ (i.e., frequency or CF in kHz). The numbers in parentheses give the approximate uncertainty (i.e., 95% confidence interval) in the final digit(s) estimated from the fits [e.g., $0.44(5) = 0.44 \pm 0.05$]; when the uncertainty is 1 or greater, the position of the decimal point is shown for clarity. The uncertainties in α and $\log\beta$ are strongly correlated, with a typical correlation coefficient between them of roughly -0.9.

$\beta\ (f/[\text{kHz}])^{\alpha}$		Cat	Guinea pig	Human
N_{SFOAE}	α	0.44(5)	0.44(3)	0.37(7)
	β	3.32(36)	3.56(26)	11.0(1.2)
Q_{ERB}	α	0.37(10)	0.35(4)	—
	β	5.0(1.1)	4.0(3)	—

D. Testing the predicted covariation of Q_{ERB} and N_{SFOAE}

We test the predicted covariation of Q_{ERB} and N_{SFOAE} in Fig. 3 by replotting the group delays $\tau_{SFOAE}(f)$ from Fig. 1 in the dimensionless form $N_{SFOAE}(f)$. Comparing the functions $N_{SFOAE}(f)$ (from Fig. 3) with $Q_{ERB}(f_{CF})$ (from Fig. 2) demonstrates that in cats and guinea pigs the frequency dependence of $N_{SFOAE}(f)$ generally parallels the CF dependence of the sharpness of tuning, at least in the basal half of the cochlea. In addition, note that although SFOAE group delays *decrease* at higher frequencies when measured in fixed units of time (e.g., milliseconds, as in Fig. 1), they

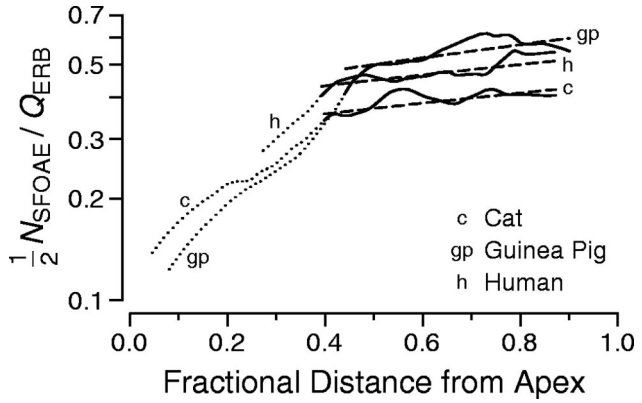

FIG. 4. Estimated tuning ratio N_{BM}/Q_{ERB} in three species. Tuning ratios were computed from the data in Figs. 2 and 3 using either the loess trend lines (solid lines) or the corresponding power-law fits (dashed lines). Values for the human Q_{ERB} were obtained by combining the otoacoustic and behavioral estimates of tuning reported by Shera *et al.* (2002; see also Oxenham and Shera, 2002). The horizontal axes represent relative cochlear location obtained by inverting the corresponding cochlear position-frequency map (Liberman, 1982; Greenwood, 1990; Tsuji and Liberman, 1997). Based on the intensity dependence of human OAE latencies reported by Neely *et al.* (1998), the values shown here may underestimate threshold-level tuning ratios by perhaps 30%, independent of frequency (see text). In the apical 40% of the cochlea, where the ratios and their dependence on frequency are of more uncertain reliability, the estimates are shown using dotted lines.

increase with frequency when measured in natural dimensionless units (i.e., periods of the stimulus waveform, as in Fig. 3). In cats, for example, the $N_{SFOAE}(f)$ trend line increases by roughly a factor of 20 from apex to base; similar variations in N_{SFOAE} are apparent in guinea pigs and humans. Given the sharpening of neural tuning at high CFs (Fig. 2), the frequency dependence of $N_{SFOAE}(f)$ demonstrated here is in qualitative agreement with expectations from filter theory about the covariation of bandwidth and group delay. Figures 2 and 3 thus support a general proportionality between N_{SFOAE} and N_{BM}, as predicted by Eq. (13).

1. The tuning ratio

The approximate proportionality between N_{SFOAE} and Q_{ERB} can be quantified by explicit calculation of the tuning ratio N_{BM}/Q_{ERB} using the theoretical estimate

$$N_{BM} \approx \tfrac{1}{2} N_{SFOAE}. \tag{15}$$

Figure 4 shows the estimated tuning ratio N_{BM}/Q_{ERB} as a function of relative cochlear location as computed from the data in Figs. 2 and 3. [Values for the human Q_{ERB} were obtained by combining the otoacoustic and behavioral estimates of tuning reported by Shera *et al.* (2002; see also Oxenham and Shera, 2002). The otoacoustic estimates of Q_{ERB} in that study were obtained by assuming approximate species-invariance of the tuning ratio (see Sec. V E 1).] Note that the values in Fig. 4 were obtained by combining measurements of N_{SFOAE} and Q_{ERB} made at somewhat different sound intensities. (The measurements of N_{SFOAE} were made at 40 dB SPL; the values of Q_{ERB} were obtained from ANF tuning curves with thresholds typically near 10 dB SPL in cat and 15 dB SPL in guinea pig.) Since OAE latencies generally decrease at higher sound levels (e.g., Neely *et al.*, 1988), the values of $\frac{1}{2}N_{SFOAE}/Q_{ERB}$ in Fig. 4 presumably underestimate the tuning ratios characteristic of threshold-level tuning. The intensity dependence of human OAE latencies reported by Neely *et al.* (1988), if generally applicable to the cat and guinea pig, suggests that the values in Fig. 4 systematically underestimate threshold-level tuning ratios by perhaps 30%.[8] (This value is likely to be an upper bound; Neely *et al.*'s characterization presumably overestimates the intensity dependence of OAE latencies at sound-levels near threshold, where cochlear mechanics is approximately linear.) Additional data are needed to determine the appropriate correction factor in each species. We focus here on the CF dependence shown in Fig. 4; since roughly the same correction applies at all frequencies (Neely *et al.*, 1988), the overall frequency dependence is largely unaffected.

Figure 4 indicates that the estimated tuning ratio behaves very differently in the base and the apex of the cochlea. In the basal 60% of the cochlea N_{BM}/Q_{ERB} increases slowly with distance from the apex, its value changing by only 20% over a region where N_{BM} and Q_{ERB} vary by at least 300%. N_{BM} and Q_{ERB} thus vary together in nearly constant proportion, as expected from filter theory and the predicted proportionality between N_{SFOAE} and N_{BM}. In the apical 40% of the cochlea, however, the tuning ratio varies more rapidly with position. This change in the form of N_{BM}/Q_{ERB} reflects a mid-frequency change in $N_{SFOAE}(f)$. Figure 3 demonstrates a ''bend'' in the function $N_{SFOAE}(f)$ at a frequency that maps in each species to a location just apical to the midpoint of the cochlea. The bend, a change of slope on log-log axes, represents a change in the power-law exponent. No bend or other change of form corresponding to that seen in Fig. 3 for $N_{SFOAE}(f)$ is apparent in the functions $Q_{ERB}(f_{CF})$ reproduced in Fig. 2. As a result, the bend in $N_{SFOAE}(f)$ appears also in the ratio N_{SFOAE}/Q_{ERB}, and the tuning ratio changes form. Note that because the tuning ratio varies more slowly than $N_{SFOAE}(f)$—thereby allowing an expanded vertical scale on the plot—the bend is much more salient in Fig. 4 than in Fig. 3. The strong variation of N_{BM}/Q_{ERB} in the apex may reflect either rapid changes with CF in the form of mechanical tuning (e.g., the effective order of the mechanical filter) and/or a systematic breakdown in the proportionality between otoacoustic and BM group delays [e.g., a violation of Eq. (1)]. Whatever its origin, the mid-cochlear bend in $N_{SFOAE}(f)$ assumes a remarkably similar form in all of the three species. Interestingly, the location of the bend corresponds approximately with the frequency at which cat ANF tuning curves change from the classic tip/tail form characteristic of high-CF fibers to the more complex shapes found in the apex (Liberman, 1978; Liberman and Kiang, 1978).

E. Apparent breakdown in the apex of the cochlea

Although Eq. (13) appears valid at high CFs, several pieces of evidence suggest that the relation breaks down in the apex of the cochlea. Figure 5 compares values of $N_{SFOAE}(f)$ with estimates of $2N_{BM}(f)$ obtained from mechanical and neural data at low CFs. In the cat, the N_{SFOAE} trend line and round-trip group delays estimated from auditory-nerve fibers (Goldstein *et al.*, 1971) part company at CFs below 3 kHz. At the apical end of the guinea pig

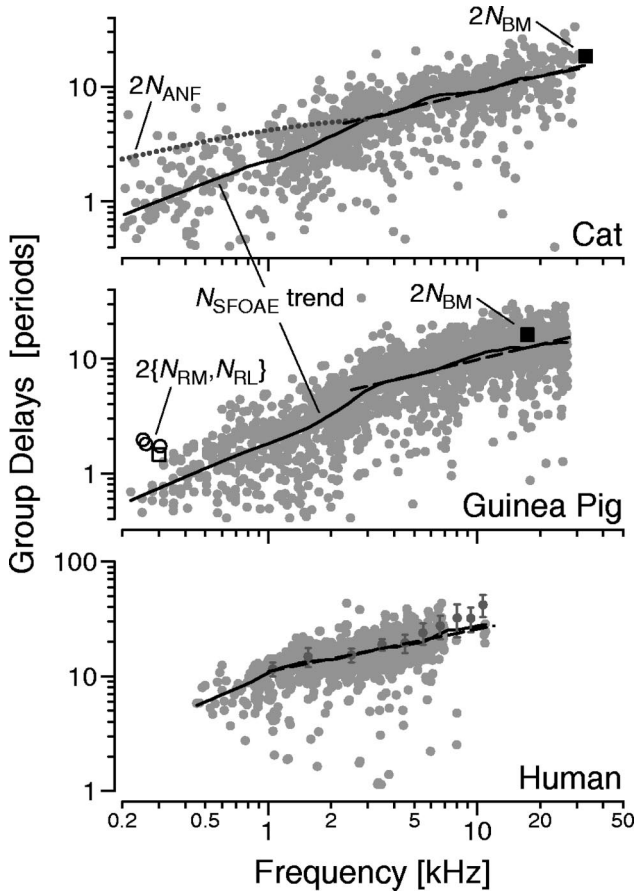

FIG. 5. N_{SFOAE} compared with mechanical and neural data in the apex. Superimposed on the data and trend lines from Fig. 3 are values of mechanical and neural group delays at low CFs. The mechanical data in the guinea pig (open symbols) were obtained from measurements on Reissner's membrane (Cooper and Rhode, 1995, □) or the reticular lamina (Khanna and Hao, 1999, ○) at high sound levels. The neural data in the cat (dotted line) is a curve fit to energy-weighted group delays obtained from auditory-nerve fiber (ANF) responses by Goldstein *et al.* (1971). The ANF values were corrected for fiber transmission delay by subtracting 1 ms. Both mechanical and neural group delays were doubled to estimate round-trip delay for comparison with N_{SFOAE}.

cochlea, similar differences between otoacoustic and mechanical group delays are seen based on measurements from Reissner's membrane (Cooper and Rhode, 1995) and the reticular lamina (Khanna and Hao, 1999). Although interpretations are complicated—both by potential problems relating neural and mechanical group delays and because the mechanical data from the apex were obtained from measurements on Reissner's membrane or the reticular lamina at high sound levels in cochleae of uncertain condition—the data suggest that $N_{\mathrm{SFOAE}}(f)$ is systematically smaller than predicted by Eq. (13) in the apex of the cochlea. Note, however, that a simple straight-line extrapolation of $N_{\mathrm{SFOAE}}(f)$ to low CFs using the slope characteristic of the high-CF region yields a curve largely consistent with the mechanical and neural data from the apex.

V. SUMMARY AND DISCUSSION

The theory of coherent reflection filtering predicts that reflection-source-emission group delay (τ_{SFOAE}) is determined by the group delay of the basilar-membrane mechanical transfer function ($\hat{\tau}_{\mathrm{BM}}$) through Eq. (1). We tested this prediction by comparing ear-canal measurements of $\tau_{\mathrm{SFOAE}}(f)$ in cats and guinea pigs with values of $2\hat{\tau}_{\mathrm{BM}}(f)$ computed from published measurements of BM transfer functions (Cooper and Rhode, 1992; Nuttall and Dolan, 1996). Although an explicit comparison is possible only at the extreme basal end of the cochlea, the mechanical and otoacoustic data appear generally consistent with the theory, especially considering the possible sources of error, and that the mechanical group delays represent only a single animal in each species. The comparison suggests, however, that the ratio $\tau_{\mathrm{SFOAE}}/\hat{\tau}_{\mathrm{BM}}$, although significantly greater than 1, may be slightly less than the value 2 predicted by the theory. Ratios somewhat less than 2 would occur if the region of wave scattering were skewed slightly basally from the peak of the traveling wave. Definitive tests of the theory using BM measurements require additional data (see Sec. V D).

A comparison between τ_{SFOAE} and $\hat{\tau}_{\mathrm{BM}}$ based on the variation in the sharpness of neural tuning with CF can be made over the entire frequency range and suggests that the proportionality $\tau_{\mathrm{SFOAE}}(f) \propto \hat{\tau}_{\mathrm{BM}}(f)$ holds in roughly the basal-most 60% of the cochlea. At low frequencies, however, the otoacoustic measurements disagree with neural and mechanical group delays from the apex of the cochlea. Human SFOAE group delays measured over a four-octave range are roughly a factor of 3 longer than their counterparts in cat and guinea pig but show similar trends across CF.

A. Global deviations from scaling

In locally scaling-symmetric cochleae, transfer functions $T(x,f)$ measured at nearby locations overlie one another when plotted as a function of the normalized frequency f/f_{CF}, where f_{CF} is the characteristic frequency (Zweig, 1976; Siebert, 1968; Sondhi, 1978). In perfectly scaling cochleae, the relative bandwidths of tuning [e.g., the functions $Q_{\mathrm{ERB}}(f_{\mathrm{CF}})$] are constant, independent of CF. Likewise, the theory of coherent reflection filtering predicts that in a perfectly scaling cochlea, SFOAE group delays—expressed in the dimensionless form $N_{\mathrm{SFOAE}}(f)$ as the number of stimulus periods—are also constant, independent of f. Although measurements of BM motion and neural tuning curves indicate that an approximate scaling symmetry applies locally (Rhode, 1971; Kiang and Moxon, 1974; Liberman, 1978), the plots of Q_{ERB} and N_{SFOAE} in Figs. 2 and 3 demonstrate global deviations from scaling whose form appears quantitatively similar in cats, guinea pigs, and humans.

We note that the systematic deviations from scaling demonstrated here imply that when the cochlear frequency-position map is logarithmic the function $T(x,f)$ cannot be symmetric about its peak in both the space and log-frequency domains simultaneously. Consider, for example, the case where the spatial envelope of the traveling wave at frequency f_0 [i.e., $|T(x,f_0)|$ vs x] is symmetric about its peak at $\hat{x}(f_0)$. Approximate symmetry about the peak of the traveling wave has recently been reported in longitudinal measurements of basilar-membrane motion (Ren, 2002). If the sharpness of frequency tuning increases with CF, other things being equal, then the amplitude of the transfer function at location $x_0 \equiv \hat{x}(f_0)$ [i.e., $|T(x_0,f)|$ vs f] must be asymmetric (on a log

TABLE II. Otoacoustic estimates of the wavelength at the peak of the traveling wave in three species. For each species, the parameters $\{\hat{\lambda}_1, \alpha\}$ characterizing the frequency dependence of $\hat{\lambda}(f_{CF}) = \hat{\lambda}_1 (f_{CF}/[\text{kHz}])^{\alpha}$ in the high-frequency region of the cochlea were computed from the parameters in Table I using the formula $\hat{\lambda} \approx l/N_{BM}$, where $N_{BM} \approx \frac{1}{2} N_{SFOAE}$ and l is the distance over which $f_{CF}(x)$ changes by a factor of e in the basal turn of the cochlea. The values of l assumed for each species were $l = \{5.2, 3.3, 7.2\}$ mm for cat, guinea pig, and human, respectively (Liberman, 1982; Tsuji and Liberman, 1997; Greenwood, 1990). As in Table I, the numbers in parentheses give the approximate uncertainty (i.e., 95% confidence interval) in the final digit(s) [e.g., $3.13(35) = 3.13 \pm 0.35$]; confidence intervals were estimated from the fits to N_{SFOAE} and do not reflect uncertainties in the values of l.

$\hat{\lambda}_1 (f_{CF}/[\text{kHz}])^{\alpha}$	Cat	Guinea pig	Human
$\hat{\lambda}_1$ [mm]	3.13(35)	1.85(15)	1.31(15)
α	−0.44(5)	−0.44(3)	−0.37(7)

frequency axis) about its peak at f_0 (i.e., CF).[9] In particular, the frequency transfer function must fall more rapidly at frequencies above CF than below. Note, however, that in addition to variations in tuning bandwidth, other, less well characterized deviations from scaling, such as possible systematic variations in transfer function height, will presumably contribute to any apparent asymmetry. Nevertheless, we note that the sign of the asymmetry in the transfer function (i.e., a steeper high-frequency slope) predicted from the variations in bandwidth reported here is similar to that measured experimentally (e.g., Robles and Ruggero, 2001; Ren, 2002).

B. Wavelength of the traveling wave

The locally scaling-symmetric form of $T(x,f)$ implies that the spatial wavelength of the traveling wave and the group delay of the transfer function [defined by partial derivatives of $\angle T$ with respect to x and f, respectively; see Eqs. (4) and (8)] are related to one another. When the cochlear position-frequency map is exponential, the wavelength and group delay at the peak are related through the equation

$$\hat{\lambda} N_{BM}/l = 1, \tag{16}$$

where l is the distance over which $f_{CF}(x)$ changes by a factor of e (Zweig and Shera, 1995). The theoretical estimate $N_{BM} \approx \frac{1}{2} N_{SFOAE}$ allows us to compute the wavelength at the peak of the traveling wave from our otoacoustic measurements and parameters of the cochlear map (e.g., Liberman, 1982; Tsuji and Liberman, 1997; Greenwood, 1990). Power-law estimates of the wavelength $\hat{\lambda}$ as a function of CF in cat, guinea pig, and human are given in Table II. The table indicates that in each of the three species $\hat{\lambda}$ decreases systematically at higher CFs at a rate of roughly 25% per octave. In humans, for example, the wavelength $\hat{\lambda}$ decreases from a value equivalent to about 130 rows of hair cells at the 1 kHz place (assuming 10 μm/row) to about 55 rows near 10 kHz.

C. Differences between base and apex

The large deviation from the predicted relation between otoacoustic and mechanical group delays [Eq. (1)] apparent at low CFs (Fig. 5) suggests that there are important differences in mechanisms of emission generation between the base and apex of the cochlea. These apparent otoacoustic differences may be related to other, more well-established differences in the mechanical and neural responses of the base and apex. For example, recent data from the guinea pig (Cooper and Dong, 2002) suggest that mechanical nonlinearities differ markedly in form and/or frequency dependence between the base and the apex. Since the suppression method used here to measure SFOAEs relies on nonlinear interactions between the probe and the suppressor to extract the emission,[10] the differences between otoacoustic and mechanical group delays in the apex may reflect changes in the form of cochlear mechanical nonlinearities with CF.

Other possibilities are suggested by the observation that mechanical and neural responses from the apex appear to result from multiple interacting mechanical drives (reviewed in Lin and Guinan, 2000). For example, auditory-nerve fibers at low CFs in cats have multi-lobed tips (Liberman and Kiang, 1978)—in their overall form apical tuning curves more nearly resemble a distorted ''W'' than the classic ''V'' shape characteristic of tuning curves from the base—and the phase-versus-frequency curves for these low-CF fibers manifest two well-defined and different group delays, separated by a transition at the ''seams'' between the lobes (Pfeiffer and Molnar, 1970; Kiang, 1984). Since different mechanical drives may couple differently to propagating pressure-difference waves and thereby produce backward-traveling waves with different characteristics, the relationship between OAEs and the motion of the organ of Corti, like the shapes of neural tuning curves, may vary systematically along the length of the cochlea. Perhaps significantly, the discrepancy between otoacoustic theory and experiment first becomes evident in cat at approximately the same frequency where neural tuning curves change from the classic tip/tail form to the more complex shapes found in the apex. Additional data and analysis are needed to explore these possibilities and to provide definitive tests of Eq. (1) in the apex.

D. Definitive tests of the theory

Rigorous tests of Eq. (1) should ideally be performed using simultaneous measurements of SFOAEs and BM motion in the same animal. In addition to eliminating uncertainty in the conclusions arising from differences among preparations, simultaneous otoacoustic and BM measurements would enable one to perform the more definitive experiment of testing the theory's prediction for the change in the reflection-source-emission spectrum caused by the introduction of artificial impedance perturbations (Zweig and Shera, 1995). For a masslike perturbation located at position x, the theory predicts that the change in the emission spectrum is proportional to $\omega T^2(x,f)$.

E. Applications of the tuning ratio

The tuning ratio N_{BM}/Q_{ERB} is equivalent to the product of BM group delay and bandwidth (as measured by the ERB); its value provides a dimensionless measure of the effective ''shape'' or ''order'' of cochlear tuning. Local scal-

ing can be used to interpret the tuning ratio in the spatial domain. The exponential form of the cochlear map implies that the spatial correlate of the ERB [sometimes called the ''equivalent rectangular spread'' or ERS (cf. Allen, 1996)] has the value $\mathrm{ERS}=l/Q_{\mathrm{ERB}}$. Combining this relation with Eq. (16) for $\hat{\lambda}$ shows that the tuning ratio, $N_{\mathrm{BM}}/Q_{\mathrm{ERB}}$, represents the ratio of the ERS to the wavelength at the peak of the traveling wave ($\mathrm{ERS}/\hat{\lambda}$).

A quantity analogous to the tuning ratio can be computed for any bandpass filter if $N_{\mathrm{BM}}(f_{\mathrm{CF}})$ is identified with the group delay at the filter peak. For example, in the family of gammatone filters widely used as models of peripheral auditory filters (e.g., Johannesma, 1972; Patterson *et al.*, 1991), the tuning ratio $N_{\mathrm{BM}}/Q_{\mathrm{ERB}}$ uniquely determines the filter order.[11] By specifying the filter order, the tuning ratio controls the asymmetry (or skewness) of the impulse-response envelope about its maximum: larger ratios correspond to higher orders, and thus to more symmetrical impulse responses (Aertsen and Johannesma, 1980).

Measurements of the tuning ratio across CF—when obtained from values of N_{SFOAE} and Q_{ERB} measured at comparable sound intensities—can thus be used to determine the characteristics of gammatone or other models of cochlear tuning. It would be instructive to compare the filter characteristics determined in this way with those obtained by fitting filter models to ANF impulse responses measured using reverse correlation (e.g., Carney and Yin, 1988). Since additional delays not directly associated with cochlear tuning (e.g., acoustic and/or neural transmission delays) are implicitly included in the definition of the revcor filter, group delays obtained otoacoustically presumably provide better estimates of mechanical group delay in the cochlea.

1. Noninvasive measurement of cochlear tuning

Rather than committing oneself to a particular type of filter (e.g., a gammatone), one can apply the tuning ratio to estimate the frequency selectivity of cochlear tuning in a more model-independent manner (Shera *et al.*, 2002). The method is based on the assumption that at corresponding cochlear locations the tuning ratio is broadly similar across mammalian species. If this assumption is correct (e.g., if the analytic structure of mammalian mechanical transfer functions is approximately conserved across species), then noninvasive estimates of the human Q_{ERB} can be obtained by combining otoacoustic estimates of the human N_{BM} with the tuning ratios measured in cat and/or guinea pig. More precisely,

$$Q_{\mathrm{ERB}}^{\mathrm{human}} \approx k_{\mathrm{gpig}} N_{\mathrm{BM}}^{\mathrm{human}}, \tag{17}$$

where $k_{\mathrm{gpig}} \equiv Q_{\mathrm{ERB}}^{\mathrm{gpig}}/N_{\mathrm{BM}}^{\mathrm{gpig}}$ is the reciprocal of the guinea-pig tuning ratio obtained by combining otoacoustic and neurophysiological measurements as in Fig. 4. Note that so long as the otoacoustic measurements are made at comparable sound intensities in the two species (in this example, human and guinea pig), systematic errors due to differences in the intensities at which N_{SFOAE} and Q_{ERB} are measured will, to first order, cancel in the product. [For example, if $N_{\mathrm{SFOAE}}^{\mathrm{gpig}}$ and $N_{\mathrm{SFOAE}}^{\mathrm{human}}$ measured at 40 dB SPL both differ by roughly the same (unknown, possibly frequency dependent) factor from their values near threshold, then the unknown factors cancel out when computing $Q_{\mathrm{ERB}}^{\mathrm{human}}$ from Eq. (17).]

We apply these ideas in another publication (Shera *et al.*, 2002), in which we combine the theory of coherent reflection filtering with otoacoustic measurements to compare cochlear tuning across species and to test the correspondence between physiological and behavioral measures of auditory frequency selectivity. The results indicate that, contrary to common belief, tuning in the human cochlea is considerably sharper than that found in the other mammals. In addition, at low sound levels human cochlear tuning appears to be more than twice as sharp as implied by standard behavioral studies and has a different dependence on frequency. These findings are consistent with new behavioral measurements designed to minimize the influence of nonlinear effects such as suppression (Oxenham and Shera, 2002). The measurements and analysis reported here thus illustrate the rich potential inherent in OAEs for obtaining valuable new information about basic cochlear properties.

ACKNOWLEDGMENTS

We thank Nigel P. Cooper, M. Charles Liberman, and Alfred L. Nuttall for generously sharing their data, Jont B. Allen and Andrew J. Oxenham for stimulating discussions, and Paul F. Fahey, K. Domenica Karavitaki, William T. Peake, and Robert H. Withnell for valuable comments on the manuscript. This work was supported by Grant Nos. DC03687 and DC00235 from the NIDCD, National Institutes of Health.

[1]Preliminary accounts of this work have been presented elsewhere (Shera and Guinan, 2000a, b).

[2]Alternative derivations of Eq. (1) are available elsewhere (Shera, 1992; Zweig and Shera, 1995; Talmadge *et al.*, 1998).

[3]By characterizing the middle-ear using transmittance and reflectance coefficients (Shera and Zweig, 1992), one can easily show that the SFOAE pressure, P_{SFOAE}, has the value

$$P_{\mathrm{SFOAE}} = P_0 \vec{T}_{\mathrm{me}} \overleftarrow{T}_{\mathrm{me}} \frac{R(1+R_{\mathrm{stapes}})}{1-RR_{\mathrm{stapes}}},$$

where P_0 is the calibrated ear-canal stimulus pressure, $\vec{T}_{\mathrm{me}}$ and $\overleftarrow{T}_{\mathrm{me}}$ are, respectively, the forward and reverse middle-ear pressure transfer functions, R_{stapes} is the reflection coefficient for retrograde cochlear waves at the stapes (Shera and Zweig, 1991; Talmadge *et al.*, 1998; Puria, 2002), and R is the cochlear traveling-wave reflectance (Shera and Zweig, 1993a; Zweig and Shera, 1995; Talmadge *et al.*, 1998), defined as the ratio of the emitted (backward-traveling) to the stimulus (forward-traveling) pressure wave at the stapes. Note that P_0, $\vec{T}_{\mathrm{me}}$, and $\overleftarrow{T}_{\mathrm{me}}$ are measured at sound intensities where $|P_{\mathrm{SFOAE}}/P_0| \ll 1$. Noncochlear contributions to τ_{SFOAE} are small when $\angle R$ dominates the frequency dependence of $\angle P_{\mathrm{SFOAE}}$.

[4]The value of τ_{SFOAE} used to compute the ratio was obtained using the power-law fits given in Table I.

[5]Measurements of ANF group delay in fibers with CFs near 12 kHz have been obtained in the guinea pig using responses to amplitude-modulated tones (Gummer and Johnstone, 1984). The authors of that study argue that the ''group delay difference,'' obtained as the difference between the near-CF group delay and the group delay measured about one octave below CF, correlates well with the sharpness of tuning measured using the Q_{10}. Although the group delay differences reported for their most sensitive units agree well with our values of τ_{SFOAE} near 12 kHz in the guinea pig, we do not show these neural data here because of our uncertainty about the interpretation of the delay difference, especially in light of other measurements suggesting that neural group delays at tail frequencies often have a nonmonotonic frequency dependence (e.g., Allen, 1983). See also van der

Heijden and Joris (2002) for another method to estimate high-frequency phase characteristics from ANF responses to complex stimuli.

[6]Although we adopt the ERB-based measure to facilitate comparisons with behavioral measurements, we obtain similar conclusions using Q_{10}, defined as f_{CF}/BW_{10}, where BW_{10} is the bandwidth 10 dB below the peak. In many filters the two measures are simply proportional: for simple harmonic oscillators $Q_{ERB}/Q_{10} \approx 1.9$, and for Gaussian filters $Q_{ERB}/Q_{10} \approx 1.7$. Analysis of ANF tuning curves (Shera, unpublished) yields similar ratios (i.e., $Q_{ERB}/Q_{10} \approx 1.7-1.8$), largely independent of species and CF.

[7]Thanks to Jont Allen for suggesting this formulation.

[8]According to the measurements and analysis of Neely *et al.* (1988), evoked OAE latencies measured at sound level $L+\Delta L$ (in dB SPL) will differ from those measured at level L by a frequency-independent factor of approximately $c^{-\Delta L/100}$, with $c=5$.

[9]As a convenient example, consider the simple Gaussian envelope

$$|T(x,f)| \propto \exp\left[\frac{x-\hat{x}(f)}{\sqrt{2}\sigma_x(f)}\right]^2,$$

where the frequency-position map $\hat{x}(f)$ is proportional to $-\log(f)$ and the width of the excitation pattern, $\sigma_x(f)$, varies with frequency. Although $|T|$ is symmetric when considered as a function of x at fixed f (the traveling wave), the function is asymmetric when considered as a function of $\log(f)$ at fixed x (the transfer function).

[10]We note the need for caution when interpreting OAE measurements obtained using the suppression method and other techniques based on nonlinear effects such as compression. As an extreme example, consider the thought experiment in which the mechanics in some region of the cochlea (e.g., the apex) is presumed completely linear. Although this region might generate strong reflection-source OAEs—the absence of nonlinearity implies neither the lack of traveling-wave amplification nor the absence of emissions—suppression and other nonlinear OAE methods would be unable to measure them. If measurable emissions at corresponding frequencies are found using these methods, then they must have come from other (nonlinear) regions of the cochlea. Similar remarks apply to the method of efferent suppression if the effective strength of efferent feedback varies strongly with position in the cochlea [as suggested, for example, by the relative sparsity of medial efferent innervation in the apex (Guinan *et al.*, 1984)].

[11]For a gammatone filter of order n

$$N_{BM}/Q_{ERB} = \tfrac{1}{2} n\Gamma(2n-1)[2^{-(n-1)}/\Gamma(n)]^2$$

(see, e.g., Aertsen and Johannesma, 1980; Hartmann, 1997). Note that all gammatone filters must satisfy $N_{BM}/Q_{ERB} \geqslant \frac{1}{2}$.

Aertsen, A. M. H. J., and Johannesma, P. I. M. (**1980**). ''Spectro-temporal receptive fields of auditory neurons in the grassfrog. I. Characterization of tonal and natural stimuli,'' Biol. Cybern. **38**, 223–234.

Allen, J. B. (**1983**). ''Magnitude and phase-frequency response to single tones in the auditory nerve,'' J. Acoust. Soc. Am. **73**, 2071–2092.

Allen, J. B. (**1996**). ''Harvey Fletcher's role in the creation of communication acoustics,'' J. Acoust. Soc. Am. **99**, 1825–1839.

Apostol, T. M. (**1969**). *Calculus*, 2nd ed. (Wiley, New York), Vol. II.

Bredberg, G. (**1968**). ''Cellular patterns and nerve supply of the human organ of Corti,'' Acta Oto-Laryngol., Suppl. **236**, 1–135.

Brillouin, L. (**1946**). *Wave Propagation in Periodic Structures* (McGraw-Hill, New York).

Carney, L. H., and Yin, T. C. T. (**1988**). ''Temporal coding of resonances by low-frequency auditory nerve fibers: Single fiber responses and a population model,'' J. Neurophysiol. **60**, 1653–1677.

Cleveland, W. S. (**1993**). *Visualizing Data* (Hobart, Summit, NJ).

Cooper, N. P., and Dong, W. (**2002**). ''Baseline position shifts and mechanical compression in the apical turns of the cochlea,'' in *Biophysics of the Cochlea: From Molecule to Model*, edited by A. W. Gummer (World Scientific, Singapore), pp. 157–163.

Cooper, N. P., and Rhode, W. S. (**1992**). ''Basilar membrane mechanics in the hook region of cat and guinea-pig cochleae: Sharp tuning and nonlinearity in the absence of baseline position shifts,'' Hear. Res. **63**, 163–190.

Cooper, N. P., and Rhode, W. S. (**1995**). ''Nonlinear mechanics at the apex of the guinea-pig cochlea,'' Hear. Res. **82**, 225–243.

de Boer, E. (**1997**). ''Cochlear models and minimum phase,'' J. Acoust. Soc. Am. **102**, 3810–3813.

Dreisbach, L. E., Siegel, J. H., and Chen, W. (**1998**). ''Stimulus-frequency otoacoustic emissions measured at low and high frequencies in untrained human subjects,'' Assoc. Res. Otolaryngol. Abs. **21**, 349.

Engström, H., Ades, H. W., and Andersson, A. (**1966**). *Structural Pattern of the Organ of Corti* (Williams and Wilkins, Baltimore).

Evans, E. F., and Wilson, J. P. (**1973**). ''Frequency selectivity in the cochlea,'' in *Basic Mechanisms in Hearing*, edited by A. R. Møller and P. Boston (Academic, New York), pp. 519–551.

Goldstein, J. L., Baer, T., and Kiang, N. Y. S. (**1971**). ''A theoretical treatment of latency, group delay, and tuning characteristics of auditory-nerve responses to clicks and tones,'' in *Physiology of the Auditory System*, edited by M. B. Sachs (National Educational Consultants, Baltimore), pp. 133–141.

Greenwood, D. D. (**1990**). ''A cochlear frequency-position function for several species—29 years later,'' J. Acoust. Soc. Am. **87**, 2592–2605.

Guinan, J. J. (**1986**). ''Effect of efferent neural activity on cochlear mechanics,'' Scand. Audiol. Suppl. **25**, 53–62.

Guinan, J. J., Warr, W. B., and Norris, B. E. (**1984**). ''Topographic organization of the olivocochlear projections from the lateral and medial zones of the superior olivary complex,'' J. Comp. Neurol. **226**, 21–27.

Gummer, A. W., and Johnstone, B. M. (**1984**). ''Group delay measurements from spiral ganglion cells in the basal turn of the guinea pig cochlea,'' J. Acoust. Soc. Am. **76**, 1388–1400.

Hartmann, W. M. (**1997**). *Signal, Sound, and Sensation* (AIP, Woodbury).

Johannesma, P. I. M. (**1972**). ''The pre-response stimulus ensemble of neurons in the cochlear nucleus,'' in *Hearing Theory 1972* (Institute for Perception Research, Eindhoven), pp. 58–69.

Kemp, D. T. (**1978**). ''Stimulated acoustic emissions from within the human auditory system,'' J. Acoust. Soc. Am. **64**, 1386–1391.

Kemp, D. T. (**1980**). ''Towards a model for the origin of cochlear echoes,'' Hear. Res. **2**, 533–548.

Kemp, D. T. (**1986**). ''Otoacoustic emissions, travelling waves and cochlear mechanisms,'' Hear. Res. **22**, 95–104.

Khanna, S. M., and Hao, L. F. (**1999**). ''Reticular lamina vibrations in the apical turn of a living guinea pig cochlea,'' Hear. Res. **132**, 15–33.

Kiang, N. Y. S. (**1984**). ''Peripheral neural processing of auditory information,'' in *Handbook of Physiology, Section 1: The Nervous System, Vol. 3 (Sensory Processes)*, edited by I. Darian-Smith (American Physiological Society, Bethesda), pp. 639–674.

Kiang, N. Y. S., and Moxon, E. C. (**1974**). ''Tails of tuning curves of auditory-nerve fibers,'' J. Acoust. Soc. Am. **55**, 620–630.

Liberman, M. C. (**1978**). ''Auditory-nerve response from cats raised in a low-noise chamber,'' J. Acoust. Soc. Am. **63**, 442–455.

Liberman, M. C. (**1982**). ''The cochlear frequency map for the cat: Labeling auditory-nerve fibers of known characteristic frequency,'' J. Acoust. Soc. Am. **72**, 1441–1449.

Liberman, M. C. (**1990**). ''Effects of chronic cochlear de-efferentation on auditory-nerve response,'' Hear. Res. **49**, 209–224.

Liberman, M. C., and Kiang, N. Y. S. (**1978**). ''Acoustic trauma in cats: Cochlear pathology and auditory-nerve activity,'' Acta Oto-Laryngol., Suppl. **358**, 1–63.

Lighthill, J. (**1981**). ''Energy flow in the cochlea,'' J. Fluid Mech. **106**, 149–213.

Lin, T., and Guinan, J. J. (**2000**). ''Auditory-nerve-fiber responses to high-level clicks: Interference patterns indicate that excitation is due to the combination of multiple drives,'' J. Acoust. Soc. Am. **107**, 2615–2630.

Lonsbury-Martin, B. L., Martin, G. K., Probst, R., and Coats, A. C. (**1988**). ''Spontaneous otoacoustic emissions in the nonhuman primate. II. Cochlear anatomy,'' Hear. Res. **33**, 69–94.

Narayan, S. S., Temchin, A. N., Recio, A., and Ruggero, M. A. (**1998**). ''Frequency tuning of basilar membrane and auditory nerve in the same cochleae,'' Science **282**, 1882–1884.

Neely, S. T., Norton, S. J., Gorga, M. P., and Jesteadt, W. (**1988**). ''Latency of auditory brain-stem responses and otoacoustic emissions using tone-burst stimuli,'' J. Acoust. Soc. Am. **83**, 652–656.

Norton, S. J., and Neely, S. T. (**1987**). ''Tone-burst-evoked otoacoustic emissions from normal-hearing subjects,'' J. Acoust. Soc. Am. **81**, 1860–1872.

Nuttall, A. L., and Dolan, D. F. (**1996**). ''Steady-state sinusoidal velocity responses of the basilar membrane in guinea pig,'' J. Acoust. Soc. Am. **99**, 1556–1565.

Olson, E. S. (**1998**). ''Observing middle and inner ear mechanics with novel intra-cochlear pressure sensors,'' J. Acoust. Soc. Am. **103**, 3445–3463.

Oxenham, A. J., and Shera, C. A. (**2002**). ''Estimates of human cochlear

tuning at low levels using forward and simultaneous masking,'' J. Assoc. Res. Otolaryngol. (in press).
Patterson, R. D., Holdsworth, J., Nimmo-Smith, I., and Rice, P. (**1991**). ''The auditory filter bank,'' MRC-APU Report 2341, Cambridge, England.
Pfeiffer, R. R., and Molnar, C. E. (**1970**). ''Cochlear nerve fiber discharge patterns: Relationship to the cochlear microphonic,'' Science **167**, 1614–1616.
Press, W. H., Teukolsky, S. A., Vetterling, W. T., and Flannery, B. P. (**1992**). *Numerical Recipes in C: The Art of Scientific Computing* (Cambridge U.P., Cambridge).
Puria, S. (**2002**). ''Measurements of human middle ear forward and reverse acoustics: Implications for otoacoustic emissions,'' J. Acoust. Soc. Am. (in press).
Puria, S., and Allen, J. (**1998**). ''Measurements and model of the cat middle ear: Evidence of tympanic membrane acoustic delay,'' J. Acoust. Soc. Am. **104**, 3463–3481.
Ren, T. (**2002**). ''Longitudinal pattern of basilar membrane vibration in the sensitive cochlea,'' Proc. Natl. Acad. Sci. U.S.A. **99**, 17101–17106.
Rhode, W. S. (**1971**). ''Observations of the vibration of the basilar membrane in squirrel monkeys using the Mössbauer technique,'' J. Acoust. Soc. Am. **49**, 1218–1231.
Robles, L., and Ruggero, M. A. (**2001**). ''Mechanics of the mammalian cochlea,'' Physiol. Rev. **81**, 1305–1352.
Shera, C. A. (**1992**). ''Listening to the Ear,'' Ph.D. thesis, California Institute of Technology.
Shera, C. A., and Guinan, J. J. (**1999**). ''Evoked otoacoustic emissions arise by two fundamentally different mechanisms: A taxonomy for mammalian OAEs,'' J. Acoust. Soc. Am. **105**, 782–798.
Shera, C. A., and Guinan, J. J. (**2000a**). ''Frequency dependence of stimulus-frequency-emission phase: Implications for cochlear mechanics,'' in *Recent Developments in Auditory Mechanics*, edited by H. Wada, T. Takasaka, K. Ikeda, K. Ohyama, and T. Koike (World Scientific, Singapore), pp. 381–387.
Shera, C. A., and Guinan, J. J. (**2000b**). ''Reflection-emission phase: A test of coherent reflection filtering and a window on cochlear tuning,'' Assoc. Res. Otolaryngol. Abs. **23**, 545.
Shera, C. A., and Zweig, G. (**1991**). ''Reflection of retrograde waves within the cochlea and at the stapes,'' J. Acoust. Soc. Am. **89**, 1290–1305.
Shera, C. A., and Zweig, G. (**1992**). ''Analyzing reverse middle-ear transmission: Noninvasive Gedankenexperiments,'' J. Acoust. Soc. Am. **92**, 1371–1381.
Shera, C. A., and Zweig, G. (**1993a**). ''Noninvasive measurement of the cochlear traveling-wave ratio,'' J. Acoust. Soc. Am. **93**, 3333–3352.
Shera, C. A., and Zweig, G. (**1993b**). ''Order from chaos: Resolving the paradox of periodicity in evoked otoacoustic emission,'' in *Biophysics of Hair Cell Sensory Systems*, edited by H. Duifhuis, J. W. Horst, P. van Dijk, and S. M. van Netten (World Scientific, Singapore), pp. 54–63.
Shera, C. A., Guinan, J. J., and Oxenham, A. J. (**2002**). ''Revised estimates of human cochlear tuning from otoacoustic and behavioral measurements,'' Proc. Natl. Acad. Sci. U.S.A. **99**, 3318–2232.
Shera, C. A., Talmadge, C. L., and Tubis, A. (**2000**). ''Interrelations among distortion-product phase-gradient delays: Their connection to scaling symmetry and its breaking,'' J. Acoust. Soc. Am. **108**, 2933–2948.
Siebert, W. M. (**1968**). ''Stimulus transformations in the peripheral auditory system,'' in *Recognizing Patterns*, edited by P. A. Kolers and M. Eden (MIT, Cambridge), pp. 104–133.
Sisto, R., and Moleti, A. (**2002**). ''On the frequency dependence of the otoacoustic emission latency in hypoacoustic and normal ears,'' J. Acoust. Soc. Am. **111**, 297–308.
Sondhi, M. M. (**1978**). ''Method for computing motion in a two-dimensional cochlear model,'' J. Acoust. Soc. Am. **63**, 1468–1477.
Strube, H. W. (**1989**). ''Evoked otoacoustic emissions as cochlear Bragg reflections,'' Hear. Res. **38**, 35–45.
Talmadge, C. L., Tubis, A., Long, G. R., and Piskorski, P. (**1998**). ''Modeling otoacoustic emission and hearing threshold fine structures,'' J. Acoust. Soc. Am. **104**, 1517–1543.
Tsuji, J., and Liberman, M. C. (**1997**). ''Intracellular labeling of auditory nerve fibers in guinea pig: Central and peripheral projections,'' J. Comp. Neurol. **381**, 188–202.
van der Heijden, M., and Joris, P. X. (**2002**). ''Retrieving cochlear phase characteristics from high-frequency auditory nerve fibers,'' Assoc. Res. Otolaryngol. Abs. **25**, 329.
Wilson, J. P. (**1980**). ''Evidence for a cochlear origin for acoustic re-emissions, threshold fine-structure and tonal tinnitus,'' Hear. Res. **2**, 233–252.
Wright, A. A. (**1984**). ''Dimensions of the cochlear stereocilia in man and in guinea pig,'' Hear. Res. **13**, 89–98.
Zweig, G. (**1976**). ''Basilar membrane motion,'' in *Cold Spring Harbor Symposia on Quantitative Biology, Volume XL, 1975* (Cold Spring Harbor Laboratory, Cold Spring Harbor, NY), pp. 619–633.
Zweig, G., and Shera, C. A. (**1995**). ''The origin of periodicity in the spectrum of evoked otoacoustic emissions,'' J. Acoust. Soc. Am. **98**, 2018–2047.
Zwicker, E. (**1989**). ''Otoacoustic emissions and cochlear travelling waves,'' in *Cochlear Mechanisms—Structure, Function, and Models*, edited by J. P. Wilson and D. T. Kemp (Plenum, New York), pp. 359–366.
Zwicker, E., and Manley, G. (**1981**). ''Acoustical responses and suppression-period patterns in guinea pigs,'' Hear. Res. **4**, 43–52.

Measurements of human middle ear forward and reverse acoustics: Implications for otoacoustic emissions

Sunil Puria[a)]
Stanford University, Mechanics and Computation Division, Palo Alto, California 94305
and California Ear Institute at Stanford, 801 Welch Road, Palo Alto, California 94304

(Received 11 July 2002; revised 1 February 2003; accepted 4 February 2003)

Middle and inner ears from human cadaver temporal bones were stimulated in the forward direction by an ear-canal sound source, and in the reverse direction by an inner-ear sound source. For each stimulus type, three variables were measured: (a) P_{ec}—ear-canal pressure with a probe-tube microphone within 3 mm of the eardrum, (b) V_{st}—stapes velocity with a laser interferometer, and (c) P_v—vestibule pressure with a hydrophone. From these variables, the forward middle-ear pressure gain (M1), the cochlear input impedance (Z_c), the reverse middle-ear pressure gain (M2), and the reverse middle-ear impedance (M3) are directly obtained for the first time from the same preparation. These measurements can be used to fully characterize the middle ear as a two-port system. Presently, the effect of the middle ear on otoacoustic emissions (OAEs) is quantified by calculating the roundtrip middle-ear pressure gain G_{me}^{RT} as the product of M1 and M2. In the 2–6.8 kHz region, $|G_{me}^{RT}|$ decreases with a slope of −22 dB/oct, while OAEs (both click evoked and distortion products) tend to be independent of frequency; this suggests a steep slope in vestibule pressure from 2 kHz to at least 4 kHz for click evoked OAEs and to at least 6.8 kHz for distortion product OAEs. Contrary to common assumptions, measurements indicate that the emission generator mechanism is frequency dependent. Measurements are also used to estimate the reflectance of basally traveling waves at the stapes, and apically generated nonlinear reflections within the vestibule. [DOI: 10.1121/1.1564018]

PACS numbers: 43.64.Ha, 43.64.Jb, 43.64.Tk [BLM]

I. INTRODUCTION

Ever since the time of Helmholtz (1868), many researchers have made measurements and proposed mathematical models in attempts to characterize the human middle ear. Table I is a survey of experimental physiology and mathematical modeling work on the human middle ear during the past century and many of the measurements can be reduced to four broad categories identified in column 4.

The first category of middle-ear measurements is the ear-canal impedance, Z_{ec} (West, 1928; Waetzmann and Keibs, 1936). Because the ear canal is readily accessible, many researchers have since measured the ear-canal impedance, the ear-canal reflectance related to Z_{ec} by a binomial transform of the normalized impedance, and the standing wave ratio (SWR) obtained from the magnitude of the reflectance. Because all three measurements are related to each other to within a scale factor and through algebraic manipulations, they are all different incarnations of the same physical quantity.

The second category of measurements reported in the literature is the stapes displacement to ear-canal pressure ratio, D_{st}/P_{ec}, starting with the work of Rubinstein *et al.* (1966). Since then, numerous researchers have reported the stapes-velocity to ear-canal pressure ratio, V_{st}/P_{ec}, which is simply the time derivative of the displacement. Again, because these two measurements are directly related to each other, they constitute one independent measurement.

The third category of measurements is the vestibule pressure to ear-canal pressure ratio, P_v/P_{ec}, or the middle-ear pressure gain. Here, the middle-ear gain in the forward direction is obtained by driving the ear canal with a sound source. Von Békésy (1941) measured the magnitude of the middle-ear pressure gain, $|P_v/P_{ec}|$, in one ear with the stapes immobilized. It was not until 1993 (Puria *et al.*, 1993a), that both the magnitude and angle of P_v/P_{ec} with normal stapes were reported in one ear, and later in four ears (Puria *et al.*, 1997).

The fourth category of measurements is the reverse middle-ear pressure gain from the cochlea, through the middle ear, and into the ear canal. This measurement, from 0.1 to 4 kHz, was reported in one ear by Puria and Rosowski in 1996. Hudde and Engle (1998b) estimated the reverse pressure gain by mechanically driving the stapes of several temporal bones. However, their measurements show significant inter-ear variability above 2–3 kHz in comparison to the measurements reported here.

From the perspective of middle ear input–output physiology, only two independent measurements of the human middle ear were available at the beginning of the 1990s. Many additional measurements such as umbo velocity, eardrum surface displacement, and lever ratio have been reported and these are important when one is interested in getting inside the middle ear. However, they do not increase the number of independent variables required to fully characterize the middle ear from an input–output perspective.

[a)]Address for correspondence: Department of Mechanical Engineering, Mechanics and Computation Division, Stanford University, Durand Bldg., Room 262, Stanford, CA 94305. Electronic mail: puria@stanford.edu

TABLE I. Previous measurement and modeling efforts of the human middle ear. Input–output middle-ear acoustic measurements can be categorized into four basic categories, indicated in the right column. Category 1 is the ear-canal impedance Z_{ec} (reflectance R_{ec}, or standing wave ratios SWR). Category 2 is the stapes velocity V_{st} (or the stapes displacement D_{st}). Category 3 is the middle-ear pressure gain $P_v/P_{ec}(F)$ measured in the forward direction. And the fourth category is $P_{ec}/P_v(R)$ the reverse middle-ear pressure gain.

Measurements	Models	Type	Category
West (1928)		Z_{ec}	1
Waetzmann and Keibs (1936)		Z_{ec}	1
Békésy (1941)		Open circuit $\lvert P_v/P_{ec}\rvert$	3
Metz (1946)		Z_{ec}	1
	Zwislocki (1948, 1957, 1962)	Z_{ec}	1
	Onchi (1949)	Z_{ec}	1
		Z_{ec}	1
Møller (1960)	Møller (1961)	Z_{ec}, Z_s, Indirect $\lvert P_v/P_{ec}\rvert$	1
Onchi (1961)	Onchi (1961)	Z_{ec}	1
	Flanagan (1962)	Predicts stapes displacement	2
Rubinstein *et al.* (1966)		Stapes displacement	2
Zwislocki and Feldman (1970)		Z_{ec}	1
Gunderson (1971)		Tympanic membrane (TM) and stapes velocity	2
Tonndorf and Khanna (1972)		TM surface vibration	
Gundersen and Høgmoen (1976)		Malleus and Incus lever ratio	
Mehrgardt and Mellert (1977)		Reflectance at TM	1
	Shaw (1977)	Z_{ec}, two-piston model	1
	Lutman and Martin (1979)	Z_{ec}, ME muscle reflex	1
Rabinowitz (1981)		Z_{ec} in living ears	1
	Shaw and Stinson (1981)	Z_{ec} and standing wave ratio (SWR)	1
McElveen *et al.* (1982)		Umbo displacement	
Huddle (1983)		Z_{ec} in living ears	1
Kringlebotn and Gundersen (1985)		Stapes displacement	2
Vlaming and Feenstra (1986)		TM and stapes displacement	2
Gyo *et al.* (1987)		Umbo and stapes displacement	2
Brenkman *et al.* (1987)		Umbo and stapes displacement	2
Rosowski *et al.* (1990)		Z_{ec}	1
Stinson (1990)		R_{ec} canal reflection coefficient	1
	Puria and Allen (1991)	Z_c	
	Wada *et al.* (1992)	Z_{ec} (static+dynamic) finite element model	1
Goode *et al.* (1993)		D_u/P_{ec}	
Keefe *et al.* (1993)		Z_{ec} in living ears	1
Puria *et al.* (1993a)		P_v/P_{ec}	3
Voss and Allen (1994)		Z_{ec} in living ears	1
	Goode *et al.* (1994)	D_{st}/P_{ec}, D_u/P_{ec}	2
Merchant *et al.* (1996)		Z_{st}, Z_c	
Puria *et al.* (1997)		P_v/P_{ec}	3
Puria and Rosowski (1996)		Forward and reverse gains pressure P_v/P_{ec}, P_{ec}/P_v	3 & 4
Hudde and Engel (1998b)		Z_{ec}, forward and reverse pressure gains	1,3 & 4
Aibara *et al.* (2001)		P_v/P_{ec}, V_{st}/P_{ec}, Z_c	2 & 3

There are two important reasons for this study. The first is to report measurements that will allow a full characterization of the human middle ear and the second is to provide an empirical basis for understanding how the middle ear modifies otoacoustic emissions (OAEs) generated by the cochlea and measured in the ear canal.

In its simplest form, the middle ear can be described as a two-port system with one port at the ear canal and the other port at the stapes footplate. Mathematically, an ABCD matrix relates the variables at the ear canal and the stapes footplate as follows:

$$\begin{bmatrix} P_{ec} \\ U_{ec} \end{bmatrix} = \begin{bmatrix} \mathbf{A} & \mathbf{B} \\ \mathbf{C} & \mathbf{D} \end{bmatrix} \begin{bmatrix} P_v \\ -U_{st} \end{bmatrix}. \quad (1)$$

In Eq. (1), P_{ec} and U_{ec} are the ear-canal pressure and volume velocity, while P_v and U_{st} are the vestibule pressure and stapes volume velocity, respectively. Velocities going into the middle ear are defined as positive (U_{ec}), and velocities coming out of the middle ear are defined as negative ($-U_{st}$). Equation (1) states that the four input–output variables are related to each other by four matrix elements, **A**, **B**, **C**, and **D** that completely characterize the middle ear. All variables in Eq. (1) are a function of frequency.

The ABCD chain matrix formalism has been used for modeling the ear canal (Egolf *et al.*, 1992), the middle ear (Peake *et al.*, 1992; Shera and Zweig, 1992), and the inner ear (Puria and Allen, 1991). Although the formalism has

been expressed, the elements of the ABCD matrix have not been measured for any middle ear, human or otherwise. An important attribute of the ABCD matrices is that they are independent of the cochlear and ear-canal loads, which allows a better comparison of the properties of the middle ear alone. The ABCD matrix formalism has the additional advantage of providing readily interpretable matrix elements (Shera and Zweig, 1992).

Solution of the four unknown complex (magnitude and angle) variables **A**, **B**, **C**, and **D** requires four complex measurements at each frequency and knowledge of the cochlear and ear canal loads. As outlined above, only two independent measurements were previously made in different ears and from different laboratories. Our goal since 1991 has been to make a sufficient number of measurements in human ears to obtain the ABCD chain matrix. The second goal has been to make all measurements from the same ears in the same laboratory, which helps reduce measurement variability.

A parallel effort is the recent work of Hudde and Engel (1998a, b). They reported a sufficient number of variables from the same ear to characterize the impedance matrix from the ear canal to the incus, not including the stapes. The impedance and ABCD matrices are related to each other through matrix transforms. However, measurements reported by Hudde and Engel are quite noisy for frequencies above about 2–3 kHz, and thus at high frequencies the middle ear remains to be characterized.

Several intermediate results that led to the development of the methods described in this paper have been reported. The first of these was the forward middle-ear pressure gain, P_v/P_{ec} (Puria *et al.*, 1993a, 1997). Development of the reverse middle-ear pressure gain was reported at a hearing mechanics conference (Puria and Rosowski, 1996). Stapes velocity was added to the forward pressure gain measurements, to provide the first measurements of middle-ear stapes velocity and vestibule pressure gains from the same ears (Aibara *et al.*, 2001). The ratio of P_v to stapes volume velocity U_{st} gave the first direct measurement of the cochlear input impedance in human ears. Previous techniques and preparations were combined and further refined to allow measurement of these three variables and the cochlear load from the same ear.

Measurements of four independent variables from five temporal bone ears are reported in this paper. These measurements include the middle-ear pressure gain in the forward direction, the cochlear input impedance (vestibule pressure to stapes volume velocity) in the forward direction, the middle-ear pressure gain in the reverse direction, and the middle-ear impedance looking out from the stapes in the reverse direction (rather than the impedance looking into the middle ear as reported by many others). All of these complex (real and imaginary components) measurements, along with assumptions of reciprocity for the middle ear (Shera and Zweig, 1992), are sufficient to fully characterize the human middle ear independently of the cochlear and ear-canal loads. The reciprocity assumption reduces the number of measurements from four to three. Only the three measurements and the cochlear load are reported in the present study. The reported measurements are compared with predictions from Shaw's (1977; Shaw and Stinson, 1983) model of the middle ear.

Generated within the inner ear, otoacoustic emissions (OAEs) travel through the middle ear and are measured in the ear canal (Kemp, 1978). The accessibility of otoacoustic emissions to measurement makes them a potentially useful clinical tool for objective evaluation of cochlear and middle-ear function. However, little is known about the effect of the middle ear on otoacoustic emissions, and thus the inner ear—as viewed through the middle ear—is clouded by incomplete knowledge of the middle ear.

Measurement of the reverse pressure gain through the middle ear could help ''clear the window'' through which the inner ear is viewed using OAEs. However, there are no direct measurements of sound-driven reverse middle-ear pressure gain in humans. The reverse pressure gain has been directly measured only in guinea pig ears (Magnan *et al.*, 1997).

The forward and reverse middle-ear pressure gain measurements (M1 and M2) are used to quantify the effect the middle ear has on ear canal measurements of otoacoustic emissions. In addition, the cochlear input impedance and the reverse impedance (Z_c and M3) are used to quantify the stapes reflection coefficient for OAEs. Measurements of OAEs and the present measurements are combined to ascertain the level versus frequency slope of the OAE generator mechanism for CEOAEs and DPOAEs. Portions of the OAE analysis were previously presented (Puria, 2003).

II. METHODS AND MATERIALS

Portions of the measurement procedures have been previously described (Puria *et al.*, 1993a; Puria and Rosowski, 1996; Puria *et al.*, 1997; Aibara *et al.*, 2001). Because there are differences in current and previous methods, the procedures are repeated here while highlighting those differences.

A. Postmortem materials

Seven temporal bone ears were used for these experiments. A complete set of measurements from five ears (E1–E5), from four donors, are reported. The other two ears were used to develop measurement techniques. Measurements were made on thawed ears extracted from human cadavers. Four temporal bones (E1–E4) were purchased from the Anatomic Gift Foundation (AGF), which solicits postmortem materials throughout the country from a whole body future donor program (http://www.anatomicgift.com/). One bone (E5) was obtained from the Oakwood Hospital Laboratory (Dearborn, MI), licensed by the state of Michigan for the procurement of donated cadaver tissue for implantation and/or research. No audiometric information on donors is available.

Temporal bone cores were extracted at the time of autopsy within 24 h of cardiac death, or within 48 h if the body was placed in refrigerated storage within 12 h of death. In either case, the cores were kept frozen at −20 °C. Standard contagious disease screenings were performed. Upon confirming all contraindications, temporal bones were packed in dry ice and shipped to the California Ear Institute at Stanford overnight.

The donors of the temporal bones were both male (2) and female (2). The ages of the donors were 53, 73, 73, 67,

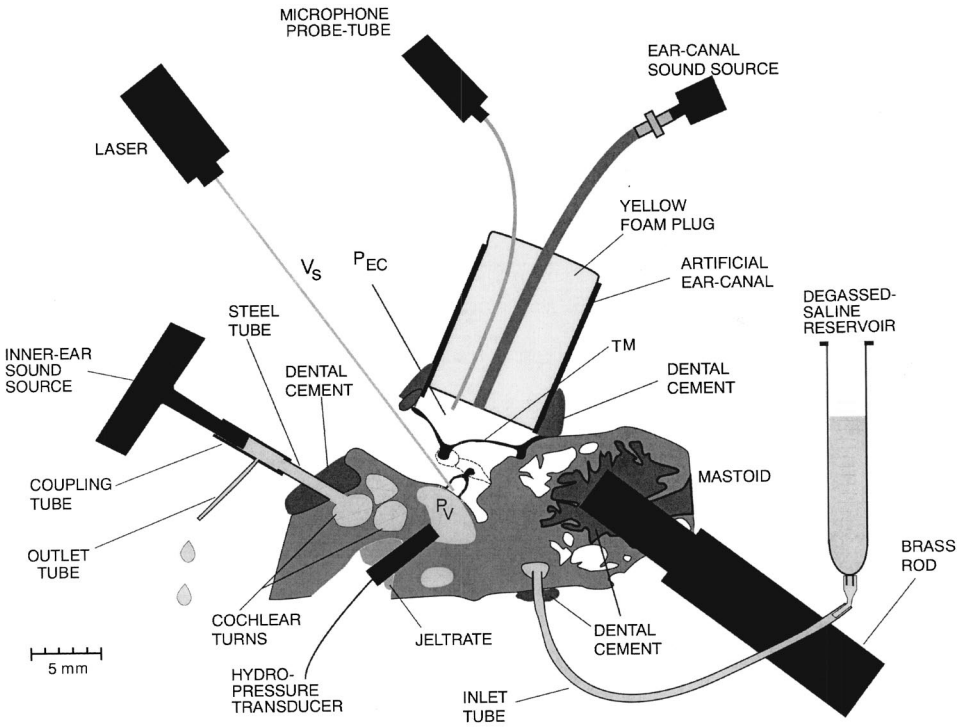

FIG. 1. A simplified horizontal cross section of a human temporal bone (right ear) preparation for driving the middle ear in the forward and reverse directions. A yellow-foam plug coupled to a Knowles receiver was used to drive the middle ear in the forward direction. The inner-ear sound source coupled to a tube cemented near the round window was used to drive the inner ear in the reverse direction. The ear-canal pressure P_{ec} was measured with an ER-7C probe-tube microphone. To measure the inner-ear pressure P_v, a hydropressure transducer was placed in the vestibule. The stapes velocity was measured with a HLV-1000 PolyTec laser vibrometer. An inlet and outlet tube allowed flushing of the inner ear to ensure that it remained fluid filled. The temporal bone was cemented, in the horizontal portion of the carotid artery, to a brass stick (shown here in the mastoid region to avoid clutter), which was clamped to a pole mounted on the vibration isolation table. The hydrophone was mounted on a micromanipulator. The temporal bone and attached materials are not necessarily on the same scale nor are they in the same plane.

and 54 for E1–E5, respectively, with an average age of 62 years. The races were Caucasian for E1–E4 and African American for E5.

B. Preparation of temporal bones

Upon removal of attached connective tissue, the bony wall of the external ear canal was drilled down to 1–2 mm from the TM annulus, keeping the posterior wall intact. A simple mastoidectomy and posterior hypotympanotomy were performed. The horizontal segment of the facial nerve and surrounding bone were removed to provide a good view of the stapes footplate, while leaving the chorda tympani and stapedius muscle tendon intact.

The internal auditory canal (IAC) was enlarged and the bone blue-lined with a drill over the vestibule. Two different locations were used. For E1–E3, the saccular wall at the inferior vestibular nerve, just anterior and superior to the singular canal (the duct for the nerve to the posterior semicircular canal), was exposed (Puria *et al.*, 1997). For E4 and E5, the vestibule was exposed at a site lateral to the transverse crest and just superior to the singular foramen, and a 1.4–1.6 mm hole was drilled (Aibara *et al.*, 2001). No differences in vestibule pressure are expected due to the two measurement locations. The latter location is preferable because the footplate can be more clearly visualized.

Two different ear canal sound-delivery and microphone systems were used. In both cases, an artificial ear canal (a small section of a 3-cc syringe with diameter 0.855 cm and length about 0.9 cm) was cemented (carboxylate dental cement ESPE, Durelon®, Norristown, PA) near the annulus after the bony ear canal of each temporal bone was shortened, by drilling bone away as shown in Fig. 1.

For ears E1, E2, and E3, the sound-source (CI-2955, Knowles Electronics, Itasca, IL) was glued with epoxy to a tube nipple (ER3-04, Etymotic Research, Elk Grove, IL), which was then coupled to the center tube of the yellow foam plug. The probe tube of the ER-7C microphone was threaded through the yellow foam plug with a household sewing needle, as shown in Fig. 1.

For ears E4 and E5, the configuration was similar to previous methods (Goode *et al.*, 1994). Two holes were drilled in the side of the artificial ear-canal tube. One hole provided the sound inlet port through a narrow tube (L=9 mm, OD=2 mm) glued to the side of the artificial ear canal with the other end of the narrow tube connected to a coupling nipple glued to the Knowles sound source. The other hole provided a way to place the ER-7C microphone probe tube, used to measure the ear-canal pressure, near the eardrum. This configuration allowed measurement of umbo velocity in the same ears (not reported here). In both sound-delivery systems, the microphone probe-tube tip was visually estimated to be within 1–3 mm of the eardrum.

As the inner ear manipulations produced the possibility of air entering the labyrinth, an ''inlet'' flush tube and an ''outlet'' flush tube allowed removal of the air. The ''inlet'' tube was placed and cemented in the readily accessible superior part of the superior semicircular canal. The length of this coupling tube varied from ear to ear but it was typically about 240 mm with a volume of about 50 μl. The ''outlet'' tube and the inner-ear sound source were coupled to the cochlea near the round window (RW). Previously, this location was used to attach the RW outlet tube (Puria *et al.*, 1997). With modifications to previous procedures, this location was also used to inject sound into the cochlea (Fig. 1).

To access the round window, the middle-ear cavity was opened widely by drilling into the hypotympanum through the jugular fossa, just anterior to the stylomastoid foramen, allowing access to the basal turn of the cochlea (Donald and Anson, 1992). A hole was drilled into the scala tympani just anterior to the RW. Dental cement was used to create a foundation on the bony surface surrounding the RW hole. After letting the cement dry, a steel tube (ID=0.73 mm, L=5.6 mm) was attached to the foundation surface using more dental cement. Care was taken, such as placing gelfoam in the oval window (OW) niche and the RW niche, to ensure that the dental cement did not damage important structures.

A polyethylene tube (ID=1.39 mm, L=13.7 mm) was inserted around the outer diameter of the steel tube. The polyethylene tube coupling helps to reduce vibrations produced by the inner ear sound source, from being transfered to the temporal bone. As shown in Fig. 1, a small steel outlet tube (ID~0.5 mm, L=17.4 mm) was inserted perpendicular to the polyethylene tube to allow fluid (and air, when present) to be drained from the cochlea.

The volume of visible fluid in the polyethylene tube (with the inner-ear sound source in place as shown in Fig. 1) was estimated to be approximately 5.6 μl, while the total volume of the RW assembly was expected to be about 8 μl. By comparison, the total volume of the cochlea is approximately 100 μl (Wever and Lawrence, 1954). It has been shown that manipulations of the scala tympani, by injecting small bubbles, affect primarily low-frequency responses (Puria *et al.*, 1997). It is expected that the attached tubes near the RW will likely decrease the cochlear input impedance magnitude primarily at low frequencies (see Sec. IV).

A brass-rod cemented to the bone (Fig. 1) allowed mounting of the bone to the measurement table. The brass rod was typically cemented into the horizontal portion of the internal carotid canal, just medial to the orifice of the bony Eustachian tube. In Fig. 1, some artistic license has been used to show the brass-stick in the mastoid region to reduce clutter on the left side of the drawing.

C. Measurement preparations

At the beginning of each measurement session, the temporal bone was attached to a fluid reservoir filled with degassed saline as shown in Fig. 1. Finger pressure was applied at the top of the reservoir to push fluid into the inner ear, causing air to be pushed out from the opening in the vestibule. The entire assembly was placed in a beaker filled with degassed saline (0.9% NaCl Irrigation USP, B. Braun Medical, Inc., Irving, CA) and then placed in a dry-seal glass vacuum desiccator (EW-08912-40, www.coleparmer.com) attached to a vacuum pump (Model C6C17N82B, Leeson Electric Corp., Grafton, MI). While being degassed for approximately 30 min, the glass chamber was periodically shaken and tapped gently to facilitate removal of air from the bone.

The temporal bone was mounted on a pneumatic isolation table (Type XJ-A, Newport Corporation, Fountain Valley, CA). A $\frac{1}{2}$-in.-diam steel pole was tightly screwed onto the table and the brass rod (cemented to the bone) was attached to the pole with a clamp. The bone was oriented to allow visualization of the stapes footplate through the facial recess. The fluid reservoir was held with a clamp attached to a second pole screwed onto the table. During the mounting process, the bone was oriented while maintaining the vestibule fluid level. The inner-ear sound source was coupled to the polyethylene tube already attached to the RW steel tube. Care was taken to ensure that air did not enter the polyethylene tube. The inner-ear sound source was held with a clamp attached to one of the poles screwed into the vibration isolation table.

The pressure sensor (EPIH-111-5P-/R, Entran Corp., Fairfield, NJ), used for measuring fluid pressure inside the vestibule, was gently pushed down to the bottom opening of a hollow brass tube (OD=1.65 mm, ID=1.39 mm, and about 25 mm in length) to house and protect the sensor and its wiring. A dab of medical grade silicone (Silastic, Dow Corning, Midland, MI) was applied on the surface of the sensor and allowed to dry overnight to waterproof it. The hollow brass tube was permanently attached to a larger brass tube mounted at an angle. The calibrated (see below) hydropressure assembly was placed on a ball-joint micromanipulator (BE-8, Narishige Corp., Japan). The manipulator was used to position the tip of the hydrophone such that most of the vestibule opening is blocked by it. An alginate liquid impression material, ''Jeltrate'' (L. D. Caulk Company, Division of Dentsply International, Inc., Milford, DE), was applied between the internal auditory canal and the body of the brass tube. When mixed and applied, the impression material is in liquid form and within about one minute it congeals into a mold. A successful application was one where there was no fluid flow from the vestibule and fluid starts to flow out from the outlet tube, as shown in Fig. 1, due to gravity.

As mentioned above, two different ear-canal sound delivery systems were used for these experiments. In both cases, fluid in the ear canal and on the eardrum was cleaned with a vacuum suction tip. For E1–E3, the yellow foam assembly consisting of the sound delivery tube and microphone probe tube was inserted into the artificial ear canal. The microphone and the sound source were attached to corresponding tubes as shown in Fig. 1. For E4 and E5, a dab of FunTack® (DAP, Inc., Dayton, OH) was used to attach the microphone probe tube to the side of the artificial ear while approximately centering the tip near the center of the eardrum. A layer of FunTack was also placed around the rim of the artificial ear canal, and a square glass cover slip ($7/8\ \text{in.}^2 \times 0.018$ in.) was used to cover the ear canal. The sound source was attached to a tube cemented to the artificial ear canal.

For E1–E3, velocity of the stapes was measured directly without a target. To improve the laser signal-to-noise ratio (SNR), a small (less than 1 mm^2) piece of reflective tape with adhesive backing was attached to the stapes footplate center for E4 and E5. For E1, the velocity from the anterior portion of the footplate was measured. Calculation of cochlear impedance measurements suggested that the measurement location on the footplate is important. Thus, footplate measurement location was explored in subsequent bones. For E2–E5, velocity measurements from the center of the foot-

plate are reported. The bones were kept moist by applying saline to the middle-ear cavity typically within 30 min, preceding each measurement. The application of fluid moistened the tympanic membrane, ossicles, annular ligament, round-window membrane, supporting ligaments, and surrounding structures.

1. Normal ear

Physiological measurements were made in pairs. The ear canal was driven with sound, and the ear canal and vestibule pressures measured. From the two responses, the middle-ear pressure gain was calculated to check for the presence of air in the cochlea as previously described (Puria *et al.*, 1997). On occasion, when it was clear that air was present, the entire degassing process was restarted, the bone remounted, and the middle-ear pressure gain measured again. One of the inputs, typically the ear canal pressure, was then switched to stapes velocity, and the vestibule pressure and stapes velocity recorded. These responses provide the M1 and Z_c measurements. The output drive was switched to the inner-ear sound source and the ear canal pressure, vestibule pressure, and stapes velocity responses recorded again in pairs. These variables provide the M2 and M3 measurements. As described below, M1, M2, M3, and Z_c were calculated using MATLAB scripts.

2. Middle-ear manipulations

Once a satisfactory number of measurements were obtained for the normal ear, a number of middle-ear manipulations were made for different experiments not reported here. Measurements of reverse pressure gain (M2), with the cut ISJ, provide a convenient way of assessing artifacts on reverse middle-ear pressure gain measurements (Puria and Rosowski, 1996). The incudo-stapedeal joint (ISJ) was cut with a sharp surgical knife; unfortunately, M2 was only measured on E1.

D. Response measurement, calibration, and analysis

1. Response measurements

All measurements were performed using the SYSid (version 6.5) audio band measurement and analysis system (www.sysid-labs.com, Berkeley, CA), a software program that interfaces a DSP-16+ board with two-channel D/A and A/D converters and a Digital Signal Processing chip running on an IBM compatible PC.

Stimulus generation and synchronous response averaging were performed with the SYSid system (Puria and Allen, 1992; Puria *et al.*, 1993b), which extracts the amplitude and phase of the response at each frequency through fast Fourier transformation (FFT).

The output of the D/A converter was amplified with a power amplifier (P2075, Yamaha Electronics) and fed to a toggle switch that allows switching between the ear canal sound source with a 200 Ohm series resistor for attenuation, and the piezo driver for the inner-ear sound source.

The stimulus delivered by the D/A conventer was either a single-frequency tone or a flat spectrum wideband chirp (swept tone with quadratic phase and linear group delay). In the single tone case, measurements were repeated several times (160–180 points) with the frequency of the tone evenly spaced on a log-frequency axis from 24.4 Hz to 25 kHz. This is often called the stepped-tone method. The magnitude and angle of the response at the primary frequency, second and third harmonic distortions, and the total harmonic distortion plus noise (THD+N) magnitude are saved to a file for all frequencies automatically (Distortion menu in SYSid). Chirp measurements were used to quickly ascertain the physiological state of variables being measured during the measurement session. All measurements reported here were made with stepped tones.

Simultaneously with the stimulus, a response waveform was sampled by the two A/Ds connected to the ER-7C probe-tube microphone amplifier (Etymotic Research, Elk Grove, IL), or the HLV-1000 laser vibrometer (PolyTec PI, Tustin, CA) and the low-noise preamplifier (DL Instruments, Ithaca, NY) coupled to the hydropressure transducer. Since the SYSid HW is a two-channel system, only two simultaneous variables can be measured at any given time. The input variables were manually switched.

The stimulus buffer was 2048 points sampled at 20 μsecs. This corresponds to a stimulus having 1024 frequency points with a frequency minimum of 24.4 Hz and maximum of 25 kHz. Typically, 20–60 stimulus buffer presentations were averaged at each tone frequency corresponding to a stimulus length of 0.8–2.4 s/frequency.

2. Calibration

A reference microphone is used as a standard for calibrating magnitude and angle of the pressure transducers used for these measurements. A sound level calibrator (type 4230) was used to determine the sensitivity of a $\frac{1}{8}$-in. reference microphone (type 4138) coupled to a pre-amp (type 2633) with a UA 160 adapter (UA 160), all from Bruel and Kjaer (Norcross, GA). The entire reference microphone assembly has a flat response ($\pm$0.5 dB) and zero phase shift ($\pm$1°) in the 0.024–12 kHz frequency range.

The probe-tube microphone and the hydrophone were independently calibrated as follows: The probe-tube tip was placed within 1 mm of the reference microphone in a small and transparent cavity (25 mm long). Sound was injected into the sealed cavity via a small tube attached to a hearing aid receiver. The ratio of the complex responses of the reference microphone and the probe-tube microphone is the calibration curve for the probe-tube microphone. The hydrophone was calibrated in exactly the same manner. Due to its high impedance, the hydrophone's sensitivity (measured after water proofing the tip, as discussed in Sec. II C) is assumed to be the same in air and water. To check the calibration of the two microphones, the probe-tube microphone and hydrophone were placed together, 1 mm apart, in a different 25-mm-long sealed cavity and their calibrated responses compared. The maximum deviation in magnitude was 1.0 dB at 1 kHz, with a maximum deviation in phase of 15° at 10 kHz. The observed differences place a bound on possible calibration errors in the measurement system.

The HLV-1000 laser Doppler vibrometer (LDV) system was calibrated by aiming the LDV at a target on top of an

accelerometer (type 4371) that was attached to a mini shaker (type 4810), both from Bruel and Kjaer (Norcross, GA). The response of the LDV was then compared to the accelerometer's, which had a known sensitivity and phase response between 0.024 and 10 kHz.

The complex gains of all amplifiers were measured and incorporated into calibration specifications. This includes the looped response of the SYSid hardware, the low noise preamp for the hydrophone, and other amplifiers used only for calibration purposes.

All of the calibration measurements were made from the ''caliBrate'' menu in SYSid which greatly simplifies calibration procedures. After all the equipment was calibrated, the calibration files were specified from this menu. When enabled, these calibration files are used to operate on the measured data. The resulting data then has physical units (Pa, mm/s) rather than volts. Calibration and gain files were specified for E3–E5. On E1 and E2, calibration files were applied to measured voltages manually.

All calibration and gain measurements were made at 32k points with a resolution of 1.53 Hz. When calibration files are specified, SYSid interpolates, effectively down-sampling, the specified calibration data to the FFT length of the measurements (2048 points) before operating on the data.

Data presentation is limited to the 0.1–10 kHz range; low-frequency limitations are due to inadequate signal-to-noise ratios and high-frequency limitations are due to calibration errors.

3. Analysis

The measured stepped-tone responses were read back into SYSid and the magnitude and phase angle of the primary responses interpolated (using cubic splines) from the log-frequency axis to a linear frequency axis (1024 frequency points). One of the advantages of interpolating the response on a frequency axis common to all measurements is that it allows easier manipulation of the data (i.e., taking ratios, averaging, etc.). For some of the measurements (E1–M2, Z_c, and M2 after separating the ISJ; E3–M1, M2, and Z_c), the magnitude and phase angles were smoothed in SYSid, with a $\frac{1}{6}$ octave (oct) band filter.

Harmonic distortion measurements confirm previous reports that for ear-canal pressures below about 120 dB SPL, corresponding to a maximum vestibule pressure of about 140 dB SPL, the middle ear behaves as a linear system (Guinan and Peake, 1967; Puria *et al.*, 1993a). When driven by the ear-canal sound source, ear-canal pressures varied as a function of frequency between 90 and 115 dB SPL with second and third harmonic distortions typically more than 30 dB down from the primary level. Inside the cochlea the corresponding harmonic distortions were also 30–40 dB down from inner-ear primary levels. When driven by the inner-ear sound source, cochlear pressures varied from 90 to 130 dB SPL with second and third harmonic distortions typically 30–40 down from the primary tone level. In the ear canal, the corresponding harmonic distortions were also 30–40 dB down from ear canal primary levels. Most of these distortions are generated by the sound generating transducers.

Custom MATLAB scripts were used to analyze the data presented in this report. Files and input channels in pairs produced the magnitude and angle of the ratio as follows:

$$\mathrm{M1} = \frac{\vec{P}_{v}}{\vec{P}_{\mathrm{ec}}}, \tag{2}$$

$$\mathrm{M2} = \frac{\overleftarrow{P}_{\mathrm{ec}}}{\overleftarrow{P}_{v}}, \tag{3}$$

$$\mathrm{M3} = \frac{\overleftarrow{P}_{v}}{\overleftarrow{V}_{\mathrm{st}} A_{\mathrm{fp}} / \mathrm{Cos}(\theta_{\mathrm{st}})}, \tag{4}$$

$$Z_c = \frac{\vec{P}_{v}}{-\vec{V}_{\mathrm{st}} A_{\mathrm{fp}} / \mathrm{Cos}(\theta_{\mathrm{st}})}. \tag{5}$$

The right arrow ($\rightarrow$) indicates forward drive while the left arrow ($\leftarrow$) indicates reverse drive. In Eqs. (4) and (5) a footplate area A_{fp} of π mm^2 (Wever and Lawrence, 1954) and a stapes angle θ_{st} of 55° relative to an axis perpendicular to the footplate and through the stapes head (based on an average of angle measurements in the Aibara *et al.* study) is assumed. With V_{st} as the rms velocity, the magnitude of the denominator in Eqs. (4) and (5) is the rms stapes footplate volume velocity, $|U_{\mathrm{st}}|$ along the stapes axis, which is perpendicular to the footplate.

Individual measurements were converted to log-magnitudes, mean and STDs computed, and the results converted back to a linear scale by taking its anti-log. All reported slopes (dB/oct, deg/oct, etc.) were computed by fitting, in a least-squares sense, a straight line in the specified frequency range.

E. Model calculations

The measured results (M1–M3) can be compared to model predictions from a number of existing middle ear models. Such comparisons allow us to determine if the current models are consistent with measurements, or if they need modification. Shaw's (1977; Shaw and Stinson, 1983) model of the middle ear was chosen because it is considered to be one of the better lumped-element models for the human middle-ear (Goode *et al.*, 1994; Hudde and Engel, 1998b). The primary difference between Shaw's middle-ear model and other lumped element models is the representation of the eardrum as two coupled pistons, instead of a single piston. Parameters of the two-piston model were updated by Goode *et al.* (1994) to more accurately represent stapes velocity measurements. In the present study, we use the Goode *et al.* parameters for Shaw's model, with two exceptions pertaining to the ear-canal load and the cochlear load.

The ear-canal load and the cochlear load are represented as two loads termed MT-A for model termination A and MT-B for model termination B. It can be expected that in the forward direction (M1) the cochlear load has a significant effect (Puria *et al.*, 1997). We look at the effect the cochlear load has by using the Aibara *et al.* measured impedance and an average resistive (zero phase) load of 100G Ohms [see

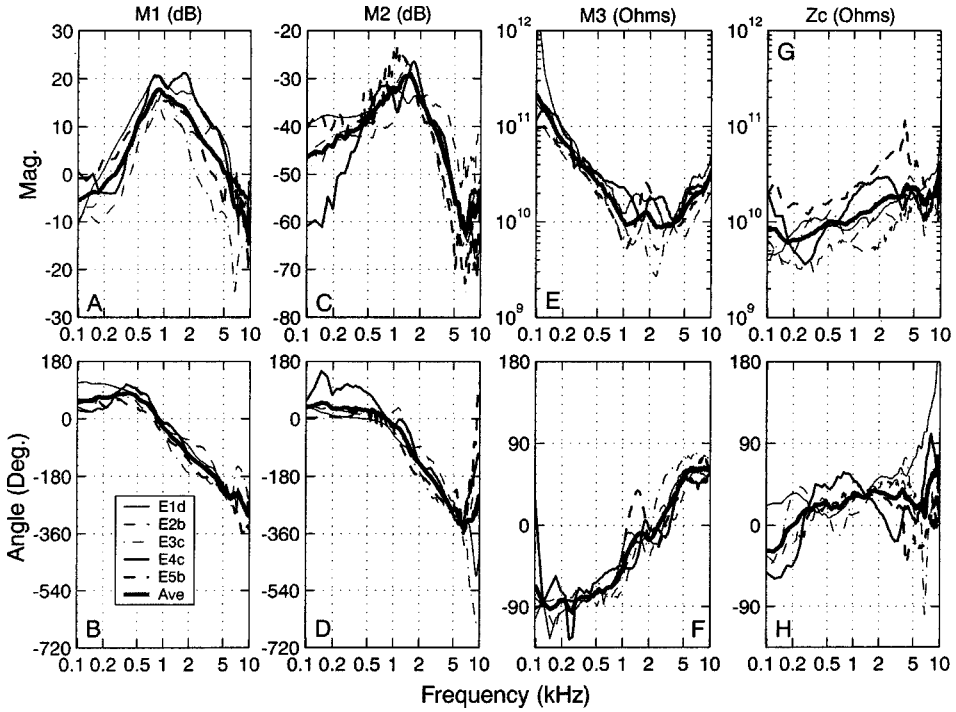

FIG. 2. Measurement of M1 [panels (a) and (b)], M2 [panels (c) and (d)], M3 [panels (e) and (f)] and Z_c [panels (g) and (h)] from five temporal bone ears. The average of the log-magnitude and angle is shown as thick-solid lines in each panel. See Eqs. (2)–(5) for definitions of M1–M3, and Z_c. M1 and Z_c were measured while the ear was stimulated, with an ear canal sound source, in the forward direction. The forward middle-ear pressure gain, M1 is the ratio of the vestibule pressure to the ear-canal pressure (P_v/P_{ec}). The cochlear input impedance $Z_c = P_v/-U_{st}$, is the ratio of the vestibule pressure to the stapes-volume-velocity U_{st} defined as the stapes-velocity times the footplate area. M2 and M3 were measured while the ear was stimulated, with the inner ear sound source, in the reverse direction. The reverse middle-ear pressure gain, M2, is the ratio of the ear-canal pressure to the inner-ear pressure (P_{ec}/P_v). The reverse middle-ear impedance, $M3 = P_v/U_{st}$, is the ratio of the vestibule pressure to the stapes-volume-velocity. For each ear, data from the same measurement session is shown.

Figs. 4(g) and (h)]. As in the forward direction, the impedance of the ear-canal sound delivery system in the reverse direction (M2) can have a significant effect (Puria and Rosowski, 1996). As discussed in Sec. II C above, the two sound delivery methods have very different impedances for most frequencies of interest. The impedance of the sound delivery mechanism with the glass cover slip and the Aibara *et al.* cochlear load make up MT-A. The impedance of the sound delivery mechanism with the yellow foam plug and the average cochlear impedance together make up MT-B.

III. RESULTS

Figure 2 shows the magnitude (top row) and angle (bottom row) of the measurements M1, M2, M3, and Z_c from five individual ears in the 0.1 to 10 kHz region. Also shown in Fig. 2 are the averages of the four measurements.

A measure of the variability across ears is the standard-deviation (STD). In addition to averages, Fig. 3 shows the STD of the measured magnitudes and angles across ears.

A. Forward pressure gain—M1

The magnitude of the forward pressure gain $|M1|$ from five ears is shown in Fig. 2(a) while the corresponding angle $\angle M1$ is shown in Fig. 2(b). The magnitude of the pressure gain has generally a bandpass shape with a five-ear-average maximum of 18 dB at 0.9 kHz. Below 0.8 kHz, average $|M1|$ has a slope of approximately 10.4 dB/oct. Between 1 and 6 kHz, average $|M1|$ has a slope of approximately -7.2 dB/oct.

The angle of the forward pressure gain $\angle M1$ five-ear-average has a maximum of 50° at 0.4 kHz with a slope of 13°/oct below the peak. The phase crosses 0° near 0.9 kHz. From 0.9 to 6 kHz, the average slope is about -73°/oct.

The STD of $|M1|$ is shown in Fig. 3(a) while STD of $\angle M1$ is shown Fig. 3(b). The STD of $|M1|$ varies from a maximum of 3.1 dB at 6.7 kHz to a minimum of 1.4 dB at 0.9 kHz, with an overall average STD of 2.1 dB. The STD of $\angle M1$ varies from a maximum of 66° at 8.2 kHz to a minimum of 12° at 5.8 kHz with an overall average STD of 38°. The overall average STD is defined as the square root of the average variance (STD^2).

B. Reverse pressure gain—M2

The magnitude of the reverse middle-ear pressure gain $|M2|$ from five ears is shown in Fig. 2(c) while the corresponding angle $\angle M2$ is shown in Fig. 2(d). Like $|M1|$, the magnitude of the reverse pressure gain has generally a bandpass shape with a five-ear average maximum of -30 dB at 1.4 kHz. There is also a local minimum of -63 dB at 6.8 kHz. Below 1.2 kHz, average $|M2|$ decreases with a slope of approximately 4.1 dB/oct. Between 1.6 and 6.4 kHz, average $|M2|$ decreases at approximately -15.6 dB/oct. Above 7 kHz average $|M2|$ increases with a 12 dB/oct slope.

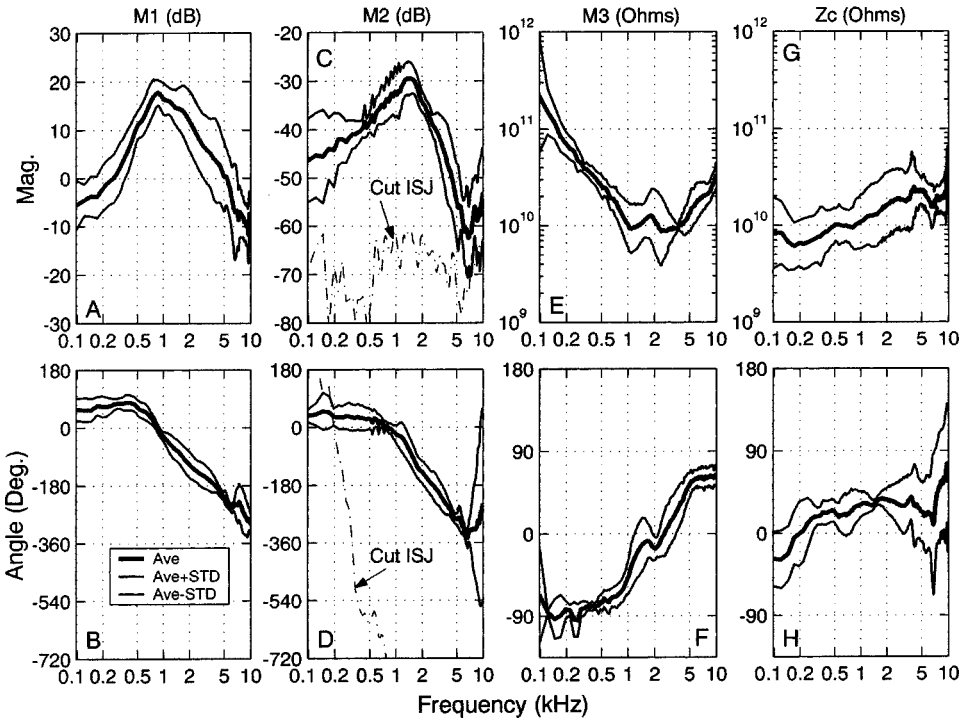

FIG. 3. Average and standard deviation (STD) of individual data from Fig. 2. Panel (c) also shows the magnitude of the reverse pressure gain after separating the incudo-stapedial joint (ISJ) while panel (d) shows the corresponding angle for frequencies below about 1 kHz (above 1 kHz, the angle continues to decrease linearly).

The average ∠M2 decreases from about 40° at 0.1 kHz, crosses 0° at 0.8 kHz, and reaches −350° at 6.8 kHz. Above 6.8 kHz, average ∠M2 increases to about −250° with a slope of 154°/oct. Below 0.4 kHz slope of ∠M2 is −7°/oct. Between 1.6 to 6.8 kHz, the slope of average ∠M2 is −105°/oct.

The individual ear data generally follow the average curves. The exception is E4, which has somewhat of a different M2 below about 1 kHz. Above about 6.7 kHz, two different responses are apparent from ∠M2. For E1 and E3 the angle continues to decrease while for the other ears the angle slope reverses sign.

The STD of |M2| is shown in Fig. 3(c) while STD of ∠M2 is shown Fig. 3(d). The STD of |M2| varies from a maximum of 3.8 dB at 9.3 kHz to a minimum of 1.2 dB at 2.2 kHz with an average STD of 2.3 dB. The STD of ∠M2 varies from a maximum of 300° at 10 kHz to a minimum of 13° at 0.8 kHz with an average STD of 116°. The large STD at the highest frequencies is due to the two different types of responses discussed above.

The reverse gain M2 after separating the ISJ is an important measurement as it provides a method for assessing artifacts and noise not related to sound transmission through the ossicular chain. The magnitude of M2, for the cut ISJ condition, is shown in Fig. 3(c) while the angle is shown in Fig. 3(d). The ear-canal pressure is 60–70 dB down from the vestibule pressure indicating that artifacts are at least that far down in the present preparation [Fig. 3(c)]. The angle linearly decreases from about 180° to about −3200° [only a portion of this curve is shown in Fig. 3(d)]. The fact that the phase decreases linearly, rather than being noisy, indicates that the M2 measurement, with cut ISJ, is due to an alternate path to the ear canal rather than due to noise. The average group delay of this path is about 0.85 ms and it is not clear what path the signal takes.

C. Reverse middle-ear impedance—M3

The reverse middle-ear impedance magnitude |M3| from five ears is shown in Fig. 2(e) while the corresponding phase ∠M3 is shown in Fig. 2(f). Generally, |M3| decreases with increasing frequency, reaches somewhat of a plateau, and increases again at high frequencies. The 1–4 kHz region shows signs of a resonance in individual ears. The magnitude and phase of the average M3 (Figs. 3e, f) indicates that it is approximately a spring (below 0.9 kHz), dashpot (1–4 kHz) and mass (5–10 kHz) system.

In the 0.2–0.9 kHz region, reverse impedance is stiffness dominated. The slope of the average |M3| is about −6.4 dB/oct while average ∠M3 is about −75° with a shallow 13°/oct slope. End-points affect some of this analysis because in the 0.25–0.75 kHz region the slope is closer to −6 dB/oct. In the 1–4 kHz transition region, reverse impedance is resistance dominated. The mean of the average |M3| is 10G Ohms and varies with nearly a flat slope of −0.7 dB/oct. The mean of the average ∠M3 is 0° with a steep 32°/oct slope. The phase crosses 0° at 2.6 kHz. In the 5–9 kHz region, reverse middle-ear impedance is mass dominated. The slope of the average |M3| is about 5.1 dB/oct while average ∠M3 is 60° with a shallow 7°/oct slope.

Figures 3(e) and (f) show the STDs of |M3| and ∠M3, respectively. Magnitude STDs were calculated on a log-magnitude scale and converted back to the linear domain. In Fig. 3(e), |M3| times the magnitude STD (upper plot) and divided by the magnitude STD (lower plot) are shown by the thin lines. Clearly, the largest STD in M3 is at the lowest frequency point (0.1 kHz), which we exclude from the STD analysis. Above 0.12 kHz, the STD of |M3| varies from a maximum of 2.3 (equivalent of 7.2 dB) at 2.4 kHz to a minimum of 1.1 (0.8 dB) at 3.7 kHz with a 1.5 (3.5 dB) average STD. The STD of ∠M3 varies from a maximum of 29° at

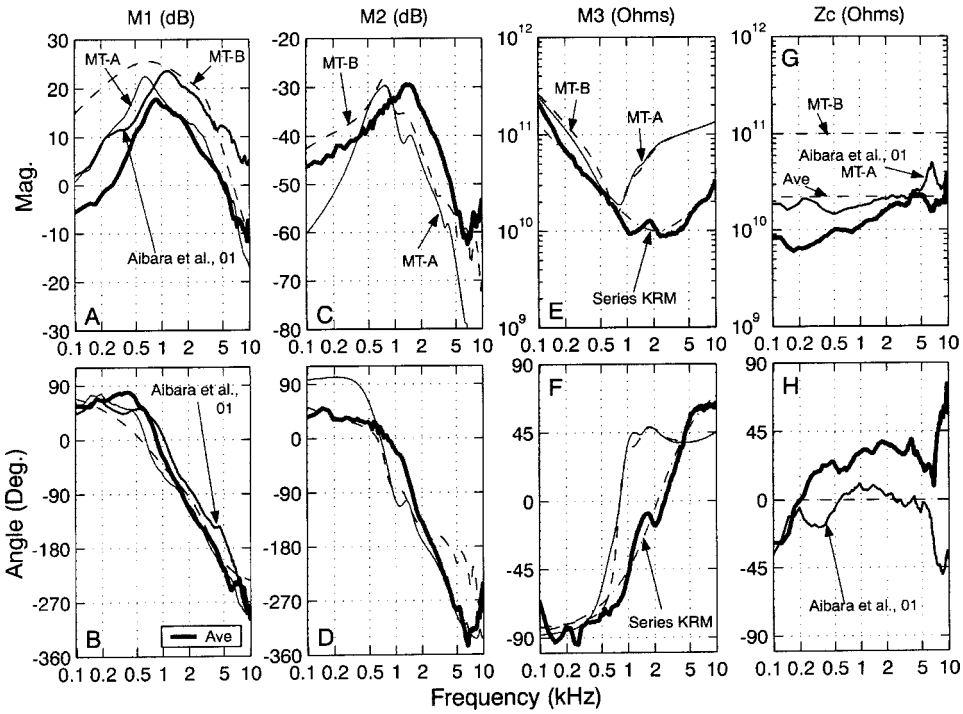

FIG. 4. Average of measurements (from Fig. 3) are compared to measurements previously reported in the literature and model computations. M1 [panels (a) and (b)] and Z_c [panels (g) and (h)] from Aibara *et al.* (2001) are less invasive than the preparation used in the present study. "Ave" curve is mid-frequency average (21.1G Ohms) of the Aibara *et al.* $|Z_c|$. A series KRM (stiffness K, resistance R, and mass M) model fit to the average M3 impedance [panels (e) and (f)] is shown (see text for parameters). Shaw's (1977; Shaw and Stinson, 1983) middle-ear model, with parameter updates by Goode *et al.* (1994,), was used for the computational results. Two different pairs of ear canal and cochlear loads were used for model terminations (MT). For MT-A, Z_c is the Aibara *et al.* measurement and the ear-canal load is the impedance of a tube terminated with a glass cover slip impedance. For MT-B, Z_c is 100G Ohms, estimated by Goode *et al.* (1994), and the ear canal load is the impedance of a short tube terminated by the impedance of a yellow foam plug.

1.4 kHz to a minimum of 2° at 0.12 kHz with an average STD of 16°. The increase in STD in the 1–3 kHz region is due to a resonance in individual ears.

D. Cochlear input impedance—Z_c

The cochlear input impedance magnitude, $|Z_c|$, from five ears is shown in Fig. 2(g) while the corresponding angle, $\angle Z_c$, is shown in Fig. 2(h). The driving point impedance of the cochlea has three distinct regions. The first is between 0.1 and 0.17 kHz, the upper frequency being the point where the average magnitude changes slope. The second region is from 0.17 to 6.8 kHz, the upper frequency being the point where the phase changes slope. The third region is in the 6.8–10 kHz range.

In the 0.1–0.17 kHz region, the slope of $|Z_c|$ is about −3.3 dB/oct with 11°/oct slope for $\angle Z_c$. At 0.17 kHz $|Z_c|$ has a minimum of 6.1G Ohms. From 0.2 to 5 kHz, $|Z_c|$ has a slope of 2 dB/oct. In the same frequency region, $\angle Z_c$ is nearly flat (−1°/oct) with an average angle of 31°. There is minimum in the angle of 8° at 6.8 kHz. In the 7.5–9 kHz region, the average $|Z_c|$ is 19G Ohms with a slope of about 2.3 dB/oct. In the same frequency region the angle of Z_c is steep with a 59°/oct slope.

Figures 3(g) and (h) show the STD of the measured cochlear input impedance magnitude and angle, respectively. As was done for |M3|, the STD of $|Z_c|$ was calculated on a log-magnitude scale and converted back to the linear domain. The STD of $|Z_c|$ varies from a maximum of 2.5 (8 dB) at 3.9 kHz to a minimum of 1.3 (2.3 dB) at 7.5 kHz with a 1.7 (4.6 dB) average STD. The maximum STD is due primarily to the peak in $|Z_c|$ of E4 (Fig. 2g). The STD of $\angle Z_c$ has minimum of 4° at 1.5 kHz. Above 1.5 kHz the STD increases and reaches a maximum of 77°. This increase in STD is partly attributed to the increase in angle of E1. The overall average STD of $\angle Z_c$ is 45°.

IV. DISCUSSION

A. Comparison with previous work

Figure 4 shows averages of the present measurements from Fig. 3 and measurements previously reported for M1 and Z_c (Aibara *et al.*, 2001). Also shown in Fig. 4 are calculations for Shaw's (1977; Shaw and Stinson, 1983) model of the middle ear with middle-ear parameters from Goode *et al.* (1994) and two pairs of middle-ear model terminations A and B (see Sec. II E).

1. Cochlear input impedance—Z_c

The average $|Z_c|$, from Fig. 3(g), is shown in Fig. 4(g) while average $\angle Z_c$, from Fig. 3(h), is shown in Fig. 4(h). Measurements of Z_c from Aibara *et al.* (2001) are also shown. Generally speaking, the average cochlear input impedance magnitude $|Z_c|$, of the present measurements is lower than our previous measurements by about 3.4 dB (18.5 vs 27.5 G Ohms) and angles tend to be higher by about 45° (34° vs −16°), in the 0.1–10 kHz region [Figs. 4(g) and (h)]. The largest discrepancy of about 8.2 dB (6.9 vs 17.7 G Ohms) is at frequencies below 0.2 kHz. Above 5 kHz, the discrepancy is approximately 4.4 dB (20.3 vs 33.8 G Ohms).

In the mid-frequency region of 0.2 to 5 kHz, the present $|Z_c|$ measurement is lower by about 2 dB (16.8 vs 21.2 G Ohms) and angles higher by about 30° (30° vs 0°). Both $|Z_c|$ measurements are approximately an order of magnitude lower than the 100G Ohms resistive load suggested by Goode *et al.* (1994).

The working hypothesis, for differences between our present and previous Z_c measurements, is that the tubing used for driving the middle ear in reverse alters the cochlear input impedance. As shown in Fig. 1, and outlined in Sec. II, sound injection into the inner ear requires coupling of an inner-ear sound source (IESS) to the cochlea near the RW. In order to reduce vibrations produced by the IESS, a polyethylene tube was used to couple the IESS to a small steel tube cemented to the scala tympani near the RW. The total volume of the added tubing is estimated to be about 8 μl. The quantitative effect of such an addition of volume in the scala tympani is beyond the scope of the present work. Qualitatively, it is known from previous measurements that injecting air into the scala tympani reduces the cochlear impedance at low frequencies while injecting air into the scala vestibule reduces the impedance at high frequencies (Puria *et al.*, 1997). Thus it can be expected that a volume of fluid in the scala tympani near the RW will have its greatest effect at low frequencies and less of an effect at high frequencies. Another possible reason is that the flush tubes used for degassing the inner ear may affect Z_c. However, it was previously shown (Aibara *et al.*, 2001) that there are no statistical differences between measurements in frozen-and-thawed bones with flush tubes (Puria *et al.*, 1997) and fresh bones without flush tubes (Aibara *et al.*, 2001).

The fact that the load to the middle ear was altered does not affect our ability to estimate the middle-ear ABCD parameters [Eq. (1)]. All that is required is that we measure the load, whatever it may be, on the middle ear.

2. Forward pressure gain

The cochlear load has a significant effect on the forward middle-ear pressure gain M1. The average |M1|, from Fig. 3, is shown in Fig. 4(a) while average ∠M1, from Fig. 3(b), is shown in Fig. 4(b). Measurement of M1 from Aibara *et al.* (2001) is also shown. Like $|Z_c|$, present |M1| is lower than previous measurements for all frequencies with a discrepancy of up to 12–13 dB. Discrepancies in angles tend to be less than 30°–40°. As discussed in the previous section, $|Z_c|$ of the present preparation is lower than in the previous preparation (Aibara *et al.*) resulting in a lower |M1| measured in the present preparation.

The present work indicates that there are inaccuracies in the middle-ear model. Figures 4(a) and (b) also shows M1 from model calculations with two different cochlear loads, or model terminations (MTs). For MT-A, the Aibara *et al.* measured Z_c was used, while for MT-B a resistive load of 100G Ohms (zero angle) was used. With the flat cochlear load (MT-B), M1 level is higher by as much as 12 dB for frequencies below 1 kHz, in comparison to the Aibara *et al.* measurement. On the other hand, M1 level is lower than the Aibara *et al.* measurement by as much as 12 dB for frequencies above about 4 kHz. There is reasonable agreement in the 1–4 kHz region. Model ∠M1 is generally lower than the measured data. Using the Aibara *et al.* cochlear load (MT-A) improves the response at frequencies below about 1 kHz. But above 1 kHz, the disagreement between the Aibara *et al.* measurements and model M1 increases (from MT-B to MT-A). M1 is a function of both the middle-ear and the cochlear load. The fact that with a realistic cochlear load (MT-A) the model calculation disagrees with measurements of M1 from the same set of ears from which the cochlear loads were measured suggests that the problem lies in the middle-ear model itself.

3. Reverse middle-ear pressure gain

The average |M2|, from Fig. 3(c), is shown in Fig. 4(c) while average ∠M2, from Fig. 3(d), is shown in Fig. 4(d). Based on driving the stapes backwards with a force transducer (rather than sound), Hudde and Engel (1998b) estimated M2. Their measurements are noisy below about 0.5 kHz and above about 3 kHz. Even in the 0.5–3 kHz range, the STD appears to be at least 10 dB. In comparison, the maximum STD of the present |M2| is 3.8 dB with an overall average STD of 2.3 dB. Overall, mean estimates of |M2| by Hudde and Engel are typically lower than the present estimate by about 20 dB in the 0.5–3 kHz region.

The only other measurements of reverse middle-ear pressure gain have been by Magnan *et al.* (1997) in guinea pig ears. Their finding, that $|M2| \approx -35$ dB from about 1.5 to 8 kHz, is significantly different from the steep slope of −15.6 dB/oct reported here from human temporal bones. There are many possible reasons for differences between the two measurements. The first is the obvious species differences between human and guinea pig middle ears. Evidence of species differences is suggested by the fact that the forward middle-ear pressure gain in the guinea pig ears is also relatively flat, 19–27 dB in the 1.5–8 kHz frequency region (Magnan *et al.*, 1997), whereas in humans the gain decreases systematically as a function of frequency. Another possible reason for differences between the two measurements is the smaller ear-canal volume: 0.1 cm^3 in guinea pig ears versus approximately 0.7 and 23 cm^3 for the yellow foam plug and the glass cover slip terminations, respectively, in these experiments. Smaller volumes increase the ear-canal load to the middle ear and thus the pressure inside the ear canal due to reverse transmission.

Figures 4(c) and (d) also show M2 from model calculations with two different ear-canal loads. These loads correspond to the acoustic impedance of two different types of sound-delivery systems used in the present experiments (see Sec. II).

A tube representing the artificial ear canal, terminated by an impedance function, was used for MT-A and for MT-B. The length of the artificial ear canal and the terminating impedance function were different for MT-A and MT-B. For MT-A, the terminating impedance function consists of the parallel combination of the impedance of the glass cover slip and the impedance of a short tube attached to the side of the artificial ear canal terminated by the sound source. For MT-B, the terminating impedance function is from the parallel combination of the impedance of the yellow foam plug

and a narrow tube terminated by the sound source. Impedance measurements of both ear canal assemblies were made and model parameters for each assembly adjusted to fit the measured impedance data (not shown).

Generally, a bandpass shape describes both model calculations and measurements. There are differences in the details. For example, the model reaches a peak at around 0.8 kHz, while the peak in the data is near 1.4 kHz.

The ear-canal load has a significant effect on the measured reverse pressure transfer function (Puria and Rosowski, 1996; Hudde and Engel, 1998b). This is seen in the model calculations for frequencies below about 0.5 kHz and above 3 kHz [Figs. 4(c) and (d)] where |M2| appears more dependent on the two terminations presently used. Puria and Rosowski (1996) measurements also show that the reverse transmission magnitude varied more outside the 0.5–1.5 kHz region than inside this frequency region. |M2| can be similar if the two canal impedances are also similar as is the case for MT-A and MT-B. In the individual M2 data, some of the differences are due to different ear-canal terminations [Figs. 2(c) and (d)]. For E1–E3, a yellow foam plug was used and this corresponds to MT-B while for E4 and E5 a glass cover slip was used corresponding to MT-A. M2 in E4 is very similar to model calculation with MT-A for the canal load. It is not clear why M2 in E5 is more similar to the model calculation with MT-B rather than like the MT-A response.

For frequencies above about 7 kHz, measured |M2| reverses slope and tends to increase, whereas in the model |M2| continues to decrease. It is not clear if this is related to errors in the model, or if it is due to potential artifacts in the reverse measurements at the highest frequencies.

Generally, the forward and reverse pressure gains |M1| and |M2| are neither a shifted version of each other, nor are they reciprocals of each other. In the simple transformer model of the middle ear with the same cochlear and ear-canal loads, the gains in the two directions are reciprocals of each other. The measurements shown here clearly suggest that the simple transformer model is not correct.

4. Reverse middle-ear impedance

The average |M3|, from Fig. 3(e), is shown in Fig. 4(e) while average ∠M3, from Fig. 3(f), is shown in Fig. 4(f). To the best of our knowledge, measurements of M3 have not been previously reported. As noted in Sec. III, average reverse impedance measurement M3 was modeled as a series spring (K_{mer}), dashpot (R_{mer}), and mass (M_{mer}). This model will be collectively called the KRM model and it is mathematically described as $\mathrm{M3}=K_{\mathrm{mer}}/j\omega+R_{\mathrm{mer}}+j\omega M_{\mathrm{mer}}$. The extracted element values are $K_{\mathrm{mer}}=8.1\times10^{13}$ N/m^5, $R_{\mathrm{mer}}=10\times10^{9}$ N-s/m^5 (or 10G Ohms), and $M_{\mathrm{mer}}=4.4\times10^{5}$ kg/m^4. The one parameter that can be directly compared to physical measurements is M_{mer}, the effective mass of the middle ear looking out from the stapes footplate. Using a footplate area of π mm^2 (Wever and Lawrence, 1954, Appendix D), we obtain a stapes weight of 4.3 mg. Wever and Lawrence (1954, Appendix D) reported a range of stapes mass from 2.05 to 4.35 mg with mean mass of 2.86 mg. More recently Nummela (1995) reported a stapes mass of 2.53 mg.

The stapes mass, based on physiological measurements reported here, is on the high side of previous reports of physically measured stapes mass. One reason for this might be that the mass of the malleus and incus contributes to the effective mass in the reverse direction. However, the effective masses of the malleus and the incus are expected to be small due to their radius of gyration. Another possible reason is the mass due to the column of fluid (Zwislocki, 1962) in the vestibule (i.e., between the footplate and the hydrophone). The present measurements suggest that the fluid mass is 1.4 mg (present stapes mass of 4.3 mg minus average stapes mass of 2.86 mg). Zwislocki (1962) estimated the fluid mass to be about 6.4 mg, which is at least a factor of 4 greater than the present estimate. The present measurements suggest that the mass of the column of fluid in the vestibule is less than half that of the stapes mass.

Merchant *et al.* (1996) drained the cochlea and made impedance measurements of just the stapes, Z_{s}. The measured impedance is well described by a series stiffness (K), resistance (R), and mass (M) model. This series model is mathematically described as: $Z_{\mathrm{s}}=K_{\mathrm{s}}/j\omega+R_{\mathrm{s}}+j\omega M_{\mathrm{s}}$. Measurements of Z_{s} and M3 can be compared while keeping some key differences in mind. First, Z_{s} was measured in the forward direction while M3 was measured in the reverse direction. It is assumed that the stapes impedance when measured in the forward or reverse directions is same. Second, Z_{s} does not include the eardrum, malleus, and incus while measurement M3 does and consequently the effective stiffness, damping, and mass terms in M3 will be higher than in Z_{s}.

The Merchant *et al.* estimates from one ear are $K_{\mathrm{s}}=22\times10^{13}$ N/m^5, $R_{\mathrm{s}}=5.7$ G Ohms, and $M_{\mathrm{s}}=4.5\times10^{5}$ kg/m^4. Merchant's stiffness is 2.7 times higher than K_{mer}, the damping is 0.6 times lower than R_{mer}, and mass is about the same as M_{mer}. Although the stapes mass is similar to present measurements, there are differences in the stiffness and damping values. The fact that K_{mer} from M3 is lower than K_{s} is surprising given that in M3 the increased stiffness of the eardrum, malleus, and incus should result in higher K_{mer}.

Figure 4 also shows the reverse impedance calculated from Shaw's middle-ear model with two different ear-canal terminations. It is clear that the two ear-canal loads have very little influence on the reverse impedance M3. There are significant differences between measurements and model calculations of M3. Like the data, model calculations are stiffness dominated at low frequencies and mass dominated at high frequencies. The effective stiffness in the model is about a factor of 1.5 times higher than in the measurements. The effective mass in the model is approximately a factor of 4 higher than in the measurements. The large effective mass in the model may also account for discrepancies between measurements and model calculations in the forward and reverse middle-ear pressure gains M1 and M2 at high frequencies [Figs. 4(a)–(d)]. Another deficiency in the model is the lack of a clear resonance in the 1–4 kHz region observed in individual ears [Figs. 2(e) and (f)].

5. Stapes velocity

The stapes-velocity to ear-canal pressure ratio, previously reported (e.g., Goode *et al.*, 1994a; Aibara *et al.*, 2001), is related to the present measurements by

$$\frac{V_{st}}{P_{ec}} = \frac{\mathrm{M1}}{A_{fp} \cdot Z_c}. \tag{6}$$

The average $|V_{st}/P_{ec}|$ of the present measurement is similar to the Aibara *et al.* (2001) measurement for frequencies below about 1 kHz and tends to diverge and is lower than the Aibara *et al.* data above 1–2 kHz (not shown). At 4 kHz, the present measurement is lower by about 6 dB. The average $|V_{st}/P_{ec}|$ by Goode *et al.* (1994) is generally higher than the current and the Aibara *et al.* measurement below 1 kHz and lies somewhere in between Aibara *et al.* and current measurement above 1 kHz. For frequencies below about 0.8 kHz, the angle of the stapes to ear-canal pressure transfer function $\angle\{V_{st}/P_{ec}\}$ is in agreement with those of Aibara *et al.* (Goode *et al.* did not report angles). Above about 1 kHz, the angles of the two measurements diverge. The angle of the present measurements is lower by about 65° at 4 kHz.

One reason why the magnitudes and angles of V_{st}/P_{ec} in the present measurements are lower than previous measurements is due to the cochlear load. As hypothesized above, the cochlear load was possibly altered by the presence of the IESS and its associated tubing. In a previous publication, a simple circuit model, of air in the cochlea, was presented (Puria *et al.*, 1997, Fig. 10). In that model, air in the cochlea effectively increases the stapes velocity. Thus, air in the cochlea is not the reason for the observed lower velocity at the high frequencies. It is not clear if these differences are due to methodological differences or differences in the sample of temporal bones.

6. Stapes footplate rocking: Forward versus reverse drive

There is more stapes footplate rocking-motion when driven from the ear canal, in the forward direction, than when driven from the cochlea, in the reverse direction. For bones E2–E5, velocity measurements were made from the center of the footplate. On the other hand, velocity from the anterior part of the footplate, for E1, was measured resulting in a Z_c angle that is higher, for frequencies above 5 kHz, than for E2–E5 [Fig. 2(h)]. Similar observations, not shown, were also made on E2. This suggests that measurement location along the footplate anterior–posterior axis can systematically bias the phase of the stapes velocity, and thus the phase angle of Z_c, when the middle ear is driven in the forward direction.

Footplate measurement location does not affect the angle of M3, and thus the angle of stapes velocity, when driven in the reverse direction. This is apparent from the fact that M3 angle measurements are all in close agreement. The lower average-STD of M3 angle (16°) in comparison to the average-STD of Z_c angle (45°) can be attributed to a reduced rocking motion when the middle ear is driven backwards. Taken together, the forward versus reverse stapes motion measurements indicates that footplate rocking is due primarily to rocking motion of the incus at the head of the stapes, rather than the stapes itself. Further measurements are needed to verify these results.

B. Effect of the middle ear on OAEs

It is now possible to resolve the effect of the middle ear on otoacoustic emissions. First, how otoacoustic emissions (OAEs) are shaped by middle-ear transmission is analyzed. Second, apically traveling nonlinear pressure reflection coefficient is estimated. Finally, the basally traveling OAE pressure reflection coefficient at the stapes is analyzed.

1. Round-trip through the middle ear

To what extent does the middle ear shape the frequency dependence of evoked otoacoustic emissions? To determine this, the round-trip gain through the middle ear, the product of the forward and reverse middle-ear pressure gains, is computed as follows:

$$G_{me}^{RT} = \mathrm{M1} \cdot \mathrm{M2}. \tag{7}$$

The magnitude of the round-trip middle-ear pressure gain $|G_{me}^{RT}|$ is shown in Fig. 5(a) while the corresponding angle is shown in Fig. 5(b). In the 0.2–1 kHz region, $|G_{me}^{RT}|$ increases with a slope of about 11.4 dB/oct, reaching a peak of −7 dB at 1.3 kHz, and then decreases with a slope of −22 dB/oct in the 2–6.8 kHz region. In the 6.8-8.2 kHz range, $|G_{me}^{RT}|$ changes slope to 11.7 dB/oct. The angle of G_{me}^{RT} decreases with increasing frequency. The slope of $\angle G_{me}^{RT}$, in the 1–2 kHz region is −220°/oct, in the 2–6.8 kHz region is −180°/oct, and in the 6.8-8.2 kHz range it is −75°/oct.

2. Evoked otoacoustic emissions

Both click evoked (CE) and distortion product (DP) OAEs involve the middle ear in the forward and reverse directions. Attention is restricted to CEOAEs and DPOAEs because these are clinically the most widely used. Smurzynski and Kim (1992) measured CEOAEs and DPOAEs in 29 normal-hearing adults ranging in age from 22 to 30 years. The average level (dB SPL, measured in 49-Hz bands) of CEOAEs is shown Fig. 5(a). There are three distinct frequency regions. In the 0.5–2 kHz region, the level shapes of CEOAE and $|G_{me}^{RT}|$ are very similar, suggesting that in this region the shape of the CEOAE is primarily determined by the middle ear. In the 2–4 kHz region, CEOAE level slope is relatively flat, −4 dB/oct, whereas $|G_{me}^{RT}|$ decreases with a slope of about −22 dB/oct, resulting in a slope difference of about −18 dB/oct.

Above 4 kHz, the level of CEOAE decreases sharply with a slope of about −50 dB/oct. CEOAE levels are almost never normalized to the stimulus. Most reports that show the stimulus spectrum indicate that the level of the stimulus decreases rapidly for frequencies below about 0.5 kHz and above 4 kHz (e.g., Spector *et al.*, 1991). The decrease in CEOAE level above 4 kHz is attributed primarily to a decrease in ear-canal stimulus.

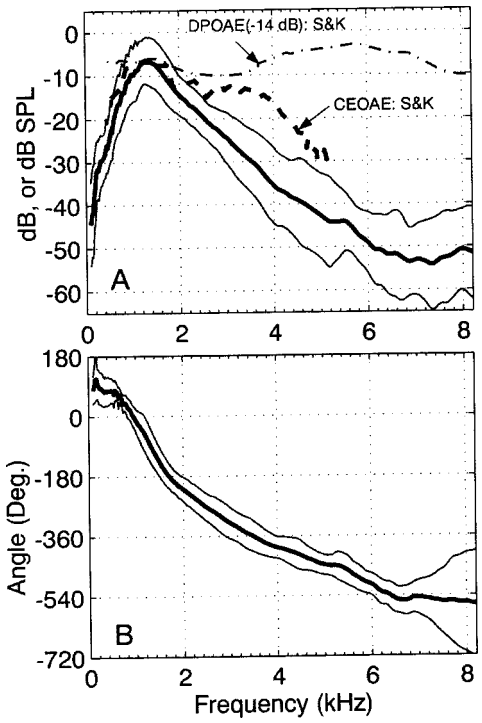

FIG. 5. Effect of the middle ear on OAEs. The magnitude (in dB) of the round-trip middle-ear pressure gain $|G_{\rm me}^{\rm RT}|$ is shown in panel (a), while the angle of the gain $\angle G_{\rm me}^{\rm RT}$ is shown in panel (b). Also shown in panel (a) is the average measurement by Smurzynski and Kim (1992) of the CEOAE level (dB SPL, in 49 Hz bandwidth) and the DPOAE level (after shifting down by 14 dB to match the peak of the $|G_{\rm me}^{\rm RT}|$). Typical stimulus levels for CEOAEs are 30–40 dB SPL in the 0.5–4 kHz region. For DPOAE measurements, the primary levels were approximately 65 dB SPL in the 0.5–8 kHz range.

3. Nonlinear apical reflectance

It is well known that a healthy and living cochlea behaves nonlinearly. For a given spectral level in the inner ear, the cochlea reflects signals due to both linear and nonlinear mechanisms. Clinical measurements of CEOAEs are a measure of the nonlinear (level dependent) properties of the inner ear (Kemp, 1978).

The shape and level of the response to a click measured in the ear canal are due to linear and nonlinear mechanisms. The ear canal pressure due to a single click at level L1 can be approximately described as (Kemp, 1980)

$$\mathrm{CE}_{\rm L1}=P_{\rm ec}^{\rm L1}\cdot \mathrm{M1}\cdot(R_{\rm l}+R_{\rm nl}^{\rm L1})\cdot \mathrm{M2}. \tag{8}$$

In Eq. (8), a signal in the vestibule $P_{\rm ec}^{\rm L1}\cdot \mathrm{M1}$ results in generation of a sum of a linear component $R_{\rm l}$ and a nonlinear component $R_{\rm nl}^{\rm L1}$ from the cochlea. As mentioned above, Eq. (8) is an approximation and a more exact analysis does not affect the basic conclusions (Shera and Puria, 2003).

Clinically, CEOAEs are measured using a nonlinear differential method of presenting four pulses in a block. The first three pulses are at low levels (L1) and the fourth pulse is inverted and three times higher in level (L2). The blocks are averaged and its Fourier transform is clinically reported in the ILO88 Otodynamic analyzer used by Smurzynski and Kim (1992) and many others. Mathematically, the nonlinear CEOAE can be described as

$$\mathrm{CEOAE}=CE_{\rm L1}+CE_{\rm L1}+CE_{\rm L1}-CE_{\rm L2}. \tag{9}$$

Substituting Eqs. (7) and (8) into Eq. (9) for L1 and L2 we obtain

$$\mathrm{CEOAE}=3\cdot P_{\rm ec}^{\rm L1}\cdot G_{\rm me}^{\rm RT}\cdot(R_1+R_{\rm nl}^{\rm L1}) - P_{\rm ec}^{\rm L2}G_{\rm me}^{\rm RT}\cdot(R_{\rm l}+R_{\rm nl}^{\rm L2}). \tag{10}$$

Since $P_{\rm ec}^{\rm L1}$ is $\frac{1}{3}$ of $P_{\rm ec}^{\rm L2}$, we can simplify as follows:

$$\mathrm{CEOAE}=P_{\rm ec}^{\rm L2}\cdot G_{\rm me}^{\rm RT}\cdot(R_{\rm nl}^{\rm L1}-R_{\rm nl}^{\rm L2}). \tag{11}$$

The difference in the nonlinear component, at the vestibule, is defined as

$$R_{\rm nl}^{\rm v}=R_{\rm nl}^{\rm L1}-R_{\rm nl}^{\rm L2}. \tag{12}$$

Thus, what is measured is

$$\mathrm{CEOAE}=P_{\rm ec}^{\rm L2}\cdot G_{\rm me}^{\rm RT}\cdot R_{\rm nl}^{\rm v}. \tag{13}$$

Note that in Eq. (13), the nonlinear component $R_{\rm nl}^{\rm v}$ is modified, or filtered by the linear component $G_{\rm me}^{\rm RT}$. For the nonlinear cochlea $R_{\rm nl}^{\rm v}$ represents the difference in the nonlinear components at the two levels. For a linear cochlea, (i.e., due to pathology) $R_{\rm nl}^{\rm v}$, and thus CEOAE vanishes because $R_{\rm nl}^{\rm L1}$ and $R_{\rm nl}^{\rm L2}$ are equal at all frequencies.

The linear component in Eq. (13) is primarily due to the middle ear, and it has been shown that the forward pressure gain (M1) in living and cadaver ears is approximately the same (Puria *et al.*, 1997). It is assumed here that the reverse pressure gain (M2) in living and cadaver ears is also approximately the same. Based on this assumption the linear component, namely $G_{\rm me}^{\rm RT}$, from cadaver ears can be used as a good representation of living ears.

The nonlinear reflection and distortion estimated at the vestibule is

$$R_{\rm nl}^{\rm v}=\frac{\mathrm{CEOAE}}{P_{\rm ec}^{\rm L2}\cdot G_{\rm me}^{\rm RT}}. \tag{14}$$

If one launches a pressure wave at low level and one at a high level from the vestibule towards the apical end of the cochlea, then the difference in the level-dependent components of the pressure waves that comes back is the level-dependent function $R_{\rm nl}^{\rm v}$.

In the 0.5–2 kHz region, the level difference between CEOAE and $|G_{\rm me}^{\rm RT}|$ is close to 0 dB (Fig. 5a) for an average $P_{\rm ec}^{\rm L2}$ of about 48 dB SPL (in 49-Hz bandwidth). This suggests, using Eq. (14), that $|R_{\rm nl}^{\rm v}|$ is approximately 0.004 in the 0.5–2 kHz region. Above 2 kHz, $|R_{\rm nl}^{\rm v}|$ increases at a rate of about 18 dB/oct. Thus at 4 kHz, $|R_{\rm nl}^{\rm v}|$ should be approximately 0.032. It is not clear if this slope continues above 4 kHz.

4. Generated DPOAEs

The average level of ear canal DPOAE, from the same subjects as the CEOAE data (Smurzynski and Kim, 1992), is also shown in Fig. 5(a). These DPOAE measurements are consistent with measurements by others (e.g., Lonsbury-Martin *et al.*, 1990). The level of DPOAE, measured with 65 dB SPL primary levels, is relatively flat in the entire frequency range from 0.5 to 8.2 kHz.

It appears that, unlike CEOAEs, DPOAE levels do not decrease in amplitude for frequencies around the peak in

$|G_{me}^{RT}|$ at 1.3 kHz. Above the peak in $|G_{me}^{RT}|$, the growth of the DPOAE generator is 22 dB/oct, reciprocal to the decrease in $|G_{me}^{RT}|$.

It is not clear why, in the 0.5–2 kHz region, CEOAEs appear to be filtered exactly by the middle ear whereas DPOAEs do not. Above about 2 kHz, and up to at least 6.8 kHz, both types of emissions have a rapid growth rate with frequency inside the cochlear vestibule.

There are several caveats that must be considered regarding the above analysis. First, the Smurzynski and Kim emissions measurements are from relatively young (average age 28 years) subjects while the measurements reported here are from an older population (average age 62) and it is possible that age affects middle-ear physiology. However, there is controversy regarding the effect of aging on middle-ear function. Below 1 kHz there is no correspondence between middle-ear function and aging (Kringlebotn and Gundersen, 1985; Feeney *et al.*, 1999). Feeney *et al.* (1999) showed an age effect on the middle-ear reflectance only in the limited frequency range of 4–5 kHz. Overall, it appears that age is a factor in a limited frequency region. Second, it is well known that the DPOAEs have multiple generation sites that result in fine structure in the observed ear canal pressure. However, due to averaging across many subjects, DPOAE fine structure (Fig. 5) is averaged out. Third, emission measurements from living ears are being compared to measurements from cadaver ears. Comparing living ears of animals to human cadaver ears, Puria *et al.* (1997) showed there is remarkable similarity in middle-ear pressure gain (M1) shapes across species. Also, Rosowski *et al.* (1990) showed that the middle-ear impedance in living and cadaver guinea pig ears are very similar up to at least 5 kHz. All of this suggests that the emission analysis discussed here is applicable to living ears. Finally, DPOAEs are generated at a frequency that is different from the frequency of the primary tones. Taking the frequency difference between the forward transfer function for the primaries and the reverse transfer function for the DP emission does not alter the approximate analysis discussed above because differences between the three frequencies are relatively small.

5. Stapes reflectance

When OAEs are generated, they travel apically toward their characteristic place and basally towards the stapes. At the stapes, OAEs are partially reflected where they travel back towards their characteristic frequency place, partially transmitted through the middle ear, and enter into the ear canal where they are measured. Estimates of R_{st} were made for cat (Shera and Zweig, 1991) and human (Talmadge *et al.*, 1998) ears based on model assumptions. Estimates of R_{st} based on measurements have not been reported.

The stapes reflection coefficient R_{st} can be calculated from measurements of the reverse middle-ear impedance M3 and the cochlear input impedance Z_c as follows (Shera and Zweig, 1991):

$$R_{st}=\frac{M3/Z_c^*-1}{M3/Z_c+1}, \tag{15}$$

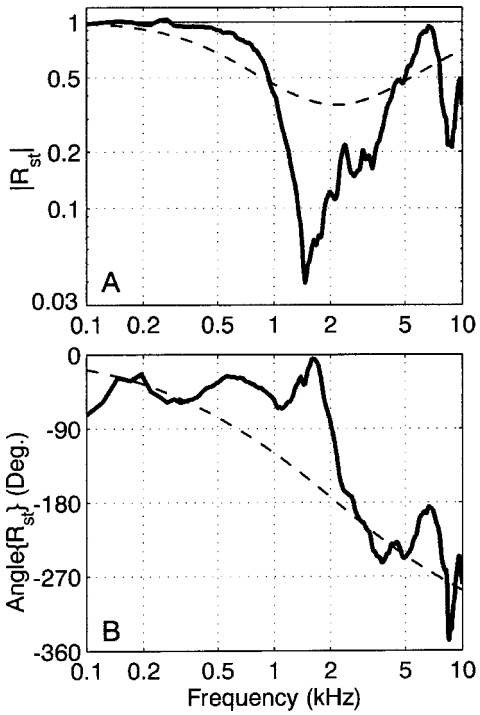

FIG. 6. Stapes reflectance R_{st}, as defined by Eq. (15), is calculated by using the average reverse middle-ear impedance M3 and cochlear input impedance Z_c (solid line) from Aibara *et al.* (2001). R_{st} calculated by using the simple KRM model and resistive Z_c [Fig. 4(e)–(g)] is also shown (dashed line).

where Z_c^* is the complex conjugate of Z_c. A review of the relationship between normalized impedance (i.e., $M3/Z_c$) and reflectance can be found in Puria and Allen (1998). Z_c from Aibara *et al.* is used because it is a better approximation to the cochlear input impedance of a normal ear than the impedance of the preparation reported here. The magnitude of the stapes reflectance $|R_{st}|$ is shown in Fig. 6(a) while the angle of the stapes reflectance $\angle R_{st}$ is shown in Fig. 6(b).

Below 0.27 kHz, $|R_{st}|$ waxes and wanes, becoming greater than unity at a few frequencies which is a clear indication of a problem in the measurements, as reflectance magnitudes must be less than or equal to unity in passive systems (as is the case for cadaveric ears). Errors arise when the angle of M3 measurements is less than $-90°$.

Above 0.3 kHz $|R_{st}|$ decreases to a minimum of about 0.04 at 1.5 kHz and then the reflectance increases reaching a local maximum of 0.96 at 6.7 kHz. Above 6.7 kHz, $|R_{st}|$ decreases and then goes back up. Below 1.5 kHz the average $\angle R_{st}$ is about $-45°$. Above about 1.8 kHz the angle goes up and down but generally decreases with frequency [Fig. 6(b)].

Figure 6 also shows the reflectance calculated from the simple KRM model fit to average M3 and a resistive cochlear load based on the mid-frequency average for Z_c [see Figs. 4(e)–(g), and above discussion]. Using the simple circuit model for R_{st} results in errors in magnitude by about a factor of 5 in the mid-frequency region while at low and high frequency there is more agreement.

In summary, at low frequencies more than $\frac{2}{3}$ of OAEs are reflected back into the inner ear, while in the 1–4 kHz region less than $\frac{1}{3}$ of OAEs are reflected back into the inner ear. Above 5 kHz, the amount of OAE reflected varies from about $\frac{1}{5}$ to 1.

6. Using OAEs to estimate forward and reverse transmission

Keefe (2002) used DPOAEs to estimate noninvasively the shape of the middle-ear pressure gain in the forward and reverse directions and Miller and Shera (2002) proposed some refinements to Keefe's method. The key assumption with these methods, based primarily on the physiology of laboratory animals, is that DPOAE generation inside the cochlea is independent of frequency. This property is often referred to as the cochlear scaling symmetry assumption (e.g., Zweig, 1976; Shera and Guinan, 1999). Estimation of the reverse transmission by the above noninvasive procedures is particularly dependent on this assumption being correct. Direct measurements of reverse transmission reported in this paper challenge the cochlear scaling symmetry assumption for the human cochlea. Even if the cochlear scaling assumption turns out to be correct, noninvasive methods yield only the shapes of the transfer function magnitudes. No information can be obtained about the absolute level of the transfer functions, or about the phase of the forward and reverse transfer functions. However, these noninvasive methods can be used, to a limited extent, to further test the applicability of cadaveric measurements to living ears.

V. SUMMARY

Four measurements from the same human temporal bone preparations are reported here for the first time. M1, the forward middle-ear pressure gain, and Z_c, the cochlear input impedance, are similar to previous measurements with some differences due to the requirement of injecting sound into the inner ear. M2, the sound-driven reverse middle-ear pressure gain, and M3, the reverse middle-ear impedance, are reported for the first time. These four measurements can be used to refine existing circuit models and anatomically based structural models, and to derive new models such as two-port descriptions of the human middle ear. Calculations of M1–M3 from Shaw's middle-ear model suggest that, although the model has the correct general behavior, there are disagreements in the details in comparison to the data reported here.

Cadaver measurements of M2 and M3, and previous reports of M1, Z_c, and otoacoustic emissions from living subjects, were used to understand how the middle ear affects emissions and how to interpret emissions generated by the inner ear. Results indicate that above about 2 kHz, both click evoked and distortion product pressures inside the cochlear vestibule increase with frequency at a rate of at least 18 dB/oct. This suggests that the OAE generator mechanism is not constant with frequency as is commonly assumed.

The nonlinear component of apical reflectance is estimated to vary from 0.004 in the 0.5–2 kHz region, increasing at a rate of about 18 dB/oct, up to at least 4 kHz. The stapes reflectance is estimated from the measurements to vary from unity to a minimum of 0.04.

ACKNOWLEDGMENTS

I would like to thank Jont B. Allen, Jonathan P. Fay, Richard L. Goode, Douglas H. Keefe, James P. Tuck-Lee, Kovid T. Puria, Euan Murugasu, Chris Shera, Charles R. Steele, Neshie Tiwari, and Michael Wittbrodt for their valuable comments and suggestions. I am also grateful to John Shaw for help with procurement and preparation of temporal bones and John Winstead with many aspects of the experiments. Rodney Perkins supported the laboratory space where this work was performed. This work was supported (in part) by research Grant No. DC03085 from the National Institute on Deafness and Other Communication Disorders.

Aibara, R., Welsh, J. T., Puria, S., and Goode, R. L. (**2001**). ''Human middle-ear sound transfer function and cochlear input impedance,'' Hear. Res. **152**(1–2), 100–109.

Békésy, G. v. (**1941**). ''Uber die messung der schwingungsamplitude der gehoknochelchen mittels einer kapazitiven sonde,'' Akust. Z. **6**, 1–16.

Brenkman, C. J., Grote, J. J., and Rutten, W. L. (**1987**). ''Acoustic transfer characteristics in human middle ears studied by a SQUID magnetometer method,'' J. Acoust. Soc. Am. **82**, 1646–1654.

Donald, J. A., and Anson, B. J. (**1992**). *Surgical Anatomy of the Temporal Bone* (Raven, New York).

Egolf, D. P., Kennedy, W. A., and Larson, V. D. (**1992**). ''Occluded-ear simulator with variable acoustic properties,'' J. Acoust. Soc. Am. **91**, 2813–2823.

Feeney, M. P., Hoffman, N. L., Mitovich, K. L., and Smith, K. L. (**1999**). ''Age effects in middle ear reflectance measurements,'' in Association for Research in Oto-Laryngology Abstracts.

Flanagan, J. L. (**1962**). ''Computational Model for Basilar-Membrane Displacement,'' J. Acoust. Soc. Am. **34**, 1370–1376.

Goode, R. L., Ball, G., and Nishihara, S. (**1993**). ''Measurement of umbo vibration in human subjects-method and possible clinical applications,'' Am. J. Otol. **14**, 217–251.

Goode, R. L., Killion, M., Nakamura, K., and Nishihara, S. (**1994**). ''New knowledge about the function of the human middle ear: development of an improved analog model,'' Am. J. Otol. **15**(2), 145–154.

Guinan, J. J., Jr., and Peake, W. T. (**1967**). ''Middle-ear characteristics of anesthetized cats,'' J. Acoust. Soc. Am. **41**, 1237–1261.

Gunderson, T. (**1971**). ''*Prosthesis in the Ossicular Chain.*'' (University Park, P., Baltimore, MD).

Gundersen, T., and Høgmoen, K. (**1976**). ''Holographic vibration analysis of the ossicular chain,'' Acta Oto-Laryngol. **82**, 16–25.

Gyo, K., Aritomo, H., and Goode, R. L. (**1987**). ''Measurement of the Ossicular Vibration Ratio in Human Temporal Bones by Use of a Video Measuring System,'' Acta Otolaryngol. (Stockh) **103**, 87–95.

Helmholtz, H. L. F. (**1868**). ''Die Mechanik der Gehorknochelchen und des Trommelfells,'' Pfluegers Arch. Gesamte Physiol. Menschen Tiere **1**, Translated from the German by A. H. Buck and N. Smith, ''The mechanism of the ossicles of the ear and membrana tympani,'' 1873.

Hudde, H. (**1983**). ''Estimation of the area function of human ear canals by sound pressure measurements,'' J. Acoust. Soc. Am. **73**(1), 24–31.

Hudde, H., and Engel, A. (**1998a**). ''Measuring and Modeling Basic Properties of the Human Middle Ear and Ear Canal. Part II: Ear Canal, Middle Ear Cavities, Eardrum, and Ossicles,'' Acust. Acta Acust. **84**, 894–913.

Hudde, H., and Engel, A. (**1998b**). ''Measuring and Modeling Basic Properties of the Human Middle Ear and Ear Canal. Part III: Eardrum Impedances, Transfer Functions and Model Calculations,'' Acust. Acta Acust. **84**, 1091–1109.

Keefe, D. H., Bulen, J. C., Arenhart, K. H., and Burns, E. M. (**1993**). ''Method to measure acoustic impedance and reflection coefficient,'' J. Acoust. Soc. Am. **94**, 2617–2638.

Keefe, D. H. (**2002**). ''Spectral shapes of forward and reverse transfer functions between ear canal and cochlea estimated using DPOAE input/output functions,'' J. Acoust. Soc. Am. **111**, 249–260.

Kemp, D. T. (**1978**). ''Stimulated acoustic emissions from within the human auditory system,'' J. Acoust. Soc. Am. **64**, 1386–1391.

Kemp, D. T. (**1980**). ''Towards a model for the origin of cochlear echoes,'' Hear. Res. **2**, 533–548.

Kringlebotn, M., and Gundersen, T. (**1985**). ''Frequency characteristics of the middle-ear,'' J. Acoust. Soc. Am. **77**, 159–164.
Lonsbury-Martin, B. L., Harris, F. P., Stagner, B. B., Hawkins, M. D., and Martin, G. K. (**1990**). ''Distortion Product Emissions in Humans. I. Basic Properties in Normally Hearing Subjects,'' Ann. Otol. Rhinol. Laryngol. **99**(5), 3–14.
Lutman, M. E., and Martin, A. M. (**1979**). ''Development of an electroacoustic analogue model of the middle ear and acoustic reflex,'' J. Sound Vib. **64**, 133–157.
Magnan, P., Avan, P., Dancer, A., Smurzynski, J., and Probst, R. (**1997**). ''Reverse middle-ear transfer function in the guinea pig measured with cubic difference tones,'' Hear. Res. **107**(1–2), 41–45.
McElveen, J. T., Goode, R. L., Miller, C., and Falk, S. A. (**1982**). ''Effect of mastoid cavity modification on middle ear sound transmission,'' Ann. Otol. Rhinol. Laryngol. **91**(5 Pt 1), 526–532.
Mehrgardt, S., and Mellert, V. (**1977**). ''Transformation characteristics of the external ear,'' J. Acoust. Soc. Am. **61**, 1567–1576.
Merchant, S. N., Ravicz, M. E., and Rosowski, J. J. (**1996**). ''Acoustic input impedance of the stapes and cochlea in Human Temporal bones,'' Hear. Res. **97**, 30–45.
Metz, O. (**1946**). *The acoustic impedance measured on normal and pathological ears*, Ed., Acta Oto-Laryngol. Suppl.
Miller, A. J., and Shera, C. A. (**2002**). *Using DPOAEs to Measure Forward and Reverse Middle-Ear Transmission Noninvasively*, in Association for Research in Oto-Laryngology Abstracts, St. Petersburg, FL.
Møller, A. R. (**1960**). ''Improved technique for detailed measurements of the middle ear impedance,'' J. Acoust. Soc. Am. **32**, 250–257.
Møller, A. R. (**1961**). ''Network model of the middle ear,'' J. Acoust. Soc. Am. **33**, 168–176.
Nummela, S. (**1995**). ''Scaling of the mammalian middle ear,'' Hear. Res. **85**(1–2), 18–30.
Onchi, Y. (**1949**). ''A study of the mechanism of the middle ear,'' J. Acoust. Soc. Am. **21**, 404–410.
Onchi, Y. (**1961**). ''Mechanism of the middle ear,'' J. Acoust. Soc. Am. **33**, 794–805.
Peake, W. T., Rosowski, J. J., and Lynch, T. J. III (**1992**). *Middle-ear transmission: Acoustic versus ossicular coupling in cat and human*, Hear. Res. **57**, 245-268.
Puria, S., and Allen, J. B. (**1991**). ''A parametric study of cochlear input impedance,'' J. Acoust. Soc. Am. **89**, 287–309.
Puria, S., and Allen, J. B. (**1992**). ''SYSid—audio-band measurement and analysis system,'' J. Acoust. Soc. Am. Suppl. 1 **92**, S2469.
Puria, S., Rosowski, J. J., and Peake, W. T. (**1993a**). ''Middle-ear pressure gain in humans: preliminary results,'' in *Biophysics of Hair Cell Sensory Systems*, edited by H. Duifhuis, J. W. Horst, P. van Dijk, and S. M. van Netten (World Scientific, Singapore), pp. 345–351.
Puria, S., Allen, J. B., Elko, G. W., Jeng, P. S., and Kirkegaard, D. L. (**1993b**). ''Measurements and analysis with SYSid,'' J. Acoust. Soc. Am. Suppl. 1 **93**, S2356.
Puria, S., and Rosowski, J. J. (**1996**). ''Measurement of reverse transmission in the human middle ear: Preliminary results,'' in *Diversity in Auditory Mechanics*, edited by E. R. Lewis *et al.* (World Scientific, Singapore), pp. 151–157.
Puria, S., Peake, W. T., and Rosowski, J. J. (**1997**). ''Sound-pressure measurements in the cochlear vestibule of human-cadaver ears,'' J. Acoust. Soc. Am. **101**, 2754–2770.
Puria, S., and Allen, J. B. (**1998**). ''Measurements and model of the cat middle ear: evidence of tympanic membrane acoustic delay,'' J. Acoust. Soc. Am. **104**, 3463–3481.
Puria, S. (**2003**). ''Growth of otoacoustic emissions with frequency: Inside the human cochlea vestibule,'' in *Biophysics of the Cochlea*, edited by A. W. Gummer (World Scientific, Singapore), pp. 454–463.
Rabinowitz, W. M. (**1981**). ''Measurement of the acoustic input immittance of the human ear,'' J. Acoust. Soc. Am. **70**, 1025–1035.
Rosowski, J. J., Davis, P. J., Merchant, S. N., Donahue, K. M., and Coltrera, M. D. (**1990**). ''Cadaver middle ears as models for living ears: Comparisons of middle ear input impedance,'' Ann. Otol. Rhinol. Laryngol. **99**(5), 403–412.
Rubinstein, M., Feldman, B., Fischler, H., Frei, E. H., and Spira, D. (**1966**). ''Measurement of Stapedial-Footplate displacements during transmission of sound through the middle ear,'' J. Acoust. Soc. Am. **40**, 1420–1426.
Shaw, E. A. G. (**1977**). ''Eardrum representation in middle-ear acoustical networks,'' J. Acoust. Soc. Am. Suppl. 1 **62**, SE5.
Shaw, E. A. G., and Stinson, M. R. (**1981**). ''Network concepts and energy flow in the human middle ear,'' J. Acoust. Soc. Am. Suppl. 1 **69**, S44.
Shaw, E. A. G., and Stinson, M. R. (**1983**). ''The human external and middle ear: Models and concepts,'' Mech. Hear., edited by E. de Boer and M. A. Viergever (Mantinus Nijhott Publishers and Delft Univeristy Press, Delft) 3–10.
Shera, C. A., and Zweig, G. (**1991**). ''Reflection of retrograde waves within the cochlea and at the stapes,'' J. Acoust. Soc. Am. **89**, 1290–1305.
Shera, C. A., and Zweig, G. (**1992**). ''Middle-ear phenomenology: the view from the three windows,'' J. Acoust. Soc. Am. **92**, 1356–1370.
Shera, C. A., and Guinan, J. J., Jr. (**1999**). ''Evoked otoacoustic emissions arise by two fundamentally different mechanisms: a taxonomy for mammalian OAEs,'' J. Acoust. Soc. Am. **105**, 782–798.
Shera, C. A., and Puria, S. (**2003**). ''Modeling click-evoked otoacoustic emissions,'' (to be submitted).
Smurzynski, J., and Kim, D. O. (**1992**). ''Distortion-product and click-evoked otoacoustic emissions of normally-hearing adults,'' Hear. Res. **58**, 227–240.
Spector, Z., Leonard, G., Kim, D. O., Jung, M. D., and Smurzynski, J. (**1991**). ''Otoacsoustic Emissions in Normal and Hearing Impaired Children and Normal Adults,'' Laryngoscope **101**(9), 965–976.
Stinson, M. R. (**1990**). ''Revision of estimates of acoustic energy reflectance at the human eardrum,'' J. Acoust. Soc. Am. **88**, 1773–1778.
Talmadge, C. L., Tubis, A., Long, G. R., and Piskorski, P. (**1998**). ''Modeling otoacoustic emission and hearing threshold fine structures,'' J. Acoust. Soc. Am. **104**, 1517–1543.
Tonndorf, J., and Khanna, S. M. (**1972**). ''Tympanic-membrane vibrations in human cadaver ears by time-averaged holography,'' J. Acoust. Soc. Am. **52**, 1221–1233.
Vlaming, M. S. M. G., and Feenstra, L. (**1986**). ''Studies of the mechanics of the normal human middle ear,'' Clin. Otolaryngol. **11**, 353–363.
Voss, S. E., and Allen, J. B. (**1994**). ''Measurement of acoustic impedance and reflectance in the human ear canal,'' J. Acoust. Soc. Am. **95**, 372–384.
Wada, H., Metoki, T., and Kobayashi, T. (**1992**). ''Analysis of dynamic behaviour of human middle ear using a finite-element method,'' J. Acoust. Soc. Am. **92**, 3157–3168.
Waetzmann, E. v., and Keibs, L. (**1936**). ''Theoretischer und experimenteller Vergleich von Hörschwellenmessungen,'' Akust. Z. **1**, 1–12.
West, W. (**1928**). ''Measurements of the acoustical impedances of human ears,'' Post Office Elect. Eng. J. **21**, 293.
Wever, E. G., and Lawrence, M. (**1954**). *Physiological Acoustics* (Princeton U.P., Princeton, NJ).
Zweig, G. (**1976**). ''Basilar membrane motion,'' Cold Spring Harb Symp. Quant Biol. **40**, 619–633.
Zwislocki, J. (**1948**). ''Theorie der schneckenmechanik,'' Acta Oto-Laryngol., Suppl. **72**, pp. 76.
Zwislocki, J. (**1957**). ''Some impedance measurements on normal and pathological ears,'' J. Acoust. Soc. Am. **29**, 1312–1317.
Zwislocki, J. (**1962**). ''Analysis of the middle-ear function. Part I: Input impedance,'' J. Acoust. Soc. Am. **34**, 1514–1523.
Zwislocki, J., and Feldman, A. S. (**1970**). ''Acoustic impedance in normal and pathological ears,'' Am Speech Hear Assoc. Monogr. **15**, 1–42.

Microsecond temporal resolution in monaural hearing without spectral cues?

Katrin Krumbholz[a] and Roy D. Patterson
Centre for the Neural Basis of Hearing, Department of Physiology, University of Cambridge, Downing Street, Cambridge CB2 3EG, United Kingdom

Andrea Nobbe and Hugo Fastl
Institute for Human-Machine Communication, Technical University Munich, Arcisstrasse 21, D-80333 München, Germany

(Received 26 April 2002; revised 5 October 2002; accepted 16 December 2002)

The auditory system encodes the timing of peaks in basilar-membrane motion with exquisite precision, and perceptual models of binaural processing indicate that the limit of temporal resolution in humans is as little as 10–20 *microseconds*. In these binaural studies, pairs of continuous sounds with microsecond differences are presented simultaneously, one sound to each ear. In this paper, a monaural masking experiment is described in which pairs of continuous sounds with microsecond time differences were combined and presented to both ears. The stimuli were matched in terms of the excitation patterns they produced, and a perceptual model of monaural processing indicates that the limit of temporal resolution in this case is similar to that in the binaural system. © *2003 Acoustical Society of America.* [DOI: 10.1121/1.1547438]

PACS numbers: 43.66.Dc, 43.66.Ba, 43.66.Mk [MRL]

I. INTRODUCTION

Physiological studies have shown that primary auditory-nerve fibers phase lock to the temporal fine structure of sinusoids up to frequencies as high as 5 kHz in the cat (Johnson, 1980). Psychophysical studies indicate that the binaural system can detect interaural time differences of a few tens of microseconds. Perceptually, interaural time differences are interpreted in terms of where the source is relative to the head, or how spatially compact it is (Durlach and Colburn, 1978). In this paper, we report a monaural perception experiment which suggests that the auditory system can also detect monaural time differences of a few tens of microseconds in continuous sounds even when they have matched excitation patterns. In this case, the perception involves distinguishing whether the sound contains one or two sources, or in the limit, how perceptually coherent the sound is. These source characteristics would appear to be defined by the monaural temporal structure of the sound rather than its spatial or spectral attributes.

The experiments were motivated by a monaural model of temporal processing that was recently used to explain a monaural masking release that is presumed to be based on the temporal microstructure of the sounds (Krumbholz *et al.*, 2001). The model and the masking release are introduced briefly in subsections I A and I B to explain the motivation for the research, which is introduced in subsection I C.

A. Models of monaural temporal processing

Much of the temporal information in the neural firing patterns generated in the cochlea is preserved up to the level of the superior olivary complex (Oertel, 1997). Beyond the brainstem, however, the temporal precision of neural firing deteriorates as the volley of firing progresses to higher stages in the system (Rouilly *et al.*, 1979). Time-interval models of auditory processing (e.g., Meddis and Hewitt, 1991a; Patterson *et al.*, 1995) assume that there is a mechanism that measures the time intervals between peaks in the phase-locked activity of auditory-nerve fibers, and thereby converts the unstable temporal information in the phase-locked response into a more stable time-interval code. The obvious assumption, although it is not explicitly stated, is that the time-interval representation might emerge at the stage of the inferior colliculus in the midbrain. This is the level in the system where the upper limit of phase locking drops to about 500 Hz, and there is a mandatory synapse with strong convergence of ascending pathways (Irvine, 1992).

Studies of temporal processing often employ a stimulus referred to as iterated rippled noise (IRN) in an effort to neutralize processing in the tonotopic dimension and focus attention on temporal processing. IRN is constructed by delaying a copy of a random noise by d ms, adding it back to the original noise, and iterating the process n times. The stimulus has a noise-like waveform with a degree of temporal regularity that increases with increasing numbers of iterations, n. When the delay, d, is between about 1 and 30 ms, IRN elicits a two-component perception, with a noisy hiss and a buzzy tone whose pitch corresponds to $1/d$. IRN is interesting because it enables the generation of sounds with any degree of tonality from almost completely tonal to completely atonal while leaving the gross temporal structure and the excitation pattern of the stimulus essentially unchanged. Perceptual differences between IRNs with matched excitation patterns are used to demonstrate the importance of time-interval analysis in auditory processing; Yost *et al.* (1996) and Patterson *et al.* (1996) have shown that the pitch and pitch strength of IRN are more readily explained by time-

[a]Current address: Institute for Medicine (IME), Forschungszentrum Jülich, D-52425 Jülich, Germany.

 0001-4966/2003/113(5)/2790/11/$19.00

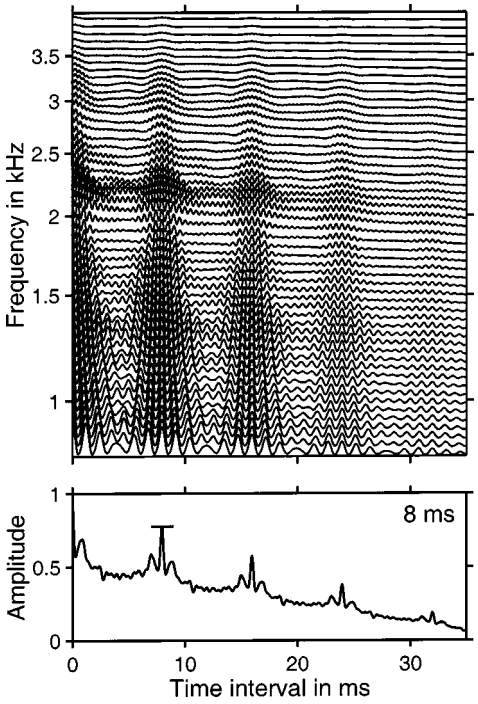

FIG. 1. Upper panel: Auditory image (AI) of an IRN with a delay of 8 ms and 16 iterations. The solid lines show time-interval histograms of the neural activity in different channels of the tonotopic array; the ordinate is the best frequency of the channel. Lower panel: Summary AI computed by averaging across channels in the AI; the short horizontal line shows the normalized height of the first peak in the summary image.

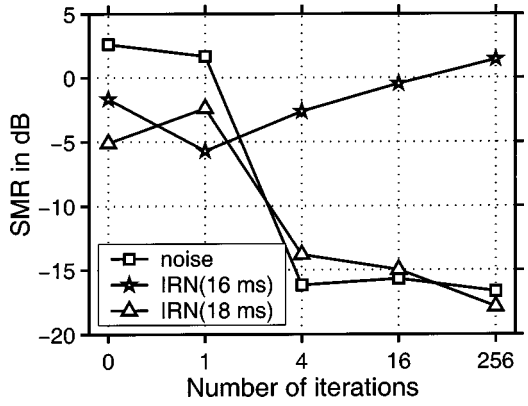

FIG. 2. Results from the IRN masking experiment of Patterson and Datta (1996). The abscissa is the number of iterations in the masker (0 iterations indicates that the masker was a noise). The signal was a noise (squares), or an IRN with 256 iterations and a delay of either 16 (stars) or 18 (triangles) milliseconds. The data show the average for three listeners and threshold is expressed in terms of the signal-to-masker ratio (SMR).

interval models of auditory processing than by models based on the excitation patterns of the stimuli.

In these time-interval models, a summary of the neural processing up to the level of the midbrain is simulated with a tonotopic array of autocorrelation functions (Meddis and Hewitt, 1991a; Slaney and Lyon, 1990) or time-interval histograms (Patterson *et al.*, 1992; Patterson, 1994). The upper panel in Fig. 1 shows the simulated neural pattern in response to an IRN with a delay of 8 ms and 16 iterations. The pattern was produced with the Auditory Image Model (AIM; Patterson *et al.*, 1995). The abscissa is time interval; the ordinate is frequency as it is represented along the frequency dimension of the cochlea. Each line in this representation shows the kind of time-interval histogram that might be calculated from the stream of spikes flowing from individual auditory-nerve fibers at a given frequency. The vertical ridges at 8 ms and integer multiples thereof demonstrate the presence of temporal regularity in the neural activity across the tonotopic array. The representation is referred to as an ''auditory image'' (Patterson, 1994). The overall form of the temporal regularity is similar in all channels, which illustrates how the stimulus neutralizes the tonotopic dimension of auditory processing. The lower panel of Fig. 1 shows the normalized sum of the activity across channels. It is referred to as a ''summary auditory image,'' and it is this representation that is typically used to summarize responses to stimuli in quantitative evaluations of time-interval models.

It is perhaps worth noting that in these representations, the autocorrelation-lag, or time-interval dimension is presented as if it were a spatial dimension similar to the frequency dimension, and that the auditory image might be thought of as the pattern of activity in a two-dimensional array of neurons at the level of the brainstem or the midbrain. This is a convenient way to conceive the processing of temporal information, but a spatial array of time intervals is not necessary for the functioning of these models; any method of representing concentrations of activity at different time intervals would suffice.

B. A monaural masking release based on temporal microstructure

Patterson and Datta (1996) reported that a noise masks an IRN much more effectively than an IRN masks a noise, even when the stimuli have the same energy and are filtered in the same spectral region. The effect is illustrated in Fig. 2, which shows the masked threshold for a noise (squares) and an IRN with a delay of 16 ms and 256 iterations (stars) in the presence of five different maskers—a random noise (0 iterations) and an IRN with 1, 4, 16, or 256 iterations and the same 16-ms delay. Threshold is expressed in terms of the signal-to-masker ratio (SMR), which is the difference between the overall level of the signal at threshold and the overall level of the masker. All of the stimuli were highpass filtered at 800 Hz, which is 12.6 times the reciprocal of the delay. The filtering ensures that the excitation patterns of the IRNs do not have sets of harmonically spaced peaks, and the long delay ensures that the stimuli contain frequency components in a frequency region with accurate phase locking to support time-interval processing. The figure shows that a noise signal is effectively masked by noise and by IRN with one iteration. But, as the number of iterations in the masker increases and its fine structure becomes more regular, there is a release from masking by as much as 18 dB. Similarly, the IRN signal with 256 iterations is effectively masked by IRN with 256 iterations. But, as the number of iterations in the masker decreases and its fine structure becomes less regular, threshold decreases. However, in this case the release from masking is only about 7 dB. Thus, there is an asymmetry of masking between noise and IRN, in that a noise (0 iterations)

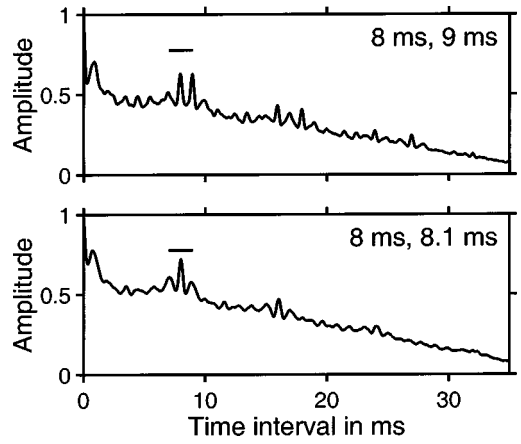

FIG. 3. Summary AIs of ''merged IRNs'' consisting of an 8-ms masker IRN and a signal IRN with a delay of either 9 (upper panel) or 8.1 (lower panel) milliseconds. The signal was added with a SMR of 0 dB. The IRNs were computed with 16 iterations of the delay-and-add process. The short horizontal lines show the height of the first peak in the summary AI of the masker alone, shown in the lower panel of Fig. 1.

masks an IRN (stars) much more effectively than an IRN (iterations$\geqslant$4) masks a noise (squares). Recently, Krumbholz *et al.* (2001) extended the range of the observations and showed that, for delays within the pitch region, the basic masking asymmetry between noise and IRN was essentially independent of the spectral region. This means that it is very unlikely that models based on the excitation patterns of the stimuli could explain the data. Krumbholz *et al.* (2001) explain the asymmetry of masking in terms of the fine-grain temporal information in the neural activity patterns of the stimuli.

There is a third condition in the study of Patterson and Datta (1996) in which the signal is an IRN with a delay of 18 ms and 256 iterations; it has a noticeably lower pitch than the IRN masker. The thresholds (triangles) show that the 18-ms IRN is masked by noise to about the same degree as the 16-ms IRN, as would be expected. However, when the number of iterations in the masker is four or more, the listener can use the difference in delay between signal and masker to detect the signal, and threshold falls to about the same levels as for the noise signal. This stands in contrast to the increase in threshold when the IRN signal has the same delay (16 ms) as the IRN masker. It is this condition where the IRNs have different pitches that provides the motivation for the current study.

The upper panel of Fig. 3 shows the summary auditory image when a 9-ms IRN signal is added to an 8-ms IRN masker with a signal-to-masker ratio (SMR) of 0 dB. The summary auditory image of the 8-ms IRN masker on its own was presented in the lower panel of Fig. 1. The summary auditory image of this ''merged'' IRN (Patterson *et al.*, 2000) exhibits peaks at both the masker delay (8 ms) and its integer multiples, and at the signal delay (9 ms) and its integer multiples. The heights of the peaks associated with the masker are, however, somewhat smaller than those for the masker alone; for reference, the short horizontal line shows the height of the 8-ms peak in the masker-alone condition. Handel and Patterson (2000) measured the pitch strength of merged IRNs with relatively large delay differences and showed that the pitch strength was greatly reduced except at octave delay ratios. Patterson *et al.* (2000) measured the pitch strength of merged IRNs with very small delay differences where the pitches of the two IRNs merge. They showed that there is still a pronounced reduction in pitch strength even when the delay difference was as little as 6% of the basic delay. So, the reduction in peak height remains audible to the listener after the pitches have merged. When the delay difference is less than about 2%, the time-interval peaks associated with the signal and masker merge in the summary auditory image (Patterson *et al.*, 2000); the lower panel of Fig. 3 shows the case where the masker is an 8-ms IRN and the signal is an 8.1-ms IRN. The form of the summary image is very similar to that for the 8-ms IRN masker on its own (Fig. 1), but the heights of the peaks are reduced, corresponding to the perceptual reduction in pitch strength. Note that the merging of the time-interval peaks for small delay differences is due to auditory processing that the stimuli undergo prior to the time-interval processing stage; Patterson *et al.* (2000) attribute it to a loss of phase-locking information in the midbrain. In any event, the degree to which the peaks merge provides information about the peripheral processing of the stimuli.

C. A masking paradigm for measuring monaural temporal resolution

In this paper, the reduction in pitch strength caused by the merging of IRNs with small delay differences is used to estimate the resolution with which time-interval information is represented in the auditory system. The listener's task is to detect a signal IRN in the presence of a masker IRN with a slightly different delay. The delay and level of the masker IRN were fixed and the level of the signal IRN was varied to determine the threshold as a function of the difference between the signal delay and the masker delay. The summary images in Figs. 1 and 3 suggest that threshold would drop as the delay of the signal begins to diverge from that of the masker. The function relating threshold to the difference in delay between the signal and masker will be referred to as a ''time-interval masking pattern.'' The traditional masking pattern reveals properties of frequency resolution in terms of the elevation of threshold for a sinusoidal signal in the frequency region around a narrow-band noise masker. Similarly, the time-interval (TI) masking pattern reveals properties of temporal resolution in terms of the elevation of threshold for an IRN signal with a delay in a time-interval region around the delay of an IRN masker.

II. METHOD

The time-interval masking pattern was measured for different masker delays and in different spectral regions to assess the effect of auditory filter width and phase locking on temporal resolution. The study of Krumbholz *et al.* (2001) showed that both variables have a pronounced effect on the asymmetry of masking between IRN and noise.

A. Stimuli

The masker and signal IRNs were generated with 16 iterations of the add-original algorithm (Yost *et al.*, 1996), using a gain, *g*, of unity. The stimuli were generated digitally with 16-bit resolution and a sampling rate of 25 kHz (TDT AP2). In order to produce the very small IRN delay differences required in this experiment, the IRN was generated in the spectral domain, by multiplying the Fourier spectrum of a Gaussian noise with the complex, comb-filter spectrum of an add-original IRN with delay, *d*, and *n* iterations

$$H(d,n)=\sum_{k=0}^{n} g^{k}[\cos(2\pi kdf)+i\cdot\sin(2\pi kdf)],$$

where *i* is the imaginary unit and *f* is frequency. The signal and masker were played out through separate channels of the TDT DD1 D/A converter and antialiasing filtered with a 10-kHz cutoff (TDT FT6-2). They were separately attenuated according to the signal and masker levels of the current trial using two programmable attenuators (TDT PA4). Finally, the signal and masker were added in an analog mixer (TDT SM3) and presented diotically to the listener, who was seated in a double-walled, sound-attenuating booth.

The stimuli were filtered into frequency bands with an equivalent rectangular bandwidth of 2.2 kHz; the lower cutoff frequency, F_c, was 0.4, 0.8, 1.6, 3.2, or 6.4 kHz. In order to avoid edge tones, the lower and upper edges of the frequency bands were rounded with a quarter cycle of a cosine function whose width was 0.2 kHz on the lower edge and 1 kHz on the upper edge (see Fig. 1 in Krumbholz *et al.*, 2001). A background of continuous pink noise was introduced to mask any distortion products that might be audible in the region below the passband of the stimuli. The pink noise was low-pass filtered half an octave below the lower cutoff frequency, F_c, of the current filter condition; the slope beyond the cutoff frequency was 96 dB/octave. The unfiltered pink noise had a level of 31.3 dB SPL in the 1/3-octave band around 1 kHz. In the 0.8- and 3.2-kHz filter conditions, thresholds were measured for several different masker delays, d_m, ranging from 4 to 64 ms for $F_c=0.8$ kHz, and from 4 to 32 ms for $F_c=3.2$ kHz. Initially, we intended to measure the same range of masker delays in both filter conditions. However, pilot work showed that the task was too difficult for $d_m=64$ ms in the 3.2-kHz filter condition. In the other filter conditions, only one masker delay, 16 ms, was used. Each masker delay was combined with six different signal delays. The delay difference, *dd*, between signal IRN and masker IRN ranged from 0 μs to a maximum of 800 μs. Pilot work revealed that signals with very small delay differences were more readily detectable in the higher filter conditions, so the maximum *dd* varied with filter cutoff, F_c, from 800 μs when F_c was 0.4 kHz, to 50 μs when F_c was 6.4 kHz. The signal and masker were gated on and off simultaneously with 25-ms cosine-squared ramps and a total duration of 800 ms (between the 0–V points).

B. Procedure

Masked threshold was measured using a two-interval, forced-choice adaptive procedure. The trials consisted of two 800-ms observation intervals that were separated by 500 ms. One interval contained the masker alone; the other interval contained masker plus signal. The listener's task was to indicate which interval contained the signal by pressing one of two buttons on a response box. Feedback was given after each response. The adaptive parameter was the level of the signal. At the beginning of each threshold run, signal level was set to a value well above the anticipated threshold. Signal level was varied according to a 3-down, 1-up rule which tracks the signal level that yields 79% correct responses (Levitt, 1971). The step size for the level changes was 5 dB up to the first reversal in signal level, 3 dB up to the second reversal, and 2 dB for the rest of the ten reversals that made up one threshold run. Each threshold estimate was the average of the last eight reversals of signal level. Threshold was measured three times in each condition; the data points and error bars in the figures show the means and standard errors of the three estimates. In some cases, the error bars are smaller than, and thus covered by, the symbols. The order in which conditions were measured was counterbalanced between the three threshold runs. The masker had a nominal overall level of 60 dB SPL. In order to reduce the salience of level cues and to encourage listeners to base their decisions on differences in sound quality, the level of the stimuli was randomized over a 10-dB range in every interval of every trial. The random level rove was expected to increase threshold in the conditions where signal and masker IRNs had the same delay, and thereby enhance the effect of sound quality differences associated with delay differences between signal and masker.

C. Listeners

A total of five listeners participated in the current experiment: authors KK and AN, as well as three students, who were paid for their services at an hourly rate. The listeners were between 20 and 32 years of age and had no history of hearing impairment or neurological disease.

III. RESULTS

The average threshold data for the detection of an IRN signal in an IRN masker are presented in Figs. 4 and 5 for filter cutoffs of 0.8 and 3.2 kHz, respectively. Threshold is expressed in terms of the signal-to-masker ratio, SMR. The parameter in both figures is the delay of the masker IRN; the number of iterations in the signal and masker IRNs was fixed at 16. In the upper panels of Figs. 4 and 5, threshold is plotted as a function of the absolute delay difference, *dd*, between the signal and masker IRNs; in the lower panels, threshold is plotted as a function of the relative delay difference, that is, delay difference normalized by the delay of the masker IRN, d_m. Each function in Figs. 4 and 5 is a ''time-interval (TI) masking pattern'' for a specific combination of masker delay and filter condition. When *dd* was 0 μs, the only detection cue was the loudness difference between the masker alone and masker plus signal. The levels of both stimuli were randomized over a 10-dB range, so threshold SMR in this condition was relatively high (about 2 dB). As soon as *dd* was increased to a few tens of *microseconds*,

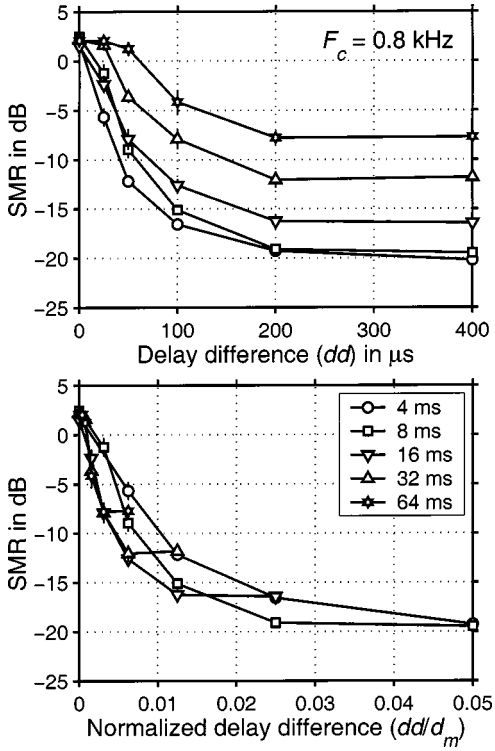

FIG. 4. Average masked threshold for detection of an IRN signal as a function of the delay difference, dd, between signal and masker IRNs; the parameter is the delay of the masker IRN (legend in lower panel). The filter cutoff was 0.8-kHz. The panels show the same thresholds but the abscissa in the lower panel is *normalized* delay difference, that is, dd divided by the masker delay, d_m. The error bars show the standard error of the threshold estimates.

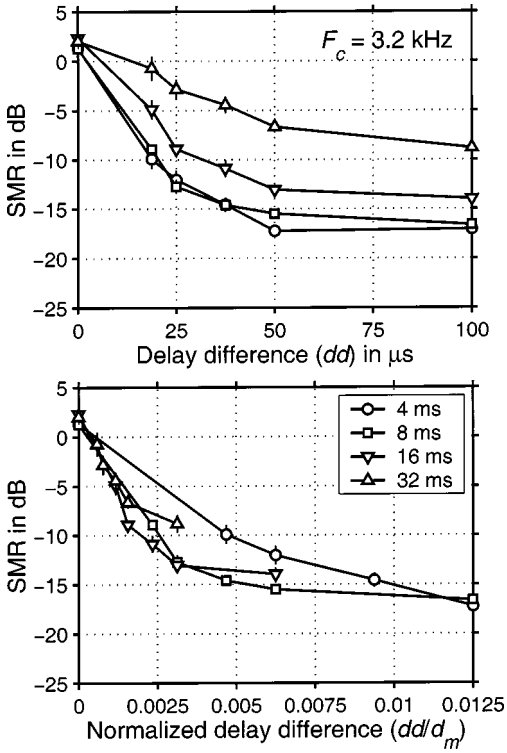

FIG. 5. Average masked threshold for detection of an IRN signal as a function of the delay difference, dd, between signal and masker IRNs; the parameter is the delay of the masker IRN (legend in lower panel). The filter cutoff was 3.2-kHz. The panels show the same thresholds but the abscissa in the lower panel is *normalized* delay difference, that is, dd divided by the masker delay, d_m. The error bars show the standard error of the threshold estimates.

however, there was a small difference in pitch strength between the two intervals, and threshold dropped by more than 10 dB in some conditions. Thereafter, threshold decreased at an ever slower rate, approaching an asymptote when dd was 200–400 μs for $F_c = 0.8$ kHz, and when dd was 50–100 μs for $F_c = 3.2$ kHz. The initial slope of the TI masking pattern was steeper, and the asymptotic level lower, for the smaller masker delays. The normalized making patterns in the lower panels of Figs. 4 and 5 show that, for d_m in the range 16–64 ms, the rate of the initial descent was inversely proportional to d_m. The masking patterns for $d_m = 4$ and 8 ms were similar in terms of their widths and asymptotic levels. The TI masking patterns were much narrower in the 3.2-kHz filter condition (Fig. 5) than in the 0.8-kHz filter condition (Fig. 4); note that in Fig. 5, the scale of the abscissas is stretched by a factor of 4 relative to Fig. 4.

Figure 6 shows the average TI masking patterns for a masker delay of 16 ms and filter cutoff frequencies ranging from 0.4 to 6.4 kHz. As before, threshold is expressed in terms of the SMR and plotted as a function of dd. Figure 6 shows that the width of the TI masking pattern *decreased* as the filter cutoff frequency increased from 0.4 to 6.4 kHz.

Overall, the TI masking patterns reveal remarkable temporal resolution. When the delay of the masker IRN is short (4–8 ms) or when the filter cutoff is high (3.2–6.4 kHz), a difference of a few tens of microseconds between the delays of the signal and masker is sufficient to produce an appreciable release from masking. Indeed, in the highest filter condition ($F_c = 6.4$ kHz), a delay difference of just 12.5 μs produced a masking release of about 7 dB relative to the condition where dd is 0 μs. The size of the delay difference producing a significant masking release, and the fact that the width of the TI masking pattern decreases with *increasing* filter cutoff means that it is unlikely that the present data could be explained by spectral differences between the stimuli when one considers the spectral resolution of the internal excitation pattern. In most of the experimental conditions, the lower filter cutoff, F_c, was greater than 12 times

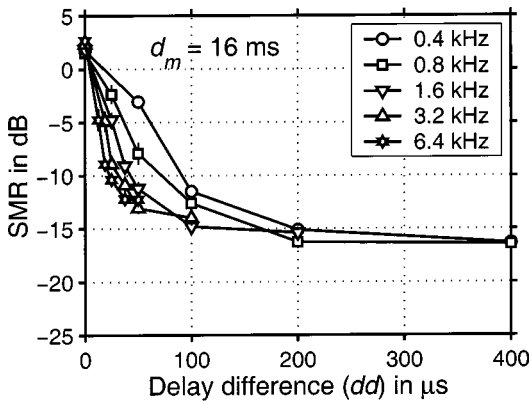

FIG. 6. Average threshold for detecting an IRN signal in the presence of a 16-ms IRN masker as a function of delay difference, dd; the parameter is the low-frequency cutoff, F_c, of the filter passband. The error bars show the standard error of the threshold estimates.

the reciprocal of the IRN delay, so the excitation patterns of the IRNs were like those for random noise filtered to the same frequency region (Krumbholz *et al.*, 2001). In some of the conditions, however, the excitation patterns of the IRNs would be expected to exhibit a few resolved harmonics by the relatively lenient criterion of Shackleton and Carlyon (1994). The fact that there are no discontinuities in the TI masking patterns suggests that resolved harmonics did not play a part in the processing, and that the masking release is associated with a single mechanism operating on the differences in the monaural *temporal* structure between the masker alone and the masker plus signal.

IV. SIMULATION OF TIME-INTERVAL MASKING PATTERNS WITH A TIME-INTERVAL MODEL OF AUDITORY PROCESSING

A computational version of Licklider's (1951) autocorrelation model of pitch was used to determine whether a simple time-interval model of auditory temporal processing could account for the basic effects in the present data. Specifically, we used a modified version of the auditory image model (AIM) presented in Patterson *et al.* (1995), implemented with the DSAM/AMS software package and MATLAB. The auditory model consisted of (i) a second-order bandpass filter with cutoffs at 0.45 and 8.5 kHz; (ii) a 60-channel gammatone filterbank (gtf) with center frequencies between 0.1 and 8 kHz, evenly distributed on the ERB scale; (iii) half-wave rectification, square-root compression, and fourth-order low-pass filtering with a 0.8-kHz cutoff (hcl) in each frequency channel; (iv) a channel-by-channel time-interval analysis performed by strobed temporal integration (sti), which is similar to autocorrelation. This version of AIM is referred to as the $gtf/hcl/sti$ model, and a detailed description of it can be found in Sec. IV of the paper by Krumbholz *et al.* (2001), who used the model to explain the masking asymmetry between noise and IRN.

The stages of the $gtf/hcl/sti$ model prior to the time-interval analysis simulate peripheral auditory processing up to the level of the auditory nerve: the initial bandpass filter represents the operation of the middle ear, the gammatone filterbank (gtf) simulates the spectral analysis performed by the cochlea, the half-wave rectification, compression, and low-pass filtering (hcl) simulate the transformation of the basilar-membrane response to the neural activity pattern (NAP) flowing up the auditory nerve. Strobed temporal integration (sti) produces a time-interval histogram of the neural activity in each tonotopic channel, which is similar to the all-order time-interval histograms produced by autocorrelation. However, sti has the advantage of preserving short-term temporal asymmetry that listeners hear (Patterson and Irino, 1998), and at the same time, it requires far less computation. The tonotopic array of time-interval histograms is referred to as an auditory image (AI), and the structure in the upper panel of Fig. 1 is the AI produced by the model in response to an IRN with an 8-ms delay.

The decision statistic was derived from the ''summary AI,'' produced by averaging the AI across frequency (as in the lower panel of Fig. 1). The summary image was normalized to the value at 0 ms which is a measure of the overall level of the stimulus. In the experiment, the roving level paradigm discouraged the use of overall level as a detection cue. The lower limit of pitch for complex sounds occurs when the period exceeds about 33 ms (Krumbholz *et al.*, 2000). Accordingly, the summary AI was limited to time intervals less than 35 ms, and the modeling was restricted to conditions where the masker delay was less than 35 ms. The stimuli in the simulations were generated using the same software as in the experiment. The maskers were set to a fixed level of 60 dB SPL. Signals were generated with SMRs ranging from -27 to 14 dB in 3-dB steps and then added to the maskers as in the experiment. The stimuli had a duration of 810 ms. For each stimulus condition, summary AIs for 15 different random samples of the stimuli were averaged to produce the summary AI used to calculate the decision statistic. Moreover, the summary AI for a given stimulus sample was itself an average of 20 summary AIs generated at 35-ms intervals throughout the stimulus duration; the first summary AI was calculated 105 ms after stimulus onset, at which point the model response had reached steady state.

A. Decision measure, D^2

Listeners reported using different detection cues in different experimental conditions. When the delay difference between the signal and masker IRNs was large, or the masker delay was small, the signal IRN produced a pitch that was distinct from that of the masker IRN, and listeners based their judgments on whether the stimulus contained one or two pitches. For small delay differences, or large masker delays, the pitches of the signal and masker merged, and listeners based their judgments on the strength, or salience, of the pitch. In the simulations, we used a Euclidean distance, D^2 (Meddis and Hewitt, 1991a) to measure the differences between the summary AI for the signal plus masker and that of the masker alone. D^2 is the integral of the squared difference between the summary AIs, so it includes differences at all time intervals within the summary images. For each experimental condition (i.e., each combination of F_c, d, and dd), D^2 was calculated as a function of SMR. Threshold was defined as the SMR at which D^2 reached a criterion level, C, and this criterion was the main parameter in the fitting process. All of the conditions of the experiment were fitted simultaneously, with a fixed value of C, which was then varied to find the value that minimized the root-mean-square (rms) deviation between the simulated and observed thresholds. The version of AIM in Krumbholz *et al.* (2001) produced a good fit to the data without modification. At the same time, it appeared that the fit could be improved by (i) modifying the *time-interval weighting function* associated with the lower limit of pitch and/or (ii) limiting the *order* of the peaks that contribute to D^2.

B. Time-interval weighting

There is a progressive reduction in pitch strength when approaching the lower limit of pitch. In the default version of AIM, the reduction in pitch strength and the lower limit of pitch are implemented with a linear weighting function that decreases from unity when the time interval is 0 ms, to zero when it is 40 ms. It is this which produces the progressive

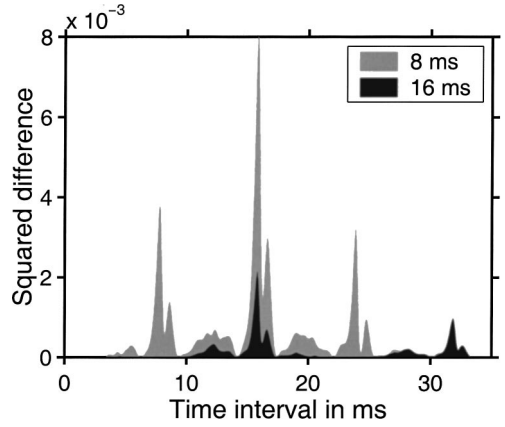

FIG. 7. Squared difference between the summary AIs for masker-plus-signal and masker alone, plotted as a function of time interval. In the case of the gray area, the masker and the signal had delays of either 8 and 8.1 ms (gray shading), or 16 and 16.1 ms (black shading).

reduction of activity level across time interval in the AI of the upper panel in Fig. 1, and thus, the slope in the summary AI of the lower panel in Fig. 1. This linear time-interval weighting function in turn produces an approximately linear decrease in the weight of the squared difference between the summary images for masker and masker plus signal across time interval. The black foreground in Fig. 7 shows the squared difference for a 16-ms masker IRN combined with a 16.1-ms signal IRN plotted as a function of time interval; the SMR is 0 dB and F_c is 0.8 kHz. The squared difference is concentrated at the signal delay, the masker delay, and their integer multiples. The gray background shows the squared difference for an 8-ms masker with an 8.1-ms signal. The first peak in the squared difference function for the 8-ms masker is about twice as large as the first peak in the difference function for the 16-ms masker because of the time-interval weighting function.

The relative weight of the time intervals was varied with a power function that reduces to the linear weighting function when the exponent, α, is unity. The weighting function is $w(ti)=1-(ti/40)^{\alpha}$, where ti is time interval and α is a parameter that determines the degree of nonlinearity. Figure 8 shows the time-interval weighting function for values of α from 0.25 to 8; they all decrease from unity at $ti=0$ ms to zero at $ti=40$ ms, but the relative weight of the short and long intervals varies considerably. When $\alpha<1$, the function is concave and longer time intervals contribute relatively less to the decision statistic; when $\alpha>1$, the function is convex and the longer time intervals contribute relatively more. The vertical, dotted line in Fig. 8 marks the time interval (35 ms) where the summary images were truncated.

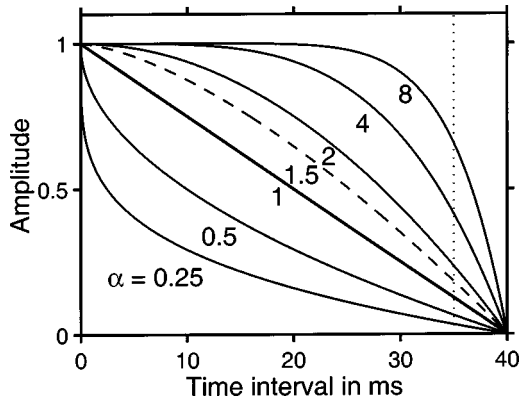

FIG. 8. Time-interval weighting functions for values of α from 0.25 to 8, plotted as a function of time interval; the vertical dotted line marks the time interval where the AI was truncated (35 ms). The function for $\alpha=1.5$, which produced the best fit to the data, is shown by the dashed line.

C. Peak-order limit

Peaks in the summary AI at multiples of a basic delay are referred to as ''higher-order'' peaks (Yost, 1996a,b). The presence of higher-order peaks is due to the fact that autocorrelation and *sti* include time intervals between nonadjacent peaks in the neural activity pattern, as well as first-order intervals. Kaernbach and colleagues have pointed out that the order of the time intervals that contribute to a given peak in the AI is usually greater, or equal, to the peak order (Kaernbach and Demany, 1998; Kaernbach and Bering, 2001).

Figure 7 shows that the squared difference associated with the second-order peak (near 16 ms) can be greater than that associated with the first-order peak (near 8 ms), despite the linear time-interval weighting in the underlying summary images. The reason is that the separation between the peaks of the signal and masker increases in proportion to peak order. So, in the current example, the delay difference of 100 μs between the 8-ms masker and the 8.1-ms signal produces a peak separation of 100 μs for the first-order peaks, but a peak separation of 200 μs for the second-order peaks, and the larger peak separation leads to a larger squared difference for the second-order peaks. It is also the case that stimuli with shorter delays produce more higher-order peaks within the time-range of the summary images than stimuli with longer delays. In the version of the model proposed by Krumbholz *et al.* (2001) all peaks with delays less than 35 ms contribute to the D^2 measure, and the higher-order peaks enable the model to simulate the general reduction in threshold that occurs as delay *decreases* in the asymmetry of masking experiment.

There are other studies, however, where listeners appear to make little, if any, use of higher-order peaks, indicating that higher-order peaks may affect the masking properties of the stimulus more, and in a somewhat different way than they do its pitch and pitch strength. Yost (1996a) and Yost *et al.* (1996) found that listeners had difficulty discriminating IRN in which the delayed copy is added back to the ''original'' noise (IRNO) from IRN in which the delayed copy was added to the ''same'' noise (IRNS). The first-order peaks in these stimuli have the same height but the higher-order peaks in IRNO are larger, and so the IRNO might have been expected to have a stronger pitch. It appears that higher-order peaks have no influence on the pitch or pitch strength, as long as they are not *larger* than the first peak (Yost, 1996b, 1997). In IRN, peak height usually decreases with increasing peak order. However, when IRN is produced with a negative gain factor, *g*, the first-order peak is inverted and it is replaced by its adjacent smaller side peaks that dominate the perception when the number of iterations, *n*, is small. When

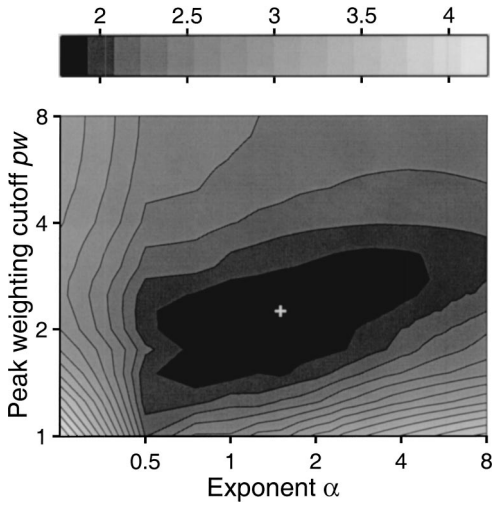

FIG. 9. Minimum root-mean-square (rms) deviation between simulated and observed thresholds, as a function of α (the parameter of the time-interval weighting function), and pw (the parameter of the peak-weighting function); the shading is black for smaller deviations and white for larger deviations (scale bar across the top of the figure). The small white cross marks the combination α of and pw for which the rms deviation is minimum (1.85 dB).

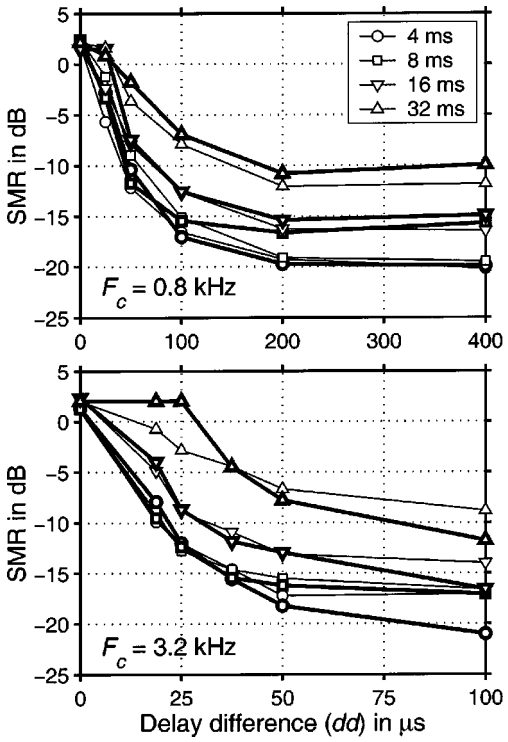

FIG. 10. Simulated thresholds (bold symbols and lines) and observed thresholds (thin symbols and lines) as a function of delay difference; the filter cutoff is 0.8 kHz (upper panel) or the 3.2-kHz (lower panel). The parameter is the delay of the masker IRN.

n increases, however, these side peaks can be smaller than the second-order peak at twice the delay, which is not inverted when g is negative. In this case, the pitch corresponds to the second-order peak (Yost, 1996b, 1997).

The data from the current study appear to be ambiguous with regard to the use of higher-order peaks. On the one hand, the width of the TI masking function decreased with delay for maskers with delays between 64 and 8 ms, which suggests that higher-order peaks are used. On the other hand, there was no further decrease for masker delays below 8 ms, which suggests that there is some relatively low limit on the order of the peaks that can be used. Accordingly, AIM was modified to include a "peak-weighting" function, p(ti), that reduced the contribution of time intervals from unity to zero between one order of peak and the next. That is, for a given peak order, pw, the function decreased linearly from unity at $ti = pw \times d_m$ to zero at $ti = (pw+1) \times d_m$, where d_m is the masker delay. The upper limit on pw is effectively 8 since the shortest delay in the current experiment was 4 ms, and its eighth-order peak would occur at 32 ms.

D. Modeling results

The simulation of the TI masking patterns with the modified version of AIM was performed repeatedly using time-interval weighting functions with α ranging from 0.25 to 8 in steps of 0.25, and peak-weighting functions with pw ranging from 1 and 8 in steps of 0.25. For each combination of α and pw, the fit was evaluated in terms of the rms deviation between the simulated and observed thresholds. Figure 9 shows the rms deviation between simulated and observed threshold plotted with α on the abscissa and pw on the ordinate (white representing large, black representing small, deviations). The figure shows that there is a local minimum in the region where pw is 1.5 to 2.5 and α is 1 to 3. The minimum rms deviation is just 1.85 dB and it occurs at $pw = 2.25$ and $\alpha = 1.5$, marked by a white cross. At this point, the time-interval weighting function is slightly convex (see the dashed line in Fig. 8), and second-order peaks in the summary images contribute to the decision measure, but higher-order peaks do not. The TI masking patterns produced by this version of the model are presented by the bold symbols and lines in Figs. 10 and 11; the thin symbols and lines show the observed thresholds.

Overall, the model produces a surprisingly good fit to the data. The upper and lower panels of Fig. 10 show the data for the 0.8- and the 3.2-kHz filter conditions, respectively; the parameter is the masker delay (legend in upper panel). The initial descent of the simulated TI masking pattern is very similar to that of the data, except in the case of the 32-ms masker in the 3.2-kHz filter condition where the tip of the simulated masking pattern is too broad. The width of the TI masking pattern increases with the delay of the masker as in the data. The asymptotic level at the larger delay differences increases with increasing masker delay as in the data, although the absolute values at the largest delay differences are a little too low when the filter cutoff is 3.2 kHz.

Figure 11 shows the results for the 16-ms masker; in this case, the parameter is filter cutoff, F_c (legend in upper panel). The width of the TI masking pattern *decreases* with increasing filter cutoff (upper panel of Fig. 11), which suggests that temporal resolution (as measured by IRN masking) is affected by the duration of the impulse response of the auditory filter, which is roughly inversely proportional to filter center frequency. In the model, the duration of the auditory filter impulse response determines the width of the ver-

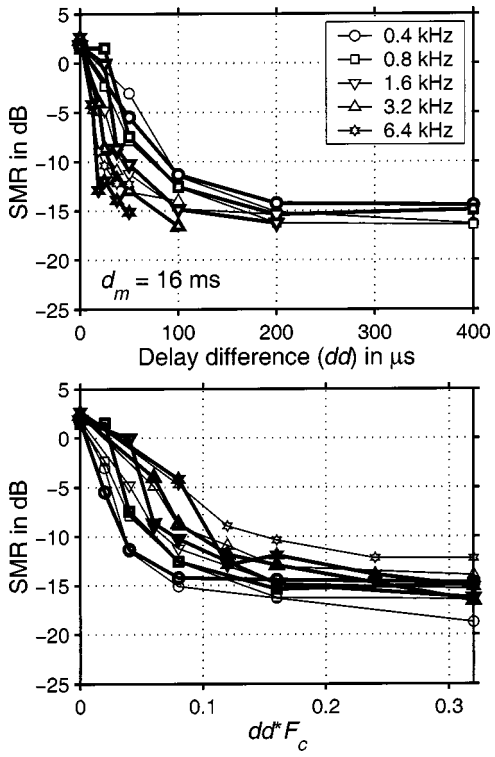

FIG. 11. Simulated thresholds (bold) and observed thresholds (thin) for the 16-ms masker as a function of delay difference; the parameter is filter cutoff, F_c. The abscissa is absolute dd in the upper panel and dd multiplied by F_c in the lower panel.

tical ridges in the AI of IRN, just as the frequency resolution of the auditory filters determines the width of the excitation pattern of a sinusoid. Consequently, the width of the ridges decreases with increasing filter frequency (see the upper panel in Fig. 1). This, in turn, explains the model's ability to account for the decrease in the width of the TI masking pattern with increasing filter cutoff frequency. In the lower panel of Fig. 11, threshold is plotted as a function of dd times F_c. This panel shows that the width of the simulated masking pattern, like that of the observed masking pattern, does not decrease in proportion to filter cutoff. The panel also shows that the model is unable to explain why the asymptotic threshold level increases with increasing filter cutoff (lower panel of Fig. 11).

V. DISCUSSION

The previous section showed that a simple time-interval model of auditory processing can produce a remarkably good fit to the present IRN masking data. The model explains the absolute width of the TI masking pattern and it accounts for the effects of masker delay and frequency region. The modeling results indicate that first- and second-order peaks in the time-interval histograms contribute to the masking release but that higher-order peaks do not, and that contribution of longer time intervals decreases approximately linearly with time interval. In the highest filter condition ($F_c = 6.4$ kHz), a delay difference of just 12.5 μs between the signal and masker IRNs produced a significant masking release (Fig. 6). The masker delay was 16 ms, and so the second-order peak at 32 ms was close to the lower limit of pitch. As a result, it would not be expected to contribute much to the detection of the signal (see the black area in Fig. 7). Thus, to the extent that the model is appropriate, the present data suggest that the monaural system processes time-interval information with a resolution of 10–20 microseconds, which is similar to the resolution of the binaural system.

The temporal resolution revealed by the TI masking pattern (tens of microseconds) is two orders of magnitude greater than the values obtained with traditional measures like gap detection or modulation detection (Forrest and Green, 1987). The discrepancy suggests that the thresholds in the TI masking pattern are based on a different perceptual cue and a different neural code. The cue in the gap and modulation experiments is rapid fluctuation in the temporal envelope of the sound, whereas the cue in the TI masking experiment is stationary—a reduction in pitch strength or precision of the perception. In models of envelope processing, it is assumed that the cue is a temporal fluctuation, and that it is represented by a *temporal* code up to the highest processing levels. In time-interval models of auditory processing, it is assumed that the cues are based on stable time-interval histograms with relatively long time constants that may involve a *spatial* representation of the time-interval information in the monaural stimulus (e.g., Patterson *et al.*, 1995).

Rate discrimination measurements yield estimates of temporal acuity that are closer to the microsecond resolution reported in the present study than the estimates from traditional measurements of temporal resolution. Rate discrimination threshold for sinusoidally amplitude-modulated (SAM) noise is about 6% for base rates up to about 300 Hz (Hanna, 1992). A 6% difference in rate at 300 Hz corresponds to a difference of 200 μs in the repetition period of the modulator. Kaernbach and Bering (2001) report that listeners could discriminate the rate of periodic click trains with an acuity of about 1.25% when the rate was 250 Hz and the click trains were high-pass filtered at 4.5 kHz to remove spectrally resolved harmonics. A 1.25% difference in rate at 250 Hz corresponds to a difference of 50 μs in the period of the sound, which is not much larger than the value suggested by the data from the current experiments. However, Kaernbach and Bering's results might be overly optimistic; using essentially the same stimuli, Cullen and Long (1986) reported rate discrimination thresholds that were considerably larger than those reported by Kaernbach and Bering. Discrimination of the frequency of a sinusoid can be interpreted to indicate temporal acuity that surpasses even the 12.5-μs resolution suggested by the current data. At 1 kHz, frequency discrimination threshold is about 0.2%. So, if changes in the frequency of sinusoids are mainly mediated by temporal cues in the phase-locking range, threshold at 1 kHz would correspond to temporal acuity on the order of 2 μs. However, changing the frequency of a sinusoid produces a change in the place of the excitation along the cochlear partition, and so this measure is probably confounded by spectral cues.

It is interesting to compare the temporal resolution derived from TI masking patterns with the frequency resolution derived from spectral masking patterns. The resolution with which temporal and spectral information is represented in the

auditory system might be expected to reflect their relative importance for the formation of perceptions. When IRN threshold is plotted as a function of the relative delay difference as in the lower panels of Figs. 4 and 5, the TI masking pattern is found to be surprisingly narrow. In the 0.8-kHz condition (Fig. 4), the width of the masking patterns is less than 1% of the masker delay, and the percentage is even smaller in the higher frequency region (Fig. 5). In percentage terms, spectral masking patterns are more than an order of magnitude wider than TI masking patterns. The relative width of spectral masking patterns is determined by the width of the excitation pattern produced by the narrowband masker, which is approximately 10%–15% of the masker frequency.

The paradigm used to generate and analyze the TI masking patterns is reminiscent of the binaural laterality paradigm. In that case, temporal resolution is measured in terms of the listener's ability to detect minute differences between the neural patterns produced by two similar sounds presented concurrently, but to separate ears. In the monaural case, the two stimuli are combined before entering the auditory system, and temporal resolution is measured in terms of the listener's ability to detect minute temporal differences in the neural pattern of the masker due to the presence of the signal. The two paradigms both yield resolution estimates on the order of 10 μs and time-interval models appear to be a reasonable basis for explaining the main effects in both domains.

In most of the current models of monaural temporal processing, the transformation from the time domain to the time-interval domain is modeled by an autocorrelation process; they effectively compute an all-order interval histogram for each channel of the tonotopic array produced in the cochlea. Although autocorrelation models can explain many perceptual phenomena in general terms (Meddis and Hewitt, 1991a,b, 1992; Meddis and O'Mard, 1997), they have been shown to be inadequate in several respects: (i) Time-interval histograms produced by autocorrelation are symmetric in the time-interval dimension. The autocorrelogram does not preserve temporal asymmetries in the stimulus which listeners may well perceive (Patterson and Irino, 1998). (ii) The autocorrelation process places no particular limit on the *length* of the time intervals that are represented in the histograms, whereas psychophysical evidence suggests that human listeners can accurately process time intervals up to 33 ms but no longer (Krumbholz *et al.*, 2000; Pressnitzer *et al.*, 2001). (iii) In autocorrelation models, there is no limit on the *order* of the time intervals that appear in the histograms. Kaernbach and colleagues (Kaernbach and Demany, 1998; Kaernbach and Bering, 2001) constructed click trains exhibiting temporal regularity in the higher-order interclick intervals but not in the first-order intervals, and concluded that ''the mechanism operates more easily on first-order...temporal regularities'' (Kaernbach and Bering, 2001, p. 1047). Moreover, pitch-strength studies suggest that higher-order peaks in the time-interval histograms, which are composed of higher-order time intervals, do not contribute to pitch strength (Yost, 1996a; Yost *et al.*, 1996; Patterson *et al.*, 2000). (iv) There are experiments involving discrimination of IRNs with positive and negative gain which show that the second-order peak contributes to the discrimination when it is similar in size to the first-order peak (Yost, 1996b, 1997). The current study corroborates the use of second-order peaks but indicates that peaks beyond second order are not used.

In the current simulation, the time-interval analysis was performed by strobed temporal integration (sti), instead of autocorrelation; sti measures time intervals from local peaks in the neural activity and, as a result, it is sensitive to temporal asymmetry in the stimulus. This is a fundamental difference between sti and autocorrelation. The contribution of higher-order peaks in the time-interval histograms was limited by multiplying the histograms with a peak-order weighting function, and the longer time intervals were reduced by a time-interval weighting function to explain the lower limit of melodic pitch. These modifications could be applied to the autocorrelogram and/or summary autocorrelogram in a similar way, but they would still represent aspects of autocorrelation that must be modified and/or limited if it is to explain pitch perception in detail.

VI. CONCLUSIONS

The current study indicates that listeners can discriminate a coherent sound, consisting of a single IRN, from a less coherent sound, consisting of two IRNs, when the delays of the two IRNs differ by only a few tens of microseconds. The magnitude of the difference and the fact that the difference decreases when the stimuli are restricted to higher frequency regions mean that it is unlikely that the discrimination is based on spectral cues. Rather, the discrimination appears to be based on small temporal differences in the monaural neural patterns produced by masker and masker plus signal.

The just-discriminable difference in IRN delay decreased with masker delay from 64 down to 8 ms, but it did not decrease further as delay decreased to 4 ms. This suggests that higher-order peaks in the time-interval histograms contributed to the resolution at the shorter masker delays, but that there is a limit on the order of the peaks that can be used. Signals with small delay differences were more readily detectable in the higher filter conditions, indicating that the resolution is affected by the duration of the impulse response of the auditory filters.

A computational model of time-interval processing (Patterson *et al.*, 2000; Krumbholz *et al.*, 2001) was modified to limit the contribution of longer time intervals and higher-order peaks, and in this modified form it could explain the main effects in the data accurately.

ACKNOWLEDGMENT

Research supported by the Medical Research Council (Grant No. G9901257).

Cullen, Jr., J. K., and Long, G. (**1986**). ''Rate discrimination of high-pass filtered pulse trains,'' J. Acoust. Soc. Am. **79**, 114–119.

Durlach, N. I., and Colburn, H. S. (**1978**). ''Binaural phenomena,'' in *Hearing, Handbook of Perception*, edited by E. C. Carterette and M. P. Friedman (Academic, New York), Vol. IV.

Forrest, T. G., and Green, D. M. (**1987**). ''Detection of partially filled gaps in noise and the temporal modulation transfer function,'' J. Acoust. Soc. Am. **82**, 1933–1943.

Hanna, T. E. (**1992**). ''Discrimination and identification of modulation rate,'' J. Acoust. Soc. Am. **91**, 2122–2128.
Handel, S., and Patterson, R. D. (**2000**). ''The perceptual tone/noise ratio of merged, iterated rippled noises with octave, harmonic and nonharmonic delay ratios,'' J. Acoust. Soc. Am. **108**, 692–695.
Irvine, D. R. F. (**1992**). ''Physiology of the auditory brain stem,'' in *The Mammalian Auditory Pathway: Neurophysiology*, edited by A. N. Popper and R. R. Fay (Springer, New York), pp. 153–231.
Johnson, D. H. (**1980**). ''The relationship between spike rate and synchrony in responses of auditory-nerve fibers to single tones,'' J. Acoust. Soc. Am. **68**, 1115–1122.
Kaernbach, C., and Demany, L. (**1998**). ''Psychophysical evidence against the autocorrelation theory of auditory temporal processing,'' J. Acoust. Soc. Am. **104**, 2298–2306.
Kaernbach, C., and Bering, C. (**2001**). ''Exploring the temporal mechanism involved in the pitch of unresolved harmonics,'' J. Acoust. Soc. Am. **110**, 1039–1048.
Krumbholz, K., Patterson, R. D., and Pressnitzer, D. (**2000**). ''The lower limit of pitch as determined by rate discrimination,'' J. Acoust. Soc. Am. **108**, 1170–1180.
Krumbholz, K., Patterson, R. D., and Nobbe, A. (**2001**). ''Asymmetry of masking between noise and iterated rippled noise: Evidence for time-interval processing in the auditory system,'' J. Acoust. Soc. Am. **110**, 2096–2107.
Levitt, H. (**1971**). ''Transformed up–down methods in psychoacoustics,'' J. Acoust. Soc. Am. **49**, 467–477.
Licklider, J. C. R. (**1951**). ''A duplex theory of pitch perception,'' Experientia **7**, 128–133.
Meddis, R., and Hewitt, M. J. (**1991a**). ''Virtual pitch and phase sensitivity of a computer model of the auditory periphery. I. Pitch identification,'' J. Acoust. Soc. Am. **89**, 2866–2882.
Meddis, R., and Hewitt, M. J. (**1991b**). ''Virtual pitch and phase sensitivity of a computer model of the auditory periphery. II. Phase sensitivity,'' J. Acoust. Soc. Am. **89**, 2883–2894.
Meddis, R., and Hewitt, M. J. (**1992**). ''Modeling the identification of concurrent vowels with different fundamental frequencies,'' J. Acoust. Soc. Am. **91**, 233–245.
Meddis, R., and O'Mard, L. (**1997**). ''A unitary model of pitch perception,'' J. Acoust. Soc. Am. **102**, 1811–1820.
Oertel, D. (**1997**). ''Encoding of timing in brain stem auditory nuclei of vertebrates,'' Neuron **19**, 959–962.
Patterson, R. D. (**1994**). ''The sound of a sinusoid: Time-interval models,'' J. Acoust. Soc. Am. **96**, 1419–1428.
Patterson, R. D., and Datta, A. J. (**1996**). ''The detection of iterated rippled noise (IRN) masked by IRN,'' Br. J. Audiol. **30**, 148.
Patterson, R. D., and Irino, T. (**1998**). ''Modeling temporal asymmetry in the auditory system,'' J. Acoust. Soc. Am. **104**, 2967–2979.
Patterson, R. D., Robinson, K., Holdsworth, J., McKeown, D., Zhang, C., and Allerhand, M. (**1992**). ''Complex sounds and auditory images,'' in *Auditory Physiology and Perception, Proceedings of the 9th International Symposium on Hearing*, edited by Y. Cazals, L. Demany, and K. Horner (Pergamon, Oxford), pp. 429–446.
Patterson, R. D., Allerhand, M., and Giguère, C. (**1995**). ''Time-domain modeling of peripheral auditory processing: A modular architecture and a software platform,'' J. Acoust. Soc. Am. **98**, 1890–1894.
Patterson, R. D., Handel, S., Yost, W. A., and Datta, A. J. (**1996**). ''The relative strength of tone and noise components of iterated rippled noise,'' J. Acoust. Soc. Am. **100**, 3286–3294.
Patterson, R. D., Yost, W. A., Handel, S., and Datta, A. J. (**2000**). ''The perceptual tone/noise ratio of merged iterated rippled noises,'' J. Acoust. Soc. Am. **107**, 1578–1588.
Pressnitzer, D., Patterson, R. D., and Krumbholz, K. (**2001**). ''The lower limit of melodic pitch,'' J. Acoust. Soc. Am. **109**, 2074–2084.
Rouilly, E., deRibaupierre, Y., and deRibaupierre, F. (**1979**). ''Phase-locked responses to low frequency tones in the medial geniculate body,'' Hear. Res. **1**, 213–226.
Shackleton, T. M. and Carlyon, R. P. (**1994**). ''The role of resolved and unresolved harmonics in pitch perception and frequency modulation discrimination,'' J. Acoust. Soc. Am. **95**, 3529-3540.
Slaney, M., and Lyon, R. F. (**1990**). ''A perceptual pitch detector,'' in *Proceedings of the IEEE International Conference on Acoustics, Speech, and Signal Processing, Albuquerque, New Mexico* (IEEE, New York), pp. 357–360.
Yost, W. A. (**1996a**). ''The pitch strength of iterated rippled noise,'' J. Acoust. Soc. Am. **100**, 3329–3335.
Yost, W. A. (**1996b**). ''The pitch of iterated rippled noise,'' J. Acoust. Soc. Am. **100**, 511–518.
Yost, W. A. (**1997**). ''Pitch strength of iterated rippled noise when the pitch is ambiguous,'' J. Acoust. Soc. Am. **101**, 1644–1648.
Yost, W. A., Patterson, R. D., and Sheft, S. (**1996**). ''A time domain description for the pitch strength of iterated rippled noise,'' J. Acoust. Soc. Am. **99**, 1066–1078.

Testing the concept of a modulation filter bank: The audibility of component modulation and detection of phase change in three-component modulators

Aleksander Sek
Institute of Acoustics, Adam Mickiewicz University, 85 Umultowska, 61-614 Poznan, Poland

Brian C. J. Moore[a)]
Department of Experimental Psychology, University of Cambridge, Downing Street, Cambridge CB2 3EB, England

(Received 12 July 2002; revised 24 January 2003; accepted 6 February 2003)

Two experiments were performed to test the concept that the auditory system contains a ''modulation filter bank'' (MFB). Experiment 1 examined the ability to ''hear out'' the modulation frequency of the central component of a three-component modulator applied to a 4-kHz sinusoidal carrier. On each trial, three modulated stimuli were presented. The modulator of the first stimulus contained three components. Within a run the frequencies of the outer two components were fixed and the frequency of the central (''target'') component was drawn randomly from one of five values. The modulators of second and third stimuli contained one component. One had a frequency equal to that of the target and the other had a frequency randomly selected from one of the other possible values. Subjects indicated whether the target corresponded to the second or third stimulus. Scores were around 80% correct when the components in the three-component modulator were widely spaced and when the frequencies of the target and comparison differed sufficiently. Experiment 2 examined the ability to hear a change in the relative phase of the components in a three-component modulator with harmonically spaced components, using a 3IFC task. The frequency of the central component, f_c, was either 50 or 100 Hz. Scores were 80%–90% correct when the component spacing was $\leqslant 0.5f_c$, but decreased markedly for greater spacings. Performance was only slightly impaired by randomizing the overall modulation depth from one stimulus to the next. The results of both experiments are broadly consistent with what would be expected from a MFB with a Q value of 1 or slightly less. [DOI: 10.1121/1.1564020]

PACS numbers: 43.66.Mk, 43.66.Nm, 43.66.Ba [NFV]

I. INTRODUCTION

The perception of amplitude modulation (AM) has often been modeled by a sequence of stages. The first stage is a bank of bandpass filters (the auditory filters), although some models assume just a single, broad ''predetection filter'' (Viemeister, 1979). Each filter is followed by a nonlinear device, such as a rectifier and compressor, and a ''smoothing'' device. Usually, this smoothing device is thought to reflect a relatively central process. The output of the smoothing device is fed to a decision device. Models of this general type have been proposed by Viemeister (1979), Festen and Plomp (1981), Moore *et al.* (1988), Plack and Moore (1990), and Oxenham and Moore (1994). The smoothing device has been implemented as a low-pass filter (Viemeister, 1979; Strickland and Viemeister, 1996) or by a sliding temporal integrator (temporal window) (Moore *et al.*, 1988; Plack and Moore, 1990; Oxenham and Moore, 1994).

More recently, it has been proposed that modulation perception depends on a second stage of filtering in the auditory system (Dau *et al.*, 1997a, b). It is assumed that the envelopes of the outputs of the auditory filters are fed to a second array of overlapping bandpass filters tuned to different envelope modulation rates. This set of filters is usually called a ''modulation filter bank'' (MFB). The concept of the MFB implies that the auditory system performs a limited resolution spectral analysis of the envelope at the output of each auditory filter.

Evidence supporting the concept of the MFB has come mainly from experiments on modulation masking (Bacon and Grantham, 1989; Houtgast, 1989; Dau *et al.*, 1997a, b, 1999; Ewert and Dau, 2000; Ewert *et al.*, 2002), which appear to show selectivity in the modulation-frequency domain. However, the interpretation of the results is not entirely clear cut, and not all authors accept that a MFB is necessary to explain the results (Strickland and Viemeister, 1996; Moore *et al.*, 1999a). It is possible that the results could be explained by the similarity of the temporal patterns of the envelopes of the signal and masker, without analysis using an MFB. Here we describe two experiments not involving modulation masking that are aimed at providing further tests of the concept of the MFB. Both experiments are analogous to experiments that have been performed in the audio-frequency domain, and which are thought to reflect the effects of filtering in the auditory periphery.

[a)]Author to whom correspondence should be addressed. Electronic mail: bcjm@cus.cam.ac.uk

II. EXPERIMENT 1—"HEARING OUT" COMPONENT MODULATION

In the audio-frequency domain, subjects are able, to some extent, to "hear out" individual components in complex tones. This has been shown both for harmonic complex tones (Plomp, 1964; Plomp and Mimpen, 1968; Soderquist, 1970; Fine and Moore, 1993) and for non-harmonic complex tones (Plomp, 1964; Moore and Ohgushi, 1993). For reviews, see Plomp (1976) and Moore (2003). In a typical task to demonstrate this ability, subjects hear three separate stimuli: a complex tone and two sinusoidal tones. One of the sinusoidal tones is a component of the complex, and the other has a frequency mistuned from that of any component in the complex. The task of the subject is to decide which of the two sinusoidal tones is contained within the complex tone. Usually, the task is performed very well if the "target" component is widely separated in frequency from neighboring components, but it is performed less well when the components are closely spaced; on average, a partial can be heard out from a complex tone with about 75% accuracy when it is separated from neighboring partials by $1.25ERB_N$ (Moore and Ohgushi, 1993; Moore, 2003), where ERB_N denotes the equivalent rectangular bandwidth of the auditory filter as measured in normal-hearing listeners at moderate sound levels (Glasberg and Moore, 1990; Moore, 2003). Hence, the ability to hear out partials has been ascribed mainly to the frequency analysis that occurs in the auditory periphery. However, musicians are better at this task than nonmusicians (Soderquist, 1970; Fine and Moore, 1993), even though auditory filter bandwidths do not differ between these groups (Fine and Moore, 1993), which suggests that other factors are involved.

In our first experiment, we assessed the extent to which subjects can hear out the component modulations in a complex modulator, as a function of the frequency separation of the components. An ability to hear out component modulation would support the concept of the MFB.

A. Rationale and method

The selectivity of the putative MFB is generally assumed to be markedly poorer than selectivity in the audio-frequency domain. Q values (center frequency divided by bandwidth) for the modulation filters are typically assumed to be 1–2 (Dau *et al.*, 1997a, b; Ewert and Dau, 2000; Lorenzi *et al.*, 2001b; Ewert *et al.*, 2002; Sek and Moore, 2002). To maximize the likelihood that subjects could perform the task, we decided to use a simple three-component modulator, with relatively wide frequency spacing between the components. We assessed whether subjects could hear out the central component of this complex modulator. We chose to use a 4-kHz sinusoidal carrier rather than a broadband noise carrier, as there is evidence that the inherent fluctuations in a noise carrier can limit the ability to detect and discriminate imposed modulation (Dau *et al.*, 1997a, b; Ewert and Dau, 2000; Verhey, 2002). To avoid any influence of resolvable spectral sidebands (Zwicker, 1956; Schorer, 1986; Sek and Moore, 1994; Kohlrausch *et al.*, 2000; Moore and Glasberg, 2001), the highest modulation frequency used was 190 Hz, which is less than one-half of ERB_N at 4 kHz (Glasberg and Moore, 1990).

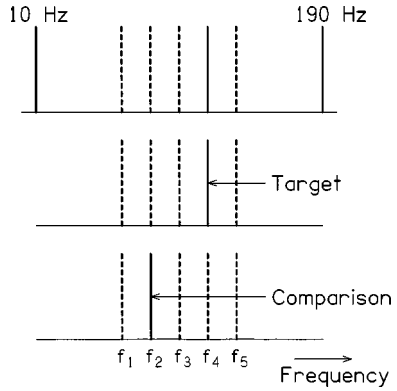

FIG. 1. Schematic illustration of the task and stimuli used in experiment 1. The top row shows the spectrum of the three-component modulator presented in the first interval, with (in this example) flanking components at 10 and 190 Hz. The inner target component could have one of five possible frequencies, selected at random on each trial, indicated by the five inner lines (four dashed and one solid). The solid line indicates the target frequency for one specific trial (f_4, equal to 111.8 Hz). The second and third rows show the possible frequencies for the single modulator components presented in the second and third intervals. In this example, the target frequency occurred in the second interval and the comparison frequency f_2 (89.4 Hz) occurred in the third interval. On each trial, the target occurred randomly in interval two or interval three. The frequency of the comparison component was selected randomly from the four possible values for each target frequency.

We designed the task so that subjects could not perform it by judging the mean rate of the complex modulator. The design is illustrated schematically in Fig. 1. On each trial, three modulated stimuli were presented. The modulator of the first stimulus contained three components. Within a run, the frequencies of the outer two components were fixed and the frequency of the central ("target") component, f_{target}, was drawn randomly from one of five possible values: 80, 89.4, 100, 111.8, and 125 Hz. In the example trial shown in Fig. 1, the target frequency is 111.8 Hz (solid line) and the flanking component frequencies are 10 and 190 Hz. The modulators of the second and third stimuli contained just a single component. In one of these, selected at random, the modulation frequency was equal to that of the target. In the other, the ("comparison") modulation frequency, f_{comp}, was randomly selected from one of the four other possible values of the target. In the example trial shown in Fig. 1, the target frequency occurs in the second stimulus (solid line) and the comparison modulation frequency is 89.4 Hz (solid line in third row). Subjects were required to indicate whether the second or third stimulus contained a modulation component that was present in the first stimulus. Feedback was provided by lights on the response box indicating the correct interval. Subjects were seated in a double-walled sound-attenuating chamber.

The results were analyzed in terms of the ratio between f_{target} and f_{comp}, taking as the numerator whichever of these two was the larger. The smallest ratio was equal to 1.118. This was chosen as it is somewhat larger than the threshold for detection of a change in modulation frequency of a sinusoidal carrier (Lemanska *et al.*, 2002) (although Lemanska

et al. used a modulation index of 0.5, while we used an index of 0.33 for each component). Clearly, if subjects cannot hear the difference between f_{target} and f_{comp} when presented in isolation, they will be unable to perform the task. A run started with five trials using the easiest condition, with the largest ratio of f_{target} and f_{comp}. Scores for these initial five trials were discarded. Then each possible value of f_{target} was paired with each possible value of f_{comp} two times, giving a total of 40 scored trials per run. Data presented are the result of at least 10 runs per subject (more usually, 13–15 runs).

B. Stimuli

Stimuli were generated using a Tucker-Davis array processor (TDT-AP2) in a host PC, and a 16-bit digital to analog converter (TDT-DD1) operating at a 50-kHz sampling rate. The stimuli were attenuated (TDT-PA4) and sent through an output amplifier (TDT-HB6) to a Sennheiser HD580 earphone. Only one ear was tested for each subject. The 4-kHz sinusoidal carrier had a level of 70 dB SPL. Each modulator component had a modulation index of 0.33. This was chosen so as to avoid over-modulation of the three-component modulator, while ensuring that the modulation was clearly audible. The starting phase of each modulator component was chosen randomly for each and every stimulus.

On each trial, the carrier was presented in three bursts separated by silent intervals of 400 ms. Each burst had a 20-ms raised-cosine rise and fall, and an overall duration (including rise/fall times) of 1000 ms. The modulation was applied during the whole of the carrier. The flanking component frequencies are given in Sec. II D.

C. Subjects

Five subjects were tested in all, although only three completed all conditions. One subject was author AS. The other subjects were paid for their services. All subjects had absolute thresholds less than 20 dB HL at all audiometric frequencies and had no history of hearing disorders. All had extensive previous experience in tasks similar to that described above; these tasks were variations on the design described here that were tried before the final design was decided.

D. Results

In our first condition, the flanking component frequencies were as illustrated in Fig. 1, namely 10 and 190 Hz. The individual results for the five subjects are shown in the top-left panel of Fig. 2. For the smallest ratio of f_{target} and f_{comp}, scores are close to the chance level of 50%. However, scores increase as the ratio increases, and for a ratio of 1.56 scores range from about 77% to 90%. A one-way within-subjects analysis of variance (ANOVA) was conducted on the arcsine-transformed percent correct scores. This showed a significant effect of frequency ratio; $F(3,12)=37.28$, $p<0.001$. This suggests an ability to hear out the target modulation in the complex modulator when the flanking components are widely spaced in frequency from the target, and when f_{target} and f_{comp} differ sufficiently.

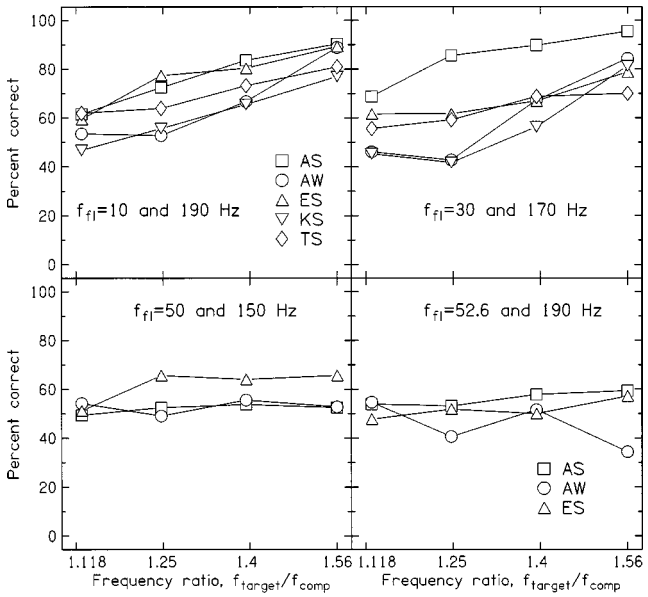

FIG. 2. Results of experiment 1. The percent correct identification of the target is plotted as a function of the ratio of the target and comparison frequencies, using as numerator whichever of the two was the larger. Each symbol denotes one subject, as indicated in the key. Each panel shows results for a specific pair of flanking component frequencies, as indicated in the key.

We next tried moving the flanking modulator components closer to the target component, while keeping them symmetrically placed (on a linear frequency scale) around the frequency of the central target component (100 Hz). The flanking component frequencies were (1) 30 and 170 Hz and (2) 50 and 150 Hz. Results are shown in the top-right and bottom-left panels of Fig. 2, respectively. For the flanking modulator frequencies of 30 and 170 Hz, performance, on average, is a little worse than for the frequencies of 10 and 190 Hz, although subject AS actually showed slightly better performance for the 30- and 170-Hz frequencies. An ANOVA showed a significant effect of frequency ratio; $F(3,12)=16.04$, $p<0.001$. Only three subjects were tested using the flanking modulator frequencies of 50 and 150 Hz. Two (AW and AS) performed very close to the chance level of 50%; they were unable to perform the task. Subject ES achieved scores of about 65% for the three larger frequency ratios. An ANOVA showed that there was no significant effect of frequency ratio; $F(3,6)=1.2$, $p=0.385$. The finding that performance did not improve with increasing ratio of f_{target} and f_{comp} may be partly due to the fact that, for the largest ratio, the lowest and highest target frequencies, 80 and 125 Hz, approached the frequencies of the lower and higher flanking components, respectively.

In the conditions described so far, the flanking components were equally spaced from the central target component on a linear frequency scale. In the final condition, the components were equally spaced on a logarithmic scale; flanking component frequencies were 52.6 and 190 Hz. The results are shown in the bottom-right panel of Fig. 2. All three subjects tested showed close to chance performance. An ANOVA showed no significant effect of frequency ratio; $F(3,6)=0.24$, $p=0.866$.

Comparing across conditions, for the largest ratio of

f_{target} and f_{comp}, performance was well above chance when the flanking component frequencies were 30 and 170 Hz (top right) but was at chance when the flanking component frequencies were 52.6 and 190 Hz. This suggests that performance when the flanking components had equal logarithmic spacing from the central target frequency was mainly limited by the lower of the two flanking components. This in turn suggests that the hypothetical modulation filter tuned to the central target component is not symmetrical on a logarithmic frequency scale. At first sight this appears inconsistent with the proposal of Ewert *et al.* (2002) that the modulation filters are roughly symmetrical on a logarithmic scale. However, their masked-threshold patterns did show some asymmetry for the highest signal modulation frequency tested (64 Hz), being steeper on the high-frequency side, and they modeled the modulation filter for this frequency with the combination of a second-order bandpass filter and a low-pass filter with a cutoff frequency of 150 Hz. Our results are consistent with theirs in suggesting that, for high center frequencies, the modulation filters have steeper upper than lower slopes on a logarithmic frequency scale.

When the lowest modulator component was relatively close in frequency to the central target component (i.e., when the lowest component frequency was 50 or 52.6 Hz), the results for some subjects showed a strong asymmetry or bias. For example, subject AS picked the interval containing the lower modulation frequency as matching the target, regardless of whether or not that was the case. As a result, he was nearly always correct when f_{target} was below f_{comp} and nearly always incorrect when f_{target} was above f_{comp}. AS reported that he based his judgments on the overall impression of fluctuation rate in the complex modulator. This appeared to be relatively low, so he picked the interval in which the single component had the lower rate. As noted above, the task was designed to prevent subjects from doing well by using a cue based on the overall rate of the complex modulator. The effect of AS using this strategy was that he performed at chance level, but with the bias noted here.

E. Discussion

One potential problem with our method is that subjects might have learned to associate the overall sound of each complex modulator with a particular target modulation frequency. There were only five possible target frequencies, so it might have been possible for subjects to learn the association over a series of trials, using the feedback information provided on each trial. There are two reasons for believing that subjects did not actually do this. First, such learning does not explain the effect of the frequency of the flanking modulator components. If subjects could learn to associate the overall sound of each complex modulator with a particular target frequency, there is no reason why they should not have done this for the cases when the flanking components were relatively close in frequency to the target frequency. However, for these cases, performance was at or close to chance level (bottom two panels in Fig. 2). Second, when subjects were switched from flanking modulator frequencies of 10 and 190 Hz to flanking modulator frequencies of 30 and 170 Hz, the overall sound of each complex modulator would have changed, but subjects showed good performance for the higher ratios of f_{target} and f_{comp} even on the early runs, when there would have been little chance for learning to occur. We conclude, therefore, that it is unlikely that subjects learned to associate the overall sound of each complex modulator with a particular target frequency.

The most plausible interpretation of our results is that subjects could hear out the target modulation in the complex modulator when the flanking components were widely spaced in frequency from the target, and when f_{target} and f_{comp} differed sufficiently. This is consistent with the subjective reports of the subjects. However, the mean score never exceeded about 85%. In comparable tasks in the audio-frequency domain, scores close to 100% are obtained for widely spaced components (Plomp, 1964; Moore and Ohgushi, 1993). Thus, the ability to hear out modulator components is relatively poor. Also, scores fell close to chance level when the lower of the two flanking components was separated by 50 Hz or less from the central target component frequency of 100 Hz. As described earlier, in the audio-frequency domain, a partial has to be separated from neighboring partials by about $1.25ERB_N$ to be heard out with 75% accuracy. For our data, most subjects scored slightly better than 75% when the flanking components were separated from the central target component by 70 Hz. Applying the same criterion as in the audio-frequency domain, this would imply a bandwidth of the modulation filter centered at 100 Hz of about 112 Hz (140/1.25), implying a Q value a little below 1. This is consistent with the relatively broad tuning of the modulation filters inferred from experiments on modulation masking (Dau *et al.*, 1997a, b; Ewert and Dau, 2000; Lorenzi *et al.*, 2001b).

III. EXPERIMENT 2—THE DETECTION OF CHANGES IN MODULATOR COMPONENT PHASE

A. Background

In the audio-frequency domain, sensitivity to the relative phases of the components in a three-component modulator has been used as a measure of the critical bandwidth (Zwicker, 1952; Schorer, 1986; Sek, 1994). It is assumed that listeners are sensitive to the relative phases of the components when all components fall within a single critical band, but become insensitive to relative phase when the components fall in separate critical bands. In one method, the threshold for detecting amplitude modulation (AM) or quasi-frequency modulation (QFM) is measured as a function of modulation frequency. For low modulation frequencies, the modulation index required for threshold is lower for AM than for FM. For higher modulation frequencies, AM and QFM are equally detectable when their modulation indices are equal. The modulation frequency at which AM and QFM first become equally detectable is called the critical modulation frequency (CMF). It has sometimes been assumed that the critical bandwidth is equal to twice the CMF (Zwicker, 1952; Schorer, 1986).

Although the validity of this method as a measure of the auditory filter bandwidth has been questioned (Sek and

Moore, 1994; Moore, 2003), it is generally accepted that human listeners are more sensitive to within-channel phase changes than to across-channel phase changes (Patterson, 1987; Uppenkamp *et al.*, 2001; Moore, 2003). Hence, changes in phase sensitivity with changes in the frequency spacing of the components probably do reflect the influence of the frequency selectivity of the auditory system.

In the modulation domain, the effect of relative modulator phase has been assessed in only a few previous studies, and these mostly involved ''modulation masking'' (detection of signal modulation in the presence of masker modulation) rather than a direct measure of the ability to detect changes in relative modulator phase. Bacon and Grantham (1989) measured thresholds for detecting sinusoidal AM of a white noise carrier in the presence of a second sinusoidal AM, acting as a modulation masker. They found no effect of relative phase using masker and signal modulation frequencies of 6 and 4 Hz, respectively. Strickland and Viemeister (1996) also examined modulation masking using a noise carrier and a sinusoidal masker and a sinusoidal signal. When the two sinusoids had a frequency ratio of 2:1, thresholds were influenced by the relative phase of the masker and signal. For example, when the masker frequency was twice the signal frequency and the masker frequency was relatively low (32 or 8 Hz), thresholds tended to be lowest (best) when the starting phase of the signal relative to the masker was 135° or 225°.

Lorenzi *et al.* (1999) studied the effect of relative modulator phase for a two-component modulator when both components were clearly detectable. A white noise carrier was modulated with the sum of two sinusoids with frequency ratio 2:1 (100, 200 and 150, 300) or 3:1 (100, 300). The task was to distinguish two stimuli in which the two sinusoidal modulators had either a fixed phase or a drifting phase. Performance was good for the 2:1 ratio, but at chance for the 3:1 ratio.

Moore and Sek (2000) explored the effect of relative modulator phase on the detection of a three-component modulator applied to a 4-kHz sinusoidal carrier. The central modulator component had a frequency of 50 Hz, and the two other components had frequencies of 50 ± 5, 10, 25, 40, or 45 Hz. Thus, the modulator waveform was always periodic. Each modulator component had the same modulation index, *m*. The relative phases of the components were chosen to give a variety of modulation waveforms differing in the ratio of maximum to minimum value (max-min) and in crest factor. Modulation detection thresholds were measured by varying *m*, using an adaptive two-interval forced-choice procedure. Thresholds were found to be independent of relative modulator phase and of the frequency spacing of the components. This experiment is analogous to experiments that have been performed in the frequency domain to measure the CMF. However, the failure to find an effect of component frequency spacing cannot be taken as disproof of the concept of the MFB, since the listeners were insensitive to relative component phase even for closely spaced components.

Moore and Sek (2000) and other researchers (Moore *et al.*, 1999a; Lorenzi *et al.*, 2001a, b) have suggested that the internal representation of the envelopes of sounds may be distorted by the presence of nonlinearities in the auditory system, such as basilar-membrane compression (Rhode and Robles, 1974) and neural saturation and adaptation effects (Shofner *et al.*, 1996). These nonlinearities can result in the introduction of components in the effective modulation spectrum that were not present in the stimulus itself, and they can also result in differences in effective ''internal'' root-mean-square (rms) value of the modulator when the relative phases of the modulator components are changed. Moore and Sek (2000) suggested that the phase effects found in some earlier studies might be partly explained by such differences in effective rms value; subjects may have used the impression of the overall depth of modulation as a cue. The distortion of the modulator waveform produced by nonlinearities in the auditory system would be small for low modulation depths, and this could explain the finding of Moore and Sek that the threshold for detecting complex modulation was unaffected by the relative phases of the modulator components.

The present experiment used stimuli similar to those of Moore and Sek (2000). However, rather than measuring thresholds for detecting complex modulation as a function of modulator component phase, we assessed whether subjects could detect changes in relative modulator phase when the modulation depth of each component was well above threshold. As in Moore and Sek (2000), the frequency spacing of the harmonically related components was varied to test the prediction based on the concept of the MFB that performance would be better for closely spaced components. To assess whether subjects used the effective rms value of the modulator as a cue, we included a condition where the modulation depth of all components was randomly varied from one stimulus to the next.

B. Stimuli

The equipment and earphone were the same as for experiment 1. Each modulator component was of equal amplitude. Subjects were required to discriminate two modulators differing in the relative phases of their components. For one modulator, the starting phase was 0° (sine phase) for all modulator components. We refer to this as 0-phase. The waveforms for this modulator, for each spacing of the modulator components, are shown as the solid lines in the left column of Fig. 3 (the right column will be explained later). The waveforms have relatively high peak factors. For the other modulator, the lowest component was phase shifted by 180° or π radians (the other two components starting at 0°). We refer to this as π-phase. The waveforms for this modulator are shown as the dotted lines in the left column of Fig. 3. They have lower peak factors than for the sine-phase modulator. The center component of the modulator had a frequency, f_c, of 50 or 100 Hz. The spacing of the components was 5, 15, 25, 35, or 45 Hz, for the 50-Hz f_c and 10, 30, 50, 70, and 90 Hz for the 100-Hz f_c.

On each trial, three stimuli were presented. Durations and levels were the same as for experiment 1. In one set of conditions, the modulation index, *m*, of each component was fixed at 0.2. In another condition, each modulator component had the same value of *m*, but the value of *m* was randomly varied from one stimulus to the next, over a range of ± 3 dB

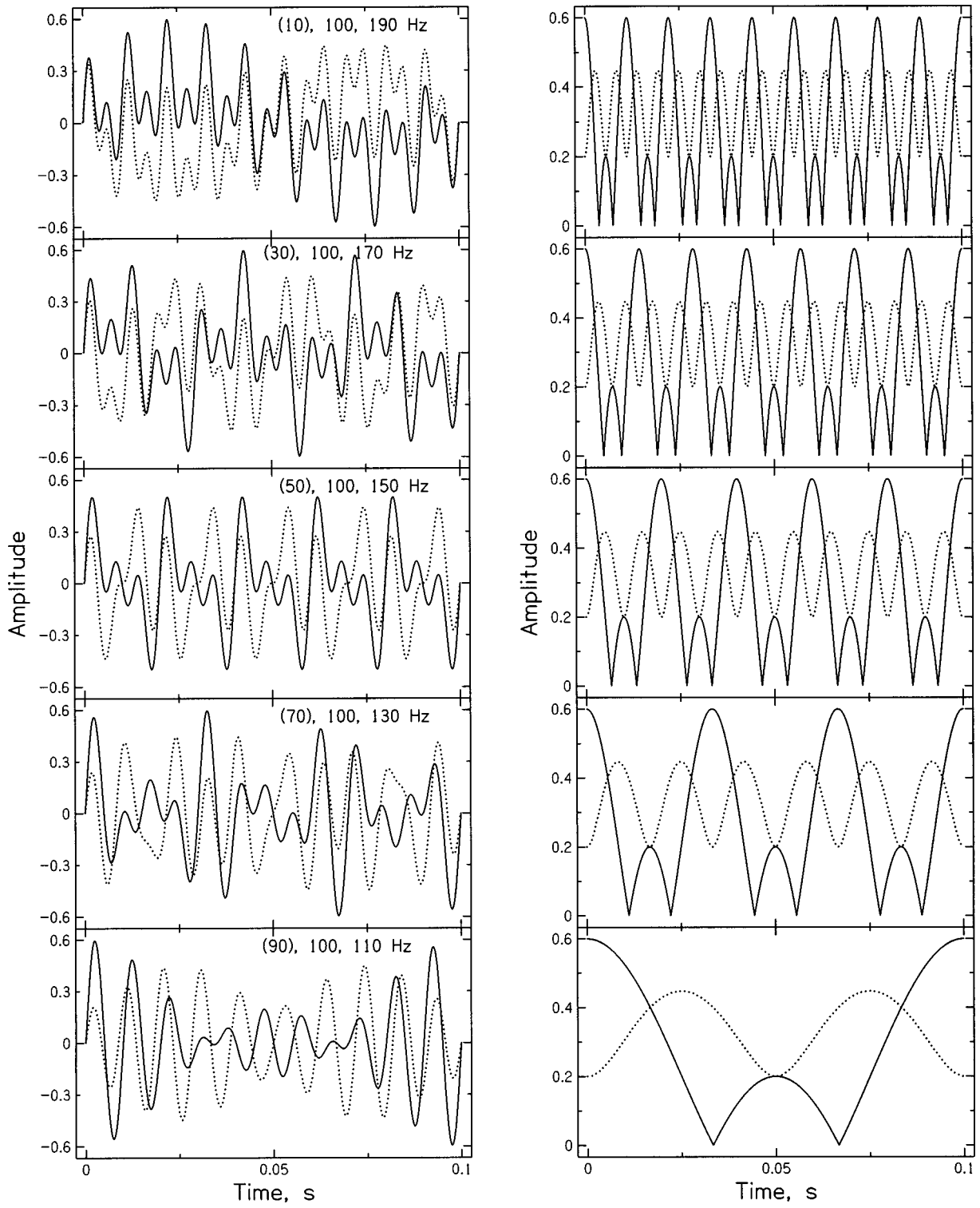

FIG. 3. The left column shows waveforms of the three-component complex modulators used in experiment 2 (without DC component) when the center frequency was 100 Hz. One modulator had components all with a starting phase of 0° (sine phase). The waveforms for this modulator, for each spacing of the modulator components, are shown as the solid lines. The other modulator had the phase of the lowest component shifted by 180° or π radians. The waveforms for this modulator are shown as the dotted lines. The frequencies of the modulator components are given within each panel. The frequency of the component whose phase was shifted is in parentheses. The right column shows the venelope (envelope of the envelope) corresponding to each modulation waveform in the left column.

in terms of $20 \log m$ (on a uniform scale in terms of $\log m$); the value of m varied between 0.1416 and 0.2825. This was done to disrupt a possible cue based on differences in effective rms value of the modulator produced by the change in relative modulator phase.

C. Procedure

A three-interval forced-choice task was used. Two intervals contained the 0-phase stimulus. The other interval, selected at random from the three intervals, contained the

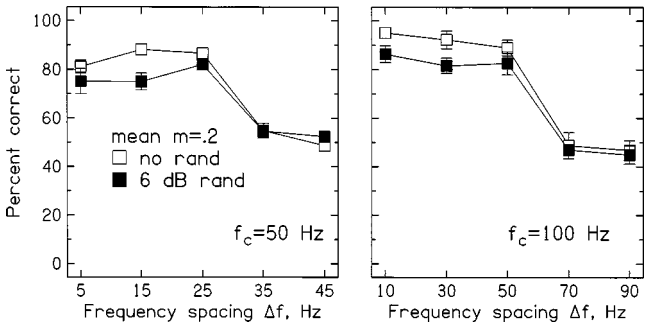

FIG. 4. Mean results of five subjects for experiment 2. The percent correct in the three-alternative forced-choice task is plotted as a function of the frequency spacing of the flanking modulator components from the center component. The left and right panels shows results when the frequency of the center modulator component was 50 and 100 Hz, respectively. Error bars show ± one standard error across subjects. They are omitted when they would be smaller than the symbol used to represent a point.

π-phase stimulus. The task of the subject was to select the interval that was different from the other two. Feedback was given via lights on the response box. A run started with five trials using the smallest frequency spacing of the modulator components; pilot trials indicated that performance was relatively good for this spacing. Then, in successive trials, stimuli with each frequency spacing were presented once, in ascending order. This sequence was repeated ten times to give a total of 55 trials per run. Results from the first five trials of each run were discarded. For each subject, each modulator center frequency, and each condition (fixed or randomized modulation depth), 20 runs were obtained, giving 200 judgments for each frequency spacing and condition.

D. Subjects

Five subjects were tested. One was author AS. The other four subjects were paid for their services. All subjects had absolute thresholds less than 20 dB HL at all audiometric frequencies and had no history of hearing disorders. All had previous experience in psychoacoustic tasks including tasks similar to the present one.

E. Results

The results were very similar across subjects, and the mean results are shown in Fig. 4. Error bars show ± one standard error (SE) across subjects. For the condition with fixed modulation depth (open squares), performance was reasonably good (80% to 95%) for frequency spacings of the modulator components up to $0.5f_c$, but worsened when the frequency spacing was increased beyond that. However, even for the largest spacing used, the means are more than 2 SEs above the chance level of 33%. These results are generally consistent with the pattern that would be expected on the basis of a MFB; subjects may be sensitive to modulator component phase when all components fall within the passband of one modulation filter, and become less sensitive when the overall spacing of the components exceeds the bandwidth of the modulation filter tuned to the central component. Interpreted in this way, the results suggest that the bandwidth of the modulation filters slightly exceeds the center frequency, i.e., the Q value is a little less than 1. Such a Q value was also suggested by the results of experiment 1.

The randomization of modulation depth (filled squares) produced a small impairment of performance for frequency spacings of the modulator components up to $0.5f_c$, but had little or no effect for greater spacings. The fact that performance remained relatively good even when the modulation depth was randomized suggests that the task could be performed when the effective internal depth of the modulation was not a reliable cue. The fact that randomization of modulation depth had some effect could be interpreted as indicating that subjects did use a cue related to differences in effective rms level for the two phase conditions, when the modulation depth was not randomized and when the spacing of the modulator components was $\leqslant 0.5f_c$. However, it might also be the case that the randomization simply distracted subjects to some extent.

To assess the significance of these effects, the arcsine-transformed data were subjected to a within-subjects analysis of variance with factors modulator center frequency (50 or 100 Hz), spacing of the components relative to the center frequency (five values), and randomization of modulation depth (absent or present). The main effect of center frequency was not significant. The main effect of frequency spacing of the components was significant; $F(4,16) = 91.97$, $p < 0.001$. The main effect of randomization was also significant; $F(1,4) = 10.2$, $p = 0.031$. Finally, the interaction of randomization and frequency spacing of the components was significant, reflecting the fact that randomization of the modulation depth had an effect for small spacings but not for large spacings; $F(4,16) = 13.58$, $p < 0.001$.

F. Discussion

As noted above, the fact that performance remained relatively good even when the modulation depth was randomized suggests that the task could be performed when the effective internal depth of the modulation was not a reliable cue. However, to be confident of this conclusion we need to assess whether the randomization of modulation depth was sufficient to effectively prevent the use of such a cue. It is difficult to give a definite answer to this question, because the nature of the nonlinearities involved is uncertain. Moore *et al.* (1999a) proposed that the main nonlinearity influencing the perception of modulation was the compressive nonlinearity on the basilar membrane (Rhode and Robles, 1974; Sellick *et al.*, 1982; Robles *et al.*, 1986), but other nonlinearities may well be involved (Shofner *et al.*, 1996; Moore and Sek, 2000) and the data of Verhey *et al.* (2002) suggest that a nonlinearity other than that on the basilar membrane is dominant.

To get some idea of the likely size of changes in ''internal'' rms value of the modulation produced by the changes in modulator component phase, relative to the changes produced by the randomization of modulation depth, we used the simple model described by Moore *et al.* (1998, 1999b). The envelopes of the stimuli were passed through a compressive nonlinearity, resembling the compressive input–output function of the basilar membrane. We do not want to argue that this is the only nonlinearity involved. We use it here

merely to illustrate the magnitudes of the effects produced by this form of nonlinearity. The nonlinearity had the following form:

$$L_{\text{out}} = 0.9L_{\text{in}} + 6 + 53(1 - (1/(1 + \exp(-0.05(L_{\text{in}} - 50))))), \quad (1)$$

where L_{in} is the input level in dB and L_{out} is the output level in dB; see Fig. 4 in Moore *et al.* (1999b). This function is based on an equation suggested by Oxenham (1995), and used subsequently by Moore *et al.* (1996) and by Oxenham and Moore (1997).

For the complex modulators used in our experiment, the effect of modulator phase on the rms value of the modulator at the output of the nonlinearity was small. For $m = 0.2$, the output rms value was between 0.094 34 and 0.094 55 for the 0-phase stimuli, and between 0.093 54 and 0.093 70 for the π-phase stimuli. In comparison, the effects of changing modulation depth were much larger. At the top end of the range of randomization ($m = 0.2825$), the output rms value was around 0.1364 for the 0-phase stimuli and 0.1340 for the π-phase stimuli. The corresponding numbers at the bottom end of the range of randomization were 0.0662 and 0.0660. We conclude that, in terms of output rms value, the range of randomization was about 106 times as large as the effect of the change in component phase. This means that, in the condition with randomization of modulation depth, any cue for phase discrimination based on a change in effective rms value of the modulation would have been rendered ineffective. Of course, other nonlinearities might produce a larger effect of component phase on effective rms value. But it is difficult to envisage any nonlinearity that would lead to changes in rms value of the modulation comparable to those produced by the randomization of modulation depth. Given that the effect of the randomization was small, we conclude that, when randomization was used, subjects did not perform the task using a cue based on the effective internal depth of the modulation.

Another possible cue introduced by nonlinearities in the auditory system is a distortion component at the envelope rate of the modulation. Such a distortion component has been proposed as an explanation for modulation masking produced by two-component ''beating'' modulators (Moore *et al.*, 1999a; Verhey *et al.*, 2002) and by ''second-order'' modulation (Lorenzi *et al.*, 2001a, b; Ewert *et al.*, 2002; Verhey *et al.*, 2002). For example, for $f_c = 50$ Hz and a frequency spacing of the components of 15 Hz (i.e., components at 35, 50, and 65 Hz), a distortion component at 15 Hz might be produced. The strength of this component might vary with the phase of the components, and this could be used as a cue to discriminate the phase changes (possibly, mediated via analysis with an MFB). However, in several of the conditions of our experiment, the use of such a cue seems unlikely. For example, for $f_c = 50$ Hz and a frequency spacing of the components of 25 Hz, the distortion component would have fallen at 25 Hz, and therefore coincided with a component that was already present. Given that the distortion component appears to be weak in amplitude relative to the primaries (Shofner *et al.*, 1996; Moore *et al.*, 1999a), it is unlikely that the change in effective modulation depth of the 25-Hz modulator component would provide a useful cue in the phase discrimination task, especially in the condition where the modulation depth was randomized.

It is of interest to consider what cue subjects might have used to perform the phase discrimination task. Some researchers have proposed that the discrimination of modulator waveforms may be based on the ratio of the maximum value to the minimum value of the modulator (max-min) (Forrest and Green, 1987; Strickland and Viemeister, 1996), although Moore and Sek (2000) found that such a decision statistic could not account for their results on the detection of three-component modulators. To assess whether the max-min statistic could account for the present results, we calculated the max-min value for each of the modulator waveforms used in our experiment. For the cases where all components were in sine phase, the max-min value was between 3.939 and 3.960 for all component spacings except $0.5f_c$. For this specific case, the max-min value was only 2.999. For the cases where the phase of the lowest modulator component was shifted by 180°, the max-min value varied from 2.565 to 2.615. The *difference* in max-min value for the two phases was markedly smaller for the spacing of $0.5f_c$ than for all other spacings. However, performance was not worse for this spacing than for the smaller spacings. This pattern of results cannot be accounted for using the max-min statistic. Use of the max-min statistic also fails to account for two other effects: (1) the worsening of performance when the frequency spacing of the components was increased above $0.5f_c$, and (2) randomization of modulation depth from one stimulus to the next had only a small effect. Other statistics that have been suggested in the literature, such as the crest factor or the skewness of the modulator (Lorenzi *et al.*, 1999), also fail to account for the effect of the frequency spacing of the components.

The most straightforward explanation of our results seems to be that subjects are sensitive to changes in the shape of the modulator waveform at the output of the modulation filter centered on (or close to) the central component of the modulator. This shape would be influenced by the relative phase of the components. When the modulator components are widely spaced (spacing greater than $0.5f_c$), they interact less at the output of the modulation filter, so the sensitivity to modulator phase is reduced. However, because of the broad tuning of the modulation filters, some interaction occurs even for wide spacings. This can explain why performance remained above chance for the largest spacing used. It was not possible to use much larger spacings, since if the spacing exceeds f_c, one of the modulator components has a negative frequency.

Ewert *et al.* (2002) and Verhey *et al.* (2002) have proposed that the auditory system somehow derives the envelope of the (ac-coupled) envelope of modulated signals. They referred to this as the ''venelope.'' They assumed that venelope extraction occurs either in parallel with processing via the MFB or prior to the MFB. For modeling purposes, they calculated the venelope as the absolute value of the analytical signal derived using the Hilbert transform of the ac-coupled envelope of the stimulus (Bracewell, 1986). To

evaluate the venelope concept we used the same approach.

For our three-component modulators, the venelope depends on the relative phase with which the modulator components are added. This is illustrated in the right column of Fig. 3. For all of the 0-phase stimuli (solid lines in the right column of Fig. 3), the venelope had a maximum value of 0.6 and a minimum value of 0. For the π-phase stimuli (dotted lines), the maximum of the venelope was always 0.447 and the minimum was 0.2. Thus, changes in the venelope peak-to-valley ratio could provide the basis for the phase sensitivity shown in experiment 2. However, the change in peak-to-valley ratio produced by the phase shift was the same for all spacings of the components, while performance worsened with increasing frequency separation of the modulator components. We can conclude either that performance was not based on the change in venelope peak-to-valley ratio with changing phase, or that venelope extraction occurs after processing via the MFB.

Changing the relative phase of the modulator components also changed the time pattern of the venelope. For all spacings of the components, changing the phase of the lowest component from 0° to 180° resulted in a doubling of the number of major peaks per second in the venelope. This doubling might have been used to detect the phase shift. However, the doubling occurred for all component spacings, but performance worsened with increasing spacing. Again, we conclude either that performance was not based on the change in venelope fluctuation rate with changing phase, or that venelope extraction occurs after processing via the MFB. A possible counter-argument here is that performance may have worsened with component spacing because the auditory system has difficulty in following rapid venelope fluctuations. However, performance was good when the modulator components were at 50, 100, and 150 Hz, and the venelope had 50 major peaks per second for the 0-phase stimuli and 100 major peaks per second for the π-phase stimuli. In contrast, performance was poor when the modulator components were at 15, 50 and 85 Hz and the venelope had 35 major peaks per second for the 0-phase stimuli and 70 major peaks per second for the π-phase stimuli. Thus the rapidity of venelope fluctuations does not seem to be the critical factor.

If venelope extraction occurs after processing by the MFB, then increasing the frequency spacing of the modulator components would result in a reduced amplitude of the extracted venelope, as the modulator components would interact less at the output of any single modulation filter. This might make it harder to detect changes in peak-to-valley ratio or fluctuation rate of the venelope, which would account for the decrease in discrimination performance with increasing spacing of the components.

Although our data are not consistent with venelope extraction prior to the MFB, the data of Moore *et al.* (1999a) and Verhey *et al.* (2002) cannot be explained in terms of the venelope concept unless it is assumed that the venelope is extracted prior to or in parallel with the MFB. They showed that the detectability of low-frequency probe modulation was affected by higher-frequency ''beating'' modulators, even when the beating modulators were centered well above the passband of the modulation filter centered at the probe frequency. If the venelope is extracted only after the MFB, there seems to be no reason why the venelope at the output of modulation filters tuned to high modulation frequencies should influence the detectability of modulation at a low frequency, unless there is an across-modulation-channel interference process. Ewert *et al.* (2002) discussed the possibility of such an across-channel process, and suggested that it might provide an alternative way of accounting for their results.

It is of interest that Moore and Sek (2000) failed to find an effect of modulator component phase on the detectability of modulation, using stimuli similar to those of the present experiment. Possibly, it is much harder to hear differences in the shape of the modulator waveform, or in the venelope, when the modulation is close to threshold. Alternatively, two modulators may sound different when close to threshold, but may nevertheless have the same detection threshold when the threshold is expressed in terms of the rms value of the modulator.

For the largest frequency spacing of the modulator components, the lowest component of the modulator had a frequency of 5 Hz (for a center frequency of 50 Hz) or 10 Hz (for a center frequency of 100 Hz). For these low modulation rates, the model of Dau *et al.* (1997a, 1997b) preserves sensitivity to modulator phase at the output of the modulation filter. Indeed, Dau (1996) showed that, for modulation rates up to about 10 Hz, subjects could discriminate changes in the starting phase of sinusoidal modulation of a 5-kHz carrier. It is possible that, for large frequency spacings of the modulator components, subjects performed our task by judging the phase of the lowest modulator component relative to the onset of the sound. However, it seems unlikely that subjects would have been sensitive to the onset phase of the lowest component when the frequency of that component was 50, 70, or 90 Hz, yet performance was very good for those conditions (see the right panel of Fig. 4).

Finally, we consider whether models of modulation processing based on a low-pass filter or sliding temporal integrator, as described in the Introduction, can account for our results. It appears to us difficult to account for the results of experiment 1 using such models. The temporal pattern at the output of a sliding temporal integrator in response to the three-component modulator would change somewhat with changes in the frequency of the target component, but there would be no obvious way for the subject to use such changes to identify which of the comparison single-component modulators was contained within a specific complex modulator. Recall that the task was designed so that subjects could not achieve high scores by using the average modulation rate as a cue. Recall also that the starting phase of each component was varied randomly from one stimulus to the next, so subjects could not perform the task by learning that a specific time pattern at the output of the temporal integrator was associated with a specific target frequency.

To assess whether the pattern of phase sensitivity found in experiment 2 could be explained using a sliding temporal integrator, the envelopes of the stimuli were first subjected to compression, by raising the instantaneous envelope magni-

tude to the power 0.5 (to simulate basilar-membrane compression), and then passing the compressed envelope through a sliding temporal integrator with the characteristics described by Oxenham and Moore (1994). The root-mean-square (rms) output of the integrator was consistently slightly greater for π-phase stimuli than for the 0-phase stimuli, so a conceivable cue was the ratio of outputs for the two phases. However, the ratio of rms values for the π-phase and 0-phase stimuli did not change with frequency spacing of the modulator components in a way that was consistent with the data. For both modulation center frequencies (50 and 100 Hz), the ratio was smaller for the middle frequency separation (25 Hz at 50 Hz and 50 Hz at 100 Hz) than for any other separations, whereas the data showed good performance at the middle separation and poorer performance for greater separations. Also, the use of a cue based on rms value would have been disrupted by the randomization of modulation depth, but little effect of this randomization was found. We conclude that the effect of frequency separation of the components on phase discrimination cannot be explained in terms of the rms output of the sliding temporal integrator. Other measures of the output of the temporal integrator (standard deviation and peak-to-valley ratio) also failed to account for the observed effects.

IV. CONCLUSIONS

We have described two experiments aimed at providing tests of the concept that the auditory system contains an MFB. Both experiments were analogous to experiments in the audio-frequency domain that are thought to reflect the filtering that occurs in the auditory periphery.

Experiment 1 examined the ability to ''hear out'' the modulation frequency of the central component of a three-component modulator applied to a 4-kHz sinusoidal carrier. Subjects showed some ability to perform the task (scores of around 80% correct), when the components in the three-component modulator were widely spaced and when the frequencies of the target and comparison differed sufficiently. Scores fell close to chance level when the lower of the two flanking components was separated by 50 Hz or less from the central target component frequency of 100 Hz. This is consistent with the relatively broad tuning of the modulation filters inferred from experiments on modulation masking

Experiment 2 examined the ability to hear a change in the relative phase of the components in a three-component modulator with harmonically spaced components. The frequency of the central component, f_c, was either 50 or 100 Hz. Performance was good (80%–90% correct) when the component spacing was $\leqslant 0.5 f_c$, but worsened markedly for frequency spacings greater than that. This is broadly the pattern of results predicted from the MFB. Performance was only slightly impaired by randomizing the overall modulation depth from one stimulus to the next. This suggests that subjects did not use the overall effective internal depth of the modulation as a cue. We argue further that performance was probably not based on detection/discrimination of a distortion product in the modulation domain. Nor was it based on the use of statistics such as the max-min value, the crest factor of the modulation, or the output of a sliding temporal integrator. The most straightforward explanation of our results seems to be that subjects are sensitive to changes in the shape of the modulator waveform or the venelope (envelope of the envelope) at the output of the modulation filter centered on (or close to) the central component of the complex modulator.

The results of both experiments are broadly consistent with what would be expected from a broadly tuned MFB; the Q value appears to be about 1, or slightly less than 1.

ACKNOWLEDGMENTS

This work was supported by the Wellcome Trust and by the MRC. We thank Hedwig Gockel, Torsten Dau and an anonymous reviewer for helpful comments on an earlier version of this paper. We also thank Christian Lorenzi and Christian Füllgrabe for helpful discussions.

Bacon, S. P., and Grantham, D. W. (**1989**). ''Modulation masking: effects of modulation frequency, depth and phase,'' J. Acoust. Soc. Am. **85**, 2575–2580.

Bracewell, R. N. (**1986**). *The Fourier Transform and its Applications* (McGraw–Hill, New York).

Dau, T. (**1996**). ''Modeling auditory processing of amplitude modulation,'' Ph.D. thesis, University of Oldenburg, Germany.

Dau, T., Kollmeier, B., and Kohlrausch, A. (**1997a**). ''Modeling auditory processing of amplitude modulation: I. Detection and masking with narrowband carriers,'' J. Acoust. Soc. Am. **102**, 2892–2905.

Dau, T., Kollmeier, B., and Kohlrausch, A. (**1997b**). ''Modeling auditory processing of amplitude modulation: II. Spectral and temporal integration,'' J. Acoust. Soc. Am. **102**, 2906–2919.

Dau, T., Verhey, J. L., and Kohlrausch, A. (**1999**). ''Intrinsic envelope fluctuations and modulation-detection thresholds for narrow-band noise carriers,'' J. Acoust. Soc. Am. **106**, 2752–2760.

Ewert, S. D., and Dau, T. (**2000**). ''Characterizing frequency selectivity for envelope fluctuations,'' J. Acoust. Soc. Am. **108**, 1181–1196.

Ewert, S. D., Verhey, J. L., and Dau, T. (**2002**). ''Spectro-temporal processing in the envelope-frequency domain,'' J. Acoust. Soc. Am. **112**, 2921–2931.

Festen, J. M., and Plomp, R. (**1981**). ''Relations between auditory functions in normal hearing,'' J. Acoust. Soc. Am. **70**, 356–369.

Fine, P. A., and Moore, B. C. J. (**1993**). ''Frequency analysis and musical ability,'' Music Percept. **11**, 39–53.

Forrest, T. G., and Green, D. M. (**1987**). ''Detection of partially filled gaps in noise and the temporal modulation transfer function,'' J. Acoust. Soc. Am. **82**, 1933–1943.

Glasberg, B. R., and Moore, B. C. J. (**1990**). ''Derivation of auditory filter shapes from notched-noise data,'' Hear. Res. **47**, 103–138.

Houtgast, T. (**1989**). ''Frequency selectivity in amplitude-modulation detection,'' J. Acoust. Soc. Am. **85**, 1676–1680.

Kohlrausch, A., Fassel, R., and Dau, T. (**2000**). ''The influence of carrier level and frequency on modulation and beat-detection thresholds for sinusoidal carriers,'' J. Acoust. Soc. Am. **108**, 723–734.

Lemanska, J., Skrodzka, E., and Sek, A. (**2002**). ''Discrimination of the amplitude modulation rate,'' Arch. Acoust. **27**, 3–22.

Lorenzi, C., Berthommier, F., and Demany, L. (**1999**). ''Discrimination of amplitude-modulation phase spectrum,'' J. Acoust. Soc. Am. **105**, 2987–2990.

Lorenzi, C., Soares, C., and Vonner, T. (**2001b**). ''Second-order temporal modulation transfer functions,'' J. Acoust. Soc. Am. **110**, 1030–1038.

Lorenzi, C., Simpson, M. I., Millman, R. E., Griffiths, T. D., Woods, W. P., Rees, A. *et al.* (**2001a**). ''Second-order modulation detection thresholds for pure-tone and narrow-band noise carriers,'' J. Acoust. Soc. Am. **110**, 2470–2478.

Moore, B. C. J. (**2003**). *An Introduction to the Psychology of Hearing*, 5th ed. (Academic, San Diego).

Moore, B. C. J., and Glasberg, B. R. (**2001**). ''Temporal modulation transfer functions obtained using sinusoidal carriers with normally hearing and hearing-impaired listeners,'' J. Acoust. Soc. Am. **110**, 1067–1073.

Moore, B. C. J., and Ohgushi, K. (**1993**). ''Audibility of partials in inharmonic complex tones,'' J. Acoust. Soc. Am. **93**, 452–461.
Moore, B. C. J., and Sek, A. (**2000**). ''Effects of relative phase and frequency spacing on the detection of three-component amplitude modulation,'' J. Acoust. Soc. Am. **108**, 2337–2344.
Moore, B. C. J., Peters, R. W., and Glasberg, B. R. (**1996**). ''Detection of decrements and increments in sinusoids at high overall levels,'' J. Acoust. Soc. Am. **99**, 3669–3677.
Moore, B. C. J., Sek, A., and Glasberg, B. R. (**1999a**). ''Modulation masking produced by beating modulators,'' J. Acoust. Soc. Am. **106**, 908–918.
Moore, B. C. J., Glasberg, B. R., Plack, C. J., and Biswas, A. K. (**1988**). ''The shape of the ear's temporal window,'' J. Acoust. Soc. Am. **83**, 1102–1116.
Moore, B. C. J., Launer, S., Vickers, D., and Baer, T. (**1998**). ''Loudness of modulated sounds as a function of modulation rate, modulation depth, modulation waveform and overall level,'' in *Psychophysical and Physiological Advances in Hearing*, edited by A. R. Palmer, A. Rees, A. Q. Summerfield, and R. Meddis (Whurr, London).
Moore, B. C. J., Vickers, D. A., Baer, T., and Launer, S. (**1999b**). ''Factors affecting the loudness of modulated sounds,'' J. Acoust. Soc. Am. **105**, 2757–2772.
Oxenham, A. J. (**1995**). ''Psychophysical consequences of peripheral auditory nonlinearity,'' Ph.D. thesis, Cambridge.
Oxenham, A. J., and Moore, B. C. J. (**1994**). ''Modeling the additivity of nonsimultaneous masking,'' Hear. Res. **80**, 105–118.
Oxenham, A. J., and Moore, B. C. J. (**1997**). ''Modeling the effects of peripheral nonlinearity in listeners with normal and impaired hearing,'' in *Modeling Sensorineural Hearing Loss*, edited by W. Jesteadt (Erlbaum, Mahwah, NJ).
Patterson, R. D. (**1987**). ''A pulse ribbon model of monaural phase perception,'' J. Acoust. Soc. Am. **82**, 1560–1586.
Plack, C. J., and Moore, B. C. J. (**1990**). ''Temporal window shape as a function of frequency and level,'' J. Acoust. Soc. Am. **87**, 2178–2187.
Plomp, R. (**1964**). ''The ear as a frequency analyzer,'' J. Acoust. Soc. Am. **36**, 1628–1636.
Plomp, R. (**1976**). *Aspects of Tone Sensation* (Academic, London).
Plomp, R., and Mimpen, A. M. (**1968**). ''The ear as a frequency analyzer II,'' J. Acoust. Soc. Am. **43**, 764–767.
Rhode, W. S., and Robles, L. (**1974**). ''Evidence from Mössbauer experiments for non-linear vibration in the cochlea,'' J. Acoust. Soc. Am. **55**, 588–596.
Robles, L., Ruggero, M. A., and Rich, N. C. (**1986**). ''Basilar membrane mechanics at the base of the chinchilla cochlea. I. Input-output functions, tuning curves, and response phases,'' J. Acoust. Soc. Am. **80**, 1364–1374.
Schorer, E. (**1986**). ''Critical modulation frequency based on detection of AM versus FM tones,'' J. Acoust. Soc. Am. **79**, 1054–1057.
Sek, A. (**1994**). ''Modulation thresholds and critical modulation frequency based on random amplitude and frequency changes,'' J. Acoust. Soc. Jpn. (E) **15**, 67–75.
Sek, A., and Moore, B. C. J. (**1994**). ''The critical modulation frequency and its relationship to auditory filtering at low frequencies,'' J. Acoust. Soc. Am. **95**, 2606–2615.
Sek, A., and Moore, B. C. J. (**2002**). ''Mechanisms of modulation gap detection,'' J. Acoust. Soc. Am. **111**, 2783–2792.
Sellick, P. M., Patuzzi, R., and Johnstone, B. M. (**1982**). ''Measurement of basilar membrane motion in the guinea pig using the Mössbauer technique,'' J. Acoust. Soc. Am. **72**, 131–141.
Shofner, S., Sheft, S., and Guzman, S. J. (**1996**). ''Responses of ventral cochlear nucleus units in the chinchilla to amplitude modulation by low-frequency, two-tone complexes,'' J. Acoust. Soc. Am. **99**, 3592–3605.
Soderquist, D. R. (**1970**). ''Frequency analysis and the critical band,'' Psychon. Sci. **21**, 117–119.
Strickland, E. A., and Viemeister, N. F. (**1996**). ''Cues for discrimination of envelopes,'' J. Acoust. Soc. Am. **99**, 3638–3646.
Uppenkamp, S., Fobel, S., and Patterson, R. D. (**2001**). ''The effects of temporal asymmetry on the detection and perception of short chirps,'' Hear. Res. **158**, 71–83.
Verhey, J. L. (**2002**). ''Modeling the influence of inherent envelope fluctuations in simultaneous masking experiments,'' J. Acoust. Soc. Am. **111**, 1018–1025.
Verhey, J. L., Ewert, S., and Dau, T. (**2002**). ''Modulation masking produced by complex tone modulators,'' J. Acoust. Soc. Am. (submitted).
Viemeister, N. F. (**1979**). ''Temporal modulation transfer functions based on modulation thresholds,'' J. Acoust. Soc. Am. **66**, 1364–1380.
Zwicker, E. (**1952**). ''Die Grenzen der Hörbarkeit der Amplitudenmodulation und der Frequenzmodulation eines Tones,'' Acustica **2**, 125–133.
Zwicker, E. (**1956**). ''Die elementaren Grundlagen zur Bestimmung der Informationskapazität des Gehörs,'' Acustica **6**, 356–381.

The relation of lung volume initiation to selected acoustic properties of speech

Peter J. Watson[a] and Angela H. Ciccia
Department of Communication Sciences, 11206 Euclid Avenue, Case Western Reserve University, Cleveland, Ohio 44106

Gary Weismer
Department of Communicative Disorders, Waisman Center, 447 Waisman Center, University of Wisconsin, Madison, Wisconsin 53705

(Received 3 August 2002; accepted for publication 24 February 2003)

This study examined the relationship of speech breathing to other elements of speech production. It was hypothesized that initiating speech from different lung volumes would have an effect on different elements of the acoustic output. It was postulated that effects may be brought about by mechanical interaction as well as a dispersion of effort to mechanically unlinked elements of speech production, such as articulatory behavior. To this end, selected acoustic variables were studied in eight young healthy women who initiated speech from low, typical, and high lung volume levels. The acoustic variables studied were selected because they have been shown to be sensitive indicators of speech production performance. It was found that with increasing lung volume initiation levels, average sound pressure level, average fundamental frequency, and declination rate of fundamental frequency increased. It was also observed that vowel space was significantly smaller during low lung volume initiation levels relative to typical lung volume initiation levels. Vowel space reduction is discussed relative to ''gaining down.'' © *2003 Acoustical Society of America.*
[DOI: 10.1121/1.1567279]

PACS numbers: 43.70.Aj, 43.70.Bk [AL]

I. INTRODUCTION

The speech production system is often organized into three distinct subsystems—breathing, laryngeal, and upper airway. This organization has often been used to understand the nature of speech production and its assessment and treatment. However, this line of thinking does not always take into account the interaction of these components in producing speech (Netsell, 1973).

When considering the interplay between the speech production subsystems, mechanical interdependence may account for certain interactions. For example, fundamental frequency ($F0$) is higher for the high vowel /i/ compared to the low vowel /ɑ/. It is believed that this is due to tongue position, which may have an effect on laryngeal position and subsequent alteration of vocal fold tension (Honda, 1983; Whalen and Levitt, 1995). In addition, intensity of phonation represents an interaction between tracheal pressure and vocal fold tension (Bouhuys *et al.*, 1966), and changes of tracheal pressure can alter F0, especially at low F0's (Titze, 1994).

There is some evidence that interactions may also occur between the amount of air in the lungs—hereafter referred to as lung volume—and certain aspects of speech production behavior. For example, Iwarsson *et al.* (1998) showed that estimates of glottal wave shape and valving during phonation were systematically related to lung volume initiation levels; these estimates suggested that laryngeal valving was less efficient at higher as compared to lower lung volumes. Hoit *et al.* (1993) reported a different kind of speech breathing-laryngeal interaction, in the form of longer voice-onset times (VOTs) for /pi/ with increasing lung volume. A preliminary report by Shipp *et al.* (1983) suggested that laryngeal muscle behavior for phonation favored lower net adductory forces at higher as compared to lower lung volumes.

A unifying explanation for these effects may be found in Zenker (1964), who proposed that the footward movement of the diaphragm at high lung volume levels may tug on the trachea which in turn influences position of the larynx within the neck and hence vocal fold adjustments. This notion is supported by an experimental demonstration (Iwarsson and Sundberg, 1998) of a systematically decreasing vertical larynx height with increasing lung volume. Presumably, the increased stiffness of laryngeal tissues that would follow from the tracheal pull at high lung volumes would account both for the reduced valving efficiency (that is, reduced adductory force because of stiffer tissues) and greater opposition of the folds to the opening–closing movements associated with voiceless obstruents (Hirose, 1976), the latter resulting in the longer VOTs described above.

Interactions between lung volume and other aspects of speech production that cannot be so easily explained by an appeal to volume-dependent anatomical linkages may be expected on both theoretical and empirical grounds. Ramig (1992), following a line of thinking introduced by Rosenbek and LaPointe (1985), has proposed that modifying one element of speech production, such as phonatory loudness, results in a dispersion of effort to other parameters of speech production. The effect of this dispersion has been observed in the treatment of speech and voice problems in patients with Parkinson's disease. By increasing voice sound pressure

[a]Electronic mail: pjw4@po.cwru.edu

 0001-4966/2003/113(5)/2812/8/$19.00

level (SPL), the following changes have been observed in phonation, represented by decreased jitter and shimmer values (Dromey *et al.*, 1995), articulation, represented by increased vowel duration and second format duration (Dromey *et al.*, 1995), and prosody, represented by a decreased monotonicity (Ramig *et al.*, 1995). Similarly, Schulman (1989) demonstrated that when healthy adult speakers increased voice SPL, displacement and velocity increased for the lips and jaw. These kinds of observations are consistent with one theoretical view of speech production in which a ''gaining up'' of one component of the speech motor system is generalized to other, and perhaps all, components of the system (Kelso *et al.*, 1986).

One of the difficulties in understanding the kinds of effects described above for voice SPL is the complex nature of this variable. As described by Sundberg *et al.* (1993) and others, voice SPL may be produced and affected by a number of factors which are difficult if not impossible to separate experimentally. For example, it is natural for voice SPL to increase with increasing starting lung volume for speech (Dromey and Ramig, 1998) because of the higher expiratory recoil forces at higher lung volumes, but some component of the increased SPL could also be due to volume-dependent adductory forces in the larynx (Sundberg *et al.*, 1993). Similarly, when speakers are requested to produce loud speech, they will sometimes initiate phonation from higher lung volumes (Hixon *et al.*, 1973).

The possibility that lung volume initiation level for speech has a ''spreading effect'' on phonatory and articulatory behaviors is interesting for at least two reasons. First, the link between lung volume initiation levels and voice SPL on the one hand, and voice SPL and phonatory/articulatory behaviors on the other hand (as discussed above), suggests a possible influence of speech breathing on other phonetic behaviors that might be consistent with the overall gaining-up principle described theoretically by Kelso *et al.* (1986) and as a clinical guiding principle by Rosenbek and LaPointe (1985). Second, among the speech breathing problems seen in cases of dysarthria, lower-than-normal lung volume levels for utterance initiation have been observed experimentally (Murdoch *et al.*, 1991) and are mentioned as a target of intervention in the clinical literature (e.g., see Duffy, 1995, pp. 390–391).

There are very few data bearing on the potential influence of lung volume on phonatory and articulatory behavior. Dromey and Ramig (1998), in a study of the effect of lung volume initiation levels on upper-lip (UL) and lower-lip plus jaw (LL+J) kinematics and selected acoustic measures for a single utterance, reported inconsistent effects for the kinematic measures but more consistent ones for measures such as SPL and $F0$. These authors suggested that this pattern of results made sense because of the relative absence of anatomical and low-level (brainstem) neural linkages between the articulators and the breathing system, as compared to the more direct anatomical linkages and neural overlap between the respiratory and laryngeal mechanisms (hence the consistent effects for measures such as SPL and $F0$). Dromey and Ramig (1998) concluded, therefore, that respiratory adjustments such as starting lung volume for utterances are not likely to have much of an effect on articulatory behavior.

This conclusion can be criticized on a number of grounds. First, the limitation of articulatory observations to lip and jaw motions places severe constraints on the theoretical question of a possible joint parametrization of speech breathing and articulatory processes. The motions of the lips and jaw during speech do not predict the motions of the tongue (Adams *et al.*, 1993), and there is no evidence that they are predictive of more global indices of articulatory behavior (such as vowel formant frequencies or consonant spectra). Second, Dromey and Ramig (1998) limited their observations to a single phrase, and within that phrase just two phases of motion for one consonant and one vowel (opening and closing in CV and VC forms where C=/p/ and V=/æ/). Finally, the logic underlying Dromey and Ramig's (1998) rejection of a possible joint parametrization of speech breathing and articulatory processes seems to be based entirely on structural and low-level neural linkages (see above). The notion of linkages in the theoretical perspective of Kelso *et al.* (1986) is *functional*, not structural (see also (Kugler and Turvey, 1987). On this view, for example, starting lung volumes outside the range of those typically used (see Hixon *et al.*, 1973) might require greater effort, which in turn might generalize to other speech behaviors as the system is gained up collectively, not piecemeal.

The single piece of information that supports the idea of an interaction between lung volume and articulatory variables is found in Chong (1994). In this single-case design, a young adult who had suffered a traumatic brain injury and had habitually low starting lung volumes for speech and impaired intelligibility was trained in initiate utterances at higher lung volumes. For those utterances that were produced at a more ''normal'' starting lung volume, listeners perceived an increase of articulatory precision and speech intelligibility as compared to utterances with habitually lower starting lung volumes. Although no acoustic analysis is available from this study, these data suggest some articulatory effects of starting lung volumes.

The current study continues this line of work, by employing some acoustic variables that are known to be sensitive indicators of speech production performance. These variables, in some cases, are of interest because they have been shown to be altered in individuals with motor speech disorders. As reviewed above, lung volume initiation issues may be seen in various dysarthric populations, and it would be beneficial to know how lung volume affects these variables. Acoustic measures such as vowel space (Weismer *et al.*, 2000) and second formant transitions (Kent *et al.*, 1989; Weismer *et al.*, 1988) have been shown to be related to intelligibility in individuals with motor speech disorders. Moreover, prosodic variables such as pitch shifts (Cooper and Sorensen, 1981) and long-term intonation changes, such as $F0$ declination (Sorensen and Cooper, 1980), are believed useful for a listener to parse linguistic information. Therefore, the purpose of this study was to examine the effect of different starting lung volumes on selected speech acoustic variables.

II. METHOD

A. Participants

Eight women between the ages of 18 and 35 years (mean=21) participated in this experiment. Each participant reported that they were in good health, had no history of pulmonary disease, had no surgery of the head, neck or torso, and were free of upper respiratory ailments on the day of testing. Participants reported no speech, language, voice, or hearing problems, each was a speaker of Standard American English and had no formal voice training. The speech of the participants was judged to be without defect by a certified speech-language pathologist.

B. Procedures

1. Tasks

a. Breathing tasks. To determine lung-volume initiation levels, each participant's breathing kinematics was monitored using Respitrace™. One band was fitted around the rib cage and the other band around the abdomen. The band for the abdomen was monitored to assure that it did not encroach upon the lower rib cage. The data were displayed on an *X*-*Y* oscilloscope screen, with rib cage volume represented on the ordinate and abdomen volume displayed on the abscissa. For lung volume calibration, each participant while seated in a chair performed isovolume maneuvers and lung-volume displacement tasks. Isovolume maneuvers were performed to establish the relationship of the motions of the two chest wall components (rib cage and abdomen) to their volume displacements (Hixon *et al.*, 1973). Isovolume maneuvers were performed by each participant at end-expiratory level (EEL) while breath holding. The single isovolume maneuver at EEL was believed to adequately represent the volume relationships of the rib cage and abdomen within the lung volume range being used. That is, isovolume lines generated between 20% and 80% of the vital capacity are relatively parallel and only become anisotropic at the extremes of vital capacity (Hixon *et al.*, 1973; Konno and Mead, 1967).

Lung-volume displacement tasks consisted of vital capacity maneuvers and breath-holding maneuvers. Lung-volume displacement tasks were performed while each participant, wearing a noseclip, breathed into a 10-L wet spirometer through a mouthpiece (W. E. Collins, Braintree, MA). The vital capacity maneuver allowed for the determination of each individual's entire breathing range. For the breath-holding maneuvers, participants were instructed to breathe in or out from EEL to 20% increments throughout their vital capacities. At each 20% interval, participants were asked to stop breathing and hold their breath for 3 s. The 20% intervals were marked on the oscilloscope screen. This was done so that the oscilloscopic display could be used to determine lung-volume initiation levels during oral reading.

b. Oral-reading task. The oral-reading stimuli consisted of a collection of 24 sentences of different lengths and having different phonetic content. Some of the words within the set of sentences contained either one of the four corner vowels /i, u, ɑ æ/, or one of two diphthongs /ɑɪ, oɪ/. These vowels and diphthongs were situated in long sentences (17–18 syllables) and short sentences (7–8 syllables), and were located at either the beginning or the end of a sentence. For each of three experimental conditions (see below), eight tokens of each of the four corner vowels and eight tokens of each of the diphthongs were produced by each participant. In addition, there was a single strong-weak syllable combination located at the beginning of eight of the sentences. Therefore, 16 strong-weak syllable combinations were produced per experimental condition. Each sentence was repeated two times so that there were 48 sentences per experimental condition. Sentences were presented in random order for each experimental condition.

For data collection, participants were seated. Written sentences were placed in front of each participant on a stand. Participants were instructed to read the sentences without trying to control their reading in any particular way.

C. Data collection and analysis

Participants initiated oral reading at three lung volume levels, hereafter referred to as typical-level (TL), high-level (HL), and low-level (LL) volume conditions. Data collection began with the TL condition. Following the TL condition, a coin was flipped to determine if either the LL or HL condition would be performed next. For the TL condition, participants were instructed to take in what they considered their normal speech breathing depth. For the HL condition, participants were asked to initiate their reading at what they judged to be 80% of their vital capacity. With regard to the LL condition, participants were instructed to initiate oral reading at EEL. Usually, lung volume initiation for speech breathing is around 60% of the vital capacity and breath groups terminate at EEL or around 40% of the vital capacity (Hixon *et al.*, 1973). It was reasoned that the HL condition of around 80% and speech at EEL (the LL condition), or 40% of the vital capacity, would be outside the range of typical speech breathing but not at the extremes of lung volume.

Before data collection began, a training session was performed by each participant to practice initiating reading at the three lung volume levels. During data collection, lung-volume initiation levels were monitored by the first author from the oscilloscope display. In all instances, no participant had difficulty in initiating speech at EEL. For the HL condition, if initiation was considered not within 5% of the 80% mark, then the participant was asked to perform the sentence again. Although not controlled, all participants usually initiated reading at or near 20% above EEL during the TL condition.

The acoustic signal was sensed by a head-mounted microphone (AKG, C420) and routed to a digital-audio tape recorder (TASCAM, DA-P1). The microphone was placed 2.5 in. and at a 45° azimuth from each participant's lips. The recording level was held constant throughout the experiment. The audio data from the tapes were then recorded to a PC and edited to produce individual files for each sentence. Acoustic analysis was performed using CSpeech (Milenkovic, 1990).

For data analysis, vowel space, slopes of second formant transitions, strong-weak syllable duration ratio (S/W duration ratio), average relative sound pressure level (Average SPL), standard deviation of sound pressure level (SPL standard de-

TABLE I. Group means and standard deviations for vowel space (Hz^2), the $F2$ transition slopes for the diphthongs /aɪ, oɪ/ (Hz/ms), and S/W duration ratio (s) for the low, typical, and high lung volume initiation level conditions.

Measures	Low volume M (SD)	Typical volume M (SD)	High volume M (SD)
Vowel space	243,103 (79,507)	348,387 (88,704)	297,168 (73,779)
$F2$ transition /aɪ/	1.155 (0.223)	1.209 (0.285)	1.150 (0.317)
$F2$ transition /oɪ/	2.397 (0.262)	2.410 (0.284)	2.260 (0.235)
S/W duration ratio	1.23 (0.09)	1.28 (0.17)	1.29 (0.14)

TABLE II. Repeated measures ANOVA for vowel space (Hz^2), $F2$ transition slopes for the diphthongs /aɪ, oɪ/ (Hz/ms), and S/W duration ratio (s) for the low, typical, and high lung volume initiation level conditions.

Measures	F value	df	Pr>F
Vowel space	4.43	2	0.037*
$F2$ transition /aɪ/	0.43	2	0.648
$F2$ transition /oɪ/	2.62	2	0.108
S/W duration ratio	0.40	2	0.679

viation), declination rate of sound pressure level (SPL declination rate), average fundamental frequency (average $F0$), standard deviation of fundamental frequency ($F0$ standard deviation), declination rate of fundamental frequency ($F0$ declination rate) and syllables per second were measured. For vowel space, the first and second formant frequencies from the corner vowels were measured. Formant frequency measures were obtained interactively using combined LPC and spectrographic analysis; measures were taken from the temporal middle of the vowels, using a 20-ms window. From these measures, a vowel quadrilateral was constructed to calculate the area (Hz^2) within it. Vowel space provides an index of acoustic space and by inference the size of the articulatory working space for vowels (Fourakis, 1991; Turner *et al.*, 1995). For the diphthongs /aɪ/ and /oɪ/, the slope of the second formant (Hz/ms) was calculated by determining the onset and offset of the transition (see Weismer *et al.*, 1988). The onset of the segment was determined as the first point where there was at least a 20-Hz change over 20 ms and the offset was defined as any point following where there was not a 20-Hz change within a 20-ms increment. Second formant transition slopes provide an index of the rate of change of vocal tract configuration and have been shown to be sensitive to speaking rate variations (Turner *et al.*, 1995) as well as the presence of neurological disease.

The relationship of strong to weak syllables was also examined. Stress prominence is related to the relative duration of strong to weak syllables. The strong-weak syllable combination was taken from a target word at the beginning of each sentence. This temporal pattern is believed to play a role in perceptual decisions concerning word boundaries in English (Liss *et al.*, 1998; Norris *et al.*, 1995). Stress duration contrast measurement was done by measuring the duration of the vowel segments of strong-weak syllable combinations, as in the sentence "**Bob**bie brought cupcakes to school" (strong syllable indicated in bold and the weak syllable is underlined). Vowel durations were measured from spectrographic displays as the interval between the first and last glottal pulses of the relevant vocalic nuclei.

For the following measures, the beginning and end of each sentence, as determined from the onset of acoustic energy and offset of acoustic energy, was delineated with cursors, and values between the cursors were calculated in successive steps. For sound pressure level analysis, the size of the analysis window was 20 ms and this window was moved through the utterance in 10-ms steps. The voltage values returned by the primary analysis were converted to relative sound pressure levels by reference to the maximum voltage output of the sound card, taken as 0 dB SPL (Milenkovic, 1990). Because the primary interest in this study was the relative change in SPL across lung volume conditions, no calibration of absolute SPL values was performed; the constant mouth-to-microphone distance and input gain for recording ensured that the relative measures could be interpreted in an unambiguous way. For fundamental frequency ($F0$), all $F0$ traces were examined to identify and edit tracking errors. The size of the analysis window for fundamental frequency analysis was 30 ms with a step size of 10 ms. Variation of fundamental frequency is believed to have linguistic importance, at both the localized level, such as pitch shifts (Cooper and Sorensen, 1981), and long term intonation changes, such as fundamental frequency declination (Sorensen and Cooper, 1980). Means and standard deviations were calculated for Average SPL (dB SPL), SPL standard deviation (dB SPL), SPL declination rate (dB/s), average $F0$ (Hz), $F0$ standard deviation (Hz), and $F0$ declination Rate (Hz/s). Declination rate was calculated from the output of the SPL and $F0$ analyses as an all-points linear regression analysis, using the slope of the regression results as the relevant index (Lieberman *et al.*, 1985).

A one-way repeated measures ANOVA was performed on each variable, with lung volume level as the repeated factor. If significance was revealed for a measure, Tukey pair-wise comparisons were performed to determine which lung volume initiation conditions were significantly different from one another. The alpha level of $p \leqslant 0.05$ was set *a priori*.

III. RESULTS

Group means and standard deviations for vowel area, second formant transition slopes for the two diphthongs, and the S/W duration ratio are presented in Table I; the ANOVA results are shown in Table II. There was no statistical difference for the second formant slopes for the diphthongs /aɪ, oɪ/ or for the S/W duration ratio between the lung volume conditions.

A significant difference was observed between the initiation levels for vowel area. For the significant vowel area effect, Tukey pair-wise analysis revealed only a single effect, with vowel areas being significantly larger in the TL, as compared to the LL condition. Figure 1 displays the average vowel quadrilateral data for the LL, TL, and HL conditions.

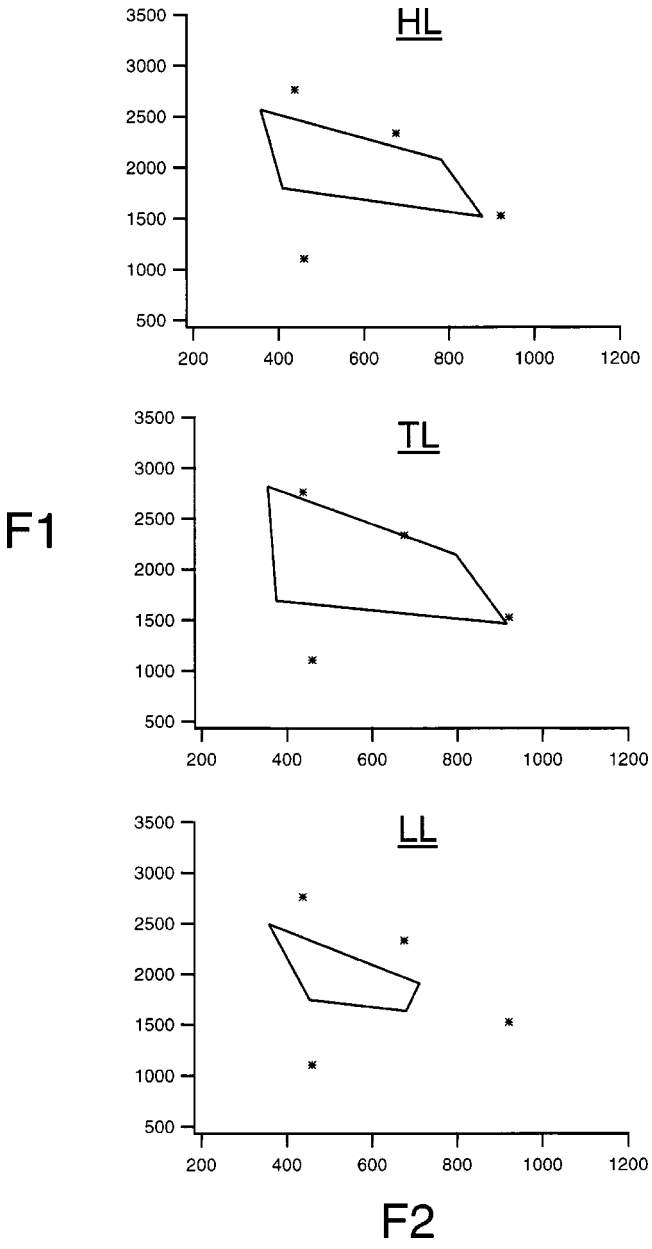

FIG. 1. Average vowel quadrilaterals for the H1, TL, and LL conditions. $F1$ (Hz) is on the horizontal axis and $F2$ (Hz) is on the vertical axis for each vowel quadrilateral display. Asterisks represent data from Hillenbrand *et al.* (1995).

The asterisks represent first and second formant frequency data for the corner vowels in young women as reported by Hillenbrand *et al.* (1995). The smaller ''normal'' area in this current study (TL condition), as compared to data published by Hillenbrand *et al.* (1995), is almost certainly due to the citation forms used. Hillenbrand *et al.* (2001) have shown how citation formant patterns are reduced by consonant context. As can be seen, vowel quadrilateral dimensions for the LL condition were decreased by changes in both $F1$ and $F2$ as compared to the TL condition.

Group means and standard deviations for SPL, $F0$, and rate variables are presented in Table III; ANOVA results are shown in Table IV. No statistical difference was found for SPL standard deviation, SPL declination rate, $F0$ standard deviation, or syllables per second.

TABLE III. Group means and standard deviations for average SPL (dB SPL), SPL standard deviation (dB SPL), SPL declination rate (dB SPL/s), Average $F0$ (Hz), $F0$ standard deviation (Hz), $F0$ declination rate (Hz/s), and syllables per second for the low, typical, and high lung volume initiation level conditions.

Measures	Low volume M (SD)	Typical volume M (SD)	High volume M (SD)
Average SPL	−30.97 (2.82)	−28.48 (3.17)	−26.00 (2.44)
SPL standard deviation	8.35 (0.55)	8.41 (0.62)	8.43 (0.77)
SPL declination rate	−3.44 (1.22)	−3.65 (0.86)	−3.88 (1.07)
Average $F0$	191.18 (11.99)	198.59 (7.47)	215.02 (20.44)
$F0$ standard deviation	36.15 (9.58)	41.50 (13.57)	42.77 (11.67)
$F0$ declination rate	−29.08 (13.57)	−39.35 (19.30)	−44.51 (17.18)
Syllables per second	4.71 (0.33)	4.59 (0.50)	4.78 (0.36)

The mean values for average SPL showed a consistent increase from low volume to high volume. The results from one-way repeated measure analysis revealed a statistical difference. Tukey comparisons showed that all pair-wise combinations were significantly different.

For average $F0$, there was a consistent increase with higher lung-volume initiation levels. The one-way repeated measures analysis showed a statistical difference. Tukey comparisons revealed a statistical difference between the LL and HL, and the TL and HL conditions. With regard to $F0$ declination rate, there was a consistent increase of declination rate from the LL condition to the HL condition. Tukey pair-wise comparisons revealed a statistical difference between LL and TL and the LL and HL volume initiation conditions. No statistical difference was found between the TL and HL conditions. The increased declination rate with higher lung volume initiation appeared to be the result of higher starting $F0$ values with increasing lung volume; the termination $F0$ values did not appear to be affected by the lung volume manipulation. Figure 2 demonstrates this effect for one subject, showing superimposed $F0$ contours for multiple utterances within each lung volume initiation condition.

TABLE IV. Repeated measures ANOVA for average SPL (dB SPL), SPL standard deviation (dB SPL), SPL declination rate (dB SPL/s), Average $F0$, (Hz), $F0$ standard deviation (Hz), $F0$ declination rate (Hz/s), and Syllables per second for the low, typical, and high lung volume initiation conditions.

Measures	F value	df	Pr>F
Average SPL	31.23	2	0.000*
SPL standard deviation	0.23	2	0.800
SPL declination rate	0.49	2	0.623
Average $F0$	13.74	2	0.000*
$F0$ standard deviation	3.29	2	0.068
$F0$ declination rate	10.19	2	0.002*
Syllables per second	1.02	2	0.387

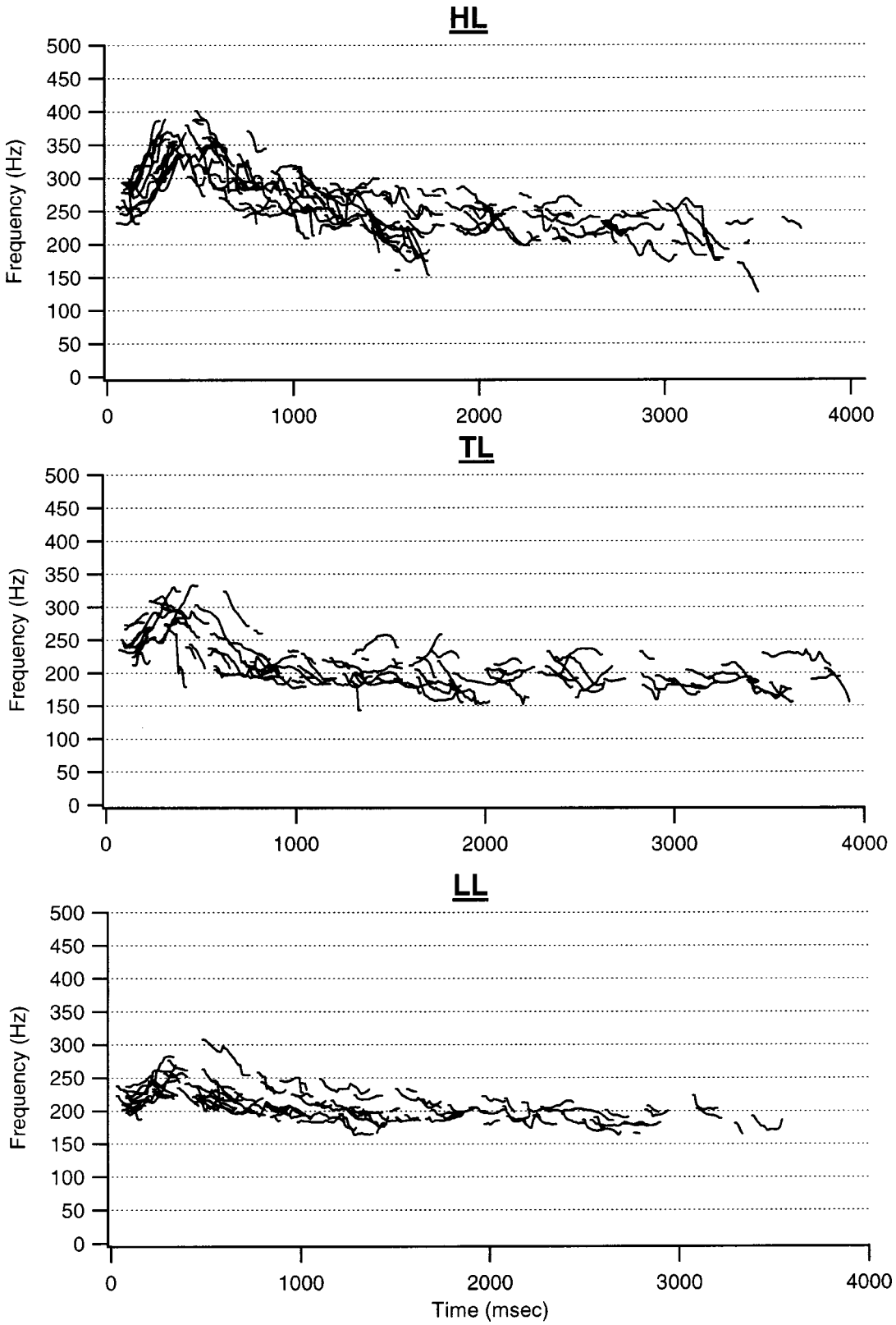

FIG. 2. Representative $F0$ declination data from one subject for the HL, TL, and LL conditions.

IV. DISCUSSION

This study demonstrated that initiating speech at different lung volume levels produced significant change in some of the acoustic variables examined. The observed changes are believed related to both the mechanical linkage existing between the breathing system and the larynx on the one hand, and to dispersion of gain to the mechanically unlinked articulatory system on the other hand.

A. Do the data suggest cross-component dispersion?

Of the acoustic variables studied that presumably reflect articulatory behavior, only vowel working space changed when initiating speech from different lung volume levels. From a perspective of spreading effects, it might have been expected that the size of the vowel space would increase systematically from the LL to TL to HL conditions, or alternatively that both the LL and HL conditions would have greater vowel spaces than the TL condition because they would be associated with overall greater speech breathing effort as compared to the TL condition. This latter expectation would follow from the greater muscular effort required to produce utterances outside the most efficient lung volume range for speech which would correspond to the TL condition in the present study (Hixon *et al.*, 1973; Weismer, 1985). However, vowel working space decreased only for the LL condition relative to the TL condition.

When considering possible reasons for the reduction of vowel space in the LL condition, rate is probably not a factor. Turner and colleagues (1995) showed that with increased rate, vowel space decreases. Dromey and Ramig (1998) observed that articulatory rate increased at low lung volume initiation conditions and speculated that this may have contributed to reduced upper lip displacement. However, there was no rate difference between the lung volume initiation conditions in the current study (Table III).

At first glance, there was no direct relationship observed between increased SPL and increased vowel space as might be predicted from the work of Schulman (1989), who found that with increased loudness production, lip and jaw displacement increased. For the current study, there was an increase of SPL between the LL and the TL conditions and a corresponding vowel area difference; however, there was a greater increase of SPL between the TL and HL conditions, but no vowel area difference was observed.

What then might explain the reduced vowel space in the LL condition? In the Introduction the notion was introduced of a collective ''gaining up'' of an entire system in response to a change in the setting of one component of the system; perhaps this is what was observed in the form of smaller vowel spaces in the LL, as compared to TL condition, but is more appropriately described as a ''gaining down'' from the most efficient lung volume range used in the TL condition. When insipiring to greater lung volume levels above EEL, expiratory recoil forces increase, thus providing adequate pressure for speech (Hixon, 1973) with no requirement to increase expiratory muscular effort. The current effect of increasing SPL with increasing lung volume level demonstrates that change in recoil pressure is not offset by muscular forces to maintain constant voice SPL when the instructions are to adjust lung volume rather than SPL. Thus, when speaking from lung volume levels at and below EEL, a ''gaining down'' of effort was observed. The apparent lowered effort at LL as compared to TL, suggested by the lower relative SPL values, may have spread to the articulatory system, resulting in reduced contrasts among vocal tract configurations for corner-vowels and therefore smaller acoustic vowel spaces.

Why did vowel space not increase from TL to HL? At this time it is not clearly apparent as to why this did not occur. It might have been that the available expiratory recoil force at higher lung volume levels did not require the increase of expiratory muscular effort and, therefore, with no increase of muscular effort, no gaining-up of the system was observed.

B. What of the relationship between the breathing system and the mechanically linked larynx?

Statistically significant differences were observed for average SPL, average $F0$, and $F0$ declination across lung volume initiation levels. The increase of SPL with increasing lung volume initiation levels was most likely related to increasing expiratory recoil pressures, as discussed above.

Average $F0$ increased from the LL condition to the HL condition by 24 Hz in the present study. Two possible mechanisms are offered as an explanation for this increase. First, increased driving pressure, as a result of greater expiratory recoil force at higher lung volume levels, may account in part for the increase of $F0$ (Titze, 1994). A second explanation for the increase of frequency may be due to indirect tensing of vocal fold tissue via a ''tracheal pull.'' At high lung volumes the diaphragm descends and in doing so pulls down on the trachea and larynx, resulting in force generation that can abduct the vocal folds (Zenker, 1964). This abductory force may result in an increase of vocal fold tension, thereby providing a mechanism for increasing frequency.

Declination rate of $F0$ increased with higher lung volume initiation levels, largely due to increasing $F0$ values at the beginning of utterances with higher lung volumes. This finding is reminiscent of Ladd's (1988) observation that declination ''resets'' occurred mainly at utterance onset, with the remainder of the $F0$ contour fairly unchanged across several different grammatical boundary conditions. In the present case there is no grammatical variable so the effect is more likely a biomechanical one, although it is not immediately obvious why the effect would be restricted to utterance onset.

These data provide evidence that modifying breathing behavior, by altering lung volume initiation levels, influences not only mechanically linked variables (breathing system and larynx) but also higher-order neural linkages such as articulatory behavior. Therefore, increasing lung volume initiation levels in individuals with motor speech disorders who initiate speech from lower than normal lung volume levels may prove beneficial by increasing vowel space, known to be related to intelligibility (Weismer *et al.*, 2000), and increasing $F0$ declination, known to be useful for parsing out sentence and phrase boundaries (Sorensen and Cooper, 1980). However, further inquiry into the effect of lung volume initiation levels in motor speech disorders (e.g., hypokinetic dysarthria) may be useful. For example, individuals with hypokinetic dysarthria, as found in Parkinson's disease, may benefit from initiating speech from higher lung volume levels which may in turn reduce the monotonicity of their speech (Duffy, 1995).

ACKNOWLEDGMENTS

We wish to thank Jennifer Cook, Erin Didde, and Beth Kades for their assistance in data collection and analysis.

Adams, S., Weismer, G., and Kent, R. (**1993**). ''Speaking rate and speech movement velocity profiles,'' J. Speech Hear. Res. **36**, 41–54.

Bouhuys, A., Proctor, D. F., and Mead, J. (**1966**). ''Kinetic aspects of singing,'' J. Appl. Physiol. **21**, 483–496.

Chong, M. (**1994**). ''Measuring the effect of lung volume treatment on speech intelligibility and ratings of articulatory precision and respiratory support: A single-subject design,'' University of Wisconsin, Madison.

Cooper, W., and Sorensen, J. (**1981**). *Fundamental Frequency in Sentence Production* (Springer-Verlag, New York).

Dromey, C., and Ramig, L. (**1998**). ''The effect of lung volume on selected phonatory and articulatory variables,'' J. Speech Lang. Hear. Res. **41**, 491–502.

Dromey, C., Ramig, L. O., and Johnson, A. B. (**1995**). ''Phonatory and articulatory changes associated with increased vocal intensity in Parkinson disease: a case study,'' J. Speech Hear. Res. **38**, 751–764.

Duffy, J. R. (**1995**). *Motor Speech Disorders: Substrates, Differential Diagnosis, and Management* (Mosby, St. Louis).

Fourakis, M. (**1991**). ''Tempo, stress, and vowel reduction in American English,'' J. Acoust. Soc. Am. **90**, 1816–1827.

Hillenbrand, J., Clark, M., and Nearer, T. (**2001**). ''Effects of consonant environment on vowel formant patterns,'' J. Acoust. Soc. Am. **109**, 748–763.

Hillenbrand, J., Getty, L. A., Clark, M. J., and Wheeler, K. (**1995**). ''Acoustic characteristics of American English vowels,'' J. Acoust. Soc. Am. **97**, 3099–3111.

Hirose, H. (**1976**). ''Posterior cricoarytenoid as a speech muscle,'' Ann. Otol. Rhinol. Laryngol. **85**, 335–342.

Hixon, T. J. (**1973**). ''Respiratory function in speech,'' in *Normal Aspects of Speech, Hearing, and Language*, edited by F. Minifie, T. Hixon, and F. Williams (Prentice-Hall, Englewood Cliffs, NJ), pp. 73–125.

Hixon, T. J., Goldman, M. D., and Mead, J. (**1973**). ''Kinematics of the chest wall during speech production: Volume displacements of the rib cage, abdomen, and lung,'' J. Speech Hear. Res. **16**, 78–115.

Hoit, J. D., Solomon, N. P., and Hixon, T. J. (**1993**). ''Effect of lung volume on voice onset time (VOT),'' J. Speech Hear. Res. **36**, 516–521.

Honda, K. (**1983**). ''Relationship between pitch control and vowel articulation,'' in *Vocal Fold Physiology*, edited by D. Bless and J. Abbs (College Hill, San Diego), pp. 286–299.

Iwarsson, J., and Sundberg, J. (**1998**). ''Effects of lung volume on vertical larynx position during phonation,'' J. Voice **12**, 149–165.

Iwarsson, J., Thomasson, M., and Sundberg, J. (**1998**). ''Effects of lung volume on the glottal voice source,'' J. Voice **12**, 424–433.

Kelso, J. A. S., Saltzman, E. L., and Tuller, B. (**1986**). ''Intentional contents, communicative context, and task dynamics: a reply to the commentators,'' J. Phonetics **14**, 171–196.

Kent, R., Kent, J., Weismer, G., Martin, R., Sufit, R., Brooks, B., and Rosenbek, J. (**1989**). ''Relationships between speech intelligibility and the slope of second-formant transitions in dysarthric subjects,'' Clin. Linguist. Phonetics **3(4)**, 347–358.

Konno, K., and Mead, J. (**1967**). ''Measurement of the separate volume changes of rib cage and abdomen during breathing,'' J. Appl. Physiol. **22**, 407–422.

Kugler, P. N., and Turvey, M. T. (**1987**). *Information, Natural Law, and the Self-assembly of Rhythmic Movement* (Erlbaum, Hillsdale, NJ).

Ladd, D. (**1988**). ''Declination 'reset' and the hierarchical organization of utterances,'' J. Acoust. Soc. Am. **84**, 530–544.

Lieberman, P., Katz, W., Jongman, A., Zimmerman, R., and Miller, M. (**1985**). ''Measures of the sentence intonation of read and spontaneous speech in American English,'' J. Acoust. Soc. Am. **77**, 649–657.

Liss, J., Spitzer, S., Caviness, J., Adler, C., and Edwards, B. (**1998**). ''Syllabic strength and lexical boundary decisions in the perception of hypokinetic dysarthric speech,'' J. Acoust. Soc. Am. **104**, 2457–2466.

Milenkovic, P. (**1990**). *CSpeech* (University of Wisconsin–Madison, Madison).

Murdoch, B., Chenery, H., Stokes, P., and Hardcastle, W. (**1991**). ''Respiratory kinematics in speakers with cerebellar disease,'' J. Speech Hear. Res. **34**, 768–780.

Netsell, R. (**1973**). ''Speech physiology,'' in *Normal Aspects of Speech, Hearing, and Language*, edited by F. Minifie, T. Hixon, and F. Williams (Prentice-Hall, Englewood Cliffs, NJ), pp. 211–234.

Norris, D., McQueen, J. M., and Cutler, A. (**1995**). ''Competition and segmentation in spoken-word recognition,'' J. Exp. Psychol. Learn Mem. Cogn. **21**, 1209–1228.

Ramig, L. O. (**1992**). ''The role of phonation in speech intelligibility: A review and preliminary data from patients with Parkinson's disease,'' in *Intelligibility in Speech Disorders: Theory, Measurement and Management*, edited by R. Kent (John Benjamin, Amsterdam), pp. 119–156.

Ramig, L. O., Countryman, S., Thompson, L. L., and Horii, Y. (**1995**). ''Comparison of two forms of intensive speech treatment for Parkinson's disease,'' J. Speech Hear. Res. **38**, 1232–1251.

Rosenbek, J., and LaPointe, L. (**1985**). ''The dysarthrias: Description, and treatment,'' in *Clinical Management of Neurogenic Communicative Disorders*, 2nd ed., edited by D. F. Johns (Little Brown, Boston), pp. 97–152.

Schulman, R. (**1989**). ''Articulatory dynamics of loud and normal speech,'' J. Acoust. Soc. Am. **85**, 295–312.

Shipp, T., Morrissey, P., and Hagland, S. (**1983**). ''Laryngeal muscle adjustments for sustained phonation at lung volume extremes,'' paper presented at the Proceedings of the Stockholm Music Acoustics Conference (SMAC '83), Stockholm.

Sorensen, J., and Cooper, W. (**1980**). ''Syntactic coding of fundamental frequency in speech production,'' in *Perception and Production of Fluent Speech*, edited by R. Cole (Erlbaum, Hillsdale), pp. 399–340.

Sundberg, J., Titze, I., and Scherer, R. (**1993**). ''Phonatory control in male singing: A study of the effects of the subglottal pressure, fundamental frequency, and mode of phonation on the voice source,'' J. Voice **7**, 15–29.

Titze, I. (**1994**). *Principles of Voice Production* (Prentice-Hall, Englewood Cliffs, NJ).

Turner, G., Tjaden, K., and Weismer, G. (**1995**). ''The influence of speaking rate on vowel space and speech intelligibility for individuals with amyotrophic lateral sclerosis,'' J. Speech Hear. Res. **38**, 1001–1013.

Weismer, G. (**1985**). ''Speech breathing: Contemporary views and findings,'' in *Speech Science—Recent Advances*, edited by R. Daniloff (Taylor & Francis, London), 47–72.

Weismer, G., Jeng, J., Laures, J., Kent, R., and Kent, J. (**2000**). ''Acoustic and intelligiblity characteristics of sentence production in neurogenic speech disorders,'' Folia Phoniatr. Logopaed. **53**, 1–18.

Weismer, G., Kent, R. D., Hodge, M., and Martin, R. (**1988**). ''The acoustic signature for intelligibility test words,'' J. Acoust. Soc. Am. **84**, 1281–1291.

Whalen, D., and Levitt, A. (**1995**). ''The universality of intrinsic *F*0 of vowels,'' J. Phonetics **23**, 349–366.

Zenker, W. (**1964**). ''Questions regarding the function of external laryngeal muscles,'' in *Research Potentials in Voice Physiology*, edited by D. Brewer (State University of New York, New York), pp. 20–40.

Tongue-surface movement patterns during speech and swallowing

Jordan R. Green and Yu-Tsai Wang
Department of Communicative Disorders, University of Wisconsin–Madison, 1975 Willow Drive, Madison, Wisconsin 53706

(Received 30 January 2002; revised 28 January 2003; accepted 31 January 2003)

The tongue has been frequently characterized as being composed of several functionally independent articulators. The question of functional regionality within the tongue was examined by quantifying the strength of coupling among four different tongue locations across a large number of consonantal contexts and participants. Tongue behavior during swallowing was also described. Vertical displacements of pellets affixed to the tongue were extracted from the x-ray microbeam database. Forty-six participants recited 20 vowel-consonant-vowel (VCV) combinations and swallowed 10 ccs of water. Tongue-surface movement patterns were quantitatively described by computing the covariance between the vertical time-histories of all possible pellet pairs. Phonemic differentiation in vertical tongue motions was observed as coupling varied predictably across pellet pairs with place of articulation. Moreover, tongue displacements for speech and swallowing clustered into distinct groups based on their coupling profiles. Functional independence of anterior tongue regions was evidenced by a wide range of movement coupling relations between anterior tongue pellets. The strengths and weaknesses of the covariance-based analysis for characterizing tongue movement are considered. © *2003 Acoustical Society of America.*
[DOI: 10.1121/1.1562646]

PACS numbers: 43.70.Bk, 43.70.Aj, 43.70.Jt [AL]

I. INTRODUCTION

The tongue has been frequently characterized as being composed of several functionally independent articulators (Hardcastle, 1976; Hoole, 1999; Mermelstein, 1973; Öhman, 1967; Perkell, 1969; Stone, 1990). The common use of such terms as tip, blade, body, dorsum, and root to refer to the ''parts'' of the tongue reflects the widespread acceptance of this assertion. The factors that give rise to functional regionality within the tongue are not fully understood but may include task demands, neuromuscular control, biomechanical tissue linkages, and constraints in motion imposed by palatal shape. The conception of the tongue as a segmented structure is particularly interesting given that studies of its internal structure have not identified morphologic features that could account for the extent of functional partitioning alluded to in the literature. For example, a recent study by Takemoto (2001) revealed the body of the human tongue to contain serially arranged replications of a ''structural unit'' that consists of several layers of highly interdigitating musculature. Presently, there is little agreement about (1) the number and location of functional regions in the human tongue, (2) the degree of functional independence among tongue regions,[1] and (3) the extent to which putative functional regions or characteristic movement patterns in the tongue are similar across speakers.

A number of studies have reported that tongue motions are generated by a small number of independent components and that the tongue assumes relatively few shapes during speech. The small number of tongue surface-deformation patterns exhibited during speech has been interpreted to reflect both speaker-strategies and constraints imposed by the physical properties of the tongue (Kent and Moll, 1972; Perkell, 1969). As early as 1967, Öhman, proposed that the tongue may be regarded as three independently controlled systems: the apical articulator serving the dentals, alveolars, and retroflex; the dorsal serving the palatal and velars; and the tongue-body serving vowels. Since then, several investigators have worked toward estimating both the number of functionally distinct parts of the tongue and the number of unique shapes it assumes during speech.

Using x-ray microbeam and ultrasound to transduce tongue motion, Stone (1990) identified four midsagittal regions that functioned quasi-independently: anterior, dorsal, middle, and posterior. Other investigators have applied factor analysis to mid-sagittal tongue contours to derive the number of distinct shapes exhibited by the tongue during speech (Harshman *et al.*, 1977; Maeda, 1990). Harshman and colleagues (1977) reported that two factors could account for the variations in sagittal tongue shapes associated with ten steady-state vowels. One factor was associated with the forward movement of the tongue-root and upward movement of the blade, and the other accounted for upward and backward movements. Maeda (1990) reported that variations in sagittal tongue shape during ten French sentences could be accounted for by three primary factors related to tongue-dorsum position (front/back), tongue-dorsum shape (arched/flat), and tongue-tip position (raised/lowered). Sanguineti and colleagues' (Sanguineti *et al.*, 1997) articulatory model corroborates these empirical descriptions of tongue behavior by showing that the repertoire of speech-related tongue behaviors can be generated from a small number of primitive movements that are distinguished by the independent activation of distinct muscle groups.

Although several investigations have quantified speech-

 0001-4966/2003/113(5)/2820/14/$19.00

related tongue shapes, few have quantified the spatiotemporal relations among adjacent and nonadjacent tongue regions during speech or swallowing. An improved understanding of the extent of functional regionality within the tongue will be important for explaining features of normal and disordered speech and swallowing. For speech, the degree of movement independence across the tongue will delimit the tongue's capacity to encode phonetic details for linguistic distinction and the time course for coarticulation. For instance, in a CV utterance where the consonant requires alveolar closure, the degree of independence in movement between tongue-tip and tongue-body will determine the time course in which speakers can begin to move the tongue-body for producing the vowel (Kent and Moll, 1972).

There is some empirical evidence that both acquired and developmental disorders of tongue function are associated with a decrease in movement independence among the different tongue regions. Using electropalatography, Gibbon (1999) reported that a majority of children with speech disorders exhibited tongue contact patterns that lacked clear differentiation between the tongue's apex, body, and lateral margins. In addition, Hardcastle and colleagues (Hardcastle *et al.*, 1991) observed the erroneous coupling of velar and alveolar elevation in a speaker with apraxia resulting in a /t/ for /k/ substitution. In an earlier study of childhood articulatory disorders, Hardcastle *et al.* (1987) identified one child who exhibited reduced control over different regions of the tongue. During speech, this child's tongue was reported to move as a ''single undifferentiated mass'' (p. 180). Similarly, in a cineradiographic study of dysarthric speech, Kent *et al.* (1975) observed tongue function in speakers with dysarthria to be characterized by ''reduced motility'' and ''limited flexibility in the directions of tongue movement.'' Such deficits in lingual coordination might be usefully described in terms of the distributions of coupling relations among adjacent and nonadjacent tongue regions. However, more information regarding the spatiotemporal features of tongue-surface movement patterns in nonimpaired speakers is required before such a measure can be used to gauge the degree of speech-motor impairment.

Swallowing also requires functional independence within the tongue's supporting musculature. For example, the transport of material through the oral cavity and into the pharynx is executed by the sequential activation of genioglossus muscle fibers from anterior to posterior (Bosma *et al.*, 1990). Thus, the study of the coupling relations among tongue regions has the potential to improve our understanding of tongue control for swallowing, as well as speech, and will provide a quantitative basis for understanding differences in the coordinative requirements for these distinct tasks.

In the present investigation, we examine the question of functional regionality by quantifying the strength of coupling among four different tongue locations across a large number of consonantal contexts and participants. Tongue behavior during swallowing will also be described. Based on this representation of tongue behavior, the following questions will be addressed regarding tongue function during speech and swallowing: (1) How much functional independence in movement is typically exhibited during speech and swallowing across the surface of the tongue? (2) How distinct is spatiotemporal organization of mid-sagittal tongue deformations for differing consonants? (3) Are lingual deformation patterns similarly affected by phonemic contexts across speakers?

The range of movement coupling relations between two regions of the tongue across a variety of tasks is taken as a *gross* indicator of their functional independence. For example, the observation of persistently high coupling between two regions across a variety of tasks would suggest limited functional independence. In contrast, the observation of a wide range of movement relations between two regions would suggest a high degree of functional independence.

II. METHODS

A. Participants

These data were obtained from the X-Ray Microbeam Speech Production Database (XRMB-SPD, Westbury, 1994), which includes 57 speakers of American English. The present study examined data from 46 of these participants. The 11 excluded participants either did not perform the selected tasks or produced an insufficient amount of data to be analyzed. The mean chronological age of participants (20 male, 26 female) was 21 years; 5 months (SD: 2;6, range: 19;2–29;4) for males and 22 years; 8 months (SD: 4;5, range: 18;4–37;0) for females. The majority of participants (85%) spoke a Midwest dialect and were students at the University of Wisconsin–Madison. All participants passed a hearing screening with thresholds at or below 25 dB HL for a range of frequencies from 500 to 8000 Hz. No participants reported a history of a speech or language disorder (including oral mechanism anomalies) or evidence of neuromotor or other health concerns.

B. Kinematic data

The x-ray microbeam (XRMB) tracked movements of pellets that were affixed to the tongue (T1,T2,T3,T4), the upper and lower lip (UL,LL), and the mandible (MI,MM). An anatomically based reference frame was used to standardize pellet placement across participants [see Fig. 5.2 and Tables 5.1 and 5.2 in Westbury (1994)]. Pellet MI was affixed to the buccal surface of the mandibular incisor and pellet MM was affixed to the junction between the first and second mandibular molars. T1 and T4 pellets were placed on regions of the tongue that are typically classified as blade and dorsum, respectively, and T2 and T3 were placed intermediately and equidistant to each other and the endpoint pellets. For purpose of discussion, T3 will be considered to be located at the body of the tongue, and T1 and T2 are considered to be located at the anterior blade and posterior blade, respectively. The gold pellets (2–3 mm diameter) were affixed to these sites mid-sagittally using dental adhesive (Ketac-Bond).

The XRMB captures the motion of radiodense pellets via computer guided positioning of a narrowly focused x-ray. The operating principles of x-ray microbeam technology for tracking articulatory movements have previously been de-

scribed in detail by Westbury (1991). Because the articulators tend to move at different speeds, articulatory movements were initially sampled at various rates per second (UL and MI=40 Hz; LL, T2, T3, and T4=80 Hz; and T1=160 Hz). However, for ease of analysis, all signals were subsequently resampled at a uniform rate of 160 samples per second. The database expresses all pellet positions relative to the maxillary occlusal plane (see Westbury, 1994). In this coordinate system, the central maxillary incisor defines the origin with the *x* axis being defined by the maxillary occlusal plane. The *y* axis was defined as the line that was normal to *x* axis in the midsagittal plane. All signals were low-pass filtered ($f_c = 10$ Hz) using a zero phase forward and reverse digital filter. The low-pass cutoff frequency was selected based on spectral analysis of over 50 movement traces, which were selected arbitrarily across participants and pellets, showing prominent spectral energy in a narrow band centered near 2.5 Hz.

C. Experimental tasks

Speech data existed for 43 of the 46 participants (19 male, 24 female) with a mean chronological age of 21;7 (SD: 3;4, range: 18;4–37;0). The remaining three participants completed only the swallowing task. Each speaker produced 20 consecutive vowel consonant vowel (V_1CV_2) combinations, with the consonant changing and the vowels remaining constant (V_1=/u/, V_2=/a/). The consonants were 20 American English phonemes (/h,m,w,b,p,f,v,t,d,n,s,z,k,g, r,j,ʃ,ʒ,tʃ,dʒ/). For several of the analyses, phonemes were grouped according to the following place of articulation scheme: laryngeal fricative /h/, bilabials /m,w,b,p/, labiodentals /f,v/, alveolars /t,d,n,s,z/, palatoalveolars /ʃ,ʒ,tʃ,dʒ/, retroflex /r/, lateral /l/, palatal /j/, velars /k,g/. All utterances were produced at a self-selected typical rate with stress assigned to the second syllable. Each VCV utterance was only produced once. Thus, the present design is predicated on the assumption that a single token provides a reasonable representation of the articulatory kinematics associated with each task. This assumption is supported by previous research showing high reliability of tongue, lip, and jaw kinematic patterns among replicates of basic speech material (Green *et al.*, 2000; Westbury *et al.*, 1998). Data from a given pellet was not included in the analysis if it contained gaps related to mistracking. Consequently, when the data were pooled across participants, the number of missing data points varied from 0% to 8% across pellet pairs, with the highest incidence of missing data observed for T1×T2 and T2×T3 (range=5%–8%).

Swallow data existed for 42 participants (19 male, 23 female) with a mean chronological age of 22;1 (SD: 3;11, range: 18;4–37;0). Participants swallowed 10 ccs of water for five trials. Because of pellet mistracking, the number of samples analyzed for each swallow trial differed, with a mean of 39 samples (range: 36–42) per trial. Differences in the percent of missing data for specific pellets were evident across the five swallow trials. The percent of missing data varied across all four tongue pellets (M: T1=13%; T2=14%; T3=19%; T4=12%) with a range of 4%–30%. Percent of missing data for the upper and lower jaw pellets also varied (M: MI=3%; MM=16%) with a range of 0%–18%.

D. Data conditioning and analysis

1. Signal processing

Prior to analysis, the positional data was transformed to achieve tongue and lower lip positions that were independent from that of jaw. Translatory and rotary components of mandibular movements were computed and used to reexpress the position of the tongue and lower lip pellets relative to the mandibular incisor and molar pellets. This computation, which is defined in Formula 1 (from Westbury *et al.*, 2002), effectively transposed these data from the maxillary occlusal plane coordinate system to one that is relative to the position of the mandible:

$$\textbf{Formula 1}: \quad \begin{bmatrix} x' \\ y' \end{bmatrix} = \begin{bmatrix} \cos\alpha & \sin\alpha \\ -\sin\alpha & \cos\alpha \end{bmatrix} \begin{bmatrix} (x - x_{\mathrm{MI}}) \\ (y - y_{\mathrm{MI}}) \end{bmatrix},$$

where

$$\alpha = \tan^{-1}[(y_{\mathrm{MM}} - y_{\mathrm{MI}})/(x_{\mathrm{MM}} - x_{\mathrm{MI}})];$$

x_{MI}, y_{MI} and x_{MM}, y_{MM} are the positions of the mandible pellets (MI=mandibular incisor, MM=mandibular molar); and *x*, *y* is the position of a flesh-point (either the lower lip or tongue) that is being reexpressed into the mandibular-based coordinate system. This transformation was necessary because analysis of the tongue data in its original reference frame (i.e., the maxillary occlusal plane) would have biased the results toward high coupling among all lingual pellet pairs due to the shared influence of the mandible on the position of each pellet.

All analyses were restricted to motions in the vertical dimension (*y* axis) as defined by the mandibular-based coordinate system. The decision to study only a single dimension of tongue motion was motivated by the need to simplify both the analysis and the interpretation of the large number of conditions being examined. This roughly ''vertical'' component of articulatory motion was specifically selected because (a) elevation of the appropriate region of the tongue toward the palate is an essential kinematic goal for these speech utterances and (b) based on previous findings, the vertical component is expected to provide better mapping to phonetic variation than the horizontal component (Lofqvist and Gracco, 1994). For example, during V /g/ V utterances, the anterior–posterior positioning of the site of palatal contact varies considerably depending on vowel context (Kent and Moll, 1972). Reduction of the two-dimensional data into a single variable that reflects the motion relative to a primary axis of motion (e.g., principle component analysis) was not pursued because the accuracy of this transformation can vary significantly from token to token with changes in the shape of the movement path. This transformation was also avoided because it makes the direction of movement relative to the palate ambiguous.

Prior to analysis, the movement associated primarily with the consonant was identified on each movement trace. For this procedure, the start- and end-points of each VCV gesture was defined algorithmically based on a near-zero

crossing (−0.03 mm/s) in a derived velocity signal. The −0.03-mm/s threshold was empirically derived and was adopted to ensure that the selected segments were associated with speech movements as opposed to those associated with small amplitude fluctuations that frequently occur at rest. The near-zero crossing associated with the beginning of consonantal closure defined the onset of each signal, and the near-zero crossing associated with the ending of consonantal release defined the offset of each signal. If more than one threshold crossing was identified for a given phase of movement, the point that was closest to the middle of the movement segment was designated as the event marker.

2. Performance measures

For each task, pairwise correlations were computed on the vertical time histories of select pellet pairs: T1×T2, T2×T3, T3×T4, T1×T3, T2×T4, T1×T4, UL×LL, LL×MI. The resulting correlation coefficients among lingual pellets quantified the strength of movement coupling of tongue-surface regions as they moved toward and away from the palate. Correlations approaching one represented highly coupled articulatory movements; correlations near zero represented independent articulatory movements; and correlations approaching negative one represented highly coupled articulatory movements that were moving in opposite directions. Although the present study was primarily concerned with movements of the tongue, lip and jaw pairs (i.e., UL×LL and LL×MI) were included to examine differences in lip and jaw coordination between lingual and labial consonants, and between labial and glottal consonants.

3. Quantification of articulatory coupling: Covariance

One interpretive limitation of representing movement-coupling solely based on zero-lag correlations is that the relative importance of a given movement on vocal tract acoustics or bolus propulsion cannot be evaluated. That is, because traditional correlation-based analyses are inherently normalized to signal amplitude, small movements cannot be distinguished from larger, potentially more functional movements. To overcome this limitation, we computed the covariance between the vertical time histories associated with each pellet pair (see Formula 2). The covariance formula is rexpressed in Formula 3 to emphasize that it represents spatiotemporal coupling that is weighted by movement amplitude. The SD represents the standard deviation of movement for each vertical time history:

$$\textbf{Formula 2}: \quad \mathrm{Cov}_{xy} = \frac{\Sigma(x-\overline{x})(y-\overline{y})}{N-1},$$

$$\textbf{Formula 3}: \quad \mathrm{Cov}_{xy} = r_{ij} \times \mathrm{SD}_i \times \mathrm{SD}_j .$$

The value of the covariance will decrease in response to both spatial and temporal differences between pellet-position time histories. The *maximum* value of $\mathrm{SD}_i \times \mathrm{SD}_j$ is expected to differ across pellet pairs because the *maximum* vertical position for a given pellet will be determined by the curvature of the palate.

The representation of tongue surface motion in terms of the *covariance* provided a quantitative means to examine patterns of functional independence for two tongue regions across a variety of phonemes. For example, the observation of consistently high covariance values between two regions and across a variety of phonemes would suggest limited functional independence, whereas the observation of consistently low covariance values would suggest a high degree of functional independence.

To examine phonemic differentiation in tongue coordination, the *covariance* values associated with each pellet pair (i.e., T1×T2, T2×T3, T3×T4, T1×T3, T2×T4, T1×T4) were grouped to form *coupling profiles* for each task and speaker. The *coupling profiles* were used to quantify the degree of coordinative distinctness among different consonants and swallowing, and the degree of variability in lingual movement patterns across tasks and participants. For example, if tongue movements for distinct phonemes were derived from common movement patterns, then *coupling profiles* would be similar for multiple phonemes. Likewise, if speakers used similar lingual movement patterns, then coupling profiles would be similar across speakers for a given task.

Figure 1 illustrates the effectiveness of the covariance analysis for capturing across-phoneme differences in lingual movement patterns. The data in this figure were obtained from a single speaker's production ''uhda'' and ''uhga.'' The top panel displays the movement path for each pellet in the midsagittal plane as shown in Tf32.exe (Milenkovic, 2000). The middle panel contains the extracted vertical time histories for each pellet, and the bottom panel contains the derived *coupling profiles*.

The vertical time histories, displayed in the middle panel, emphasize the kinematic differences between these tasks. As expected, the location of maximum constriction is more anterior for the alveolar than for the velar. During ''uhda'' T1, T2, and T3 moved toward the palate relatively synchronously, while T4 moved away from the palate; during consonantal closure for ''uhga,'' all tongue pellets moved relatively synchronously toward the palate. The derived *coupling profiles*, which are displayed in the bottom panels, quantify the observed trends in the vertical time histories. During the production of ''uhda,'' T1×T2 coupling was highly positive; T1×T4 and T2×T4 coupling was negative; and the other three pellet pairs exhibited low positive coupling. In contrast, during the production of ''uhga,'' the covariance values for all tongue pellet pairs were high and positive.

III. RESULTS

A. Distribution of coefficients and $\mathrm{SD}_i \times \mathrm{SD}_j$ values as a function of task and pair

Tongue pellets exhibited differing degrees of functional independence across task (i.e., across different phonemes and swallowing). Panel (a) in Fig. 2 shows the distribution of average $\mathrm{SD}_i \times \mathrm{SD}_j$ values as a function of average correlation coefficient for each place of articulation and swallowing. Each data point represents the average value across participants. Panel (b) in Fig. 2 shows the same data plotted as a function of pellet pair. In these figures, high degrees of

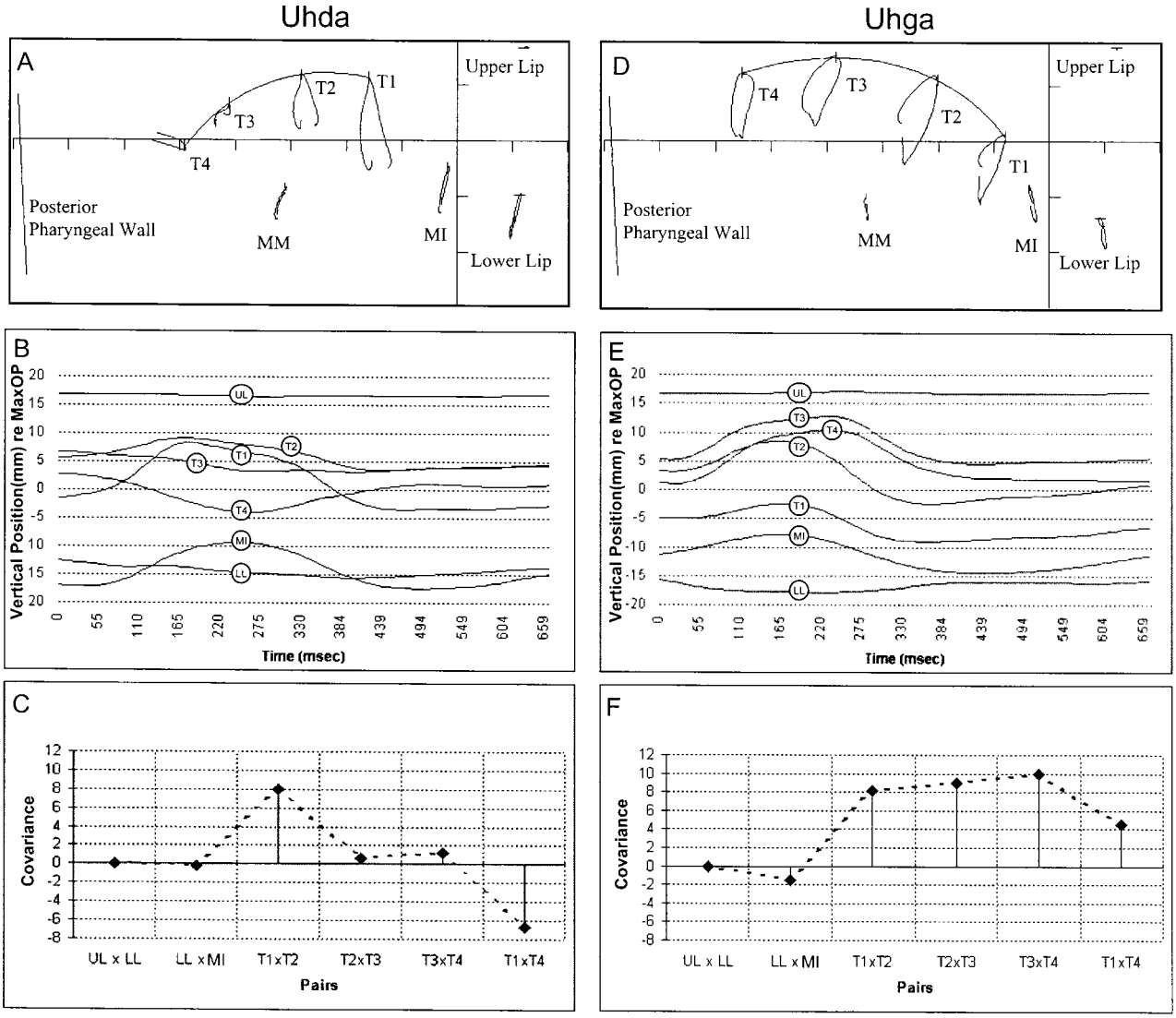

FIG. 1. Movement data and associated *coupling profiles* for the utterances "uhda" and "uhga" from a single participant. Top panels: the movement path for each pellet in the mid-sagittal plane. Middle panels: the extracted vertical time histories for each pellet. Bottom panels: *coupling profiles* based on *covariance* values derived from the traces in the middle panels. The *coupling profiles* highlight the differences in tongue motion for these two tasks. The alveolar, as displayed in panel (c), exhibits greatest coupling between pellets T1 and T2 with little activity at other adjacent tongue regions. In addition, coupling between T1 and T4 was negative, suggesting oppositional movement. In contrast, the velar was produced with uniformly strong, positive coupling across all tongue regions. Coupling profiles provided a quantitative means to describe differences in tongue surface motion across all tasks.

movement independence between any two pellets would be represented by the observation of a relatively large $SD_i \times SD_j$ value that was associated with a low coefficient value. Another indicator of coordinative flexibility between pellets is the range of coefficient values across tasks. That is, a high degree of movement independence for a given pellet pair would be suggested by the observation of a large range of coefficient values across different speech contexts and swallowing. Conversely, limited movement independence would be supported by the observation of a small cluster of coefficient values near either 1 or -1 across tasks.

The large range of coefficient values and movement amplitudes exhibited for most of the pellet pairs suggests that many of these anatomic regions are capable of functioning quasi-independently. Conversely, limitations in motion independence are indicated by the absence of data points in the upper middle region of these figures. This finding was anticipated on the basis that the maximum degree of movement decoupling across different tongue regions was expected to be limited by tissue linkages and volume displacement effects.

As displayed in panel (b) of Fig. 2, the range of coefficient values differed considerably across pellet pairs. Adjacent pellets tended to be only positively coupled, and therefore exhibited a relatively smaller range of coupling relations than nonadjacent pellets, which for some tasks exhibited negative coupling. T3×T4 exhibited the smallest range (0.46) of average coefficient values and T1×T3 exhibiting the largest range (1.35). With the exception of LL×MI, coefficient values for most pellet pairs tended to vary along a continuum.

These data also illustrate the potential limitations of relying solely on the correlation coefficient as a measure of tongue-pellet coupling. As displayed in panel (a) of Fig. 2,

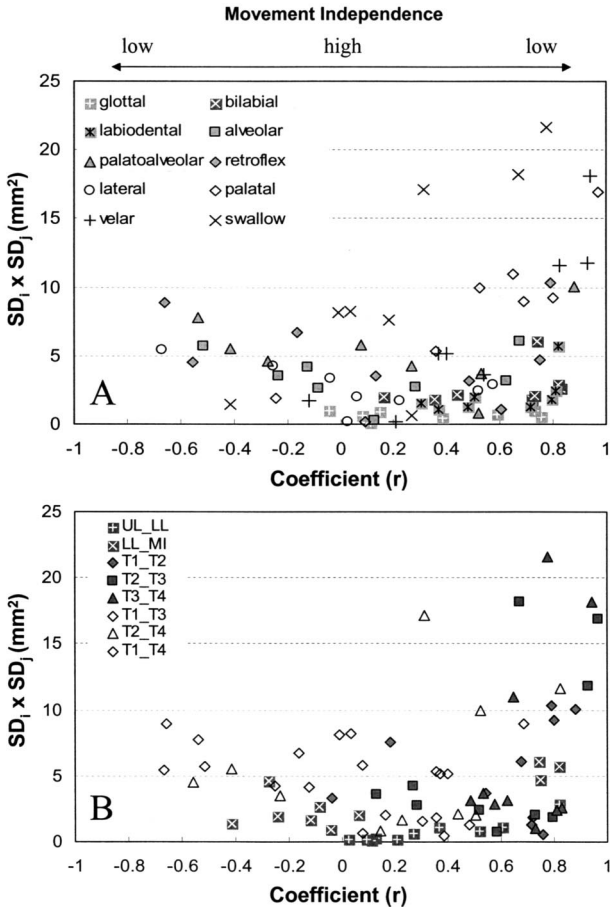

FIG. 2. Panel (a) shows the distribution of $SD_i \times SD_j$ terms as a function of average coefficient for each place of articulation and swallowing. Each data point represents the average value taken across participants. Panel (b) shows the same data plotted as a function of pellet pair.

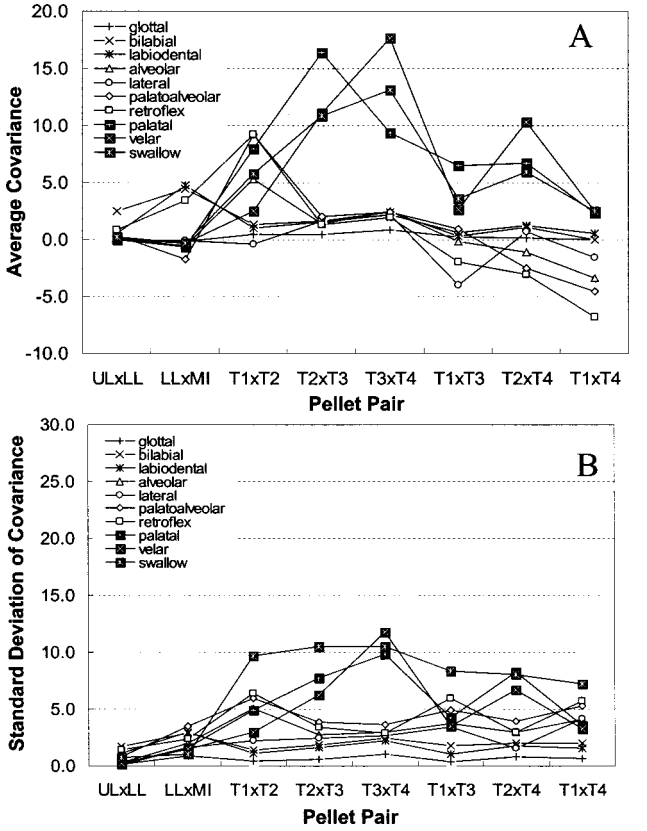

FIG. 3. Panel (a) shows the average across-participant *covariance* values plotted as a function of pair and grouped by task. Panel (b) shows the standard deviation values associated with the mean values displayed in Panel (a).

the *coefficient* values do not distinguish the differences in coupling relations among pellets displayed in the lower right-hand corner of the figure (high coupling–small movements) from those displayed in the upper right-hand corner (high coupling–large movements). Covariance values, in contrast, distinguish between movements that reasonably may be assumed to have a greater influence (i.e., large amplitude) on vocal tract acoustics from those that might have only a minimal influence (i.e., small amplitude). Although we also recognize that, in accordance with quantal theory of speech (Stevens, 1989), articulatory to acoustic relations are highly nonlinear, with small articulatory movements producing disproportionately large acoustic changes in some vocal tract regions.

B. Task-related differences in tongue-surface movement patterns

Covariance values were plotted as a function of pair and grouped by task. The resultant *coupling profiles* for each place of articulation and swallowing are presented in panel (a) of Fig. 3. A comparison of the *coupling profiles* provides a quantitative means to assess task-related differences in tongue-surface movement patterns. The average *covariance* values are listed in Table I as a function of pair and task.

Overall, different places of articulation were distinguished by their *coupling profiles*, with *covariance* values being greatest for adjacent pellet pairs located near the expected primary place of articulation. Task differences among *coupling profiles* were tested statistically using multiple repeated measures MANOVAs (task×pair). To reduce the potentially large number of statistical comparisons, the data were grouped by place of articulation and the statistical tests were restricted to lingual pellets. Prior to statistical analysis, normality of the covariance data was examined using histograms and normal probability plots. These plots revealed that the covariance scores were distributed symmetrically about their mean with the exception of a few outliers. The results of the omnibus and main effect analyses are reported in Table II. For these *repeated measures* comparisons, a Bonferroni correction was applied to each familywise comparison (15 possible tongue-pellet pair comparisons per task) resulting in a corrected α level of 0.003. With the exception of palatoalveolar versus retroflex, all omnibus comparisons achieved statistical significance using this criterion. This finding suggests that mid-sagittal lingual movement patterns, as represented by the *coupling profile*, were distinct across different places of articulation. In the main effect analysis, each place of articulation exhibited at least one across-pair comparison that achieved statistical significance with the exception of palatoalveolar versus retroflex and velar versus swallow.

The *coupling profiles* for each phonemic context were

TABLE I. Covariance summary statistics as a function of pellet pair and place of articulation.

Place	Pellet pairs								Total
	T1×T2	T2×T3	T3×T4	T1×T3	T2×T4	T1×T4	LL×J1	UL×LL	M (SD): Range
Alveolar	5.07(5.10)	1.34(2.79)	2.48(2.98)	−0.17(3.70)	−1.01(3.00)	−3.37(4.11)	−0.51(2.01)	0.06(0.27)	0.49(3.37):29.69
Bilabial	1.35(1.42)	1.65(1.84)	2.35(2.47)	0.32(1.78)	1.11(1.99)	0.01(2.04)	4.49(2.93)	2.46(1.70)	1.72(2.00):14.76
Glottal	0.48(0.42)	0.47(0.58)	0.86(1.02)	0.20(0.40)	0.13(0.82)	−0.03(0.65)	−0.17(0.92)	0.03(0.13)	0.24(0.74):8.11
Labiodental	1.01(1.11)	1.56(1.65)	2.20(2.27)	0.64(1.07)	1.30(1.80)	0.51(1.60)	4.76(3.00)	0.52(1.12)	1.55(2.04):17.06
Palatal	7.94(4.92)	16.42(7.80)	9.37(9.83)	6.49(4.27)	6.68(8.27)	2.38(3.60)	−0.66(1.61)	0.03(0.11)	5.92(7.81):42.10
Palatal-alveolar	9.34(5.99)	1.97(3.89)	2.53(3.67)	0.91(4.91)	−2.48(3.95)	−4.66(5.31)	−1.74(3.50)	0.43(0.81)	0.77(5.42):39.53
Velar	2.57(2.95)	11.09(6.29)	17.62(11.76)	2.68(3.53)	10.11(6.75)	2.45(3.32)	−0.32(1.50)	0.10(0.23)	5.75(7.99):50.61
Retroflex	9.20(6.40)	1.29(3.41)	1.97(2.90)	−1.99(5.97)	−3.04(3.01)	−6.82(5.76)	3.47(2.40)	0.83(1.39)	0.61(6.14):54.17
Lateral	−0.42(2.27)	1.63(2.46)	2.18(2.67)	−3.97(3.42)	0.71(1.59)	−1.57(4.15)	−0.05(1.67)	0.03(0.19)	−0.21(3.13):29.98
Swallow	3.37(6.32)	12.93(9.18)	17.38(9.48)	0.33(3.84)	6.06(7.41)	−0.23(3.92)	−0.55(1.48)	0.34(1.04)	5.30(8.64):41.30
Total: M (SD)	4.45(5.38)	5.45(7.39)	6.26(8.61)	0.63(4.49)	2.10(6.18)	−1.25(4.71)	1.04(3.19)	0.55(1.10)	
Range	35.24	37.52	49.58	31.69	39.39	42.00	28.66	9.65	

subjected to a multidimensional scaling (MDS) procedure to derive an articulatory coordination space based on pellet coupling. This analysis provided a novel means for evaluating task specificity of lingual movement patterns by reducing the multivariate data associated with each task into three factors. Three factors were used because this combination of factors accounted for a greater proportion of the variance ($R^2=70\%$, *stress*$=0.25$) than did the two-dimension model ($R^2=64\%$, *stress*$=0.32$). Panel (a) of Fig. 4 displays the MDS solution, which is plotted as Euclidian distances from a common centroid. Similarities among *coupling profiles* across place of articulation and task are represented by spatial proximity. When interpreting the MDS solution it is important to consider that the impression of data clusters varies dramatically depending on figure orientation. The individual participant weights for each dimension are presented in panel (b) of Fig. 4.

Based on visual inspection, the MDS solution identified between five and seven clusters that distinguished the different tongue sounds (e.g., alveolar fricatives from velars and alveolar stops). As expected, all labial sounds occupied a similar location of the MDS space. With the exception of /t/ and /d/, homorganic consonants were in close proximity. The retroflex, lateral, and swallowing each occupied a unique location in the MDS solution. Velars and the palatals appeared to form a unique cluster. Interestingly, /s/ and /z/ did not cluster with other alveolar sounds. The retroflex was primarily distinguished from the other alveolars and the palatoalveolars by its relatively high dimension 3 value, which was more similar to the values associated with labial sounds.

C. Pellet pair by task interactions

Pellet pair effects were tested using multiple *posthoc* comparisons for swallowing and place of articulation. Due to the large number of comparisons being tested, statistical reporting was abbreviated in the form "$p<0.003$, for each comparison" when the same alpha level was used for a family of comparisons. In general, pellet pair effects tended to vary predictably with place of articulation. As anticipated, glottals were associated with weak coupling across all pellet pairs. The alveolars, retroflex, and palatoalveolars exhibited significantly stronger coupling for T1×T2 than for all other pellet pairs ($p<0.001$, for all comparisons) and significantly stronger negative coupling for T1×T4 than for all other pairs ($p<0.001$, for all comparisons) except T2×T4. In contrast to the more "fronted" sounds, the palatal and velars were associated with positive correlations among all pellet pairs. In the present study, the /l/ was characterized by uniformly low coupling except for T1×T3, which showed significantly greater negative coupling than all other pellet-pairs ($p<0.001$, for all comparisons). The palatal was produced with significantly greater coupling for T2×T3 than for all other pellet pairs ($p<0.001$, for all comparisons). In contrast, velars were produced more posteriorly than was the palatal with significantly stronger coupling for T3×T4 than for all other pairs ($p<0.001$, for all comparisons). For velars, pellet pair coupling was also significantly stronger for T2×T3 than for all other pairs ($p<0.001$, for all comparisons) except T3×T4 and T2×T4. Like the palatal and velars, swallowing was characterized by a high degree of positive coupling across all tongue pellets with significantly stronger coupling for T3×T4 than for all other pellet-pairs ($p<0.001$, for all comparisons) and greater coupling for T2×T3 for all pellet pairs ($p<0.001$, for all comparisons) except T3×T4.

D. Across-speaker variation in lingual movement patterns

The present analyses provide several parameters that could be examined to assess across-speaker differences in lingual movement patterns. Figure 3(b) presents the across-speaker standard deviation for each mean value displayed in panel (a). These values show marked individual variability, most notably in the expected place of primary constriction for each consonant. In general, the standard deviation values appear to scale closely with their associated means. Swallowing was associated with high degrees of variability across all lingual pellet pairs. The results in Fig. 4(b) support the findings in Fig. 3(b) by showing a wide range of weights, most notably for dimension 1. The weights for the MDS solution measure the importance of each dimension to each participant. A participant with weights proportional to the

TABLE II. Results of pairwise comparisons testing for differences in covariance values across pairs and tasks. All *p* values were Bonferroni corrected. Nonsignificant findings are shown in bold. Pa: Palatoalveolar.

Pairwise comparison	Omnibus			T1×T2			T2×T3			T3×T4			T1×T3			T2×T4			T1×T4		
	df	F	p	df	F	p	df	F	p	df	F	p	df	F	p	df	F	p	df	F	p
Alveolar vs Palatal	(6,31)	38.4	0.0001	1	13.4	**0.0008**	1	170.7	0.0001	1	13.9	**0.0007**	1	86.7	0.0001	1	40.9	0.0001	1	92.1	0.0001
Alveolar vs Pa	(6,35)	8.9	0.0001	1	34.3	0.0001	1	1.9	**0.1802**	1	0.0	**0.9450**	1	5.0	**0.0317**	1	11.5	**0.0016**	1	6.4	**0.0151**
Alveolar vs Velar	(6,34)	48.8	0.0001	1	16.5	0.0002	1	115.7	0.0001	1	61.5	0.0001	1	14.7	**0.0004**	1	148.3	0.0001	1	74.2	0.0001
Alveolar vs Retroflex	(6,33)	7.3	0.0001	1	21.7	0.0001	1	0.0	**0.9658**	1	1.7	**0.1984**	1	2.9	**0.0983**	1	17.3	0.0002	1	11.3	**0.0018**
Alveolar vs Lateral	(6,30)	34.8	0.0001	1	108.3	0.0001	1	0.5	**0.4722**	1	3.6	**0.0673**	1	54.2	0.0001	1	16.67	0.0002	1	21.8	0.0001
Alveolar vs Swallow	(6,26)	44.2	0.0001	1	0.9	**0.3448**	1	66.3	0.0001	1	117.3	0.0001	1	0.8	**0.3746**	1	39.9	0.0001	1	16.3	0.0003
Palatal vs Pa	(6,31)	42.1	0.0001	1	2.2	**0.1481**	1	186.0	0.0001	1	14.4	**0.0005**	1	57.9	0.0001	1	71.0	0.0001	1	97.9	0.0001
Palatal vs Velar	(6,30)	27.5	0.0001	1	53.0	0.0001	1	31.8	0.0001	1	57.0	0.0001	1	32.5	0.0001	1	9.1	**0.0047**	1	0.2	**0.6848**
Palatal vs Retroflex	(6,29)	20.0	0.0001	1	1.1	**0.3053**	1	115.2	0.0001	1	19.1	0.0001	1	56.4	0.0001	1	49.7	0.0001	1	65.8	0.0001
Palatal vs Lateral	(6,28)	38.9	0.0001	1	78.5	0.0001	1	100.4	0.0001	1	20.0	0.0001	1	115.0	0.0001	1	21.4	0.0001	1	19.4	0.0001
Palatal vs Swallow	(6,24)	8.5	0.0001	1	10.1	**0.0035**	1	1.6	**0.2153**	1	20.8	0.0001	1	25.2	0.0001	1	0.0	**0.9509**	1	5.2	**0.0306**
Pa vs Velar	(6,34)	50.9	0.0001	1	55.4	0.0001	1	91.7	0.0001	1	62.9	0.0001	1	3.7	**0.0631**	1	225.3	0.0001	1	79.5	0.0001
Pa vs Retroflex	(6,33)	4.3	**0.0025**	1	0.0	**0.8741**	1	0.7	**0.4198**	1	1.3	**0.2567**	1	6.5	**0.0149**	1	0.9	**0.3488**	1	3.9	**0.0545**
Pa vs Lateral	(6,30)	42.5	0.0001	1	117.5	0.0001	1	0.2	**0.6841**	1	1.8	**0.18461**	1	38.2	0.0001	1	22.0	0.0001	1	24.8	0.0001
Pa vs Swallow	(6,26)	35.4	0.0001	1	16.82	0.0003	1	51.1	0.0001	1	106.0	0.0001	1	0.12	**0.73089**	1	50.89	0.0001	1	21.4	0.0001
Velar vs Retroflex	(6,32)	28.3	0.0001	1	38.6	0.0001	1	64.7	0.0001	1	76.7	0.0001	1	11.6	**0.0016**	1	154.7	0.0001	1	61.3	0.0001
Velar vs Lateral	(6,29)	18.7	0.0001	1	22.66	0.0001	1	69.5	0.0001	1	58.4	0.0001	1	55.2	0.0001	1	61.69	0.0001	1	17.68	0.0002
Velar vs Swallow	(6,25)	10.5	0.0001	1	2.2	**0.1485**	1	4.2	**0.0504**	1	0.8	**0.39337**	1	3.7	**0.06287**	1	6.6	**0.01528**	1	8	**0.0084**
Retroflex vs Lateral	(6,28)	16.6	0.0001	1	78.4	0.0001	1	0.3	**0.6128**	1	0.0	**0.94993**	1	3.6	**0.06572**	1	41.1	0.0001	1	35.0	0.0001
Retroflex vs Swallow	(6,25)	46.8	0.0001	1	11.1	**0.0023**	1	53.3	0.0001	1	160.4	0.0001	1	2.7	**0.11342**	1	64.4	0.0001	1	25.5	0.0001
Lateral vs Swallow	(6,22)	32.7	0.0001	1	13.1	**0.0012**	1	85.3	0.0001	1	115.3	0.0001	1	28.3	0.0001	1	36.9	0.0001	1	1.6	**0.2109**

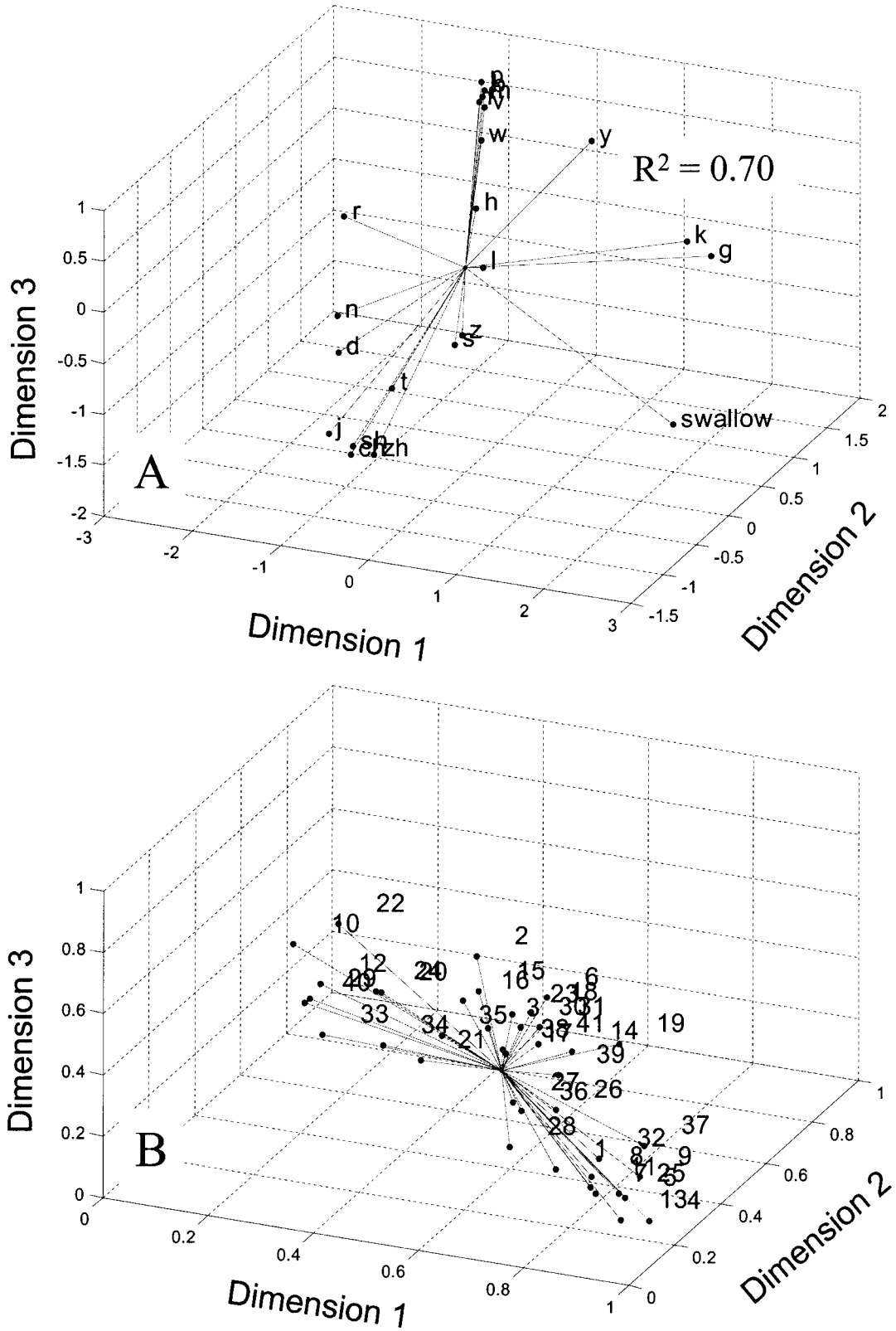

FIG. 4. The *coupling profiles* for each phonemic context were subjected to a multidimensional scaling (MDS) procedure to derive an articulatory coordination space based on pellet coupling. This analysis provided a means to evaluate task specificity of lingual deformation patterns by reducing the multivariate data associated with each task into three factors or dimensions. Similarities among *coupling profiles* across place of articulation and task are represented by spatial proximity. Panel (a) shows the MDS solution plotted as Euclidian distances from a common centroid. Panel (b) shows the individual participant weights for each dimension.

average weights has a weirdness of zero, the minimum value. A participant with one large weight and many low weights has a weirdness value approaching one. A participant with only one positive weight has a weirdness of one, the maximum value for non-negative weights.

Although oppositional movement between T1×T4 was a distinguishing feature of front consonants, not all of the participants exhibited this pattern and some exhibited

oppositional movement for back consonants. For T1×T4, negative coupling (oppositional movement) occurred in 90% of the participants for front consonants, in 20% of the participants for /g,k/, and in 28% of the participants for /j/.

IV. DISCUSSION

The *coupling profile* analysis provided a relatively simple quantitative method for describing tongue-surface movement patterns and for evaluating the behavioral flexibility exhibited by the tongue during speech and swallowing. Across all tasks, speakers exhibited a moderate degree of movement independence among adjacent and nonadjacent tongue regions. However, several constraints in movement independence were suggested by patterns of persistent high coupling across and within tasks. Specifically, adjacent pairs exhibited the least amount of movement independence, and large movements of posterior pellets (i.e., T3 and T4) were strongly associated with movements of anterior pellets (i.e., T1 and T2). Although *coupling profiles* describe lingual coordination of only four tongue regions, they effectively captured changes in tongue-surface deformation patterns that distinguish between one place of articulation from another and speech from swallowing. The basic movement patterns captured by the *coupling profiles* reflect regional organization of the tongue and underscore the importance of local surface elevations in determining constriction location. The patterns of tongue movement identified in the present study may be useful for forming some expectations for tongue behavior during speech, which may potentially be used to gauge the degree of disordered tongue function.

A. Task differentiation in lingual coordination

1. Phonemic differentiation

Overall, the coupling profiles captured the expected features of tongue, lip, and jaw behavior of consonants across participants. Specifically, the predominant peak of each coupling profile exhibited in Fig. 3 varied systematically from anterior to posterior and occurred in locations that are roughly consistent with those identified by conventional places of articulation schemes (Ladefoged, 2001; Nicolosi *et al.*, 1996). This finding provides some evidence for the face validity of covariance as a quantitative index of lingual-surface coordinative organization.

In the present study, the number of distinct profiles grossly represented the degree of phonemic specificity encoded by motions of the tongue in the mandibular anatomic reference plane. Based on visual inspection, the MDS solution (Fig. 4) identified between five and seven clusters that distinguished between, for instance, alveolar fricatives from velars and alveolar stops. This number of distinct lingual movement patterns is greater than might be expected based on previous estimates (Harshman *et al.*, 1977; Maeda, 1990; Stone, 1990). However, a visual inspection of panel (a) of Fig. 3 suggests that if scaling differences among profiles were accounted for, the number of distinct patterns might decrease to four: (1) blade elevation with dorsum depression, (2) body elevation, (3) dorsum elevation, and (4) anterior-blade elevation with body depression. The blade elevation with dorsum depression pattern was observed for alveolars, palatoalveolars, and the retroflex, which exhibited positive T1×T2 coupling and negative T1×T4 coupling. As revealed by the MANOVA the MDS solution, the retroflex was primarily distinguished from the alveolars and the palatoalveolars by the relatively greater covariance values for LL and MI. This finding agrees with prior work suggesting that lip rounding is an additional feature of the retroflex (Westbury *et al.*, 1998). The body elevation pattern, which was observed for the palatal /j/, tended to be produced with positive coupling among all pellet pairs, but with the strongest coupling between T2×T3. The third pattern was associated with swallowing and velars, which, like /j/, was characterized by positive coupling for all pellet pairs, but differed in that the greatest coupling occurred between T3×T4. Finally, the fourth pattern was associated with the lateral, which was distinct from the other fronted sounds in that T1×T2 were weakly coupled, and T1×T3 were negatively coupled.

The four basic tongue-surface movement patterns observed in the present study are similar to those described by Stone and Lundberg (1996). Using electropalatographic and three-dimensional ultrasound techniques, these investigators identified four fundamental tongue-surface shapes: front-raising for /n/ and /ʃ/, complete groove for /s/ and /ɵ/, back-raising for /k/, and two-point displacement for /l/. In the present experiment, front-raising was a prominent movement pattern for alveolars, palatoaveolars, and the retroflex and was indicated by strong coupling for anterior pellets (T1 ×T2), relatively weak coupling among posterior pellets (T3 ×T4), and negative coupling for T1×T4. Central grooving may explain why /s/ and /z/ did not cluster with other alveolars in the multidimensional solution, as this type of posturing may restrict motion of the mid-sagittal tongue. Future investigations should explore this within-place category difference. Stone and Lundberg's ''back-raising'' gesture for velars was quantitatively supported in the present investigation by the relatively high T3×T4 coupling observed for these consonants. The present analysis also revealed that velars were characterized by the simultaneous elevation of all tongue regions (i.e., positive, moderate to high coupling across all tongue pairs). This ''whole tongue'' movement pattern is fundamentally different from that observed for alveolars and palatoalveolars, which exhibited a greater diversity of covariance values across tongue regions, and thus more complicated patterns of lingual movement. The coupling profiles for /l/ did not exhibit the anterior–posterior elevation pattern (i.e., ''two-point displacement'') described by Stone and Lundberg, although both studies similarly observed tongue behavior for this sound to be distinct from other sounds. In the present study, the /l/ was characterized by uniformly low coupling except for T1×T3, which showed moderate, negative coupling. The similarities between the lingual patterns described by Stone and Lundberg and those identified in the present study provide additional evidence for the strength of covariance as a method for parametrizing tongue-surface movement patterns across a large number of participants.

2. Scaling of basic movement templates across consonants

The present suggestion of four tongue-surface coupling patterns is consistent with the assertion that a small set of movement patterns or shapes form the bases for phonemic distinctions and that differences among closely related sounds may result from a scaling of these basic templates (Stone and Lundberg, 1996). The observation of limited variations in tongue configurations across a variety of phonemes is consistent with motor control theories that rely on neuromuscular synergies. Synergies, in theory, simplify the task of movement control from the central nervous system by reducing the number of independent elements that need to be regulated across a variety of motor tasks (see Bernstein, 1967; Turvey *et al.*, 1978). For the present discussion, we adopt the definition of synergy proposed by Saltiel *et al.*, (2001) as ''a fixed group of muscles whose activity scales together'' (p. 1).

If synergies, as previously defined, were evoked for lingual motion during speech, then we would expect lingual phonemes to be primarily distinguished by the relative level of excitation across a shared set of muscles. Moreover, to the extent that these putative modulations of muscle excitation map to articulatory displacement, we would also expect that some phonemes are primarily distinguished by the amplitude scaling of a common movement pattern. Although synergies are central to many prevailing theories of motor control, including those related to speech production (Browman and Goldstein, 1989; Kelso *et al.*, 1986), empirical verification of their physical manifestation has proven to be challenging and requires further work (Macpherson, 1991; Perkell, 1997).

3. Speech versus swallowing

Despite the fact that the average coupling profile for swallowing was similar in shape to that for velars, swallowing occupied a unique region of the MDS space. This result may be accounted for, in part, by the large variability across participants that was observed for swallowing covariance values [Fig. 3(b)]. The vertical time histories observed for lingual pellets during swallowing were distinct from those observed during speech. During swallowing, lingual pellet motions were initiated sequentially starting at the anterior T1 and ending at the posterior T4. This observation is consistent with reports describing tongue motion during swallowing to propagate in a wavelike manner from apex to dorsum (Bosma *et al.*, 1990; Martin, 1991). In contrast, the pellet motions during speech appeared to be relatively synchronous (for example, see Figs. 1(b) and (e)]. Based on these observations, we suspect that the high, positive covariance values observed during swallowing were not the result of greater movement coupling, but instead were due to the overlapping of periods of stillness that occurred when each pellet assumed a relatively stationary position after achieving palatal closure. This observation suggests that a time-lagged cross-correlational analysis would be a more appropriate method for describing the sequential movement patterns characteristic of swallowing than the zero-lag method used in this investigation.

B. Functional movement independence in mid-sagittal tongue

The degree of movement independence, as measured by covariance, varied considerably among pellet pairs. Of all the adjacent pellet pairs, the anterior pair (i.e., T1×T2) appeared to exhibit the greatest across-task variation in coupling. This observation is consistent with the expectation that speakers have the finest control over the tongue's distal regions. Interestingly, morphologic differences between the anterior and posterior tongue musculature have been reported in primates. DePaul and Abbs (1996) reported that in the Macaca fascicularis, type IIA fibers were predominant in the apex of the tongue, with the number of type I fibers increasing posteriorly. These authors speculated that the different fiber types may be activated separately, with the type IIA fibers associated with rapid tongue tip movements and the type I fibers associated with the relatively slower movements of the posterior tongue.

The distribution for covariance values for some pellet pairs (i.e., T2×T3, T3×T4, T2×T4) formed several primary clusters, which suggest that the relative motions between these regions are, in practice, limited. For example, the covariance values for T2×T4 formed two primary clusters, one representing back sounds (positive coupling) and one representing front consonants (negative coupling). Similarly, covariance values associated with T3×T4 and T2×T3 formed two primary clusters that were restricted in range: one cluster representing weak coupling for more anterior tongue consonants and the other cluster representing strong coupling for more posterior tongue consonants. The observation of strong coupling within a restricted range for more posterior consonants is consistent with the extreme convex posturing of the tongue dorsum during back consonants, which has been previously described by other investigators (Perkell, 1969; Stone and Lundberg, 1996). Collectively, these findings reveal that during back-raising gestures, movements of posterior pellets (e.g., T4) were highly coupled with those of more anterior pellets (e.g., T1, T2, T3), whereas during front-raising gestures, anterior pellets exhibited functional independence from more posterior pellets. These observed tendencies in lingual surface motion might be interpreted to represent a general feature of tongue motion for speech: large amplitude movement of anterior tongue can be independent from movement of posterior regions, but large amplitude movements of posterior regions are not independent from movement of anterior regions.

C. Across-speaker variation

In the present investigation, *coupling profiles* were examined to assess across-speaker variation in tongue movement patterns for very basic speech utterances. There have been relatively few comprehensive reports of across-speaker differences in tongue kinematics largely because the instrumentation for tracking lingual kinematic data is expensive, as are the work hours required for data reduction (hence the impetus for the XRMB database; see Westbury, 1994). Consequently, most investigations of tongue function have studied seven or fewer participants (e.g., Guenther *et al.*, 1999;

Harshman *et al.*, 1977; Hoole, 1999; Kent and Moll, 1972; Lofqvist and Gracco, 1994; Perkell and Nelson, 1985; Stone, 1990). The few existing investigations that have studied tongue kinematics in a large number of participants have reported large differences across speakers (Hashi *et al.*, 1998; Westbury *et al.*, 1998). Based on these findings, and the widely reported kinematic changes with regard to speech rate and context, we anticipated observing considerable across-participant differences in *coupling profiles*, even for the relatively basic speech utterances studied. The expectation for across-participant differences in tongue movement patterns was further strengthened by factors such as individual differences in vocal tract anatomy and pellet placement. Of course, differences in coupling profiles across phonemes will be directly affected by differences in movement amplitude across participants. Vocal tract size may be one factor that contributes to across-speaker differences in the magnitude of displacement (Kuehn and Moll, 1976). However, a direct relationship between vocal tract size and articulatory displacement is not supported by experiments showing that young children exhibit similar articulatory displacements to adults (Goffman and Malin, 1999; Smith and Gartenberg, 1984). Knowledge of how individual differences in vocal tract morphology influence articulatory strategies is surprisingly limited.

Despite the expectation for across-speaker differences, the present findings suggest that covariance is at the appropriate level of analysis for capturing across-speaker similarities in tongue movement patterns. Similarities across-participants were most strongly supported by the phoneme effects observed in the repeated measures MANOVA. Because this analysis statistically controlled for systematic subject effects on covariance values, it was able to detect across-participant similarities in the shape of coupling profiles. In contrast, across participant differences were suggested by the data in Figs. 3(b) and 4(b), where covariance values appeared to vary considerably across participants for most contexts, as indicated by the high standard deviations and weirdness values, respectively. Some of these differences might be explained by systematic differences in movement amplitude. As a whole, the results of the different levels of analysis suggest that although speakers exhibited a wide degree of variation in their covariance values for a given phoneme, their overall profile shapes were similar.

D. Putative mechanisms for observed tendencies in lingual motion

Some of the present findings may represent biomechanical constraints on tongue movements. For example, mechanical linkages between contiguous tongue regions may have accounted for the relatively high maximum coupling observed between adjacent pellets. This possibility was also suggested by Dembowski and colleagues (1998), who reported that the strength of pairwise correlations of pellet-point positions decreased as the distance between their locations on the tongue increased. Moreover, the consistently high levels of movement coupling observed across the entire tongue during back consonants may be the result of extrinsic muscle activity (e.g., styloglossus), which simultaneously raises the tongue body and dorsum toward the palate (MacNeilage and Sholes, 1964).

The basis for the regular negative coupling observed between anterior and posterior tongue during front consonants is not obvious. One possibility is that speakers produce this lowering gesture to provide clearance for the ensuing air stream posterior to the primary site of constriction. This gesture may also be the result of (a) a motor strategy in which the posterior muscles of the tongue are stiffened to form a stable support for more anterior regions, (b) a coarticulation effect from surrounding vowels (Stone, 1990), and (c) a redistribution of volume within the tongue (Smith and Kier, 1989). The latter possibility considers the hydrostatic mechanisms in the tongue by which depression of the dorsum and root could potentially facilitate anterior elevation through shifting the volume within the tongue anteriorly.

Some of the observed across-pellet differences in coupling may be also explained, in part, by pellet placement effects and palatal constraints on lingual mobility. For example, alveolars may have exhibited lower covariance values than did palatoalveolars because T1 (the most anterior pellet) was located posterior to the tongue tip, which is the primary location of constriction for the alveolars. Moreover, maximum coupling as represented by covariance may have been greater for posterior tongue than for anterior tongue because the high-arching, posterior palate affords more space to move than does the downward-sloping, anterior palate.

E. Design limitations and interpretive caveats

Several aspects of our experimental design should be considered when attempting to generalize the present findings to all tongue behavior. Specifically, a greater diversity of lingual movement patterns may have been observed if vowel context was varied or if more natural speech stimuli were used and if observations of tongue motion were not restricted to the vertical dimension of the mid-sagittal plane. For example, Stone (1990) reported that the oppositional movement between anterior and posterior tongue regions (i.e., negative coupling) during alveolars was somewhat vowel context dependent. Moreover, previous research has shown some consonants to be distinguished by tongue maneuvers outside the mid-sagittal plane such as palatal bracing (Stone, 1990) and cross-sectional movements for linguapalatal sounds (Stone *et al.*, 1992).

In addition, several issues should be considered regarding interpretive limitations of tongue and lower lip data that are referenced relative to the mandibular reference plane. Specifically, the interpretation that this transformation (i.e., Formula 1) yields tongue positions that are independent from the motion of jaw becomes particularly challenging during instance when the tongue is stationary while the jaw is moving. In this case, the kinematic traces of tongue pellets will reflect the movement characteristics of the jaw more than that of the tongue. It is likely that the composition of our utterances minimized this effect because the low vowel context of each VCV utterance encouraged movement of the jaw for both oral opening and closing. Interpreting lingual kinematic traces in the mandibular reference plane will also be

challenged if jaw motion does not uniformly influence the motion of different tonque pellets. In this case, the positions of pellets whose motions are not tightly coupled to the jaw's will be effectively ''overcorrected.'' At present, the extent of this effect is not known. Finally, this transformation does not account for the inertial forces that jaw motion imposes on the tongue and lower lip. The effects of these forces, however, are not of particular interest to the present study because it is principally concerned with characterizing tongue-surface movement patterns rather than the forces that generate them.

F. Summary and future directions

In summary, the coupling profile analysis effectively captured probable tongue movement patterns for distinguishing different places of articulation and speech from swallowing. In general, pellet-motion coupling patterns varied predictably with place of articulation. This analysis revealed four basic patterns of lingual coordination in the mid-sagittal tongue that could potentially be elaborated on to form further distinction.

The usefulness of covariance as a quantitative means for describing basic lingual function is pending on additional work directed toward evaluating the extent to which the observed trends in tongue-surface coupling apply to less constrained speech tasks. For instance, it is not evident how surrounding vowels, speech rate, and intensity influence coupling profiles. Nonetheless, the present level of success in capturing across-speaker tendencies in tongue-surface movement patterns suggests that with further development, *covariance* might be a useful metric for gauging the extent of disordered tongue function. For example, the present analysis might be particularly well suited for quantifying the relative increases or decreases in constraints imposed by the neuromotor system that may underlie neurologically impaired tongue function (e.g., the decreased inhibition by the neuromotor system associated with Huntington's Chorea or the decrease excitation by the neuromotor system associated with Parkinson's).

ACKNOWLEDGMENTS

We are very grateful to Gary Weismer, Erin Wilson, Rita Patel, and two anonymous reviewers for helpful feedback on earlier versions of this manuscript. We would also like to thank Steven Pittelko for his assistance with data analysis, Dave Wilson for programming assistance, Doris Kistler for statistical consulting, and Carl Johnson and John Westbury for generating and providing access to the XRMB database. This research was supported in part by Research Grant No. R03 DC4643-01 from the National Institute on Deafness and Other Communication Disorders.

[1]Throughout this manuscript, the degree of functional movement independence refers to the degree of movement decoupling that is observed for different tongue regions across a variety of tasks (e.g., different speech sounds and swallowing). The identification of a high degree of functional movement independence among different tongue regions cannot be taken as direct evidence of independence of neural control for these regions because tongue-surface movement patterns during swallowing and speech will be determined by the combined influences of task demands, neural innervation patterns, palatal shape, and biomechanic architecture and tissue linkages.

Bernstein, N. (**1967**). *The Coordination and Regulation of Movement* (Pergamon, Oxford).

Bosma, J. F., Hepburn, L. G., Josell, S. D., and Baker, K. (**1990**). ''Ultrasound demonstration of tongue motions during suckle feeding,'' Dev. Med. Child Neurol. **32**, 223–229.

Browman, C., and Goldstein, L. (**1989**). ''Articulatory gestures as phonological units,'' Phonology **6**, 201–251.

Dembowski, J., Lindstrom, M. J., and Westbury, J. R. (**1998**). ''Articulator point variability in the production of stop consonants,'' in *Neuromotor Speech Disorders: Nature, Assessment, and Management*, edited by M. P. Cannito, K. M. Yorkston, and D. R. Beukelman (Brookes, Baltimore, MD), pp. 27–46.

DePaul, R., and Abbs, J. H. (**1996**). ''Quantitative morphology and histochemistry of intrinsic lingual muscle fibers in Macaca fascicularis,'' Acta Anat. (Basel) **155**, 29–40.

Gibbon, F. E. (**1999**). ''Undifferentiated lingual gestures in children with articulation/phonological disorders,'' J. Speech Lang. Hear. Res. **42**, 382–397.

Goffman, L., and Malin, C. (**1999**). ''Metrical effects on speech movements in children and adults,'' J. Speech Lang. Hear. Res. **42**, 1003–1015.

Green, J. R., Moore, C. A., Higashikawa, M., and Steeve, R. W. (**2000**). ''The physiologic development of speech motor control: Lip and jaw coordination,'' J. Speech Lang. Hear. Res. **43**, 239–255.

Guenther, F. H., Espy-Wilson, C. Y., Boyce, S. E., Matthies, M. L., Zandipour, M., and Perkell, J. S. (**1999**). ''Articulatory tradeoffs reduce acoustic variability during American English /r/ production,'' J. Acoust. Soc. Am. **105**, 2854–2865.

Hardcastle, W. J. (**1976**). *Physiology of Speech Production* (Academic, London).

Hardcastle, W. J., Gibbon, F. E., and Jones, W. (**1991**). ''Visual display of tongue-palate contact: Electropalatography in the assessment and remediation of speech disorders,'' Br. J. Communi. Disorders **26**, 41–74.

Hardcastle, W. J., Morgan-Barry, R. A., and Clark, C. J. (**1987**). ''An instrumental phonetic study of lingual activity in articulation-disordered children,'' J. Speech Hear. Res. **30**, 171–184.

Harshman, R., Ladefoged, P., and Goldstein, L. (**1977**). ''Factor analysis of tongue shape,'' J. Acoust. Soc. Am. **62**, 693–327.

Hashi, M., Westbury, J. R., and Honda, K. (**1998**). ''Vowel posture normalization,'' J. Acoust. Soc. Am. **104**, 2426–2437.

Hoole, P. (**1999**). ''On the lingual organization of the German vowel system,'' J. Acoust. Soc. Am. **106**, 1020–1032.

Kelso, J. A. S., Saltzman, E. L., and Tuller, B. (**1986**). ''The dynamical perspective on speech production: Data and Theory,'' J. Phonetics **14**, 29–59.

Kent, R., and Moll, K. (**1972**). ''Cinefluorographic analyses of selected lingual consonants,'' J. Speech Hear. Res. **15**, 453–473.

Kent, R. D., Netsell, R., and Bauer, L. L. (**1975**). ''Cineradiographic assessment of articulatory mobility in the dysarthrias,'' J. Speech Hear Disord. **40**, 467–480.

Kuehn, D. P., and Moll, K. L. (**1976**). ''A cineradiographic study of VC and CV articulatory velicities,'' J. Phonetics **4**, 303–320.

Ladefoged, P. (**2001**). *A Course in Phonetics*, 4th ed. (Harcourt Brace, Fort Worth).

Lofqvist, A., and Gracco, V. L. (**1994**). ''Tongue body kinematics in velar stop production: influences of consonant voicing and vowel context,'' Phonetica **51**, 52–67.

MacNeilage, P., and Sholes, G. (**1964**). ''An electromyographic study of the tongue during vowel production,'' J. Speech Hear. Res. **7**, 209–232.

Macpherson, J. M. (**1991**). ''How flexible are muscle synergies?'' in *Motor Control: Concepts and Issues*, edited by D. R. Humphrey and H-J. Freund (Wiley, New York), pp. 33–47.

Maeda, S. (**1990**). ''Compensatory articulation during speech: Evidence from the analysis and synthesis of vocal-tract shapes using an articulatory model,'' in *Speech Production and Speech Modeling*, edited by W. J. Hardcastle and A. Marchal (Kluwer, Dordrecht), pp. 131–149.

Martin, R. E. (**1991**). ''A Comparison of Lingual Movement in Swallowing and Speech Production,'' Ph.D. dissertation, University of Wisconsin–Madison.

Mermelstein, P. (**1973**). ''Articulatory model for the study of speech production,'' J. Acoust. Soc. Am. **53**, 1070–1082.

Milenkovic, P. (**2000**). ''Time-frequency analysis for 32-bit windows (computer program),'' University of Wisconsin–Madison.

Nicolosi, L., Harryman, E., and Kresheck, J. (**1996**). *Terminology of Com-*

munciative Disorders: Speech-Language-Hearing, 4th ed. (Lippincott, Williams, & Wilkins, Baltimore, MD).
Öhman, S. E. G. (**1967**). ''Numerical model of coarticulation,'' J. Acoust. Soc. Am. **41**, 310–320.
Perkell, J. S. (**1969**). ''Physiology of Speech Production: Results and Implications of a Quantitative Cineradiographic Study,'' Research Monograph No. 53 (MIT, Cambridge, MA).
Perkell, J. S. (**1997**). ''Articulatory processes,'' in *The Handbook of Phonetics Sciences*, edited by W. Hardcastle and J. Laver (Blackwell, Cambridge, MA), pp. 333–370.
Perkell, J. S., and Nelson, W. L. (**1985**). ''Variability in production of the vowels /i/ and /a/,'' J. Acoust. Soc. Am. **77**, 1889–1895.
Saltiel, P., Wyler-Duda, K., D'Avella, A., Tresch, M. C., and Bizzi, E. (**2001**). ''Muscle synergies encoded within the spinal cord: evidence from focal intraspinal NMDA iontophoresis in the frog,'' J. Neurophysiol. **85**, 605–619.
Sanguineti, V., Laboissière, R., and Payan, Y. (**1997**). ''A control model of human tongue movements in speech,'' Biol. Cybern. **77**, 11–22.
Smith, B. L., and Gartenberg, T. E. (**1984**). ''Initial observations concerning development characteristics of labio-mandibular kinematics,'' J. Acoust. Soc. Am. **75**, 1599–1605.
Smith, K. K., and Kier, W. M. (**1989**). ''Trunks, tongues, and tentacles: Moving with skeletons of muscles,'' Am. Sci. **77**, 29–35.
Stevens, K. (**1989**). ''On the quantal nature of speech,'' J. Phonetics **17**, 3–46.
Stone, M. (**1990**). ''A three-dimensional model of tongue movement based on ultrasound and x-ray microbeam data,'' J. Acoust. Soc. Am. **87**, 2207–2217.
Stone, M., and Lundberg, A. J. (**1996**). ''Three-dimensional tongue surface shapes of English consonants and vowels,'' J. Acoust. Soc. Am. **99**, 3728–3737.
Stone, M., Faber, A., Raphael, L., and Shawker, T. (**1992**). ''Cross-sectional tongue shapes and linguopalatal contact patterns in [s], [sh], and [l] syllables,'' J. Phonetics **20**, 253–70.
Takemoto, H. (**2001**). ''Morphologic analysis of the human tongue musculature for three-dimensional modeling,'' J. Speech Hear. Res. **44**, 95–107.
Turvey, M. T., Shaw, R. E., and Mace, W. (**1978**). ''Issues in theory of action: degrees of freedom, coordinative structures and coalitions,'' in *Attention and Performance*, edited by J. Requin (Hillsdale, Erlbaum), pp. 557–595.
Westbury, J. R. (**1991**). ''The significance and measurement of head position during speech production experiments using the x-ray microbeam system,'' J. Acoust. Soc. Am. **89**, 1782–1791.
Westbury, J. R. (**1994**). *X-ray Microbeam Speech Production Database User's Handbook* (Univ. of Wisconsin, Madison, WI).
Westbury, J. R., Hashi, M., and Lindstrom, M. J. (**1998**). ''Differences among speakers in lingual articulation for American English /ɹ/,'' Speech Commun. **26**, 203–226.
Westbury, J. R., Lindstrom, M. J., and McClean, M. D. (**2002**). ''Tongues and lips without jaws: A comparison of methods for decoupling speech movements,'' J. Speech Hear. Res. **45**, 651–662.

Effects of prosodic boundary on /aC/ sequences: articulatory results

Marija Tabain[a)]
Institut de la Communication Parlée, Institut National Polytechnique de Grenoble, 46, av. Félix Viallet, 38031 Grenoble, France

(Received 3 January 2002; accepted for publication 10 February 2003)

This study presents EMA (electromagnetic articulography) data on articulation of the vowel /a/ at different prosodic boundaries in French. Three speakers of metropolitan French produced utterances containing the vowel /a/, preceded by /t/ and followed by one of six consonants /b d g f s ʃ/ (three stops and three fricatives), with different prosodic boundaries intervening between the /a/ and the six different consonants. The prosodic boundaries investigated are the Utterance, the Intonational phrase, the Accentual phrase, and the Word. Data for the Tongue Tip, Tongue Body, and Jaw are presented. The articulatory data presented here were recorded at the same time as the acoustic data presented in Tabain [J. Acoust. Soc. Am. **113**, 516–531 (2003)]. Analyses show that there is a strong effect on peak displacement of the vowel according to the prosodic hierarchy, with the stronger prosodic boundaries inducing a much lower Tongue Body and Jaw position than the weaker prosodic boundaries. Durations of both the opening movement into and the closing movement out of the vowel are also affected. Peak velocity of the articulatory movements is also examined, and, contrary to results for phrase-final lengthening, it is found that peak velocity of the opening movement into the vowel tends to increase with the higher prosodic boundaries, together with the increased magnitude of the movement between the consonant and the vowel. Results for the closing movement out of the vowel and into the consonant are not so clear. Since one speaker shows evidence of utterance-level articulatory declension, it is suggested that the competing constraints of articulatory declension and prosodic effects might explain some previous results on phrase-final lengthening. [DOI: 10.1121/1.1564013]

PACS numbers: 43.70.Fq [AL]

I. INTRODUCTION

Work within the framework of articulatory prosody examines the strategies used by speakers at the supralaryngeal level to delineate prosodic boundaries. Much work in articulatory prosody has been based on EPG (electropalatographic) data, in order to study consonant articulations (Fougeron and Keating, 1997; Fougeron, 2001; Cho and Keating, 2001; Keating *et al.*, in press). Studies that have used EMA (electromagnetic articulography) have focused mainly on bilabial stops or interarticulator timing (Byrd and Saltzman, 1998; Byrd, 2000; Byrd *et al.*, 2000). It is the purpose of the present paper to examine primarily intraarticulator effects of the prosodic hierarchy on /aC/ sequences, based on EMA data for the Jaw, Tongue Body, and Tongue Tip.

We begin with an overview of the main work that has been carried out in the area of articulatory prosody, and move on to a discussion of the prosody of French, the language under examination here.

A. Supralaryngeal correlates of linguistic accent

In an EPG study using reiterations of the syllable /no/ based on English mathematical expressions, Fougeron and Keating (1997) found greater contact for /n/ at the beginning of a prosodic domain (and less contact for /o/ at the end of the previous domain) the greater the strength of the prosodic boundary. The four prosodic domains examined were (in order of increasing strength) the phonological Word,[1] the Phonological (or intermediate) phrase, the Intonational phrase, and the Utterance [these categories following Beckman and Pierrehumbert (1986)]. In general, three or four levels were distinguished. However, speakers differed as to what levels were distinguished. For /n/, for example, of three speakers examined, two distinguished the Syllable from the Word, two distinguished the Word from the Phonological phrase, and three distinguished the Phonological phrase from some higher level, either the Intonational phrase or the Utterance. Fougeron and Keating also found that the acoustic duration of /n/ was affected by prosodic position. Like linguo-palatal contact, duration increased as the prosodic boundary became stronger; however, duration and linguo-palatal contact were only weakly correlated, since more levels were distinguished by duration. Fougeron and Keating argued that there was an articulatory ''strengthening'' at the edges of prosodic domains, in particular, between the vowel which ends one domain, and the consonant which begins another, as the strength of the prosodic boundary increased.

So far, articulatory prosody effects such as these have been described for at least five languages: English (Fougeron and Keating, 1997; Byrd and Saltzman, 1998; Byrd, 2000; Cho, 2002); French (Fougeron, 2001); Korean (Cho and Keating, 2001); Tamil (Byrd *et al.*, 2000); and Taiwanese

a)Current address: Speech, Hearing and Language Research Centre & Macquarie Centre for Cognitive Science, Division of Linguistics and Psychology, Macquarie University, Sydney NSW 2109, Australia. Electronic mail: mtabain@maccs.mq.edu.au

(Keating *et al.*, in press). Fougeron (2001) observed articulatory strengthening of the domain-initial segment in French using EPG, nasal airflow, and acoustic measures. As observed for /n/ in English by Fougeron and Keating (1997), the stop consonants in French show overall greater contact at higher prosodic boundaries, with the alveolars having greater alveolar as well as lateral contact, and the velars having greater and more forward contact. /s/ shows fewer effects of the prosodic boundary [in line with its resistance to coarticulatory strategies—cf. Recasens (1999)]. Fougeron also found that nasal airflow is *lesser* at higher prosodic domains: although this result may seem surprising at first, it can perhaps be explained by the fact that the nasal becomes more ''stoplike'' at the higher prosodic boundaries, and is hence maximally distinct from surrounding vowels. Finally, Fougeron found that vowels are more likely to be glottalized at stronger prosodic boundaries, a result in line with Dilley *et al.*'s (1996) results (a study which was not explicitly couched in terms of articulatory prosody, but which described results very much in line with articulatory prosody).

Cho and Keating (2001) examined Korean alveolar stop and nasal consonants. Their results were similar to Fougeron's (2001) results, with the exception of their VOT data, which showed significantly greater values for higher prosodic boundaries. Fougeron, by contrast, did not find any significant results for VOT values, possibly because VOT is quite short for both the unvoiced and the voiced stops in French. Cho and Keating also found that the (acoustic) nasal energy minimum was *lesser* in the higher prosodic boundaries. This was in complement to Fougeron's results on nasal airflow in French. Thus, both articulatory and acoustic measures suggest that nasals become less nasal, and therefore less vowellike and more stoplike, at higher prosodic boundaries. Cho and Keating found no significant effect of prosodic boundary on rms energy.

While the underlying articulatory strategies involved in producing these effects are not clear, the end result is (presumably) enhancement of the speech signal for the listener, who is perhaps given some extra cues to the strength of the prosodic boundary in the signal.

Whereas the studies mentioned so far have looked at consonants using EPG and some acoustic measures, work by Byrd and colleagues has used EMA to look at certain aspects of vowel–consonant coordination at prosodic boundaries, in particular at lip movement in /V #$C_{BILABIAL}$/ sequences, where # denotes a prosodic boundary. Byrd and Saltzman (1998) examined lip movements in the sequence /mə # m/. They examined five prosodic boundaries (Utterance, Vocative, List, Word, and Syllable) and found that both the magnitude and the duration of the opening lip movement into the vowel, as well as of the closing movement into the second /m/, increased with the stronger prosodic boundaries (although the effect was more reliable for the opening movement than for the closing movement). Byrd *et al.* (2000) examined tongue tip and upper lip movement in Tamil /m # n/ and /n # m/ sequences, and found less overlap of gestures at the higher prosodic boundaries than at the lower prosodic boundaries. Byrd (2000) examined the tongue raising gesture for the vowel sequence /ə/ to /i/ in relation to an intervening /m/ in the sequence /ə # mi/. Duration results at the prosodic boundary were consistent with previous results; however, for two of the three speakers, there was no consistent difference in relative /# CV/ timing according to prosodic boundary (the remaining speaker showed relatively later peak velocities for the vowel /i/ following a stronger prosodic boundary). These results are consistent with Fougeron and Keating's (1997) results in that prosodic boundary effects occur precisely at the edges of the boundary, and not internal to the prosodic unit.

It should be observed that these results in articulatory prosody are not completely unlike results on strategies used by speakers to mark stressed syllables in speech. For example, de Jong (1995) presents consonant data showing that stressed syllables have ''tighter'' closures than unstressed syllables, and Harrington *et al.* (1995) present vowel data showing that unstressed syllables are ''truncated'' versions of stressed syllables, with shorter duration and amplitude of movement, but similar peak velocities. For this reason, prosodic accent effects on speech could potentially be confused with effects of lexical stress. This becomes apparent if one considers that in studies of lexical stress, when the target word is uttered in isolation, effects of lexical stress may be compounded with effects of the nuclear pitch accent (Harrington *et al.*, 1998), with an end effect of much greater hyperarticulation of speech segments. As Harrington *et al.* (1998) showed, differences between primary-stressed and secondary-stressed syllables are greatly reduced if the effects of pitch accent are removed. This consideration is of importance to the present study, since French is a language in which lexical stress and prosodic accent cannot be combined, given that French has only prosodic accent, and no lexical stress. Therefore, differences in articulatory strategies at prosodic boundaries for the jaw and tongue, for example, must be due to the prosodic boundary itself, rather than to a combination of the boundary with the intrinsic realizations of lexical stress[2] (however, see the section ''Prosodic accent in French'' below for some qualifications regarding lexical stress and prosodic ''stress'').

It is perhaps worth noting that Fletcher (1991) has shown that French has similar effects of rhythm and final lengthening in accentual domains as do ''stress-timed'' languages such as English [syllables at the edges of domains show greater lengthening than do syllables internal to the domain—cf. Turk and Sawusch (1996)]. For this reason, it is expected that accentual effects on supralaryngeal articulation will be similar in French and English.

The following section contains a brief account of the prosodic structure of French.

B. Prosodic accent in French

In French, words do not carry lexical stress, but they can attract prosodic accent at the sentence level. Following Fougeron and Jun (1998), the prosodic structure of French is based on the accentual phrase (AP), which is dominated by the intonational phrase (IP).

According to Fougeron and Jun, the AP has the underlying tonal representation /L Hi L H*/, with a more common phonetic realization being (LH*) [their approach is based on

Pierrehumbert (1980); Beckman and Pierrehumbert (1986), and subsequent work]. The initial high tone, Hi, has been described as the peak of the ''accent secondaire;'' and the final high tone, H*, has been described as the peak of the ''accent primaire.'' The H* is realized on the phrase-final full syllable. In neutral utterances, the Hi, when it appears, is usually shorter and has a lower *F*0 value than the following H*. In these cases it is not considered to have a pitch accent. However, in producing a focused word, the Hi is often promoted to pitch accent status. As regards the L tone, it is realized on the syllable preceding the H tone syllable. The reader is referred to Jun and Fougeron (2000) for further discussion of the status of Hi and H*, respectively, as well as other issues of debate in the study of French prosody.

The IP is marked by a major continuation rise (H%) or fall (L%) and also by a significant final lengthening, often followed by a pause.[3]

It has already been mentioned that French has no lexical stress, and that effects of the prosodic hierarchy cannot therefore be confused with effects of lexical stress. However, as just described, the AP is characterized by the presence of a pitch accent on the final syllable of the phrase. For this reason, placement of pitch accent and prosodic structure interact in French: the presence of an AP boundary, or any higher boundary, denotes the presence of a phrase-final pitch accent. Nevertheless, it is true that effects of *lexical* stress, rather than prosodic ''stress,'' cannot be confounded with effects of the prosodic hierarchy, and for this reason French is an important contrast to English in the study of articulatory prosody.

In the present study it is assumed that an Utterance dominates an Intonational-phrase level, which dominates an Accentual-phrase level, which in turn dominates a Word level.

C. Aims

Given the above discussions, a major aim of this study is to build on results from previous studies by looking at effects of articulatory prosody on different /aC/ sequences using EMA. Since previous studies had used EPG, often with reiterant speech (e.g., Fougeron and Keating, 1997), or had only looked at bilabial consonants using EMA (e.g., Byrd and Saltzman, 1998), the present study aims to examine various consonants, in particular lingual consonants, using EMA with real sentences instead of reiterated speech.

In particular, attention will be paid to the different articulators which contribute to the production of the vowel, in case they show differing patterns. This approach was adopted based on results presented in Harrington *et al.* (2000) which showed that the jaw and the tongue adopt apparently contradictory strategies in the articulation of stressed /i/—even though both the tongue and the jaw strategies are phonologically well motivated. Using as their point of departure the fact that the vowel /a/ becomes lower (and hence, due to a lower jaw position, more ''sonorous'' as well as more peripheral) in a stressed syllable, Harrington *et al.* examined the vowel /i/ in stressed versus unstressed syllables. Their motivation was the fact that a more peripheral vowel and a more sonorous vowel are less compatible in the case of a high vowel than in the case of a low vowel (since a more peripheral /i/ involves a greater constriction in the oral cavity, and hence reduces sonority). Harrington *et al.* found that speakers attempt to make the /i/ more peripheral by fronting the tongue, as well as making it more sonorous by lowering the jaw. It is therefore clear that both the increased sonority and increased peripherality strategies, which are on the surface contradictory, may be implemented by a single speaker.

These results are relevant to the present study because acoustic data presented in Tabain (2003) suggested that there may be an effect of articulatory declension (Vayra and Fowler, 1992; Krakow *et al.*, 1994; Johnson and Martin, 2001) on the /a/ vowel at the Utterance boundary for one speaker. Briefly, articulatory declension predicts that supralaryngeal articulations become *hypo*-articulated the later they occur in an utterance, whereas articulatory prosody (as discussed above) predicts that supralaryngeal articulations are *hyper*-articulated at the beginnings and ends of utterances. For instance, in the one-word utterances in Creek examined by Johnson and Martin (2001), the acoustic vowel space is larger (and hence, the vowels more peripheral) in the first syllable than in the last syllable of the word. At an articulatory level, this phenomenon has been described for velum position in oral stop consonants by Krakow *et al.* (1994), where the velum position is lower at the ends of utterances; and for vowel articulations by Vayra and Fowler (1992), where the /a/ vowel is higher at the ends of utterances (although results for /i/ were less clear).

Articulatory declension only applies in the spatial domain, and, for this reason, it is expected to have an effect on the consonant or vowel peak displacements, rather than on durations. Articulatory prosody, by contrast, describes effects both in the spatial and temporal domains, and would therefore have effects on both duration and on peak displacement. Furthermore, articulatory declension relates exclusively to the Utterance boundary, whereas articulatory prosody makes predictions about other kinds of boundaries as well. [Vayra and Fowler (1992) make the important point that the phenomenon of articulatory declension occurs at the level of the Utterance, rather than the Word for example, since this effect is often observed in isolated words.] Since the predictions made for the Utterance boundary by articulatory declension are contrary to those made by articulatory prosody, it is possible that different articulators may show different effects, as Harrington *et al.* (2000) observed in their study. For this reason, Jaw, Tongue Tip, and Tongue Body articulators will all be examined for different aspects of the /a/ vowel production.

In order to provide a basic description of the /aC/ sequences under study here, the following will be examined: vowel and consonant durations; percentage vowel duration of the VC syllable (this measure is used to examine whether the vowel or the consonant is more affected by prosodic boundary—it is expected that both vowel and consonant duration will increase with the strength of the prosodic boundary, but it is not clear which will be relatively more affected); peak displacements of the vowel and consonants;[4] magnitude, duration, and peak velocities of the opening and closing movements (into the /a/ and out of the /a/ respectively); and

TABLE I. Location of the transducers on the Tongue Tip and Tongue Back for each speaker. Magnitude from the tip of the tongue is given in cm.

Speaker	Tip	Back
AV (female)	0.85	4.76
CV (male)	1.25	5.18
GR (male)	1.04	4.78

pathlength of the tongue movement during consonant closure.

The measures relating to movement perhaps require further explanation of hypotheses. Following various studies by Beckman, Edwards, and Fletcher (Beckman and Edwards, 1990; Edwards *et al.*, 1991; Beckman *et al.*, 1992), it is expected that at the ends of stronger prosodic boundaries, articulatory movements will be greater in magnitude and duration, and that peak velocity will be concomitantly slower.

The measure of tongue pathlength during consonant closure (cf. Lofqvist, 1999) is included in order to further explore the relationship between the vowel and the consonant, since if the vowel is reduced more in time than the consonant, it is possible that much of the vowel movement occurs during consonant closure.

In sum, this study aims to provide a basic description of the articulation of /aC/ sequences at different prosodic boundaries in French, and to compare the results to certain previous results described in the literature.

II. METHOD

A. Speakers, stimuli, and recordings

Three native speakers of metropolitan French (two male—CV and GR—and one female—AV) were recorded in a sound-treated room. Articulatory (EMA—electromagnetic articulography) and acoustic data were recorded simultaneously and time-synchronized. Details on the collection and labeling of the acoustic data are given in Tabain (2003).

The Carstens Electromagnetic Articulograph at ICP in Grenoble was used for the collection of these data. Data were sampled at 200 Hz. EMA transducers were placed at four measurement points, and one reference point, for each speaker. The reference transducer was placed on the gums above the upper teeth. The four measurement points were the Jaw (transducer placed on the gums beneath the lower teeth); the Tongue Tip; the Tongue Back; and the Upper Lip (transducer placed just above the vermilion border of the upper lip). The two tongue transducers were attached with Ketac bond and the reference, Jaw, and Lip transducers were attached with Cyano. Table I gives the distances of the Tongue Tip and Tongue Back transducers from the tip of the tongue for each speaker, as measured when the tongue was slightly protruded.

Stimuli consisted of four sentences (based on Fougeron, 2001), each containing a prosodic boundary of interest between the fourth and fifth syllables. These sentences were (with the intended type of prosodic boundary listed in brackets as follows):

(1) Paul aime Tata. **B**aba les protège en secret. (Utterance)
(2) La pauv' Tata, **B**aba et Paul arriveront demain. (Intonational phrase)
(3) Tonton, Tata, **B**aba et Paul arriveront demain. (Accentual phrase)
(4) Paul et Tata **B**aba arriveront demain. (Word)

The consonant in bold was varied to be one of /b d g f s ʃ/, and the vowel following this consonant was varied to be one of /a i u y ø/ (where "ø" is the vowel found in the word "feu"). There was thus a total of 120 sentences (4 prosodic contexts×6 consonants×5 vowels). Two of the speakers [AV (female) and GR (male)] produced four repetitions of the corpus, giving a total of approximately 480 utterances. The second male speaker, CV, produced two repetitions of the corpus, giving a total of approximately 240 utterances.

Speakers were encouraged to produce a final intonation contour followed by a pause for the Utterance boundary, and a continuation contour while avoiding a pause for the Intonational boundary. Speakers tended to read the stimuli for the Accentual boundary as a list.

Present at each recording were a phonetically trained, fluent though not native, French speaker (the author), and two native French speakers, both involved in speech research. To verify that the correct intonation had been produced for each utterance, a ToBl-trained French speaker (not present at the recording) listened to a random selection of utterances from speaker AV, and found that the *F*0 traces and auditory effect were consistent with her knowledge of Accentual- and Intonational-phrases in French. Based on this judgment, and on the presence of the three speech researchers mentioned above at the recordings, it was felt that the intonational data from speakers CV and GR were also natural.

The current paper focuses on the relationship between the /a/ at the end of "Tata" and the three stop and three fricative consonants following. Although the vowel following the consonant was varied, with the aim of examining vowel-to-vowel coarticulation, these results will not be presented here. Data are therefore collapsed across the different vowels following the consonant.[5]

B. Labeling and analysis environment

Details on the acoustic labeling can be found in Tabain (2003).

The articulatory data were labeled by hand using EMU (Cassidy and Harrington, 2001) and the R statistical package (Ihaka and Gentleman, 1996).[6] All analyses of the data were carried out using the EMU database speech analysis system (Harrington *et al.*, 1993), interfaced with the R statistical package.

Prior to labeling, *x*- and *y*-data were smoothed using a Tukey's median filter with a window-width of three samples (i.e., 10 ms); values for the reference transducer were subtracted from values for the four movement transducers; and the resulting data were rotated according to the measured occlusal plane of the speaker. The kinematic signal was ex-

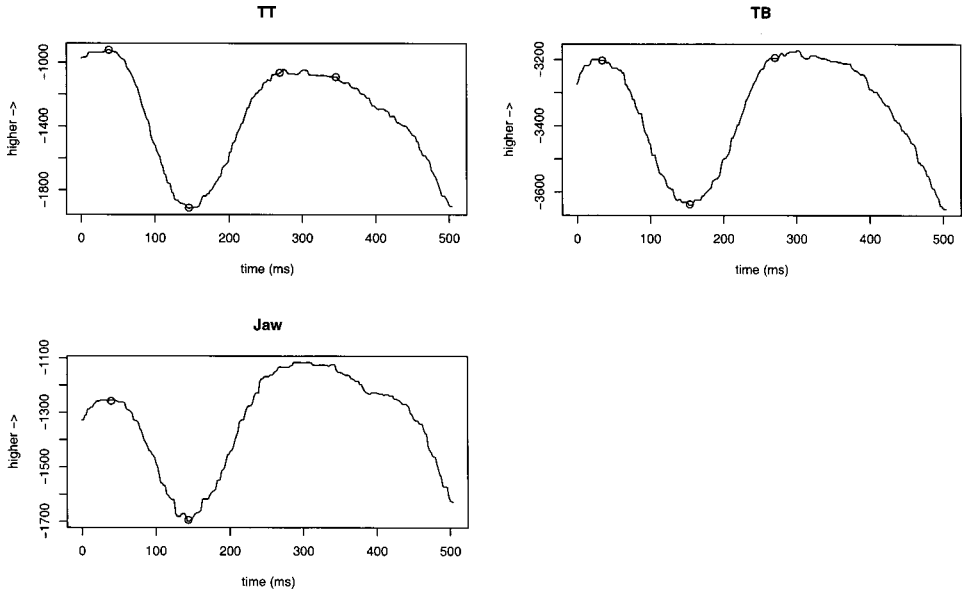

FIG. 1. Tongue Tip, Tongue Body, and Jaw data from the same token of the sequence /ta # s/, as spoken by speaker CV. The /a/ and the /s/ are separated by an Intonational-phrase boundary. Circles on each panel show the hand-marked measurement points. In each panel, the left-most point represents the maximum for the /t/, and the second point represents the /a/. In the TT panel, the third and final points represent the onset and offset of the closure for the /d/. Units on the *y*-axis are hundredths of a millimeter from the reference transducer.

amined from a point before the acoustic release of the second /t/ in ''Tata'' to a point after the acoustic offset of the consonant under investigation. All labeling of data was done in the *y* plane only (however, Jaw movement data are described in the *x*-*y* plane—see details below). Velocity was calculated as the first differential of this smoothed displacement signal, and this first differential was also smoothed using a Tukey's median filter.

It should be noted that measurements from the Upper Lip transducer were not used. This is primarily due to the influence of the vowel following the consonant, which was originally varied with the aim of studying vowel-to-vowel coarticulation (see details on stimuli above). These vowels varied in rounding, making lip data according to the prosodic boundary more difficult to interpret. Jaw data will therefore be used instead of Upper Lip data for the labial consonants. It is of course recognized that the Jaw is not the end articulator for the labial consonants, and that data for these consonants will therefore not be as reliable as data for the lingual consonants (for which Tongue Tip and Tongue Body data are available).

1. Definition of measures

Figure 1 shows an example of the labeling criteria. These Tongue Tip, Tongue Body, and Jaw data are taken from speaker CV's utterance of the sequence /ta # s/, where an intonational-phrase boundary occurs between the /a/ and the /s/. The labeled points are marked as circles, and are explained in the following paragraphs.

a. Duration and peak displacement. Duration and peak Displacement for the vowel and for the consonant were defined as follows (TT=Tongue Tip, TB=Tongue Body):

(i) Vowel Duration preceding a lingual consonant—/d g s ʃ/—was defined as the difference in time between the TB displacement maximum for /t/ (the first point in the top right panel in Fig. 1) and the TB displacement maximum for the consonant (third point in the top right panel of Fig. 1)—or the onset of TB closure in the case of /g/.

(ii) Vowel Duration preceding a labial consonant—/b f/—was defined as the difference in time between the TB maximum for /t/ and the Jaw maximum for the /b/ or /f/. (This approach was used for the labials because there was not always a TB closing movement for these consonants, since the vowel following the consonant varied.)

(iii) Consonant Duration was defined as the difference between the articulatory closure and release of the active articulator [TT in the case of /d s ʃ/ (the third and fourth points on the top left panel in Fig. 1), TB in the case of /g/, and Jaw in the case of /b f/].

(iv) Vowel peak Displacement in the *y*-plane was defined as the TB minimum for the vowel (second point in top right panel of Fig. 1). The Jaw minimum was also examined for the vowel (second point in bottom left panel of Fig. 1).

(v) Consonant peak Displacement was defined as the greater (''higher'' in articulatory terms) value of the closure and the release of the active articulator (TT in the case of /d s ʃ/, TB in the case of /g/, and Jaw in the case of /b f/). For example, in the top left panel of Fig. 1, the onset of the closure is slightly higher than the release of the closure (though of course not significantly), and this point was chosen as the peak displacement value.

b. Tongue Body Pathlength. The TB pathlength is calculated as the sum of the Euclidean distances in an *x*-*y* plane between each TB sample during consonant closure. Since the TB is the active articulator for /g/, these data are presented for the other five consonants only.[7]

Two sets of Movement data will be presented: data for the Opening movement from the /t/ into the /a/, and data for the Closing movement from the /a/ into the consonant. The following definitions apply:

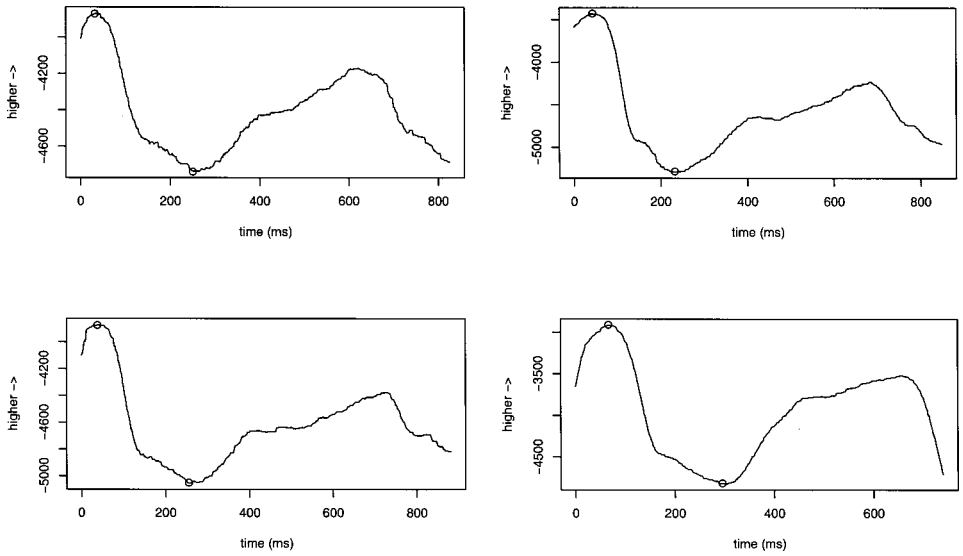

FIG. 2. Four tokens of the sequence /ta # ʃ/ as produced by speaker GR. The articulator shown is the Tongue Body. In each case, an Utterance boundary separates the /a/ and the /ʃ/. In each panel, circles represent (from left to right) the maximum for the /t/, and the minimum for the /a/. Units on the *y* axis are hundredths of a millimeter from the reference transducer.

c. Opening movement.

(i) For the TB, Magnitude of the Opening gesture is defined as the difference between the ''release'' of the preceding /t/ and the minimum for /a/ (the first and second points in the top right panel of Fig. 1). For the Jaw, Magnitude is calculated as the Euclidean distance in an *x*-*y* plane between the ''release'' of the preceding /t/ (first point in the bottom left panel of Fig. 1) and the minimum for /a/ (second point in the same panel). The *x*-values were taken at the hand-marked *y*-values. This approach was adopted because Jaw movement is not perpendicular to the occlusal plane, and might even be described as a rotation in the *x*-*y* plane (Ostry and Munhall, 1994; Vatikiotis-Bateson and Ostry, 1995).

(ii) Duration of the Opening gesture is defined as the difference in time between the two values used to calculate Opening Magnitude.

(iii) Peak Velocity for the Opening gesture is defined as the minimum value (since velocity of the opening movement is expressed in negative values) of the first differential of the movement in the *y*-plane of the articulator.

d. Closing movement.

(i) Magnitude of the Closing gesture is defined as the difference between the minimum for /a/ of the active articulator (TT in the case of /d s ʃ/, TB in the case of /g/, and Jaw in the case of /b f/), and the onset of consonant closure for the same active articulator.

(ii) Duration of the Closing gesture is defined as the difference in time between the two values used to calculate closing Magnitude.

(iii) Peak Velocity for the Closing gesture is defined as the maximum value of the first differential of the movement in the *y*-plane of the articulator.

An important effect was observed during labeling, and is illustrated in Fig. 2, which presents four TB signals from different tokens produced by speaker GR. All tokens are for the sequence /ta # ʃ/, where the /a/ and the /ʃ/ are separated by an Utterance boundary. The maxima for the /t/ and the minima for the /a/ are marked. What should be noted here is that following the minimum for the /a/, the articulator achieves what is apparently a neutral, rest position, lasting up to 100 ms in each case, before movement begins towards the /ʃ/. In each panel except the bottom left, where it begins slightly later, this rest-plateau begins at about 400 ms. The rest-plateau position is clearly a reflection of the acoustic pause at the end of the Utterance. This was observed to be a reasonably common articulatory pattern for the Utterance boundary data, and it is likely that some of the effects of articulatory prosody discussed below are related to the presence of this pause. However, much smoother transitions from the /a/ to the following consonant were common as well at the Utterance boundary, so that the presence of the pause cannot fully account for the nature of the Utterance boundary. One might also note in passing that the opening movement from the /t/ into the /a/ in these panels shows a slowing down of the movement before the minimum for /a/ is reached.

It should be noted that for speaker AV, certain coronal consonant tokens were rejected due to excessive error on the TT transducer. However, the TB and Jaw data from these tokens were used (for example, for vowel duration data). Nine tokens in total were concerned.

The statistical test used is an ANOVA, followed by least significant difference *posthoc* tests. The *posthoc* tests are adjusted according to the Bonferroni method. An eta^2 analysis will also be presented for the various measures. This analysis describes the proportion of total observed variability accounted for by a given independent variable—in this case, prosodic boundary—and is presented as a value between zero and one.

Results will be presented in the following order: Duration data; peak Displacement data; pathlength data; and other Movement data.

TABLE II. (a) Durational data for three speakers of metropolitan French. Results are listed separately for each prosodic boundary context (U=Utterance boundary, I=Intonational-phrase boundary; A=Accentual-phrase boundary; W=Word boundary). See text for details on measurement criteria for these articulatory data. (b) Significance results according to prosodic context for vowel duration and consonant duration. For each speaker, results from a one-way ANOVA are presented in the first column, and *posthoc* pairwise comparisons are presented for adjacent pairs in the prosodic hierarchy in the second column (with p set at 0.017 following the Bonferroni method). The direction of the difference is marked by either "<" or ">," or "=" in the case where the result is not significant. In this and in subsequent tables, "$p=0.00$" means that the statistical program returned a value of p which was zero to six decimal places.

		Vowel duration (ms)		Consonant duration (ms)		Percentage duration: Vowel/syllable		
(a)		Mean	s.d.	Mean	s.d.	Mean	s.d.	*N*
AV	U	810.4	231.06	247.1	133.00	75.6	13.62	126[a]
	I	280.1	95.38	140.8	56.34	66.2	12.27	127[a]
	A	241.9	101.13	132.1	54.40	63.9	13.34	128[a]
	W	212.5	76.93	127.4	56.52	61.5	20.53	127[a]
CV	U	373.6	87.09	150.96	87.35	73.3	12.25	62
	I	266.0	42.75	61.62	36.26	81.8	8.72	63
	A	258.6	42.83	64.25	36.82	80.8	8.77	63
	W	174.9	44.15	52.05	32.38	77.8	11.37	63
GR	U	489.8	148.76	233.3	85.52	67.4	11.42	126
	I	295.8	70.55	114.0	43.62	72.5	8.32	126
	A	286.5	64.74	105.6	41.10	73.5	8.42	126
	W	202.9	50.74	88.3	37.62	70.2	9.86	127

	AV		CV		GR	
(b)	d.f.=3,504		d.f.=3,247		d.f.=3,501	
Vowel Duration	$F=521.07$ $p=0.00$	U>I=A=W	$F=126.37$ $p=0.00$	U>I=A>W	$F=220.24$ $p=0.00$	U>I=A>W
Consonant Duration	$F=52.77$ $p=0.00$	U>I=A=W	$F=47.01$ $p=0.00$	U>I=A=W	$F=179.71$ $p=0.00$	U>I=A>W

[a]Note that nine NAs in speaker AV's Consonant Duration data were excluded in these calculations (this includes the percentage duration data), so that the number of tokens is 9 less than the number listed for Consonant Duration and Percentage Duration only.

III. RESULTS

A. Duration

Table II(a) presents durational data based on the measures described above. Data are collapsed across consonant context, and are presented according to the prosodic boundary. Vowel duration, consonant duration, and the derived measure "percentage duration of the vowel in the VC syllable" are presented. Table II(b) presents the significance results for the vowel duration and consonant duration data. It is evident that the values for the Utterance boundary are far greater than those for any other boundary. This is partly due to the presence of an acoustic pause between /a/ and the consonant for this boundary type (cf. Fig. 2).

A pattern emerges in the durational data of greater duration the stronger the prosodic boundary. This is true for both the vowel and the consonant data, though there appears to be a slightly stronger effect for the vowel data. If the Utterance boundary is ignored (due to the presence of the pause, as mentioned above), it will be seen that the vowel takes up a slightly greater percentage of the syllable the stronger the prosodic boundary. This is consistent with a greater effect on vowel duration than on consonant duration of the prosodic boundary.

B. Peak displacement

1. Vowel

Figure 3 shows TB and Jaw data for each of the three speakers. The vowel is /a/, preceding the six consonants examined in this study. Data are presented according to prosodic context. Table III presents the statistical significance results for these data.

It is evident that the TB position becomes lower the stronger the prosodic boundary. With one exception (the Utterance boundary for speaker GR), this is also true for the Jaw data. These effects were observed across consonant classes (separate data for each consonant class according to prosodic boundary are not presented here).

A note must be made of the Jaw data for the Utterance context in speaker GR's vowel articulations. As Fig. 3 shows, the Utterance context Jaw data are nested between the Accentual-phrase and Word contexts. This result is consistent with predictions made by the articulatory declension model (as outlined in the introduction section) since GR's Jaw data show *hypo*-articulation at the Utterance boundary. It should also be noted, however, that speaker GR's TB data are consistent with effects of the prosodic hierarchy. This point will be discussed further in the final discussion section.

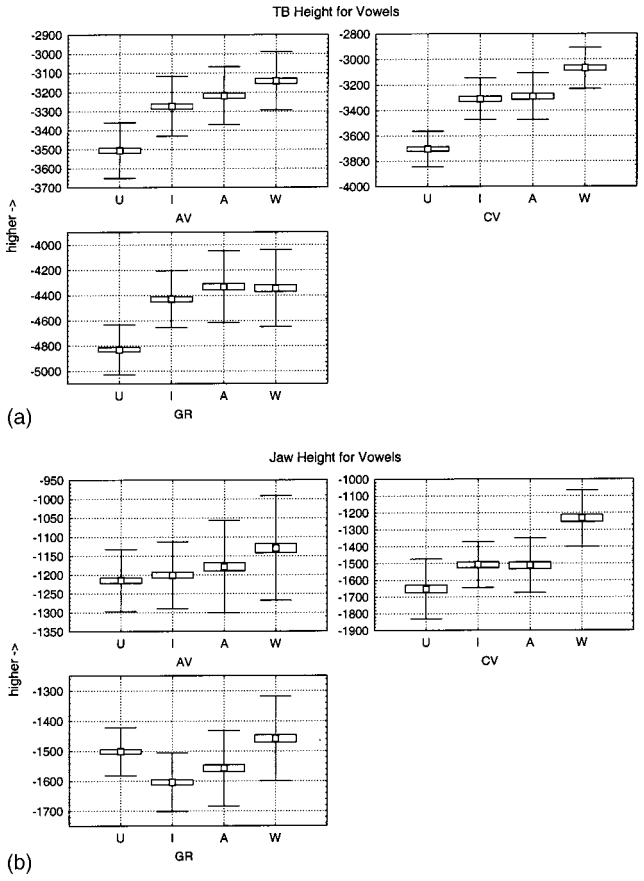

FIG. 3. Boxplots of TB and Jaw peak displacement for the vowel /a/, plotted according to prosodic boundary: (a) TB data and (b) Jaw data. The square in the middle of each box represents the mean, the box represents the standard error, and the whiskers represent the standard deviation. Units on the *y* axis are hundredths of a millimeter from the reference transducer.

In sum, with one exception (speaker GR's Jaw data), there is a strong prosodic effect on TB position and Jaw position in the vowel, with lower TB and Jaw positions at stronger prosodic boundaries.

2. Consonant

There was no effect of prosodic context on consonant peak displacement for either the TT, TB, or Jaw transducers. This is undoubtedly due to the fact that EMA, rather than EPG, was used for the present study, since EPG measures the extent of the tongue-palate contact rather than simply peak displacement of the active articulator. Other researchers (such as Fougeron and Keating, 1997; Fougeron, 2001; Cho and Keating, 2001), using EPG, have found significant effects of prosodic boundary on amount of contact between the tongue and the palate. We turn now to a measure in which EMA provides more information than EPG does: the TB pathlength.

C. TB pathlength during consonant closure

Figure 4 presents data for the TB pathlength during consonant closure. Data are shown for each prosodic context, for each speaker. As explained earlier, data for /g/ are not included in these results due to the small amount of TB movement involved during closure. Table IV presents the statistical significance results.

It can be seen that there is indeed an overall effect of prosody, though different speakers group the data in different ways. Speakers AV and GR clearly separate the Utterance data from the other data,[8] while speaker CV consistently separates the Word data from the rest.

D. Intraarticulator movement

The presentation of the Movement data will be split into two parts. The first part presents data for the Opening movement from the /t/ into the vowel /a/, and the second part for the Closing movement from the vowel /a/ into the following consonant. For the Opening movement, data will be presented according to prosodic boundary, but not according to the consonant context following the vowel (since no systematic effects from the consonant following the vowel could be found). For the Closing movement, data were examined according to the prosodic boundary for each consonant separately. However, only selected results will be presented from the Closing movement data, for reasons which will be discussed during the presentation.

Each set of data is analyzed using three measures. They are the Magnitude of the movement between the /t/ maximum and the /a/ minimum for the Opening movement, or between the /a/ minimum and the onset of consonant closure for the Closing movement; the Duration between these two respective time points for Opening movement and for Closing movement; and the peak Velocity of the movement, calculated as the maximum value (a negative value for Opening movement, since peak velocity is negative in this case, and a positive value for the Closing movement) of the first differential of the movement.

Since Opening Duration can be inferred from the total

TABLE III. Significance results according to prosodic context for TB and Jaw peak displacement in the *y*-plane for the vowel /a/. For each speaker, results from a one-way ANOVA are presented in the first column, and *posthoc* pairwise comparisons are presented for adjacent pairs in the prosodic hierarchy in the second column (with *p* set at 0.017 following the Bonferroni method). The direction of the difference is marked by either "<" or ">," or "=" in the case where the result is not significant.

	AV d.f.=3,504		CV d.f.=3,247		GR d.f.=3,501	
Vowel TB *y*-min.	$F=135.71$ $p=0.00$	U<I<A<W	$F=164.44$ $p=0.00$	U<I=A<W	$F=105.62$ $p=0.00$	U<I<A=W
Vowel Jaw *y*-min.	$F=14.47$ $p=0.00$	U=I=A<W	$F=73.21$ $p=0.00$	U<I=A<W	$F=39.39$ $p=0.00$	U>I<A<W

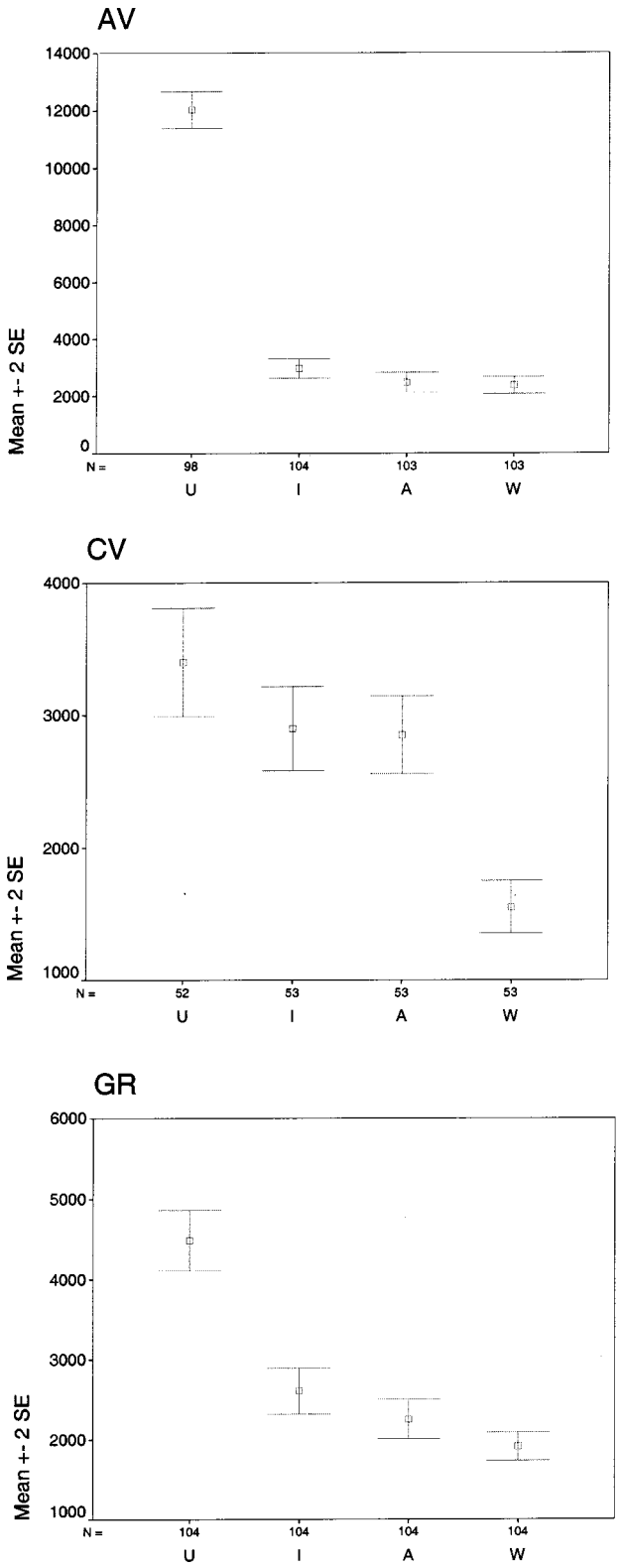

FIG. 4. Error plots showing TB pathlength during consonant closure. The square in the middle of each error bar represents the mean, and the whiskers represent two standard errors. Pathlength was calculated as the sum of the Euclidean distances between successive TB samples during the consonant closure. Data are presented separately for each speaker and for each prosodic context. Units on the *y* axis represent hundredths of a millimeter.

vowel duration data presented in Table II, these data are not plotted separately here. Likewise, since Opening Magnitude can be inferred from the Vowel peak Displacement data presented in Fig. 3, these data are also not plotted separately.

1. Opening movement

It will be remembered from presentation of previous data that both Magnitude and Duration increase with the stronger prosodic boundaries. The exception is speaker GR's Jaw data at the Utterance boundary, which pattern between the Accentual- and Word-boundary data.

Figure 5 shows boxplots for the peak Velocity of the Opening movement into the vowel for the TT, TB, and Jaw (note that data for the TT include only data from the coronal consonant-context, whereas TB and Jaw data include all consonants). Both TT and TB data are included here since the TT is responsible for the release of the /t/ closure, while the TB is responsible for the attainment of the /a/ target. (Although TT data were not presented for the vowel displacement data above, they patterned similarly to the TB data.) The Jaw data are included given the interesting results for speaker GR's Jaw data for the vowel /a/ at the Utterance level. Data for each speaker are presented separately according to the prosodic context. Table V presents the statistical significance results for the TT, TB, and Jaw Opening movement Magnitude, Duration, and Velocity.

It can be seen in Fig. 5 that there is a general trend for peak Velocity to increase the stronger the prosodic boundary. The pattern is stronger in the TT and TB data than in the Jaw data. This may be due to the fact that the TB and TT data include some contribution from the Jaw, or it may be that the Jaw, being a slower articulator which shows less overall movement than either the TT or TB, tends to be less prone to variation in peak velocity.

An important point to note from Table V is that speaker GR's data for the Jaw Opening Duration do not show a significant difference between the Utterance data and the Intonational-phrase data. The same is true for the peak Velocity data. These observations will be mentioned again in the final discussion section.

Table VI presents eta^2 values for all of the data presented thus far.

It can be seen in Table VI that between about 55% and 75% of the variability in vowel Duration is accounted for by the factor of prosodic boundary, whereas only about 25% to 50% of the variability in consonant Duration is accounted for by the prosodic boundary (presumably, consonant identity accounts for a large proportion of the variability). It can also be seen that prosodic boundary accounts for more of the variance in TB vowel peak Displacement (between about 40% and 65% of the variability) than in Jaw vowel peak Displacement. Although the amount of variability accounted for by prosodic boundary for speaker AV's Jaw vowel peak Displacement is relatively small (8%), it is much greater for speaker CV (47%) and still quite important for speaker GR (19%). Prosodic boundary was also a very important factor in the TB pathlength during consonant closure (between 27% and 78%) and for the Opening movement Magnitude and Duration of all the articulators. The effect of prosodic boundary on peak Velocity was reasonably important for the TT (between 15% and 20%), but less so for the TB and Jaw for speakers AV and GR. However, for speaker CV, the effect of prosodic boundary on TB and Jaw peak Velocity was very important (54% and 26%, respectively).

TABLE IV. Significance results according to prosodic context for TB pathlength during consonant closure. For each speaker, results from a one-way ANOVA are presented in the first column, and *posthoc* pairwise comparisons are presented for adjacent pairs in the prosodic hierarchy in the second column (with p set at 0.017 following the Bonferroni method). The direction of the difference is marked by either "<" or ">," or "="in the case where the result is not significant.

	AV d.f.=3,404		CV d.f.=3,207		GR d.f.=3,412	
TB pathlength	$F=482.81$ $p=0.00$	U>I=A=W	$F=25.46$ $p=0.00$	U=I=A<W	$F=67.69$ $p=0.00$	U>I=A=W

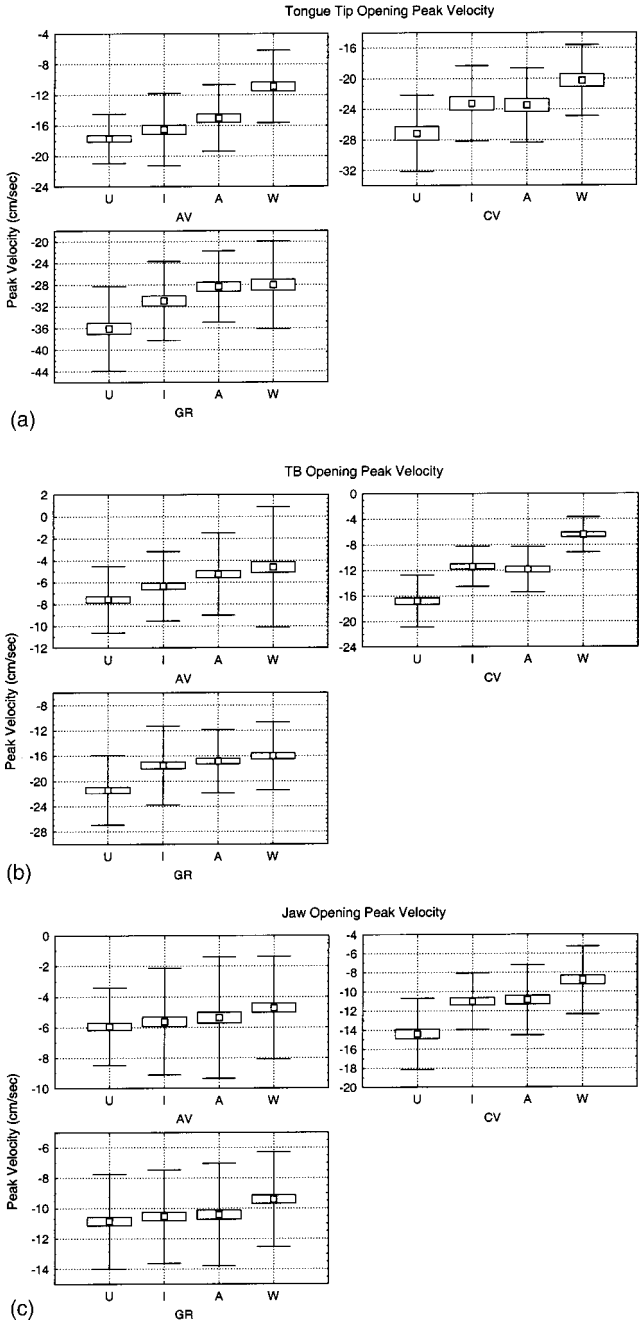

FIG. 5. Boxplots of Peak Velocity data for (a) TT, (b) TB, and (c) Jaw Opening movement into the vowel /a/. The preceding consonant is /t/. Data are presented separately for each prosodic context and for each speaker, although data are collapsed across the consonant context which follows the vowel. Note that data are expressed in negative values for the Opening movement.

To summarize the section on Opening movement: there is a strong effect of prosodic boundary on the Magnitude of the movement between the /t/ and the /a/ (with increased magnitude the stronger the prosodic boundary), on Duration (with increased duration the stronger the prosodic boundary), and on peak Velocity (with increased velocity the stronger the prosodic boundary). It can be hypothesized that while speakers AV and GR rely mainly on increased duration to effect the increased magnitude at the higher prosodic boundaries (since their Duration results are more affected by prosodic boundary than their peak Velocity results), speaker CV uses a combination of increased duration as well as increased peak velocity to cover the greater magnitude in the higher prosodic boundaries (as evidenced by his eta^2 results).

The results showing increased peak Velocity at stronger prosodic boundaries, together with increased Magnitude and Duration, are consistent with known strategies to effect an increased distance between targets: a speaker can either increase duration, or increase velocity, or both (Nelson *et al.*, 1984). However, these results are also contrary to other results in the literature (e.g., Beckman and Edwards, 1990; Edwards *et al.*, 1991; Beckman *et al.*, 1992), which have reported increased lengthening and decreased velocity at stronger phrase boundaries. This apparent contradiction in the present results will be discussed further in the final section.

Data are now presented for the Closing movement.

2. Closing movement

Several observations can be made regarding the data for the Closing movement. First of all, the results are more difficult to interpret than the results for the Opening movement. While this may be due to the fact that, in the present study, one of six consonants could follow the open vowel, whereas the vowel was preceded only by /t/, one could equally note that Byrd (2000) encountered similar problems in analyzing the Closing movement for the sequence /mə # mi/ at various prosodic boundaries. Byrd found greater intersubject differences in interarticulator timing for the Closing movement than for the Opening movement of the /ə/, and, indeed, in the present study, there was much less consistency in the Closing movement data than in the Opening movement data. The differences between the Closing movement and the Opening movement will be mentioned again in Sec. IV.

An examination of the Closing movement data showed that the results were similar to the Opening movement results as regards the Magnitude and the Duration of the movement.

TABLE V. Significance results according to prosodic context for various measures of the Opening movement into the vowel /a/. For each speaker, results from a one-way ANOVA are presented in the first column, and *posthoc* pairwise comparisons are presented for adjacent pairs in the prosodic hierarchy in the second column (with p set at 0.017 following the Bonferroni method). The direction of the difference is marked by either "<" or ">," or "=" in the case where the result is not significant.

	AV d.f.=3,244		CV d.f.=3,123		GR d.f.=3,244	
TT opening Magnitude	$F=103.98$ $p=0.00$	U>I=A>W	$F=110.23$ $p=0.00$	U>I=A>W	$F=129.97$ $p=0.00$	U>I>A=W
TT Opening Duration	$F=52.49$ $p=0.00$	U>I=A>W	$F=33.08$ $p=0.00$	U=I=A>W	$F=94.30$ $p=0.00$	U>I=A>W
TT Opening Peak Velocity	$F=19.97$ $p=0.00$	U=I=A>W	$F=9.00$ $p=0.00$	U>I=A>W	$F=13.85$ $p=0.00$	U>I=A=W
	d.f.=3,495		d.f.=3,247		d.f.=3,501	
TB Opening Magnitude	$F=144.74$ $p=0.00$	U>I>A>W	$F=322.17$ $p=0.00$	U>I=A>W	$F=61.47$ $p=0.00$	U>I=A>W
TB Opening Duration	$F=179.43$ $p=0.00$	U>I>A>W	$F=206.35$ $p=0.00$	U>I=A>W	$F=293.01$ $p=0.00$	U>I=A>W
TB Opening Peak Velocity	$F=12.92$ $p=0.00$	U>I=A=W	$F=98.06$ $p=0.00$	U>I=A>W	$F=23.44$ $p=0.00$	U>I=A=W
Jaw Opening Magnitude	$F=40.43$ $p=0.00$	U>I>A=W	$F=109.58$ $p=0.00$	U>I=A>W	$F=115.71$ $p=0.00$	U<I>A>W
Jaw Opening Duration	$F=138.61$ $p=0.00$	U>I>A=W	$F=67.06$ $p=0.00$	U=I>A>W	$F=139.59$ $p=0.00$	U=I>A>W
Jaw Opening Peak Velocity	$F=2.87$ $p<0.05$	U=I=A=W	$F=28.87$ $p=0.00$	U>I=A>W	$F=4.94$ $p=0.00$	U=I=A>W

However, as regards peak Velocity, there was little consistency across speakers for the different consonants. The striking exception was the TB data for /g/, which were most consistent across speakers. It might be hypothesized that this result for /g/ is due to the fact that the TB is actively involved in the closure of the /g/; for this reason, the TT data for /d/ were also examined a little more closely. It will be seen below that the pattern is not as strong for /d/ as it is for /g/.

TABLE VI. Eta^2 results for the various measures examined thus far. The eta^2 value gives the proportion of total variance accounted for by the independent variable of prosodic boundary.

	AV	CV	GR
Vowel Duration	0.756	0.606	0.569
Consonant Duration	0.266	0.363	0.518
Vowel TB *y*-min.	0.447	0.666	0.387
Vowel Jaw *y*-min.	0.079	0.471	0.191
TB Pathlength	0.782	0.270	0.330
TT Opening Magnitude	0.561	0.729	0.615
TT Opening Duration	0.392	0.447	0.537
TT Opening Peak Velocity	0.197	0.180	0.146
TB Opening Magnitude	0.467	0.796	0.269
TB Opening Duration	0.521	0.715	0.637
TB Opening Peak Velocity	0.073	0.544	0.123
Jaw Opening Magnitude	0.197	0.591	0.409
Jaw Opening Duration	0.457	0.449	0.455
Jaw Opening Peak Velocity	0.017	0.260	0.029

Figure 6 presents the TT data for /d/ and the TB data for /g/ according to prosodic contexts for all three speakers.[9] For ease of presentation, data are normalized by subtracting the mean and dividing by the standard deviation (Lobanov normalization). The normalization for this figure was carried out across all the data for the given articulator, i.e., data for the TT were normalized across /d s ʃ/ and data for the TB were normalized across /d g s ʃ/. The Magnitude, Duration, and peak Velocity data are superimposed on the plot for each consonant. Table VII gives the statistical significance results for these data.

It can be seen in Fig. 6 and Table VII that the results for Closing movement Magnitude and Duration are very similar to the results for Opening movement Magnitude and Duration (i.e., with greater Magnitude and Duration the stronger the prosodic boundary). However, the results for Closing movement peak Velocity are quite different to those for the Opening movement. There is a tendency, particularly for /g/, for peak Velocity to increase at the *weaker* prosodic boundaries, rather than at the stronger prosodic boundaries, as was the case with the Opening movement data. However, the pattern is not so clear for /d/, where only speaker CV seems to show the same pattern as for /g/, but without the results reaching statistical significance. Moreover, speaker GR has statistically significant results for /d/ peak Velocity which fail to show expected effects of the prosodic hierarchy altogether.

It is perhaps worth noting that once again, the strongest differences are observed between the Utterance and the Intonational boundaries, in particular with respect to Duration

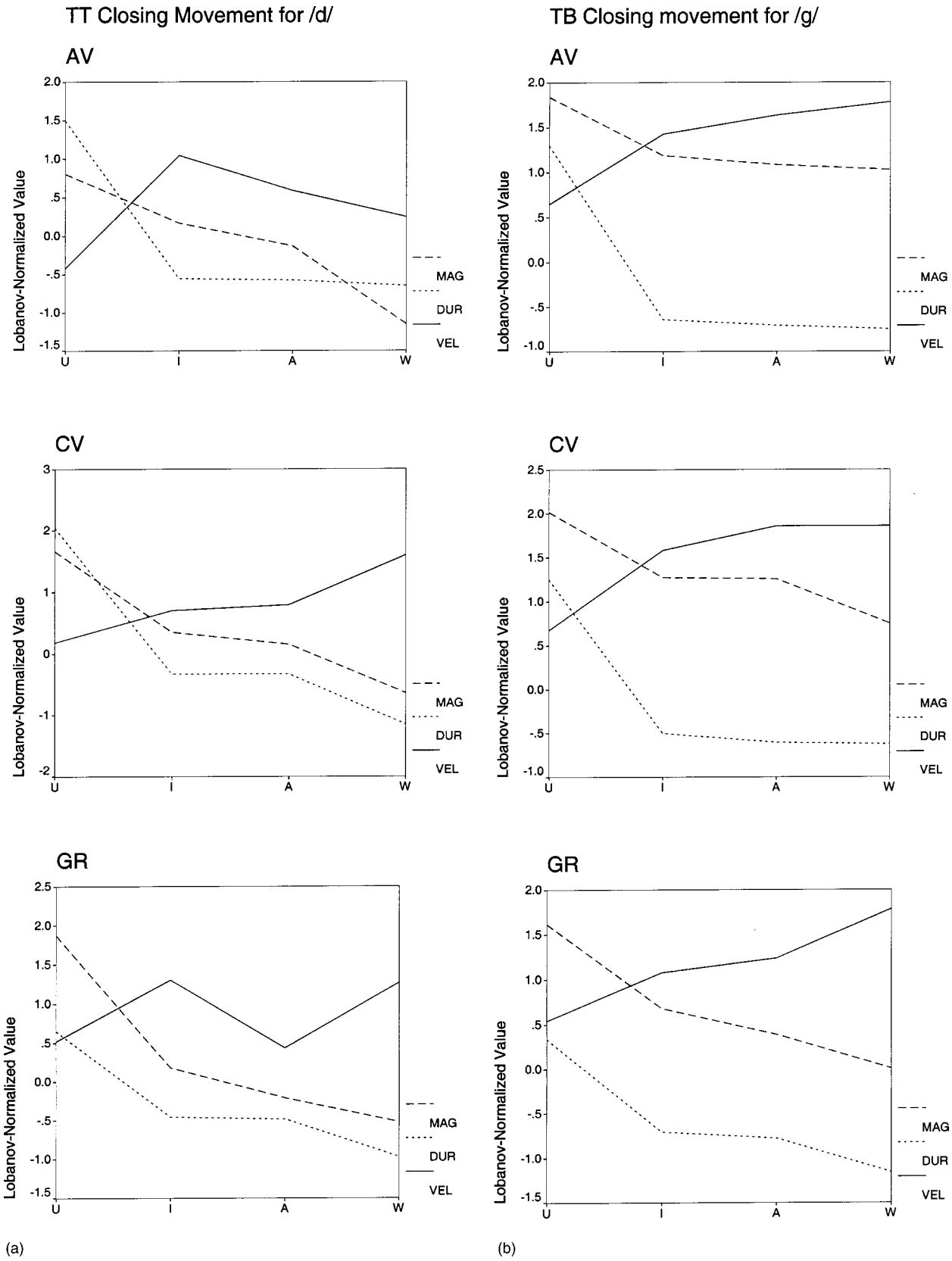

FIG. 6. Plots showing the interaction between Magnitude, Duration, and Velocity for (a) TT data for /d/ and (b) TB data for /g/ for all three speakers. Data are Lobanov-normalized for ease of presentation (see text for details).

and peak Velocity. This is quite possibly due to the presence of the pause at the Utterance boundary (as seen in Fig. 2). Clearly, the much greater Duration between the vowel target and the consonant target means that peak Velocity is much lesser in this context. The effect of the pause on articulatory timing needs to be explored further, but unfortunately this is beyond the scope of the present paper.

As mentioned above, the Closing movement results are

TABLE VII. Significance results according to prosodic context for the closing movement into the consonant /d/ (for the TT data) and the consonant /g/ (for the TB data) out of the vowel /a/. For each speaker, results from a one-way ANOVA are presented in the first column, and *posthoc* pairwise comparisons are presented for adjacent pairs in the prosodic hierarchy in the second column (with p set at 0.017 following the Bonferroni method). The direction of the difference is marked by either "<" or ">," or "=" in the case where the result is not significant.

	AV d.f.=3,76		CV d.f.=3,35		GR d.f.=3,84	
TT Closing Distance	$F=37.41$ $p=0.00$	U>I=A>W	$F=44.25$ $p=0.00$	U>I=A>W	$F=126.25$ $p=0.00$	U>I>A>W
TT Closing Duration	$F=119.24$ $p=0.00$	U>I=A=W	$F=92.37$ $p=0.00$	U>I=A>W	$F=127.87$ $p=0.00$	U>I=A>W
TT Closing Peak Velocity	$F=17.05$ $p=0.00$	U<I=A=W	$F=4.20$ $p<0.00$	U=I=A=W	$F=127.87$ $p<0.00$	U<I>A<W
	d.f.=3,83		d.f.=3,36		d.f.=3,85	
TB Closing Magnitude	$F=7.23$ $p=0.00$	U>I=A=W	$F=13.83$ $p=0.00$	U>I=A>W	$F=40.69$ $p=0.00$	U>I=A>W
TB Closing Duration	$F=267.88$ $p=0.00$	U>I=A=W	$F=95.09$ $p=0.00$	U>I=A=W	$F=158.79$ $p=0.00$	U>I=A>W
TB Closing Peak Velocity	$F=11.56$ $p=0.00$	U<I=A=W	$F=11.70$ $p=0.00$	U<I=A=W	$F=11.44$ $p=0.00$	U<I=A<W

much more stable across speakers for /g/. The TB movement for /g/ is of course greater than for other consonants given that the TB must achieve full closure for /g/ but not for the other consonants. This can be seen in Fig. 6 by the fact that the mean Magnitude of the movement is greater than zero (these Lobanov-normalized data were generated across all the TB data, and not just across the TB data for /g/). It can also be seen in Fig. 6 that the mean Duration for /g/ is less than zero—hence, the mean Duration for /g/ is less than that of the other consonants. It could also be suggested that there is very little variability in Duration for /g/, since for speakers AV and CV, the difference in Duration between the three weaker prosodic boundaries is not statistically significant. This is contrary to Duration results for the Opening movements of these two speakers. It might therefore be inferred that the difference in Duration across prosodic boundaries for the /g/ Closing movement does not make up for the difference in Magnitude of the movement, and that as a result, peak Velocity must increase at the weaker prosodic boundaries.

Based on the results for /g/, it might be concluded that the articulator active in achieving consonant closure shows an increase in peak Velocity at the weaker prosodic boundaries. However, the fact that the results were not so clear for /d/ suggests that caution is needed with this interpretation of the results. Why the results should be clear for /g/ and not for /d/ is not immediately apparent. (It should be noted in passing that neither the TT nor the TB data gave consistent results across speakers for the sibilant fricatives' peak Velocity data.) It is possible that the timing of the peak Velocity with respect to movement duration will provide additional information. A brief examination of peak Velocity timing suggested that there were indeed prosodic effects to be found, though as with the peak Velocity data presented above, the results would not be uniform across consonant contexts.

Table VIII shows the eta^2 results for the Closing movements of /d/ and /g/. While it is not straightforward to compare these results directly with those of the Opening movement (since the Opening movement data had different consonants following the /a/), it should nevertheless be observed that these results show a very strong effect of the prosodic boundary on the Closing movement. It should be remembered that the eta^2 analysis is not affected by the number of tokens, so that the smaller number of tokens analyzed in the Closing movement should make no difference to the amount of variance accounted for. One might tentatively conclude that the prosodic hierarchy has at least an equal effect on the Closing movement as on the Opening movement.

In sum, the Magnitude and Duration data of the Closing movement are similar to those of the Opening movement (both are greater at stronger prosodic boundaries), whereas the peak Velocity data show the opposite pattern to that observed for the Opening movement: for the Closing movement, peak Velocity tended to increase at the *weaker* prosodic boundaries, whereas for the Opening movement, peak Velocity tended to increase at the *stronger* prosodic boundaries.

TABLE VIII. Eta^2 results for the Closing movement into /d/ (TT data) and into /g/ (TB data). The eta^2 value gives the proportion of total variance accounted for by the independent variable of prosodic boundary.

	AV	CV	GR
TT Closing Magnitude	0.596	0.791	0.832
TT Closing Duration	0.825	0.888	0.637
TT Closing Peak Velocity	0.402	0.265	0.183
TB Closing Magnitude	0.207	0.536	0.589
TB Closing Duration	0.906	0.888	0.849
TB Closing Peak Velocity	0.295	0.494	0.288

IV. DISCUSSION

Throughout this paper, many effects have been observed of the prosodic hierarchy at the boundary between two prosodic units at the same hierarchical level. Quite often, though not always, the Accentual-phrase and Intonational-phrase boundaries were treated as a single class. The Utterance boundary and Word boundary, by contrast, were almost always treated as a separate class, each on its own in terms of Magnitude, Duration, and Velocity of movement. Thus, the present data suggest that in French, major articulatory adjustments occur for pausing (Utterance versus other boundaries) and for the presence or absence of a major phrasal boundary (Word versus other boundaries). The present data do not appear to support a view of the prosodic hierarchy where different phrasal categories (in this case, Accentual- versus Intonational-phrase) give rise to statistically different articulatory behavior. Whether this result is coincidence due to a small number of subjects or a true reflection of suprasegmental prosodic organization in French can only be determined by further studies of French articulatory prosody.

The discussion below will focus to a large extent on the result shown by speaker GR's Jaw data. At this point, it is worth emphasizing that this focus is on one prosodic condition for one articulator for one speaker. The remaining data all strongly support the view of the prosodic hierarchy in which supralaryngeal articulations are strengthened the stronger the prosodic boundary. The reader is asked to keep this in mind during the discussion below. However, the implications of GR's Jaw data results are important, and although they are apparently only a small part of the system, they are nevertheless an important part that must be accounted for.

Before going on to speaker GR's Jaw data, it is worth recalling the observation, made in the Introduction, that articulatory strategies used to delineate prosodic boundaries are very similar to strategies used to mark stress (cf. de Jong, 1995). de Jong *et al.* (1993) showed that coarticulatory resistance is weaker when stress is also weaker. It is tempting to paraphrase their conclusion to describe the present results, saying that coarticulatory resistance is weaker (for /a/) the weaker the prosodic boundary. However, there is at least one set of results for which the analogy breaks down: the TB pathlength data. It is often thought that the greater the TB movement during consonant closure, the greater the coarticulation [since the gesture for the vowel overlaps more in time with the closure for the consonant—cf. Lofqvist (1999)]. In the present results, however, the greater TB movement is found at the stronger prosodic boundaries, which are the ones we have just referred to as being more resistant to coarticulation. This is no doubt due to the fact that duration is greater at stronger prosodic boundaries. It is nevertheless clear that comparisons between coarticulatory strategies and strategies to delineate prosodic boundaries must be made very carefully indeed.

We turn now to the two sets of unusual results observed in the present study: (a) speaker GR's Jaw data at the Utterance level, and (b) the increase in peak Velocity together with an increase in Magnitude and Duration of the opening movement at the stronger prosodic boundaries. The first set of results is contradictory in the sense that GR's Jaw Utterance data do not pattern in accord with the prosodic hierarchy. The second set of results is contradictory in that it goes against previous results in the literature showing that at the ends of large phrases, duration becomes greater while velocity decreases. The two sets of unusual results will be discussed in turn.

It was mentioned above that speaker GR's Jaw results in the Utterance context may be due to articulatory declension [and that acoustic data presented in Tabain (2003) support this view]. It has already been noted that the articulatory prosody and articulatory declension approaches are mutually incompatible with regard to the Utterance: articulatory declension predicts that articulations are greatly reduced at the end of an utterance, whereas articulatory prosody predicts that they are strengthened at the end of an utterance. (Of course, both approaches predict a strengthening of the articulation at the beginning of an utterance.) A full discussion of these apparently competing constraints is beyond the scope of this paper. However, a few speculative comments will perhaps prove useful.

It may be noted, first of all, that the effects of the prosodic hierarchy are linguistically motivated [like both of the competing constraints in Harrington *et al.*'s (2000) study], whereas the motivation for articulatory declension is less well understood (biological control?). One might suggest that the purpose of representing the prosodic structure of an utterance in the supralaryngeal articulations (in addition to the F0 structure and the rhythmic structure of the utterance) is to provide the listener with extra cues to the linguistic structure of the utterance. This is then a listener-oriented function of speech, as described in the Hyper- and Hypo-Speech model of Lindblom (1990). By contrast, it could be argued that the purpose of having articulations become more ''lax'' as the utterance becomes longer is to save articulatory effort on the part of the speaker (a speaker-oriented effect). Such declension is assisted by the fact that during online processing of speech, the number of ''candidate'' words or syllables is reduced as the utterance becomes longer [see Cutler *et al.* (1997) for a summary], so that the listener is less in need of cues to the identity of individual consonants and vowels. It may be that in a more natural setting, where communication is less listener-oriented due to the role played by semantics, pragmatics and syntax in constraining the set of consonants and vowels which can occur later in the utterance, the effects of articulatory declension are more prevalent than they are in the laboratory, and more speakers would show articulatory declension at the ends of utterances. (One could hypothesize that speaker GR may permit articulatory declension at the Utterance level—so that there is a resetting with each new utterance—whereas within the Utterance, effects of the prosodic hierarchy are in operation.)

In the sense that speech serves a communicative function, it is important to note that the competing constraints on GR's TB and Jaw vowel articulations are resolved in the acoustic data (Tabain, 2003) in favor of articulatory declension, with centralization of the vowel at the end of the Utterance. The lower F1 associated with such centralization is most likely due to the fact that the first formant of a low

vowel, where there is no critical constriction in the vocal tract, is largely determined by the size of the orifice at the anterior end of the vocal tract.

Turning to the second apparent contradiction mentioned above in relation to the present dataset, it is possible that the articulatory declension results observed in speaker GR's data may explain why previous studies looking at phrase-final lengthening did not necessarily find an increase in peak velocity between phrase-internal and phrase-final gestures, despite differences in duration given similar magnitude. Previous studies on phrase-final lengthening (Beckman and Edwards, 1990; Edwards *et al.*, 1991; Beckman *et al.*, 1992) primarily looked at phrase-final position versus phrase-internal position. Although the phrase-internal boundary could be between two words (''Pop # opposed'') or between two syllables (''Pop#pa posed''),[10] the phrase-final position was always some sort of Intonational-phrase boundary. There was therefore no Utterance level nor an Accentual-phrase level controlled for explicitly. Although the studies by Beckman and colleagues were designed to examine the effects of stress, pitch-accent, and tempo as well as prosodic effects (and are therefore not completely comparable with the present study), it was apparent that phrase-final gestures in their studies were longer and slower than phrase-internal gestures, with no apparent difference in the magnitude of the gesture. However, if one allows that the effects of articulatory declension may have applied at the phrase-final position of these utterances (as evidenced by speaker GR's Jaw data in the present study), then it can be understood that there would be no difference in magnitude of the movement between phrase-final and phrase-medial position for these utterances, since the phrase-medial position is a simple Word (or Syllable) boundary. In turn, due to the fact that duration is greater in phrase-final position, peak velocity in this position is lesser. To lend some support to this interpretation, it should be noted that although speaker GR's Opening movement peak Velocity was significantly greater in the Utterance context for the TT and TB (which did not show effects of articulatory declension), there was no significant difference in the Utterance context for the Jaw data (which did show an effect of articulatory declension).

It will be recalled that results for the VC closing movement did not show the clear trends of increasing peak velocity with stronger prosodic boundaries that the CV opening movement data showed. In fact, there appeared to be a trend for peak velocity to increase with the weaker prosodic boundaries in the VC movement. Kozhevnikov and Chistovish (1965) hypothesized that CV syllable onset movements (in the present study, the opening movement into the vowel /a/) constitute elementary planning units for speech production. It could further be hypothesized that the VC movement dynamics depend on the time available between the end of the preceding CV movement and the start of the following CV movement. Under such a view, the dynamics of the VC movement would be much more variable than those of the CV movement, and indeed this appears to be the case in the present data.

It is also worth pointing out that the results on phrase-final lengthening reported by Edwards and colleagues relate to the closing movement into a bilabial consonant, whereas in the present study, phrase-final position is the opening movement into a low vowel. Given the hypotheses regarding CV vs VC syllable timing just outlined above, it is clear that much work remains to be done in order to fully describe the interaction of prosodic boundary with syllable structure for the many different speech segments that humans can produce.

ACKNOWLEDGMENTS

This work was supported by the French Ministère de l'Education Nationale, de la Recherche et de la Technologie (MENRT), and by the Fondation Fyssen. I would like to thank Gérard Bailly, Hélène Loevenbruck, and in particular Pascal Perrier for discussion; Jonathan Harrington for assistance with the kinematic analysis; Christophe Savariaux for help in collecting the EMA data; Anders Lofqvist for editorial help; two anonymous reviewers for their constructive criticisms; and my speakers for their time. Most of all I would like to thank everyone at ICP Grenoble for welcoming me so warmly during my postdoctoral year there.

[1]Throughout this paper, an abstract phonological entity is denoted by a capital letter at the beginning of the word. For instance, ''Word'' denotes the abstract entity which forms part of the prosodic hierarchy, whereas ''word'' denotes the instantiation of that entity in real time and space (either acoustically or visually). Similarly ''Utterance'' versus ''utterance,'' and ''Syllable'' versus ''syllable.''

[2]It should be noted that in Byrd (2000) and Byrd and Saltzman (1998), which looked at American English, the domain-final vowel examined is a schwa due to primary stress being placed on the preceding (first) syllable in ''mamma,'' whereas in the present study, the domain-final vowel is a full /a/, since French has no vowel reduction.

[3]It should be noted that Jun and Fougeron (2000) have proposed an additional level, the Intermediate Phrase (ip), between the AP and the IP. However, they note that further research is needed to support this level of the ip, and for this reason, the hypothesized ip is ignored in the present study.

[4]The term ''peak displacement'' is used as a cover term to mean either the minimum for the vowel, or the maximum for the consonant.

[5]The reader may wonder what the effect was on the various measures examined here of the following vowel contexts, which are being ignored in the present study. As a partial answer, it may be mentioned that an eta[2] analysis of several acoustic measures (vowel and consonant duration, and F1 and F2) showed that the effects of following vowel were minimal (always less than 10%, and usually less than 5% of the variance accounted for) compared to the effects of prosodic boundary (usually well above 50% of the variance accounted for, except for consonant duration, which is not as affected by prosodic boundary as vowel duration is—see results below).

[6]It was felt that hand-labeling was more reliable than automatic labeling of the data, which seemed to be prone to error. However, in order to determine whether test–retest reliability would be an issue with the hand-labeled data, a comparison of the means and standard deviations of the hand-labeled versus automatically labeled data was carried out for the vowel TB and Jaw displacement minima for speaker CV. Once errors had been removed or corrected for the automatic data, it was found that there was minimal difference between the two methods.

[7]The TB may of course move during closure for /g/. However, as Lofqvist and Gracco (2002) have shown, this movement is minimal compared to the movement during closure for consonants where the TB is not the active articulator.

[8]An additional four tokens were removed from speaker AV's data, due to the duration of the consonant closure being less than 5 ms (i.e., less than the time between successive EMA samples). The consonants concerned were /d/ and /s/.

[9]It will be noted that the Closing movement Jaw data are not presented. This is mainly because the Velocity data were both inconsistent across speakers, and because they did not show any effect of the prosodic hierarchy. In particular, the Jaw data did not give any useful information regarding Ve-

locity for the Closing movement into /b/ or /f/—presumably, the lower lip, which was not recorded, would give more useful information for these consonants.

[10]A Syllable boundary was originally included in the present study. Although the Syllable-boundary context data were recorded, they could not be used since it was later discovered that the phonetic context was not comparable to that of the other sentences.

Beckman, M., and Edwards, J. (**1990**). ''Lengthenings and shortenings and the nature of prosodic constituency,'' in *Papers in Laboratory Phonology I: Between the Grammar and Physics of Speech*, edited by J. Kingston and M. Beckman (Cambridge U.P., Cambridge), pp. 152–178.

Beckman, M., Edwards, J., and Fletcher, J. (**1992**). ''Prosodic structure and tempo in a sonority model of articulatory dynamics,'' in *Papers in Laboratory Phonology III: Gesture, Segment, Tone*, edited by G. Docherty and D. R. Ladd (Cambridge U.P., Cambridge), pp. 68–86.

Beckman, M., and Pierrehumbert, J. (**1986**). ''Intonational structure in English and Japanese,'' Phonology **3**, 255–310.

Byrd, D. (**2000**). ''Articulatory vowel lengthening and coordination at phrasal junctures,'' Phonetica **57**, 3–16.

Byrd, D., Kaun, A., Narayanan, S., and Saltzman, E. (**2000**). ''Phrasal signatures in articulation,'' in *Papers in Laboratory Phonology V: Acquisition and the Lexicon*, edited by M. Broe and J. Pierrehumbert (Cambridge U.P., Cambridge), pp. 70–87.

Byrd, D., and Saltzman, E. (**1998**). ''Intragestural dynamics of multiple prosodic boundaries,'' J. Phonetics **26**, 173–199.

Cassidy, S., and Harrington, J. (**2001**). ''Multi-level annotation in the EMU speech database management system,'' Speech Commun. **33**, 61–77.

Cho, T. (**2002**). *Effects of Prosody on Articulation in English* (Routledge, New York).

Cho, T., and Keating, P. (**2001**). ''Articulatory and acoustic studies on domain-initial strengthening in Korean,'' J. Phonetics **29**, 155–190.

Cutler, A., Dahan, D., and von Donselaar, W. (**1997**). ''Prosody in the comprehension of spoken language: a literature review,'' Lang. Speech **40**, 141–201.

de Jong, K. (**1995**). ''The supraglottal articulation of prominence in English: linguistic stress as localized hyperarticulation,'' J. Acoust. Soc. Am. **97**, 491–504.

de Jong, K., Beckman, M., and Edwards, J. (**1993**). ''The interplay between prosodic structure and coarticulation,'' Lang. Speech **36**, 197–212.

Dilley, L., Shattuck-Hufnagel, S., and Ostendorf, M. (**1996**). ''Glottalization of word-initial vowels as a function of prosodic structure,'' J. Phonetics **24**, 423–444.

Edwards, J., Beckman, M., and Fletcher, J. (**1991**). ''The articulatory kinematics of final lengthening,'' J. Acoust. Soc. Am. **89**, 369–382.

Fletcher, J. (**1991**). ''Rhythm and final lengthening in French,'' J. Phonetics **19**, 193–212.

Fougeron, C. (**2001**). ''Articulatory properties of initial segments in several prosodic constituents in French,'' J. Phonetics **29**, 109–135.

Fougeron, C., and Jun, S-A. (**1998**). ''Rate effects on French intonation: prosodic organization and phonetic realization,'' J. Phonetics **26**, 45–69.

Fougeron, C., and Keating, P. (**1997**). ''Articulatory strengthening at edges of prosodic domains,'' J. Acoust. Soc. Am. **101**, 3728–3740.

Harrington, J., Beckman, M., and Fletcher, J. (**2000**). ''Manner and place conflicts in the articulation of accent in Australian English,'' in *Papers in Laboratory Phonology V: Acquisition and the Lexicon*, edited by M. Broe and J. Pierrehumbert (Cambridge U.P., Cambridge), pp. 40–51.

Harrington, J., Fletcher, J., and Roberts, C. (**1995**). ''Coarticulation and the accented/unaccented distinction,'' J. Phonetics **23**, 305–322.

Harrington, J., Beckman, M., Fletcher, J., and Palethorpe, S. (**1998**). ''An electropalatographic, kinematic, and acoustic analysis of supralaryngeal correlates of word and utterance-level prominence contrasts in English,'' in *Proceedings of the 5th International Conference on Spoken Language Processing*, Sydney, Australia, pp. 1851–1854.

Harrington, J., Cassidy, S., Fletcher, J., and McVeigh, A. (**1993**). ''The mu + system for corpus based speech research,'' Comput. Speech Lang. **7**, 305–331.

Ihaka, R., and Gentleman, R. (**1996**). ''R: A Language for Data Analysis and Graphics,'' J. Comput. Graph. Stat. **5**, 299–314.

Johnson, K., and Martin, J. (**2001**). ''Acoustic vowel reduction in Creek: effects of distinctive length and position in the word,'' Phonetica **58**, 81–102.

Jun, S-A., and Fougeron, C. (**2000**). ''A phonological model of French intonation,'' in *Intonation: Analysis, Modelling and Technology*, edited by A. Botinis (Kluwer, Dordrecht), pp. 209–242.

Keating, P., Cho, T., Fougeron, C., and Hsu, C-S. (**in press**). ''Domain-initial articulatory strengthening in four languages,'' in *Papers in Laboratory Phonology VI*, edited by J. Local, R. Ogden, and R. Temple (Cambridge U.P., Cambridge).

Kozhevnikov, V., and Chistovish, L. (**1965**). *Speech: Articulation and Perception* (Joint Publication Research Service, Washington, DC).

Krakow, R., Bell-Berti, F., and Wang, Q. (**1994**). ''Supralaryngeal declension: evidence from the velum,'' in *Producing Speech: A Festschrift for Katherine Safford Harris*, edited by F. Bell-Berti and L. Raphael (AIP, Woodbury, NY), pp. 333–353.

Lindblom, B. (**1990**). ''Explaining phonetic variation: a sketch of the H & H theory,'' in *Speech Production and Speech Modelling*, edited by W. Hardcastle and A. Marchal (Kluwer, Dordrecht), pp. 403–439.

Lofqvist, A. (**1999**). ''Interarticulator phasing, locus equations and degree of coarticulation,'' J. Acoust. Soc. Am. **106**, 2022–2030.

Lofqvist, A., and Gracco, V. (**2002**). ''Control of oral closure in lingual stop consonant production,'' J. Acoust. Soc. Am. **111**, 2811–2827.

Nelson, W., Perkell, J., and Westbury, J. (**1984**). ''Mandible movements during increasingly rapid articulations of single syllables: preliminary observations,'' J. Acoust. Soc. Am. **75**, 945–951.

Ostry, D., and Munhall, K. (**1994**). ''Control of jaw orientation and position in mastication and speech,'' J. Neurophysiol. **71**, 1528–1545.

Pierrehumbert, J. (**1980**). ''The phonology and phonetics of English intonation,'' Ph.D. thesis, MIT, Cambridge, MA.

Recasens, D. (**1999**). ''Lingual coarticulation,'' in *Coarticulation: Theory, Data and Techniques*, edited by W. Hardcastle and N. Hewlett (Cambridge U.P., Cambridge), pp. 80–104.

Tabain, M. (**2003**). ''Effects of prosodic boundary on /aC/ sequences: acoustic results,'' J. Acoust. Soc. Am. **113**, 516–531.

Turk, A., and Sawusch, J. (**1996**). ''The processing of duration and intensity cues to prominence,'' J. Acoust. Soc. Am. **99**, 3782–3790.

Vatikiotis-Bateson, E., and Ostry, D. (**1995**). ''An analysis of the dimensionality of jaw movement in speech,'' J. Phonetics **23**, 101–117.

Vayra, M., and Fowler, C. (**1992**). ''Declension of supralaryngeal gestures in spoken Italian,'' Phonetica **49**, 48–60.

Using links between speech perception and speech production to evaluate different acoustic metrics: A preliminary report

Rochelle S. Newman[a)]
Department of Hearing and Speech Sciences, Program in Neuroscience and Cognitive Science, University of Maryland, Lefrak Hall, College Park, Maryland 20742

(Received 22 May 2001; accepted for publication 20 February 2003)

This paper examines whether correlations between speech perception and speech production exist, and, if so, whether they might provide a way of evaluating different acoustic metrics. The cues listeners use for many phonemic distinctions are not known, often because many different acoustic cues are highly correlated with one another, making it difficult to distinguish among them. Perception-production correlations may provide a new means of doing so. In the present paper, correlations were examined between acoustic measures taken on listeners' perceptual prototypes for a given speech category and on their average production of members of that category. Significant correlations were found for VOT among stop consonants, and for spectral peaks (but not centroids or skewness) for voiceless fricatives. These results suggest that correlations between speech perception and production may provide a methodology for evaluating different proposed acoustic metrics. © *2003 Acoustical Society of America.* [DOI: 10.1121/1.1567280]

PACS numbers: 43.70.Fq, 43.71.Es, 43.71.An [CWT]

I. INTRODUCTION

A great deal of research in speech perception has focused on the cues listeners use to distinguish different phonetic categories. Although the cues to some phonemic distinctions have been well specified (for example, VOT for voicing among stop consonants), the cues to other distinctions (such as place of articulation) are less clear.

One reason for this uncertainty is that the acoustic spectrum for many phonemes is quite complex, and the differences between spectra can therefore be described in a number of ways. Different alternatives are often highly correlated with one another, making it difficult to distinguish among them experimentally. For instance, Syrdal and Gopal (1986) have suggested that differences between formant peaks may be a cue to stop consonant place of articulation, whereas Sussman and colleagues (Sussman *et al.*, 1993, 1991) have suggested that the starting point of the second formant may be a cue by itself. Since both of these cues are based (at least in part) on the location of the second formant, changes in one cue almost necessitate changes in the alternative as well. Thus attempts to specify the acoustic changes to which listeners are sensitive often fail to differentiate between different proposed cues.

The present paper is an attempt to develop a new method of distinguishing between alternative cues, based on links between speech perception and speech production. Some phonemic distinctions can be articulated in multiple ways, with slightly different muscle movements (for example, see Johnson *et al.*, 1993b; Perkell and Matthies, 1992). Different people may articulate the same sound with different combinations of muscle and articulatory action. This could then influence what these individuals expect to hear from other speakers. Those individuals who produce a sound in a particular manner are likely going to judge others' productions according to the same metric. By examining which acoustic properties demonstrate these types of links between perception and production, it is possible to assess the likelihood that a particular cue is being used by a given listener.

There are a number of reasons to predict that these types of links should occur. Infants learn to speak their native language by hearing what other people produce. They must in some way associate the sounds they hear with the proper way of producing them, suggesting some basic sort of linkage between the systems (see, for example, Kuhl and Meltzoff, 1982). Moreover, since people are likely to have heard their own productions more than those of any other single individual, their productions are likely to have an especially important role in their perceptual prototypes. Thus, perceptual expectations should be skewed towards one's own productions, again suggesting at least an indirect link between the two systems.

Evidence for a more direct link comes from studies that have found that particular experiences in either perception or production often result in changes in the other modality as well (Bradlow *et al.*, 1997; Cooper, 1974; Cooper and Lauritsen, 1974; Cooper and Nager, 1975; Jamieson and Rvachew, 1992). For example, Bradlow *et al.* (1997) found that training Japanese speakers on perception of the English /ɹ/-/l/ distinction also resulted in improved production. Cooper (1974) found that after repeated presentation of /pi/, listener's productions of that syllable were more ''/bi/-like'' (that is, had shorter VOTs).

Several theories also make claims regarding the existence of links between perception and production. For example, motor theory (Liberman *et al.*, 1962, 1967; Liberman and Mattingly, 1985) argues that adults perceive speech by making reference to their own articulation. The authors even go so far as to claim that the word ''link'' really is not cor-

a)Electronic mail: rnewman@hesp.umd.edu

 0001-4966/2003/113(5)/2850/11/$19.00

rect, since it implies that speech perception and production ''though tightly bonded, are nevertheless distinct.'' Rather, they feel that ''for language, perception and production are only different sides of the same coin'' (Liberman and Mattingly, 1985, p. 30). Fowler's direct perception theory (Fowler, 1986) suggests that listeners directly perceive the gestures (or productions) of the speaker. Nearey's double weak theory (1992) also claims that the perceptual system has knowledge about relations between speech-production capabilities and the resulting acoustic output, which may require a link between the perception and production systems. Thus, these theories all suggest that there should be some connection between the two systems, although the strength of the predicted linkage varies between theories.

Experimental evidence for the existence of these perception-production correlations is somewhat mixed, however. Bell-Berti *et al.* (1979) found that there are two different manners of producing the tense-lax distinction among American English vowels, and that the strategy selected by different individuals (based on EMG data) was related to how those individuals performed in a perceptual task. Fox (1982) examined perceptual scaling data on vowels, and found that while three dimensions (representing tongue height, tongue ''frontness,'' and the presence of lip-rounding) were an adequate fit to listeners' data, the listeners differed in the weightings (or saliences) they gave to each dimension. Furthermore, there was a relationship between the weightings used by any given listener and acoustic measures of that listener's productions.

There has also been some evidence of correlations between perception and production of consonants, using cues such as VOT (Flege and Eefting, 1986; Hoffman *et al.*, 1984). These correlations appear to be limited to proficient speakers of the language (Flege, 1999), suggesting that they may be related to learning the appropriate pronunciation in the language.

Other studies have failed to find such perception-production correlations, however. For example, Bailey and Haggard (1973, 1980) failed to find a correlation between average produced VOTs for voiced and voiceless consonants and listener's category boundaries on a /g/-/k/ continuum. Ainsworth and Paliwal (1984) asked listeners to both produce English glides and identify synthetic tokens, and measured the F2 and F3 loci for these items. But they found that the variability within subjects was as high as that between subjects, arguing against perception-production links. Many of these failed attempts to find perception-production links have used relatively coarse-grained distinctions between stimuli (for example, Ainsworth and Paliwal, 1984; Bailey and Haggard, 1973, 1980; Paliwal *et al.*, 1983), or have averaged productions across different phoneme categories (such as labial and velar stop consonants; see Bailey and Haggard, 1973, 1980). Other studies have used relatively simple production measures, such as individual formants (Ainsworth and Paliwal, 1984; Frieda *et al.*, 2000; Paliwal *et al.*, 1983).

The variability in these results clearly demonstrates that correlations between speech perception and speech production are inconsistent. Finding such correlations appears to require not only a task that is sensitive to small variations in perception and production, but also an appropriate acoustic correlate as a production measure. In fact, there is no reason to expect correlations between perception and production unless the acoustic property being measured is one that is at least related to the cues actually used by listeners. The variability in previous research may suggest that these correlations could serve as a means of telling us something about the cues being investigated, specifically about the likelihood that listeners actually use those cues.

Another possible reason for this variability in findings is the hyperspace effect (Johnson *et al.*, 1993a). When asked to judge the best examples of a phonetic category, listeners often choose tokens with more extreme articulation than is common in fluent speech. Listeners' perceptual prototypes might better match exaggerated productions than typical ones. Although this would not necessarily eliminate a perception-production correlation, it would be likely to reduce it, making it more difficult to find significant results (especially with relatively insensitive tasks).

The present paper explores the feasibility of using perception-production correlations as a means of evaluating the appropriateness of speech production measures. Experiment 1 demonstrates the existence of perception-production correlations in a case where an appropriate cue is known. It focuses on VOT differences between voiced and voiceless stop consonants, an acoustic measure of voicing that has received substantial support in the literature (Lisker and Abramson, 1964, 1970). If correlations are not clearly apparent in this case, it would suggest either that our methodology is not sufficiently sensitive, or that these correlations vary across speakers. In either case, correlations could not be relied upon as a research tool. Given a significant correlation in experiment 1, experiment 2 then examines a phoneme for which there have been multiple proposed acoustic cues, with the goal of determining whether perception-production correlations can distinguish among related metrics.

II. EXPERIMENT 1

This experiment investigates whether correlations between individuals' perception of speech contrasts and their production of those contrasts can be found when an appropriate acoustic cue is used. Listeners participated in both a production and a perception task focusing on voice onset time (VOT), a result of laryngeal timing differences which are the primary cue to the voiced-voiceless distinction among stop consonants (Lisker and Abramson, 1964, 1970). The relationship between each individual's measures on the two tasks was examined.

The perception task was modeled on work by Miller and Volaitis (1989). In the present version of the task, listeners heard a VOT series ranging from /bɑ/ to /p/ɑ/ to something beyond a good /pɑ/ (labeled as */pɑ/, following Miller and Volaitis). These extreme stimuli sound like a very breathy ''pah,'' and have VOTs that are far longer than would normally occur in speech. Listeners were asked to rate the items for their goodness as members of the category /p/. Miller and Volaitis found that this task results in an orderly rating scale, with only one or a few items receiving the highest rating, and

ratings dropping off to either direction. The item with the highest mean rating was considered the listener's category prototype, and correlations between this perceptual prototype and the individual's production prototype—the average acoustic measure across a number of different productions—were examined.

These two tasks provide measures of each individual's perceptual prototype and average production, using the same acoustic measure (VOT). If correlations exist between perception and production within individuals, those individuals who produce /p/'s with longer VOTs would be expected to also rate items with longer VOTs as being better examples of the category than would individuals who produce tokens with shorter VOTs. Thus, correlations between each individual's perception and production measures would be expected.

A. Method

1. Subjects

The 25 paid participants were native speakers of English with no reported history of a speech or hearing disorder. They participated in two 1-h sessions. Data from two additional participants were dropped for being a non-native speaker ($n=1$) or for missing the second visit ($n=1$). During debriefing one of our listeners reported that he had misunderstood the instructions, and had identified whether the items were /p/'s or not, rather than rating their degree of goodness; his data were removed from analysis, as were that of a speaker whose highest rated item had a VOT more than 4 standard deviations beyond the mean of the other participants (221 ms). Data from three additional participants were removed because a central member of the /pɑ/ category could not be determined from their perceptual data, as discussed in the procedure below. Leaving out these listeners resulted in 20 participants for this experiment.[1]

2. Stimuli

To create models for our production task, a female native talker of English (RSN) recorded one token each of the 48 CV syllables formed from pairings of the English stop consonants (/p/, /b/, /t/, /d/, /k/, /g/) and the eight vowels /i, e, æ, u, o, ɔ, ɑ, ʌ/. These vowels represent the range of vowels in English which can occur in an open syllable. Two additional tokens of the syllable /pɑ/ (for a total of three) were recorded to provide a greater range of examples of the target syllable. All tokens were amplified, low-pass filtered at 9.5 kHz, and digitized via a 16-bit, analog-to-digital converter at a 20-kHz sampling rate.

Rather than create a synthetic speech series for our perceptual task (as did Miller and Volaitis, 1989), items from natural speech were edited in order to make the items as natural-sounding as possible. The same native speaker recorded the tokens /bɑ/, /pɑ/ and */pɑ/. A 21-item continuum ranging from /b/ to /p/ was created from the /bɑ/ base by removing successively longer sections from the /b/ onset and replacing them with the corresponding portions of the /p/ onset. Formant transitions in the original items were approximately 35 ms for /bɑ/ and 75 ms for /pɑ/, but the formants during the transitions were more broad for the /p/. This increase in bandwidth would have helped to mask any mismatches in formant values during these transitions; moreover, any such mismatches would have occurred only in the first two or three items in the series, none of which were within the range of prototypical /p/ tokens. Steady-state formants were at 950, 1350, and 3200 Hz for /b/, and at 1000, 1275, and 2950 Hz for /p/. Although these values are not identical, the formant frequencies are sufficiently close that cross-splicing did not result in sudden changes in formant values. All editing was done at zero crossings in the digital waveform to avoid audible clicks. The first stimulus was created by removing the /b/ release burst and replacing it with the release burst from /pɑ/. The second through twenty-first stimuli were each made by removing one additional vocal pulse from the onset of the /bɑ/ syllable, and replacing this with the equivalent duration of burst release and aspiration from /p/. Durations of vocal pulses were not exactly equal, but averaged 4.2 ms. The next 40 items were each generated by removing an additional 5 ms of aspiration from the */pɑ/ token and adding this to the end of the aspiration in the last item of the /b-p/ series (i.e., the 21st, or most ''p''-like item).

This resulted in a 61-item series, which would have been overly tedious for the participants. Pilot testing showed that most individuals placed their prototypes between 55 and 140 ms VOT (or between stimulus items 13 and 31). In order to maintain sensitivity to small differences between listeners, all stimuli within this range were included in the experiment. Beyond this range, every other stimulus was included in the experiment, and the remaining stimuli were removed. This resulted in a 40-item series, with VOTs ranging from 8.25 to 291 ms. Adjacent stimuli in the series differed in VOT by 4.6 ms at intermediate VOTs and by 9.4 ms at both longer and shorter VOTs.

3. Procedure

Listeners participated individually in both a production task and a perception task across two sessions; the production task occurred at the start of the first session.[2] The production task was an imitation task; pilot work suggested that when asked to read aloud written representations of syllables, talkers tend to speak progressively more quickly as recording continues. To encourage talkers to maintain a fairly even speaking rate, our participants listened to an example of each syllable over a loudspeaker and then repeated that syllable in the way they would normally produce it. This method of recording has previously been used by Forrest *et al.* (1988). Although it is possible that this method could induce listeners to mimic the acoustic characteristics of the model, the variability in participant's productions suggest this was not the case: average /pɑ/ productions ranged from VOTs of 51 to 125 ms.

The model stimuli for this production task were converted to analog from by a 16-bit, digital-to-analog converter at a 20-kHz sampling rate, low-pass filtered at 9.5 kHz, and presented in random order. Trials were repeated if productions were peak-clipped, if the participant failed to respond within 4 s, or if the participant indicated that he or she

wished to redo that trial (either because of uncertainty as to the target syllable, or because some other noise, such as a cough, interfered with recording). Listeners heard (and recorded) each of the 50 syllables in a single block, and participated in two such blocks. This resulted in two recordings of each CV syllable (and six tokens of the target item /pá/) to be used for later acoustic measurement.

Listeners then participated in the perceptual task. The stimuli for this task were converted to analog form in the same manner as above, and were presented binaurally through TDH-39 headphones at a comfortable listening level. Listeners heard the syllables in random order, and were asked to rate each initial phoneme for its goodness as a member of the category /p/. They responded using the numbers 0–9 on a numeric keypad. Listeners were instructed to use the ''0'' label whenever the item did not sound like a ''p'' at all, to use the ''1'' when they were unclear whether the item was a ''p'' or not, and to use the range ''2''–''9'' for items which were definitely members of the category ''p,'' but differed in how good of an example they were. Listeners were given a reference sheet containing this scale in case they wished to refer back to it. Responses from the first block of trials (one repetition of each item) were considered practice and were not included in subsequent data analysis. Listeners then participated in six test blocks (of two repetitions per item) in each of the two sessions, for a total of 24 responses to each stimulus.

4. Acoustic and perceptual measures

A mean perceptual rating was computed for each stimulus for each participant. The single item with the highest rating (regardless of where it occurred) was considered the listener's perceptual prototype, and that item's VOT was recorded. One participant had equally high ratings for two items in the continuum; the VOT values for these items were averaged as that listener's prototype. Listeners were excluded if they did not show at least a half of a ranking difference between their peak item and the final item in the series, suggesting there was no clear peak item.

For the production experiment, the time interval from syllable release to the onset of vocal pulsing was measured for each token produced by each speaker. The six values for the recordings of ''pa'' were averaged as the produced ''pa'' VOT. The values for the 14 other ''p'' recordings were averaged to find a mean VOT for the remaining ''p'' tokens. Likewise, the values for the 16 recordings for each of the other stop consonants were averaged, to determine its mean VOT. Prevoicing was ignored since this is a different cue from bursts/aspiration and it may be inappropriate to average across the two cues.

A second coder remeasured VOT for all 52 voiceless items for two participants for reliability purposes. Only voiceless items were considered because the large difference between voiced and voiceless items would have resulted in a high correlation across coders even had the VOT measures been relatively coarse; by restricting the range, we focus the correlation on the consistency within the category (as well as making it more difficult to find a high correlation in general). Despite this restricted range, correlations were 0.94 and 0.95 for the two talkers (average absolute differences were 3.5 and 5.3 ms, respectively), suggesting that VOT measures were quite reliable.

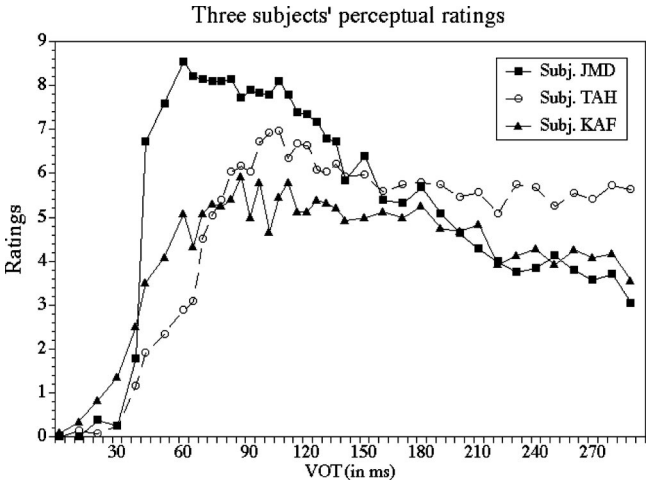

FIG. 1. Three subjects' perception data. Subject's ratings generally increase with increasing VOT until they reach their peak rating, then begin to decrease as the items sound more and more extreme.

B. Results and discussion

Listeners generally showed clear prototypes, with ratings dropping to either side, although they did vary in the number of items receiving high rankings. On average, listeners showed a rating drop-off of 2.5 units between their peak item and the series */pɑ/ endpoint; average rating on the /b/ endpoint was 0.27, suggesting it was not heard as a member of the /p/ category. Listeners' prototypes ranged from VOTs of 60.9 to 150.9 ms, suggesting that this perceptual measure is sensitive to differences between individuals. Figure 1 shows three listeners' perception data; these individuals were selected as demonstrating a range of prototype values (60.9, 88.0, and 105.3 ms) and drop-offs (5.5, 2.4, and 1.3 units).

The calculations resulted in one perceptual measure (VOT of the prototype), and seven production measures (average VOT for /pɑ/, average VOT for other /p/ items, and average VOT for /b/, /t/, /d/, /k/, and /g/ items). A stepwise hierarchical regression was performed using the perceptual measure as the dependent variable, and all seven production measures as independent variables. A hierarchical regression is less likely to capitalize on chance relationships than is a stepwise regression (Cohen and Cohen, 1983), but requires an *a priori* ordering of the IVs in terms of their likelihood of having a correlation with the DV. On the basis of phonological theory it was assumed that items differing from the target in one phonetic feature would be more closely related to the target than those differing from it in two features, and that items matching on the measure of interest (VOT; that is, /t/ and /k/) would be more closely related than the phoneme /b/, which matches on place of articulation. As alveolars tend to be more similar to bilabials than are velars (Dorman *et al.*, 1977; Klatt, 1975; Lisker and Abramson, 1964), alveolars were placed higher in the ordering. This resulted in the ordering /pɑ/, /p/, /t/, /k/, /b/, /d/, /g/.

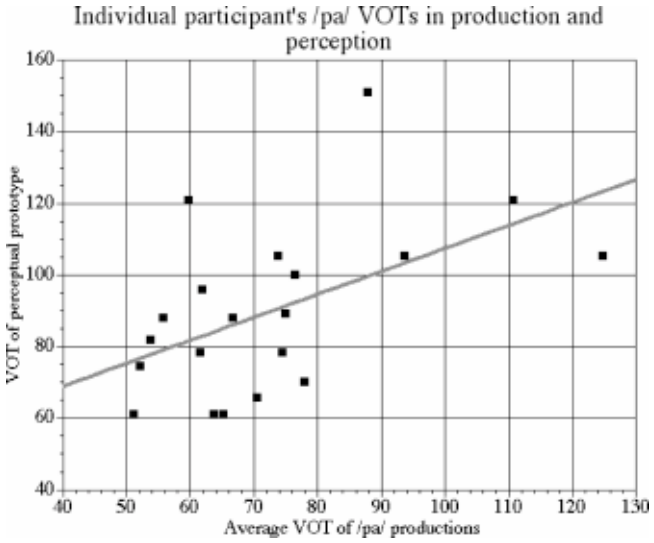

FIG. 2. Scatter-plot showing the correlation between the average VOT in production for /pɑ/ and the VOT of the highest-rated ''*p*'' in the perception task.

All production measures were independently correlated with the prototype VOT. However, only the VOT values from the /pɑ/ item contributed significantly to the regression formula, and the /b/ items added marginally significant additional information; the other items did not add additional information to the equation. The variation in produced /pɑ/ VOT was responsible for 27% of the variance in listeners' perceptual ratings [$F(1,18)=6.73,\ p<0.02$], whereas the variation in /b/ VOT was responsible for an additional 15% [$F(1,14)=3.94,\ p=0.07$]. Figure 2 shows the regression line with /pɑ/ VOT as the predictor. A complete listing of the regression coefficients, r^2, change in r^2, and statistics are given in Table I. It is apparent from Fig. 2 that the /pɑ/ correlation was augmented by the unusually high perceptual scores for two individuals; however, the correlation remains significant even if data from these individuals are removed, suggesting they are not the primary cause of the correlation ($r=0.49,\ p<0.05$).

These results suggest that the present methodology was successful at finding a link between perception and production. There was a significant relationship between participants' productions and their perceptual prototypes. Individuals whose perceptual prototype for ''p'' occurred at longer VOTs also tended to produce longer VOTs themselves.

It is interesting to note that while the listeners' productions of the voiceless stops did not provide additional information above and beyond their production of the target item itself, their production of the first voiced stop in the hierarchy approached doing so. This suggests that production of the voiceless items may be highly correlated within each individual, but that production of voiced items may not be as correlated with the voiceless tokens. Indeed, the p, t, and k measures were highly correlated, with correlations ranging from 0.88 to 0.96; the b, d, and g items, while correlated with one another, did not correlate so highly with the voiceless items (correlations among the voiced items ranged from 0.54 to 0.75; correlations between voiced and voiceless items ranged from 0.37 to −0.06). The additional voiceless stops may not have added additional information because they were highly correlated with the production of the target item; the marginal effect of adding the /b/ items into the equation suggest that the voiced stops contained additional information beyond that provided by the production of the target item. Perhaps these provide information about the degree of category separability the individual prefers (participants whose /b/ productions had relatively short VOTs tended to have prototype /p/s with longer VOTs, suggesting a preference for more easily discriminable categories).

Something more akin to listeners' category boundaries were also examined: the minimum VOTs they considered acceptable for a /p/. In production, this was estimated as the minimum /p/ VOT that speakers produced—across listeners this averaged 46.7 ms. In the perception task, the VOT of the earliest member of the continuum that listeners rated as being a member of the /p/ (rather than /b/) category was measured—this averaged 44.7 ms across listeners. These two measures showed a significant correlation across participants ($r=0.48,\ p<0.05$), suggesting that the lower ends of listeners' categories were comparable in perception and production, much as were their category prototypes.

There was also evidence for a hyperspace effect (Frieda *et al.*, 2000; Johnson *et al.*, 1993a), as has previously been found for vowels. Perceptual prototypes had an average VOT of 90 ms, whereas VOTs of the participants' productions averaged only 73 ms. This difference was significant by a paired *t*-test, $t=3.61$, $p<0.002$. Fifteen of the 20 participants showed this pattern of longer VOTs for their perceptual prototype than in their speech production.

The results from this experiment suggest that individual differences in production are related to differences in perception. Both the best exemplar of the category, and the lowest acceptable member of the category, were similar in production and perception within each individual. It appears that production-perception correlations can be found with an ap-

TABLE I. Results from multiple regression from experiment 1.

Step	Individual *r*	Multiple *r*	Multiple r^2	Change in r^2	Change in F	Significance
pɑ	0.522	0.522	0.272	0.272	6.73	0.018
p	0.361	0.550	0.303	0.031	0.75	0.398
t	0.311	0.551	0.303	0.000	0.00	0.960
k	0.362	0.561	0.315	0.012	0.27	0.614
b	−0.442	0.682	0.466	0.150	3.94	0.067
d	−0.297	0.688	0.474	0.008	0.20	0.662
g	−0.323	0.756	0.572	0.098	2.75	0.123

propriate perceptual task and an appropriate acoustic correlate.

One possibility is that this task can be used to evaluate different acoustic cues. Often, there are multiple proposals for how a given phonemic distinction should be described. It might be possible to evaluate different metrics by determining the degree to which perception and production measures using these proposed cues are correlated. Such an approach requires that correlations occur only for those cues that are actually used by listeners. Given that different proposed cues are generally highly correlated with one another, perception-production correlations might be present for all proposed cues. If so, the correlations would not provide additional information to distinguish among them. This approach can only be useful if correlations exist for some acoustic cues, but not for all. Experiment 2 examines this in more detail.

III. EXPERIMENT 2

Unlike the /p/-/b/ distinction examined in experiment 1, there are some phonemic distinctions where multiple metrics or measures appear to be equally plausible. One such phoneme is the fricative /ʃ/ (''sh''). Fricatives are produced by creating a partial obstruction in the mouth. Forcing air through this narrow constriction causes turbulence in the airstream, resulting in a ''noisy'' sound, with energy at a broad range of frequencies (Pickett, 1980). The location of the obstruction differs between an /s/ and an /ʃ/, and a number of studies have examined the possible acoustic correlates of this difference. Research has focused on four attributes as being particularly important for fricatives in general: spectral properties of the fricative noise, noise duration, noise amplitude, and spectral properties of the transition between the fricative and the following vowel (Jongman *et al.*, 2000).

Of these four types of cues, spectral properties of the noise appear to be most important for the /s/-/ʃ/ distinction. Noise duration and overall amplitude appear particularly important for distinguishing the sibilant fricatives (/s/ and /ʃ/) from the nonsibilants (/f/ and /θ/), but do not appear to distinguish between the two sibilants (Behrens and Blumstein, 1988b). Relative amplitude differences do appear to be important, but this may be a result (at least in part) of concomitant changes in spectral properties (Hedrick, 1997; Hedrick and Ohde, 1993). Although some research has examined transition information (Sussman, 1994; Sussman and Shore, 1996; but see Fowler, 1994) as cues to place of articulation within fricatives, most researchers have focused on spectral properties of the noise as being the most important cues for distinguishing /s/ and /ʃ/. This information has been shown to be sufficient for a high degree classification in several studies (Tabain, 1998; Tomiak, 1991).

There have been many proposals as to the best ways to characterize this spectral information. Harris (1958; see also Heinz and Stevens, 1961; Hughes and Halle, 1956; May, 1976) found that the noise center frequency information (roughly the frequency mean) is the primary cue for distinguishing these particular phonemes. Strevens (1960) reported that the frication range for /s/ was shifted higher than that for /ʃ/, which would likewise imply that the mean frequency for /s/ would be higher (although he measured only the range of frequencies at which energy occurred, and did not actually calculate average values). Forrest and colleagues (1988) examined three spectral moments [centroid (or frequency mean), skewness, and kurtosis], and found that skewness of frication was the primary feature distinguishing these phonemes, although centroids might also aid in their discriminability [but see Shadle and Mair (1996) for contrasting data on the role of skewness]. In contrast, other work has examined spectral peaks, which are more akin to a statistical mode than a mean (Behrens and Blumstein, 1988a; Jassem, 1965; Seitz *et al.*, 1987). Thus, while there is wide agreement that the frication noise is the primary acoustic cue for distinguishing /s/ and /ʃ/, there is less agreement on the appropriate way of measuring this cue.

One reason for this disagreement is that these measures are highly correlated in these phonemes. They do not refer to independent information in the spectrum, but instead are different ways of describing the same information. It is therefore very difficult to distinguish between these measures experimentally; any modification of one cue results in changes in the other cues as well.

In recent work, Jongman *et al.* (2000) examined a variety of cues to fricatives. They found that while many of these cues were successful at classifying fricatives, discriminant analysis suggested that spectral peak location was a more important cue than were spectral moments.

The present experiment proposes a different way of evaluating these measures. If the degree of perception-production correlation for a given cue is based on the extent to which that cue is related to the dimensions utilized by the listener, then the degree of correlation can be used as means of evaluating this relation. Correlations should be stronger for the cue most similar to that which listeners are actually using.

Given that the different cues are themselves highly correlated, one concern is that all cues may result in strong perception-production correlations. If so, these types of correlations would not be useful as a means of evaluating metrics. Thus the primary goal in the present experiment is to determine whether perception-production correlations can distinguish among different acoustic measures, even when those measures are themselves related.

A. Method

1. Subjects

Twenty-four volunteers participated in exchange for a cash payment. Ratings from five of these participants did not fall off towards the extremes of the continuum; their data were not analyzed.[3] (For this experiment, in which both endpoints of the series were clearly not /ʃ/ tokens, a minimum of a one category rating drop-off to either side was required for data inclusion.) This left a total of 19 listeners, one of whom was also in experiment 1. The average rating drop-offs were 4.1 units towards the velar side, and 6.3 units toward the /s/ side.

2. Stimuli

For the model stimuli for the production task, a female native talker of English (RSN) recorded four tokens of each

CV syllable consisting of either /s/ or /ʃ/ followed by one of the seven vowels /i, e, æ, u, o, ɑ, ʌ/. The recording manner for these 56 items was identical to that in experiment 1.

For the perception task, the stimuli consisted of series ranging from /sæ/ to /ʃæ/ and from /ʃæ/ to beyond-/ʃæ/ (or */ʃæ/). The vowel /æ/ was chosen because it does not entail lip-rounding or protrusion, which can alter the spectral information in the fricative (Soli, 1981). These stimuli were produced synthetically, as the type of editing used in experiment 1 can only be used to create duration-based series, not frequency-based series. The synthetic stimuli were modeled on a male voice chosen because it is well-mimicked by our speech synthesis program.

Use of a male voice in the perception task and a female voice in the production task should prevent listeners from hearing the items as coming from the same individual, and from judging the voice in the perceptual task on the basis of the speech from the talker in the production task. This avoids one potential criticism of experiment 1, that the talker used in the perceptual study and the model for the production component were the same individual. If listeners in the production task were trying to mimic that talker's speaking style, correlations could have occurred for that reason alone. If perception-production correlations are found in this experiment where the voices clearly differed, it would suggest that these relationships are not an artifact of having used the same talker for both tasks.

The model speaker produced tokens of /sæ/ and /ʃæ/ in the context of the carrier phrase, ''Please say _____ to me.'' The transition and vowel portions of the /s/ and /ʃ/ syllables were temporarily removed, leaving only the 215-ms frication portion of the syllables. These two frications were synthesized using the parallel mode of a cascade/parallel synthesizer (Klatt, 1980). Formant frequencies, amplitudes, and bandwidths were carefully adjusted to make the synthetic tokens both sound as similar to the original items as possible and look as similar as possible in spectral cross-section. The vowel portion from one of the two syllables was likewise synthesized and its formant values, bandwidths, and amplitudes adjusted. This vowel portion was then appended to both the /s/ and /ʃ/ tokens, resulting in two endpoints which had identical synthesis parameters after the first 215 ms (or 43 frames). Values for the initial frication portion were then interpolated between the two endpoints to make a 21-item series. This interpolation was performed on all parameters that differed across the endpoints: the amplitudes and bandwidths of all formants, and the location of formants 2, 4, and 5 (the location of formants 1 and 3 were the same in both endpoints, as was the bandwidth of formant 3). The transition and vowel portions (which occurred after the initial 215 ms) were held constant across items.

Rather than make the series continue beyond /ʃ/ acoustically (by continuing to adjust formant and amplitude values in the same manner as in the first half of the continuum), the series continued beyond /ʃ/ in an articulatory sense, towards a more extreme place of articulation. Continuing to adjust formant and amplitude values in the same manner could have resulted in an endpoint that was not possible from a human vocal tract. A linguist was asked to produce fricatives from a variety of places of articulation: alveolar (as in /s/), palatal (/ʃ/), and velar and uvular fricatives (which do not occur in English but do occur in other languages; uvular fricatives occur in one of the languages in which she was fluent). The first five formant movements between her tokens were analyzed, and the formants, amplitudes, and bandwidths in our synthetic continua were adjusted to move in the same manner. Thus our formant movements beyond /ʃ/ were such that they moved towards a more velar/uvular place of articulation. A 20-item series was created in this manner, resulting in a total of 41 stimuli (the /s/ endpoint, 19 interpolated items between /s/ and /ʃ/, the /ʃ/ endpoint, 19 interpolated items beyond /ʃ/, and the most velar endpoint).

3. Procedure and measures

This study was combined with that of another perceptual rating study using other syllables, not reported here. Participants recorded their speech at the onset of the first session, and then took part in the two perceptual tasks; the order of these tasks was counterbalanced across participants.

Procedures for both the production and perception tasks were identical to those in experiment 1, with the exception that listeners were asked to rate the phonemes as examples of the sound ''sh,'' rather than as examples of the sound ''p.'' There were 16 blocks of trials in the perceptual task and 2 blocks of trials in the production task.

Three types of acoustic measurements were taken on the participants' productions: frication centroid, skewness, and peaks. For centroids and skewness, analysis was modeled after that of Forrest *et al.* (1988); a 20-ms analysis window was used to compute a sequence of Fourier spectrum; the initial analysis window centered on the frication onset and each subsequent spectra was computed over a window centered 10 ms further into the signal, resulting in a series of measurements containing 50% overlap. The speech signal was preemphasized by first differencing (with preemphasis of 0.94), and a 400-point Hamming window was used for analysis. (For the synthetic speech in the perceptual task, the stimuli had a 10-kHz sampling rate, so a 20-ms window resulted in a 200-point Hamming window). The spectra were treated as random probability distributions, and the centroid (or mean) and skewness of the distribution were calculated. The number of analysis windows was set at 10; analysis thus occurred over a total of 110 ms and the means and skewness values were averaged across the 10 frames. [This duration was suggested by Tomiak (1991) to provide a valid estimate of the fricative, based on results from a masking study.] The measured portions were at the onset of the fricatives.

Peak frequency measures were performed using the CSRE software package from AVAAZ. Each production was analyzed using a fast Fourier transform over a 128-point Hamming window with 50% overlap, averaged across the initial 100 ms. This analysis was then treated as a random probability distribution, but instead of finding the moments of the distribution, the mode was found instead (or the frequency at which the greatest amount of energy was present). Some speakers' productions did appear to have more than one peak frequency; however, the single frequency value

TABLE II. Acoustic measures from experiment 2.

Participant	/ʃæ/ centroid	/ʃæ/ skewness	/ʃæ/ peak
ggg	5197	−0.001	2822
ddy	5302	−0.059	3628
clk	5315	−0.051	3461
ic	5174	−0.028	3528
cer	5107	+0.031	2871
hem	5122	+0.001	4111
jg	5202	−0.060	4692
nv	5316	−0.064	3477
cab	5303	−0.088	4199
acy	5450	−0.138	5966
jem	5124	+0.023	3374
bam	5268	−0.053	4590
iaf	5036	+0.089	4316
kjp	5355	−0.117	5429
kfb	4999	+0.041	3828
vjl	5302	−0.092	5410
mlt	5101	+0.040	4423
ksk	5367	−0.082	3916
tlg	5272	−0.064	4033

with the greatest energy was selected. These acoustic measurements are shown in Table II.

For the perceptual task, the single item in the continuum with the highest rating was considered the listener's prototype, as in experiment 1. This prototype was measured for its frication centroid, skewness, and peak, in the same manner as the participants' productions described above. For one listener, three adjacent items received equally high ratings; the values for these three items were averaged on each measure to find the prototype for that listener.

B. Results and discussion

As expected, the three production measures were highly correlated, especially the two spectral moments measures. For centroids and skewness, the correlations for the /ʃ/ measures across participants was -0.94, $p<0.0001$. For centroids and peaks, the correlation was marginal, $r=0.43$, $p<0.07$, and for skewness and peaks it was -0.54, $p<0.02$. Thus, all three measures do seem to be based on related aspects of the same information.

The perception-production correlations were examined using all three measures. In experiment 1, it was found that measurements from the single syllable identical to the perceptual item were the most relevant; the relationship between the /ʃæ/ prototypes and the average /ʃæ/ productions were therefore examined here (that is, the average value across the eight different productions of the /ʃæ/ syllable, rather than the average across all 56 /ʃ/ tokens).

For centroids, the correlation was not significant ($r=-0.30$, $p>0.10$). Moreover, it was actually negative. While negative correlations across different measures would be unsurprising, correlations between production and perception using the same measure should be positive. It would be rather odd for those individuals who produced the most extreme /ʃ/ tokens to prefer the least extreme versions perceptually. Thus finding a negative correlation here suggests that individuals' perceptual prototypes are not determined by the tokens' centroid measures.

For skewness, correlations were again both negative and nonsignificant ($r=-0.19$, $p>0.40$). Skewness likewise does not appear to be a primary factor in individuals' prototypes.

The correlation for peak frequency, however, was not only positive but also was significant ($r=0.50$, $p<0.03$). The correlation was almost identical in size to that found in experiment 1 ($r=0.52$). This suggests that frequency peaks may be a better indication than centroids of what makes a particular fricative token sound better to a listener. Those listeners who showed more extreme values in their frequency peaks for /ʃ/ also preferred listening to more extreme tokens. This was not the case for either fricative centroid or skewness measures.

More importantly for the present purposes, the findings also suggest that correlations between speech perception and speech production can differentiate between different acoustic cues. Only acoustic measurements based on the peaks in the spectrum appeared to be related to listeners' goodness ratings. This is in accord with recent findings by Jongman *et al.* (2000), also suggesting that spectral peaks are better cues to fricative discrimination than are spectral moments. This suggests that even when different acoustic cues are highly correlated, perception-production correlations can be used to discriminate among different measures.

The present results also extend the general finding from experiment 1 that correlations exist between speech perception and speech production. Finding these correlations in two different experiments, for two different phonemic contrasts, suggests that these results are fairly common. Furthermore, one potential problem in experiment 1 was that the talker whose voice served as the model for the production study was the same talker as that judged in the perceptual study. If the correlations in that experiment were actually the result of participants trying to mimic that talker, such results would not be expected in the present experiment, where the talker that served as the base for the perceptual study and the talker that served as the model for the production component were not only different individuals, but also were of different genders.

The next logical step would be to directly test the idea that peaks are more important than centroids by orthogonally varying these dimensions. Unfortunately, it is not possible to vary these two properties in this manner (at least not while maintaining good endpoint stimuli), which is why the finding of an alternative method of differentiating cues is so important. As an example of the difficulty, the synthetic /s/ endpoint in this study had a mean frequency of approximately 4500 Hz, and a peak frequency of approximately 4700 Hz. In order to manipulate peak and centroid independently, it would be necessary to create a series that maintained this centroid at 4500 Hz while the peak frequency moved from 4700 Hz down to a value appropriate for an /ʃ/ (approximately 3400 Hz based on our /ʃ/ endpoint). Lowering the peak is relatively easy in synthetic speech; however, in order to keep the centroid from changing along with the peak, this would require adding diffuse high-frequency energy to compensate for the loss of energy at 4700 Hz (and the increase in energy at 3400 Hz). With an unlimited frequency range, this

would be easily doable. However, the implementation of the Klatt synthesizer used here was limited to 5000 Hz, making it impossible to add sufficient high-frequency energy without creating a high-frequency peak. This limits the comparison of peaks and centroids to indirect measures, such as the correlations discussed here.

IV. GENERAL DISCUSSION

These two experiments demonstrate that individual differences in production are related to differences in perception. Listeners whose productions are more extreme along an acoustic continuum appear to prefer hearing more extreme productions from other speakers as well. This is in addition to a hyperspace effect, in which individuals prefer listening to more extreme tokens than they themselves produce.[4]

However, these production-perception correlations are not ubiquitous. Although they will occur for acoustic cues known to be used by listeners (such as VOT), they do not occur for all possible acoustic measures. Despite the fact that the three acoustic measures used in experiment 2 were highly correlated with one another, significant perception-production correlations were found only for one of them—in particular, for the one most supported by a recent comparative analysis by Jongman *et al.* (2000). Nor did the lack of an effect in the other two measures appear to be caused by a lack of power: the results were not only nonsignificant, but were in the opposite direction as that expected.

These findings suggest that this task can be used to evaluate different acoustic measures. For many phonemic distinctions, there is no apparent ''best'' measure. Many different metrics may be proposed, and it is often difficult to discriminate among such metrics experimentally. Looking for links between perception and production may provide another means for making such comparisons.

Clearly, this conclusion must be taken as tentative at this point. More research is necessary to ensure that these correlations only exist (and consistently exist) when the appropriate measure is used. Furthermore, since the degree of variability among individuals can influence the likelihood of finding a significant correlation, this task is likely to be best used in a converging methods approach, in combination with more traditional ways of contrasting metrics (such as that of Richardson, 1992 and Tomiak, 1991). Still, the results are at least suggestive that this task can provide a better indication of the types of acoustic cues most likely to be used by listeners, and may be particularly useful in situations where other contrastive methods are not possible.

One limitation of the present approach is that it requires the use of a single cue, such as frequency centroid or VOT. For some phonemic distinctions, sets of cues have been proposed that work as a whole. For example, peak differences (Syrdal and Gopal, 1986) have been proposed as cues to stop consonant place of articulation. These were proposed as a set of values, and there is no reason to believe that the individual peak differences would of necessity correlate with one another. If each component is a dimension in multi-dimensional space, the overall location of a value in space would depend on the values from the set of measures, but need not correlate highly with any single measure. Since there is no statistical test that provides an overall measure of the strength of a relationship between two sets of variables (see Cohen and Cohen, 1983), the present methodology of examining correlations between perceptual prototypes and average productions is likely to be limited to cases in which there is a single acoustic property that can be measured.

Although significant correlations between speech production and speech perception were found in both of the present experiments, these correlations were quite modest, accounting for approximately 27% of the variance in listeners' perceptual prototypes. There are several possible reasons why this might be the case. One possibility is that the representations for perception and production are at least partially distinct. If this were the case, it could be taken as an argument against models such as motor theory (Liberman and Mattingly, 1985), which rely on identical representations for both input and output. However, there are other potential explanations for the small size of these effects that limit the strength of this conclusion. The effect size may be due, in part, to the existence of a hyperspace effect (Johnson *et al.*, 1993a); listeners highest-rated item may be more strongly related to a hyperarticulated production than to a typical one. Since participants were not asked to exaggerate their productions, the correlation may be less strong than would otherwise be the case. It is also possible that a stronger correlation might have arisen with more participants, or more acoustic measures per participant.

Anecdotal evidence suggests that people are often surprised by the sound of their own voice when they hear a recording of it. This is due to the fact that one's own voice is heard both via air conduction (as others hear us) and via bone conduction within the head, which emphasizes low frequencies. This makes our own voices sound more resonant to ourselves than to others. Perception-production correlations might therefore be expected to be strongest for temporally-based contrasts and for sounds without vocal fold vibration, as these would be unaffected by a low-frequency emphasis.

As expected from previous research, correlations between speech perception and speech production do appear to exist, although they are not as strong as might be expected on the basis of some theoretical models. These correlations appear to distinguish between different acoustic cues, suggesting that they may be usable as a way of evaluating different proposed metrics. Future research will be needed to examine this proposal in more depth.

ACKNOWLEDGMENTS

Some of this research was from a doctoral dissertation, directed by James R. Sawusch. Special thanks to him, and also to Peter Jusczyk and Paul Luce for helpful discussions, and to Sheryl Clouse for performing the peak measurements described in experiment 2. Also, thanks to Jim Sawusch for the use of his acoustic measurement program, NMEASURE, which was used for the centroid and skewness measures in experiment 2, Nina Azhdam for the reliability measures in experiment 1, and to Rob Fox, Chris Turner, and an anonymous reviewer for comments on a previous draft.

[1]As a comparison, Frieda *et al.* (2000) report that 11 of their 35 participants did not meet their criteria for prototype designation.

[2]Because of a computer recording error, one subject's production task had to be recorded at the start of the second session.

[3]Four of these five participants failed to show a drop-off towards the /s/ end of the series, rather than towards the velar end; that is, they gave high rankings to the most /s/-like member of the series. In contrast, the 19 participants whose data were kept gave this item an average rating of 0.6, indicating that they did not hear this item as a member of the /ʃ/ category at all. One possibility is that the individuals whose data were dropped were confused by English orthography, in which /s/ and /ʃ/ both contain ''s.''

[4]Hyperspace effects could only be explored in experiment 1: in experiment 2, the perceptual items were based on synthetic speech with a limited frequency range. This makes the direct comparison to natural productions difficult.

Ainsworth, W. A., and Paliwal, K. K. (**1984**). ''Correlation between the production and perception of the English glides /w, r, l, j/,'' J. Phonetics **12**, 237–243.

Bailey, P. J., and Haggard, M. P. (**1973**). ''Perception and production: Some correlations on voicing of an initial stop,'' Lang. Speech **16**, 189–195.

Bailey, P. J., and Haggard, M. P. (**1980**). ''Perception-production relations in the voicing contrast for initial stops in 3-year-olds,'' Phonetica **37**, 377–396.

Behrens, S. J., and Blumstein, S. E. (**1988a**). ''Acoustic characteristics of English voiceless fricatives: a descriptive analysis,'' J. Phonetics **16**, 295–298.

Behrens, S. J., and Blumstein, S. E. (**1988b**). ''On the role of the amplitude of the fricative noise in the perception of place of articulation in voiceless fricative consonants,'' J. Acoust. Soc. Am. **84**, 861–867.

Bell-Berti, F., Raphael, L. J., Pisoni, D. B., and Sawusch, J. R. (**1979**). ''Some relationships between speech production and perception,'' Phonetica **36**, 373–383.

Bradlow, A. R., Pisoni, D. B., Akahane-Yamada, R., and Tohkura, Y. (**1997**). ''Training Japanese listeners to identify English /r/ and /l/: IV. Some effects of perceptual learning on speech production,'' J. Acoust. Soc. Am. **101**, 2299–2310.

Cohen, J., and Cohen, P. (**1983**). *Applied Multivariate Regression/ Correlation Analysis for the Behavioral Sciences*, 2nd ed. (Erlbaum, Hillsdale, NJ).

Cooper, W. E. (**1974**). ''Perceptual-motor adaptation to a speech feature,'' Percept. Psychophys. **16**(2), 229–234.

Cooper, W. E., and Lauritsen, M. R. (**1974**). ''Feature processing in the perception and production of speech,'' Nature (London) **252**, 121–123.

Cooper, W. E., and Nager, R. M. (**1975**). ''Perceptuo-motor adaptation to speech: an analysis of bisyllabic utterances and a neural model,'' J. Acoust. Soc. Am. **58**, 256–265.

Dorman, M. F., Studdert-Kennedy, M., and Raphael, L. J. (**1977**). ''Stop-consonant recognition: Release bursts and formant transitions as functionally equivalent, context dependent cues,'' Percept. Psychophys. **22**(2), 109–122.

Flege, J. E. (**1999**). ''Age of learning and second-language speech,'' in *Second Language Acquisition and the Critical Period Hypothesis*, edited by D. P. Birdsong (Erlbaum, Mahwah, NJ).

Flege, J. E., and Eefting, W. (**1986**). ''Linguistic and developmental effects on the production and perception of stop consonants,'' Phonetica **43**, 155–171.

Forrest, K., Weismer, G., Milenkovic, P., and Dougall, R. N. (**1988**). ''Statistical analysis of word-initial voiceless obstruents: Preliminary data,'' J. Acoust. Soc. Am. **84**, 115–123.

Fowler, C. A. (**1986**). ''An event approach to the study of speech perception from a direct-realist approach,'' J. Phonetics **14**, 3–28.

Fowler, C. A. (**1994**). ''Invariants, specifiers, cues: An investigation of locus equations as information for place of articulation,'' Percept. Psychophys. **55**(6), 597–610.

Fox, R. A. (**1982**). ''Individual variation in the perception of vowels: Implications for a perception-production link,'' Phonetica **39**, 1–22.

Frieda, E. M., Walley, A. C., Flege, J. E., and Sloane, M. E. (**2000**). ''Adults' perception and production of the English vowel /i/,'' J. Speech Lang. Hear. Res. **43**, 129–143.

Harris, K. S. (**1958**). ''Cues for the discrimination of American English fricatives in spoken syllables,'' Lang. Speech **1**(1), 1–7.

Hedrick, M. (**1997**). ''Effect of acoustic cues on labeling fricatives and affricates,'' J. Speech Lang. Hear. Res. **40**, 925–938.

Hedrick, M. S., and Ohde, R. N. (**1993**). ''Effect of relative amplitude of frication on perception of place of articulation,'' J. Acoust. Soc. Am. **94**, 2005–2026.

Heinz, J. M., and Stevens, K. N. (**1961**). ''On the properties of voiceless fricative consonants,'' J. Acoust. Soc. Am. **33**, 589–596.

Hoffman, P. R., Daniloff, R. G., Alfonso, P. J., and Schuckers, G. H. (**1984**). ''Multiple-phoneme-misarticulating children's perception and production of voice onset time,'' Percept. Mot. Skills **58**, 603–610.

Hughes, G. W., and Halle, M. (**1956**). ''Spectral properties of fricative consonants,'' J. Acoust. Soc. Am. **28**, 303–310.

Jamieson, D. G., and Rvachew, S. (**1992**). ''Remediating speech production errors with sound identification training,'' J. Speech-Language Patholo. Audiol. **16**, 201–210.

Jassem, W. (**1965**). ''The formants of fricative consonants,'' Lang. Speech **8**, 1–16.

Johnson, K., Flemming, E., and Wright, R. (**1993a**). ''The hyperspace effect: phonetic targets are hyperarticulated,'' Language **69**(3), 505–528.

Johnson, K., Ladefoged, P., and Lindau, M. (**1993b**). ''Individual differences in vowel production,'' J. Acoust. Soc. Am. **94**, 701–714.

Jongman, A., Wayland, R., and Wong, S. (**2000**). ''Acoustic characteristics of English fricatives,'' J. Acoust. Soc. Am. **108**, 1252–1263.

Klatt, D. H. (**1975**). ''Voice onset time, friction, and aspiration in word-initial consonant clusters,'' J. Speech Hear. Res. **18**, 686–706.

Klatt, D. H. (**1980**). ''Software for a cascade/parallel formant synthesizer,'' J. Acoust. Soc. Am. **67**, 971–995.

Kuhl, P. K., and Meltzoff, A. N. (**1982**). ''The bimodal perception of speech in infancy,'' Science **218**, 1138–1141.

Liberman, A. M., and Mattingly, I. G. (**1985**). ''The motor theory of speech revised,'' Cognition **21**, 1–36.

Liberman, A. M., Cooper, F. S., Harris, K. S., and MacNeilage, P. F. (**1962**). ''A motor theory of speech perception,'' in *Speech Communication Seminar*, Speech Transmission Laboratory, Royal Institute of Technology, Stockholm, Sweden.

Liberman, A. M., Cooper, F. S., Shankweiler, D. P., and Studdert-Kennedy, M. (**1967**). ''Perception of the speech code,'' Psychol. Rev. **74**(6), 431–461.

Lisker, L., and Abramson, A. S. (**1964**). ''A cross-language study of voicing in initial stops: Acoustical measurements,'' Word **20**(3), 384–422.

Lisker, L., and Abramson, A. S. (**1970**). ''The voicing dimension: Some experiments in comparative phonetics,'' in *Proceedings of the Sixth International Congress of Phonetic Sciences*, Prague, 1967 (Academia, Prague), pp. 563–567.

May, J. (**1976**). ''Vocal tract normalization for /s/ and /ʃ/,'' Haskins Laboratories: Status Report on Speech Research, SR-48, pp. 67–73.

Miller, J. L., and Volaitis, L. E. (**1989**). ''Effect of speaking rate on the perceptual structure of a phonetic category,'' Percept. Psychophys. **46**, 505–512.

Nearey, T. M. (**1992**). ''Context effects in a double-weak theory of speech perception,'' Lang. Speech **35**(1,2), 53–171.

Paliwal, K. K., Lindsay, D., and Ainsworth, W. A. (**1983**). ''Correlation between production and perception of English vowels,'' J. Phonetics **11**, 77–83.

Perkell, J. S., and Matthies, M. L. (**1992**). ''Temporal measures of anticipatory labial coarticulation for the vowel /u/: Within- and cross-subject variability,'' J. Acoust. Soc. Am. **91**, 2911–2925.

Pickett, J. M. (**1980**). *The Sounds of Speech Communication: A Primer of Acoustic Phonetics and Speech Perception* (University Park, Baltimore).

Richardson, K. H. (**1992**). ''An analysis of invariance in English stop consonants,'' Diss. Abstr. Int., B **53**(3-B), 1633.

Seitz, P. F. D., Bladon, R. A. W., and Watson, I. M. C. (**1987**). ''Across-speaker and within-speaker variability of British English sibilant spectral characteristics,'' J. Acoust. Soc. Am. Suppl. 1 **82**, S37.

Shadle, C. H., and Mair, S. J. (**1996**). ''Quantifying spectral characteristics of fricatives,'' 4th International Conference on Spoken Language Processing (ICSLP).

Soli, S. D. (**1981**). ''Second formants in fricatives: Acoustic consequences of fricative-vowel coarticulation,'' J. Acoust. Soc. Am. **70**, 976–984.

Strevens, P. (**1960**). ''Spectra of fricative noise in human speech,'' Lang. Speech **3**, 32–49.

Sussman, H. M. (**1994**). ''The phonological reality of locus equations across manner class distinctions: Preliminary observations,'' Phonetica **51**, 119–131.

Sussman, H. M., and Shore, J. (**1996**). ''Locus equations as phonetic de-

scriptors of consonantal place of articulation,'' Percept. Psychophys. **58**, 936–946.
Sussman, H. M., Hoemeke, K. A., and Ahmed, F. S. (**1993**). ''A cross-linguistic investigation of locus equations as a phonetic descriptor for place of articulation,'' J. Acoust. Soc. Am. **94**, 1256–1268.
Sussman, H. M., McCaffrey, H. A., and Matthews, S. A. (**1991**). ''An investigation of locus equations as a source of relational invariance for stop place categorization,'' J. Acoust. Soc. Am. **90**, 1309–1325.
Syrdal, A. K., and Gopal, H. S. (**1986**). ''A perceptual model of vowel recognition based on the auditory representation of American English vowels,'' J. Acoust. Soc. Am. **79**, 1086–1100.
Tabain, M. (**1998**). ''Non-sibilant fricatives in English: Spectral information above 10 kHz,'' Phonetica **55**, 107–130.
Tomiak, G. R. (**1991**). ''An acoustic and perceptual analysis of the spectral moments invariant with voiceless fricative obstruents,'' Diss. Abstr. Int., B **51**(8-B), 4082–4083.

The resolution of complex spectral patterns by cochlear implant and normal-hearing listeners

Belinda A. Henry[a] and Christopher W. Turner
Department of Speech Pathology and Audiology, The University of Iowa, Iowa City, Iowa 52242

(Received 5 April 2002; accepted for publication 26 January 2003)

The differences in spectral shape resolution abilities among cochlear implant (CI) listeners, and between CI and normal-hearing (NH) listeners, when listening with the same number of channels (12), was investigated. In addition, the effect of the number of channels on spectral shape resolution was examined. The stimuli were rippled noise signals with various ripple frequency-spacings. An adaptive 4IFC procedure was used to determine the threshold for resolvable ripple spacing, which was the spacing at which an interchange in peak and valley positions could be discriminated. The results showed poorer spectral shape resolution in CI compared to NH listeners (average thresholds of approximately 3000 and 400 Hz, respectively), and wide variability among CI listeners (range of approximately 800 to 8000 Hz). There was a significant relationship between spectral shape resolution and vowel recognition. The spectral shape resolution thresholds of NH listeners increased as the number of channels increased from 1 to 16, while the CI listeners showed a performance plateau at 4–6 channels, which is consistent with previous results using speech recognition measures. These results indicate that this test may provide a measure of CI performance which is time efficient and non-linguistic, and therefore, if verified, may provide a useful contribution to the prediction of speech perception in adults and children who use CIs. [DOI: 10.1121/1.1561900]

PACS numbers: 43.71.Ky, 43.71.Es, 43.66.Fe, 43.66.Ts [KRK]

I. INTRODUCTION

While many cochlear implant (CI) users achieve high levels of open-set speech recognition with current speech processors, there is a wide range in performance, with some CI listeners relying on the use of lipreading cues in order to communicate (e.g., Skinner *et al.*, 1994). This significant variability in speech understanding is thought to be a product of variations among implantees in factors such as the number and function of surviving spiral ganglion cells, the placement of the electrodes within the scala tympani, patterns of current distribution within the cochlea, and the status of the central auditory system. Identifying variables in postlinguistically deafened adults that are presumably related to these factors, including the duration of deafness, the duration of CI use, etiology of deafness, and preoperative sentence scores, allows some level of prediction of postoperative speech perception ability (Battmer *et al.*, 1995; Blamey *et al.*, 1992, 1996; Dorman *et al.*, 1990; Gantz *et al.*, 1993; Rubinstein *et al.*, 1999). However, in order to design improved speech processing strategies, and to optimize these strategies for individual CI listeners, it is necessary to develop an understanding of the perceptual mechanisms employed by CI listeners of different performance levels in recognizing speech.

The resolution of complex spectral patterns is one important aspect in perceiving speech. The ability to resolve the spectral peaks associated with the first two or three formants of speech is of primary importance in the identification of vowels, as well as other phonemes. In multichannel CIs, the speech processor typically resolves the frequency components in the signal using bandpass filtering, and the spectral shape information in the speech signal is then represented in the pattern of stimulation across the electrode array. The spectral resolution abilities of CI listeners depend first on the ability of the CI system to provide the spectral detail in the signal, which will be limited by the finite number of discrete channels provided in the particular CI system, and also on the way in which the acoustic signal is processed and represented in the electrical stimulation. Second, spectral resolution will depend on the ability of the individual CI listener to perceive this electrical representation of the spectral information.

The number of stimulating channels in current CI systems is generally limited to between 6 and 22, depending on the device and speech processing strategy, and therefore these speech processors do not preserve the fine spectral detail in the speech signal. It may seem logical to assume that optimizing the transmission of fine spectral detail by maximizing the number of channels may lead to improved speech perception. However, studies of speech recognition in normal-hearing (NH) listeners through acoustic simulations of CI processing indicate that high levels of speech recognition do not require a finely detailed spectral representation of the speech signal (Dorman *et al.*, 1997; Friesen *et al.*, 2001; Shannon *et al.*, 1995; Turner *et al.*, 1995). Rather, these studies have shown that high levels of speech understanding can be achieved in quiet listening conditions with 4 to 12 spectral bands, depending on the speech materials used (a larger number of channels is generally required for high levels of performance when more difficult speech materials are used,

[a]Current affiliation: Department of Communicative Disorders, University of Wisconsin–Madison, Madison, WI 53706. Electronic mail: bahenry@wisc.edu

such as those comprised of multiple talkers and/or those with low levels of linguistic context). However, when listening in background noise, NH listeners utilize more channels to recognize speech, with performance continuing to increase to at least 16 to 20 channels, depending on the level of the noise (Dorman *et al.*, 1998; Friesen *et al.*, 2001).

While most current CI speech processors therefore provide a sufficient number of channels to represent the spectral detail in the speech signal, at least in quiet listening conditions, most CI listeners are unable to fully utilize this spectral information. The results of speech recognition testing have indicated that spectral resolution is one major factor limiting CI speech perception. Vowel recognition, for example, which as noted above relies primarily on the perception of spectral cues, has been shown in many studies to be highly variable among CI listeners. Ranges in vowel recognition performance of 14% to 79%, reported by van Wieringen and Wouters (1999) for 25 users of the Laura CI system with the Continuous Interleaved Sampling (CIS) strategy, and 36% to 100%, reported by Skinner *et al.* (1994) for 59 users of the Nucleus CI22M implant and SPEAK strategy, are typical. In addition, while speech perception performance in CI listeners improves as the number of channels is increased, there is an asymptote in performance at four to seven channels, regardless of whether testing is performed in quiet or noisy listening conditions (Dorman and Loizou, 1997, 1998; Dorman *et al.*, 1997; Fishman *et al.*, 1997; Friesen *et al.*, 2001), which is in contrast to NH listeners (see above). These results provide further evidence that CI listeners generally cannot utilize all of the spectral information that is provided by CI speech processors and multiple electrode arrays. Furthermore, while the better-performing CI users can achieve performance levels similar to those of NH listeners when listening with the same number of channels, there is a wide range of abilities across CI listeners, and there is some evidence that poorer-performing CI listeners may not be able to utilize as many channels as better-performing CI listeners (Friesen *et al.*, 2001).

One factor which may limit spectral resolution with a CI is the degree of spectral contrast (the difference in amplitude between the peak and valley). For CI listeners, the wide acoustic dynamic range must be compressed into the small electrical dynamic range (typically 3–30 dB), resulting in a reduction in spectral contrast. While NH listeners only require a spectral contrast of between 1 and 3 dB for reasonably accurate vowel identification (Leek *et al.*, 1987; Alcantara and Moore, 1995; Turner and Van Tassell, 1984), Loizou and Poroy (2001) found that the minimal spectral contrast required for high levels of vowel identification accuracy was 4–6 dB for CI listeners.

Psychophysical studies which have investigated the ability to discriminate between stimulation on different electrodes also indicate that the perception of spectral cues is a performance-limiting factor in CI speech perception (Collins *et al.*, 1997; Donaldson and Nelson, 2000; Henry *et al.*, 2000; Nelson *et al.*, 1995; Throckmorton and Collins, 1999). Henry *et al.* (2000) showed a correlation between speech perception and electrode discrimination in the frequency regions below approximately 2.7 kHz when the stimuli in the electrode discrimination task were presented with randomly varying levels, but no correlation between the two measures in the frequency regions above 2.7 kHz, indicating that fine spectral discrimination may be relatively more important in the vowel-formant regions than in the high-frequency regions, where the cues are mostly broadband. The relationship between the two measures indicates the usefulness of electrode discrimination measures as a method of predicting speech perception in CI users. However, these measures are time consuming to conduct since they are multi-point measures, which are made at multiple positions along the electrode array.

Electrode discrimination measures can only provide an indirect assessment of frequency discrimination ability for acoustic signals. The ability of CI listeners to resolve peaks in the *acoustic* signal, when listening through their speech processors, is not currently well understood. The present study was therefore designed to address the following specific questions:

(1) How closely can peaks in the acoustic spectrum be spaced and still be resolved by CI users of varying performance levels, and does this differ between CI and NH listeners, when listening with the same number of channels?
(2) Is the ability to resolve spectral peaks related to speech recognition with a CI?
(3) How does the ability to resolve spectral peaks vary with the number of processing channels in CI and NH listeners?

Spectral shape resolution was investigated in this study using a method based on the ''ripple phase reversal test'' (e.g., Supin *et al.*, 1994, 1999), which was originally developed to measure the resolution of spectral patterns in NH listeners. Using this method, the threshold for resolvable spectral peak spacing is determined using rippled noise stimuli, which are broadband noise signals with spectral ripples. The listeners' task is to discriminate between two rippled noise stimuli in which the frequency positions of the peaks and valleys are reversed. Ripple density is varied and the threshold is taken as the highest or maximum ripple density at which an interchange in the peak and valley positions in the rippled spectrum (i.e., a ripple phase reversal) can be detected. It is hypothesized that a listener can only discriminate the spectral ripple phase reversal if the rippled spectrum pattern can be resolved. If the spectral pattern is not resolvable due to the ripples being spaced too closely, the reversal cannot be detected. This test is hypothesized to provide a one-point measure of the listeners' ability to perceive the frequency locations of the peaks in a generic speech-like acoustic signal.

In experiment 1, a modified version of the ripple phase reversal test was used to investigate differences in spectral ripple resolution thresholds among CI listeners having a range of speech perception abilities, when listening to signals through a 12-channel CIS speech processor. In order to estimate the upper limit of spectral shape resolution provided by CI speech processors, spectral ripple resolution was also measured in NH subjects, who listened to noise-band acous-

TABLE I. Individual subject details. The number of maxima is 8 for the ACE strategy and 6 for the SPEAK strategy unless noted otherwise prog=progressive, pps/ch=pulses per second/channel, NA=not available.

Subject	Age (years)	Duration of profound deafness (years)	CI experience (years)	Etiology	Clinical map: strategy, # maxima	Clinical map: rate (pps/ch), # channels	CNC phoneme score (% correct)	Dynamic range (dB) (average, 12-ch map)	Vowel score (% correct) (12-ch map)
CI1	73	12	5	Infection	ACE	720, 22	83.3	9.5	54.2
CI2	46	13	2.5	Congenital, prog	ACE	1800, 22	47.3	13.0	37.9
CI3	62	4	4	Unknown	ACE, 16	720, 18	71	9.7	62.1
CI4	37	2	2.5	Autoimmune	SPEAK	250, 19	73.3	12.0	52.5
CI5	72	8	3	Congenital, prog	SPEAK	250, 20	85.3	11.3	43.3
CI6	72	1	1	Meniere's disease	SPEAK	250, 20	71.3	8.6	26.3
CI7	43	0.5	2.5	Autoimmune	ACE	1200, 22	74.7	14.6	32.9
CI8	51	2.5	1.5	Congenital, prog	SPEAK	250, 20	48.7	5.5	28.8
CI9	41	5	1	Unknown	ACE	1800, 22	76	17.9	32.1
CI10	74	25	4	Congenital, prog	ACE, 12	720, 22	81.3	10.6	30.4
CI11	76	40	2	Unknown	CIS	900, 6	NA	5.5	23.3
CI12	40	18	3	Autoimmune	SPEAK	250, 20	83.3	8.6	55.8
CI13	48	2	1	Unknown	CIS	2400, 6	69.3	5.6	29.2
CI14	54	5	3	Unknown	ACE, 10	1200, 22	30.7	6.3	9.2
CI15	80	3	3	Unknown	SPEAK	250, 19	62	3.2	20.4
CI16	37	2	1	Unknown	ACE	720, 22	49.3	10.9	45.4
CI17	48	2	3	Ototoxicity	ACE	1800, 22	82.7	5.3	45.8
CI18	56	36	5	Unknown	ACE	1800, 22	71.3	7.4	45.4
CI19	78	0.5	4	Viral infection	SPEAK	250, 20	87.3	5.5	32.1
CI20	46	7	3.5	Unknown	ACE	20, 900	54.7	15.7	30.8
CI21	78	4	5	Unknown	ACE	22, 900	71.3	7.2	44.2

tic simulations of 12-channel CI processing. It is hypothesized that since the identification of vowels relies primarily on the ability to resolve and identify the frequencies of spectral peaks, measuring the ability to perceive the frequency locations of the peaks in a complex acoustic spectrum using the spectral ripple resolution test may show a relationship with vowel recognition. Therefore, the relationship between spectral peak resolution and vowel identification ability was also examined. In experiment 2, the effect on spectral ripple resolution of limiting the spectral detail that is presented in the acoustic signal, by varying the number of processing channels, was investigated both in CI and NH listeners. The purpose of the second experiment was to investigate the number of effective channels utilized by NH and CI listeners in resolving spectral peaks, and to further investigate the degree of similarity between results obtained using the spectral peak resolution test and those obtained using speech recognition tasks.

II. EXPERIMENT 1: SPECTRAL RIPPLE RESOLUTION AND VOWEL RECOGNITION

A. Methods

1. Subjects

Eight NH subjects (six female, two male), ranging in age from 19 to 39 years, participated in this experiment. Normal hearing was defined as having pure-tone air conduction thresholds $\leqslant$15 dB HL at octave frequencies from 125 to 8000 Hz in the tested ear. Twenty-one postlinguistically deafened adults (14 female, 7 male) with CIs also participated. All were users of the Cochlear Corp. CI24M implant and the SPrint speech processor, and had a wide range of speech perception abilities. The individual subject details are shown in Table I. All participants were native American English speakers.

2. Stimuli

a. Rippled noise stimuli. Rippled noise stimuli of 500-ms duration and with peak-to-valley ratios of approximately 30 dB were created from white noise. The white noise was recorded in 16-bit digital form at a 44.1 kHz sampling rate from a white noise generator onto a Macintosh G4 computer. The technique of adding a white noise to a copy of itself with a delay of T seconds, where the reciprocal of the delay gives the frequency of the rippled noise, was employed using Sound Designer II (DigiDesign, Audio Media III) software. The resulting spectrum has peaks linearly spaced at $1/T$ Hz. The first peak in the spectrum of the noise occurs at 0 Hz when the delayed version of the noise is added to the original in phase (*standard* stimulus). When the polarity of the delayed noise is reversed, the first peak occurs at $0.5/T$ Hz (*inverted* stimulus).

The frequency spacings of the ripples were 8000, 6000, 4000, 3000, 2000, 1500, 1000, 500, 250, 125, 64, 32, and 16 Hz. Examples of rippled noise spectra, both *standard* and *inverted*, with ripple frequency spacings of 8000, 2000, and 500 Hz are shown in Fig. 1. The rippled noise stimuli were then processed in two different ways, as described in the signal processing section below, depending on whether they were to be presented to the CI or the NH listeners.

b. Vowel stimuli. Vowel recognition was measured using a closed-set 12-alternative identification procedure. Medial vowel tokens were presented in a /h/-vowel-/d/ context (had, hod, hawed, head, hayed, heard, hid, heed, hoed, hood, hud, who'd). The tokens were digitized natural productions from

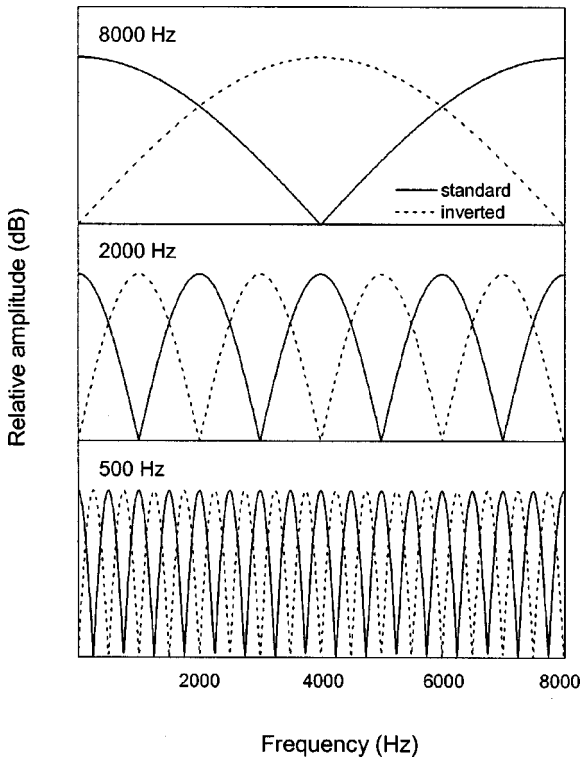

FIG. 1. Rippled noise spectra. Ripple frequency-spacings of 8000, 2000, and 500 Hz, with both *standard* and *inverted* peak positions are shown.

ten male and ten female talkers, taken from the materials recorded by Hillenbrand *et al.* (1995). The vowel stimuli were stored in a digital form on a Macintosh G4 computer, after being transferred from CD.

3. Signal processing

a. Cochlear implant subjects. The final processing of the rippled noise stimuli to be presented to the CI listeners was accomplished using the Sound Designer II program. The rippled noise signals were first filtered with a filter that approximated the long-term speech spectrum (Byrne *et al.*, 1994). This low-pass filtering resulted in a distribution of energy across the entire frequency range for the processed signals (since the width of the filters in the CI processor increase with frequency, the energy in the processed signals would be concentrated in the high frequencies if the signals were not low-pass filtered). The overall levels of the rippled noise sound files were then approximately equalized, and linear rise/fall times of 150-ms applied to each stimulus to avoid click effects and other idiosyncratic cues which were shown to be perceptible by NH listeners in a pilot study.

The stimuli were presented to the CI subjects using the Nucleus CI24M implant system and the SPrint speech processor. The CI24M electrode array has 22 intracochlear and 2 extracochlear electrodes. All CI subjects used a pulse width of 25 μs, and stimulus pulses were presented using the monopolar MP1+2 stimulation mode, where current flows between the active intracochlear electrode and both extracochlear electrodes. The CIS speech processing strategy was used to present both the rippled noise and vowel stimuli, with 12 channels, a Q-value of 20, and a pulse rate of 900 pulses per second (pps)/channel, and therefore a total stimulation rate across electrodes of 10 800 pps. In the 12-channel CIS strategy implemented in the SPrint processor, the amplitude envelope is estimated within each of the 12 bands during each stimulation period. These amplitudes are converted to electrical stimulus levels, and stimulus pulses representing each band are presented sequentially on the associated electrodes, in a basal to apical order in this experiment. The default frequency to channel allocation for 12-channel CIS [as set by the Cochlear Diagnostic and Programming System (DPS) software] was used, and this provided a frequency range of 187–7937 Hz, and the filter cutoff frequencies shown in Table II. The post-processing spectra for the rippled noise stimuli with peak spacings of 8000, 2000, and 500 Hz (from Fig. 1) are shown in Fig. 2. These channel output levels were measured using the SCILAB (Swiss Cochlear Implant Laboratory software) program, which records the RF transmissions from the speech processor and provides either a graphical display or a list of the electrodes activated and the current levels. The speech processor settings were the same as used in the experiment (i.e., 12-channel CIS, 900 Hz pulse rate), with the electrical stimulation levels set to the average across CI subjects [threshold level (T)=150, comfortably loud level (C)=200]. Note the reduction in spectral contrast from 30 dB in the acoustic signal to between 2 and 5 dB for the processed spectra.

b. Normal-hearing subjects. The NH subjects were presented with both rippled noise and vowel stimuli processed using a 12-channel simulation of CI processing. The acoustic simulation of electrical hearing was accomplished using multiple channels of narrow-band noise modulated by the signal, using MATLAB software. The original rippled noise and vowel signals were band-pass filtered into 12 frequency bands using filters whose cutoff frequencies (see Table II) and frequency response slopes approximated those used in the CI speech processor. Within each band, the signal was transformed into broadband signal correlated noise by randomly assigning negative or positive signs, with a probability of 0.5, to the sampled waveform points (Schroeder, 1968; Shannon *et al.*, 1995; Turner *et al.*, 1995). This resulted in a white noise carrier signal whose amplitude was modulated by the original speech waveform envelope. This broadband noise was then refiltered to spectrally limit the signal to the bandwidth corresponding to the originally filtered signal bands, and the overall amplitudes of each band were corrected to correspond to those of the original stimulus bands. The output of all of the bands was then recombined. The processed rippled noise stimuli underwent a final filtering with a filter that approximated the long-term speech spectrum, an equalizing of the overall levels of the processed signals, and an application of linear rise/fall times of 150 ms, which was identical to that of the rippled noise stimuli to be presented to the CI subjects.

4. Procedures

a. Spectral ripple resolution. Each CI subject was programmed with an experimental speech processor program (map), which differed in all cases from the normal maps used by the subjects (Table I). The 12 active electrodes to be in-

TABLE II. Channel lower and upper cutoff frequencies (Hz) for signal processors with 1, 2, 4, 6, 8, 12, and 16 channels. The active electrode used for each channel is shown in brackets.

	No. of channels condition						
Channel	1	2	4	6	8	12	16
1	187–7937 (16)	187–1062 (18)	187–1062 (22)	187–562 (22)	187–437 (22)	187–312 (22)	187–312 (22)
2		1062–7937 (8)	1062–2062 (16)	562–1062 (19)	437–687 (20)	312–562 (20)	312–437 (21)
3			2062–4062 (10)	1062–1812 (15)	687–1062 (18)	562–812 (19)	437–562 (20)
4			4062–7937 (4)	1812–2937 (11)	1062–1562 (16)	812–1062 (18)	562–812 (19)
5				2937–4812 (7)	1562–2312 (13)	1062–1312 (16)	812–1062 (18)
6				4812–7937 (4)	2312–3437 (10)	1312–1687 (15)	1062–1312 (17)
7					3437–5187 (7)	1687–2187 (14)	1312–1562 (16)
8					5187–7937 (4)	2187–2812 (12)	1562–1812 (15)
9						2812–3687 (10)	1812–2187 (14)
10						3687–4812 (8)	2187–2687 (13)
11						4812–6187 (6)	2687–3187 (12)
12						6187–7937 (4)	3187–3812 (11)
13							3812–4562 (10)
14							4562–5437 (8)
15							5437–6562 (6)
16							6562–7937 (4)

cluded in each subject's speech processor program (see Table II) were determined by the default setting in the DPS software. In the cases where a map contained deactivated electrodes which corresponded to the electrodes selected for the experimental map, the next closest available electrode was included instead. T and C levels were measured for each electrode, using standard clinical procedures. Apart from these subject-dependent settings, it was important that all other speech processing parameters be constant across subjects. Therefore, the same speech processor, with the same sensitivity setting (a value of 8), was used for all subjects. Since the audibility of conversational-level signals is controlled mostly by the sensitivity setting of the speech processor and does not vary significantly among CI users, providing the T and C levels are set optimally, a constant sensitivity setting minimizes individual variation in the audibility of the signals. An optimal combination of signal level and sensitivity setting was selected, by measuring the output of the speech processor using the SCILAB program, so that the signal peaks resulted in stimulation at approximately 90% of the dynamic range.

The rippled noise stimuli were output via custom software routines using a 16-bit digital-to-analog converter (DigiDesign, Audio Media III), which has a built-in antialiasing filter at 20 kHz. For the CI listeners, the stimuli were presented via a direct input into the speech processor, using a 3.5-mm mono phone plug, which defeats the headset microphone so that no external input occurs, while at the same time preserving the microphone pre-emphasis. The stimuli were presented to the NH subjects monaurally using Sennheiser HD 25-SP1 circumaural headphones at an average level of 65 dB SPL. Participants were tested using the same ear throughout the experiment.

A four-interval forced-choice (4IFC) procedure, in which three intervals contained the *standard* (reference) rippled noise stimulus, while the other interval, chosen at random, contained the *inverted* (test) stimulus, was used to measure the discrimination abilities of the listeners. The stimuli were separated by silent intervals of 500 ms. The level of the stimuli was varied randomly for each interval within an 8-dB range in 1-dB steps using a Tucker-Davis programmable attenuator (model PATT), in order to minimize the ability of subjects to use loudness cues for identification. Subjects were asked to select one of four buttons labeled numerically on a touch-screen, corresponding to the ''different'' interval, ignoring any loudness differences between intervals. Feedback was provided. Practice testing was provided at a range of ripple frequency spacings. Following this, psychometric functions were obtained for 18 of the CI listeners (CI1 to CI18) and for 4 of the NH listeners. Percent

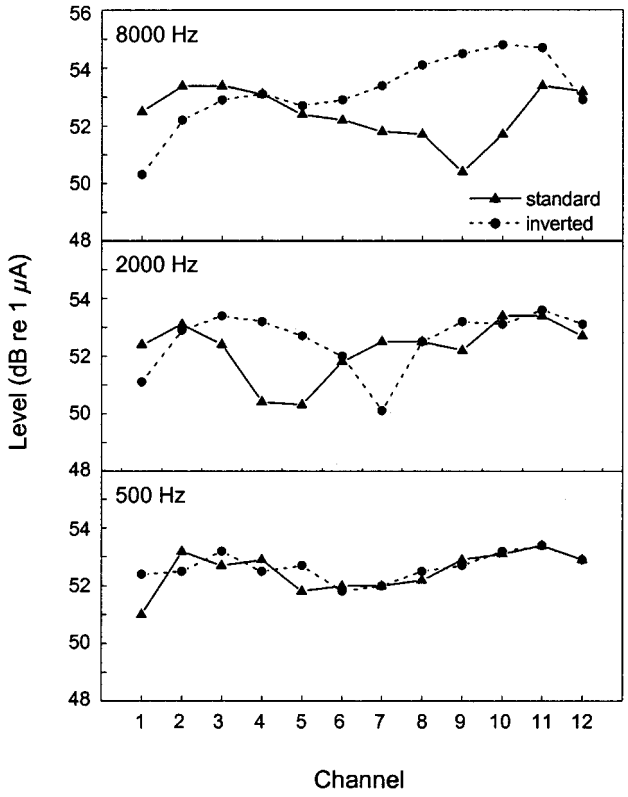

FIG. 2. Cochlear implant channel output levels for the rippled noise spectra. The speech processing strategy was 12-channel CIS, with a 900-Hz pulse rate, and with T and C levels set to the average across the CI subjects in the study (see text for details). Ripple frequency-spacings of 8000, 2000, and 500 Hz with both *standard* and *inverted* peak positions are shown.

correct scores for the psychometric functions were based on the average of between one and four runs (or sets) of 20 trials of the 4IFC task. In general, scores of 95% or 100% are based on one run (i.e., only one run of the task was administered), scores of less than 40% are based on two runs, and scores between these values (i.e., those near or on the steepest portion of the function) are based on three to four runs of the 4IFC task. Detailed psychometric functions were obtained for all subjects except CI19, C20, and CI21, who were recruited to participate in experiment 2. A threshold for ripple resolution was estimated from the psychometric functions at the 70.7% correct level for each subject. To determine this threshold, the data points in the 20% to 100% range were examined, and a straight line fitted to those four data points distributed around the 70.7% level. Each run of 20 trials of the 4IFC task took approximately 5 min to complete.

An adaptive procedure was also used to estimate ripple resolution thresholds for all CI and NH subjects. Thresholds were obtained using a two-down, one-up 4IFC procedure, converging on the 70.7% correct point (Levitt, 1971). The 4IFC task was the same as that detailed above. An experimental run proceeded until 13 reversals were obtained, and the threshold for the run was taken as the mean of the final 8 reversals. All 13 ripple frequency spacings were included in the adaptive procedure, a run of which commenced at the 6000-Hz ripple frequency spacing. Several practice runs (between four and six) were completed initially for each subject. The final threshold values for each subject were taken as the average of the final five to six adaptive runs.

Using this adaptive procedure, spectral ripple resolution was assessed in two conditions; a broadband condition (0–8000 Hz) and a 3000-Hz low-pass filtered condition. A Kemo filter (VBF8.04) was used, with filter slopes of 30 dB/oct. The reason for this was to compare spectral shape resolution ability over the entire speech frequency range with that in the frequency region which is most relevant to vowel perception, and had previously been shown to be the frequency region in which electrode discrimination and speech recognition were correlated (Henry *et al.*, 2000). All subjects were tested in a double-walled sound treated room.

b. Vowel recognition. The vowel stimuli were output via custom software routines using a 16-bit digital-to-analog converter (see above). These stimuli were presented to the CI subjects in the free-field, positioned approximately 1 m from a speaker, at an average level of 65 dB SPL, and to NH subjects monaurally through Sennheiser HD 25-SP1 circumaural headphones at an average level of 65 dB SPL. All CI and NH subjects participated in the vowel recognition test.

Initial training was provided for the vowel identification task. Each of the 12 words containing the medial vowels was displayed as buttons on a touch-screen. The subject was asked to select the word they wanted to hear, and five examples of that word (i.e., the word was spoken by five different talkers) were then presented. Fifty trials of the training task were conducted (or more as desired by the individual subject) in order to allow the subject to familiarize themselves with the tokens and their labels.

Following the vowel training, two runs (a practice and a test run) of the vowel identification test were administered. A single run of the test consisted of 240 trials (12 vowels×20 talkers). On each trial, a stimulus token was chosen randomly, without replacement, and following presentation of each token the subject responded by pressing 1 of the 12 buttons on the touch-screen. Feedback was provided during the practice run, but not during the test run. Each run of the vowel test took approximately 25 min to complete.

B. Results

1. Spectral ripple resolution

The psychometric functions representing ripple frequency spacing versus percent correct score are shown for four of the NH listeners in Fig. 3, and for the CI listeners (CI1 to CI18) in Fig. 4. Also shown are the estimates of the 70.7% correct thresholds derived from the psychometric functions. As the spacing between spectral peaks decreases, there is a reasonably monotonic decrease in the ability to discriminate between the *standard* and *inverted* stimuli. The consistently monotonic nature of these functions supports the use of an adaptive procedure as a more time-efficient method of estimating ripple resolution thresholds.

The thresholds determined using the adaptive procedure for the NH and CI listeners, and for both the broad-band and low-pass conditions, are shown in Fig. 5. The mean spectral ripple resolution threshold for the NH subjects was 391 Hz, in the low-pass condition. The range was 309 to 555 Hz. The

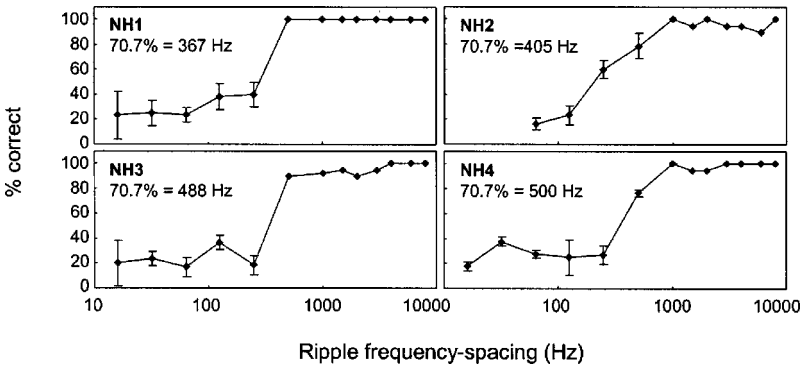

FIG. 3. Psychometric functions showing percent correct scores versus ripple frequency-spacing for NH listeners with 12 processing channels. Error bars represent ±one standard deviation. The 70.7%-correct thresholds, estimated from the psychometric functions, are shown for each subject.

performance of CI14, CI15, and CI20 on the ripple resolution task was too poor to perform the adaptive procedure, since their thresholds (around 8000 Hz) were above the starting point for the adaptive procedure. Thus, the ripple resolution thresholds shown in Fig. 5 for these listeners were derived from their psychometric functions. The mean spectral ripple resolution threshold for the CI listeners as a group was 2977 Hz in the low-pass condition. Thus, spectral ripple resolution ability was substantially poorer in the CI than the NH subjects. In addition, spectral ripple resolution abilities varied substantially among the CI group, with a range of 802 to approximately 8000 Hz. Thresholds at or near 8000 Hz (CI14, CI15, and CI20) imply very limited spectral shape resolution abilities.

Paired *t*-tests showed no significant differences between the spectral ripple resolution thresholds obtained in the broadband condition compared to the low-pass condition for the CI listeners (broadband mean=3093 Hz, low-pass mean =2977 Hz; $p=0.078$). While the difference between the two conditions was mildly significant for the NH listeners (broadband mean=418 Hz, low-pass mean=391 Hz; $p=0.038$), the mean difference is small and is therefore not of practical importance.

The accuracy of the thresholds determined using the adaptive procedure compared to those derived from the psychometric functions was investigated using regression analysis. Figure 6 shows the adaptively determined threshold plotted against the threshold derived from the psychometric function for each subject. The slope of the regression line was 0.97, which, being very close to 1, and along with the significant correlation between the two measures ($r=0.98$, $p<0.0001$), indicates a high degree of similarity between the results from the two threshold-estimating methods.

The possible effect of learning through the course of the experiment on the results was assessed by comparing the threshold obtained in the broadband condition at the start compared to the end of the experiment. This analysis is based on data for all CI subjects except CI14, CI15, and CI20, whose thresholds were too high to perform the adaptive procedure, as mentioned above. The results of a paired *t*-test indicate no significant difference between the first and last runs for either the CI (mean start threshold=2587 Hz, mean end threshold=2488 Hz; $p=0.316$) or the NH (mean start threshold=490 Hz, mean end threshold=508 Hz; $p=0.361$) subjects. This indicates that the adaptive ripple discrimination task does not suffer from a lengthy training period to reach stable performance.

The post-processing rippled noise spectra in Fig. 2 show a significant reduction in spectral contrast at the output of the speech processor, which is due to the compression of the acoustic dynamic range into the small electrical dynamic range of CI listeners. It may be hypothesized that dynamic range may contribute to the variability in ripple resolution thresholds among CI listeners. However, the results of a regression analysis between the average dynamic range across electrodes (shown in Table I) and ripple resolution threshold did not indicate a significant relationship between these two measures ($r=-0.17$, $p=0.47$).

2. The relationship between spectral ripple resolution and vowel recognition

The average vowel recognition score for the NH subjects was 80.5% (range 72.1%–89.2%), and for the CI subjects was 37.2% (range 9.2%–62.1%). The relationship between ripple resolution ability and vowel recognition for the CI listeners is shown in Fig. 7. The ripple resolution thresholds shown in this figure are from the low-pass condition, and were determined using the adaptive procedure, except for CI14, CI15, and CI20, for whom they were derived from the psychometric function (see above). A regression analysis showed a significant correlation between the ripple resolution threshold and vowel identification scores ($r=-0.65$; $p=0.001$). Similar results were obtained when the ripple resolution thresholds determined in the broadband condition were used in the analysis.

III. EXPERIMENT 2: THE EFFECT OF THE NUMBER OF CHANNELS ON SPECTRAL RIPPLE RESOLUTION

In the second experiment, the effect of varying the number of processing channels on spectral ripple resolution in both CI listeners and NH listeners was investigated. Previous studies (see the Introduction) employing speech recognition measures have shown an asymptote in performance at between around 4 to 7 channels for CI listeners, compared to around 4 to 12 channels for NH listeners (in quiet), depending on the speech material used. The purpose of this experiment was to further investigate the degree of similarity between results obtained using the spectral ripple resolution test and those obtained using speech recognition tasks.

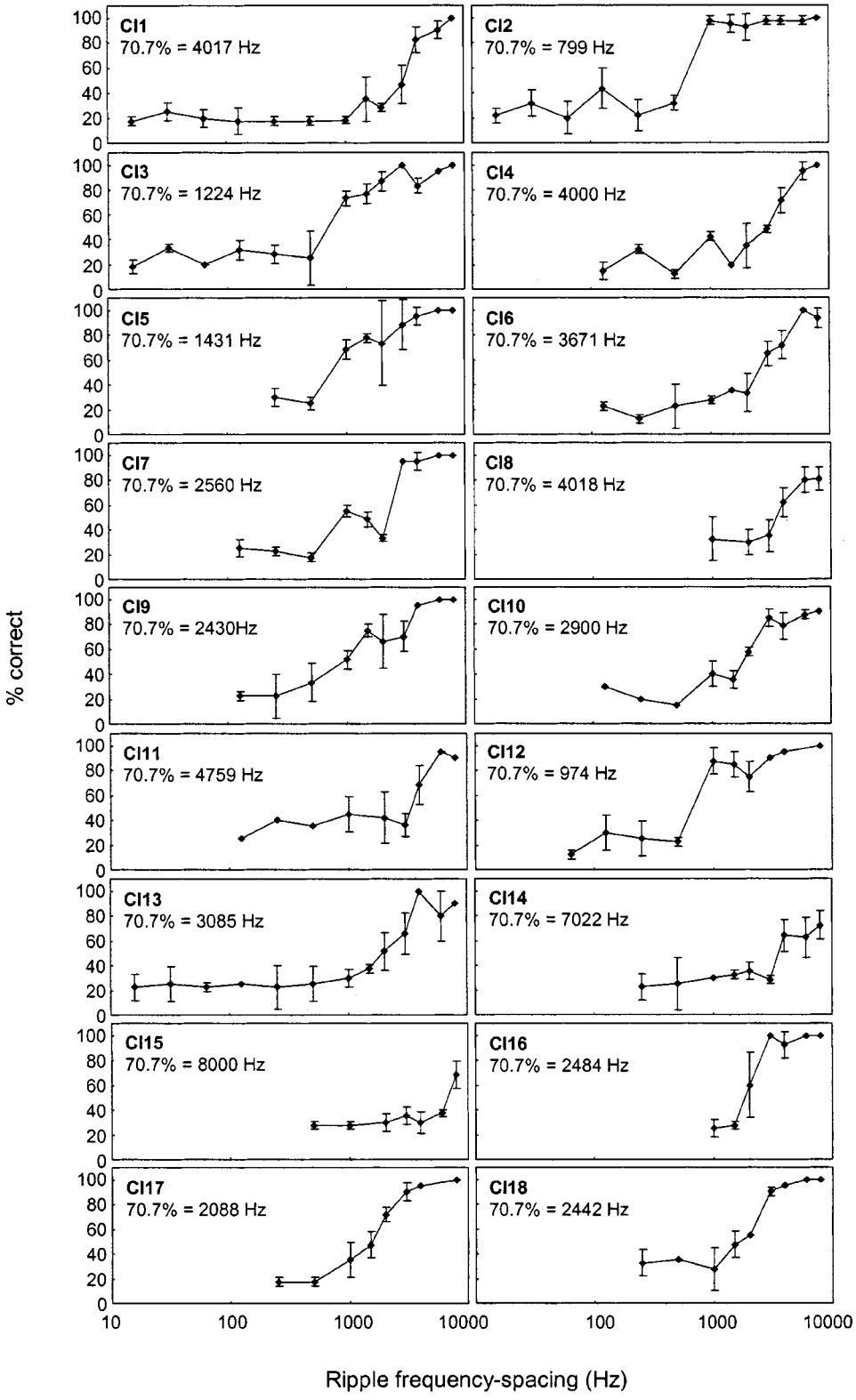

FIG. 4. Psychometric functions showing percent correct scores versus ripple frequency-spacing for CI listeners with 12 processing channels. Error bars represent ± one standard deviation. The 70.7%-correct thresholds, estimated from the psychometric functions, are shown for each subject.

A. Methods

1. Subjects

A different group of eight NH adult subjects (seven female, one male, age range 21–22 years) participated in experiment 2. Normal hearing was defined as in experiment 1, and all NH participants were native American English speakers. Eleven of the CI subjects from experiment 1 (CI1, CI2, CI3, CI5, CI6, CI9, CI13, CI17, CI18, CI20, and CI21) also participated in experiment 2.

2. Stimuli

The effect of the number of channels on spectral ripple resolution was assessed using the same rippled noise stimuli as in experiment 1. The signal processing is described below.

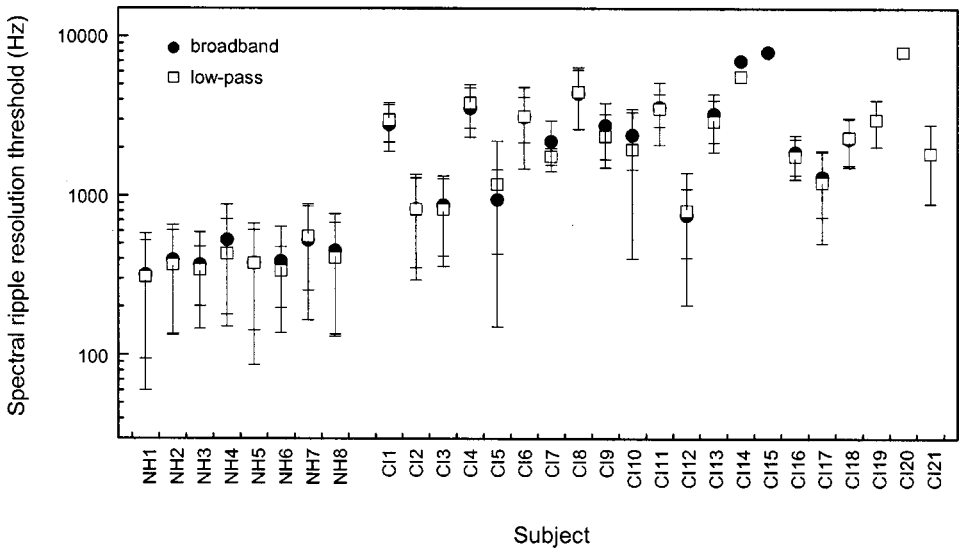

FIG. 5. Thresholds for spectral ripple resolution for NH and CI subjects (both listening with 12 channels) in both the broadband and low-pass conditions. Thresholds were determined using the adaptive procedure. Error bars represent ± one standard deviation.

3. Signal processing

a. Cochlear implant subjects. The SPrint processor and CIS strategy was again used in experiment 2, and the number of channels was varied using the Cochlear DPS software. Spectral ripple resolution was assessed in seven different conditions, which were with 1, 2, 4, 6, 8, 12, and 16 channels. The filter cutoff frequencies, which are shown in Table II, were determined by the default settings used in the CIS strategy for each of these conditions. As the number of frequency bands was varied, the total bandwidth of 187–7937 Hz remained the same, and the frequency range associated with each electrode increased. The pulse rate *per channel* was held constant at 900 pps as the number of channels was varied. The electrodes activated for each of the channels are shown in Table II. If a selected electrode was unavailable for activation in an individual's map, the next closest available electrode was used instead. If testing was conducted on the same day as experiment 1, each subject used the same T and C levels as in experiment 1 for all conditions (and the extra 4 channels were added to the map for the 16-channel condition). If the testing for experiment 2 was conducted during a separate test session, the T and C levels were checked prior to commencing the experiment.

b. Normal-hearing subjects. Spectral shape resolution was assessed in the NH subjects in the same conditions as for the CI subjects. The rippled noise stimuli were processed into the various number-of-channels acoustic CI simulations using the same general methods as those described previously for experiment 1. The cutoff frequencies of the filters used in the simulations approximated those used in the CI speech processor for each condition (see Table II).

4. Procedures

The stimuli were presented in the broadband condition (0 to 8000 Hz). The 12-channel condition was administered

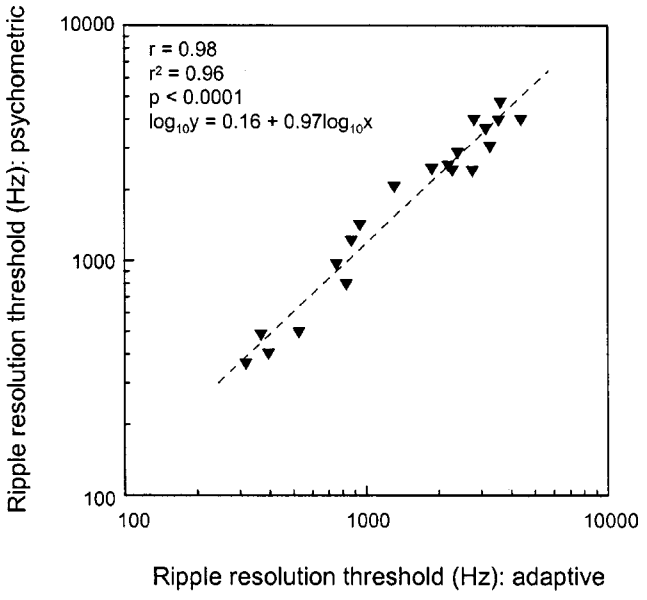

FIG. 6. The relationship between spectral ripple resolution thresholds determined using the adaptive procedure and those derived from the psychometric functions. Data for both NH and CI subjects are included.

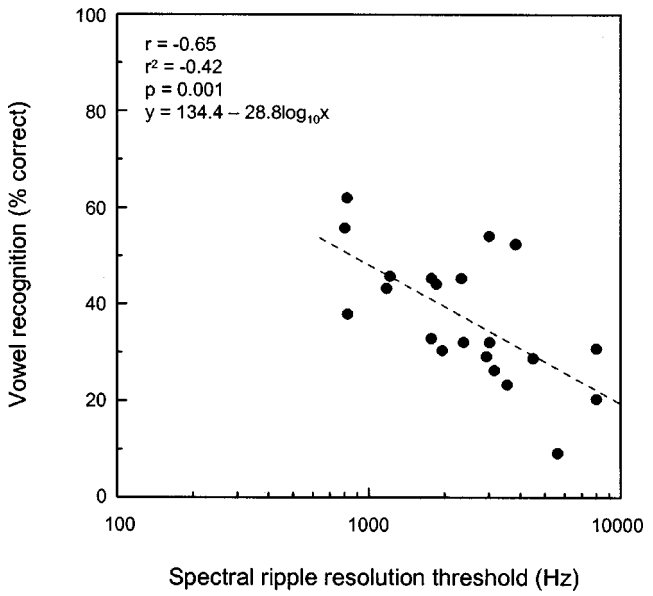

FIG. 7. The relationship between spectral ripple resolution and vowel recognition.

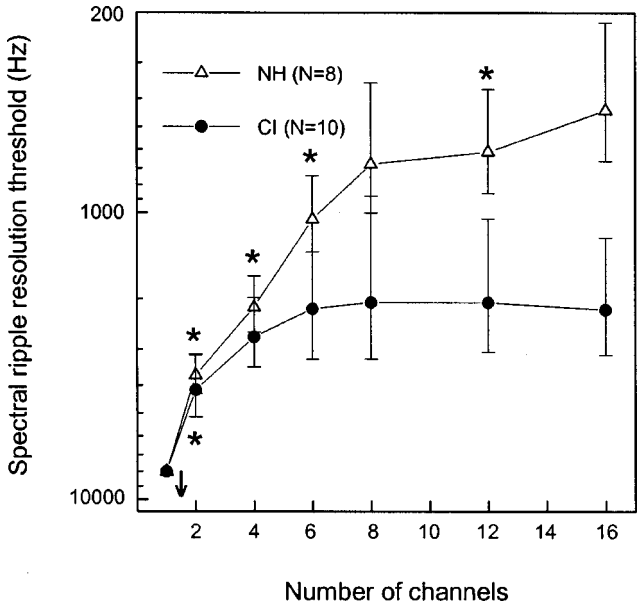

FIG. 8. Average spectral ripple resolution thresholds as a function of the number of processing channels for NH and CI listeners. CI subjects: circles; NH subjects: triangles. Error bars represent ± one standard deviation. The downward-pointing arrow indicates that no threshold could be obtained in the one-channel condition. Asterisk symbols represent a statistically significant difference between that condition and the next highest number-of-channels condition.

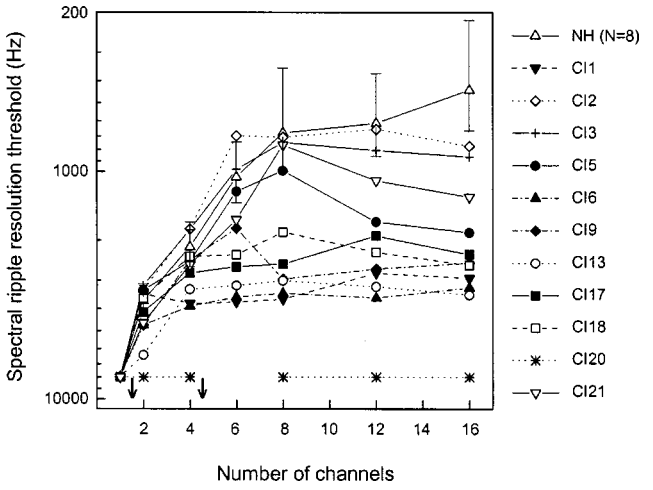

FIG. 9. Spectral ripple resolution thresholds as a function of the number of processing channels for the NH group and for individual CI listeners. Vowel scores are shown in the legend for individual CI subjects. Error bars represent ± one standard deviation. The downward-pointing arrow indicates that no threshold could be obtained in the one-channel condition.

as the first and last test conditions, in order to assess any learning effects over the course of the experiment. The remaining conditions were presented in a randomized order. The average of four runs of the adaptive procedure (see experiment 1) was taken as the ripple resolution threshold for each condition for each listener.

B. Results

Figure 8 shows the average spectral ripple resolution thresholds versus the number of channels for both the NH and CI subject groups. In general, for both NH and CI listeners, as the number of channels increased, more closely spaced peaks were able to be resolved, although the extent of this trend varied between the two subject groups, and among individual CI listeners, as described below.

Both NH and CI subjects were unable to resolve any peaks using a one-channel processor, as indicated by the downward-pointing arrow in Fig. 8. Therefore, the results for this trivial condition could not be included in the statistical analyses. In addition, the data of CI20 were excluded from the statistical analyses, since this subject performed too poorly in all conditions to complete the adaptive task. A mixed model ANOVA, with number of channels (2 to 16) and subject group (NH versus CI) as factors, showed main effects of both the number of channels ($p<0.0001$) and of the subject group ($p=0.004$), as well as a channel by group interaction ($p=0.004$). To further analyze the channel by group interaction, separate repeated measures ANOVAs were conducted on the two subject groups. For the NH subject group, a repeated measures ANOVA showed a significant effect of number of channels ($p<0.0001$). *Post hoc* tests (Sidak) showed statistically significant increases in performance as the number of channels was increased to 16. In Fig. 8, a significant difference between one condition and the next highest number-of-channels condition is represented by an asterisk symbol above the NH curve. All differences were shown to be significant in *post hoc* tests, except the difference in ripple resolution thresholds between the 8- and 12-channel conditions. For the CI subject group, a repeated measures ANOVA also showed a significant effect of number of channels ($p<0.0001$). *Post hoc* tests (Sidak) indicated a statistically significant difference between the two-channel condition and all other conditions (as shown by the asterisk symbol below the CI curve in Fig. 8), but no other statistically significant differences between conditions. However, the difference between the four- and six-channel condition was close to significance ($p=0.06$). These results indicate a plateau in performance at between four and six channels for the CI subject group.

Figure 9 shows the variation in thresholds with number of channels across the individual CI subjects (as well as the average thresholds for the NH group, as shown in Fig. 8). There was substantial variability among CI subjects in the effect of the number of channels on spectral ripple resolution ability. For example, while more closely spaced peaks could be resolved by CI21 as the number of channels increased to 8, increasing the number of channels did not result in an increased ability to resolve spectral peaks for CI20.

The possible effects of learning over the course of the experiment were assessed by comparing the average threshold values from the 12-channel condition at the start to those at the end of the experiment. The results of paired *t*-tests for both the NH (mean start threshold=614 Hz, mean end threshold=666 Hz; $p=0.142$) and the CI (mean start threshold=2106 Hz, mean end threshold=2105 Hz; $p=0.495$) subjects do not suggest any influence of learning on the experimental results.

IV. DISCUSSION

The average spectral ripple resolution threshold for the CI group compared to the NH group differed by nearly an order of magnitude when listening with 12 spectral channels (ripple frequency-spacing of approximately 3000 Hz compared to approximately 400 Hz, experiment 1). While acoustic simulations of CI processing cannot exactly replicate CI signals, since, for example, they cannot simulate the effects of current distribution patterns in the cochlea, they do allow some understanding of perceptual abilities with CI-like signal processing. Thus, to the extent that CI simulations provide an estimate of optimal performance, these results indicate that the spectral shape resolution abilities of most CI listeners are considerably poorer than those of NH listeners when listening with the same number of channels. Performance on the spectral ripple resolution task varied widely among CI listeners, with the best-performing CI subject able to achieve a level of performance (threshold of 800 Hz) close to the range of the NH subjects (300 to 600 Hz), while at the other end of the performance range three subjects showed thresholds of approximately 8000 Hz.

It is interesting that as the spectral detail provided in the signal was increased, by increasing the number of processing channels from 1 to 16, the NH listeners were able to use the additional spectral detail to resolve more closely spaced peaks, showing significant increases in performance to the maximum number of channels tested (16 channels). In contrast, while the CI listeners as a group showed significant increases in performance as the number of channels was increased to between four and six channels, as the number of channels was increased further, this increased spectral detail was not able to be used by these listeners to resolve more closely spaced peaks. Furthermore, the number of effective channels utilized by CI subjects to resolve spectral peaks varied widely, from one to eight channels (Fig. 9). These findings are significant in two respects. First, they provide additional evidence that CI listeners are not able to take advantage of the spectral detail provided in the processed signal. Second, these results are generally consistent with the results of previous studies which have investigated the effect of the number of channels on speech recognition (e.g., Fishman *et al.*, 1997; Friesen *et al.*, 2001). As such, they indicate that patterns of performance obtained using the spectral ripple resolution test are similar to those obtained using speech recognition tests, the potential implications of which are discussed below.

In CIs and CI simulations, acoustic spectral shapes are represented by the relative amplitude across channels. Therefore, in order to discriminate between spectral shapes, such as between different formants, or in the specific case of the present study, between the *standard* and *inverted* stimuli, listeners must be able to detect and discriminate between relative changes in amplitude across channels. The generally poorer ability of CI listeners to utilize the spectral detail provided in the processed signal is not well understood, but may be due to a lower specificity of neural populations activated in electrical stimulation, due to factors related to the patterns of neural survival and function, and patterns of current distribution in the cochlea. An inability of CI users to discriminate electrodes, which is an ability which has previously been shown to be related to speech recognition ability (see the Introduction), and to detect and discriminate changes in level between electrodes, may therefore be associated with a ''blurring'' of the spectral peaks in acoustic signals. In addition, the reduced spectral contrast at the output of CI processors, due to the compression of the acoustic dynamic range into the narrow electrical dynamic range, may also affect the ability to resolve the spectral peaks in acoustic signals. Indeed, Loizou and Poroy (2001) found that CI listeners required 4–6 dB of spectral contrast for maximal vowel perception, in comparison to 1–3 dB for NH listeners (see the Introduction). While it might be hypothesized therefore that spectral shape resolution may be related to the dynamic range of an individual, studies on the effect of dynamic range on vowel recognition in quiet listening conditions have shown mixed results (Zeng and Galvin, 1999; Loizou *et al.*, 2000). In this study, there was no apparent relation between spectral peak perception and dynamic range (at least when expressed as an average value across frequency). Clearly, further research regarding the effects of the dynamic range of electrical stimulation on the ability to resolve the spectral peaks in acoustic signals is required.

We hypothesized that a listeners' ability to perceive the frequency locations of the peaks in a generic speech-like acoustic signal (as measured in the spectral ripple resolution task in this study) may be related to vowel recognition. Indeed, there was a significant relationship between ripple resolution thresholds and vowel recognition for CI listeners, with the r^2 value of 0.42 indicating that 42% of the variability in vowel scores is accounted for by the regression of vowel score and spectral ripple resolution threshold. These results indicate that those listeners who are better able to determine the positions of the spectral peaks in the acoustic signal, as shown by lower ripple resolution thresholds, are, on average, more readily able to extract vowel information from the signal. While further research is required to investigate the potential clinical applications of these results, it seems possible that the adaptive spectral ripple resolution test may provide a time-efficient and non-linguistic measure which may contribute to the prediction of performance in both adult and child CI users. Should this test be verified, and extended to other speech perception measures, it may be potentially applicable in a clinical setting in guiding the selection of re/habilitation strategies, and selecting and optimizing speech processing strategies for individual CI users, and also in improving the predictive power of models which use variables such as duration of deafness and preoperative sentence scores (e.g., Rubinstein *et al.*, 1999) to describe the variance in CI speech recognition, via the inclusion spectral ripple resolution thresholds as an additional factor.

Finally, while some of the variance in vowel scores is accounted for by the regression of vowel score on spectral ripple resolution threshold, more than half of the variance remains unaccounted for. As discussed in the Introduction, there are many factors, both peripheral and central, which may contribute to the variance in speech perception among CI users, and some of these may be unrelated to the resolution of spectral ripples. For example, one factor which may

have contributed more to the variance in speech perception scores than the variance in ripple resolution scores is the age of the participants, which varied widely from 37 to 80 years in this study. While it does seem highly likely that other factors account for the remaining variance in speech recognition scores, it may also be possible to optimize the rippled noise stimuli to improve the predictive power of this test. For instance, the effects measured in this study might depend to some extent on whether a linear or logarithmic scale is used for the ripple frequency spacing. While ripple spacing on a logarithmic scale would reflect the properties of the normal auditory system, the filters in the CIS strategy implemented in this study use a combination of linear and logarithmic division of the frequency scale (see Table II), and therefore linear spacing of ripples was chosen to provide an initial estimate of ripple resolution abilities in the present study.

V. CONCLUSIONS

The main findings in this study were the following.

(1) There was wide variation in the ability of CI listeners to resolve spectral shapes in the acoustic signal, with spectral ripple resolution thresholds ranging from 800 to 8000 Hz.
(2) Spectral shape resolution was poorer in CI users than NH listeners when listening with the same number of channels (12). While the average ripple resolution threshold for NH listeners was 400 Hz, the average for CI listeners was 3000 Hz.
(3) NH listeners were able to utilize more channels to resolve spectral peaks than CI listeners. Spectral shape resolution increased with the number of channels to 16 for the NH group, while the CI listeners showed a performance plateau at 4–6 channels, which is consistent with previous studies of the effect of the number of channels on speech recognition.
(4) There was a significant correlation between spectral shape resolution and vowel recognition for the CI listeners.

ACKNOWLEDGMENTS

We are grateful to the subjects for their considerable time and effort in participating in this research. We wish to thank Keith Kluender, Fan-Gang Zeng, and two anonymous reviewers for their comments on an earlier version of this manuscript. Thanks also to James Hillenbrand for use of the multi-talker vowel test materials, to Norbert Dillier and Waikong Lai for use of the SCILAB program, and also to Arik Wald, Bomjun Kwon, Kristine Melis, Anne Torkelson, Courtney Burke, and Jenny Klein for their assistance. Funding for this research was provided in part by NIDCD Grant No. 1R01DC00377.

Alcantare, J., and Moore, B. (**1995**). ''The identification of vowel-like harmonic complexes: Effects of component phase, level and fundamental frequency,'' J. Acoust. Soc. Am. **97**, 3818–3824.
Battmer, R. D., Gupta, S. P., Allum-Mecklenburg, D. J., and Lenarz, T. (**1995**). ''Factors influencing cochlear implant perceptual performance in 132 adults,'' Ann. Otol. Rhinol. Laryngol. **104** (Suppl. 166), 185–187.
Blamey, P. J., Pyman, B. C., Gordon, M., Clark, G. M., Brown, A. M., Dowell, R. C., and Hollow, R. D. (**1992**). ''Factors predicting postoperative sentence scores in postlinguistically deaf adult cochlear implant patients,'' Ann. Otol. Rhinol. Laryngol. **101**, 342–348.
Blamey, P. J., Arndt, P., Bergeron, F., Bredberg, G., Brimacombe, J., Facer, G., Larky, J., Lindstrom, B., Nedzelski, J., Peterson, A., Shipp, D., Staller, S., and Whitford, L. (**1996**). ''Factors affecting auditory performance of postlinguistically deaf adults using cochlear implants,'' Audiol. Neuro-Otol. **1**, 293–306.
Byrne, D., Dillon, H., Tran, K., Arlinger, S., Wilbraham, K., Cox, R., Hagerman, B., Hetu, R., Kei, J., Lui, C., Kiessling, J., Kotby, M. N., Nasser, N. H. A., El Kholy, W. A. H., Nakanishi, Y., Oyer, H., Powell, R., Stephens, D., Meredith, R., Sirimanna, T., Tavartkiladze, G., Frolenkov, G. I., Westerman, S., and Ludvigsen, C. (**1994**). ''An international comparison of long-term average speech spectra,'' J. Acoust. Soc. Am. **96**, 2108–2120.
Collins, L. M., Zwolan, T. A., and Wakefield, G. H. (**1997**). ''Comparison of electrode discrimination, pitch ranking, and pitch scaling data in postlingually deafened adult cochlear implant subjects,'' J. Acoust. Soc. Am. **101**, 440–455.
Donaldson, G. S., and Nelson, D. A. (**2000**). ''Place-pitch sensitivity and its relation to consonant recognition by cochlear implant listeners using the MPEAK and SPEAK speech processing strategies,'' J. Acoust. Soc. Am. **107**, 1645–1658.
Dorman, M. F., and Loizou, P. C. (**1997**). ''Speech intelligibility as a function of the number opf channels of stimulation for normal-hearing listeners and patients with cochlear implants,'' Am. J. Otolaryngol. **18**, S113–S114.
Dorman, M. F., and Loizou, P. C. (**1998**). ''The identification of consonants and vowels by cochlear implant patients using a 6-channel Continuous Interleaved Sampling processor and by normal-hearing subjects using simulations of processors with two to nine channels,'' Ear Hear. **19**, 162–166.
Dorman, M. F., Loizou, P. C., and Rainey, D. (**1997**). ''Speech understanding as a function of the number of channels of stimulation for processors using sine-wave and noise-band outputs,'' J. Acoust. Soc. Am. **102**, 2403–2411.
Dorman, M. F., Loizou, P. C., Fitzke, J., and Tu, Z. (**1998**). ''The recognition of sentences in noise by normal-hearing listeners using simulations of cochlear-implant signal processors with 6–20 channels,'' J. Acoust. Soc. Am. **104**, 3583–3585.
Dorman, M. F., Dankowski, K., McCandless, G., Parkin, J. L., and Smith, L. (**1990**). ''Longitudinal changes in word recognition by patients who use the Ineraid cochlear implant,'' Ear Hear. **11**, 455–459.
Fishman, K., Shannon, R. V., and Slattery, W. H. (**1997**). ''Speech recognition as a function of the number of electrodes used in the SPEAK cochlear implant speech processor,'' J. Speech Lang. Hear. Res. **40**, 1201–1215.
Friesen, L. M., Shannon, R. V., Baskent, D., and Wang, X. (**2001**). ''Speech recognition in noise as a function of the number of spectral channels: Comparison of acoustic hearing and cochlear implants,'' J. Acoust. Soc. Am. **110**, 1150–1163.
Gantz, B. J., Woodworth, G. G., Knutson, J. F., Abbas, P. J., and Tyler, R. S. (**1993**). ''Multivariate predictors of audiological success with multi-channel cochlear implants,'' Ann. Otol. Rhinol. Laryngol. **102**, 909–916.
Henry, B. A., McKay, C. M., McDermott, H. J., and Clark, G. M. (**2000**). ''The relationship between speech perception and electrode discrimination in cochlear implantees,'' J. Acoust. Soc. Am. **108**, 1269–1280.
Hillenbrand, J., Getty, L. A., Clark, M. J., and Wheeler, K. (**1995**). ''Acoustic characteristics of American English vowels,'' J. Acoust. Soc. Am. **97**, 3099–3111.
Leek, M., Dorman, M., and Summerfield, Q. (**1987**). ''Minimum spectral contrast for vowel identification by normal-hearing and hearing-impaired listeners,'' J. Acoust. Soc. Am. **81**, 148–154.
Levitt, H. (**1971**). ''Transformed up-down methods in psychoacoustics,'' J. Acoust. Soc. Am. **49**, 467–477.
Loizou, P. C., and Poroy, O. (**2001**). ''Minimal spectral contrast needed for vowel identification by normal hearing and cochlear implant listeners,'' J. Acoust. Soc. Am. **110**, 1619–1627.

Loizou, P. C., Dorman, M., and Fitzke, J. (**2000**). ''The effect of reduced dynamic range on speech understanding: Implications for patients with cochlear implants,'' Ear Hear. **21**, 25–31.
Nelson, D. A., Van Tassell, D. J., Schroder, A. C., Soli, S., and Levine, S. (**1995**). ''Electrode ranking of 'place pitch' and speech recognition in electrical hearing,'' J. Acoust. Soc. Am. **98**, 1987–1999.
Rubinstein, J. T., Parkinson, W. S., Tyler, R. S., and Gantz, B. J. (**1999**). ''Residual speech recognition and cochlear implant performance: effects of implantation criteria,'' Am. J. Otol. **20**, 445–452.
Schroeder, M. R. (**1968**). ''Reference signal for signal quality studies,'' J. Acoust. Soc. Am. **44**, 1735–1736.
Shannon, R. V., Zeng, F-G., Kamath, V., Wygonski, J., and Ekelid, M. (**1995**). ''Speech recognition with primarily temporal cues,'' Science **270**, 303–304.
Skinner, M. W., Clark, G. M., Whitford, L. A., Seligman, P. M., Staller, S. J., Shipp, D. B., Shallop, J. K., Everingham, C., Menapace, C. M., Arndt, P. L., Antogenelli, T., Brimacombe, J. A., Pijl, S., Daniels, P., George, C. R., McDermott, H. J., and Beiter, A. L. (**1994**). ''Evaluation of a new spectral peak coding strategy for the Nucleus 22 channel cochlear implant system,'' Am. J. Audiol. **15(2)**, 15–27.
Supin, A., Popov, V. V., Milekhina, O. N., and Tarakanov, M. B. (**1994**). ''Frequency resolving power measured by rippled noise,'' Hear. Res. **78**, 31–40.
Supin, A., Popov, V. V., Milckhina, O. N., and Tarakanov, M. B. (**1998**). ''Ripple density resolution for various rippled-noise patterns,'' J. Acoust. Soc. Am. **103**, 2042–2050.
Supin, A., Popov, V. V., Milekhina, O. N., and Tarakanov, M. B. (**1999**). ''Ripple depth and density resolution of rippled noise,'' J. Acoust. Soc. Am. **106**, 2800–2804.
Throckmorton, C. S., and Collins, L. M. (**1999**). ''Investigation of the effects of temporal and spatial interactions on speech-recognition skills in cochlear-implant subjects,'' J. Acoust. Soc. Am. **105**, 861–873.
Turner, C. W., and Van Tassell, D. (**1984**). ''Sensorineural hearing loss and the discrimination of vowel-like stimuli,'' J. Acoust. Soc. Am. **75**, 562–566.
Turner, C. W., Souza, P. E., and Forget, L. N. (**1995**). ''Use of temporal envelope cues in speech recognition by normal and hearing-impaired listeners,'' J. Acoust. Soc. Am. **97**, 2568–2576.
Van Wieringen, A., and Wouters, J. (**1999**). ''Natural vowel and consonant recognition by Laura cochlear implantees,'' Ear Hear. **20**, 89–103.
Zeng, F.-G., and Galvin, J. (**1999**). ''Amplitude mapping and phoneme recognition in cochlear implant users,'' Ear Hear. **20**, 60–74.

Numerical and experimental modal analysis of the reed and pipe of a clarinet[a)]

Matteo L. Facchinetti
Laboratoire de Mécanique des Solides and Laboratoire d'Hydrodynamique, CNRS-École Polytechnique, 91128 Palaiseau Cedex, France

Xavier Boutillon[b)]
Laboratoire d'Acoustique Musicale, CNRS-Université Paris 6-Ministère de la Culture, 11 rue de Lourmel, 75015 Paris, France

Andrei Constantinescu
Laboratoire de Mécanique des Solides, CNRS-École Polytechnique, 91128 Palaiseau Cedex, France

(Received 12 December 2001; revised 8 August 2002; accepted 24 January 2003)

A modal computation of a complete clarinet is presented by the association of finite-element models of the reed and of part of the pipe with a lumped-element model of the rest of the pipe. In the first part, we compare modal computations of the reed and the air inside the mouthpiece and barrel with measurements performed by holographic interferometry. In the second part, the complete clarinet is modeled by adjoining a series of lumped elements for the remaining part of the pipe. The parameters of the lumped-resonator model are determined from acoustic impedance measurements. Computed eigenmodes of the whole system show that modal patterns of the reed differ significantly whether it is alone or coupled to air. Some modes exhibit mostly reed motion and a small contribution of the acoustic pressure inside the pipe. Resonance frequencies measured on a clarinet with the mouthpiece replaced by the cylinder of equal volume differ significantly from the computed eigenfrequencies of the clarinet taking the actual shape of the mouthpiece into account and from those including the (linear) dynamics of the reed. This suggests revisiting the customary quality index based on the alignment of the peaks of the input acoustical impedance curve. [DOI: 10.1121/1.1560212]

PACS numbers: 43.75.Ef [NHF]

I. INTRODUCTION

The clarinet is usually considered as the association of a linear resonator, the pipe, and a nonlinear excitor, the reed, subject to the air flow from the mouth. Alternatively, one can consider the air column and the reed as a linear system subject to nonlinear boundary conditions. This is the approach retained in this article where the reed is considered as a linear mechanical system coupled to the pipe and where the interaction with the player is not treated. Nonlinear phenomenon such as the interaction between the reed and the jet across the reed-slit, the contact forces between the reed and the lay, and the interaction between the reed and the player's lip will be included in a subsequent piece of work as nonlinear boundary conditions to the normal modes that are described here. Humidity of the reed and the player's lip also have a damping role which is not considered in this modal analysis of a pipe coupled to a (dry) reed.

Acoustical studies of the clarinet have so far represented the mouthpiece of a wind instrument by its equivalent volume. This study goes beyond this approximation and presents the three-dimensional distribution of the pressure in the upper part of the instrument.

Studies of the pipe of the clarinet have traditionally been expressed in the frequency domain and were based on measurements or computations of input acoustic impedance. However, numerical simulations of this instrument operate in the time domain and are usually based on the reflection function of the pipe. Recent experimental studies have adopted the time domain approach with direct measurements of this reflection function. Abundant literature extensively covers these subjects: for general presentations, see Refs. 1–4.

Studies of the reeds are far less extensive and the mechanical behavior of cane is still subject to discussion. The simplest reed model, a spring, is implicitly used by reedmakers when they rate them by their so-called ''strength,'' which corresponds to the mechanical compliance. Experimental studies have proposed values for the compliance of the reed.[1,5,6] Associated with various models of the pipe and excitation, this model has been used in numerical simulations which were successful in describing basic features of the dynamics of clarinet-like system.[7–9] Music-oriented algorithms have also been proposed in which the values of the parameters describing the excitor and the resonator are adjusted in order to obtain realistic sounds instead of accurately describing their mechanical behavior.[10,11] However, this model is obviously insufficient to describe quality-based criteria: otherwise all reeds in a given commercial box (with

[a)]Part of this work was presented in ''Application of modal analysis and synthesis of reed and pipe to numerical simulations of a clarinet,'' invited paper at the 140th meeting of the ASA, Newport Beach, CA, December 2000 [J. Acoust. Soc. Am. **108**, 2590(A)], in ''Etude modale d'une clarinette,'' Proceedings of the Colloque National en Calcul de Structures, Giens, France, May 2001, and in ''Modal analysis of a complete clarinet,'' Proceedings of the International Conference on Acoustics, Rome, Italy, September 2001.

[b)]Electronic mail: boutillon@lms.polytechnique.fr; present address: Laboratoire de Mecanique des Solides, Ecole Polytechnique, 91128 Palaiseau Cedex, France.

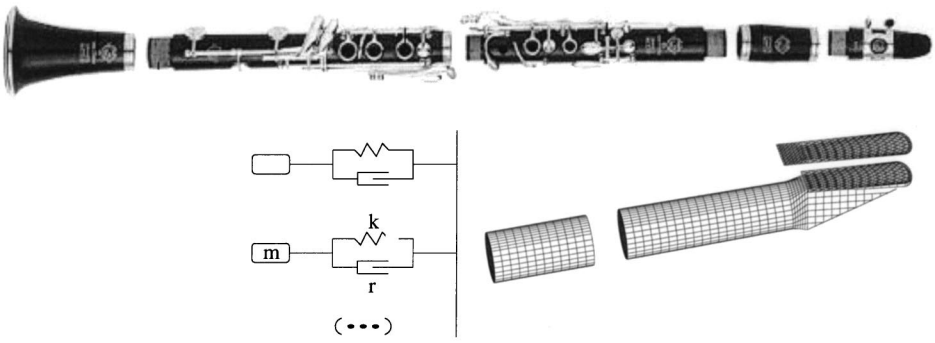

FIG. 1. The clarinet: its parts and their respective models (not to scale).

similar strength) would suit a given player, but this is not the case.

The next modeling step is the single-degree-of-freedom oscillator. Although some simulation algorithms[12] have been very successful in producing realistic sounds,[13,14] this is not sufficient in itself to assert the physical validity of a model. One degree of freedom is not sufficient to account for criteria such as reed quality. Stewart and Strong[15] and Sommerfeld and Strong[16] used a refined model of the reed as a nonuniform beam. In the latter study, the pipe was only slightly simplified compared to a real clarinet and the player's air column (including the lungs) was also taken into account. There is no fundamental difference between this simulation and those based on a simple oscillator model for the reed since the interaction with the rest of the system is averaged along the beam. The beam model is needed if one wants to take into account the curved shape of the mouthpiece on which the reed beats during large amplitude motions. Gazengel[17] derived a simple oscillator model from a beam equation. In his time-domain simulation, the mass of the oscillator is recalculated at each time step as a function of the position of the reed, introducing by this means the nonlinear behavior of the reed contact.

Modeling the reed as a continuous system is the current state of research. Several examples of modal analysis of clarinet reeds with holographic interferometry have been presented in conferences over the recent years,[18–20] but never published. One example of finite-element modeling based on measurements of the mechanical properties of cane has been reported.[21] Another (unpublished) pioneering study has been done by Pinard and Laine when they were students at the École Polytechnique (France). The experimental modal analysis and the finite-element modeling of isolated reeds that are presented in the following are a development of this unpublished work. To our knowledge, no model of the reed as a continuous system in association with the air column has been proposed.

The model proposed here is aimed at overcoming several limitations of previous approaches. Besides giving a means to review the approximations of the classical model, this new approach is also a first step toward numerical simulations of the instrument based on modal projection[22,23] rather than on propagation schemes represented by reflection functions.

The different parts of a clarinet—reed, mouthpiece, barrel, upper and lower parts of the pipe, bell—are shown in Fig. 1 together with their respective models. Fluid and solid finite-element models (FEM) for the reed and the beginning of the pipe and a lumped elements model for the main part of the pipe are used.

The work presented here begins with the modal analysis of the isolated reed. In each subsequent section, another element of the model is added, finally resulting in a complete instrument. In addition, the modes of the reed associated with the mouthpiece and barrel are compared with the results of experimental modal analysis.

II. THE REED

A. Construction of the numerical model

Establishing a finite element model requires the determination of the geometry of the reed, the choice of a constitutive law, the determination of the mechanical parameters, as well as the appropriate boundary conditions.

A series of three reeds have been measured. The thickness of each reed was measured with a coordinate measuring machine (Mitutoyo EURO-M 574 and Johansson Saphir 7 were used). Approximately 200 points, arbitrarily chosen on the reed surface, have been measured [Fig. 2(a)]. The geometrical data for the model are interpolated from the measured values. Interpolation between measured points was done by using a fourth-order polynomial, resulting in and giving the thickness map shown in Fig. 2(b). The reed is assumed to be symmetrical with regard to its longitudinal axis.

The shape of the reed was measured using a high precision optical projector (Macro Dynascope 5D, by Vision Engineering with Metronics Quadra-Check 4000 interpolating software) with the results shown in Fig. 2(c). The precision of the geometrical measurements of the reed can be estimated to ≈ 2 μm.

Reeds are made out of cane which is considered here as a purely elastic, transversely isotropic, homogeneous material. Viscosity and plasticity, related to energetic losses, have been neglected at this step of the analysis. The homogeneity hypothesis will be analyzed a posteriori in Sec. V. In the current state of knowledge, we have found no other plausible description that could be expressed quantitatively.

A discussion of losses in cane has been given lately by Marandas *et al.*[24] and Obataya and Norimoto.[25] The former found out that dry cane is viscoelastic and turns viscoplastic when wet. This implies that static tests on wet cane are not appropriate to measure Young's moduli. Obataya proposed values of the quality factor Q of the order of magnitude of

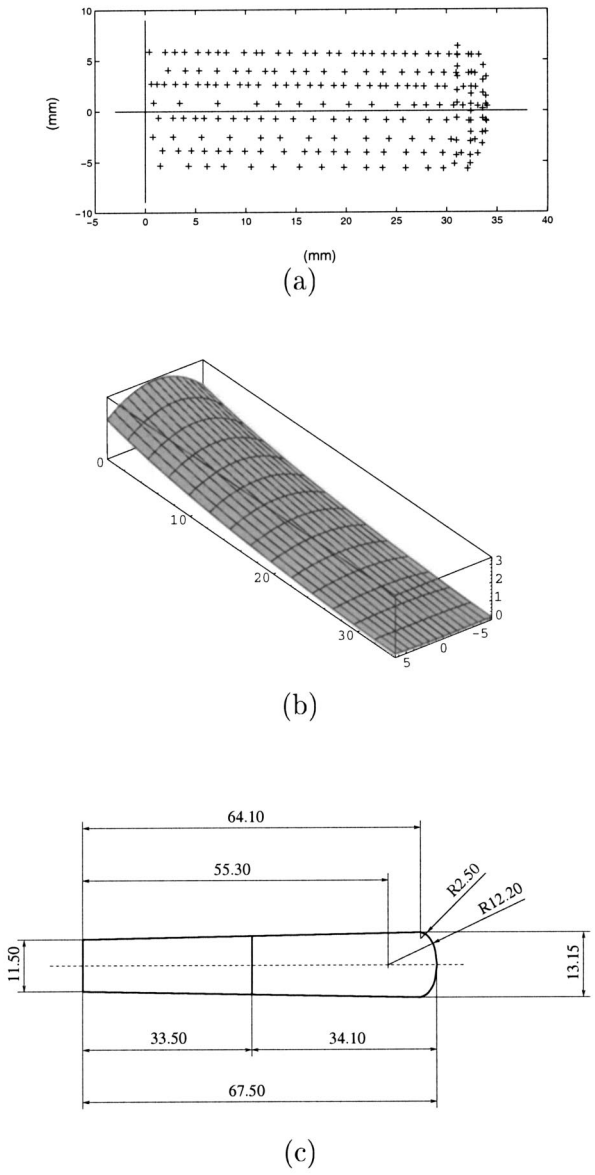

FIG. 2. Geometry of the reed, with dimensions in mm: (a) points actually measured, (b) interpolated thickness, (c) estimated contour.

100 varying with frequency, relative humidity, and internal state of cane. Since only individual modes of the reed are considered here losses can be ignored. They would need to be taken into account in modeling the actual dynamics of the instrument.

Under these assumptions, five parameters are needed to describe the material: density ρ_s, longitudinal and transverse Young's moduli E_L and E_T, transverse to longitudinal shear modulus G_{LT}, and longitudinal-transverse Poisson ratio ν_{LT}. The values adopted here are given in Table I. The values for ρ_s, E_L, and ν_{LT} were obtained by Pinard and Laine and result from static measurements on a piece of dry cane given by a reed maker. Obataya and Norimoto give roughly the same value for the main Young's modulus E_L of dry cane in the frequency that is relevant here (2–6 kHz). Their measurements show that this value decreases linearly with the relative humidity level (RH), E_L decreasing by around 30% for a variation of 100% in RH. The other parameters were

TABLE I. Material properties for dry cane used in reeds, as given by Pinard and Laine.

Density	$\rho_s = 450$ kg/m^3
Longitudinal Young modulus	$E_L = 10\,000$ MPa
Transverse Young modulus	$E_T = 400$ MPa
Shear modulus	$G_{LT} = 1300$ MPa
Poisson ratio	$\nu_{LT} = 0.22$

also obtained by Pinard and Laine. Their work has been pioneering in several respects. In particular, they were the first to match eigenfrequencies and modal patterns of reeds obtained by holographic interferometry with those obtained with a finite-element model.

As boundary condition, we consider the reed rigidly clamped on the section corresponding to the ligature and having a stress-free boundary elsewhere.

B. Computed eigenmodes

This model has been implemented on a standard PC (450 MHz, 250 Mbyte RAM, Linux) using linear Love–Kirchoff plate elements in the CAST3M finite-element code. The first modes of a reed are presented in Fig. 3. A classification of the modes is needed for referencing and an attempt is made here. Since modal patterns with closed modal lines have not been encountered, it is intuitively appealing to label the modes according to the number of intersections between the nodal lines and the edges of the reed. For the symmetric reed considered here, a mode is labeled *LnTm*. "*L*" stands for longitudinal and the first index *n* is the number of intersections of nodal lines with the edge(s) parallel to the main axis. Such nodal lines include the one imposed by the boundary condition at the ligature. "*T*" stands for transverse and the index *m* is the number of intersections of the nodal lines with the tip edge of the reed. Modes appear in an order which can be expected ($L1T0$, $L1T1$, $L2T0$, $L1T2$, $L2T1$), given the larger flexibility in the direction transverse to the reed and the thickness distribution.

The generalized mass of a mode is:

$$m = \mathbf{u}^T \mathbf{M}_s \mathbf{u}, \tag{1}$$

where $\mathbf{u}$ represents the reed displacement for the mode and $\mathbf{M}$ is the mass matrix of the reed. For a unit value of the maximum displacement in each mode, the modal masses are 7, 0.35, 0.47, 0.063, and 0.094 mg for the $L1T0$, $L1T1$, $L2T0$, $L1T2$, and $L2T1$ modes, respectively. Along with modal patterns, these values establish a comparison between modes. These mass values can also be compared to the order of magnitude of the real mass of the moving reed. At the tip of the reed, the thickness is about 1/10 mm and the width 13 mm. For a density $\rho_s = 450\,\mathrm{kg\,m^{-3}}$, the mass of a moving portion of the reed of length l (in mm) is $(0.59 \times l)$ mg.

III. MODAL COMPUTATION OF THE REED ASSOCIATED WITH MOUTHPIECE AND BARREL

This section analyzes how the dynamics of the reed is influenced by air loading and provides a comparison between results given by the model and experiments presented in Sec.

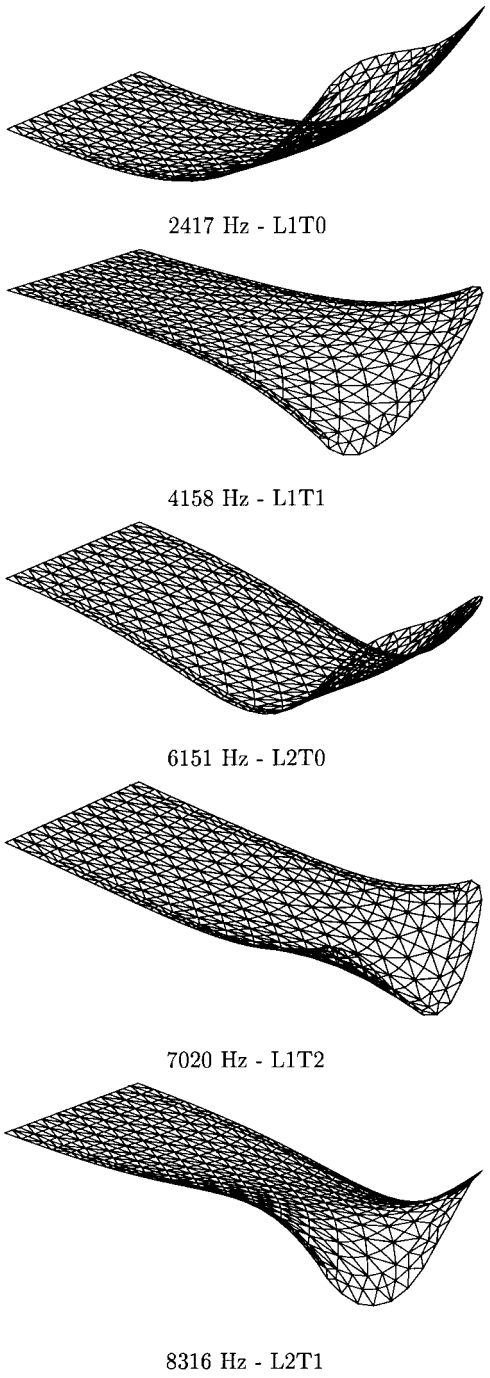

FIG. 3. First five computed modes of an isolated reed. Modes are labeled according to the number of modal lines perpendicular to the main axis (*Ln*) and parallel to it (*Tm*).

II. The system considered now is composed of the reed, the mouthpiece, and the barrel and is represented using a coupled fluid–solid model.

A. Numerical model

The full model of reed, mouthpiece, and open barrel is shown in Fig. 4. The internal shape of the mouthpiece (a Selmer HS*) has been carefully measured by means of the coordinate measuring machine used for the reed. The barrel is considered as a cylindrical bore with a diameter of 15 mm. The air volume inside the mouthpiece and the barrel is modeled with linear tetrahaedric and prismatic finite elements of compressible elastic fluid.

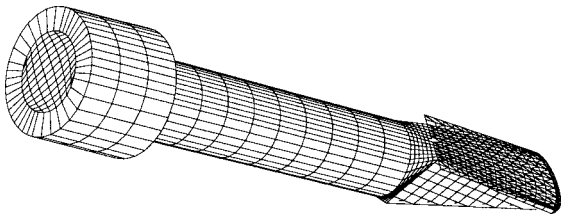

FIG. 4. Reed and volume of air inside the mouthpiece mounted on an open barrel.

The acoustic pressure at points of the open air surfaces is considered to be zero. The normal derivative of the acoustic pressure on the walls of the mouthpiece and the barrel, corresponding to air flow, is also set to zero. The boundary condition coupling the reed and the mouthpiece involves the stress in the solid and the velocity of the fluid and will be given explicitly in the following.

The eigenvalue problem for a coupled solid–fluid system is expressed in the continuous formulation by the following:[26]

$$\mathrm{div}\,\mathbf{C}\nabla\mathbf{u}-\omega^2\rho_s\mathbf{u}=0, \tag{2}$$

$$\mathrm{div}\,\frac{1}{\rho_f}\boldsymbol{\nabla} p+\omega^2\frac{1}{c^2\rho_f}p=0, \tag{3}$$

where p represents the acoustic pressure in the fluid. The densities of solid and fluid are ρ_s and ρ_f, respectively. The speed of sound is c, the angular frequency of the motion is ω, and $\mathbf{C}$ denotes the elasticity matrix of the solid.

The boundary conditions coupling the fluid and the solid parts are

$$\boldsymbol{\sigma}\cdot\mathbf{n}=-p\mathbf{n}, \tag{4}$$

$$\frac{\partial p}{\partial\mathbf{n}}=\rho_f\omega^2\mathbf{u}\cdot\mathbf{n}, \tag{5}$$

where $\mathbf{n}$ represents the unit vector normal to the solid surface and $\boldsymbol{\sigma}=\mathbf{C}\nabla\mathbf{u}$ the stress tensor.

In order to formulate these equations as a standard eigenvalue problem, a new variable $\pi=-(1/\omega^2)p$ must be introduced.[26] The equations and boundary conditions become

$$\mathrm{div}\,\mathbf{C}\nabla\mathbf{u}-\omega^2\rho_s\mathbf{u}=0, \tag{6}$$

$$\mathrm{div}\,\frac{1}{\rho_f}\boldsymbol{\nabla}\pi-\frac{1}{c^2\rho_f}p=0, \tag{7}$$

$$\omega^2\pi+p=0, \tag{8}$$

$$\boldsymbol{\sigma}\cdot\mathbf{n}=-p\mathbf{n}, \tag{9}$$

$$\frac{\partial\pi}{\partial\mathbf{n}}=-\rho_f\mathbf{u}\cdot\mathbf{n}. \tag{10}$$

To the preceding equations, we can associate the following Lagrangian $\mathcal{L}$ denoting the variational formulation of the problem:

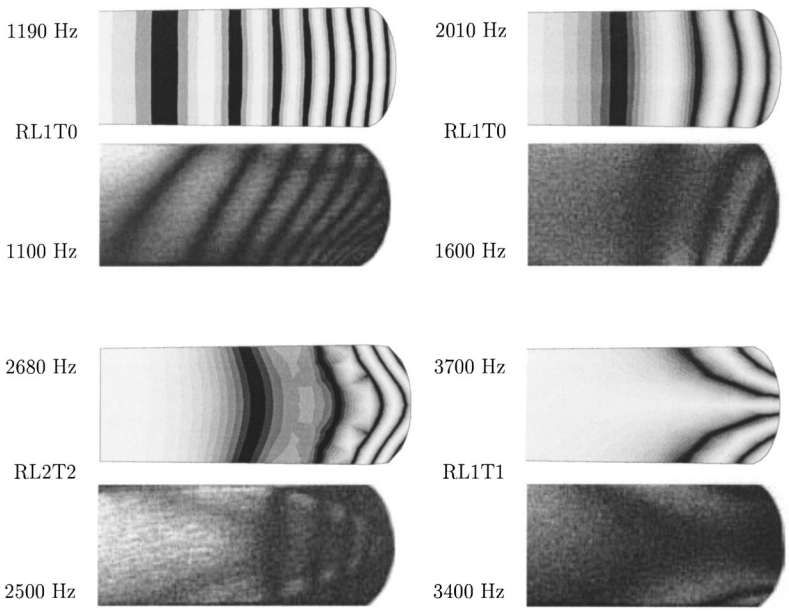

FIG. 5. Projection of four eigenmodes on the reed (see the text for labels). Top pictures: computed normalized eigenmodes of the association of a reed with mouthpiece and barrel. In this representation, a cyclic gray scale produces fringes of equal differences in normal displacement, allowing a comparison with the modal patterns observed experimentally. Bottom pictures: modal patterns measured by holographic interferometry on one good reed mounted on the mouthpiece attached to the barrel. The resonance is not very sharp owing to damping, hence the rounded eigenfrequencies. The photographed section of the reed does not have the same height between the various experiments and the simulations.

$$\mathcal{L}=\frac{1}{2}\int_{\Omega_s}\nabla\mathbf{u}\mathbf{C}\nabla\mathbf{u}\,dv+\frac{1}{2}\int_{\Omega_f}\frac{1}{\rho_f c^2}p^2\,dv - \omega^2\left(\frac{1}{2}\int_{\Omega_s}\rho_s\mathbf{u}^2\,dv-\frac{1}{2}\int_{\Omega_f}\frac{1}{\rho_f c^2}(\boldsymbol{\nabla}\pi)^2 dv - \int_{\Omega_f}\frac{1}{\rho_f c^2}p\,\pi\,dv-\int_{\partial\Omega}\pi\boldsymbol{\sigma}\cdot\mathbf{n}\,ds\right), \tag{11}$$

where Ω_s and Ω_f represent the solid and fluid volumes, respectively, and $\partial\Omega$ represents the boundary between these volumes.

Finally, the problem is expressed in its discrete form by the following eigenvalue problem:

$$\left(\begin{bmatrix}\mathbf{K}_s & 0 & 0\\ 0 & \mathbf{K}_f & 0\\ 0 & 0 & 0\end{bmatrix}-\omega^2\begin{bmatrix}\mathbf{M}_s & 0 & -\mathbf{N}\\ 0 & 0 & \mathbf{K}_f\\ -\mathbf{N}^T & \mathbf{K}_f^T & -\mathbf{M}_f\end{bmatrix}\right)\begin{bmatrix}\mathbf{u}\\ p\\ \pi\end{bmatrix}=\begin{bmatrix}0\\ 0\\ 0\end{bmatrix},$$

where $\mathbf{K}_s$ (respectively, $\mathbf{K}_f$) and $\mathbf{M}_s$ (respectively, $\mathbf{M}_f$) are rigidity and mass matrices of the solid (respectively, fluid) part of the system and $\mathbf{N}$ is the operator corresponding to the coupling boundary condition (10) related to the normal vector $\mathbf{n}$. Details of the derivation can be found in Ref. 26.

B. Experimental modal analysis

An experimental modal analysis on reeds by means of holographic interferometry was performed in order to check the validity of the numerical model of the reed coupled to air. Recent works have been reported in short communications.[18–20] For various reeds mounted on a mouthpiece under dry conditions Pinard and Laine observed one mode corresponding to a longitudinal flexion at around 2200 Hz; one family of modes around 3500–3700 Hz, with patterns varying from reed to reed, some of them being indicative of torsion, others being closer to flexion; and one family of modes around 5800–6000 Hz, with more complex patterns.

In measurements presented here, the reed was attached to the mouthpiece exactly as on the real instrument. Since the ligature was producing strong light reflexions, it was replaced with adhesive tape placed slightly further from the tip. A sinusoidally driven loudspeaker was placed close to the reed to excite its vibration. For determining the resonance frequencies a very thin PVDF piezoelectric film [poly(vinylidenefluoride), thickness 0.05 mm, mass 0.06 g, of which only a part was actually moving] was glued onto the lower thicker part of the reed, yielding the average deformation near the ligature. Resonance frequencies were determined using the maximum of the piezoelectric signal. The experiments were performed under natural humidity. A saturated atmosphere would have been preferable but was not possible with the interferometry equipment.

The eigenmodes were visualized by means of laser transmission interferometry. Complete details of the implementation of this classical method are described in Ref. 27. The images in Fig. 5 represent variations of equal normal-displacement of the reed. The resolution of the system is half the wavelength of the laser, approximately 0.3 μm.

The reed was measured either alone, associated with an open mouthpiece, or with the mouthpiece mounted on an open barrel. The first four measured modes shown in Fig. 5 correspond to the barrel configuration (see Fig. 4). They are compared with the corresponding computed modal patterns (see the next section for computation of the eigenmodes) on top. Results of the holographic measurements show that the maximum displacement of the reed is negligible compared to the distance between the mouthpiece and the reed at that level of excitation. Thus one can be confident that contact between the reed and the lay, which could possibly make the system nonlinear, does not occur.

TABLE II. Sensitivity analysis: changes in eigenfrequencies when mechanical characteristics of the reed and acoustical properties of the air vary. Changes are given in % for a 10% variation of each parameter.

$\Delta = 10\%$ mean values	E_L 10^4 MPa	E_T 400 MPa	G_{LT} 1300 MPa	ν_{LT} 0.22	ρ_s 450 kg m^{-3}	c 340 m s^{-1}	ρ_f 1.23 kg m^{-3}
1190 Hz	0	0	0	0	0	9.8	0
2010 Hz	2.4	0	0	0	−2.2	0.7	−0.4
2680 Hz	0.1	0	0	0	−0.2	9.6	0
3700 Hz	1.5	0	3.1	0	−4.6	0	0
4010 Hz	0.2	0	0	0	−0.2	9.3	0
4740 Hz	4.9	0	0	0	−4.8	2.7	−0.1
5280 Hz	0.6	0	0	0	−0.9	8.1	−0.1
6300 Hz	1.7	0.9	4.9	0	−6.4	3.2	0

C. Results

A comparison between computed and measured modes is displayed in Fig. 5 for the situation described by Fig. 4. In this comparison with holographic measurements, the ''ligature'' of the reed had to be placed slightly beyond its normal position. This led to a slightly more flexible reed than in the normal situation. When the reed is coupled to air, one should stress that eigenmodes concern the whole system, not just the reed. Strictly speaking, expressions such as ''reed modes'' are inappropriate and refer instead to modes for which energy is *mostly* localized in the reed. Each mode has been labeled using the notation proposed earlier. The ''*R*'' prefix indicates that we regard the result just as the *projection* of the four first eigenmodes on the reed subspace. In order to simplify the discussion, we have not attempted to label the air configuration. One can notice that the $L2T2$ pattern did not appear in the isolated reed case. One can also notice that the $L1T0$ pattern of the reed appears in the two first modes of the coupled system.

The computed modes appear in the same order as the measured ones with eigenfrequencies deviating by 10%–20% from measured resonance frequencies. The modal patterns are globally the same despite the fact that no real reed is symmetric whereas the numerical model has been chosen symmetric. As expected, the modes are mainly localized at the tip of the reed where it becomes very thin, showing the importance of a precise measurement of the geometry. Although some of the mechanical parameters come themselves from a fit between observation and computation of modes of an isolated reed, the mixed fluid–solid model can be considered as valid within the range of approximations retained here.

Real reeds have natural asymmetries due to their geometry or to nonuniform mechanical properties. One notices that the asymmetry seems stronger for the lowest mode than for any other one.

D. Sensitivity analysis

The sensitivity analysis of the eigenfrequencies to variations in mechanical parameters describing the reed and in acoustical properties of the air is presented in Table II. The air volume is that of Fig. 4. Parameters are varied by 5% above and below their average values (i.e., 10% overall) and the corresponding overall variations of eigenfrequencies are reported. The value of the Poisson ratio appears to be irrelevant. Eigenfrequencies 1190, 2680, and 4010 Hz vary linearly with the speed of sound. This is also almost the case for the mode at 5280 Hz. Without looking at the modal pattern of air pressure or reed displacement, one can infer that they correspond to '' 'air modes,'' with energy mostly localized in the (short) pipe. Conversely, the mode at 3700 Hz is not influenced by air characteristics; sensitivity to the shear modulus G_{LT} indicates that the reed is subject to torsion (see the second mode of Fig. 3) and is poorly coupled to the pipe (Fig. 6). To a lesser degree, this is also the case of the mode at 6300 Hz. The mode at 4740 reveals a $(E_L/\rho_s)^{1/2}$ dependency of the eigenfrequency. It is mostly a ''reed mode'' involving primarily a longitudinal deformation. The mode at 2010 Hz is apparently a mode in which air and reed are strongly coupled. It is interesting to notice that the transverse Young's modulus does not seem to influence any frequency. The measurement of its precise value is therefore less particularly important.

E. Evolution of the eigenfrequencies

Another way of examining how the reed is coupled to the acoustic field is to follow the evolution of the eigenfrequencies when the reed is loaded by the air volume of mouthpiece and barrel. A decrease of the eigenfrequencies and a dominance of the longitudinal flexion occurs in the eigenmodes (Fig. 7).

The frequencies of the first two modes of the {reed, mouthpiece, barrel} system are mainly imposed by the resonance of the air cavity. In both modes, the reed undergoes mainly longitudinal flexion. The frequency of the torsion mode $L1T1$ (3257 Hz for the isolated reed) does not vary

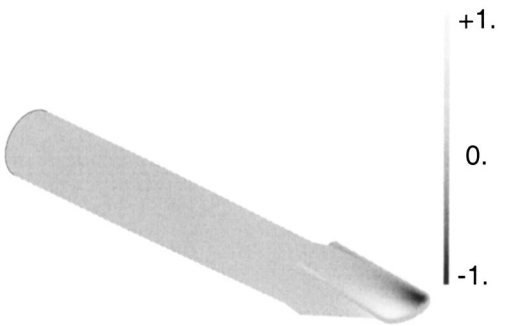

FIG. 6. Computed eigenmode at 4119 Hz in a mixed solid-air situation: acoustic pressure inside the mouthpiece and barrel.

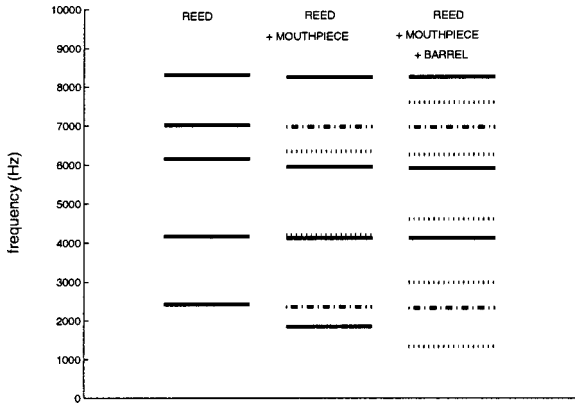

FIG. 7. Evolution of the eigenfrequencies (left scale, in hertz) when the system evolves from the isolated reed (left) to {reed+mouthpiece} (middle) and {reed+mouthpiece+barrel} (right). Black lines represent ''primary reed'' modes, dotted lines ''primary air'' modes, and dash-dot lines, ''mixed'' modes.

significantly, meaning that this mode is weakly coupled to the air cavity. The same phenomenon can be noticed for the mode $L1T2$ at 5840 Hz for the isolated reed. One can conclude from Fig. 7 and from the observation of the rather uniform pressure in the pipe at these modes (not shown here) that this mode also is weakly coupled to the pipe.

IV. MODAL COMPUTATION OF THE WHOLE CLARINET

In order to simulate the modal behavior of the complete clarinet, we have associated a finite-element model of $\approx$10 cm of pipe with lumped elements representing the rest of the pipe and matching its acoustic input impedance. This can be done since at the outlet of the barrel, the acoustic field consists essentially of plane waves. An example of acoustic pressure in the mouthpiece is represented in Fig. 8. The mode is that of a complete clarinet and corresponds to the lowest mode at 311 Hz of the medium C$\sharp$ fingering combined with the opening of the register key (see the following for the complete list of modes in this configuration). The length of mouthpiece represented here is 32 mm and corresponds to the tapered part. One can see that the acoustic waves can already be considered as plane waves within a very good approximtation.

The lumped-element oscillators (shown in generic form in Fig. 1) are coupled to the finite-element barrel by means

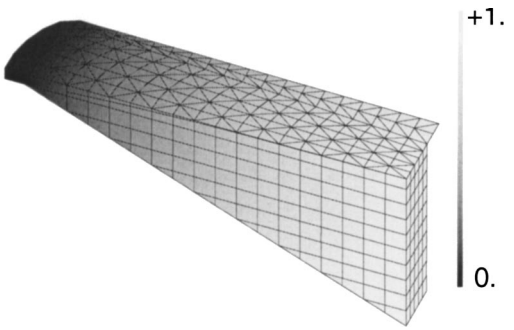

FIG. 8. Acoustic pressure inside the tip part of the mouthpiece for a 311 Hz mode of the complete clarinet. The acoustic pressure decreases monotonically from the tip to the largest section by 14%.

of a rigid plate of negligible mass, as shown in Fig. 9. The plate and the lumped-element oscillators are supposed to move only in the longitudinal axis of the instrument. The lumped elements are placed at the (virtual) junction between the barrel and the lower part of the clarinet.

It is now explained how the numerical values of the lumped elements are calculated on the basis of measurements provided by Gibiat[28] on several notes of a Noblet B$\flat$ clarinet. Results of these measurements are supposed to represent the *input* acoustical impedance of the instrument. In order to measure this input impedance, a reference plane was defined by Gibiat *et al.* by replacing the mouthpiece with a portion of cylindrical tube of equal volume. This is the usual ''equivalent volume'' approximation which we discuss later on. Prior to matching the impedance of the lumped elements to the measured input acoustical impedance of the pipe, the latter must therefore be transported from the input plane toward the open end of the pipe. The ''transportation distance'' is equal to the length of a cylinder having the volume of the mouthpiece and the barrel.[22,29]

An oscillator is associated with each measured impedance peak. At the angular frequency ω the mechanical impedance of each elementary oscillator in Fig. 1 is

$$Z_m(\omega)=i\left(\frac{1}{m\omega}-\frac{\omega}{k+i\omega r}\right)^{-1}, \tag{12}$$

where *m, r, k* are respectively the mass, damping, and stiffness of the lumped elements.

In this ''comb-like'' association, the impedances of the oscillators add. The dual association where the admittances add is ''chain-like.'' Each elementary oscillator of Fig. 1 is a mass chained with a comb of a damper and a spring, leading to Eq. (12).

The parameters m_i, r_i, k_i of each oscillator (a tooth of the large comb) are identified by minimizing a cost functional $\mathcal{J}$ measuring the distance between computed and measured moduli and phase of the impedance:

$$\mathcal{J}=\alpha|\mathrm{Mod}(Z_{\mathrm{comp}})-\mathrm{Mod}(Z_{\mathrm{meas}})| + \beta|\mathrm{Arg}(Z_{\mathrm{comp}})-\mathrm{Arg}(Z_{\mathrm{meas}})|. \tag{13}$$

The initial values of the parameters for each oscillator are obtained by identifying each single resonance peak and the final values are obtained by running a Nelder–Mead simplex search algorithm. A comparison between the measured and the identified modulus and phase of the acoustic impedance of the lowest F fingering (E$\flat$ heard) of the clarinet is presented in Fig. 10. The impedance represented is not the input acoustical impedance but the impedance of the lower part taken at the (virtual) junction between the barrel and the lower part of the clarinet. Therefore, the peak frequencies are not the eigenfrequencies of the instrument. The acoustical impedance represented here is the ratio of the acoustical pressure to the air velocity, normalized by ρc. The average modulus on a logarithmic scale would be 1 for an ideal long cylindrical pipe. According to Gibiat, it is less here due to internal losses, radiation, and presumably the complexity of the pipe.

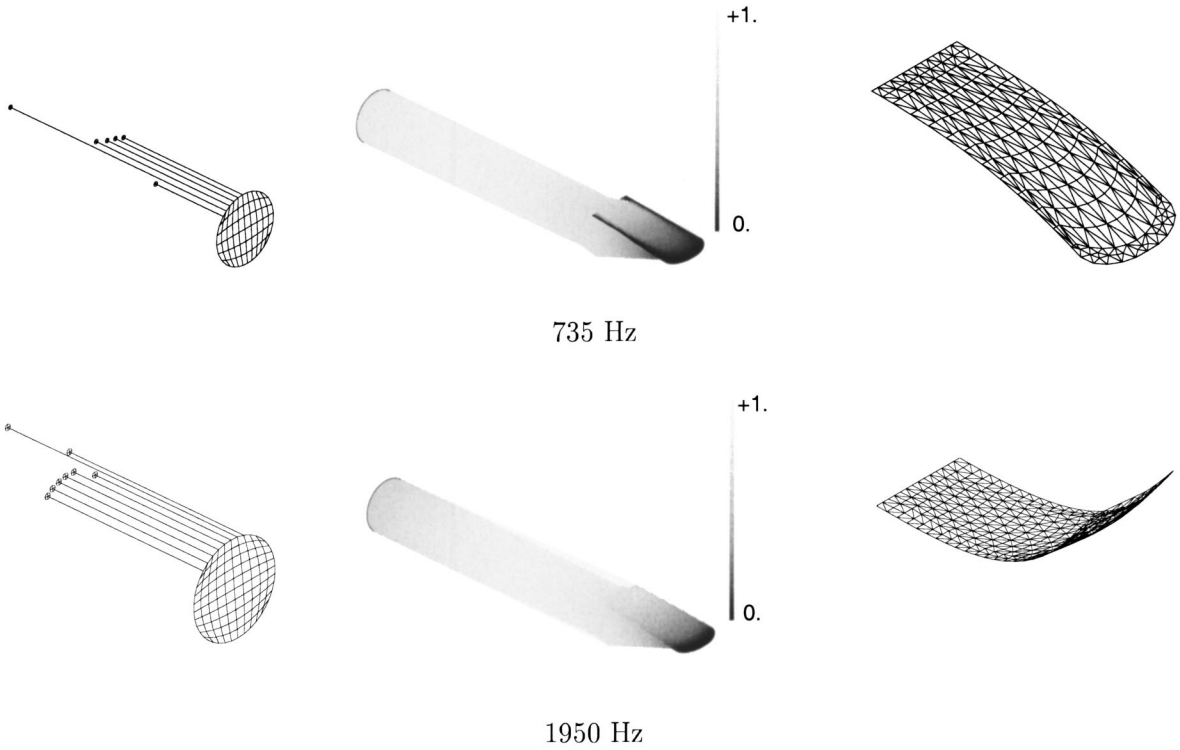

FIG. 9. Modal representation of a complete clarinet: amplitude of the motion of the lumped-element oscillators (left), air pressure in the upper part of the pipe (middle), and deformation of the reed (right). Eigenmode 2 for note treeble F# (fingering of C# medium plus opening of register key) and eigenmode 8 for note low E♭ (low F fingering).

Two eigenmodes of the complete instrument for different fingerings are shown in Fig. 9. One eigenmode has no amplitude *per se*. For each eigenmode in Fig. 9 the (relative) amplitude of the motion of the oscillators is represented by the length of a straight line extending from the plate. One notices that the pressure distribution is not uniform in the mouthpiece. Examining other similar figures reveals that the motion of the reed can differ significantly from mode to mode of a given note, even if it follows a $L1T1$ pattern. This means that, although the first modes of the isolated reed occur at significantly higher frequencies than those considered here, a single degree of freedom for the reed is not appropriate since it would not account for these differences. When the reed undergoes mostly longitudinal flexion, it is to be expected that the beam model used by several authors[15,16,30] would give comparable results.

For the low F fingering (sounding one tone lower), the first eigenfrequencies are 166, 464, 743, 1147, 1436, 1620, 1950, 2058, and 2201 Hz. They are 373, 1035, 1541, 1687, 1893, 1930, and 2309 Hz for the medium G fingering and 311, 735, 1213, 1467, 1578, 1865, and 2211 Hz for the high G♯, played with medium C♯ fingering and opening of the register key. These frequencies are represented in Fig. 11 in order to evaluate their harmonicity. Eigenfrequencies are normalized by their ratio to the theoretical musical frequency for the note under consideration (respectively, 156, 349, and 740 Hz), rounded to the nearest integer. For example, a 900 Hz eigenfrequency for note A4 (440 Hz) would be normalized by 2, nearest integer to 900/440. For this high note, the register key does not eliminate the first mode of the instrument but the sound will be locked approximately on the second mode. The lowest mode is very roughly at half the pitch of the note and is therefore normalized by the integer 2.

The sets of solid lines in Fig. 11 represent the computed eigenfrequencies listed above of the complete instrument. The sets of dashed lines are resonances of the pipe as extracted from the measurements of the input impedance of the pipe. This set represents the traditional view of the instru-

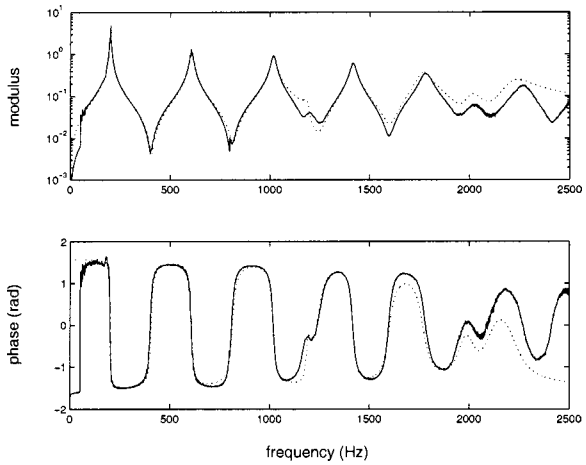

FIG. 10. Acoustical impedances (ratio of the acoustical pressure to the air velocity, normalized by ρc) for the low F note of the clarinet. Solid lines: acoustical impedance of the pipe as measured at the closed end of the pipe and transported at the (virtual) junction between the barrel and the lower part of the clarinet. Dashed lines: impedance of the set of lumped oscillators best matching the impedance of the pipe at the junction.

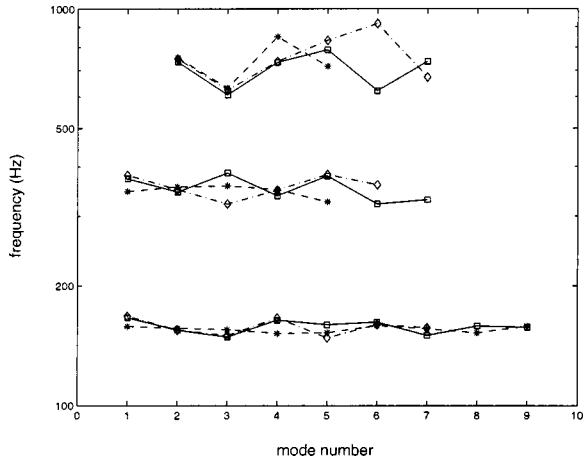

FIG. 11. Normalized eigenfrequencies (logarithmic scale) of the complete clarinet, pipe with reed (solid symbols), of the pipe with a fixed reed (dash dot), and normalized resonance frequencies measured on the pipe where the mouthpiece replaced by its equivalent volume (dashed). See the text for the definition of the normalization. Fingerings are low F, medium G, and high G♯ (medium C♯ with register key) corresponding to notes E♭ 3, F 4, and G♯ 5.

ment where the volume of the mouthpiece has been replaced by a cylindrical pipe having the same volume and closed at one end. The sets of dotted lines represent computed eigenfrequencies of the air column with a rigid boundary on the reed surface. Instead of the completely closed pipe of the traditional modeling, one assumes here a slight opening between the reed surface and the lay of the mouthpiece with a zero pressure condition.

V. DISCUSSION AND PERSPECTIVES

A. Alignment of resonances and low-frequency approximation

The traditional model of the mouthpiece is that of a cylinder of equivalent volume. Within this approximation there is no point in measuring the input acoustic impedance above a certain limit. This limit can be evaluated by the length scale at which the mouthpiece geometry differs from a cylinder. Taking as an order of magnitude for these geometrical differences a length of 1 cm is consistent with a 2.5 kHz frequency limit beyond which input acoustical impedances would begin to differ noticeably. In the approach followed in this paper, the equivalent volume approximation is abandoned and the acoustical input impedance of the pipe would keep full utility and validity up to the frequency of the first transverse mode of the pipe (13.3 kHz for the clarinet).

The cylinder of equivalent volume approximation for the mouthpiece is assumed to be correct for low frequencies. It appears in Fig. 11 that this approximation is not acceptable enough to be used in conjunction with an alignment of peaks criteria. One can see in Fig. 11 that variations in eigenfrequencies due to the model change are significant with regard to the alignment of resonances, *even at low frequencies*. In other words, the deviations from alignment in the traditional view (equivalent volume approximation) are of the same order of magnitude as the frequency shifts due to the presence of the reed and the prismatic shape of the mouthpiece.

B. Coupling of torsion modes to the air

The association of reed, mouthpiece, and a short open portion of the pipe is shown in Fig. 6. The modal acoustic pressure at an eigenfrequency of 4119 Hz is displayed in Fig. 6. In this mode, the reed undergoes torsion in a pattern very similar to the $L1T1$ mode of the isolated reed (Fig. 3). The characteristic distance of this modal deformation is significantly smaller than half the wavelength in air at that frequency ($\lambda \approx 10$ cm); the resulting acoustical short-circuit prevents any efficient coupling of the reed to the air in the mouthpiece. This explains the fairly uniform acoustic pressure for this mode, except very near to the reed. However, there are several reasons why these modes may be important in the actual playing.

First of all, the flow entering the air channel between the reed and the lay is governed by a nonlinear equation. Therefore, antisymmetric reed modes may have an influence on the global flow entering the pipe.

It has been shown that the antisymmetric reed modes are very weakly coupled to the acoustic (far)field in the clarinet. This is not to say that these modes play no role in the dynamics. Asymmetries or, better said, unevenness in the geometric or constitutive properties of reeds induce asymmetries of longitudinal reed modes and consequently an asymmetry in the local acoustical field. Due to its small relative modal mass, the torsion mode can be easily excited at a frequency different from its resonant frequency and therefore may play a significant role in the actual dynamics of the reed. The coupling factor would then be the local acoustic field. This may be an explanation for the player's experience that for different mouthpieces, the preferred reeds are also different.

This modal analysis is performed on a symmetric reed. This is not the case in reality as shown for example by the first mode in Fig. 5. The so-called torsion modes are likely to be associated in the fluid domain to a flow different from zero and therefore couple to the plane waves inside the pipe.

C. Symmetry

Experimental modal analysis shows that some reeds have strong asymmetries. Makers can be expected to be successful in controlling the symmetry of the geometry; therefore, the cause of modal asymmetries lies most probably in the lack of homogeneity of the cane used for the reed due to its natural character. Pinard, Laine, and Vach [31] examined 24 reeds, ranked by two professional players. They observed that the two reeds ranked as good and very good were symmetric whereas the poor reed had asymmetrical high modes. Based on limited sampling of reeds and players, no definite conclusion can be drawn. Intuition would suggest that asymmetry is not a desirable feature for a reed. However, we think that it might not be so.

Visualizing the lip motion in brass playing shows that lips do not move symmetrically and that this factor varies from player to player. Since brass mouthpieces are symmetric, one can conclude that the mechanical properties of lips (possibly coupled to dentition and the mouth cavity) are not symmetric for all brass players. One can hypothesize that the same is true among clarinet and saxophone players. Another

observation is that different players do not always prefer the same reeds in a given box, even for common musical tasks, style, etc., and the same clarinet and mouthpiece. A good match between a player and a reed could mean that a given asymmetry in a reed would fit well the natural asymmetry of a given player and not so well with another one. It has even been observed that a few players use reeds which fit almost none of their colleagues. It would be interesting to test these players and their preferred reeds with regard to the symmetry hypothesis.

VI. CONCLUSION

The modal analyses of reeds and of a few notes of the whole clarinet were performed. Results have shown the following points.

(1) A numerical model of cane based on the hypothesis of transverse isotropy is suited to describe modal patterns of reeds. Some of the numerical hypotheses (homogeneity, symmetry, damping) can be released but this would necessitate additional measurements.

(2) When coupled to air, the reed is subject to deformation patterns which are not always those of its own normal modes. Therefore, the normal modes of isolated reeds cannot be taken as a source for the acoustic field in the mouthpiece. Specifically, coupling must be taken into account.

(3) Torsion modes of reeds generate a strong but very localized acoustic field in the mouthpiece. It remains to be examined how this would interact with asymmetries in lower modes through the excitation process.

(4) Acoustic waves are already plane within a very good approximation in the cylindrical part of the mouthpiece. Since finite-element modeling of air is interesting insofar as the waves are not plane, the air volume in the barrel and a large proportion of that in the mouthpiece can be included in the lumped-element model, reducing significantly the computational burden.

(5) The shape of the mouthpiece and the dynamics of the reed influence the alignment of resonances in the same proportion as the misalignment derived from the customary observation of the input acoustical impedance. Therefore, the approximation of the equivalent volume is too coarse to be used when looking at harmonicity of resonances.

This study shows the need for input impedance measurements at higher frequencies than usually performed. It calls for simplified formulations of the acoustic field in the mouthpiece. The procedure outlined here could be used to test these formulations. Finally, the method paves the way for numerical simulations of the dynamics of the clarinet based on modal projection and taking into account the whole complexity of the reed.

ACKNOWLEDGMENTS

We express our gratitude to Holger Vach for his decisive help in the experimental part of this study, to Vincent Gibiat for providing us with the measurements of the acoustic input impedances and the associated software, and to Brian Katz for many language corrections.

[1] C. J. Nederveen, *Acoustical Aspects of Woodwind Instruments* (Illinois University Press (first ed. Frits Knuf Pub., Amsterdam), Dekalb, 1998 (first ed. 1968)).
[2] A. H. Benade, *Fundamentals of Musical Acoustics* (Oxford University Press, New York, 1976).
[3] J. Kergomard, ''Elementary considerations on reed-instrument oscillations,'' in *Mechanics of Musical Instruments* (Springer, New York, 1995).
[4] D. Campbell, ''Nonlinear dynamics of musical reed and brass wind instruments,'' Contemp. Phys. **40**, 415–431 (1999).
[5] J. Gilbert, ''Étude des instruments à anche simple'' (On simple reed instruments), Ph.D. thesis, Université du Maine-Le Mans, 1991.
[6] X. Boutillon and V. Gibiat, ''Evaluation of the acoustical stiffness of saxophone reeds under playing conditions by using the reactive power approach,'' J. Acoust. Soc. Am. **100**, 1178–1189 (1996).
[7] R. Schumacher, ''*Ab initio* calculations of the oscillations of a clarinet,'' Acustica **48**, 73–85 (1981).
[8] M. Mcintyre, R. Schumacher, and J. Woodhouse, ''On the oscillations of musical-instruments,'' J. Acoust. Soc. Am. **74**, 1325–1345 (1983).
[9] C. Maganza, R. Causse, and F. Laloe, ''Bifurcations, period doublings and chaos in clarinet-like systems,'' Europhys. Lett. **1**, 295–302 (1986).
[10] X. Rodet and C. Vergez, ''Nonlinear dynamics in physical models: Simple feedback-loop systems and properties,'' Comput. Music J. **23**, 18–34 (1999).
[11] J. Smith, ''Physical modeling using digital wave-guides,'' Comput. Music J. **16**, 74–98 (1992).
[12] B. Gazengel, J. Gilbert, and N. Amir, ''Time-domain simulation of single reed wind instrument—From the measured input impedance to the synthesis signal—Where are the traps?,'' Acta Acustica **3**, 445–472 (1995).
[13] E. Ducasse, ''Modelisation et simulation dans le domaine temporel d'instruments à vent a anche simple en situation de jeu'' (Time-domain model and simulation of simple-reed instruments in playing conditions), Ph.D. thesis, Université du Maine-Le Mans, 2001.
[14] E. Ducasse, ''Models of musical-instruments for sound synthesis: Application to woodwind instruments,'' J. Phys. (France) **51**, 837–840 (1990).
[15] S. Stewart and W. Strong, ''Functional-model of a simplified clarinet,'' J. Acoust. Soc. Am. **68**, 109–120 (1980).
[16] S. Sommerfeldt and W. Strong, ''Simulation of a player clarinet system,'' J. Acoust. Soc. Am. **83**, 1908–1918 (1988).
[17] B. Gazengel and J. Gilbert, ''Numerical simulations in time and frequency domains—Comparative-study, application to single-reed woodwind instruments,'' J. Phys. IV **4**, 577–580 (1994).
[18] P. Hoekje and G. Roberts, ''Observed vibration patterns of clarinet reeds,'' J. Acoust. Soc. Am. **99**, 2462(A) (1996).
[19] I. Lindevald and J. Gower, ''Vibrational modes of clarinet reeds,'' J. Acoust. Soc. Am. **102**, 3085(A) (1997).
[20] B. Richardson (private communication).
[21] D. Casadonte, ''The perfect clarinet reed? Vibrational modes of realistic clarinet reeds,'' J. Acoust. Soc. Am. **94**, 1807(A) (1993).
[22] M. Facchinetti, ''Etude des vibrations de l'anche de la clarinette'' and ''Analisi del comportamento dinamico di un clarinetto,'' Ecole Polytechnique-Paris and Politecnico-Milano (1999).
[23] M. Facchinetti, X. Boutillon, and A. Constantinescu, ''Application of modal analysis and synthesis of reed and pipe to numerical simulations of a clarinet,'' J. Acoust. Soc. Am. **108**, 2590(A) (2000).
[24] E. Marandas, V. Gibiat, C. Besnainou, and N. Grand, ''Mechanical characterization of woodwind reeds,'' J. Phys. IV **4**, 633–636 (1994).
[25] E. Obataya and M. Norimoto, ''Acoustic properties of a reed (Arundo donax L.) used for the vibrating plate of a clarinet,'' J. Acoust. Soc. Am. **106**, 1106–1110 (1999).
[26] R.-J. Gibert, *Vibrations des Structures-Interactions avec les Fluides* (Eyrolles, Paris, 1988).
[27] K. Menou, B. Audit, X. Boutillon, and H. Vach, ''Holographic study of a vibrating bell: An undergraduate laboratory experiment,'' Am. J. Phys. **66**, 380–385 (1998).
[28] V. Gibiat and F. Laloe, ''Acoustical impedance measurements by the 2-microphone-3-calibration (tmtc) method,'' J. Acoust. Soc. Am. **88**, 2533–2545 (1990).
[29] V. Gibiat, ''Mesures d'impédance acoustique pour la clarinette,'' proprietary software and private communication, 1999.
[30] B. Gazengel, ''Caractérisation ... des instruments à anche simple'' (Characterization ... of simple reed instruments), Ph.D. thesis, Université du Maine-Le Mans, 1994.
[31] F. Pinard, B. Laine, and H. Vach, ''Musical quality assessment of clarinet reeds using optical holography,'' J. Acoust. Soc. Am. **113**, 1736–1742 (2003).

Ultrasonic absorption in aqueous solutions of amino acids at neutral pH

S. Nishikawa,[a] T. Ohno, and H. Huang
Department of Chemistry and Applied Chemistry, Faculty of Science and Engineering, Saga University, Saga 840-8502, Japan

K. Yoshizuka
Department of Chemical Processes and Environments, Faculty of Environmental Engineering, The University of Kitakyushu, Kitakyushu 808-0135, Japan

F. Jordan
Department of Chemistry, Rutgers, The State University of New Jersey, Newark, New Jersey 07102

(Received 30 August 2002; revised 5 February 2003; accepted 10 February 2003)

Ultrasonic absorption coefficients in aqueous solutions of glycine, L-alanine, imidazole, L-phenylalanine, L-histidine and L-tryptophan at neutral pH were measured in the range from 0.8 to 220 MHz at 25 °C. A characteristic ultrasonic relaxation phenomenon was observed only in the solution of L-histidine with a relaxation frequency at around 2 MHz at neutral pH. It was proposed from the concentration independent relaxation frequency and the linear concentration dependence of the maximum absorption per wavelength that the relaxation mechanism was associated with a perturbation of the rotational isomeric equilibrium of the L-histidine molecule. The existence of two rotational isomeric forms of L-histidine in water was examined by semiempirical quantum chemical methods, in order to determine the free energy difference between the two states. The forward and backward rate constants were determined from the relaxation frequency and the energy change. Also, the standard volume change of the reaction was estimated from the concentration dependence of the maximum absorption per wavelength. It was speculated that L-histidine fulfills a specific function among amino acids because of the rotational motion in the molecule, in addition to its well-established acid-base properties.
[DOI: 10.1121/1.1564012]

PACS numbers: 43.80.Cs, 43.80.Ev [FD]

I. INTRODUCTION

Great attention has been directed towards assessing the importance of ultrasonic absorption mechanisms in aqueous solutions of biological materials. Especially, the clarification of the absorption mechanisms in aqueous solutions of polypeptides is earnestly desired for applications of ultrasound to medically important compounds. In order to clarify the absorption mechanisms in solutions, many studies have been performed previously in model systems. One of the characteristic relaxational absorption mechanisms in aqueous solutions of amino acids is a proton-transfer reaction associated with amino and carboxylic groups.[1] This phenomenon is also observed in aqueous solutions of various amines and carboxylic acids.[2,3] Other mechanisms such as conformational change have also been proposed. Recently, Holmes and Challis[4] reported detailed studies of the ultrasonic absorption mechanism in aqueous solutions of peptides and compounds related to peptides at neutral pH. It is well accepted that one of the essential amino acids, L-histidine, has characteristic acid-base properties and plays an important role in the active site of enzymes. Kremkau[5] reported a small relaxational absorption in aqueous solution of L-histidine though the relaxation mechanism was not elucidated.

From many kinetic studies in aqueous solutions of amines, it has been found that the proton-transfer reaction gives rise to a large ultrasonic absorption under high pH conditions.[6] In solutions of imidazole ($pK_b = 6.99$), for example, the relaxation associated with the proton-transfer reaction is clearly observed and the rate and thermodynamic parameters have been determined by the present authors.[7] This relaxational absorption disappears when the solution pH is around 7.

In order to clarify the ultrasonic relaxation mechanisms in aqueous solution of L-histidine in detail, we have measured the ultrasonic absorption coefficients in the aqueous solutions in a wide frequency range, along with solutions of several other amino acids, and the possible relaxational mechanisms observed in aqueous solution of L-histidine are considered.

II. EXPERIMENTS

Glycine, L-alanine, L-phenylalanine, L-histidine, L-tryptophan and imidazole were purchased from Wako Pure Chemical Co., Ltd. and Tokyo Kasei Kogyou Co., Ltd. All of these were the purest grade (>98%), and were used without further purification. Sample solutions were prepared by weight using distilled water filtered through the MilliQ SP-TOC system from Japan Millipore Ltd. and solutions were stored in an N_2 gas atmosphere.

[a]Author to whom correspondence should be addressed; electronic mail: nishikas@cc.saga-u.ac.jp

 0001-4966/2003/113(5)/2884/5/$19.00

Ultrasonic absorption coefficients, α, were measured by both pulse and resonance methods. The two cells with 5 and 20 MHz *x*-cut fundamental quartz crystals for the pulse apparatus were used in the frequency range from 15 to 220 MHz.[8] The cells were immersed in a water bath maintained within ± 0.1 °C by Eyela Univ Ace NCB-2200. For the resonance method,[9,10] we used three resonators with 3, 5, and 7 MHz fundamental X-cut quartz crystals in the range from 0.8 to 9 MHz. The temperature of the sample solutions in the cells was maintained by circulating water controlled within ± 0.01 °C using a Lauda RM-20B temperature controller. The relationship between the absorption coefficient and the half-bandwidth, Δf, is given by $\Delta f/f = (\alpha/f^2)(f\nu/\pi) + Q^{-1}$, where f is the frequency, ν is the sound velocity, and Q^{-1} is the mechanical loss of the resonator. The values of Q^{-1} at individual frequencies were determined using NaCl solutions with the same acoustic impedance as that of the sample solutions.[10]

Sound velocity was measured by the resonator at around 3 MHz, with an accuracy of ± 0.1 m s^{-1}. Density was obtained by Anton Paar vibrating density meter (DMA60/602) and solution pH was measured with a HM-60S Toa Denpa pH meter with a glass electrode. All of the measurements were carried out at 25 °C.

Molecular modeling computation for L-histidine conformers was carried out with the program MOPAC2000 on the molecular modeling software WinMOPAC v.3.0 (Fujitsu, Co. Ltd.), to obtain the optimal structures and free energies.[11,12] AM1 type and PM3 type of semiempirical molecular orbital (AM1–SMO and PM3–SMO) calculations were employed under the precise mode which sets the convergence criteria for GNORM = 0.001, SCFCRT = 0.00001 and DDMIN = 0.0 as control parameters of MOPAC2000.

For the calculations of all the molecules, conductor-like screening model calculations were conducted in addition to the AM1–SMO and PM3–SMO methods, to evaluate the solvent effects of organic diluents on the free energies of L-histidine conformers.[10] The dielectric constant necessary to calculate with the COSMO method was 78.3 for water.

III. RESULTS AND DISCUSSION

One of the characteristic ultrasonic relaxations in aqueous solutions of amino acids is due to the proton-transfer reaction associated with amino and carboxyl groups.[1] They are observed at pH values away from the isoelectric points. Figure 1 shows the ultrasonic absorption spectra in aqueous solutions of glycine, L-phenylalanine, imidazole, L-alanine and L-tryptophan at around neutral pH. It is seen that the absorption coefficients divided by the square of the measurement frequency, (α/f^2), are independent of the measurement frequency, showing that there is no relaxation in these solutions. Figure 2 displays the representative absorption spectra in aqueous solutions of L-histidine at neutral pH. There is clear evidence that an ultrasonic relaxation exists in the solutions. As can be seen in this figure, the values of α/f^2 are almost constant above 35 MHz. The most widely used equation to analyze the frequency dependence of the absorption with a single relaxation frequency, f_r, is a Debye-type one as follows:

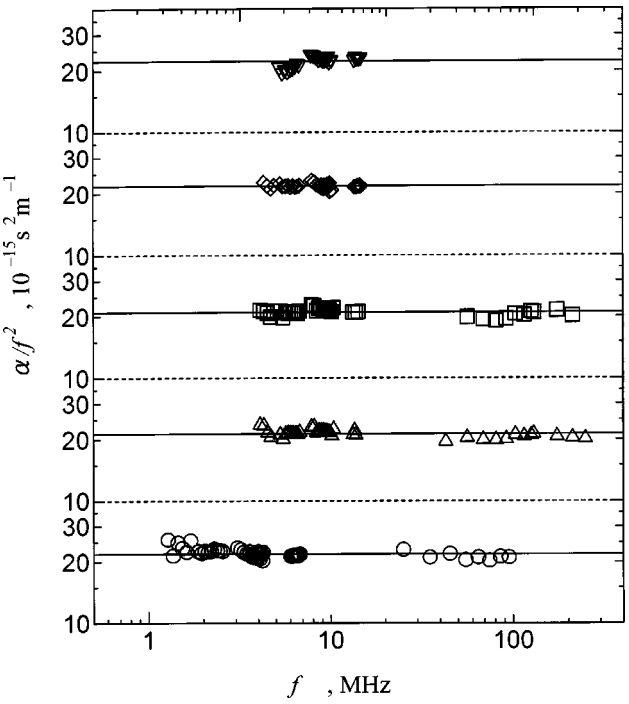

FIG. 1. Ultrasonic absorption spectra in aqueous solutions of several amino acids at 25 °C. No excess absorption has been found in these solutions. (○) 0.25 mol diam^{-3} glycine at pH 7.7; (◇) 0.10 mol diam^{-3} L-phenylalanine at pH 7.6; (□) 0.20 mol diam^{-3} imidazole at pH 7.7, (△) 0.20 mol diam^{-3} L-alanine at pH 7.7; (▽) 0.050 mol diam^{-3} L-tryptophan at pH 8.0. The dashed lines are drawn for distinguishing the vertical scales for the individual samples.

$$\alpha/f^2 = A/[1+(f/f_r)^2] + B, \tag{1}$$

where A is the amplitude of the relaxational absorption and B is the background absorption associated with the viscosity

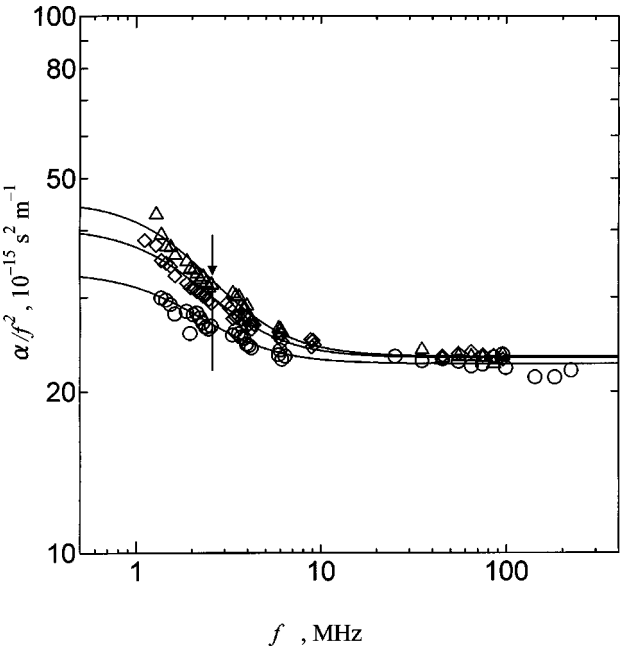

FIG. 2. Representative ultrasonic absorption spectra in aqueous solution of L-histidine at 25 °C. The arrows show the position of the relaxation frequency and the solution pH's are 7.7. (△) 0.200 mol diam^{-3}; (◇) 0.151 mol diam^{-3}; (○) 0.101 mol diam^{-3}. The solid lines are the calculated relaxation curves.

TABLE I. Ultrasonic and thermodynamic parameters for aqueous solutions of L-histidine at 25 °C.

Co mol dm^{-3}	pH	f_r MHz	A 10^{-15} s^2 m^{-1}	B	ν ms^{-1}	ρ kg m^{-3}
0.200	7.71	2.15±0.10	22.22±1.20	23.2	1513.9	1008.4
0.187	7.70	2.40±0.09	17.54±0.78	23.2	1512.4	1007.7
0.178	7.68	2.04±0.14	21.77±1.82	23.3	1512.7	1007.1
0.166	7.69	2.09±0.08	17.39±0.78	23.1	1510.3	1006.4
0.151	7.70	2.22±0.04	16.65±0.44	22.8	1510.7	1006.2
0.128	7.68	1.75±0.09	14.22±0.90	23.1	1507.2	1004.2
0.101	7.67	2.03±0.16	10.96±1.04	22.5	1506.7	1002.9
0.050	7.74			23.0		

and thermal conductivity of the medium, as well as that due to any processes with relaxation frequencies much higher than the f_r for the process in question. The background absorption, B, can be readily estimated from the experimental α/f^2 values at the higher frequency (>35 MHz). Therefore, the modified equation, $(\alpha/f^2-B)f=Af/[1+(f/f_r)^2]$ was utilized to determine A and f_r. The reason for multiplying both sides of the above equation by the frequency is that the α/f^2 values are a monotonous decreasing function with the frequency, and the similar weights to the experimental data for determination of the parameters, A and f_r, may be given as the function of the frequency by the multiplication. The B value was gradually varied until the smallest standard deviation resulted. A nonlinear least mean square program was used to obtain the two ultrasonic relaxation parameters, A and f_r.[13] The solid curves in Fig. 1 are generated with the values obtained by the above calculation procedure. It is seen that the calculated curves are well fitted to the experimental data, the results of which confirm that a single relaxational absorption is operative. Thus determined A and f_r values at various concentrations of L-histidine are listed in Table I along with the background absorption, B, sound velocity, ν, density, ρ, and solution pH. The concentration dependence of the relaxation frequency in the solutions at around pH=7.7 is shown in Fig. 3. The relaxation frequency is found to be independent of L-histidine concentration.

Another important parameter obtained from the absorption measurement is a maximum absorption per wavelength which is given by $\mu_{\max}=0.5Af_r\nu$, and is related to the standard volume change and the standard enthalpy change of a reaction occurring in solution. The concentration dependence of $\mu_{\max}$ is shown in Fig. 4, indicating a straight line going through the origin.

The independence of the relaxation frequency of the concentration, and the linear increase of the maximum absorption per wavelength prompt us to claim that the relaxation is associated with a unimolecular reaction.

$$\mathrm{A} \underset{k_b}{\overset{k_f}{\rightleftharpoons}} \mathrm{B}, \tag{2}$$

where k_f and k_b are the forward and backward rate constant, respectively. For the perturbation of the equilibrium expressed by Eq. (2), the relaxation frequency is given as,

$$2\pi f_r = k_f + k_b. \tag{3}$$

The maximum absorption per wavelength, μ_m, is given by Eq. (4) for the reaction expressed as Eq. (2),[14]

$$\mu_{\max} = \pi\rho\nu^2(\Delta V_s)^2(K/(1+K)^2)C_0/2RT, \tag{4}$$

where K is the equilibrium constant of the two states and C_0 is the analytical concentration of solute. The ΔV_s contains the two terms, i.e., the standard volume change of the reaction, ΔV, and the standard enthalpy change, ΔH, and it is expressed as $\Delta V_s=\Delta V-(\theta/\rho C_p)\Delta H$, here θ is the thermal expansion coefficient and C_p is the specific heat at constant pressure. In relatively dilute aqueous solutions, the thermal expansion coefficient is considered to be close to liquid water. The contributions of the solution density and sound velocity to the maximum absorption per wavelength is not dominant because the concentration dependences of these quantities are small when compared with those in the amplitude of the relaxational absorption as is seen in Table I. Also, the specific heat in the solution may be expected to be close to that of liquid water. Then, the $(\theta/\rho C_p)\Delta H$ term is very small when it is compared with the standard volume change. As a result, the plots of $\mu_{\max}$ vs C_0 appear to be linear, going

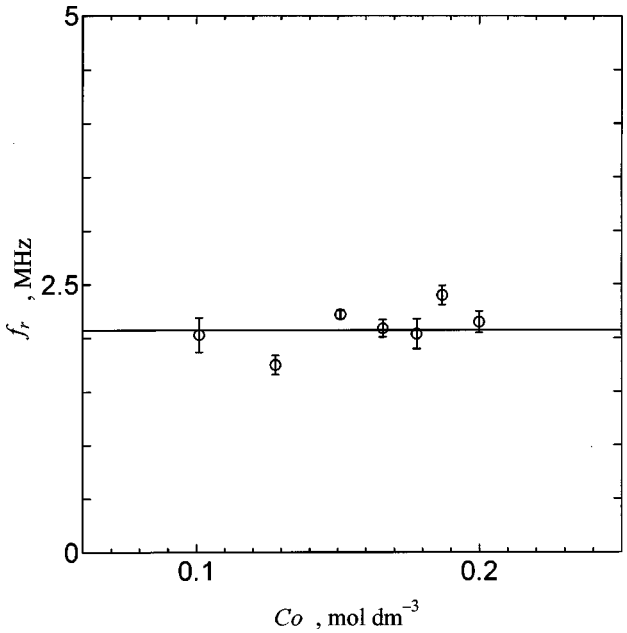

FIG. 3. The concentration dependence of the relaxation frequency for aqueous solution of L-histidine at 25 °C. The solid line going through the data points is only drawn to guide the eye, using the mean value of the obtained relaxation frequencies.

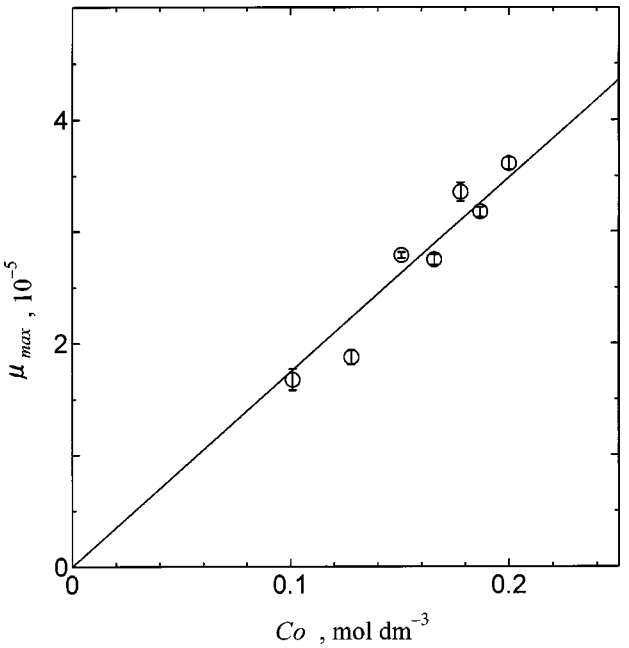

FIG. 4. The concentration dependence of the maximum absorption per wavelength for aqueous solution of L-histidine at 25 °C. The solid line is the calculated one by a linear least mean square method.

through the origin as is seen in Fig. 4. Logically, the plots of $\mu_{\max}/\rho\nu^2$ vs C_0 gave the straight line and the value of the slope allowed us to calculate the $(\Delta V)^2(K/(1+K)^2)$ value. This result is consistent with the speculation that the cause of the relaxation is due to the unimolecular reaction.

From the experimental facts that no relaxation is observed in the solutions of glycine, L-phenylalanine, L-tryptophan and imidazole at neutral pH's, and that the clear relaxation is evident only in the solution of L-histidine, we suggest that the characteristic relaxation in the solution arises from the specific molecular structure of L-histidine. One of the possibilities for the unimolecular reaction of L-histidine in aqueous media is a perturbation of the equilibrium associated with the rotational isomerization around α- and β-carbon in the L-histidine molecule.

To identify the stable conformations of L-histidine in aqueous solution, a molecular modeling computation was carried out with the molecular modeling software (MOPAC) to obtain the optimal structures and free energies. Prior to this calculation on L-histidine, the validity of the method was examined by calculating structures and energies of a number of esters in which the relaxation was attributed to the perturbation of an equilibrium between two planar isomers formed by rotation about the C–O bond.[15] The calculated free energy differences are compared with the experimental ones in Table II. Although both AM1–SMO and PM3–SMO methods give different values from the experimental ones, the trend of the free energy change is similar. Further, there also exist considerable errors in the experimental values and therefore the following estimation for L-histidine in aqueous medium is obviously a gross simplification. The two stable conformations estimated by MOPAC2000 are shown in Fig. 5. The AM1–SMO method gave the free energy difference of 0.9 kJ mol^{-1}and the PM3–SMO gave a value of 1.1 kJ mol^{-1}. We therefore accepted the mean value of the free energy changes given by the two methods. There were also conformations giving rise to the minimum free energy change in the two states. However, the free energy difference between the two states by AM1–SMO gave largely different values from that given by the PM3–SMO method. Using the relationship, $K=k_f/k_b=\exp(-\Delta G/RT)$ and Eq. (3), we estimated the forward and backward rate constants as $k_f=6\times10^6$ s^{-1} and $k_b=8\times10^6$ s^{-1}. Also, the equilibrium constant was substituted into Eq. (4) in order to obtain the stan-

TABLE II. The reference and calculated values of the free energy difference of carboxylic esters at room temperature for the reaction as

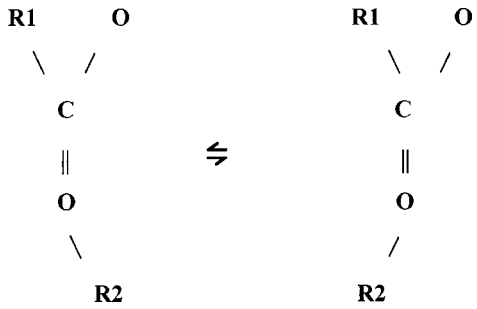

	R1	R2	Reference values[a]	Calculated values AM1 (kJ mol^{-1})	Calculated values PM3 (kJ mol^{-1})
Methyl formate	H	CH_3	0.46	11.86	4.88
Methyl acetate	CH_3	CH_3	18.00	10.25	6.59
Methyl propionate	CH_2CH_3	CH_3	19.02	12.98	11.44
Ethyl formate	H	CH_2CH_3	−0.39	12.29	4.37
Ethyl acetate	CH_3	CH_2CH_3	17.56	11.08	6.27
Ethyl propionate	CH_2CH_3	CH_2CH_3	22.25	14.68	13.87
Propyl formate	H	$CH_2CH_2CH_3$	14.08	11.80	4.82

[a]Reference 15.

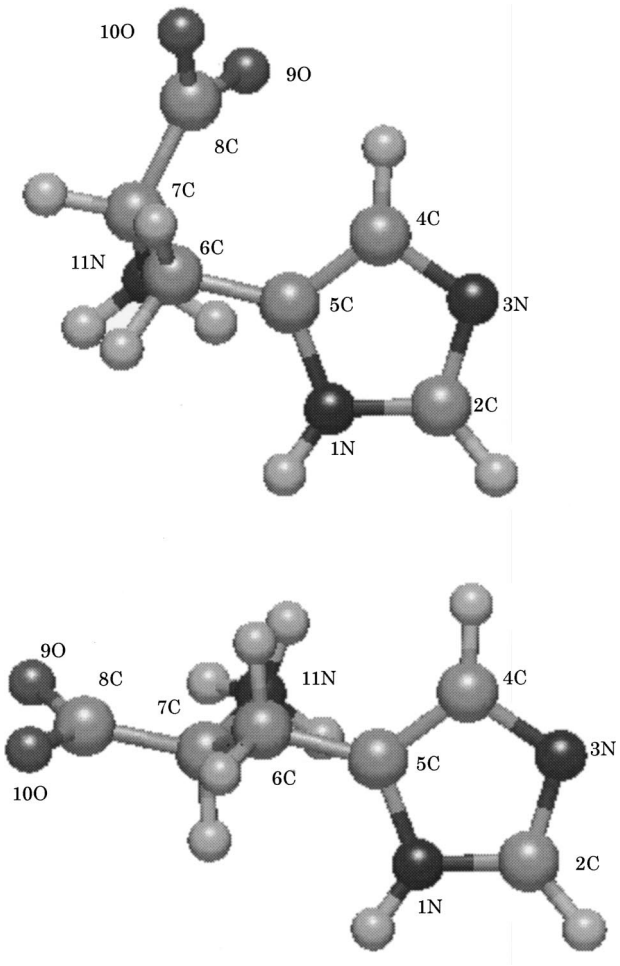

FIG. 5. The two stable conformations of L-histidine molecule calculated with semiempirical quantum chemical methods.

dard volume change of the reaction as 0.7×10^{-6} $m^3 mol^{-1}$. It is interesting to note that the ultrasonic relaxation is not observed in the aqueous solution of L-phenylalanine and L-tryptophan, but it is present in the solution of L-histidine. This may be because L-phenylalanine and L-tryptophan have more nonpolar hydrophobic groups than L-histidine and the hydrophobic hydrations around the hydrophobic groups may affect to decrease the rate of structural changes in molecules. Then, the L-histidine molecule might have higher flexibility in the aqueous solution than L-phenylalanine and L-tryptophan. The flexible L-histidine may result in the easier rotation around single bonds. Therefore, the rotational motion for L-phenylalanine and L-tryptophan would be predicted in a lower frequency range than that used in this study.

Another point which needs to be addressed is the possibility of the relaxation due to a proton-transfer reaction.[6] At neutral pH, most of the carboxylic and amino groups are ionized, hence the source of the relaxation cannot be associated with these groups. The relaxation due to the imidazole group is only observed above pH=9.5 and the position of the relaxation frequency is above 4 MHz.[7]

In conclusion, the ultrasonic relaxation observed in aqueous solution of L-histidine is specific only to this amino acid and the cause of the relaxation has been attributed to the isomerization reaction of the molecule. L-histidine molecules seem to have ability of the rapid rotational motion around single bonds in a hydrophilic environment. Given sufficient space in a protein active site, it may be also likely that rotation of the imidazole side chain can readily accommodate the needs of the surrounding protein. An interesting example of this is the different conformers found in serine and cysteine proteases, both of which have an essential L-histidine at their active centers in each case carrying out general acid-base functions.[16]

[1] K. Applegate, L. S. Slutsky, and R. C. Parker, "Kinetics of proton-transfer reactions of amino acids and simple polypeptides," J. Am. Chem. Soc. **90**, 6909–6913 (1968).
[2] H. Huang and S. Nishikawa, "Ultrasonic absorption spectra in aqueous solutions of alkylamines. Effect of isotopic solvents on kinetics of hydrolysis and aggregation reactions," J. Phys. Chem. **104**, 5910–5915 (2000), and references therein.
[3] S. Nishikawa, T. Fukahori, and K. Ishikawa, "Ultrasonic relaxations in aqueous solutions of propionic acid in the presence and absence of β-cyclodextrin," J. Phys. Chem. **106**, 3029–3033 (2002).
[4] A. K. Holmes and R. E. Challis, "Acoustic absorption due to proton transfer in solutions of proteins, peptides and amino acids at neutral pH," J. Acoust. Soc. Am. **100**, 1865–1877 (1998).
[5] F. W. Kremkau, "Biomolecular absorption of ultrasound. III. Solvent interactions," J. Acoust. Soc. Am. **83**, 2410–2415 (1988).
[6] L. J. Slutsky, L. Madsen, R. D. White, and J. Harkness, "Kinetics of the exchange of protons between hydrogen phosphate ions and a histidyl residue," J. Phys. Chem. **84**, 1325–1329 (1980).
[7] S. Nishikawa and M. Satoh, "Ultrasonic relaxation associated with proton transfer reaction in aqueous solutions of heterocyclic amines," J. Acoust. Soc. Am. **102**, 3779–3784 (1997).
[8] S. Nishikawa and K. Kotegawa, "Structure and kinetics in aqueous solution of butyl cellosolve from the temperature dependence of ultrasonic properties," J. Phys. Chem. **89**, 2896–2900 (1985).
[9] N. Kuramoto, M. Ueda, and S. Nishikawa, "Solvent effect on proton transfer reaction rate by ultrasonic absorption method," Bull. Chem. Soc. Jpn. **67**, 1560–1564 (1994).
[10] A. Labhardt and G. Schwarz, "A high resolution and low volume ultrasonic resonator method for fast chemical relaxation measurements," Ber. Bunsenges. Phys. Chem. **80**, 83–92 (1976).
[11] J. J. P. Stewart, MOPAC 2000, a molecular orbital package, Stewart Computational Chemistry, Colorado Springs, 2000.
[12] A. Klamt and G. Schumann, "COSMO: A new approach to dielectric screening in solvents with explicit expressions for the screening energy and its gradient," J. Chem. Soc., Perkin Trans. 2 **2**, 799 (1993).
[13] S. Nishikawa, M. Tanaka, and M. Mashima, "Structure and kinetics in aqueous solutions of ethers by ultrasonic methods," J. Phys. Chem. **85**, 686–689 (1981).
[14] R. Behrends, M. K. Cowman, F. Eggers, E. M. Eying, U. Kaatze, J. Majewski, S. Petrucci, K. Richmann, and M. Riech, "Ultrasonic relaxation and fast chemical kinetics of some carbohydrate aqueous solutions," J. Am. Chem. Soc. **119**, 2182–2186 (1997).
[15] E. Wyn-Jones and W. J. Orville-Thomas, "Molecular acoustic and spectroscopic studies. Part 1. Rotational isomerization in some halogenated hydrocarbons," Trans. Faraday Soc. **64**, 2907–2918 (1968).
[16] L. Abrahmsen, J. Tom, J. Burnier, K. A. Butcher, A. Kossiakoff, and J. A. Wells, "Engineering subtilisin and its substrates for efficient ligation of peptide bond in aqueous solution," Biochemistry **30**, 4151–4159 (1991).

Multiple scattering in a trabecular bone: Influence of the marrow viscosity on the effective properties

Francine Luppé,[a] Jean-Marc Conoir, and Hervé Franklin
Laboratoire d'Acoustique Ultrasonore et d'Electronique, UMR 6068, Université du Havre, Place R. Schuman, 76610 Le Havre, France

(Received 18 July 2002; revised 18 November 2002; accepted 30 October 2002)

The Foldy and the Waterman and Truell approximations are used to determine the effective properties of the coherent wave that emerges after multiple scattering of a plane longitudinal fast wave by the largest pores in a trabecular bone. The unit scattering cell considered is either a single pore or two close cylindrical pores (cluster), at a fixed overall bone porosity. In the cluster case, the effective attenuation is about twice that obtained with one single pore *per* scatterer. It is shown that taking into account the marrow viscosity leads only to minor differences on the effective dispersion and attenuation. © *2003 Acoustical Society of America.* [DOI: 10.1121/1.1554695]

PACS numbers: 43.80.Cs, 43.20.Jr [FD]

I. INTRODUCTION

Ultrasound is a useful tool in the diagnosis of osteoporosis. A few devices use the well-established correlation between the bone mineral density and the ultrasonic attenuation in cancellous bones such as the calcaneus[1] to infer bone status. The pertinent physical quantity is then the *normalized broadband attenuation* (nBUA) which is the slope, in dB/(cm MHz) of the measured attenuation in the 0.2–1 MHz frequency range. In a human marrow-saturated calcaneus, the nBUA values usually lay in the [5–20] dB/(cm MHz) range.[1] The other measured quantity is the ultrasound velocity through the bone, which is often (but not always) found to be decreasing as the frequency is increased.[1–3]

Numerous attempts have been made to explain the high nBUA values observed. Most of them are based on the modeling of the tabecular bone as a porous medium obeying the Biot model, with different dissipation effects added to the original theory.[4] On the other hand, a few attempts have been made to model it as a fluid in which single scattering, due to the solid trabeculae, would occur.[5,6] We have recently[7,8] proposed another standpoint. We consider the bone as a porous Biot medium, in which the largest pores, which size is actually the order of, or even greater than, the ultrasonic wavelengths,[7] would act as scatterers. Up to now, we used the Foldy–Twersky approximation to determine the effective complex wave number of the coherent wave that would be due to multiple scattering by those pores, in an otherwise nondissipative Biot medium, as we neglected the marrow viscosity.

The main default of our original work,[7] to our point of view, was to neglect the mode conversions that occur at each scattering process between the three waves which propagate in the Biot medium. In a later work,[8] we considered clusters composed of two close large pores, instead of only one. Mode conversions were then taken into account in the scattering amplitude of each cluster. In all cases, however, we used the same approximation, and neglected the marrow viscosity. As two questions are often asked, we study in this letter the marrow viscosity influence on the coherent wave properties, and compare the Foldy–Twersky approximation[9] to the Waterman and Truell one.[10]

Section II is devoted to the coherent wave properties obtained from the Foldy–Twersky approximation when the marrow viscosity is neglected. In Sec. III, the marrow viscosity is shown to be indeed negligible, as well as the Waterman and Truell correction to the Foldy–Twersky approximation.

II. COHERENT WAVE PROPERTIES WITH THE MARROW VISCOSITY NEGLECTED AND THE FOLDY–TWERSKY APPROXIMATION

The trabecular bone is considered as a porous, marrow saturated, Biot medium. The marrow viscosity is neglected, and no dissipation at all is taken into account: in such a medium, two homogeneous longitudinal waves may propagate, a fast one and a slow one, as well as a homogeneous transverse wave. The solid part (trabeculae) elastic properties and density are those of cortical bone, given in Ref. 11, along with the marrow density and elastic constant. The way we derived the porous dried medium properties is explained in Ref. 7. Let β_{Biot} be this nondissipative porous medium porosity. Dissipation is introduced by a multiple scattering process of a plane incident fast longitudinal wave by large marrow-filled pores, which are modeled as infinitely long cylinders, diameter 2 mm, whose axes are all perpendicular to the plane incident wave propagation direction, in such a way that they all are insonified at normal incidence. The actual porosity of the bone is then β, equal to the sum of β_{Biot} and of the ratio of the largest pores volume to the bone volume.

We suppose a harmonic time dependence $e^{-i\omega t}$, which will be omitted in the following. Let $\Phi(\alpha,\theta)$ be the displacement potential of the scattered fast longitudinal wave, when a fast longitudinal plane wave, propagating in the direction indicated by α, is incident on a single scatterer; θ is the observation direction. In that scatterer far field, $\Phi(\alpha,\theta)$ may be written as

[a]Author to whom correspondence should be addressed; electronic mail: luppe@iut.univ-lehavre.fr

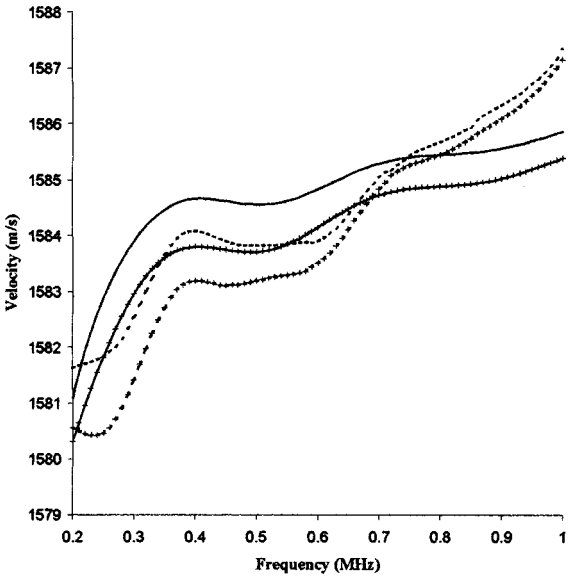

FIG. 1. Coherent fast wave velocity dispersion. Solid line: scatterer=one single cylinder, no marrow viscosity. Solid line with +: scatterer=one single cylinder, marrow viscosity taken into account. Dotted lines: scatterer =two close cylinders in the eclipse configuration, no marrow viscosity. Dotted line with +: scatterer=two close cylinders in the eclipse configuration, marrow viscosity taken into account.

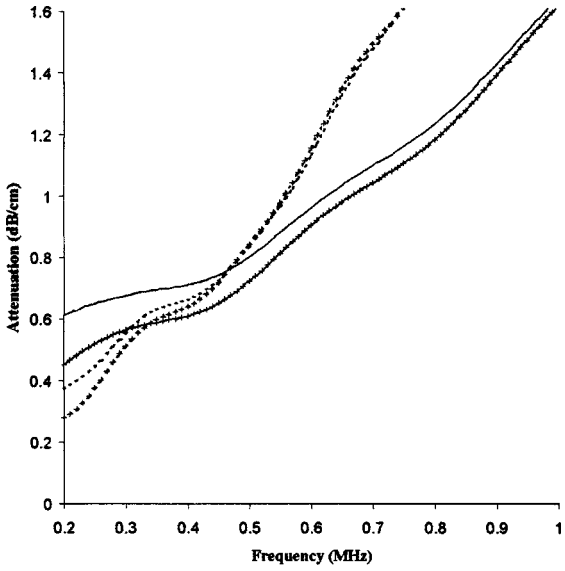

FIG. 2. Coherent fast wave attenuation versus frequency. Solid line: scatterer=one single cylinder, no marrow viscosity. Solid line with +: scatterer=one single cylinder, marrow viscosity taken into account. Dotted lines: scatterer=two close cylinders in the eclipse configuration, no marrow viscosity. Dotted line with +: scatterer=two close cylinders in the eclipse configuration, marrow viscosity taken into account.

$$\Phi(\alpha,\theta)=-\frac{i}{4}f(\alpha,\theta)\sqrt{\frac{2}{\pi k_1 r}}\exp\left[i\left(k_1 r-\frac{\pi}{4}\right)\right], \quad (1)$$

with (r,θ) the observation point polar coordinates, and k_1 the homogeneous fast wave real wave number.

Using the Foldy–Twersky approximation, as described in Ref. 9, the complex wave number K of the coherent fast wave that results from multiple scattering is

$$K=k_1\left(1-n\frac{f(\alpha,\alpha)}{2k_1^2}\right), \quad (2)$$

with n the density of scatterers.

The coherent wave effective velocity and attenuation are easily derived from relation (2), provided that the free field response of one single scatterer, to a plane incident wave, is known.

If one single marrow filled cylinder is considered as one scatterer, the forward scattered amplitude $f(\alpha,\alpha)$ in Eq. (2) is given by relation (36) in Ref. 7, and the corresponding coherent wave dispersion and attenuation are plotted as solid lines in Figs. 1 and 2. These curves have been plotted for an overall bone porosity β equal to 0.9 and a density n of cylinders equal to 40 000 m^{-2}. If one considers no scatterers at all ($\beta=\beta_{\text{Biot}}=0.9$), then the nondispersive fast wave velocity c_1 is 1680 m/s. Scattering, then, lowers the mean effective velocity. A linear fit of the attenuation solid curve in Fig. 2 provides a nBUA value equal to 1.28 dB/(cm MHz), with a determination coefficient $R^2\simeq 0.96$.

If one considers now clusters composed of two close cylinders, the fast scattered wave amplitude in the far field takes into account the mode conversions that take place at each interaction of a given type of wave (fast, slow, or transverse) with each cylinder. Let the two cylinders, be, respectively, centered at $O_1(d_1\cos\chi_1, d_1\sin\chi_1)$ and $O_2(d_2\cos\chi_2, d_2\sin\chi_2)$, as in Fig. 3. The $f(\alpha,\theta)$ function is then given by

$$f(\alpha,\theta)=4i\sum_{p=1}^{2}\sum_{m=-\infty}^{\infty} i^{-m}C_m^{(p)1}(\alpha)e^{-ik_1 d_p\cos(x_p-\theta)}e^{im\theta}. \quad (3)$$

The summation over m is theoretically infinite; in practice, however, it is performed from $m=-M$ to $m=+M$, with M depending on frequency. $C_m^{(p)1}(\alpha)$ is the amplitude of the mth fast mode, that is scattered by the pth cylinder. It is a component of vector $\mathbf{C^{(p)}}$, composed of the $2M+1$ $C_m^{(p)1}(\alpha)$ fast wave amplitudes, followed by the $2M+1$ $C_m^{(p)2}(\alpha)$ slow wave amplitudes and then by the $2M+1$ $C_m^{(p)t}(\alpha)$ shear wave amplitudes. The whole $\mathbf{C^{(p)}}$ vectors are obtained from the following:

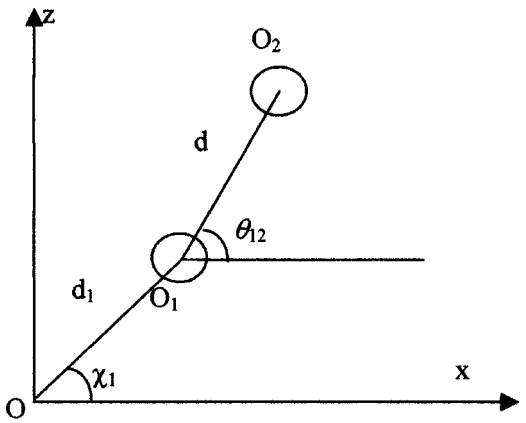

FIG. 3. One scatterer is composed of two close cylinders. The plane incident fast wave propagates in the Ox direction, so that $\theta_{12}=0$ corresponds to the eclipse configuration.

$$\mathbf{C^{(p)}}=[I-T^{(p)}M^{(pq)}T^{(q)}M^{(qp)}]^{-1}\times[\mathbf{A^{(p)}}+T^{(p)}M^{(pq)}\mathbf{A^{(q)}}],\quad p,q=1,2,\quad q\neq p, \tag{4}$$

with I the identity matrix.

$T^{(p)}$ is the block transition matrix of cylinder p composed as

$$T^{(p)}=\begin{pmatrix} T^{(p)11} & T^{(p)12} & T^{(p)1t} \\ T^{(p)21} & T^{(p)22} & T^{(p)2t} \\ T^{(p)t1} & T^{(p)t2} & T^{(p)tt} \end{pmatrix}, \tag{5}$$

with $T^{(p)jl}$ the diagonal matrix of the pth cylinder, defined by its diagonal elements:

$$T_n^{(p)jl}=\tfrac{1}{2}(s_n^{(p)jl}-\delta_{jl}),\quad j,l=1,2,t. \tag{6}$$

The $s_n^{(p)jl}$ that appear in relation (6) are the scattering matrix elements defined in Ref. 7. The $\mathbf{A^{(p)}}$ vector is defined by

$$\mathbf{A^{(p)}}=e^{i\mathbf{k_1}\cdot\mathbf{OO_p}}\begin{pmatrix} T^{(p)11}a(\boldsymbol{\alpha}) \\ T^{(p)21}a(\boldsymbol{\alpha}) \\ T^{(p)t1}a(\boldsymbol{\alpha}) \end{pmatrix}, \tag{7}$$

$$a(\boldsymbol{\alpha})=\begin{pmatrix} \cdot \\ \cdot \\ a_n=i^n e^{-in\alpha} \\ \cdot \\ \cdot \end{pmatrix},$$

with $\mathbf{k_1}$ the fast incident plane wave vector.

The $M^{(pq)}$ matrices are block matrices, that allow one, *via* the Graf addition theorem, to express the waves scattered by cylinder q as incident waves on cylinder p,

$$M^{(pq)}=\begin{pmatrix} M_1^{(pq)} & 0 & 0 \\ 0 & M_2^{(pq)} & 0 \\ 0 & 0 & M_t^{(pq)} \end{pmatrix}, \tag{8}$$

$$M_{jnm}^{(21)}=(-1)^{m-n}e^{-i(n-m)\theta_{12}}H_{n-m}^{(1)}(k_j d),$$
$$M_{jnm}^{(12)}=e^{-i(n-m)\theta_{12}}H_{n-m}^{(1)}(k_j d),\quad j=1,2,t. \tag{9}$$

In order to work at a fixed number of cylinders, the density of scatterers in relation (2) is now $n=20\,000\ \mathrm{m}^{-2}$, while the β_{Biot} porosity remains unchanged. The corresponding dispersion and attenuation curves are plotted in Figs. 1 and 2 with dotted lines. The distance d between the two cylinders is 2.1 a, with a the cylinders radius ($a=1$ mm). The θ_{12} angle, defined in Fig. 3, is 0°, so that the cylinders are in the eclipse configuration with respect to the plane incident wave, which propagates in the x direction ($\alpha=0$). Actually, the coherent wave attenuation is greater in this configuration than in all other configurations corresponding to nonzero θ_{12} values.[8] A linear fit of the attenuation gives a nBUA value equal to 2.74 dB/(cm MHz), with $R^2\simeq 0.97$. Taking into account the mode conversions, then, increases the effective attenuation.

III. THE MARROW VISCOSITY INFLUENCE ON THE COHERENT WAVE PROPERTIES

Taking into account the marrow viscosity in the Biot modeling of the bone, while neglecting it in the marrow-filled cylinders that are considered as scatterers leads to dispersion and attenuation curves that are plotted with + superimposed on either solid or dotted lines in Figs. 1 and 2. The solid lines (with +) correspond to the case of one cylinder *per* scatterer, and the dotted ones (with +) to the case of two cylinders *per* cluster. One can observe that taking into account the marrow viscosity lowers the effective propagation speed as well as the attenuation, at fixed frequency. The nBUA values, however, are slightly increased. In the one cylinder *per* scatterer assumption, indeed, it is found to be 1.42 dB/(cm MHz), with $R^2\simeq 0.97$, while it is 2.82 dB/(cm MHz), with $R^2\simeq 0.98$, in the two cylinders *per* cluster assumption.

The Foldy–Twersky approximation we used in relation (2) assumes the ratio of the forward to backwards scattered amplitude to be large, i.e., $=[f(\alpha,\alpha)/f(\alpha,\alpha+\pi)]\gg 1$, which is not the case in our frequency range (this ratio is only slightly greater than unity). This is the reason why we used the Waterman and Truell approximation,[10] which gives the corrected effective wave number in such cases:

$$\left(\frac{K}{k_1}\right)^2=\left(1-n\frac{f(\alpha,\alpha)}{2k_1^2}\right)^2-\left(n\frac{f(\alpha,\alpha+\pi)}{2k_1^2}\right)^2. \tag{10}$$

Relation (10), however, leads to non-noticeable changes in the dispersion and attenuation curves of Figs. 1 and 2.

IV. CONCLUSION

Wear's study[5] of backscatter from calcaneus shows that single scattering from the trabeculae may explain the quasi-cubic frequency dependence measured. Forward scattering by the trabeculae is also shown to be much lower than backward scattering, so that Wear concludes that multiple scattering by the trabeculae cannot explain the attenuation coefficient measured in the forward direction. He then suggests that "absorption is likely to be a larger component of attenuation than scattering." We do agree with him, as far as "scattering" means "scattering by the trabeculae." In that letter, absorption is taken into account in the Biot model as the marrow viscosity is introduced, but we show that multiple scattering by the largest pores induces a non-negligible attenuation. The nBUA values we obtain are still lower than those usually measured, and the effective fast wave velocity, although not increasing monotonically with frequency, is still globally increasing on the frequency range under study. This shows our model still needs improvement. This should be done by a better modeling of multiple scattering in a porous medium, as the approximations we used so far have been established in fluid media only, i.e., when only one type of wave may propagate. This work is in progress.

[1] P. Laugier, P. Drouin, A. M. Laval-Jeantet, and G. Berger, "*In vitro* assessment of the relationship between acoustic properties and bone mass density of the calcaneus by comparison of ultrasound parametric imaging

and quantitative computed tomography,'' Bone (N.Y.) **20**, 157–165 (1997).
[2] P. Droin, G. Berger, and P. Laugier, ''Velocity dispersion of acoustic waves in cancellous bone,'' IEEE Trans. Ultrason. Ferroelectr. Freq. Control **45**, 581–592 (1998).
[3] K. A. Wear, ''Measurements of phase velocity and group velocity in human calcaneus,'' Ultrasound Med. Biol. **26**, 641–646 (2000).
[4] T. J. Haire and C. M. Langton, ''Biot theory: A review of its application to ultrasound propagation through cancellous bone,'' Bone (N.Y.) **24**, 291–295 (1999).
[5] K. A. Wear, ''Frequency dependence of ultrasonic backscatterer from human trabecular bone: Theory and experiment,'' J. Acoust. Soc. Am. **106**, 3659–3664 (1999).
[6] F. Padilla and P. Laugier, ''Prediction of ultrasound attenuation in cancellous bones using poroelasticity and scattering theories,'' IEEE Ultrasonics Symposium, Piscataway, NJ, 2001, Proceedings (Cat. No. 01CH37263) IEEE; (2), 1754-1201-4 Vol. 2.
[7] F. Luppé, J. M. Conoir, and H. Franklin, ''Scattering by a fluid cylinder in a porous medium: Application to trabecular bone,'' J. Acoust. Soc. Am. **111**, 2573–2582 (2002).
[8] F. Luppé, J. M. Conoir, and H. Franklin, ''Scattering-induced attenuation of a fast longitudinal wave propagating in a trabecular bone modeled as a nondissipative porous medium,'' J. Acoust. Soc. Am. **110**, 2622(A) (2001).
[9] A. Ishimaru, *Wave Propagation and Scattering in Random Media* (Academic, New York, 1978).
[10] P. C. Waterman and R. Truell, ''Multiple scattering of waves,'' J. Math. Phys. **2**, 512–537 (1961).
[11] M. L. McKelvie and S. B. Palmer, ''The interaction of ultrasound with cancellous bone,'' Phys. Med. Biol. **36**, 1331–1340 (1991).

Modeling the frequency dependence (5–120 MHz) of ultrasound backscattering by red cell aggregates in shear flow at a normal hematocrit

Isabelle Fontaine[a] and Guy Cloutier[b]
Laboratory of Biorheology and Medical Ultrasonics, Research Center, University of Montreal Hospital, Notre-Dame Hospital, 2099 Alexandre de Sève (room Y-1619), Montréal, Québec H2L 2W5, Canada and Department of Radiology, Radio-Oncology and Nuclear Medicine, University of Montreal, C.P. 6128, Succ. Centre-ville, Montréal, Québec H3C 3J7, Canada

(Received 18 November 2002; accepted for publication 3 February 2003)

The frequency dependence of the ultrasound signal backscattered by blood in shear flow was studied using a simulation model. The ultrasound backscattered signal was computed with a linear model that considers the characteristics of the ultrasound system and tissue acoustic properties. The tissue scattering properties were related to the position and shape of the red blood cells (RBCs). A 2D microrheological model simulated the RBC dynamics in a Couette shear flow system. This iterative model, described earlier [Biophys. J. **82**, 1696–1710 (2002)], integrates the hydrodynamic effect of the flow, as well as adhesive and repulsive forces between RBCs. RBC aggregation was simulated at 40% hematocrit and shear rates of 0.05–2 s^{-1}. The RBC aggregate sizes ranged, on average, from 3.3 RBCs at 2 s^{-1} to 33.5 cells at 0.05 s^{-1}. The ultrasound backscattered power was studied at frequencies between 5–120 MHz and insonification angles between 0–180°. At frequencies below approximately 30 MHz, the ultrasound backscattered power increased as the shear rate was decreased and the size of the aggregates was raised. A totally different scattering behavior was noted above 30 MHz. Typical spectral slopes of the backscattered power (log–log scale) between 5–25 MHz equaled 3.8, whereas slopes down to 0.6 were measured at 0.05 s^{-1}, between 40–60 MHz. The ultrasound backscattered power was shown to be angle dependent at low frequencies (5–25 MHz). The anisotropy persisted at high frequencies (>25 MHz) for small aggregates (at 2 s^{-1}). In conclusion, this study sheds some light on the blood backscattering behavior with an emphasis on the non-Rayleigh regime. Additional experimental studies may be necessary to validate the simulation results, and to fully understand the relation between the ultrasound backscattered power, level of RBC aggregation, shear rate, frequency, and insonification angle. © *2003 Acoustical Society of America.* [DOI: 10.1121/1.1564606]

PACS numbers: 43.80.Cs, 43.80.Jz, 43.80.Qf [FD]

I. INTRODUCTION

The backscattering of an acoustic wave by a linear biological tissue is governed by the size of the tissue microstructure with respect to the acoustic wavelength, and by the acoustical impedance mismatches produced by the tissue inhomogeneities. Weakly scattering particles much smaller than the wavelength are referred to as Rayleigh scatterers. The power backscattered by randomly distributed Rayleigh scatterers is known to increase with the fourth power of the incident wave frequency. In contrast, scattering by reflectors of dimension much larger than the wavelength is generally frequency independent. Intermediate sizes of biological scatterers from various tissues were shown to be characterized by a wide range of frequency dependence (f^0 to $f^{4.5}$, approximately).[1–3] Even greater dependencies (up to f^6) were predicted for densely packed scatterers.[4] For small particles with respect to the wavelength, the deviation from the Rayleigh scattering theory (f^4) can be explained by the existence of organized patterns diminishing the randomness in the positioning of the biological scattering cells.

Within the last 25 years, several studies have aimed at elucidating the backscattering of ultrasound by blood. Rayleigh scattering was observed, between 3.5 and 12.5 MHz, for suspensions of nonaggregating red blood cells (RBCs washed and resuspended in a saline solution to eliminate the plasma proteins responsible for the aggregation).[5] The spectral slope of the backscattering coefficient for a suspension of nonaggregating bovine RBCs was 3.95, when corrected for attenuation (a slope of 4.0 was theoretically expected). In contrast, the frequency dependence of porcine whole blood at a low shear rate was lower in the same range of frequencies, presumably because of the presence of RBC aggregates[5] (shear rates below ≈1 s^{-1} promote the aggregation of RBCs, and RBC aggregates may still exist up to ≈50 s^{-1} and even higher shear rates under pathological conditions[6]).

At higher frequencies (22–37 MHz), a mean spectral slope around 1.0 (not corrected for the frequency-dependent attenuation) was measured for normal human whole blood flowing at a low shear rate.[7] At these frequencies, the spectral slope for suspensions of nonaggregating RBCs differed from the Rayleigh scattering theory (slope ≈3.0). Similar spectral slopes (1.3–1.4, attenuation compensated) to those found by Van der Heiden *et al.*[7] were reported, between

[a]Ms. Fontaine left the laboratory in 2001. She is now with ORTHOsoft, Inc., Montréal, Canada.
[b]Electronic mail: guy.cloutier@umontreal.ca

35–65 MHz, for normal human blood circulating in a flow phantom.[8] Foster *et al.*[9] measured an attenuation compensated spectral slope as low as 0.4, between 40–60 MHz, for normal human blood sheared in a Couette flow at 0.16 s^{-1}. In the above studies,[5,7–9] the hematocrit was in the normal physiological range (between 35%–45%). Hematocrit changes well beyond normal physiological values can affect the spectral slope of the backscattering coefficient.[5] Other factors such as the temperature, flow shearing condition, and plasma protein contents must be known if one attempts to systematically compare the spectral slope of the backscattering coefficient from blood.

Particles of the size of an RBC can be considered Rayleigh scatterers when insonified by a plane wave at frequencies below 30 MHz, approximately.[10] However, backscattering by blood cannot simply be described by considering independently distributed finite scatterers. Blood is characterized by a high number density of RBCs that are subjected to various levels of aggregation under flowing condition. As a consequence, this implies various structural arrangements of RBCs, and thus various patterns of acoustic interference between the different scattered echoes. According to recent models,[10–12] the frequency dependence of the backscattered signal from blood depends not only on the scatterers' size, but also on their spatial arrangement. Savéry and Cloutier[12] developed an analytical backscattering model based on the Neyman–Scott random point process, predicting the frequency dependence of aggregating particles at a low hematocrit (<5%). The purpose of the present study is to extend these results to a normal physiological hematocrit by considering the shearing effect of the flow on the RBC spatial organization.

II. METHODS

As performed earlier,[13] RBC aggregates can be viewed as large distinct scatterers containing numerous cells. However, a more effective way to model the backscattering properties is to consider individual RBCs, identical in shape, whose positions vary in space with the hematocrit and the level of aggregation. This approach was recently adopted to study the effect of the shear rate and anisotropy on ultrasound backscattering by aggregating RBCs at 10 MHz.[14] The backscattered signal was predicted by considering the ultrasonic transducer properties, the backscattering cross section of a single cell, and the spatial arrangement of RBCs.

The simulation model used in the present study is described in detail elsewhere.[14] In summary, the radio-frequency (rf) signal backscattered by blood was modeled in two dimensions by the following equation:

$$\mathrm{rf}(x,y)=\frac{\partial^2}{\partial y^2}T(x,y)\otimes C(x,y)\otimes N(x,y), \tag{1}$$

where y is the direction of propagation of the ultrasonic waves perpendicular to the flow direction x, $T(x,y)$ is the ultrasound system transfer function, $C(x,y)$ represents the spatial inhomogeneity due to a single RBC, and $N(x,y)$ is the microscopic density function describing the RBC positioning. The transducer transfer function (T) was modeled as

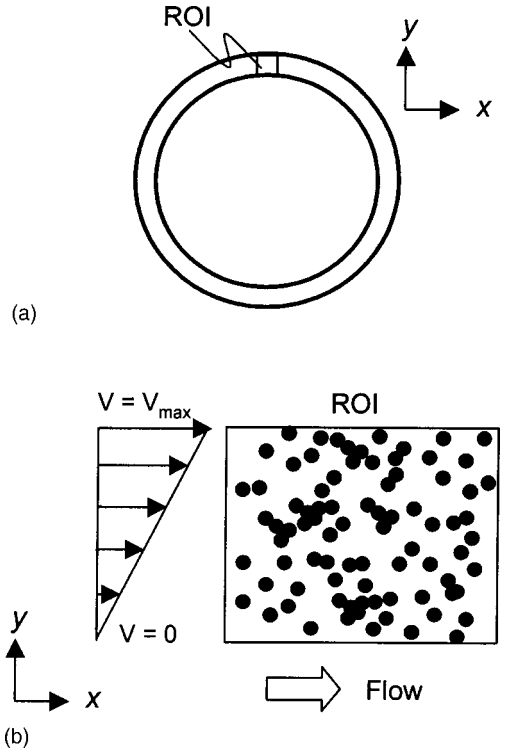

FIG. 1. (a) Top view of the two coaxial cylinders composing the Couette flow system. The region of interest (ROI) is located in the small gap between the two cylinders. The x axis refers to the direction of the flow parallel to the cylinders, and the y axis refers to the radial direction between the cylinders. (b) Magnification of the ROI and illustration of the velocity profile, assuming a constant shear rate in the ROI.

a Gaussian envelope modulated by a cosine function

$$T(x,y)=\exp\left[\frac{-1}{2}\left(\frac{x^2}{\psi_x^2}+\frac{y^2}{\psi_y^2}\right)\right]\cos\left(\frac{4\pi f y}{c}\right), \tag{2}$$

where ψ_x and ψ_y are the standard deviations of the 2D Gaussian function representing the beamwidth and the bandwidth of the transmitted waves. They were kept constant to $\psi_x=0.43$ mm and $\psi_y=0.03$ mm for all frequencies studied. The selected value of ψ_y corresponds to a bandwidth of approximately 10 MHz at -3 dB. The parameter f in Eq. (2) is the ultrasonic frequency and c is the speed of sound in blood (1570 m/s).

The function C in Eq. (1) was defined as the 2D projection of a 5.5-μm-diameter sphere [Eq. (11) of Fontaine *et al.*[14]]. The function N was obtained from 2D dynamical simulations of the RBC aggregation process in a shear flow.[14] It consists of an iterative microrheological model that considers the effect of the adhesive and repulsive forces between RBCs, and the hydrodynamic effect of the flow shear rate on the positioning of the cells. The motion of the particles resulting from the flow was between two coaxial cylinders (Couette flow—see Fig. 1), where the shear rate is maintained constant for a given relative rotational speed of one of the two cylinders. Shear rates varying between 0.05 and 2 s^{-1} were modeled. Different levels of aggregation were obtained by modifying the balance of forces acting on RBCs under physiological conditions (adhesion due to adsorption or depletion of plasma macromolecules between neighboring RBCs, repulsion due to steric and electrostatic

TABLE I. Effect of the shear rate on the mean numbers of RBCs per aggregate, and on the slopes of the frequency dependence of the ultrasound backscattered power between 5–25 MHz and 40–60 MHz (means±s.d., $n=8$). The spectral slopes were obtained for an insonification angle of 90° with respect to the flow.

Shear rate (s^{-1})	Number of RBCs per aggregate	Spectral slope (5–25 MHz)	Spectral slope (40–60 MHz)
0.05	33.5±2.4 [a]	3.3±0.3	0.6±1.1 [a]
0.1	23.0±2.2 [a]	3.3±0.2	0.9±1.0 [a]
0.3	11.9±0.2 [a]	3.4±0.1	3.4±1.0
2	3.3±0.1 [a]	3.1±0.2	3.6±0.7

[a] $p<0.001$.

forces, and the effect of the flow). In the present study, the simulated conditions are limited to the intermediate level of aggregation described by Fontaine *et al.*[14] All simulations were performed in an area of 300 by 300 μm at a hematocrit of 40%, which gives approximately 1500 particles in the region of interest (ROI). At each time step considered, the vector displacements resulting from each force (adhesion, repulsion, and flow) were summed for every RBC included between the two coaxial cylinders. Once the displacements were computed for all particles, they were moved for the next iteration. Starting with randomly positioned nonaggregated particles at the first iteration, the process was continued until the size of the aggregates reached a steady state (stable aggregate size—see Fig. 5 of Fontaine *et al.*[14]).

The backscattered power was computed from the 2D spectrum of the rf images obtained by Eq. (1). The spectrum of the rf image was evaluated from the central portion (256 by 256 μm) of the simulated ROI to avoid errors from the edges (the boundaries could promote the formation of artifactual aggregate structures). The backscattered power (POW) was determined for the steady state of aggregation by

$$\mathrm{POW}=\frac{1}{M_S}\sum_{f_x}\sum_{f_y}\left|\Im\left(\frac{\partial^2}{\partial y^2}T\right)\ \Im(C)\Im(N)\right|^2, \tag{3}$$

where M_S is the number of samples in the frequency domain (f_x,f_y). For a given simulation, the spectra of five functions N (i.e. $\Im(N)$), taken at the steady state of aggregation, were averaged to reduce the statistical variance. Then, the backscattered power obtained from Eq. (3) was computed and averaged over eight simulations performed under the same conditions. The initial random positioning of nonaggregated and nonoverlapped RBCs was changed between simulations, thus resulting in different aggregate structures.

TABLE II. Effect of the insonification angle, for a shear rate of 0.05 s^{-1}, on the slopes of the frequency dependence of the ultrasound backscattered power between 5–25 MHz and 40–60 MHz (means±s.d., $n=8$).

Angle (degrees)	Spectral slope (5–25 MHz)	Spectral slope (40–60 MHz)
0	2.6±0.2 [a]	1.2±0.4
45	[b] 2.7±0.4	1.6±0.7
90	3.3±0.3 [b]	0.6±1.1
135	2.7±0.2	1.3±0.4

[a] $p<0.001$.
[b] $p=0.002$.

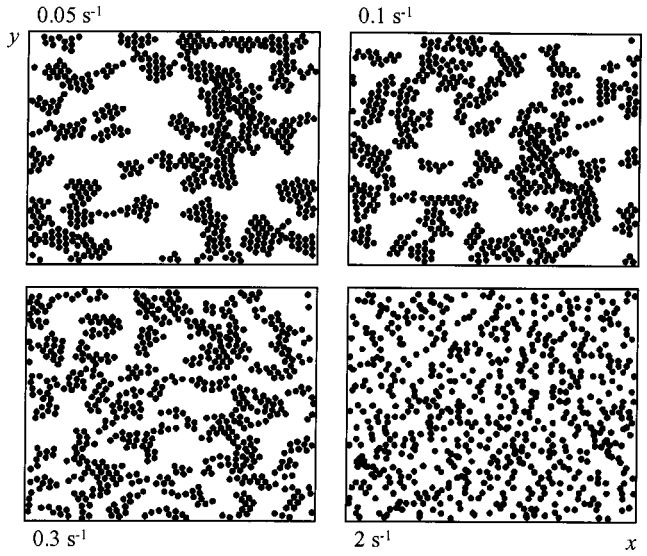

FIG. 2. Simulation results of RBC aggregation at 40% hematocrit for shear rates of 0.05, 0.1, 0.3, and 2 s^{-1}. The simulated areas are 300 by 300 μm, and the zoomed areas represent a dimension of 200 by 200 μm. Each panel was obtained at the steady state of aggregation of the iterative microrheological model. The x and y coordinates correspond to the direction of the flow and of the radial direction between the cylinders of the Couette flow system, respectively.

To allow the study of the anisotropy of the backscattered power, the rf signal was modeled at various angles of insonification by doing a rotation of the transducer transfer function. As performed earlier,[13,14] the $x-y$ plane was mapped onto the $p-q$ plane. The function characterizing the transducer was computed on the rotated axes. The following equations were used to transform the $x-y$ plane onto the $p-q$ plane:

$$\begin{bmatrix}p\\q\end{bmatrix}=\begin{pmatrix}\sin\theta & \cos\theta\\ -\cos\theta & \sin\theta\end{pmatrix}\begin{bmatrix}x\\y\end{bmatrix}, \tag{4}$$

where θ represents the angle of rotation of the axes. Thus, 0° and 90° correspond, respectively, to a direction of insonification parallel and perpendicular to the flow x.

A. Statistical analyses

All results were expressed as means±standard deviations (s.d.). One-way analyses of variance with Bonferroni's method for multiple comparisons were used to assess the differences in the mean aggregate sizes and spectral slopes listed in Tables I and II (SIGMASTAT statistical software, version 2.0, SPSS Science, Chicago, IL). A significance level of 0.05 was considered in all analyses.

III. RESULTS

A key feature of the current model is the possibility to simulate various RBC aggregate structures and the corresponding ultrasound backscattered signal in response to the shear rate intensity. Figure 2 shows examples of RBC spatial arrangements obtained at the steady state of aggregation (after more than 15 000 iterations), for shear rates of 0.05, 0.1, 0.3, and 2 s^{-1} and a hematocrit of 40%. As expected, the fraction of aggregated RBCs and the size of the aggregates increased as the shear rate was decreased. At low shear rates

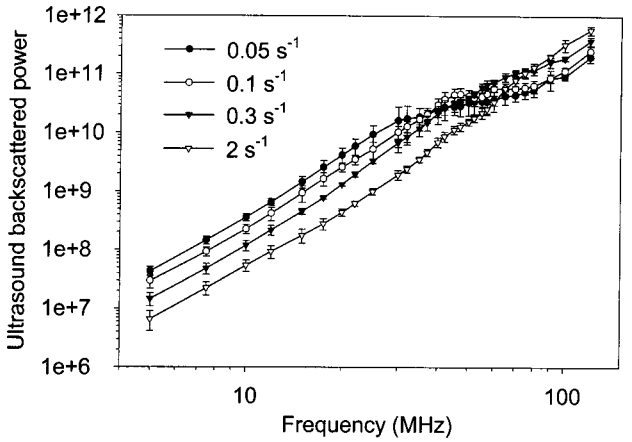

FIG. 3. Frequency dependence of the ultrasound backscattered power (relative units, means±s.d., $n=8$) at an insonification angle of 90° with respect to the flow, for shear rates of 0.05, 0.1, 0.3, and 2 s^{-1}.

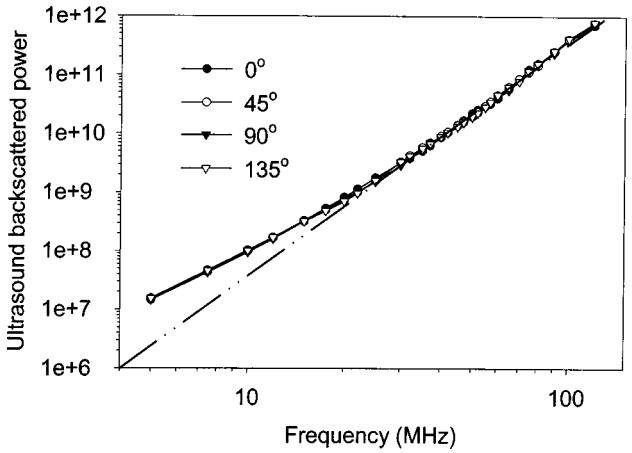

FIG. 4. Frequency dependence of the ultrasound backscattered power (relative units) for the initial random positioning of nonaggregated and nonoverlapped RBCs, at different insonification angles with respect to the flow. The dash-dotted line represents the theoretical fourth-power frequency relationship of Rayleigh scattering.

(e.g., 0.05 and 0.1 s^{-1}), clump types of aggregates were obtained with the model. The compactness of the aggregates increased as the shear rate was decreased. Rouleaux of a few RBCs were more often observed at higher shear rates (e.g., 2 s^{-1}).

The frequency dependencies of the ultrasound backscattered power at an insonification angle of 90° with respect to the flow are presented in Fig. 3, for shear rates of 0.05, 0.1, 0.3, and 2 s^{-1}. At frequencies below approximately 30 MHz, the ultrasound backscattered power increased as the shear rate was decreased and the level of aggregation was raised. The mean increase of the backscattered power between shear rates of 0.05 and 2 s^{-1} was 9.1±1.2 dB. The mean numbers of RBCs per aggregate at these shear rates were 33.5 (0.05 s^{-1}), 23.0 (0.1 s^{-1}), 11.9 (0.3 s^{-1}), and 3.3 (2 s^{-1}) (see Table I, $p<0.001$). As also seen in Table I, the slopes on a log–log scale of the frequency dependence of the backscattered power, between 5–25 MHz, were independent of the shear rate (mean values around 3.3, $p=0.06$).

Above 30 MHz, a totally different scattering behavior was observed in Fig. 3. The backscattered power was no longer positively correlated with the mean size of the aggregates, or inversely with the shear rate. For instance, at a given shear rate, changes in the slope of the backscattered power as a function of frequency were noted. As emphasized in Table I, the slope at 0.05 s^{-1} was 3.3 between 5–25 MHz, and decreased to 0.6 between 40–60 MHz. At higher shear rates between 40–60 MHz, the slope increased from 0.9 at 0.1 s^{-1} to 3.6 at 2 s^{-1} ($p<0.001$). Because the change in the slope was more pronounced at 0.05 s^{-1} than at other shear rates, the backscattered power was lower at 0.05 s^{-1} than at 0.1 s^{-1} above 37 MHz, was lower at 0.05 s^{-1} than at 0.3 s^{-1} above 45 MHz, and was lower at 0.05 s^{-1} than at 2 s^{-1} above 65 MHz (see Fig. 3). The frequency at which the transition in the slope occurred increased as a function of the shear rate.

According to the Rayleigh scattering theory for particles much smaller than the acoustic wavelength (particle, continuum, or hybrid modeling approaches), the backscattering properties are independent of the insonification angle.[15] To verify the validity of the current model, in terms of angular independencies for a scatter's diameter of 5.5 μm and a cell concentration of 40%, the backscattered power was estimated from the initial random positioning of nonaggregated and nonoverlapped RBCs (before the first iteration of the microrheological dynamical model of RBC aggregation). The spectra of the function N in Eq. (3) were averaged over 50 independent RBC realizations performed over the simulated area of 300 by 300 μm, and the backscattered power was then computed for each frequency considered. As shown in Fig. 4, the insonification angle had no effect on the ultrasound backscattered power. However, the spectral slope of the backscattered signal differed, in the lower frequency range, from the fourth-power frequency dependence predicted by the Rayleigh scattering theory. The reasons for this discrepancy are postulated in Sec. IV.

The possible influence of the insonification angle on the ultrasound signal backscattered by aggregating RBCs was also investigated over the range of frequencies considered (see Fig. 5, shear rate=0.05 s^{-1}). It can be recalled that an angle of 0° refers to a direction of propagation of the ultrasound beam parallel to the flow, whereas 90° corresponds to

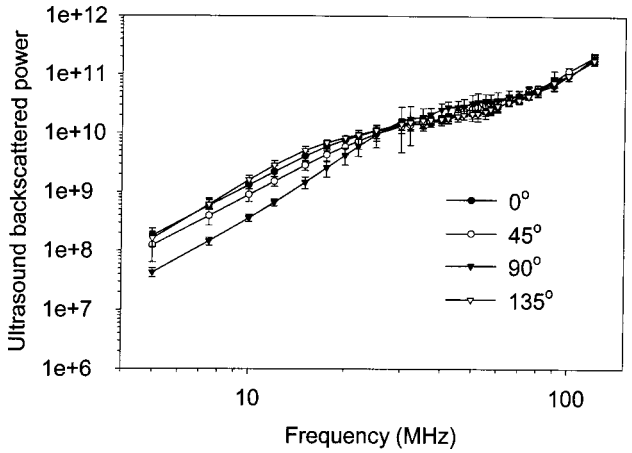

FIG. 5. Frequency dependence of the ultrasound backscattered power (relative units, means±s.d., $n=8$) for a shear rate of 0.05 s^{-1}, at different insonification angles with respect to the flow.

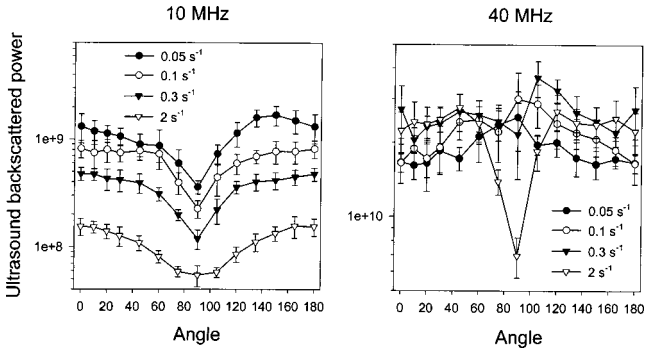

FIG. 6. Changes in the ultrasound backscattered power (relative units, means ± s.d., $n=8$) as a function of the insonification angle, for shear rates of 0.05, 0.1, 0.3, and 2 s^{-1}, and mean frequencies of 10 and 40 MHz.

a perpendicular orientation. Significant variations of the backscattered power as a function of the insonification angle were noted at frequencies between 5–20 MHz, approximately. At 90°, the backscattered power was consistently lower than the values observed at the other angles. The strongest backscattering was noted at 0° and 135°. The maximum difference in the mean backscattered power as a function of the insonification angle was 6.5 dB (at 10 MHz). Between 25–120 MHz, the ultrasound backscattered power was angle independent for that low shear rate of 0.05 s^{-1}. Table II shows the effect of the insonification angle on the spectral slopes at the same shear rate value of 0.05 s^{-1}. Statistically significant differences ($p<0.005$) were observed between 5–25 MHz. At higher frequencies (40–60 MHz), the spectral slopes were similar on average ($p=0.06$).

Figure 6 is presented to further emphasize the relationship between the ultrasound backscattered power, insonification angle, shear rate (aggregation level), and frequency. At 10 MHz, the anisotropy (angular dependence) of the ultrasound backscattered power was relatively similar as a function of the shear rate. The range of variation of the mean backscattered power as a function of the angle was 6.7 dB at 0.05 s^{-1}, 5.6 dB at 0.1 s^{-1}, 6.0 dB at 0.3 s^{-1}, and 4.6 dB at 2 s^{-1}. For each shear rate, the minimum backscattering was found at an angle of 90°. With the exception of the shear rate at 2 s^{-1}, the anisotropic behavior of the backscattered power was more erratic at 40 MHz. As for the observation made at 10 MHz, the anisotropic behavior at 2 s^{-1} was characterized by a minimum of the backscattered power at 90°, and a range of variation of 6.0 dB. For the other shear rates and a frequency of 40 MHz, the angular variations were below 2.6 dB.

IV. DISCUSSION

A common belief, based on experimental observations and the Rayleigh scattering theory, is to consider that an increase in the level of RBC aggregation results in a raise of the ultrasound backscattered signal strength.[16] The simulation results presented in Fig. 3, at frequencies below 30 MHz, are consistent with this postulation because the backscattered power is shown to increase with a reduction of the shear rate and an increase in the size of the aggregates (see Table I). According to the Rayleigh scattering theory, a linear increase in the backscattering coefficient (a measure proportional to the backscattered power) as a function of the scatterers' volume is expected, for a constant hematocrit and a spatial organization not affected by the scatterers' size.[1,10] According to Table I and Fig. 3, the simulation results seemed to deviate slightly from this prediction. As listed in Table I, the mean volume of RBC aggregates increased by a factor of 10.2 between shear rates of 2 and 0.05 s^{-1}. For the same shear rate changes, the backscattered power at 90° increased, on average, by a factor of only 8.1 (9.1 dB) below 30 MHz. Although this difference may be attributed to the variance of the simulated results, the fact that RBC aggregation influences the structure factor, a main determinant of the ultrasound backscattering properties, may also be a reasonable explanation. It can be recalled that the structure factor reflects the spatial organization (pair correlation) of scatterers in the frequency domain.[12,14,17] The spatial arrangement of RBCs due to aggregation had an influence on the backscattered power at frequencies below 30 MHz, but as seen in Fig. 3, the impact of the structure factor was more dominant at frequencies between 30–120 MHz (non-Rayleigh regime), as reflected by the changes in spectral slopes.

A. Effect of the insonification angle

Another common belief is to consider the backscattering from blood (with or without RBC aggregates) possibly angle dependent only in the non-Rayleigh regime.[18,19] It may be worth mentioning that although judged negligible by the authors, Kuo and Shung[19] predicted slight differences in magnitude of the backscattering cross section (backscattering from a single particle) between sphere, disk, and biconcave disk having the size of a RBC below 30 MHz, by using the T-matrix method. In the current study, the anisotropy of the backscattered power at frequencies below 25 MHz (expected Rayleigh regime) and a shear rate of 0.05 s^{-1} was not negligible and reached values up to 6.5 dB (see Fig. 5). As shown in Fig. 6, the shear rate did not seem to affect the anisotropy at low frequencies. Surprisingly, at a first glance, the anisotropy disappeared in the non-Rayleigh regime (frequencies above 25 MHz) for shear rates promoting the formation of large RBC aggregates. This may be explained by the structure of RBC aggregates simulated in Couette flow, which had more the form of clusters than oriented rouleaux at low shear rates (see Fig. 2). Another observation that can be made from Figs. 5 and 6 is the maximum backscattering, at low frequencies, that generally occurred at angles close to 0° or 180°. This would suggest that the privileged macroscopic orientation of the blood structure was close to parallel with the ultrasound beam in these simulations. In summary, to fully understand the relationship between the ultrasound backscattered power, insonification angle, and frequency, one needs to refer to the frequency dependence of the structure factor, as performed by Fontaine *et al.*[14] Additional experimental validations would be necessary to better understand the anisotropic behavior of the backscattered power from blood as a function of the frequency. To our knowledge, the only experimental results available were performed at 10 MHz.[18]

B. Deviation from the fourth-power frequency dependence under Rayleigh scattering

As observed in Fig. 4, the frequency dependence of the backscattered power from nonaggregated and nonoverlapped RBCs, at a hematocrit of 40%, differed from the fourth-power relationship in the lower frequency range. This is clearly an artifact of the simulation model related to the filtering induced by the frequency response of the point spread function [Eq. (2)]. In theory, the incident wave should be plane and monochromatic (Dirac impulse in the frequency domain) to validate the definition of the backscattering coefficient.[1] In the current study, ψ_y in Eq. (2) was kept constant to 0.03 mm whatever the frequency studied. This resulted in a bandwidth of the point spread function, at -3 dB, of 10 MHz (or relative bandwidths varying between 200% to 8.3% between 5–120 MHz). There were three main reasons to select a bandwidth of 10 MHz. It first allowed the transmitted power to remain constant whatever the frequency selected. Second, the constant value of $\psi_y = 0.03$ mm allowed us to constrain the size of the point spread function entirely within the ROI. But, more importantly, this bandwidth was selected to reduce the variance of the backscattered power computation as a function of the frequency. For instance, averaging was performed by computing, with Eq. (3), the backscattered power over f_y frequency samples. A smaller bandwidth would have required several additional realizations of the function N (the positioning of RBCs, as illustrated in Fig. 2) to obtain acceptable standard deviations. The obtaining of the functions N used to compute the backscattered power with Eq. (3) could necessitate several days (on a Pentium III computer) because up to 30 000 iterations could be required to obtain the steady state of aggregation with the microrheological model.

To estimate the bias induced in the low-frequency range (5–25 MHz) with the current model, additional simulations were performed by using a single RBC in the middle of the ROI. For such simulations, a fourth-power frequency dependence should be obtained. We did not evaluate the bias of the spectral slopes from the results of Fig. 4 because the random positioning of a large number of nonoverlapped and nonaggregated scatters is constrained by the exclusion volume effect (in theory, the spectral slope for such cases could be higher than 4.0[20,21]). By performing the simulations over individual RBCs with the current definition of the point spread function, the mean spectral slope had a value of 3.5 instead of 4.0 between 5–25 MHz (the slope was 4.0 between 40–60 MHz). Table III presents the corrected values of the spectral slopes as a function of the shear rate. To do so, a value of 0.5 was added to the results of Table I between 5–25 MHz. As seen in Table III, values closer to 4.0 were obtained in the low-frequency range. Thus, for the simulated conditions of RBC aggregation, close to Rayleigh scattering was obtained between 5–25 MHz, whatever the shear rate ($p = 0.06$). The corrections performed in Table III can also be applied to modify the results of Table II (new table not shown). In the low-frequency range, the corrected mean values of the spectral slopes would thus vary between 3.1 and 3.8 as a function of the insonification angle.

TABLE III. Spectral slopes between 5–25 MHz and 40–60 MHz (means $\pm$s.d., $n = 8$), corrected for the bias induced by the broadband frequency response of the transducer, as a function of the shear rate (a value of 0.5 was added to the results of Table I between 5–25 MHz). The spectral slopes were obtained for an insonification angle of 90° with respect to the flow. Note that the same corrections could be performed with Table II (results not shown).

Shear rate (s^{-1})	Spectral slope (5–25 MHz)	Spectral slope (40–60 MHz)
0.05	3.8 ± 0.3	0.6 ± 1.1
0.1	3.8 ± 0.2	0.9 ± 1.0
0.3	3.9 ± 0.1	3.4 ± 1.0
2	3.6 ± 0.2	3.6 ± 0.7

C. Effect of RBC aggregation on the spectral slopes

Experimentally, Rayleigh scattering was observed for nonaggregating RBCs at frequencies below 30 MHz (hematocrits = 6%–44%, attenuation-compensated backscattering coefficient).[5,19] In the presence of RBC aggregation for frequencies slightly above 10 MHz, spectral slopes below 4.0 were found.[5] According to Table III, spectral slopes between 3.6–3.9 were obtained between 5–25 MHz, whatever the shear rate. In the experimental study of Yuan and Shung,[5] the fibrinogen concentration was changed to promote the formation of RBC aggregates in tube flow. The current simulations are in agreement with the experimental results reported by others,[5] although the type of flow (tube versus Couette flow) and the geometry of the scattering ROI (3D versus 2D for the current simulations) differed between both studies. At frequencies between approximately 40–60 MHz, attenuation-compensated spectral slopes varying between 0.4–1.4 were measured experimentally at low shear rates for normal human blood.[8,9] To our knowledge, these results on whole-blood backscattering are the only ones available in the literature in this range of frequency. Although they may be erroneous because they were obtained with focused wideband transducers (by definition, a monochromatic plane wave should be used to measure the backscattering coefficient in steradian-cm^{-1}), it may be worth mentioning that these slopes between 0.4–1.4 are within the range of values reported in Table III for shear rates of 0.1 and 0.05 s^{-1}.

D. Comparison to other modeling strategies

Models were proposed to predict the frequency dependence of ultrasound backscattering from the microstructure of soft biological tissues.[1,4,22,23] The different modeling strategies adopted in these studies are difficult to apply to a complex medium such as blood, because angulated fibers, aligned scatterers regularly spaced, independently distributed particles, isotropic media, or dilute systems of particles are poor descriptors of aggregated packed RBCs. The modeling of blood scattering is quite complex due to the high density of scatterers, the phenomenon of RBC aggregation, and the flow dependency of the scatterers' position. To our knowledge, very few studies addressed the issue of modeling blood scattering as a function of the frequency.

In 1999, the acoustic framework of the current model was proposed to study ultrasound backscattering from non-aggregated RBCs at hematocrits of 0%–100%, and frequencies of 2–500 MHz.[10] The effect of both the scatterers' shape and positioning on the backscattered power was studied in 3D. The mathematical relationship between the positioning of RBCs (function N) and the structure factor was given in that study. Because the ROI was infinite, a narrow-band signal could be used ($\psi_y = 0.21$ mm, bandwidth≈ 0.7 MHz) and the filtering artifact produced by the frequency response of the transducer was limited. In Savéry and Cloutier,[24] the backscattering coefficient (monochromatic plane wave) was determined analytically for 3D diluted suspensions of RBC aggregates modeled as Gaussian-shaped inhomogeneities being either isotropic or anisotropic. The non-Rayleigh changes in the spectral slope were observed as the frequency or scatterers' size were increased. Recently, a totally different modeling strategy was adopted by the same authors to consider the positioning of RBCs forming aggregates.[12] Instead of using aligned Gaussian-shaped particles,[24] the Neyman–Scott point process was proposed to simulate RBC clustering in 3D. A monochromatic plane wave was considered in that study, but a limitation was the validity of the model at only a low hematocrit ($<5\%$), as the exclusion volume effect was not taken into account. Very interestingly, the changes in the spectral slope found in the current study, as a function of the level of RBC aggregation, were also noticed in the previous 3D model at 5% hematocrit.[12] This suggests that the current 2D model may adequately describe the frequency dependence of ultrasound backscattering by blood. However, we are aware that the current model would have to be developed in 3D to satisfactorily describe the backscattering behavior as a function of the hematocrit.

V. CONCLUSION

By using a microrheological iterative model previously developed,[14] various structures of RBC aggregates at a physiological hematocrit of 40% were obtained by varying the flow shear rate between Couette cylinders. Simulations were performed over a wide range of frequencies (5–120 MHz) for shear rates varying between 0.05 and 2 s^{-1}. The main prediction of the model is that the growing of RBC aggregates at low shear rates causes an increase in the backscattered power at low frequencies (<30 MHz), and a diminution of the spectral slope (backscattered power versus frequency on a log–log scale) at frequencies between 30–90 MHz, approximately. Additional studies may be required to fully understand the backscattering behavior above 120 MHz. Another observation of the model is the important angular dependencies of the backscattered power at frequencies between 5–25 MHz. At higher frequencies, anisotropy of the backscattered power may still exist depending on the shear rate (level of RBC aggregation and spatial organization of RBCs). Consequently, it can be concluded that a scalar index, such as the mean size of the scatterers, may not fully characterize the phenomenon of RBC aggregation. The anisotropic behavior of the backscattered power and spectral slope may be other parameters to consider.

According to the results of the present study, the following question can be raised. For a given insonification angle, does the combination of measurements performed at low and high frequencies bring more information to the characterization of RBC aggregation? It appears, from the results, that the variations in backscattered power, spectral slope, and anisotropy convey complementary information. Dual frequency characterization was proposed before to characterize other types of biological tissue. The detection of malignant liver tumors, kidney microstructures, and vascular emboli are some examples.[4,25,26] The use of dual frequency may be a direction to proceed in the future.

ACKNOWLEDGMENTS

This work was supported by operating grants from the Institutes of Health Research of Canada (No. MOP-36467) and the Heart and Stroke Foundation of Quebec, and by a research scholarship from the Fonds de la Recherche en Santé du Québec. The authors would like to acknowledge Mr. David Savéry for reviewing the manuscript.

[1] K. K. Shung and G. A. Thieme, *Ultrasonic Scattering in Biological Tissues*, 1st ed. (CRC Press, Boca Raton, 1993).
[2] F. S. Foster, C. J. Pavlin, K. A. Harasiewicz, D. A. Christopher, and D. H. Turnbull, "Advances in ultrasound biomicroscopy," Ultrasound Med. Biol. **26**(1), 1–27 (2000).
[3] E. L. Madsen, F. Dong, G. R. Frank, B. S. Garra, K. A. Wear, T. Wilson, J. A. Zagzebski, H. L. Miller, K. K. Shung, S. H. Wang, E. J. Feleppa, T. Liu, W. D. O'Brien, Jr., K. A. Topp, N. T. Sanghvi, A. V. Zaitsev, T. J. Hall, J. B. Fowlkes, O. D. Kripfgans, and J. G. Miller, "Interlaboratory comparison of ultrasonic backscatter, attenuation, and speed measurements," J. Ultrasound Med. **18**(9), 615–631 (1999).
[4] M. F. Insana, "Modeling acoustic backscatter from kidney microstructure using an anisotropic correlation function," J. Acoust. Soc. Am. **97**(1), 649–655 (1995).
[5] Y. W. Yuan and K. K. Shung, "Ultrasonic backscatter from flowing whole blood. II. Dependence on frequency and fibrinogen concentration," J. Acoust. Soc. Am. **84**(4), 1195–1200 (1988).
[6] H. Schmid-Schönbein, P. Gaehtgens, and H. Hirsch, "On the shear rate dependence of red cell aggregation *in vitro*," J. Clin. Invest. **47**, 1447–1454 (1968).
[7] M. S. Van Der Heiden, M. G. M. De Kroon, N. Bom, and C. Borst, "Ultrasound backscatter at 30 MHz from human blood: Influence of rouleau size affected by blood modification and shear rate," Ultrasound Med. Biol. **21**(6), 817–826 (1995).
[8] G. R. Lockwood, L. K. Ryan, J. W. Hunt, and F. S. Foster, "Measurement of the ultrasonic properties of vascular tissues and blood from 35–65 MHz," Ultrasound Med. Biol. **17**(7), 653–666 (1991).
[9] F. S. Foster, H. Obara, T. Bloomfield, L. K. Ryan, and G. R. Lockwood, "Ultrasound backscatter from blood in the 30 to 70 MHz frequency range," IEEE Ultrasonics Symposium Proceedings, 1599–1602 (1994).
[10] I. Fontaine, M. Bertrand, and G. Cloutier, "A system-based approach to modeling the ultrasound signal backscattered by red blood cells," Biophys. J. **77**, 2387–2399 (1999).
[11] I. Fontaine and G. Cloutier, "Frequency Dependence of Simulated Ultrasound Signals Backscattered by Aggregating Red Blood Cells," in *Acoustical Imaging*, edited by M. Halliwell and P. N. T. Wells (Kluwer Academic/Plenum, New York, 2000), pp. 297–302.
[12] D. Savéry and G. Cloutier, "A point process approach to assess the frequency dependence of ultrasound backscattering by aggregating red blood cells," J. Acoust. Soc. Am. **110**(6), 3252–3262 (2001).
[13] B. G. Teh and G. Cloutier, "The modeling and analysis of ultrasound backscattering by red blood cell aggregates with a system-based approach," IEEE Trans. Ultrason. Ferroelectr. Freq. Control **47**(4), 1025–1035 (2000).
[14] I. Fontaine, D. Savéry, and G. Cloutier, "Simulation of ultrasound backscattering by red cell aggregates: Effect of shear rate and anisotropy," Biophys. J. **82**(4), 1696–1710 (2002).

[15] L. Y. L. Mo and R. S. C. Cobbold, ''Theoretical Models of Ultrasonic Scattering in Blood,'' in *Ultrasonic Scattering in Biological Tissues*, edited by K. K. Shung and G. A. Thieme (CRC Press, Boca Raton, 1993), Chap. 5, pp. 125–170.
[16] G. Cloutier and Z. Qin, ''Ultrasound backscattering from nonaggregating and aggregating erythrocytes—A review,'' Biorheology **34**(6), 443–470 (1997).
[17] V. Twersky, ''Transparency of pair-correlated, random distributions of small scatterers, with application to the cornea,'' J. Opt. Soc. Am. **65**(5), 524–530 (1975).
[18] L. Allard, G. Cloutier, and L. G. Durand, ''Effect of the insonification angle on the Doppler backscattered power under red blood cell aggregation conditions,'' IEEE Trans. Ultrason. Ferroelectr. Freq. Control **43**(2), 211–219 (1996).
[19] I. Y. Kuo and K. K. Shung, ''High frequency ultrasonic backscatter from erythrocyte suspension,'' IEEE Trans. Biomed. Eng. **41**(1), 29–34 (1994).
[20] J. A. Campbell and R. C. Waag, ''Ultrasonic scattering properties of three random media with implications for tissue characterization,'' J. Acoust. Soc. Am. **75**(6), 1879–1886 (1984).
[21] J. F. Chen, J. A. Zagzebski, and E. L. Madsen, ''Experimental demonstration of the frequency dependence of the effective scatterer number density,'' J. Acoust. Soc. Am. **99**(4), 1932–1936 (1996).
[22] M. F. Santarelli and L. Landini, ''A model of ultrasound backscatter for the assessment of myocardial tissue structure and architecture,'' IEEE Trans. Biomed. Eng. **43**(9), 901–911 (1996).
[23] J. H. Rose, M. R. Kaufmann, S. A. Wickline, C. S. Hall, and J. G. Miller, ''A proposed microscopic elastic wave theory for ultrasonic backscatter from myocardial tissue,'' J. Acoust. Soc. Am. **97**(1), 656–668 (1995).
[24] D. Savéry and G. Cloutier, ''Modeling of the Acoustic Signal Backscattered by a Biphasic Suspension: Application to the Characterization of Red Blood Cell Aggregation,'' in *Acoustical Imaging*, edited by M. Halliwell and P. N. T. Wells (Plenum, New York, 2000), pp. 289–295.
[25] G. Sommer, E. W. Olcott, and L. Tai, ''Liver tumors: Utility of characterization at dual-frequency US,'' Radiology **211**(3), 629–636 (1999).
[26] M. A. Moehring and J. A. Ritcey, ''Sizing emboli in blood using pulse Doppler ultrasound. I. Verification of the EBR model,'' IEEE Trans. Biomed. Eng. **43**(6), 572–580 (1996).

Reliability of sound attenuation in Florida scrub habitat and behavioral implications

Brian S. Nelson[a)]
Department of Biology, Indiana University, Bloomington, Indiana 47405-3700

(Received 20 May 2002; revised 24 January 2003; accepted 11 February 2003)

Attenuation over distance in natural habitat is often difficult to predict when measured without respect to sound frequency. The physical-acoustic structure of Florida scrub habitat is described and both attenuation and reliability of attenuation are measured as a function of sound frequency, over several distances, speaker elevations, and microphone elevations. The spatial context of sound propagation in Florida scrub habitat is discussed and a model designed to describe contributions to overall attenuation from individual factors is presented. Sound frequencies below ~3.5 kHz attenuate more reliably than higher sound frequencies, suggesting that animals should pay greatest attention to relatively low sound frequencies when they assess attenuation or estimate sound-pressure level. © *2003 Acoustical Society of America.* [DOI: 10.1121/1.1564817]

PACS numbers: 43.80.Ev, 43.80.Lb [WA]

I. INTRODUCTION

Attenuation over distance in natural habitat is often difficult to predict when measured without respect to sound frequency (e.g., Morton, 1975; Wiley and Richards, 1982). Nevertheless, playback experiments with amplified or attenuated stimuli have demonstrated that eastern towhees, *Pipilo erythrophthalmus* (Emberizidae, Passeriformes) in Florida are able to assess attenuation with surprisingly little error (Nelson, 2000; Nelson and Stoddard, 1998). More specifically, this small bird appears to estimate source sound-pressure level (SPL) using at least one correlated sound frequency or temporal variable and assess auditory distance using the difference between perceived (incident) and source SPL. One explanation for the towhee's ability to assess attenuation may be that subjects are able to process sound frequencies that attenuate reliably separately from those that do not. In fact, it has long been recognized that attenuation is frequency dependent and a recent experiment has demonstrated that towhees use SPL as an auditory distance cue only when they hear relatively low sound frequencies (below 3.5 kHz; Nelson, 2002).

Physical objects typically reflect (scatter) incident sound waves, and the magnitude of this sound reflection decreases as sound wavelength approaches and exceeds object diameter/2π, corresponding with the transition between Rayleigh and diffractive (Mie) scattering (Bowman *et al.*, 1987; Bradbury and Vehrencamp, 1998; Pye and Langbauer, Jr., 1998). Sound frequency can be derived directly from sound wavelength (frequency=c/wavelength, where c=speed of sound in air) and, as a result, a direct relationship exists between sound frequency and magnitude of sound reflection. Thus, if a broadband sound is reflected by a single object, or by many objects of similar size, then one should expect to observe an increase in sound reflection magnitude above a relatively narrow range of sound frequencies. For example, 1.5-cm objects should begin to reflect sound frequencies above about 3.65 kHz [(34 400 cm/1.5 cm)/$2\pi\approx$3.65 kHz].

Sound reflections with greater magnitude should interfere with sound transmission to a greater extent than reflections with lower magnitude. In addition, an increase in interference should, on average, result in greater attenuation over distance. Thus, an increase in sound reflection magnitude over relatively high sound frequencies should, on average, result in increased attenuation over these same relatively high sound frequencies. For example, if 1.5-cm objects begin to reflect sound frequencies above about ~3.65 kHz, then increased attenuation might also be expected above ~3.65 kHz. In fact, frequency-dependent attenuation has been described in numerous previous investigations and differential scattering has been recognized as an important process that can produce frequency-dependent attenuation (Wiley and Richards, 1982).

Florida scrub habitat has a relatively simple physical-acoustic structure. For example: (1) these vegetation associations are dominated by only a few xerophilous plant species (Abrahamson *et al.*, 1984); (2) leaves are abundant in relation to other potential reflective surfaces (e.g., stems and branches); (3) leaves are located within a relatively dense, 1–2-m-high matrix above the ground; (4) this matrix of leaves lies above a flat and relatively homogeneous sandy soil; and (5) leaves are structurally rigid (sclerophyllous), revolute and linear. Given these habitat characteristics, leaves of dominant Florida scrub plant species should function as an important source of interference during sound transmission.

In this study, I collect leaves in Florida scrub habitat and predict that leaf diameter will be distributed narrowly. I then obtain sound attenuation measurements over several sites, days, speaker elevations, and microphone elevations and predict that sound frequencies will attenuate less reliably as sound wavelength (wavelength=c/frequency) approaches and exceeds the diameter of the most abundant leaf size observed [i.e., as wavelength approaches and exceeds (c/leaf size)/2π]. Finally, I present a model in which I estimate the relative contributions to overall attenuation from atmo-

a)Electronic mail: brsnelso@indiana.edu

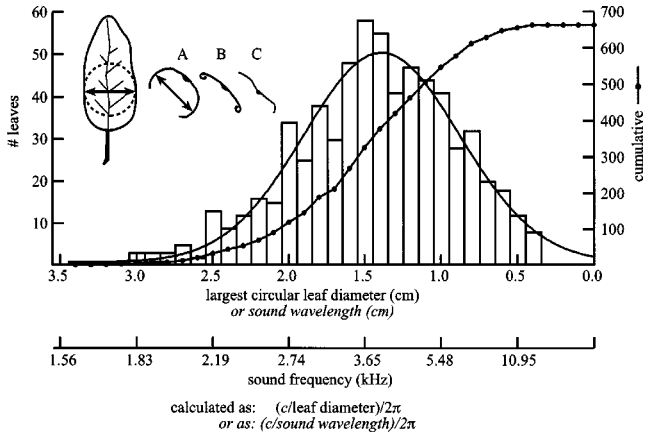

FIG. 1. Nonaccumulating and cumulative distributions of largest circular leaf diameter calculated from 663 leaves collected along sixteen 100-m transects (0.1-cm bins). Inset is an illustration of how largest circular leaf diameter was measured. The distribution is dominated by three species: Quercus inopina (46%; cross section depicted as inset A); Q. geminata (20%; inset B); and Q. chapmanii; (12%; inset C). Reciprocal bottom axis predicts the sound frequency at which sound should begin to reflect with substantial magnitude as a function of largest circular leaf diameter [frequency=(c/leaf diameter)/2π; c=speed of sound].

spheric absorption, ground reflections, and interference from vegetation.

II. EXPERIMENT 1. PHYSICAL-ACOUSTIC HABITAT STRUCTURE

A. Methods

I collected a single leaf every meter along 16 100-m linear transects. I chose sites with variable plant density, species distribution, and time since fire (natural or prescribed) and all sites were located within either a scrubby flatwoods or sand pine scrub vegetation association (Abrahamson *et al.*, 1984). Leaves, not lying on the ground, nearest each 1-m mark on the 100-m measuring tape were chosen, but no leaf was collected if the nearest leaf was closer to the previous or next 1-m mark. Leaves were selected at an elevation above the ground that was determined by the elevation of the 100-m measuring tape stretched above each transect and then allowed to rest naturally within the vegetation. I collected palmetto (*Serenoa repens* and *Sabal etonia*) fronds if they were nearest to each 1-m mark, but did not include these fronds in my analysis.

Leaves were placed in a plastic bag during collection and scanned into a computer (300 dots per inch resolution) within 3 h of collection. Leaves were placed flat along their widest side so that they lay stable on the scanner's bed but were not compressed prior to scanning. Leaf shape did not appear to change prior to scanning.

Leaf images were analyzed digitally by overlaying the largest diameter circle that fit completely within the outside edges of each leaf (inset in Fig. 1). Thus, largest circular leaf diameter is defined as twice the length of radius that can be rotated 360° from a single point without extending beyond the edge of a leaf displayed as a two-dimensional object on its widest side (Fig. 1, inset). Largest circular leaf diameter, as just defined, encompasses what appears to be the most relevant dimension in analyses of several simple shapes (e.g., a disk, thin strip, cylinder, sphere, etc., Bowman *et al.*, 1987, see below) and, as a result, this measurement is assumed to represent the most relevant dimension in this analysis.

Variation in leaf shape and orientation decreases the effective size of a leaf depending on the leaf's exact three-dimensional shape. For example, a flat 0.1-cm-thick leaf with a largest circular diameter of 1.5 cm should reflect sound as if it had a largest circular diameter of between 0.1 and 1.5 cm depending on direction of sound incidence upon the leaf. In other words, the function between leaf orientation and magnitude of sound reflection is comparable to what is observed when direction of sound incidence is varied relative to the orientation of, for example, a thin rigid strip (Bowman *et al.*, 1987). As a result, an accounting of variation in leaf shape and orientation should, on average, skew a nonaccumulating distribution of leaf diameter towards a smaller average value, increase the number of small leaves in a cumulative distribution, and accentuate the inflection point of the cumulative distribution. This shift towards a smaller effective leaf diameter is expected to magnify the relationships I describe and, as a result, I do not attempt to account for variation in leaf shape or orientation.

B. Results

Largest circular leaf diameter measurements are distributed normally (mean±s.d.=1.46±0.54; $N=663$, Fig. 1) with 68% of values falling between 0.92 and 2.0 cm. The distribution has a mode near 1.5 cm and is described well by a Gaussian function despite having a slightly positive skew (0.61) and negative kurtosis (−1.04; Fig. 1). The distribution is dominated by leaves of *Quercus inopina* [Fig. 1(A); 46±5% mean±s.d., s.d. calculated across the 16 transects], *Q. geminata* [Fig. 1(B); 20±8.4%], and *Q. chapmanii* [Fig. 1(C); 12±3.8%]. The remaining 22% of leaves collected and analyzed were collected from *Lyonia* spp., *Vaccinium* spp., *Befaria racemosa, Palafoxia feayi*, and a few other less abundant species. After adjusting for palmetto (*Serenoa repens* and *Sabal etonia*) fronds which were excluded from this analysis, these percentages correspond well with estimates of percent cover obtained previously for sand pine scrub (oak understory phase) and scrubby flatwood (inopina phase) vegetation associations (Abrahamson *et al.*, 1984).

III. EXPERIMENT 2. RELIABILITY OF SOUND ATTENUATION

A. Methods

I obtained sound attenuation measurements over five sites in 1998 and over five additional sites in 1999. I obtained recordings at each site on at least 2 different days in May and June between 0600–0800. Recordings were obtained when no birds were near the microphones, and all recordings included in my analyses were preceded and followed by ambient sound with a spectrum level at least 6 dB below spectra of experimental recordings (1.6–8 kHz; see Results).

In both 1998 and in 1999 I recorded at least 6 s of Gaussian noise (Brüel & Kjaer WB 1314, −24-dB/octave passband filter 1.6–10 kHz) played from a single 1-in. dome

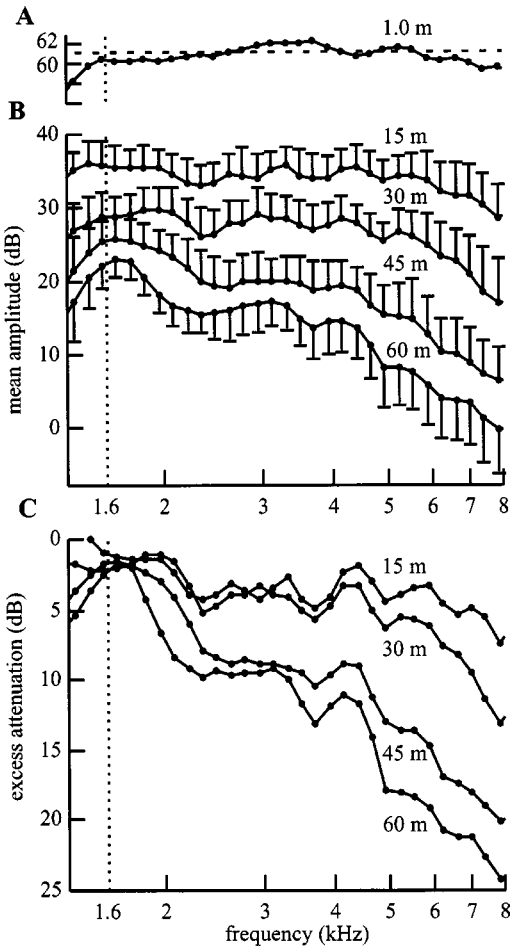

FIG. 2. Attenuation as a function of sound frequency and distance between speaker and microphone positions in 1998 (Fig. 2). (A) Spectrum level (dB, $re{:}20\,\mu$Pa) of Gaussian noise measured under free-field conditions at a distance of 1 m used to assess sound attenuation in 1998 (the average noise level in 1999 was 4 dB greater, 1.6–8 kHz). Values are averages within 1/12th-octave bands. (B) Mean level of Gaussian noise recordings obtained over 15-, 30-, 45-, and 60-m distances calculated across all recordings obtained with the speaker and microphone placed 1.5 or 2.0 m above the ground ($N=20$ over each distance, error bars=1 s.d.); (C) excess attenuation calculated as: source spectrum-level—mean level of recording—attenuation expected from spherical spreading. The vertical dashed line marks the location of the 1.6 kHz high-pass filter.

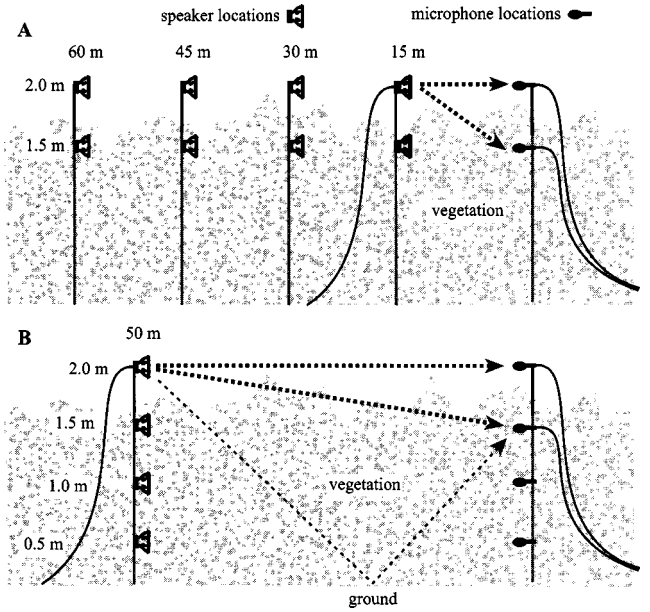

FIG. 3. Distances and elevations of the speaker and microphones used to measure attenuation in 1998 (A) and in 1999 (B). On average, the 2.0-m elevation placed the speaker and a microphone just above surrounding vegetation. In contrast, the 1.5-m elevation usually placed the speaker and a microphone just within surrounding vegetation and the 1.0- and 0.5-m elevations usually placed the speaker and microphone within surrounding vegetation (see the text). The third dashed line in (B) depicts a reflection from the ground.

speaker (MB Quart QTC 25.01 driven by a Soundstream D200 amplifier, Bescor 14-V, battery and 0.5 farad capacitor) using two calibrated omnidirectional measuring microphones (Brüel & Kjaer 4189), two microphone preamplifiers (Brüel & Kjaer 2671), and a digital audiotape recorder (HHB PortaDAT, 16-bit, 44.1 kHz). Noise was played from the speaker at 94 dB in 1998 [rms at 1 m; 61±1.5-dB spectrum level between 2–8 kHz, Fig. 2(A)], and at 98 dB in 1999 (rms at 1 m). Source output levels at a distance of 1 m were obtained in an open field with both the speaker and microphone placed 2 m above two stacked acoustic foam panels positioned on the ground between the speaker and the microphone (cutting wedge 48×48×3 in., 122×122×7.6 cm, Systems Development Group). Output from the noise-generating system was verified several times each year and only minor (<±1-dB) adjustments were required throughout the 2-year period to maintain a consistent output level (±1 dB between 1.6 and 8 kHz) under these free-field conditions [Fig. 2(A)].

In 1998, I recorded Gaussian noise with speaker and microphone elevations of 1.5 or 2.0 m [Fig. 3(A)]. I chose these elevations because an elevation of 2 m placed the speaker and microphone, on average, just above surrounding vegetation while an elevation of 1.5 m placed the speaker and microphone, on average, within the maximum elevation (1–2 m) of surrounding vegetation (Abrahamson *et al.*, 1984). For example, from an elevation of 2 m, and over a distance of 60 m, I could usually see a small, 5-cm-diameter brightly colored object (speaker) that was also placed at an elevation of 2 m. In contrast, I could rarely see this same object from an elevation of 1.5 m. These elevations were also chosen because towhees often forage on the ground, but typically perch at an elevation between 1.5 and 2.0 m when vocalizing (personal observation) or when interacting with real or perceived rival conspecifics (Nelson and Stoddard, 1998; Nelson, 2000). During this same year the speaker and microphones were separated by distances of 15, 30, 45, and 60 m [Fig. 3(A)]. Towhees often communicate over 15–60 m (see Discussion) and these four distances were chosen because they span the distances from which stimuli were played to towhee subjects in sound localization experiments (Nelson and Stoddard, 1998; Nelson, 2000).

In 1999, I recorded Gaussian noise with the speaker and microphones positioned at additional elevations of 0.5, 1.0 m [Fig. 3(B)]. These two lower elevations were included to better describe elevation as a source of variation and because towhees often perch at these lower elevations when not vocalizing or interacting with real or perceived rival conspecifics. A single distance of 50 m was used as both a regular

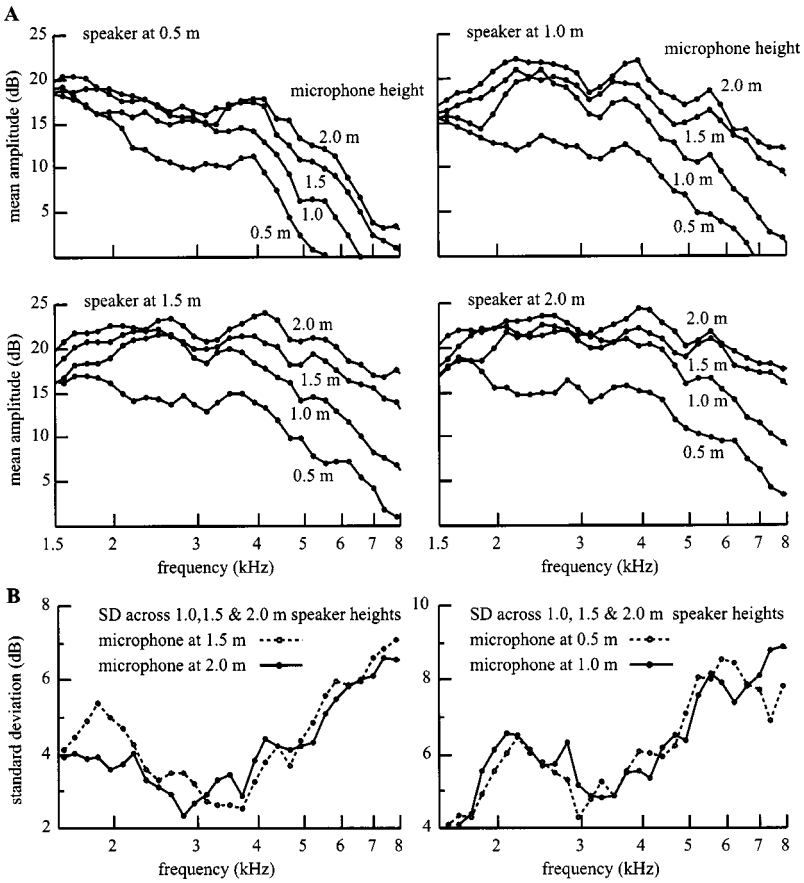

FIG. 4. Attenuation as a function of sound frequency, speaker height, and microphone height above the ground in 1999 (Fig. 2). (A) Mean level of Gaussian noise recordings, averaged within 1/12th-octave bands obtained over a single 50-m distance in 1999. Each plot illustrates mean values obtained with a microphone elevation of 0.5, 1.0, 1.5, and 2.0 m when noise was played from one of the four speaker elevations (0.5, 1.0, 1.5, or 2.0 m, $N=10$ for each condition). (B) Standard deviation (s.d.) calculated across the 1.0-, 1.5-, and 2.0-m speaker elevations for recordings obtained at each microphone elevation (0.5, 1.0, 1.5, and 2.0 m, $N=30$ for each microphone elevation) as well as across sites sampled and between days. Measurements of s.d. demonstrate that sound frequencies below ~3.5 kHz attenuate more reliably in comparison with sound frequencies above ~3.5 kHz.

(standard) and intermediate distance between the 45- and 60-m distances tested in 1998.

Outputs from the two microphones were recorded simultaneously on separate channels of the stereo recorder (HHB PortaDAT, 16-bit, 44.1 kHz). In 1999, simultaneous recordings were obtained from the 2.0- and 1.5-m elevations and then from the 1.0- and 0.5-m elevations (or vice versa). Gaussian noise recordings on each stereo channel were transferred to a microcomputer (Digigram PCXPocket A/D 44.1 kHz, 16-bit, SPDIF digital interface) and scaled to a proper absolute SPL using reference 1-kHz, 94-dB calibration tones (Brüel & Kjaer 4321) recorded just before and after each recording period. Power spectral densities (PSD) were produced with a Hanning window and 2048-point FFT over 5.99 s (129×2048 point) noise selections (Igor Pro). Magnitudes for each 43.07-Hz linear bin were then averaged within 1/12th-octave bands.

Attenuation and variation in attenuation (s.d.) are both difficult to assess as a function of sound frequency for reasons described below. However, attenuation and variation in attenuation (s.d.) should be positively correlated above ~3.5 kHz if both attenuation and s.d. are produced by interference from vegetation (experiment 1). I used line-fit procedures (Igor Pro) to evaluate these correlations as a function of sound frequency below 3.3 kHz and above 3.5 kHz. In all cases, s.d. was calculated over 50 m and across the 1.0-, 1.5-, and 2.0-m speaker elevations.

In a second related analysis I used iterative line-fit procedures to calculate the frequency range over which the maximum correlation coefficient could be obtained. In all cases this variable frequency range included sound frequencies above 5 kHz but was allowed to include any sound frequency between 2 to 5 kHz if doing so resulted in a larger correlation coefficient. I interpret the lowest frequency included in this iterative analysis as the frequency at which the correlation between attenuation and s.d. begins to change from relatively weak (<0.5) or negative to relatively strong and positive.

Finally, I measured ambient noise level at each microphone elevation (0.5, 1.0, 1.5, and 2.0 m) prior to and after each Gaussian noise recording ($N=20$ for 0.5-, 1.0-, 1.5-, and 2.0-m microphone elevations). Ambient noise level was measured as a function of sound frequency using methods described above over 9.98 s (215×2048 point) waveform selections.

B. Results

Sound attenuation and excess attenuation (i.e., attenuation in addition to that expected from spherical spreading of sound from a single point source) increased with recording distance (Fig. 2). Excess attenuation also increased markedly between the 30- and 45-m recording distances (Fig. 2). Finally, attenuation decreased with speaker and microphone elevation [Fig. 4(A), $N=10$ each elevation] and increased substantially when either the speaker or a microphone was placed at an elevation of 0.5 m.

Attenuation varies as a function of sound frequency (ANOVA $P<0.01$), although statistical contrasts cannot be drawn because, as predicted, there is significant variation in

variance as a function of sound frequency (i.e., the data are heteroscedastic; Levene's test, $P<0.05$). *Post hoc* tests for unequal variance (e.g., Dunnett's pairwise comparison with a control) are also inappropriate because there is no control against which attenuation over each distance might be compared. Finally, there seems to be little justification for transforming these data both because the relationship between s.d. and mean attenuation appears to depend on speaker and microphone elevation and because a relationship between mean attenuation and s.d. can be defined only over relatively high sound frequencies (above ~3.5 kHz; see below).

Variation in sound attenuation (s.d.) increases above 3–4 kHz under the following conditions: (1) when calculated across the 1.0-, 1.5-, and 2.0-m speaker elevations; (2) when limited to recordings obtained at each microphone elevation [Fig. 4(B), $N=10$]; (3) when calculated across recordings obtained at all microphone elevations ($N=40$, not illustrated); and (4) when assessed across all speaker elevations (including the 0.5-m speaker elevation), although overall variation observed in this last analysis is greater due to the large increase in attenuation that is observed when either the speaker or the microphone is placed at an elevation of 0.5 m (not illustrated). Variation in sound attenuation (s.d.) also increases between approximately 2 and 3 kHz, although much of this variation appears to be produced by ground reflections (experiment 3 and Discussion).

Attenuation levels observed over 45 m in 1998 correspond well with attenuation levels obtained over 50 m in 1999 after adjusting for variation in source spectrum level (94 dB vs 98 dB rms) and the 5-m difference in sound propagation distance. In addition, spectra obtained over 50 m in 1999 correspond will with spectra obtained over 15, 30, 45, and 60 m in 1998. As a result, attenuation trends observed as a function of speaker and microphone elevation in 1999 do not appear to occur only over a 50-m propagation distance.

The Levenberg–Marquardt best-fit algorithm (Igor Pro) reports relatively small chi-square values (1.70 ± 0.64; mean $\pm$s.d.; Fig. 4) for power functions describing attenuation over 50 m, whereas larger chi-square values are reported for line fits (2.52 ± 0.93). Thus, attenuation is frequency dependent and appears to be described best over 50 m using a power function in which attenuation is approximately equal to sound frequency (in kHz) raised to a power between 1 and 2 ($f^{1\text{ to }2}$, where f is frequency in kHz). Residuals reveal that a spectral ripple is imposed on amplitude spectra and that peaks and notches occur at relatively constant frequency intervals above ~3 kHz regardless of speaker or microphone elevation (Fig. 5).

Positive linear correlations were observed between attenuation and variation in attenuation (s.d.) above ~3.5 kHz in all tests (Table I, Fig. 6). In contrast, relatively weak or negative correlations were observed over sound frequencies below ~3.3 kHz. Correlations above 3.5 kHz become stronger as speaker elevation decreases from 2.0 to 0.5 m. In addition, slope values (b) calculated above 3.5 kHz decrease as speaker elevation decreases from 2.0 to 0.5 m (Table I, Fig. 6).

Iterative line fits revealed that stronger positive correlations between attenuation and variation in attenuation (s.d.) could often be obtained by including sound frequency points just below or above 3.5 kHz (Table I, Fig. 6). The lowest frequency measurement included to obtain a larger correlation coefficient decreases with microphone elevation and decreases markedly when the microphone is at 0.5 m. On average, and across the 1.0-, 1.5-, and 2.0-m microphone elevations, the lowest frequency measurement included to obtain a maximum correlation coefficient was 3.612 ± 0.30 kHz (mean$\pm$s.d.; Table I).

Ambient sound levels attenuate rapidly over distance above ~4 kHz (Fig. 7). In addition, ambient sound levels decrease between ~1.5 and 2.5 kHz and rise again below ~1.5 kHz (not illustrated). Ambient sound levels are lower at the 0.5- and 1.0-m microphone elevations than at the 1.5- and 2.0-m microphone elevations.

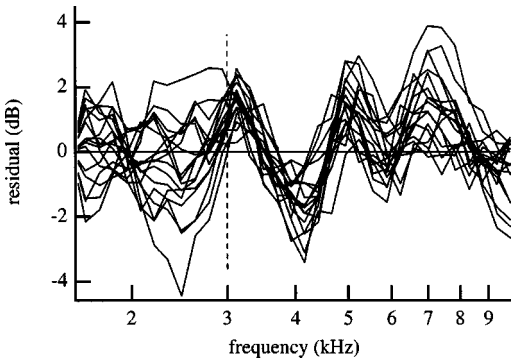

FIG. 5. Residuals from power functions fit to attenuation curves obtained in 1999 over 50 m and across each speaker and microphone elevation. Residuals reveal that a spectral ripple is imposed on amplitude spectra and that peaks and notches in this ripple occur at relatively constant frequency intervals above ~3 kHz regardless of speaker or microphone elevation.

TABLE I. Relationship between attenuation and variation in attenuation (s.d.). Correlation coefficients (r) are calculated for each speaker and microphone elevation across sound frequencies either below 3.3 kHz or above 3.5 kHz. Slopes (b) are also reported for sound frequencies above 3.5 kHz. In the last column I report the lowest frequency (kHz) that could be included to obtain a larger correlation coefficient over higher sound frequencies (Fig. 6).

Elevation speaker, mic.	r <3.3 kHz	r >3.5 kHz	b >3.5 kHz	Lowest kHz to obtain larger r
0.5, 0.5	0.345	0.734	0.136	2.473
1.0, 0.5	0.305	0.697	0.170	2.473
1.5, 0.5	0.274	0.726	0.221	2.473
2.0, 0.5	0.482	0.689	0.239	2.334
0.5, 1.0	0.305	0.943	0.206	2.941
1.0, 1.0	−0.621	0.926	0.259	3.498
1.5, 1.0	−0.747	0.938	0.332	3.301
2.0, 1.0	−0.801	0.919	0.315	3.705
0.5, 1.5	−0.905	0.961	0.241	3.926
1.0, 1.5	0.267	0.898	0.424	3.498
1.5, 1.5	−0.529	0.907	0.537	3.498
2.0, 1.5	−0.691	0.759	0.639	3.705
0.5, 2.0	−0.805	0.938	0.197	3.926
1.0, 2.0	−0.015	0.894	0.343	3.498
1.5, 2.0	−0.313	0.822	0.444	3.926
2.0, 2.0	−0.278	0.765	0.466	3.926

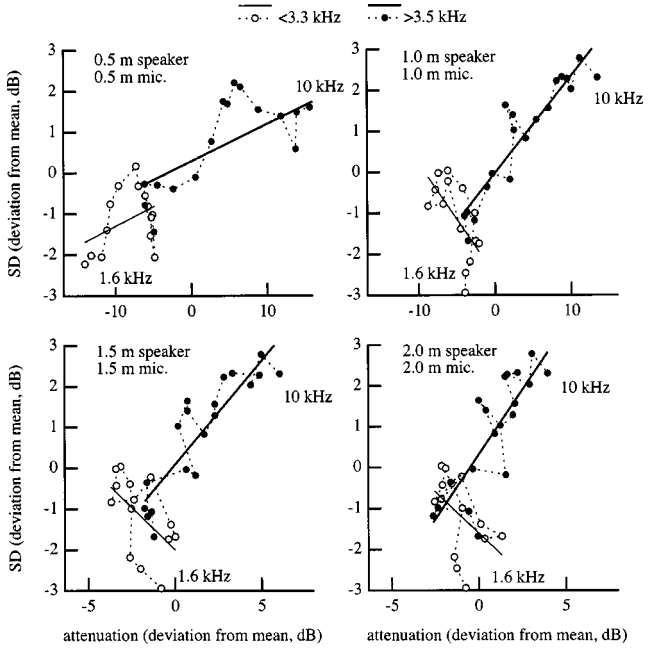

FIG. 6. Relationship between attenuation and reliability of attenuation (s.d.) as a function of sound frequency. A positive relationship exists for sound frequencies above approximately 3.5 kHz. In contrast, a relatively weak or negative relationship exists for sound frequencies below approximately 3.3 kHz. Correlation coefficients are reported in Table I.

IV. EXPERIMENT 3. CONTRIBUTIONS TO ATTENUATION

A. Methods

Attenuation in Florida scrub habitat appears to be due to three primary factors: (1) atmospheric absorption; (2) interference from vegetation; and (3) interference from ground reflections. I present a simple model of sound transmission in Florida scrub habitat and use the results of this model to estimate the contributions to both attenuation and variation in attenuation from each individual factor.

Wiley and Richards (1982) suggested that attenuation (dB) should be approximately equal to sound frequency raised to a power of between 1 and 2. Power coefficients between 1 and 1.3 appear to approximate attenuation when the speaker and microphone are located above vegetation, while larger coefficients (1.3 to 1.7) appear to approximate attenuation when the speaker or microphone are located within vegetation (experiment 2). I therefore approximate attenuation (in dB) due to atmospheric absorption as sound frequency (kHz) raised to a power between 1 and 1.3 [Fig. 8(A)] and attenuation due to both atmospheric absorption and interference from vegetation as sound frequency (in kHz) raised to a power between 1 and 1.7 [Fig. 8(A)].

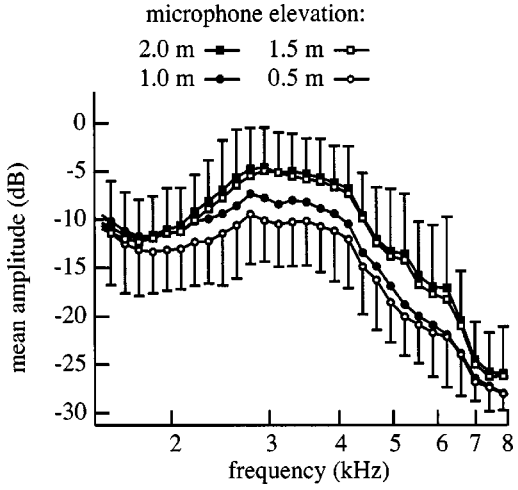

FIG. 7. Ambient noise levels measured at 0.5-, 1.0-, 1.5-, and 2.0-m microphone elevations in 1999 ($N=20$, 9.98 s. samples). Error bars (1 s.d.) are plotted only for the 0.5- and 2.0-m elevations; however, error measured at 1 m is similar to error measured at 0.5 m and error measured at 1.5 m is similar to error measured at 2 m.

Ground reflections are often difficult to predict in natural habitats due to soil heterogeneities (Martens *et al.*, 1985; e.g., Wiley and Richards, 1982). However, the soils where I obtained attenuation measurements can be described as sandy, well drained (1.8 to >3 m), and relatively homogeneous (Abrahamson *et al.*, 1984). Sandy soils are acoustically "hard" because reflection coefficients have relatively large real parts (0.7–1.0) and relatively small imaginary parts (0.0–0.2, Bolen and Bass, 1981; Martens *et al.*, 1985). As a result, ground reflections should arrive at microphone positions with both substantial magnitude and minimum phase shift [Fig. 3(B)].

I calculate the delay time (Dt) of reflections from the ground

$$\mathrm{Dt}=\left(\left(\sqrt{S^2+\left(d\cdot\frac{S}{S+M}\right)^2}+\sqrt{M^2+\left(d\cdot\frac{M}{M+S}\right)^2}\right)-d\right)\div c, \quad (1)$$

where S is speaker elevation, M is microphone elevation, d is the distance from the speaker to the microphone (50 m), and c is the speed of sound in air (340 m/s).

Sound propagating down to the ground should experience substantial frequency-dependent attenuation from vegetation. Furthermore, sound that is reflected back upwards from the ground should experience additional attenuation if both the speaker and microphone are positioned within or above the vegetation (Fig. 3). As a result, I attenuate ground reflections using a relatively large reflection coefficient (0.7) and power coefficient (2)

$$A=0.7\cdot 10^{-f^2/20}, \quad (2)$$

where f is sound frequency (kHz). I then calculate amplitude as a function of sound frequency at a (nondirectional) receiver's location by summing both direct and reflected sound waves

$$W(t)=\cos(2\cdot\pi\cdot Hz\cdot t)+A\cdot\cos(2\cdot\pi\cdot Hz\cdot(t+\mathrm{Dt})), \quad (3)$$

$$\mathrm{dB}=20\cdot\log(\mathrm{rms}(W(t))), \quad (4)$$

where A is the amplitude of the ground reflection [Eq. (2)], t is time (s), Dt is the delay time of the ground reflection [s; Eq. (1)], $W(t)$ is a waveform, and rms is a function computing root mean square (rms) amplitude over the waveform defined by $W(t)$.

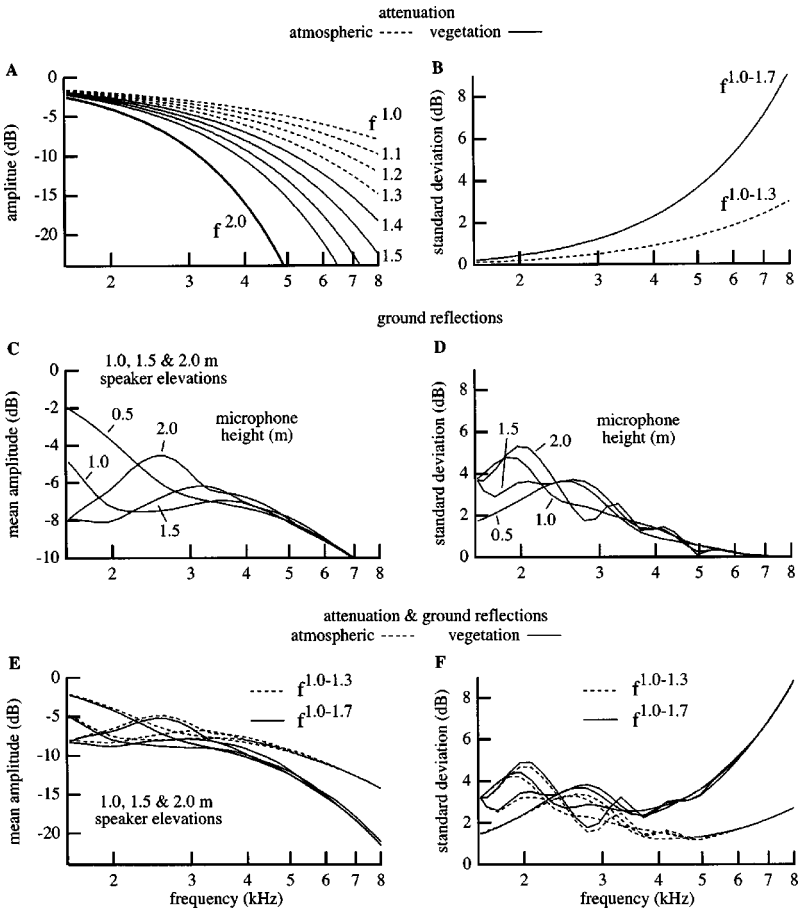

FIG. 8. Estimated contributions to overall attenuation from atmospheric absorption, interference from vegetation, and interference from ground reflections. (A) Attenuation derived from power functions ($f^{1.0\text{ to }1.7}$) where f is sound frequency in kHz. (B) Variation in attenuation (calculated across power coefficients) describing attenuation due to atmospheric absorption ($f^{1.0\text{ to }1.3}$) and interference from vegetation ($f^{1.4\text{ to }1.7}$). (C) Attenuation due to ground reflections at each microphone elevation; calculated as an average across speaker elevations. (D) Variation in attenuation due in ground reflections; calculated across speaker elevations. (E) Attenuation curves derived both from power functions and ground reflections. (F) Variation in attenuation due to atmospheric absorption ($f^{1.0\text{ to }1.3}$), interference from vegetation ($f^{1.4\text{ to }1.7}$), and ground reflections; calculated across speaker elevations.

For comparison with empirical data I calculated attenuation and variation in attenuation (s.d.) over 50 m and across the same 0.5-, 1.0-, 1.5-, and 2.0-m speaker and microphone elevations evaluated during 1999 in experiment 2. I calculated attenuation for individual sound frequencies in this model for clarity but verified results in a second comparable model that employed Fourier analyses of Gaussian noise waveforms that were similarly attenuated (filtered), delayed, and summed (results not presented).

B. Results

Variation in attenuation (s.d.) increases with sound frequency when attenuation is described by a power function [Fig. 8(A)] and when the power coefficient describing attenuation is varied between 1.0 and 1.3 [Fig. 8(B); s.d. $=0.11*f^{1.6}$, where f is frequency in kHz]. Thus, s.d. might be expected to increase with sound frequency even when there is minimum variation in attenuation due to atmospheric absorption. s.d. increases more rapidly with sound frequency when the power coefficient describing attenuation is varied between 1.0 and 1.7 [Fig. 8(B); s.d.$=0.186*f^{1.88}$]; a range of coefficient values that would appear to more closely approximate attenuation through vegetation [Fig. 4(B)].

Ground reflections undergo substantial frequency-dependent attenuation in this model and, as a result, these reflections appear to produce interference primarily over relatively low sound frequencies [Fig. 8(C)]. In addition, interference appears to depend on both speaker and microphone elevation [Fig. 8(D)]. In fact, the combined effects of attenuation and ground interference [Figs. 8(E) and (F)] are not vastly different from empirical measurements obtained in experiment 2 (Fig. 4). Finally, results lend support to the hypothesis that the relationship observed between attenuation and variation in attenuation (s.d., Fig. 6) might be due primarily to ground reflections below ~3 kHz and by atmospheric absorption and interference from vegetation above ~3.5 kHz (Fig. 9).

V. DISCUSSION

A. Physical-acoustic structure of the habitat

Natural outside environments are complex, and numerous factors can lead to both increased attenuation and de-

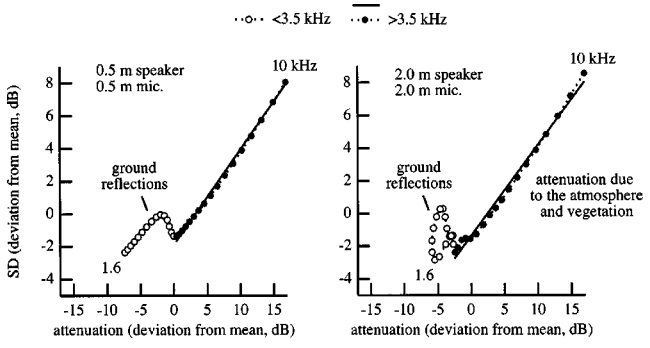

FIG. 9. Relationship between attenuation and variation in attenuation (s.d.) observed in the output of the model (Fig. 8). The relationship is complex and dependent on both speaker and microphone elevation below ~3.5 kHz but becomes both positive and linear above ~3.5 kHz.

creased reliability of attenuation. For example, the variable and frequency-dependent nature of atmospheric absorption might alone often produce substantial variation in attenuation over relatively high sound frequencies [Fig. 8(B)]. Nevertheless, vegetation is likely to be an important factor in determining how sound attenuates in Florida scrub habitat (experiment 1).

Leaves in Florida scrub habitat can be described as having a relatively narrow size distribution with a peak near 1.5 cm (Fig. 1), which led to the following three predictions: (1) sound frequencies above ~3.5 kHz (3–4 kHz) should attenuate rapidly with distance and attenuate with greater variation in attenuation over distance in comparison with lower sound frequencies because sound frequencies above ~3.5 kHz are likely to face strong interference from numerous leaves with a largest circular diameter larger than 1.5 cm; (2) a moderate amount of attenuation should occur between ~2.75 and 3 kHz as a result of interference from a moderate number of leaves with diameter between 1.5 and 2 cm; and (3) a negligible amount of attenuation should occur below ~2.75 kHz as a result of negligible interference from a relatively low number of leaves with a circular diameter larger than 2 cm. These predictions are illustrated graphically in Fig. 1 by reciprocal bottom axes.

Sound is not normally transmitted along a single direct pathway between a signaler and a receiver but is, instead, dispersed upon production and then (in most cases) resolved by directional hearing mechanisms during reception. As a result, the role that sound propagation plays during communication is likely to be substantial in comparison with the role that is normally attributed by analyses of monaural sound recordings. For example, monaural sound recordings may often need to be interpreted with caution because we do not yet fully understand the mechanisms by which animals resolve direct sound from reverberant sound. In addition, while neither birds nor humans localize sound reflections (lagging stimuli) that arrive within a few milliseconds of direct sound (e.g., Blauert, 1997; Litovsky *et al.*, 1999; Dent and Dooling, 2003), it has been demonstrated that humans pay attention to these reflections when discriminating sound level (Freyman *et al.*, 1998).

With these cautions in mind, attenuation measurements might often be interpreted most clearly in relation to the physical-acoustic structures of the habitats in which measurements are obtained. I suggest that sound frequencies below ~3.5 kHz are likely to attenuate more reliably than higher sound frequencies because these lower sound frequencies encounter a lower level of interference from leaves lying along the direct pathway between a speaker (signaler) and microphone (listener). In contrast, sound frequencies above ~3.5 kHz attenuate less reliably because they are more likely to experience a variable level of interference during propagation.

Previous investigators often emphasize how natural environments can ''degrade'' temporally modulated vocalizations during transmission. I do not investigate temporal changes that sound might undergo after transmission through Florida scrub habitat and, as a result, I do not describe how Florida scrub habitat might degrade temporally modulated vocalizations. Leaves are expected to reflect sound frequencies above ~3.5 kHz with greater magnitude in comparison with lower sound frequencies and, as a result, one might expect to observe increased degradation above ~3.5 kHz. On the other hand, leaves are scattered diffusely throughout Florida scrub habitat and this interpretation must, again, be viewed with caution until we learn more about mechanisms for hearing in natural environments.

B. Attenuation due to ground reflections

Ground reflections can sum together with direct sound and produce pronounced spectral peaks and notches in sound recordings (Bradbury and Vehrencamp, 1998; Roberts *et al.*, 1979; Wiley and Richards, 1982). This is especially true when recordings are obtained with a single omnidirectional microphone that is sensitive to both direct and reflected sound. Ground reflections are important because, when they exist, attenuation at any single sound frequency can depend to a large extent on several factors including the height of a sound source (signaler), height of a receiver (listener), and the distance between a sound source and a receiver (Fig. 3). Ground reflections are important in this study because sound frequencies below ~3.5 kHz are not expected to reflect from leaves, and are therefore expected to reflect from the ground and sum together with direct sound with substantial magnitude.

Spectral peaks and notches are evident below ~5 kHz in field recordings obtained where scrub vegetation had been cleared or burned within the last year. These peaks and notches can be attributed to ground reflections because they vary predictably with changes in both the elevation of the speaker or microphone and with the distance over which the speaker and microphones are separated (unpublished data). However, when otherwise identical recordings are obtained over vegetation (i.e., over at a site where vegetation has not been cleared or burned within the previous year), peaks and notches are most evident below ~3 kHz (unpublished data). As a consequence, variation in attenuation observed between ~2 and 2.5 kHz would appear to occur primarily as result of increased interference due to ground reflections (Fig. 4).

Animals may experience similar ambiguity (i.e., variation in attenuation) when unable to resolve indirect sound reflections separately from direct sound. However, directional hearing may allow subjects to avoid some of this variation if reflections can be suppressed or otherwise distinguished from direct sound. For example, if the auditory system can suppress sound reflections (lagging stimuli) that arrive within a few milliseconds of direct sound (e.g., Blauert, 1997; Litovsky *et al.*, 1999; Dent and Dooling, 2003), then it remains possible that ground reflections will not interfere with mechanisms for assessing the SPL of direct sound. In fact, some of these reflections may improve assessment of attenuation if reflections can contribute to an animal's overall assessment of SPL (e.g., Freyman *et al.*, 1998).

C. Frequency-dependent attenuation

Ground reflections can produce variable attenuation patterns over relatively low sound frequencies (<3 kHz) but are

not expected to produce variable attenuation patterns over relatively high sound frequencies (Wiley and Richards, 1982). Instead, it would appear that attenuation over relatively high sound frequencies is best approximated as sound frequency (kHz) raised to a power of between 1 and 2 in many habitats including Florida scrub (Wiley and Richards, 1982, experiment 2).

That attenuation increases as a function of sound frequency has long been recognized. However, that variation in attenuation should also increase with sound frequency has received less attention. In this study, I demonstrate that variation in attenuation increases above ~3.5 kHz (experiment 2). Furthermore, I suggest that variation in attenuation above ~3.5 kHz may be due simply to variation in the function describing attenuation with respect to sound frequency (experiment 3).

Spectra obtained in both 1998 and in 1999 undulate with sound frequency, and the ripple that results from this undulation is most pronounced between 3 and 5 kHz (Figs. 4 and 5). This ripple does not appear to be due to ground reflections because peaks and notches in this ripple are pronounced only over relatively high sound frequencies (>~3 kHz) and occur at roughly constant frequency intervals regardless of speaker and microphone elevation (Figs. 4 and 5). In addition, this ripple exists in recordings obtained using different equipment (unpublished data) and as thus does not appear to be an artifact. Spectral ripples are normally observed in reflected sound when wavelength exceeds object diameter/π (Bowman *et al.*, 1987; Bradbury and Vehrencamp, 1998; Pye and Langbauer, Jr., 1998). Thus, one potential explanation for this ripple may be that sound is reflecting from numerous similarly sized objects during propagation. In fact, while this interpretation remains hypothetical, measurements of leaf diameter are narrowly distributed and leaves are expected to begin reflecting sound above approximately 3 kHz (Fig. 1).

D. Factors contributing to attenuation

Numerous factors can contribute to increased attenuation. Similarly, these same factors can often contribute to increased variation in attenuation (i.e., decreased reliability of attenuation). Nevertheless, individual contributions are often difficult to discern in empirical measurements. As a result, I present a relatively simple model intended to estimate the relative contributions to both attenuation and variation in attenuation from atmospheric absorption, interference from vegetation, and interference from ground reflections (experiment 3).

Attenuation due to atmospheric absorption is ubiquitous and will often limit the distance over which relatively high sound frequency vocalizations will propagate. On the other hand, variation in attenuation due to atmospheric absorption does not appear to decrease reliability of attenuation substantially as long as the function describing atmospheric absorption is not highly variable [Fig. 8(B)]. In contrast, attenuation due to increased interference from vegetation would appear to both increase attenuation and introduce substantial variation in attenuation over relatively high sound frequencies [Fig. 8(B)]. In fact, the use of a variable power coefficient to describe attenuation in this model, as opposed to a linear function, appears to produce relatively strong variation in attenuation primarily above ~3–4 kHz [Fig. 8(B)].

Ground reflections appear to be common in many habitats and may introduce substantial variation in attenuation over relatively low sound frequencies (e.g., Roberts *et al.*, 1979; Wiley and Richards, 1982). Variation in attenuation due to speaker elevation in this model does not appear to differ markedly from empirical measurements [Figs. 4(B) and 8(D)]. Nevertheless, nonsandy soils can often introduce phase shifts in ground reflections (e.g., Bolen and Bass, 1981; Martens *et al.*, 1985) and it should be recognized that such phase shifts can often produce highly variable attenuation patterns over relatively low sound frequencies.

Finally, it should be noted that additional factors are expected to contribute to both attenuation and variation in attenuation. For example, Wiley and Richards (1982) suggested that atmospheric turbulence can alone result in strong attenuation of relatively high sound frequencies. In fact, much of the frequency-dependent attenuation I attribute to atmospheric absorption and interference from vegetation might also be attributed to increased atmospheric turbulence.

E. Effects of signaler and listener elevation above the ground

Previous investigators have demonstrated that both a signaler's and listener's elevation above the ground can have substantial influences on characteristics of sound propagation (e.g., Dabelsteen *et al.*, 1993; Holland *et al.*, 1998; Mathevon *et al.*, 1996). In fact, these studies demonstrate that a change in speaker or microphone elevation can, in many ways, resemble a change in horizontal distance. A listener presumably often knows its own elevation and location within local habitat and, as a result, a listener might often be able to account for these factors when assessing attenuation. In contrast, listeners may rarely be able to assess the elevation of a distant signaler. Thus, while a greater amount of overall variation in attenuation is observed as a function of microphone elevation in comparison with variation assessed as a function of speaker elevation (Dabelsteen *et al.*, 1993), the results of this latter analysis may be of greater biological interest.

The attenuation levels that I observed as a function of microphone elevation in 1999 suggest that eastern towhees in Florida scrub habitat should move to an elevation of at least ~1 m to avoid a high level of excess attenuation [Fig. 4(A)]. In addition, results suggest that subjects should move to an elevation above ~1 m to avoid increased variation in attenuation [Fig. 4(B)]. Towhees may benefit additionally by perching above a 2-m elevation but can often do so in Florida scrub habitat only if willing to fly a considerable distance to one of a few relatively tall trees typically located within a towhee territory.

Towhees spend a substantial amount of time on or near the ground but nearly always move to an elevation between 1 and 2 m when interacting actively with real or perceived conspecific rivals that are located within or near their territory boundaries (Nelson and Stoddard, 1998; Nelson, 2000,

and personal observations). In addition, towhees often move to an elevation between 1 and 2 m just before vocalizing even if they return to the ground shortly after vocalizing (personal observations). These movements are likely to produce substantial variation in attenuation above ~3.5 kHz but are less likely to produce substantial variation in attenuation below ~3.5 kHz.

F. Implication for sound frequency windows

Morton (1975) described a sound frequency ''window'' for long distance communication in a forested habitat (see below) and argued that vocalizations may propagate farthest when produced within this range of sound frequencies. Sound frequency windows have subsequently been identified across a surprisingly broad range of habitats and, in most cases, these windows appear to be bounded by increased attenuation due to ground effects over relatively low sound frequencies and by increased attenuation due to atmospheric absorbance and interference from vegetation over relatively high sound frequencies (e.g., Marten and Marler, 1977a; Brenowitz, 1982; Marten and Marler, 1977b). For example, in a Panamanian forest both Morton (1975) and Marten and Marler (1977a) identified a sound frequency window between ~0.5 and 2.5 kHz (depending on interpretation). Similarly, Marten and Marler (1977b) defined a sound frequency window between ~1 and 3 kHz in several temperate habitats and Brenowitz (1982) defined a window between ~2.5 and 4 kHz in an open field. Roberts *et al.* (1979) suggested that many of these sound frequency windows might be explained by ground reflections (see Discussion above); however, it remains interesting that sound frequency windows have been identified in such variable habitats.

Attenuation increases with sound frequency in Florida scrub habitat and ground reflections introduce variable attenuation patterns below ~2–3 kHz. As a result, a sound window for long-distance communication often appears to exist between approximately 2.5 and 4.5 kHz in Florida scrub habitat.

Towhee calls are highly variable in acoustic structure but span a range of sound frequencies between ~1.8 and 4.5 kHz (Nelson, 2000). As a result, one might expect calls to propagate over relatively long distances. However, calls are also produced with variable source SPL (~70–84 dB, $re{:}20\,\mu$Pa; Nelson, 2000) and estimates of propagation distance are, ultimately, dependent both on ambient noise levels (Fig. 6) and mechanisms for hearing in noise (Dent *et al.*, 1997). As a result, it remains difficult to estimate how far any single towhee call might propagate before it can no longer be detected or discriminated. For example, a 3.3-kHz signal (selected arbitrarily) might be produced with a source spectrum level of 45 dB (equivalent to a 75-dB rms SPL; $re{:}20\,\mu$Pa; Nelson 2000) and be emitted from a height of 1.5 m. This signal might then attenuate ~46 dB over 50 m and arrive at a receiver's position with a spectrum level that is approximately 1 dB below ambient noise level at least ~84% of the time. However, this same signal can also be expected to arrive with an amplitude that is approximately 8 dB above ambient noise level ~16% of the time. Binaural release from masking might decrease threshold by an additional 9 dB (Dent *et al.*, 1997) and, thus, this same 45-dB signal might sometimes be detected over an additional ~150 m depending on environmental conditions and the physiological mechanisms that listeners may employ for hearing in noisy environments (assuming ~7.5-dB attenuation per doubling of distance). In summary, this variation is substantial and does not incorporate additional variation in active space that is expected to occur as a function of sound frequency or as a result of variation in source SPL (Nelson, 2000).

These results suggest that a bird like the eastern towhee may rarely be able to predict how far any single vocalization will propagate before it can no longer be detected or discriminated. However, much of this variation results from difficulty in quantifying when a vocalization falls below threshold and does not result from variation in attenuation. Thus, these results say little about variation in attenuation. In fact, sound frequencies below ~3.5 kHz may often attenuate reliably even if the active space of any single sound frequency or vocalization cannot be easily predicted.

G. Generality of results and behavioral implications

There are two main tasks to understanding ecological systems. The first task is to understand how individual processes operate and the second task is to understand how individual processes operate together. Florida scrub habitat has a relatively homogeneous physical-acoustic structure and, as a consequence, the results I present may be particularly robust. In fact, even a relatively simple model of sound propagation appears to produce similar results (experiment 3). On the other hand, the processes that contribute to attenuation in Florida scrub habitat are not specific to this habitat but are known to influence how sound propagates in numerous other habitats. For example, ground reflections, atmospheric absorbance, and interference from vegetation are all processes that are expected to produce attenuation in other habitats.

Eastern towhees use SPL as an auditory distance cue when they hear sound frequencies below 3.5 kHz but use another auditory distance cue when they hear sound frequencies above 3.5 kHz (Nelson, 2002). These results suggest that neural circuits used for judging attenuation might receive inputs primarily from low-frequency neural pathways (e.g., Irvine, 1992; Takahashi *et al.*, 1984). Alternatively, these circuits might select against high-frequency inputs during development if high frequencies do not normally attenuate reliably.

Use of SPL as an auditory distance cue can demonstrate that an animal is able to assess attenuation. However, if attenuation is reliable then variation in SPL might also convey additional information. For example, if distance can be judged using a visual cue or second auditory cue, then an ability to compensate for attenuation might allow an animal to assess source SPL. In fact, experiments have suggested that birds vary SPL when learning to sing (Brumm and Hultsch, 2001) and when vocalizing as adults (e.g., Brumm and Todt, 2002; Nelson, 2000; Cynx *et al.*, 1998; Manabe *et al.*, 1998).

ACKNOWLEDGMENTS

I thank Roderick Suthers, Sumit Dhar, Erica Goss, Ellen Ketterson, Bill Rowland, Troy Smith, and Philip Stoddard for helpful comments. Support was provided, in part, by NSF Grant No. BIR-9413220 to the Center for the Integrative Study of Animal Behavior at Indiana University and NIH Grant No. NS-29467 to Roderick Suthers. Archbold Biological Station provided access to research facilities.

Abrahamson, W. G., Johnson, A. F., Layne, J. N., and Peroni, P. A. (**1984**). ''Vegetation of the Archbold Biological Station, Florida: An example of the southern Lake Wales Ridge,'' Florida Sci. **47**, 209–250.

Blauert, J. (**1997**). *Spatial Hearing: The Psychophysics of Human Sound Localization, revised edition* (The MIT Press, Cambridge, MA).

Bolen, L. N., and Bass, H. E. (**1981**). ''Effects of ground cover on the propagation of sound through the atmosphere,'' J. Acoust. Soc. Am. **69**, 950–954.

Bowman, J. J., Senior, T. B. A., and Uslenghi, P. L. E. (**1987**). *Electromagnetic and Acoustic Scattering by Simple Shapes* (Hemisphere, New York).

Bradbury, J. W. and Vehrencamp, S. L. (**1998**). *Principles of Animal Communication* (Sinauer Associates, Sunderland, MA).

Brenowitz, E. A. (**1982**). ''Long-range communication of species identity by song in the red-winged blackbird,'' Behav. Ecol. Sociobiol. **10**, 29–38.

Brumm, H., and Hultsch, H. (**2001**). ''Pattern amplitude is related to pattern imitation during the song development of nightingales,'' Anim. Behav. **61**, 747–754.

Brumm, H., and Todt, D. (**2002**). ''Noise-dependent song amplitude regulation in a territorial songbird,'' Anim. Behav. **63**, 891–897.

Cynx, J., Lewis, R., Tavel, B., and Tse, H. (**1998**). ''Amplitude regulation of vocalizations in noise by a songbird, *Taeniopygia guttata*,'' Anim. Behav. **56**, 107–113.

Dabelsteen, T., Larsen, O. N., and Pedersen, S. B. (**1993**). ''Habitat-induced degradation of sound signals: Quantifying the effects of communication sounds and bird location on blur ratio, excess attenuation, and signal-to-noise ratio in blackbird song,'' J. Acoust. Soc. Am. **93**, 2206–2220.

Dent, M. L., and Dooling, R. (**2003**). ''Investigations of the precedence effect in budgerigars: Effects of stimulus type, intensity, duration, and location,'' J. Acoust. Soc. Am. **113**, 2146–2158

Dent, M. L., and Dooling, R. J. (**2003**). ''Investigations of the precedence effect in budgerigars: Perceived location of auditory images,'' J. Acoust. Soc. Am. **113**, 2159–2170.

Dent, M. L., Larsen, O. N., and Dooling, R. J. (**1997**). ''Free-field binaural unmasking in budgerigars (*Melopsittacus undulatus*),'' Behav. Neurosci. **111**, 590–598.

Freyman, R. L., McCall, D. D., and Clifton, R. K. (**1998**). ''Intensity discrimination for precedence effect stimuli,'' J. Acoust. Soc. Am. **103**, 2031–2041.

Holland, J., Dabelsteen, T., and Larsen Ole, N. (**1998**). ''Degradation of wren Troglodytes troglodytes song: Implications for information transfer and ranging,'' J. Acoust. Soc. Am. **103**, 2154.

Irvine, D. R. F. (**1992**). ''Physiology of the auditory brainstem,'' in *The Mammalian Auditory Pathway: Neurophysiology*, edited by A. N. Popper and R. R. Fay (Springer, New York), pp. 153–231.

Litovsky, R. Y., Colburn, H. S., Yost, W. A., and Guzman, S. J. (**1999**). ''The precedence effect,'' J. Acoust. Soc. Am. **106**, 1633–1654.

Manabe, K., Sadr, E. I., and Dooling, R. J. (**1998**). ''Control of vocal intensity in budgerigars (*Melopsittacus undulatus*): Differential reinforcement of vocal intensity and the Lombard effect,'' J. Acoust. Soc. Am. **103**, 1190–1198.

Marten, K., and Marler, P. (**1977a**). ''Sound transmission and its significance for animal vocalization. I. Temperate habitats,'' Behav. Ecol. Sociobiol. **2**, 271–290.

Marten, K., and Marler, P. (**1977b**). ''Sound transmission and its significance for animal vocalization. II. Tropical forest habitats,'' Behav. Ecol. Sociobiol. **2**, 291–2302.

Martens, M. J. K., van der Heijen, L. A. M., Walthaus, H. H. J., and van Rens, W. J. J. M. (**1985**). ''Classification of soils based on acoustic impedance, air flow resistivity and other physical parameters,'' J. Acoust. Soc. Am. **78**, 970–980.

Mathevon, N., Aubin, T., and Dabelsteen, T. (**1996**). ''Song degradation during propagation: Importance of song post for the wren *Troglodytes troglodytes*,'' Ethology **102**, 397–412.

Morton, E. S. (**1975**). ''Ecological sources of selection on avian sounds,'' Am. Nat. **109**, 17–34.

Nelson, B. S. (**2000**). ''Avian dependence on sound-pressure level as an auditory distance cue,'' Anim. Behav. **59**, 57–67.

Nelson, B. S. (**2002**). ''Duplex auditory distance assessment in a small passerine bird (*Pipilo erythrophthalmus*),'' Behav. Ecol. Sociobiol. **53**, 42–50.

Nelson, B. S., and Stoddard, P. K. (**1998**). ''Accuracy of auditory distance and azimuth perception by a passerine bird in natural habitat,'' Anim. Behav. **56**, 467–477.

Pye, J. D., and Langbauer, Jr., W. R. (**1998**). ''Ultrasound and infrasound,'' in *Animal Acoustic Communication: Sound Analysis and Research Methods*, edited by S. L. Hopp, M. J. Owren, and C. S. Evans (Springer, Berlin).

Roberts, J., Kacelnik, A., and Hunter, M. J. (**1979**). ''A model of sound interference in relation to acoustic communication,'' Anim. Behav. **27**, 1271–1273.

Takahashi, T. T., Moiseff, A., and Konishi, M. (**1984**). ''Time and intensity cues are processed independently in the auditory system of the owl,'' J. Neurosci. **4**, 1781–1786.

Wiley, R. H., and Richards, D. G. (**1982**). ''Adaptations for acoustic communication in birds: Sound transmission and signal detection,'' in *Acoustic Communication in Birds*, edited by D. E. Kroodsma and E. H. Miller (Academic, New York), pp. 132–163.

Effect of pulse polarity and energy on ultrasound-induced lung hemorrhage in adult rats

Leon A. Frizzell[a)]
Bioacoustics Research Laboratory, Department of Electrical and Computer Engineering, University of Illinois at Urbana-Champaign, 405 North Mathews, Urbana, Illinois 61801

James F. Zachary
Bioengineering Program, University of Illinois at Urbana-Champaign, 1406 West Green Street, Urbana, Illinois 61801

William D. O'Brien, Jr.
Bioacoustics Research Laboratory, Department of Electrical and Computer Engineering, University of Illinois at Urbana-Champaign, 405 North Mathews, Urbana, Illinois 61801

(Received 14 June 2002; accepted for publication 21 January 2003)

The objective of this study was to further assess the role of inertial cavitation in ultrasound-induced lung hemorrhage by examining the effect of pulse polarity at a common *in situ* (at the lung surface) peak rarefactional pressure [$p_{r(in\ situ)}$] and at a common *in situ* pulse intensity integral ($\mathrm{PII}_{in\ situ}$). A total of 60 rats was divided into three experimental groups of 20 animals per group and randomly exposed to pulsed ultrasound. The groups were exposed as follows: Group 1 to 0° polarity pulses (compression followed by rarefraction) at a $p_{r(in\ situ)}$ of 3.48 MPa and a $\mathrm{PII}_{in\ situ}$ of 4.78 Ws/m^2, group 2 to 180° polarity pulses (rarefraction followed by compression) at a $p_{r(in\ situ)}$ of 3.72 MPa and a $\mathrm{PII}_{in\ situ}$ of 2.55 Ws/m^2, and group 3 to 180° polarity pulses at a $p_{r(in\ situ)}$ of 4.97 MPa and a $\mathrm{PII}_{in\ situ}$ of 4.79 Ws/m^2. For all experimental groups, the frequency was 2.46 MHz, the exposure duration was 240 s, the pulse repetition frequency was 2.5 kHz, and the pulse duration was 0.42 μs. Six sham animals were also randomly distributed among the experimental animals. The lesion surface area and depth were determined for each rat as well as lesion occurrence (percentage of rats with lesions) per group. It was found that lesion occurrence and size correlated better with $\mathrm{PII}_{in\ situ}$ than with $p_{r(in\ situ)}$, suggesting that a mechanism other than inertial cavitation was responsible for the damage. © *2003 Acoustical Society of America.* [DOI: 10.1121/1.1559176]

PACS numbers: 43.80.Gx [FD]

I. INTRODUCTION

Several research groups have observed ultrasonically produced hemorrhage in the lung. These groups have also been interested in the mechanism of damage.[1–20] Several studies have indicated that heating is not responsible for ultrasound-induced lung hemorrhage,[1,21] and there is agreement that gas in the lung plays a role in ultrasound-induced damage.[2,16] Even though the aerated lung requirement suggests cavitation as the mechanism responsible for lung damage, a distinction must be made between mechanisms involving large gas bodies, such as gas in the alveoli of the lung (38–49 μm[22–24]), and classical inertial cavitation that involves small microbubbles as nuclei (radii on the order of 1 μm or less[25]). Evidence has been slowly accumulating that suggests that the mechanism of damage in the lung may not be inertial cavitation.[17,26,27] There seems to be no dependence on whether the negative or positive pressure components of the ultrasonic pulse cause lithotripter-induced lung damage; however, inertial cavitation is associated with the negative pressure.[28] The frequency dependence may not be the same as that associated with effects due to the presence of contrast agents that quite clearly nucleate inertial cavitation.[29] The hydrostatic pressure dependence of ultrasound-induced lung hemorrhage in mice is not the same as that associated with effects due to inertial cavitation.[17] Albunex does not seem to increase the sensitivity of the lung to pulsed ultrasound.[30] However, there is evidence that suggests the mechanism of damage in rat lung may be inertial cavitation,[10,31] and at least one investigator argues that previously reported studies using overpressure[17] may not conclusively demonstrate that inertial cavitation is not responsible.[32–35]

This study has been designed to further investigate the possible role of inertial cavitation in lung hemorrhage. The peak negative pressure is known to be associated with the onset of inertial cavitation. This fact was the basis for including $p_{r.3}$, the water-based value of the peak rarefactional pressure derated by 0.3 dB/cm-MHz, in the definition of the mechanical index (MI). The MI is the output display quantity intended to indicate the relative likelihood of mechanically induced biological effects associated with an ultrasound examination. Further, it has been shown theoretically that the threshold for inertial cavitation is lower when the rarefaction portion of a pulse precedes the compression portion, rather than when the sequence is reversed.[36–38]

Flynn[36] showed theoretically that there were differences in the temporal response of the bubble radius and the quan-

a)Electronic mail: frizz@uiuc.edu

 0001-4966/2003/113(5)/2912/7/$19.00

TABLE I. Exposimetry quantities. The pulse duration, ultrasonic frequency, and exposure duration for all exposures were 0.42 μs, 2.46 MHz, and 240 s, respectively. For the shams, the pulse repetition frequency was 10 Hz, and for the three experimental groups, the pulse repetition frequency was 2.5 kHz.

Group	Polarity (degrees)	$p_{r(in\ situ)}$ (MPa)	$p_{c(in\ situ)}$ (MPa)	$\mathrm{PII}_{in\ situ}$ ($\mathrm{Ws/m^2}$)	$I_{\mathrm{TA}(in\ situ)}$ ($\mathrm{W/cm^2}$)	MI
Shams	0	0.15	0.18	0.0044	4.4×10^{-6}	0.070
1	0	3.48	9.05	4.78	1.20	1.60
2	180	3.72	4.23	2.55	0.64	1.75
3	180	4.97	6.80	4.79	1.20	2.31

tities associated with bubble collapse depending upon polarity of the pulse. He showed that for the 180° polarity pulse (rarefaction followed by compression) the maximum values for the collapse pressure, $P_{\max}$, and temperature, $T_{\max}$, within the bubble were greater than for the 0° polarity pulse (compression followed by rarefaction), i.e., $P_{\max}=9$ kbar [900 MPa] versus 4.2 kbar [420 MPa], and $T_{\max}=4775$ K versus 3105 K for an acoustic pulse of amplitude 3 bar [0.3 MPa] incident on a 1-μm-radius bubble in water. However, the maximum bubble radius achieved was slightly greater for the 0° polarity pulse. Flynn[36] attributed the lower values of $P_{\max}$ and $T_{\max}$ associated with a 0°-polarity acoustic pulse that gave a larger maximum bubble radius to the ''absence of a positive pressure peak that can do appreciable work on the expanded cavity.''

Consistent with this hypothesis is the work of Apfel and Holland,[39,40] who explored theoretically the threshold for inertial cavitation associated with a single-cycle acoustic pulse. They considered only a pulse that had a rarefaction preceding a compression (180° polarity pulse), clearly implying that they expected this sequence would yield the lowest threshold for inertial cavitation.

Morgan *et al.*[37,38] showed theoretically and experimentally that the acoustic echo amplitude from encapsulated gas contrast agents was greater from incident 180° polarity pulses than from incident 0° polarity pulses. Also, the initiation of the echo pulse coincided with the negative portion of the incident pulse in both cases. Thus, the echo pulse associated with the 0°-polarity pulse did not begin with the initial compression portion of the incident pulse but was delayed until occurrence of the rarefaction portion of the incident pulse. For the 180°-polarity pulse the rarefactional portion of the incident waveform is followed by a compression, which results in a higher bubble wall velocity during collapse and a higher center frequency for the echo. Thus, experimentally and theoretically the 180°-polarity pulse gave a greater response.

The first hypothesis tested for the study reported herein was that inertial cavitation is not responsible for ultrasound-induced lung hemorrhage. To test this hypothesis two different temporal pulse waveforms with the same value of $p_{r(in\ situ)}$ were used, and will be referred to as the 180° (rarefaction followed by compression) and 0° (compression followed by rarefaction) polarity pulses. If this hypothesis were supported, then the 180° polarity pulse would not produce a greater effect on lung than the 0°-polarity pulse. This represents the first test of the effects of pulse polarity on lung hemorrhage with diagnostic-like ultrasound pulses.

Another aspect of this study was to examine the role of the energy associated with the ultrasound exposure. In previous studies[41,27] the energy incident on the lung had been shown to relate to lesion occurrence and lesion size under superthreshold conditions. Thus, we designed this study so that we could also test a second hypothesis, which was that superthreshold lung hemorrhage would correlate with the value of the $\mathrm{PII}_{in\ situ}$ or energy associated with the exposure. To test this hypothesis both the 180°- and 0°-polarity waveforms were used, except that the value of $\mathrm{PII}_{in\ situ}$ was held constant. If this hypothesis were supported, then the effect on the lung would be similar for the two pulses.

II. MATERIALS AND METHODS

A. Exposimetry

Ultrasonic exposures were conducted using a focused, 2.54-mm-diameter, PZT ultrasonic transducer (Valpey Fisher, Hopkinton, MA). Water-based (degassed water, 22 °C) pulse-echo ultrasonic field distribution measurements were performed according to established procedures,[42,19] and yielded a center frequency of 2.46 MHz, a fractional bandwidth of 38%, a −6-dB beamwidth of 1.54 mm, a −6-dB depth of focus of 14.4 mm, and a focal length of 39 mm. An automated procedure was used to routinely calibrate the ultrasound fields[43,44,19] (Table I) that was based on established standards.[45,46] Briefly, the source transducer's drive voltage was supplied by a RAM5000 (Ritec, Inc., Warwick, RI). A calibrated PVDF membrane hydrophone (Marconi model Y-34-6543, Chelmsford, UK) was mounted to the computer-controlled micropositioning system (Daedal, Inc., Harrisburg, PA). The hydrophone's signal was digitized with an oscilloscope (500 Ms/s, LeCroy model 9354TM, Chestnut Ridge, NY), the output of which was fed to the same computer (Dell Pentium II, Dell Corporation, Round Rock, TX) that controlled the positioning system. Off-line processing (MATLAB, The Mathworks, Natick, MA) yielded the peak water-based rarefactional pressure $p_{r(in\ vitro)}$, the peak water-based compressional pressure $p_{c(in\ vitro)}$, and the water-based pulse intensity integral ($\mathrm{PII}_{in\ vitro}$). The temporal-average intensity (I_{TA}) at the focus was calculated. The mechanical index (MI) was also determined.[45] The MI is reported because it is a regulated quantity[47,48] of diagnostic ultrasound systems, and its value is available to system operators. Thus, there is value to provide the MI for each of our exposure settings in order to give general guidance to manu-

facturers and operators as to the levels we are using in this study. Further, it is a quantity that cannot be determined directly from $p_{r(in\ situ)}$.

The two different polarity pulses were obtained by changing the polarity of the applied electrical signal; examples of the recorded acoustic waveforms measured in water are shown in Fig. 1. It is readily seen that these waveforms contain more than one cycle. As expected for experimental sources the pulse increases in amplitude to a maximum and then decreases, in this case including on the order of three complete cycles. This necessitates a very clear definition of the 0°- and 180°-polarity waveforms used in this study. The 0°-polarity waveform is defined as one having the first of the two largest half-cycles as a compression, while the 180°-polarity waveform has the first of the two largest half-cycles as a rarefaction. This is entirely consistent with the definition of 0°- and 180°-polarity pulses as used by Morgan *et al.*[38] for their pulses that consisted of approximately two complete cycles.

Fourteen independent calibrations were performed weekly during the time period of the experiment. One set of calibrations was performed before exposures were initiated each week and one set of calibrations was performed after exposures were concluded for each week. Relative standard deviations (standard deviation/mean) of $p_{r(in\ vitro)}$ and $p_{c(in\ vitro)}$ were 6% and 9%, respectively. The relative standard deviation of $\mathrm{PII}_{in\ vitro}$ was 11%.

The *in situ* (at the pleural surface) peak rarefactional pressures, peak compressional pressures, and pulse intensity integrals were estimated from their respective *in vitro* values, the mean attenuation coefficient of the chest wall's intercostal tissue (2.5 dB/cm at 2.46 MHz),[49] and the mean chest-wall thickness (66 rats: 4.76 ± 0.11 mm). The experimental findings were analyzed and reported in terms of the *in situ* peak rarefractional pressure $p_{r(in\ situ)}$, *in situ* peak compressional pressure $p_{c(in\ situ)}$, *in situ* pulse intensity integral $\mathrm{PII}_{in\ situ}$, the temporal-average intensity $I_{\mathrm{TA}(in\ situ)}$, and mechanical index MI (Table I).

B. Animals

The experimental protocol was approved by the campus' Laboratory Animal Care Advisory Committee and satisfied all campus and National Institutes of Health rules for the humane use of laboratory animals. Animals were housed in an AAALAC-approved animal facility, placed in groups of three or four in polycarbonate cages with beta-chip bedding and wire bar lids, and provided food and water *ad libitum*. The AAALAC (Association for Assessment and Accreditation of Laboratory Animal Care, Rockville, MD) is a private nonprofit organization that promotes the humane treatment of animals in science through a voluntary accreditation program.

A total of 60 10- to-11-week-old 327 ± 22-gram female Sprague-Dawley rats (Harlan, Indianapolis, IN) were assigned to one of three experimental groups at random (Table I). An additional six rats were assigned as shams and incorporated into the randomized design. All experimental animals were exposed to 2.46-MHz ultrasound with a 2.5-kHz pulse repetition frequency and a 240-s exposure duration.

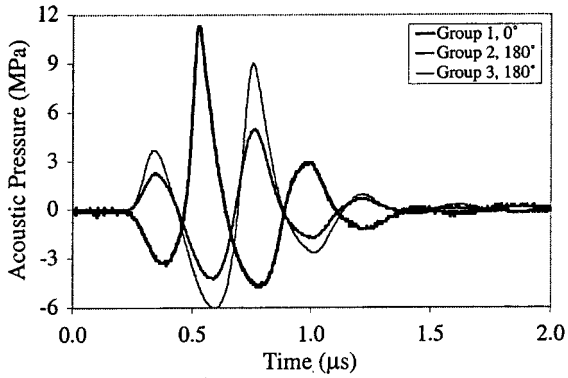

FIG. 1. Measured ultrasonic pressure waveforms in water for the three experimental groups: Group 1, 0° polarity, $p_{r(in\ situ)} = 3.48$ MPa, $\mathrm{PII}_{in\ situ} = 4.78$ Ws/m^2; group 2, 180° polarity, $p_{r(in\ situ)} = 3.72$ MPa, $\mathrm{PII}_{in\ situ} = 2.55$ Ws/m^2; and group 3, 180° polarity, $p_{r(in\ situ)} = 4.97$ MPa, $\mathrm{PII}_{in\ situ} = 4.79$ Ws/m^2.

Experimental group 1 consisted of animals exposed with 0°-polarity pulses and served as the baseline comparison group [$p_{r(in\ situ)} = 3.48$ MPa and $\mathrm{PII}_{in\ situ} = 4.78$ Ws/m^2]. The other two groups were both exposed with pulses of polarity 180°. Group 2 was designed to have the same peak rarefactional pressure [$p_{r(in\ situ)} = 3.72$ MPa and $\mathrm{PII}_{in\ situ} = 2.55$ Ws/m^2] as group 1, and group 3 was designed to have the same pulse intensity integral [$p_{r(in\ situ)} = 4.97$ MPa and $\mathrm{PII}_{in\ situ} = 4.79$ Ws/m^2] as group 1. The actual values for quantities designed to be the same vary slightly because of variation in the mean chest-wall thickness among the groups. Sample waveforms measured in water are shown in Fig. 1 for the three experimental groups. The baseline exposure for group 1 was chosen to be at a superthreshold level corresponding to approximately 50% lesion occurrence based on previous results,[18,19,49] so that changes in lesion occurrence and size could be easily compared among the groups.

Rats were weighed and then anesthetized with ketamine hydrochloride (87.0 mg/kg) and xylazine (13.0 mg/kg) administered intraperitoneally. The skin of the left thorax was exposed by removing the hair with an electric clipper, followed by a depilatory agent (Nair® Carter-Wallace, Inc., New York, NY) to maximize sound transmission. A black dot was placed on the skin over the ribs at approximately the sixth to ninth rib to guide the positioning of the ultrasonic beam. Anesthetized animals were placed in a specially designed holder to which the ultrasonic transducer was attached. A removable pointer, attached to the transducer, was used to position the ultrasonic beam perpendicular to the skin at the position of the black dot with the beam's focal region approximately at the lung surface.[19] The ultrasonic beam was incident on the lateral surface of the lung.

The holder with the animal and mounted transducer was placed in highly degassed, temperature-controlled (30 °C) water. The low-power pulse-echo capability of the RAM5000 exposure system displayed on an oscilloscope was used to adjust the axial center of the focal region to within 1 mm of the lung surface. It was during this part of the experimental procedure that the 13-ohm in-line attenuator was placed between the RAM5000 and transducer to obtain very low exposure values (see the row ''shams'' in

TABLE II. Percentage of animals with lesions and means (±s.d.) for lesion depth, surface area, and volume for shams and experimental groups.

Group	Number of animals	Lesion occurrence (percent)	Lesion depth (mm)	Lesion surface area (mm^2)	Lesion volume (mm^3)
Shams	6	17	0.18 (±0.43)	0.62 (±1.5)	0.22 (±0.54)
1	20	50	0.49 (±0.53)	1.58 (±2.4)	0.57 (±0.99)
2	20	10	0.08 (±0.24)	0.14 (±0.49)	0.04 (±0.13)
3	20	60	0.64 (±0.85)	2.29 (±3.0)	1.23 (±0.99)

Table I for these low-level ultrasonic pressure levels). Also, the pulse repetition frequency was reduced to 10 Hz during this alignment procedure. The ultrasound propagation medium between the transducer and the animal's skin surface was highly degassed water, as was used for transducer calibrations. Animals were exposed to pulsed ultrasound with a pulse repetition frequency of 2.5 kHz and an exposure duration of 240 s. Following exposure, rats were removed from the water and holder, and euthanized under anesthesia by cervical dislocation.

The left thoracic wall was opened and the thickness of the intercostal tissue (skin, fat, fascia, muscle, and parietal pleura) between the ribs was measured with a digital micrometer (accuracy: 10 μm) at the black dot used for transducer alignment. These chest-wall measurements were used for later calculation of the *in situ* ultrasonic pressures at the visceral pleural surface. The lungs were removed from each animal and the left lung was scored for the presence or absence of hemorrhage. As previously reported,[17,19] and also observed in this study, lung hemorrhage formed along the pathway of the ultrasound beam and the lesion assumed a conical shape. The base of the lesion originated at the visceral pleural surface and was elliptical in shape. The lesion extended into lung parenchyma to form its apex at varied depths within the lung. The left lung was fixed by immersion in 10% neutral-buffered formalin for a minimum of 24 h. After fixation, the elliptical dimensions of each lung lesion at the visceral pleural surface were measured using a digital micrometer where ''a'' is the semimajor axis and ''b'' is the semiminor axis. The lesion was then bisected and the depth ''d'' of the lesion within the pulmonary parenchyma was also measured. The surface area (πab) and volume (πabd/3) of the lesion were calculated for each animal. Each half of the bisected lesion was embedded in paraffin, sectioned at 5 μm, stained with hematoxylin and eosin, and evaluated microscopically.

C. Statistics

The lesions' depth, surface area, and volume were compared among the groups to determine if differences were significant. Groups were determined to be significantly different at the 0.05 level if the ranges defined by their (mean) ± 1.96× (standard error of the mean) did not overlap. Otherwise the differences were not significant.

III. RESULTS

The fraction of animals with lesions was determined for the shams and each of the three experimental groups (Table II and Figs. 2 and 3). The fraction of animals with hemorrhage in the shams was 17% (one out of six rats) and for groups 1, 2, and 3 was 50%, 10%, and 60% (each out of 20 rats), respectively.

The means and standard deviations for depth, surface area, and volume of the lesions for the shams and groups 1, 2, and 3 are shown in Table II and Fig. 3. Although the lesion volume was not measured directly, it was calculated from the surface area and the depth of the lesion and is provided here for completeness. For all three lesion size quantities, there was a statistically significant difference between groups 1 and 2, but no significant difference between groups 1 and 3.

IV. DISCUSSION

Two hypotheses related to the determination of the mechanism for lung hemorrhage were tested in this study. The first hypothesis was that ultrasound-induced lung hemorrhage is not caused by inertial cavitation. The threshold for inertial cavitation depends upon peak rarefactional pressure, and both theoretical and experimental results predict that quantities associated with bubble collapse (maximum collapse pressure, maximum collapse temperature, and wall speed during collapse) are greater when the rarefactional portion of a pulse precedes the compressional portion of the pulse. These theoretical and experimental observations were

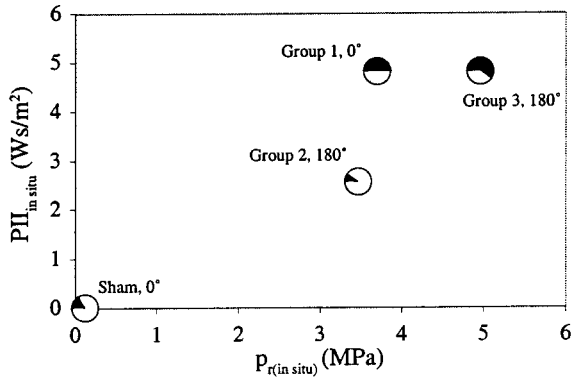

FIG. 2. Fraction of animals with lesions versus $p_{r(in\ situ)}$ and $PII_{in\ situ}$ for sham and experimental groups. The fraction of the circles colored black represents the fraction of animals with lesions.

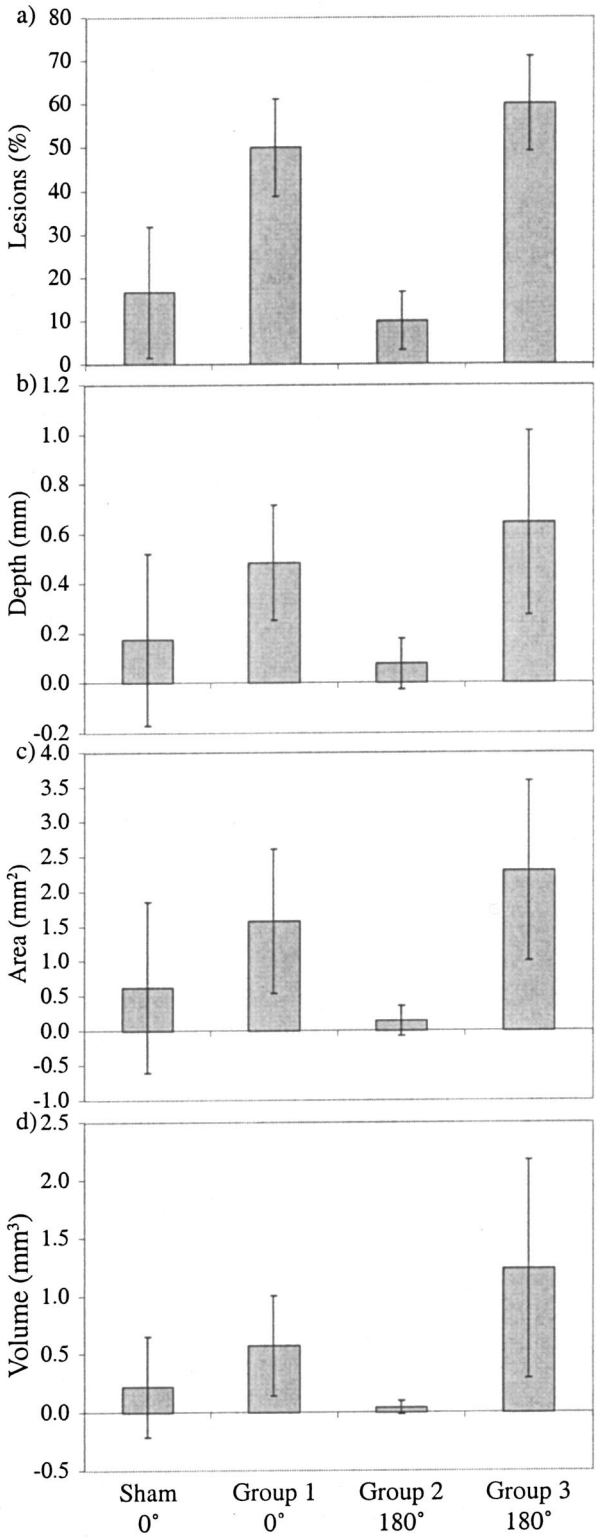

FIG. 3. Lesion (a) occurrence; (b) depth; (c) surface area; and (d) volume for sham and experimental groups.

the basis for the design of two of the experimental groups in this study. Experimental groups 1 and 2 were designed to have the same peak rarefactional pressure; one group had the compressional portion first (group 1, 0°) and the other had the rarefactional portion first (group 2, 180°). The actual peak rarefactional pressures were slightly different for the two groups because the mean chest-wall thicknesses differed. Note that the largest two pulses in the waveform were used to determine whether the rarefactional peak was second or first and that this was consistent with the definition of 0° and 180° pulses, respectively, as used by Morgan *et al.*[38] If inertial cavitation was the primary mechanism responsible for lesion production, then the lesion percentage for group 2 should have been greater than that for group 1. Instead, exactly the opposite occurred (Table II and Figs. 2 and 3), which supports the hypothesis by providing direct evidence that inertial cavitation was not the primary mechanism responsible for the lung damage.

The second hypothesis tested was that the lung hemorrhage would correlate with the value of the $PII_{in\ situ}$ or energy associated with the exposure. In previous studies,[41,27] the energy incident on the lung had been shown to relate to lesion occurrence and lesion size under superthreshold conditions. Thus, another experimental group (group 3, $PII_{in\ situ}=4.79\ Ws/m^2$) was established to have the same pulse intensity integral as group 1 ($PII_{in\ situ}=4.78\ Ws/m^2$). Again, there was a very small difference in the value of the pulse intensity integral between the two groups due to chest-wall thickness differences. Because the transducer, frequency, pulse repetition frequency, and exposure duration were the same for all three groups, the power and energy incident on the lung surface for these two groups were proportional to $PII_{in\ situ}$. The results show that lesion occurrence was nearly the same for these two groups (group 1 = 50% and group 3 = 60%). This result supported the second hypothesis and lends even further experimental evidence that inertial cavitation was not involved because lesion occurrence at these superthreshold conditions correlated better with incident energy than with peak rarefactional pressure.

Similar results were observed when lesion depth, surface area, and volume were examined. For all three of these lesion size quantities, there were statistically significant differences between groups 1 and 2, but no significant differences between groups 1 and 3 (Table II and Fig. 3).

The pulses used in this study consisted not of a simple single cycle or half-cycle but of multiple cycles that were much more representative of diagnostic pulses. In this respect, they were similar to pulses used by Morgan *et al.*[37,38] and had the advantage of mimicking real-world ultrasound exposures. However, they had the disadvantage that as a result of transducer response and nonlinear propagation, the pulses for the three groups differed in ways other than simply the pulse polarity and amplitude adjustment for common peak rarefactional pressure or common pulse intensity integral. For example, the peak compressional pressure was greater for groups 1 and 3 than for group 2. However, this difference also supported the conclusion that inertial cavitation was not responsible for the lung hemorrhage because inertial cavitation is not associated with the peak compressional pressure.

This analysis is of course not complete without considering the sham exposed animals. One of the six sham animals used in this study had a lesion. In the last several years, we have conducted experiments involving exposure of the lung in approximately 1500 rats. Each of these experiments involved shams and we have used approximately 150 rats as

shams. Prior to this study in no case has there ever been any lesions found in the shams. That previous experience and the fact that the lesion in the one sham animal reported herein was quite large leads us to believe that this lesion is an outlier. Even though we are convinced that is the case, the results for this animal had to be included with our analysis. The sham exposed animals exhibited a lesion occurrence and lesion dimensions that were greater than in group 2, but smaller than groups 1 and 3 (Table II and Figs. 2 and 3). Statistical comparisons between any of the experimental groups and the shams have limited meaning because only one sham animal had a lesion, leading to a very large standard error of the mean and no real statistical significance between the shams and any of the three experimental groups. This in no way lessens the statistical comparisons among the experimental groups that were presented above.

Finally, the MI was developed to provide an estimate of the potential for mechanically induced bioeffects,[45] and is given by

$$\mathrm{MI}=\frac{p_{r.3}}{\sqrt{f}}, \tag{1}$$

where $p_{r.3}$ is the water-based peak rarefactional pressure derated by 0.3 dB/cm-MHz at the location where the derated pulse intensity integral $\mathrm{PII}_{.3}$ is a maximum and f is the ultrasonic frequency in megahertz. The MI measurement procedure[45] was that used to determine the MI reported herein (Table I). The frequency dependence built into the MI was developed specifically to reflect the best idea as to the dependence of the likelihood for inertial cavitation on frequency under specified conditions.[16,40,45] The results of this study provide further evidence that the MI is not a good predictor of lung hemorrhage.

ACKNOWLEDGMENTS

We thank J. Blue, R. Miller, K. Norrell, and B. Zierfuss for technical contributions. This work was supported by NIH Grant HL58218 awarded to W.D.O. and J.F.Z.

[1] S. Z. Child, C. L. Hartman, L. A. Schery, and E. L. Carstensen, "Lung damage from exposure to pulsed ultrasound," Ultrasound Med. Biol. **16**, 817–825 (1990).
[2] C. Hartman, S. Z. Child, R. Mayer, E. Schenk, and E. L. Carstensen, "Lung damage from exposure to the fields of an electrohydraulic lithotripter," Ultrasound Med. Biol. **16**, 675–679 (1990).
[3] D. P. Penney, E. A. Schenk, K. Maltby, C. Hartman-Raeman, S. Z. Child, and E. L. Carstensen, "Morphologic effects of pulsed ultrasound in the lung," Ultrasound Med. Biol. **19**, 127–135 (1993).
[4] C. H. Raeman, S. Z. Child, and E. L. Carstensen, "Timing of exposures in ultrasonic hemorrhage of murine lung," Ultrasound Med. Biol. **19**, 507–517 (1993).
[5] L. A. Frizzell, E. Chen, and C. Lee, "Effects of pulsed ultrasound on the mouse neonate: Hind limb paralysis and lung hemorrhage," Ultrasound Med. Biol. **20**, 53–63 (1994).
[6] C. K. Holland, K. Sandstrom, X. Zheng, J. Rodriguey, and R. A. Roy, "The acoustic field of a pulsed Doppler diagnostic ultrasound system near a pressure-release surface," J. Acoust. Soc. Am. **95**, 2855(A) (1994).
[7] A. F. Tarantal and D. R. Canfield, "Ultrasound-induced lung hemorrhage in the monkey," Ultrasound Med. Biol. **20**, 65–72 (1994).
[8] J. F. Zachary and W. D. O'Brien, Jr., "Lung lesions induced by continuous- and pulsed-wave (diagnostic) ultrasound in mice, rabbits, and pigs," Vet. Pathol. **32**, 43–54 (1995).
[9] R. Baggs, D. P. Penney, C. Cox, S. Z. Child, C. H. Raeman, D. Dalecki, and E. L. Carstensen, "Thresholds for ultrasonically induced lung hemorrhage in neonatal swine," Ultrasound Med. Biol. **22**, 119–128 (1996).
[10] C. K. Holland, C. X. Deng, R. E. Apfel, J. L. Alderman, L. A. Ferandez, and K. J. W. Taylor, "Direct evidence of cavitation *in vivo* from diagnostic ultrasound," Ultrasound Med. Biol. **22**, 917–925 (1996).
[11] C. H. Raeman, S. Z. Child, D. Dalecki, C. Cox, and E. L. Carstensen, "Exposure-time dependence of the threshold for ultrasonically induced murine lung hemorrhage," Ultrasound Med. Biol. **22**, 139–141 (1996).
[12] D. Dalecki, S. Z. Child, C. H. Raeman, C. Cox, D. P. Penny, and E. L. Carstensen, "Age dependence of ultrasonically induced lung hemorrhage in mice," Ultrasound Med. Biol. **23**, 767–776 (1997).
[13] D. Dalecki, S. Z. Child, C. H. Raeman, C. Cox, and E. L. Carstensen, "Ultrasonically induced lung hemorrhage in young swine," Ultrasound Med. Biol. **23**, 777–781 (1997).
[14] W. D. O'Brien, Jr. and J. F. Zachary, "Lung damage assessment from exposure to pulsed-wave ultrasound in the rabbit, mouse, and pig," IEEE Trans. Ultrason. Ferroelectr. Freq. Control **44**, 473–485 (1997).
[15] WFUMB Symposium on Safety of Ultrasound in Medicine: Issues and Recommendations Regarding Non-Thermal Mechanisms for Biological Effects of Ultrasound [Ultrasound Med. Biol. **24**, Supplement 1, S1–S55 (1998)].
[16] *Mechanical Bioeffects from Diagnostic Ultrasound: AIUM Consensus Statements* (American Institute of Ultrasound in Medicine, Laurel, MD, 1998). Also, J. Ultrasound Med. **19**, 67–168 (2000).
[17] W. D. O'Brien, Jr., L. A. Frizzell, R. M. Weigel, and J. F. Zachary, "Ultrasound-induced lung hemorrhage is not caused by inertial cavitation," J. Acoust. Soc. Am. **108**, 1290–1297 (2000).
[18] W. D. O'Brien, Jr., L. A. Frizzell, D. J. Schaeffer, and J. F. Zachary, "Superthreshold behavior of ultrasound induced lung hemorrhage in adult mice and rats: Role of pulse repetition frequency and pulse duration," Ultrasound Med. Biol. **27**, 267–277 (2001).
[19] J. F. Zachary, J. M. Sempsrott, L. A. Frizzell, D. G. Simpson, and W. D. O'Brien, Jr., "Superthreshold behavior and threshold estimation of ultrasound-induced lung hemorrhage in adult mice and rats," IEEE Trans. Ultrason. Ferroelectr. Freq. Control **48**, 581–592 (2001).
[20] J. F. Zachary, L. A. Frizzell, K. S. Norrell, J. P. Blue, Jr., R. J. Miller, and W. D. O'Brien, Jr., "Temporal and spatial evaluation of lesion reparative responses following superthreshold exposure of rat lung to pulsed ultrasound," Ultrasound Med. Biol. **27**, 829–839 (2001).
[21] C. L. Hartman, S. Z. Child, D. P. Penney, and E. L. Carstensen, "Ultrasonic heating of lung tissue," J. Acoust. Soc. Am. **91**, 513–516 (1992).
[22] M. L. Crosfill and J. G. Widdicombe, "Physical characteristics of the chest and lungs and the work of breathing in different mammalian species," J. Physiol. (London) **158**, 1–14 (1961).
[23] S. M. Tenney and J. E. Remmers, "Comparative quantitative morphology of the mammalian lung: Diffusing area," Nature (London) **197**, 54–56 (1963).
[24] E. R. Weibel, "Dimensions of the tracheobronchial tree and alveoli," in *Biological Handbooks: Respiration and Circulation*, edited by P. L. Altman and D. S. Dittmer (Federation of American Societies for Experimental Biology, Bethesda, MD), Chap. 51.
[25] H. G. Flynn and C. C. Church, "Transient pulsations of small gas bubbles in water," J. Acoust. Soc. Am. **84**, 985–998 (1988).
[26] E. L. Carstensen, S. Gracewski, and D. Dalecki, "The search for cavitation *in vivo*," Ultrasound Med. Biol. **26**, 1377–1385 (2000).
[27] W. D. O'Brien, Jr., J. M. Kramer, T. G. Waldrop, L. A. Frizzell, and J. F. Zachary, "Ultrasound-induced lung hemorrhage: Role of acoustic boundary conditions at the pleural surface," J. Acoust. Soc. Am. **111**, 1102–1109 (2002).
[28] M. R. Bailey, D. Dalecki, S. Z. Child, C. H. Raeman, D. P. Penney, D. T. Blackstock, and E. L. Carstensen, "Bioeffects of positive and negative acoustic pressures *in vivo*," J. Acoust. Soc. Am. **100**, 3941–3946 (1996).
[29] E. L. Carstensen, D. Dalecki, S. M. Gracewski, and T. Christopher, "Nonlinear propagation and the output indices," J. Ultrasound Med. **18**, 69–80 (1999).
[30] C. H. Raeman, D. Dalecki, S. Z. Child, R. S. Meltzer, and E. L. Carstensen, "Albunex does not increase the sensitivity of the lung to pulsed ultrasound," Echocardiography **14**, 553–557 (1997).
[31] C. K. Holland, R. A. Roy, R. W. Biddinger, C. J. Disimile, and C. Cawood, "Cavitation mediated rat lung bioeffects from diagnostic ultrasound," J. Acoust. Soc. Am. **109**, 2433(A) (2001).
[32] R. E. Apfel, Comment on "Ultrasound-induced lung hemorrhage is not caused by inertial cavitation," J. Acoust. Soc. Am. **110**, 1737 (2001).

[33] R. E. Apfel, ''Reply to Frizzell *et al.*'s comment to our comment,'' J. Acoust. Soc. Am. **110**, 1740 (2001).
[34] L. A. Frizzell, J. M. Kramer, J. F. Zachary, and W. D. O'Brien, Jr., Response to ''Comment on 'Ultrasound-induced lung hemorrhage is not caused by inertial cavitation,'' J. Acoust. Soc. Am. **110**, 1738–1739 (2001).
[35] L. A. Frizzell, J. M. Kramer, J. F. Zachary, and W. D. O'Brien, Jr., ''Comment on Apfel's second comment,'' J. Acoust. Soc. Am. **110**, 1742 (2001).
[36] H. G. Flynn, ''Generation of transient cavities in liquids by microsecond pulses of ultrasound,'' J. Acoust. Soc. Am. **72**, 1926–1932 (1982).
[37] K. Morgan, M. Averkiou, and K. Ferrara, ''The effect of the phase of transmission on contrast agent echoes,'' IEEE Trans. Ultrason. Ferroelectr. Freq. Control **45**, 872–875 (1998).
[38] K. E. Morgan, J. S. Allen, P. A. Dayton, J. E. Chomas, A. L. Klibanov, and K. W. Ferrara, ''Experimental and theoretical evaluation of microbubble behavior: Effect of transmitted phase and bubble size,'' IEEE Trans. Ultrason. Ferroelectr. Freq. Control **47**, 1494–1509 (2000).
[39] R. E. Apfel, ''Possibility of microcavitation from diagnostic ultrasound,'' IEEE Trans. Ultrason. Ferroelectr. Freq. Control **33**, 139–142 (1986).
[40] C. K. Holland and R. E. Apfel, ''An improved theory for the prediction of microcavitation due to pulsed ultrasound,'' IEEE Trans. Ultrason. Ferroelectr. Freq. Control **36**, 204–208 (1989).
[41] W. D. O'Brien, Jr., D. G. Simpson, L. A. Frizzell, and J. F. Zachary, ''Superthreshold behavior and threshold estimates of ultrasound-induced lung hemorrhage in adult rats: Role of beamwidth,'' IEEE Trans. Ultrason. Ferroelectr. Freq. Control **48**, 1695–1705 (2001).
[42] K. Raum and W. D. O'Brien, Jr., ''Pulse-echo field distribution measurement technique of high-frequency ultrasound sources,'' IEEE Trans. Ultrason. Ferroelectr. Freq. Control **44**, 810–815 (1997).
[43] J. M. Sempsrott and W. D. O'Brien, Jr., ''Experimental Verification of Acoustic Saturation,'' in Proceedings of the 1999 IEEE Ultrasonics Symposium, 1999, pp. 1287–1290.
[44] J. M. Sempsrott, ''Experimental Evaluation of Acoustic Saturation,'' MS thesis, Department of Electrical and Computer Engineering, University of Illinois, Urbana, IL, 2000.
[45] *Acoustic Output Measurement Standard for Diagnostic Ultrasound Equipment* (American Institute of Ultrasound in Medicine, Laurel, MD, and National Electrical Manufacturers Association, Rosslyn, VA, 1998).
[46] *Standard for the Real-Time Display of Thermal and Mechanical Acoustic Output Indices on Diagnostic Ultrasound Equipment, Rev 1* (American Institute of Ultrasound in Medicine, Laurel, MD, and National Electrical Manufacturers Association, Rosslyn, VA, 1998).
[47] *Use of Mechanical Index in Place of Spatial Peak, Pulse Average Intensity in Determining Substantial Equivalence* (Center for Devices and Radiological Health, US Food and Drug Administration, Rockville, MD, 14 April 1994).
[48] *Information for Manufacturers Seeking Marketing Clearance of Diagnostic Ultrasound Systems and Transducers* (Center for Devices and Radiological Health, US Food and Drug Administration, Rockville, MD, 30 September 1997).
[49] G. A. Teotico, R. J. Miller, L. A. Frizzell, J. F. Zachary, and W. D. O'Brien, Jr., ''Attenuation coefficient estimates of mouse and rat chest wall,'' IEEE Trans. Ultrason. Ferroelectr. Freq. Control **48**, 593–601 (2001).

Pulse register phonation in Diana monkey alarm calls

Tobias Riede[a)]
Department of Psychology, 245 Uris Hall, Cornell University, Ithaca, New York 14853

Klaus Zuberbühler[b)]
School of Psychology, University of St. Andrews, St. Andrews, Fife KY 16 9JU, Scotland, United Kingdom

(Received 4 October 2002; revised 7 February 2003; accepted 24 February 2003)

The adult male Diana monkeys (*Cercopithecus diana*) produce predator-specific alarm calls in response to two of their predators, the crowned eagles and the leopards. The acoustic structure of these alarm calls is remarkable for a number of theoretical and empirical reasons. First, although pulsed phonation has been described in a variety of mammalian vocalizations, very little is known about the underlying production mechanism. Second, Diana monkey alarm calls are based almost exclusively on this vocal production mechanism to an extent that has never been documented in mammalian vocal behavior. Finally, the Diana monkeys' pulsed phonation strongly resembles the pulse register in human speech, where fundamental frequency is mainly controlled by subglottal pressure. Here, we report the results of a detailed acoustic analysis to investigate the production mechanism of Diana monkey alarm calls. Within calls, we found a positive correlation between the fundamental frequency and the pulse amplitude, suggesting that both humans and monkeys control fundamental frequency by subglottal pressure. While in humans pulsed phonation is usually considered pathological or artificial, male Diana monkeys rely exclusively on pulsed phonation, suggesting a functional adaptation. Moreover, we were unable to document any nonlinear phenomena, despite the fact that they occur frequently in the vocal repertoire of humans and nonhumans, further suggesting that the very robust Diana monkey pulse production mechanism has evolved for a particular functional purpose. We discuss the implications of these findings for the structural evolution of Diana monkey alarm calls and suggest that the restricted variability in fundamental frequency and robustness of the source signal gave rise to the formant patterns observed in Diana monkey alarm calls, used to convey predator information. [DOI: 10.1121/1.1567278]

PACS numbers: 43.80.Ka [WA]

I. INTRODUCTION

The vocalizations of many mammals are the result of two distinct components: the oscillating vocal folds within the larynx produce a primary acoustic signal, which then undergoes a filtering process within the vocal tract where various frequency bands are dampened to different degrees (van den Berg, 1958; Fant, 1960; Titze, 1994; Owren and Linker, 1995). Basic vocal fold behavior can be described as the following: *Bernoulli* forces cause the vocal folds (if close to each other) to be sucked together, creating a closed airspace below the glottis. Continued subglottal air pressure from the lungs builds up underneath the closed folds. Once this pressure becomes high enough, the folds are blown outward, thus opening the glottis and releasing a single ''puff'' of air (van den Berg, 1958). As the subglottal pressure increases, two effects can be observed. First, the motion of the vocal folds becomes faster (demonstrated in computer models: Ishizaka and Flanagan, 1972; Steinecke and Herzel, 1995, and *in vitro*: Titze, 1989). Second, the sound pressure level increases (Gramming, 1988; Titze, 1994). The fundamental frequency of the sound produced by the vocal folds is additionally directly related with the tension of the vocal fold tissue (Titze, 1989, 1991).

Adult male Diana monkeys (*Cercopithecus diana*) produce acoustically distinct alarm calls to two of their predators, the crowned eagle and the leopard (Zuberbühler *et al.*, 1997; Zuberbühler, 2000a). Playback experiments have shown that nearby listeners respond to these alarm calls as if the corresponding predator were present, suggesting that these calls inform nearby recipients about important ongoing events in the environment (Zuberbühler *et al.*, 1999; Zuberbühler, 2000b). Acoustically, the Diana monkeys' alarm vocalizations consist of a bout of calls. Bouts vary in the number of calls from one to more than a dozen. Individual calls are characterized by a highly stereotypic pulse pattern and calls are interspersed by short harmonic elements (Fig. 1).

The single pulses within each call resemble a damped oscillation: a rapid, transient change in signal amplitude from a baseline value to a higher or lower value, followed by a rapid return to the baseline value. Elsewhere, we showed that the formant peak frequency and formant transition of the pulse elements is the single most important parameter to differentiate eagle versus leopard alarm calls (Riede and Zuberbühler, in press), suggesting that similar to human speech sounds, some primate vocalizations convey important semantic information by formant structures. Although research

[a)]Present address and address for correspondence: Tobias Riede, 315 Jordan Hall, School of Medicine, Indiana University, Bloomington, IN 47405. Electronic mail: tobiasriede@web.de
[b)]Electronic mail: kz3@st-andrews.ac.uk

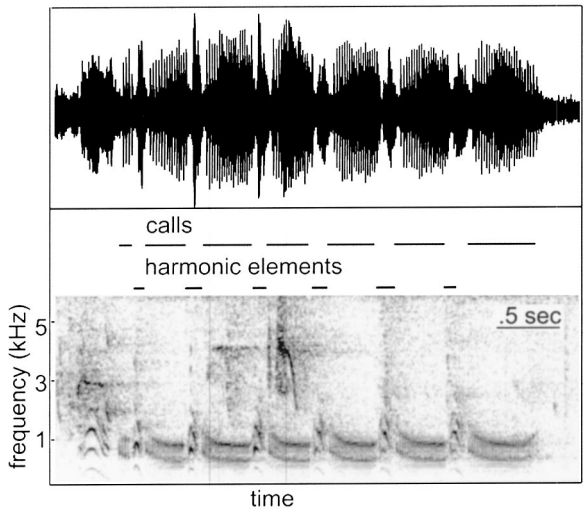

FIG. 1. Time domain and spectrogram of a leopard alarm bout, consisting of seven calls. Basic unit of the call is the pulse as shown in the ''zoom in'' picture of Fig. 2.

on the structural evolution of animal vocalizations is not new (Morton, 1977), comparatively little is still known about how natural and sexual selection affected the acoustic structure of primate alarm calls (Zuberbühler, 2003). Here, we provide a detailed acoustic analysis of the source characteristics of Diana monkey alarm calls to elucidate the adaptive significance and physiological constraints of this remarkable vocalization.

Human speech sounds can be produced using three different registers. A register can be described by the frequency range covered and by the specific mode of vocal fold behavior by which it is produced (e.g., Hollien, 1974; Titze, 1994; Svec *et al.*, 1999). Although each register covers a certain frequency range, neighboring registers overlap significantly. Normal speech is delivered in the so-called modal (or chest) register (fundamental frequency range 100–300 Hz). Humans are also capable to produce speech using either the falsetto (or flagolet) register (fundamental frequency $>$300 Hz) or the pulse (or vocal fry) register [fundamental frequency $<$100 Hz (Blomgren *et al.*, 1998)]. Recent studies suggest the existence of a separate fourth register, i.e., the vocal-ventricular phonation mode, like pulse register covering the frequency range below 100 Hz but unlike pulse register involving the ventricular folds (''false folds'') into the mode of production (Fuks *et al.*, 1998; Lindestad *et al.*, 2001). According to this terminology we used the term ''pulse register'' to describe the Diana monkey calls, because these vocalizations strongly resemble the pulse register of humans [see Blomgren *et al.* (1998) for a review].

Pulse register differs in acoustical, physiological, and perceptual characteristics from other phonation types [reviewed in Gerratt and Kreiman (2001)]. Vocal fold vibration during pulse register is characterized by glottal pulses of alternating amplitudes or by irregular trains of pulses (Hollien and Michel, 1968). The vocal fold length is shorter for the pulse register than for even the lowest frequency of phonation in the modal register (Hollien *et al.*, 1969). The vocal fold vibratory pattern of the pulse register in humans exhibits a very short open period (probably less than 25% of the entire cycle) and a very long period where the vocal folds are completely adducted and a small vocal fold excursion (Hollien *et al.*, 1977).

The fundamental frequency is affected by different factors in each of the three registers. In the modal register, the fundamental frequency is mainly determined by changes in vocal fold length and stiffness (Murry and Brown, 1971). Moreover, there is a positive correlation between vocal fold thickness (i.e., mass, length, and stiffness) and fundamental frequency [reviewed in Titze (1994)]. This relationship is absent in the pulse register (Hollien *et al.*, 1969; Allen and Hollien, 1973). Instead, the fundamental frequency of the pulse register appears to be predominantly determined by changes in subglottal air pressure.

To investigate the vocal production mechanism of the Diana monkey, we analyzed the relationship between call amplitude (a reliable estimator of subglottal pressure) and fundamental frequency. We predicted a positive relationship between these two parameters if Diana monkey alarm calls are the product of the same source production mechanism that is responsible for the human pulse register.

A second aim of this study was to investigate the role of nonlinear phenomena in the vocalizations of Diana monkey alarm calls. Nonlinear phenomena are relevant in this context because they can be directly related to events at the laryngeal source. Several lines of research suggest that nonlinear phenomena are common and ubiquitous in mammalian vocalization behavior (Wilden *et al.*, 1998; Mergell *et al.*, 1999; Riede *et al.*, 1997, 2000; Fischer *et al.*, 2000). Phenomena such as frequency jumps, subharmonics, biphonation, and deterministic chaos are commonly observed, usually the result of deviations from the regular harmonic vibration pattern of the vocal folds, such as nonsynchronously oscillating left and right vocal folds or simultaneously oscillating horizontal and vertical components of the vocal folds (e.g., Herzel *et al.*, 1994; Berry, 2001; Berry *et al.*, 1994; Steinecke and Herzel, 1995; Tigges *et al.*, 1997; Neubauer *et al.*, 2001). The two combined approaches are likely to yield important insights into the sound production mechanism underlying male Diana monkey alarm calls.

II. MATERIAL AND METHODS

A. Study site and subjects

Data were collected in an approximately 40-km^2 study-area of primary rain forest surrounding the Centre en Recherche d'Ecologie (University of Cocody, Abidjan) research station (5°50′N, 7°21′W) in the Taï National Park, Côte d'Ivoire, between June 1994 and June 1997. Seven monkey species are regularly observed in the area: the western red colobus (*Colobus badius*), the western black-and-white colobus (*Colobus polykomos*), the olive colobus (*Procolobus verus*); the Diana monkey (*Cercopithecus diana*), the lesser white-nosed monkey (*Cercopithecus petaurista*), the Campbell's monkey (*Cercopithecus campbelli*), and the sooty mangabey (*Cercocebus torquatus*). Diana monkey groups typically consist of about 20–25 individuals with one adult male and several adult females with their offspring. Groups occupy stable home ranges of approximately 60 ha. Diana monkeys eat primarily fruit and insects and they are

found at all levels of the forest but prefer the main upper canopy. None of the animals were habituated to human presence. However, all data were so that the animals were unaware of the observer's presence.

B. Recordings and acoustic analysis

We recorded Diana monkey alarm vocalizations given in response to playbacks of African leopard (*Panthera pardus*) and crowned eagle (*Stephanoaetus coronatus*) vocalizations, using a Sony WMD6C tape recorder and a Sennheiser microphone (ME88 head with K3U power module) on 90-min type IV metal tapes. The frequency response of the microphone (40 Hz to 20 kHz; ±2.5 dB) and the tape recorder (40 Hz to 14 kHz, ±3 dB; distortion of 0.1%; signal-to-noise-ratio of 57 dB) are flat and within the frequency range of analysis. Playbacks of predator vocalizations were conducted randomly throughout the day, usually between 08:00 and 17:00 GMT. Daytime therefore cannot explain the differences in the vocal patterns. All recordings were made at distances of about 50 m from the focal animal, i.e., the adult male of a Diana monkey group. Individual distances varied randomly across trials and therefore cannot explain the patterns. Male alarm calls transmit to about 700 m, i.e., sound attenuation at short distances was unlikely to have affected the acoustic variables. The study area contained between 40 and 80 different groups of Diana monkeys with one adult male each. Because we did not know the exact location of these groups' home ranges, we selected ten different groups for experimental playbacks that were located at least 1 km apart from each other, which guaranteed that data came from ten different groups, i.e., were independent. This data set resulted in a set of 25 eagle alarm bouts (5 bouts from 5 different males) and 25 leopard alarm bouts (5 bouts from 5 different males). We digitized all recordings at a 16-bit quantization and a 44-kHz sampling rate using Signalize software. We performed signal analysis on a PC using the signal processing software HYPERSIGNAL-Macro™ using a DSP32C PC System Board. We completed the spectrographic analysis by using 512-point fast Fourier transforms, with 75% frame overlapping, a 44-kHz sampling frequency, and a Hanning window. To avoid aliasing effects we low-passed filtered all calls at 22 kHz.

C. Call parameters

A male Diana monkey alarm vocalization consists of one to many calls per bout (Fig. 1). The basic acoustic unit within a call is the pulse, defined as a rapid, transient change in the amplitude of the signal from a baseline value to a higher or lower value, followed by a rapid return to the baseline value, resembling a damped oscillation (Fig. 2).

Pulse duration is measured as the interval between the onset of a pulse to the onset of the subsequent pulse. Fundamental frequency is defined as the inverse (i.e., 1/pulse duration in Hz; pulse duration measured in seconds). Throughout the paper we use the term ''fundamental frequency'' to refer to the inverse value of ''pulse duration'' in the waveform. We quantified the variation of the fundamental frequency within calls by the parameter within-call jitter, defined as cycle-to-cycle variability in the fundamental frequency (Titze, 1994). Fundamental frequency ranges between 8.3 and 24 ms (mean±SD 16.1±2.0) in eagle alarm calls and between 13.3 and 29.9 ms (mean±SD 17.4±2.4) in leopard alarm calls (Riede and Zuberbühler, in press). Call duration and jitter ranges in eagles and leopard alarm calls between 6.4% and 9.2% (Riede and Zuberbühler, in press). In this study we investigate the development of the two parameters maximum amplitude of a pulse and fundamental frequency within a call. Both parameters were normalized within calls. For the correlation between maximum amplitude of a pulse and fundamental frequency we considered the means of the pulses at position 0%, 25%, 50%, 75%, and 100% within the call. Only calls with more than ten pulses and with very low background noise level, i.e., a high signal-to-noise ratio, were considered, resulting in a data set of 10 leopard and 21 eagle alarm calls, respectively.

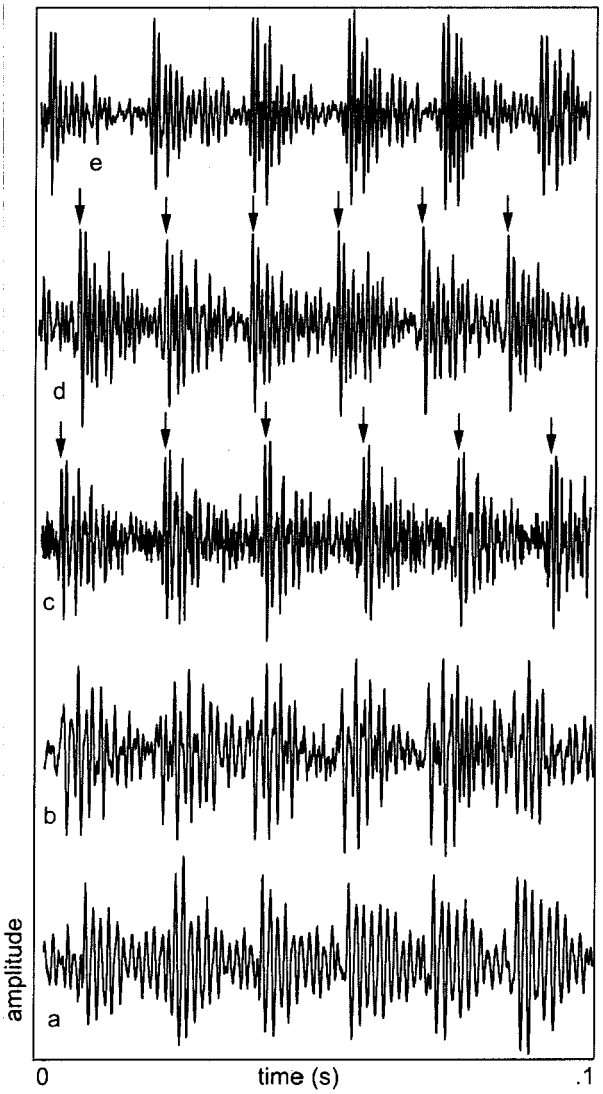

FIG. 2. Time series of pulses of five different individuals. The pulse is the basic acoustic unit in the alarm call; it is defined as a rapid, transient change in the amplitude of the signal from a baseline value to a higher or lower value, followed by a rapid return to the baseline value. Arrows point to the first or second peak in the pulse waveform.

To test if pulse time series are the result of individual-

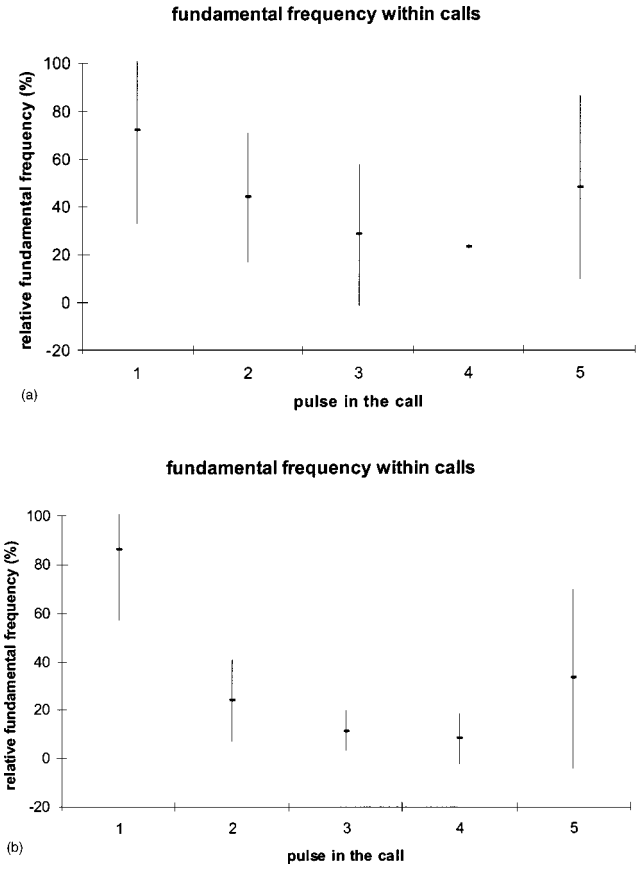

FIG. 3. Fundamental frequency over syllables in (a) leopard alarm calls ($N=10$ syllables) and (b) in eagle alarm calls ($N=21$ syllables). Each data point in the diagram represents the mean ± standard deviation of the relative fundamental frequency within $N=10$ calls (leopard alarm) and $N=21$ calls (eagle alarm). Since calls are of different duration, i.e., they consist of a different number of pulses, call duration was standardized. The five pulses on positions 0%, 25%, 50%, 75%, and 100% of the total number of pulses within a call were considered for the graphs.

specific patterns, cross correlations between pulse time series were undertaken. Five pulses were selected from each of five calls, cut and saved as a text compatible ASCII file. In NCSS 2001 statistical software single cross correlations were run (a) on the within-call level, (b) the between-call and within-individual level, and (c) on the between-individual level. Finally, we were interested in the occurrence of nonlinear phenomena (frequency jumps, subharmonics, biphonation, deterministic chaos) in the alarm calls. For this purpose we inspected the call spectrograms visually for consistency of the pulse pattern, using a data set of 50 calls plus an additional data set of 100 calls from other individuals.

III. RESULTS

A. Fundamental frequency versus maximum amplitude of a pulse

Fundamental frequency depended on the position of the pulse within the call. Fundamental frequency was lower at the beginning and at the end of the call than in the middle of the call. Figure 3 summarizes the development of fundamental frequency over a call of leopard alarm calls ($N=10$ calls) and eagle alarm calls ($N=21$ calls).

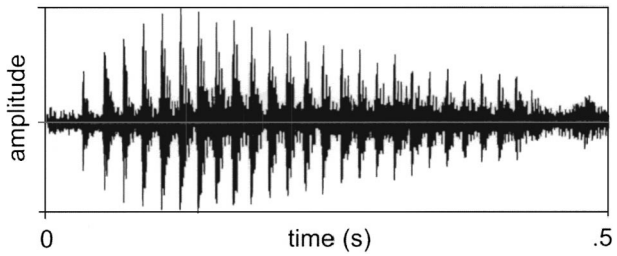

FIG. 4. Time domain of a call. Note the increase in amplitude toward the middle of the call and the amplitude decreases toward the end.

Even maximum amplitude of pulses depended on the position of the pulse within a call. Pulses in the middle of the call were louder than those at the beginning or the end of the call (Fig. 4).

Figure 5 summarizes the development of maximum amplitude of pulses within calls of leopard alarm calls ($N=10$ calls) and eagle alarm calls ($N=21$ calls).

Comparing both parameters, there is a suggestive positive correlation between fundamental frequency and maximum amplitude of pulses within a call in leopard alarm calls (Pearson, $N=5$, $r=0.8$, $P=0.1$) and there is a significant positive correlation between fundamental frequency and maximum amplitude of pulses in eagle alarm calls (Pearson, $N=5$, $r=0.96$, $P=0.0089$). For the correlation the five mean values, as shown in Figs. 3 and 4, have been used.

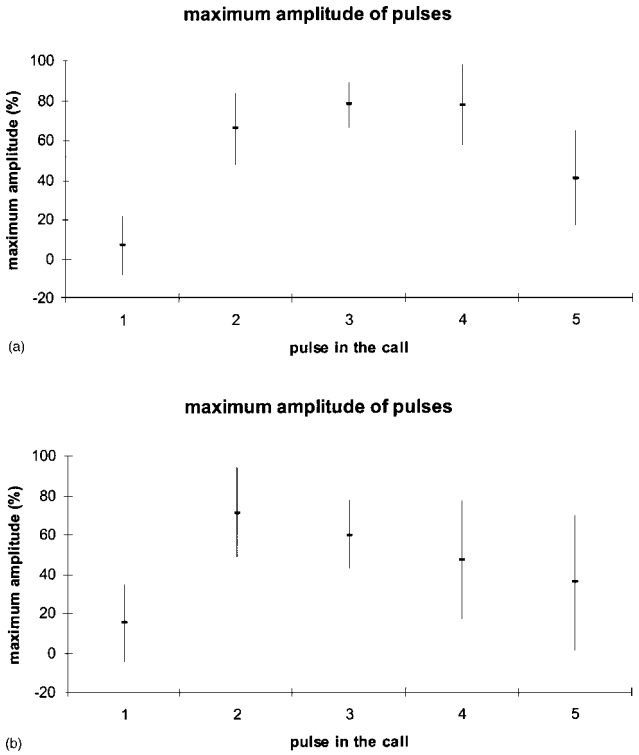

FIG. 5. Maximum amplitude of pulses (a) in leopard alarm calls ($N=10$ calls) and (b) in eagle alarm calls ($N=21$ calls). Each data point within the diagram represents the mean ± standard deviation of the maximum amplitude of pulses of $N=10$ calls (leopard alarm) and $N=21$ calls (eagle alarm). Since calls are of different duration, i.e., they consist of a different number of pulses, call duration was standardized. The five pulses on positions 0%, 25%, 50%, 75%, and 100% of the total number of pulses within a call were considered for the graphs.

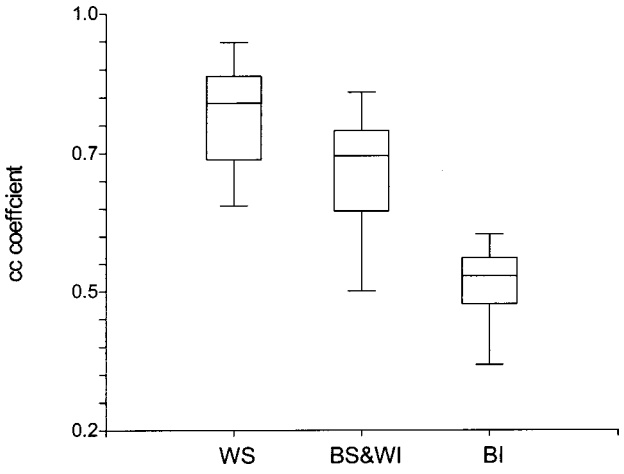

FIG. 6. Cross correlations of pulse time series on three levels. WS—within calls, BS&WI—between calls and within individuals, BI—between individuals. Cross correlation values can be considered as similarity indexes between two time series, saying the higher the cross correlation coefficient the higher the similarity. Within calls the similarity between pulses is highest.

B. Similarity in the pulse waveform

The waveform of a pulse varied within and between individuals. For instance, the maximum amplitude of a pulse can be consistent within the first single cycle of a pulse or alternatively, within one of the later cycles (indicated by arrows in Fig. 2). Cross correlations between single pulses showed an individual specific pattern, delivering highest cross correlation values within calls, being less similar between calls within individuals, and being least between individuals (Fig. 6). The differences between conditions were significant ($N_1=25$, $N_2=25$, $N_3=25$, $F=89.2$, $P<0.001$) with *posthoc* comparisons showing that all means differed from one another. As illustrated in Fig. 6, the means of the two ''within individual'' conditions (within calls and between calls) were closer to each other than the ''between individual'' condition to each of the other two conditions (Fig. 6).

C. Nonlinear phenomena

We investigated the calls for the occurrence of nonlinear phenomena. Pulses occurred in a very regular pattern, i.e., visual inspection of the spectrograms delivered no deviations from the pulse pattern, suggesting a rigid and not deviating vibration pattern of the oscillating system (of the sound source). This was true for the whole data set of 50 calls. Even in the additional data set of 100 additional calls no nonlinear phenomena were discovered.

IV. DISCUSSION

The acoustic structure of male Diana monkey alarm calls is remarkable. These vocalizations consist of trains of loud and low-pitched calls that carry over long distances of up to a kilometer through dense tropical forest habitat. A pulse of 8- to 30-ms duration is the basic unit of male Diana monkey alarm vocalizations. Up to 30 pulses are associated to a call. Several calls build a bout. Between two calls there is a short harmonic element, a sound probably uttered during inspiration. The pulse pattern is very robust, being not interrupted by other phonation types (vibration modes of the source). In 150 different calls produced by more than a dozen different males we did not find any other than the pulse pattern. The fundamental frequency of male Diana monkey alarm calls ranges between 33 and 120 Hz (Riede and Zuberbühler, in press) similar to fundamental frequency ranges of pulsed phonation in *Felidae* [$F0$ in purring between 10 and 45 Hz (Peters and Tonkin-Leyhausen, 1999)] and humans [$F0$ in pulse register between 10 and 90 Hz (Henton and Bladon, 1988)]. Although similar patterns were found for instance in felids (Peters and Tonkin-Leyhausen, 1999) or humans (Titze, 1994) unlike to male Diana monkey, cats do produce all kinds of other vocalizations (Peters, 1981) and in humans the occasional occurrence of a subharmonic regime within a pulse register utterance is reported (Titze, 1994).

The aim of the present study was to investigate the acoustic characteristics of pulsed phonation in Diana monkeys. The sound production mechanism in this species is of particular interest since it has been shown that formant characteristics of a single pulse conveys important information to nearby listeners about ongoing predation events (Zuberbühler, 2000b; Riede and Zuberbühler, in press). Our data confirmed the very narrow range in fundamental frequency in the Diana monkey pulse register, suggesting very limited vocal fold adjustments. In a given adjustment of the vocal folds (i.e., a given length and tension), which is not changed during a single utterance, fundamental frequency seems to be exclusively regulated by the one variable—subglottal pressure (Murry and Brown, 1971). This stands in contrast to the modal phonation type, where the fundamental frequency is controlled mainly by vocal fold tension. Subglottal pressure has been found to correlate both with fundamental frequency (Ishizaka and Flanagan, 1972; Steinecke and Herzel, 1995; Titze, 1989) and with signal amplitude (Gramming, 1988; Titze, 1994).

In male Diana monkeys, we found a positive correlation between the fundamental frequency and the maximum amplitude of a pulse. Since signal amplitude is mainly controlled by subglottal pressure (Gramming, 1988; Titze, 1994), we conclude that fundamental frequency in male Diana monkey alarm calls is similarly controlled by subglottal pressure. Male Diana monkeys differ from humans in that they apparently do not switch to a higher register to produce vocalizations with higher fundamental frequencies. Male Diana monkeys, it appears, are constrained by a pulsed phonation mechanism whose fundamental frequencies are entirely regulated by subglottal pressure.

A. The evolution of Diana monkey alarm calls

Previous work has shown that the fundamental frequency of mammalian vocalizations tends to covary with context relevant aspects, like individual identity, sex or degree of arousal [reviewed in Tembrock (1996)]. If, however, the primary signal is rigid, repetitive and broadband and shows little variability in its most important parameter fundamental frequency, as it is the case in the Diana monkey,

TABLE I. Examples of pulsed utterances in other species than Diana monkeys, giving the name of the utterance, the extent of occurrence, and the reference.

Species	Call type	Description	Reference
Primates			
Human, *Homo sapiens*	Creaky voice	Voluntarily, end-of utterance phenomenon or as a pathological voice	Reviewed in Henton and Bladon (1988)
Chacma baboon, *Papio ursinus*	Wahoo	End of call with some few pulses	Fischer *et al.* (2002)
Gelada baboon, *Theropithecus gelada*			Richman (1976)
Pigtailed macaque, *Macaca nemestrina*	Intention notes, inspiratory note, vibrato growl, bark	A group of calls subsummarized as ''harsh sounds''	Grimm (1967)
Squirrel monkey, *Saimirisciureus*	Girren, churr	A separate call within the repertoire	Winter (1969) (Fig. 9); Ploog *et al.* (1975)
Red howling monkey, *Alouatta seniculus*	Roars	In the climax of the roar	Schön Ybarra (1986) (p. 209)
Other mammals			
Several felidae	Purring		Peters (1981)
Koala, *Phascolarctos cinereus*	Bellow	Seemingly the whole utterance is pulsed	Smith (1980) (p. 21, Figs. 9 and 10)
Cetaceans	Clicks	Part of the sonar system or of other repertoire	Au (1993)

then this might provide a reliable and fruitful basis for the evolution of more sophisticated vocal tract performance. Indeed, other work has shown that formant modulation plays the most important role in the acoustic differentiation of eagle and leopard alarm calls in male Diana monkeys (Zuberbühler, 2000b; Riede and Zuberbühler, in press). Diana monkeys manage to filter the primary source signal produced by the vocal folds in their vocal tracts to product acoustically distinct eagle and leopard alarm calls. Because of their broad bandwidth, pulses are particularly well suited to picture the resonance characteristics of the vocal tract and serve as acoustic raw material for filtering effects in the vocal tract.

Interestingly, human singing tutelage is often based on using pulse register phonation as an exercise to ''tune'' the vocal tract (Miller *et al.*, 1997). By singing a particular vowel in pulse register the trainee can examine his or her vocal tract performance. Once successful, the trainee switches back to the actual singing voice while maintaining the vocal tract configuration. This exercise should enable the performer to tune the formants and fundamental frequency optimally.

This example illustrates that the simple and robust pulse signal is physiologically easy to produce, but is insufficient as a source of acoustic variation to be useful to convey contextual information. Instead, phonation based on a pulse signal is likely to favor the evolution of vocal tract characteristics that enable the caller to engage in sophisticated molding of the source, i.e., to engage in articulatory maneuvers. Research focusing on the signal production mechanisms will be necessary to determine the general evolutionary trends that were likely to have affected Diana monkey vocal behavior.

In recent years it became more evident that the mammalian larynx can be considered as a nonlinear system; several studies showed that sudden changes in the vibration mode of the vocal folds are more the normal picture rather than an exception (Wilden *et al.*, 1998; Riede *et al.*, 2000). Those studies are contrasted by the findings presented here, showing that male Diana monkey alarm call pulsed phonation was free of any interruption of the pulse pattern. Anatomical data on the male Diana monkey larynx will be necessary to illuminate the evolution of this special kind of vocalizations. Possibly, anatomical adaptations make the vocal folds ''special'' for this kind of vibration behavior, leading to the observed highly stabilized vibration pattern.

B. Pulse phonation—an exclusive vocal pattern in male Diana monkeys?

Table I reviews studies that mention pulsed phonation as part of a species repertoire or present spectrograms, which suggest the occurrence of pulsed vocal utterances.

In land mammals, the felids seem to be the most intensively studied group that show pulsed phonation (Peters and Tonkin-Leyhausen, 1999). The time series of purring, however, appears different from Diana monkey alarm calls and humans pulse register (Fig. 7). In humans, pulse register

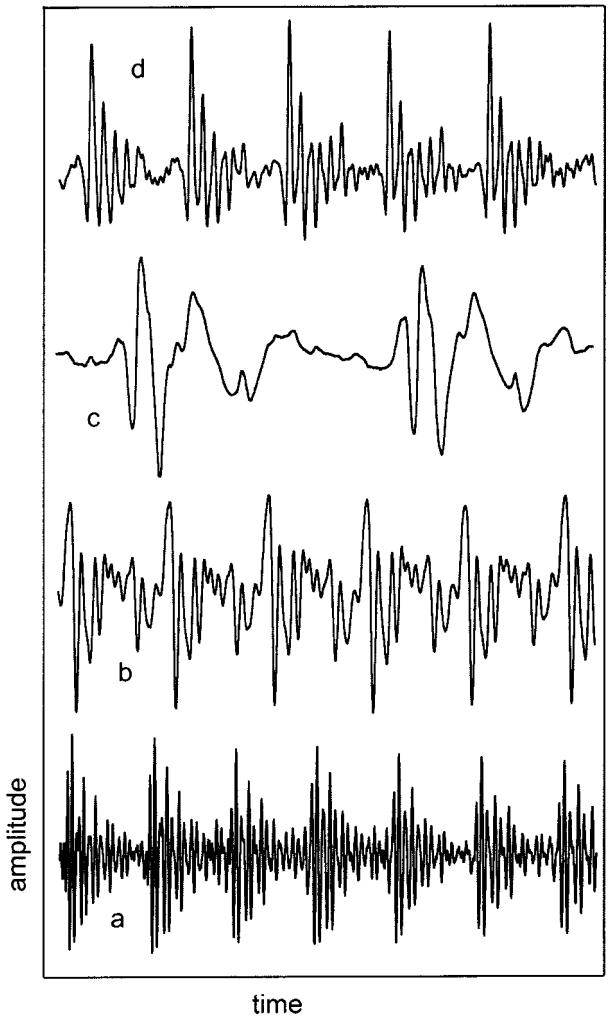

FIG. 7. Time series of pulsed phonation in different land mammals. (d) Domestic cat, (c) leopard, (b) human creaky voice, and (a) Diana monkey.

does not seem to play an important role in everyday speech. Instead it is considered an ''end-of-utterance'' phenomenon, indicating that pulses often occur at the end of words or sentences, and in men more often than in women (Henton and Bladon, 1988). However, no studies have dealt in any depth with the incidence of vocal fry in natural, unprovoked conditions in humans (Henton and Bladon, 1988). For other species this kind of a ''single mode'' source signal was apparently not yet described. In contrast to all these findings, our results suggest that in male Diana monkeys pulse register is the main mode at the source.

C. Implications for the receiver

Animal alarm calls have often been shown to be repetitive, i.e., consisting of short and similarly structured segments which are repeated, for instance in the vervet monkey snake alarm calls (Owren, 1990). Studies on the psychological value of visual and acoustic signals have shown that repeating short elements to form a signal are the most effective way to attract attention and alert others [reviewed in Bradbury and Vehrencamp (1998)]. Diana monkey alarm call pulses are short and repetitive. It is interesting to note that silent gaps of about 5 ms can still be detected by humans (e.g., Abel, 1972; Buus and Florentine, 1985). Assuming the gap detection ability of nonhuman primates is comparable to that of humans, the pulse duration of male Diana monkey alarm calls lies comfortably above that threshold, suggesting the pulsed structure of Diana monkey alarm calls is perceived as an attention attracting structure. Psychophysical experiments manipulating the number of pulses might be suitable to determine the minimum amount of information necessary for a Diana monkey to discern eagle from leopard alarm calls or to identify calls as those of a conspecific.

V. CONCLUSION

To investigate the mechanisms of sound production in Diana monkeys, eagle and leopard alarm calls from ten different Diana monkey males were digitized and subjected to spectrographic analysis. Results showed that the fundamental frequency of these calls ranged between 33 and 120 Hz, comparable to the human pulse register, which tends to range between 10 and 90 Hz. Jitter was very small and did not vary significantly between individuals or alarm call type. Nonlinear phenomena were virtually absent in male Diana monkey vocalization and pulses were not interrupted by any other vibration modes of the vocal folds. Over the entire calls, fundamental frequency was low at the beginning and at the end of the syllable and highest in the middle of the call, while the amplitudes of pulses increase towards the middle and then decrease toward the end of the call, indicating that fundamental frequency and maximum amplitude of a pulse were correlated, which suggested that the fundamental frequency in Diana alarm calls is controlled by subglottal pressure rather than vocal fold stiffness changes. The pulsed phonation in male Diana monkey alarm call, therefore, appeared to be a special adaptation delivering a robust source broadband signal for subsequent vocal tract filtering.

ACKNOWLEDGMENTS

We thank Michael Owren and two anonymous reviewers for important comments on an earlier version of the manuscript. This work was supported by a fellowship within the Postdoc Program of the German Academic Exchange Service (DAAD) to TR.

Abel, S. M. (**1972**). ''Discrimination of temporal gaps,'' J. Acoust. Soc. Am. **52**, 519–524.

Allen, E., and Hollien, H. (**1973**). ''A laminagraphic study of pulse (vocal fry) phonation,'' Folia Phoniatr. **25**, 241–250.

Au, W. W. L. (**1993**). *The Sonar of the Dolphin* (Springer Verlag, New York).

Berry, D. A. (**2001**). ''Mechanisms of modal and nonmodal phonation,'' J. Phonetics **29**, 431–450.

Berry, D. A., Herzel, H., Titze, I. R., and Krischer, K. (**1994**). ''Interpretations of biomechanical simulations of normal and chaotic vocal fold oscillations with empirical eigenfunctions,'' J. Acoust. Soc. Am. **95**, 3595–3604.

Blomgren, M., Chen, Y., Ng, M. L., and Gilbert, H. R. (**1998**). ''Acoustic, aerodynamic, physiologic, and perceptual properties of modal and vocal fry registers,'' J. Acoust. Soc. Am. **103**, 2649–2658.

Bradbury, J. W., and Vehrencamp, S. L. (**1998**). *Principles of Animal Communication* (Sinauer, Sunderland).

Buus, S., and Florentine, M. (**1985**). ''Gap detection in normal and impaired listeners: The effect of level and frequency,'' in *Time Resolution in Auditory Systems*, edited by A. Michelsen (Springer, New York).

Fant, G. (**1960**). *Acoustic Theory of Speech Production* (Mouton, The Hague).
Fischer, J., Hammerschmidt, K., Cheney, D. L., and Seyfarth, R. M. (**2002**). ''Acoustic features of male baboon loud calls: influences of context, age, and individuality,'' J. Acoust. Soc. Am. **111**, 1465–1474.
Fuks, L., Hammarberg, B., and Sundberg, J. (**1998**). ''A self-sustained vocal-ventricular phonation mode: acoustical, aerodynamic and glottographic evidences,'' TMH-QPRS **3**, 49–59.
Gerratt, B., and Kreiman, J. (**2001**). ''Toward a taxonomy of nonmodal phonation,'' J. Phonetics **29**, 365–381.
Gramming, P. (**1988**). ''The phonetogram: An experimental and clinical study,'' Malmoe Sweden, Dept. Otolaryngology, Univ. of Lund.
Grimm, R. J. (**1967**). ''Catalogue of sounds of the pigtailed macaque (Macaca nemestrina),'' J. Zool. Lond. **152**, 361–373.
Henton, C., and Bladon, A. (**1988**). ''Creak as a sociophonetic marker,'' in *Language, Speech, and Mind: Studies in Honour of Victoria A. Fromkin*, edited by L. M. Hyman and C. N. Li (Routledge, London), pp. 3–29.
Herzel, H., Berry, D., Titze, I. R., and Saleh, S. (**1994**). ''Analysis of vocal disorders with methods from nonlinear dynamics,'' J. Speech Hear. Res. **37**, 1008–1019.
Hollien, H. (**1974**). ''On vocal registers,'' J. Phonetics **2**, 125–143.
Hollien, H., and Michel, J. (**1968**). ''Vocal fry as a phonational register,'' J. Speech Hear. Res. **11**, 600–604.
Hollien, H., Damsté, H., and Murry, T. (**1969**). ''Vocal fold length during vocal fry phonation,'' Folia Phoniatr. **21**, 257–265.
Hollien, H., Girard, G. T., and Coleman, R. F. (**1977**). ''Vocal fold vibratory patterns of pulse register phonation,'' Folia Phoniatr. **29**, 200–205. (**1972**).
Ishizaka, K., and Flanagan, J. L. (**1972**). ''Synthesis of voiced sounds from a two-mass model of the vocal cords,'' Bell Syst. Tech. J. **51**, 1233–1268.
Lindestad, P., Soedersten, M., Merker, B., and Granqvist, S. (**2001**). ''Voice source characteristics in Mongolian 'throat singing' studied with high-speed imaging technique, acoustic spectra, and inverse filtering,'' J. Voice **15**, 78–85.
Mergell, P., Fitch, W. T., and Herzel, H. (**1999**). ''Modeling the role of non-human vocal membranes in phonation,'' J. Acoust. Soc. Am. **105**, 2020–2028.
Miller, D. G., Sulter, A. M., Schutte, H. K., and Wolf, R. F. (**1997**). ''Comparison of vocal tract formants in singing and nonperiodic phonation,'' J. Voice **11**, 1–11.
Morton, E. S. (**1977**). ''On the occurrence and significance of motivation—structural rules in some bird and mammal sounds,'' Am. Nat. **111**, 855–869.
Murry, T., and Brown, W. S., Jr. (**1971**). ''Subglottal air pressure during two types of vocal activity: vocal fry and modal phonation,'' Folia Phoniatr. **23**, 440–449.
Neubauer, J., Mergell, P., Eysholdt, U., and Herzel, H. (**2001**). ''Spatio-temporal analysis of irregular vocal fold oscillations: biphonation due to desynchronization of spatial modes,'' J. Acoust. Soc. Am. **110**, 3179–3192.
Owren, M. J. (**1990**). ''Acoustic classification of alarm calls by veret monkeys (*Cercopithecus aethiops)*,'' J. Acoust. Soc. Am. **101**, 2951–2963.
Owren, M., and Linker, C. D. (**1995**). ''Some analysis techniques that may be useful to acoustic primatologists,'' in *Current Topics in Primate Vocal Communication*, edited by E. Zimmermann, J. Newman, and U. Jürgens (Plenum, New York), pp. 1–27.
Peters, G. (**1981**). ''Das Schnurren der Katzen,'' Säugetierkundl. Mitteilungen **29**, 30–37.
Peters, G., and Tonkin-Leyhausen, B. A. (**1999**). ''Evolution of communication signals of mammals: friendly close range vocalizations in felidae (Carnivora),'' J. Mammalian Evol. **6**, 129–159.
Ploog, D., Hupfer, K., Jürgens, U., and Newman, J. D. (**1975**). ''Neuroethological studies of vocalization in squirrel monkeys with special reference to genetic differences of calling in two subspecies,'' in *Growth and Development*, edited by M. A. B. Brazier (Raven, New York).
Richman, B. (**1976**). ''Some vocal distinctive features used by gelada monkeys,'' J. Acoust. Soc. Am. **60**, 718–724.
Riede, T., and Zuberbühler, K. (in press). ''The relationship between acoustic structure and semantic information in Diana monkey alarm calls.'' J. Acoust. Soc. Am.
Riede, T., Wilden, I., and Tembrock, G. (**1997**). ''Subharmonics, biphonations, and frequency jumps—common components of mammalian vocalization or indicators for disorders,'' Z. Säugetierkunde **62**, 198–203.
Riede, T., Herzel, H., Mehwald, D., Seidner, W., Trumler, E., Böhme, G., and Tembrock, G. (**2000**). ''Nonlinear phenomena in the natural howling of a dog-wolf mix,'' J. Acoust. Soc. Am. **108**, 1435–1442.
Schoen Ybarra, M. A. (**1986**). ''Loud calls of adult male red howling monkeys (*Alouatta seniculus*),'' Folia Primatol (Basel) **47**, 204–216.
Smith, M. (**1980**). ''Behavior of the Koala, Phascolarctos cinereus (Goldfuss), in captivity, III. Vocalizations,'' Aust. Wildl. Res. **7**, 13–34.
Steinecke, I., and Herzel, H. (**1995**). ''Bifurcations in an asymmetric vocal fold model,'' J. Acoust. Soc. Am. **97**, 1874–1884.
Svec, J. G., Schutte, H. K., and Miller, D. G. (**1999**). ''On pitch jumps between chest and falsetto registers in voice: Data from living and excised human larynges,'' J. Acoust. Soc. Am. **106**, 1523–1531.
Tembrock, G. (**1996**). *Akustische Kommunikation der Säugetiere. Wissenschaftl* (Buchgesell, Darmstadt).
Tigges, M., Mergell, P., Herzel, H., Wittenberg, T., and Eysholdt, U. (**1997**). ''Observation and modeling of glottal biphonation,'' Acustica **83**, 707–714.
Titze, I. R. (**1989**). ''On relation between subglottal pressure and fundamental frequency in phonation,'' J. Acoust. Soc. Am. **85**, 901–906.
Titze, I. R. (**1991**). ''Mechanisms underlying the control of fundamental frequency,'' in *Vocal Fold Physiology: Acoustic, Perceptual and Physiological Aspects of Voice Mechanisms*, edited by J. Gauffin and B. Hammarberg (Singular, San Diego), pp. 129–138.
Titze, I. R. (**1994**). *Principles of Voice Production* (Prentice Hall, Englewood Cliffs, NJ).
van den Berg, J. (**1958**). ''Myoelastic-aerodynamic theory of voice production,'' J. Speech Hear. Res. **1**, 227–244.
Wilden, I., Herzel, H., Peters, G., and Tembrock, G. (**1998**). ''Subharmonics, biphonation, and deterministic chaos in mammal vocalization,'' Bioacoustics **9**, 171–196.
Winter, P. (**1969**). ''Dialects in squirrel monkeys: vocalization of the roman arch type,'' Folia Primatol (Basel) **10**, 216–229.
Zuberbühler, K. (**2000a**). ''Causal knowledge of predators' behavior in wild Diana monkeys,'' Anim. Behav. **59**, 209–220.
Zuberbühler, K. (**2000b**). ''Referential labeling in Diana monkeys,'' Anim. Behav. **59**, 917–927.
Zuberbühler, K. (**2003**). ''The effects of natural and sexual selection on the evolution of guenon loud calls,'' in *The Guenons*, edited by M. Glenn and M. Cords (Plenum, New York).
Zuberbühler, K., Cheney, D. L., and Seyfarth, R. M. (**1999**). ''Conceptual semantics in a non-human primate,'' J. Comp. Psychol. **113**, 33–42.
Zuberbühler, K., Noe, R., and Seyfarth, R. M. (**1997**). ''Diana monkey long-distance calls: messages for conspecifics and predators,'' Anim. Behav. **53**, 589–604.

Responses of squirrel monkeys to their experimentally modified mobbing calls

Claudia Fichtel[a,c] and Kurt Hammerschmidt[b]
Deutsches Primatenzentrum, Abteilung Neurobiologie, Kellnerweg 4, 37077 Göttingen, Germany

(Received 10 June 2002; accepted for publication 23 December 2002)

Previous acoustic analyses suggested emotion-correlated changes in the acoustic structure of squirrel monkey (*Saimiri sciureus*) vocalizations. Specifically, calls given in aversive contexts were characterized by an upward shift in frequencies, often accompanied by an increase in amplitude. In order to test whether changes in frequencies or amplitude are indeed relevant for conspecific listeners, playback experiments were conducted in which either frequencies or amplitude of mobbing calls were modified. Latency and first orienting response were measured in playback experiments with six adult squirrel monkeys. After broadcasting yaps with increased frequencies or amplitude, squirrel monkeys showed a longer orienting response towards the speaker than after the corresponding control stimuli. Furthermore, after broadcasting yaps with decreased frequencies or amplitude, squirrel monkeys showed a shorter orienting response towards the speaker than after the corresponding manipulated calls with higher frequencies or amplitude. These results suggest that changes in frequencies or amplitude were perceived by squirrel monkeys, indicating that the relationship between call structure and the underlying affective state of the caller agreed with the listener's assessment of the calls. However, a simultaneous increase in frequencies and amplitude did not lead to an enhanced response, compared to each single parameter. Thus, from the receiver's perspective, both call parameters may mutually replace each other. [DOI: 10.1121/1.1548158]

PACS numbers: 43.80.Ka, 43.80.Jz, 43.80.Lb [WA]

I. INTRODUCTION

According to Darwin (1872), animal signals should be predominantly understood as expressions of emotions (see also Marler, 1977, 1992). However, several studies have been demonstrated that some animal vocalizations, such as alarm calls, can also function to designate specific objects or events in the external environment (Seyfarth *et al.*, 1980; Gyger *et al.*, 1987; Macedonia, 1990; Zuberbühler, 1999; Manser, 2001; Fichtel and Kappeler, 2002). Nevertheless, in several contexts, the acoustic structure of calls appears to be related to the signaler's affective state (Morton, 1977; Owings and Morton, 1998), but this relationship has been clearly demonstrated in only a few recent studies. For example, Barbary macaques (*Macaca sylvanus*) calls given immediately after disturbances at their sleeping site were significantly higher in peak frequency than at the end of the call series (Fischer *et al.*, 1995). Contact calls in marmoset monkeys (*Callithrix j. jacchus*) had a higher maximum and mean fundamental frequency when the animals were visually and acoustically isolated than when isolation was only visual; fundamental frequency was higher in visually isolated animals than in animals that were spatially separated but could see each other (Schrader and Todt, 1993). Similarly, changes in frequencies of vocalizations were associated with changes in the affective state or perceived pain in other mammal species, such as vocalizations of domestic cattle (*Bos primigenius f. taurus*: Watts and Stookey, 1999) during branding or vocalizations of piglets (*Sus scrofa domestica*) during castration (Weary *et al.*, 1998; Taylor and Weary, 2000). Together, these studies led us to the assumption that it is a widespread phenomenon in mammal species that changes in frequencies and amplitude of vocalizations are influenced by the affective state of the caller.

Therefore, we focused on a study conducted by Jürgens (1979), in which he identified the aversive or pleasant emotional character underlying the production of different vocalizations of squirrel monkeys (*Saimiri sciureus*). In this study, squirrel monkeys were given the opportunity to control vocalization-eliciting brain stimulations, which allowed the aversive or pleasant quality of the emotional state underlying the production of specific calls to be determined independently of the call produced. In a subsequent acoustic analysis of these vocalizations, Fichtel *et al.* (2001) demonstrated that the aversive or pleasant character of different call types, as well as calls within the same type, is characterized by an upward shift of the peak frequency (the maximum frequency amplitude in the power spectrum), an increase in frequency range, and/or an increase in the ratio of nonharmonic to harmonic structure. Additionally, in many cases there was a positive correlation between call frequencies and amplitude (Hammerschmidt and Jürgens, 2000). These results suggested that a shift in frequencies and amplitude might characterize different affective states.

In this paper, we present results of a set of playback experiments that were designed to test whether changes in

[a]Electronic mail: fichtel@eva.mpg.de
[b]Current address: University Hospital, Department of Psychiatry, Section of Addiction Research, Tübingen.
[c]Current address: Max-Planck Institut for Evolutionary Anthropology, Department of Cultural Phylogeny, Inselstr. 22, 04103 Leipzig, Germany. Electronic mail: Fichtel@eva.mpg.de

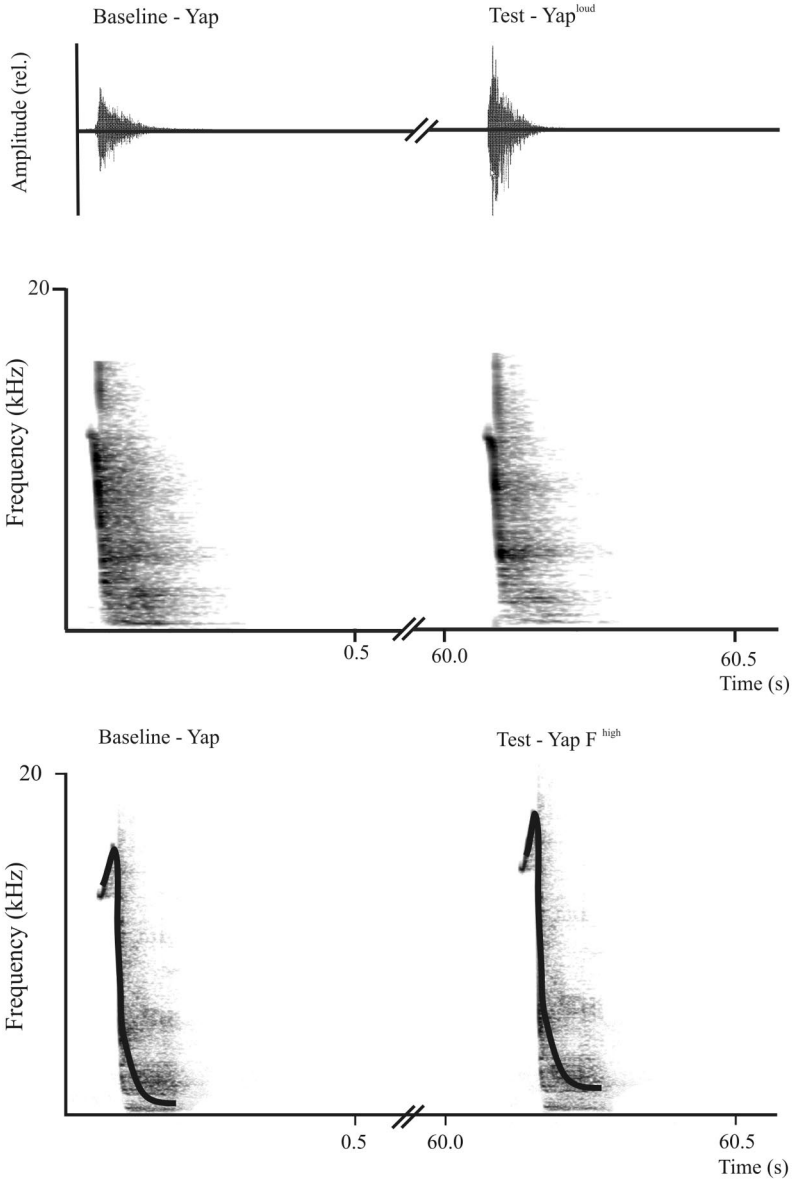

FIG. 1. (a) Waveform and spectrogram of an unmanipulated soft and loud yap and (b) spectrogram of an unmanipulated and in frequencies manipulated yap used for the playback experiments. Black line in the spectrograms (Fig. 1b) shows the course of the mean DFA2.

frequencies or amplitude are meaningful for squirrel monkeys. We conducted playback experiments using squirrel monkeys mobbing calls (yap) that we artificially increased either in frequencies or amplitude. To exclude call manipulation or novelty as a cause for differences in responses we also broadcast calls that we artificially decreased in frequencies or amplitude. Additionally, we used as control stimuli either unmanipulated calls with naturally higher frequencies and amplitude compared to control stimuli. We predicted that yaps with higher frequencies or amplitude would elicit a stronger response (as measured by duration of orienting response towards the speaker) than the respective control stimulus, independent of whether the call was manipulated or not.

II. METHODS

A. Subjects

We tested six adult male squirrel monkeys which were born in captivity, group-reared and between 5 and 12 years old. They were housed in two groups of three in two neighboring cages with $1.70\times1.60\times2.50$ m and $1.70\times80\times2.50$ m, respectively. Both cages were equipped with branches and chaff, and the room was kept at constant temperature (25 °C) in a 12/12 h LD cycle. Animals were fed twice a day, and their diet included monkey chow, fruits, vegetables, and a protein supplement.

B. Call manipulations

The yap serves to inform conspecifics about the presence of a mammalian predator and is often uttered in a chorus as a mobbing reaction (Herzog and Hopf, 1983; Winter *et al.*, 1966). The yap appears to indicate increased flight motivation and arousal of the sender, but it also has an appellant character to receivers to join the mobbing of the predator. We considered the yap to be suitable for playback experiments because we expected receivers to exhibit a strong motivation to respond. Moreover, in previous studies

the yap showed an aversion-correlated increase in frequencies, in the sense that more aversive yaps had higher frequencies (Fichtel *et al.*, 2001).

We chose test calls out of sequences recorded with a Sony WM TCD-100 DAT recorder and a Sennheiser directional microphone K6 power module and ME66 recording head with MZW66 pro windscreen during approaches of an animal keeper. For call manipulation we used 'Cool-edit 2000' (Synthrillium Software Cooperation, Phoenix, AZ). The fast Fourier transformation (1024-pt FFT; time step: 5 ms; frequency range: 22.05 kHz; Frequency resolution: app. 43 Hz was conducted with AVISFOFT-SASLab pro 3.0 (R. Specht, Berlin, Germany). Peak frequency and DFA were measured with a custom software program (LMA 9.2) developed by (Hammerschmidt, 1990). In order to avoid pseudoreplications (Kroodsma, 1989) we selected for each experimental subject ($n=6$) a different set of two calls. Both calls differed in frequencies and amplitude whereas the call with lower frequencies and amplitude was manipulated and the call with higher frequencies and amplitude was used as control (Fig. 1). We measured changes in frequencies by calculating the statistical distribution of the frequency amplitudes in the spectrum, hereafter 'distribution of frequency amplitudes'. These values represent the frequency at which the summed up frequency amplitudes reaches 25% (DFA1), 50% (DFA2), and 75% (DFA3) of the total distribution of the power spectrum. Furthermore, we measured the peak frequency (maximum energy in the power spectrum).

C. Amplitude

First, we either increased or decreased the amplitude of the softer call about 6 dB applying the same amount of change throughout the audio signal. This difference in amplitude was equivalent to the naturally occurring differences between softer and louder calls. Sound pressure level was measured for each call with a sound level meter (Rion NL-05) at a distance of 1 m with a flat weighting over the entire frequency range. The average maximum sound pressure level for the soft calls was 70.7 ± 4.4 dB, for calls with increased amplitude 76.2 ± 4.7 dB, for calls with decreased amplitude 65.22 ± 4.32 dB, for calls with increased frequencies 70.1 ± 4.1 dB, for calls with decreased frequencies 69.8 ± 3.56 dB, and for the unmanipulated louder calls 76.7 ± 4.2 dB.

D. Frequencies

We used the pitch shift algorithm from 'Cool-edit 2000' (Synthrillium Software Cooperation, Phoenix, AZ) with preserved tempo to increase or decrease the frequencies of the whole call (only soft calls) about two semitones. This led on average to an increase in the distribution of frequency amplitudes (mean DFA2) from 7312 ± 1332 Hz for the unmanipulated calls to 8477 ± 1304 Hz of the increased calls, and from 6713 ± 1675 Hz to 7931 ± 1644 Hz for the mean peak frequency. This represents a change of about apparently 15%. The decreased calls had a mean DFA2 of 5362 ± 1673 and a mean peak frequency of 4696 ± 1885 Hz. The calls with increased or decreased amplitude had nearly the same values as the unmanipulated soft calls (mean DFA2, increased amplitude: 7180 ± 1211 Hz; mean peak frequency, increased amplitude: 6692 ± 1675; mean DFA2, decreased amplitude: 7649 ± 1089 Hz; mean peak frequency, decreased amplitude: 7104 ± 1305). The natural louder calls had a DFA2 of 7637 ± 1599 Hz and a mean peak frequency of 7018 ± 1710 Hz.

In total, each experimental animal was broadcast once a pair of unmanipulated control calls, four pairs of calls existing of an unmanipulated and a manipulated call as well as one pair of unmanipulated low and louder call. In total, each subject was exposed to six different pairs of calls, which were presented in a randomized but counterbalanced order.

E. Playback-design

For the experiments, subjects were caught by a keeper, placed in a cage with a size of $60\times30\times40$ cm^2 and brought into the experimental room. Afterwards, we left the animals alone for 30 min to recover from the stress associated with the handling and to become familiar with the new surroundings.

The loudspeaker was placed at the same height as the individuals at a distance of 3 m and 30° on either the left or right side behind the test animal. For each session, the loudspeaker was positioned randomly on the left or right side. Test calls were played back in a randomized order with a Sony TCD-D100 DAT recorder connected to a DMS Nagra amplifier loud-speaker. Playback experiments were videotaped with a Sony DCR-PC100E Video DAT-Recorder connected to a Sennheiser directional microphone (K6 power module and ME 66 recording head with MZW66 pro windscreen) positioned at a distance of 2 m in front of the individuals.

Each playback-session lasted about 50 min with two playback-experiments each. A playback session was conducted as follows: for the first playback experiments the observer came into the experimental room, sat quietly next to the video camera, and started the playback 10 min later. We videotaped the behavior of the animals 2 min before, 1 min during and 2 min after the end of the playback. After the first playback-experiment, the observer left the room and started the next playback-experiment half an hour later with the same procedure. To avoid habituation, each individual was tested only once a weak.

We used a ''baseline-and-test-call design'' for playback-experiments, in which the baseline call was first broadcasted and used as a control stimulus for the following test call. As baseline call we used an unmanipulated call. After a silent interval of 60 s the same call that had been manipulated was used as test call (Fig. 1). This design allowed us to examine how the attention of an animal was affected by hearing a manipulated call in comparison to an unmanipulated call. By first presenting an unmanipulated call, we ensured that all individuals were attracted initially in the same way, providing a baseline for the subsequent test calls. The ''mean difference of responses'' between baseline and test call was used as the dependent measure of subject behavior (for calculation see below).

TABLE I. Difference (duration of the test call-control call) of the first orienting response towards the speaker after broadcasting the playback calls for each individual and playback design, respectively.

Subject	yap-yap	yap-yap$^{\text{amplitude high}}$	yap-yap$^{\text{amplitude low}}$
1	−0,84 s	0,76 s	0,22 s
2	−0,88 s	3,36 s	0,08 s
3	−1,60 s	0,36 s	−1,44 s
4	−1,96 s	4,64 s	1,88 s
5	−0,36 s	0,44 s	0,80 s
6	−2,72 s	9,32 s	−0,40 s
	yap-yap$^{\text{loud}}$	yap-yap$^{\text{frequencies high}}$	yap-yap$^{\text{frequencies low}}$
1	−0,44 s	2,12 s	0,16 s
2	−0,08 s	1,32 s	−1,00 s
3	1,88 s	−1,08 s	−0,28 s
4	0,32 s	1,16 s	−11,64 s
5	0,68 s	1,84 s	−1,12 s
6	0,80 s	2,76 s	−0,36 s

F. Data analyses

Videotapes were analyzed with the software-tool ''Adobe Premiere D1-4.2'' using a frame-by-frame analysis with 25 frames per second. We measured the latency of response, defined as the duration between the onset of the playback and head or body movement in any direction, and the duration of the immediately following first orienting response, i.e., head or body movements towards the speaker (with a toleration of 45° deviation to either side), after the onset of the playback.

In order to compare responses after the baseline and test call between different playback-designs, we calculated the ''mean difference of response'' of latency and the duration of orienting towards the speaker. We therefore subtracted, for example, the duration of the latency after the test call from that after the baseline call.

To compare differences in latency between baseline and test call, we used the GLM repeated measure analysis of variance with the different playback designs as different treatments. To examine whether there were differences in latency dependent on the types of test calls, we used the Friedman test. To compare the ''differences of response'' in duration of the first orienting response between test call and baseline call, we used the exact Wilcoxon paired ranks test (two tailed). All tests were carried out with SPSS 10.0.

III. RESULTS

A. Latency

Individuals responded immediately (mean latency: 0.1 $\pm$0.06) after the onset of each playback. There were no significant differences in either the latency of response between baseline and test calls (GLM repeated measure, $F=0.081$, $df=1$, $p=0.782$), or in the difference of response in mean latency between control playback trials and other playback trials (Friedman test, chi$^2=3.438$, $N=6$, $df=3$, $p=0.308$).

B. First orienting response

During the control playback (yap-yap) all individuals spent less time orienting towards the loudspeaker after broadcasting the second call, the test call (Table I). Thus, individuals showed a measurable habituation to repeated playback is of the same call. After broadcasting calls with increased frequencies (yap$^{\text{freq high}}$) or amplitude (yap$^{\text{amp high}}$) all individuals spent more time orienting towards the loudspeaker than after the baseline call (Table I). After the calls with decreased frequency or amplitude (yap$^{\text{freq low}}$ or yap$^{\text{amp low}}$), individuals spent less time orienting towards the speaker than after the baseline calls. We found the same results after broadcasting the original louder yap, which also had higher frequencies.

The differences in duration of the orienting response between control playbacks and playbacks with increased frequencies or amplitude were significant [Fig. 2; (yap-yap$^{\text{amplitude high}}$): Wilcoxon, $T=21$, $N=6$, $p=0.031$ or (yap-yap$^{\text{frequencies high}}$): Wilcoxon, $T=21$, $N=6$, $p=0.031$]. The difference in duration of the orienting response after broadcasting the unmanipulated louder call following the baseline call was also significant [Fig. 2; (yap-yap$^{\text{loud}}$): Wilcoxon, $T=21$, $N=6$, $p=0.031$]. Further, differences in duration of the first orienting response between the manipulated frequencies$^{\text{high}}$ and frequencies$^{\text{low}}$ calls were significant [(yap$^{\text{frequencies high}}$-yap$^{\text{frequencies low}}$): Wilcoxon, $T=21$, $N=6$, $p=0.031$]. Thus, individuals spent significantly more time

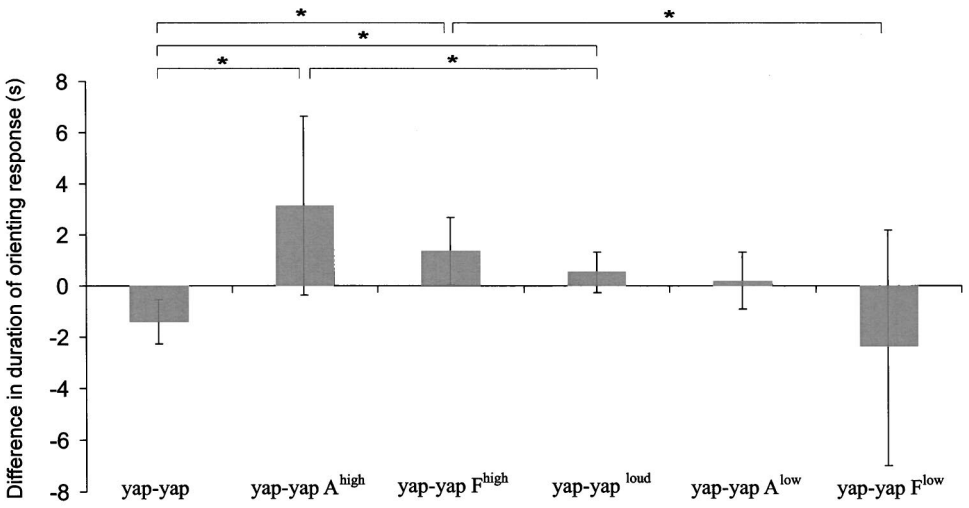

FIG. 2. Mean differences ($\pm$s.d.) in the difference of duration of the first orienting response after broadcasting the baseline and test-calls.

orienting towards the loudspeaker after broadcasting calls with increased frequencies or amplitude, irrespective of whether the call was manipulated or not.

However, differences in duration of the first orienting response between the manipulated amplitude^{high} and amplitude^{low} calls failed to reach significance [(yap$^{amplitude\ high}$-yap$^{amplitude\ low}$): Wilcoxon, $T=20$, $N=6$, $p=0.063$].

IV. DISCUSSION

Squirrel monkeys responded with a significantly longer orienting response towards the speaker after playbacks of calls with higher frequencies or amplitude than to control stimuli. They also showed significantly shorter orienting responses after playbacks of calls with lower frequencies or amplitude than to calls with higher frequencies and amplitude. Thus, longer orienting responses after calls with increased frequencies or amplitude were not due to manipulation or the novelty of calls. These results demonstrate that squirrel monkeys are able to discriminate subtle differences in frequencies, i.e., they paid more attention to calls with higher frequencies and amplitude. Because of the already characterized relationship between call structure, and the underlying affective state of squirrel monkey mobbing calls (Fichtel *et al.* 2001), we conclude that higher frequencies and amplitudes might function to communicate the severity of the eliciting threat and that this was perceived as such from conspecific recipients.

The importance of vocalizations as a source of information about the affective state of a signaler has been demonstrated in different mammal species, including nonhuman primates and humans. For example, an upward shift in frequencies is related with the perceived stress of the vocalizer. For example, barks of female Chacma baboons (*Papio cynocephalus*) constitute a graded continuum where harsher variants are given as alarm calls and more tonal variants as contact call. Alarm calls, which are presumably linked to higher arousal or affective state of the caller, are higher in frequencies, shorter and noisier (Fischer *et al.* 2001a). Subsequent playback studies demonstrated that such differences are salient for receivers (Fischer *et al.* 2001b). Schrader and Todt (1998) demonstrated that squeal grunts given by domestic pigs under social isolation stress differ from normal grunts by a lower peak frequency. These studies support the hypothesis that changes in frequency are reliable indicators of the affective state of a caller. This is in line with findings of vocal expression of emotions in humans. Expressions of emotions and their corresponding perception are a fundamental aspect of human communication (Bachorowski, 1999). Emotional differences in vocalizations are mainly characterized by changes in amplitude and frequency, whereas basic physical properties of the call remained unchanged (Banse and Scherer, 1996; Scheiner *et al.* 2002).

In many cases higher call amplitude is positively related to the affective state of the caller (Smith, 1977). For example, yellow-bellied marmots (*Marmota flaviventris*) responded more strongly to playbacks of disturbance calls with higher amplitude than to those with lower amplitudes (Blumstein and Armitage, 1997). In humans, Hammerschmidt and Mundry (2000) demonstrated that an upward shift in frequencies was used to estimate the loudness of spoken vowels, and, interestingly, the unpleasant character underlying the production of these vowels. These studies indicate that changes in amplitude may be related to different levels of perceived risk or affective states of the caller.

In contrast, eastern chipmunks, *Tamias striatus*, failed to respond more strongly to alarm calls broadcast with a higher amplitude or at closer distance (Weary and Kramer, 1995). Also, vervet monkeys, *Cercopithecus aethiops*, did not respond more strongly to broadcast alarm calls with higher amplitude (Seyfarth *et al.*, 1980). However, these results may have occurred because listeners did perceive that the caller was at greater risk, but did not reveal this perception in their response.

Because the amplitude of vocalizations flucutates for a fixed propagation distance and broadcast volume in forests (Wiley and Richards, 1978), amplitude seems to be a critical feature to provide reliable information of the affective state of the caller, when the affective state or the proximity of the caller cannot be estimated by additional cues. Thus, changes in frequencies may be a more reliable feature to provide information about the affective state than amplitude in cases of low visibility or longer distances. In our study changes in both either frequencies or amplitude attracted the attention of conspecific recipients.

Interestingly, calls with a simultaneous increase in frequencies and amplitude did not attract the attention of recipients more strongly than calls increased in only one parameter. Thus, from the receiver's perspective, both call parameters may mutually replace each other.

Owren and Rendall (2001) suggested that physical properties of calls such as noisy frequency spectra or rapid amplitude fluctuations might be responsible to induce changes in the affective state of recipients. In contrast, Fichtel and Kappeler (2002) demonstrated that redfronted lemurs (*Eulemur fulvus rufus*) did not respond with startle responses to other nonhuman primate alarm calls, i.e., 'wahoos' of chacma baboons, although 'wahoos' are acoustically similar to their own alarm calls, indicating that acoustic properties alone did not induce startle responses. The results of our study demonstrated that subtle changes in frequency or amplitude, led to a different assessment of the calls in recipients, whereas basic physical properties of the calls remained unchanged (see Figs. 1a, b). Similarly Fichtel and Hammerschmidt (2002) showed that redfronted lemurs perceived urgency based changes in frequency and amplitude in general alarm calls in the same way as squirrel monkeys. Manser (2001) demonstrated that suricates' alarm calls, tonal calls with several overtones, could convey information about the type of predator and different levels of urgency. Different levels of urgency were expressed by changes in frequencies of their alarm calls and were also perceived as such from conspecific recipients (Manser 2001). Moreover, calls of piglets that had been removed from their mothers immediately before suckling had higher peak frequencies than those of piglets that had been removed from their mothers immediately after suckling (Weary & Fraser 1995). Playbacks of calls given by piglets removed immediately before suckling

elicited a stronger response, i.e., orienting towards the speaker, in sows than those given by piglets removed after suckling (Weary 1997). In all these cases, changes in frequencies and amplitude were meaningful in these species although the respective calls are characterized by different basic physical properties.

We, therefore, suggest that recipients might be able to infer differences in the affective state of a caller on the basis of frequency changes in calls, independent from the basic physical properties of the respective calls. However, further investigations of calls given in contexts associated with changes in the affective state and subsequent playback experiments are needed to gereralize these findings.

ACKNOWLEDGMENTS

We thank Heino Hartung and Achim Lück for assistance with the experiments and for taking excellent care of the animals. We thank Uwe Jürgens for discussions and support of this study. Julia Fischer, Peter Kappeler, Elisabeth Scheiner, Robert Seyfarth, and two anonymous referees provided helpful comments on the manuscript.

Bachorowski, J-A. (**1999**). ''Vocal expression and perception of emotion'', Current Directions in Psychological Science **8**, 53–57.

Banse R. and Scherer K. R. (**1996**). ''Acoustic profiles in vocal emotion expression'', J. Pers. Soc. Psychol. **70**, 614–636

Beeman, K. (**1996**). *SIGNAL Operation Manual* (Engineering Design, Belmont).

Blumstein, D. T., and Armitage, K. B. (**1997**). ''Alarm calling in yellow-bellied marmots: I: The meaning of situationally variable alarm calls,'' Anim. Behav. **53**, 143–171.

Darwin, C. (**1872**). *The Expression of the Emotions in Man and Animals* (Muray, London).

Fichtel, C., and Hammerschmidt, K. (**2002**). ''Responses of redfronted lemurs (*Eulemur fulvus rufus*) to experimentally modified alarm calls: evidence for urgency-based changes in call structure,'' Ethology **108**, 763–777.

Fichtel, C., Hammerschmidt, K., and Jürgens, J. (**2001**). ''On the vocal expression of emotion. A multi-parametric analysis of different states of aversion in the Squirrel monkey,'' Behaviour **138**, 97–116.

Fichtel, C., and Kappeler, P. M. (**2002**). ''Anti-predator behavior of group-living Malagasy primates: mixed evidence for a referential alarm call system,'' Behav. Ecol. Sociobiol. **51**, 262–275.

Fischer, J., Hammerschmidt, K., and Todt, D. (**1995**). ''Factors affecting acoustic variation in Barbary macaque (*Macaca sylvanus*) disturbance calls,'' Ethology **101**, 51–66.

Fischer, J., Hammerschmidt K., Cheney D. L., and Seyfarth R. M. (**2001a**). ''Acoustic structure of female chacma baboons,'' Ethology **107**, 33–54.

Fischer J., Metz M., Cheney D. L., and Seyfarth R. M. (**2001b**). ''Categorical responses of Chacma baboons to graded bark variants?'', Anim. Behav. **61**, 925–931.

Hammerschmidt, K. (**1990**). ''Individuelle Lautmuster bei Berberaffen (*Macaca sylvanus*): Ein Ansatz zum Verständnis ihrer vokalen Kommunikation,'' PhD Thesis, Freie Universität Berlin, Berlin.

Hammerschmidt, K., and Jürgens, U. (**2000**). ''Amplitude correlated changes in the vocalization of squirrel monkeys (*Saimiri sciureus*), '' Folia Primatol **71**, 195–196.

Hammerschmidt, K., and Mundry, R. (**2000**). ''Amplitude correlated changes in the vocalization of squirrel monkeys and humans,'' 17 ETHOLOGENTREFFEN, Utrecht.

Herzog, M., and Hopf, S. (**1983**). ''Effects of species-specific vocalisation in the behaviour of surrogate-reared squirrel monkeys,'' Behaviour **86**, 197–214.

Jürgens, U. (**1979**). ''Vocalization as an emotional indicator. A neuroethological study in the Squirrel monkey,'' Behaviour **69**, 88–117.

Kroodsma, D. (**1989**). ''Suggested experimental designs for song playbacks,'' Anim. Behav. **37**, 600–609.

Macedonia, J. M. (**1990**). ''What is communicated in the antipredator calls of lemurs: evidence from playback experiments with ringtailed and ruffed lemurs,'' Ethology **86**, 177–190.

Manser, M. B. (**2001**). ''The acoustic structure of alarm calls in suricates varies with predator type and level of response urgency,'' Proc. R. Soc. London, Ser. B **268**, 2315–2324.

Marler, P. (**1977**). ''Primate vocalizations: affective or symbolic?'' in *Progress in Ape Research*, edited by G. H. Bourne (Academic, New York), pp. 85–96.

Marler, P. (**1992**). ''Functions of arousal and emotion in primate communication: a semiotic approach,'' in *Topics in Primatology: Volume 1: Human Origins*, edited by T. Nishida, W. S. McGrew, P. Marler, M. Pichford, and J. M. Macedonia (Univ. of Tokyo, Tokyo), pp. 225–233.

Morton, E. S. (**1977**). ''On the occurrence and significance of motivation-structural rules in some bird and mammal sounds,'' Am. Nat. **111**, 855–869.

Owings, D. H., and Morton, E. S. (**1998**). *Animal Vocal Communication: A New Approach* (Cambridge U. P., Cambridge).

Owren, M. J., and Rendall, D. (**2001**). ''Sound on the rebound: Bringing form and function back to the forefront in understanding nonhuman primate vocal signaling,'' Evol. Anthr. **10**, 58–71.

Scheiner E., Hammerschmidt K., Jürgens U., and Zwirner P. (**2002**). ''Acoustic analysis of developmental changes and emotional expression in the preverbal vocalizations of infants'', J. Voice **16**, 509–529.

Schrader, L., and Todt, D. (**1993**). ''Contact call parameters covary with social context in common marmosets, *Callithrix j. jacchus*,'' Anim. Behav. **46**, 1026–1028.

Schrader, L., and Todt, D. (**1998**). ''Vocal quality is correlated with levels of stress hormones in domestic pigs,'' Ethology **104**, 859–876.

Seyfarth, R., Cheney, D. L., and Marler, P. (**1980**). ''Vervet monkey alarm calls: semantic communication in a free-ranging primate,'' Anim. Behav. **28**, 1070–1094.

Smith, W. J. (**1977**). *The Behavior of Communicating: An Ethological Approach* (Havard U. P., Cambridge, MA).

Taylor, A. A., and Weary, D. M. (**2000**). ''Vocal responses of piglets to castration: identifying procedural sources of pain,'' Appl. Anim. Behav. Sci. **70**, 17–26.

Weary, D. M., and Fraser, D. (**1995**). ''Calling by domestic piglets: reliable signals of need?'' Anim. Behav. **50**, 1047–1055.

Weary, D. M., and Kramer, D. L. (**1995**). ''Response of eastern chipmunks to conspecific alarm calls,'' Anim. Behav. **49**, 81–93.

Weary, D. M., Braithwaite, L. A., and Fraser, D. (**1998**). ''Vocal response to pain in piglets,'' Appl. Anim. Behav. Sci. **56**, 161–172.

Weary, D. M., Ross, S., and Fraser, D. (**1997**). ''Vocalizations by isolated piglets: a reliable indicator of piglet need directed towards the sow,'' Appl. Anim. Behav. Sci. **53**, 249–257.

Watts, J. M., and Stookey, J. M. (**1999**). ''Effects of restraint and branding on rates and acoustic parameters of vocalization in beef cattle,'' Appl. Anim. Behav. Sci. **62**, 125–135.

Wiley, R. H., and Richards, D. G. (**1978**). ''Physical constraints on acoustic communication in the atmosphere: implications for the evolution of animal vocalization,'' Behav. Ecol. Sociobiol. **3**, 69–94.

Winter, P., Ploog, D., and Latta, J. (**1966**). ''Vocal repertoire of the squirrel monkey, its analysis and significance,'' Exp. Brain Res. **1**, 359–384.

Zuberbühler, K. (**1999**). ''Conceptual semantics in a nonhuman primate,'' J. Comp. Psychol. **113**, 33–42.

Correlations between acoustic properties and bone density in bovine cancellous bone from 0.5 to 2 MHz

Kang Il Lee, Heui-Seol Roh, and Suk Wang Yoon
Acoustics Research Laboratory and BK21 Physics Research Division, Department of Physics, SungKyunKwan University, Suwon 440-746, Republic of Korea

(Received 16 August 2002; revised 23 December 2002; accepted 24 February 2003)

Correlations between acoustic properties and bone density were investigated in the 12 defatted bovine cancellous bone specimens *in vitro*. Speed of sound (SOS) and broadband ultrasonic attenuation (BUA) were measured in three different frequency bandwidths from 0.5 to 2 MHz using three matched pairs of transducers with the center frequencies of 1, 2.25, and 3.5 MHz. The relative orientation between ultrasonic beam and bone specimen was the mediolateral (ML) direction of the bovine tibia. SOS shows significant linear positive correlation with apparent density for all three pairs of transducers. However, BUA shows relatively weak correlation with apparent density. SOS and BUA are only weakly correlated with each other. The linear combination of SOS and BUA in a multiple regression model leads to a significant improvement in predicting apparent density. The correlations among SOS, BUA, and bone density can be effectively and clearly represented in the three-dimensional space by the multiple regression model. These results suggest that the frequency range up to 1.5 MHz and the multiple regression model in the three-dimensional space can be useful in the osteoporosis diagnosis. © *2003 Acoustical Society of America.* [DOI: 10.1121/1.1567733]

PACS numbers: 43.80.Qf [FD]

I. INTRODUCTION

Quantitative ultrasound (QUS) technique is now widely used for noninvasive assessment of osteoporosis.[1–7] Bone mineral density (BMD) is regarded as the most important parameter for the assessment of osteoporotic fracture risk. BMD can be measured at specific fracture-related skeletal sites by dual energy X-ray absorptiometry (DEXA). Ultrasound has been found to measure bone characteristics of calcaneus, tibia, and patella. This technique has some advantages over DEXA. It is less expensive, relatively simple, portable, and does not apply ionizing radiation. Moreover, ultrasonic parameters reflect bone structural characteristics as well as BMD. Most commercial devices report values for speed of sound (SOS), broadband ultrasonic attenuation (BUA), or their combination in the os calcis.[5] SOS is related in a predicted manner to elasticity and density of cancellous bone, whereas BUA is related to both density and structure.

In recent years, the relationships between ultrasonic parameters and bone density have been extensively studied *in vitro*. Many studies[8–10] report a strong correlation between BUA and apparent density in human cancellous bone. Serpe *et al.*[10] showed a strong correlation between apparent density and both SOS and BUA in low density cancellous bone from bovine tibiae. In denser bovine cancellous bone, however, the correlation is much weaker or even completely absent, and both positive and negative regression slopes have been reported.[6,9–12] These results suggest that the relationship between BUA and density over a large density range of cancellous bone is not linear.[9,10] Similar trends have been also reported in bone phantom materials, suggesting that this nonlinear behavior is a general feature of fluid-saturated porous media.[13] The nonlinearity for BUA in cancellous bone is not present in the relationship between SOS and bone density. Significant linear correlations have been reported between SOS and density.[8–10,14,15] The correlation is still significant for bovine samples over wide ranges of density.[12,16]

Most recent ultrasonic studies of cancellous bone have been conducted at frequencies below 1 MHz. Consequently, little is known about the ultrasonic properties of cancellous bone at higher frequencies comparable to those used for diagnostic imaging. The main objective of the present study is to investigate the correlations between acoustic properties and bone density over a broad frequency range up to 2 MHz. SOS and BUA of the 12 defatted bovine cancellous bone specimens were measured in the mediolateral (ML) direction over three different frequency bandwidths from 0.5 to 2 MHz using three matched pairs of transducers with the center frequencies of 1, 2.25, and 3.5 MHz.

II. MATERIALS AND METHODS

Twelve cancellous bone specimens were obtained from the proximal ends of one fresh frozen bovine tibia. Using a rotary electric saw the specimens were cut to make parallel and smooth surfaces without any soft tissue. The surfaces of each specimen were finished with fine silicon carbide abrasive paper. Care was taken to produce parallel surfaces. The resulting specimens had flat and parallel faces with thicknesses varying from 12 to 20 mm. The angle between opposing planar surfaces was confirmed to be confined within $\pm 0.5°$ by caliper measurements of thickness throughout each specimen. The cross-sectional areas of the specimens were greater than 30 mm$\times$30 mm, the dimensions of the smallest specimen. The specimens were all oriented in the same direction in relation to the bone. Their orientations were chosen so that the ultrasound could pass through the specimens along the ML direction of the tibia. They are the same orientations with those *in vivo* measurements commonly performed with commercial bone sonometers. The specimens

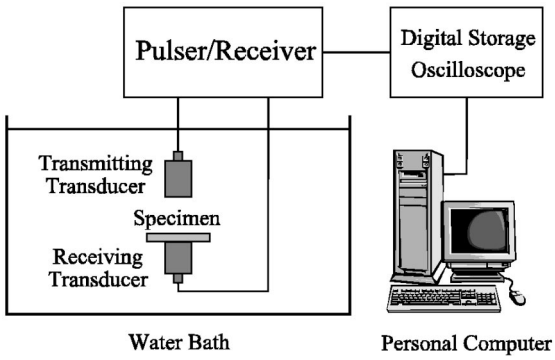

FIG. 1. Schematic diagram of the experimental setup for the ultrasonic measurements.

were defatted by boiling them for 1 h in water. Defatting process was assumed not to significantly affect their acoustic properties because the acoustic properties of defatted trabecular bone have showed just slightly different from those of bone with marrow left intact.[17] To remove air bubbles, they were degassed under vacuum. After removing air bubbles, the specimens were kept at room temperature prior to ultrasonic measurements.

Apparent density defined as the ratio of defatted bone mass to bulk volume of the specimen was assessed from separate measurements of mass and volume. Mass was measured with a balance. Volume was determined by measuring the volume difference with and without the specimen using a mass cylinder.

A schematic diagram of the experimental setup for the ultrasonic measurements is shown in Fig. 1. Ultrasonic measurements were performed in a water bath maintained at room temperature. The temperature was measured for each experiment and ranged between 16 °C and 19 °C. A 200 MHz computer controlled pulser/receiver (Panametrics 5900PR) was used. Three matched pairs of coaxially aligned transducers (Panametrics, 0.5 in. diameter) with the center frequencies of 1 MHz (V303), 2.25 MHz (V306), and 3.5 MHz (V382) were vertically oriented to make it possible to place the specimens directly on the face of the receiving transducer. The faces of the transducers were separated by 100 mm, a distance greater than the near-field distances stated by the manufacturer. For the pair of 1 MHz transducers, the near-field distance is given as 26.5 mm by the manufacturer. It is 60.3 mm for the pair of 2.25 MHz transducers and 93.9 mm for the pair of 3.5 MHz transducers. Received ultrasonic signals were acquired using a 500 MHz digital storage oscilloscope (LeCroy LT322) and stored on computer for off-line analysis. A through-transmission method was used to measure SOS and BUA. Using two opposing coaxially aligned transducers, transmitted signals were recorded both with and without the bone specimen in the acoustic path. The bone specimens were large enough to cover the receiving transducer face.

The estimation of SOS was carried out in the time domain, according to the straightforward principle of time of arrival of signal energy. The estimation of SOS can be also achieved in the frequency domain, through the use of phase unwrapping and linear models. However, since most commercial bone QUS devices have employed the pulse transit time method, we choose to use that method here as well. To measure SOS, arrival times of received broadband pulses were measured with and without the specimen in water path. SOS, c_s, can be estimated from

$$c_s = \frac{c_w}{1 - \frac{c_w \Delta t}{d}}, \tag{1}$$

where d is the thickness of the specimen and Δt is the difference in arrival times. The temperature-dependent speed of sound in distilled water, c_w, is given by[18]

$$c_w = 1402.9 + 4.835 \times T - 0.047\,016 \times T^2 + 0.000\,127\,25 \times T^3, \tag{2}$$

where T is the temperature in °C. Each arrival time was taken to the first zero crossing time. Five measurements were obtained from at five spatially independent sites on the specimen. The measurements were repeated for opposite direction in the same specimen. A total of ten measurements of two directions in each specimen were averaged to obtain a single value of SOS for each pair of transducers with the center frequencies of 1, 2.25, and 3.5 MHz.

BUA was analyzed using the same signals acquired for our SOS measurements. A fast Fourier transform (FFT) was used to obtain the power spectra of the transmitted signals with and without the specimen in water path. The signal loss as a function of frequency was obtained by subtracting the power spectrum obtained through the specimen from the nonattenuating reference power spectrum obtained through water. A linear fit was performed over the bandwidth of interest, and the slope of the fitted line was divided by the thickness of the specimen to obtain a value of BUA in units of dB/cm MHz. This parameter is often referred to as ''normalized broadband ultrasonic attenuation'' (nBUA). Clinical systems do not generally normalize attenuation to calcaneal thickness. Due to the anatomical variations in the bone size of human subjects, it is reasonable to normalize for bone thickness. The frequency bandwidth was selected to reduce the effect of noise at low signal levels particularly at the upper frequency limit, due to the high attenuation of the denser bone specimens. For the first pair of 1 MHz transducers, the usable frequency bandwidth was 0.5–1.0 MHz. It was 0.5–1.5 MHz for the second pair of 2.25 MHz transducers and 0.5–2.0 MHz for the third pair of 3.5 MHz transducers. These frequency bandwidths used in this study provided good signal to noise ratios.

To assess the signal-to-noise ratio of the measurement system, data from a bone specimen with an intermediate density of 0.71 g/cm^3 were analyzed according to the following procedure. Signal power spectrum was determined by centering a rectangular window on the signal of interest and performing an FFT to determine the signal power spectrum in decibels. The window was then repositioned on a portion of the acquired trace immediately preceding the arrival of the ultrasonic signal. An FFT was performed to determine the noise power spectrum in decibels. The signal to noise ratio was analyzed by subtracting the noise spectrum from the signal spectrum, and averaging the result over the frequency

TABLE I. Summary of an analysis that was performed to determine the signal-to-noise ratio of the measurement system for each pair of transducers with the center frequencies of 1, 2.25, and 3.5 MHz.

Signal type	Center frequency (bandwidth) [MHz]	Signal-to-noise ratio [dB]
Reference signal transmitted through water only	1 (0.5–1.0)	44.3±5.6
	2.25 (0.5–1.5)	25.9±7.9
	3.5 (0.5–2.0)	22.5±8.7
Specimen signal transmitted through a bone specimen	1 (0.5–1.0)	51.2±5.6
	2.25 (0.5–1.5)	29.5±6.3
	3.5 (0.5–2.0)	19.4±9.7

bandwidths that were used for the analysis of BUA for each pair of transducers with the center frequencies of 1, 2.25, and 3.5 MHz. Table I summarized the results of this analysis.

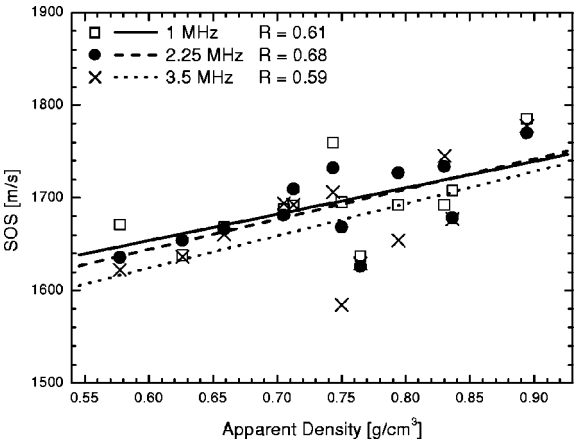

FIG. 2. Correlation between SOS and apparent density, and separate linear fit performed for each of three pairs of transducers.

III. RESULTS

Table II shows the mean value and the standard deviation (s.d.) of SOS, BUA, and correlation coefficient of the linear fit for the attenuation coefficient as a function of frequency in the 12 defatted bovine cancellous bone specimens for each pair of transducers with the center frequencies of 1, 2.25, and 3.5 MHz.

Figure 2 shows the correlation between SOS and apparent density. Separate linear fit was performed for each of three pairs of transducers. SOS shows significant linear positive correlations with apparent density for all three pairs of transducers of 1 MHz ($r=0.61$, $p<0.03$), 2.25 MHz ($r=0.68$, $p<0.01$), and 3.5 MHz ($r=0.59$, $p<0.04$), respectively. A p value is the probability that the correlation coefficient r is zero.

Figure 3 shows the correlation between BUA and apparent density. BUA shows moderate linear positive correlations with apparent density for the pairs of transducers of 1 MHz (bandwidth 0.5–1.0 MHz: $r=0.55$, $p<0.06$) and 2.25 MHz (bandwidth 0.5–1.5 MHz: $r=0.45$, $p<0.14$). However, in the measurement with the pair of 3.5 MHz transducers (bandwidth 0.5–2.0 MHz), BUA is independent of apparent density ($r=-0.03$, $p<0.93$).

Figure 4 shows the correlation between SOS and BUA. Separate linear fit was performed for each pair. SOS and BUA are only weakly correlated with each other (1 MHz: $r=0.33$, $p<0.28$; 2.25 MHz: $r=0.37$, $p<0.23$; 3.5 MHz: $r=0.21$, $p<0.50$).

The linear combination of SOS and BUA shows significant correlation with apparent density for all three pairs of transducers (1 MHz: $r=0.71$; 2.25 MHz: $r=0.71$; 3.5 MHz: $r=0.61$). The multiple regression model for the prediction of apparent density is based on the following regression equation:

$$\text{apparent density } [\text{g/cm}^3] = A + B_1 \times \text{SOS}[\text{m/s}] + B_2 \times \text{BUA } [\text{dB/cm MHz}], \tag{3}$$

where A is the intercept and B's are the regression coefficients to be chosen according to the principle of least squares, representing the independent contribution of each independent variable (SOS and BUA) to the prediction of the dependent variable (apparent density). The results of the multiple regression analysis are shown in Table III.

When there are two independent variables, the regression line cannot be visualized in the two-dimensional space but in the three-dimensional space. Figure 5 shows the multiple regression model of the linear combination of SOS and BUA in the three-dimensional space for the pair of 2.25 MHz transducers. Each projection of the multiple regression line on each two-dimensional plane is related to each two-dimensional correlation. Therefore, the correlations among SOS, BUA, and bone density can be effectively and clearly represented in the three-dimensional space by the multiple regression model.

The SOS measurements for three different transducer pairs are compared in Fig. 6. Separate linear fit was performed for each of three pairs of SOS measurements. SOS measured with the 2.25 MHz pair shows strong positive correlation with SOS measured with the 1 and 3.5 MHz pairs, respectively (2.25 MHz vs 1 MHz: $r=0.82$, $p<0.001$; 3.5 MHz vs 2.25 MHz: $r=0.82$, $p<0.001$). However, linear

TABLE II. Mean value and standard deviation (s.d.) of SOS, BUA, and correlation coefficient of the linear fit for the attenuation coefficient as a function of frequency in the 12 defatted bovine cancellous bone specimens for each pair of transducers with the center frequencies of 1, 2.25, and 3.5 MHz.

Center frequency	SOS [m/s]		BUA [dB/cmMHz]		Correlation coefficient	
	Mean±s.d.	Range	Mean±s.d.	Range	Mean±s.d.	Range
1 MHz	1694±43	1637–1786	26.0±3.8	19.7–32.7	1.00±0.01	0.98–1.00
2.25 MHz	1690±44	1626–1770	25.5±3.3	20.9–31.8	0.98±0.01	0.96–0.98
3.5 MHz	1673±54	1585–1778	19.6±3.5	14.9–24.1	0.94±0.02	0.91–0.97

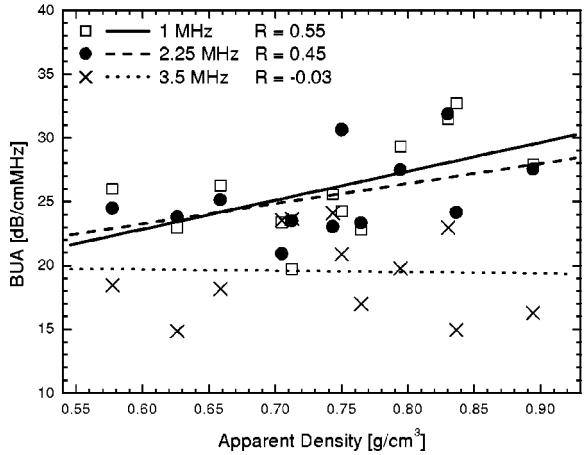

FIG. 3. Correlation between BUA and apparent density, and separate linear fit performed for each of three pairs of transducers.

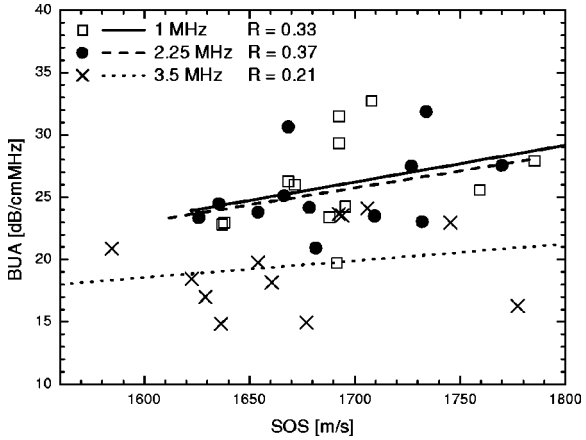

FIG. 4. Correlation between SOS and BUA, and separate linear fit performed for each of three pairs of transducers.

correlation between SOS measured with the 1 MHz pair and SOS measured with the 3.5 MHz pair is not relatively strong (3.5 MHz vs 1 MHz: $r=0.68$, $p<0.01$).

The BUA measurements for three different pairs of transducers are compared in Fig. 7. BUA measured with the 1 MHz pair shows a moderate correlation with BUA measured with the 2.25 MHz pair, but a weak negative correlation with BUA measured with the 3.5 MHz pair (2.25 MHz vs 1 MHz: $r=0.48$, $p<0.11$; 3.5 MHz vs 1 MHz: $r=-0.25$, $p<0.43$). However, BUA measured with the 2.25 MHz pair is independent of BUA measured with the 3.5 MHz pair (3.5 MHz vs 2.25 MHz: $r=0.05$, $p<0.88$).

IV. DISCUSSION

In the present study, the relative orientation between ultrasonic beam and bone specimen was the ML direction of the bovine tibia where the trabeculae are aligned in the perpendicular direction to propagation at normal incidence. Although the experiments were carefully performed, the separation of the fast and slow[19,20] waves was not observed from the signals transmitted through any bone specimens. The fast and slow waves were completely overlapped and observed as if a single wave propagated. Figure 8 shows a reference signal only through water and a typical transmitted signal through a bone specimen using the pair of 1 MHz transducers. The bone signal arrived earlier due to the faster speed of sound in bone than that in water. The center frequency downshift due to frequency-dependent attenuation was also evident.

In order to investigate the consequences of changing nominal ultrasonic transducer frequencies, the SOS measurements were performed using three matched pairs of transducers with the center frequencies of 1, 2.25, and 3.5 MHz in this study. SOS showed significant linear positive correlations with apparent density for all three pairs of transducers.

BUA has been measured in three different frequency bandwidths using three different pairs of transducers. As shown in Table II, BUA measured in the higher frequency range (0.5–2.0 MHz) is lower than those measured in the lower frequency ranges (0.5–1.0 and 0.5–1.5 MHz). This could be due in part to nonlinear frequency dependence of attenuation at high frequencies. Figure 9 shows the attenuation coefficients obtained with three matched pairs of transducers for a typical specimen, and linear fits for the attenuation coefficient as a function of frequency over three different frequency bandwidths. In Fig. 9 and Table II, it can be seen that the higher correlation values are associated with the lower frequency ranges and higher BUA values. This supports that the high frequency data are influenced by the system noise due to the poor signal to noise ratio at high frequency performance of transducer pairs. Since the BUA itself is a calculated value based on the difference of two measured data sets, it would be expected that, if the difference is small, then the relative contribution from the system noise will be more significant. This would increase the uncertainty and poor reproducibility of each individual data point.

It was observed that there was no correlation between apparent density and BUA in the higher frequency range up to 2 MHz when the pair of 3.5 MHz transducers was used. The role of scattering and absorption in the attenuation of the ultrasound signal provides qualitative explanation for the nonlinear relationship of BUA with density. Han *et al.*[5] and

TABLE III. Regression coefficient, standard error (SE), and correlation coefficient of the linear combination of SOS and BUA with apparent density for each pair of transducers with the center frequencies of 1, 2.25, and 3.5 MHz.

Center frequency	A	B_1	B_2	Correlation coefficient
1 MHz	$-1.228\,30\pm0.860\,67$	$0.001\,02\pm0.000\,53$	$0.009\,39\pm0.006\,02$	0.71
2.25 MHz	$-1.509\,13\pm0.840\,55$	$0.001\,23\pm0.000\,53$	$0.006\,41\pm0.007\,14$	0.71
3.5 MHz	$-0.945\,02\pm0.751\,20$	$0.001\,06\pm0.000\,46$	$-0.004\,21\pm0.007\,21$	0.61

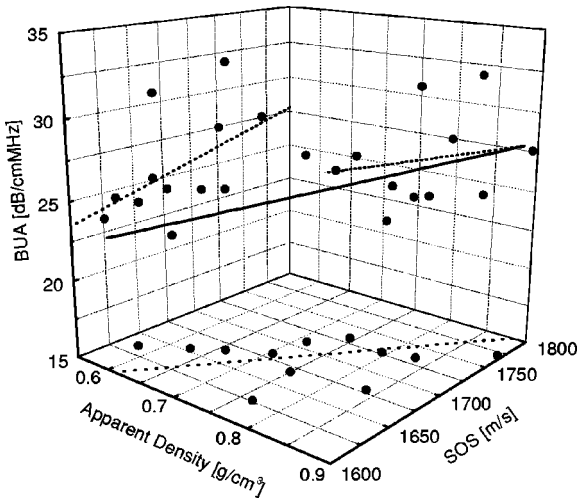

FIG. 5. Multiple regression model of the linear combination of SOS and BUA in the three-dimensional space for the pair of 2.25 MHz transducers.

Serpe *et al.*[10] suggested that attenuation in low density cancellous bone and in cortical bone may be primarily due to absorption. In dense cancellous bone, however, the predominant effect may be scattering due to significant interaction of the sound with the cancellous structure. The frequency dependence of attenuation has been studied in bovine cancellous bone by Hoffmeister *et al.*[21] An abrupt breakpoint in the slope of attenuation near 1 MHz was observed in the approximately half of the samples. To explain this behavior, they assumed that scattering is an important mechanism of attenuation in high density cancellous bone. It was also assumed that the density dependence of backscatter is not linear over a wide range of densities and the frequency dependence of backscatter can change considerably over a sufficiently broad frequency range. Based on this consideration, we propose that the nonlinearity of BUA with bone density in high density cancellous bone increases as the frequency increases. This is consistent with the observations of the present study, because the lower correlation values were associated with the higher frequency ranges as shown in Fig. 3.

A linear combination of SOS and BUA, known as ''stiffness,'' is currently used in commercial ultrasound bone

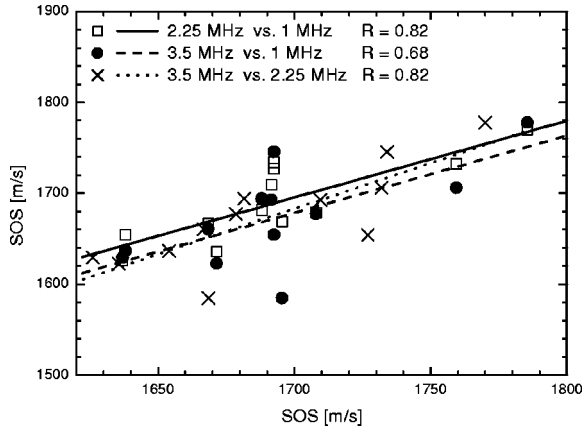

FIG. 6. Correlation among SOS measurements, and separate linear fit performed for each of three pairs of SOS measurements.

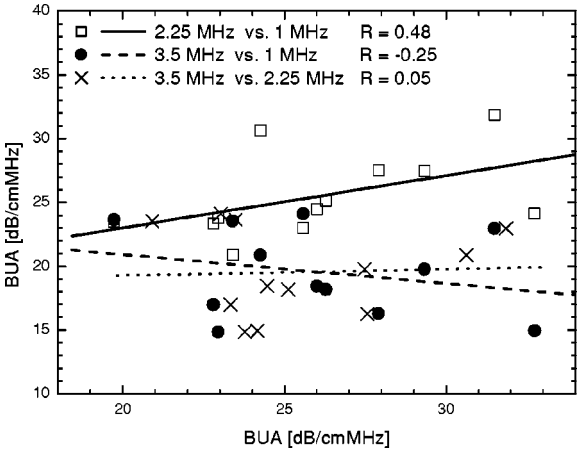

FIG. 7. Correlation among BUA measurements, and separate linear fit performed for each of three pairs of BUA measurements.

sonometer (Achilles+, Lunar Co). Lees *et al.*[22] showed that stiffness measured at the calcaneus was correlated better than SOS or BUA with the BMD of the femoral neck. Grimm *et al.*[23] demonstrated that a combination of SOS and BUA improved the predictability of Young's modulus. In the present study, the linear combination of SOS and BUA in a multiple regression model was more predictive for apparent density than SOS or BUA alone. Although the correlation of BUA with apparent density was so weak in the higher frequency range of 0.5–2.0 MHz, the linear combination of SOS and BUA led to a significant improvement in predicting apparent density.

Future studies will be required to address some of the limitations of the present study. The one limitation of this study is the small number of specimens. In order to duplicate the orientation of the trabeculae as closely as possible, we used only one bovine tibia. Twelve specimens were obtained from the proximal ends of one bovine tibia so that all specimens could be oriented in the same direction in relation to the bone (ML direction). The most significant limitation involves the fact that all measurements were performed *in vitro* using the specimens of bovine cancellous bone with relatively high bone mineral density. The higher density of bo-

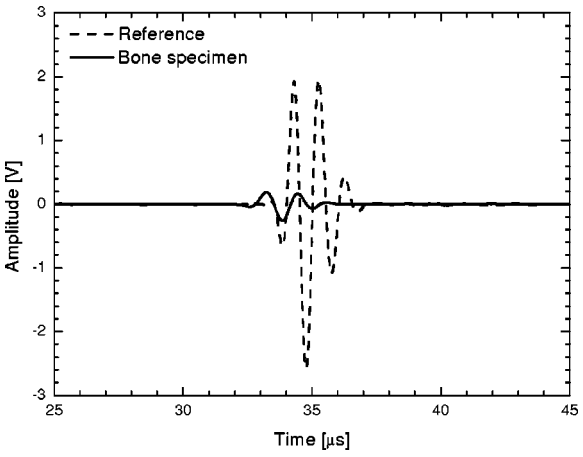

FIG. 8. Reference signal only through water and a typical transmitted signal through a bone specimen using the pair of transducers with the center frequency of 1 MHz.

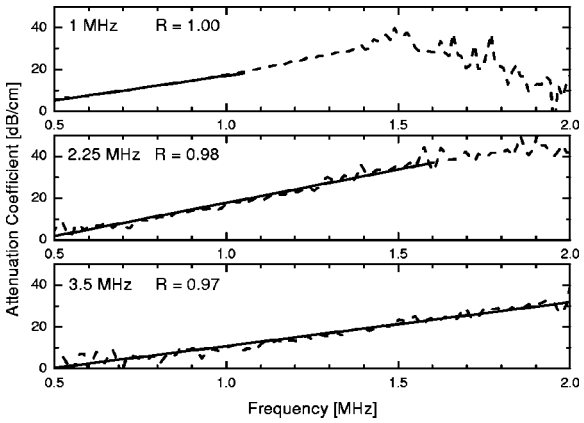

FIG. 9. Attenuation coefficient for a typical specimen, and separate linear fit performed for the attenuation coefficient as a function of frequency over three different frequency bandwidths from different transducer pairs.

vine cancellous bone may cause ultrasonic absorption and scattering in a fundamentally different manner compared with the lower density of human cancellous bone. Repeating this study on specimens of human cancellous bone would be valuable using a similar *in vitro* procedure.

V. CONCLUSIONS

Correlations of SOS, BUA, and their linear combination with bone density were investigated in bovine cancellous bone. Three matched pairs of transducers with the center frequencies of 1, 2.25, and 3.5 MHz were used in order to cover a broad frequency range up to 2 MHz. SOS shows significant linear positive correlation with apparent density for all three frequency ranges. BUA shows moderate linear positive correlations with apparent density for the lower frequency ranges (0.5–1.0 and 0.5–1.5 MHz) and no correlation for the higher frequency range (0.5–2.0 MHz). Based on these results, we propose that the nonlinearity of BUA with bone density in high density cancellous bone increases as the frequency increases. The correlation between BUA and apparent density is relatively weakened for high density bovine cancellous bone. It is clear that for the range of bone densities studied, SOS is a more consistent and accurate predictor of apparent density than BUA. The linear combination of SOS and BUA in a multiple regression model leads to a significant improvement in predicting apparent density. The correlations among SOS, BUA, and bone density can be effectively and clearly represented in the three-dimensional space by the multiple regression model. These results suggest that the frequency range up to 1.5 MHz and the multiple regression model in the three-dimensional space can be useful in the osteoporosis diagnosis.

ACKNOWLEDGMENTS

This work was supported by Korea Research Foundation Grant (KRF-2000-015-DP0178), Korea Science and Engineering Foundation Grant (2000-1-11100-002-2), and the BK21 Program of the Ministry of Education.

[1] M. Raggozino, "Analysis of the error in measurement of ultrasound speed of sound in tissues due to waveform deformation by frequency-dependent attenuation," Ultrasonics **19**, 73–89 (1981).
[2] C. M. Langton, S. B. Palmer, and R. W. Porter, "The measurement of broadband ultrasonic attenuation in cancellous bone," Eng. Med. **13**, 89–91 (1984).
[3] R. Strelitzki, A. J. Clarke, and J. A. Evans, "The measurement of the velocity of ultrasound using broadband pulses and single-frequency tone-bursts," Phys. Med. Biol. **41**, 743–753 (1996).
[4] R. Strelitzki and J. A. Evans, "An investigation of the measurement of broadband ultrasonic attenuation in trabecular bone," Ultrasonics **34**, 785–791 (1996).
[5] S. Han, J. Medige, and I. Ziv, "Combined models of ultrasound velocity and attenuation for predicting trabecular bone strength and mineral density," Clin. Biomech. (Los Angel. Calif.) **11**, 348–353 (1996).
[6] J. Toyras, H. Kroger, and J. S. Jurvelin, "Bone properties as estimated by mineral density, ultrasound attenuation, and velocity," Bone **25**, 725–731 (1999).
[7] C. F. Njeh, D. Hans, T. Fuerst, C. C. Gluer, and H. K. Genant, *Quantitative Ultrasound: Assessment of Osteoporosis and Bone Status* (Martin Dunitz, London, 1999).
[8] P. H. F. Nicholson, M. J. Haddaway, and M. W. J. Davie, "The dependence of ultrasonic properties on orientation in human vertebral bone," Phys. Med. Biol. **39**, 1013–1024 (1994).
[9] S. Han, J. Y. Rho, and I. Ziv, "Ultrasound velocity and broadband attenuation over a wide range of bone mineral density," Osteoporosis Int. **6**, 291–296 (1996).
[10] L. Serpe and J. Y. Rho, "The nonlinear transition period of broadband ultrasound attenuation as bone density varies," J. Biomech. **29**, 963–966 (1996).
[11] J. A. Evans and M. B. Tavakoli, "Ultrasonic attenuation and velocity in bone," Phys. Med. Biol. **35**, 1387–1396 (1990).
[12] J. M. Alves, W. Xu, D. Lin, R. S. Stiffert, J. T. Ryaby, and J. J. Kaufman, "Ultrasonic assessment of human and bovine trabecular bone: A comparison study," IEEE Trans. Biomed. Eng. **43**, 249–258 (1996).
[13] R. Strelitzki, J. A. Evans, and A. J. Clarke, "The influence of porosity and pore size on the ultrasonic properties of bone investigated using a phantom material," Osteoporosis Int. **7**, 370–375 (1997).
[14] C. F. Njeh, C. W. Kuo, C. M. Langton, H. I. Atrah, and C. M. Boivin, "Prediction of human femoral bone strength using ultrasound velocity and BMD: An *in vitro* study," Osteoporosis Int. **7**, 471–477 (1997).
[15] P. Laugier, P. Droin, A. M. Laval-Jeantet, and G. Berger, "*In vitro* assessment of the relationship between acoustic properties and bone mass density of the calcaneus by comparison of ultrasound parametric imaging and quantitative computed tomography," Bone **20**, 157–165 (1997).
[16] C. F. Njeh, R. Hodgskinson, J. D. Currey, and C. M. Langton, "Orthogonal relationships between ultrasonic velocity and material properties of bovine cancellous bone," Med. Eng. Phys. **18**, 373–381 (1996).
[17] K. A. Wear, "Ultrasonic attenuation in human calcaneus from 0.2 to 1.7 MHz," IEEE Trans. Ultrason. Ferroelectr. Freq. Control **48**, 602–608 (2001).
[18] G. W. C. Kaye and T. H. Laby, *Table of Physical and Chemical Constants* (Longman, London, 1973).
[19] M. A. Biot, "Theory of propagation of elastic waves in a fluid-saturated solid. II. Higher frequency range," J. Acoust. Soc. Am. **28**, 179–191 (1956).
[20] A. Hosokawa and T. Otani, "Ultrasonic wave propagation in bovine cancellous bone," J. Acoust. Soc. Am. **101**, 558–562 (1997).
[21] B. K. Hoffmeister, S. A. Whitten, and J. Y. Rho, "Low-megahertz ultrasonic properties of Bovine cancellous bone," Bone **26**, 635–642 (2000).
[22] B. Lees and J. Stevenson, "Preliminary evaluation of a new ultrasound bone densitometers," Calcif. Tissue Int. **53**, 149–152 (1993).
[23] M. Grimm and J. Williams, "Prediction of Young's modulus in trabecular bone with a combination of ultrasound velocity and attenuation measurements," ASME Bioengineering Conference **24**, 608–609 (1993).

Erratum: "A perturbation method for the modes of cylindrical acoustic waveguides in the presence of temperature gradients" [J. Acoust. Soc. Am. 102, 160–163 (1997)]

Brian J. McCartin
Applied Mathematics, Kettering University, 1700 West Third Avenue, Flint, Michigan 48504-4898

(Received 27 January 2003; accepted for publication 10 February 2003)

This note concerns itself with the correction of an algebraic mistake as well as its consequences for the results and conclusions of J. Acoust. Soc. Am. **102**(1), 160–163 (1997). An addendum is attached which outlines the modifications necessary for the correct treatment of degenerate modes.
 [DOI: 10.1121/1.1564607]

PACS numbers: 43.20.Mv, 43.10.Vx

I. INTRODUCTION

A mathematical model for cylindrical acoustic waveguides in the presence of temperature gradients induced by an applied temperature distribution along the duct walls was presented in Ref. 1. The Rayleigh-Schrödinger perturbation procedure[2] was then applied to this model to study the effect of mild temperature variations on the spectrum and modes of the waveguide. Unfortunately, an algebraic error crept into that computation thus requiring modifications to the equations and resulting conclusions of that paper. This note comprises such correction and includes an addendum addressing the issue of degenerate modes.

II. CORRECTION

The difficulties commence with Eq. (9) which should read

$$\frac{1}{\hat{\rho}}=\frac{1}{\hat{\rho}_0}[1+\epsilon f-\epsilon^2 A_2-\epsilon^3(A_2 f+A_3)+\cdots], \tag{1}$$

and continue with Eq. (12) which should read

$$\begin{aligned}&\Delta p+\epsilon[\nabla\cdot(f\nabla p)-k_0^2 fp]-\epsilon^2[\alpha_2\Delta p+(\nabla f\cdot\nabla f)p]\\&\quad+\epsilon^3[\alpha_3\Delta p+\alpha_2 f k_0^2 p-\alpha_2\nabla\cdot(f\nabla p)+(f\nabla f\cdot\nabla f)p]+\cdots\\&\quad=\lambda p[1+\epsilon f-\epsilon^2\alpha_2+\epsilon^3(-\alpha_2 f+\alpha_3)\cdots].\end{aligned} \tag{2}$$

Thus, upon discretization, the matrix generalized eigenvalue problem, Eq. (13), should instead read

$$\begin{aligned}&[A+\epsilon(C-k_0^2 D_0)-\epsilon^2(\alpha_2 A-D_1)\\&\quad+\epsilon^3(\alpha_3 A+\alpha_2 k_0^2 D_0-\alpha_2 C+D_2)+\cdots]p\\&\quad=\lambda[B+\epsilon D_0-\epsilon^2\alpha_2 B+\epsilon^3(-\alpha_2 D_0+\alpha_3 B)+\cdots]p,\end{aligned} \tag{3}$$

where A is symmetric and nonpositive-definite, C is symmetric, B is positive and diagonal, and D_0, D_1, and D_2 are diagonal.

Upon the application of the Rayleigh-Schrödinger perturbation procedure,

$$\lambda(\epsilon)=\sum_{n=0}^{\infty}\epsilon^n\lambda_n;\quad p(\epsilon)=\sum_{n=0}^{\infty}\epsilon^n p_n, \tag{4}$$

and under the assumption that λ_0 is a simple eigenvalue with corresponding eigenvector p_0 for the unperturbed problem

$$Ap_0=\lambda_0 Bp_0, \tag{5}$$

Eqs. (16)–(19) should now read

$$(A-\lambda_0 B)p_0=0, \tag{6}$$

$$(A-\lambda_0 B)p_1=\lambda_1 Bp_0-Cp_0+\beta^2 D_0 p_0, \tag{7}$$

$$\begin{aligned}(A-\lambda_0 B)p_2&=\lambda_2 Bp_0+\lambda_1 Bp_1-Cp_1-D_1 p_0\\&\quad+\beta^2 D_0 p_1,\end{aligned} \tag{8}$$

$$\begin{aligned}(A-\lambda_0 B)p_3&=\lambda_3 Bp_0+\lambda_2 Bp_1+\lambda_1 Bp_2-Cp_2\\&\quad+(\alpha_2 A-D_1-\alpha_2\lambda_0 B)p_1\\&\quad+(\alpha_2 C-D_2-\alpha_2\lambda_1 B)p_0\\&\quad+\beta^2(D_0 p_2-\alpha_2 D_0 p_0).\end{aligned} \tag{9}$$

With the normalization $\langle p_0,Bp_0\rangle=1$, we still have $\lambda_0=\langle p_0,Ap_0\rangle$. However, Eq. (20) should now read

$$\lambda_1=\hat{\lambda}_1-\beta^2\langle p_0,D_0 p_0\rangle;\quad \hat{\lambda}_1=\langle p_0,Cp_0\rangle. \tag{10}$$

We next employ the pseudoinverse to solve Eq. (7) above for p_1

$$\begin{aligned}&\hat{p}_1=-(A-\lambda_0 B)^{\dagger}(C-\beta^2 D_0-\lambda_1 B)p_0;\\&p_1=-\langle\hat{p}_1,Bp_0\rangle p_0+\hat{p}_1,\end{aligned} \tag{11}$$

thus ensuring that $\langle p_1,Bp_0\rangle=0$ for later convenience.

With p_1 so computed, Eqs. (21)–(23) should now read

$$\begin{aligned}&\lambda_2=\hat{\lambda}_2-\beta^2\langle p_0,D_0 p_1\rangle;\\&\lambda_3=\hat{\lambda}_3-\beta^2(\langle p_1,D_0 p_1\rangle-\alpha_2\langle p_0,D_0 p_0\rangle),\end{aligned} \tag{12}$$

$$\hat{\lambda}_2=\langle p_0,Cp_1+D_1 p_0\rangle, \tag{13}$$

TABLE I. Computed modal eigenvalue corrections ($\beta=0$).

Mode	λ_0	$\hat{\lambda}_1$	$\hat{\lambda}_2$	$\hat{\lambda}_3$
(0,0)	0	0	−0.1317	0.0368
(1,0)	−0.0987	−0.0165	−0.1140	0.0302
(1,1)	−0.4935	0.0552	−0.1145	0.0028
"(0,1)"	−0.3948	0.0126	−0.1110	0.0710
"(2,0)"	−0.3948	−0.0150	−0.0619	0.0853

$$\hat{\lambda}_3=\langle p_1,(C-\lambda_1 B)p_1\rangle+\langle p_0,(2D_1-\alpha_2 A)p_1 + [D_2-\alpha_2(C-\lambda_1 B)]p_0\rangle. \quad (14)$$

Note that the computation of only a single pseudoinverse suffices to produce *all* of the modal corrections, p_n.

III. CONSEQUENCES

Consequently, modifications are also required to the results and conclusions of Ref. 1.

- It is only the third term of Eq. (5) of Ref. 1 which makes no $O(\epsilon)$ contribution to Eq. (2) above and is thus of "higher order" than the first and second terms.
- For degenerate modes, expansion in terms of fractional powers of ϵ (Puiseux series) is necessary only in the event of eigenvector deficiency.
- The first-order correction, λ_1, *is* frequency dependent. Thus the expressions for λ_1 and p_1 of Ref. 1 are correct only at cut-off ($\beta=0$).
- Figures 3, 4, and 5 of Ref. 1 should have displayed the (1,0) mode rather than the (0,1) mode as this latter mode is degenerate with the (2,0) mode of the numerical example of Ref. 1. (See Addendum.)
- The cut-off frequencies are given by $\omega_c^2/c_0^2=-\lambda$ where λ is calculated for $\beta=0$, so that Eq. (26) of Ref. 1 is only accurate to first-order. Hence, Fig. 6 of Ref. 1 is only accurate for correspondingly small ϵ.

Table I displays the corresponding computed eigenvalue corrections at cut-off for the five lowest order modes ($\alpha_2=-0.2108$, $\alpha_3=-0.0882$).

Equations (12)–(14) are then used to determine $\lambda_2^{(i)}$, $\lambda_3^{(i)}$ ($i=1,2$) with λ_1, p_0, p_1 replaced by $\lambda_1^{(i)}$, $p_0^{(i)}$, $p_1^{(i)}$, respectively.

V. CONCLUDING REMARK

For higher order degeneracy and/or degeneracy that is not fully resolved at first-order, similar but more complicated modifications are necessary.[2]

IV. ADDENDUM

When a mode is degenerate, the Rayleigh-Schrödinger procedure must be modified accordingly.[2] We illustrate this modification for the case of a double eigenvalue with degeneracy resolved at first-order. This occurs, for example, for the (0,1) and (2,0) modes of the rectangular waveguide of Ref. 1 which accounts for the "·" of Table I.

In this case, we seek Rayleigh-Schrödinger expansions in the form

$$\lambda^{(i)}(\epsilon)=\lambda_0+\sum_{n=1}^{\infty}\epsilon^n\lambda_n^{(i)};\quad p^{(i)}(\epsilon)=\sum_{n=0}^{\infty}\epsilon^n p_n^{(i)}\quad (i=1,2). \quad (15)$$

Let $\{q_0^{(1)},q_0^{(2)}\}$ be a B-orthonormal basis for the solution space of Eq. (6) above. What is required is the determination of an appropriate linear combination of these generalized eigenvectors so that Eq. (7) above will then be solvable.

Specifically, we seek a B-orthonormal pair of generalized eigenvectors

$$p_0^{(i)}=a_1^{(i)}q_0^{(1)}+a_2^{(i)}q_0^{(2)}\quad (i=1,2). \quad (16)$$

This requires that $[a_1^{(i)},a_2^{(i)}]^T$ be orthonormal eigenvectors, with corresponding eigenvalues $\lambda_1^{(i)}$, of the 2×2-matrix M with components

$$M_{i,j}=\langle q_0^{(i)},(C-\beta^2 D_0)q_0^{(j)}\rangle. \quad (17)$$

Consequently, $\lambda_1^{(i)}$ ($i=1,2$) are then given by Eq. (10) above with p_0 replaced by $p_0^{(i)}$. For convenience, all subsequent $p_n^{(i)}$ ($n=1,2,\ldots$) are chosen to be B-orthogonal to $p_0^{(i)}$ ($i=1,2$).

Likewise, $p_1^{(i)}$ ($i=1,2$) must be chosen so that Eq. (8) above is then solvable. This is achieved by first solving Eq. (7) above as

$$\hat{p}_1^{(i)}=-(A-\lambda_0 B)^{\dagger}(C-\beta^2 D_0-\lambda_1^{(i)}B)p_0^{(i)}\quad (i=1,2), \quad (18)$$

and then defining

$$p_1^{(i)}=k_1^{(i)}p_0^{(1)}+k_2^{(i)}p_0^{(2)}+\hat{p}_1^{(i)}\quad (i=1,2);\qquad k_i^{(i)}=-\langle\hat{p}_1^{(i)},Bp_0^{(i)}\rangle, \quad (19)$$

$$k_j^{(i)}=\frac{\langle\hat{p}_1^{(i)},(C-\beta^2 D_0-\lambda_1^{(i)}B)p_0^{(j)}\rangle-\langle\hat{p}_1^{(i)},Bp_0^{(i)}\rangle\langle p_0^{(i)},(C-\beta^2 D_0)p_0^{(j)}\rangle+\langle p_0^{(j)},D_1 p_0^{(i)}\rangle}{\lambda_1^{(i)}-\lambda_1^{(j)}}\quad (j\neq i). \quad (20)$$

[1] B. J. McCartin, "A perturbation method for the modes of cylindrical acoustic waveguides in the presence of temperature gradients," J. Acoust. Soc. Am. **102**(1), 160–163 (1997).

[2] F. W. Byron, Jr. and R. W. Fuller, *Mathematics of Classical and Quantum Physics* (Dover, New York, 1992).